

SPACE SCIENCES SERIES OF ISSI

Planetary Atmospheric Electricity

F. Leblanc, K.L. Aplin, Y. Yair,
R.G. Harrison, J.P. Lebreton,
M. Blanc (Eds.)



 Springer

 Europlanet
European Planetary Network

 INTERNATIONAL
SPACE
SCIENCE
INSTITUTE

F. Leblanc • K.L. Aplin • Y. Yair • R.G. Harrison •
J.P. Lebreton • M. Blanc
Editors

Planetary Atmospheric Electricity

Previously published in *Space Science Reviews* Volume 137,
Issues 1–4, 2008



Springer

F. Leblanc
Service d'Aeronomie du CNRS/IPSL
Université Versailles Saint Quentin
Verrières Le Buisson, France

K.L. Aplin
Space Science and Technology Department
Rutherford Appleton Laboratory
Oxon, UK

Y. Yair
Department of Life and Natural Sciences
Open University of Israel
Ra'anana, Israel

R.G. Harrison
Department of Meteorology, University of Reading
Reading, UK

J.P. Lebreton
Space Science Department of ESA
Noordwijk, The Netherlands

M. Blanc
CESR. Université Paul Sabatier
Toulouse, France

Cover illustration: The image shows Chaiten Volcano. Image #: 5036478

© UPI photo / Landov Media

All rights reserved.

Library of Congress Control Number: 2008936088

ISBN-978-0-387-87663-4

e-ISBN-978-0-387-87664-1

Printed on acid-free paper.

© 2008 Springer Science+Business Media, BV

No part of this work may be reproduced, stored in a retrieval system, or transmitted in any form or by any means, electronic, mechanical, photocopying, microfilming, recording or otherwise, without the written permission from the Publisher, with the exception of any material supplied specifically for the purpose of being entered and executed on a computer system, for the exclusive use by the purchaser of the work.

Contents

FOREWORD

Foreword

R.-M. Bonnet · M. Blanc **1**

PREFACE

Planetary Atmospheric Electricity

R.G. Harrison · K.L. Aplin · F. Leblanc · Y. Yair **5**

INTRODUCTORY OVERVIEWS

Investigating Earth's Atmospheric Electricity: a Role Model for Planetary Studies

K.L. Aplin · R.G. Harrison · M.J. Rycroft **11**

Updated Review of Planetary Atmospheric Electricity

Y. Yair · G. Fischer · F. Simões · N. Renno · P. Zarka **29**

Physical Processes Related to Discharges in Planetary Atmospheres

R. Roussel-Dupré · J.J. Colman · E. Symbalisty · D. Sentman · V.P. Pasko **51**

An Overview of Earth's Global Electric Circuit and Atmospheric Conductivity

M.J. Rycroft · R.G. Harrison · K.A. Nicoll · E.A. Mareev **83**

Ions in the Terrestrial Atmosphere and Other Solar System Atmospheres

R.G. Harrison · H. Tammet **107**

Charge Generation and Separation Processes

Y. Yair **119**

Physics of Electric Discharges in Atmospheric Gases: An Informal Introduction

R.A. Treumann · Z. Kłos · M. Parrot **133**

IONISATION PROCESSES IN PLANETARY ATMOSPHERES

Cosmic Ray Induced Ion Production in the Atmosphere

G.A. Bazilevskaya · I.G. Usoskin · E.O. Flückiger · R.G. Harrison · L. Desorgher · R. Bütkofer · M.B. Krainev · V.S. Makhmutov · Y.I. Stozhkov · A.K. Svirezhevskaya · N.S. Svirezhevsky · G.A. Kovaltsov **149**

Meteoric Layers in Planetary Atmospheres

J.G. Molina-Cuberos · J.J. López-Moreno · F. Arnold **175**

Profiles of Ion and Aerosol Interactions in Planetary Atmospheres
S.N. Tripathi · M. Michael · R.G. Harrison **193**

Composition and Measurement of Charged Atmospheric Clusters
K.L. Aplin **213**

Atmospheric Ions and Aerosol Formation
F. Arnold **225**

Tropospheric New Particle Formation and the Role of Ions
J. Kazil · R.G. Harrison · E.R. Lovejoy **241**

MEASUREMENTS EFFECTS AND HAZARDS OF THUNDERSTORMS AND LIGHTNING

Ground-Based and Space-Based Radio Observations of Planetary Lightning
P. Zarka · W. Farrell · G. Fischer · A. Konovalenko **257**

Atmospheric Electricity at Saturn
G. Fischer · D.A. Gurnett · W.S. Kurth · F. Akalin · P. Zarka · U.A. Dyudina ·
W.M. Farrell · M.L. Kaiser **271**

Atmospheric Electricity Hazards
R.D. Lorenz **287**

Electrical Effects on Atmospheric Chemistry
R.D. Lorenz **295**

NEW MISSIONS

TARANIS—A Satellite Project Dedicated to the Physics of TLEs and TGFs
F. Lefeuvre · E. Blanc · J.-L. Pinçon · R. Roussel-Dupré · D. Lawrence · J.-A. Sauvaud ·
J.-L. Rauch · H. de Feraudy · D. Lagoutte **301**

Lightning Detection by LAC Onboard the Japanese Venus Climate Orbiter, Planet-C
Y. Takahashi · J. Yoshida · Y. Yair · T. Imamura · M. Nakamura **317**

CHARGE GENERATION AND SEPARATION

Charge Separation Mechanisms in Clouds
C. Saunders **335**

Charge Structure and Dynamics in Thunderstorms
M. Stolzenburg · T.C. Marshall **355**

Formation of Charge Layers in the Planetary Atmospheres
E.A. Mareev **373**

Electrical Charging of Volcanic Plumes
M.R. James · L. Wilson · S.J. Lane · J.S. Gilbert · T.A. Mather · R.G. Harrison ·
R.S. Martin **399**

Electrical Activity and Dust Lifting on Earth, Mars, and Beyond
N.O. Renno · J.F. Kok **419**

The Charging of Planetary Rings
A.L. Graps · G.H. Jones · A. Juhász · M. Horányi · O. Havnes **435**

ELECTROMAGNETIC SIGNATURES OF DISCHARGES IN THE ATMOSPHERE

**Schumann Resonances as a Means of Investigating the Electromagnetic Environment
in the Solar System**

F. Simões · M. Rycroft · N. Renno · Y. Yair · K.L. Aplin · Y. Takahashi **455**

Blue Jets: Upward Lightning

E.V. Mishin · G.M. Milikh **473**

VLF Studies During TLE Occurrences in Europe: A Summary of New Findings

Á. Mika · C. Haldoupis **489**

DEMETER Observations of EM Emissions Related to Thunderstorms

M. Parrot · J.J. Berthelier · J.P. Lebreton · R. Treumann · J.L. Rauch **511**

On ULF Signatures of Lightning Discharges

T. Bösinger · S.L. Shalimov **521**

Foreword

Roger-Maurice Bonnet · Michel Blanc

Originally published in the journal Space Science Reviews, Volume 137, Nos 1–4.
DOI: [10.1007/s11214-008-9418-0](https://doi.org/10.1007/s11214-008-9418-0) © Springer Science+Business Media B.V. 2008

“Planetary Atmospheric Electricity” is the first publication of its kind in the Space Science Series of ISSI. It is the result of a new and successful joint venture between ISSI and Europlanet.

Europlanet is a network of over 110 European and U.S. laboratories deeply involved in the development of planetary sciences and support to the European planetary space exploration programme. In 2004, the Europlanet consortium obtained support from the European Commission to strengthen the planetary science community worldwide, and to amplify the scientific output, impact and visibility of the European space programme, essentially the European Space Agency’s Horizon 2000, Cosmic Vision programmes and their successors. Its present contract with the Commission extends from 2005 to 2008, and includes 7 networking activities, including discipline-based working groups covering the main areas of planetary sciences. A new contract with the Commission, presently under negotiation, will extend Europlanet’s activities into the period 2009–2012. With the broad community connection made through its Discipline Working Groups and other activities, Europlanet offers an ideal base from which to identify new fields of research for planetary sciences and to stimulate collaborative work among its member laboratories. For Europlanet, developing collaboration with ISSI in holding workshops and producing books on these new and emerging subjects is both natural and extremely stimulating, considering the high profile, international standing and proven success of ISSI. For ISSI, collaboration with Europlanet offers a very interesting opportunity to extend its successful series of workshops and books within the area of planetary sciences and to deepen its links with this community.

Working from this clear convergence of interests, in 2006 ISSI and Europlanet initiated implementation of a series of joint workshops, soon after the establishment of Europlanet’s

R.-M. Bonnet (✉)
International Space Science Institute (ISSI), Bern, Switzerland
e-mail: rmbonnet@issibern.ch

M. Blanc
Centre Etude Spatiale des Rayonnements (CESR), Toulouse, France

Discipline Working Groups. Each of Europlanet's nine Discipline Working Groups were invited to select one or two promising subjects for ISSI workshops, which were presented and discussed at a working group meeting at ESAC, Villafranca, Spain, April 24th–26th. The Board of Coordinators of Europlanet then selected a shortlist. Finally, on May 18th, 2006, the Science Committee of ISSI, chaired by Prof. Len Culhane, selected the “Planetary Atmospheric Electricity” proposal, initially formulated by Jean-Pierre Lebreton and François Leblanc, to become the first joint ISSI-Europlanet workshop.

In retrospect, the choice of this subject has indeed been particularly good. As this volume nicely illustrates, Planetary Atmospheric Electricity happened to be an outstanding theme to stimulate the dialogue between a “traditional” field of geosciences—atmospheric electricity was initiated as a science by Benjamin Franklin—and the emerging field of planetary electricity, a promising development of comparative planetology. Once again, the synergistic alchemy of ISSI operated beautifully between these two communities, leading to many exciting scientific exchanges and finally to a fundamentally interdisciplinary book, merging the expertise and prospects of the two communities.

Electrical phenomena have been studied for centuries in the Earth’s atmosphere, leading to a progressively better understanding of electrification sources (galactic cosmic rays, deep cloud convection, etc.), their manifestations (lightning, discharges and electromagnetic emissions...) and their hazards. Atmospheric electricity still offers outstanding challenges to modern environmental research. For example, the very mechanism of charging of cloud droplets is only partly understood, and understanding the complex 3-D geometry of thunderstorm convection cells is only beginning. Even more, a significant fraction of electrostatic discharges, those which occur between the cloud tops and the ionosphere base and manifest themselves through spectacular optical phenomena such as sprites, elves, coronae, have only recently been discovered. Taranis, the first European in-depth global study of these phenomena from space is still only in its preparation phase. Many discoveries are ahead of us!

While terrestrial atmospheric electricity is well established yet rapidly evolving, its planetary counterpart is in its infancy. One of the major merits of this book is to show the *universality*, the *diversity* and the *importance* of atmospheric electrical phenomena across the solar system.

Standing as a good example of a *universal process*, lightning is common and currently observed at Jupiter and Saturn, it is likely at Uranus and Neptune, and evidence of its existence in the atmosphere of Venus accumulates from Venus Express data. But many basic questions about its generation and occurrence are open: does cloud convection need water to generate electrification and lightning? Is there a global electrical circuit at any other planet than Earth?

Space exploration of the solar system has also illustrated the broad *diversity* of charging and discharge phenomena, in Martian dust storms or on planetary rings and dust particles, for instance, or through levitation processes at the surfaces of airless bodies.

Finally, the *importance* of electrical phenomena in the history of solar system evolution is also emerging more and more as research progresses. Did atmospheric discharges play a role in the dynamics and chemical activity of the primordial solar nebula? Or in the synthesis of the first prebiotic molecules of early Earth as suggested by Miller and Urey more than fifty years ago? Or in the growth and dynamics of atmospheric aerosol?

Based on this first inventory of electrical phenomena in the solar system, the next phase of detailed investigations of these phenomena by future planetary missions can be expected to be planned with great effectiveness, through taking advantage of the terrestrial experience both to design the best possible diagnostic instruments and to anticipate and better understand what they will observe. We are convinced that this first ISSI-Europlanet volume on

Planetary Atmospheric Electricity will become and remain a key reference for the planning of future missions.

In achieving this goal, all credit must be given to those whose hard work and dedication made this first joint workshop and publication of ISSI and Europlanet possible. Many thanks, first, to the leadership of ISSI and Europlanet who designed this collaborative project, and to the leaders of the Discipline Working Groups of Europlanet, Norbert Krupp and Ari-Matti Harri, who managed and inspired their working groups to produce challenging new subjects for future planetary science workshops. Many thanks to the Science Committee of ISSI, chaired by Prof. Len Culhane, who did the selection and made useful suggestions on the workshop contents. Our special gratitude goes to François Leblanc and Jean-Pierre Lebreton, who originally proposed the workshop's topic, and to François for masterly leadership of the whole process, from the first Conveners Meeting to book production. The team of conveners and editors did a fantastic job in defining the structure of the workshop and of the book, in managing the writing and the overall review process: as usual, all chapters were carefully reviewed by independent experts to whom we would also like to extend our gratitude.

Last, but not least, our warmest appreciation goes to the wonderful staff of ISSI, Andrea Fischer, Vittorio Manno, Saliba Saliba, Brigitte Schutte, Irmela Schweizer, Silvia Wenger, and all their colleagues whose kindness and dedication make ISSI such a nice place for a visit and for work. They are the greatest asset on which this new and promising collaboration between ISSI and Europlanet will continue to develop and flourish in the years to come.

Roger-Maurice Bonnet
Executive Director, International Space Science Institute

Michel Blanc
Europlanet Coordinator

Preface

Planetary Atmospheric Electricity

R.G. Harrison · K.L. Aplin · F. Leblanc · Y. Yair

Originally published in the journal Space Science Reviews, Volume 137, Nos 1–4.
DOI: [10.1007/s11214-008-9419-z](https://doi.org/10.1007/s11214-008-9419-z) © Springer Science+Business Media B.V. 2008

Abstract Electrification is a fundamental process in planetary atmospheres, found widely in the solar system. It is most evident through lightning discharges, which can influence an atmosphere's chemical composition, but electrification also affects the physical behaviour of aerosols and cloud droplets that determine an atmosphere's radiative balance. In the terrestrial atmosphere, lightning has been implicated in the origin of life.

Keywords Charge · Lightning · Electrostatic discharge · Comparative planetology · Primordial atmosphere · Cosmic rays · Electromagnetic radiation

1 Electrification in Atmospheres

Electrification occurs commonly in planetary atmospheres, although it is present in different forms. The most direct evidence to remote observers is presented by lightning, which is definitively known to occur on Earth, Jupiter, Saturn and, most probably, Venus, with lightning on Mars thought very likely but as yet undetected. In addition, Uranus and Neptune have yielded possible signals of lightning discharges. Taken across the solar system, the probability of lightning occurring in a planetary atmosphere (Venus, Earth, Mars, Jupiter, Saturn, Uranus and Neptune, but neglecting moons) is therefore confidently at least (4 ± 1) in 7. Thus, as lightning can also result from volcanic activity, it is reasonable to expect electrical discharges in a solar system atmosphere, with odds considerably better than evens.

R.G. Harrison (✉)

Department of Meteorology, University of Reading, Earley Gate, Reading, UK

e-mail: r.g.harrison@reading.ac.uk

K.L. Aplin

Space Science and Technology Department, Rutherford Appleton Laboratory, Didcot, Oxon, UK

F. Leblanc

Service d'Aéronomie du CNRS, Osservatorio Astronomico di Trieste, 34131 Trieste, Italy

Y. Yair

Department of Life and Natural Sciences, Open University of Israel, Ra'anana 43107, Israel

Planetary electrification has generally been explained by analogy with terrestrial processes. Lightning on both Saturn and Jupiter is thought to originate from water clouds deep in their atmospheres, with temperatures ~ 300 K (Fischer et al. 2008) where water is likely to exist in more than one phase. Charge separation is therefore expected to develop in a similar way to terrestrial thunderclouds (Saunders 2008). Martian lightning, though not yet measured, is likely to originate in dust storms. These storms are probably directly analogous to terrestrial dust devils, in which high electric fields are generated by triboelectric charge separation¹ (Farrell and Desch 2001). There is, however, no terrestrial analogue for the sulphuric acid clouds on Venus. Observations of lightning on Venus are increasingly convincing (e.g. Russell et al. 2007), but a scientific consensus on the existence of Venusian lightning has been slow to develop, probably because of the clear differences between Venusian and other solar system lightning (Gurnett et al. 2001). This illustrates that much of our acceptance of planetary atmospheric electricity is rooted in comparison with terrestrial models.

Lightning highlights atmospheric electrification localised in space and time. Charge released by high-energy particles, such as Galactic Cosmic Rays (GCR) is, however, spatially and temporally widespread in an atmosphere. The incessant GCR flux sweeping across the solar system from stellar and galactic sources ensures that planetary atmospheres are constantly permeated by energetic particles. Their arrival rate is modulated by solar activity (with the 11-year Schwabe cycle, though this effect decreases with distance from the Sun), and by the planetary magnetic field (Bazilevskaya et al. 2008). Together with the ultraviolet part of the solar spectrum, GCRs constitute energetic ionisation agents, although the depth of penetration and the nature of ionisation products are specific to each planetary atmosphere.

2 Ion Production, Clouds and Atmospheric Discharges

As well as GCR ionisation, rocky planetary bodies have a low-altitude ionisation source from the radioactive minerals contained within the surface rocks, whose decay products emanate and ionise the air immediately above it. Charging of aerosols generated mechanically from the planet's surface is expected to be a direct consequence. In the presence of condensable compounds, varying in composition between atmospheres, ion production may affect the nucleation of ultra-fine aerosol particles (Arnold 2008; Kazil et al. 2008) or droplet condensation, thus providing a link between ionisation and cloud formation. The connection between ions and clouds is especially important in Earth's atmosphere because of the central role clouds play in the climate system, now studied more intensively than ever because of the challenging context presented by climate change.

The presence of ionisation in cloud-forming atmospheric regions indicates that charging can affect many microphysical processes in clouds (e.g. ion-droplet attachment, droplet activation, droplet coalescence and aerosol-droplet scavenging) which determine cloud lifetime, cloud thickness and ultimately precipitation, and also the complex charging processes leading to electric field growth. Cloud microphysical processes and charging occur simultaneously as thunderclouds mature, and are intricately inter-related. Modern theories suggest that GCR-induced free electrons within a developing thundercloud are actually responsible for triggering the breakdown process, which culminates in an avalanche, propagating between charge centres or to the ground as a lightning flash. Electrons and ions also exist

¹On Earth, however, the breakdown voltage is sufficiently large that discharges in dust devils generally do not occur.

above cloud tops, where they are subjected to transient electric fields following lightning discharges; acceleration of electrons and ions upwards above terrestrial cloud tops creates spectacular transient luminous events (TLEs), known as sprites and elves. Terrestrial gamma flashes (TGFs) may also result from lightning's aftermath.

When a lightning channel passes through an atmosphere (N_2 or CO_2 based), it initiates chains of chemical reactions whose long-lived products can be remotely detected, permitting elucidation of the atmospheric composition. On Earth, NO_x from lightning is transported over large distances in the anvils of thunderstorms; the chemical effects are prolonged, ultimately providing a source of dissolved solutions at the surface.

3 Evidence for Planetary Atmospheric Electrification

Non-terrestrial electricity in upper atmospheres has generally been studied by ion and electron spectrometers, electric and magnetic field measurements and plasma wave instruments, as well as remotely, from earth, by radio-occultation, optical spectrometry, electromagnetic and radar measurements (Aplin et al. 2008). Upper atmosphere measurements characterise the ionospheres produced by energetic ultra-violet ionisation but, in some cases, a secondary peak in electron concentration due to meteors has been discovered, below the ionospheric electron region (Molina-Cuberos et al. 2008).

Considering lower atmospheres, no definitive evidence for lightning has yet emerged from the *Huygens* descent through the atmosphere of Saturn's satellite Titan. No Martian lightning activity has ever been measured but, so far, no electrical instrument has deployed at its surface and therefore scope for its detection remains. Very recently, *Venus Express* magnetic measurements have strongly suggested lightning on Venus, although without a coincident optical observation, a small ambiguity over the precise source remains. Ground-based observations of NO abundance in the Venusian atmosphere also suggest lightning activity (Krasnopolksy 2006). *Voyager 1* first detected optical lightning and the electromagnetic signatures of whistlers² at Jupiter. It subsequently detected sferics³ and whistlers at Saturn, a discovery recently confirmed by the *Cassini* mission (Fischer et al. 2008). *Voyager 2* measured sferics at Neptune and Uranus, interpreted as the signatures of lightning activity (Yair et al. 2008; Zarka et al. 2008).

As an alternative to direct optical detection (Takahashi et al. 2008), electromagnetic emissions have assumed to present clear signatures of lightning activity in planetary atmospheres (Zarka et al. 2008). However recent work arising from terrestrial atmospheric electricity has suggested some new approaches to studying planetary atmospheric electricity. Very low frequency measurements (3 Hz–3 kHz) can indicate the Schumann resonance, which is caused by lightning and its presence presents an important clue to the existence of a global circuit (Aplin et al. 2008; Simoes et al. 2008). The uppermost ultra low frequency present in the spectrum may be associated with lightning activity (Bosinger and Shalimov 2008). Transient luminous events discovered above active thunderstorms provide a further possibility for characterising lightning activity optically, even on planets completely covered by clouds (Yair et al. 2008). Terrestrial gamma and X-ray flashes associated with intra-cloud discharges are other potentially detectable

²Whistlers are radio signals below $f \sim 30$ kHz. In physical terms they propagate in the frequency interval between the ion and electron cyclotron frequencies $f_{ci} \ll f < f_{ce}$.

³Sferics (a word derived originally from “atmospherics” in radio work) describes high frequency electromagnetic emissions.

phenomena which may occur more widely in the solar system (Lefevre et al. 2008; Roussel-Dupré et al. 2008).

4 Atmospheric Current Flow and Global Electrical Circuits

The balance between charge generation, lightning and local ionisation results, on earth at least, in a planetary scale current flow between disturbed and fair weather regions. More generally, this conceptual circuit model provides a framework unifying atmospheric electrical processes operating in disturbed weather regions (e.g. thunderclouds, dust devils, volcanic plumes) and the ionisation processes occurring throughout the atmosphere. Conceived by CTR Wilson, the terrestrial global circuit model is based on the generation of a global potential difference between conducting upper and lower regions, separated by a poorly conducting atmosphere (Rycroft et al. 2008). This potential difference drives a current of cluster ions (and/or electrons) created by cosmic rays and natural radioactivity between the two conducting layers. Through the global circuit current, the source energy from thunderstorms is globally dissipated by the transport of trace species, and a steady flow of ions is maintained throughout the widespread non-thunderstorm regions.

As the study of terrestrial atmospheric electricity is long established, there is much that can be learnt from its history (Aplin et al. 2008). Understanding the terrestrial concepts, and synthesising them to produce the global circuit model was protracted, taking two centuries. Identifying the key stages in the synthesis could be used to optimise future measurements of extraterrestrial environments. For example, the Schumann resonance (low frequency radiation caused by the lightning excitation of the cavity formed between the atmosphere's lower and upper conducting layers) is one of the more recently discovered aspects of the terrestrial global circuit (1950s). It has been identified as the most informative single measurement to make (Aplin et al. 2008), and therefore deserves priority when proposing future planetary atmospheric electrical instrumentation.

5 Significance of Atmospheric Electrification

Clearly, our knowledge of terrestrial lightning can be applied in mitigating electrostatic hazards. This is put to very practical application when designing lightning protection systems for spacecraft. All spacecraft are under threat from lightning after launch, or sometimes before (Lorenz 2008), particularly because the tropical locations where spacecraft are launched are also where lightning is most common. Planetary probes need additional protection against electrostatic discharge (ESD) hazards when passing through atmospheres or landing on other planets. For the *Huygens* and *Galileo* probes, ESD protection technology was directly borrowed from the aircraft industry (Lorenz 2008).

There are, however, two broader scientific issues extending well beyond the essential protection of spacecraft. Firstly, fossil evidence confirms that terrestrial lightning has existed for at least 250 million years (Harland and Hacker 1966), so, as well as being abundant in the solar system, electrification is probably a long-lived phenomenon extending to geological timescales. The abundance and longevity of terrestrial lightning has caused it to be suggested as a possible factor in the formation of molecules central to the origin of life (Miller 1953). Secondly, as outlined above, charge can modify cloud formation processes and the collision rates between droplets, crystals and aerosols. Although the effect of electrification

on individual aerosols and droplets may be small, it can also be widespread, acting, in total, to influence an atmosphere's radiative balance.⁴

Beyond lightning in planetary atmospheres, aspects in their infancy include the role of electrical forces in lifting dust (Renno and Kok 2008), as well as the importance of cluster ions and charged aerosols (Tripathi et al. 2008; Harrison and Tammet 2008; Aplin 2008). Some further aspects of non-terrestrial planetary electricity have also hardly been characterised, such as the charging of planetary rings (Graps et al. 2008), volcanic electrical activity on Io (James et al. 2008) and the charge carried by asteroids.

6 Conclusions

Atmospheric electricity can originate from many different causes, specific to the kind of atmosphere and the altitude above the planetary surface. In all gaseous planetary atmospheres charge is generated by cosmic rays or ultraviolet radiation, but also by friction, meteoric impacts, atmospheric circulation, cloud charging, volcanism, and dust. The presence of aerosols modifies the charging process, facilitating charge transfer between ions and aerosols. In other planetary environments, dust storms or impacts are responsible for charge production. Rings around planets can become charged both actively and passively—for instance in the presence of magnetic fields and plasma—with their dynamics being at least affected, if not completely determined, by the build-up of electric fields. In one or other of these ways, charged atmospheric layers can be produced near most of the planets.

Information about planetary atmospheric electricity has been obtained by spacecraft observations, and the extraordinarily valuable measurements made *in situ* when spacecraft pass through a planetary atmosphere or even land instrumentation on the planet. On Earth, the violent discharge from large atmospheric electric fields is common and evident through lightning. On other planets, however, most discharges manifest themselves through secondary effects such as non-optical electromagnetic radiation, which can leak from their atmospheres to be detected remotely. Consequently detailed study of terrestrial lightning remains very important, and therefore many of the articles in this book are in one or the other way concerned with lightning, its causes, mechanism, effects, intracloud lightning, cloud to ground lightning, and cloud to space lightning like TLEs, as well as the generation of electromagnetic radiation from Schumann resonances through the spectrum to X-rays, and TGFs. The latter two are signatures of high-energy particles generated in the lightning discharges; they may indicate planetary atmospheric electric fields which could present hazards for missions to the planets.

In this volume (Leblanc et al. 2008), a detailed and up to date summary is given of the various problems in planetary atmospheric electricity outlined above. A feature is that it begins with an introductory overview section. These introductory overviews are intended to provide a brief, though fairly-founded, tutorial concerning the physics and chemistry of atmospheric electricity on Earth and the planets, the charging, ion production, current flow, current systems, electrical conductivities, and the observable processes involved into the quiet and the violent discharges. Based on these articles, the student and researcher of the many and various forms of atmospheric electricity should be prepared to deal with the more specialised papers that follow.

⁴This was memorably described at the EuroPlanet-ISSI workshop in Bern as “the tail wagging the dog”.

References

- K.L. Aplin, Composition and measurement of charged atmospheric clusters. *Space Sci. Rev.* (2008, this issue). doi:[10.1007/s11214-008-9397-1](https://doi.org/10.1007/s11214-008-9397-1)
- K.L. Aplin, R.G. Harrison, M.J. Rycroft, Investigation of Earth's atmospheric electricity: a role model for planetary studies. *Space Sci. Rev.* (2008, this issue). doi:[10.1007/s11214-008-9372-x](https://doi.org/10.1007/s11214-008-9372-x)
- F. Arnold, Atmospheric ions and aerosol formation. *Space Sci. Rev.* (2008, this issue). doi:[10.1007/s11214-008-9390-8](https://doi.org/10.1007/s11214-008-9390-8)
- G.A. Bazilevskaya, I.G. Usoskin, E. Flückiger et al., Cosmic ray induced ion production in terrestrial and planetary atmospheres. *Space Sci. Rev.* (2008, this issue). doi:[10.1007/s11214-008-9339-y](https://doi.org/10.1007/s11214-008-9339-y)
- T. Bösinger, S.L. Shalimov, On ULF signatures of lightning discharges. *Space Sci. Rev.* (2008, this issue). doi:[10.1007/s11214-008-9333-4](https://doi.org/10.1007/s11214-008-9333-4)
- W.M. Farrell, M.D. Desch, *J. Geophys. Res.* **E4**, 7591–7595 (2001)
- G. Fischer, D.A. Gurnett, W.S. Kurth et al., Atmospheric electricity at Saturn. *Space Sci. Rev.* (2008, this issue). doi:[10.1007/s11214-008-9370-z](https://doi.org/10.1007/s11214-008-9370-z)
- A. Graps, G. Jones, A. Jubasz et al., Charging of planetary rings. *Space Sci. Rev.* (2008, this issue). doi:[10.1007/s11214-008-9362-z](https://doi.org/10.1007/s11214-008-9362-z)
- D.A. Gurnett, P. Zarka, R. Manning et al., *Nature* **409**, 313–315 (2001)
- W.B. Harland, J.L.F. Hacker, *Adv. Sci.* **22**, 663–671 (1966)
- R.G. Harrison, H. Tammet, Ions in the terrestrial atmosphere and other solar system atmospheres. *Space Sci. Rev.* (2008, this issue). doi:[10.1007/s11214-008-9356-x](https://doi.org/10.1007/s11214-008-9356-x)
- M.R. James, L. Wilson, S.J. Lane et al., Electrical charging of volcanic plumes. *Space Sci. Rev.* (2008, this issue). doi:[10.1007/s11214-008-9362-z](https://doi.org/10.1007/s11214-008-9362-z)
- J. Kazil, R.G. Harrison, E.R. Lovejoy, Tropospheric new particle formation and the role of ions. *Space Sci. Rev.* (2008, this issue). doi:[10.1007/s11214-008-9388-2](https://doi.org/10.1007/s11214-008-9388-2)
- V.A. Krasnopol'sky, *Planet. Space Sci.* **54**(13–14), 1352–1359 (2006)
- F. Leblanc, K.L. Aplin, Y. Yair et al., *Planetary Atmospheric Electricity. Space Sciences Series of ISSI*, vol. 30 (2008)
- F. Lefèuvre, E. Blanc, R. Roussel-Dupré et al., Taranis—a microsatellite project dedicated to the physics of TLEs and TGFs. *Space Sci. Rev.* (2008, this issue). doi:[10.1007/s11214-008-9414-4](https://doi.org/10.1007/s11214-008-9414-4)
- R. Lorenz, Atmospheric electricity hazards. *Space Sci. Rev.* (2008, this issue). doi:[10.1007/s11214-008-9364-x](https://doi.org/10.1007/s11214-008-9364-x)
- S.L. Miller, *Science* **117**, 528 (1953). doi:[10.1126/science.117.3046.528](https://doi.org/10.1126/science.117.3046.528)
- G. Molina-Cuberos, J.J. Lopez-Moreno, F. Arnold, Meteoritic ions in planetary atmospheres. *Space Sci. Rev.* (2008, this issue). doi:[10.1007/s11214-008-9340-5](https://doi.org/10.1007/s11214-008-9340-5)
- N. Renno, J. Kok, Electric activity and dust lifting on Earth, Mars and beyond. *Space Sci. Rev.* (2008, this issue). doi:[10.1007/s11214-008-9377-5](https://doi.org/10.1007/s11214-008-9377-5)
- R. Roussel-Dupré, J.J. Colman, E. Symbolisty et al., Physical processes related to discharges in planetary atmospheres. *Space Sci. Rev.* (2008, this issue). doi:[10.1007/s11214-008-9385-5](https://doi.org/10.1007/s11214-008-9385-5)
- C.T. Russell, T.L. Zhang, M. Delva et al., *Nature* **450**, 661–662 (2007). doi:[10.1038/nature05930](https://doi.org/10.1038/nature05930)
- M.J. Rycroft, R.G. Harrison, K.A. Nicoll et al., Physical processes related to discharges in planetary atmospheres. *Space Sci. Rev.* (2008, this issue). doi:[10.1007/s11214-008-9368-6](https://doi.org/10.1007/s11214-008-9368-6)
- C. Saunders, Charge separation mechanisms in clouds. *Space Sci. Rev.* (2008, this issue). doi:[10.1007/s11214-008-9345-0](https://doi.org/10.1007/s11214-008-9345-0)
- F. Simoes, M. Rycroft, N. Renno et al., Schumann resonances as a means of investigating the electromagnetic environment in the solar system. *Space Sci. Rev.* (2008, this issue). doi:[10.1007/s11214-008-9398-0](https://doi.org/10.1007/s11214-008-9398-0)
- Y. Takahashi, J. Yoshida, Y. Yair et al., Lightning detection by LAC onboard the Japanese Venus Climate Orbiter Planet-C. *Space Sci. Rev.* (2008, this issue). doi:[10.1007/s11214-008-9400-x](https://doi.org/10.1007/s11214-008-9400-x)
- S. Tripathi, M. Michael, R.G. Harrison, Profiles of ion and aerosol interactions in planetary atmospheres. *Space Sci. Rev.* (2008, this issue). doi:[10.1007/s11214-008-9367-7](https://doi.org/10.1007/s11214-008-9367-7)
- Y. Yair, G. Fischer, F. Simoes et al., Updated review of planetary atmospheric electricity. *Space Sci. Rev.* (2008, this issue). doi:[10.1007/s11214-008-9349-9](https://doi.org/10.1007/s11214-008-9349-9)
- P. Zarka, W. Farrell, G. Fischer et al., Ground-based and space-based radio observations of planetary lightning. *Space Sci. Rev.* (2008, this issue). doi:[10.1007/s11214-008-9366-8](https://doi.org/10.1007/s11214-008-9366-8)

Introductory Overviews

Investigating Earth's Atmospheric Electricity: a Role Model for Planetary Studies

K.L. Aplin · R.G. Harrison · M.J. Rycroft

Originally published in the journal Space Science Reviews, Volume 137, Nos 1–4.
DOI: [10.1007/s11214-008-9372-x](https://doi.org/10.1007/s11214-008-9372-x) © Springer Science+Business Media B.V. 2008

Abstract The historical development of terrestrial atmospheric electricity is described, from its beginnings with the first observations of the potential gradient to the global electric circuit model proposed by C.T.R. Wilson in the early 20th century. The properties of the terrestrial global circuit are summarised. Concepts originally needed to develop the idea of a global circuit are identified as “central tenets”, for example, the importance of radio science in establishing the conducting upper layer. The central tenets are distinguished from additional findings that merely corroborate, or are explained by, the global circuit model. Using this analysis it is possible to specify which observations are preferable for detecting global circuits in extraterrestrial atmospheres. Schumann resonances, the extremely low frequency signals generated by excitation of the surface-ionosphere cavity by electrical discharges, are identified as the most useful single measurement of electrical activity in a planetary atmosphere.

Keywords Atmospheric electricity · Lightning · History of science · Comparative planetology · Planetary atmospheres

PACS 92.60.Pw · 01.65.+g · 96.30.Bc · 96.15.Hy

K.L. Aplin (✉)

Space Science and Technology Department, Rutherford Appleton Laboratory, Chilton, Didcot,
Oxon OX11 0QX, UK

e-mail: k.aplin@rl.ac.uk

R.G. Harrison

Department of Meteorology, University of Reading, Earley Gate, PO Box 243, Reading
Berkshire RG6 6BB, UK

M.J. Rycroft

International Space University, 1 rue Jean-Dominique Cassini, 67400 Illkirch-Graffenstaden, France

M.J. Rycroft

CAESAR Consultancy, 35 Millington Road, Cambridge CB3 9HW, UK

1 Historical Introduction

The understanding of electricity is a relatively recent development in human endeavour, although lightning is known to have existed on Earth for much longer than *homo sapiens*. Lightning will almost definitely have been known to all human civilisations, some of whom recorded it in their literature, or linked the phenomena with gods unleashing thunderbolts. According to Schiffer (2003), William Gilbert (1540–1603), the physician to Queen Elizabeth I, was the first person to investigate electrical phenomena in what is now referred to as a “scientific” way. It was known amongst natural philosophers that amber and other insulators could attract straw fragments and chaff, but Gilbert was first to identify that it was only lightweight items that were subject to the mysterious attraction, and to generalise the types of material that could act as attractors.

The study of what might now be called electrostatics progressed throughout the seventeenth and eighteenth centuries (Schiffer 2003), through the development of scientific instrumentation such as the Leyden jar (Falconer 2004) and also the start of scientific academies such as the Royal Society (London) and the Académie des Sciences (Paris). Benjamin Franklin (1706–1790), the famous American polymath, is credited with suggesting that lightning was electricity, proposing an experiment later undertaken by Thomas-Francois d’Alibard (1703–1799) in 1752, who extracted sparks from a cloud. As well as making further measurements under thunderstorms, John Canton (1718–1772) observed in experiments in England that electricity was also present in cloudless air (Canton 1753). In the late eighteenth century a two-year series of quantitative atmospheric electrification measurements was made by John Read (1726–1814), who monitored, at least daily, the deflection of a pith ball electrometer connected to an insulated mast on the roof of his house in Knightsbridge, London (Read 1791). This monitoring approach was inspired by the earlier work of Giovanni Battista Beccaria (1716–1781) in Piedmont, Italy (Beccaria 1775). Beyond static electricity, the possibility of charge flow was emerging from laboratory experiments at around the same time. Charles-Augustin Coulomb (1736–1806) noticed that the charge on an object slowly decayed in air with time, and that this decay was more rapid when the air was more humid:

L'électricité des deux balles diminue un peu pendant le temps que dure l'expérience... si l'air est humide et que l'électricité se perd rapidement... (Coulomb 1784)

For this Coulomb is widely credited with discovering the electrical conductivity of air, though it is not clear that he realised the significance of his findings. He certainly did not have the theoretical understanding to explain the effect, as will be explained. To Coulomb, an experimentalist, the conductivity of air was just another difficulty encountered during his investigations of the inverse square law of electrostatic repulsion.

Detailed observation, but a lack of explanatory power, was a characteristic of this early work. Scientific theory did not exist to explain the electrical conductivity of gases until the discovery of the electron over a hundred years later. Similarly, the lack of an explanatory framework for an atmospheric electric potential in the absence of electrified cloud, which was well-established by the mid-nineteenth century, precluded systematic study of the phenomena. For example, early experimenters had noted that an atmospheric measuring electrode developed a positive charge during fine weather (Bennett and Harrison 2007), and that it varied considerably with the weather conditions, but Beccaria’s suggestion that it might one day be possible to use atmospheric electricity for weather prediction was drawn only from experience rather than a theoretical understanding. At this stage, therefore, the theory did not exist to permit a more sophisticated approach than simple inductive empiricism.

In the nineteenth and early twentieth centuries the study of atmospheric electricity was approached more systematically. With scientific giants such as Faraday and Maxwell researching electricity and electromagnetism, a better physical context for the measurements was starting to be developed. The advent of more reliable instrumentation and, in particular, the ability to make continuous automatic measurements of the atmospheric electric field (more conventionally now known as the Potential Gradient, PG¹), was very important during this period. Lord Kelvin² (1824–1907) was one of the pioneers of this autographic recording, developing an electrometer that measured the PG by letting water dribble through a pipe from an isolated tank, which, through charge exchange, caused the tank to acquire the potential of the atmosphere where the stream broke into a droplet spray. Kelvin's "water dropper" was used with photographic recording to produce continuous atmospheric electrical measurements for the first time in 1862 (Everett 1868). As a result, Kelvin concluded that electrification was a property of the fair weather atmosphere. This equipment began continuous measurements of the atmospheric PG in the UK at Kew Observatory³ (Harrison and Aplin 2002), and at new scientific research facilities such as at the top of the Eiffel Tower in Paris (Harrison and Aplin 2003).

As well as surface measurements, new opportunities were presented by manned balloons which provided measurements of PG above the surface (Table 1). However, it was not just the PG that was measured. After the almost simultaneous discovery of the electron and ionising radiation (X-rays and radioactivity) in the last years of the nineteenth century, study of the conduction of electricity in gases progressed rapidly. Most of this work was carried out at the Cavendish Laboratory at Cambridge, first under J.J. Thomson (1856–1940), and then Lord Rutherford (1871–1937). It was during this period that many of the terms used to characterise ions in air were defined, for instance, the concept of mobility (the speed of an ion at terminal velocity in a unit electric field) (Aplin 2000). In parallel with the Cavendish laboratory studies, in Europe, Ebert, Gerdien, Elster and Geitel developed instrumentation to measure atmospheric ions *in situ* (Elster and Geitel 1900; Ebert 1901; Gerdien 1905a). Gerdien's instrumentation permitted the air conductivity to be measured on balloon ascents, providing further data on ion properties (Table 1). Wigand's ascent was one of the first to measure reliably both PG and conductivity to 9 km. This permitted determination of the conduction current, which was found to be essentially independent of height in the free troposphere (Wigand, 1914, 1921; Everling and Wigand 1921).

The beginning of the twentieth century is often considered to mark a transition between "classical" and "modern" physics. Atmospheric electricity also moved into a new phase at this time. There was new instrumentation with which to make systematic measurements of spatially varying quantities, supported by the rapid advances in contemporary physical theory. This set the scene for unification of previously disparate measurements, through the concept of the global circuit. The development of the global circuit model will be outlined in Sect. 2 followed by more detail on its properties and parameters in Sect. 3. The final Discussion section will conclude by summarising the historical development of the terrestrial global circuit and outlining its application to planetary studies.

¹The potential gradient (PG) and electric field have equal magnitudes, but are of opposite sign by convention. In fair weather, when the vertical electric field is negative, the PG is considered positive.

²Lord Kelvin was formerly W. Thomson and his papers are listed under this name.

³Observations at Kew continued virtually uninterrupted from 1860 until 1981, although their absolute calibration improved (Harrison 2003).

Table 1 Summary of the early European research balloon flights in atmospheric electricity listing quantities measured by different investigators (after Harrison and Bennett 2007a). (Atmospheric Electricity (AE) quantities: PG = Potential Gradient, surface air conductivity σ_0 , positive air conductivity σ_+ , negative air conductivity σ_- , air temperature T , relative humidity RH). Hess's 1912 ascent measured ion production, not atmospheric electrical quantities, but is significant because this flight discovered cosmic rays

Investigator	Launch date	Launch site	Max height (m)	AE quantities				Met data	Source
				PG	σ_0	σ_+	σ_-		
				T	RH				
Tuma	1892, 1894 (22nd Sep); 7 flights 1894 to 1898	Near Salzburg	3000	✓				✓	✓
Le Cadet	1893 (1st and 9th Aug)	Meudon-Valhermay, Paris	2520	✓					Andre 1893
Börnstein	1893	Berlin		✓					Chauveau 1925
Gerdien	1903 (1st July, 2nd Aug, 1st Oct, 5th Nov)	Göttingen and Berlin	7100		$\mu \pm n \pm$			✓	Gerdien 1903
Gerdien	1903 (14th April), 1904 (5th May), 1905 (11th May, 30th Aug)	Charlottenberg (Berlin)	6030	✓	✓	✓		✓	Gerdien 1904, 1905b, 1905c
Hess	1912 (7th Aug)	Aussig	5000	Ion production rate					Hess 1912
Wigand	1913 (12th and 27th July, 4th Aug, 9th Sep)	Bitterfeld	9005	✓	✓	✓	✓	✓	Wigand 1914, 1921; Everling and Wigand 1921
Wigand	1919 (18th Dec)	?	2950	✓	✓	✓			Everling and Wigand 1921
Gish Explorer 2	1935 (11th Nov)	South Dakota	22000		✓		✓		Gish and Sherman 1936

2 Development of the Global Circuit Concept

From the studies in the eighteenth and nineteenth centuries, basic facts of atmospheric electricity emerged. By the beginning of the twentieth century it was well-established that:

- (1) a positive potential gradient was present in fair weather,
- (2) ions were formed naturally in air,
- (3) air had a finite electrical conductivity (known originally as the property of “dissipation”).

It was known that the PG and conductivity were inversely related (Gockel 1903; Zolss 1904), and this result was extended by Simpson (1906a) to be related to “clarity” (visibility) of the air. Simpson (1906b) remarked that, from balloon ascents, the observed reduction in PG provided an inference that charge existed through the lower layers of the atmosphere. The balloon ascents of Gerdien, Wigand, and others found, from PG and conductivity measurements, that the air-Earth conduction current was constant with height. This provided evidence of current flow in an electric field between the upper atmosphere and the sur-

face. C.T.R. Wilson (1869–1959) developed new apparatus for direct measurements of the air-Earth current, which was able to make measurements in different conditions without precipitation⁴ (Wilson 1906, 1908).

The mechanism to sustain the current observed in fair weather was a matter of scientific speculation, though it was known to be generated within the atmosphere (Simpson 1906b). Wilson (1921, 1929) proposed that thunderstorms and rain clouds provided the current. It was possible to consider current flow from distant storms to fair weather regions, as the conductive properties of the upper atmosphere had then been deduced from radio wave studies. This will be discussed further in Sect 4.1.

A test for the theory that the thunderstorms, highly conductive ionosphere and surface, and partially conductive lower atmosphere together constituted a global atmospheric electrical circuit (the “Wilson circuit”) came from the cruises of the geophysical research ship *Carnegie* in the 1920s. During these voyages, a characteristic daily variation (with Universal Time) of the atmospheric PG—known as the *Carnegie* curve—was found; it was noted that this was largely independent of the global position of the ship. (Oceanic air was particularly favourable for these measurements, because of its remoteness from continental aerosol pollution.) Using thunderday⁵ statistics (Brooks 1925) from meteorological stations, and summing the diurnal variations in thunderstorm area for each of Africa, Australia and America, a strong positive correlation was found between the Carnegie curve and the diurnal variation in global thunderstorm area⁶ (Whipple 1929; Whipple and Scrase 1936). Seasonal changes in the Carnegie curve variations are considered in Rycroft et al. (2008).

These findings confirmed one of the predictions of a global circuit hypothesis, namely that the variations in PG were linked to the electrical activity of thunderstorms elsewhere on the planet. Further evidence for the global circuit was provided when measurements of the ionospheric potential V_I were obtained in the late 1950s, by integration of the vertical PG profile using balloon or aircraft carried field sensors (Imyanitov and Chubarina 1967; Markson 2007). Soundings made by Mülheisen (Budyko 1971) from Weissenau, Germany between 1959 and 1972 included a period in March–April 1967 that showed common simultaneous variations in V_I measured over Weissenau and above the research ship *Meteor* in the Atlantic (Mülheisen 1971). The same V_I measurements made over the Atlantic have been shown to correlate closely with surface measurements of PG made at Lerwick, Shetland Islands, UK (Harrison and Bennett 2007b). Simultaneous variations of V_I at two locations coupled with synchronous changes in the PG provide important support for the global circuit concept. The existence of a Carnegie-like diurnal variation in V_I (Mülheisen 1977) provides further confirmation of the coupling and integrating properties of the global circuit.

3 Properties of the Global Electric Circuit

The Earth possesses, on average, a surface which is a good conductor of electricity. Land conductivity ranges from 10^{-8} Sm^{-1} for marble up to $\sim 10^{-2} \text{ Sm}^{-1}$ for wet clay or limestone, a typical mean value being 10^{-2} Sm^{-1} (Lowrie 2007); the main mechanism of crustal

⁴These were continued in a very similar manner by the UK Met Office between 1909 and 1979 (Harrison and Ingram 2005).

⁵A *thunderday* is a calendar day on which thunder is heard at a meteorological observing station.

⁶The original Carnegie and thunderday data is tabulated in Harrison (2003).

conduction is through impurity semi-conduction in dry silicate rocks. The ocean conductivity ranges from 3 to 4 Sm^{-1} , depending on salinity and temperature, the mean value being $\sim 3.2 \text{ Sm}^{-1}$ (Olsen and Kuvshinov 2004). Kamra and Ravichandran (1993) point out that the Earth's surface cannot universally be considered a conductor, particularly in hot dry areas and at the poles, where the land conductivity $< 10^{-9} \text{ Sm}^{-1}$. However, this is not thought to be important for the global circuit due to the specific geographical regions concerned combined with the paucity of lightning over the less conductive surface regions. At altitudes above $\sim 80 \text{ km}$, the ionospheric plasma produced by the action of solar extreme ultraviolet and X-radiation on the tenuous upper atmosphere is also a good conductor of electricity (Schunk and Nagy 2000). Between these two conductors lies the atmosphere, which behaves like a leaky insulator (an imperfect dielectric), as discussed by Rycroft et al. (2000), Williams (2002, 2007), Harrison (2004), Rycroft (2006) and Markson (2007). The atmospheric conductivity increases with height as the ionisation produced by cosmic rays increases, from a surface value of $\sim 10^{-14} \text{ Sm}^{-1}$ (mostly from natural radioactivity emanating from the Earth) by seven orders of magnitude, to reach the large values ($\sim 10^{-7} \text{ Sm}^{-1}$) characterising the electrically conducting ionosphere.

Complex microphysical processes acting within thunderclouds generally cause the build up of reservoirs of positive electric charge at $\sim 10\text{--}16 \text{ km}$ altitude and, in regions well below these, reservoirs of negative charge; a vertical electric dipole is thereby formed. Details of the physical mechanisms operating are given in Yair (2008) and Saunders (2008), and more complicated geometrical arrangements of charge—multipoles—often exist in a thundercloud. These thunderclouds constitute giant “batteries” which drive an upward current (i.e. positive ions moving upwards, and negative ions moving downwards) through the stratosphere and mesosphere up to the ionosphere, as was first discussed in the seminal paper by Wilson (1921). This upward thunderstorm conduction current contributes to causing the potential of the ionosphere to reach $\sim +250 \text{ kV}$ with respect to that of the Earth's surface. As a good electrical conductor, the ionosphere is an equipotential surface which is approximately spherically symmetric about the Earth.

Remote from thunderstorms, in the so called “fair weather” regions of the globe, an electric current flows downwards through the atmosphere to the Earth; positive ions move downwards and negative ones upwards. The value of the vertical conduction current density $J_c \sim 2 \text{ pA m}^{-2}$ (Wilson 1906; Wahlin 1994, Rycroft et al. 2000; Markson 2007). The current flowing in this DC global circuit is closed by point discharge currents (sometimes termed coronal currents) which are created in the large electric fields existing below thunderclouds, as was first pointed out by Wilson (1921). These processes are illustrated in Fig. 1, taken from Rycroft and Füllekrug (2004). This figure was originally produced to introduce the activities of the SPECIAL (Space Processes and Electrical Charges Influencing Atmospheric Layers) Scientific Network of the European Science Foundation. The arrows show the electric currents flowing through the global atmospheric electric circuit. Further, Fig. 1 indicates that the ionosphere and atmosphere below it respond to heliospheric phenomena, such as the solar wind flowing radially away from the Sun at $\sim 400 \text{ km s}^{-1}$, energetic charged particles precipitating from the magnetosphere, and also to cosmic rays coming from beyond the solar system.

Figure 1 also shows lightning discharges from the top and from the bottom of a thundercloud to ground; these radiate electromagnetic waves across the spectrum from Extremely Low Frequency (ELF, 3 Hz to 3 kHz), and Very Low Frequency (VLF, 3 to 30 kHz) to High Frequency (HF, 3 to 30 MHz). At Ultra Low Frequency (ULF, $< 3 \text{ Hz}$) lightning generates transient signals (see Fukunishi et al. 1997); pulsations at ULF are generated in the magnetosphere. Lightning acts as a source of electromagnetic radiation which excites the

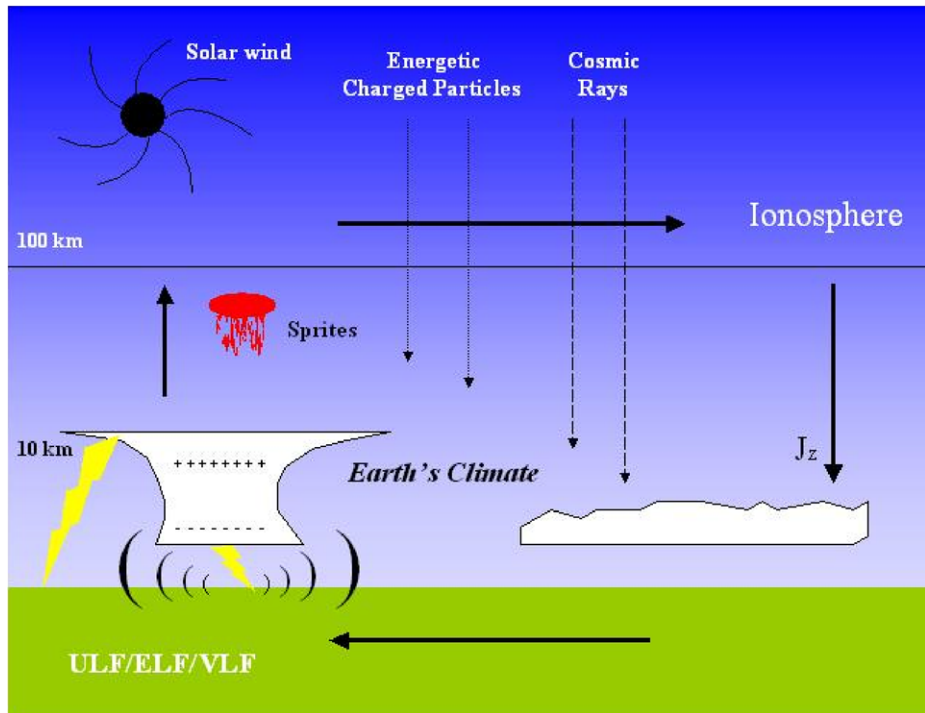
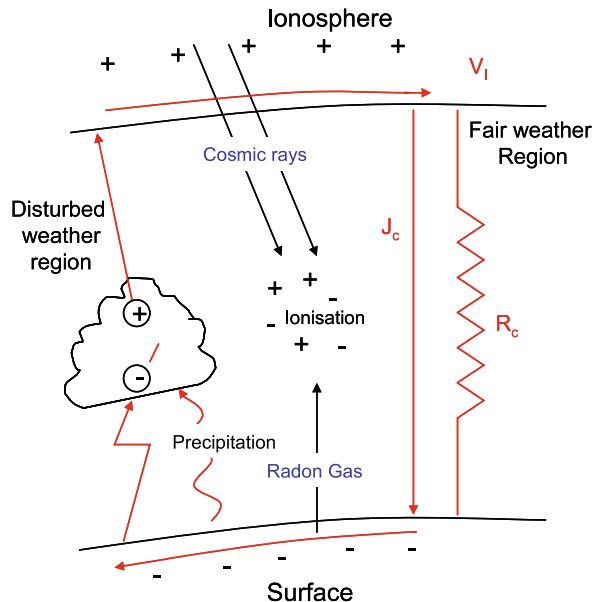


Fig. 1 Essential features of the global atmospheric electric circuit, from Rycroft and Füllekrug (2004)

AC global circuit; Schumann resonances of the Earth-ionosphere cavity exist at frequencies of 8, 14, 20, 26, ... Hz (Simoes et al. 2008). Above the thundercloud is shown a sprite, a type of upward lightning discharge—for details of sprites and associated phenomena, see Füllekrug et al. (2006), Mika and Haldoupis (2008) and Mishin and Milikh (2008).

Other than thunderstorms, there are two further major mechanisms which act as drivers for current flows around the global electric circuit. Interactions between the solar wind and the Earth's magnetic field generate additional currents (Rycroft et al. 2000), and PG modulation may arise from coupling of geomagnetically-induced changes in the magnetospheric dynamo through the global circuit. These perturbations generate polar cap potential differences, which can cause surface PG variations of $\pm 20\%$ (Roble and Tzur 1986). The ionospheric/magnetospheric generator is thought only to affect the global circuit appreciably at high latitudes, although weak geomagnetic influences have been detected at lower latitudes (Märcz 1976; Harrison and Märcz 2007). Another process driving current around the global circuit is precipitation (commonly called “rain”) from electrified clouds (Wilson 1921; Williams and Heckman 1993). A cloud transferring negatively charged water droplets constitutes another “battery” which causes currents to flow in the same direction as does the thundercloud mechanism already discussed. The total current flowing in the global atmospheric electric circuit $\sim 1\text{--}2$ kA. Together with its physical dimensions (the Earth's radius = 6378 km, and the base of the ionosphere at ~ 80 km), it is the profiles of the atmospheric conductivity at all locations over the Earth which determine, via Ohm's law, the properties (namely, the electric fields and current densities everywhere) of the global atmospheric electric circuit. An “electrical engineering” model of the circuit, originally involving only resistors, was devised by Markson

Fig. 2 Simplified “electrical engineering” model of the global circuit, illustrating charge generation in disturbed weather regions, conduction through the ionosphere (upper layer) and surface (lower layer), and discharge through the finite conductivity of fair weather regions. In fair weather regions, the ionospheric potential V_i , conduction current density J_c and unit area columnar resistance R_c are related by Ohm’s Law



(1978). Some more realistic models, with capacitors as well as resistors (see Rycroft 2006; Rycroft et al. 2007), are introduced in Rycroft et al. (2008). A simplified model of the global circuit is shown in Fig. 2.

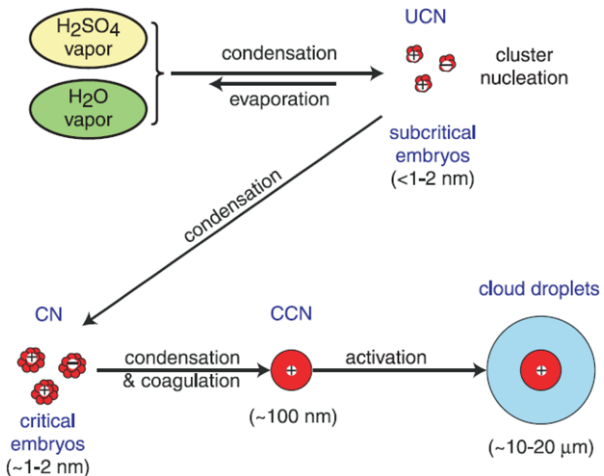
Any of the electrical processes operating in the Earth’s climate system may respond to climate change (*i.e.* global warming or, specifically, increased concentrations of greenhouse gases in the atmosphere). There is also the possibility that sensitive components of the climate system can respond to atmospheric electrical changes. One sensitive aspect of the climate system is clouds.

It has been suggested that changes in the electrical properties of the atmosphere could alter the properties of clouds, resulting in a climate response. Plausible possible mechanisms have been discussed by Carslaw et al. (2002). In one scenario (the “ion-aerosol clean air mechanism”), cluster ions contribute to the formation of aerosol particles in clean air, on which cloud droplets subsequently form; in another scenario (the “ion-aerosol near cloud mechanism”), the atmospheric electrical conduction current causes particle and droplet charging which modify the cloud properties.

The clean air mechanism is illustrated in Fig. 3. In this process, condensation of vapour on freshly-formed cluster ions leads to the formation of new ultrafine particles. Laboratory and atmospheric evidence exists which demonstrates that, in the absence of other sinks of the condensable vapour, such ultrafine particle formation can occur. Ultrafine particles are not, however, able to form water clouds because of their small size. A particle needs to reach 100 nm radius to permit condensation of water in atmospheric conditions—known as a Cloud Condensation Nucleus (CCN)—but the ultrafine particles formed are about two orders of magnitude smaller. The growth stage of the ultrafine particles is therefore critical, if there is to be a later influence on the formation of cloud droplets. Modelling by Yu and Turco (2001) indicates that the growth timescale is typically 5 to 10 hours.

The near cloud mechanism results from the difference in electrical conductivity of air within and outside a cloud. In the simple case of a horizontal layer cloud, charge accumulates at the cloud boundary with clear air, as a result of the vertical current density within

Fig. 3 Nucleation of ultrafine condensation nuclei (UCN), catalysed by ions from water or sulphuric acid vapour in the atmosphere, which could grow into cloud condensation nuclei (CCN). Reproduced with permission from AAAS from Carslaw et al. (2002)



the global circuit (Fig. 4). The effect of charge on cloud has not been investigated in detail, but, for the special case of supercooled water clouds, Tinsley and Heelis (1993) suggested that electrification might enhance the effectiveness of aerosol as ice-forming nuclei—which are relatively rare in the atmosphere—and therefore the amount of cloud ice formed. This was called *electrofreezing*. A possible mechanism for electrofreezing is the electrically-enhanced collection of charged ice nuclei by supercooled water droplets, which has been quantified through detailed modelling (Harrison 2000; Tripathi 2000; Tinsley et al. 2001; Tripathi and Harrison 2002; Tripathi et al. 2006). Such an electrically-enhanced aerosol scavenging process, known as *electroscavenging*, may lead to electrofreezing on the cloud boundary. There are laboratory observations of electroscavenging, but no direct atmospheric observations of electrofreezing. If electrofreezing does occur, there could be appreciable local latent heat release. As indicated on the right hand side of Fig. 4, the charge density on the cloud boundary is proportional to the vertical current density flowing in the global circuit. Harrison and Shine (1999) and Tinsley (2000) suggested that the global circuit may be involved in climate change via electrical effects on cloud microphysical processes in fair weather regions.

The global circuit model has recently been extended by Rycroft et al. (2007) to include the generator associated with electrified clouds; this was found to be of the same magnitude as that due to thunderstorms. Further refinements of the model could be attempted. Rycroft et al. (2007) also showed that a sprite (Füllekrug et al. 2006; Mika and Haldoupis 2008; Mishin and Milikh 2008) following a cloud to ground lightning flash which transports positive charge to ground varies the ionospheric potential in only a minuscule way. However, the effects of gigantic jets (Pasko et al. 2002; Su et al. 2003) on the ionosphere and the global atmospheric electric circuit have yet to be modelled.

4 Discussion

Based upon many observations performed and experiments conducted in the Earth's atmosphere over the last 250 years, the concept of a global atmospheric electrical circuit is one which orders the diverse measurements satisfactorily and is able to explain subsequent

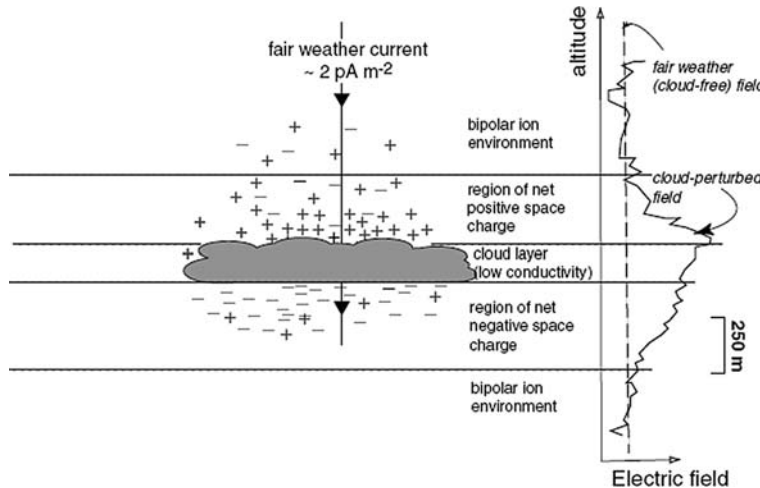


Fig. 4 Electric charge distributed around an isolated cloud in the fair weather part of the global circuit. The upward electric field is shown at the right hand side. From Harrison and Carslaw (2003)

findings adequately. Though it still has some inadequacies—notably the absence of upper atmosphere discharges and no allowance for electron density variations in the ionosphere—it still provides the best overall model available with which to unify the many disparate measurements and theoretical concepts associated with electricity in the atmosphere. Recently, other approaches to understanding the global circuit, such as simple “electrical engineering” models (e.g. Fig. 2), have provided a reasonable theoretical framework within which atmospheric electrical phenomena can be understood.

Starting from the origin of electrostatics with William Gilbert in the 16th century, the concept of a global circuit took around four hundred years to emerge in the 20th century; it is arguably still incomplete. As the word “theory” implies a still greater level of predictive power (Hesse 2000), the global circuit is referred to throughout this paper as a “model” or a “concept”. In this section the development of the model is discussed so that the key concepts can be identified and used to prescribe the simplest possible measurements that could detect an extraterrestrial global circuit.

4.1 Concepts Needed in Originating the Idea of a Global Circuit

The findings leading to the development of the global circuit model were discussed in Sects. 1 and 2 above. They can be categorised into concepts that were absolutely necessary for the model to be established, and those that support or are supported by the global circuit model, but were not essential to establish it. Here the two types of finding are defined as “central tenets” and “confirming ideas”, summarised in Fig. 5.

Chronologically, the first central tenet to be established was the existence of a positive potential gradient in all fair weather regions. Kelvin was probably one of the earliest to become aware of the ubiquity of the PG through his own measurements, and a compilation of the many disparate observations described in Sect. 1. For example, he described Beccaria’s, “incessant observations on atmospheric electricity, night and day, sleeping in the room with his electrometer in a lofty position” (Thomson 1859; Bennett and Harrison 2007). As is also described in Sect. 1, the conductivity of the air was observed but not explained by Coulomb (1784) and attributed to the continual formation of ion pairs in air by Wilson (1897, 1899).

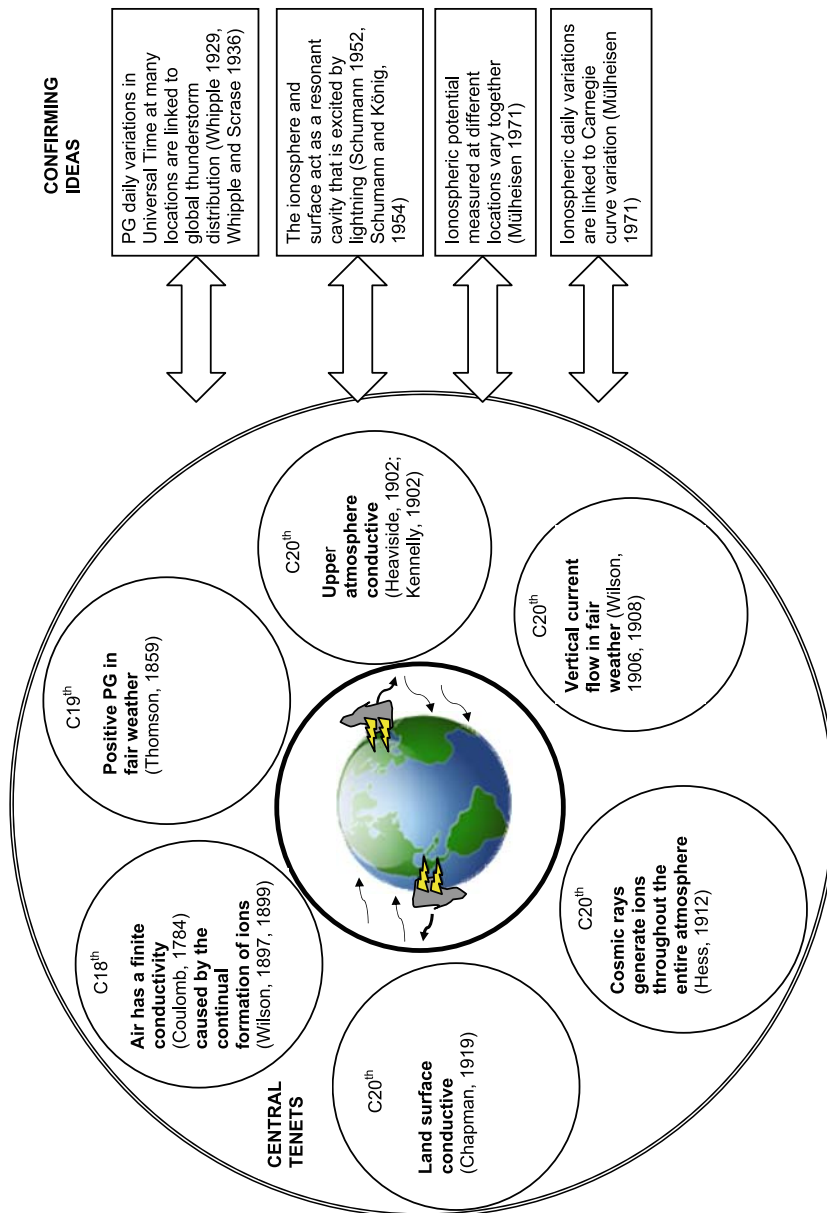


Fig. 5 Historical development of the global circuit model. Central tenets are shown on the *left*, and confirming ideas are on the *right*. The central tenets are ordered chronologically clockwise from the *top left*

The next central tenet came from the discovery of cosmic rays by Hess (1912) through atmospheric soundings. This was important for development of the global circuit model, since it explained how ionisation was sustained throughout the entire atmosphere. Contemporary experimenters such as those within the Cavendish in Cambridge were well aware of the contribution of radioisotopes to air ionisation at the surface but, if radioactivity was the only source of atmospheric ionisation, air conductivity would become negligible above ~ 1 km. Hess's historic balloon ascent showed that "penetrating radiation", a uniquely persistent form of ionising radiation that could not be screened out like other forms of radioactivity, came from outside Earth's atmosphere.

Two further central tenets for the global circuit model were the conducting upper and lower layers, needed to sustain current flow from thunderstorm regions around the Earth. The development of these concepts is intimately linked with the history of radio science. Besser (2007) explains that the first postulation of an upper conducting layer followed from Gauss's expansion of spherical harmonics for the Earth's magnetic field in 1839, and it was later suggested by several 19th century scientists, such as Kelvin in 1860, and Balfour Stewart in 1882, who is often credited with proposing the idea (e.g. Simpson 1941). Fitzgerald publicly conjectured the existence of a conducting layer high in the atmosphere at a British Association meeting in 1893. In the same presentation, he presciently proposed that thunderstorms could be the excitation mechanism (Besser 2007). Fitzgerald's suggestions could also have been inspired by discussions with his friend Lodge, who gave the first public demonstration of radio transmission at a subsequent British Association meeting in 1894 (Lovell 1997). The *observation* of this conducting layer, however, needed long-distance radio transmission. Radio transmission beyond line of sight requires the existence of an ionised layer in the upper atmosphere to reflect the radio waves around the Earth. Marconi was internationally recognised for transmitting a radio signal across the Atlantic in late 1901 (Franklin 1902), using technology largely developed by Lodge, to demonstrate potential for the commercial development of radio. Marconi's achievement was first explained in terms of this conducting layer by Kennelly, and, independently and slightly later, Heaviside (Heaviside 1902; Kennelly 1902; McAdie 1925). The lowest ionospheric conducting region was subsequently named the Kennelly-Heaviside layer.

As implied in Sect. 3, the Earth's surface also needs to be conductive relative to the atmosphere for a global circuit to exist. A finite surface conductivity had been assumed for many years simply based on the mean conductivity of the salt water covering most of the planet. Chapman (1919), building on investigations of the terrestrial magnetic field, was first to calculate the Earth's surface conductivity accurately, stating that it was "similar to that of moist earth".

C.T.R. Wilson himself had developed the instrumentation to establish the next central tenet: the vertical fair weather current (1906, 1908). His work on what became the global circuit seems to have begun around the same time, no doubt inspired by the same fascination with the weather that motivated the cloud chamber work for which he ultimately became famous (Galison 1997). As early as January 1909, Wilson's notebooks show he was trying to understand where the Earth's negative charge (which can be deduced from the direction of the fair weather PG) came from, "It is conceivable that negative charge might be continually acquired to earth by beta rays from atmosphere" (Wilson 1909). Wilson (1909) rejected an experimental test of this idea due to the impossibility of excluding "penetrating radiation". In notes on a paper by Simpson (1909), Wilson (1909) realised that charge was carried downwards by rain. This is the one of the building blocks of the global circuit model, but the ionising upper layer, of which Wilson does not seem to have been aware in 1909, is needed

to “close” the circuit.⁷ In Wilson’s 1921 paper the first principles of the global circuit model are presented:

Thus far no account has been taken of the conducting layer in the higher levels of the atmosphere, to the existence of which the phenomena of terrestrial magnetism seem to point.

The normal potential gradient at the surface of the ground in clear weather is of the order of 100 volts per metre, falling off with increasing height and becoming negligible above 10 km; thus the potential in the conducting layer over regions of fine weather is not likely to exceed a value of the order of 1,000,000 volts. If we assume... that the conductivity of the upper atmosphere is high enough to prevent any large potential differences within it, then even above a thunderstorm the potential in the conducting layer may not greatly exceed 1,000,000 volts. (Wilson 1921)

The final unifying concept, of the fair weather current balancing the current flow from thunderstorms and other electrified clouds (referred to slightly ambiguously by Wilson as “shower clouds”) is sketched out in notebooks of the 1920s (Wilson 1926) and presented in the second global circuit paper (1929):

I have long held that we must look to showers and thunderstorms as the main agents in the maintenance of the negative charge on the earth in fine weather regions; that they act as electric generators which remove positive electricity from the earth and supply it to the conducting upper atmosphere by which it is distributed over the whole earth. The upper atmosphere is thus maintained at a potential of nearly one million volts... There are on average nearly 2,000 thunderstorms in action at a given moment. An upward current of one ampere per thunderstorm would be more than sufficient to balance the downward current of the fine weather regions. (Wilson 1929)

In this paper Wilson refers to Brooks’ (1925) thunderday data and the results from the Carnegie voyages (discussed here in Sect. 2). As shown in Fig. 5, these measurements were not actually necessary for development of the global circuit concept, but it is likely that Wilson took them as corroboration of the validity of his “long held” ideas. Subsequent work has continued to validate and elaborate Wilson’s model, as was described in Sect. 2.

4.2 Detection of Planetary Atmospheric Global Circuits

The concept of a global atmospheric electric circuit is of value in studies both of terrestrial and planetary atmospheres. In the last decade it has been suggested that other planets could have a global circuit, with Mars as the prime candidate (Aplin 2006). In this final section a comparative approach will be used to suggest what could be learnt about other planets based on terrestrial atmospheric electricity. A more systematic study of extraterrestrial global circuits will also be proposed based on the experience gained from development of the terrestrial circuit.

The existence of physical mechanisms linking the terrestrial global circuit with climate is vigorously debated, as summarised in Sect. 3. A key role for the global circuit is that it continuously distributes ions throughout the atmosphere, and moves freshly-formed ions

⁷It is possible that Wilson could have learnt about the ionising upper atmosphere from conversations with E.V. Appleton (1892–1965) who was based in the Cavendish Laboratory from 1920–1924. In the cramped surroundings of the old laboratory in Free School Lane, interactions on topics of mutual scientific interest would seem very likely.

vertically in the fair weather conduction current. This transfer of ions may introduce ions to regions where they can grow, and new particle formation results. In addition, electrical transport could be important for some trace chemical species, particularly in extraterrestrial atmospheres where other transport mechanisms (e.g. convection) can be less important. On Earth, the global circuit forms part of a linking framework between the sun, space, and upper and lower atmospheres. Recent analysis of a long series of terrestrial potential gradient measurements shows that a quasi-periodicity known to be generated in the heliosphere (at 1.68 years) is also present in surface atmospheric electricity: should the common periodicities indeed have the same origin this provides direct evidence for the global circuit acting to couple heliospheric changes with the lower troposphere (Harrison and Märzc 2007). The relevance of electrical processes to the climate in extraterrestrial planetary atmospheres is more likely where solar radiation plays a more minor role, such as on Titan. Here, electrical interactions may control, for example, cloud formation and lifetime (Aplin 2006).

To define the optimal measurements to be made in another planetary environment, it is helpful to remember what defines a global circuit. The necessary requirements have been discussed elsewhere (e.g. Aplin 2006) and can be briefly summarised as:

- an upper conductive layer
- a lower conductive layer
- discharges or precipitation, to “charge” the circuit
- current flow in fair weather, to “discharge” the circuit

Detection of all these aspects is necessary to establish the existence of a planetary global circuit. (This should be distinguished from the central tenets discussed in Sect. 4.1 needed to originate the concept of a global circuit.) Table 2 shows which of these necessary parameters could be detected by measurements made from an orbiter or *in situ*. It is clear that Schumann resonance measurements are by far the most valuable single atmospheric electrical observation, since the existence of the Schuman resonance requires the existence of both upper and lower conducting layers, and electrical discharges for excitation (see e.g., Simoes et al. 2008). If Schumann resonances are detected, then only one further factor of vertical current flow is needed to confirm the existence of a global circuit. Non-detection of the Schumann resonances does not show there is no global circuit, as it is possible to have a circuit in which charge is only transferred by precipitation, with no discharges to excite the cavity. Measurement of Schumann resonance is most likely to result from *in situ* instrumentation, though it may be possible from an orbiter alone, through sensitive detection of leakage of the ELF radiation outside the cavity. At the moment there is no established remote sensing technology to measure vertical current flow (though this may ultimately be achieved through detection of charged species using their infra-red absorption properties, Aplin and McPheat 2005). *In situ* measurements are therefore necessary for the unambiguous identification of a global circuit.

The only *in situ* extraterrestrial atmospheric electrical measurements so far, made in Titan’s atmosphere during the descent of the Huygens probe in 2005, may have detected a Schumann resonance frequency at 36 Hz, though it is not yet established beyond doubt (Simoes et al. 2007; Béghin et al. 2007). The excitation mechanism is uncertain due to the probable rarity of electrical discharges; however, it is still possible that Titan could have a global circuit with precipitation as the major charge carrier (Owen et al. 2008), if the surface is adequately conductive compared to the atmosphere close to the surface. This surface-lower atmosphere conductivity ratio could be important, since on Earth it is very high ($\sim 10^{12}$) whereas the other “terrestrial” planets tend to have more conductive lower atmospheres and less conductive surfaces e.g. the same ratio for Mars ~ 100 . Future *in situ*

Table 2 Necessary conditions for a global circuit in a planetary atmosphere, and which of them could be determined from different measurements (indicated with a tick)

Condition measurement	Charge generation		Lower conductive surface	Upper conductive surface	Vertical current flowing
	Electrical discharges	Precipitation			
Schumann resonances	✓		✓	✓	
Atmospheric electric field	✓	✓ ^a			✓ ^b
Electrical conductivity					✓
Radar		✓	✓		
Broadband radio	✓				
Optical	✓				

^aIf measurements are made on rapid timescales

^bIf Ohm's Law is obeyed, i.e. little mechanical transport of aerosol particles

measurements currently planned for the ExoMars mission, e.g. a radio instrument and an electric field detector (Berthelier et al. 2000), should contribute to understanding some of these issues.

The classical Wilson global circuit model can probably only be applied to "Earth-like" planets or moons, with a well-defined surface and atmosphere, principally Venus, Mars and Titan. It is likely that very different circumstances, at, for instance, the giant planets, where there is no solid surface, will make any global circuit work in an entirely different way (Aplin 2006). For example, recent observations from the Cassini spacecraft suggest coupling between Saturn's thunderstorms and rings (Jones et al. 2006); this can only hint at the surprises planetary atmospheric electrical systems may have in store.

Acknowledgements K.A. Nicoll (University of Reading) provided Fig. 2. K.L. Aplin was partially supported by the U.K. Science and Technology Facilities Council.

References

- C. Andre, Comptes Rendus **117**, 729–732 (1893)
- K.L. Aplin, PhD thesis, The University of Reading, UK, 2000
- K.L. Aplin, Surv. Geophys. **27**, 63–108 (2006). doi:[10.1007/s10712-005-0642-9](https://doi.org/10.1007/s10712-005-0642-9)
- K.L. Aplin, R.A. McPheat, J. Atmos. Sol.-Terr. Phys. **67**(8–9), 775–783 (2005). doi:[10.1016/j.jastp.2005.01.007](https://doi.org/10.1016/j.jastp.2005.01.007)
- G. Beccaria, Della Elettricità Terrestre Atmosferica a Cielo Sereno (Turin, 1775)
- C. Béghin, F. Simões, V. Karnoselskikh et al., Icarus **191**(1), 251 (2007). doi:[10.1016/j.icarus.2007.04.005](https://doi.org/10.1016/j.icarus.2007.04.005)
- J.J. Berthelier, R. Grard, H. Laakso et al., Planet. Space Sci. **48**(12–14), 1193–1200 (2000)
- A.J. Bennett, R.G. Harrison, Weather **62**, 10 (2007). doi:[10.1002/wea.97](https://doi.org/10.1002/wea.97)
- B.P. Besser, Radio Sci. **42**, RS2S02 (2007). doi:[10.1029/2006RS003495](https://doi.org/10.1029/2006RS003495)
- C.E.P. Brooks, Geophys. Memo. **3**(24), 147–164 (1925)
- M.I. Budyko, Results of observations of atmospheric electricity (The World Network, Additional Issue, 1965–1969). (USSR Chief Administration of the Hydro-Meteorological Service, Leningrad, 1971)
- J. Canton, Philos. Trans. **48**, 780–785 (1753)
- K.S. Carslaw, R.G. Harrison, J. Kirkby, Science **298**, 1732 (2002)
- S. Chapman, Philos. Trans. R. Soc. Lond. A **218**, 1 (1919)

- B. Chauveau, *Électricité Atmosphérique*, vol. 3 (Librairie Octave Doin, Paris, 1925)
- C.A. Coulomb, in *Collection de Mémoires Relatifs à la Physique, Tome I* (Gauthier-Villars, Paris, 1784), pp. 113–114. Available online at <http://cnum.cnam.fr/fSYN/8CA121-1.html>
- H. Ebert, Phys. Z. **2**, 662–664 (1901)
- J.E. Elster, H. Geitel, Phys. Z **2**, 116 (1900)
- J.D. Everett, Philos. Trans. R. Soc. Lond. **158**, 347–361 (1868)
- E. Everling, A. Wigand, Ann. Phys. **66**(20), 261–282 (1921)
- I. Falconer, Metrologia **41**, S107–S114 (2004)
- W.S. Franklin, Science **15**(368), 112–113 (1902)
- H. Fukunishi, Y. Takahashi, M. Sato et al., Geophys. Res. Lett. **24**, 2973 (1997)
- M. Füllekrug, E.A. Mareev, M.J. Rycroft (eds.), *Sprites, Elves and Intense Lightning Discharges* (Springer, Dordrecht, 2006)
- P. Galison, *Image and Logic: A Material Culture of Microphysics* (University of Chicago Press, Chicago, 1997)
- H. Gerdien, Nachr. Ges. Wiss. Gött. **1903**, 383–399 (1903)
- H. Gerdien, Nachr. Ges. Wiss. Gött. **1904**, 277–299 (1904)
- H. Gerdien, Phys. Z. **6**, 800–801 (1905a)
- H. Gerdien, Nachr. Ges. Wiss. Gött. **1905**, 258–270 (1905b)
- H. Gerdien, Nachr. Ges. Wiss. Gött. **1905**, 447–458 (1905c)
- O.H. Gish, K.L. Sherman, in *Nat. Geogr. Soc. Techn. Papers. Stratosphere Series*, vol. 2, Washington, DC (1936)
- A. Gockel, Phys. Z. **4**, 871 (1903)
- R.G. Harrison, Space Sci. Rev. **94**, 381–396 (2000)
- R.G. Harrison, Weather **58**, 11–19 (2003)
- R.G. Harrison, Surv. Geophys. **25**, 441 (2004)
- R.G. Harrison, K.L. Aplin, Atmos. Env. **36**(25), 4037–4043 (2002)
- R.G. Harrison, K.L. Aplin, Atmos. Env. **37**(38), 5319–5324 (2003). doi:[10.1016/j.atmosenv.2003.09.042](https://doi.org/10.1016/j.atmosenv.2003.09.042)
- R.G. Harrison, A.J. Bennett, J. Atmos. Sol.-Terr. Phys. **69**, 515–527 (2007a). doi:[10.1016/j.jastp.2006.09.008](https://doi.org/10.1016/j.jastp.2006.09.008)
- R.G. Harrison, A.J. Bennett, Adv. Geosci. **13**, 17–23 (2007b)
- R.G. Harrison, K.S. Carslaw, Rev. Geophys. **41** (2003). doi:[10.1029/2002RG000114](https://doi.org/10.1029/2002RG000114)
- R.G. Harrison, W.J. Ingram, Atmos. Res. **76**(1–4), 49–64 (2005). doi:[10.1016/j.atmosres.2004.11.022](https://doi.org/10.1016/j.atmosres.2004.11.022)
- R.G. Harrison, F. März, Geophys. Res. Lett. **34**, L23816 (2007). doi:[10.1029/2007GL031714](https://doi.org/10.1029/2007GL031714)
- R.G. Harrison, K.P. Shine, in: *Hadley Centre Technical Note 6* (Met Office, Exeter, 1999)
- O. Heaviside, in: *Encyc. Brit. 10th*, vol. 9 (London, 1902), pp. 213–218
- V.F. Hess, Phys. Z. **13**, 1084 (1912)
- M. Hesse, in *A Companion to the Philosophy of Science*, ed. by W.H. Newton-Smith (Blackwell, Oxford, 2000), pp. 299–307
- I.M. Imyanitov, E.V. Chubarina, Electricity of the Free Atmosphere (Israel program for Scientific Translations, Jerusalem, 1967)
- G.H. Jones, N. Krupp, H. Krüger et al., Geophys. Res. Lett. **33**, L21202 (2006). doi:[10.1029/2006GL028146](https://doi.org/10.1029/2006GL028146)
- A.K. Kamra, M. Ravichandran, J. Geophys. Res. **98**(D12), 22,875–22,885 (1993)
- A.E. Kennelly, Electr. World Eng. **32**, 473 (1902)
- B. Lovell, Notes Rec. R. Soc. Lond. **51**(1), 151–153 (1997)
- W. Lowrie, in *Fundamentals of Geophysics*, 2nd edn. (Cambridge University Press, Cambridge, 2007), pp. 274–276
- F. März, J. Geophys. Res. **81**(25), 4566 (1976)
- R. Markson, Nature **273**, 103 (1978)
- R. Markson, Bull. Am. Meteorol. Soc. **88**, 1 (2007)
- A. McAdie, Science **61**(1586), 540 (1925)
- A. Mika, C. Haldoupis, Space Sci. Rev. (2008, this issue)
- E. Mishin, G. Milikh, Space Sci. Rev. (2008, this issue). doi:[10.1027/s11214-008-9346-z](https://doi.org/10.1027/s11214-008-9346-z)
- R.P. Mülheisen, Pure Appl. Geophys. **84**, 112–115 (1971)
- R.P. Mülheisen, in *Electrical Processes in Atmospheres*, ed. by H. Dolezalek, R. Reiter (Steinkopf, Darmstadt, 1977), pp. 467–476
- N. Olsen, A. Kuvshinov, Earth Planets Space **56**, 525 (2004)
- N.R. Owen, K.L. Aplin, P.A. Stevens, J. Phys. Conf. Ser. (2008 in press). Available online at <http://epubs.cclrc.ac.uk/index>
- V.P. Pasko, M.A. Stanley, J.D. Mathews, U.S. Inan, T.G. Woods, Nature **416**, 152 (2002)
- J. Read, Philos. Trans. R. Soc. Lond. **81**, 185–212 (1791)
- R.G. Roble, I. Tzur, in *The Earth's Electrical Environment*, ed. by E.P. Krider, R.G. Roble (National Academy Press, Washington, 1986), pp. 206–231

- M.J. Rycroft, J. Atmos. Sol.-Terr. Phys. **68**, 445 (2006)
- M.J. Rycroft, M. Füllekrug, J. Atmos. Sol.-Terr. Phys. **66**, 1103 (2004)
- M.J. Rycroft, S. Israelsson, C. Price, J. Atmos. Sol.-Terr. Phys. **62**, 1563–1576 (2000). doi:[10.1016/S1364-6826\(00\)00112-7](https://doi.org/10.1016/S1364-6826(00)00112-7)
- M.J. Rycroft, A. Odzimek, N.F. Arnold et al., J. Atmos. Sol.-Terr. Phys. (2007). doi:[10.1016/j.jastp.2007.09.004](https://doi.org/10.1016/j.jastp.2007.09.004)
- M.J. Rycroft et al., Space Sci. Rev. (2008, this issue). doi:[10.1007/s11214-008-9368-6](https://doi.org/10.1007/s11214-008-9368-6)
- C.P.R. Saunders, Space Sci. Rev. (2008, this issue). doi:[10.1007/s11214-008-9345-0](https://doi.org/10.1007/s11214-008-9345-0)
- W.B. Schiffer, in *Draw the Lightning Down: Benjamin Franklin and Electrical Technology in the Age of Enlightenment* (University of California Press, Berkeley, 2003), pp. 1–11
- R.W. Schunk, A.F. Nagy, *Ionospheres—Physics, Plasma Physics and Chemistry* (Cambridge University Press, Cambridge, 2000)
- F. Simoes, R. Grard, M. Hamelin et al., Planet. Space Sci. **55**, 1978–1989 (2007). doi:[10.1016/j.pss.2007.04.016](https://doi.org/10.1016/j.pss.2007.04.016)
- F. Simoes et al., Space Sci. Rev. (2008, this issue)
- G.C. Simpson, Philos. Trans. R. Soc. A **205**, 61–97 (1906a)
- G.C. Simpson, Mon. Wea. Rev. **34**(1), 16–17 (1906b)
- G.C. Simpson, Philos. Trans. R. Soc. A **209**, 379–413 (1909)
- G.C. Simpson, Geogr. J. **97**(6), 383–385 (1941). doi:[10.2307/1788175](https://doi.org/10.2307/1788175)
- H.T. Su, R.R. Hsu, A.B. Chen et al., Nature **423**, 974 (2003)
- W. Thomson, *Report of 29th Meeting*, British Association for the Advancement of Science, Aberdeen, 1859
- B.A. Tinsley, Space Sci. Rev. **94**(1–2), 231–258 (2000)
- B.A. Tinsley, R.A. Heelis, J. Geophys. Res. **98**, 10375–10384 (1993)
- B.A. Tinsley, R.P. Rohrbaugh, M. Hei, Atmos. Res. **59–60**, 115–135 (2001)
- S.N. Tripathi, PhD thesis, The University of Reading, UK, 2000
- S.N. Tripathi, R.G. Harrison, Atmos. Res. **62**, 57–70 (2002)
- S.N. Tripathi, S. Vishnoi, S. Kumar et al., Q. J. R. Met. Soc. **132**, 1717 (2006)
- J. Tuma, Sitz. Akad. Wiss. Wien, 227–260 (1899)
- L. Wahlin, J. Geophys. Res. **99**(D5), 10,767 (1994)
- F.J.W. Whipple, Q. J. R. Meteorol. Soc. **55**, 351 (1929)
- F.J.W. Whipple, F.J. Scrase, Meteorol. Off. Geophys. Mem. 68 (1936)
- A. Wigand, Terr. Mag. Atm. Elect. **19**, 93–101 (1914)
- A. Wigand, Ann. Phys. **60**(18), 81–109 (1921)
- E.R. Williams, in *Encyclopedia of Atmospheric Sciences*, ed. by J.R. Holton, J.A. Pyle, J.A. Curry (Academic, New York, 2002), pp. 724–733
- E.R. Williams, In Proc. 13th Int. Conf. Atm. Elect., Beijing, China, 13–17 August 2007
- E.R. Williams, S.J. Heckman, J. Geophys. Res. D **98**(3), 5221 (1993)
- C.T.R. Wilson, Philos. Trans. R. Soc. Lond. A **189**, 265–307 (1897)
- C.T.R. Wilson, Philos. Trans. R. Soc. Lond. A **189**, 403–453 (1899)
- C.T.R. Wilson, Proc. Camb. Philos. Soc. **13**, 364 (1906)
- C.T.R. Wilson, Proc. R. Soc. Lond. A **80**(542), 537–547 (1908)
- C.T.R. Wilson, Notebook entitled “Thunderstorms; Condensation” ref CW/A/9 (1909)
- C.T.R. Wilson, Philos. Trans. R. Soc. Lond. A **221**, 73 (1921)
- C.T.R. Wilson, Notebook entitled “Atmospheric electricity” ref CW/B/7 (1926)
- C.T.R. Wilson, J. Franklin Inst. **208**(1), 1–12 (1929)
- Y. Yair, Space Sci. Rev. (2008, this issue). doi:[10.1007/s11214-008-9348-x](https://doi.org/10.1007/s11214-008-9348-x)
- F. Yu, R.P. Turco, J. Geophys. Res. **106**(D5), 4797–4814 (2001). doi:[10.1029/2000JD900539](https://doi.org/10.1029/2000JD900539)
- B. Zolss, Phys. Z. **5**, 106 (1904)

Updated Review of Planetary Atmospheric Electricity

Y. Yair · G. Fischer · F. Simões · N. Renno · P. Zarka

Originally published in the journal Space Science Reviews, Volume 137, Nos 1–4.
DOI: [10.1007/s11214-008-9349-9](https://doi.org/10.1007/s11214-008-9349-9) © Springer Science+Business Media B.V. 2008

Abstract This paper reviews the progress achieved in planetary atmospheric electricity, with focus on lightning observations by present operational spacecraft, aiming to fill the hiatus from the latest review published by Desch et al. (*Rep. Prog. Phys.* 65:955–997, 2002). The information is organized according to solid surface bodies (Earth, Venus, Mars and Titan) and gaseous planets (Jupiter, Saturn, Uranus and Neptune), and each section presents the latest results from space-based and ground-based observations as well as laboratory experiments. Finally, we review planned future space missions to Earth and other planets that will address some of the existing gaps in our knowledge.

Keywords Lightning · Thunder · Radio emissions · Whistlers · Transient luminous events · Charging processes · SED—Saturn Electrostatic Discharges · Optical emissions · Dust · Dust devils · Triboelectric charging · Ionosphere · Spectrum · Cassini · Voyager · Mars Express · Venus Express · Remote sensing · Flash rate · Terrestrial gamma-ray flashes · Satellite · Mars · Venus · Jupiter · Titan · Saturn · Uranus · Neptune · Pioneer Venus Orbiter · Galileo · Electric field · Conductivity · Schumann resonance · Optical efficiency · Hydrocarbon · Cloud

Y. Yair (✉)

Department of Life and Natural Sciences, Open University of Israel, Ra'anana 43107, Israel
e-mail: yoavya@openu.ac.il

G. Fischer

Department of Physics and Astronomy, University of Iowa, Iowa City, IA 52242, USA

F. Simões

Centre d'Etude des Environnements Terrestre et Planétaires, 4, Avenue de Neptune, Saint Maur, France

N. Renno

Department of Atmospheric, Oceanic and Space Sciences, University of Michigan, Ann Arbor, MI 48109, USA

P. Zarka

Observatoire de Paris, Meudon, France

1 Introduction

There is now numerous evidence of lightning activity in atmospheres of the planets of our solar system. The most unequivocal and strong observations are optical emissions detected by cameras of orbiting or flying-by spacecraft. The intense lightning light is caused by the heating of the discharge channel, which emits continuum and line spectra that are observed directly as scattered light by clouds (on Earth, Jupiter; controversial for Venus). Lightning can also be observed indirectly by measurements of transient luminous events (TLE) caused by them in the region above the cloud layers (Earth). In addition, indirect electromagnetic evidence for lightning activity is provided by whistlers propagating along magnetic field-lines penetrating the ionosphere, high frequency (HF) and very high frequency (VHF) emissions above the ionospheric cut-off frequency (discussed by Zarka et al. (2008) in this issue), low-frequency radio emission by the current channel acting as an antenna in a broad spectrum peaking (at Earth) at $\sim 1\text{--}10$ kHz (decreasing as f^{-1} to f^{-2} at higher frequencies) and finally by detecting the signature of Schumann Resonances at extremely low frequencies (< a few tens of Hz), which are trapped in the surface-ionosphere cavity. The major properties of the ionospheres of various planets are summarized in Table 1. Spectroscopic observations by ground-based telescopes or orbiting spacecraft offer chemical evidence of lightning by identifying non-equilibrium concentrations of certain compounds and the presence of exotic species, which cannot be explained by other phenomena. Indeed, the prediction that lightning takes place in other planetary atmospheres dates back to the mid-1970s, when data on the chemistry and meteorology of different planets was obtained from spacecraft and ground-based spectroscopy (e.g. Bar-Nun 1975, 1979). The importance of lightning as an agent for chemical reactions in pre-biotic circumstances was recognized even earlier, in the famous Urey–Miller experiments (Miller 1953), where electrical sparks were

Table 1 Characteristics of planetary ionospheres

Body	Characteristic	Reference
Venus	Ionospheric layer peak at ~ 140 km / electron density $\sim 4 \cdot 10^5 \text{ cm}^{-3}$	Knudsen et al. (1987)
Mars	Ionospheric layer peak at ~ 120 km / electron density $\sim 1.5 \cdot 10^5 \text{ cm}^{-3}$ Sporadic ionospheric layer in the range 65–110 km / electron density $\sim 8 \cdot 10^3 \text{ cm}^{-3}$	Wang and Nielsen (2003) Pätzold et al. (2005)
Titan	Ionospheric layer peak ~ 1250 km / electron density $\sim 3.8 \cdot 10^3 \text{ cm}^{-3}$ Atmospheric conductive layer at ~ 60 km / electron density $\sim 650 \text{ cm}^{-3}$	Wahlund et al. (2005) Hamelin et al. (2007)
Jupiter	Ionospheric layer peak ~ 1000 km / electron density $\sim 10^5 \text{ cm}^{-3}$, another layer ~ 2000 km with $\sim 10^4 \text{ cm}^{-3}$ Lower ionospheric layers (~ 200 km) might attenuate HF radio waves	Schunk and Nagy (2000) Zarka (1985a, 1985b)
Saturn	Ionospheric peaks from 1200–2500 km / electron density $\sim 5 \cdot 10^4 \text{ cm}^{-3}$ Low frequency cutoff of Saturn lightning suggests diurnal variation of factor ~ 100	Nagy et al. (2006) Kaiser et al. (1984)
Uranus	Two sharp ionospheric layers from 1500–2000 km with peak electron densities $\sim 10^5 \text{ cm}^{-3}$	Lindal et al. (1987)
Neptune	Ionospheric layer peak ~ 1400 km / electron density $\sim 2.5 \cdot 10^3 \text{ cm}^{-3}$	Tyler et al. (1989)

used to simulate atmospheric lightning activity supposedly prevalent in the Archaean Earth. These two lines of research have since converged with many other aspects of planetary science. Thus, planetary atmospheric electricity has become a field that involves multiple disciplines such as atmospheric thermodynamics, heterogeneous chemistry, cloud physics, spectroscopy, electromagnetic wave propagation, remote sensing and natural hazards and spaceflight risk assessment.

The present contribution follows in the footsteps of earlier reviews on the subject which appeared in the scientific literature. Among these are Levin et al. (1983), Williams et al. (1983), Rinnert (1985), Russell et al. (1993), Desch et al. (2002) and Aplin (2006). It aims to give the reader an updated description of the latest advances and new understanding which relate to electrical phenomena in the solar system gained through observations, laboratory work, numerical simulations and theoretical studies. We limit this review to those processes occurring below the ionosphere, and thus shall not discuss auroral processes or radiation belt phenomena, unless they are strongly coupled to lightning activity.

1.1 Existing and New Observation Platforms and Technologies

1.1.1 *Spacecraft*

Cassini/Huygens: The Cassini/Huygens mission was launched more than 10 years ago in October 1997 and arrived at Saturn in July 2004. On its way to Saturn it made two flybys of Venus in 1998 and 1999, one of Earth in 1999, and one of Jupiter at the end of 2000. Instruments on the Cassini orbiter capable of detecting lightning are the ISS (Imaging Science Subsystem) and the RPWS (Radio and Plasma Wave Science) instrument. The ISS platform consists of two cameras (wide and narrow-angle), each of them equipped with a charge-coupled device (CCD) sensor of 1024 pixels squared (Porco et al. 2004). They have a large number of filters, spanning the wavelength range from 200 to 1100 nm, including a narrow-band H_α filter for the atomic hydrogen line at 656 nm. The RPWS instrument consists of three electric and magnetic antennas and various receivers in the frequency range from a few Hz up to 16 MHz (Gurnett et al. 2004). It is capable of detecting either lightning whistlers or HF radio emissions (also called “sferics”) above the ionospheric cutoff frequency of the respective planet, and the three electric antennas enable polarization and direction finding measurements. The Huygens Probe landed on Titan in January 2005 and the PWA (Permittivity, Wave, and Altimetry) package of the HASI (Huygens Atmospheric Structure Instrument) was equipped with several sensors capable of detecting lightning (Fulchignoni et al. 2002). It was able to measure AC electric fields up to 11.5 kHz, and a special Schumann mode could measure the power spectral density below 100 Hz with 3 or 6 Hz resolution. Each AC electric field data packet consisted of 80 integrated spectra with either 32 (above 60 km) or 14 lines (below 60 km); each spectrum was also split, then integrated in 3 frequency ranges, to provide impulsive event dynamics over shorter time scales.

New Horizons: This Pluto-bound spacecraft was launched on January 19th 2006 and made a Jupiter fly-by on February 28th, 2007. It carries a 7-instrument payload, designed to study the surface properties of the icy worlds of the Pluto–Charon system and to monitor interplanetary dust and solar wind particles. The LORRI (Long Range Reconnaissance Imager) instrument consists of an 8.2-inch (20.8-centimeter) telescope with a CCD and provides images of high angular resolution, $\sim 5 \mu\text{rad}$. This instrument detected multiple lightning flashes on Jupiter’s night side (Baines et al. 2007; details in Sect. 3.1). The spacecraft also carries LEISA (Linear Etalon Infrared Spectral Imager) and ALICE—an ultraviolet imaging spectrometer which was capable of detecting the Ly- α nightglow on Jupiter (Gladstone et al. 2007).

Mars Express (MEX): This spacecraft was launched on June 2nd 2003, and entered a nearly-polar orbit around Mars on December 25th 2003. While the Beagle-2 Lander mission was lost, the MEX orbiter accomplished most of its intended scientific objectives. The main atmospheric instruments on board MEX are the Energetic Neutron Atoms Analyzer (ASPERA), the Radio Science Experiment (MaRS) for atmospheric and environmental sounding, the Planetary Fourier Spectrometer (PFS) for atmospheric composition and circulation, and the SPICAM, an ultraviolet and infrared atmospheric spectrometer. The MEX also carries a high-resolution stereo camera (HRSC) used for surface imaging. The spacecraft is equipped with the MARSIS instrument ionospheric and surface sounding radar, whose receivers could potentially detect electromagnetic impulses from Martian dust storm discharges.

Venus Express (VEX): Launched on November 9th 2005, this European spacecraft entered a Venusian orbit on April 11th 2006. It is an upgraded version of the MEX mission with similar instruments. The spacecraft monitors the atmosphere with an array of 7 instruments. VEX (but not MEX) has a magnetic field instrument called MAG, which is considered to be optimal for detection of lightning-associated electromagnetic bursts (Russell et al. 2006). The main camera on board is the Venus Monitoring Camera (VMC) that takes images of Venus in 4 narrow band filters from UV to near-IR all sharing one CCD. The spatial resolution is 0.2 km to 45 km per pixel, depending on the distance from the planet. The full disc of Venus is in the VMC field-of-view near the apocentre of the orbit. Additional instruments include the SPICAV (identical to the MEX SPICAM), the VeRa for radio sounding and the VIRTIS (Visible and Infrared Thermal Imaging Spectrometer) which operates at wavelengths between 0.3 and 5 μm . The infrared capability of VIRTIS is especially well fitted to the thermal sounding of the night side atmosphere allowing a tomography of the atmosphere down to the surface.

Earth Orbiting Spacecraft: Monitoring of terrestrial lightning from space on a continuous basis was first achieved by the Optical Transient Detector (OTD), a payload on board the NASA Micro-Lab-1 satellite that was launched in April 1995. The orbital inclination of the satellite was 70 degrees and enabled the coverage of almost the entire planetary thunderstorm activity from an altitude of 740 km. The OTD instrument optically detects lightning flashes occurring within its $1300 \times 1300 \text{ km}^2$ field-of-view during both day and night. A statistical examination of OTD lightning data reveals that nearly $1.4 \cdot 10^9$ flashes occur annually on Earth, translating to a rate of 44 ± 5 flashes per second (Christian et al. 2003). The OTD was an engineering prototype for the LIS instrument on board the TRMM (Tropical Rainfall Measuring Mission) satellite which was launched in 1997 to a 35 degrees inclination orbit, that focused its lightning mapping capability on the tropics, reaching 90% detection efficiency of both cloud-to-ground and intracloud flashes. With additional instruments on-board such as the Precipitation Radar (PR), the Visible and Infrared Scanner (VIRS) and the TRMM Microwave Imager (TMI), this satellite provides unique insights into precipitation patterns in the tropics and the relationships between lightning and rain. The data from both instruments is readily available on-line at NASA's Global Hydrology and Climate Center (<http://thunder.nsstc.nasa.gov/>).

Terrestrial lighting is also being monitored by spaceborne VHF detectors on the FORTE and DEMETER satellites. The Fast On-orbit Recording of Transient Events (FORTE) satellite was launched on August 29th 1997, to a nearly circular, 70° inclination orbit. It carries two tunable receivers that have a 22 MHz analog bandwidth, covering the frequency range from 20 to 300 MHz (HF and VHF bands), as well as an optical sensor with a 10 nm pass-band filter centered at 777.4 nm. It also carries a single-element silicon photodiode (PDD),

which has a 6% detection efficiency of cloud-to-ground flashes, and thus is able to geolocate only the strongest flashes (e.g., superbolts; Turman 1977). The DEMETER mission is reviewed by Parrot et al. (2008) in another chapter of this issue.

Boeck et al. (1994) utilized the space shuttle payload-bay cameras to observe the Earth's limb above thunderstorms and demonstrate that transient luminous events can be observed from low earth orbit. Such episodic observations were repeated with more sensitive instruments by Yair et al. (2004) and Blanc et al. (2004). The capability for a continuous monitoring of TLE activity on a global scale was achieved by the FORMOSAT satellite, launched on May 20th 2004 to a 99.1° inclination, 891 km high, circular orbit. The Imager of Sprites and Upper Atmosphere Lightning (ISUAL) payload comprises an array photometer, an intensified imager and a spectrophotometer with 6 wavelengths, covering the main emissions of sprites and elves. The global coverage of FORMOSAT enables detailed mapping of the occurrence of TLEs (see Sect. 2.1.2 below). The RHESSI satellite is being used to monitor terrestrial gamma flashes (TGFs), originally discovered by the BATSE instrument on board the Compton Gamma-Ray Observatory (see Sect. 2.1.3 below). There is now considerable evidence linking TGFs with lightning (Smith et al. 2005).

1.1.2 Telescopes

UTR-2: This is the world largest radio-telescope in the decametric frequency range (operated from about 8–32 MHz) located in Kharkov, Ukraine. It consists of 2040 dipoles and has an effective area of 150,000 m² (Konovalenko et al. 2001). Its sensitivity of a few Jansky (Jy) enables it to detect lightning from Saturn that is expected to produce a flux of the order of 100 Jy at Earth (Zarka et al. 2004).

LOFAR: The future Low Frequency Array (LOFAR) will be a large baseline next-generation radio-telescope that is being built in Northern Europe. It will operate in the frequency range from 30 to 240 MHz, and its effective area should be $>10^5$ m² (Kassim et al. 2004). Besides astronomical observations, it could also be used to monitor lightning on Saturn and Uranus (Zarka et al. 2004).

NASA/IRTF: This is the largest infrared telescope available for planetary science, with a 3-m diameter mirror. Several upgrades and technological improvements have been made and the observatory now contains five operational instruments: (a) SpeX, a 1–5 micron cross-dispersed medium-resolution spectrograph (b) CSHELL, a 1–5 μm high-resolution spectrograph; (c) MIRSI, a 5–25 μm camera and low-resolution spectrometer; (d) NSFCAM2, a 2048 × 2048 pixel, 1–5 μm camera with a 0.04 arcsec/pixel scale; and (e) Low-resolution 3–14 μm spectrograph and high-resolution spectrographs for 8–25 μm. The IRTF allocates 50% of its observation time to solar-system bodies and made numerous contributions to the study of the outer planets' atmospheres (Sánchez-Lavega et al. 2001; Orton et al. 2006; Simon-Miller et al. 2006; and many others). The IRTF is able to identify trace molecular constituents in planetary atmospheres, thus providing indirect evidence of the presence of lightning, based on the fact that lightning is a high-temperature discharge process that produces non-equilibrium chemical compounds (Bar-Nun 1975).

2 Lightning Activity and Atmospheric Electricity on Solid Surface Bodies

2.1 Earth

Hundreds of new papers and several comprehensive book chapters have been published since the brief phenomenology of terrestrial lightning activity given in Desch et al. (2002),

the most comprehensive one is the book by Rakov and Uman (2003). We shall present here only those aspects that are essential for comparative studies of the meteorological and microphysical conditions conducive to the generation of lightning. Admittedly, there is a huge body of new knowledge concerning the properties of lightning initiation and propagation, the very nature of which may be different in alien circumstances. New techniques and observation systems have been developed that yield exciting insights into the intricate details of the lightning phenomenon. However, the limited scope of this review dictates a focus on the most basic and important aspects. Detailed information is found in the chapter by Stolzenburg and Marshall (2008) in this issue.

2.1.1 Lightning

Lightning on Earth is concentrated between $\pm 60^\circ$ latitude, with the large majority (>90%) above continental land-masses. The region of maximum lightning activity displays a distinct seasonal dependence and migrates with the Intertropical Convergence Zone (ITCZ) as it moves across the equator to the summer hemisphere. The global planetary rate was estimated by Christian et al. (2003) to be ~ 45 flashes per second based on the OTD and LIS space-borne sensors, a frequency similar to that which was estimated based on Cassini's HF measurements during its Earth flyby in 1999 (70 s^{-1} , Gurnett et al. 2001). The global lightning activity is concentrated in the convectively active continental tropical regions, and shows a clear maximum around 16–17 LT and a minimum in the early morning hours 06–09 LT. The oceanic lightning activity has a marginal contribution to the global rate and is spread evenly along the day (the reader is invited to view the statistics published at <http://thunder.msfc.nasa.gov/>). Most lightning occurs inside thunderclouds (IC or intracloud flashes) and only the minority connects with the surface (CG or cloud-to-ground flashes). For obvious reasons, CG lightning discharges have been the main focus of research and the typical values of all their parameters are known quite accurately (see Table 1.1, page 7 in Rakov and Uman 2003). The details of the discharge process in its various stages are also well documented on the sub-millisecond scale (Table 1.2, ibid.).

In our solar system, cloud-to-ground lightning might be unique to Earth, because there are no similar conditions in any other planet to allow the propagation of a (stepped) leader from the clouds to the ground (with the possible exception of Mars). Thus, intracloud flashes are probably the typical type of planetary lightning and hence we devote more attention to their features. Intracloud discharges in terrestrial clouds often begin within the negative charge center and are accompanied by strong initial breakdown pulses which last 50–80 μs . They produce strong HF emissions whose amplitudes are 10 times larger than in CG flashes, and are termed “compact intracloud discharges”. These discharges are thought to be responsible for the Trans-Ionospheric Pulse Pairs (TIPPs) detectable by satellites (FORTE; Jacobson and Light 2003) and ground-based VLF/LF sensors (Smith et al. 2004). TIPPs appear as pairs of very brief dispersed HF radio bursts, each lasting a few microseconds and separated by a few tens of microseconds (Massey and Holden 1995), that were identified as the direct and reflected signals of compact intracloud discharges.

Interestingly, Shao and Jacobson (2002) found the TIPPs observed with the FORTE satellite to be highly polarized emissions on the contrary to other VHF signals accompanying more common discharge processes like initial ground strokes, dart leaders or K-streamers. The intracloud discharge process is slow and the initial breakdown pulses are separated by 600–800 μs , a factor ~ 10 longer compared to a CG flash. The processes in the late stages of intracloud flashes resemble the J- and K-changes found in the interstroke intervals of regular CGs. Recent advances in 3D VHF source mapping technology showed

the bipolar nature of the intracloud discharge process (Thomas et al. 2001) and measured the peak powers in the 60–66 MHz pass-band where they varied from a typical minimum of about 1 W up to 10–30 kW. The radiation sources indicate the location of the main charge regions in a storm and the strongest ones were found to reside in the upper positive charge center. Coleman et al. (2003) also used 3D VHF mapping and showed good agreement between the altitudes of horizontal lightning channels and the altitudes of maximum electric potential (measured by balloons). Lightning flashes appear to deposit charge of opposite polarity in relatively localized volumes within the clouds, thus modifying the tri-polar state and creating a complex, multi-polarity structure (Stolzenburg et al. 2001; Stolzenburg and Marshall 2008, this issue).

2.1.2 Transient Luminous Events

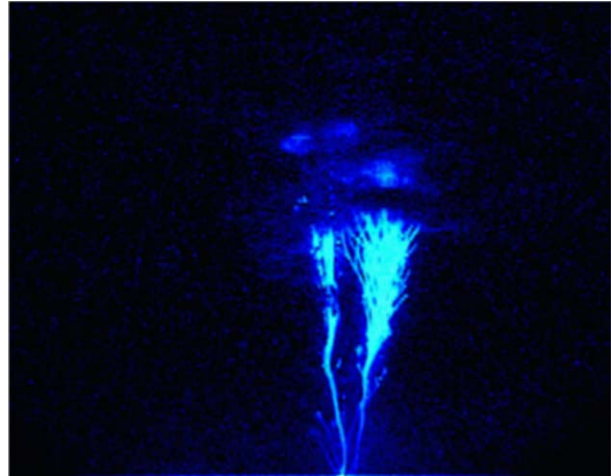
Transient Luminous Events (TLEs) is the collective name given to a wide variety of optical emissions which occur in the upper terrestrial atmosphere above active thunderstorms. Since their discovery these very brief, colorful phenomena have been studied from the ground, balloons, aircraft, the space shuttle, the ISS (International Space Station) and orbiting satellites. There is a growing body of literature which covers the phenomenology and theory of TLE generation (we refer the interested reader to the comprehensive volume edited by Füllekrug et al. (2006)). Distinct classes and names were given to the various forms of TLEs, all of which allude to their rapid unpredictable nature: Jets, Sprites, Elves, Pixies to name but a few. Telescopic imaging (Gerken and Inan 2001) and the use of high-speed imagers (Cummer et al. 2006a) have greatly improved the knowledge of the fine structure of these emissions and their initiation and propagation mechanisms. The inhomogeneous and transient variability of the terrestrial atmosphere at these heights is believed to play a crucial role in the initiation of TLEs—e.g. gravity waves, chemical reactions and meteors modify the local electrical properties of the mesosphere, making it more conducive to electrical breakdown processes. The molecular basis for the emissions observed in sprites is thoroughly discussed by Pasko (2007). Sprites are usually associated with intense positive cloud-to-ground lightning and are initiated at a height of 70–80 km, from which they propagate in visible tendrils downwards and upwards. Elves occur higher up, around 90–95 km above the ground and are a result of the interaction between the propagating Electromagnetic Pulse (EMP) from the lightning and the ionosphere (Inan et al. 1997). They have not been found to correlate with the polarity of the parent lightning.

A new class of TLE which extends from cloud tops all the way up toward the ionosphere was discovered by Pasko et al. (2002) and Su et al. (2003) and was nicknamed “gigantic jets” (Fig. 1). It is believed to short-circuit the cloud charge to the upper atmosphere. The Earth’s global rate of TLEs was estimated to be a few per minute based on observations from the space shuttle (Yair et al. 2004), the International Space Station (Blanc et al. 2004) and from the continuing monitoring by the FORMOSAT satellite (Cummer et al. 2006b). Though TLEs have not been detected in any other planetary atmosphere, their existence is theoretically possible and they are likely to occur (Yair et al. 2007).

2.1.3 Terrestrial Gamma Ray Flashes (TGFs)

Relativistic runaway electrons were considered by various authors (e.g. Gurevich et al. 1992; Roussel-Dupré and Gurevich 1996; Lehtinen et al. 1997) as a potential source of ionization and optical emissions related to sprites. In fact, runaway electrons necessarily must produce X-rays and gamma rays in interaction with air particles. However, due to their attenuation in

Fig. 1 Enhanced color image of a gigantic jet, observed by Pasko et al. (2002). The propagation of the discharge was from cloud top until the base of the ionosphere at ~ 95 km



air, their detection is difficult. Suszcynsky et al. (1996) showed that for energies of the order of MeV, the X-ray attenuation length is around 100 m to 1 km at thunderstorm altitudes. Suszcynsky et al. (1996) also reviewed the ground-based and low-altitude measurements of previous X-ray measurements and remained somewhat skeptical about positive results. But, X-ray observations with balloon-borne measurements within thunderclouds were reported by Eack et al. (1996), and Moore et al. (2001) associated their X-ray measurements with stepped leaders from ground flashes observed on a mountain top. The first observations of Terrestrial Gamma Ray Flashes (TGFs) from space were related to thunderstorms on Earth by Fishman et al. (1994). The Burst and Transient Signal Experiment (BATSE) onboard the Compton Gamma Ray Observatory detected 50 X-ray bursts with a typical duration of a few milliseconds in four years. This detection was later confirmed by the RHESSI (Reuven Ramaty High Energy Solar Spectroscopic Imager) satellite, which typically detects 10 to 20 TGFs per month (Smith et al. 2005). Dwyer and Smith (2005) inferred from Monte Carlo simulations of TGF spectra in comparison with RHESSI observations that the TGFs might stem from a source altitude around 15–21 km, which was also confirmed by Williams et al. (2006). Dwyer et al. (2005) also reported the production of X-ray bursts by laboratory sparks in air. In a recent paper, Stanley et al. (2006) link TGFs to intracloud discharges which transport electrons upward. Although the detection of atmospheric gamma-ray bursts and X-rays are somewhat difficult due to their attenuation in the surrounding medium, they might open a new wavelength window for future detection and studying of lightning also in other planetary atmospheres.

2.2 Venus

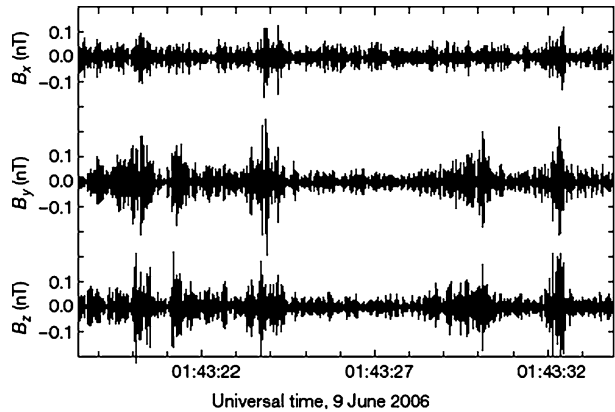
Venus is completely covered by a thick, optically opaque layer of sulfuric acid clouds, which rotate faster than the planet (super-rotate). There are at least three cloud decks, between ~ 50 and 70 km above ground, whose altitude, composition and size distribution (in 4 discrete particle-size modes) was derived from descent probes measurements. There is little evidence for small scale convective structures or for vigorous vertical motions within this essentially stratus-like planetary scale envelope. Venus has an induced “magnetosphere”, where the interplanetary magnetic field is draped around the planet. After the Magellan radar mapping mission of the early 90s, Venus has become in the words of Schilling (2005) “our neglected

neighbor", and relatively little research effort was directed to what was once considered to be "*our sister planet*". As a result, the controversy concerning the very existence, location and frequency of lightning on Venus remains unresolved.

Radio wave observations that were interpreted as likely due to lightning (Ksanfomaliti 1979; Russell 1991; Russell et al. 1993, 2006) have not been firmly confirmed by measurements in the visible spectrum, though two optical observations are claimed—one performed onboard Venera 9 (Krasnopol'sky 1980) and another with a ground-based telescope (Hansell et al. 1995). Similar radio waves detected by the Galileo and Cassini spacecraft during their respective flybys were given different interpretations (Gurnett et al. 1991, 2001). The crux of the matter is that apart from that single attempt by Hansell et al. (1995), no systematic search for Venusian lightning by a dedicated instrument on a spacecraft or on the ground was conducted, and the existing optical and electromagnetic data is insufficient to elucidate the matter completely. As Desch et al. (2002) state: "*Progress in resolving the central controversy of Venusian lightning will probably require either an extensive ground-based optical search or an orbiter with a camera and HF receiver*". The non-detection of HF signals by the Cassini spacecraft (Gurnett et al. 2001) sets a lower limit on lightning activity, but it can be argued that the short sampling time during the two flybys coincided with a quiet period with subdued lightning activity, and thus misrepresents the true planetary rate (see Zarka et al. 2008 in this issue for further discussion). The little numerical work done on the possible charging mechanisms and electrical field build-up within Venusian clouds all date back to the early 80 s, and lack the sophistication of contemporary terrestrial cloud models (reviewed by Yair 2008 in this issue). This leaves the question on the ability of the multiple stratiform cloud layers in Venus to actually separate sufficient charge for electrical breakdown largely open.

Recently, high-resolution spectra of Venus in the NO band at 5.3 μm were acquired using the TEXES spectrograph at the IRTF (Krasnopol'sky 2006). An NO mixing ratio of 5.5 ± 1.5 ppb was detected below 60 km. The photochemical impact of the measured NO abundance is significant and cannot be explained by chemical reactions induced by cosmic ray ionization alone, leaving lightning as the only possible source (Krasnopol'sky 2006). The required flux of NO corresponds to a lightning energy deposition of $0.19 \pm 0.06 \text{ erg cm}^{-2} \text{ s}^{-1}$. For an assumed flash energy of $\sim 10^9 \text{ J}$, the global flash rate should be $\sim 90 \text{ s}^{-1}$ or $\sim 6 \text{ km}^{-2} \text{ y}^{-1}$. Such a high flash rate is consistent with the analysis of the Pioneer Venus Orbiter (PVO) VLF data, that yielded a rate of 250 s^{-1} based on the assumption that lightning occurs only between $\pm 30^\circ$ latitude and during 18–24 h LT (Ho et al. 1995). Even if that calculation can be considered overly optimistic, additional supporting evidence for at least some lightning activity in the Venusian atmosphere was given by Strangeway (1995), who maintained that lightning is the most probable explanation for the plasma waves detected at low altitudes in the nightside ionosphere of Venus by the PVO. The Venus Express mission has yet to produce optical images of lightning by the VMC and VIRTIS instruments. However, Russell et al. (2007) reported clear indications of lightning activity. A 128 Hz sampling rate was used by MAG for 2 minutes at periapsis for each orbit until December 2006, and from that time onwards the high-rate sampling switched to 10 minutes at periapsis. The received data show elliptically polarized signals that propagate along the background magnetic field. When the field is horizontal the waves are not observed, yet at larger inclinations the wave energy can reach the instrument in the whistler mode. Most recently, Russell et al. (2007) discussed the measurements obtained in 37 orbits of VEX that took place between May and June 2006. When VEX passed through the magnetic field lines at altitudes around 300 km (which is above the Venusian ionopause and in a magnetic field strength $\sim 23 \text{ nT}$), the MAG instrument observed magnetic field fluctuations of the order of 0.1 nT indicative of whistler mode waves. The fluxgate magnetometer

Fig. 2 The three components of the magnetic field as recorded by the fluxgate magnetometer (MAG) on-board the Venus Express spacecraft. Signals exhibit repeated bursts with alerting amplitudes and duration, hinting at lightning as the probable source. The x -component is towards the Sun, z along the orbit plane and y in opposite planetary motion. This measurement was made from a range of 305 km of the Venusian surface as the spacecraft was travelling at 24,000 km/h (from Russell et al. 2007)



detected bursts of clear signals, with rapidly varying amplitudes and variable durations and intermissions between successive bursts (Fig. 2). The typical durations were found to be 0.2–0.5 s.

The possibility that these signals were due to spacecraft interference was excluded by subtracting the signals received by the two magnetometers. Russell et al. (2007) argues that there is no other possible source for natural whistler-mode waves propagating from the atmosphere to the ionosphere except lightning. However, the possibility that these waves stem from ionospheric plasma waves should not be discarded yet, since on Earth lightning whistlers at comparable altitudes are typically a factor of 10 shorter in duration (e.g. Holzworth et al. 1999) than the VEX-MAG whistler mode waves. Their deduced planetary flash rate on Venus, based on the detector footprint of 0.06% of the planet's surface, is 50 s^{-1} . Such a flash rate is comparable to Earth's and is inconsistent with the lack of correlative optical data. As the mission progresses there is hope that optical signatures will be received on top of the robust electromagnetic data.

Obviously, lightning on Venus should be completely intracloud, namely occurring within a given cloud layer or between layers. This is because the height of the cloud layer above the surface and the extreme atmospheric pressure requires an extremely high electric field for cloud-to-ground breakdown to be produced. It is possible that Venusian intracloud discharges will not resemble terrestrial intracloud flashes, and will have different signatures in the electromagnetic and optical bands. It may well be that the luminosity of Venusian lightning is significantly lower than that of terrestrial ones and that they are completely obscured by the upper cloud layers. Hopefully future missions such as the Japanese Planet-C (Takahashi 2008, this issue) will enable us to conduct better and prolonged observations.

2.3 Mars

The Martian environment has been studied using remote sensing and in situ observations, but the electrical properties, such as those related to atmospheric electricity, are still poorly known. The atmosphere consists mostly of CO₂ with a mole fraction of ~ 0.95 ; the near-surface atmospheric density is about 70 times smaller than on Earth and the electron conductivity is a few orders of magnitude higher than on Earth at similar altitudes. Surface conductivity estimates evaluated by theoretical models vary between 10^{-12} and 10^{-7} Sm^{-1} . Berthelier et al. (2000) tentatively restrict the range down to $10^{-12}\text{--}10^{-10}\text{ Sm}^{-1}$. Furthermore, the composition of the surface at low and high latitudes is quite different due to the

presence of ice deposits in the polar region, suggesting large variations in surface conductivity with latitude. Electrical discharges on Mars certainly would differ from that on Earth because the environmental properties and discharge processes are markedly different on the two planets (Farrell and Desch 2001). Aplin (2006) presents a comprehensive review of atmospheric electricity that also includes relevant information about the Martian environment.

Large electric fields have been measured in terrestrial dust storms, dust devils and regular wind-blown saltation (Stow 1969; Farrell et al. 1999; Renno et al. 2004; Schmidt et al. 1998). Melnik and Parrot (1998) used a numerical model to study the electrification of Martian dust storms and predicted that large electric fields are generated in them. In dust storms, charge transfer occurs during collisions between sand/dust particles with each other and the surface. After collisions, the smaller dust particles become negatively charged with respect to the larger sand particles and the surface, although the exact mechanism by which this occurs is still under debate (Lowell and Truscott 1986; Desch and Cuzzi 2000; Kok and Renno 2008). Gravitational and aerodynamic forces then separate the heavier, positively charged particles from the lighter, negatively charged particles. The resulting charge separation produces the observed bulk electric fields. On Earth these fields can exceed 100 kV/m, but on Mars they are limited by the electric breakdown of the thin Martian air at about 20 kV/m, except perhaps at very short distances (smaller than a few cm) from the surface. This happens because the breakdown electric field decreases with the distance between electrodes and the value of 20 kV/m is for a distance of the order \sim 1 m (Naidu and Kamaraju 1999; Ito and Terashima 2002).

The maximum charge of airborne dust particles can be calculated assuming that during saltation, charging is limited by field emission (Bernhard et al. 1992) in collisions between dust and sand particles. Then, a micro-discharge occurs while the particles move away from each other and the particles are left with a residual charge of the order of that necessary to produce electric discharges (Renno et al. 2003). Negatively charged dust particles of a few μm in diameter then rise with the updraft while the larger positively charged sand particles stay in the saltation layer. This produces charge separation and the bulk electric fields observed in dusty phenomena. Then, knowing the dust particle concentration and distribution, the bulk electric field can be calculated. Renno et al. (2004) showed theoretical evidence that Martian dusty phenomena should emit non-thermal microwave radiation, and supported it by the observation of terrestrial dust devil analogues. More recently, Renno and his collaborators found evidence that electric discharges in Martian dust storms not only should emit non-thermal radiation but also might excite Schumann resonance in the surface-ionosphere cavity.

Delory et al. (2006) and Atreya et al. (2006) showed that the electric activity on Mars may potentially produce large quantities of hydrogen peroxide, a powerful oxidant that could make the surface inhospitable to life as we know it. Similar to the observations of Venus, the TEXES spectrograph on the IRTF was used to study the Martian atmosphere. Measurements on one NO line show some power increasing over the continuum, hence suggesting that discharging processes might play a role in the atmosphere (Krasnopolsky 2006). The inferred NO concentration is above the predictions of photochemical models by a factor of 3 but no definite explanation is provided for such a difference.

2.4 Titan

Saturn's largest satellite Titan (radius of 2575 km) possesses a thick atmosphere dominated by nitrogen and methane with a surface pressure and temperature of 1.5 bar and 94 K, respectively. Since the Voyager 1 flyby of Titan in November 1980 the possibility of lightning

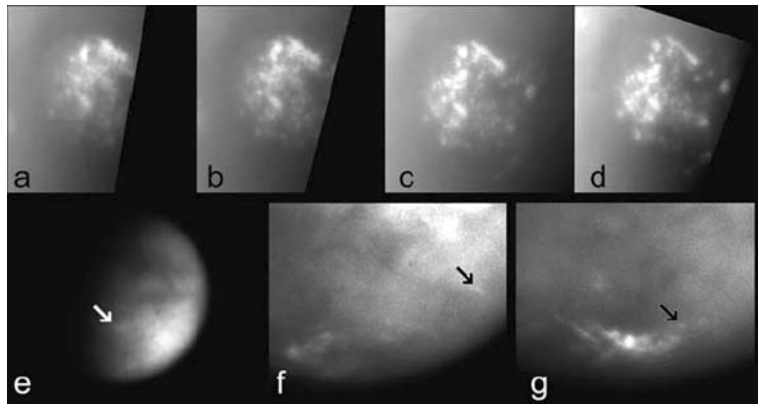


Fig. 3 Tropospheric cloud features observed by Cassini/ISS on Titan. The sequence **a–d** shows the development of Titan's South polar cloud as imaged on July 2, 2004. Panels **e–g** show three examples of discrete mid-latitude clouds, which are marked by arrows. They were imaged on May 29, October 23 and 25 (all 2004), respectively (taken from Porco et al. 2005a). Could lightning discharges develop in such clouds?—Cassini/RPWS did not detect lightning associated radio emissions

on Titan has been investigated by theoretical and experimental studies of its complex atmospheric chemistry (Gupta et al. 1981; Borucki et al. 1984, 1988; Navarro-González et al. 2001), mostly with positive and promising results. The non-detection of Titan lightning radio emissions by Voyager's radio instrument (Desch and Kaiser 1990) still could be explained by Titan's low or episodic flash rate (Lammer et al. 2001), and Tokano et al. (2001) developed a model for thundercloud and lightning generation on Titan.

The multiple Cassini flybys of Titan as well as the descent of the Huygens Probe on its surface in January 2005 revealed a fascinating Earth-like landscape with lakes and river beds, bright high-land regions and dark flat lowlands. Besides geological processes, this landscape is shaped mostly by weather, because there is wind, haze, drizzle, and most likely rain in Titan's atmosphere (Tomasko et al. 2005; Tokano et al. 2006). The Earth-based infrared observations of methane clouds on Titan (Griffith et al. 1998) were clearly confirmed by Cassini imaging observations (Porco et al. 2005a; see Fig. 3). Convective clouds over the South pole of Titan were observed for several months in 2004 before they vanished in December of that year and reappeared shortly in December 2005 (Rodriguez et al. 2007). Furthermore, elongated mid-latitude tropospheric clouds (Porco et al. 2005a) as well as ethane clouds (Griffith et al. 2006) have been observed. The most likely places for lightning on Titan are the convective-type methane clouds as those that appeared over the South Pole. Such clouds were modeled by Hueso and Sánchez-Lavega (2006) who found strong updrafts with velocities up to 20 m s^{-1} in such methane storms. In a similar model Barth and Rafkin (2007) got mixing ratios of cloud particles of the order of $1\text{--}10 \text{ g kg}^{-1}$. Such updraft velocities and mixing ratios are comparable to terrestrial thunderstorms (Rakov and Uman 2003).

Despite such promising conditions, the existence of lightning on Titan has not been proven yet. Fulchignoni et al. (2005) reported the possible detection of the signature of lightning by the Huygens Atmospheric Structure Instrument (HASI), that measured impulsive electric field events with the mutual impedance receiver during the descent of the Huygens Probe. These impulses, recorded in the frequency range from 180 Hz to 11.5 kHz, could be due to lightning, but one has to be careful in the interpretation with impulsive signals since they could be as well caused by interferences from on-board instruments or particle impacts.

Nevertheless, the number of events detected during the descent of the Huygens Probe establishes a maximum stroke rate not higher than 1% compared to stratospheric balloon campaigns. A peak in the power spectrum detected at 36 Hz is most likely not a lightning caused Schumann resonance since its frequency is not consistent with most models of Titan's ionospheric cavity (Simões et al. 2007), and its signal level is also much too high. Bégin et al. (2007) favor waves created in Titan's ionosphere as a possible source, and future laboratory experiments at low temperatures could show if the 36 Hz line is simply created by a mechanical vibration of the HASI antennas or not. The acoustic sensor on-board Huygens did not record any thunder claps (Grard et al. 2006). The Huygens Probe also detected an ionized layer at about 60 km altitude with a maximum conductivity of 3 nS/m (Hamelin et al. 2007), which is a few times higher than the surface conductivity measured at the landing site (Grard et al. 2006). This layer, induced by cosmic rays, certainly plays a role in atmospheric electrification, aerosol kinetics, and on the possible global electric circuit of Titan.

The Cassini/RPWS instrument searched for radio emissions from Titan lightning, but nothing was found during any of the first 35 Titan close flybys (Fischer et al. 2007a). In case of a Titan lightning storm RPWS should easily detect bursty signals above Titan's ionospheric cutoff frequency of about 500 kHz (Bird et al. 1997) that also show a quadratic fall-off of signal intensity with spacecraft distance. The non-detection of RPWS tells us that Titan lightning is an extremely rare event if it exists at all. Despite the similarities between methane clouds on Titan and terrestrial thunderclouds, one key question is still whether an efficient microscale electrification process can work in a Titan cloud given the low relative dielectric constant of 1.7 of methane. The RPWS result does not rule out the existence of other forms of atmospheric electricity like corona discharges. The search for Titan lightning with RPWS will continue at least until the end of Cassini's extended mission in mid-2010, which will increase the total number of close Titan flybys to 70.

3 Lightning Activity and Atmospheric Electricity at the Gas Giants

Lightning is a very interesting phenomenon in the atmospheres of the four gas giants, Jupiter, Saturn, Uranus and Neptune. It is likely to be more powerful than terrestrial lightning and also acts as a diagnostic tool of the dynamics of the respective atmosphere. Equilibrium cloud condensation models (Atreya and Wong 2004) suggest a similar cloud structure for Jupiter and Saturn, as well as for Uranus and Neptune. For Jupiter and Saturn the outermost cloud layer consists of ammonia (NH_3) ice particles, which is followed by an intermediate ammonium hydrosulfide cloud layer (NH_4SH) and a deep water cloud (H_2O). For Uranus and Neptune there should be a methane (CH_4) ice particle cloud around the 1-bar level followed by nearly the same cloud layering as on Jupiter and Saturn, except that also hydrogen sulfide (H_2S) should be present at the same altitude where ammonia condenses (de Pater et al. 1991).

At Jupiter, the water cloud at a pressure level around 4–5 bar has been identified as the source of lightning by optical observations. Usually, the bright dots due to Jovian lightning imaged by the cameras extend over more than one hundred kilometers, since the flashes are scattered at various cloud layers. A Monte-Carlo model of this scattering process has lead Borucki and Williams (1986) as well as Dyudina et al. (2002) to the same (already mentioned) conclusion regarding the origin of Jovian lightning. The non-detection of optical emissions from lightning on Saturn (Burns et al. 1983; Dyudina et al. 2007), Uranus (Smith et al. 1986), and Neptune (Borucki and Pham 1992) could be due to very deep atmospheric sources, as well as scattered ring light. The deep water cloud is a primary candidate, because

it is located around the freezing level for all four gas giants and cloud particle charging could work in a similar manner as in terrestrial thunderclouds. The smaller gravitation at Saturn, Uranus, and Neptune compared to Jupiter leads to smaller temperature lapse rates and the water clouds condense at higher pressure levels. According to the models of Atreya and Wong (2004) the base of the water ice cloud should be around 5 bars and 10 bars for Jupiter and Saturn, respectively, and around 40 bars for Uranus and Neptune.

A decisive parameter for the possibility of lightning discharges in planetary atmospheres is the value of the breakdown electric field for the specific atmosphere. The measured value for dry terrestrial air under standard conditions is $3 \cdot 10^6$ V/m and it scales with pressure. Such high electric fields have never been directly measured in thunderclouds and observed values are typically smaller by one order of magnitude (Rakov and Uman 2003) suggesting that besides the conventional breakdown the so-called runaway breakdown might play an important role in initiating lightning discharges. For Jupiter's atmosphere, Yair et al. (1995a) estimated the conventional breakdown field to be $2.3 \cdot 10^6$ V/m at a pressure of 5 bars. Recent modeling work by Dwyer et al. (2006) indicate that the electric field threshold for the so-called runaway breakdown could be 10 times smaller in the atmospheres of the gas planets compared to the conventional breakdown field. Kinetic calculations of runaway and conventional breakdown fields in planetary atmospheres have been performed by Sentman (2004) and are supplemented in the paper by Roussel-Dupré et al. (2008) in this issue. The hydrogen–helium atmospheres of the gas planets facilitate electric breakdown, but breakdown fields are still larger than at Earth at the pressure level where the deep water clouds reside.

3.1 Jupiter

Lightning at Jupiter was first detected optically with the camera on-board Voyager 1 (Cook et al. 1979), and further observations were made with Voyager 2 as well as by Galileo (Little et al. 1999). The Voyager plasma wave instrument detected lightning whistlers in Jupiter's magnetosphere (Gurnett et al. 1979), and sferics attributed to lightning were observed with the Galileo Probe inside Jupiter's atmosphere (Rinnert et al. 1998). These observations as well as the theoretical modeling of water clouds in Jupiters's atmosphere (Gibbard et al. 1995; Yair et al. 1995a, 1995b) have been extensively reviewed by Desch et al. (2002). Here we will focus on the recent optical observations obtained during the Jupiter flybys of Cassini at the end of 2000 and New Horizons in 2007, respectively.

Nightside images by the Cassini/ISS camera using the H _{α} filter revealed four lightning clusters, one at 24°N (North), one at 34°N, and two were repeated observations of the same storm located around 14°S (South; all planetocentric latitudes), in the turbulent wake region of the Great Red Spot (Dyudina et al. 2004). The observations were performed from a relatively large distance (140 to 200 Jovian radii). To diminish the scattered light, ISS used the narrowband H _{α} filter. Interestingly, the H _{α} line was about ten times weaker than expected from previous Galileo observations and laboratory simulations of Borucki et al. (1996) of the Jovian lightning spectrum. This could suggest that lightning is generated in atmospheric layers even deeper than 5 bar or that simply lightning frequency and intensity or cloud coverage varied between Galileo and Cassini observations (Dyudina et al. 2004). Cassini/ISS also studied the dayside appearance of the Jovian lightning storms.

On its way to Pluto and the Kuiper Belt, the New Horizons spacecraft flew by Jupiter as close as 32 Jovian radii at the end of February 2007. Recent observations by the spacecraft as well as ground-based thermal imagery have in fact revealed that the Jovian cloud cover in 2007 has thinned substantially since the Cassini 2000 flyby (Baines et al. 2007). Furthermore, the New Horizons LORRI (Long Range Reconnaissance Imager) camera identified

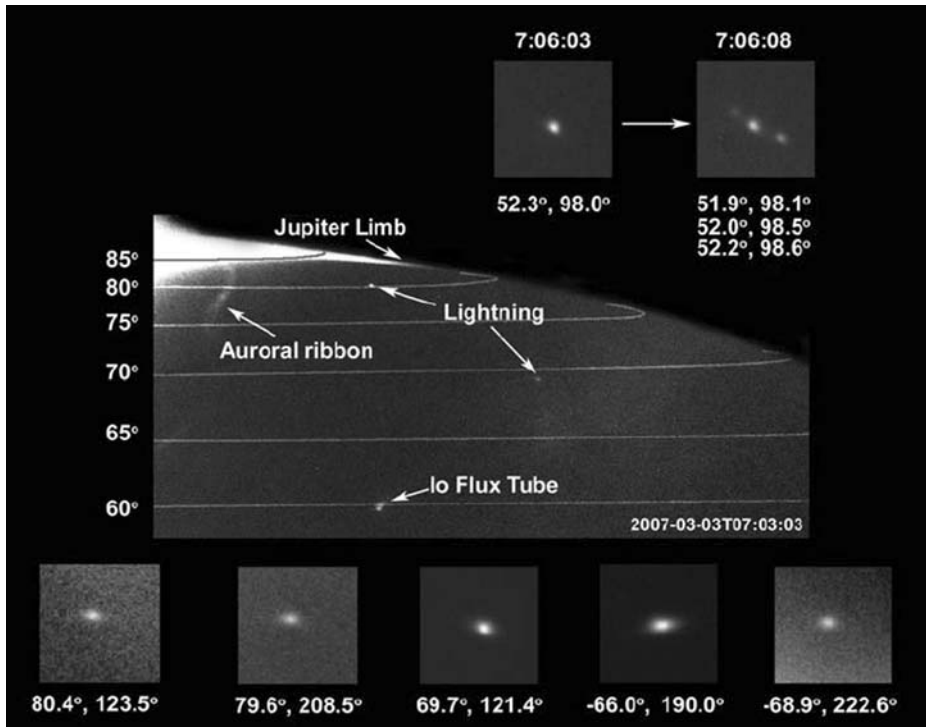


Fig. 4 Jovian lightning flashes as imaged by New Horizons/LORRI at various latitudes (planetographic) and longitudes. Exposure time was typically 5 seconds, and the spatial extension is due to diffusive scattering of flashes originating near the 5-bar water cloud level by aerosols and clouds above (taken from Baines et al. 2007)

Jovian lightning at high latitudes up to 80°N and 74°S (planetographic). Figure 4 displays some representative lightning flashes. Previous lightning observations have found Jupiter lightning only at lower latitudes, typically at the southern edges of westward-moving jets in regions of cyclonic shear (Borucki and Magalhaes 1992). New Horizons has found flashes also at the anticyclonic sides of eastward jets (60°S and 66°S), and the polar strikes (80°N, 74°S) are located in regions of relatively weak winds. All investigating spacecraft (including New Horizons) have found Jovian lightning to be most optically active around 50°N (Baines et al. 2007). Jupiter lightning is more powerful than terrestrial lightning, since the optical energy of a Jovian flash is of the order of 10^9 J, which corresponds to the typical *total* energy of a terrestrial flash (the median value for the optical energy in terrestrial lightning is $4.5 \cdot 10^5$ J; Kirkland et al. 2001). When considering the optical efficiency of the Jovian atmosphere (Borucki and McKay 1987), the total energy of a Jovian flash is $\sim 10^{12}$ J, comparable to terrestrial “superbolts” (Turman 1977). These estimates were corroborated in the numerical simulations by Yair et al. (1995b).

3.2 Saturn

Following the Voyager discovery (Warwick et al. 1981) and extensive studies (see e.g. the review by Zarka 1985a, 1985b), our knowledge about atmospheric electricity at Saturn has been greatly increased by the Cassini mission and this is reviewed in more detail in a separate

article in this issue by Fischer et al. (2008). Several thousands of lightning sferics termed SEDs (Saturn Electrostatic Discharges) have been measured by Cassini/RPWS in six SED storms (Gurnett et al. 2005; Fischer et al. 2006, 2007b), but only one lightning whistler has been identified (Akalin et al. 2006). As opposed to Jupiter, until now only two latitudes at Saturn (whistler latitude excluded) have been found to produce lightning storms and these are the equatorial region and the “storm alley” at 35°S. The lightning flashes on Saturn have not yet been detected optically, most probably because the lightning source is located very deep in Saturn’s atmosphere, approximately at the 10-bar level. But, Cassini/ISS imaged prominent cloud features in Saturn’s atmosphere, whose occurrence, longitudinal drift rate, and brightness were strongly related to the SEDs (Porco et al. 2005b; Dyudina et al. 2007). Images of these cloud features can be found in this issue in the article by Fischer et al. (2008). During the Cassini mission there have been long time intervals with no SED activity. A giant lightning storm in early 2006 (Fischer et al. 2007b) was followed by 21 months of “silence”, but a seventh SED storm started in the end of November 2007. The intense radio signals of SEDs (about 10^4 times more powerful compared to HF radio emissions from terrestrial lightning) have been detected also by the giant UTR-2 radio-telescope in the Ukraine (Konovalenko et al. 2006). SED characteristics and implications for ionospheric studies are discussed in Zarka et al. (2008) in this issue.

3.3 Uranus and Neptune

High frequency radio signals similar to SEDs have been detected by the Voyager 2 radio instrument at Uranus and they were termed UED for Uranus Electrostatic Discharges (Zarka and Pedersen 1986). At Neptune Voyager 2 detected 16 lightning whistler like events (Gurnett et al. 1990) as well as 4 possible lightning sferics (Kaiser et al. 1991). Since no other spacecraft except Voyager 2 has ever visited Uranus and Neptune, the progress in our knowledge concerning lightning activity on those two icy giants has been limited in the last years. Considerable progress has been made concerning Earth-based cloud observations of Uranus and Neptune in the infrared as well as visible wavelength region (e.g. Karkoschka 1998; Hammel et al. 2001; Roe et al. 2001; de Pater et al. 2002; Gibbard et al. 2003; Sromovsky and Fry 2005; Irwin et al. 2007). However, the lightning source might be in the water clouds located at a pressure level of about 40 bar, which is not accessible with these observations (Encrenaz et al. 2004). On the other hand, using a particle-growth and charge-separation model Gibbard et al. (1999) suggested that lightning is inhibited in the deep water or NH_4SH cloud because of the high atmospheric pressures there and that lightning seems possible in the $\text{H}_2\text{S}-\text{NH}_3$ cloud layer. Finally, Zarka et al. (2004, 2008) concluded that the sensitivity of the future giant Low Frequency Array (LOFAR) would allow us to detect and monitor lightning activity on Uranus (but not on Neptune) from Earth.

4 Laboratory Experiments

The early work done in laboratories in order to predict and to determine the production of chemical compounds by lightning in planetary atmospheres is discussed in detail by Desch et al. (2002), and we shall briefly touch upon some results that are of special relevance to on-going missions. Conceptually, these experiments are mostly based on discharging electrical sparks or on producing high-temperature plasma (LIP or laser induced plasma) inside a vessel containing the proper gas mixture at the relevant temperature and pressure, simulating the atmosphere being studied. Alternatively, concentrated lasers can be used to

produce shock waves in order to study shock-induced chemistry. Borucki et al. (1996) have obtained the spectra of simulated lightning in gas mixtures of the atmospheres of Jupiter, Venus and Titan, by observing laser-induced plasmas with a scanning spectrometer and an optical multi-channel analyzer in the range 380–820 nm. The results show that atomic line and continuum dominate the spectra, with some weak molecular band from CN for Venus and Titan. At higher pressures, the dominance of the continuum over the atomic spectra increased and some lines disappeared. That work was a continuation of earlier experiments reported by Borucki and McKay (1987) which were aimed at obtaining the optical efficiencies of different atmospheres, namely, the capability of lightning light emanating from the deep atmosphere to be detected by a sensor on an orbiting spacecraft. The results showed that the fraction of the energy in lightning discharge channels that is radiated in the visible spectrum is similar for Earth, Venus and Titan, but quite different for Jupiter. However, this conclusion can be challenged based on our lack of detection, after numerous orbits, of visible light from flashes neither on Venus (Sect. 2.2) nor on Titan (Sect. 2.4). Arguably the assumption that electrical discharges are essentially similar to terrestrial flashes may be incorrect and it may well be that the characteristics of flashes in these two atmospheres is completely different (for example, slower rise-time, shorter channels, smaller peak currents and lower total energies). This calls for re-evaluation of the simulation philosophy of planetary lightning in laboratory-type atmospheres.

Due to its unique (pre-) biological aspect, considerable attention is being dedicated to the study of Titan's atmosphere. The notion that lightning can produce disequilibrium chemistry and lead to the formation of amino-acids and other complex organic compounds in its N₂-based atmosphere is not new and is considered, in the words of Desch et al. (2002), "*a tantalizing possibility*". Numerous new publications appeared since that review, especially in the exobiology literature, with a focus on production of organic pre-biotic chemical compounds by electrical processes. Navarro-González et al. (2001) studied the chemical effects of corona and lightning discharges in CH₄–N₂ mixtures. They found that lightning is approximately 2 orders of magnitude more efficient than corona discharges in producing hydrocarbons and nitriles, and that corona discharges are producing linear and branched hydrocarbons whereas lightning produces mainly unsaturated ones. Majumdar et al. (2005) studied reactions in CH₄/Ar and CH₄/N₂ gas mixtures at ambient pressures of 250–300 mbar. The products were higher order hydrocarbon molecules, typically C_nH_m with n up to 9, and also different functional CN groups. In a different type of experiment, Somogyi et al. (2005) studied the chemical reactions taking place in Titan's stratosphere, by exposing a mixture of 5% CH₄ and 95% N₂ to an AC electrical discharge at a temperature of 195 K inside a glass reaction vessel. The chemical reactions produced a thin layer of tholin on the wall, that was scraped and analyzed by mass spectrometry using electrospray ionization (ESI) and laser desorption (LD) techniques. The samples mimic the chemistry of aerosol particles in Titan's upper atmosphere, exhibiting the general formula of C_xH_yN_z. Most recently, Plankenstein et al. (2007) conducted discharge experiments in order to simulate the chemical evolution on the surface of Titan by allowing the hydrocarbon chemistry to be exposed to water ice.

Electric discharges of 60 kV and 60 mA were pulsed with 5 Hz into the reaction chamber, which was kept at a pressure of 1.46 bar (Titan's atmospheric surface pressure) and at a temperature of −32°C. One electrode of the discharge gap was situated below a layer of water ice simulating discharges into Titan's surface. The results showed a robust production of C–H–O, C–H–N and C–H–O–N compounds including several molecules important for the formation of amino acids and nucleic acids. The uniqueness of this new experiment is the introduction of oxygen atoms into the compounds, believed to be a "first step" in any possible chemical evolution on the surface of Titan.

Interesting experiments were conducted in rarefied gas mixtures subjected to high external voltage in order to study the light emissions from transient luminous events (namely sprites). This type of discharge is very different to the high-energy high-temperature regime of LIP experiments. The first successful set of experiments was conducted by Williams (2001) for an N₂–O₂ mixture. The optical spectrum in the (red) positive column was found to resemble the spectrum of the sprite body as observed by Hampton et al. (1996). Lately, Goto et al. (2007) conducted similar experiments and proceeded to simulate a Venus-like composition of nearly pure CO₂ in different pressures. The results of the Venus experiment show dominance of the oxygen atomic line O 777.6 nm (the one used for lightning detection by Hansell et al. 1995), with additional CO and CO₂ lines at shorter wavelengths. This type of experiments is useful for searching for sprites above the clouds of other planets (see Takahashi 2008, in this issue).

5 Summary and Future Prospects

Considerable progress has been made in our understanding of lightning discharges since the latest review by Desch et al. (2002), and new insights have been gained from observations of electrical activity on other planets. Additionally, laboratory studies have shed light on the physics of charging and discharging processes in the atmospheres of other planets. The continuation of observations from spacecraft and ground-based instruments is bound to increase our inventory of data, and to enable us to gain deeper understanding of one of the basic phenomena in nature. At Venus the VEX mission will continue to increase our knowledge of atmospheric electricity at “our sister planet”. The occurrence of the detected whistler-mode waves (Russell et al. 2007) as a function of local time should be evaluated. The future Japanese Planet-C mission (to be launched in 2010) will have a sensitive camera on-board for the detection of optical emissions from lightning and sprites. On our own planet Earth, atmospheric electricity is under investigation by an increasing number of scientists. The future Earth satellite mission, Taranis, described in this issue by Lefevre et al. (2008), and the proposed Global Lightning Mapper on board a NOAA GOES geostationary satellite which is due to be launched in 2012 will provide new insights on the physics of lightning. On Mars, an instrument package for the investigation of atmospheric electricity and dust storms to the surface of the red planet is overdue (Aplin 2006). An instrument capable of measuring the electric field and the flux of charged particles has been developed for future in-situ measurements on Mars and other bodies of the solar system (Renno and Kok 2008). The future JUNO mission to Jupiter (to be launched in 2011) will provide further insights into the dynamics of the Jovian atmosphere by using instruments to determine the water content and to derive further physical characteristics of the atmosphere down to a pressure level of about 100 bar. An optical camera as well as a plasma wave instrument are also able of detecting optical or radio emissions (whistlers) from lightning. At Saturn the current Cassini mission continues to monitor Saturn Electrostatic Discharges, and it searches for evidence of Titan lightning. A future mission to Titan could be in the form of a balloon, and Tokano and Lorenz (2006) simulated possible balloon trajectories. To our knowledge there are presently no definite plans to revisit the icy giants Uranus and Neptune.

References

- F. Akalin, D.A. Gurnett, T.F. Averkamp et al., Geophys. Res. Lett. **33**, L20107 (2006)
- K.L. Aplin, Surv. Geophys. **27**, 63–108 (2006)
- S.K. Atreya, A.-S. Wong, Space Sci. Rev. **114**, 121–136 (2004)

- S.K. Atreya, A.-S. Wong, N.O. Renno et al., *Astrobiology* **6**(3), 439–450 (2006)
- K.H. Baines, A.A. Simon-Miller, G.S. Orton et al., *Science* **318**, 226–229 (2007)
- A. Bar-Nun, *Icarus* **24**, 86–94 (1975)
- A. Bar-Nun, *Icarus* **38**, 180–191 (1979)
- E.L. Barth, S.C.R. Rafkin, *Geophys. Res. Lett.* **34**, L03203 (2007)
- C. Béghin, F. Simões, V. Krasnoselskikh et al., *Icarus* **191**, 251–266 (2007)
- A.K. Bernhard, K. Sattler, H.C. Siegmann, *J. Phys. D* **25**, 139–146 (1992)
- J.-J. Berthelier, R. Grard, H. Laakso, M. Parrot, *Planet. Space Sci.* **48**, 1193–1200 (2000)
- M.K. Bird, R. Dutta-Roy, S.W. Asmar, T.A. Rebolt, *Icarus* **130**, 426–436 (1997)
- E. Blanc, T. Farges, R. Roche et al., *J. Geophys. Res.* **109**(A2), A02306 (2004)
- W.L. Boeck, O.H. Vaughan, R.J. Blakeslee et al., *J. Geophys. Res.* **100**(D1), 1465–1475 (1994)
- W.J. Borucki, M.A. Williams, *J. Geophys. Res.* **91**(D9), 9893–9903 (1986)
- W.J. Borucki, C.P. McKay, *Nature* **328**, 509–510 (1987)
- W.J. Borucki, P.C. Pham, *Icarus* **99**, 384–389 (1992)
- W.J. Borucki, J.A. Magalhaes, *Icarus* **96**, 1–14 (1992)
- W.J. Borucki, C.P. McKay, R.C. Whitten, *Icarus* **60**, 260–273 (1984)
- W.J. Borucki, L.P. Giver, C.P. McKay, T. Scattergood, J.E. Parris, *Icarus* **76**, 125–134 (1988)
- W.J. Borucki, C.P. McKay, D. Jebens, H.S. Lakkaraju, C.T. Vanajakshi, *Icarus* **123**, 336–344 (1996)
- J.A. Burns, M.R. Showalter, J.N. Cuzzi, R.H. Durisen, *Icarus* **54**, 280–295 (1983)
- H.J. Christian, R.J. Blakeslee, D.J. Boccippio et al., *J. Geophys. Res.* **108**(D1), 4005 (2003)
- L.M. Coleman, T.C. Marshall, M. Stolzenburg et al., *J. Geophys. Res.* **108**(D9), 4298 (2003)
- A.F. Cook, T.C. Duxbury, G.E. Hunt, *Nature* **280**, 794–795 (1979)
- S. Cummer, N. Jaugey, J. Li et al., *Geophys. Res. Lett.* **33**, L04104 (2006a). doi: [10.1029/2005GL024969](https://doi.org/10.1029/2005GL024969)
- S.A. Cummer, H.A. Frey, S.B. Mende et al., *J. Geophys. Res.* **A10315** (2006b). doi: [10.1029/2006JA011809](https://doi.org/10.1029/2006JA011809)
- G.T. Delory, W.M. Farrell, S.K. Atreya et al., *Astrobiology* **6**(3), 451–462 (2006)
- M.D. Desch, M.L. Kaiser, *Nature* **343**, 442–444 (1990)
- S.J. Desch, J.N. Cuzzi, *Icarus* **143**, 87–105 (2000)
- S.J. Desch, W.J. Borucki, C.T. Russell, A. Bar-Nun, *Rep. Prog. Phys.* **65**, 955–997 (2002)
- I. de Pater, P.N. Romani, S.K. Atreya, *Icarus* **91**, 220–233 (1991)
- I. de Pater, S.G. Gibbard, B.A. Macintosh et al., *Icarus* **160**, 359–374 (2002)
- U.A. Dyudina, A.P. Ingersoll, A.R. Vasavada, S.P. Ewald, the Galileo SSI Team, *Icarus* **160**, 336–349 (2002)
- U.A. Dyudina, A. Del Genio, A.P. Ingersoll et al., *Icarus* **172**, 24–36 (2004)
- U.A. Dyudina, A.P. Ingersoll, P.E. Shawn et al., *Icarus* **190**, 545–555 (2007)
- J.R. Dwyer, D.M. Smith, *Geophys. Res. Lett.* **32**, L22804 (2005)
- J.R. Dwyer, H.K. Rassoul, Z. Saleh et al., *Geophys. Res. Lett.* **32**, L20809 (2005)
- J.R. Dwyer, L.M. Coleman, R. Lopez et al., *Geophys. Res. Lett.* **33**, L22813 (2006)
- K.B. Eack, W.H. Beasley, W.D. Rust, T.C. Marshall, M. Stolzenburg, *J. Geophys. Res.* **101**, 29,637–29,640 (1996)
- Th. Encrenaz, E. Lellouch, P. Drossart et al., *Astron. Astrophys.* **413**, L5–L9 (2004)
- W.M. Farrell, M.D. Desch, *J. Geophys. Res.* **106**, 7591–7595 (2001)
- W.M. Farrell, M.L. Kaiser, M.D. Desch et al., *J. Geophys. Res.* **104**(E2), 3795–3802 (1999)
- G. Fischer, M.D. Desch, P. Zarka et al., *Icarus* **183**, 135–152 (2006)
- G. Fischer, D.A. Gurnett, W.S. Kurth et al., *Geophys. Res. Lett.* **34**, L22104 (2007a)
- G. Fischer, W.S. Kurth, U.A. Dyudina et al., *Icarus* **190**, 528–544 (2007b)
- G. Fischer, D.A. Gurnett, W.S. Kurth et al., *Space Sci. Rev.* (2008, this issue)
- G.J. Fishman, P.N. Bhat, R. Mallozzi et al., *Science* **264**, 1313–1316 (1994)
- M. Füllekrug, E. Mareev, M. Rycroft, *Sprites, Elves and Intense Lightning Discharges* (Springer, Dordrecht, 2006)
- M. Fulchignoni, F. Ferri, F. Angrilli et al., *Space Sci. Rev.* **104**, 395–431 (2002)
- M. Fulchignoni, F. Ferri, F. Angrilli et al., *Nature* **438**, 785–791 (2005)
- E.A. Gerken, U.S. Inan, Asia-Pacific Radio Sci. Conf., 2001aprs.conf.135G (2001)
- S.G. Gibbard, E.H. Levy, J.I. Lunine, *Nature* **378**, 592–595 (1995)
- S.G. Gibbard, E.H. Levy, J.I. Lunine, I. de Pater, *Icarus* **139**, 227–234 (1999)
- S.G. Gibbard, I. de Pater, H.G. Roe et al., *Icarus* **166**, 359–374 (2003)
- G.R. Gladstone, S.A. Stern, D.C. Slater et al., *Science* **318**, 229 (2007)
- R. Grard, M. Hamelin, J.J. López-Moreno et al., *Planet. Space Sci.* **54**, 1124–1136 (2006)
- C.A. Griffith, T. Owen, G.A. Miller, T.R. Geballe, *Nature* **395**, 575–578 (1998)
- C.A. Griffith, P. Penteado, P. Rannou et al., *Science* **313**, 1620–1622 (2006)
- S. Gupta, E. Ochiai, C. Ponnampерuma, *Nature* **293**, 725–727 (1981)
- Y. Goto, Y. Ohba, K. Narita, *J. Atmos. Electr.* **27**, 105–112 (2007)
- A.V. Gurevich, G.M. Milikh, R. Roussel-Dupré, *Phys. Lett. A* **165**, 463–468 (1992)

- D.A. Gurnett, R.R. Shaw, R.R. Anderson, W.S. Kurth, *Geophys. Res. Lett.* **6**, 511–514 (1979)
- D.A. Gurnett, W. S Kurth, I.H. Cairns, L.J. Granroth, *J. Geophys. Res.* **95**, 20,967–20,976 (1990)
- D.A. Gurnett, W.S. Kurth, A. Roux et al., *Science* **252**, 1522–1525 (1991)
- D.A. Gurnett, P. Zarka, R. Manning et al., *Nature* **409**, 313–315 (2001)
- D.A. Gurnett, W.S. Kurth, D.L. Kirchner et al., *Space Sci. Rev.* **114**, 395–463 (2004)
- D.A. Gurnett, W.S. Kurth, G.B. Hospodarsky et al., *Science* **307**, 1255–1259 (2005)
- M. Hamelin, C. Béghin, R. Grard et al., *Planet. Space Sci.* **55**, 1964–1977 (2007)
- H.B. Hammel, K. Rages, G.W. Lockwood, E. Karkoschka, I. de Pater, *Icarus* **153**, 229–235 (2001)
- D.L. Hampton, M.J. Heavner, E.M. Wescott, D.D. Sentman, *Geophys. Res. Lett.* **23**, 89–92 (1996)
- S.A. Hansell, W.K. Wells, D.M. Hunten, *Icarus* **117**, 345–351 (1995)
- C.-M. Ho, R.J. Strangeway, C.T. Russell, *Adv. Space Res.* **15**, 493–498 (1995)
- R.H. Holzworth, R.M. Winglee, B.H. Barnum, Y.Q. Li, M.C. Kelley, *J. Geophys. Res.* **104**(A8), 17369–17378 (1999)
- R. Hueso, A. Sánchez-Lavega, *Nature* **442**, 428–431 (2006)
- U.S. Inan, C. Barrington-Leigh, S. Hansen et al., *Geophys. Res. Lett.* **24**, 583–586 (1997)
- P.G.J. Irwin, N.A. Teanby, G.R. Davis, *Astrophys. J.* **665**, L71–L74 (2007)
- T. Ito, K. Terashima, *Appl. Phys. Lett.* **80**(16), 2854 (2002)
- A.R. Jacobson, T.E.L. Light, *J. Geophys. Res.* **108**(D9), 4266 (2003)
- M.L. Kaiser, M.D. Desch, W.M. Farrell, P. Zarka, *J. Geophys. Res.* **96**, 19,043–19,047 (1991)
- M.L. Kaiser, M.D. Desch, J.E.P. Connerney, *J. Geophys. Res.* **89**(A4), 2371–2376 (1984)
- E. Karkoschka, *Science* **280**, 570–572 (1998)
- N.E. Kassim, T.J.W. Lazio, P.S. Ray et al., *Planet. Space Sci.* **52**, 1343–1349 (2004)
- J.F. Kok, N.O. Renno, *Phys. Rev. Lett.* **100** (2008). doi:[10.1103/PhysRevLett.100.014501](https://doi.org/10.1103/PhysRevLett.100.014501)
- A.A. Konovalenko, A. Lecacheux, C. Rosolen, H.O. Rucker, in *Planetary Radio Emissions V*, ed. by H.O. Rucker, M.L. Kaiser, Y. Leblanc (Austrian Academy of Sciences Press, Vienna, 2001), pp. 63–76
- A.A. Konovalenko, A. Lecacheux, H.O. Rucker et al., European Planetary Science Congress. Berlin, Germany, 2006, p. 229
- V.A. Krasnopol'sky, *Cosmic Res.* **18**(3), 325–330 (1980)
- V.A. Krasnopol'sky, *Icarus* **182**, 80–91 (2006)
- M.W. Kirkland, D.M. Suszcynsky, J.L.L. Guillen, J.L. Green, *J. Geophys. Res.* **106**(D24), 33499–33510 (2001)
- W.C. Knudsen, A.J. Kilore, R.C. Whitten, *J. Geophys. Res.* **92**, 13391–13408 (1987)
- L.V. Ksanfomaliti, Kosmicheskie Issledovaniia **17**, 747–762 (1979) (in Russian)
- H. Lammer, T. Tokano, G. Fischer et al., *Planet. Space Sci.* **49**, 561–574 (2001)
- F. Lefèuvre, E. Blanc, R. Roussel-Dupré, J.A. Sauvad, *Space Sci. Rev.* (2008, this issue)
- N.G. Lehtinen, T.F. Bell, V.P. Pasko, U.S. Inan, *Geophys. Res. Lett.* **24**, 2639–2642 (1997)
- Z. Levin, W.J. Borucki, O.B. Toon, *Icarus* **56**, 80–115 (1983)
- G.F. Lindal, J.R. Lyons, D.N. Sweetnam et al., *J. Geophys. Res.* **92**(A13), 14,987–15,001 (1987)
- B. Little, C.D. Anger, A.P. Ingersoll et al., *Icarus* **142**, 306–323 (1999)
- J. Lowell, W.S. Truscott, *J. Phys. D: Appl. Phys.* **19**, 1281–1298 (1986)
- A. Majumdar, J.F. Behnke, R. Hippler, K. Matyash, R. Schneider, *J. Phys. Chem. A* **109**, 9371–9377 (2005)
- R.S. Massey, D.N. Holden, *Radio Science* **30**(5), 1645–1659 (1995)
- O. Melnik, M. Parrot, *J. Geophys. Res.* **103**(A12), 29,107–29,118 (1998)
- S.L. Miller, *Science* **117**, 528–529 (1953)
- C.B. Moore, K.B. Eack, G.D. Aulich, W. Rison, *Geophys. Res. Lett.* **28**, 2141–2144 (2001)
- M.S. Naidu, V. Kamaraju, *High Voltage Engineering* (McGraw-Hill, New York, 1999)
- R. Navarro-González, S.I. Ramírez, J.G. de la Rosa, P. Coll, F. Raulin, *Adv. Space Res.* **27**(2), 271–282 (2001)
- A.F. Nagy, A.J. Kliore, E. Marouf et al., *J. Geophys. Res.* **111**(A6), A06310 (2006)
- G.S. Orton, P.A. Yanamandra-Fisher, P.D. Parrish et al., *Bull. Am. Astron. Soc.* **38**, 554 (2006)
- M. Parrot, J.J. Berthelier, J.P. Lebreton, R. Treumann, J.L. Rauch, *Space Sci. Rev.* (2008, this issue). doi:[10.1007/s11214-008-9347-y](https://doi.org/10.1007/s11214-008-9347-y)
- V.P. Pasko, *Plasma Sources Sci. Technol.* **16**, S13–S29 (2007). doi:[10.1088/0963-0252/16/1/S02](https://doi.org/10.1088/0963-0252/16/1/S02)
- V.P. Pasko, M.A. Stanley, J.D. Mathews, U.S. Inan, T.G. Wood, *Nature* **416**, 152–154 (2002)
- M. Pätzold, S. Tellmann, B. Häusler, D. Hinson, R. Schaa, G.L. Tyler, *Science* **310**, 837–839 (2005)
- K. Plankenstein, H. Reiner, B.M. Rode et al., *Icarus* **187**, 616–619 (2007)
- C.C. Porco, R.A. West, S. Squyres et al., *Space Sci. Rev.* **115**, 363–497 (2004)
- C.C. Porco, E. Baker, J. Barbara et al., *Nature* **434**, 159–168 (2005a)
- C.C. Porco, E. Baker, J. Barbara et al., *Science* **307**, 1243–1247 (2005b)
- V.A. Rakov, M.A. Uman, *Lightning, Physics and Effects* (Cambridge Univ. Press, Cambridge, 2003)
- N.O. Renno, A.-S. Wong, S.K. Atreya, I. de Pater, M. Roos-Serote, *Geophys. Res. Lett.* **30**, 2140 (2003)

- N.O. Renno, V. Abreu, J. Koch et al., *J. Geophys. Res.* **109**, E07001 (2004). doi:[10.1029/2003JE002219](https://doi.org/10.1029/2003JE002219)
- N.O. Renno, J.F. Kok, *Space Sci. Rev.* (2008, this issue)
- K. Rinnert, *J. Geophys. Res.* **90**, 6225–6237 (1985)
- K. Rinnert, L.J. Lanzerotti, M.A. Uman et al., *J. Geophys. Res.* **103**, 22,979–22,992 (1998)
- H.G. Roe, D.T. Gavel, C.E. Max et al., *Astron. J.* **122**(3), 1636–1643 (2001)
- S. Rodriguez, S. Le Mouelic, G. Tobie et al., *Lunar Planet. Sci.* **XXXVIII** (2007)
- R. Roussel-Dupré, A.V. Gurevich, *J. Geophys. Res.* **101**(A2), 2297–2311 (1996)
- R. Roussel-Dupré, J. Colman, E. Symbalisty, D. Sentman, V. Pasko, *Space Sci. Rev.* (2008, this issue)
- C.T. Russell, *Space Sci. Rev.* **55**, 317–356 (1991)
- C.T. Russell, R.N. Clayton, P.R. Buseck et al., *Annu. Rev. Earth Planet. Sci.* **21**, 43–87 (1993)
- C.T. Russell, R.J. Strangeway, T.L. Zhang, *Planet. Space Sci.* **54**, 1344–1351 (2006)
- C.T. Russell, T.L. Zhang, M. Delva et al., *Nature* **450**, 661–662 (2007)
- A. Sánchez-Lavega, G.S. Orton, R. Morales et al., *Icarus* **149**, 491–495 (2001)
- D.D. Sentman, 1st ISUAL scientific workshop, Taiwan, 08-O013-O016 (2004)
- G. Schilling, *Science* **310**(5747), 431 (2005)
- D.S. Schmidt, R.A. Schmidt, J.D. Dent, *J. Geophys. Res.* **103**(D8), 8997–9002 (1998)
- R.W. Schunk, A.F. Nagy, *Ionospheres, Physics, Plasma Physics and Chemistry* (Cambridge Univ. Press, Cambridge, 2000)
- X.-M. Shao, A.R. Jacobson, *J. Geophys. Res.* **107**(D20), 4430 (2002)
- F. Simões, R. Grard, M. Hamelin et al., *Planet. Space Sci.* **55**, 1978–1989 (2007)
- A.A. Simon-Miller, B.J. Conrath, P.J. Gierasch et al., *Icarus* **180**, 98–112 (2006)
- B.A. Smith, L.A. Soderblom, R. Beebe et al., *Science* **233**, 43–64 (1986)
- D.A. Smith, M.J. Heavner, A.R. Jacobson et al., *Radio Sci.* **39**(1), RS1010 (2004)
- D.M. Smith, L.I. Lopez, R.P. Lin, C.P. Barrington-Leigh, *Science* **307**, 1085–1088 (2005)
- A. Somogyi, C.-H. Oh, M. Smith, J. Lunine, *J. Am. Soc. Mass. Spec.* **16**(6), 850–859 (2005). doi:[10.1016/j.jasms.2005.01.027](https://doi.org/10.1016/j.jasms.2005.01.027)
- L.A. Sromovsky, P.M. Fry, *Icarus* **179**, 459–484 (2005)
- M.A. Stanley, X.-M. Shao, D.M. Smith et al., *Geophys. Res. Lett.* **33**, L06803 (2006)
- M. Stolzenburg, T.C. Marshall, W.D. Rust, *J. Geophys. Res.* **106**(D12), 12,371–12,380 (2001)
- M. Stolzenburg, T.C. Marshall, *Space Sci. Rev.* (2008, this issue). doi:[10.1007/s11214-008-9338-z](https://doi.org/10.1007/s11214-008-9338-z)
- C.D. Stow, *Rep. Prog. Phys.* **32**(1), 1–67 (1969)
- R.J. Strangeway, *Adv. Space Res.* **15**, 489–492 (1995)
- H.T. Su, R.R. Hsu, A.B. Chen et al., *Nature* **423**, 974–976 (2003)
- D.M. Suszcynsky, R. Roussel-Dupré, G. Shaw, *J. Geophys. Res.* **101**, 23,505–23,516 (1996)
- Y. Takahashi, *Space Sci. Rev.* (2008, this issue)
- B.N. Turman, *J. Geophys. Res.* **82**(C18), 2566–2568 (1977)
- R.J. Thomas, P.R. Krehbiel, W. Rison et al., *Geophys. Res. Lett.* **28**(1), 143–146 (2001)
- T. Tokano, G.J. Molina-Cuberos, H. Lammer, W. Stumptner, *Planet. Space Sci.* **49**, 539–560 (2001)
- T. Tokano, C.P. McKay, F.M. Neubauer et al., *Nature* **442**, 432–435 (2006)
- T. Tokano, R.D. Lorenz, *Planet. Space Sci.* **54**, 685–694 (2006)
- M.G. Tomasko, B. Archinal, T. Becker et al., *Nature* **438**, 765–778 (2005)
- G.L. Tyler, D.N. Sweetnam, J.D. Anderson et al., *Science* **246**, 1466–1473 (1989)
- J.-E. Wahlund, R. Boström, G. Gustafsson, D.A. Gurnett, W.S. Kurth et al., *Science* **308**, 986–989 (2005)
- J.-S. Wang, E. Nielsen, *Planet. Space Sci.* **51**, 329–338 (2003)
- J.W. Warwick et al., *Science* **212**, 239–243 (1981)
- E.R. Williams, *Phys. Today* **54**(11), 41–47 (2001)
- E.R. Williams, R. Boldi, J. Bor et al., *J. Geophys. Res.* **111**, D16209 (2006)
- M.A. Williams, E.P. Krider, D.M. Hunten, *Rev. Geophys. Space Phys.* **21**, 892–902 (1983)
- Y. Yair, Z. Levin, S. Tzivon, *Icarus* **115**, 421–434 (1995a)
- Y. Yair, Z. Levin, S. Tzivon, *Icarus* **114**, 278–299 (1995b)
- Y. Yair, P. Israelevich, A.D. Devir et al., *J. Geophys. Res.* **109**(D15), D15201 (2004)
- Y. Yair, Y. Takahashi, D. Sentman, R. Yaniv, *Proc. XIV Int. Con. Atmos. Elec.* (2007)
- Y. Yair, *Space Sci. Rev.* (2008, this issue). doi:[10.1007/s11214-008-9348-x](https://doi.org/10.1007/s11214-008-9348-x)
- P. Zarka, in *Planetary Radio Emissions*, ed. by H.O. Rucker, S.J. Bauer (Austrian Acad. Sci. Press, Vienna, 1985a), pp. 237–270
- P. Zarka, *Astron. Astrophys.* **146**, L15–L18 (1985b)
- P. Zarka, B.M. Pedersen, *Nature* **323**, 605–608 (1986)
- P. Zarka, W.M. Farrell, M.L. Kaiser, E. Blanc, W.S. Kurth, *Planet. Space Sci.* **52**, 1435–1447 (2004)
- P. Zarka, W.M. Farrell, G. Fischer, A. Konovalenko, *Space Sci. Rev.* (2008, this issue). doi:[10.1007/s11214-008-9366-8](https://doi.org/10.1007/s11214-008-9366-8)

Physical Processes Related to Discharges in Planetary Atmospheres

R. Roussel-Dupré · J.J. Colman · E. Symbalisty ·
D. Sentman · V.P. Pasko

Originally published in the journal Space Science Reviews, Volume 137, Nos 1–4.
DOI: [10.1007/s11214-008-9385-5](https://doi.org/10.1007/s11214-008-9385-5) © Springer Science+Business Media B.V. 2008

Abstract This paper focuses on the rudimentary principles of discharge physics. The kinetic theory of electron transport in gases relevant to planetary atmospheres is examined and results of detailed Boltzmann kinetic calculations are presented for a range of applied electric fields. Comparisons against experimental swarm data are made. Both conventional breakdown and runaway breakdown are covered in detail. The phenomena of transient luminous events (TLEs), particularly sprites, and terrestrial gamma-ray flashes (TGFs) are discussed briefly as examples of discharges that occur in the terrestrial environment. The observations of terrestrial lightning that exist across the electromagnetic spectrum and presented throughout this volume fit well with the broader understanding of discharge physics that we present in this paper. We hope that this material provides the foundation on which explorations in search of discharge processes on other planets can be based and previous evidence confirmed or refuted.

R. Roussel-Dupré (✉) · J.J. Colman · E. Symbalisty
Earth and Environment Sciences Devision, Atmospheric, Climate, and Environmental Dynamics Group,
MS F665, Los Alamos National Lab, Los Alamos, NM 87545, USA
e-mail: boberdnm@comcast.net

J.J. Colman
e-mail: jonah@lanl.gov

E. Symbalisty
e-mail: esymbalisty@lanl.gov

D. Sentman
Physics Department, University of Alaska Fairbanks, 108 Natural Sciences Facility,
708E Elvey Building, Fairbanks, AK 99775, USA
e-mail: dsentman@gi.alaska.edu

V.P. Pasko
Department of Electrical Engineering, Communications and Space Sciences Laboratory (CSSL),
The Pennsylvania State University, 211B Electrical Engineering East, University Park,
PA 16802-2706, USA
e-mail: vpasko@psu.edu

Keywords Planetary atmospheres · Electrical discharges · Electrical breakdown · Lightning · Kinetic theory · Swarm · Electron transport · Atmospheric electricity · Boltzmann equation · Fokker-Planck equation · Relativistic breakdown · Ionization · Drift velocity · Characteristic energy · Electron impact cross-sections · Electron attachment

1 Electron Transport and Avalanche in Gases

The acceleration, scattering, and energy loss or gain experienced by an electron as it moves through a gas subject to an applied electric field depends entirely on the gas composition, the details of the electron interactions with the constituent particles, and the boundary conditions. For weak fields the electrons drift and diffuse through the gas while undergoing elastic and inelastic collisions that together with the field define their momentum and energy distribution. The inelastic interactions that can occur include rotational, vibrational, and electronic excitations of the gas particles as well as losses by way of attachment and recombination. For stronger fields it is possible for ionizing collisions to take place. A gas discharge is initiated when the applied electric field exceeds the threshold value necessary for a sufficient population of electrons to overcome collisional drag and accelerate to energies beyond the gas ionization potential. In addition the ionization rate must exceed the net dissociative attachment rate (if extant) in order to have a net growth in the electron population. The energy or electric field at which the two balance each other defines the threshold for a discharge to initiate. Three-body attachment may also play an essential role in defining the overall development of the discharge as in air.

To date, two electrical breakdown mechanisms are known to operate in dielectrics. The first is the conventional breakdown (CB) process that has been studied extensively in the laboratory for a century or more and that is recognized as the sparks, arcs, and glow discharges of routine occurrence (cf., Loeb 1939; Raether 1964; Raizer 1991; Bazelyan and Raizer 1998). The second is a relatively new mechanism called runaway breakdown (RB) that was first advanced by Gurevich et al. (1992) and involves an avalanche of relativistic electrons that are collimated by the applied field to form an electron beam. RB may play an important role in lightning discharges on Earth (cf., Gurevich and Zybin 2005). Many of the fundamental ideas associated with electron runaway in thunderstorm electric fields were discussed by Wilson (1925, 1956).

Both breakdown mechanisms can be understood in the context of Fig. 1 where the frictional force, normalized to the minimum value at high energies, experienced by an electron moving through air is plotted as a function of the electron energy. This plot was derived by calculating the electron energy loss per unit length due to translational, rotational, vibrational, electronic, and ionizing collisions with air molecules. At high energies beyond ~ 10 keV the plotted values agree well with the Bethe energy loss expression (Bethe 1930; Bethe and Ashkin 1953) which is often referred to as the dynamical friction force. We see that a local minimum corresponding to 218 keV/m in sea level air exists at approximately 1.4 MeV. Clearly, if an electric field whose magnitude exceeds the minimum is applied to the medium then electrons with energies greater than the critical value ε_c at which the electric force equals the frictional force (see Fig. 1 for the case of an applied field equal to the conventional breakdown field where ε_c is approximately 10 keV) will be maintained and accelerated (runaway) to higher energies. It is also true that impact ionization of the air by energetic electrons will lead to the production of energetic secondary electrons. Those secondary electrons whose energies exceed the critical value ε_c become part of the runaway population and contribute to further ionization that also populates the runaway regime. The

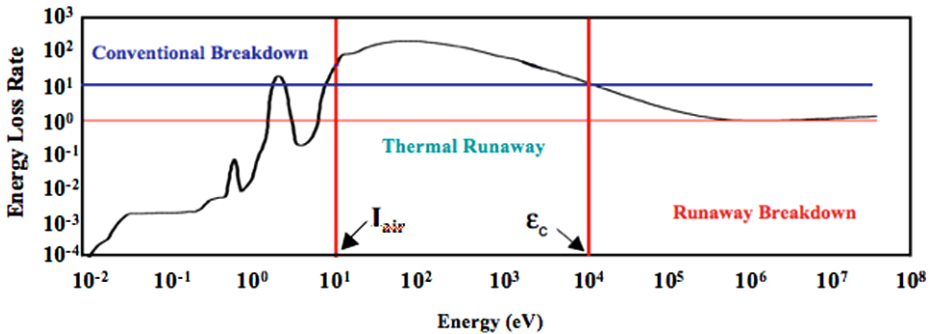


Fig. 1 Rough sketch of the electron energy loss rate in air, normalized to the local minimum at approximately 1.4 MeV, as a function of electron energy. The *blue line* represents the threshold for conventional breakdown which is ten times the threshold for runaway (shown in *red*). The critical energy ϵ_c at which electrons runaway in the presence of the conventional breakdown threshold field is shown at ~ 10 keV. The ionization potential for air (~ 14.9 eV) is also shown

net result is an avalanche in which the electron population grows exponentially. Collimation of these relativistic electrons by the electric field leads to the formation of an electron beam that grows exponentially as it propagates through the medium as long as the electric field exceeds a threshold defined near the minimum of the frictional force. In general, RB initiation requires a seed energetic electron with energy of order 1–10s of keV depending on the field strength. In planetary atmospheres, at altitudes below the ionosphere or the layer where solar UV and EUV radiation is absorbed, cosmic ray (CR) interactions provide the necessary seed population for initiation.

In the case of CB an applied electric field accelerates seed thermal electrons (~ 0.03 eV at STP) against the frictional drag such that some fraction of the electrons reach or exceed the ionization potential of air and eject additional secondary electrons that accelerate to sufficient energies to produce additional tertiary electrons and so on. The ensuing avalanche is limited in its energy extent by the large and broad maximum in the ionization energy loss rate depending on the field strength. Near the threshold for CB the electron distribution function is characterized by a mean energy of a few eV (controlled by the nitrogen resonant vibrational peak near 2 eV) together with a high-energy tail (tens of eV) that drives the avalanche. When the electric force exceeds the maximum energy loss rate due to ionization then a process referred to as cold or thermal runaway develops and feeds the RB mechanism. In fully and partially ionized gases (Dreicer 1959, 1960) the threshold is known as the Dreicer field which was derived using the Fokker-Planck treatment for electron transport described below. The question of whether or not such high fields (~ 10 times the CB threshold) can be established in the natural environment remains an ongoing topic of debate. This mechanism would compete with cosmic rays as seeds for the runaway process.

One important feature of RB is that the threshold electric field needed to initiate the avalanche is a factor of ten below that for conventional breakdown (see Fig. 1). Interestingly, macroscopic field strengths near or exceeding the threshold for CB have never been measured in terrestrial thunderstorms while values near and exceeding the threshold for RB have often been measured (see e.g., Marshall et al. 2005; Stolzenburg et al. 2007). At the same time it is important to note that positive and negative leaders can propagate in long gaps with sizes exceeding several tens of meters at ground pressure (Raizer 1991, p. 362) at fields that are significantly below the CB threshold but the question of how the leader is initiated in the first place particularly for lightning remains unanswered (e.g., Uman 2001, p. 79; Raizer

1991, p. 370; Bazelyan and Raizer 1998, pp. 203, 253). One of the unique signatures of runaway breakdown is the strong γ -ray flux produced by the beam interaction with the gas. The past several decades of research into the phenomenon of terrestrial lightning has in fact seen an accumulation of evidence for the existence of penetrating radiation (X- and γ -rays) in direct association with many forms of the lightning discharge (McCarthy and Parks 1985; McCarthy and Parks 1992; Fishman et al. 1994; Eack et al. 1996; Moore et al. 2001; Dwyer 2003; Smith et al. 2005). At high altitudes above 25 km, the Earth's atmosphere becomes transparent to the gamma rays produced by RB and remote detection becomes feasible as in the case of the terrestrial gamma ray flashes (TGFs) measured by the BATSE and RHESSI satellite based detectors (Fishman et al. 1994; Smith et al. 2005; Østgaard et al. 2008; Grefenstette et al. 2008).

While the basic properties of the electron beam formed in runaway breakdown such as the full electron energy distribution function (Symbalisty et al. 1998; Babich et al. 2001), the physical dimensions (Roussel-Dupré and Gurevich 1996; Babich et al. 2008), the diffusion coefficients (Gurevich et al. 1994), and the avalanche rates (Symbalisty et al. 1998; Lehtinen et al. 1999; Babich et al. 2001; and Dwyer 2003) have been studied with detailed kinetic calculations and some initial laboratory experiments have been performed (Gurevich et al. 1999; Babich et al. 2002), precise and comprehensive experimental validation is not presently available. Recently a new source of high-energy electrons in the Earth's magnetosphere due to Compton scattering and pair production by TGFs near the tropopause has been identified (Dwyer et al. 2008). Because of the large avalanche scale lengths (of order tens of meters at atmospheric pressure) necessary to produce an observable effect, RB is not easily reproduced in the laboratory. As a result, the natural environment provides the primary means for studying the details of this mechanism and satellite missions directed towards Earth and other planets provide important platforms for fielding critical diagnostics.

The RB mechanism can be suppressed by an applied magnetic field when the energy dependent electron gyro-frequency ($= eB/\gamma mc$, where B is the magnetic field strength and γ is the Lorentz factor) becomes comparable to the electron scattering rate (cf., Gurevich et al. 1996; Lehtinen et al. 1999). This condition is met for the relativistic electrons above approximately 30–40 km altitude in the terrestrial atmosphere. Once the electron becomes magnetized it follows the field lines. In this way the geomagnetic field acts as an energy filter as a function of height. The pitch angle distribution of the electrons once magnetized will span a broad angular range that depends on the angle of the magnetic field relative to the driving electric field and the runaway distribution function itself in the region above the thunderstorm. Another important effect is that the total current generated in an RB discharge can be significant (tens of kA) and can lead to a self magnetic field approaching and exceeding the geomagnetic field. This beamed plasma is subject to various forms of plasma instabilities that can affect the development of RB and further broaden electron pitch-angle distributions. This RB regime has yet to be explored and may be accessed in TLEs and TGFs.

2 Kinetic Theory

The kinetic theory of non-uniform gases was put on a firm mathematical and statistical foundation by Maxwell and Boltzmann by the end of the 19th century. The kinetic treatment of electron transport in gases that was also formulated nearly a century ago (see discussion in Chapman and Cowling 1970) forms the basis even today for calculating the momentum distribution and the statistical motion of electrons through a gas subjected to an applied

electric field. Cross-sections that quantify the probability of elastic or inelastic collisions are an important ingredient in the kinetic formulation and can also be derived from the interaction potentials for specific processes (e.g., rotational, vibrational, electronic, or ionizing interactions) or measured in the laboratory.

The Boltzmann equation in its most general form is a six dimensional integro-differential equation. The frequently referenced and utilized Maxwell-Boltzmann distribution function is a solution of this equation and it describes the probability distribution of particle momentum and energy for a uniform gas in thermodynamic equilibrium. The Boltzmann equation is still used even today to study the kinetic properties of gases and how they evolve in time. Much of the progress made in our understanding since the seminal works of Maxwell and Boltzmann is based on approximations that make the Boltzmann equation mathematically more tractable. In particular the assumption that the mean-free-path between binary collisions is small compared to the scale lengths that characterize non-uniformities in gases forms the basis for an expansion about the uniform state. Chapman and Enskog employed this approximation to develop a rigorous mathematical formulation that yielded the transport coefficients of particle diffusion, viscosity, the stress tensor, electrical conduction, heat conduction, and thermal diffusion. Inherent to this analysis is the assumed form of the interaction potential that characterizes the outcome of collisions between two particles. Simple models that ranged from rigid elastic spheres to spherically symmetric fields of force that fall off as a specified power of the distance from the particle center were utilized.

These overly simplified forms for the interaction potentials proved inadequate as more and more detail showing the complexity of molecular structures was gathered by spectroscopic means. Eventually, these problems were circumvented in part by relying on measurements of cross-sections that describe the probability of a certain outcome (scattering, momentum transfer, and/or energy loss) following a collision. In the modern computing era in fact it is possible to solve the Boltzmann equation numerically without resorting to analytic formulations and other simplifications. This approach is outlined below in our treatment of electrical discharges. With a full accounting of the relevant cross-sections as a function of the electron energy and scattering angle it is possible to compute the electron velocity distribution function from either the Boltzmann equation or from statistical Monte Carlo calculations that simulate many electron encounters. The Boltzmann equation when solved numerically can be effected by significant numerical diffusion depending on the details of the grid chosen to represent the momentum and spatial domains. The accuracy of Monte Carlo calculations on the other hand depends strongly on the number of particles and trajectories chosen per simulation and the extent of the spatial and momentum volumes. Generally, the Boltzmann formulation has an advantage at high gas densities (large numbers of collisions) and vice versa. However, the two methods have been checked against each other in the case of RB with discrepancies in the avalanche rates of only a few to tens of percent (Babich et al. 2001). Good agreement between discharge characteristics obtained by both methods has also been demonstrated in the conventional breakdown regime (e.g., Moss et al. 2006, and references therein). Our discussions below will focus on the Boltzmann treatment of electron transport.

2.1 Kinetic Equations for Runaway Breakdown

Assuming a spatially uniform applied electric field (no spatial dependence) we need only consider two momentum coordinates (azimuthal symmetry exists about the electric field direction) which in a spherical geometry are the momentum amplitude p and the cosine of

the angle between the applied electric field and the electron momentum direction μ . In this coordinate system the relativistic Boltzmann equation can be written:

$$\frac{\partial f}{\partial t} - \left[\frac{(1 - \mu^2)}{p} \frac{\partial f}{\partial \mu} + \mu \frac{\partial f}{\partial p} \right] eE = \frac{\partial_e f}{\partial t} \quad (2.1)$$

where $f(t, p, \mu)$ is the electron distribution function, m is the electron mass, E is a self-consistent or applied electric field, and $\partial_e f / \partial t$ is the Boltzmann collision integral for electron-gas interactions. Electron-gas interactions are, at high energies, primarily Coulomb in nature and the electrons undergo small deflections in both velocity space and configuration space. In this limit, the collision integral reduces to a Fokker-Planck form (derivation provided in Chapman and Cowling 1970; Krall and Trivelpiece 1973) that is given by:

$$\frac{\partial_e f}{\partial t} = \frac{1}{p^2} \frac{\partial(p^2 F_D f)}{\partial p} + \frac{(1 + Z/2)F_D}{4\gamma p} \frac{\partial}{\partial \mu} \left[(1 - \mu^2) \frac{\partial f}{\partial \mu} \right] + Q_{ion} \quad (2.2)$$

where Z is the mean molecular charge, γ is the Lorentz factor ($= 1/\sqrt{1 - \beta^2}$, $\beta = v/c$, v = electron speed, c = speed of light), F_D is the dynamical friction force first obtained by Bethe, namely,

$$F_D = \frac{4\pi Ze^4 N_m}{mc^2} \frac{\gamma^2}{\gamma^2 - 1} \left[\ln \left(\frac{mc^2 \sqrt{(\gamma^2 - 1)(\gamma - 1)}}{I\sqrt{2}} \right) + \left(\frac{2}{\gamma} - \frac{1}{\gamma^2} \right) \frac{\ln 2}{2} + \frac{1}{2\gamma^2} + \frac{(\gamma - 1)^2}{16\gamma^2} \right] \quad (2.3)$$

with I equal to the mean excitation potential of the gas, e is the electron charge, N_m is the molecular gas density, and Q_{ion} is an ionization term that accounts for the production of secondary energetic electrons by more energetic primary electrons. This term is essential for modeling the effects of runaway breakdown (e.g. Gurevich et al. 1992, 1996, 1998; Roussel-Dupré et al. 1994; Roussel-Dupré and Gurevich 1996) and is given by,

$$Q_{ion} = N_m c \frac{\beta}{\gamma^2 - 1} \frac{2\pi Ze^4}{mc^2} \int_{\varepsilon_L}^{\infty} d\varepsilon' \gamma'^2 Q_M(\varepsilon, \varepsilon') \frac{1}{\pi} \int_0^\pi d\alpha f(t, \varepsilon', \mu') \quad (2.4)$$

where ε is the electron kinetic energy, and the Møller cross section Q_M is given by,

$$Q_M(\varepsilon, \varepsilon') = \left[\frac{1}{\varepsilon^2} - \frac{1}{\varepsilon(\varepsilon' - \varepsilon)} \frac{(2\varepsilon' + mc^2)mc^2}{(\varepsilon' + mc^2)} + \frac{1}{(\varepsilon' - \varepsilon)^2} + \frac{1}{(\varepsilon' + mc^2)^2} \right]. \quad (2.5)$$

Experimental results are in agreement with the Møller formula to within 8% (see e.g. Scott et al. 1951). Equation (2.5) is valid for $\varepsilon > \varepsilon'$, and the integration is over all incident electrons with energy ε' greater than ε_L ($= 2\varepsilon$), and with

$$\mu' = \mu \mu_0 + \sqrt{(1 - \mu_0^2)(1 - \mu^2)} \cos \alpha \quad (2.6)$$

where $\mu_0 = \sqrt{\frac{\varepsilon(\varepsilon' + 2mc^2)}{\varepsilon'(\varepsilon + 2mc^2)}}$ is the cosine of the angle between the primary μ' and secondary μ electron momentum vectors and α is the azimuthal angle around the primary electron's momentum vector.

2.2 Kinetic Equations for Conventional Breakdown

Under the same approximations of a uniform applied electric field and azimuthal symmetry around the field, the non-relativistic Boltzmann equation for the electron distribution function, $f(v, \mu, t)$, can be written in a spherical coordinate system as:

$$\frac{\partial f}{\partial t} - \left[\frac{(1 - \mu^2)}{v} \frac{\partial f}{\partial \mu} + \mu \frac{\partial f}{\partial v} \right] eE = \frac{\partial_e f}{\partial t} \quad (2.7)$$

where t represents time, e the charge on an electron, m the electron mass, and E the applied field. The right hand side of this equation defines changes to the distribution function due to encounters with neutral gas molecules (the collision operator) and can be broken down as:

$$\begin{aligned} \frac{\partial_e f_s}{\partial t} = & N_m v \int_0^{2\pi} d\alpha \int_0^\pi \sin \beta d\beta \sigma_e(\beta, v) [f_s(v, \mu') - f_s(v, \mu)] \\ & - N_m \frac{m}{M} \frac{1}{v^2} \frac{\partial}{\partial v} \left\{ \int_0^{2\pi} d\alpha \int_0^\pi \sin \beta d\beta (1 - \cos \beta) \sigma_e(\beta, v) v^4 f_s(v, \mu') \right\} \\ & + \sum_h N_h v \int_0^{2\pi} d\alpha \int_0^\pi \sin \beta d\beta \left[f_s(w, \mu') \frac{w^2}{v^2} \sigma_h(\beta, w) - f_s(v, \mu) \sigma_h(\beta, v) \right] \\ & + \sum_I N_I v \int_0^{2\pi} d\alpha \int_0^\pi \sin \beta d\beta \left[\int_0^\infty d\varepsilon_I f_s(\varepsilon_I, \mu') \frac{\varepsilon_I}{v^2} \sigma_I(\varepsilon_I, \varepsilon_b) - f_s(v, \mu) \sigma_{Itot}(v) \right] \end{aligned} \quad (2.8)$$

where

$$w^2 = v_h^2 + v^2, \quad \varepsilon_I = v_I^2 + v^2 + \varepsilon_b, \quad \text{and} \quad \mu' = \mu \mu_\beta + \sqrt{1 - \mu^2} \sqrt{1 - \mu_\beta^2} \cos \alpha.$$

Sums are taken over all inelastic states h and ionization states I . N_m is the molecular gas density; σ_e the elastic differential cross-section (angular); σ_h the inelastic differential cross-section (angular); σ_I the ionization differential cross-section (energy); σ_{Itot} the total ionization cross-section; ε_I the incident electron energy in ionizing collisions; ε_b the scattered electron energy in ionizing collisions; v_h the inelastic threshold velocity for excitation; v_I the threshold velocity for ionization; v the electron velocity; and M the molecular mass.

3 Interaction Cross-Sections for Planetary Gases

3.1 Input to Non-relativistic Boltzmann Collision Integral

In order to solve the Boltzmann equation for electrons a collision integral ($\partial_e f / \partial t$) must be formulated that represents the interactions between the electrons and the medium through which they travel. At high electron energies the Fokker-Planck form may be used, as the interactions are primarily Coulomb in nature and small angle scattering dominates. At lower electron energies the interactions begin to couple to internal states of the medium, e.g. an electronic excitation of molecular nitrogen, and collisions characterized by large angle scattering and/or energy loss become important. In this case it is necessary to have knowledge of the various internal states of the medium, as well as its susceptibility to ionization and

attachment, in order to properly formulate the collision integral. Here we will quickly review the current state of knowledge of the cross sections for elastic, inelastic (rotational, vibrational, and electronic), attachment (both three body and dissociative), and ionizing interactions between electrons and those gases relevant to planetary atmospheres: molecular nitrogen (N_2), molecular oxygen (O_2), molecular hydrogen (H_2), carbon dioxide (CO_2), methane (CH_4), and helium (He).

We have taken data from the peer-reviewed and institutional literature at times, but there are two additional sources of relevant cross sections available on the Internet. The first is the well-known ‘public private communication’ by A.V. Phelps, available by ftp at ftp://jila.colorado.edu/collision_data (availability checked as of January 11, 2008); the second is the set of cross sections employed by the Magboltz code maintained by CERN and copyrighted by Biagi (1999). Plots of the Magboltz cross sections are available at <http://rjd.web.cern.ch/rjd/cgi-bin/cross> and the tabular data can be extracted from the code itself which is available at <http://consult.cern.ch/writeups/magboltz/magboltz-7.1.f> (availability checked as of January 11, 2008). Both of these sources have references to some of their source publications, and both include modifications or interpretations of their primary sources. The Phelps compilation does not include the elastic cross section for any of the gasses, providing instead an effective momentum transfer cross section, which is appropriate for use in the two-term spherical harmonic expansion treatment. The effective momentum transfer cross section is equal to the sum of the (angular integrated) inelastic cross sections plus the elastic momentum transfer cross section (Pitchford and Phelps 1982). We are not concerned with any form of the momentum transfer cross section here.

It is not our intent to attempt a comprehensive review of the literature here. The most recent ‘best value’ compilations owe much to earlier work and references can be found in papers referred to here. Our intent is to inform our readers of where readily available tabulated data resides, and give references to the most recent publications that include tabulated data. We will mention two early works in this introduction, both of which were helpful to the authors: the text “The diffusion and drift of electrons in Gases” by Huxley and Crompton (1974), and the review “Electron Scattering by Molecules II. Experimental Methods and Data” by Trajmar et al. (1983). A good deal of additional recent information is available in a review article by Brunger and Buckman (2002), which helps outline the uncertainties in the cross sections but does not recommend specific values.

3.1.1 Nitrogen

Both the Phelps and Magboltz compilations cover N_2 , and in fact the Magboltz compilation references Phelps as its source. Recently Itikawa (2006) published a compilation of his recommended values of the N_2 cross-sections; here we focus on those three sources. The various compilations are in reasonable agreement but there are some differences as well. Table 1 lists the various inelastic interactions along with their associated energy loss terms.

In Table 1 we see that Itikawa only specifically recommends values for the $v = 0 \rightarrow 1$ transition, he does discuss and provide references to the higher transitions all the way up to $v = 0 \rightarrow 17$. The vibrational cross sections utilized by Magboltz are identical to the Phelps compilation. For the electronic transitions the Magboltz treatment starts from work published by Phelps and Pitchford (1985) (JILA Report No. 26), but combines some transitions that are close together in energy. Individual electronic states sometimes show large differences with Itikawa recommending a peak value of $4.73 \times 10^{-17} \text{ cm}^2$ for the $a'^1\Pi_g$ transition at 16.5 eV while Phelps recommends a peak value of $2.023 \times 10^{-17} \text{ cm}^2$ at 17 eV. Some of these differences are compensated for with respect to the total scattering cross section by differences in other cross sections.

Table 1 Inelastic processes excited by electron impact with N₂ and the associated energy loss

Excited State	Energy Loss (eV)	Reference
Rotation	0.02, 0.00148	Phelps, Itikawa
Vibrational ($v = 0 \rightarrow 1$)	0.29	Phelps, Itikawa
Vibrational ($v = 0 \rightarrow 2$)	0.59	Phelps, Magboltz
Vibrational ($v = 0 \rightarrow 3$)	0.88	Phelps, Magboltz
Vibrational ($v = 0 \rightarrow 4$)	1.17	Phelps, Magboltz
Vibrational ($v = 0 \rightarrow 5$)	1.47	Phelps, Magboltz
Vibrational ($v = 0 \rightarrow 6$)	1.76	Phelps, Magboltz
Vibrational ($v = 0 \rightarrow 7$)	2.06	Phelps, Magboltz
Vibrational ($v = 0 \rightarrow 8$)	2.35	Phelps, Magboltz
$A^3\Sigma_u^+$, Triplet1	6.17, 6.169, 6.17	Phelps, Itikawa, Magboltz
$B^3\Pi_g$, Triplet3	7.35, 7.353, 7.35	Phelps, Itikawa, Magboltz
$W^3\Delta_u$	7.36, 7.362	Phelps, Itikawa
Triplet5	7.80	Magboltz
$B'^3\Sigma_u^-$	8.16, 8.165	Phelps, Itikawa
$a'^1\Sigma_u^-$	8.40, 8.399	Phelps, Itikawa
$a^1\Pi_g$, Singlet2	8.55, 8.549	Phelps, Itikawa, Magboltz
$W^1\Delta_u$	8.89, 8.890	Phelps, Itikawa
$C^3\Pi_u$, Triplet7	11.03, 11.032, 11.03	Phelps, Itikawa, Magboltz
$E^3\Sigma_g^+$, Triplet8	11.88, 11.875, 11.87	Phelps, Itikawa, Magboltz
$a''^1\Sigma_g^+$	12.25, 12.255	Phelps, Itikawa
$b^1\Pi_u$	12.500	Itikawa
$c'_4\Sigma_u^+$	12.935	Itikawa
$b'^1\Sigma_u^+$	12.854	Itikawa
Sum of singlet, Singlet5	13.0, 13.0	Phelps, Magboltz

Figure 2a shows a plot of the various N₂ cross-sections represented as energy loss per distance traveled at sea level as a function of energy. To construct this plot we have taken the elastic cross section from Magboltz, the inelastic cross sections from Phelps, and the ionization cross section from Itikawa. Figure 2a also shows the relativistic energy loss calculated from the Bethe formula (2.3).

3.1.2 Oxygen

Both the Phelps and Magboltz compilations cover O₂. Jeon (2003) has also published a full set of cross sections for O₂, which started from the set compiled by Phelps along with higher energy electronic states from a personal communication with M. Hayashi, and adjusted to match experimentally determined transport coefficients calculated from a two-term approximation of the Boltzmann equation. Magboltz again starts with the Phelps compilation but has done more extensive adjustments to match more recent experimental work, including work by Jeon and Nakamura (1998). The various compilations are in reasonable agreement with differences of less than 30% in most cases. Table 2 lists the various inelastic interactions along with their associated energy loss terms. Figure 2b shows a plot of the various O₂ cross-sections represented as energy loss per distance traveled at sea level as a function of energy. To construct this plot we have taken the cross sections from the Magboltz compila-

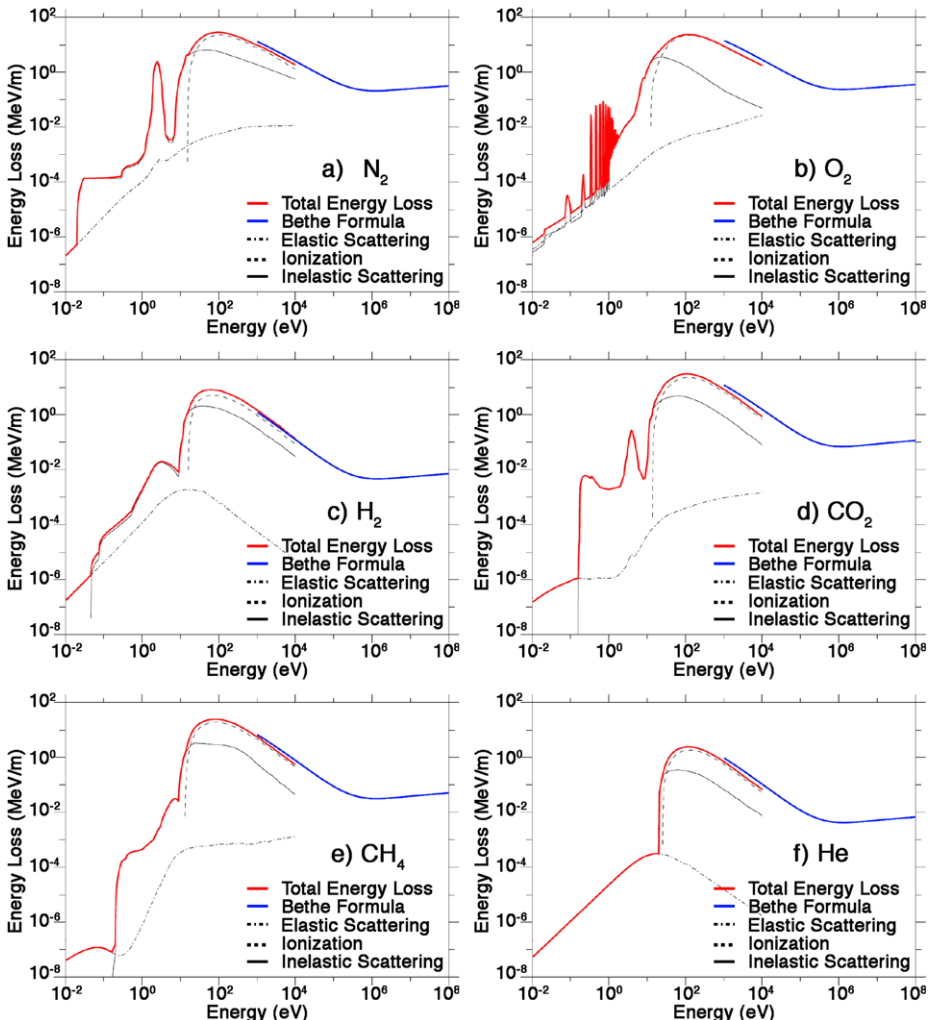


Fig. 2 a–f Energy loss in MeV/m for an electron traveling through pure gasses at sea level plotted as a function of electron energy. The total energy loss is represented by the thick red line, elastic scattering by the dash dot pattern, ionization by the dash pattern, and inelastic processes by the thin black line. The blue line was calculated from the Bethe formula (2.3). Figures a–f represent the gases N_2 , O_2 , H_2 , CO_2 , CH_4 , and He respectively

tion along with an elastic cross section taken from Kanik et al. (1993). It is worth noting that there is large variation among the various published elastic scattering cross section determinations and recommendations. Figure 2b also shows the relativistic energy loss calculated from the Bethe formula (2.3).

3.1.3 Hydrogen

Both the Phelps and Magboltz compilations cover H_2 . There is also a useful review by Tawara et al. (1990a), which unfortunately does not include tabulated data. It is important to keep in mind that the dissociation energy of molecular hydrogen is about 4.5 eV, therefore

Table 2 Inelastic processes excited by electron impact with O₂ and the associated energy loss

Excited State	Energy Loss (eV)	Reference
Three Body Attachment		Phelps, Jeon, Magboltz
Dissociative Attachment		Phelps, Jeon, Magboltz
Rotation	0.02, 0.02, 0.02	Phelps, Jeon, Magboltz
Vibrational ($v = 0 \rightarrow 1$)	0.19, 0.19, 0.193	Phelps, Jeon, Magboltz
Vibrational ($v = 0 \rightarrow 2$)	0.38, 0.38, 0.386	Phelps, Jeon, Magboltz
Vibrational ($v = 0 \rightarrow 3$)	0.57, 0.57, 0.579	Phelps, Jeon, Magboltz
Vibrational ($v = 0 \rightarrow 4$)	0.75, 0.75, 0.772	Phelps, Jeon, Magboltz
$a^1\Delta_g$	0.977, 0.977, 0.977	Phelps, Jeon, Magboltz
$b^1\Sigma_g^+$	1.627, 1.627, 1.627	Phelps, Jeon, Magboltz
4.5 Loss, $c^1\Sigma_u^- + c^3\Delta_u$	4.5, 4.5	Phelps, Magboltz
6.0 Loss, $A^3\Sigma_u^+$	6.0, 6.0, 6.1	Phelps, Jeon, Magboltz
8.4 Loss, $B^3\Sigma_u^-$	8.4, 8.4, 8.4	Phelps, Jeon, Magboltz
9.97 Loss	9.97, 9.97, 9.3	Phelps, Jeon, Magboltz
10.29 Loss	10.29	Jeon
13.3 Loss	13.3	Jeon

Table 3 Inelastic processes excited by electron impact with H₂ and the associated energy loss

Excited State	Energy Loss (eV)	Reference
Dissociative Attachment		Magboltz
Rotation ($J = 0 \rightarrow 2$)	0.044, 0.0439	Phelps, Magboltz
Rotation ($J = 1 \rightarrow 3$)	0.073, 0.727	Phelps, Magboltz
Vibration ($v = 0 \rightarrow 1$)	0.516, 0.516	Phelps, Magboltz
Vibration ($v = 0 \rightarrow 2$)	1.0, 1.023	Phelps, Magboltz
Vibration ($v = 0 \rightarrow 3$)	1.5, 1.48	Phelps, Magboltz
$b^3\Sigma_u^+$, Triplet States	8.9, 8.85	Phelps, Magboltz
$B^1\Sigma_u^+$	11.3	Phelps
$c^3\Pi_u$	11.75	Phelps
$a^3\Sigma_g^+$	11.8	Phelps
Singlet States	12.0	Magboltz
$C^1\Pi_u$	12.4	Phelps
Lyman Alpha	15.0	Phelps
Rydberg Sum	15.2	Phelps
Balmer Alpha	16.6	Phelps

many electronic excitations lead to dissociation. Table 3 lists the various inelastic interactions along with their associated energy loss terms. Figure 2c shows a plot of the various H₂ cross-sections represented as energy loss per distance traveled at sea level as a function of energy. To construct this plot we have taken the cross sections from the Phelps compilation along with an elastic cross section estimated from data compiled by Brunger and Buckman (2002), and a plot in the Tawara et al. (1990a). Figure 2c also shows the relativistic energy loss calculated from the Bethe formula (2.3).

3.1.4 Carbon Dioxide

Both the Phelps and Magboltz compilations cover N₂. In 2002, Itikawa published a compilation of his recommended values of the CO₂ cross-sections (Itikawa 2002). This work by Itikawa includes tabulations for the total, elastic, momentum transfer, three vibrations (100,010,001), ionization, and the dissociative attachment cross sections. In the conclusion Itikawa acknowledges the omission of electronic states from his compilation saying that they are either small or not known quantitatively. Indeed his review of even the state assignments show little agreement, nor do they agree with the compilations looked at here. He also discusses the vibrational resonance region around 3.8 eV saying that there are likely significant overtone bands in this region, indicated by the difference between total and elastic cross sections there. This assessment is consistent with the differences seen between the Phelps and Magboltz compilations, which are significant especially in the light of energy loss rather than total cross section. The Magboltz compilation includes ‘Polyad’ transitions, which we take to be vibrational resonances sometimes referred to as Fermi dyads; these contribute significantly to the energy loss if not so much the total cross section. Table 4 lists the various inelastic interactions along with their associated energy loss terms. Figure 2d shows a plot of the various CO₂ cross-sections represented as energy loss per distance traveled at sea level as a function of energy. To construct this plot we have taken the cross sections from the Magboltz compilation. Figure 2d also shows the relativistic energy loss calculated from the Bethe formula (2.3).

3.1.5 Methane

Methane is the only gas we address that is not covered by the Phelps compilation. Magboltz does include it, and there is some additional information in the paper by Kanik et al. (1993). Kanik estimates and tabulates integral elastic, vibrational, and electronic cross sections. Summing over Magboltz cross sections to give an appropriate comparison shows large differences between the compilations, exceeding a factor of 2 in some cases. Tawara et al. (1990b) also published a review in 1990, but does not include tabulated data and does not recommend any electronic transitions. Table 5 lists the various inelastic interactions along with their associated energy loss terms. Figure 2e shows a plot of the various CH₄ cross-sections represented as energy loss per distance traveled at sea level as a function of energy. To construct this plot we have taken the cross sections from the Magboltz compilation, as it is the most complete. Figure 2e also shows the relativistic energy loss calculated from the Bethe formula (2.3).

3.1.6 Helium

Helium is an important gas because it is commonly used as the standard in relative flow techniques to obtain absolute scattering cross-sections. It has the useful property that only elastic scattering is available below its inelastic threshold of about 19.8 eV. Both the Phelps and Magboltz compilations cover Helium. Comments in the Magboltz code claim an accuracy of 0.2% at all fields. We have not found this level of agreement in the open literature (see e.g. Brunger et al. 1992). Table 6 lists the various inelastic interactions along with their associated energy loss terms. Figure 2f shows a plot of the various He cross-sections represented as energy loss per distance traveled at sea level as a function of energy. To construct this plot we have taken the cross sections from the Magboltz compilation. Figure 2f also shows the relativistic energy loss calculated from the Bethe formula (2.3).

Table 4 Inelastic processes excited by electron impact with CO₂ and the associated energy loss

Excited State	Energy Loss (eV)	Reference
Dissociative Attachment		
Asymmetric Stretch, V(010) Bend Mode	0.083, 0.08275	Phelps, Magboltz
Vibration 2, V(020) Bend Mode Resonance	0.167, 0.15937	Phelps, Magboltz
V(100) Symmetric Stretch	0.17211	Magboltz
0.252 Loss, V(030) + V(110)	0.252, 0.251	Phelps, Magboltz
Vibration 3, V(001) Asymmetric Stretch	0.291, 0.29126	Phelps, Magboltz
0.339 Loss, Polyad 3	0.339, 0.335	Phelps, Magboltz
0.422 Loss, V(130) + V(210)	0.422, 0.422	Phelps, Magboltz
0.505 Loss, Polyad 4	0.505, 0.505	Phelps, Magboltz
Polyad 5	0.685	Magboltz
Polyad 6	0.825	Magboltz
Polyad 7	0.995	Magboltz
Polyad 8	1.16	Magboltz
Polyad 9	1.32	Magboltz
2.5 Loss, Sum Higher Polyads	2.5, 2.5	Phelps, Magboltz
3.85 Loss	3.85	Phelps
7.0 Loss	7.0	Phelps
Excitation 1	7.9	Magboltz
Excitation 2	8.9	Magboltz
10.5 Loss, Excitation 3	10.5, 10.5	Phelps, Magboltz
Excitation 4	12.2	Magboltz
13.3 Loss, Excitation 5	13.3, 13.2	Phelps, Magboltz
Excitation 6	15.0	Magboltz

Table 5 Inelastic processes excited by electron impact with CH₄ and the associated energy loss

Excited State	Energy Loss (eV)	Reference
Dissociative Attachment		
VIB V2 + V4	0.1625	Magboltz
VIB V1 + V3	0.3743	Magboltz
VIB HAR1	0.544	Magboltz
VIB HAR2	0.736	Magboltz
EXC DISOCIATION1	9.000	Magboltz
EXC DISOCIATION2	10.000	Magboltz
EXC DISOCIATION3	11.000	Magboltz
EXC DISOCIATION4	11.800	Magboltz

3.2 Input to Relativistic Boltzmann Equation

In the Fokker-Planck treatment described in Sect. 2.1 the electron encounters with gas molecules are represented as a mean drag (energy loss) plus a scattering in angle. The gas parameters that enter into this formulation are the mean charge Z and the mean excitation energy I . Values appropriate for planetary gases are listed in Table 7. The resulting energy loss is plot-

Table 6 Inelastic processes excited by electron impact with He along and associated energy loss

Excited State	Energy Loss (eV)	Reference
Triplet State, 19.8 Loss	19.82, 19.8	Phelps, Magboltz
Singlet Excitation	20.61	Magboltz

Table 7 Mean charge and excitation energy for planetary gases. Data taken from ICRU (1993)

GAS	Mean Charge (Z)	Mean Excitation Energy (I in eV)
H ₂	2	19.2
N ₂	14	82.0
O ₂	16	95.0
CH ₄	10	41.7
CO ₂	22	85.0
He	2	41.8

ted in Figs. 2a–f. The corresponding numbers for gas mixtures are found by weighting the values for the individual constituents by the gas fractional concentration. We note that the energy loss calculated from the Bethe formula and that calculated from the tabulated cross sections do not always agree. The source of this disagreement, and how best to address it, is not yet clear to us.

4 Solutions of the Kinetic Equations

4.1 Numerical Solution Techniques

4.1.1 Relativistic Boltzmann Equation

In this section we describe the numerical solution of the relativistic Boltzmann kinetic equation for the electron distribution function, $f(t, p, \mu)$, in a uniform atmosphere and with an applied, fixed, external electric field. Recall that p is the magnitude of the electron momentum, μ is the cosine of the angle between the electric field and the momentum vector, and δ_0 is the ratio of the electric field strength to the runaway threshold field or the over-voltage. This parameter represents the natural scaling for runaway breakdown and has been used extensively in the literature. It is related to the scaled electric field E/N_m expressed in Townsend or Td (where N_m is the molecular gas density and $1 \text{ Td} = 10^{-21} \text{ V m}^2$) in air by $E/N_m = 8 \cdot \delta_0$. The corresponding formula for the other planets can be derived from the values given in the last column of Table 8. From $f(t, p, \mu)$, we can compute the avalanche time, the average electron beam energy, and the spread in the beam energy. We recast the relativistic Boltzmann equation into a form, through a change of variables, that allows one to use the machinery of computational fluid dynamics for its numerical solution. The new, normalized, variables are:

$$\begin{aligned} p &= p/mc; & F &= F_D/F_{D,min}; & \varepsilon &= \varepsilon/mc^2; \\ \rho &= pf; & t &= (F_{D,min}/mc)(N_m/N_m^0)t. \end{aligned}$$

With these variables, (2.1) and (2.2) can be written as:

$$\frac{\partial \rho}{\partial t} + \nabla \cdot (\rho v) = \frac{\partial}{\partial \mu} \left\{ \Gamma \frac{\partial \rho}{\partial \mu} \right\} + p S_{ion} \quad (4.1)$$

Table 8 Relative concentrations of the constituent gases that make up the atmosphere's of the major planets as well as Titan and Triton are listed along with the corresponding mean molecular charge (Z), mean excitation energy (I), and threshold electric field at STP. The scaled electric field (E/N_m) in Td is also provided in each case. The asterisks indicate the specific gas mixtures (planets or moons) for which detailed kinetic calculations have been performed

Planet *Modeled	Gas Mixture	Mean Charge (Z)	Mean Excitation Energy I (eV)	Runaway Threshold E_{th} (kV/m)
Venus*	96.5% CO ₂ 3.5% N ₂	21.7	85	320 (11.9 Td)
Earth*	78% N ₂ , 21% O ₂ , 1% Ar	14.5	80.5	215 (8.00 Td)
Mars	95.5% CO ₂ 2.8% N ₂ 1.7% Ar	21.7	85	320 (11.9 Td)
Jupiter*	89% H ₂ 10.9% He 0.1% CH ₄	2.01	19.2	34.1 (1.27 Td)
Saturn	96.3% H ₂ 3.6% He 0.1% CH ₄	2.01	19.2	34.1 (1.27 Td)
Neptune	80% H ₂ 18.5% He 1.5% CH ₄	2.12	19.2	36.0 (1.34 Td)
Uranus	82.5% H ₂ 15.2% He 5% CH ₄	2.18	19.2	37.0 (1.38 Td)
Triton*	95% N ₂ 5% CH ₄	13.8	82	204 (7.59 Td)
Titan	95% N ₂ 5% CH ₄	13.8	82	204 (7.59 Td)

where the effective velocities in (p, μ) space are

$$v_\mu = -\frac{\delta_0(1-\mu^2)}{p}, \quad v_p = -(F + \mu\delta_0) \quad (4.2)$$

and the diffusion coefficient, due to elastic scattering, is

$$\Gamma = \frac{(1+Z/2)}{4} \frac{F}{\gamma} \frac{(1-\mu^2)}{p}. \quad (4.3)$$

We have now reduced the problem to solving a continuity equation with a diffusion term and source term. The effective velocity field is constant for a given electric field strength. We use a finite volume, cell centered, time explicit, spatially second order accurate algorithm from the CAVEAT code (Addessio et al. 1992) to solve this equation. The finite volume solution requires a discretization of the ionization term over a finite volume element. Our code runs

were initialized with an isotropic distribution of electrons having a specified mean energy, typically around several MeV though other values were tested to ensure that the distribution function evolved to the same steady state form. The model was run to a final time such that the distribution function was no longer changing, or was self-similar in the cases where the distribution function magnitude or electron density continues to change due to the runaway avalanche. Details of the solution can be found in Symbalisty et al. (1998).

4.1.2 Non-relativistic Boltzmann Equation

The numerical method used to solve the non-relativistic Boltzmann equation revolves around the technique described above and in Symbalisty et al. (1998). We first choose a new independent variable $\rho = vf$ and then recast the advective terms in (2.7) into a form that is equivalent to the usual hydrodynamic equations (see Symbalisty et al. 1998 for details). Then we use the well-known and well-tested numerical solution algorithms from computational fluid dynamics to derive an operator that acts on ρ and represents the change in ρ due to the left hand side of (2.7). Cross sections are weighted according to the number concentration presented in Table 8. The collision term (2.8) is discretized and an operator that acts on ρ at each cell in our grid is derived. The final solution is obtained by expressing the modified distribution function ρ as a vector with each element representing a cell defined by a specific momentum and angle in our grid. The flow and encounter terms were then formulated as matrices within the same dimensional space. The encounter matrix/operator was notated A , and the flow matrix/operator as S . The differential equation was then solved using an explicit time stepping method, with a time-step picked to ensure that the change of velocity remains smaller than our smallest grid volume in velocity space, i.e., satisfies the Courant condition. Thus, we rearrange the Boltzmann equation to:

$$\rho(t + \Delta t) = \rho(t) \times (1 + A\Delta t - ES\Delta t). \quad (4.4)$$

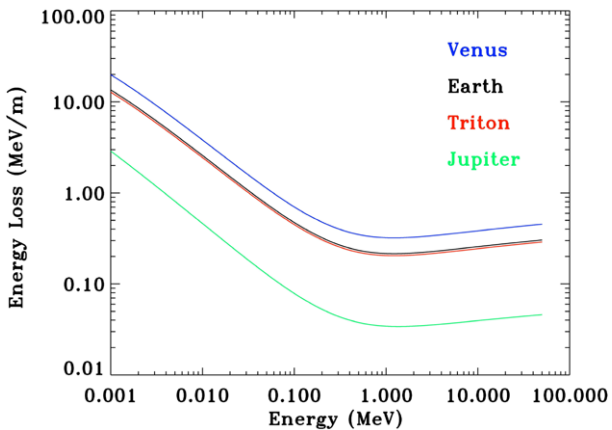
E is again the applied field.

The model initializes with an isotropic distribution of electrons having a specified mean energy, typically this value was 0.38 eV though other values were tested to ensure that the distribution function evolved to the same steady state form regardless of the starting energy. The model was run to a final time such that the distribution function was no longer changing, or was self-similar in the cases where the distribution function magnitude continues to change due to ionization or attachment. The model was run with all terms normalized to Standard Temperature and Pressure (STP) equivalents, but the output could be adapted to any altitude by rescaling the length (L) and time scales (τ) such that $NL = \text{constant}$ and $N\tau = \text{constant}$ and applying an additional correction for the three body attachment rate (in the case of oxygen and air). Thus, velocity and energy have no scaling factor while rates and accelerations (e.g., E) are proportional to the density (N) and hence the utility of the scaled parameter E/N (i.e., independent of gas density). Though we have all the mechanisms in place to employ differential cross sections, and we intend to do so in the future, we are currently assuming all processes to be isotropic.

4.2 Results

Solutions of both the relativistic (runaway breakdown regime) and non-relativistic (conventional breakdown or swarm regime) Boltzmann equations were obtained for gas mixtures relevant to a number of planetary and lunar atmospheres. The relative concentrations of the

Fig. 3 Electron energy loss rate or dynamical friction force as a function of electron energy for Venus, Earth, Triton, and Jupiter



constituent gases that make up the atmosphere's of the major planets as well as Titan and Triton are listed in Table 8 along with the corresponding mean molecular charge (Z), mean excitation energy (I), and threshold electric field at STP. Detailed calculations were performed for Venus (similar to Mars), Earth, Jupiter (representing the gas giants), and Triton (identical to Titan) as indicated by the asterisks in Table 8. The results are presented below for STP and for a range of scaled values of the electric field (E/N_m) given in Td. The electron distribution function was evolved in time until a self-similar solution was obtained.

4.2.1 Runaway Breakdown Regime

One of the primary inputs to the relativistic Boltzmann equation is the dynamical friction force or drag, F_D , resulting from electron-gas interactions. A plot showing the energy dependence of F_D for Venus, Earth, Triton, and Jupiter is provided in Fig. 3. Immediately evident from this plot as from Table 8 is the fact that the local minimum around 1.4 MeV (or the runaway threshold) is much lower in magnitude for the gas giants (Jupiter) than for Earth (by a factor of ~ 6.3) or the other planets and moons. Thus, runaway breakdown is more likely to be initiated on Jupiter provided the same electric field environments can be attained.

Table 9 lists the avalanche time τ , the average beam energy $\langle \epsilon \rangle$, and the spread (or standard deviation) σ in the beam energy derived from solutions of the relativistic Boltzmann equations for a number of electric field strengths and for the Earth at 1 atmosphere of pressure. The final time of the simulation, TMAX, is also listed. TMAX is always greater than 5 times the avalanche time, in order to allow a similarity solution to develop for the electron distribution function. The avalanche time is found to equilibrate 2 to 3 times faster than the average beam energy.

Similar calculations were performed for Venus, Jupiter, and Triton. The results are shown in Figs. 4a–c where the avalanche time, mean energy, and spread in energy, are plotted as a function of the scaled electric field (E/N) in Td, respectively. One key result is that the avalanche time is smaller for Jupiter than for Earth by large factors at low E/N and by factors of 2–3 at high E/N , in agreement with the findings of Dwyer et al. (2006). The indication again is that runaway breakdown initiates more easily and proceeds faster on the gas giants for the same applied electric field. In addition, the mean energy and spread in energy tends to be smaller. As a result we can expect diagnostics such as gamma ray flashes from bremsstrahlung radiation produced by a runaway discharge on Jupiter to be

Table 9 The avalanche time τ , average beam energy $\langle \varepsilon \rangle$, and the spread (or standard deviation) σ in the beam energy are listed for a number of scaled electric field strengths E/N or overvoltages δ_0 . These results were obtained from solutions of the relativistic Boltzmann equation for the Earth at STP. The final time of the simulation, TMAX, is also listed

E/N (Td)	δ_0	TMAX (ns)	τ (ns)	$\langle \varepsilon \rangle$ (MeV)	σ (MeV)
15	1.85	1000	194	6.91	10.8
16.22	2.0	900	158	7.05	11.3
20	2.466	600	100	7.24	12.1
24.33	3.0	435	70.8	7.34	12.5
28.39	3.5	300	55.4	7.35	12.5
32.44	4.0	279	45.5	7.39	12.8
35	4.316	248	40.8	7.40	12.9
40.55	5.0	200	33.3	7.39	12.9
50	6.165	140	25.3	7.34	12.8
56.77	7.0	125	21.5	7.32	12.9
64.9	8.0	110	18.2	7.26	12.9
72.99	9.0	95	15.7	7.20	12.8
75	9.248	80	15.2	7.16	12.6
81.10	10.0	70	13.8	7.10	12.4
100	12.33	60	10.7	6.92	12.3
125	15.41	55	7.93	6.64	11.9
150	18.50	50	6.24	6.36	11.5
200	24.66	25	4.23	5.82	10.6

significantly different. In particular, the spectrum of the gamma rays would be softer on Jupiter than on Earth.

Results for the electron distribution at high energies for the various planets and moons and for $E/N = 20$ Td and $E/N = 200$ Td are presented in Figs. 5 and 6, respectively. Clearly evident in these plots is the collimation of the electrons anti-parallel to the electric field. The collimation increases significantly at the larger field strength. Also evident is that the electrons are significantly more aligned with the electric field in the Jovian atmosphere for the same field strength. This result indicates that the gamma emissions produced by a runaway discharge on Jupiter would be significantly more forward directed (along the electric field) for the same electric field.

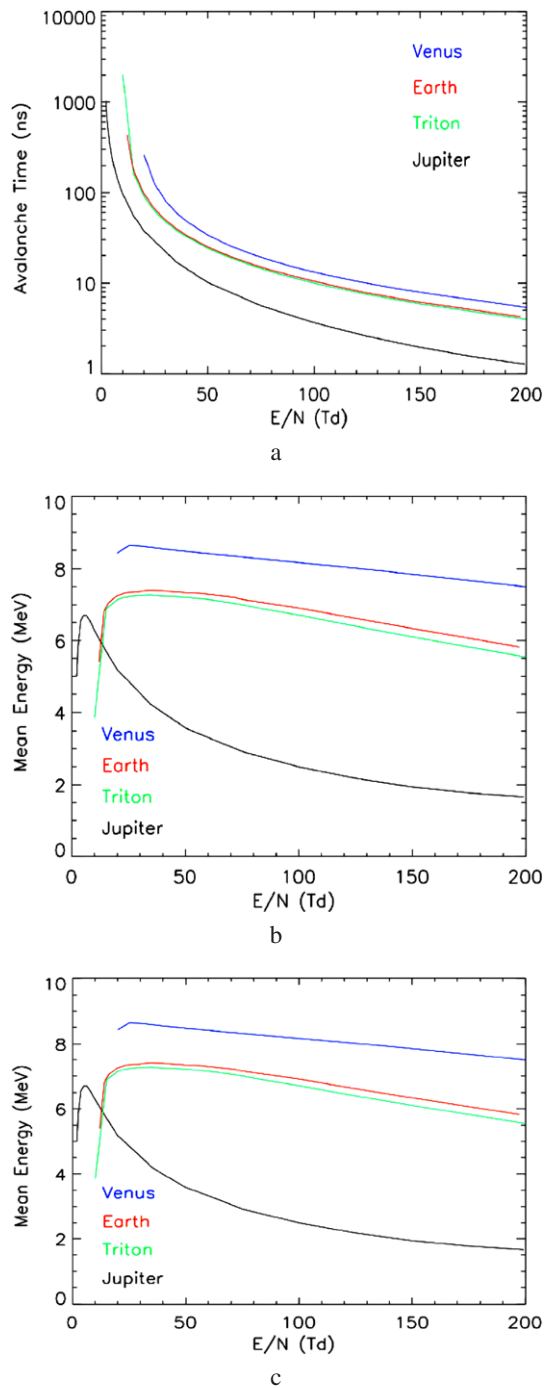
4.2.2 Non-relativistic Regime

Here we present representative results from our kinetic calculations of electron swarms in various pure gases and compare them to various experimental determinations.

Summary of Planets

Figures 7, 8, 9, 10 show that we are accurately representing the bulk properties of the electron swarm within this range of applied fields. We do not have the data necessary to benchmark calculations of the gas mixtures that mirror the planetary atmospheres. Nevertheless we have performed those calculations and some of the results are presented below. Figures 11 and 12 show the self-similar distribution functions obtained for calculations of the atmospheres of Jupiter, Triton, and Venus at applied fields of 20 and 200 Townsend respectively. At 20 Td, Fig. 11, the applied electric field lies below the ionization threshold for all gas mixtures and we see that the mean electron energy and shape of the distribution function

Fig. 4 **a** Avalanche time in ns, **b** Mean electron energy, and **c** Electron energy spread in MeV as a function of scaled electric field (E/N) in Td for Venus, Earth, Triton, and Jupiter



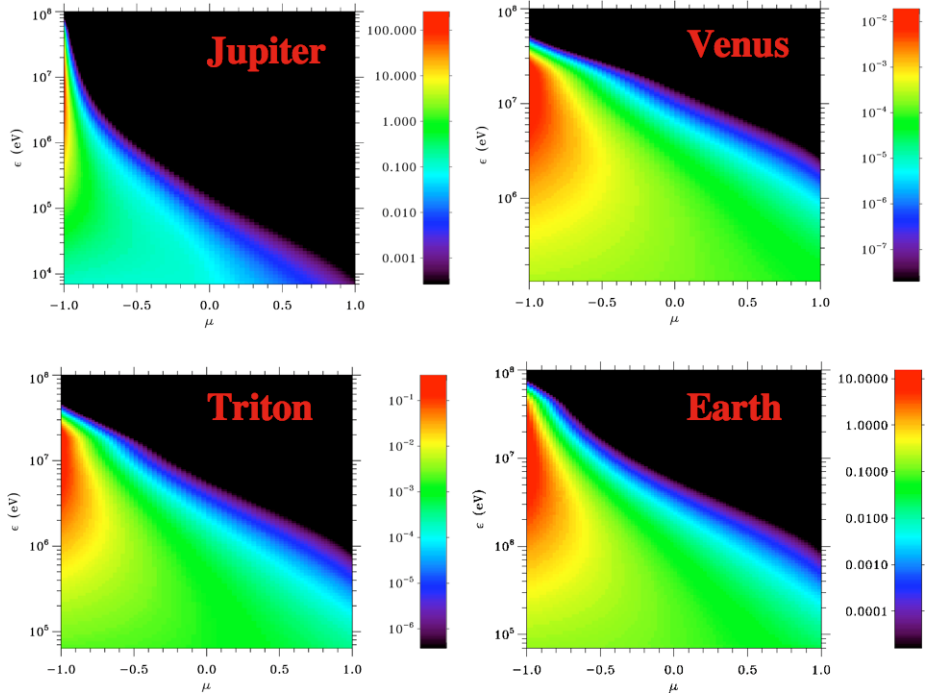


Fig. 5 Two-dimensional plots of the electron distribution functions as a function of the cosine of the angle μ between the electric field and the electron momentum and as a function of the electron energy ϵ for Venus, Earth, Triton, and Jupiter and for $(E/N) = 20$ Td

depends strongly on the details of the vibrational collision cross-sections around several eV (plotted along side the distribution functions for reference). In particular, the distribution function is depleted by the energy loss associated with vibrational excitation of N₂ (Triton) and CO₂ (Venus) but not H₂ (Jupiter). See also Figs. 2a–f. At 200 Td, Fig. 12, the electric field exceeds the threshold for ionization in all cases and we see a splitting of the distribution function in the case of N₂ and CO₂ caused by the strong energy loss associated with vibrational transitions. In the case of Jupiter we see a broader, more energetic distribution function peaked in the direction of the electric field. Note that the energy scales vary from plot to plot.

5 Earth's High-Altitude Discharges

In this section we briefly describe the recently discovered discharge phenomena of transient luminous events (TLEs) and terrestrial gamma-ray flashes (TGFs). Sprites are covered in more detail because of the large body of relevant data that exists and because of their close tie to well known discharge processes. Examples of diagnostics that can and have provided information about the physical nature and origin of sprites is included. The phenomena of TLEs and TGFs may well have counterparts on other planetary systems and it is important to understand their characteristics as manifested on Earth, their impact on the terrestrial environment, and how to detect them.

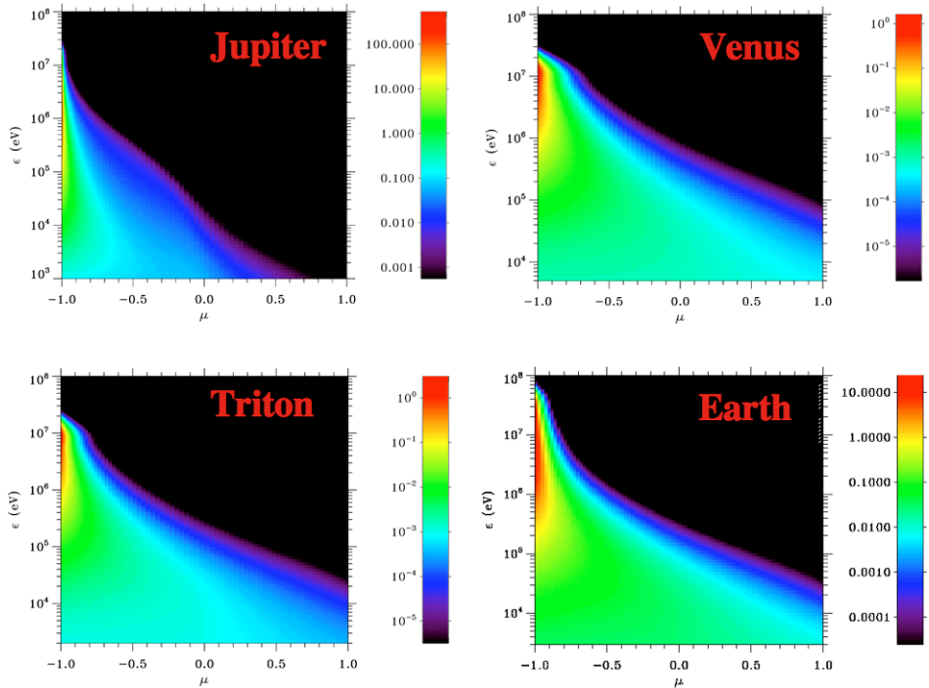


Fig. 6 Two-dimensional plots of the electron distribution functions as a function of the cosine of the angle μ between the electric field and the electron momentum and as a function of the electron energy ϵ for Venus, Earth, Triton, and Jupiter and for $(E/N) = 200$ Td

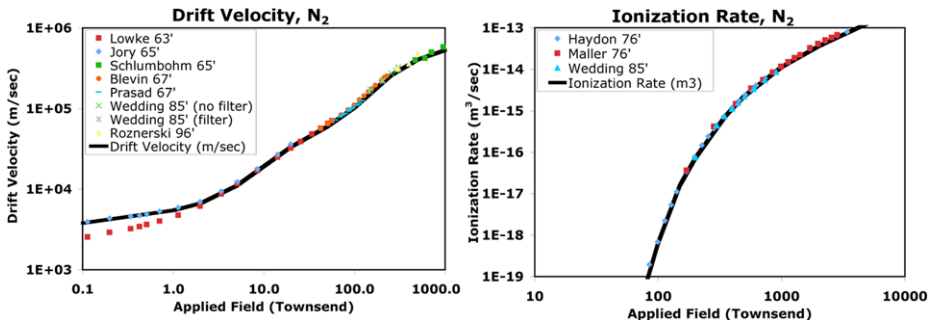


Fig. 7 Calculated Drift Velocities and Ionization rates in $N_2(g)$ (at STP) plotted along with experimental determinations

TLEs are believed to result from a discharge process that develops in the quasi-electrostatic fields that appear in the upper atmosphere following a cloud-to-ground lightning discharge in which large quantities of positive charge (~ 100 to several hundred Coulombs) and occasionally negative charge are transferred to ground. The optical measurements of TLEs (over 10000 events have been recorded) both from the ground (Lyons 2006) and from orbit (e.g., ISUAL on FORMOSAT-2, Mende et al. 2006) have resulted in the phenomenological identification of a large number of processes that have been organized

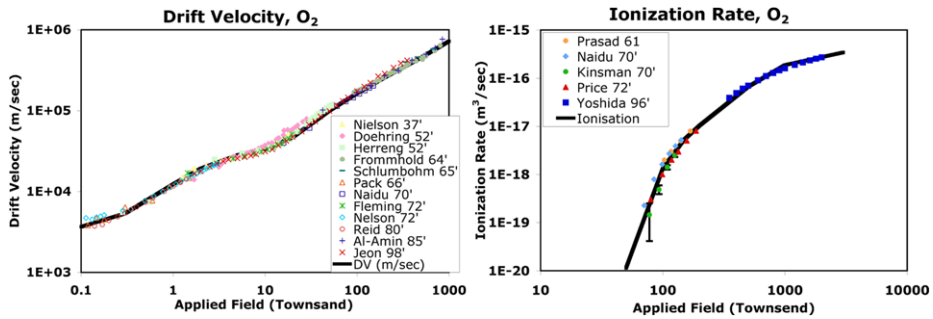


Fig. 8 Calculated Drift Velocities and Ionization Rates in $O_2(g)$ (at STP) plotted along with experimental determinations

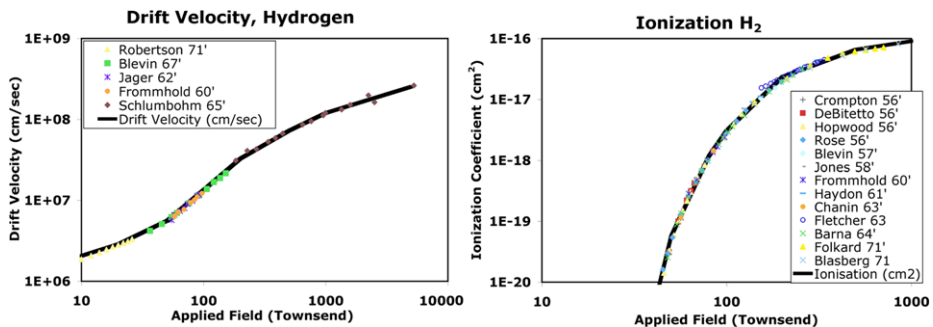


Fig. 9 Calculated Drift Velocities and Ionization Rates in $H_2(g)$ (at STP) plotted along with experimental determinations

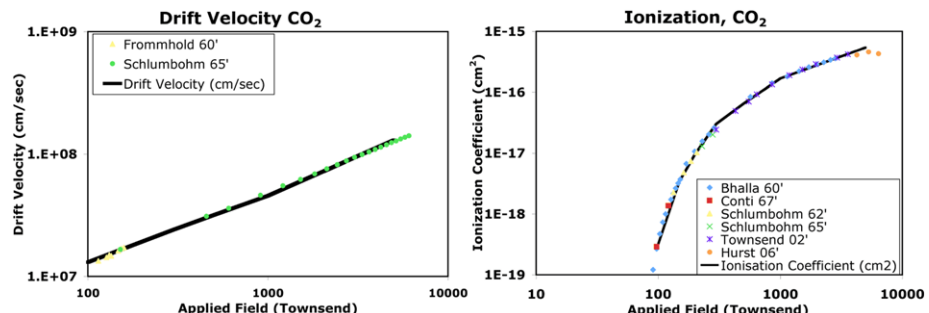


Fig. 10 Calculated Drift Velocities and Ionizations Rates in $CO_2(g)$ (at STP) plotted along with experimental determinations

into a taxonomy that includes many descriptive and non-descriptive names such as column and carrot sprites, angels, trolls, jets, giant jets, halos, elves, and beads (i.e. Sentman and Wescott 1993; Lyons et al. 2003a, 2003b; Lyons 2006; Cummer et al. 2006a, 2006b; Asano et al. 2008). The relevant scale lengths range from tens of meters to tens and hundreds of kilometers while the temporal scales range from hundreds of μ s to hundreds of ms. The total energy dissipated in individual events is generally around tens of MJ with power mea-

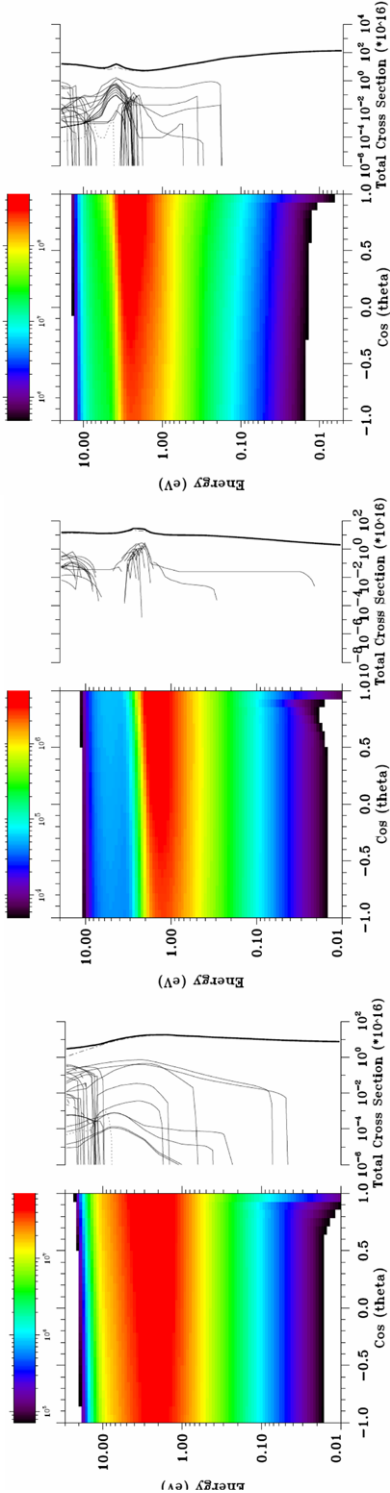


Fig. 11 Electron distribution functions for Jupiter, Triton, and Venus at an applied field of 20 Td at STP. The relevant cross sections are plotted to the *right* of the distribution functions

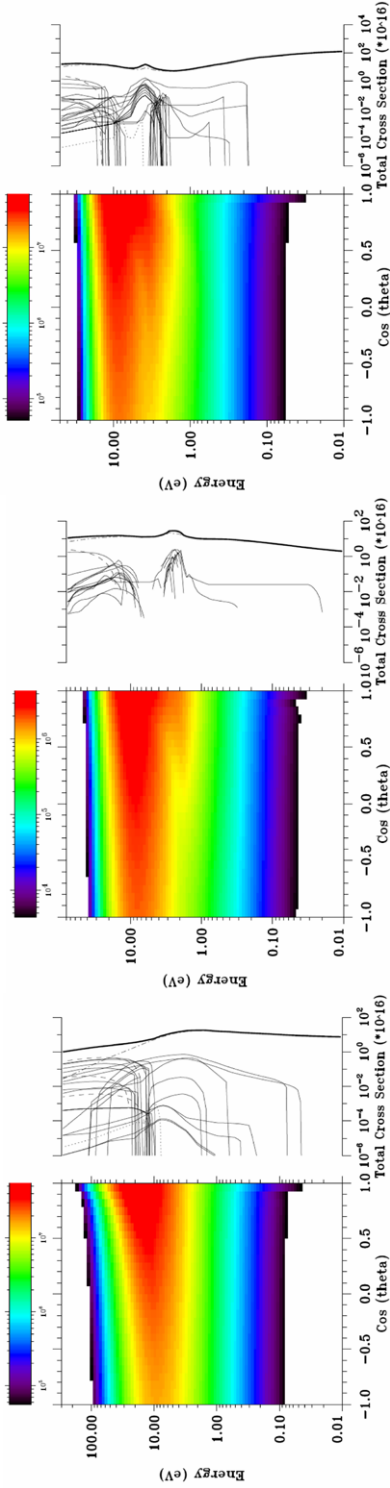


Fig. 12 Electron distribution functions for Jupiter, Triton, and Venus at an applied field of 200 Td at STP. The relevant cross sections are plotted to the right of the distribution functions

sured in gigawatts (Heavner et al. 2000). The electron densities generated in the mesosphere can exceed 10^6 cm^{-3} (cf., Liu and Pasko 2004) while the individual electron energies in these postulated electrical discharges can range from a few eV to tens of MeV and produce emissions throughout the electromagnetic spectrum. While our understanding of certain aspects of TLEs, e.g., elves, halos, and sprites, is progressing or in hand, many of the details, especially concerning their chemical effects in the atmosphere (e.g., Enell et al. 2008; Sentman et al. 2008), are not. Dedicated satellite missions are presently in planning to further study energetics and chemical effects of sprites and other transient luminous events on the upper atmosphere (e.g., Blanc et al. 2007).

TGFs are thought to be a manifestation of a RB process that occurs inside thunderstorms. These energetic phenomena were first discovered by the Burst and Transient Source Experiment (BATSE) on the Compton Gamma Ray Observatory (CGRO, Fishman et al. 1994) and are presently being monitored by the Reuven Ramaty High Energy Solar Spectroscopic Imager (RHESSI) satellite, which to date has observed some 10–20 TGFs per month (Smith et al. 2005). The time duration of individual events ranges from hundreds of μs to ms. The geographical distribution of TGFs roughly corresponds to the geographical distribution of lightning over continents at low latitude and also to the distribution of sprites (Christian et al. 2003; Chen et al. 2005). However TGF emissions are rarely detected over the Southern US where many sprites are observed at ground level (Smith et al. 2005). TGF spectra measured by RHESSI reveal energies up to 30 MeV (Smith et al. 2005), in agreement with energies predicted by the RB mechanism triggered by cosmic rays (Roussel-Dupré and Gurevich 1996; Roussel-Dupré et al. 2005; Dwyer and Smith 2005; Østgaard et al. 2008). The low energy part of the TGF spectrum (below 100 keV) is most sensitive to the TGF emission altitude, due to the large attenuation of low energy gamma rays in the atmosphere. However, in the case of RHESSI, which was not designed to look for TGFs, the instrument response to terrestrial events precludes using the low energies to ascertain source altitude. The analysis of the RHESSI spectra around 1 MeV suggests that their source is in the range of 15–21 km, implying that thunderstorms and not sprites may initiate TGFs (Dwyer and Smith 2005). A recent analysis, however, of BATSE spectra shows that the source of BATSE TGFs could extend continuously from 15 km to 60 km altitude rather than in a narrow altitude range (Østgaard et al. 2008). The possibility of two kinds of TGFs corresponding to low and high altitude sources can be envisaged. A lightning leader as a source of TGFs is predicted by Moss et al. (2006) who show that thermal electrons can be accelerated in the leader streamer zone up to energies of several hundreds of keV and possibly up to several tens of MeV. This mechanism then predicts that some TGFs can be produced by high altitude leader processes.

5.1 General Phenomenology of Sprites

Sprites are large luminous discharges, which appear in the altitude range <40–90 km above large thunderstorms typically following intense positive cloud-to-ground lightning discharges (Sentman et al. 1995; Boccippio et al. 1995; see also Fig. 13). The evolution of these discharges and their optical emissions are strongly dependent on the details of the electron distribution functions associated with the coupled, self-consistent electric fields that drive the process. The kinetic calculations and methodology outlined above are essential to modeling and understanding these phenomena. Below we describe the observations.

Recent telescopic imaging of sprites at standard video rates (i.e. with 16 ms time resolution) revealed an amazing variety of generally vertical fine structure with transverse spatial scales ranging from tens to a few hundreds of meters (Gerken et al. 2000;

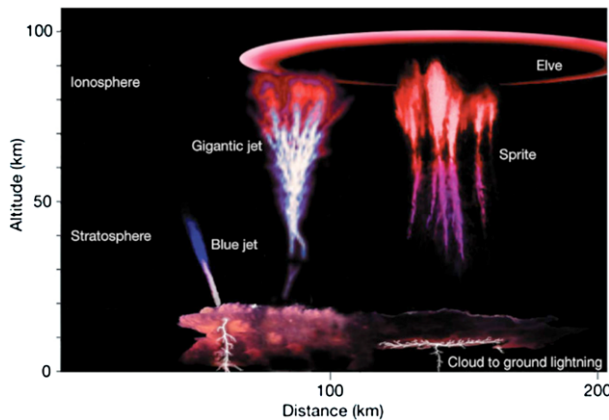


Fig. 13 Lightning related TLEs. Several types of TLEs are known, and some examples are shown here: relatively slow-moving fountains of blue light, known as ‘blue jets’, which emanate from the top of thunderclouds up to an altitude of 40 km (Wescott et al. 1995; Lyons et al. 2003a), ‘sprites’ that develop at the base of the ionosphere and move rapidly downwards at speeds up to $10\,000\text{ km s}^{-1}$ (Sentman et al. 1995; Lyons 1996; Stanley et al. 1999), ‘elves’, which are lightning induced flashes that can spread over 300 km laterally (Fukunishi et al. 1996; Inan et al. 1997; Kuo et al. 2007), and upward moving ‘gigantic jets’, which establish a direct path of electrical contact between thundercloud tops and the lower ionosphere (Pasko et al. 2002; Su et al. 2003; Pasko 2003). Reprinted from (Pasko 2003) with permission from *Nature*

Gerken and Inan 2002, 2003, 2005). First high-speed (1 ms) telescopic imaging of sprites has been reported indicating that streamer-like formations in sprites rarely persist for more than 1–2 ms (Marshall and Inan 2005, 2006). Also recently, it has been demonstrated that sprites often exhibit a sharp altitude transition between the upper diffuse and the lower highly structured regions (Gerken and Inan 2002, 2003; Stenbaek-Nielsen et al. 2000; Pasko and Stenbaek-Nielsen 2002). Many sprites are observed with an amorphous diffuse glow at their tops, the so-called sprite ‘halo’ (cf., Gerken and Inan 2003; Barrington-Leigh et al. 2001).

The appearance of fine structure in sprites has been interpreted in terms of positive and negative streamer coronas, which are considered as scaled analogs of small-scale streamers, which exist at high atmospheric pressures at ground level (cf., Pasko et al. 1998; Sentman et al. 2008). Streamers are filamentary plasma structures, which can initiate spark discharges in relatively short (several cm) gaps at near ground pressures in air and which are commonly utilized in applications such as ozone production and pollution control (Raizer 1991; van Veldhuizen 2000) and references cited therein), and also represent important components involved in the triggering of combustion in spark ignition engines (Tardiveau et al. 2001; Tardiveau and Marode 2003). An excellent recent review of various applications of streamers is provided in Ebert et al. (2006). In ground air pressure applications a typical transverse scale of individual streamer filaments is a fraction of a millimetre (Pancheshnyi et al. 2005; Briels et al. 2005). It is quite remarkable that the filamentary structures observed in sprites (Gerken and Inan 2005) are the same phenomenon known as streamer discharges at atmospheric pressure, only scaled by reduced air density at higher altitudes (Pasko et al. 1998; Liu and Pasko 2004, 2006; Pasko 2006). These aspects of sprite phenomenology are important for interpretation of optical emissions observed from them.

Table 10 (Liu et al. 2006) summarizes emissions documented in sprites. These include the First Positive (1PN_2) and Second Positive (2PN_2) band systems of N_2 , N_2 Lyman–Birge–Hopfield (LBH) band system and the First Negative band system of N_2^+ (1NN_2^+).

Table 10 Summary of observed emissions from sprites (Liu et al. 2006)

Emission band System	Transition	Excitation energy threshold (eV)	Lifetime at 70 km Alt.	Quenching Alt. (km)
1PN ₂	N ₂ (B ³ Π _g) → N ₂ (A ³ Σ _u ⁺)	~7.35	5.4 μs	~53
2PN ₂	N ₂ (C ³ Π _u) → N ₂ (B ³ Π _g)	~11	50 ns	~30
LBH N ₂	N ₂ (a ¹ Π _u) → N ₂ (X ¹ Σ _g ⁺)	~8.55	14 μs	~77
1NN ₂ ⁺	N ₂ ⁺ (B ² Σ _u ⁺) → N ₂ ⁺ (X ² Σ _g ⁺)	~18.8	69 ns	~48

The collisional excitation rates needed to obtain the fluorescence efficiencies are derived from kinetic calculations of the electron distribution function; the relevant states are noted in Table 1.

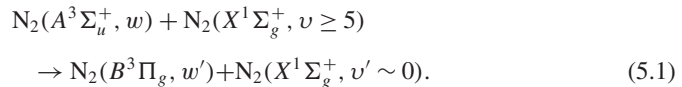
In this section we provide a review of related observations. Spectra of sprites in the stratosphere/mesosphere above electrically active cumulonimbus clouds were first acquired by Hampton et al. (1996) on 22 June, 1995, from an observation site atop Mt. Evans, and independently by Mende et al. (1995) on 16 July 1995, from an observation site near Fort Collins, Colorado. The Hampton et al. (1996) observations used a video slit spectrograph to obtain optical spectra of sprites. Twenty-five events were observed in the wavelength range 540–840 nm with spectral resolution approximately 6 nm and recorded with a 33 ms time resolution. The Mende et al. (1995) observations were conducted with a spectral resolution of approximately 9 nm and spectra recorded at a normal video rate (33 ms/frame) using an imaging spectrometer covering the wavelength range ~450–800 nm. Both sets of observations detected four distinct features in the 600–760 nm region which were identified as the N₂ First Positive system with $\Delta = 2, 3$ and 4 from the $v = 2, 4, 5, 6$ vibrational levels of the N₂ (B³Π_g) state.

The spectral observations of both groups were analyzed in detail by Green et al. (1996) using energy dependent electron excitation cross sections and laboratory data to extract information on the vibrational distributions of the excited N₂ (B³Π_g) state and the energies of electrons producing the red sprite radiance. It was concluded that the sprite electrons appear to be of energy sufficient to dissociate and ionize N₂. Results indicated excitation by electrons with a Boltzmann temperature of 1 eV (range 0.4–2 eV). Green et al. (1996) also derived an estimate for the electric field magnitude driving sprite phenomenon of 100–200 V m⁻¹ at 70 km altitude. This field appears to be fully consistent with the breakdown field.

The spectral resolution (6–9 nm) employed in Mende et al. (1995), Hampton et al. (1996) has not permitted accurate rotational temperature determination (Green et al. 1996), and we note that up to the present date there are no data available on the rotational temperature in sprites. In existing sprite models the rotational lines are computed at a temperature 220–230 K (Green et al. 1996; Bucsel et al. 2003). Recently, well-distinguishable infrasound signatures of sprite events have been reported (Liszka 2004; Farges et al. 2005; Liszka and Hobara 2006), indicating a possibility of heating of ambient atmospheric gas by sprite discharges. The measurements of rotational intensity distributions of N₂ molecular bands may be potentially used for remote sensing of variations of gas temperature in sprite discharges (Phillips 1976; Vallance-Jones 1974, p. 157).

A time-dependent N₂ vibrational level population model has been used in (Morrill et al. 1998) to simulate the spectral distributions and absolute intensities observed in sprites. Comparison of modeling results with the sprite spectrum taken at the TV field rate (17 ms resolution) measured with 7–11 nm resolution from the Wyoming Infrared Observatory (WORO)

on Jelm Mountain during July 1996 led to a vibrational distribution of the $\text{N}_2 (B^3\Pi_g)$, which required an average electron energy of only 1–2 eV, generally consistent with earlier results reported in (Green et al. 1996). Analysis also indicated the presence of weak spectral features that were attributed to N_2^+ Meinel emissions (Morrill et al. 1998). Additional analysis of a sprite spectrum from 53 km altitude from the same data set has been conducted in Buc-sela et al. (2003). The obtained $\text{N}_2 (B^3\Pi_g)$ vibrational distribution appeared to be consistent with those observed in laboratory afterglows, indicating an energy transfer process at lower altitudes in sprites (i.e. in sprite tendrils) between vibrationally excited N_2 ground state and the lowest-energy, metastable electronic state:



The recently reported altitude-resolved sprite spectra (Kanmae et al. 2007) recorded with an imaging spectrograph with 3 ms and 3 nm temporal and spectral resolution, respectively, are consistent with this hypothesis. The metastable oxygen molecules $\text{O}_2 (a^1\Delta_g)$ are abundantly produced in streamer discharges (Lowke 1992; Naidis 1999), and a possible contribution to sprite $\text{N}_2 (B^3\Pi_g)$ emissions of energy transfer between $\text{O}_2 (a^1\Delta_g)$ and $\text{N}_2 (A^3\Sigma_u^+)$ metastable species has recently been discussed in Kamaratos (2006). However, in a simulation of the plasma chemistry associated with sprite streamers at 70 km altitude Sentman et al. (2008) found that this process is not a major contributor to sprite optical emissions.

The low temporal resolution (<17–33 ms) of spectral measurements in Mende et al. (1995), Hampton et al. (1996), and in the spectra used for subsequent analysis reported in Green et al. (1996), Bucsela et al. (2003), Morrill et al. (1998), represents a likely reason why more energetic electrons and higher electric fields, associated with streamer tips, have not been detected in these early measurements. A sub-millisecond time resolution is needed for accurate studies of sprite streamers. Following original observations of Mende et al. (1995), Hampton et al. (1996), narrow band photometric and blue-light video observations of sprites had been conducted (Armstrong et al. 1998, 2000; Suszcynsky et al. 1996), which indicated presence of a short (<1 ms) energetic ionizing event at the initial stage of sprite formation sufficient to ionize and excite molecular nitrogen, followed by secondary lower energy processes which give rise to the dominant and relatively long-lasting red emission. Specifically, sub-millisecond time resolution data on the 399.8 nm $\text{N}_2 (1, 4)$ Second Positive band, 427.8 nm $\text{N}_2^+ (0, 1)$ and 470.9 nm $\text{N}_2^+ (0, 2)$ First Negative bands generated by sprites were analyzed in conjunction with supporting video imaging in Armstrong et al. (1998, 2000), Suszcynsky et al. (1996). The measured impulsive ionization emission during the sprite initiation exhibited an exponential decay time constant of only 0.3 ms. The presence of more energetic electrons at the initial stage of sprite formation has also been confirmed by subsequent photometric observations reported in Miyasato et al. (2003), Takahashi et al. (2000).

During the EXL98 aircraft mission, sprites were observed by narrow band cameras that measure the N_2^+ First Negative (0, 1) band at 427.8 nm and the N_2 Second Positive (0, 0) band at 337.0 nm (Morrill et al. 2002). The observations integrated the sprite emissions over 33 ms so that temporal information was limited. The analysis indicated characteristic electron energies on the order of 2 eV and electric field magnitudes which closely followed the breakdown threshold field up to 55 km altitude and dropped below that level above 55 km (Morrill et al. 2002). These results are generally consistent with previous observations conducted with similar time resolution.

The recently launched FORMOSAT-2 satellite carries the Imager for Sprites and Upper Atmospheric Lightning (ISUAL) instrument (Chern et al. 2003; Mende et al. 2005, 2006; Frey et al. 2005). The ISUAL science payload provides a unique opportunity to conduct a global survey of sprites and other TLEs from space using an intensified CCD imager, a six channel spectrophotometer and two array photometers (Mende et al. 2006), avoiding many complications associated with observations from ground-based and airborne platforms due to atmospheric transmission and absorption effects in the blue, violet and ultraviolet regions of the spectrum. Recently, in addition to the high time resolution photometric data on 1PN_2 , 2PN_2 and 1NN_2^+ sprite emissions, the ISUAL instrument has successfully observed far-UV (FUV) emissions from sprites due to the N_2 Lyman–Birge–Hopfield (LBH) band system (Mende et al. 2005, 2006; Frey et al. 2005).

6 Implications for Planetary Atmospheres

The kinetic theory and computational results presented in this introductory section form the basis for understanding the initiation and development of discharges in the gas mixtures that comprise planetary and lunar atmospheres. Both conventional breakdown and the recently discovered runaway mechanism were addressed and detailed solutions of the non-relativistic and relativistic Boltzmann equations presented. Our preliminary findings lead us to the following relevant conclusions:

- The threshold electric field for runaway breakdown is \sim 6.3 times lower on the gas giants, about equal on the moons, and \sim 1.5 times larger on Venus and Mars.
- For the same electric field and atmospheric density, the runaway avalanche time is (a) smaller on the gas giants by large factors near the runaway threshold on Jupiter and by a factor of \sim 2 to 3 at the higher electric fields, (b) larger on Mars and Venus by a factor of \sim 1.3, and (c) approximately equal on the moons when compared to the equivalent avalanche time on Earth.
- The Bremsstrahlung spectrum expected from a runaway discharge would be softer on the gas giants, slightly softer on the moons, and harder on Mars and Venus for the same electric field and atmospheric density.
- Emissions (RF and γ -ray) from the runaway beam would be highly collimated on the gas giants.
- The threshold electric field for conventional breakdown is a factor of \sim 2 times lower for the gas giants, \sim 1.3 time larger for Mars and Venus, and about the same for the moons compared to Earth.

The precise manner in which an electrical discharge would evolve on a given planet depends on the magnitude and atmospheric profile of the electric fields. In other words, the charging mechanisms and the gas density profile are crucial to establishing the conditions that are conducive to gas breakdown. These issues are addressed in other parts of this manuscript. We can however indicate, in agreement with Dwyer et al. (2006), that under similar conditions runaway breakdown is more likely to occur on the gas giants than conventional breakdown when compared to Earth or the other planets.

With these results in mind it is relevant to ask what we might expect to see on the other planets in light of what we observe on Earth given that our present understanding is that both conventional breakdown and runaway breakdown are at work. Of the many forms that a discharge can take in the terrestrial environment, lightning is by far the most spectacular and the most dangerous. The amount of energy expended in a single event is generally

more than gigajoules with power levels reaching tens to hundreds of gigawatts. The currents that flow in a cloud-to-ground (CG) discharge range in magnitude from hundreds of amps to hundreds of kiloamps and transfer Coulombs to tens of Coulombs of charge. The bulk of this electrical energy flows through small cross-sectional areas with radii ranging from centimeters to tens of centimeters and over long distances extending to many kilometers. The kinetic energy density in lightning is sufficient in many cases to heat the air to tens of thousands of degrees Kelvin and to generate acoustic shock waves that can be heard out to tens of kilometers. Terrestrial lightning is easily observed from the ground and from space in the optical, the radio frequency, and most recently in the X-ray and gamma ray parts of the electromagnetic spectrum. The physical manifestations of the lightning discharge are so diverse as to precipitate the proliferation of a descriptive and non-descriptive taxonomy that includes ribbons, balls, jets, sprites, elves, halos, angels, starters, trolls, beads, carrots, superbolts, and spiders.

The temptation to extrapolate the properties of terrestrial lightning to other planets and astrophysical systems is great. However, our present understanding of this seemingly well understood and extensively studied physical process is undergoing a significant change as a result of the many recent measurements of penetrating radiation in coincidence with stepped leader processes, intra-cloud discharges, and potentially high-altitude discharges. Early attempts to rely on laboratory discharge experiments to understand the lightning phenomenon met with some success but ultimately could not explain the almost ubiquitous presence of energetic radiation. Our final understanding of this incredibly fascinating natural phenomenon will not rest on a phenomenological taxonomy nor on extrapolation of small-scale laboratory experiments but rather on a fundamental shift in our thinking that must ultimately include a role for cosmic rays, relativistic electron beams, large scales, and energetic feedback processes. The detection of lightning on other planets by means of diagnostics that span the electromagnetic spectrum will help us understand the fundamental nature of the discharge process.

Acknowledgements The participation of V.P. Pasko has been supported by the United States National Science Foundation under the NSF ATM-0741589 grant to Penn State University.

References

- F.L. Adessio, J.R. Baumgardner, J.K. Dukowicz et al., *Caveat: A computer code for fluid dynamics problems with large distortion and internal slip*, 1992
- R.A. Armstrong, J.A. Shorter, M.J. Taylor et al., *J. Atmos. Sol. Terr. Phys.* **60**, 787 (1998)
- R.A. Armstrong, D.M. Suszcynsky, W.A. Lyons et al., *Geophys. Res. Lett.* **27**, 653 (2000)
- T. Asano, M. Hayakawa, M. Cho et al., *J. Geophys. Res.—Space Phys.* **113**, A02308 (2008)
- L.P. Babich, E.N. Donskoy, I.M. Kutsyk et al., *IEEE Trans. Plasma Sci.* **29**, 430 (2001)
- L.P. Babich, E.N. Donskoy, K.F. Zelenskii et al., *Dokl. Phys.* **47**, 1 (2002)
- L.P. Babich, A.Y. Kudryavtsev, M.L. Kudryavtseva et al., *J. Exp. Theor. Phys.* **106**, 65 (2008)
- C.P. Barrington-Leigh, U.S. Inan, M. Stanley, *J. Geophys. Res.* **101**, 1741 (2001)
- E.M. Bazelyan, Y.P. Raizer, *Spark Discharge* (CRC Press, Boca Raton, 1998)
- H.A. Bethe, *Ann. Phys.* **5**, 325 (1930)
- H.A. Bethe, J. Ashkin, in *Experimental Nuclear Physics*, ed. by E. Segre (Wiley, New York, 1953), p. 277
- S.F. Biagi, *Nucl. Inst. Methods A* **421**, 234 (1999)
- E. Blanc, F. Lefevre, R. Roussel-Dupré et al., *Adv. Space Res.* **40**, 1268 (2007)
- D.J. Boccippio, E.R. Williams, S.J. Heckman et al., *Science* **269**, 1088 (1995)
- T.M.P. Briels, E.M. van Veldhuizen, U. Ebert, *IEEE Trans. Plasma Sci.* **33**, 264 (2005)
- M.J. Brunger, S.J. Buckman, L.J. Allen et al., *J. Phys. B: At. Mol. Opt. Phys.* **25**, 1823 (1992)
- M.J. Brunger, S.J. Buckman, *Phys. Rep.* **357**, 215 (2002)
- E. Bucsela, J. Morrill, M. Heavner et al., *J. Atmos. Sol. Terr. Phys.* **65**, 583 (2003)

- S. Chapman, T.G. Cowling, *The Mathematical Theory of Non-uniform Gases* (Cambridge University Press, London, 1970)
- B. Chen, Y. Lee, R. Hsu et al., Global distribution and seasonal distribution variation of transient luminous events. AGU Fall meeting, San Francisco, 2005
- J.L. Chern, R.R. Hsu, H.T. Su et al., J. Atmos. Sol. Terr. Phys. **65**, 647 (2003)
- H.J. Christian, R.J. Blakeslee, D.J. Boccippio et al., J. Geophys. Res. **108** (2003)
- S.A. Cummer, N. Jaugey, J. Li et al., Geophys. Res. Lett. **33**, L04104 (2006a)
- S.A. Cummer, H.U. Frey, S.B. Mende et al., J. Geophys. Res. **111**, A10315 (2006b)
- H. Dreicer, Phys. Rev. **115**(2), 238 (1959)
- H. Dreicer, Phys. Rev. **117**(2), 343 (1960)
- J.R. Dwyer, Geophys. Res. Lett. **30**, 2055 (2003)
- J.R. Dwyer, D.M. Smith, Geophys. Res. Lett. **32**, L22804 (2005)
- J.R. Dwyer, L.M. Coleman, R. Lopez et al., Geophys. Res. Lett. **33**, L22813 (2006)
- J.R. Dwyer, B.W. Grefenstette, D.M. Smith, Geophys. Res. Lett. **35**, L02815 (2008)
- K.B. Eack, W.B. Beasley, W.D. Rust et al., Geophys. Res. Lett. **23**, 2915 (1996)
- U. Ebert, C. Montijn, T.M.P. Briels et al., Plasma Sources Sci. Technol. **15**, S118 (2006)
- C.F. Enell, E. Arnone, T. Adachi et al., Ann. Geophys. **26**, 12 (2008)
- T. Farges, E. Blanc, A. Le Pichon et al., Geophys. Res. Lett. **32**, L01813 (2005)
- G.J. Fishman, P.N. Bhat, R. Mallozzi et al., Science **264**, 1313 (1994)
- H.U. Frey, S.B. Mende, S.A. Cummer et al., Geophys. Res. Lett. **32**, L13824 (2005)
- H. Fukunishi, Y. Takahashi, M. Kubota et al., Geophys. Res. Lett. **23**, 2157 (1996)
- E.A. Gerken, U.S. Inan, J. Geophys. Res **107**, 1344 (2002)
- E.A. Gerken, U.S. Inan, J. Atmos. Sol. Terr. Phys. **65**, 567 (2003)
- E.A. Gerken, U.S. Inan, IEEE Trans. Plasma Sci. **33**, 282 (2005)
- E.A. Gerken, U.S. Inan, C.P. Barrington-Leigh, Geophys. Res. Lett. **27**, 2637 (2000)
- B.D. Green, M.E. Fraser, W.T. Rawlins et al., Geophys. Res. Lett. **23**, 2161 (1996)
- B.W. Grefenstette, D.M. Smith, J.R. Dwyer et al., Geophys. Res. Lett. **35**, L06802 (2008)
- A.V. Gurevich, K.P. Zybin Phys. Today **37** (2005)
- A.V. Gurevich, G.M. Milikh, R.A. Roussel-Dupré, Phys. Lett. A **165**, 463 (1992)
- A.V. Gurevich, G.M. Milikh, R.A. Roussel-Dupré, Phys. Lett. A **187**, 197 (1994)
- A.V. Gurevich, J.A. Valdavia, G.M. Milikh et al., Radio Sci. **31**, 1541 (1996)
- A.V. Gurevich, R.A. Roussel-Dupré, K.P. Zybin, Phys. Lett. A **237**, 240 (1998)
- A.V. Gurevich, K.F. Sergeichev, I.A. Sychov et al., Phys. Lett. A **260**, 269 (1999)
- D.L. Hampton, M.J. Heavner, E.M. Wescott et al., Geophys. Res. Lett. **23** (1996)
- M.J. Heavner, D.D. Sentman, D.R. Moudry et al., in *Geophysical Monograph Series*, ed. by D.E. Siskind, S.D. Eckerman, M.E. Summers (Am. Geophys. Union, Washington, 2000)
- L.G.H. Huxley, R.W. Crompton, *The Diffusion and Drift of Electrons in Gases* (Wiley, New York, 1974)
- ICRU, ICRU Report No. 49, ed. by Bethesda, 1993
- U.S. Inan, C. Barrington-Leigh, S. Hansen et al., Geophys. Res. Lett. **24**, 583 (1997)
- Y. Itikawa, J. Phys. Chem. Ref. Data **31**, 3 (2002)
- Y. Itikawa, J. Phys. Chem. Ref. Data **35**, 31 (2006)
- B.-H. Jeon, J. Korean Phys. Soc. **43**, 513 (2003)
- B.-H. Jeon, Y. Nakamura, J. Phys. D **31**, 2145 (1998)
- E. Kamaratos, Chem. Phys. **323**, 271 (2006)
- I. Kanik, S. Trajmar, J.C. Nickel, J. Geophys. Res. **98**, 7447 (1993)
- T. Kanmae, H.C. Stenbaek-Nielsen, M.G. McHarg, Geophys. Res. Lett. **34**, L07810 (2007)
- N.A. Krall, A.W. Trivelpiece, *Principles of Plasma Physics* (McGraw-Hill, New York, 1973)
- C.-L. Kuo, A.B. Chen, Y.J. Lee et al., J. Geophys. Res. **112**, A11312 (2007)
- N.G. Lehtinen, T.F. Bell, U.S. Inan, J. Geophys. Res. **104**, 24 (1999)
- L. Liszka, J. Low Freq. Noise, Vib. Act. Control **23**, 85 (2004)
- L. Liszka, Y. Hobara, J. Atmos. Sol.-Terr. Phys. **68**, 1179 (2006)
- N. Liu, V.P. Pasko, J. Geophys. Res.—Space Phys. **109**, A04301 (2004)
- N. Liu, V.P. Pasko, J. Phys. D: Appl. Phys. **39**, 327 (2006)
- N. Liu, V.P. Pasko, D.H. Burkhardt et al., Geophys. Res. Lett. **33**, L01101 (2006)
- L.B. Loeb, *Fundamental Processes of Electrical Discharge in Gases* (Wiley, New York, 1939)
- J.J. Lowke, J. Phys. D: Appl. Phys. **25**, 202 (1992)
- W.A. Lyons, J. Geophys. Res. **101**, 29641 (1996)
- W.A. Lyons, in *Sprites, Elves and Intense Lightning Discharges*, ed. by M. Füllekrug, E.A. Mareev, M.J. Rycroft (Springer, Berlin, 2006)
- W.A. Lyons, T.E. Nelson, R.A. Armstrong et al., Am. Meteorol. Soc. **445** (2003a)
- W.A. Lyons, T.E. Nelson E, R. Williams et al., Mon. Weather Rev. **131**, 2417 (2003b)

- R.A. Marshall, U.S. Inan, Geophys. Res. Lett. **32**, L05804 (2005)
- R.A. Marshall, U.S. Inan, Radio Sci. **41**, RS6S43 (2006)
- T.C. Marshall, M. Stolzenburg, C.R. Maggio et al., Geophys. Res. Lett. **32**, L03813 (2005)
- M.P. McCarthy, G.K. Parks, Geophys. Res. Lett. **12**, 393 (1985)
- M.P. McCarthy, G.K. Parks, J. Geophys. Res. Lett. **97**, 5857 (1992)
- S.B. Mende, R.L. Raideren, G.R. Swenson et al., Geophys. Res. Lett. **22**, 2633 (1995)
- S.B. Mende, H.U. Frey, R.R. Hsu et al., J. Geophys. Res. **110**, A11312 (2005)
- S.B. Mende, Y.S. Chang, A.B. Chen et al., in *Sprites, Elves and Intense Lightning Discharges*, ed. by M. Füllekrug, E.A. Mareev, M.J. Rycroft (Springer, Berlin, 2006)
- R. Miyasato, H. Fukunishi, Y. Takahashi et al., J. Atmos. Sol. Terr. Phys. **65**, 573 (2003)
- C.B. Moore, K.B. Eack, G.D. Aulich et al., Geophys. Res. Lett. **28**, 2141 (2001)
- J.S. Morrill, E.J. Bucsela, V.P. Pasko et al., J. Atmos. Sol. Terr. Phys. **60**, 811 (1998)
- J. Morrill, E. Bucsela, C. Seifring et al., Geophys. Res. Lett. **29**, 1462 (2002)
- G.D. Moss, V.P. Pasko, N. Liu et al., J. Geophys. Res. **111**, A02307 (2006)
- G.V. Naidis, J. Phys. D: Appl. Phys. **32**, 2649 (1999)
- N. Østgaard, T. Gjesteland, J. Stadsnes et al., J. Geophys. Res. **113**, A02307 (2008)
- S.V. Pancheshnyi, M. Nudnova, A.Y. Starikovskii, Phys. Rev. E **71**, 016407 (2005)
- V.P. Pasko, Nature **423**, 927 (2003)
- V.P. Pasko, in *Sprites, Elves and Intense Lightning Discharges*, ed. by M. Füllekrug, E.A. Mareev, M.J. Rycroft (Springer, Berlin, 2006)
- V.P. Pasko, U.S. Inan, T.F. Bell, Geophys. Res. Lett. **25**, 2123 (1998)
- V.P. Pasko, M.A. Stanley, J.D. Matheus et al., Nature **416**, 152 (2002)
- V.P. Pasko, H.C. Stenbaek-Nielsen, Geophys. Res. Lett. **29**, 1440 (2002)
- A.V. Phelps, L.C. Pitchford, Technical Report #26, JILA Information Center Report, University of Colorado, Boulder, CO, USA (1985)
- D.M. Phillips, J. Phys. D: Appl. Phys. **9**, 507 (1976)
- L.C. Pitchford, A.V. Phelps, Phys. Rev. A **25**, 540 (1982)
- H. Raether, *Electron Avalanches and Breakdown in Gase* (Butterworths, London, 1964)
- Y.P. Raizer, *Gas Discharge Physics* (Springer, New York, 1991)
- R.A. Roussel-Dupré, A.V. Gurevich, J. Geophys. Res. **101**, 2297 (1996)
- R.A. Roussel-Dupré, A.V. Gurevich, T. Tunnell et al., Phys. Rev. E **49**, 2257 (1994)
- R.A. Roussel-Dupré, E.M.D. Symbalisty, L. Triplett et al., Cal Meeting, Crete, 2005
- M.B. Scott, A.O. Hanson, E.M. Lyman, Phys. Rev. **84**, 638 (1951)
- D.D. Sentman, E.M. Wescott, Geophys. Res. Lett. **22**, 1205 (1993)
- D.D. Sentman, E.M. Wescott, D.L. Osborne et al., Geophys. Res. Lett. **22**, 1205 (1995)
- D.D. Sentman, H.C. Stenbaek-Nielsen, M.G. McHarg et al., J. Geophys. Res.: Atmos. (2008, in press)
- D.M. Smith, L.I. Lopez, R.P. Lin et al., Science **307**, 1085 (2005)
- M. Stanley, P. Krehbiel, M. Brook et al., Geophys. Res. Lett. **26**, 3201 (1999)
- H.C. Stenbaek-Nielsen, D.R. Moudry, E.M. Wescott et al., Geophys. Res. Lett. **27**, 3829 (2000)
- M. Stolzenburg, T.C. Marshall, W.D. Rust et al., Geophys. Res. Lett. **34**, L04804 (2007)
- H.T. Su, R.R. Hsu, A.B. Chen et al., Nature **423**, 974 (2003)
- D.M. Suszcynsky, R. Roussel-Dupré, G. Shaw, J. Geophys. Res. **101**, 23 (1996)
- E.M.D. Symbalisty, R. Roussel-Dupré, V. Yukhimuk, IEEE Trans. Plasma Sci. **26**, 1575 (1998)
- Y. Takahashi, M. Fujito, Y. Watanabe et al., Adv. Space Res. **26**, 1205 (2000)
- P. Tardieu, E. Marode, J. Phys. D: Appl. Phys. **36** (2003)
- P. Tardieu, E. Marode, A. Agneray et al., J. Phys. D: Appl. Phys. **34**, 1690 (2001)
- H. Tawara, Y. Itikawa, H. Nishimura et al., J. Phys. Chem. Ref. Data **19**, 617 (1990a)
- H. Tawara, Y. Itikawa, H. Nishimura et al., NIFS-DATA-6, 1990b
- S. Trajmar, D.F. Register, A. Chutjian, Phys. Rep. **97**, 219 (1983)
- M.A. Uman, *The Lightning Discharge* (Dover, New York, 2001)
- A.V. Vallance-Jones, *Aurora* (Reidel, Norwell, 1974)
- E.M. van Veldhuizen, *Electrical Discharges for Environmental Purposes: Fundamentals and Applications* (Nova Science, New York, 2000)
- E.M. Wescott, D. Sentman, D. Osborne et al., Geophys. Res. Lett. **22**, 1209 (1995)
- C.T.R. Wilson, Proc. R. Soc. Lond. **37**, 32D (1925)
- C.T.R. Wilson, Proc. R. Soc. Lond. **236**, 297 (1956)

An Overview of Earth's Global Electric Circuit and Atmospheric Conductivity

Michael J. Rycroft · R. Giles Harrison · Keri A. Nicoll ·
Evgeny A. Mareev

Originally published in the journal Space Science Reviews, Volume 137, Nos 1–4.
DOI: [10.1007/s11214-008-9368-6](https://doi.org/10.1007/s11214-008-9368-6) © Springer Science+Business Media B.V. 2008

Abstract The Earth's global atmospheric electric circuit depends on the upper and lower atmospheric boundaries formed by the ionosphere and the planetary surface. Thunderstorms and electrified rain clouds drive a DC current (~ 1 kA) around the circuit, with the current carried by molecular cluster ions; lightning phenomena drive the AC global circuit. The Earth's near-surface conductivity ranges from 10^{-7} S m $^{-1}$ (for poorly conducting rocks) to 10^{-2} S m $^{-1}$ (for clay or wet limestone), with a mean value of 3.2 S m $^{-1}$ for the ocean. Air conductivity inside a thundercloud, and in fair weather regions, depends on location (especially geomagnetic latitude), aerosol pollution and height, and varies from $\sim 10^{-14}$ S m $^{-1}$ just above the surface to 10^{-7} S m $^{-1}$ in the ionosphere at ~ 80 km altitude. Ionospheric conductivity is a tensor quantity due to the geomagnetic field, and is determined by parameters such as electron density and electron–neutral particle collision frequency. In the current source regions, point discharge (coronal) currents play an important role below electrified clouds; the solar wind-magnetosphere dynamo and the unipolar dynamo due to the terrestrial rotating dipole moment also apply atmospheric potential differences.

M.J. Rycroft (✉)
CAESAR Consultancy, 35 Millington Road, Cambridge CB3 9HW, UK
e-mail: michaelrycroft@btinternet.com

M.J. Rycroft
International Space University, 1 rue Jean-Dominique Cassini, 67400 Illkirch-Graffenstaden, France

R.G. Harrison · K.A. Nicoll
Department of Meteorology, University of Reading, Earley Gate, PO Box 243, Reading,
Berkshire RG6 6BB, UK

R.G. Harrison
e-mail: r.g.harrison@reading.ac.uk

K.A. Nicoll
e-mail: k.a.nicoll@reading.ac.uk

E.A. Mareev
Institute of Applied Physics, Russian Academy of Sciences, 46 Ulyanov str., 603950 Nizhny Novgorod,
Russian Federation
e-mail: mareev@appl.sci-nnov.ru

Detailed measurements made near the Earth's surface show that Ohm's law relates the vertical electric field and current density to air conductivity. Stratospheric balloon measurements launched from Antarctica confirm that the downward current density is $\sim 1 \text{ pA m}^{-2}$ under fair weather conditions. Fortunately, a Solar Energetic Particle (SEP) event arrived at Earth during one such balloon flight, changing the observed atmospheric conductivity and electric fields markedly. Recent modelling considers lightning discharge effects on the ionosphere's electric potential ($\sim +250 \text{ kV}$ with respect to the Earth's surface) and hence on the fair weather potential gradient (typically $\sim 130 \text{ V m}^{-1}$ close to the Earth's surface). We conclude that cloud-to-ground (CG) lightning discharges make only a small contribution to the ionospheric potential, and that sprites (namely, upward lightning above energetic thunderstorms) only affect the global circuit in a minuscule way. We also investigate the effects of mesoscale convective systems on the global circuit.

Keywords Atmospheric electric circuit · Conductivity models · Fair weather observations · Electrostatic modelling

1 The Global Atmospheric Electric Circuit

The conceptual model of the Earth's global electric circuit has been introduced by Aplin et al. (2008). In brief, the circuit is formed between the Earth's surface, which is a good conductor of electricity, and the ionosphere, a weakly-ionized plasma at $\sim 80 \text{ km}$ altitude. Between them is the atmosphere; this is a reasonably good electrical insulator, i.e. it is a leaky dielectric medium. Electrical "batteries" exist below or inside electrified clouds (e.g., thunderclouds); these cause an electric current to flow up to the ionosphere. The "DC" (direct current) electric circuit is completed by downward currents flowing through the majority of the Earth's atmosphere in the "fair weather" region remote from thunderstorms, and through the rocks and oceans of the Earth's crust (Williams 2002; Harrison 2004a; Rycroft 2006; Markson 2007; Rycroft et al. 2007 and references therein).

There is a corresponding "AC" (alternating current) circuit in which phenomena are produced by lightning discharges (Williams 2002). Lightning discharges radiate radio signals across the electromagnetic spectrum, the lowest frequencies of which propagate completely around the globe. These standing wave signals at $\sim 10 \text{ Hz}$ excite the resonant cavity formed between the Earth and the ionosphere; these are the so-called Schumann resonances (Schumann 1952). Details of Schumann resonance phenomena are dealt with by Simoes et al. (2008).

2 Conductivities in the Circuit

In general, when considering electromagnetic wave propagation in partially conducting media, with a wave field proportional to $e^{-i\omega t}$, the wave vector \mathbf{k} in the medium is defined as ω/v_ϕ . Here v_ϕ is the phase velocity of the wave of angular frequency ω ; it is equal to the velocity of light in free space c , divided by the refractive index, η . The refractive index squared, which is equal to the relative permittivity of the medium, ϵ_r , is given by

$$\eta^2 = \epsilon_r = 1 + \left(\frac{i\sigma}{\epsilon_0\omega} \right), \quad (2.1)$$

where $i = \sqrt(\epsilon - 1)$, ϵ_0 is the permittivity of free space, $8.85 \times 10^{-12} \text{ F m}^{-1}$, and σ is the conductivity of the medium (Jackson 1962, p. 223). This equation clearly shows why it is crucial to consider the conductivities in the constituent parts of the global circuit. The medium behaves as a good conductor, when $\sigma/\epsilon_0\omega \gg 1$. So, for $\omega \sim 60 \text{ s}^{-1}$, at 10 Hz, the medium can thus be considered to be a good conductor if $\sigma \gg 5 \times 10^{-10} \text{ S m}^{-1}$. Conversely, it will behave like a poor conductor if $\sigma \ll 5 \times 10^{-10} \text{ S m}^{-1}$.

The amplitude of an electromagnetic wave decreases exponentially with distance as it propagates into a conductor. The scale length for penetration into a medium whose relative magnetic permeability is 1, termed the skin depth δ , is given by

$$\delta^2 = \frac{2}{\mu_0\omega\sigma}, \quad (2.2)$$

where μ_0 is the permeability of free space, $4\pi \times 10^{-7} \text{ H m}^{-1}$, or $12.6 \times 10^{-7} \text{ H m}^{-1}$. Thus, at 10 Hz, $\delta = 160/(\sqrt{\sigma}) \text{ m}$. Putting the value of σ at the boundary between good and bad conductors, $\delta \sim 7000 \text{ km}$. For media of different conductivities, δ increases as σ decreases, being inversely proportional to $\sqrt{\sigma}$.

3 Conductivity of the Earth near the Surface

The Earth's surface and subsurface is composed of many different rock types whose conductivities vary greatly, from 10^{-8} S m^{-1} for marble to 10^{-7} S m^{-1} for poorly conducting rocks, and up to 10^{-2} S m^{-1} for clay or wet limestone. Thus the skin depth at 10 Hz would be expected to vary from $\sim 1.6 \text{ m}$ to $\sim 1600 \text{ km}$. The average value of the near-surface conductivity used in most geophysical models is near 10^{-2} S m^{-1} (see Lowrie 2007; Uyeshima 2007, his Fig. 14), and so the average near-surface skin depth can be taken to be $\sim 1.6 \text{ km}$. For ocean water, the conductivity varies with salinity and temperature, but an overall value of 3.2 S m^{-1} may be taken (Olsen and Kuvshinov 2004). The skin depth for the oceans at 10 Hz is $\sim 100 \text{ m}$. For all components of the Earth's surface and subsurface, the medium is a good conductor at 10 Hz.

When discussing propagation near 10 Hz, therefore, the important factor is the ocean conductivity to a depth of 100 m, and the continental conductivity to 1.6 km and somewhat greater depths. Information on surface and subsurface conductivities is derived from comprehensive studies of induction effects, in the field termed magnetotellurics, details of which may be found in Bahr and Simpson (2005), Bedrosian (2007), Korja (2007) and Uyeshima (2007). Based on this technique, Olsen and Kuvshinov (2004) have published a valuable global map which shows the conductance, i.e. the conductivity multiplied by a depth of 4 km. Figure 1 is based upon that work; a typical conductance value for the land is $10^{-2} \text{ S m}^{-1} \times 4000 \text{ m} = 40 \text{ S}$, as shown in yellow. For future work on detailed theoretical treatments of the AC global circuit, this compilation should be extremely useful.

4 Air Conductivity in the Lower Troposphere

The electrical conductivity of air results from the concentration of small ions which it contains. Immediately above the continental surface, the total conductivity (the sum of the positive and negative ion conductivity) ranges typically between $2 \times 10^{-15} \text{ S m}^{-1}$ and

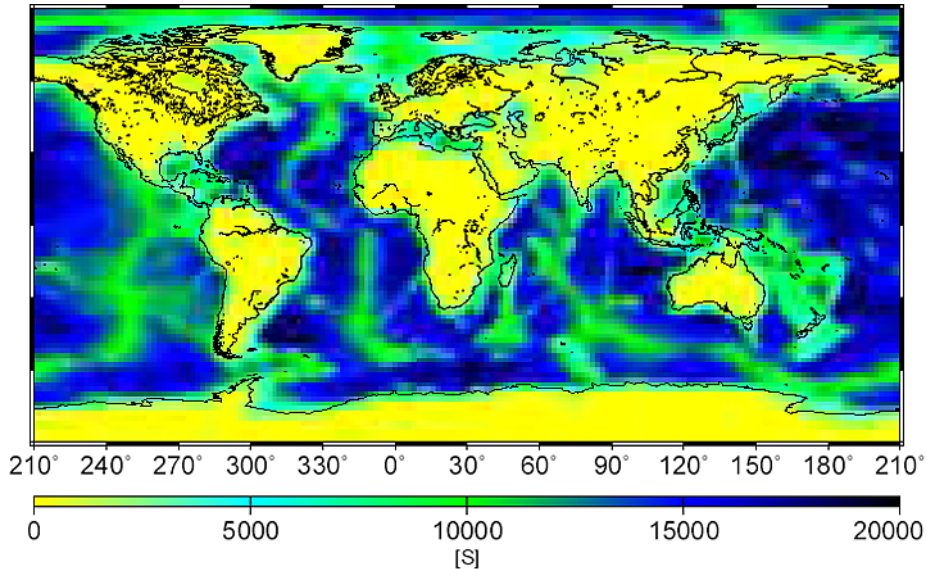


Fig. 1 Map of the conductance in Siemens [S], of the Earth's surface and subsurface, to a depth of 4 km. Over the land the value is ~ 40 S (shown as yellow), and for the oceans, $\sim 3.2 \times 4000 = 12,800$ S (greenish blue); values for the deeper ocean are in blue, whereas for the mid-ocean ridges they are green (based on Olsen and Kuvshinov 2004)

2×10^{-14} S m $^{-1}$ (Chalmers 1967) and is up to 4×10^{-14} S m $^{-1}$ in clean marine air (Cobb and Wells 1970). The air's total conductivity is defined by

$$\sigma_t = e(\mu_+ n_+ + \mu_- n_-), \quad (4.1)$$

where n_+ and n_- are the positive and negative small ion number concentrations, respectively, and μ_+ and μ_- are the mean positive and negative ion mobilities. (The ion mobility, in units of m 2 V $^{-1}$ s $^{-1}$, is the velocity acquired by an ion in unit electric field.)

In general, the ion concentrations are described by the ion balance equation (Harrison and Carslaw 2003), which describes the production and loss of ions. For an ion pair production rate of q per unit volume, in steady-state with the ion loss rate, the ion balance equation is

$$q - \alpha \bar{n}^2 - \bar{n} \beta N = 0, \quad (4.2)$$

where \bar{n} is the mean bipolar ion number concentration, α is the ion–ion recombination coefficient and β is the ion-aerosol attachment coefficient. This determines the loss rate to monodisperse aerosol particles (i.e. all with the same radius) of number concentration N ; β is proportional to the aerosol particle radius (Gunn 1954).

Air conductivity varies with height, because the ion sources q (cosmic rays, radon isotopes and terrestrial radioactivity) and the primary sink (to aerosol particles) all have height profiles. In addition, the recombination rate α and ion mobility μ vary with temperature and pressure. In terms of the individual sources, the ion production rate q can be expressed as a function of height z as

$$q(z) = q_1(z) + q_2(z) + q_3(z), \quad (4.3)$$

where $q_1(z)$ is the ion production rate from radioactive gases, $q_2(z)$ is the ion production contributed by radioactive substances in the soil, and $q_3(z)$ is the ion production rate from cosmic rays. $q_1(z)$ is determined by vertical turbulent transport. Sophisticated models for $q_3(z)$ are now available which include the effect of geomagnetic shielding on cosmic rays (Bazilevskaya et al. 2008). At the continental surface, typical values are $q_1 = 4$ ion pairs $\text{cm}^{-3} \text{s}^{-1}$, $q_2 = 4$ ion pairs $\text{cm}^{-3} \text{s}^{-1}$ and $q_3 = 2$ ion pairs $\text{cm}^{-3} \text{s}^{-1}$ (Chalmers 1967).

The major ion loss in air near the continental surface is through the attachment of ions to aerosol particles. Aerosol particle concentrations vary with height, generally having their greatest concentration in the atmospheric boundary layer.¹ Considering the particles to be monodisperse, the variation with height can be represented by an exponential vertical profile (or profiles), such as

$$N(z) = N_s \exp(-z/z_{\text{sh}}), \quad (4.4)$$

where N is the particle number concentration at a height z , N_s is the surface aerosol number concentration, and z_{sh} is an appropriate scale height. Combining (4.2) and (4.1) gives air conductivity in terms of ion production rate and aerosol concentration, both of which vary with height.

Combining all these effects, the variation of total conductivity with height is given by

$$\sigma_t(z) = e^{\frac{\mu(T, P)}{\alpha(T, P)}} \sqrt{[\beta(T, P)^2 N(z)^2 + 4\alpha(T, P)q(z)] - \beta(T, P)N(z)}, \quad (4.5)$$

where T and P are the temperature and pressure evaluated at height z . From the air conductivity profile, the columnar resistance, namely the resistance of a unit area column of atmosphere from the surface to the ionosphere, can be found. The columnar resistance R_c is defined by

$$R_c = \int_0^\infty \frac{dz}{\sigma_t(z)}. \quad (4.6)$$

R_c was first measured directly from the measured air conductivity profile during the 1935 stratospheric balloon flight of *Explorer II* (Gish 1944). An alternative method is to use simultaneous measurements of the ionospheric potential V_I and vertical conduction current density J_z , which are related by Ohm's law as

$$R_c = \frac{V_I}{J_z}. \quad (4.7)$$

Using this approach, the columnar resistance was determined above the urban site at Kew Observatory, London, for 37 values obtained between 1969 and 1971 (Harrison 2005). The values of R_c range from $64 \text{ P}\Omega \text{ m}^2$ to $310 \text{ P}\Omega \text{ m}^2$, with a median value of $145 \text{ P}\Omega \text{ m}^2$, and these are shown in Fig. 2.

The major contribution to the columnar resistance is the resistance of the boundary layer, where the ion production rate is relatively small and the loss rate is large. To account for this, Harrison and Bennett (2007b) proposed a simple parameterization for R_c which separated the boundary layer and free troposphere resistances. For a free troposphere columnar

¹The boundary layer is the part of the troposphere in which motions are directly influenced by the presence of the Earth's surface. Its thickness shows a diurnal variation over land and is typically between 100 m and 3 km (Stull 1988).

Fig. 2 Histogram of the frequency distribution of columnar resistance R_c values found above Kew Observatory, London, during 1969 to 1971; it shows that 7 of the 37 columnar resistance values lie between 50 and $100 \text{ P}\Omega \text{ m}^2$, and 14 between 100 and $150 \text{ P}\Omega \text{ m}^2$, etc.

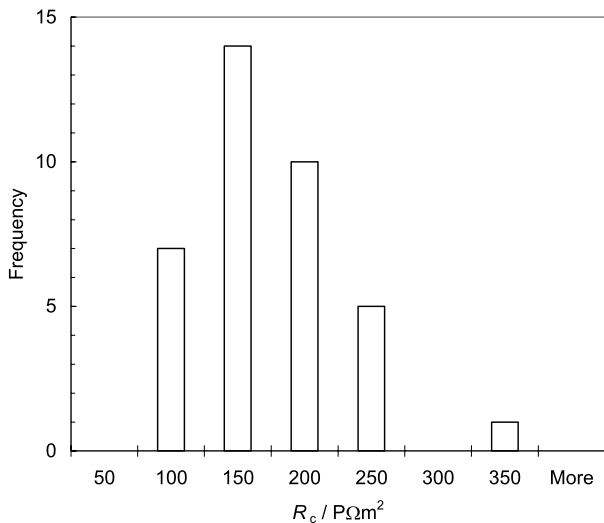
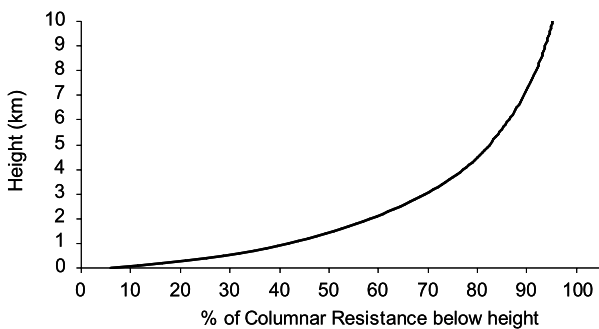


Fig. 3 Proportional contribution to the total columnar resistance R_c , as a function of height (from Harrison and Bennett 2007a, their Fig. 2)



resistance R_{FT} , and using the surface air conductivity σ_s to determine the resistance near the surface, R_c was represented as

$$R_c = \frac{k}{\sigma_s} + R_{FT}, \quad (4.8)$$

where k is a constant. For Kew, the quantities were found as $R_{FT} = (93 \pm 18) \text{ P}\Omega \text{ m}^2$ and $k = (270 \pm 90) \text{ m}$. k is related to the conductivity profile in the polluted layer, but could also be understood as representing the height of a constant conductivity layer near the surface.

Generally, $>95\%$ of the columnar resistance lies at altitudes below 10 km (Harrison and Bennett 2007a, 2007b). This is shown by the proportional contributions to the total R_c as a function of altitude in Fig. 3. There are few measurements of the conductivity profile made through the surface atmospheric layer. Measurements by Israelsson et al. (1994) show the important role played by turbulence in the formation of this profile.

5 Atmospheric Conductivity, and Properties of a Model Profile

For the Earth's atmosphere, or indeed that of any planetary body, the most significant variation of the pressure (or density) with height is due to gravity. For Earth, the density of the

neutral gas decreases exponentially with increasing height, with a scale height of ~ 7 km. Thus, for each 15 km of altitude, the density decreases by an order of magnitude (see, e.g., Rycroft 2003).

The atmosphere is weakly conducting due to ionization by galactic cosmic rays. These extremely energetic (>100 MeV) charged particles originating beyond the solar system are incident from all directions at the top of the atmosphere. The maximum production rate of ionization (up to 3×10^7 ion pairs $m^{-3} s^{-1}$ (Bazilevskaya et al. 2000, 2008; Usoskin et al. 2004)) occurs at altitudes between 12 and 20 km (Carslaw et al. 2002; Harrison and Carslaw 2003; Aplin and McPheat 2005; Tinsley and Zhou 2006). Another source of ionization, at sub-auroral latitudes (~ 60 degrees geomagnetic latitude) is relativistic electron precipitation (REP, ~ 1 MeV) from the magnetosphere, i.e. precipitation from the van Allen radiation belts (Tinsley and Zhou 2006). Further, within the polar cap, (>67 degrees geomagnetic latitude) there is occasional ionization due to solar energetic protons (SEP, ~ 100 MeV). At the Earth's surface, and up to ~ 2 or 3 km over land, the radioactive element radon emanating from the Earth produces up to 10×10^6 ion pairs $m^{-3} s^{-1}$.

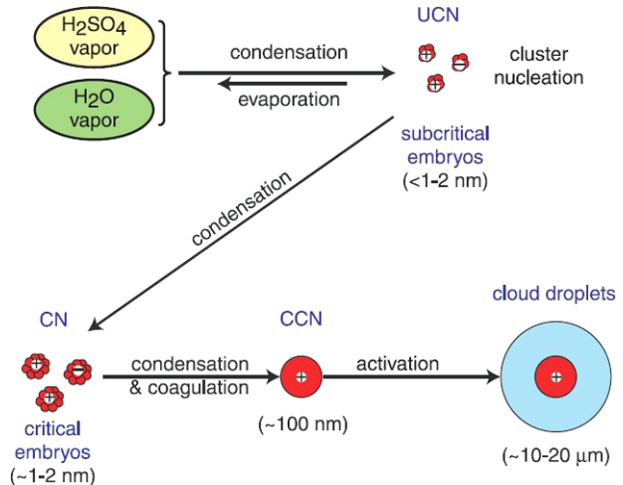
These atmospheric ions collide with, and attach to, molecules to form small cluster ions, e.g. $H^+(H_2O)_n$. It is clear that, to quantify this process, the humidity of the air is an important parameter (Harrison and Aplin 2007). Small cluster ions then attach to pollutants and to aerosols in the atmosphere, forming large ions. Thus, there is a spectrum of sizes of charged particles some of which, in the absence of competing processes, could in principle grow large enough to act as cloud condensation nuclei (termed CCN, see Yu and Turco 2001; Carslaw et al. 2002; Harrison and Carslaw 2003). Figure 4, taken from Carslaw et al. (2002, their Fig. 3), illustrates how this could work, and the sizes of particles involved.

Recent studies emphasize the significance of a poorly understood phenomenon, namely the “nucleation burst”, which is the intense emission of ultrafine (nm size) aerosols (abbreviated as ENA²), and their relation to intermediate-ion production (e.g., Smirnov 2005). In ENA events, the concentration of nano-particles initially grows rapidly to values of $10^9 - 10^{11} m^{-3}$. One or two hours later, the so-called nuclei fraction with diameters $D = 3 - 15$ nm is produced. The appearance of the Aitken fraction with $D = 20 - 80$ nm and the enlargement of aerosol particles in the accumulation fraction $D = 80 - 200$ nm may occur during the following 4–6 h. Thus, the cycle of formation and growth of atmospheric aerosol particles in the size range from a few to some 200 nanometers happens over 6–8 h. A specific synoptic feature of ENA events over land is that they occur when polar air is transported to the measuring sites and the temperature difference between day and night is large. During ENA periods, the formation rate of condensation nuclei with a diameter of 100 nm increases 10- to 100-fold. Observations made during an experiment carried out in the spring of 2000, in Finland, showed that each nucleation burst of particles with diameters between 3 and 100 nm was preceded by the emission of intermediate-ions with mobilities ranging from 0.25 to $0.8 \times 10^{-4} m^2 V^{-1} s^{-1}$. The physical nature and the role of intermediate ions in atmospheric electric processes is one of the most intriguing questions in atmospheric ion/aerosol studies today (Smirnov and Savchenko 2006).

For positive and negative ions mixed in equal concentrations ($n_+ = n_- = \bar{n}$), the air conductivity is defined by (4.1). The ion number density at ground level is typically $3 \times 10^8 m^{-3}$ (Usoskin et al. 2004, their Fig. 4), rising to a maximum value of $\sim 3 \times 10^9 m^{-3}$ at 15 km altitude. Key, representative values of conductivity σ_t are $\sim 10^{-14} S m^{-1}$ ($= 10 fS m^{-1}$) just above the Earth's surface (e.g., Harrison 2007), $\sim 10^{-11} S m^{-1}$ at 30 km altitude (as observed

²Emission of Nanometer Aerosol.

Fig. 4 This shows a possible mechanism by which ion-induced nucleation of ultrafine condensation nuclei (UCN), from trace condensable vapours, may eventually grow into cloud condensation nuclei (CCN). It is thought that the presence of charge lowers the nucleation barrier and stabilizes the embryonic particles, allowing nucleation to occur at lower ambient vapour concentrations than in a non-ionized atmosphere (from Carslaw et al. 2002, their Fig. 3)



on many stratospheric balloons, see, e.g., Bering et al. 2005), $\sim 10^{-10} \text{ S m}^{-1}$ at 55 km altitude, and 10^{-7} S m^{-1} at the bottom of the night-time ionosphere.

Using Ohm's law, conductivity relates the current density J to the electric field E by

$$J = \sigma E. \quad (5.1)$$

In the atmosphere, σ is a scalar quantity. However, in the ionosphere it is a tensor quantity, due to the Earth's magnetic field (see Rishbeth and Garriott 1969).

By Gauss' law,

$$\nabla \cdot E = \frac{\rho}{\epsilon_0}, \quad (5.2)$$

where ρ is the electric charge density and ϵ_0 is the permittivity of free space, $8.85 \times 10^{-12} \text{ F m}^{-1}$. In one dimension, the vertical direction z being positive upwards, this becomes

$$\frac{dE(z)}{dz} = \frac{\rho(z)}{\epsilon_0}. \quad (5.3)$$

This equation readily shows that, wherever $E(z)$ changes markedly with z , a layer of electric charge exists.

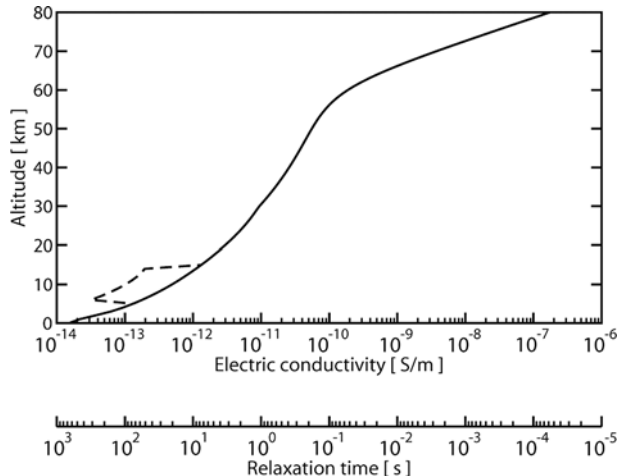
Referring back to Fig. 1 of Aplin et al. (2008), in the fair weather region, remote from thunderstorms and electrified shower clouds, the downward current density $J_z \sim 2 \text{ pA m}^{-2}$ and the fair weather electric field at the surface is $\sim -130 \text{ V m}^{-1}$ (Rycroft et al. 2000). The electric field is considered positive upwards, if it would cause a positive test charge to move upwards under the influence of the field. The potential gradient (PG) has the same magnitude as the electric field, but the opposite sign. This is because $E = -\nabla V = -dV/dz$, in one dimension.

For a 1 m² column from the ionosphere down to the Earth's surface,

$$I = \frac{V_1}{R_c} = \frac{250 \text{ kV}}{125 \text{ P}\Omega \text{ m}^2} = 2 \text{ pA}. \quad (5.4)$$

Based upon the measurements compiled by Hale (1984), (see Rakov and Uman 2003, p. 9), and the method of Makino and Ogawa (1985), Rycroft et al. (2007) presented a model

Fig. 5 Model conductivity profile for the atmosphere up to 80 km altitude; the dashed line variation is within a thundercloud. Also shown is the relaxation time τ , defined in the text. (From Rycroft et al. 2007)



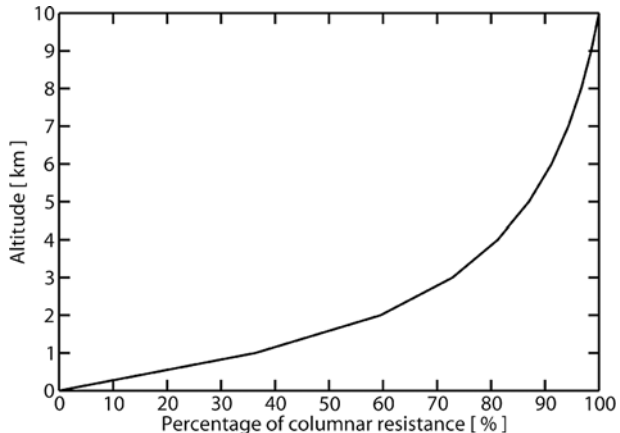
atmospheric conductivity profile (Fig. 5.) This profile fits closely to the four representative values mentioned earlier, and the profile of Pasko and George (2002, their Fig. 2). This profile demonstrates that the Earth's atmosphere behaves as an insulator at ~ 10 Hz up to 60 km altitude, where the conductivity approaches $5 \times 10^{-10} \text{ S m}^{-1}$. Also plotted is the electrostatic (or dielectric) relaxation time constant defined as $\tau = \epsilon_0/\sigma$. τ varies from ~ 15 minutes at the Earth's surface to ~ 1 s at 30 km, 0.1 s at 55 km and 0.1 ms at 80 km.

Unfortunately, very few measurements of conductivity have been made aloft, especially within clouds. Evans (1969) reported dropsonde measurements of conductivity made to about 50% accuracy, which showed regions of enhanced conductivity (up to $5 \times 10^{-11} \text{ S m}^{-1}$) in thunderstorm clouds. Rust and Moore (1974) used a tethered balloon to carry an electric field meter and a Gerdien condenser designed for measuring conductivity within large electric fields. The conductivity reduced rapidly as the instrument entered the first few metres of visible cloud. The mean polar air conductivities (with standard deviations) in cloudy air were $\sigma_- = (2.3 \pm 0.8) \text{ fS m}^{-1}$ and $\sigma_+ = (2.1 \pm 1.0) \text{ fS m}^{-1}$, respectively. Rust and Moore (1974) noted that the conductivity of cloudy air was about 1/6th that of the adjacent clear air, and about 1/10th of that of clear air at the same level but in the absence of any cloud. However, the conductivity of air within the heart of a thunderstorm remains a significant unknown parameter (MacGorman and Rust 1998).

Some theoretical treatments suggest that the electrical conductivity within a thundercloud is several times less than in the surrounding free air (Phillips 1967). Makino and Ogawa (1985) considered the ion attachment coefficient inside the thundercloud to be larger than outside. This accounts for the six-fold reduction of conductivity inside the thundercloud as modelled by Rycroft et al. (2007) and illustrated in Fig. 5. (Although the relative permittivity of water is rather large, 81, the water vapour concentration even in a dense cloud is insufficient to change the real part of the relative permittivity of air from its value of 1 assumed in (2.1).)

To compare with Fig. 3 (taken from Harrison and Bennett 2007a, their Fig. 2), Fig. 6 shows, for the model conductivity profile presented here, the columnar resistance at low altitudes as a percentage of the total columnar resistance between the surface and 10 km. Some 50% of the columnar resistance occurs in the lowest 1.5 km, which is generally within the planetary boundary layer. Almost 80% of the columnar resistance shown occurs below 4 km ($\sim 13,100$ feet) altitude. This means that, on a mountain of the same height, the columnar

Fig. 6 Variation of the percentage of columnar resistance up to 10 km altitude plotted for the non-thunderstorm model conductivity profile given in Fig. 5



resistance to the ionosphere is only a little more than a quarter of that from sea level. This is because the model columnar resistance to 10 km altitude is $156 \text{ P}\Omega \text{ m}^2$, whilst the total columnar resistance from the surface to the ionosphere is $167 \text{ P}\Omega \text{ m}^2$. For this model profile, $\sim 93\%$ of the total columnar resistance is below 10 km altitude.

Tinsley and Zhou (2006) presented a comprehensive model of the atmospheric conductivity in the fair weather part of the global circuit. Their model incorporates varying galactic cosmic ray fluxes from solar minimum to solar maximum, a realistic latitude/longitude and seasonal dependence of radon ionization at ground level and its transport by winds, varying aerosol populations, and the effects of large volcanic explosions on stratospheric aerosols (and hence on the electrical conductivity of the stratosphere). Following a northern hemisphere volcanic eruption introducing sulphur dioxide and water vapour into the lower stratosphere, ultrafine aerosol particles participate in the inter-hemispheric circulation of the stratosphere/mesosphere (see Karlsson et al. 2007). Thus, these particles are incident from above over the Antarctic.

Figure 7 (Fig. 10 in Tinsley and Zhou 2006) shows the particle effect in reducing the stratospheric conductivity dramatically; the solid line in panel (d) is for solar minimum conditions and the dot-dash line is for solar maximum. For low volcanic activity conditions, the dotted and dashed lines are for solar minimum and maximum conditions, respectively. Panel (a) shows conditions over the ocean where there is no radon source, (b) over the desert where there is a significant radon source, and (c) above the Himalayas.

Figure 8 shows a new compilation of measurements made from 1966 to 1979 by the UK Met Office at Kew Observatory, just to the west of London, U.K. (52°N , 0°W). These measurements determined the potential gradient PG, total air conductivity σ_t and the vertical conduction current density J_z on all fine (i.e. electrically undisturbed) days at 15 hours Universal Time (UT). The PG ranges from 57 V m^{-1} to 1197 V m^{-1} , and has a mean value of 358 V m^{-1} . More than 95% of the PG values measured at Kew exceed our model typical value of 130 V m^{-1} . The values of J_z are generally small, ranging from 0.1 pA m^{-2} to 3.6 pA m^{-2} , with a mean value of 1.4 pA m^{-2} . The total air conductivity was not measured directly, but calculated as J_z/PG using the Wilson method (Harrison and Ingram 2005). From the distribution of σ_t , 95% of the values are less than 10 fS m^{-1} , and the mean value of σ_t is 4.5 fS m^{-1} . The low conductivity values and high PGs measured at Kew indicate that this was a polluted site.

By contrast, at Marsta, a rural site 10 km north of Uppsala, Sweden (60°N , 17°E), from 1993 to 1998 the mean conductivity was found to be large, $\sim 40 \text{ fS m}^{-1}$, due to the relatively

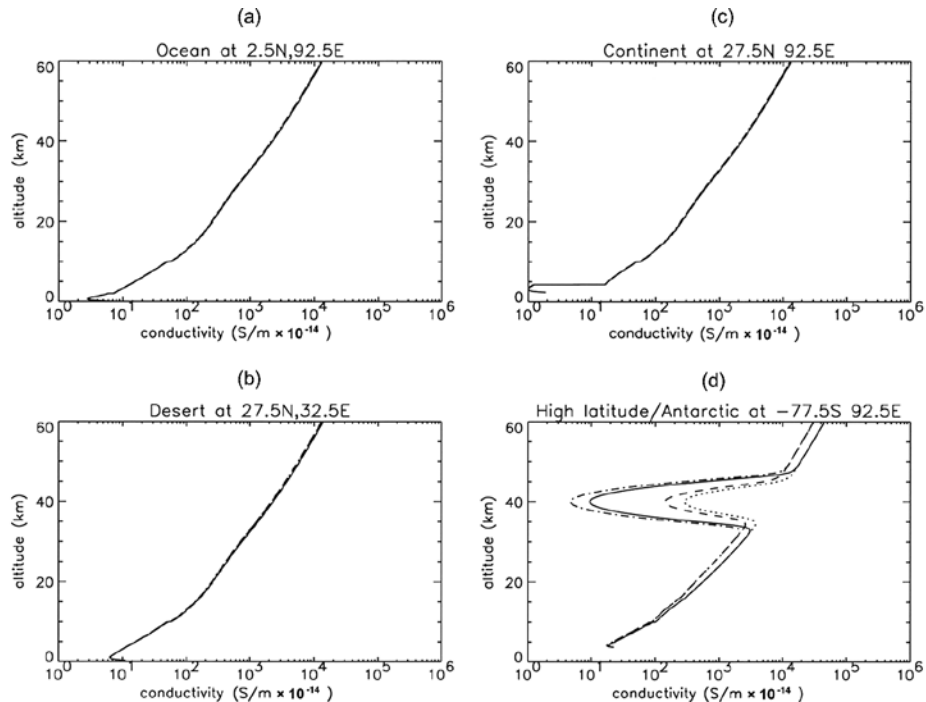


Fig. 7 Plots (a) to (c) are model conductivity profiles for a variety of surface types, (a) ocean, (b) desert, (c) Himalayas. Plot (d) shows conductivity at high latitudes during periods of solar minimum (solid line), solar maximum (dot-dash line), low volcanic activity (dotted line) and high volcanic activity (dashed line). (Taken from Tinsley and Zhou 2006)

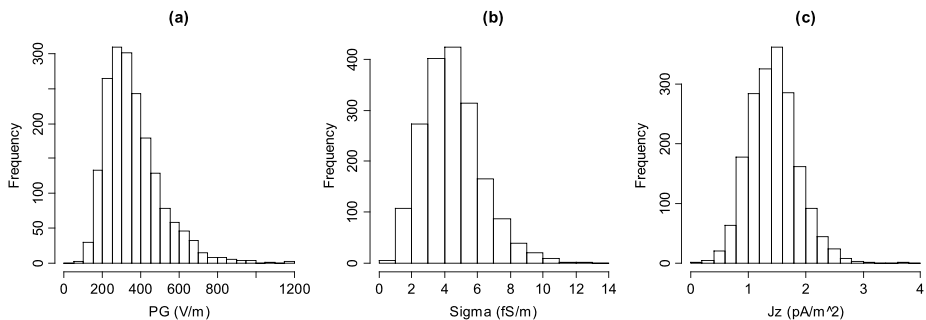


Fig. 8 Histograms of the frequency distributions of potential gradient (PG), total air conductivity (σ_t) and vertical conduction current density (J_z) as measured at the Kew Observatory, London, from 1966 to 1979

large concentration of radon there, and the mean electric field small, $\sim 65 \text{ V m}^{-1}$ (Israelsson and Tammet 2001, their Fig. 1). These values lead to a mean J_z of $\sim 2.6 \text{ pA m}^{-2}$. Both the electric field and conductivity values vary, typically by a factor of two.

It is concluded from these results that atmospheric conductivity is the most important determinant of the global electric circuit and its properties.

6 Ionospheric Conductivity

In the lowest ionosphere, at heights ~ 80 or 90 km, where electron–neutral collisions are very frequent ($\sim 10^6$ s $^{-1}$), the ionospheric conductivity is due to electrons. It is equal to $n_e e \mu_e$, using (4.1), where, by definition $\mu_e = e/(m_e v)$, and v is the velocity gained in unit electric field \underline{E} . The conductivity may also be expressed as

$$\sigma = \frac{n_e e^2}{m_e v}, \quad (6.1)$$

where n_e is the electron density, e is the charge on the electron, m_e is the mass of the electron and v is the electron–neutral collision frequency (Rishbeth and Garriott 1969, p. 133, Schunk and Nagy 2000, p. 131). This may also be expressed as

$$\sigma = \frac{\varepsilon_0 \omega_p^2}{\nu}, \quad (6.2)$$

with ω_p^2 being $n_e e^2 / \varepsilon_0 m_e$. Near 90 km at night the plasma frequency and e–n collision frequency are essentially equal so that the conductivity is $\varepsilon_0 \omega_p$, which is $\sim 5 \times 10^{-6}$ S m $^{-1}$; the ionosphere is evidently an extremely good conductor at ~ 10 Hz.

In the presence of the geomagnetic field \underline{B} , charged particles do not move directly along an electric field \underline{E} applied from above; they move in cycloidal paths across the planetary magnetic field as well as up or down it (Rishbeth and Garriott 1969, their Fig. 31). Therefore the ionospheric conductivity is a tensor quantity (Rishbeth and Garriott 1969, p. 137), because currents can flow

- (a) parallel to \underline{E} , parallel to \underline{B} , when the “direct” conductivity (as in the previous paragraph) is used,
- (b) parallel to \underline{E} , perpendicular to \underline{B} , when the Pedersen conductivity is appropriate, and
- (c) perpendicular to \underline{E} , perpendicular to \underline{B} , when the Hall conductivity is used (Schunk and Nagy 2000, p. 131).

Up to 105 km altitude, electrons dominate when considering the Earth’s ionosphere and its magnetic field, and from 105 to 140 km ions are important. More complicated expressions for the refractive index of a plasma result when the geomagnetic field is included. These involve magnetoionic theory and the Appleton-Hartree dispersion relation for waves which can propagate in the plasma, and are given, e.g., by Budden (1985) and Stix (1962).

7 Observations of Global Atmospheric Electric Circuit Parameters

7.1 Surface Potential Gradient Measurements in Clean Air

Locating global circuit signals in continental surface station measurements is difficult as these are often masked by local changes due to aerosol pollution, space charge, radioactive pollution, and disturbed weather conditions. In order, the most suitable parameters for monitoring the global circuit are the ionospheric potential V_I , the vertical air–Earth conduction current J_z , and the PG. Even so, clear evidence of the atmospheric electric circuit exists in potential gradient (PG) data obtained in remote locations, far from sources of pollution, and during fair weather conditions. One of the first such PG data sets, with enduring importance, is that obtained by the research ship *Carnegie*.

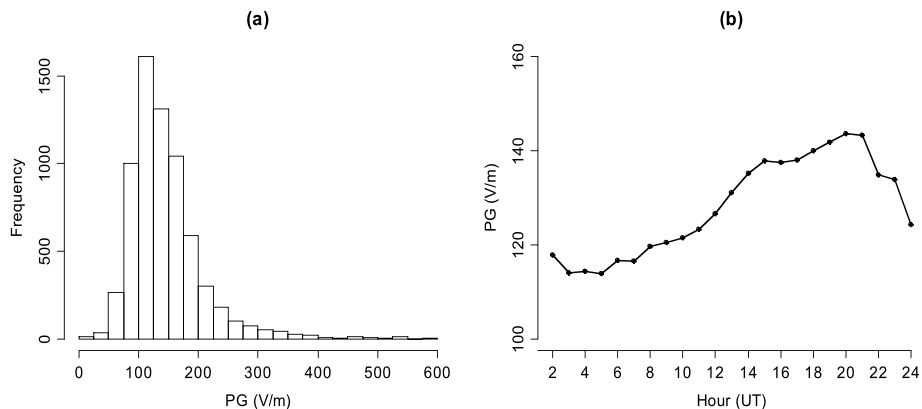


Fig. 9 (a) Histogram of the frequency distribution of hourly PG values obtained on Carnegie cruises 4, 5, and 7 (1915–1929). (Note that the 36 values above 600 V m^{-1} have been excluded for clarity, and there are 6784 data points remaining.) (b) Diurnal variation of the Carnegie mean hourly PG with values selected to illustrate fair weather conditions: hourly values $>200 \text{ V m}^{-1}$ have been excluded, as have days on which there were less than 12 hours of fair weather

The Carnegie's ocean cruises occurred between 1915 and 1921 (cruises 4, 5 and 6), with its final cruise (cruise 7) between 1928 and 1929 before the vessel was destroyed by fire. Figure 9(a) shows the distribution of all available positive hourly PG values measured by the Carnegie during cruises 4, 5, 6 and 7. The maximum PG was 1137 V m^{-1} , but the few values above 600 V m^{-1} (36 out of a total of 6820 values) have been excluded from the following analysis. (This was primarily for clarity, but such large positive values are not known to occur in fair weather conditions and are therefore expected to have resulted from local effects unrepresentative of the global circuit, such as fog, mist or sea-spray. These outliers did not contribute to the shape of the PG distribution, and the long right hand tail contains very little information compared to the rest of the distribution.) On cruises 4, 5, and 6, the PG was measured hourly during “diurnal runs”, which were made twice a month and only when there was “no abnormal weather”. Cruise 7 measured the hourly PG on most days, and in all weather conditions. On all cruises the PG was not recorded if it was negative. From Fig. 9(a) it is clear that most of the values lie between approximately 50 and 250 V m^{-1} . The interquartile range is from 106 to 168 V m^{-1} , and the median value is 134 V m^{-1} .

It is possible to select only fair weather (FW) PG data by utilizing the simultaneous weather records from cruise 7, and noting that from Fig. 9(a) 85% of PG values are less than 200 V m^{-1} . Figure 9(b) shows the Carnegie diurnal variation of mean hourly FW PG, selected using the above criteria. This characteristic diurnal variation in PG, which was independent of the global position of the ship, is one of the most famous results in atmospheric electricity, widely known as the *Carnegie curve*. It has a single diurnal cycle variation, with a maximum at about 19UT, and a minimum at 04UT. It was later shown that the Carnegie diurnal variation has a similar shape to the average UT variation of global thunderstorm activity (Whipple and Scrase 1936), providing corroborating evidence (Aplin et al. 2008) that thunderstorms play an important role in the global circuit. The Carnegie curve is regarded as the standard against which measurements are compared to demonstrate a global circuit variation. If the correlation between measured data and the Carnegie curve is good, then it is inferred that the measurements are likely to be globally representative (Markson 2007).

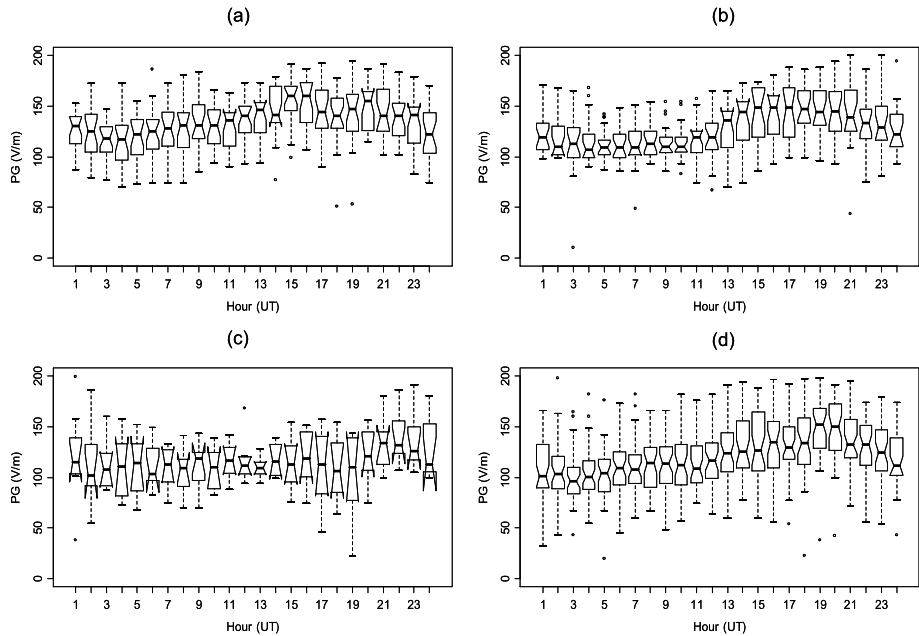


Fig. 10 Seasonal variation in PG data obtained during cruises 4, 5, 6 and 7 of the *Carnegie* for the four seasons, representing the distribution of hourly values with notched box plots, for (a) DJF = December, January, and February, (b) MAM = March, April, and May, (c) JJA = June, July and August, (d) SON = September, October and November. All PG values are for fair weather and $<200 \text{ V m}^{-1}$. (The box width is proportional to the square root of the number of values in each interval, and the edges, and line in the centre, of each box show the upper and lower quartiles, and the median, respectively. Notches indicate the 95% confidence limits on the medians and the whiskers extend to 1.5 times the inter-quartile range)

This curve emerges when hourly PG data are averaged over a suitably long time period, but is rarely seen in a single day's data, as local effects tend to dominate over the global circuit variation.

Figure 10 shows plots of Carnegie diurnal variation in FW PG for four different seasons, (a) DJF, (b) MAM, (c) JJA, (d) SON. (DJF = December, January, and February, MAM = March, April, May, JJA = June, July and August, and SON = September, October and November.) From Fig. 10 it is clear that most seasons have similar single cycle diurnal variations, with the exception of JJA. A possible explanation for the difference during JJA is that the small number of FW values available was insufficient to give a true indication of the hourly PG. (The mean number of points used in the calculation of the mean hourly PG was 56 in DJF, 46 in MAM, 94 in SON, but only 31 in JJA.) From Fig. 10, we see that the times of the maxima differ with season, ranging from 15UT in DJF, to 20UT in SON, whilst the minima occur more consistently between 03UT and 04UT. It can also be seen that the difference between the hourly maxima and minima median PG is statistically significant at the 95% confidence level for DJF, MAM and SON.

7.2 Ionospheric Potential Measurements

The ionospheric potential V_I is measured by integrating the vertical electric field profile from the surface to the ionosphere, using balloon ascents or aircraft. The ionosphere is thought to

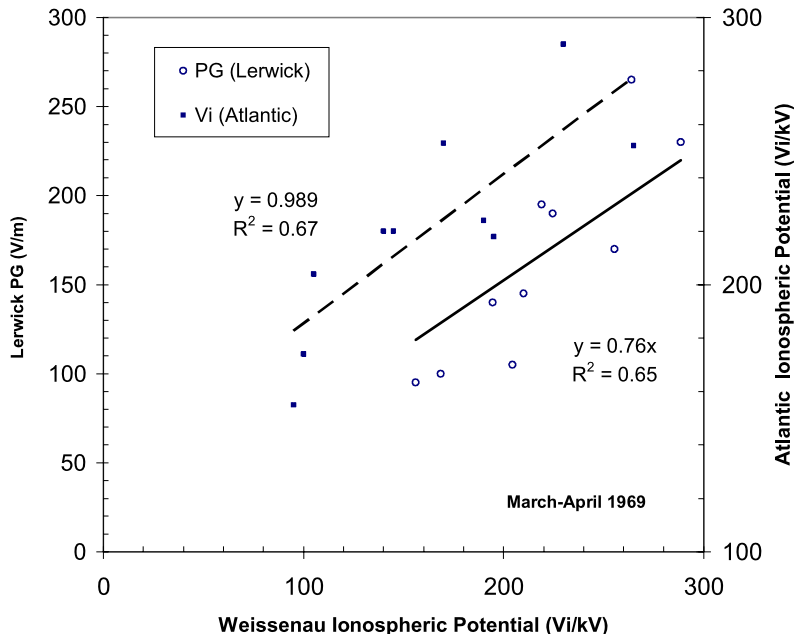


Fig. 11 Plot of V_I data measured by the research ship *Meteor* in the Atlantic (vertical scale at right, solid points, and dashed line), and surface PG data, measured at Lerwick, Scotland (vertical scale at left, open points, and solid line), against simultaneously measured V_I data from Weissenau, Germany from 17 March–2 April 1969

be an equipotential surface (i.e. the ionospheric potential has the same value everywhere), except near the poles, where the solar wind interacts most strongly with the geomagnetic field. Mülheisen (1971) plotted V_I data, measured by the research ship *Meteor* in the Atlantic, against simultaneously measured V_I data from Weissenau, Germany in 1969. This plot can be seen in Fig. 11; the gradient of 0.989 is very close to unity, which would be the case if the simultaneous values at both sites were exactly equal. With the square of the correlation coefficient between the two variables, R^2 , being 0.67, it is clear that there is a close link between V_I as measured at both sites. The additional set of points in Fig. 11 shows surface PG data, measured at Lerwick, Scotland (a remote location in the Shetland Isles) on fair weather days for the same period, against the Weissenau V_I . There is also a linear relationship, indicating that the surface PG at Lerwick is related to the ionospheric potential above (Harrison and Bennett 2007b).

7.3 Atmospheric Electrical Measurements in Polluted Air

The PG is primarily determined by conditions near the Earth's surface, and is sensitive to surface layer aerosol pollution and space charge (Chalmers 1967). Unlike PG, the vertical conduction current J_z is controlled by the total columnar resistance from the surface to the ionosphere, and is thus not so susceptible to local surface conditions. Figure 12 shows an example from the atmospheric electrical measurements at Kew observatory, London, during 1966–1978. Figure 12(a) displays PG, (b) total air conductivity σ_t , and (c) J_z . The air conductivity in Fig. 12(b) was not measured directly, but calculated from Ohm's law when simultaneous measurements of PG and J_z were available. It is clear that there is a

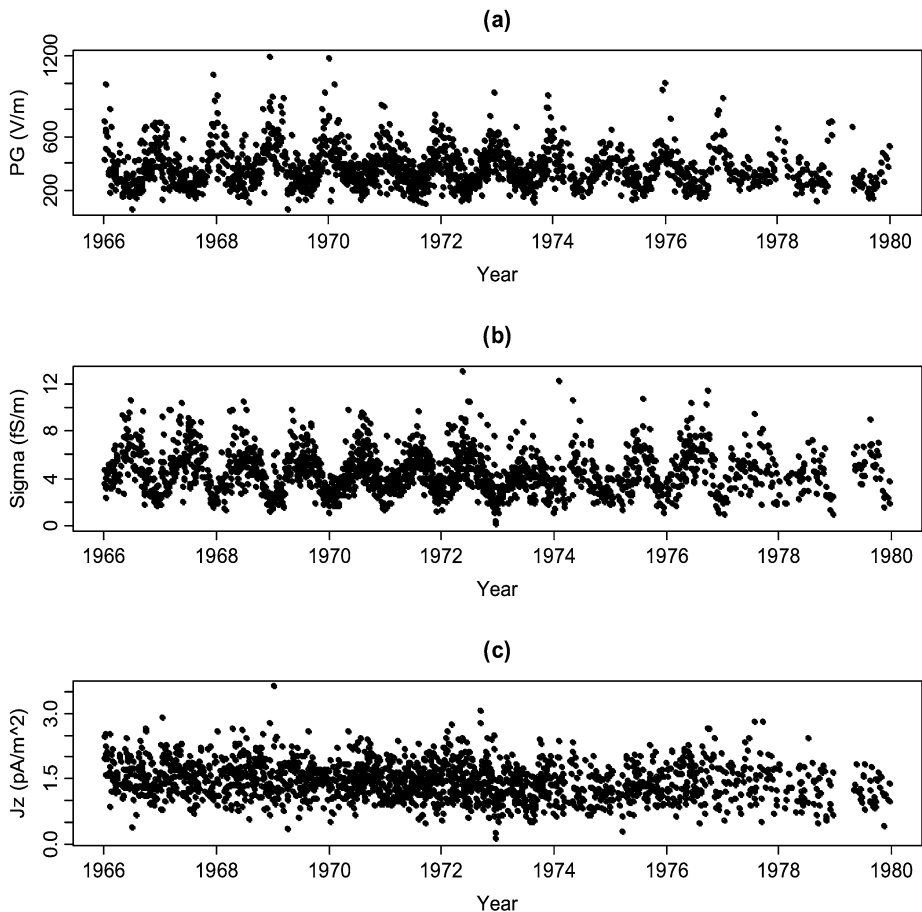


Fig. 12 (a) PG, (b) total air conductivity σ , and (c) J_z data from Kew observatory during 1966 to 1978

strong annual cycle in the PG and conductivity, but not in J_z . This is a result of local aerosol pollution, which affects the conductivity, and in turn the PG. In regions having large aerosol concentrations, the small ions, which are responsible for the conductivity of atmospheric air, are scavenged by the much larger aerosol particles; as a result the conductivity decreases. If J_z is constant, or shows only a small variation, a conductivity decrease will increase the PG.

The diurnal variation in surface PG in clean air has a single daily maximum, as shown by the Carnegie curve. However, at polluted sites, there are usually two maxima, coincident with the time of maximal local aerosol concentrations (Harrison 2006). Because of the low sensitivity of J_z to conductivity changes, there is a greater chance of detecting global signals from long-term surface measurements of J_z . However, it must be recognized that J_z observations are rare compared with observations of PG.

7.4 Similarities in Electrical Measurements at Different Sites

Synchronous variations of the electric field recorded at widely spaced stations are a direct manifestation of the operation of the global atmospheric electric circuit. One such example is

the Carnegie curve diurnal variation. Another example is the similar variation of the electric current density at Vislandi, Estonia, and Waldorf (USA), stations approximately 8000 km apart (Ruhnke et al. 1983).

Simultaneous observations of atmospheric electric field have been performed in the summers of 2005 and 2006 at three Russian stations—Borok ($58^{\circ}04'N$, $38^{\circ}14'E$), Prozorovo ($58^{\circ}23'N$, $37^{\circ}39'E$) and Gorodets ($56^{\circ}41'N$, $43^{\circ}26'E$)—where the station separations lie between 100 and 370 km (Anisimov et al. 2007). Variations of the electric currents and the atmospheric conductivities were also measured at the two stations (Anisimov et al. 2007). Cross-correlation of the electric field data from 27 July to 8 August 2005, under fair weather conditions, revealed two statistically significant maxima for the stations of Borok and Gorodets, shown in Fig. 13(a). The first corresponds to synchronous data, while the second exhibits a time lag of 10 hours, from which we conclude that both global and regional (i.e. synoptic meteorological) scale perturbations exert an influence on the global circuit. Using wavelet spectra on 2 and 3 August 2005, the amplitude of harmonics with 8–16 hour periods (at Gorodets) and 6–10 hour periods (at Borok) increased simultaneously. Accounting for the detailed geophysical and meteorological conditions occurring enabled correlated observations to be associated with geophysical events, particularly a magnetic storm on 19–20 August 2006.

Recent observations clearly demonstrate the important role played by local and regional (convective) generators; these arise due to the mixing of charged particles in the boundary

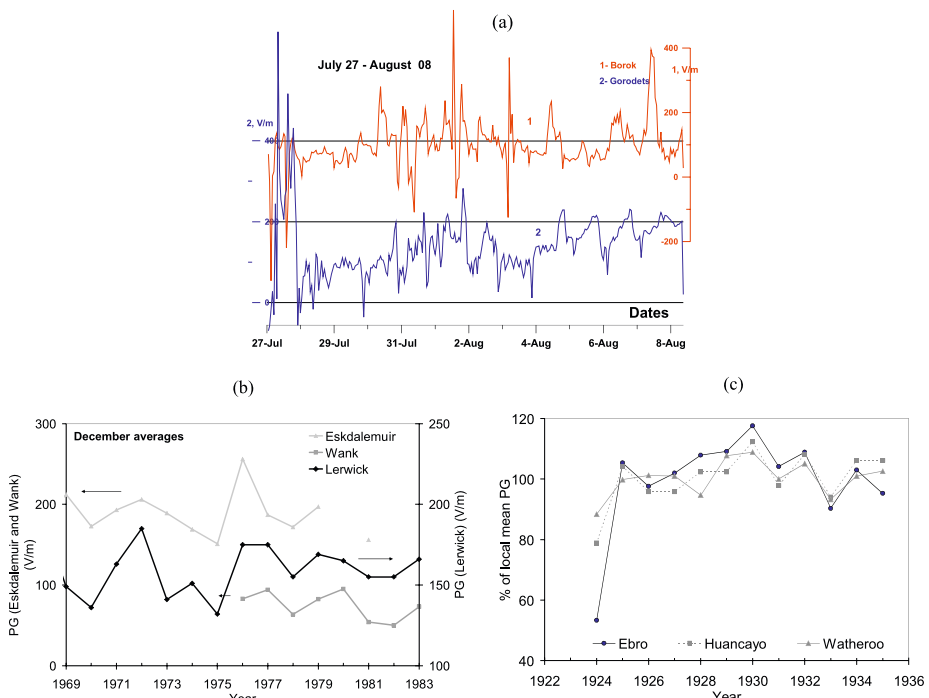


Fig. 13 (a) Recordings of the electric field at spaced stations from 27 July to 8 August 2005 (upper trace Borok, lower trace Gorodets). Data are smoothed by a low pass, 1 h, filter (Anisimov et al. 2007). (b) Comparison of monthly mean PG for December at Wank, Eskdalemuir and Lerwick, adapted from Harrison (2004b, Fig. 4a). (c) Percentage deviations of mean annual PG from the 12 year mean from 1924–1936 at Ebro, Watheroo and Huancayo, as measured by the Carnegie Institute (Wait and Mauchly 1937)

layer over the land surface and lead to short-period (with periods from 1 to 1000 s) electric field, current and conductivity perturbations (Anisimov et al. 2002). Studies of the spectra of these perturbations can be used to distinguish between local and global perturbations of the global circuit.

Similarities between PG values measured at Mt Wank in the Bavarian Alps ($47^{\circ}30'N$, $11^{\circ}09'E$), and the Scottish stations of Eskdalemuir ($55^{\circ}19'N$, $3^{\circ}12'W$) and Lerwick ($60^{\circ}8'N$, $1^{\circ}11'W$), can be seen in Fig. 13(b), adapted from Harrison (2004b). The monthly mean values of PG for December were calculated for each site, and plotted in Fig. 13(b) as a comparison of the annual December values. The similar PG variations demonstrate a long-range correlation between the three sites, as the distances from Eskdalemuir to Wank, and Lerwick to Wank are 1320 and 1620 km, respectively.

Further evidence of the influence of the global circuit can be seen in Fig. 13(c), adapted from Wait and Mauchly (1937). In addition to their survey vessels, the Carnegie Institute of Washington ran three observatories, Ebro (Spain, $40^{\circ}43'N$, $00^{\circ}44'E$), Watheroo (Western Australia, $30^{\circ}16'S$, $116^{\circ}4'E$), and Huancayo (Peru, $12^{\circ}4'S$, $75^{\circ}13'W$), all chosen for their lack of pollution. Figure 13(c) shows the percentage deviations of the mean annual PG from its 12 year mean value, for 1924–1936. Again there are substantial similarities between the three stations, providing further evidence of the global electric circuit concept.

7.5 Influence of Solar Energetic Particles on Electrical Parameters

A small number of large helium-filled balloons instrumented to measure tropospheric and stratospheric electric fields and both positive and negative ion conductivities have been launched from interesting locations since the 1970s. As an example of the results obtained by such studies, Fig. 14 shows observations made near $71^{\circ}S$, $10^{\circ}20'W$, between 30 and 33 km altitude, on 20 January 2005 by Kokorowski et al. (2006) on a balloon launched from SANE station, Antarctica. To the left of the vertical dashed line at 06.51 UT, panel (a) shows measurements of the total ion conductivity of $10 \times 10^{-12} \text{ S m}^{-1}$ (the legend on the scale should be pS m^{-1}) and panel (b) shows a measured downwards electric field, which is rather variable, but has a typical value of 0.1 V m^{-1} . Using Ohm's law, the fair weather vertical current density J_z is calculated and plotted in panel (d); its typical value is 1 pA m^{-2} .

Farrell and Desch (2002) predicted that a solar proton event could change the fair weather electric field at ground level by $\sim 5\%$. At 06.51 UT on 20 January 2005, a Solar Energetic Particle (SEP) event occurred, providing, serendipitously, an unusual experimental opportunity for investigating solar influences on the global circuit. The additional ionization created by the SEP in the stratosphere increased the total conductivity by an order of magnitude. In the observations, the vertical electric field falls to near zero, and gradually recovers over the next few hours until 14.00 and 15.56 UT when sudden changes occur; these are unexplained as yet. For four hours from 10–14 UT the deduced fair weather current density increased from ~ 2 to up to 6 pA m^{-2} at this location, inside the southern polar cap. Taking the area of the polar caps bounded by the auroral ovals to be $\sim 2.5\%$ of the Earth's surface area, the fair weather current density would presumably decrease by $\sim 10\%$ over the remainder of the Earth to compensate for this, on the assumption that nothing else changed in the DC global circuit. It would be very interesting to examine simultaneous atmospheric electricity data from stations around the world to investigate whether related changes were indeed observed, or whether the situation was more complex.

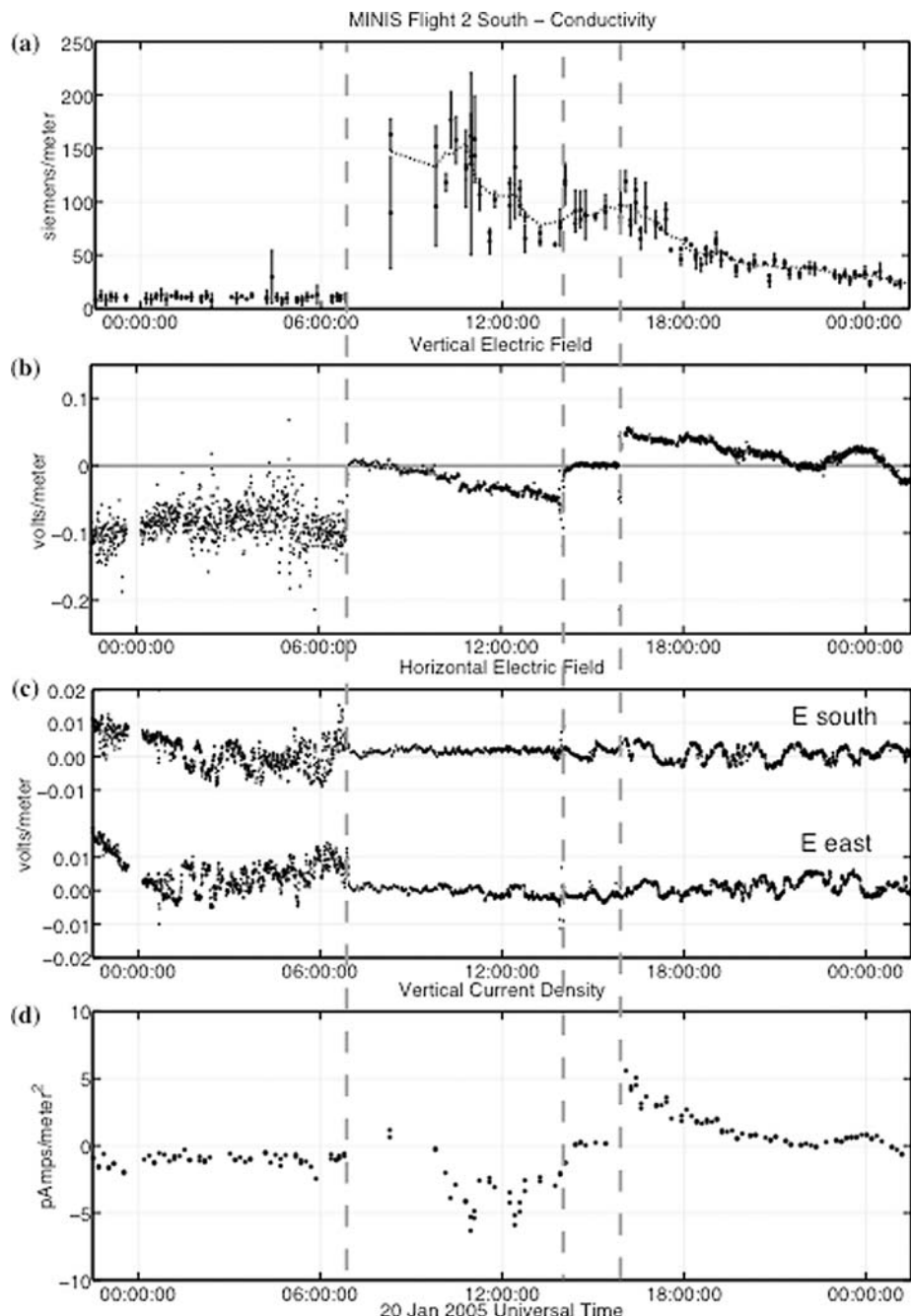


Fig. 14 Balloon observations made between 31 and 33 km altitude on 20 January 2005 of (a) atmospheric conductivity in pS m^{-1} , (b) vertical electric field (positive upwards) in V m^{-1} , (c) weak horizontal electric fields in V m^{-1} , and (d) calculated vertical current density through the atmosphere in pA m^{-2} . At 06:51 U.T. (left hand vertical dashed line) the onset of a solar energetic particle (SEP) event occurred; at 14:00 and 15:56 U.T. (two vertical dashed lines towards the right) the observed vertical electric field suddenly changed. (Taken from Kokorowski et al. 2006, their Fig. 2) (Copyright American Geophysical Union, reproduced with permission)

8 Model Studies

Global circuit modelling is a subject of long-term interest (see, e.g., Volland 1995, and references therein). Recent studies are based on new experimental results, and they seem to provide a deeper understanding of how the global circuit operates.

In terms of possible comparisons with the atmospheric electricity of other planets, recent studies of global circuit energetics are of especial interest. In particular, Mareev and Anisimov (2007) estimated the total electrostatic (not electromagnetic) energy of the atmosphere and the total mean rate of energy dissipation; this has allowed an estimate to be made of the lifetime of electric energy in the atmosphere. This time turns out to be rather small, from about 30 to 120 seconds, depending on the assumptions made about the parameters controlling the global electric circuit. In particular, the energy lifetime is less than the relaxation time of the global capacitor (~ 125 s, see Rycroft et al. 2007), and of the field relaxation time near the Earth's surface (~ 15 minutes). This is explained by the fact that the main contributions to the total energy and its dissipation rate are related to the higher altitudes of the most active parts of thunderstorm clouds.

The important role of mesoscale convective systems (MCSs) in the global electric circuit has been quantified through model calculations. Davydenko et al. (2004) developed a 3-D model which allowed the electric field and current distribution, based upon experimental results, to be calculated. Depending on the polarity, magnitude, and thickness of the stratiform region, an MCS can either serve as a generator for, or a discharger (Davydenko et al. 2004) of, the global circuit. The electrostatic energy in a typical thunderstorm is estimated to be 10^{10} – 10^{11} J, while for the most intense thunderstorms it can exceed 10^{12} J (see Davydenko et al. 2004; Mareev and Anisimov 2007).

In recent work, Rycroft et al. (2007) used the model atmospheric conductivity profile presented here as Fig. 5 in an “electrical engineering” software model of the global atmospheric electric circuit. Their model has thunderstorm generators and precipitation from electrified shower cloud generators of comparable magnitude which maintain the ionosphere at a potential of 250 kV with respect to the Earth at zero potential, and provide a fair weather current density (vertically downwards) of 2 pA m^{-2} through a resistance $r = 250 \Omega$. The time constant of the fair weather circuit is $rC = 125$ s.

Rycroft et al. (2007) calculated the electric field distribution and charge density below, through and above a model thunderstorm which produces either negative cloud-to-ground (−CG) or +CG lightning discharges. They found that 1 ms after a +CG discharge (having significant continuing current) the electric field from 76 km down to 55 km exceeded the threshold for the creation of positive streamers. Thus, a sprite, a mesospheric discharge (for a full discussion of these, see Fullekrug et al. 2006) could develop there, with downward moving positive streamers. They also found that the ionospheric potential was reduced by ~ 40 V following the +CG model discharge, after which the potential recovered with the rC time constant.

Further, Rycroft et al. (2007) modelled a sprite as a high conductivity region (10^{-7} S m^{-1}) moving from 70 km altitude down to 50 km in 4 ms. This caused a reduction of 1 V in the ionospheric potential and, hence, a $\sim 4 \times 10^{-4}\%$ reduction in the fair weather electric field. It would be interesting to investigate whether, under quiet conditions, a superposed epoch analysis “triggered” by large +CG discharges, occurring anywhere on the Earth's surface, could detect such a tiny change. Such large +CG discharges are known preferentially to cause sprites (see Fullekrug et al. 2006) and to be the source of the so-called “Q bursts” (Ogawa et al. 1967), strong radio signals at ~ 10 Hz which propagate all the way around the Earth.

Recently a numerical model of the transient electric field due to CG and inter-cloud (IC) lightning flashes and their Maxwell relaxation (slow transients) has been developed (Mareev et al. 2007). The electric field and current distributions, the electric field decay time, and the total charge transferred to the ionosphere and to the ground have been calculated. Balloon electric field data have been used to verify the theory. The CG flash efficiency (i.e. the percentage of net charge contributed to the circuit by both fast and slow lightning transients) depends strongly on the height of the localized charge in the conducting atmosphere. It varies from about 15% to 90% as the altitude of the region of charge ranges from 1 to 14 km, for a model with an exponential atmospheric conductivity profile unperturbed by the thunderstorm. Typical CG flash efficiencies are 55–75%, and IC flash efficiencies 5–15%. Both CG and IC lightning flashes drive significant slow (~ 100 s) transient currents to the ionosphere and to the ground, in addition to the rapid (~ 100 ms) transfer of charge by such flashes. A comparison of transient (fast) and sustained (slow) currents for particular storms is extremely important in order to make more definite conclusions on the current balance in the global circuit, and its variations.

For the study of the general properties of planetary electricity, it is necessary to consider additional electrical sources in the global circuit besides thunderstorms. One of these is a unipolar dynamo mechanism caused by the non-rigid rotation of the planet-plasmasphere system (Bespalov and Chugunov 1996). A magnetized rotating planet, whose magnetic moment is M , and the surrounding plasma envelope form a planetary generator with an output voltage of $\sim \mu_0 M \omega_0 / (4\pi R)$ volts (where ω_0 and R are the angular velocity and radius of the planet, respectively, and μ_0 is the magnetic permeability of free space), which is applied to the upper atmosphere. Distributions of the electric potential, current density and charge density in the atmosphere and in the magnetosphere have been determined, taking into account the altitude variation of the atmospheric conductivity for fair weather conditions (Bespalov et al. 1996). The model gives a reasonable value for the electric current density in the atmosphere near the Earth's surface, about 10^{-12} A m $^{-2}$. Davydenko et al. (2004) emphasized the significance of the conductivity exponentially increasing with height for this mechanism. They also showed that the variation of the atmospheric conductivity distribution with latitude gives rise to an additional, latitudinally uniform, radial electric field in the lower atmosphere. For the Earth, the additional potential arising from this effect is of the order of 15% of the potential difference applied to the atmosphere.

9 Conclusions

In the Earth–atmosphere–ionosphere system, the vertical profile of the electrical conductivity from the surface to the ionosphere is such that it fortuitously bounds a low conductivity region (the atmosphere) by two high conductivity regions (at the Earth's surface and the ionosphere). This has interesting and important consequences for electric current flow and the propagation of electromagnetic waves. In the first case, electric currents generated in disturbed weather regions (i.e. thunderstorms and electrified shower clouds) permit current flow in fair weather regions (the “DC global circuit”) whereas, in the second case, electromagnetic waves radiated by lightning discharges propagate an Extremely Low Frequency (ELF) radio wave all the way around the world in the surface–ionosphere waveguide (the “AC global circuit”).

For the DC global circuit, measurements made close to the surface are relatively the most abundant, particularly those of the PG. Local variations in aerosol frequently dominate such PG measurements, causing a diurnal cycle in the PG which is that of the local smoke or

aerosol variations. In clean air, or air with small aerosol variations over the diurnal cycle, a diurnal variation known as the Carnegie curve can be obtained through averaging. This variation is independent of location and local time of day, and is a characteristic of the global circuit. A global circuit parameter measured at the surface less sensitive to local aerosol pollution is the vertical air–Earth current density. This current density is associated with the potential difference between the two bounding equipotential regions of the ionosphere and surface; Ohm’s law applies. Several results of recent modelling studies of atmospheric electric phenomena are discussed, and these complement the observational results well.

The most important conclusion drawn is that the atmospheric conductivity profile determines the existence of both DC and AC global electric circuits, and substantially influences their properties.

Acknowledgements The authors are most grateful to Dr. Kuvshinov and Dr. Olsen for their help with obtaining information on variations of the Earth’s surface conductivity on a global scale. K.A. Nicoll acknowledges a studentship from the Natural Environment Research Council.

References

- S.V. Anisimov, E.A. Mareev, N.M. Shikhova et al., *Geophys. Res. Lett.* **29**, 2217 (2002)
- S.V. Anisimov, E.A. Mareev, N.M. Shikhova et al., in *Proc. 13th Int. Conf. on Atmos. Electr.* (Beijing, China, 2007), p. 33
- K.L. Aplin, R.A. McPheat, *J. Atmos. Sol.-Terr. Phys.* **67**, 775 (2005)
- K.L. Aplin, R.G. Harrison, M.J. Rycroft, *Space. Sci. Rev.* (2008, this issue)
- K. Bahr, F. Simpson, *Practical Magnetotellurics* (Cambridge University Press, Cambridge, 2005), pp. 270
- G.A. Bazilevskaya, M.B. Krainev, V.S. Makhmutov, *J. Atmos. Sol.-Terr. Phys.* **62**, 1577 (2000)
- G.A. Bazilevskaya, I.G. Usoskin, E. Flückiger et al., *Space. Sci. Rev.* (2008, this issue). doi:[10.1007/s11214-008-9339-y](https://doi.org/10.1007/s11214-008-9339-y)
- E.A. Bering, R.H. Holzworth, B.D. Reddell et al., *Adv. Space Res.* **35**, 1434 (2005)
- P.A. Bedrosian, *Surv. Geophys.* **28**, 121 (2007)
- P.A. Bespalov, Yu.V. Chugunov, *J. Atmos. Terr. Phys.* **58**, 601 (1996)
- P.A. Bespalov, Yu.V. Chugunov, S.S. Davydenko, *J. Atmos. Terr. Phys.* **58**, 605 (1996)
- K.G. Budden, *The Propagation of Radio Waves* (Cambridge University Press, Cambridge, 1985), pp. 669
- K.S. Carslaw, R.G. Harrison, J. Kirkby, *Science* **298**, 1732 (2002)
- J.A. Chalmers, *Atmospheric Electricity*, 2nd edn. (Pergamon Press, 1967)
- W.E. Cobb, H.J. Wells, *J. Atmos. Sci.* **27**, 814 (1970)
- S.S. Davydenko, E.A. Mareev, T.C. Marshall, M. Stolzenburg, *J. Geophys. Res.* **109** (2004). doi:[10.1029/2003JD003832](https://doi.org/10.1029/2003JD003832)
- W.H. Evans, *J. Geophys. Res.* **74**, 939 (1969)
- W.M. Farrell, M.D. Desch, *Geophys. Res. Lett.* **29** (2002). doi:[10.1029/2001GL013908](https://doi.org/10.1029/2001GL013908)
- M. Fullekrug, E.A. Mareev, M.J. Rycroft (eds.), *Sprites, Elves and Intense Lightning Discharges* (Springer, New York, 2006), pp. 398
- O.H. Gish, *Terr. Magn. Atmos. Electr.* **49**, 15 (1944)
- R. Gunn, *J. Meteor.* **11**, 339 (1954)
- L.C. Hale, *Adv. Space Res.* **4**, 175 (1984)
- R.G. Harrison, *Surv. Geophys.* **25**, 441 (2004a)
- R.G. Harrison, *J. Atmos. Sol.-Terr. Phys.* **66**, 1127 (2004b)
- R.G. Harrison, *J. Atmos. Sol.-Terr. Phys.* **67**, 763 (2005)
- R.G. Harrison, *Atmos. Environ.* **40**, 3327 (2006)
- R.G. Harrison, *Atmos. Res.* **84**, 182 (2007)
- R.G. Harrison, K.L. Aplin, *Atmos. Res.* **79** (2007). doi:[10.1016/j.atmosres.2006.12.006](https://doi.org/10.1016/j.atmosres.2006.12.006)
- R.G. Harrison, A.J. Bennett, *J. Atmos. Sol.-Terr. Phys.* **69**, 515 (2007a)
- R.G. Harrison, A.J. Bennett, *Adv. Geosci.* **13**, 17 (2007b)
- R.G. Harrison, K.S. Carslaw, *Rev. Geophys.* **41** (2003). doi:[10.1029/2002RG000114](https://doi.org/10.1029/2002RG000114)
- R.G. Harrison, W.J. Ingram, *Atmos. Res.* **76**(1–4), 49 (2005)
- S. Israelsson, E. Knudsen, S.V. Anisimov, *J. Atmos. Terr. Phys.* **56**, 1545 (1994)
- S. Israelsson, H. Tammet, *J. Atmos. Sol.-Terr. Phys.* **63**, 1693 (2001)

- J.D. Jackson, *Classical Electrodynamics* (Wiley, New York, 1962), pp. 641
- B. Karlsson, H. Kornich, J. Gumbel, *Geophys. Res. Lett.* **34**(L16806) (2007). doi:[10.1029/2007GL030282](https://doi.org/10.1029/2007GL030282)
- M. Kokorowski, J.G. Sample, R.H. Holzworth et al., *Geophys. Res. Lett.* **33**(L20105) (2006). doi:[10.1029/2006GL027718](https://doi.org/10.1029/2006GL027718)
- T. Korja, *Surv. Geophys.* **28**, 239 (2007)
- W. Lowrie, *Fundamentals of Geophysics*, 2nd edn. (Cambridge University Press, Cambridge, 2007)
- M. Makino, T. Ogawa, J. *Geophys. Res.* **90**(D4), 431 (1985)
- E.A. Mareev, S.V. Anisimov, in *Proc. 13th Int. Conf. on Atmos. Electr.* (Beijing, China, 2007), p. 21
- E.A. Mareev, S.A. Yashunin, S.S. Davydenko et al., *Geophys. Res. Lett.* (2007, in press)
- D.R. MacGorman, W.D. Rust, *The Electrical Nature of Storms* (Oxford University Press, New York, 1998), pp. 422
- R. Markson, *Bull. Am. Met. Soc.* **88** (2007). doi:[10.1175/BAMS-88-2-223](https://doi.org/10.1175/BAMS-88-2-223)
- R.P. Mühlheisen, *Pure Appl. Geophys.* **84**, 112 (1971)
- T. Ogawa, Y. Tanaka, T. Miura et al., *J. Geomag. Geoelectr.* **19**, 115 (1967)
- N. Olsen, A. Kuvshinov, *Earth Planets Space* **56**, 525 (2004)
- V.P. Pasko, J.J. George, *J. Geophys. Res.* **107** (2002). doi:[10.1029/2002JA009473](https://doi.org/10.1029/2002JA009473)
- B.B. Phillips, *Mon. Weather Rev.* **95**, 854 (1967)
- V.A. Rakov, M.A. Uman, *Lightning. Physics and Effects* (Cambridge University Press, Cambridge, 2003), pp. 687
- H. Rishbeth, O.K. Garriott, *Introduction to Ionospheric Physics* (Academic Press, New York, 1969), pp. 331
- W.D. Rust, C.B. Moore, *Quart. J. R. Met. Soc.* **100**, 450 (1974)
- L.H. Ruhnke, H.F. Tammet, M. Arold, in *Proc. Atmospheric Electricity*, ed. by L.H. Ruhnke, J. Latham (Hampton, Virginia, A. Deepak, 1983), p. 6
- M.J. Rycroft, in *The Standard Handbook for Aeronautical and Astronautical Engineers*, ed. by M. Davies (McGraw Hill, New York, 2003), pp. 16.1–16.23
- M.J. Rycroft, *J. Atmos. Sol.-Terr. Phys.* **68**, 445 (2006)
- M.J. Rycroft, S. Israelsson, C. Price, *J. Atmos. Sol.-Terr. Phys.* **62**, 1563 (2000)
- M.J. Rycroft, A. Odzimek, N.F. Arnold et al., *J. Atmos. Sol.-Terr. Phys.* **69** (2007). doi:[10.1016/j.jastp.2007.09.004](https://doi.org/10.1016/j.jastp.2007.09.004)
- W.O. Schumann, *Naturforsch. Z. A* **7**, 149 (1952)
- R.W. Schunk, A.F. Nagy, *Ionospheres: Physics, Plasma Physics and Chemistry* (Cambridge University Press, Cambridge, 2000), pp. 554
- F. Simoes, M. Rycroft, N. Renno et al., *Space Sci. Rev.* (2008, this issue)
- V.V. Smirnov, *Izv. RAN, Atmos. Ocean. Phys.* **51**, 750 (2005)
- V.V. Smirnov, A.V. Savchenko, *Atmos. Res.* **82**, 554 (2006)
- T.H. Stix, *The Theory of Plasma Waves* (McGraw-Hill, New York, 1962), pp. 283
- R.B. Stull, *An Introduction to Boundary Layer Meteorology* (Kluwer, London, 1988), p. 22
- B.A. Tinsley, L. Zhou, *J. Geophys. Res.* **111**(D16205) (2006). doi:[10.1029/2005JD006988](https://doi.org/10.1029/2005JD006988)
- I.G. Usoskin, O.G. Gladysheva, G.A. Kovaltsov, *J. Atmos. Sol.-Terr. Phys.* **66**, 1791 (2004)
- M. Uyeshima, *Surv. Geophys.* **28**, 199 (2007)
- H. Volland, in *Handbook of Atmospheric Sciences*, ed. by H. Volland, vol. 1 (CRC Press, Boca Raton, 1995), pp. 65–109
- G.R. Wait, J.W. Mauchly, *Transactions of the AGU*, 18th Annual Meeting, 1937
- F.J. Whipple, F.J. Scrase, *Geophys Mem.* **7**, Meteorol. Off., London, 1936
- E.R. Williams, in *Encyclopedia of Atmospheric Sciences*, ed. by J.R. Holton, J.A. Pyle, J.A. Curry (Academic Press, New York, 2002), p. 724
- F. Yu, R.P. Turco, *J. Geophys. Res.* **106**(D5), 4797 (2001)

Ions in the Terrestrial Atmosphere and Other Solar System Atmospheres

R. Giles Harrison · Hannes Tammet

Originally published in the journal Space Science Reviews, Volume 137, Nos 1–4.
DOI: [10.1007/s11214-008-9356-x](https://doi.org/10.1007/s11214-008-9356-x) © Springer Science+Business Media B.V. 2008

Abstract Charged molecular clusters, traditionally called *small ions*, carry electric currents in atmospheres. Charged airborne particles, or *aerosol ions*, play an important role in generation and evolution of atmospheric aerosols. Growth of ions depends on the trace gas content, which is highly variable in the time and space. Even at sub-ppb concentrations, electrically active organic compounds (*e.g.* pyridine derivatives) can affect the ion composition and size. The size and mobility are closely related, although the form of the relationship varies depending on the critical diameter, which, at 273 K, is about 1.6 nm. For ions smaller than this the separation of quantum levels exceeds the average thermal energy, allowing use of a molecular aggregate model for the size-mobility relation. For larger ions the size-mobility relation approaches the Stokes-Cunningham-Millikan law. The lifetime of a cluster ion in the terrestrial lower atmosphere is about one minute, determined by the balance between ion production rate, ion-ion recombination, and ion-aerosol attachment.

Keywords Atmospheric electricity · Lightning · Atomic and molecular clusters · Electrical properties · Particles and aerosols in meteorology

PACS 92.60.Pw · 36.40.-c · 51.50.+v · 92.60.Mt

1 Sources of Ions and Ionization Rate

The ionization rate q quantifies how many ion pairs are created per unit volume of gas per unit time (Israël 1970). Ions and free electrons are generated in a gas when a molecule or atom is excited with an energy exceeding the ionization potential. Typical ionization potentials for some gases in the terrestrial atmosphere are: H₂ 15.4 eV, N₂ 15.6 eV, and O₂

R.G. Harrison (✉)

Department of Meteorology, University of Reading, Earley Gate, Reading, Berks RG6 6BB, UK
e-mail: r.g.harrison@reading.ac.uk

H. Tammet

Department of Environmental Physics, University of Tartu, 18 Ülikooli St., Tartu 50090, Estonia

12.1 eV. Ions are also created when an ion or electron encounters a neutral molecule in a strong electric field, which leads to an ionization avalanche and electric breakdown, such as in a lightning discharge.

In the terrestrial upper atmosphere, the mean free path of ions is long and even a relatively low electric field can cause ionization by ion-molecule collisions. This is not, however, a dominant ionization process in planetary upper atmospheres, where the main ionizing agents are electromagnetic and corpuscular radiation emitted by the Sun.

Thermal ionization is generally negligible in atmospheres, which can be demonstrated from the Saha-Langmuir theory (Engel 1965). Using this theory, the concentration of ions (in cm^{-3}) generated by thermal collisions is roughly estimated as $1.3 \times 10^{17} \sqrt{p\sqrt{T}} \exp(-11600\phi/T)$, where the gas pressure p is in mbar, the ionization potential ϕ is in eV, and temperature T in Kelvin. For an ionization potential of 10 eV, an ion concentration of $\sim 1 \text{ cm}^{-3}$ requires a temperature of $\sim 1300 \text{ K}$ at 1000 mbar pressure, and $\sim 1400 \text{ K}$ at 1 mbar. As typical maximum temperatures in planetary atmospheres are about 850 K, the probability of thermal ionization is therefore small.

Electromagnetic ultra-violet radiation ionizes dayside planetary atmospheres for wavelengths λ less than the Lyman beta wavelength ($\lambda = 103 \text{ nm}$). Only exceptional gases like NO (ionization potential 9.3 eV) can be ionized by the more intense Lyman alpha radiation ($\lambda = 122 \text{ nm}$), although dayside photoionization also seems important in the Martian atmosphere (Tripathi et al. 2008). Another important factor in upper atmosphere ionization is the precipitation of solar electrons and protons, and meteoritic sources (Molina-Cuberos et al. 2008). The maximum ionization rate in the terrestrial upper atmosphere is of order $10^3 \text{ cm}^{-3} \text{ s}^{-1}$.

Solar corpuscular and shortwave electromagnetic radiation are efficiently absorbed in the terrestrial upper atmosphere and do not generally directly affect the lower atmosphere. In the terrestrial lower troposphere, some ions are generated by photoemission of electrons from aerosol particles, a process which requires less than half the energy necessary for ionization of gas molecules. Photoemission is usually neglected in the terrestrial atmosphere. In Titan's atmosphere, photoemission charging has been considered important (Borucki et al. 2006), from assuming that the photoemission threshold appropriate for Titan's haze is that for graphitic particles (Bakes et al. 2002). Predictions of the Titan conductivity profile derived from such assumptions differ from the Huygens probe's preliminary findings however, therefore photoemission may be considerably less important (Borucki and Whitten 2008).

The terrestrial lower atmosphere is ionized by galactic cosmic rays, from which the ionization rate reaches a maximum of about $50 \text{ cm}^{-3} \text{ s}^{-1}$ in the stratosphere, between 10 and 20 km (Bazilevskaya et al. 2008). Ion transport occurs in planetary atmospheres having global circuits, which leads to vertical ion transport in the earth's atmosphere (Aplin 2006; Aplin et al. 2008). Near to the terrestrial surface, an additional source of ionization is from natural radioactivity, and the decay of radon and airborne radon daughter nuclides. In summary, the ionizing factors in the terrestrial lower atmosphere are (Israël 1970):

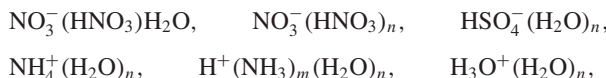
- Galactic cosmic rays (~ 2 ion pairs $\text{cm}^{-3} \text{ s}^{-1}$ in the lowest kilometre, increasing with height up to $50 \text{ cm}^{-3} \text{ s}^{-1}$ in the stratosphere). Terrestrial magnetic field variations cause the cosmic ray ion production rate to vary with geomagnetic latitude.
- Gamma rays emitted from soil and rocks (~ 4 ion pairs $\text{cm}^{-3} \text{ s}^{-1}$ up to 200–300 m from surface).
- Alpha radiation from ^{222}Rn and its progeny (~ 3 ion pairs $\text{cm}^{-3} \text{ s}^{-1}$ up to 1–2 km from surface).

The typical ionization rate from all sources near to the terrestrial continental surface is 4 to 8 cm⁻³ s⁻¹ (Hirsikko et al. 2007) but during calm nocturnal conditions accumulations of radon (²²²Rn) and thoron (²²⁰Rn) occasionally enhance the ionization rate up to at least 100 cm⁻³ s⁻¹ in the lowest metre (Nagaraja et al. 2003, 2006). Additionally, deposited radon daughters can create ions immediately adjacent to the surface. Willett (1985) modelled the atmospheric electric field close to the surface in calm conditions (known as “the electrode effect”) over a grass surface, and pointed out that despite the short path of alpha particles, radon daughter nuclide deposition is an important ionizing factor.

2 Evolution and Classification of Ions in the Terrestrial Troposphere

A free electron and a positive ion are the primary particles resulting from ionization. In a typical lower atmosphere, the electron encounters an electronegative molecule (*e.g.* O₂) during the first microsecond, forming a negative molecular ion. If the collision frequency is high, minor traces of electronegative gases will scavenge all the electrons. In general, electrons can remain free at low pressure in upper atmospheres, but can only remain free in lower atmospheres if electronegative gases are absent. For example, in Titan’s atmosphere, no electrophilic species are present, and free electrons and positive ions remain.

The enhanced chemical activity of ions results in a chain of ion-molecule reactions from ion-neutral collisions, and a charged molecular cluster known as a “cluster ion” or “small ion” is formed. The cluster ion lifetime in earth’s lower atmosphere is about one minute, during which it undergoes thousands of ion-molecular reactions (Luts and Salm 2004; Beig and Brasseur 2000). The corresponding evolution in ion size and electric mobility depends on the air’s trace gas content, which is highly variable in the time and space. Theoretical calculations indicate that, in terrestrial air free of exotic trace gases, the following cluster ions would be typical (Luts and Salm 2004; Beig and Brasseur 2000):



where *n* and *m* are small integers. If the air contains trace gases with high electron or proton affinity then longer-lived cluster ions will also include molecules of these gases (Beig and Brasseur 2000; Parts and Luts 2004). Some electrically-active compounds like pyridine derivatives can affect the ion composition and size, even at concentrations of less than one ppb. Thus the measured size and mobility distributions of the cluster ions depend on the minor contaminants present in the air, therefore the ion property measurements contain some indirect information about air pollution.

Most cluster ions will be lost through their attachment to an aerosol particle or through their recombination with another cluster ion having the opposite polarity. In some situations the cluster ions can continue their growth and become charged aerosol particles, called aerosol ions. This is known as ion-induced or ion-mediated nucleation (Curtius et al. 2006; Yu 2006; Kazil et al. 2008; Arnold 2008). This is one mechanism by which new aerosol particle formation occurs in the earth’s atmosphere (Harrison and Carslaw 2003; Kulmala 2003; Kanawade and Tripathi 2006). The aerosol particles formed encounter further small ions, and will be neutralized or recharged on timescales of minutes. Many new neutral aerosol particles form through other mechanisms, becoming aerosol ions by the attachment of cluster ions.

Table 1 Classification of terrestrial atmospheric ions according to Hörrak et al. (2000)

Class of air ions		Mobility μ ($\text{cm}^2 \text{V}^{-1} \text{s}^{-1}$)	Diameter d (nm)	Typical concentrations n_{typ} (cm^{-3})
Cluster ions	Small cluster ions	1.3–3.2	0.36–0.85	250
	Big cluster ions	0.5–1.3	0.85–1.6	100
Aerosol ions	Intermediate ions	0.034–0.5	1.6–7.4	100
	Light large ions	0.0042–0.034	7.4–22	400
	Heavy large ions	0.00087–0.0042	22–80	1300

Cluster ions and aerosol ions may be discriminated by the ratio of the average separation of internal energy levels ΔE to the thermal energy kT , where k ($k = 1.38 \times 10^{-23} \text{ J K}^{-1}$) is Boltzmann's constant and T is temperature. If $\Delta E \gg kT$, the internal energy will be unaffected by thermal collisions and the scattering of gas molecules by ions will be elastic. If $\Delta E \ll kT$, then the colliding molecules will acquire the ion's internal temperature, causing the scattering to be inelastic. In the first case ($\Delta E \gg kT$) the ion can be considered as a charged molecular aggregate, *i.e.* a cluster ion. In the second case ($E \ll kT$) the ion can be considered to be a macroscopic particle, *i.e.* an aerosol ion. At standard temperature (273 K), the transition diameter between terrestrial cluster ions and aerosol ions is about 1.6 nm, from theoretical considerations and measurements of ion masses and mobilities (Tammet 1995). This concept can be extended to other atmospheres, as the transition diameter varies with temperature T as $T^{-1/3}$, but it does not depend on the pressure and gas composition.

A detailed classification is based on the measurements of distribution of ions according to their electric mobility. The mobility μ is a directly measurable parameter defined by $\mu = v/E$, where v is the drift speed of an ion in electric field E . Traditionally, terrestrial atmospheric ions have been classified according to their mobility as *small* (or fast) ions, *intermediate* ions and *large* (or slow or Langevin) ions. The mobility and size range of small ions is essentially the same as that of cluster ions, with the boundary between intermediate and large ions arising by convention. Hörrak et al. (2000) analyzed the correlations between narrow mobility fractions of atmospheric ions and proposed a classification based on factor analysis, which is summarised in Table 1.

Concentrations of air ions vary in space and time, and, in general, are different for positive and negative ions. The typical concentrations n_{typ} presented in Table 1 are close to the long-term averages of measurements made at a rural site in Estonia (Hörrak 2001).

3 Relations Between Ion Size, Mass, and Mobility

Mass and mobility are well-defined concepts for any particle. Measurements provide good information about the mobilities for all ion classes, but only limited information about masses for small ions and poor information about sizes for the largest ions. Time-of-flight methods (Eiceman and Karpas 1994; Eiceman et al. 2001) permit measurement of cluster ion mobilities, whereas aspiration methods (Tammet 2006; Mirme et al. 2007) allow measurement of both cluster ion and aerosol ion mobilities. Mass spectrometers can measure cluster ion masses (Viggiano 1993), but determining sizes of large aerosol ions requires an electron microscope. Radiative methods, permitting remote sensing of ions in planetary

atmospheres, may also become possible (Aplin and McPheat 2005). There are no known methods for direct measurements of the geometric sizes of cluster ions and intermediate ions: sizes of these ions are usually calculated from their measured mobility or mass, using theoretical models.

The geometric size is an unambiguous and well-defined parameter only in the case of spherical macroscopic particles. In the nanometre size range, the traditional macroscopic model of a spherical particle with an exactly determined geometric surface is inadequate. Although the concept of “mobility diameter” is widely used, this requires that the appropriate mobility-size relationship is known. This presents a paradox, as the mobility-size relation cannot be established if size itself is not able to be defined. Calculating the cluster ion size by the Stokes-Cunningham-Millikan equations is unjustified, as these ideas do not apply to such small particles. Atomic ions are characterized by continuous coordinate functions, in which the concept of the size does not play any fundamental role. Instead, an acceptable geometric parameter for a cluster ion is the mass diameter d_p , defined as

$$d_p = \sqrt[3]{\frac{6m}{\pi\rho}}, \quad (1)$$

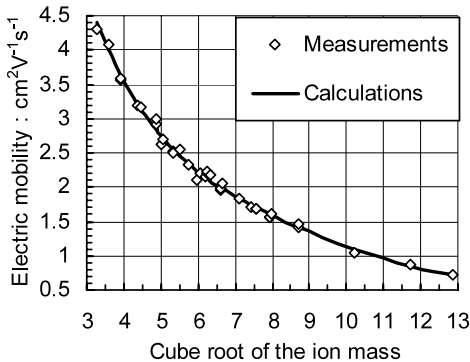
where m is the particle mass and the particle density ρ is considered independent of the particle size. The internal density of the particles will exceed the bulk macroscopic density. An array of packed spheres has a density of 0.52ρ for a simple cubic lattice and 0.74ρ for the closest packing. Uncertainty in the mass diameter arises from uncertainty in the density of the particulate matter, which depends on the bond length within a cluster. The variation in bond lengths is a few percent, which presents a lower boundary on the uncertainty of mass diameter.

In the kinetic theory of particle mobility (Chapman and Cowling 1970; Mason and McDaniel 1988) the concept of size is explicitly used in the $(\infty - 4)$ potential model. This model approximates an ion by a virtual rigid sphere, which attracts gas molecules by the electric polarization force. The mobility is expressed via the collision cross-section. Collision cross-section calculation is complicated by several factors: (1) the effect of inelastic scattering of the gas molecules, (2) the diameter dependence of the virtual rigid sphere on temperature and (3) the effect of van der Waals’ forces. The physics of collisions is rather complicated and the existing knowledge is not sufficient for *ab initio* calculation of cluster ion collision cross-sections. Tammet (1995) proposed a semi-empirical model for cluster ion and nanometre particle mobility, where the transition from the elastic to inelastic scattering was described by the Einstein factor for melting a cluster’s internal degrees of freedom. The model approaches the kinetic theory results in the zero size limit, and the Stokes-Cunningham-Millikan law in the large particle limit. Differences between carrier gases can be considered through the choice of gas viscosity, mass and polarizability. The three parameters of the model were validated by a fit to laboratory measurements (Kilpatrick 1971), as shown in Fig. 1.

A theory of cluster ions and nanometre particle mobility was developed by Li and Wang (2003a, 2003b), and Shandakov et al. (2005). The associated mass-mobility relation was tested by Loscertales (2000) and Fernandez de la Mora et al. (2003). Discrepancies between recent theoretical and experimental results, with values calculated from the semi-empirical model (Tammet 1995) are small. Thus the semi-empirical model is used for the calculations which follow.

In the zero-size limit studied by Langevin (Mason and McDaniel 1988) the ion mobility appears inversely proportional to the gas density. Thus ion mobilities are often reduced to

Fig. 1 Measured (Kilpatrick 1971) and calculated (Tammet 1995) mass-mobility correlation for ions in nitrogen. Calculations are made assuming $p = 1013$ mbar, $T = 473$ K, and ion density = 2.07 g cm^{-3}



standard conditions on this basis, according to the Langevin formula:

$$\mu_{reduced} = \mu_{measured} \frac{273.15 \text{ K}}{T} \frac{p}{101325 \text{ Pa}}. \quad (2)$$

The Langevin theory is only a rough approximation when considering real cluster ions. The mobility can be formally reduced according to (2) for an ion of any size, but the result can differ substantially from the actual mobility of the same ion when measured in standard conditions (Tammet 1998). However, (2) will flatten the dependence of mobility on the gas temperature, pressure and ion diameter. The size-mobility relationships can be trimmed further using the approximate inverse proportionality of mobility to the expression $(d + d_0)^2$, where $d_0 = 0.3 \text{ nm}$ is a good choice for ions in nitrogen or air. The “trim mobility”, which is conventionally defined as

$$\mu_{trim} = \mu \frac{273 \text{ K}}{T} \frac{p}{1013 \text{ mb}} \left(\frac{d}{1 \text{ nm}} + 0.3 \right)^2, \quad (3)$$

equals the actual mobility of typical 0.7 nm cluster ions in standard terrestrial conditions. Figure 2a shows the trim mobility dependence on the ion mass diameter, for three values of the ionic matter density. A typical density for ionic matter of terrestrial atmospheric ions is about 2 g cm^{-3} . The example shows that the density of ionic matter affects the mobility only for cluster ions smaller than 1.6 nm . The mobility of intermediate and large ions depends only on the geometric size and is practically independent of the ionic matter density.

Figure 2b shows that the proportionality of the mobility to temperature, also described in the Langevin model, is only a very rough approximation. According to the Langevin theory, the curves in Fig. 2b should be horizontal lines. Intuitively this suggests that the mobilities of large particles, which can be described by the Stokes-Cunningham-Millikan model, may not follow the temperature proportionality. However, even in case of small cluster ions with diameter 0.5 nm in Fig. 2b, the deviation from horizontal lines is substantial. A final point is that, in accordance with the Langevin theory, mobility should be inversely proportional to gas pressure and therefore the curves in Fig. 2c should be horizontal. The 0.5 nm ions satisfy this condition well, with only small deviation from the inverse proportionality even for 1 nm cluster ions. In conclusion, the Langevin model is more effective in describing the pressure variation of mobility than the temperature variation.

Cluster ions in different carrier gases usually have different chemical compositions and sizes. If it were possible for ions of the same composition and size to exist in different carrier gases then the mobility will be, very roughly, inversely proportional to the square

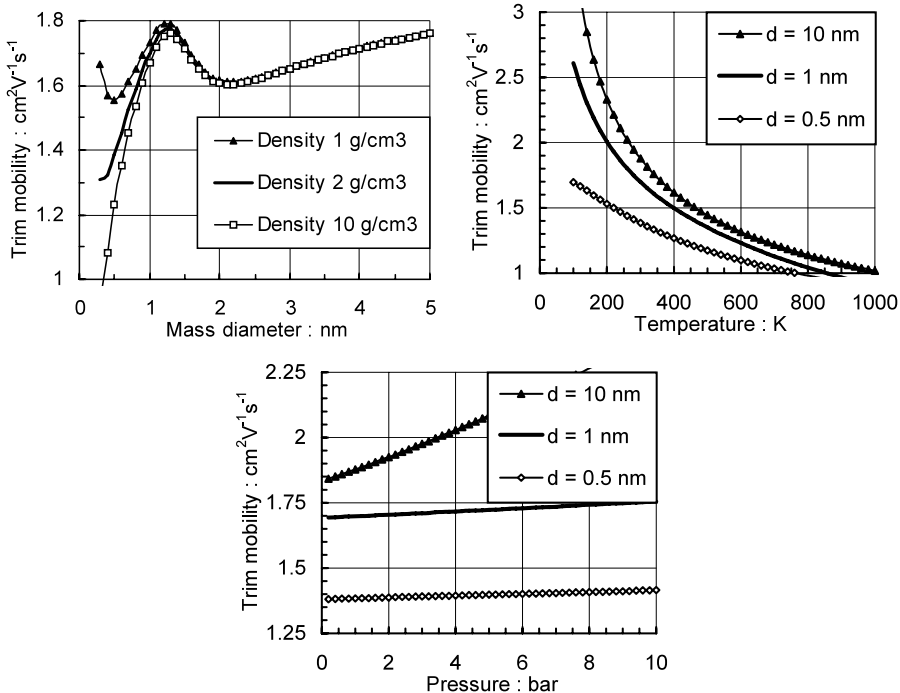
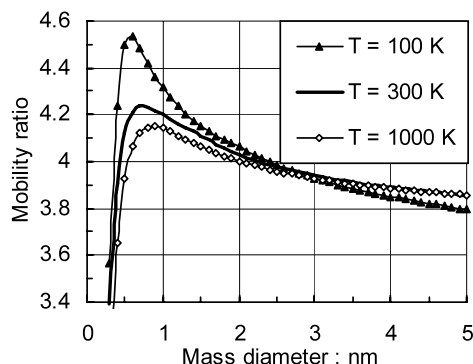


Fig. 2 (a) Trim mobility of ions of three different densities in nitrogen ($p = 1000$ mbar, $T = 300$ K). (b) Trim mobility of ions of three different sizes in nitrogen ($p = 1000$ mbar, density of ionic matter 2 g cm^{-3}). (c) Trim mobility of ions of three different sizes in nitrogen ($T = 300$ K, density of ionic matter 2 g cm^{-3})

Fig. 3 Ratio of ion mobility in H₂ to the mobility of the same ion in N₂ at three different temperatures ($p = 1000$ mbar, density of ionic matter 2 g cm^{-3})



root of the molecular mass of the gas. For example, the ion mobility in hydrogen should be about $\sqrt{14} \approx 3.7$ times greater than in nitrogen. The actual mobility ratio is not far from this value, although it also varies with environmental parameters, see Fig. 3.

4 Ion Balance Equations

The concentration of cluster ions arises from the balance between ion production, and losses from ion-ion mutual recombination and ion-aerosol attachment to background aerosol particles, which occurs in many atmospheres (Tripathi et al. 2008). For positive and negative cluster ion concentrations n_+ and n_- , the bipolar ion balance equations are

$$\begin{aligned}\frac{dn_+}{dt} &= q - \alpha n_- n_+ + s_p^+ n_+, \\ \frac{dn_-}{dt} &= q - \alpha n_+ n_- + s_p^- n_-,\end{aligned}\quad (4)$$

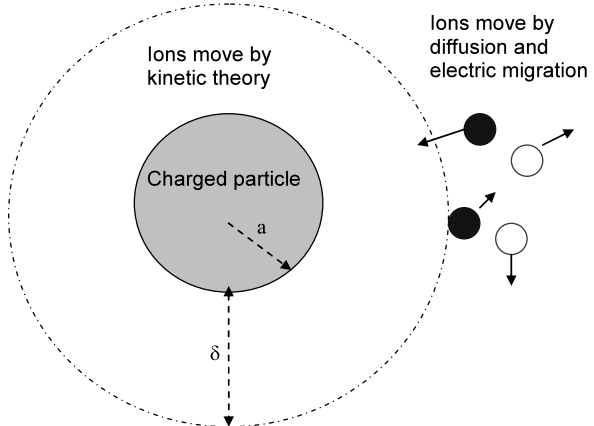
where α is the cluster ion-ion recombination coefficient and s_p is the sink rate of cluster ions to aerosol particles. The cluster ion recombination coefficient α for the terrestrial lower atmosphere is generally in the range of $1.4\text{--}1.6 \times 10^{-12} \text{ m}^3 \text{ s}^{-1}$ (Israël 1970; Hoppel and Frick 1986), close to values calculated from the three-body recombination theory of Thomson (1924). In the simplest case of a clean atmosphere, when ion-ion recombination is the only loss term ($s_p = 0$), $n_+ = n_-$. Measurement of the bipolar ion concentrations therefore provides a test on whether aerosol is present in an atmosphere and if the aerosol is charged.

To consider the ion loss rates in an atmosphere containing aerosol particles, the sink rates s_p need to be evaluated. These coefficients are predicted using an attachment theory, which considers the collection rate of ions by a particle. This can be illustrated by considering the effect on a spherical particle of radius a exposed to a bipolar concentration of ions, see Fig. 4. Ions pass to the particle by diffusion and electric migration, with a net local ion flux I_r given by

$$I_r = D \frac{dn}{dr} + \mu E(r) n(r), \quad (5)$$

where the first term represents diffusive transport (ion diffusivity D) and the second term electrical transport under an electric field E , if no account is taken of the relative polarities of ions and particle. The radial electric field $E(r)$ experienced by an ion at a distance r from

Fig. 4 Motion of ions close to a charged aerosol particle, and the limiting sphere concept



a sphere carrying a total charge je is

$$E(r) = \frac{e}{4\pi\epsilon_0} \left(\frac{j}{r^2} + \frac{2(2r^2 - a^2)e}{r^3(r^2 - a^2)^2} \right), \quad (6)$$

in which the first term arises from the Coulomb potential, and the second term from image charge effects (Jackson 1975). (The elementary charge $e = 1.6 \times 10^{-19}$ C and the permittivity of free space, $\epsilon_0 = 8.85 \times 10^{-12}$ F m⁻¹.) Gunn (1954) neglected image effects, using only the Coulomb force, leading to a particularly simple form for the local ion flux to the particle

$$D \frac{dn}{dr} - \frac{je}{4\pi\epsilon_0 r^2} \mu n(r) = \frac{I}{4\pi r^2 e}, \quad (7)$$

to which an analytical solution can be found using an integrating factor. Up to a small distance δ (of order one ionic mean free path) from the particle, the ions are considered to move by kinetic theory.

Within this *limiting sphere* region, the ion current can be estimated from ion concentrations and thermal speeds as

$$I = 4\pi a^2 e c n(\delta), \quad (8)$$

where c is the mean ion speed. Equating the two ion fluxes at the limiting sphere, Gunn (1954) found analytic attachment coefficient expressions

$$\beta_{\pm 1j}(a) = \frac{je\mu_{\pm}}{\epsilon_0[\pm \exp(\pm 2Lj) \mp 1]}, \quad (9)$$

where $\beta_{\pm 1j}$ is the attachment coefficient for ions (sign ± 1) to a particle carrying j elementary charges, $L = e^2/8\pi\epsilon_0 a k T$, and μ_+ and μ_- are the positive and negative ion mobilities respectively. (In terms of the sink rate s_p , $s_p = \beta Z$.) For the special case of neutral particles, the limiting value is

$$\beta(a) = \frac{4\pi k T \mu_{\pm}}{e} a. \quad (10)$$

Using this relationship for neutral particles, it can be shown that

$$\frac{n_+}{n_-} = \frac{\mu_-}{\mu_+}. \quad (11)$$

Thus if the bipolar ion concentrations have the inverse ratio to the ion mobilities, there is aerosol present which is uncharged. (This condition is equivalent to equal positive and negative air conductivities.) However, this leads to the presence of space charge and a corresponding electric field, which will complicate the problem.

Table 2 presents the ratios between ion concentrations and ion mobilities for the three cases of no aerosol, neutral aerosol and charged aerosol.

In general, charged aerosol consists of particles of different sizes carrying different charges. The charge distributions can be found by detailed balance equations for charge-exchange between ions and particles (e.g. Boisdon and Brock 1970; Yair and Levin 1989; Clement and Harrison 1992).

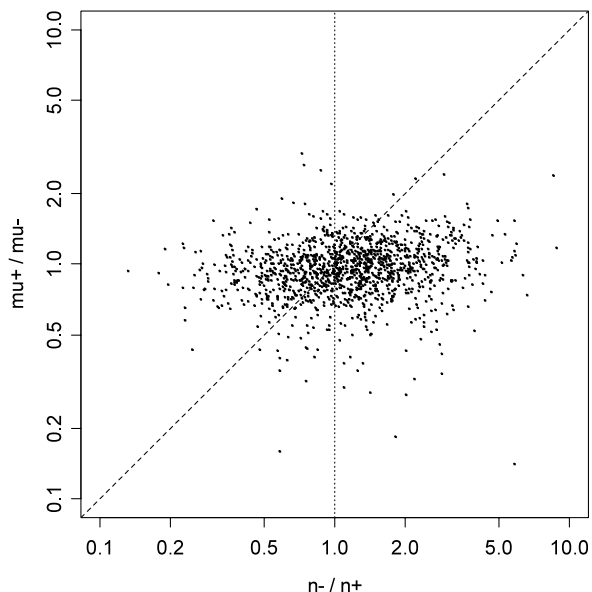
Figure 5 summarises measurements of ion mobility and ion concentration made in urban air at Reading during 2006. The instrument used (Aplin and Harrison 2001) determines both polarities of ion mobility and ion concentration (Harrison and Aplin 2007), which are plotted

Table 2 Ratio of bipolar ion concentrations with different aerosol properties

Aerosol concentration	Electrical state*	Ion concentration ratio
Aerosol-free air		$\frac{n_+}{n_-} = 1$
Aerosol-laden air	Neutral ($j = 0$)	$\frac{n_+}{n_-} = \frac{\mu_-}{\mu_+}$
	Charged ($j \neq 0$)	$\frac{n_+}{n_-} = \frac{\mu_-}{\mu_+} \exp\left(\frac{je^2}{4\pi\epsilon_0akT}\right)$

* j is the mean number of elementary charges carried by each aerosol particle

Fig. 5 Ion mobility ratio and ion concentration ratio determined using a Programmable Ion Mobility Spectrometer instrument (PIMS) at Reading during 2006, obtained on year days 44–61 and 143–180 with a 30 min measurement cycle. The dotted line marks the clean air (no aerosol) case, and the dashed line the uncharged aerosol case



as bipolar ratios. Referring to Table 2, it is clear that data points do not cluster around the zero aerosol case or the neutral aerosol case, but show a spread associated with the presence of charged aerosol. The greater relative variability in n_-/n_+ than μ_+/μ_- illustrates that, in relative terms, ion concentrations vary more than ion compositions.

For smaller aerosol particles the Gunn assumption of no image forces breaks down, and a more sophisticated theory is required (Fuchs 1963; Hoppel and Frick 1986; Jensen and Thomas 1991; Stommel and Riebel 2007). A simple mathematical approximation (Tammet et al. 2006) is

$$\begin{aligned} s_p^+ &= 2\pi \frac{kT}{e} \mu_+ \left((d_p - 1.5 \text{ nm}) - \frac{d_p + 9 \text{ nm}}{d_p + 23 \text{ nm}} q_p d_q \right) Z, \\ s_p^- &= 2\pi \frac{kT}{e} \mu_- \left((d_p - 1.5 \text{ nm}) + \frac{d_p + 9 \text{ nm}}{d_p + 23 \text{ nm}} q_p d_q \right) Z, \end{aligned} \quad (12)$$

where Z and d_p are the concentration and the mean diameter of particles, q_p is the dimensionless algebraic mean charge of aerosol particles expressed in elementary charges, and d_q

is the characteristic length of Coulomb attachment

$$d_q = \frac{e^2}{4\pi\epsilon_0 kT} \approx 1.671 \times 10^4 / (T : \text{K}) \text{ nm.} \quad (13)$$

In the general case of steady-state charging, the derivatives of the ion concentrations become equal to zero and $s_p^+ n_+ = s_p^- n_-$. The solutions for n_+ and n_- are

$$\begin{aligned} n_+ &= \frac{\sqrt{(s_p^-)^2 + 4\frac{s_p^-}{s_p^+}\alpha - s_p^-}}{2\alpha}, \\ n_- &= \frac{\sqrt{(s_p^+)^2 + 4\frac{s_p^+}{s_p^-}\alpha - s_p^+}}{2\alpha}, \end{aligned} \quad (14)$$

although (14) is not an explicit solution of the ion balance problem because the ratio s_p^+/s_p^- weakly depends on the average charge of aerosol particles q_p . This, in turn, depends on the ion concentrations. If charge exchange by electric currents can be neglected, the space charge density $n_+ - n_- + q_p N = 0$ and $q_p = (n_- - n_+)/N$. In this case the ion concentrations can be easily calculated in a rapidly converging iterative process using (14) and starting from the first approximation $q_p = 0$.

5 Conclusion

The properties of cluster ions are influenced by the properties of the atmosphere in which they are formed, both in terms of their composition, which is related to the trace gases present, and their concentration, which primarily depends on the amount of aerosol. Because of the large variability in aerosol concentrations, the concentration of ions varies more than the mobility. In most cases charge exchange between the cluster ions and the aerosol present will cause the aerosol to become charged. The possible role of ions and charged aerosol in cloud formation in planetary atmospheres presents a new frontier in this science area.

Acknowledgement This work was partially supported by the Estonian Science Foundation under Grant No. 6223.

References

- K.L. Aplin, Surv. Geophys. **27**, 63–108 (2006). doi:[10.1007/s10712-005-0642-9](https://doi.org/10.1007/s10712-005-0642-9)
- K.L. Aplin, R.G. Harrison, M.J. Rycroft, Space Sci. Rev. (2008, this issue)
- K.L. Aplin, R.G. Harrison, Rev. Sci. Instrum. **72**(8), 3467–3469 (2001)
- K.L. Aplin, R.A. McPheat, J. Atmos. Sol.-Terr. Phys. **67**(8–9), 775–783 (2005). doi:[10.1016/j.jastp.2005.01.007](https://doi.org/10.1016/j.jastp.2005.01.007)
- F. Arnold, Space Sci. Rev. (2008), this volume
- E.L.O. Bakes, C.P. McKay, C. Bauschlicher, Icarus **157**, 464–475 (2002)
- G.A. Bazilevskaya, I.G. Usoskin, E.O. Flückiger et al., Space Sci. Rev. (2008, this issue)
- G. Beig, G.P. Brasseur, J. Geophys. Res. **105**, 22671–22684 (2000)
- Y. Boisdran, J.R. Brock, Atmos. Environ. **4**, 35–50 (1970)
- W.J. Borucki, R.C. Whitten, E.L.O. Bakes et al., Icarus **181**, 527–544 (2006)
- W.J. Borucki, R.C. Whitten, Planet. Space Sci. **56**, 19–26 (2008)

- S. Chapman, T.G. Cowling, *The Mathematical Theory of Non-uniform Gases* (Cambridge University Press, Cambridge, 1970)
- C.F. Clement, R.G. Harrison, J. Aerosol Sci. **23**(5), 481–504 (1992)
- J. Curtius, E.R. Lovejoy, K.D. Froyd, Space Sci. Rev. **125**, 159–167 (2006). doi:[10.1007/s11214-006-9054-5](https://doi.org/10.1007/s11214-006-9054-5)
- G.A. Eiceman, Z. Karpas, *Ion Mobility Spectrometry* (CRC Press, Boca Raton, 1994)
- G.A. Eiceman, E.G. Nazarov, J.E. Rodriguez, Rev. Sci. Instrum. **72**, 3610–3621 (2001). DOI: [10.1063/1.1392339](https://doi.org/10.1063/1.1392339)
- A. Engel, *Ionized Gases*, 2nd edn. (Clarendon, Oxford, 1965)
- J. Fernandez de la Mora, L. de Juan, K. Liedke et al., J. Aerosol Sci. **34**, 79–98 (2003)
- N. Fuchs, Geofis. Pura Appl. **56**, 185–193 (1963)
- R. Gunn, J. Meteorol. **11**, 339–347 (1954)
- R.G. Harrison, K.L. Aplin, Atmos. Res. **85**, 199–208 (2007). doi:[10.1016/j.atmosres.2006.12.006](https://doi.org/10.1016/j.atmosres.2006.12.006)
- R.G. Harrison, K.S. Carslaw, Rev. Geophys. **41**(3), 1012 (2003). doi:[10.1029/2002RG000114](https://doi.org/10.1029/2002RG000114)
- A. Hirsikko, J. Paatero, J. Hatakka et al., Boreal Environ. Res. **12**, 265–278 (2007)
- W.A. Hoppel, G.M. Frick, Aerosol Sci. Technol. **5**, 1–21 (1986)
- U. Hörrak, *Air ion mobility spectrum at a rural area*. Doct. thesis, Dissertationes Geophysicales Universitatis Tartuensis, Tartu Univ. Press, Tartu (2001)
- U. Hörrak, J. Salm, H. Tammet, J. Geophys. Res. D **105**, 9291–9302 (2000)
- H. Israël, *Atmospheric Electricity*, vol. I (Israel Program for Sci. Transl. & NSF, Jerusalem, 1970)
- J.D. Jackson, *Classical Electrodynamics*, 2nd edn. (Wiley, New York, 1975)
- E.J. Jensen, G.E. Thomas, J. Geophys. Res. D **96**(10), 18,603–18,615 (1991)
- V. Kanawade, S.N. Tripathi, J. Geophys. Res. D **111**, 02209 (2006). doi:[10.1029/2005JD006366](https://doi.org/10.1029/2005JD006366)
- J. Kazil, R.G. Harrison, E.R. Lovejoy, Space Sci. Rev. (2008, this issue)
- W.D. Kilpatrick, in *Proc. Ann. Conf. Mass Spectrosc. 19th.* (1971), pp. 320–325
- M. Kulmala, Science **302**, 1000–1001 (2003)
- G. Molina-Cuberos, J.J. Lopez-Moreno, F. Arnold, Space Sci. Rev. (2008, this issue). doi:[10.1007/s11214-008-9340-5](https://doi.org/10.1007/s11214-008-9340-5)
- Z. Li, H. Wang, Phys. Rev. E **68**, 061206 (2003a)
- Z. Li, H. Wang, Phys. Rev. E **68**, 061207 (2003b)
- I.G. Loscertales, J. Aerosol Sci. **31**, 923–932 (2000)
- A. Luts, J. Salm, J. Geophys. Res. **99**, 10781–10785 (2004)
- E.A. Mason, E.W. McDaniel, *Transport Properties of Ions in Gases* (Wiley, New York, 1988)
- A. Mirme, E. Tamm, G. Mordas et al., Boreal Environ. Res. **12**, 247–264 (2007)
- K. Nagaraja, B.S.N. Prasad, N. Srinivasa et al., J. Atmos. Sol.-Terr. Phys. **68**, 757–768 (2006). doi:[10.1016/j.jastp.2005.12.005](https://doi.org/10.1016/j.jastp.2005.12.005)
- K. Nagaraja, B.S.N. Prasad, M.S. Madhava et al., Radiat. Meas. **36**, 413–417 (2003)
- T.-E. Parts, A. Luts, Atmos. Environ. **38**, 1283–1289 (2004)
- S.D. Shandakov, G. Nasibulin, E.I. Kauppinen, J. Aerosol Sci. **36**, 1125–1143 (2005). doi:[10.1016/j.jaerosci.2005.01.003](https://doi.org/10.1016/j.jaerosci.2005.01.003)
- Y.G. Stommel, U. Riebel, Aerosol Sci. Technol. **41**, 840–847 (2007)
- H. Tammet, J. Aerosol Sci. **26**, 459–475 (1995)
- H. Tammet, J. Geophys. Res. D **103**, 13933–13937 (1998)
- H. Tammet, Atmos. Res. **82**, 523–535 (2006). doi:[10.1016/j.atmosres.2006.02.009](https://doi.org/10.1016/j.atmosres.2006.02.009)
- H. Tammet, U. Hörrak, L. Laakso et al., Atmos. Chem. Phys. **6**, 3377–3390 (2006)
- J.J. Thomson, Philos. Mag. **47**, 337–378 (1924)
- S.N. Tripathi, M. Michael, R.G. Harrison, Space Sci. Rev. (2008, this issue)
- A.A. Viggiani, Mass Spectrom. Rev. **12**(2), 115–137 (1993). doi:[10.1002/mas.1280120203](https://doi.org/10.1002/mas.1280120203)
- J. Willett, J. Geophys. Res. D **90**, 5901–5908 (1985)
- Y. Yair, Z. Levin, J. Geophys. Res. D **94**, 13,085–13,091 (1989)
- F. Yu, Atmos. Chem. Phys. **6**, 5193–5211 (2006)

Charge Generation and Separation Processes

Y. Yair

Originally published in the journal Space Science Reviews, Volume 137, Nos 1–4.
DOI: [10.1007/s11214-008-9348-x](https://doi.org/10.1007/s11214-008-9348-x) © Springer Science+Business Media B.V. 2008

Abstract This paper presents a short overview of our current understanding of the generation of charged particles in different environments and circumstances (e.g. thunderclouds, dust storms, volcanic plumes, rings, and planetary surfaces) and the subsequent spatial separation that leads to the formation of electrical fields. Different mechanisms are involved on various scales, starting from the molecular level, through the single particle (droplet, crystal, solid) and finally the entraining volume (cloud, plume etc.). Encapsulated within a dynamic and turbulent medium, particles need to come into contact and to immediately separate, to be later transported away from each other. In order to explain the observed electrical fields and ensuing lightning or other forms of discharge, these processes need to be extremely effective. The section will briefly review laboratory results and modeling efforts of charge separation and electric field build-up in various planetary settings, and cite the appropriate observations of electrical activity on different planets.

Keywords Lightning · Inductive charging · Non-inductive charging · Graupel · Electric field · Polarization · Breakdown electric field · Cloud · Ice · Liquid water drops · Deposition · Sublimation · Freezing · Triboelectricity · Fracto-emission · Planetary rings · Dust · Dust devil · Photoelectric charging · Numerical models

1 Charging of Thunderstorm

Thunderstorm evolution and the occurrence of lightning are a familiar and clear manifestation of processes that generate, separate and eventually neutralize electrical charges in nature. The numerous processes operating synergistically within the tumultuous environment of a mature convective cloud have been studied for more than a century, and thousands of research papers were published on this topic alone. For the interested reader we recommend the detailed summaries published as chapters in the books by MacGorman and Rust (1998), Pruppacher and Klett (2003), Rakov and Uman (2003) and Jayaratne (2003), and Saunders

Y. Yair (✉)

Department of Life and Natural Sciences, Open University of Israel, Ra'anana 43107, Israel
e-mail: yoavya@openu.ac.il

(2008) and Stolzenburg and Marshall (2008) in this issue. Clearly, there is no single process that is solely responsible for cloud electrification, but rather we expect a co-operation of numerous processes with varying effectiveness and time-dependent dominance.

In the context of planetary lightning, we implicitly assume that identical or analogous processes to those thought to be important in terrestrial thunderclouds are taking place in the clouds of other planets. Even though the composition and dynamics of thunderstorms in other planetary atmospheres may differ substantially from the clouds of our home planet, it is highly likely that the generation of electric fields, which lead to breakdown and to lightning with its associated phenomena (TLEs—Transient Luminous Events (namely, sprites, elves and jets), chemical processes), involves the interaction between large (e.g. precipitation size) particles. Based on our current understanding of condensation processes in planetary atmospheres (Weidenschilling and Lewis 1973; Atreya 1986) one of the most abundant condensable substances in the solar system is water, and hence we shall briefly review the main charge generation processes that are involved in the electrification of H_2O clouds.

In order to evaluate the relative importance of various charging mechanisms and to quantify the amount and polarity of charges carried by the interacting particles, laboratory experiments that closely replicate the conditions prevailing within the charged medium are essential. Few research groups have endeavored to address this complicated issue and those that deal with water clouds are described in detail in the chapter by Saunders (2008) in this issue. Such experiments show that during freezing, melting, evaporation and deposition, the intricate dynamic interplay between the environmental conditions (temperature and vapor fields) and the properties of the particles (size, shape, fall velocity) leads to different charging regimes which are independent of any pre-existing external field.

1.1 Inductive Charging

Inductive charging refers to processes that are induced by the presence of an existing electrical field. There is little knowledge of the existence and properties of electric fields below the ionospheres and within the deep atmospheres of other planets in the solar system. No spacecraft measurements, from entry probes (in Venus, Jupiter and Saturn) or from landers (Venus and Mars), have supplied quantitative and reliable data yet. Such knowledge is essential if one wishes to evaluate the importance of processes whose efficiency is critically dependent on the strength and orientation of an external field. The pre-existence of a global background electric field (usually referred to as “fair weather” field, see the chapter by Aplin et al. 2008 in this issue) ensures that the water particles suspended in the atmosphere will become polarized. In a vertical, downward directed field (conventionally defined to be negative), such polarization will cause an excess of positive charge to accumulate in the lower part of the particle, while negative charge will be preferably located in the upper part. Of course, in other planetary atmospheres, the ambient electric field may be tilted or reversed compared to the one existing on Earth, but this fact merely complicates the geometry of the polarization of cloud particles. Any polarized configuration can lead, due to the occurrence of various processes, to the creation of oppositely and unequally charged parts of the original particle, that can be later separated and carried away from each other by cloud dynamics.

The present consensus in the literature judges inductive processes to have little importance in the early stages of cloud electrification and to be of secondary importance in later stages, when the intensity of the in-cloud electric field becomes much stronger than the fair-weather field. The following quote succinctly summarizes our understanding: “*The inductive mechanism is attractive because it is simple but in view of the difficulties it is hard*

to imagine how it may operate as a viable charge generation mechanism in thunderstorms” (Jayaratne 2003). That being said, there is recently a renewed interest in the inductive mechanisms, as being able to explain the formation of the lower center of positive charge found in maturing thunderstorms. Inductive charging is believed to play a role in charging the stratiform region of mesoscale convective systems, where vertical motions and particle interactions are subdued.

Clearly the importance of inductive processes may be different in other planetary clouds, though it is hard to evaluate this qualitatively. For example, if liquid drops contain high concentrations of solute (in the water-sulfuric acid system in Venus), or if ice particles are highly conductive (in the ammonia-water clathrates in Jupiter), the effectiveness of inductive charging by rebound collisions may prove to be significant to the electrification of clouds on those planets.

1.2 Non-inductive Charging

Contrary to field-dependent processes, the term “non-inductive” refers to those charging processes which are independent of the presence of an external electric field, and whose efficiency is not impacted by its strength. In the context of thunderstorm charging, the basic description of this process calls for rebound collisions between graupel and cloud-ice particles and the selective transfer of a distinct polarity to the larger particle. In ordinary thunderclouds, the smaller ice crystals are charged positively and then carried to the upper regions, while the larger graupel particles charge negatively and descend relative to the smaller particles. Thus, the charge transfers during encounters of ice crystals and graupel pellets in the prevalent conditions of temperature, liquid water content and mixing in thunderstorms will lead to the normal polarity (positive-over-negative charge) usually found in observations of terrestrial clouds. A variant of these conditions may eventually lead to a reversed polarity. Measurements of the charge transfer during collisions of vapor-grown ice crystals and a riming (graupel) target were reported by Takahashi (1984), Jayaratne (1993), Saunders et al. (1991), Caranti et al. (1991), Brooks et al. (1997), Pereyra et al. (2000), Berdeklis and List (2001) and by many others, with different results, some of which can be attributed to differences in the experimental set-up and/or the choice of variables used (e.g. liquid water content (LWC) vs. effective water content (EW)). A detailed discussion of the various results is beyond the scope of this introductory chapter and they are thoroughly described in the following section by Saunders (2008).

The detailed physical basis for the non-inductive collisional process is still open to speculation. A phenomenological hypothesis involving the growth conditions of the interacting ice particles in mixed phase conditions, states that the more rapidly growing of the two colliding particles charges positively. In this context, sublimation (induced by warming in the riming process) is a state of negative growth. A microscopic description of the collisional encounter between graupel and ice was suggested by Baker and Dash (1994), who stated that ice in equilibrium with vapor has a disordered quasi-liquid layer at the ice-vapor interface. The exact nature of the growth rate of the impacting particles at the point of contact determines the direction of mass transfer between their quasi-liquid layers. This exchanged mass carries with it charge from the upper part of the electrical double layer and thus determines the polarity of the charge transfer between the particles. The particle with the higher temperature (and thicker quasi-liquid layer) would lose mass and negative charge to the colder (with a thinner quasi-liquid layer) particle, thereby leaving the warmer particle positively charged. Thus, the faster growing particles (by vapor transfer) acquire positive charge (Williams et al. 1991). The full description of the non-inductive process requires the accurate characterization of particle surfaces, collisions and ambient conditions where ice and graupel interact.

Any change in the ambient conditions may flip the polarity of charging, making an accurate prediction of the sign carried by each particle very difficult.

2 Charging Process of Solid Particles

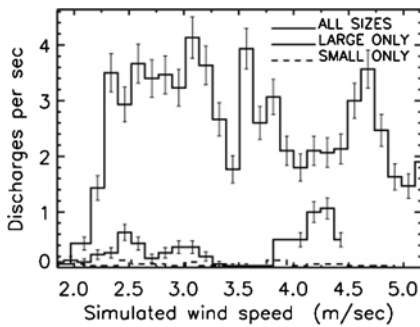
2.1 Triboelectric Charging

The oldest known process by which solid particles can charge is by frictional contact, commonly named triboelectric charging (from the word *tribos* in Greek, to rub). There is still no complete theory that fully explains the microphysics of triboelectric charging. A *tribo-electric series* is often used to express the strength and polarity by which a certain material would charge upon rubbing. This list was conceived in the early experiments by the French physicist Du Fay who in 1773 determined the relative intensity by which certain materials attract or repel others after rubbing. The triboelectric series can be interpreted as the tendency of any substance to lose surface electrons and become positively charged through the mechanical friction by another substance. The triboelectric charging process involves a transient contact between the surfaces of two materials, and the amount of induced charge on each of the surfaces as they separate depends on such factors as chemical composition, conductivity, surface properties and morphology.

Dust or ash particles that come into contact with other suspended particles, or that rub against a solid planetary surface will be charged electrically. Upon separation, the triboelectric accumulation of charges on their solid surfaces leads to an electric field and can cause sparks and corona discharges, depending on the amount of charge and the properties and pressure of the atmospheric gas. One dominant factor which controls the effectiveness of triboelectric charging is the contact time between the colliding particles (or the particle and the surface), determined by such factors as the surface roughness and impact geometry. The bigger the surface contact, the greater is the net charge that is induced on the two surfaces after separation. Rough surfaces—for example, a planetary rocky surface—reduce the surface contact area and thus decrease the amount of charge. Polished and clean surfaces offer a better contact, a larger contact area and hence would better support triboelectric charging. An intrinsic property of the materials involved in the processes is the surface work function, a measure of the ability of the substance to retain the free electrons (occupying the outermost orbits) of its atoms closest to the interface. Substances with a low work function are more likely to lose electrons and acquire net positive charge. Qualitatively we can say that materials with high values of the work function will acquire electrons from materials with lower work functions, but this of course depends on the intricate details of the contact between them.

Recent studies have focused on the fact that triboelectric charging occurs in granular insulating systems even when the colliding particles have identical composition. In such scenarios smaller particles tend to charge negatively and larger ones positively. Lacks and Levandovsky (2007) conducted numerical simulations of the charge transfer between colliding solid particles made of identical (insulating) materials. The results are explained by the presence of trapped electrons in high-energy states which are released and transferred to a particle with no high-energy electrons. When the simulation was ran with a perfectly unimodal size distribution, triboelectric charging did not occur, but it was much more pronounced for a polydispersed size distribution. This result in line with wind-tunnel experiments by Krauss et al. (2003) and Zheng et al. (2003) that showed substantially greater triboelectric charging for broad size distributions of dust and sand (Fig. 1). Kok and Renno

Fig. 1 Discharge rate in the horizontal-mixing set-up in the laboratory experiments of Krauss et al. (2003), as a function of wind speed for three particle-size distributions, with ambient pressure of 8 Torr in a simulated Martian atmosphere. A clear increase in the number of discharges occurs for a mixture of particle sizes. Used with permission



(2008) used a numerical sand-saltation model that includes the effects of electrification due to triboelectric charging and showed that sand electrification increases the particle concentration at a given wind shear velocity and better match observations of sand trajectories.

In the context of planetary electrical phenomena, triboelectric charging will be important in scenarios involving large amounts of solid particles suspended and colliding with each other within an atmospheric medium or in vacuum, or impacting the surface of a solid planetary body. Such scenarios include dust storms on Earth and on the surface of Mars (see chapter by Renno and Kok 2008 in this issue) and volcanic plumes on Earth and on Jupiter's moon Io, the icy volcanoes on Saturn's moons Enceladus, Tethys and Dione, and on Neptune's moon Triton (see chapter by James et al. 2008, in this issue). The saltation of sand particles due to wind near the surface will induce numerous impacts of the dust with the solid layer below, and lead to triboelectric charging of the surface. Laboratory work on Martian and Lunar soil simulants showed that the average contact charge varies linearly with the work function of the contacting surface (Sternovski et al. 2002). Charging of dust devils and the surface can lead to discharge events due to the low pressure on Mars, supporting sparks and corona (Farell et al. 1999a, 1999b; Farrell and Desch 2001).

In order to quantitatively assess the intensity of various charging processes and their impacts on the electrical properties of dust storms and lofted dust, Sickafoose et al. (2000, 2001), Sternovski et al. (2002) and Krauss et al. (2003) conducted a series of laboratory experiments. These teams developed an experimental setup that was used to simulate various charging regimes, involving simulated Martian and lunar regoliths (Sternovski et al. 2002) and other materials like copper, zinc graphite and glass (Sickafoose et al. 2000). The dust particles were falling off a thin metal disk with a small central hole that was agitated by an electromagnet. A Faraday cup was attached to a sensitive electrometer and the height of the output pulse indicated the charge on the grain. In one set of experiments, dust particles were impinged on various surfaces in the form of thin discs laid horizontally inside a vacuum chamber. These surfaces were made of materials with known work functions (metals: Co, Ni, Au, Pt, and silica glass). It was found that the charge on a 100 micron dust grain was usually larger than 10^5 elementary charges and it varied linearly with dust size. The effective work functions of the planetary analogs were extrapolated to be 5.8 eV for the lunar and 5.6 eV for the Martian dust regoliths.

2.2 Charging by Fracto-Emission

A sub-class of triboelectric charging is the emission of electrons from freshly exposed cracks, fractures and fissures in a solid particle surface. This process is known as fracto-emission and it includes the emission of photons and other particles due to the fracture of

materials. There is a great variety in the rates and species of the emitted particles, and laboratory experiments are conducted in order to evaluate the characteristic intensity and time evolution of photon emission (phE), electron emission (EE), positive ion emission (PIE), and neutral emission (NE) due to the fracturing processes. In natural settings, fractoemission charging should be important in volcanic plumes (Gilbert et al. 1991; James et al. 2000; Mather and Harrison 2006), where huge amounts of particles collide, explode and break apart. Charging of volcanic pumice fragments was studied in laboratory experiments by James et al. (2000), where small silicate particles were produced by collisions between two samples cut from pumice and their charge was measured. They deduced that the electrification of volcanic plumes results from brittle fragmentation of magma or pumice clasts within the upper regions of the conduit and in the jet region of the plume. A complete description is given in another chapter in this issue by James et al. (2008). A unique setting for charging may occur in the Martian polar regions where sand and ice particles collide frequently, especially during dust storms occurring in the seasonal thawing-freezing cycle onset. It was already demonstrated by Jayaratne (1991) that non-sublimating ice particles are charged positively by impacts of sand grains. The charge is transferred from the ice surface to the dust grains, which carry a net negative charge. This process may complement the triboelectric charging that would be dominant in drier regions.

2.3 Photoelectric Charging

In photoelectric charging, incident energetic radiation leads to the release of free electrons from the outermost layer of a solid particle or surface. Atmospheric aerosol particles are known to accumulate positive electric charge as a result of the photoemission of electrons. Under the influence of external irradiation, solid particles with a photoelectric work function below the photon energy will emit electrons and thus remain positively charged. The effect of strong UV radiation on the charging of suspended dust particles will be most pronounced in vacuum, where no atmospheric absorption diminishes the intensity of the UV component of the solar spectrum. It was suggested that particle lifting on the lunar surface is a result of photoelectric charging of the dust by solar UV (Horányi et al. 1998). Sickafoose et al. (2000) investigated photoelectric charging of dust particles by their own photoemission current and by photoemission from an adjacent surface by illuminating the dropped dust particles with a high intensity UV source. The results indicate that isolated grains reach a positive-equilibrium floating potential, dependent upon the work function of the particle, which causes the emitted electrons to be returned. Dust grains dropped past a photo-emitting surface reach a negative floating potential for which the sum of the emitted and collected currents is zero. The organic haze in Titan's atmosphere is also susceptible to photoelectric charging, even though the composition of the particles is carbon-based. The day-night variation in photoelectric charging leads to changes in the aerosol and macromolecule charge distribution, which can in turn influence coagulation rates. Consequently, electrical processes on a molecular scale can have seasonal, global effects on the albedo of Titan (Bakes et al. 2002).

Another environment where photoelectric charging is important is found in planetary rings, where enormous amounts of tiny particles are exposed to direct sunlight. In another chapter of this issue, Graps et al. (2008) review various charging processes operating in the rings of Saturn, Jupiter and Uranus. The particles in these rings are a mixture of ice and rocky minerals, with large variations in their physical properties. Charging causes dust particles to respond to electric and magnetic forces and plays a role in electric field generation. In Saturn's E-ring, charged dust is assumed to be levitated above the plane of the rings to form

“spokes”, which may have long-term effects on angular momentum transport in those rings (Hartquist et al. 2003) (a different mechanism was recently suggested by Jones et al. (2006) who contend that the source of the spokes is lightning-induced electron beams hitting the rings).

2.4 Effect of Chemical Composition

The presence of soluble ionic substances in the liquid and ice phases has a significant effect on the charging process, and since nature seldom presents pure materials, these effects will significantly alter the outcomes of particle interaction and charging processes. In the laboratory experiments reported by Jayaratne (1999), a rime ice target made of pure ice with various concentrations of different soluble compounds was hit by ice crystals and sand particles. When the target ice contained NaCl in concentrations as low as 10^{-5} N, the ice charged negatively at all temperatures, and the magnitude of the charging increased with increasing concentration and decreasing temperature. The picture became more complicated for different ammonium salts such as NH₄OH and (NH₄)₂SO₄. The target ice acquired positive charge with its magnitude increasing as the temperature was decreased. These observations are best explained by difference in ion mobilities in liquid water and ice, that account for a depletion of Cl⁻ ions in the liquid, leading to a surplus of Na⁺ ions in the quasi-liquid layer (see Sect. 1.2 above), which will be ejected upon collision. This will leave the graupel negatively charged. The opposite is true for NH₄⁺ ions. The effect of impurities of NH₃, HF and HCl were explained by Nelson and Baker (2003) in terms of molecular dissociation and release of ions from the ice lattice to the surface.

Different chemical compositions of CCNs are expected in different planetary settings: halogen, ammonium and sulfur compounds will undoubtedly comprise CCN and IN within the giant planets’ atmospheres (West et al. 1986). In Venus, we can expect sulfur-rich particles to exist in the cloud-forming regions. Such chemical compositions will undoubtedly affect the charging process and the final charge structure of the clouds, and the locations of the major charge centers which dictate the locations of lightning discharges in these atmospheres. Clearly, experimental data on the charge separation efficiency in these compounds is essential for any attempt to model and simulate lightning generation in planetary atmospheres.

3 Numerical Models

3.1 Terrestrial Thunderstorm Models

Computer models of thunderstorm electrification are used for studying the dynamical and microphysical evolution of the different fields as the cloud grows, matures and decays. These models usually rely on parameterizations of the charge separation mechanisms, in order to compute the charge distribution on various particles and the resultant electric field. Sophisticated formulations of the lightning process, including branching and neutralization of charge centers, are crucial for any realistic depiction of the electrical behavior of the storm. As numerical experiments are becoming more accurate and move from single cloud to multi-cell simulations they can be compared with observational data, thus offering a sensitive tool for assessing the relative importance of charge separation processes in different parts of the cloud life cycle. There was a considerable progress in the past 10 years in this field and we shall briefly review important contributions which possess a potential for addressing the existing uncertainties reviewed in Sect. 1.2.

Scavuzzo et al. (1998) used a three dimensional thundercloud model in order to evaluate the different formulations of the charging regimes in the non-inductive process (e.g. Takahashi 1984, henceforth T78 vs. Keith and Saunders 1990 and Saunders et al. 1991, henceforth S91). In this model, the cloud fields are simulated separately from the electrical aspects and are used as a background against which different parameterizations are tested. The model deals with an idealized, isolated, almost symmetric mature cloud and thus cannot be compared to any real measurements, and its predictions are tested against the “ordinary” thunderstorm defined by Williams (1995). Their results showed that the non-inductive mechanism can by itself produce high electric fields in times comparable to what is observed in nature. The tripolar charge structure and the charge magnitudes are better reproduced by the T78 formulation although it over-estimates the extent of the lower positive charge center. The T91 formulation resulted in an inverted polarity where negative charge overlies a lower positive center, without an upper positive center but it leads to a better structure in the lateral parts of the cloud. The difference was attributed to the different predictions of positive charging at low LWC. Consistent results showing similar differences between the T78 and S91 schemes were also obtained by Helsdon et al. (2001) using a 2D cloud model to study a Montana thunderstorm and by Altaratz et al. (2005) who used a 3D mesoscale model to study Mediterranean winter thunderstorms. Both these models calculated the electric field development until the first lightning flash and thus testified to the importance of the non-inductive process on its own in the initial stages of cloud evolution.

Significant progress in simulating the propagation of the lightning channel within a numerical thundercloud model was achieved by Mansell et al. (2002). They simulated various types of lightning, including positive cloud-to-ground, negative cloud-to-ground and intracloud flashes. The propagation of the lightning channel is done by using a step-by-step stochastic bi-directional dielectric breakdown discharging process, where the probability of the direction of the lightning channel in each grid point is determined by the local net electric field. The results for negative cloud-to-ground flashes show that the existence of a lower positive charge center below the main negative charge center is essential for the generation and propagation of this type of flash. Mansell et al. (2005) used a sophisticated 3D dynamic cloud model, with a multi category single-moment bulk microphysical scheme to simulate a multicell storm. The model was also used to evaluate five different formulations of the non-inductive process. These included the TAK scheme (a modified T78 formulation based on Takahashi 1984; see Fig. 2 below), the S91 scheme, the RR (Riming Rate) scheme which is a modification of the S91 formulation using the rime-accretion-rate instead of the LWC in the charge separation efficiency matrix, the Gardiner/Ziegler (GZ) scheme (based on the experiments of Jayarante et al. 1983) and the SP98 scheme (based on the experiments of Saunders and Peck 1998). The electrical part also included inductive charging parameterization and charging by ions, as well as a lightning discharge parameterization. Results showed that the TAK, GZ and S91 schemes all produced normal-polarity storms with negative cloud-to-ground flashes. The RR and SP98 formulations gave an inverted dipole structure. Mansell et al. (2005) indicate that the inductive charging process based on graupel-droplet rebound collisions may have a secondary yet possibly important role in cloud electrification and note that other inductive processes not included in this model version (such as charging during melting and break-up) can be important as well. Similar indications to the importance of inductive charging processes in the stratiform region of storms was reported recently by Barthe and Pinty (2007), who employed a 3D mesoscale model to study the electrical development of several convective storms.

Although 3D models enable comparisons with real-world thunderstorms data, simpler 1D models can still be used as exploratory tools to assess various aspects of thunderstorm

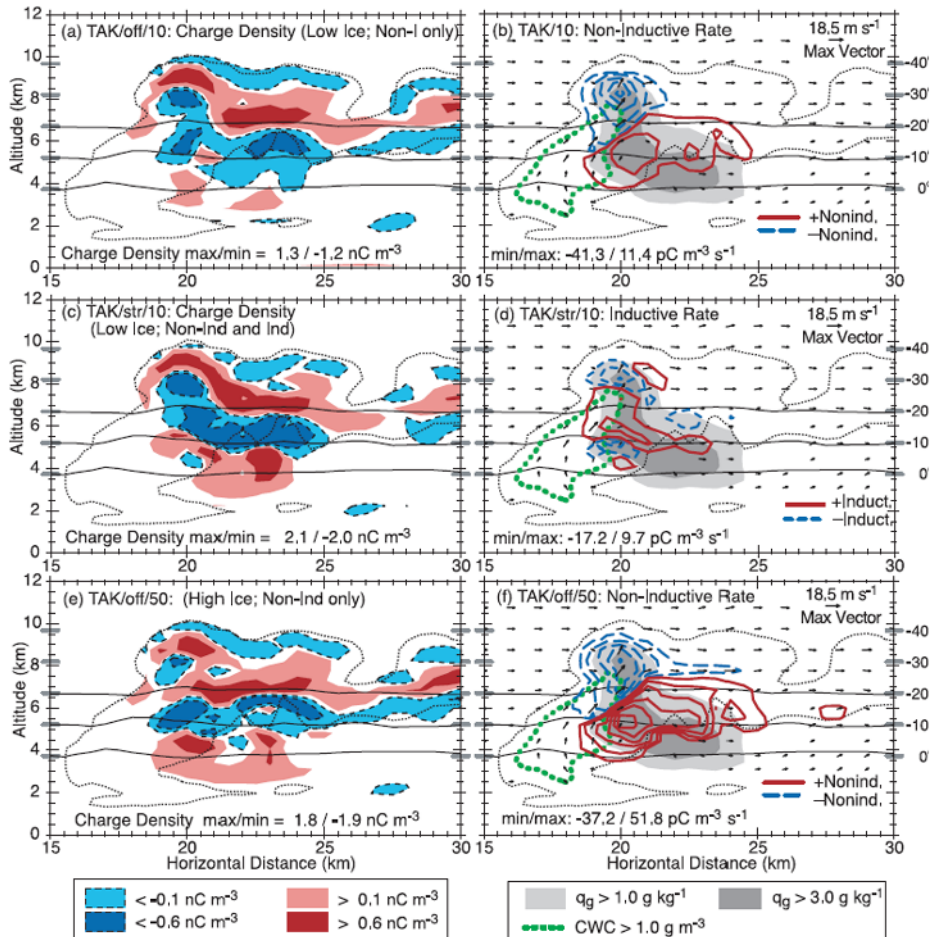


Fig. 2 The charge structure (left) and charge separation rates (right) at 52 min in a model run by Mansell et al. (2005), with the TAK (Takahashi 1984) non-inductive charging scheme. Cloud boundary (thin dotted line) and isotherms are drawn. The blue colors indicate negative charge and the red shades indicate positive charge. Shaded grey areas depict the total graupel mixing ratio in g kg^{-1} . “Non-Ind” and “Ind” refer to the inductive and non-inductive processes, and the str/off/10/50 annotations refer to specific model runs, detailed in Fig. 2 of that paper. Used with permission

electrification. For example, Mitzeva et al. (2006a) modeled convective cloud development in order to address the marked differences observed in lightning activity within maritime and continental thunderstorms. The parameterization of non-inductive charge separation was based on laboratory data of Brooks et al. (1997). The results suggest that increased fallout of precipitation in maritime clouds lowers the efficiency of charge separation and the total cloud charge. The same 1D model was used to evaluate charging regimes in areas completely devoid of liquid water droplets (namely, no riming), where the temperature is below -40°C (Mitzeva et al. 2006b). The results show that in such conditions, even though the amount of charge separated per collision is small, it may still influence the charge distribution by carrying positive charges to the uppermost parts of the cloud.

3.2 Planetary Cloud and Lightning Models

Our knowledge of the ambient conditions in the deep atmospheres of the planets, where thunderstorms are believed to occur, is insufficient and partial. Thus, it is almost impossible to adapt the detailed and extensive models used for terrestrial clouds in other planetary atmospheres unless a significant amount of free parameters are assumed. Rather, it seems more beneficial to utilize simpler models in order to evaluate basic features such as cloud life-times, mass loading and spatial dimensions. Few modeling attempts have been presented thus far. The early 1D parcel model of Stoker (1986) was used to simulate the formation of the Jovian equatorial plumes. Del-Genio and McGratten (1990) used the GISS GCM model to study Jovian convective cloud generation. A 2D axi-symmetric cloud model with detailed bin-microphysics was developed by Yair et al. (1995a, 1995b, 1998) to study lightning generation in Jupiter. It was later complemented by the 1D model of Gibbard et al. (1995). The deep H₂O clouds in Jupiter's atmosphere were shown to be the most suitable candidate for lightning generation, based on non-inductive processes equivalent to those operating in terrestrial clouds. Studying a different convective cloud Tokano et al. (2001) used a 1D time-dependent thundercloud model of Titan's methane clouds, simulating the formation of the cloud and hydrometeors including charging and several transport effects. They showed that collisional charging mechanisms in methane are probably ineffective, and suggest that sufficient charging is caused by electron attachment to cloud particles. The buildup of the mono-polar (negative) electric field is rapid and leads to breakdown of the nitrogen atmosphere, culminating in a 20-km long lightning flash. The abovementioned models are all good examples for utilizing terrestrial models in alien conditions. They should be further employed to explore the circumstances for lightning generation in Saturn, Uranus and Neptune.

Another class of models was developed to specifically address the question of lightning initiation and properties in Hydrogen-Helium atmospheres. The unique differences between the terrestrial case and the Jovian planets were discussed by Farrell et al. (1999b) and most recently by Dwyer et al. (2006). Farrell et al. (1999b) presented a discharge, radiation and propagation model from a Jovian flash. They show that HF (High Frequency) emissions from a slow lightning discharge best explain the electromagnetic data obtained by the Voyager and Galileo spacecraft. Dwyer et al. (2006) used Monte-Carlo calculations to determine the properties of runaway breakdown in the four giant planets' atmospheres. They conclude that the threshold for runaway breakdown is 10 times smaller as compared to the conventional breakdown field for these gaseous compositions, and that the process is more efficient than on earth due to the avalanche lengths and thresholds. The expected results are not sensitive to compositional differences between the four planets, emphasizing the importance of runaway breakdown for lightning in their atmospheres.

The global circuit of the dusty Martian atmosphere and the electrical conditions within Martian dust devils were numerically studied by Farrell et al. (1999a) and Farrell and Desch (2001). Assuming triboelectric charging to be the dominant mechanism, the model predicts strongly electrified dust devils, capable of sprite-like discharges in the thin atmosphere. The strength of the radiated electric field is highly dependant on the dust concentration within the devil. These results are further discussed in the chapter by Renno and Kok (2008) in this issue.

4 Gaps in Knowledge

Our present understanding of the charging processes, electric field build-up and subsequent lightning discharge in terrestrial thunderstorms is far from complete. The field is vibrant

with new experimental and observational technologies, remote-sensing platforms and ever-sophisticated numerical models. When it comes to planetary lightning, the level of understanding is several orders of magnitude lower. There are several major gaps in our knowledge which limit our understanding of the electrical processes operating in other planets' atmospheres:

1. Incomplete understanding of charge separation processes in ice—in spite of major progress made in the past two decades, some basic unknowns remain. The microphysics of charge separation in different meteorological conditions (like the melting layer in stratiform regions of Mesoscale Convective Systems) is still poorly understood.
2. Limited number of lightning observations—the harvest from the latest spacecraft flybys and orbital observations is encouraging. However, it only allows us glimpses and snapshots of what is probably a seasonal, global phenomenon. Remote sensing from Earth by optical and electromagnetic means should be encouraged and improved.
3. Incomplete cloud data—we still lack high quality in-situ measurements of cloud properties in different planetary settings. Remote controlled platforms offer some compensating data but they are essentially restricted to the upper most cloud layers.
4. Insufficient laboratory data—we have few measurements of charge generation and separation in substances other than H₂O. Even for water, the role of impurities is not well understood, both in the bulk and in the molecular levels. This gap can be addressed by conducting experiments involving different compositions of the interacting particles. The same goes for solid particles composed of other substances, representing volcanic plumes and sand-dust scenarios.
5. Simplistic models—though the benefits of 1D models for simulations of planetary clouds was shown, we still lack a comprehensive 3D, full-microphysics model as a research tool to explore cloud properties and charging mechanisms in other planetary settings. Such models are available for Earth and they need adaptation to alien conditions. They can certainly be used to set constraints on the electrical conditions and lightning frequency on other planets.

5 Conclusion

Lightning is a universal atmospheric phenomenon that is important in many aspects for planetary physics. It is an energy source in a planet's atmosphere, coupling different layers and outer spheres such as its ionosphere and magnetosphere. The study of thunderclouds on Earth, with their related transient luminous events, electron beams and energetic particles emissions, electromagnetic wave propagation and persistent chemical effects, are an active research field. It is clear that comparative research by using analogies and scaling, offers a potent tool to promote the understanding of storms occurring in other planetary atmospheres. There are still several gaps that need to be covered, as specified above. When we achieve this goal, it may well be that lightning observations conducted in a remote and alien place in our solar system will shed light on some of the unsolved questions in our home planet.

References

- O. Altaratz, O.T. Reisin, Z. Levin, J. Geophys. Res. **110**, D20205 (2005)
K. Aplin et al., Space Sci. Rev. (2008, this issue)

- S.K. Atreya, *Atmospheres and Ionospheres of the Outer Planets and Their Satellites* (Springer, Berlin, 1986), 224 p.
- M.B. Baker, J.G. Dash, *J. Geophys. Res.* **99**, 10,621 (1994)
- E.L.O. Bakes, C.P. McKay, C.W. Bauschlicher, *Icarus* **157**(2), 464–475 (2002)
- C. Barthe, J.P. Pinty, *J. Geophys. Res.* **112**, D19204 (2007)
- T. Berdeklis, R. List, *J. Atmos. Sci.* **58**, 2751 (2001)
- M. Brooks, C.P.R. Saunders, R.P. Mitzeva, S.L. Peck, *Atmos. Res.* **43**, 277–295 (1997)
- J.M. Caranti, E. Avila, M. Re, *J. Geophys. Res.* **96**, 15,365 (1991)
- A.D. Del-Genio, D.M. MacGratten, *Icarus* **84**, 29 (1990)
- J.R. Dwyer, L.M. Coleman, R. Lopez et al., *Geophys. Res. Lett.* **33**, L22813 (2006). doi:[10.1029/2006GL027633](https://doi.org/10.1029/2006GL027633)
- W.M. Farrell, M.L. Kaiser, M.D. Desch et al., *J. Geophys. Res.* **104**(E2), 3795 (1999a)
- W.M. Farrell, M.L. Kaiser, M.D. Desch, *Geophys. Res. Lett.* **26**(16), 2601–2604 (1999b)
- W.M. Farrell, M.D. Desch, *J. Geophys. Res.* **106**, 7591–7595 (2001)
- S. Gibbard, E.H. Levy, J.I. Lunine, *Nature* **378**, 592–595 (1995)
- J.S. Gilbert, S.J. Lane, R.S.J. Sparks, T. Koyaguchi, *Nature* **249**, 598–600 (1991)
- A.L. Graps, G.H. Jones, A. Juhász et al., *Space Sci. Rev.* (2008, this issue)
- T.W. Hartquist, O. Havnes, G.E. Morfill, *Astron. Geophys.* **44**(5), 5.26–5.30 (2003). doi:[10.1046/j.1468-4004.2003.44526.x](https://doi.org/10.1046/j.1468-4004.2003.44526.x)
- M. Horányi, B. Walch, S. Robertson, D. Alexander, *J. Geophys. Res.* **103**, 8575 (1998)
- M.R. James, S.J. Lane, J.S. Gilbert, *J. Geophys. Res.* **105**(B7), 16,641 (2000)
- M.R. James, L. Wilson, S.J. Lane, J.S. Gilbert et al., *Space. Sci. Rev.* (2008, this issue)
- E.R. Jayaratne, C.P.R. Saunders, J. Hallet, Q. J. R. Meteorol. Soc. **109**, 609 (1983)
- E.R. Jayaratne, *Atmos. Res.* **26**, 407–424 (1991)
- E.R. Jayaratne, *J. Atmos. Sci.* **50**(18), 3185–3193 (1993)
- E.R. Jayaratne, in *Proc. XI Int. Conf. Atmos. Electr.* (1999), pp. 312–315
- R. Jayaratne, in *The Lightning Flash*, ed. by V. Cooray (Institution of Electrical Engineers, London, 2003), pp. 17–44
- G.H. Jones, N. Krupp, H. Krüger et al., *Geophys. Res. Lett.* **33**, L21202 (2006). doi:[10.1029/2006GL028146](https://doi.org/10.1029/2006GL028146)
- J.H. Helsdon, W.A. Wojcik, R.D. Farley, *J. Geophys. Res.* **92**, 5661–5675 (2001)
- W.D. Keith, C.P.R. Saunders, *Atmos. Res.* **25**, 445 (1990)
- E.C. Krauss, M. Horanyi, S. Robertson, *New J. Phys.* **5**, 70 (2003)
- J.F. Kok, N.O. Renno, *Phys. Rev. Lett.* **100**, 014501 (2008)
- D.J. Lacks, A. Levandovsky, *J. Electrost.* **65**(2), 107–112 (2007). doi:[10.1016/j.elstat.2006.07.010](https://doi.org/10.1016/j.elstat.2006.07.010)
- D.R. MacGorman, W.D. Rust, *The Electrical Nature of Storms* (Oxford University Press, London, 1998)
- E.R. Mansell, D.R. McGorman, L. Ziegler, J.M. Straka, *J. Geophys. Res.* **107**(D9), 4075 (2002). doi:[10.1029/2000JD000244](https://doi.org/10.1029/2000JD000244)
- E.R. Mansell, D.R. McGorman, L. Ziegler, J.M. Straka, *J. Geophys. Res.* **110**, D12101 (2005). doi:[10.1029/2004JD005287](https://doi.org/10.1029/2004JD005287)
- T.A. Mather, R.G. Harrison, *Surv. Geophys.* **27**, 387 (2006)
- R. Mitzeva, J. Latham, S. Petrova, *Atmos. Res.* **82**, 26–36 (2006a)
- R. Mitzeva, C.P. Saunders, B. Tsanova, *Atmos. Res.* **82**, 102–111 (2006b)
- J. Nelson, M. Baker, *Atmos. Chem. Phys.* **3**, 1327–1252 (2003)
- R.G. Pereyra, A.E. Avila, N.E. Castellano, C.P.R. Saunders, *J. Geophys. Res.* **105**, 20803 (2000)
- H.R. Pruppacher, J.D. Klett, *Microphysics of Clouds and Precipitation* (Kluwer Academic, Dordrecht, 2003)
- V.A. Rakov, M.A. Uman, *Lightning, Physics and Effects* (Cambridge University Press, Cambridge, 2003), 690 p.
- N.O. Renno, J.F. Kok, *Space Sci. Rev.* (2008, this issue)
- C.P.R. Saunders, W.D. Keit, R.P. Mitzeva, *J. Geophys. Res.* **96**, 11,007 (1991)
- C.P.R. Saunders, S.L. Peck, *J. Geophys. Res.* **103**, 13,949–13,956 (1998)
- C.P.R. Saunders, *Space Sci. Rev.* (2008, this issue). doi:[10.1007/s11214-008-9345-0](https://doi.org/10.1007/s11214-008-9345-0)
- C.M. Scavuzzo, S. Masuelli, G.M. Caranti, E.R. Williams, *J. Geophys. Res.* **103**(D12), 13,963–13,973 (1998)
- A.A. Sickafuse, J.E. Colwell, M. Horányi, S. Robertson, *Phys. Rev. Lett.* **84**, 6034 (2000)
- A.A. Sickafuse, J.E. Colwell, M. Horányi, S. Robertson, *J. Geophys. Res.* **106**, 8343–8356 (2001)
- Z. Sternovski, S. Robertson, A. Sickafuse et al., *J. Geophys. Res.* **107**(E11), 5101 (2002)
- C. Stoker, *Icarus* **67**, 106 (1986)
- M. Stolzenburg, T. Marshall, *Space Sci. Rev.* (2008, this issue). doi:[10.1007/s11214-008-9338-z](https://doi.org/10.1007/s11214-008-9338-z)
- T. Takahashi, *J. Atmos. Sci.* **41**, 2541–2558 (1984)
- T. Tokano, G.J. Molina-Cuberos, H. Lammer, W. Stumptner, *Planet. Space Sci.* **49**, 539–560 (2001)
- S.J. Weidenschilling, J.S. Lewis, *Icarus* **20**, 465 (1973)
- R.A. West, D.F. Strobel, M.G. Tomasko, *Icarus* **65**, 161–217 (1986)

- E.R. Williams, R. Zhang, J. Rydock, *J. Atmos. Sci.* **48**, 2195–2203 (1991)
E.R. Williams, *J. Geophys. Res.* **100**, 1503–1505 (1995)
Y. Yair, Z. Levin, S. Tzivon, *Icarus* **115**, 421–434 (1995a)
Y. Yair, Z. Levin, S. Tzivon, *Icarus* **114**, 278–299 (1995b)
Y. Yair, Z. Levin, S. Tzivon, *J. Geophys. Res.* **103**(D12), 14,157–14,166 (1998)
X.J. Zheng, N. Huang, Y.-H. Zhou, *J. Geophys. Res.* **108**(D10), 4322 (2003)

Physics of Electric Discharges in Atmospheric Gases: An Informal Introduction

Rudolf A. Treumann · Zbigniew Kłos · Michel Parrot

Originally published in the journal Space Science Reviews, Volume 137, Nos 1–4.
DOI: [10.1007/s11214-008-9355-y](https://doi.org/10.1007/s11214-008-9355-y) © Springer Science+Business Media B.V. 2008

Abstract A short account of the physics of electrical discharges in gases is given from the viewpoint of its historical evolution and application to planetary atmospheres. As such it serves as an introduction to the papers on particular aspects of electric discharges contained in this issue, in particular in the chapters on lightning and the discharges which in the last two decades have been observed to take place in Earth's upper atmosphere. In addition to briefly reviewing the early history of gas discharge physics we discuss the main parameters affecting atmospheric discharges like collision frequency, mean free path and critical electric field strength. Any discharge current in the atmosphere is clearly carried only by electrons. Above the lower boundary of the mesosphere the electrons must be considered magnetized with the conductivity becoming a tensor. Moreover, the collisional mean free path in the upper atmosphere becomes relatively large which lowers the critical electric field there and more easily enables discharges than at lower altitudes. Finally we briefly mention the importance of such discharges as sources for wave emission.

Keywords Atmosphere · Quasi-stationary electric fields · Discharges · Avalanches · Sprites-jets · Electrostatic waves

R.A. Treumann (✉)

Department of Geophysics and Environmental Sciences, Munich University, Munich, Germany
e-mail: treumann@geophysik.uni-muenchen.de

R.A. Treumann

Department of Physics and Astronomy, Dartmouth College, Hanover NH 03755, USA

Z. Kłos

Space Research Centre, Polish Academy of Sciences, Warsaw, Poland
e-mail: klos@cbk.waw.pl

M. Parrot

Laboratoire de Physique et Chimie de l'Environnement, CNRS, 45071 Orleans, France
e-mail: mparrot@cnrs-orleans.fr

1 A Brief Historical Overview

The physics of electrical discharges in gases has a long history (Bowers 1991, 1998) reaching back into the 17th century; in 1672 Otto von Guericke reported the production of static electric sparks when rubbing sulphur balls with the hand. Three years later the astronomer Jean Picard reported that shaking a mercury barometer caused the tube to glow. At the end of that century (around 1698) sparks had been extracted from rubbed amber and formed the subject of intense investigation by the Comte Charles François de Cisternay du Fay. Based on Picard's observation Johann Heinrich Winckler in Leipzig invented what we can call a 'fluorescent tube' in 1745, and in 1802 Vasilii Petrov in St Petersburgh produced electric arcs between two carbon electrodes independently of, but almost at the same time as, Sir Humphry Davy (Knight 1992) in London. Davy invented the carbon arc lamp, presenting it in 1807 to the Royal Institution, and established the subject of arc physics (Davy 1807). For their experiments they both used the chemical battery invented in 1799 by Count Alessandro Volta.

The famous experiments of Benjamin Franklin in 1750 on sparks led him to coin the notions of positive and negative charging which survive until today and to invent the lightning rod. Mikhail V. Lomonosov in 1743 (Lomonosov 1748) had already suggested that lightning, and the polar lights (aurorae) as well, would be atmospheric electric discharge phenomena. With respect to the similarity between lightning and sparks they were both right, while they could not know that auroral discharges are phenomena quite different from spark discharges. Charles-Augustin de Coulomb (1785) discovered dark discharges (Gillmor 1971). In the 19th century interest in gas discharges increased due to Michael Faraday's and James Clerk Maxwell's formulation of the physics of electromagnetic phenomena. Faraday himself even experimented with sparks and glow (or corona) discharges, thereby uncovering the dependence of the latter on the pressure in the tube (Faraday 1833, 1834). It is interesting to note that such investigations were made possible by improved glass blowing techniques, the evacuation of glass tubes and the separation of gases.

Experimenting on dilute gases, Johann Hittorf (1879) determined the electrical conductivity of air and different gases which, in 1900, culminated in Paul Drude's seminal formula for the electrical conductivity of a gas, introducing the concept of collision frequency ν_c . The collision frequency received its physical explanation when Ernest Rutherford found the now famous Rutherford collisional cross section, σ_c , in terms of which the collision frequency can be written as $\nu_c = n\sigma_c v$, where n is the gas density, and v the velocity of the moving particle. Equivalently this allowed the introduction of the collisional free flight distance $\lambda_{\text{ff}} = v/\nu_c$ of a particle between two collisions. When v was taken to be the thermal velocity v_{th} this became the mean free path $\lambda_{\text{mfp}} = v_{\text{th}}/\nu_c = 1/n\sigma_c$.

Hittorf somewhat later published the first investigations on cathode rays which were crucial for the later formulation of atomic physics. Indeed, any deeper understanding of gas discharges had to wait until the advent of atomic physics, which became possible only via reference to the investigation of gas discharges. William Crookes (1879) found that cathode rays were deflected by magnetic fields and called them the fourth state of matter, claiming that their investigation would lead to the deepest insight into the nature of matter. This prediction was in fact true. From the deflection of cathode rays in a magnetic field and based on the electrodynamics of charged particle motions in electromagnetic fields, Sir J.J. Thomson (1897) determined the elementary charge-to-mass ratio which led to the discovery of the electron. Two years earlier Wilhelm Conrad Roentgen (1895) experimenting with cathode rays had discovered X-rays.

The last decade of the 19th century and the first decade of the next were devoted to investigations of spectral phenomena with the help of dilute gas tubes, leading on the one hand

to the determination of the Johann Balmer (1885), Walther Ritz (1908), Theodore Lyman (1914) and Friedrich Paschen (1908) series of spectral lines, and on the other hand to the precise mapping of the temperature dependence of black body radiation, and the energetic or collisional excitation of electrons in atoms at specific energies by James Franck and Gustav Hertz (1914). These investigations culminated in the formulation of quantum and atomic theory, going hand in hand with the development of gas discharge physics. It is thus no surprise that most of the Nobel laureates of the first three decades of the 20th century had worked on the physics of gas discharges, among them Rutherford, John S. Townsend, Owen W. Richardson, Karl Compton, Irving Langmuir and Peter Debye. In particular Townsend's (1901, 1915) and Richardson's (1908, 1928) investigations of the different types of discharges were crucial for the further development of gas discharge physics. Clearly the peak of gas discharge physics coincided with the development of atomic physics and quantum mechanics, i.e. with the quantum theory of the atom.

The first three decades of the 20th century saw the physics of gas discharge phenomena blossoming. With the investigation of the various processes of the ionisation of gases, by either radiation or collisions, the understanding of atomic spectra and of the excitation processes achieved quite a high level of sophistication and maturity. At the same time the physics of gaseous discharges bifurcated into two quite separate disciplines, proper gas discharges and plasma physics. The notion of a plasma was introduced by Irving Langmuir in 1927 (Mott-Smith 1971) reserving it to highly ionised gases, with only a small residual admixture of a non-ionised neutral component or even lacking such a component. Due to the dominance of electromagnetic interactions in a plasma, the physics of plasmas turned out to be completely different from that of neutral gases. Peter Debye and Erich Hückel (1923) showed that electrical charges in a plasma are screened beyond a distance $\lambda_D = v_e/\omega_{pe}$, termed the Debye radius, where $v_e = v_{the}$ is the electron thermal velocity, and ω_{pe} is the electron plasma frequency, the oscillation frequency of electrons around their equilibrium position (discovered by Langmuir 1923).

The notion that the upper atmosphere of the Earth must be electrically conducting goes back to Carl Friedrich Gauss (1776–1855) who, expanding the Earth's magnetic field in spherical harmonics, discovered that it contained a substantial component due to outer sources which he suspected to be currents somewhere at large altitude above the surface. It was only in 1902 that Oliver Heaviside (Nahin 1990; Appleton 1947; Watson-Watt 1950) proposed the existence of a high-altitude conducting layer that reflects radio waves. This was confirmed experimentally in 1924–1927 by Edward V. Appleton (1947). The formation and nature of this layer was understood when Sydney Chapman (1931) realised that solar UV radiation was capable of ionising the upper atmospheric layers at around 100–130 km altitude, being absorbed there. H. Kallmann (1953) ultimately proved that taking into account the full solar spectrum the ionisation effectively reached down to below 80 km altitude. It became clear that atmospheric constituents below 80 km can also be ionised by precipitating energetic particles from the Sun and the magnetosphere and by cosmic rays. These processes are reviewed elsewhere in this issue (Chapter 2 and Chapter 6).

In the early 1930s several extended reviews were written on this subject, among them the famous accounts of Compton and Langmuir (1930, 1931). After the golden twenties and thirties the physics of proper gas discharges lost its importance in fundamental physics, becoming a branch of applied physics, while plasma physics—its fully ionised twin—shifted to centre stage. This was mainly for two reasons, the interest in fusion research and the advent of the space age. Space plasma physics became attractive to both the public and politicians. Still, interest in ionospheric physics and in the mechanism of lightning enabled the physics of gas discharges to stay alive throughout this period of relative drought.

In the last twenty years gas discharges became more interesting again, in relation to natural transient luminous events (TLEs) (Franz et al. 1990; Sentman et al. 1995; Neubert 2003) that had been discovered in the Earth's upper atmosphere above thunderstorms. Such spectacular phenomena are sprites, electric jets, and elves (Fullekrug et al. 2006b); evidence for lightning and related electrical effects on other planets, in planetary rings and even in astrophysical objects, accumulated. In addition, the relation of TLEs to space weather phenomena has provided another impetus to their investigation. [The processes of the generation and separation of charges which are required before a discharge can be generated are reviewed in this issue (Roussel-Dupré et al. 2008; Yair et al. 2008) and also form the content of Chapters 2 and 6. Some of the theory and the observation of such effects as blue jets and sprites are summarized in Chapter 7 (Mishin and Milikh 2008; Mika and Haldoupis 2008).] Because of the importance of such effects the physics of gaseous discharges is far from being exhausted, in particular in view of the newly discovered fine structuring of streamers (Ebert et al. 2006).

There is one particular aspect of this that in the future will certainly regain more attention. This is the problem of the energetic coupling between near-Earth space and the atmosphere. More generally, the question of how a planetary atmosphere couples to its space environment poses a problem that is of fundamental importance for climatology and the understanding of how energy is fed into processes that are important for the planetary climate from the outside, the interplanetary and magnetospheric plasmas through coupling via the ionosphere to the atmosphere. Sprites, elves and jets suggest that this is indeed an important problem which has only just been realised and has not yet been investigated to the extent that it deserves. There are extended recent reviews of these phenomena available (Fullekrug et al. 2006b; Pasko 2007, for instance).

2 Parameters and Theory

The electric discharge is the final step of a whole sequence of processes going on in a gas that is subject to ionisation and internal gas dynamics. Most of these processes have been or will in subsequent sections in this issue be described for Earth and other planets surrounded by an atmosphere. At the end of all these processes there is an electric field of strength E that is maintained in some way over a sufficiently long time, and positive and negative electrical charge layers that are separated from each other by a distance L . This electric field can be maintained only up to a certain strength $|E| \leq |E|_{\text{crit}}$ which, when exceeded, causes a spectacular breakdown of the field. The processes of electric field build-up are related to the various processes of ionisation and take up considerable space in this issue. Here we restrict ourselves to a very basic and by no means complete discussion of the breakdown processes. Several aspects of these will be given in great detail in Chapter 7.

The atmosphere is considered to be collisional, with the collision frequency ν_c being determined mainly by collisions between electrons and the various neutral components. A more sophisticated theory must take into account the composition of the atmosphere including aerosols, various excitation and ionisation processes such as, for instance, cosmic ray ionisation or frictional ionisation, the presence of a magnetic field, the horizontal and vertical dynamics of the atmosphere, its water content, temperature distribution, and its altitudinal inhomogeneity. All these factors (including those we are not considering here) enter into the real discharge process, and some of them are considered in great detail elsewhere in this issue (Roussel-Dupré et al. 2008). Here we merely mention them as hard-to-treat complications of a realistic atmospheric discharge process encountered, for instance, in a

lightning discharge or the recently discovered high-altitude discharges in sprites, blue jets and giant jets.

In the simplest model of a resistive atmosphere the collisions are treated classically (and we will not deviate from this in this introductory paper). This implies that $\sigma_c \approx 4.5 \times 10^{-18} \text{ m}^{-2}$ (Aguilar-Benitez et al. 1990; Bernshtam et al. 2000) is the constant classical two-body collisional cross section. In addition the neutral gas density obeys the barometric law $n_n(h) = n_0 \exp[-m_n g(h)h/k_B T_n(h)]$, where the subscript n means neutrals, h is the height above sea level, n_0 the density at ground level, $g(h)$ the gravitational acceleration at altitude h , m the mass, $T(h)$ the temperature at h , and k_B Boltzmann's constant. By contrast in a fully ionised plasma the cross section is the Rutherford or (when averaged over the thermal distribution function) the Spitzer-Braginskii cross section (Baumjohann and Treumann 1996, Chapter 4) which strongly depends on plasma density and particle speed, thus implying a completely different physics. Since in the uppermost layers of the atmosphere and in particular in the ionosphere the gas is weakly ionised with a mixture of electrons and ions, the relevant cross section will be a mixture of the classical and Spitzer cross sections. In the neutral atmosphere on the other hand several other effects have to be considered which are related to the excitation cross sections of the different gas molecules, the molecular nature of the gas and the composition of the atmosphere at different altitudes, as well as the different ionisation energies. Moreover, the eventual presence of an electric field and the background convective wind motions of the gas as well as the effects of the external radiation change the conditions existing. All such effects are ignored here but for realistic cases should be taken into account in their relative importance.

With the above notations the collision frequency becomes

$$\nu_c(h) = \nu_0 \exp\left[-\frac{m_n g(h)h}{k_B T_n(h)}\right] \sqrt{\frac{T_n(0)}{T_n(h)}}, \quad \nu_0 \equiv n_0 \sigma_c \sqrt{\frac{2k_B T_0}{m_n}}. \quad (1)$$

On Earth, the temperature and density of air at ground level are roughly $T_0 \approx 300 \text{ K}$ and $n_0 \simeq 2 \times 10^{25} \text{ m}^{-3}$. The latter value depends on what is assumed for the composition of air. In the above formula the height dependence of the gravitational acceleration $g(h) \simeq g(0)(1 - 2h/R_E)$ can safely be ignored since in the altitude range from 0 to 100 km the variation of the ratio of height to Earth radius R_E is $\lesssim 1\%$. The temperature (see Fig. 1) in this altitude range changes by a factor of $T_n(h)/T_0 \leq 3$. Thus its change is important only in the exponential factor. At zero level, the Earth's surface, we have for the neutral-neutral collision frequency $\nu_0 \sim 10^9 \text{ Hz}$.

Figure 1 summarises the vertical profile of the Earth's atmospheric temperature, mass density and binary collision frequency in a simplified way with the neutral-neutral collision frequency $\nu_c = \nu_{nn}$ and electron-neutral collision frequency $\nu_c = \nu_{en}$ calculated for an 80% nitrogen and 20% oxygen mass-dominated atmosphere. The reason for the latter being large is the proportionality of the collision frequency to the thermal velocity v_e of the electrons which are generated by ionisation and therefore have energies $>$ a few eV. At higher electron energies than those they gain during a discharge this collision frequency becomes obsolete because other processes (excitation, Coulomb interaction) set on. Since the Earth is magnetized the collision frequency is, in principle, a tensor (Rycroft et al. 2008, e.g.) giving rise to a tensorial electrical conductivity $\sigma = (\sigma_{||}, \sigma_P, \sigma_H)$, where σ_P is the conductivity perpendicular to $\mathbf{b} \equiv \mathbf{B}/B$, the unit vector parallel to Earth's magnetic field \mathbf{B} , and σ_H is the Hall conductivity perpendicular to both, the electric and magnetic fields. The expressions for the

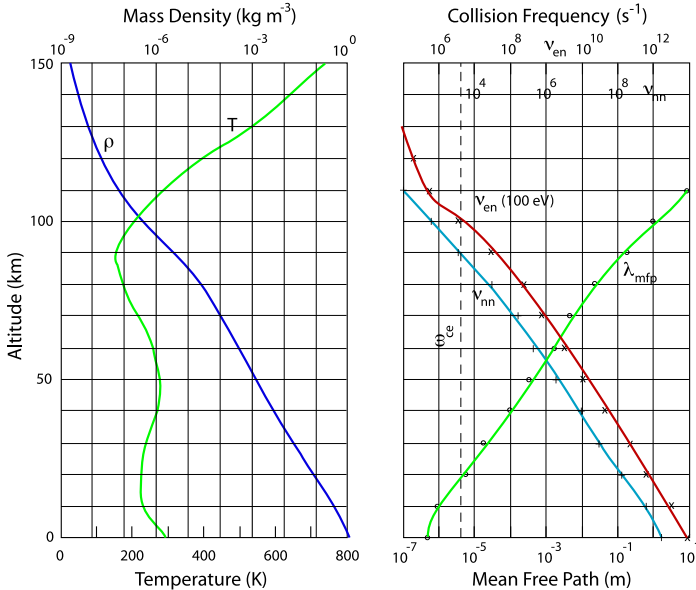


Fig. 1 *Left:* Average altitude profiles of temperature $T(h)$ and mass density $\rho(h)$ in the Earth's atmosphere consisting of 80% N₂ and 20% O₂. *Right:* Rough models of collisional mean free path λ_{mfp} , based on the data on the left for neutral-neutral binary collisions with collision frequency $v_c = v_{nn}(h)$, and the electron-neutral collision frequency for collisions between electrons of 100 eV energy and neutrals as functions of altitude above ground level. The *light line* shows the altitude dependence of the binary collisional mean free path $\lambda_{mfp}(h)$. In the middle atmosphere the mean free path and collision frequencies vary about exponentially with altitude. The *dashed vertical line* shows the electron cyclotron frequency $\omega_{ce} \simeq 4.5 \times 10^6$ Hz which is nearly constant over this height range. The estimate of the electron collision frequency neglects excitation and Coulomb interactions which should be included above roughly 10 eV electron energy for a more realistic model. This would lead to a substantial modification of $v_c = v_{en}$

components of σ are $\sigma_{\parallel} = e^2 n_e / m_e v_c = \epsilon_0 \omega_{pe}^2 / v_c$ parallel to \mathbf{b} , and

$$\sigma_P = \frac{v_c^2}{v_c^2 + \omega_{ce}^2} \sigma_{\parallel}, \quad \sigma_H = -\frac{v_c \omega_{ce}}{v_c^2 + \omega_{ce}^2} \sigma_{\parallel}, \quad (2)$$

where $\omega_{ce} = eB/m_e$ and $\omega_{pe} = e\sqrt{n/\epsilon_0 m_e}$ are the electron cyclotron and plasma frequencies, respectively, and ϵ_0 is the dielectric constant of free space. Below the mesosphere these expressions simplify to $\sigma_P = \sigma_{\parallel}$, $\sigma_H \simeq -\omega_{ce}/v_c \ll 1$. Hence the atmosphere is practically isotropic with zero Hall conductivity. As Fig. 1 suggests, this changes at altitudes above 90 km at the top of the mesosphere. Here the collision frequency drops below the electron cyclotron frequency (the vertical line in the figure) which has a weak altitude dependence only according to the weak variation of the Earth's magnetic field $B \simeq B_0(1 - 3h/R_E)$ with height h through the atmosphere; B_0 is the value at the Earth's surface on a particular geomagnetic field line. The full conductivity tensor comes into play, and this has consequences for the development of electric discharges at these altitudes. The conductivity σ_{\parallel} is low in the atmosphere meaning that the atmosphere is a poor conductor. Under discharge conditions this may change, though. In contrast, the ions are practically collisionally isotropic because $v_c \gg \omega_{ci}$ by far exceeds the ion cyclotron frequency $\omega_{ci} = Z(m_e/m_i)\omega_{ce}$ up to the altitudes of the ionosphere (Z is the ionic charge number, and m_i the ion mass).

Introducing the more detailed papers collected in Chapter 7 on the most interesting special cases of atmospheric discharges in the upper atmosphere and their effects on radio wave propagation, we will, in the following, briefly review the types of electrical discharges that may be relevant under gaseous atmospheric conditions. We explicitly exclude here other important discharges such as those in charged dust and sand storms which are considered in detail elsewhere in this volume (Renno and Kok 2008). On Earth they occur in volcanic eruptions which inject large amounts of dust and ashes into the atmosphere where they trigger lightning. They are also known to occasionally occur in sand storms in the big terrestrial sand deserts. In the atmosphere of the dusty planet Mars they could become important if not dominant (Melnik and Parrot 1998; Farrell et al. 1999).

3 Different Types of Discharges

In order to ignite an electric discharge in an otherwise neutral gas like the atmosphere, electrons have to be set free by some process. Subsequently an electric field must be present that can accelerate electrons to energies far above the ionisation energy fast enough in order to cause an avalanche of newly generated electrons by collisional (or other kinds of) ionisation. For this to happen the electric field must be strong, which implies that by some external force the initially present negatively and positively charged layers must become separated over a sufficiently large distance L . Processes capable of providing such initial charge distributions are discussed elsewhere in this issue. One of the basic processes is the weak ionisation of the atmosphere produced by the continuous inflow of highly energetic cosmic rays into the atmosphere and the cascades of nuclear fission products and elementary particles which are produced by them. Charge layer separation in a thunderstorm is a complicated process closely related to the physics of clouds and their internal dynamics. The reader is referred to the respective sections of this volume for information.

3.1 Townsend, Glow, and Spark Discharges

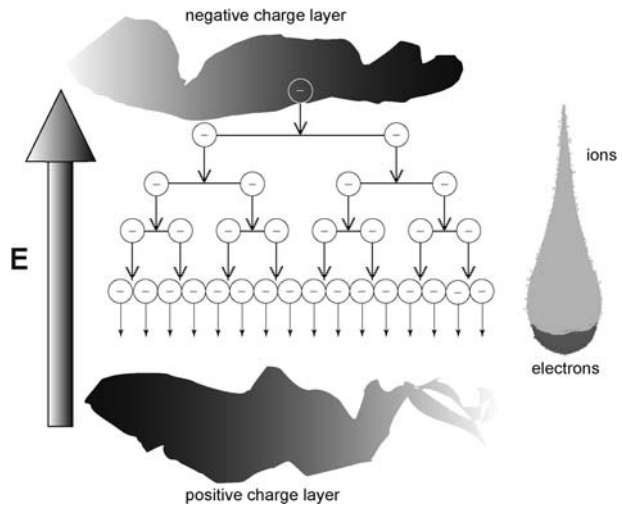
Once sufficient charge has accumulated to form a charge layer and oppositely charged layers have become separated from each other, a macroscopic electric field is built up. As long as this field is weaker than some threshold field E_{crit} , discharges go on only slowly due to recombination and may be balanced by newly created ionisation. However, when the electric field exceeds the threshold, a violent discharge process sets in, causing breakdown and the electric field is shorted out. In laboratory gas discharge physics one distinguishes a number of discharges. Two of them, which are accompanied by light emission, are shown in Fig. 2. To the left is the typical blue arc discharge between cathode and anode, and to the right is a typical red glow discharge observed in a glass tube at low pressure.

In addition there are dark (or Townsend) discharges which, as the name implies, are not accompanied by visible light emission. Moreover, one distinguishes non-stationary discharges in connection with spark discharges. In Townsend dark discharges the current flow is rather weak and the current densities are low; the voltage remains constant over the time of the discharge. When the current strength increases the Townsend discharge makes the transition to a glow discharge. Now the energy of the flowing electrons is large enough to excite an atom collisionally, which emits light from the infrared to the visible and up to the ultraviolet. Arc discharges acquire large current densities, strong electric fields, and may emit radiation deep into the ultraviolet and even weak X-rays. These processes have been described in textbooks (Lieberman and Lichtenberg 1994;



Fig. 2 Two types of electric discharges. *Left:* A typical arc discharge, and *Right:* a glow discharge in an evacuated glass tube. Glow discharges are quiet and low temperature which is in contrast to the noisy and unsteady spark discharges. Because of this reason they can be used for illumination. Arc discharges, on the other hand, develop high temperatures and find technical application in welding

Fig. 3 *Left:* Avalanche generation in electron collisions with neutrals in presence of a sufficiently strong electric field (the Townsend process). *Right:* The resulting charge distribution in the avalanche. The head of the avalanche consists of fast and dense electrons. An extended wake of slow ions is left behind which try to follow the electrons but are accelerated in the opposite direction by the externally applied electric field which, however, is partially cancelled inside the ion cloud wake



Raizer 1997, for instance). In atmospheric physics of most interest are discharges of the kind which lead to breakdown as, for instance, when lightning discharges are generated.

3.2 Electron Avalanches

For the purposes of atmospheric discharges the formation of current carrying electron avalanches is most important, as shown in Fig. 3. The continuous slow discharges of electric fields produced by the persistent inflow of cosmic rays into the atmosphere provide the seed population of electrons for the ignition of an avalanching discharge. In an avalanche the electron number density increases exponentially since $dn_e/dt = \alpha_i n_e$, the production of electrons being proportional to the existing electron number density and with the proportionality factor being the Townsend ionisation rate coefficient α_i (Raizer 1997). This relation has the solution $n_e(t) = n_e(0) \exp[\int_0^t dt' \alpha_i(t')]$. The exponential factor indicates the temporal multiplication rate of the avalanche, which also corresponds to the spatial multiplication rate over the distance of the evolution of the avalanche.

Avalanches have a typical structure with a negative head consisting of the fast electrons and an extended positively charged tail containing the slow freshly produced ions which tend to retard the advancement of electrons but are kept back by the external electric field that accelerates them in the opposite direction. It is clear that in such a process the electric field

must become strong enough in order to overcome recombination collisions and accelerate electrons in one mean free path length (see Fig. 1) up to ionisation energies. The latter are of the order of a eV, for hydrogen typically $\mathcal{E}_{\text{ion}} \simeq 13.6$ eV. The accelerated electrons must be able to both run away and ionise. From this reasoning follows a simple condition for the necessary strength of the external field E for igniting a gaseous electric discharge

$$|E| \gtrsim E_{\text{crit}} \equiv 2(\mathcal{E}_{\text{ion}}/e\lambda_{\text{mfp}}). \quad (3)$$

At 10 km altitude this field is quite large, amounting to $> (2 - 3) \times 10^6$ V m⁻¹, but decreases with altitude deep into the mesosphere (~ 70 km altitude) by roughly four orders of magnitude (see Fig. 1) to become only a few 100 V m⁻¹ there. Hence, in the higher atmosphere considerably smaller electric field strengths are required in order to ignite an electric discharge than in the troposphere. The problem therefore consists less in exceeding the threshold at these altitudes than in generating charged layers with an electric field between them which requires vertical transport. But once this is achieved at lower altitudes breakdown at higher altitudes becomes possible. In this respect it is noteworthy that sprites and jets have been observed to be closely related to low altitude thunderstorm discharges starting from the tops of thunderstorm clouds at < 10 km.

The high threshold electric field must in fact be exceeded at low altitudes of a few km, which poses a serious problem. One solution, theoretically realised and proven by kinetic simulations (Gurevich et al. 1992, 2000, 2001, 2002; Roussel-Dupré et al. 1994; 1996; Lehtinen et al. 1997; Babich et al. 1998) was that a proper kinetic description of the avalanching process should take into account not only the generation of secondary electrons but also the production of high energy run-away electrons. This causes what these authors call “runaway breakdown” (RBD). A complete review of the theory can be found elsewhere (Gurevich and Zybin 2001). The idea is that a small number of fast seed electrons initially reach high energy ($\gtrsim 10$ keV) in the electric field. At these energies the electrons are fast enough to ignore the neutral state of matter. They take the outer shell valence electrons and the nuclei of the air molecules as free particles. For them the ordinary collisional cross section σ_{en} for ionisation is replaced with the energy dependent Rutherford-Coulomb cross section σ_C when passing through the interior of the neutral molecules. This drastically increases the efficiency of ionisation since the Coulomb cross section is inversely proportional to the square of the particle energy; it decreases with energy which allows for energetic particles after collision to “run away” in the field, and obey a power law distribution function $f(\mathcal{E}) \propto \mathcal{E}^{-1.1}$ at energies below some threshold energy above which they lose their motional energy by radiation. It has been shown (Gurevich et al. 1992, 2000, 2001, 2002) that this self-consistent power law distribution is a function of the ratio of the electric to breakdown-threshold electric fields.

The RBD threshold electric field as a function of altitude h is proportional to the neutral atmospheric density

$$|E| \gtrsim E_{\text{crit,RBD}} \simeq 0.2 \left[\frac{n_n(h)}{n_0} \right] = 2.0 \exp \left[-\frac{m_n g h}{k_B T_n(h)} \right] \times 10^5 \frac{\text{V}}{\text{m}}. \quad (4)$$

This value is one order of magnitude less than the value obtained from (3). Due to the dependence of $n_n(h)$ on altitude, it decreases exponentially with h , and at higher altitudes becomes very low indeed. The Townsend coefficient now becomes a function of the ratio of electric field to critical electric field (Gurevich et al. 1992, 2000, 2001, 2002)

$$\alpha_{i,\text{RBD}} \simeq 0.07(E/E_{\text{crit,RBD}})^{3/2}, \quad (5)$$

showing the pronounced nonlinearity of the self-feeding process, i.e. avalanche formation. The numerical factor 0.2 in (4) has been determined from numerical simulations of runaway discharges at different pressures.

4 Secondary Effects

The avalanches produced in these spark discharges in the atmosphere cause a number of secondary effects. Sparks are bright, emitting light due to the excitation of both atoms and ions which emit in various lines of the electromagnetic spectrum. Moreover, space charges that are built up over macroscopic vertical and horizontal length scales by the dynamics of the neutral atmosphere due to moving the charges act back on the dynamics, braking it due to the large electrostatic forces that develop when the charges become sufficiently large. Finally, the ionisation of the atmosphere affects the atmospheric chemistry. Other effects are the excitation of several kinds of waves, the generation of radio waves and modification of propagation conditions. These have been observed to occur during and in the wake of thunderstorms and in coincidence with sprites and jets (Bosinger and Shalimov 2008; Mika and Haldoupis 2008; Simões et al. 2008). Low frequency electromagnetic radiation (VLF, ELF, ULF, Schumann resonances) which accompanies TLEs is well understood (Rodger 1999; Reising et al. 1996; Cummer and Inan 1997; Füllekrug et al. 1998, 2001, 2006a; Füllekrug and Reising 1998). In the following we list some secondary *microscopic* processes in avalanches but are less familiar. Some of them might affect the physics of the discharge and might result in observable effects.

4.1 Waves

Ion sound The simplest wave type is the mechanical distortion of the atmosphere during discharges which cause thunder and mechanical oscillations of the atmosphere. During such disturbances the ionic component of the atmosphere undergoes similar distortions which may result in low frequency ($0 < \omega_{is}/\omega_{pe} < \sqrt{m_e/m_i}$) sonic waves $\omega_{is} = kc_{is}$ of speed $v_i \ll c_{is} \simeq \sqrt{m_e/m_i} v_e \sim 40 \text{ km s}^{-1}$, where v_e , v_i are the thermal velocities of electrons and ions, respectively.

It is usually believed that these waves are strongly damped due to the high collision frequency at low altitudes (see Fig. 1). Landau damping can be neglected because of the low ion temperature. At higher altitudes than at the top of the mesopause ion sound turbulence should accompany any discharge. We must compare the mean free path of electrons with the Debye length $\lambda_D = v_e/\omega_{pe}$, where the plasma frequency $\omega_{pe} \simeq 60\sqrt{n_e} \text{ s}^{-1}$, and the electron density is measured in m^{-3} . The electron density produced in a discharge is some small altitude-dependent fraction $\zeta(h) \ll 1$ of the neutral density $n_n(h)$. The ratio of the Debye length to the mean free path $\lambda_{\text{mfp}} = 1/n_n(h)v_e$ is $\lambda_D/\lambda_{\text{mfp}} \sim 10^{-2}\sqrt{(k_B T_e/e)(n_n(h)/n_0\zeta(h))} < 1$ for any finite electron temperature of a few 10 eV, and $\zeta(h) < n_n(h)/n_0$. Hence, the plasma properties dominate inside the avalanche.

Moreover, the electrons being of energy $\gtrsim 10 \text{ eV}$, are much hotter than the ions, $T_e \gg T_i$. They carry the current $j = -en_e V_d$, where V_d is the current drift velocity. This makes excitation of ion sound waves probable if only the growth rate $\gamma_{ia} > v_c$ exceeds the collisional electron damping rate. In an avalanche the latter is given by the Spitzer collision frequency ν_C . This condition, which can be written $1 > V_d/v_e > 200/N_D$, is then always satisfied, then. With $N_D = (n_e \lambda_D^3)^{-1} \gg 1$ the number of electrons in a Debye sphere, its right-hand side is a small number. The ion-sound waves cause the avalanche to develop magnetic field-aligned striations (Davidson 1972; Treumann and Baumjohann 1997, e.g., for the discussion of the instabilities and their nonlinear evolution).

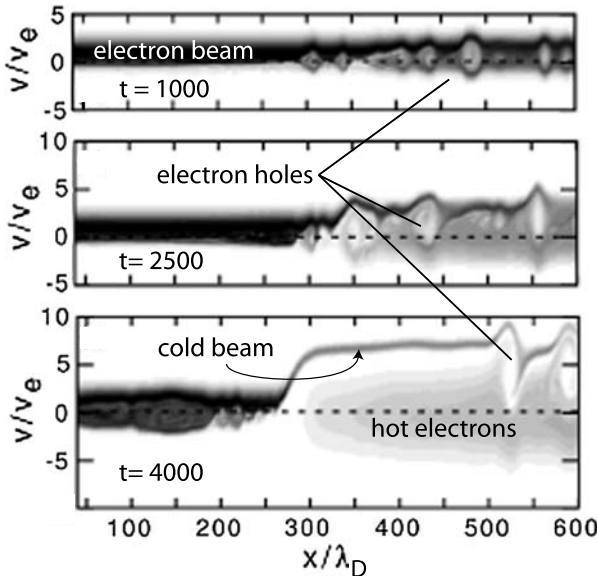


Fig. 4 Electron phase space plots at three successive simulation times (measured in plasma times ω_{pe}^{-1}) of the formation of electron holes in a two-stream unstable plasma. Instability is forced by the presence of a density dip (potential wall for electrons) in the centre of the simulation box which interacts with an injected electron beam current (after Newman et al. 2002). The box has one space (measured in Debye length) and one velocity coordinate (measured in electron thermal speeds v_e). Hole formation is seen on the right. The holes move to the right with beam velocity. They trap electrons and cause strong electron heating of the trapped electrons. In addition acceleration of a narrow (cold) beam is observed which escapes from the hole region at about 7 times the initial velocity

Buneman two-stream instability For $V_d > v_e$ the avalanche plasma is Buneman two-stream unstable (Buneman 1958). RBD discharges with their comparably high electron density and electron kinetic energy (Gurevich and Zybin 2001) are candidates for the two-stream instability. The two-stream instability is riding on the beam, i.e. it propagates at about the same velocity as the beam, being for long time in resonance with the current carrying electrons and thus giving rise to high wave intensities. This instability saturates by formation of localised electron (and also ion) holes, which correspond to locally (a few 10 Debye lengths long) very strong electric fields. This has been demonstrated in numerical simulations (Newman et al. 2002). [The existence of holes has been confirmed in the auroral plasma (Carlson et al. 1998; Ergun et al. 1998, 2001, 2003; Newman et al. 2002; Elphic et al. 1998).] Depending on its polarity, the localised electric field traps electrons or ions. The trapped avalanche electrons bounce back and forth in the holes and become violently heated, dissipating a substantial part of the beam current and electric field energy. Conversely, passing (untrapped) electrons are accelerated further and are at the same time cooled to low temperatures, as seen in Fig. 4.

Phase space hole effects The holes resulting from the two-stream instability are regions of high electric field pressure which affects the equilibrium between the avalanche and its neutral environment. Force balance requires $\nabla_n P_n = -\nabla_e P_e - \nabla_E P_E$, where $P_n = n_n k_B T_n$ is the atmospheric pressure, $P_e = n_e k_B T_e$ is the electron pressure in the avalanche, and $P_E = \frac{1}{2} \epsilon_0 |\mathbf{E}|^2 \{\partial [\omega \epsilon(\omega)] / \partial \omega\}$ is the field pressure. The electron and field pressures together in the avalanche act to expel the neutral gas from the avalanche region. But the forces on the right

and left act on different scales. The scale height L_n of the pressure is several kilometers, while the scales $L_e \sim L_E$ of the holes are only a few tens of Debye lengths long. The local force balance thus becomes

$$P_n = \frac{L_n}{10\lambda_D} (P_e + P_E).$$

Moreover, $P_n \simeq 3 \times 10^4 n_n(h)/n_0 \text{ J m}^{-3}$. Assume that the electrons have an energy of 10 keV (just a fraction of the energy assumed in Gurevich's RBD mechanism). Then, $P_e \simeq 10^{-15} n_e \text{ J m}^{-3}$. To calculate the electric field pressure one needs the wave dielectric constant $\epsilon(\omega)$. For the two-stream instability we have $\partial[\omega\epsilon(\omega)]/\partial\omega \sim \omega_{pe}^2/(0.03\omega_{pe})^2 \sim 10^3$. Thus, $P_E \simeq 5 \times 10^{-9} |E|^2 \text{ J m}^{-3}$. The Debye length is $\lambda_D \sim (0.7/\sqrt{n_e}) \text{ m}$. The balance equation becomes

$$10^4 n_n(h) \sim 10^2 L_n (\text{km}) n_e^{\frac{1}{2}} (10^{-15} n_e + 5 \times 10^{-9} |E|^2).$$

This condition can be satisfied with moderate avalanche densities $n_e < 10^{10} \text{ m}^{-3}$ and electric fields $|E| \sim \text{a few V m}^{-1}$. Stronger fields and higher avalanche densities will completely blow the neutral atmosphere away from the region of the hole. This crude estimate shows that the localisation of the electric field in electron holes and trapping of electrons as a consequence of the two-stream instability causes a substantial local dilution of the neutral atmospheric gas in the holes in the avalanche. It causes a filamentation of the avalanche into striations and narrow packets of trapped electrons and strong fields.

Fine structuring has been observed in streamers (Ebert et al. 2006) though this important observation is interpreted differently. Ebert et al. (2006) describe their observations as a multiscale structure of streamers occurring mainly in the head of the streamers. We should, however, note that the holes ride on the beam and move with about beam velocity. Thus the effect described here also happens mainly in the narrow head layer of the avalanche where the electron density, energy and velocity are highest.

Local whistlers Avalanches can serve as sources of locally excited whistlers. This is obvious from considering the trapped electron distribution in Fig. 4. The electrons that are trapped in the electron hole potentials bounce back and forth along the magnetic field. Due to their gyroscopic motion in the geomagnetic field they possess magnetic moments $\mu_e = T_{e\perp}/B$ ($T_{e\perp}$ is the electron temperature perpendicular to the geomagnetic field). As a consequence of the bounce motion of the trapped electrons, the electron holes become unstable (Ergun et al. 1998, 2001, 2003; Newman et al. 2002) with respect to whistlers of frequency $\omega_{ci} \ll \omega \ll \omega_{ce}$. While moving with the parallel hole velocity along the magnetic field, they radiate whistlers acting like point sources. In a spatially varying magnetic field this parallel motion gives rise to a saucer-like frequency-time appearance of the whistlers. [Such whistler-saucer emissions were indeed observed first under the conditions in the auroral ionosphere (Ergun et al. 1998, 2001, 2003; Newman et al. 2002). Similar phenomena during thunderstorms have been reported (Parrot et al. 2008) from the low-altitude spacecraft DEMETER.] Their propagation direction is oblique to the geomagnetic field at the whistler-resonance cone, with frequency near the lower-hybrid frequency $\omega_{lh} \simeq \omega_{pi}/(1 + \omega_{pe}^2/\omega_{ce}^2)^{\frac{1}{2}}$. In the strong geomagnetic field this is close to the ion plasma frequency ω_{pi} . Their frequency-time dependence maps the avalanche plasma density along the whistler path. Propagating obliquely, these short-perpendicular long-parallel wavelength whistlers are trapped in the avalanche. Being multiply reflected from its boundaries, the whistlers ultimately escape on the top-side with Alfvén velocity $V_A = B/\sqrt{\mu_0 m_n}$ mostly in the perpendicular direction to the magnetic field thereby spreading over a large hollow

horizontal area of narrow opening angle, centred on the source before being absorbed. Excitation of the mesospheric or exospheric gas might lead to emissions over the whole area of these whistlers resembling the ELVE emission.

4.2 Radiation

Several types of electromagnetic radiation have been observed in relation to atmospheric electric discharges, both natural and artificially triggered (Dwyer et al. 2003) lightning, in addition to the above mentioned spherics and the whistlers propagating in the ionosphere and magnetosphere caused by them. Lightning discharges have been observed to be accompanied by radiation in the optical, UV, X rays and even up to the gamma ray energy range and, also in the ELF and ULF radio wave ranges (Simões et al. 2008; Bosinger and Shalimov 2008; Mika and Haldoupis 2008). Moreover, spacecraft observations of other planets (Jupiter, Saturn) provide evidence of short duration radio emissions in connection with lightning on those planets (Fischer et al. 2008).

Gamma- and X-rays (Bremsstrahlung) Referring to the above discussion of the general physics of breakdowns it can be expected that radiation is emitted from breakdown discharges in the optical to X-ray ranges. An early prediction (Wilson 1925, 1956) based on the Townsend mechanism that lightning should be accompanied by the generation of energetic electrons and possibly by the emission of X-rays has been confirmed by the more recent BATSE experiment aboard the Compton Gamma Ray Observatory (Fishman et al. 1994) and by the Alexis spacecraft observations (Blakeslee et al. 1989; Holden et al. 1995). Gamma radiation is believed to be caused by the energetic electron component generated in the runaway phase of the discharge when avalanches of electrons are formed. In the light of the above discussion on holes it is the fast cold high energy electron beam that is responsible for their emission. The radiation mechanism has been investigated theoretically (Gurevich et al. 1992, 2000, 2001, 2002; Roussel-Dupré et al. 1994, 1996). Since very high energy electrons are required to generate these Gamma ray bursts the observations completely falsify Wilson's mechanism while they are in excellent agreement with the RBD mechanism, providing a strong argument in favour of runaway breakdown and lowering of the avalanching threshold. The gamma rays observed are not caused in a nuclear interaction, and no gamma lines have been detected yet. They form the high energy tail of the energetic X-ray emission resulting from free-free ('bremsstrahlung') radiation of the most energetic runaway electrons. The absence of lines is an indication for the existence of an upper threshold of the accelerating electric field.

Radio waves: Plasma processes Any emitted high-frequency radio radiation can hardly be via the synchrotron process (Rybicki and Lightman 1979) as this requires much higher emission measures, i.e. large volumes occupied by energetic electrons in addition to much stronger magnetic fields, than those which are available. The only imaginable mechanisms are plasma mechanisms like the head-on interaction of beam generated Langmuir (L) waves due to a process $L + L' \rightarrow T$ (where T is the transverse long-wavelength radio wave). This process is shown schematically in Fig. 5.

Generated by the cold fast electron beam, L-waves propagate in the direction of the beam. The backward moving L' -wave can be generated by backscattering of the L-wave by the slow cold ion component according to the process $L + i \rightarrow L' + i^*$. Here i is the involved ion, L' the backscattered Langmuir wave, the wave vector direction of which is reversed, and i^* is the excited ion (which emits light). L-waves can also interact with low frequency ion sound

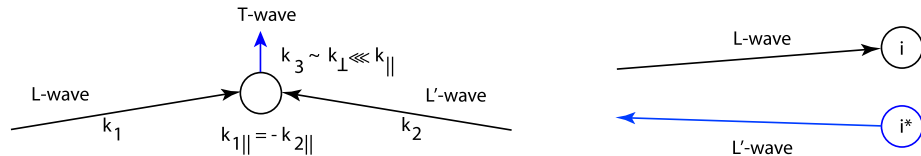


Fig. 5 *Left:* The $L + L' \rightarrow T$ plasma wave process for generation of electromagnetic radiation T . The large parallel wave numbers k_{\parallel} of the counterstreaming Langmuir waves cancel, and a transverse wave of frequency $\omega_3 = \omega_1 + \omega_2 \approx 2\omega_{pe}$ (with very small perpendicular wave number $k_3 \sim k_{\perp} \ll k_{\parallel}$ and therefore large phase and group velocities $\sim c$) is emitted. *Right:* Scattering of an L -wave by an ion i as a process in which an L' -wave is generated. i^* is the excited ion which is left over after the ‘collision’ with the L -wave

waves (IS) according to the reaction $L + IS \rightarrow T$, following the same scheme as shown in Fig. 5. This process has a lower efficiency than the $L + L'$ process, though. In the former case the frequency of the emitted radio wave is close to twice the plasma frequency $\omega_3(L+IS) \approx 2\omega_{pe}$. Because the frequency $\omega_{is} \ll \omega_{pe}$ of the IS -wave is much smaller than the electron plasma frequency, the process $L + IS$ emits radiation of frequency near the plasma frequency: $\omega_3(L+IS) \sim \omega_{pe}$. For avalanche beams of density $n_e \sim 10^{10} \text{ m}^{-3}$ this frequency is about $\sim 1 \text{ MHz}$.

Excitation of electron-acoustic waves (EA) of frequency close to a fraction of ω_{pe} can also contribute to HF-radio emission. The reaction equation is $L + EA \rightarrow T$, and the frequency is above but close to ω_{pe} , typically $\omega_3(L + EA) \lesssim 1.5 \omega_{pe}$. All these mechanisms depend crucially on the presence of a hot plasma electron component, of cool ions, and only a small admixture of cold background electrons. These requirements imply that a substantial fraction of the neutral atmospheric components has been locally expelled from the avalanche region.

Radio waves: Electron-cyclotron maser Very intense HF-radio waves can be generated by the electron-cyclotron maser (Treumann 2006, for a recent review). This is an extraordinarily efficient process. Its requirements are a strong field-aligned electric potential difference, parallel current flow and a strong geomagnetic field in addition to a negligible component of cold electrons and neutrals. It also requires some pitch angle scattering of the electron distribution such that the electrons have a substantial velocity component perpendicular to the geomagnetic field. Again, this mechanism can be realised only if the neutral atmospheric gas is expelled from the avalanching electron cloud. The electron-cyclotron maser is a direct process in which no other catalysing waves are involved. It generates long wavelength ($\lambda_{ecm} \sim$ few 100 m) electromagnetic radiation at the local electron cyclotron frequency $\omega_{ecm} \sim \omega_{ce}$, which in the atmosphere is in the MHz range. The bandwidth of the emitted radiation depends on the electron beam temperature ranging from very narrow ($\ll \omega_{ce}$) up to a substantial part of the electron cyclotron frequency.

References

- M. Aguilar-Benitez et al., Reviews of particle properties. Phys. Lett. B **239** (1990)
- E.V. Appleton, *Nobel Lectures 1947, Physics 1942–1962* (Elsevier, Amsterdam, 1964), pp. 79–86
- L.P. Babich et al., Phys. Lett. A **245**, 460 (1998)
- J.J. Balmer, Annalen Phys. Chem. **25**, 80–85 (1885)
- W. Baumjohann, R.A. Treumann, *Basic Space Plasma Physics* (Imperial College Press, London, 1996)
- V.A. Bernshtam, Yu.V. Ralchenko, Y. Maron, J. Phys. B: Atm. Mol. Opt. Phys. **33**, 5025–5032 (2000)
- T. Bosinger, S. Shalimov, Space Sci. Rev. (2008, this issue). doi:[10.1007/s11214-008-9333-4](https://doi.org/10.1007/s11214-008-9333-4)

- R.J. Blakeslee, H.J. Christian, B. Vonnegut, *J. Geophys. Res.* **94**, 13135 (1989)
- B. Bowers, *A History of Electric Light and Power* (Peter Peregrinus Ltd., London, 1991)
- B. Bowers, *Lightening the Day. A History of Lighting Technology* (Oxford Univ. Press, Oxford, 1998)
- O. Buneman, *Phys. Rev. Lett.* **1**, 8–9 (1958)
- C.W. Carlson et al., *Geophys. Res. Lett.* **25**, 2017 (1998)
- S. Chapman, *Proc. Phys. Soc.* **43**, 26 (1931)
- K.T. Compton, I. Langmuir, *Rev. Mod. Phys.* **2**, 123–242 (1930)
- I. Langmuir, K.T. Compton, *Rev. Mod. Phys.* **3**, 191–258 (1931)
- W. Crookes, *Phil. Trans. R. Soc. Lond.* **170**, 135 (1879)
- S.A. Cummer, U.S. Inan, *Geophys. Res. Lett.* **24**, 1731–1734 (1997)
- H. Davy, *Phil. Trans. R. Soc. Lond.* **97**, 1–56 (1807)
- R.C. Davidson, *Methods in Nonlinear Plasma Theory* (Academic Press, New York, 1972)
- P. Debye, E. Hückel, *Physikalische Zeitschrift* **24**, 185–206 (1923)
- J.R. Dwyer et al., *Science* **299**, 694–697 (2003)
- U. Ebert et al., *Plasma Sourc. Sci. Technol.* **15**, S118–S129 (2006)
- R.C. Elphic et al., *Geophys. Res. Lett.* **25**, 2025 (1998)
- R.E. Ergun et al., *Geophys. Res. Lett.* **25**, 2033 (1998)
- R.E. Ergun et al., *Geophys. Res. Lett.* **28**, 3805 (2001)
- R.E. Ergun et al., *Phys. Plasmas* **10**, 454 (2003)
- M. Faraday, *Experimental Researches, Series III* (1833)
- M. Faraday, *Phil. Trans. R. Soc.* **124**, 77 (1834)
- W.M. Farrell et al., *J. Geophys. Res. E* **104**, 3795 (1999)
- G. Fischer et al., *Space Sci. Rev.* (2008, this issue)
- G.J. Fishman et al., *Science* **264**, 1313 (1994)
- J. Franck, G. Hertz, *Verh. Dtsch. Phys. Ges.* **16**, 457–467 (1914)
- R.C. Franz, R.J. Nemzek, J.R. Winckler, *Science* **249**, 48–50 (1990)
- M. Füllekrug, S.C. Reising, *Geophys. Res. Lett.* **25**, 4145–4148 (1998)
- M. Füllekrug, A.C. Fraser-Smith, S.C. Reising, *Geophys. Res. Lett.* **25**, 3497–3500 (1998)
- M. Füllekrug, D.R. Moudry, G. Dawes, D.D. Sentman, *J. Geophys. Res.* **106**, 20189–20194 (2001)
- M. Füllekrug, M. Ignaccolo, A. Kuvshinov, *Radio Sci.* **41**, RS2S19 (2006a). doi:[10.1029/2006RS003472](https://doi.org/10.1029/2006RS003472)
- M. Füllekrug, E.A. Mareev, M.J. Rycroft (eds.), *Sprites, Elves and Intense Lightning Discharges*. NATO Sci. Ser. II (Springer, Heidelberg, 2006b), p. 225
- C.S. Gillmor, *Charles Augustin Coulomb* (Princeton Univ. Press, Princeton, 1971)
- A.V. Gurevich, K.P. Zybin, *Phys. Usp.* **44**, 1119–1140 (2001)
- A.V. Gurevich, G.M. Milikh, R. Roussel-Dupré, *Phys. Lett. A* **165**, 463 (1992)
- A.V. Gurevich et al., *Phys. Lett. A* **275**, 101 (2000)
- A.V. Gurevich et al., *Phys. Lett. A* **282**, 180 (2001)
- A.V. Gurevich et al., *Phys. Lett. A* **301**, 320 (2002)
- W. Hittorff, *Wiedemannsche Annalen* **7**, 613 (1879)
- D.N. Holden, C.P. Munson, J.C. Devenport, *Geophys. Res. Lett.* **22**, 889 (1995)
- H.K. Kallmann, *Phys. Rev.* **90**, 153 (1953)
- D. Knight, *Humphry Davy, Science and Power* (Cambridge Univ. Press, Cambridge, 1992)
- I. Langmuir, *Phys. Rev.* **22**, 357 (1923)
- N.G. Lehtinen et al., *Geophys. Res. Lett.* **24**, 2639 (1997)
- M.A. Lieberman, A.J. Lichtenberg, *Principles of Plasma Discharges and Materials Processing* (Wiley, New York, 1994)
- M.V. Lomonossov, Letter to Euler, July 5 (1748)
- T. Lyman, *Nature* **93**, 241 (1914)
- O. Melnik, M. Parrot, *J. Geophys. Res.* **103**, 29107–29118 (1998). doi:[10.1029/98JA01954](https://doi.org/10.1029/98JA01954)
- A. Mika, C. Haldoupis, *Space Sci. Rev.* (2008, this issue)
- E. Mishin, G. Milikh, *Space Sci. Rev.* (2008, this issue). doi:[10.1007/s11214-008-9346-z](https://doi.org/10.1007/s11214-008-9346-z)
- H.M. Mott-Smith, *Nature* **233**, 219 (1971)
- P.J. Nahin, *Scientific Am.*, June issue, 122–129 (1990)
- T. Neubert, *Science* **300**, 747–749 (2003)
- D.L. Newman, M.V. Goldman, R.E. Ergun, *Phys. Plasmas* **9**, 2337 (2002)
- M. Parrot et al., *Space Sci. Rev.* (2008, this issue). doi:[10.1007/s11214-008-9347-y](https://doi.org/10.1007/s11214-008-9347-y)
- F. Paschen, *Ann. Phys.* **27**, 537–570 (1908)
- V.P. Pasko, *Plasma Sources Sci. Technol.* **16**, S13–S29 (2007)
- Yu.P. Raizer, *Gas Discharge Physics* (Springer, New York, 1997)
- S.C. Reising, U.S. Inan, T.F. Bell, *Geophys. Res. Lett.* **23**, 3639–3642 (1996)
- N.O. Renno, J. Kok, *Space Sci. Rev.* (2008, this issue)

- O.W. Richardson, Phil. Mag. **16**, 740 (1908)
O.W. Richardson, Nobel Lectures 1928 (Elsevier, 1964), pp. 224–236
W. Ritz, Ann. Phys. **25**, 660–696 (1908)
C.J. Rodger, Rev. Geophys. **37**, 317–336 (1999)
W.C. Roentgen, Sitzber. Physik. Med. Ges. **137**, 1 (1895)
R. Roussel-Dupré et al., Phys Rev. E **49**, 2257 (1994)
R. Roussel-Dupré et al., J. Geophys. Res. **101**, 2297 (1996)
R. Roussel-Dupré et al., Space Sci. Rev. (2008, this issue)
G.B. Rybicki, A.P. Lightman, *Radiative Processes in Astrophysics* (Wiley, New York, 1979)
M.J. Rycroft et al., Space Sci. Rev. (2008, this issue). doi:[10.1007/s11214-008-9368-6](https://doi.org/10.1007/s11214-008-9368-6)
D.D. Sentman et al., Geophys. Res. Lett. **22**, 1205–1208 (1995)
F. Simões et al., Space Sci. Rev. (2008, this issue)
J.J. Thomson, Phil. Mag. **44**, 293 (1897)
E. Townsend, Phil. Mag. **1**, 198 (1901)
E. Townsend, *Electricity in Gases* (Oxford Univ. Press., Oxford, 1915)
R.A. Treumann, Rev. Astron. Astrophys. **13**, 229–315 (2006)
R.A. Treumann, W. Baumjohann, *Advanced Space Plasma Physics* (Imperial College Press, London, 1997)
R. Watson-Watt, Sir, The Scientific Monthly, December issue, 353–358 (1950)
C.T.R. Wilson, Proc. R. Soc. Lond. **37**, 32D (1925)
C.T.R. Wilson, Proc. R. Soc. Lond. **236**, 297 (1956)
Y. Yair et al., Space Sci. Rev. (2008, this issue). doi:[10.1007/s11214-008-9349-9](https://doi.org/10.1007/s11214-008-9349-9)

Ionisation Processes in Planetary Atmospheres

Cosmic Ray Induced Ion Production in the Atmosphere

**G.A. Bazilevskaya · I.G. Usoskin · E.O. Flückiger · R.G. Harrison · L. Desorgher ·
R. Bütkofer · M.B. Krainev · V.S. Makhmutov · Y.I. Stozhkov · A.K. Svirzhevskaya ·
N.S. Svirzhevsky · G.A. Kovaltsov**

Originally published in the journal Space Science Reviews, Volume 137, Nos 1–4.
DOI: [10.1007/s11214-008-9339-y](https://doi.org/10.1007/s11214-008-9339-y) © Springer Science+Business Media B.V. 2008

Abstract An overview is presented of basic results and recent developments in the field of cosmic ray induced ionisation in the atmosphere, including a general introduction to the mechanism of cosmic ray induced ion production. We summarize the results of direct and indirect measurements of the atmospheric ionisation with special emphasis to long-term variations. Models describing the ion production in the atmosphere are also overviewed together with detailed results of the full Monte-Carlo simulation of a cosmic ray induced atmospheric cascade. Finally, conclusions are drawn on the present state and further perspectives of measuring and modeling cosmic ray induced ionisation in the terrestrial atmosphere.

Keywords Atmosphere · Ionisation · Cosmic rays

1 Introduction

Cosmic rays are energetic particles of extra-terrestrial origin, which impinge upon the Earth's atmosphere. The galactic cosmic rays (CRs) are charged particles (comprising

G.A. Bazilevskaya (✉) · M.B. Krainev · V.S. Makhmutov · Y.I. Stozhkov · A.K. Svirzhevskaya ·
N.S. Svirzhevsky
Lebedev Physical Institute Russian Academy of Sciences, Leninsky Prospect, 53, Moscow 119991,
Russia
e-mail: bazilevs@fian.fiandns.mipt.ru

I.G. Usoskin
Sodankylä Geophysical Observatory, University of Oulu, P.O. Box 3000, Oulu, Finland
e-mail: ilya.usoskin@oulu.fi

E.O. Flückiger · L. Desorgher · R. Bütkofer
Physikalisches Institut, University of Bern, Sidlerstrasse 5, 3012 Bern, Switzerland

R.G. Harrison
University of Reading, Earley Gate, P.O. Box 243, Reading RG6 6BB, UK

G.A. Kovaltsov
Ioffe Physical-Technical Institute, St. Petersburg 194021, Russia

mostly protons, $\sim 10\%$ He nuclei and $\sim 1\%$ other elements; electrons comprise $\sim 1\%$) with energies from about 1 MeV ($1 \text{ MeV} = 1.6 \cdot 10^{-13} \text{ J}$) up to at least $5 \cdot 10^{13} \text{ MeV}$ (8 J) (Grieder 2001; Dorman 2004). Low-energy particles are just absorbed in the atmosphere, but those with energies above some 1000 MeV generate new particles through interactions with atomic nuclei in air. Energetic cosmic rays initiate nuclear-electromagnetic cascades in the atmosphere, causing a maximum in secondary particle intensity at the altitude of 15–26 km depending on latitude and solar activity level, the so-called Pfotzer maximum (Bazilevskaya and Svirzhevskaya 1998). The galactic CRs arrive at the Earth constantly but their intensity is modulated by the 11-year cycle of solar activity with the opposite phase i.e. the higher solar activity, the lower the intensity of galactic CRs. Solar CRs (also called solar energetic particles, SEP) are particles accelerated during the explosive energy release at the Sun and by acceleration processes in the interplanetary space (Lario and Simnett 2004). They intrude into the atmosphere sporadically, with a higher probability during periods of high solar activity. Due to their steep energy spectrum, only a small fraction of SEPs with energy around several GeV generates cascades in the atmosphere sufficiently to allow neutron monitors to record a so-called ground-level enhancement, GLE (Miroshnichenko 2004). Another energetic particle population is that of magnetospheric electrons which can precipitate into the atmosphere. They are absorbed in the upper atmosphere, but the X-rays produced by these electrons can penetrate down to the altitude of about 20 km. Electron precipitation occurs more often during the declining phase of the 11-year solar cycle.

The geomagnetic field determines which particles arrive at the Earth at different latitudes, i.e. the geomagnetic field acts as a charged particle discriminator. Motion of a charged particle in the geomagnetic field depends on the particle rigidity $R = cP/ze$, where c is the speed of light, P and z are the particle momentum and ionic charge number respectively and e is the elementary charge. Particles with equal rigidities move in a similar way in a given magnetic field. Roughly speaking, each geomagnetic latitude may be characterised by a cutoff rigidity, R_c , such that particles with less rigidity cannot arrive at this latitude (Cooke et al. 1991). Low-energy particles can therefore only arrive at high latitudes. Only particles with $R > 15 \text{ GV}$ (kinetic energy $> 14 \text{ GeV}$) are able to reach equatorial regions.

In the course of last decades CRs have attracted growing attention as a major source of atmospheric ionisation. This is because CRs are the most important contributor to ion-pair production from $\sim 3\text{--}4 \text{ km}$ up to about 50 km. Ions are involved in many atmospheric processes. In particular numerous studies suggest that ionisation due to CR may affect different climate parameters such as cloud cover (Pudovkin and Veretenenko 1995; Svensmark and Friis-Christensen 1997; Feynman and Ruzmaikin 1999; Marsh and Svensmark 2000; Pallé et al. 2004; Usoskin et al. 2004b; Harrison and Stephenson 2006; Usoskin et al. 2006; Voiculescu et al. 2006), precipitation (Stozhkov et al. 1996; Kniveton and Todd 2001; Stozhkov 2003; Kniveton 2004), cyclogenesis in mid- to high-latitude regions (Tinsley et al. 1989; Tinsley and Deen 1991; Pudovkin and Veretenenko 1996; Veretenenko and Thejll 2004), atmospheric transparency (Roldugin and Vashenyuk 1994; Veretenenko and Pudovkin 1997; Roldugin and Tinsley 2004), aerosol formation (Shumilov et al. 1996; Mironova and Pudovkin 2005; Kazil et al. 2006). Some investigations offer possible mechanisms responsible for the observed phenomena, such as the effect of the cosmic ray induced ionisation (CRII) on the global electric circuit (Tinsley and Zhou 2006; Tinsley et al. 2007) or ion-induced nucleation (Svensmark et al. 2007). However, despite extensive theoretical and phenomenological studies, detailed physical mechanisms connecting CRs with the climate parameters remain not fully understood. Thus, it is crucially important to increase the level of understanding of the CR-related changes in the atmospheric ionisation via both systematic and improved measurements and reliable modeling.

2 Measurements of Ionisation in the Atmosphere

2.1 Measurements of Ionisation in the Lower Atmosphere

Although direct measurements of CRs were not made until the twentieth century, early observations of atmospheric electricity measured CRs indirectly, through determining the electrical properties of air. From the late eighteenth century it was known that an electric field continually existed in the fair weather atmosphere, and air had a finite electrical conductivity (Harrison 2004). If there is no appreciable contribution from surface sources of radioactivity, the electrical conductivity arises from the small ions produced by CRs.

2.1.1 Air Conductivity in the Troposphere

The electrical conductivity of aerosol-free air in the troposphere is related to the number concentration of small ions (cluster ions) contained. The total conductivity, σ , is given by

$$\sigma = e(\mu_+ n_+ + \mu_- n_-), \quad (1)$$

where n_+ and n_- are the positive and negative small ion number concentrations respectively, and μ_+ and μ_- are the positive and negative ion mobilities. An important factor in determining the ion concentration is the volumetric ion production rate, q , which, away from the continental surface, is dominated by CR ion production. In aerosol-free air, the mean ion concentration n is given by

$$n = \sqrt{q/\alpha}, \quad (2)$$

where α is the ion-ion recombination rate, which, for cluster ions in surface air, is typically $1.6 \cdot 10^{-6} \text{ cm}^3 \text{ sec}^{-1}$ (Chalmers 1967). In polluted air, containing Z aerosol particles per unit volume, n is given by

$$n = \frac{q}{\beta Z}, \quad (3)$$

where β is the ion-aerosol attachment rate. Both Z and β are local properties of the air concerned, however α generally has an approximately constant value.

Clean air therefore provides the simplest case for retrieval of ion production rate information, and in suitable circumstances, such as marine air or on balloon ascents, air conductivity measurements provide a measure of CR ion production. Routine air conductivity measurements were made by the UK Meteorological Office (Dobson 1914) from the first decade of the twentieth century using the Ebert (Ebert 1901; Harrison 2007) or Wilson (Wilson 1908; Harrison and Ingram 2004) methods, and historical measurements from other occasional campaigns (Wilson 1908; Carse and MacOwan 1910; Ansel 1912; Wright and Smith 1916; Ault and Mauchly 1926) are also available.

2.1.2 Air Conductivity Measurements on Manned Balloon Ascents

Manned hydrogen-filled balloons provided the primary measurement platform for early research into the electrical properties of the atmosphere, including air conductivity (Harrison and Bennett 2007). The altitude reached was limited to about 10 km, as no oxygen was carried for the aeronauts. The first measurements of ion concentration were obtained using an Ebert ion counter (Ebert 1901), but a new air conductivity instrument was developed for balloon ascents by Gerdien (Gerdien 1905), which bears his name. The Gerdien

condenser operates using an aspirated concentric cylinder electrode system, with an inner, well-insulated electrode charged to a large potential from a battery. From the voltage decay time, the air conductivity was calculated (Chalmers 1967). Alternate measurements of the positive and negative conductivity were made by varying the polarity chose for the central electrodes' bias voltage. Modern balloon measurements of the ion concentration in the atmosphere (Rosen and Hofmann 1988; Ermakov et al. 1997) have yielded a great diversity of results. Even accounting for different latitudes and solar activity levels, the ion concentrations obtained are not consistent with each other, which appears likely to be due to the varying extent of aerosol pollution.

2.1.3 Measurement of Air Conductivity at Various Latitudes

Oceanic measurements of air conductivity using Gerdien instruments were made by geo-magnetic survey ships from about 1907, notably on the voyages of the *Galilee* and *Carnegie*. Analysis of these air conductivity measurements showed an aerosol effect in the North Atlantic (Wait 1946), but this was not present in measurements made in the Pacific (Cobb and Wells 1970). Using equation (2), and assuming a mean ion mobility μ of $1.2 \text{ cm}^2 \text{ V}^{-1} \text{ s}^{-1}$, q is found to be $1.6 \pm 0.2 \text{ cm}^{-3} \text{ s}^{-1}$, which is close to the typical “modern” value for cosmic ray ion production at the ocean surface of $2 \text{ cm}^{-3} \text{ s}^{-1}$ (Hensen and van der Hage 1994).

2.2 Direct Observations of the Ion Production Rate and Ionising Particle Fluxes in the Atmosphere

2.2.1 Early Investigations in the Atmosphere

Early quantitative investigations of CRs measured the ions produced in a fixed volume of gas, within a device known as an ionisation chamber. Victor Hess, who discovered CRs, used ionisation chambers on his balloon ascents, notably the landmark flight of 7th August 1912 (Hess 1912), from which the extra-terrestrial and non-solar origin of cosmic rays was confirmed.

An ionisation chamber contained a fixed amount of gas at atmospheric pressure, with a collecting electrode biased to a constant initial potential. The electrode's potential was measured using an electrometer. Radiation passing through the chamber generated ion pairs, some of which (unipolar ions of opposite sign to the collecting electrode potential) were collected by the electrode. The measured current was proportional to the number of ion pairs created (Smith 1966). Practical disadvantages of ionisation chambers were that they excluded the ionisation effect of the lower part of the CR energy spectrum (Simpson 2000), and radioactivity within the material comprising the chamber walls could lead to erroneous findings.

The ascent made by Hess on 7 August 1912 is an important event in the history of cosmic ray research. Three different ionisation chamber instruments were used to measure ionisation rate, and the ionisation was by γ -radiation due to the thick zinc walls of the ionisation chambers. One instrument was not made airtight and had thinner walls to allow “soft rays” (β -radiation) to penetrate. The ionisation rate profile, produced from the mean of the three instruments recordings averaged from 88 observations, is shown in Fig. 1.

Starting in the 1930s, investigations of CRs in the atmosphere were actively developed using ionisation chambers, Geiger counters, emulsions and other techniques. Unlike ionisation chambers measuring the rate of ion production, gas-discharged Geiger counters and scintillation counters return the flux of ionising particles. In 1933–1934, E. Regener found

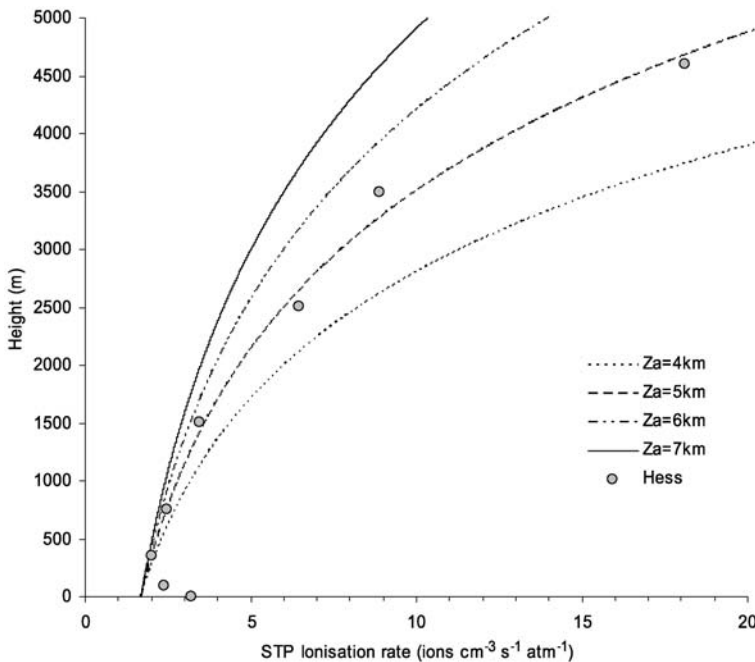


Fig. 1 Profile of the average volumetric ion production rate observations from the 7th August 1912 ascent by Victor Hess, compared with different modelled scale height reference altitudes Z_a (from Harrison and Bennett 2007)

a general form of altitude profile of ionising particle flux in the atmosphere (Regener 1934). However it was not until 1935 that Regener's pupil G. Pfotzer established for certain that the ionising particle flux in the atmosphere reached a maximum value at heights of ~ 15 km (Pfotzer 1936). The dependence of particle flux or ionisation rate on the residual atmospheric depth¹ (or the height in the atmosphere) is called a transition curve with the Pfotzer maximum. Later cosmic ray observations in the atmosphere were directed to investigating the nature of the primary radiation, exploration of geomagnetic effects and the influence of solar activity on charged particle fluxes (Neher and Pickering 1942; Winckler and Anderson 1957; Nerukar and Webber 1964; Neher 1967; Neher 1971). In the spacecraft era these investigations became possible outside the Earth's atmosphere.

2.2.2 Ground-Based Cosmic Ray Flux Monitoring

As well as on the primary instrument in balloon ascents, ionisation chambers were also carried on geophysical exploration cruises. Chambers were carried on the geophysical and atmospheric electrical research ship *Carnegie*, on its voyages between 1915 and 1929. The ionisation chamber used on the *Carnegie* was a copper chamber of about 22 litres in volume, larger than those commonly used at the time (Ault and Mauchly 1926). “Penetrating radia-

¹ Atmospheric depth is the amount of the atmospheric matter in g/cm² overburden at a given level in the atmosphere. It is directly related to the barometric pressure so that the sea level (1013 hPa barometric pressure) corresponds to the atmospheric depth of 1033 g/cm².

tion” measurements were made on Carnegie cruises IV and VI, between 1915 and 1921 and show a variation with geomagnetic latitude, up to about $\sim 50^\circ$ (Aplin et al. 2005).

In the middle of the 1930s a special ionisation chamber was developed for permanent ground-based monitoring of CR fluxes (Compton et al. 1934). Continuous data have been obtained from the identical chambers situated at Godhavn (Greenland), Cheltenham (Maryland), Huancayo (Peru), and Christchurch (New Zealand). Their main drawback was a possible uncontrolled instrumental drift due to the “decay of radioactive contamination in the main chamber or in the balance chamber” (Forbush 1954; McCracken and Beer 2007), which is difficult to account for. Recovery of historical data to extend data series backwards in time is not a trivial task and yields controversial results. For example, Ahluwalia (1997) suggested, using data from ionisation chambers operating at Cheltenham/Fredericksburg (1937–1972) and Yakutsk (1953–1994), that the ionisation and the CR flux remained at roughly the same level throughout the last century (see also Okhlopkov and Stozhkov 2005). Recently however, McCracken and Beer (2007) revised this conclusion, using calibration against the intermittent balloon-borne ionisation data available since 1933 (e.g., Bowen et al. 1934), and found a significant trend in CR induced ionisation between 1930’s and 1950’s. The question on the long-term trend in ionisation data still remains open, and therefore recovering indirect sources of data is important in establishing the long-term behaviour of atmospheric ionisation (Harrison and Bennett 2007).

In the 1950s, J. Simpson established a world-wide ground-based neutron monitor network for permanent observation of cosmic ray temporal variations (Simpson 2000). This proved to be extremely fruitful both for cosmic ray investigation and study of links between cosmic rays and other solar and terrestrial phenomena. The neutron monitor network is now an indispensable source of information for investigation of both space and atmospheric CR effects. However the neutron monitor is sensitive to the nucleon component of CRs which, although substantial in the stratosphere, contributes little in the particle fluxes in the troposphere.

2.3 Ionising Particle Fluxes at Various Latitudes and Heights in the Atmosphere

2.3.1 Long-Term Cosmic Ray Observations in the Atmosphere

A detailed series of atmospheric ion production rate observations was conducted in the late 1960s (Neher 1967; Neher 1971; Anderson 1973). The measurement was performed using balloon-carried ionisation chambers. The standard chambers had steel walls 0.6 mm thick and were filled with air at 740 mm Hg pressure. The chamber temperature of 24°C was regulated to within $\pm 10^\circ\text{C}$ during a balloon flight, and the temperature sensitivity of the chamber was less than $0.02^\circ/\text{C}$. A latitude survey with long-term observations covering 1954–1969 was accomplished. In 1969–1970 another series of cosmic ray atmosphere ionisation and charged particle fluxes measurements was conducted by Lowder et al. (1972). Balloon flights were made at geomagnetic latitudes of 42°N and $52\text{--}54^\circ\text{N}$. These flights used an ionisation chamber similar to the one, used by the Neher group, but the results appeared about 20% lower than the Neher data although the claimed accuracy was $\sim 5\%$. This discrepancy remains unexplained. Later we use the Neher results on ionisation rate for intercalibration.

There is a close relation between the charged particle flux and the ion production rate in the atmosphere (Bazilevskaya et al. 2000; Ermakov et al. 2007; Stozhkov et al. 2007). The most long-lasting observations of charged particles fluxes in the atmosphere (actually the ionising component of cosmic rays) have been performed by the cosmic ray group

of Lebedev Physical Institute (LPI) from 1957 to the present time (Charakhchyan 1964; Bazilevskaya and Svirzhevskaya 1998; Stozhkov et al. 2004, 2007a). The experiment is directed to investigations of CR modulation by solar activity. Meteorological balloon programmes using radiosondes carrying a double-Geiger counter detector system are summarised in Table 1.

The charged particle detector consists of two Geiger counters with 0.05 g cm^{-2} steel walls arranged as a vertical telescope, with a 7 mm (2 g cm^{-2}) thick aluminium filter inserted between the counters. The operating sizes of the counters are: 9.8 cm length and 1.8 cm in diameter. A single counter records the omnidirectional flux of charged particles: electrons with energy $E_e \geq 0.2 \text{ MeV}$, protons with $E_p \geq 5 \text{ MeV}$, and muons $E_m \geq 1.5 \text{ MeV}$. The counters are also sensitive to γ -rays but with efficiency lower than 1%, whereas the efficiency for charged particle recording is $\sim 100\%$. Simulation of secondary CR fluxes in the atmosphere showed a good agreement with the fluxes measured by an omnidirectional counter (Desorgher et al. 2005). A telescope records a vertical flux of charged particles within a solid angle of about 1 sr: electrons with $E_e \geq 5 \text{ MeV}$, protons with $E_p \geq 30 \text{ MeV}$, and muons $E_m \geq 15 \text{ MeV}$ (muons with $E_m \leq 100 \text{ MeV}$ are virtually absent in the atmosphere). The radiosonde sensor returns data both on the omnidirectional and vertical fluxes of charged particles in the atmosphere alongside with the residual air pressure (the atmospheric depth), which can be converted to altitude using the standard atmosphere. Homogeneity of the data is maintained through the use of standard detectors (which were unchanged during the whole period of measurement) and careful calibration. Only omnidirectional counter data are presented in this paper.

Measurement of the Neher group and the LPI group overlapped during 1957–1969 allowing rather detailed comparison of the two series. Figure 2 demonstrates the flux of ionising particles, J , and the ion production rate, q and Q , at several latitudes as observed in the minimum of solar activity in 1964–1965. Neher performed a latitude survey in 1965 (Neher 1967). For comparison the CR data are taken from observations at the stationary locations of CR balloon measurements for $R_c = 0.6 \text{ GV}$ and $R_c = 2.4 \text{ GV}$ exactly at the months of Neher's observation. It should be noticed that there was no latitude attenuation in the CR fluxes between $R_c = 0.0 \text{ GV}$ and $R_c = 0.6 \text{ GV}$ because of the “knee-effect” (see below). For the lower latitudes, the CR measurements for 1964 (Charakhchyan et al. 1976a) are compared in Fig. 2 with the ion production data obtained in 1965. However at those latitudes the changes between 1964 and 1965 could not be large. The similarity in altitude dependence of CR flux, J , (left panel of Fig. 2) and ion production rate in the chamber at the atmospheric pressure, Q , (central panel of Fig. 2) is noticeable at middle and low latitudes ($R_c \geq 2.4 \text{ GV}$). The shapes of transition curves for the two groups of data at the polar latitudes ($R_c = 0.0\text{--}0.6 \text{ GV}$) and heights above 20 km are different because of the presence of low-energy, highly-ionising particles (especially, nuclei). The right panel of Fig. 2 gives the ion production rate in free air (ambient atmosphere), q , as derived from the ion chamber measurements. The ion production in free air depends on the flux of ionising particles and the density of ambient air, therefore, the maximum of transition curves shifts to lower altitudes. The relation between q and J is presented in Fig. 3 for different phases of solar activity cycle at polar latitudes ($R_c = 0.0\text{--}0.6 \text{ GV}$) and for different R_c in the solar activity minimum. The ratio q/J is strongly dependent on the height H in the atmosphere and can be approximated as

$$q/J = A \exp(-B \cdot H). \quad (4)$$

It is seen in Fig. 3 that q/J slightly decreases with increase of R_c and growth of solar activity that is due to changes in the ionising particle energy spectrum and composition.

Table 1 Locations and operating modes of the LPI balloon CR measurements

Site	Coordinates	R_c (GV)	Period of measurements	Launches per week
Murmansk region	68°57'N 33°03'E		1957–2002	6–7*
	67°33'N 33°20'E	0.6	since 2002	
Dolgoprudny, Moscow region	55°56'N 37°31'E	2.35	since 1957	5–7*
Alma-Ata, Kazakhstan	43°15'N 76°55'E	6.7	1962–1991	6
Mirny, Antarctica	66°34'S 92°55'E	0.03	since 1963	7*
Simeiz, Crimea	44°N 34°E	5.9	1958–1961, 1964 (Mar–Jul), 1969–1970	3–5
St.-Petersburg (Leningrad)	60°00'N 30°42'E	1.7	1964–1970	3
Norilsk	69°N 88°E	0.6	1974–1982	3
Yerevan, Armenia	40°10'N 44°30'E	7.6	1976–1989	3
Tixie-Bay	71°36'N 128°54'E	0.5	1978–1987	3
Dalnerechensk	45°52'N 133°44'E	7.35	1978–1982	1–3
Barentsburg, Svalbard	78°36'N 16°24'E	0.06	1982 (May), 1983 (Mar–Jul)	2–3
Campinas, Brazil	23°00'S 47°08'W	10.9	1988–1989, 1990–1991	1–3 occasionally
Vostok, Antarctica	78°47S 106°87E	0	1980 (Jan–Feb)	7
Main latitude surveys		0.1–17	1962–1965, 1968–1969, 1970–1971, 1975–1976, 1979–1980, 1986–1987	

*From early 1990s, the launches were made 3–4 times weekly

Averaged over an 11-year cycle and over the latitude dependence, $A = 122.6 \pm 1.3 \text{ cm}^{-1}$, $B = -0.152 \pm 0.001 \text{ km}^{-1}$, H is in km, q in $\text{cm}^{-3} \text{ s}^{-1}$, J in $\text{cm}^{-2} \text{ s}^{-1}$. It should be stressed that expression (4) is not true for SEP events and electron precipitation. Using the approximation (4) and the results of ionising particle measurements, it is possible to derive the ion

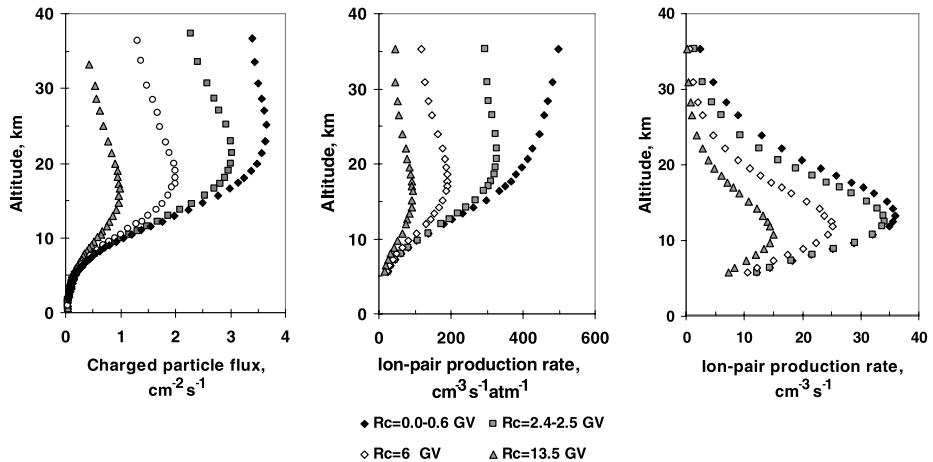


Fig. 2 Left panel: height dependence of ionising particle fluxes J at latitudes with different threshold cutoff rigidities R_c (LPI data). Middle panel: similar to the left panel but for the ion pair production rate in the ionisation chamber (Q) (Neher 1967, 1971). Right panel: the same as at the middle panel but converted to ionisation in free ambient air (q)

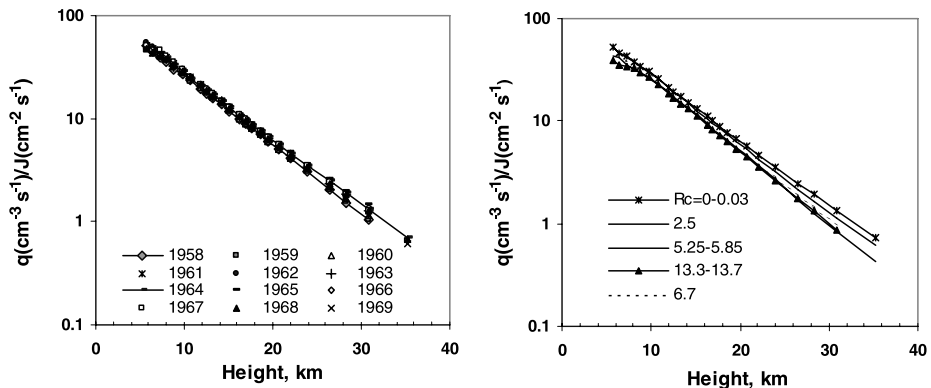


Fig. 3 Ratio of the ion production rate to the charged particle flux vs. altitude in the atmosphere. Left panel: results at polar latitudes during 1958–1969. Right panel: results for different latitudes in the solar activity minimum

production rate. An example is presented in Fig. 4 where the monthly averaged ion production rate inferred from the particles flux measurements is given for three heights in the atmosphere at polar latitude. The Neher data obtained during 1958–1969 are also plotted. Note that the ionisation rate q ($\text{cm}^{-3} \text{s}^{-1}$) at 24 km is smaller than at 6.5 and 11 km. This is because of the small density of ambient air at higher altitudes, and as can be seen in Fig. 2, this would not be so for the ionisation rate Q ($\text{cm}^{-3} \text{s}^{-1} \text{atm}^{-1}$) if the density effect were removed.

2.3.2 Ionising Particles Fluxes at Various Latitudes in the Atmosphere

A geomagnetic effect becomes apparent in the latitudinal dependence of particle fluxes which is different at higher and lower altitudes in the atmosphere. Results of observations

Fig. 4 Time dependence of ion production rate at 24, 11 and 6.5 km at polar latitude as inferred from observation of ionising particles fluxes (LPI monthly averaged data). Results of direct measurement of ionisation rate (Neher 1971) are plotted as black diamonds

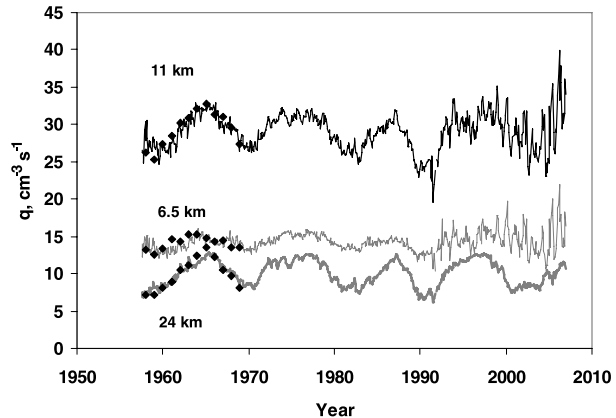
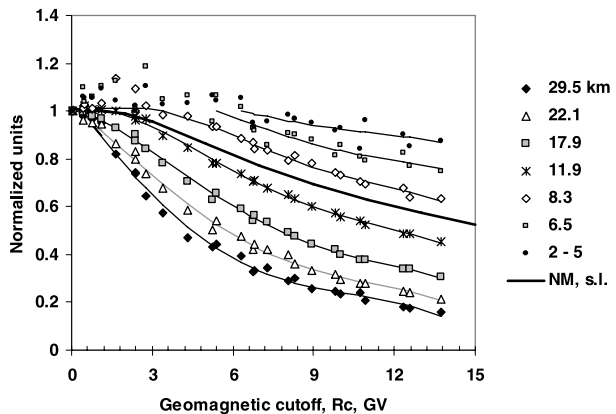


Fig. 5 Latitudinal attenuation (R_c dependence) in the CR ionising component at various heights in the atmosphere (symbols and fitting lines) in comparison with the effect in the neutron monitor count rates (black solid curve, Stoker 1994). Data are normalised at $R_c = 0$ GV



taken during the latitudinal survey in 1987 (Golenkov et al. 1990) normalised to values at $R_c = 0$ GV are plotted in Fig. 5. The balloons were launched from a ship, so the results are not affected by background radioactivity from the continental crust, but the sampling is still poor in the lower altitude. It is seen that the particle flux is virtually constant below a certain value of R_c . This is the CR knee-effect. At high altitudes, the knee-effect is due to the flat CR energy spectrum around hundreds of MeV (rigidity ~ 1 GV). While proceeding to lower altitude, the knee shifts to higher R_c since the progenies of low energy primary particles cannot reach these altitudes. The latitude attenuation in the neutron monitor count rates also measured in the solar activity minimum is presented in Fig. 5 by the solid black curve (Stoker 1994).

2.4 Temporal Variations of Ionising Particle Fluxes in the Atmosphere

Figure 6 presents monthly averaged ionising particle fluxes at selected heights in the atmosphere over the Murmansk region (LPI results). Days when solar or magnetospheric particles invaded atmosphere are excluded. At the altitudes above ~ 8 km, the most prominent variation is an 11-year solar cycle which is in opposite phase to the sunspot number. An important characteristic feature of the long-term solar modulation of CR fluxes—variation in shape between subsequent CR intensity maxima, is clearly evident in Fig. 6. In epochs

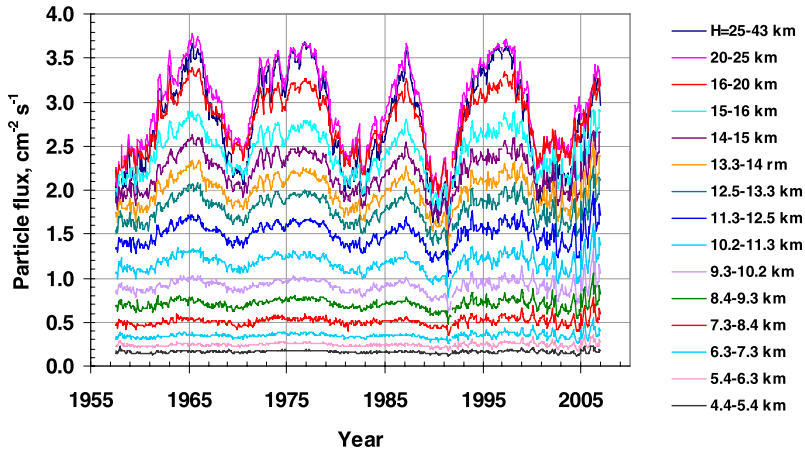


Fig. 6 Monthly averaged fluxes of ionising particles in the atmosphere over Murmansk region as measured by an omnidirectional Geiger counter. Various colors present fluxes at various heights. Days when solar or magnetospheric particles invaded atmosphere are excluded from averaging

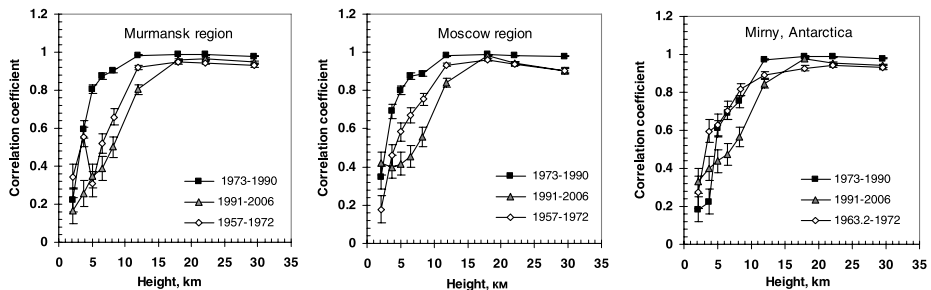


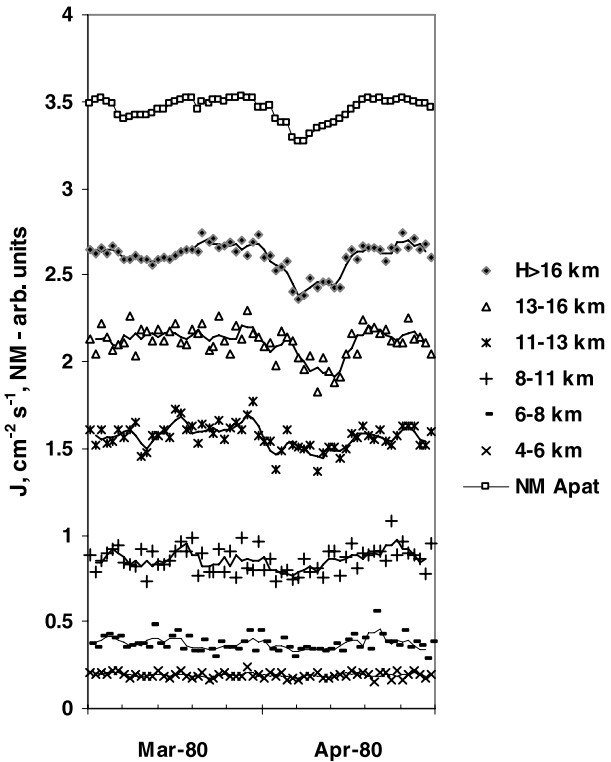
Fig. 7 Correlation between the monthly means of ground-based polar neutron monitor data and fluxes of ionising particles at various heights in the atmosphere. (After Bazilevskaya et al. 2007)

with a positive magnetic field in the northern hemisphere of the Sun (the 1970s and 1990s) the 11-year maximum in CR intensity has a flat top, whereas during the alternate epochs the maximum has a sharp peak (e.g., in 1965, 1987, and forthcoming one in 2007 or later). A similar behaviour should be expected in any atmospheric phenomenon closely connected to CRs.

At altitudes below ~ 6 km, the 11-year modulation becomes weak. Its amplitude is about 15% and it is masked by some other variations. As demonstrated in Fig. 7 above 15 km the correlation coefficient between the values of charged particle flux in the stratosphere and count rates of a ground-based neutron monitor is close to 1 for both high- and mid-latitude stations. While moving deeper in the atmosphere the correlation decreases. Moreover, the height dependence of the correlation coefficient was different before 1973, in 1973–1991, and after 1991. Therefore, neutron monitor data may be correctly used as a proxy of ionising component only for the stratospheric altitudes. No significant trend is observed in the charged particle fluxes in the atmosphere during the last 50 years.

The most prominent short-term changes of the CR flux are Forbush decreases caused by disturbances in the interplanetary magnetic field. Forbush decreases modulate CR with

Fig. 8 Daily data of the Apatity neutron monitor (upper curve, arbitrary units) and charged particle fluxes at various atmospheric heights. Symbols are the daily data, averaged for Murmansk region and obs. Mirny (Antarctica). Curves are the 3-day running mean

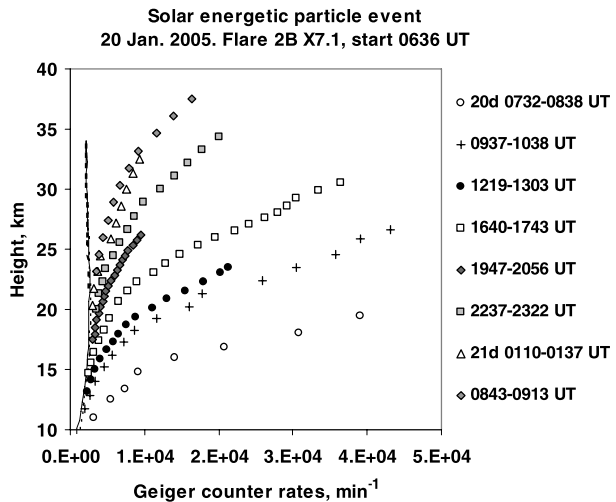


rather high energy thus affecting the atmospheric particle flux at all altitudes and latitudes. The amplitude of a Forbush decrease is only weakly attenuated in the atmosphere. Figure 8 presents a Forbush decrease as recorded by the sea-level Apatity neutron monitor ($\sim 8\%$) along with simultaneous measurements by the LPI instrument at several heights in the atmosphere. The amplitude of the Forbush decrease is $\sim 13\%$ at the heights above ~ 16 km, and $\sim 11\%$ at 6–8 km. However, the Forbush effect is hardly discernible in the LPI data at heights below 6 km because of presence of other variations and poor statistical accuracy.

Solar energetic particles (SEPs) intrude into the atmosphere sporadically (Bazilevskaya 2005). Most of SEPs are just absorbed in the atmosphere leading to the enhanced ionisation in the polar stratosphere. An example is given in Fig. 9. During the first hours after the solar flare start on 20 January 2005, the enhanced ionisation was observed over Murmansk region at the heights above 10 km, where protons with energy $E > 780$ MeV can penetrate. Next morning, 26 hours after the flare, ionisation was increased only above ~ 23 km, where only protons with $E > 220$ MeV can arrive. Because of geomagnetic cutoff, only high-energy SEPs can reach the mid- and low-latitudes, and the SEP effect there is rare and short lasting. The SEP events happen more often in periods of high solar activity. Usually there are between 20 and 30 events for an 11-year solar cycle which produce additional ionisation at heights below 30 km in the polar atmosphere. It should be noted, that only about half of them are powerful enough to essentially enhance the nucleonic component of the atmospheric cascade at the surface, leading to a ground level enhancement (GLE) of neutron monitor count rates.

Another kind of particle invasion in the atmosphere is precipitation of magnetospheric electrons (Makhmutov et al. 2001). Precipitating relativistic electrons form a maximum in

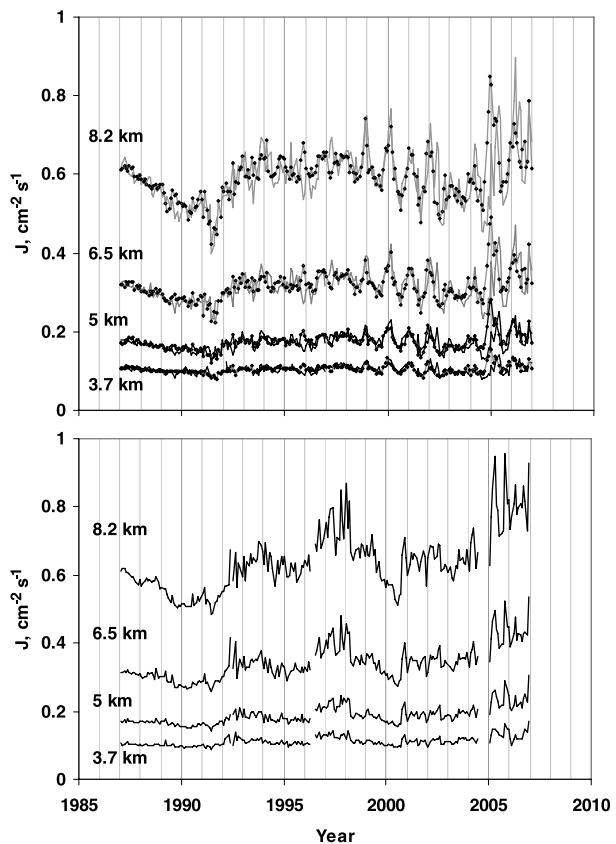
Fig. 9 Intrusion of solar energetic particles during the 20-Jan-2005 event into the atmosphere as recorded in Murmansk region by a Geiger counter versus heights. The dashed curve presents a background due to galactic cosmic rays. Symbols refer to different time of observations



the ion production rate at heights between 50 and 90 km where their energy deposit may sometimes be higher than that of solar UV radiation and CRII. The second maximum in the ion production at about 30 km is due to the bremsstrahlung X-rays generated by precipitating electrons. Here the ionisation rate from X-rays is significantly less than that from galactic CRs (Pesnell et al. 2001). Gamma and X-rays are also generated by galactic CRs in the cascades in the atmosphere, the photon fluxes ($E > 20$ keV) being an order of magnitude higher than the electron ($E > 200$ keV) fluxes (Charakhchyan et al. 1976b). Roughly speaking, the electron and photon fluxes are in equilibrium in the atmosphere. While interacting with the air atoms, X-ray photons generate Compton and photo-electrons; γ -ray photons with $E > 1$ MeV can produce an electron-positron pair. Most of these charged particles have energy below the thresholds of the LPI measurements.

As it is seen in Fig. 6 charged particle fluxes in the atmosphere became more disturbed after 1990, especially at the heights below ~ 12 km. In the same period, the balloon launches became less frequent (see Table 1) therefore enhanced variability could be due to less observational accuracy. However, the disturbances appear to be very similar at Murmansk and Moscow regions and, besides, an annual periodicity can be traced, especially beginning from 1998. There is no such periodicity at Mirny (Antarctica) although an enhanced level of variability is also present. This can be clearly seen in Fig. 10 where the time history of ionising fluxes in the troposphere of Murmansk and Moscow regions (upper panel) and of Mirny (lower panel) is presented. It should be noted that the annual oscillation at the heights 2–6 km is much lower in the Antarctic ($\sim 3\%$) than in the Arctic (8–9%) (Fleming et al. 1990). Maximum particle fluxes are observed in the winter period in the northern hemisphere as it is expected due to the temperature effect of cosmic ray muon component. However, the expected effect is $\sim 5\%$ which is consistent with observations in 1973–1991 (Kurguzova and Charakhchyan 1983). In 1999–2002 and 2005–2006 the annual change in the ionising particle fluxes comprised 15–10%, and $\sim 30\%$, respectively. This annual temperature oscillation can be traced in the atmosphere up to 10–15 km. At the moment, the nature of these variations is not clear.

Fig. 10 Temporal variations of ionising particle fluxes in the troposphere in 1987–2006.
Upper panel: Murmansk region (solid curve) and Moscow region (curve with rhombs); *lower panel:* Mirny (Antarctica)



3 Modelling of Cosmic Ray Induced Ionisation

3.1 Atmospheric Cascade Induced by Cosmic Rays

When an energetic CR particle enters the atmosphere, it first moves straight in the upper layers suffering mostly ionisation energy losses that lead to ionisation of the ambient rarefied air. Therefore, the cosmic ray induced ionisation (CRII) of the upper atmospheric layers (above approximately 25 km) can be easily calculated analytically (Velinov and Mateev 1990). However, after traversing some amount of matter (the nuclear interaction mean free path is of the order of 100 g/cm² for a proton in the air) the CR particle may collide with a nucleus in the atmosphere, producing a number of secondaries. These secondaries have their own fate in the atmosphere, in particular they may suffer further collisions and interactions forming the so-called atmospheric cascade (Dorman 2004). Because of the large amount of matter in the Earth's atmosphere (1033 g/cm²) the number of subsequent interactions can be large leading to a fully developed cascade consisting of secondary rather than primary particles. It is common to divide the cascade into three main components: the “soft” or electromagnetic component which consists of electrons, positrons and photons; the “hard” or muon component consisting of muons (pions are short-lived and decay almost immediately); and the “hadronic” nucleonic component consisting mostly of superthermal protons and neutrons. All charged secondaries ionise the ambient air and their relative role changes with the

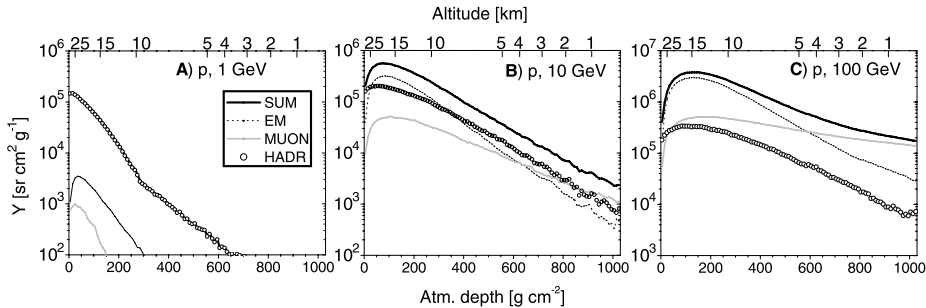


Fig. 11 Ionisation by atmospheric cascade induced by primary CR protons with energy 1 GeV, 10 GeV and 100 GeV (resp. left to right panels) isotropically impinging on the Earth's atmosphere (computations by Usozkin and Kovaltsov 2006). Curves represent: ionisation by the electromagnetic (dotted), the muon (grey) and the hadronic components (open dots) of the cascade, as well as the total ionisation (solid curve). Top X-axis depicts approximate altitude for the standard static atmosphere

energy of primary particles and altitude in the atmosphere. When describing the cascade it is usual to deal with the residual atmospheric depth rather than with the altitude. The reason is that the development of cascade is mostly defined by the amount of matter traversed, while the actual altitude may vary depending on the exact atmospheric density profile. Figure 11, based on a full Monte-Carlo simulation of the atmospheric cascade (Usozkin and Kovaltsov, 2006—see next section) shows the relative role of the three components in ionising the air as a function of the atmospheric depth for three energies of the primary CR proton. For low-energy cosmic rays, CRII is defined only by the hadronic component (Fig. 11A) at all altitudes. The role of the other components increases with increasing CR energy. All the three components are equally important at middle energies of CR particles (Fig. 11B), but they dominate at different altitudes: the soft component at high altitudes ($h < 300 \text{ g/cm}^2$), the muon component near the sea level ($h > 900 \text{ g/cm}^2$), and the hadronic component in the troposphere. The ionisation induced by high-energy cosmic rays (Fig. 11C) is dominated by secondary muons in the lower troposphere ($h > 600 \text{ g/cm}^2$) and by the electromagnetic component at higher altitudes, while the contribution from the hadronic component can be neglected in this case. Therefore, all the three components are important, but play their roles at different altitudes and different energy ranges of primary particles.

3.2 Numerical Models

Because of the atmospheric cascade it is a complicated task to model the CRII process. Earlier it was common to use an analytical approximation for the cascade (O'Brien 1979, 2005), but such models become less reliable in the lower atmosphere. With the progress in computational methods and knowledge of nuclear processes, precise models, based on full Monte-Carlo simulations of the atmospheric cascade, have been developed. There are currently two basic numerical approaches to CRII Monte-Carlo simulations. One is the Bern model (Desorgher et al. 2005) called ATMOCOSMIC/ PLANETOCOSMIC, which is based on the GEANT-4 simulation package. The PLANETOCOSMIC code is available at <http://cosray.unibe.ch/~laurent/planetocosmics/>. Another approach is based on the CORSIKA+FLUKA Monte-Carlo package and has been primarily developed as the Oulu model (Usozkin et al. 2004a; Usozkin and Kovaltsov 2006) and later adopted by other groups (Mishev and Velinov 2007). The two models have recently been the subject of a comparison (Usozkin et al. 2008b) in the framework of the COST-724 action (see

<http://www.cost.esf.org>). Results of the two simulations agree within 10%, the difference being mainly due to the different atmospheric models used and, to a lesser extent, to different cross-section approximations in CORSIKA and GEANT-4 packages. Note that an analytical approximation model of CRII (O'Brien 2005) also shows a reasonable agreement with the present models, especially at higher altitudes.

Generally CRII rate (number of ion pairs produced in one gram of the ambient air per second) at a given atmospheric depth h can be represented in as follows:

$$q(h, \phi, R_c) = \sum_i \int_{E_{c,i}}^{\infty} S_i(E, \phi) Y_i(h, E) dE, \quad (5)$$

where the summation is performed over different i -th species of CR (protons, α -particles, heavier species), $Y_i(h, E)$ is the ionisation yield function (the number of ion pairs produced at altitude h in the atmosphere by one primary CR particle of the i -th type, isotropically impinging on the Earth's magnetosphere with kinetic energy E), $S_i(E, \phi)$ is the differential energy spectrum² of galactic cosmic rays in the Earth's vicinity (given in units of $[\text{cm}^2 \text{ sec sr (GeV/nuc)}]^{-1}$). Integration is performed above $E_{c,i}$, which is the kinetic energy of a particle of i -th type, corresponding to the local geomagnetic cutoff rigidity R_c . Full details of the CRII computations, including a detailed numerical procedure and tabulated Y , are given in Usoskin and Kovaltsov (2006). Note that CRII at a given location and time depends on three variables: altitude (atmospheric depth h) via the integrand yield function Y , geographical location via the geomagnetic cutoff rigidity R_c (integration limits), and solar modulation (the modulation potential ϕ) via the integrand CR spectrum S . Since these three variables are mutually independent, they can be separated in order to solve the problem numerically in an efficient way.

Firstly, using a full Monte-Carlo simulation of the atmospheric cascade, one can compute the yield function Y depending on the atmospheric depth and energy of primary CR particles (see Fig. 11). Then the ionisation can be computed for any given time (i.e., CR modulation potential ϕ) and geographical location (i.e., geomagnetic cutoff rigidity R_c) by integrating equation (5). The effective energy of primary cosmic rays available for ionisation varies with the atmospheric depth, being about 1 GeV/nuc for stratosphere and increasing to about 10–30 GeV/nuc in the low troposphere. An example³ of the dependence of CRII on ϕ and R_c is shown in Fig. 12 for two atmospheric depths of 300 and 700 g/cm². One can see that CRII may vary by a factor of two between polar region at solar minimum and equatorial region during solar maximum. On the other hand, CRII is very sensitive to the altitude as apparent from Fig. 13. The ionisation rate varies by two orders of magnitude between sea level and the maximum (known as the Pfotzer maximum) which is located at 18–20 km in polar regions and moves slightly downwards (about 15 km) in equatorial regions.

3.3 Comparison with Measurements

The modeled CRII can be compared with real measurements of the ionisation rate in the atmosphere. Figure 14 shows a comparison of the model calculations (curves) to the measurements (symbols) for three different conditions: in the polar atmosphere during a solar maximum (panel A); in the equatorial atmosphere during a solar minimum (panel B); and

²The CR spectrum can be uniquely parameterised via the modulation potential ϕ , which is ultimately defined by the solar magnetic activity—see Usoskin et al. (2005). Note that ϕ grows with the solar magnetic activity.

³Results in Figs. 12–16 is given for the Oulu model but the Bern model yields essentially similar results.

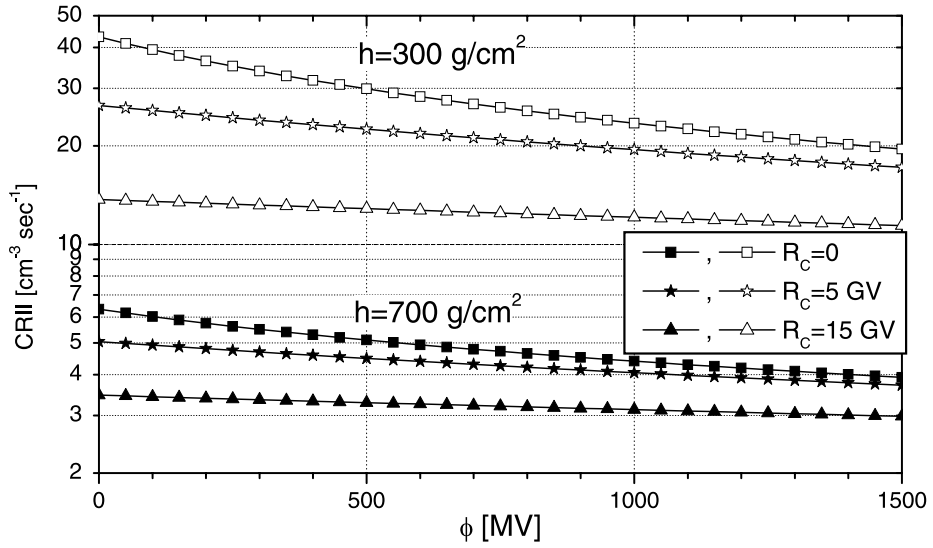


Fig. 12 Modelled CRII as a function of the modulation potential ϕ for different locations and altitudes (computations by Usoskin and Kovaltsov 2006) for two values of the atmospheric depth (700 g/cm^2 —about 3 km altitude; and 300 g/cm^2 —about 9 km). The results are shown for the geomagnetic pole ($R_c = 0$), mid-latitude ($R_c = 5 \text{ GV}$, about 40° geomagnetic latitude) and equator ($R_c = 15 \text{ GV}$)

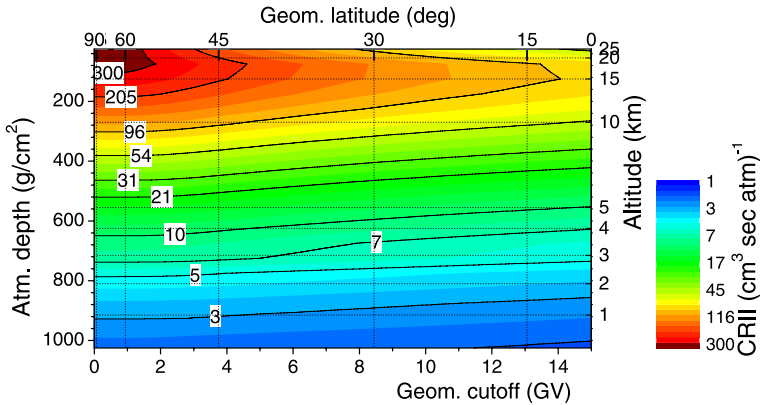


Fig. 13 Modelled CRII as a function of the atmospheric depth h (or altitude—right axis) and R_c (or geomagnetic latitude—upper axis) for medium CR modulation ($\phi = 500 \text{ MV}$)

in the southern UK during moderate solar activity. One can see a good agreement between the model and the measured ionisation rates below $h = 50 \text{ g/cm}^2$ (about 20 km) for all conditions. We note that individual measurements, performed during short balloon flights, can vary depending, e.g., on the exact atmospheric profile, the instrumentation used, exact energy spectrum of CR, etc. On the other hand, the model CRII is computed for average conditions (the standard atmospheric profile, mean modulation potential). Therefore, the observed agreement within 10% is considered good. This is clearly seen in Fig. 14c where the ionisation measured during a single balloon flight is shown and depicts some layer-like

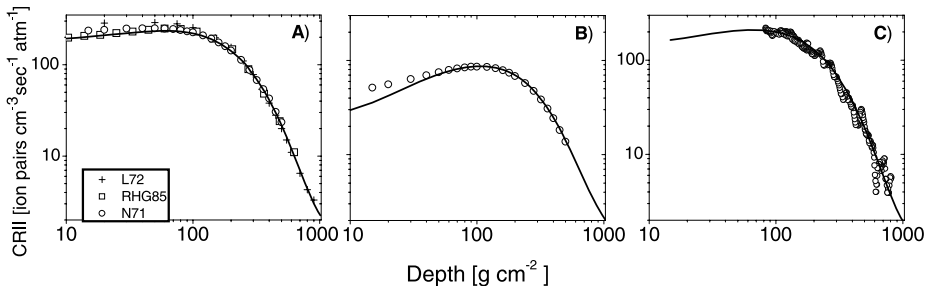


Fig. 14 Agreement between measured (symbols) and modeled (curves) CRII for different conditions. **A)** Polar region at solar maximum. Symbols denote measurements by (L72—Lowder et al. 1972), (RHG85—Rosen et al. 1985), (N71—Neher, 1971), curve depicts CRII at $R_c = 1$ GV, $\phi = 1000$ MV. **B)** Equatorial region at solar minimum. Dots denote measurements by Neher (1971) in July 1965. Curve depicts CRII at $R_c = 15$ GV, $\phi = 420$ MV. **C)** Medium conditions. Dots denote measurements at the University of Reading (Harrison 2005) in the afternoon 18/08/2005. Curve depicts CRII at $R_c = 2.5$ GV and $\phi = 650$ MV

structures and strong fluctuations, especially in the low troposphere. However, the measurements lie close to the modeled smooth curve. In order to precisely reproduce an individual observation, one needs to know the exact atmospheric density and temperature profile appropriate to the instantaneous measurement. In the upper part of the atmosphere (above 50 g/cm²), the model yields somewhat lower CRII than the measurements. This is most likely related to the action of additional ionising agents other than CR (e.g., solar UV-radiation, precipitating low-energetic particles), and possibly due to a wall effect of the detector. Thus, the model CRII calculations agree (within 10%) with the actual measurements in the whole range of possible parameters, for the troposphere and lower stratosphere, and slightly underestimate the ionisation at altitudes above 50 g/cm² (20 km), where other ionising agents become important.

The fact that the model results agree with the real measurements in the wide range of parameters as well as between the different models confirms the validity of the models and their applicability in studying ionisation effects due to cosmic rays in the atmosphere.

3.4 Long-Term Changes

CRII varies quite essentially both spatially (altitude and geomagnetic latitude) and temporally. The temporal variations are dominated by the 11-year solar cycle as discussed in Sect. 2, but CRII demonstrates changes also on longer time scales. E.g., a significant long-term decreasing trend was reported in the ionisation data between 1933 and 1950's (McCracken and Beer 2007). Using intermittent balloon measurements of the air conductivity, Harrison and Bennett (2007) found a systematic decrease of ionisation by roughly 0.15%/year between 1910 and 1950 associated with increasing solar activity. However, because of the lack of systematic direct or indirect measurements, it is difficult to study longer term changes using real data. On the other hand, CRII can be realistically modelled in the past using independent estimates of solar activity and geomagnetic field variations. An example of the modelled CRII variations on multi-centennial time scale is shown in Fig. 15, that is consistent with the observed trends in the first half of 20-th century. One can see that the long-term variations of CRII are comparable or even exceed the 11-year cycle range. The estimated CRII during the Maunder minimum of solar activity (1645–1715) was nearly constant at the level of ≈24% greater than during the recent minima or 31% higher than the average ionisation rate for the last 50 years. It is noteworthy that the period after 1700 AD

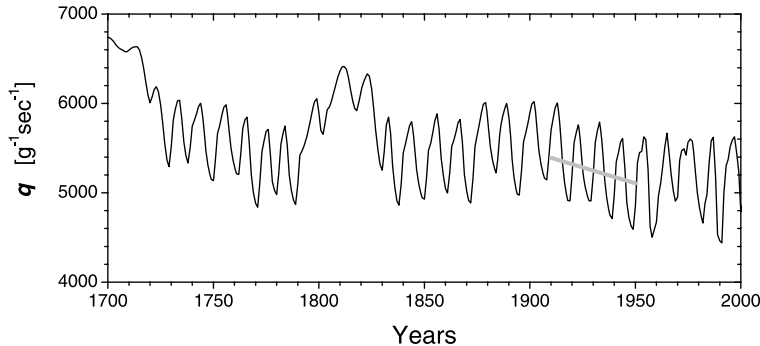


Fig. 15 Time profile of CRII in polar region at $h = 700 \text{ g/cm}^2$ since 1700 AD computed using the solar modulation reconstruction by Usoskin et al. (2002) (adapted from Usoskin and Kovaltsov 2006). Grey line illustrates the 0.15%/year decrease of the atmospheric ionisation between 1910 and 1950 (Harrison and Bennett 2007)

shown in Fig. 15 includes the whole range of solar activity variability, from the deep Maunder minimum to the modern Grand maximum of solar activity (Usoskin et al. 2007). Therefore, the CRII variability due to solar activity changes is not expected to exceed this range. However, changes of the geomagnetic field, leading to the changing cutoff rigidity R_c , can be also quite significant and even more important on the centennial-millennial time scale than solar variability, especially in mid-latitude regions (Kovaltsov and Usoskin 2007; Usoskin et al. 2008a). Because of these geomagnetic changes, the long-term variability of CRII may depend on the geographical location and its effects on, e.g., climate should be studied regionally as global averaging may smear out the effect.

Thus, CRII may undergo variations on long-term timescales caused by both solar activity and geomagnetic changes.

3.5 Effect of Solar Energetic Particles

While the ionisation due to galactic CR is always present in the atmosphere, strong transient changes of the fluxes of energetic particles can occur related to solar eruptive phenomenon (solar flares or coronal mass ejections). In particular SEP events can lead to significant increase of the atmosphere ionisation especially at high altitude in the polar atmosphere (Schröter et al. 2006). As an example, we consider here the ionisation effect of a severe SEP/GLE event of 20/01/2005, which was one of the strongest GLEs ever observed. Time profile of the neutron monitor count rate for this event is shown in Fig. 16A. During the peak at 06:55–07:00 UT, the flux of cosmic ray as measured by the South Pole NM increased by about 500% due to arrival of highly anisotropic SEPs (Vashenyuk et al. 2006; Plainaki et al. 2007). The gradual decay of the GLE event over a few hours was due to nearly isotropic component of SEP. A noteworthy aspect is that the GLE occurred during the continuing effect of a strong Forbush decrease caused by the interplanetary shock, when the CR level was reduced by 10–15% for a week (Fig. 16A). The net effect of the sequence of events is negative in the neutron monitor count rate (i.e., the long-lasting Forbush decrease over-compensates the CR increase during the transient GLE). Figure 16B shows the calculated net CRII effect of the active period of 18–23 Jan. 2005 with respect to the undisturbed period 12–17 Jan. (the ratio between the former and the latter is shown) for different atmospheric depths and geomagnetic latitudes. One can see that the event-integrated net effect is negative in the entire troposphere, even in the polar region. Strong positive effect of

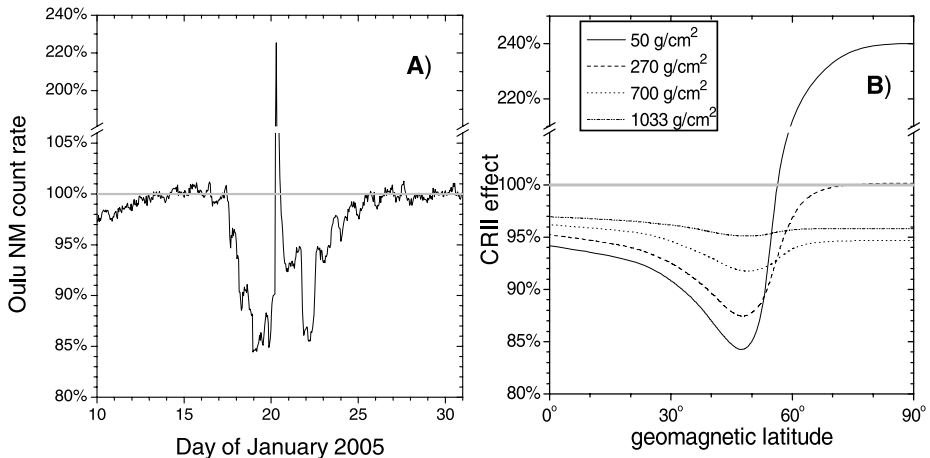


Fig. 16 Combined effect of solar and galactic CR for the event of January 2005. **A)** Count rate of the Oulu NM in January 2005, normalised to the period 12–17 Jan. 2005. **B)** Ionisation effect (see text) as a function of the atmospheric depth (different curves as denoted in the legend) and geomagnetic latitude (X-axis). Note breaks in the Y-axis

enhanced CRII exists only in polar stratosphere where it may become very strong at high altitudes. Thus, the net event-integrated ionisation effect of SEP is relatively small or even negative.

On the other hand, many processes, including chemistry of the upper atmosphere, are sensitive not only to the time-integrated effect but also to the instantaneous flux of particles, which can be enhanced by orders of magnitude during the peak phase of event. The peak phase of GLE is often highly anisotropic so that a strong collimated beam of SEPs impinges on a relatively small spot in the atmosphere. The peak effects of such a beam are considered below for the same event of 20/01/2005. The spectrum and the angular distribution of solar protons outside the magnetosphere have been computed from the neutron monitor network data (Bütkofer et al. 2008). For the peak time the pitch angle distribution of the solar protons was very narrow with the flux at 55° pitch angle being only 10% of the flux in the main direction. Using the Bern CRII model, the ionisation rate was computed globally in a 5° × 5° geographic grid (Fig. 17) for the upper troposphere. The top panel represents the momentary ionisation rate accounting for both SEP and CR fluxes, while in the bottom panel the ionisation induced only by CR is plotted as reference. One can see that the increase in CRII due to SEPs strongly depends on the location and, for this particular event, can be up to a factor of 100 in a very localised region around 70°S 140°E. This is a direct consequence of the high anisotropy of the solar particles at this specific time.

Thus, the ionisation effect of SEP events is local and of most importance in the polar atmosphere. The global effect of CRII solar particles is tiny, even for the most severe events.

3.6 Application to Other Planets

Galactic cosmic rays play also a major role in the ionisation of the atmosphere of other planets and moons of our solar system (Aplin 2005). Several authors have modeled this ionisation in the past. Capone et al. (1977, 1979) have computed the contribution of cosmic rays to the ionisation of the atmosphere of giant planets. The cosmic ray induced ionisation of the atmosphere of Venus and Titan has been calculated by Borucki et al. (1982, 1987) by

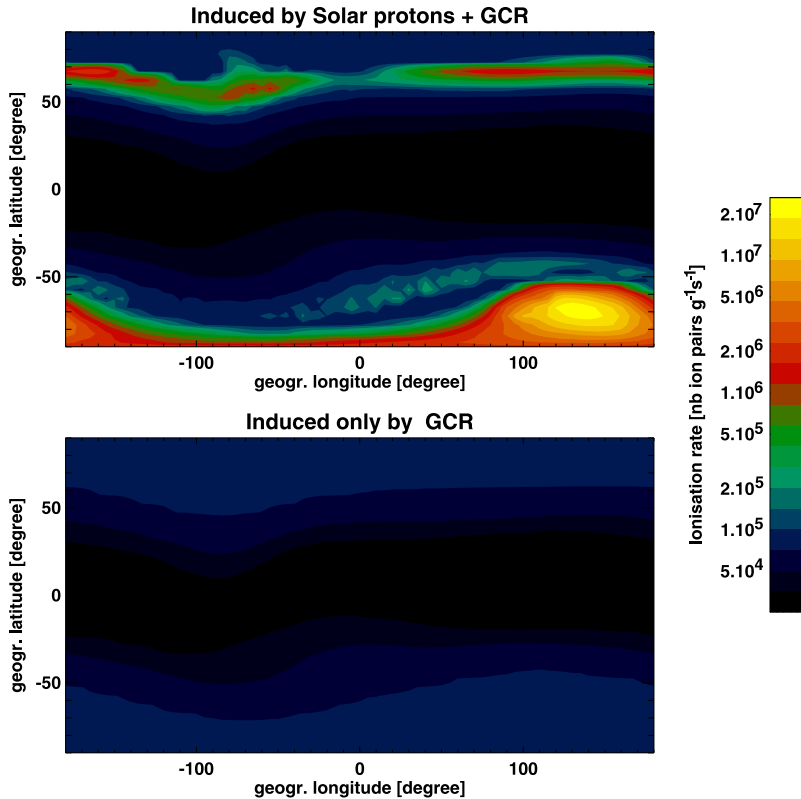


Fig. 17 Computed ionisation rate of the upper troposphere ($h = 300 \text{ g/cm}^2$), at 06:55 UT on January 20, 2005: the total ionisation rate (top panel) and that due to GCR only (bottom panel)

using a modified version of the code developed for the Earth's atmosphere by O'Brien et al. (1979). The same Earth code has been modified by Molina-Cuberos et al. (1999, 2001) to compute the ionisation of the Titan's and Martian atmosphere.

When computing the ionisation of the atmosphere by cosmic rays for other planetary bodies, some important differences have to be taken into account compared to the Earth. The first difference is that the amplitude of the modulation of the cosmic rays by the heliosphere is decreasing with the solar distance, resulting in a higher flux of cosmic rays in the outer heliosphere. While the flux of GCR is roughly similar at Earth's and Mars's orbits, it is not true for other planets since the GCR intensity increases with the heliocentric distance. Another important difference is the presence or not of a planetary dynamo. Mars does not have an internal magnetic field any more, and even the high crustal field on some region of Mars is not high enough to deflect significantly cosmic rays (Acuña et al. 2001; Dartnell et al. 2007). In the case of Jupiter the internal magnetic field is much higher than the geomagnetic field leading to a maximum cut-off rigidity (at the equator) of the order of 1 TV (roughly two order of magnitude higher than on Earth). To compute the access of CR to the moon of a magnetised planet, the positions of the moon's orbit in the magnetosphere of the planet has also to be known. On Titan the magnetic shielding effect can be neglected, as only a part of its orbits is contained within the Saturnian magnetosphere, in a region where the field is too low to significantly deflect cosmic rays (Backes et al. 2005). Finally the most

obvious difference to consider is the variation of the composition and of the density profile of the atmosphere itself.

A cosmic ray code that can treat all the planets and would be available for all the scientific community does not exist yet. The PLANETOCOSMICS code, based on the Geant4 Monte Carlo toolkit, has been recently developed to provide such an application. It simulates the electromagnetic and hadronic interaction of energetic particles with the Earth, Mars and Mercury (Desorgher et al. 2005; Dartnell et al. 2007; Gurtner et al. 2005; Gurtner et al. 2006), and an extension to Jupiter, Saturn and their satellites is under development. The code computes the magnetic shielding of the planet magnetosphere in function of position, the energy deposited by cosmic ray shower particles in the atmosphere and the soil (and therefore can be used to compute the ionisation rate), as well as the flux of any kind of particles at given depth and altitude in the atmosphere and in the soil. The source code for PLANETOCOSMICS can be downloaded from the url <http://cosray.unibe.ch/laurent/planetocosmics>.

4 Summary and Conclusions

More than 100 years of research in ionising particle behavior in the atmosphere has yielded a huge amount of observational data and general understanding of the related processes which control evolution of particle composition and their spatial-temporal distribution. Recognition of the role CR-induced ionisation plays in atmospheric processes, including cloudiness and precipitation requires careful and detailed analysis of ionising particles relation with the condition in the atmosphere. In spite of many correlations found between the particle flux temporal changes and various weather phenomena, no well-established physical connections and mechanisms are yet able to explain the observations. Monitoring of cosmic ray fluxes both with balloon-borne devices and ground-based installations gives a rich source of information for research in this field.

Dedicated simultaneous measurements of ion-production rate, aerosol concentration and ion properties, particularly independent measurements of ion concentration and mobility, should be obtained in the atmosphere.

Essential progress has been achieved recently in developing models of cosmic ray induced ionisation in the atmosphere. Models based on full Monte-Carlo simulation of the nucleonic-electromagnetic-muon cascade induced by CR in the atmosphere are able to properly simulate the 3D time dependent ionisation rate with high accuracy in the troposphere and lower stratosphere (below ~ 20 km). Thus, the modern CRII models provide a reliable tool to study ionisation effects due to cosmic rays in the atmosphere.

Modelling based on the neutron monitor data provides properties of the CR nucleon component. As shown in this paper, fluxes of the ionising CR component in the atmosphere demonstrate existence of both long-term and short-term variations which are not reflected by the neutron monitors. Further work is needed to understand nature of these variations and to input the proper parameters in the models.

Acknowledgements The LPI group is partly supported by the Russian Foundation for Basic Research (grants 08-02-00054, 08-02-00418, 08-02-91006, 08-02-10018, 07-02-01019) and the Program of Presidium RAS “Neutrino physics”. Support from the Academy of Finland and the Finnish Academy of Science and Letters Vilho, Yrjö and Kalle Väisälä Foundation are gratefully acknowledged. GAK was partly supported by the Program of Presidium RAS N16-3-5.4. We are grateful to the teams operating ground based neutron monitors for their publicly available data used in this work. LD, RB and EOF acknowledge support by the Swiss National Foundation (grants 2000020-105435/1, 200020-113704/1), by the Swiss State Secretariat for Education and Research (grant COST-724/C05. 0034), and by the COST-724 action.

References

- M.H. Acuña et al., J. Geophys. Res. **106**, 23403 (2001)
- H.S. Ahluwalia, J. Geophys. Res. **102**, 24229 (1997)
- H.R. Anderson, J. Geophys. Res. **78**, 3558 (1973)
- A. Ansel, *Die luftelektrischen und meteorologischen Ergebnisse der Beobachtungen in Island vom 10. Mai bis 2. Juni 1910 anlaßlich des Durchganges des Halleyschen Kometen*, Nachrichten von der Gesellschaft der Wissenschaften zu Göttingen, Mathematisch-Physikalische Klasse 1912, 42 (1912)
- K.L. Aplin, Surv. Geophys. **27**, 63 (2005)
- K.L. Aplin, R.G. Harrison, A.J. Bennett, Adv. Space Res. **35**, 1484 (2005)
- J.P. Ault, S.J. Mauchly, *Atmospheric-electric results obtained aboard the Carnegie 1915–1921*. Carnegie Institution of Washington publication **175**, 3 (1926)
- H. Backes, F.M. Neubauer, M.K. Dougherty et al., Science **308**, 992 (2005)
- G.A. Bazilevskaya, Adv. Space Res. **35**, 458 (2005)
- G.A. Bazilevskaya, A.K. Svirzhevskaya, Space Sci. Rev. **85**, 431 (1998)
- G.A. Bazilevskaya, M.B. Krainev, V.S. Makhmutov, J. Atmos. Sol.-Terr. Phys. **62**, 1577 (2000)
- G.A. Bazilevskaya, M.B. Krainev, V.S. Makhmutov, A.K. Svirzhevskaya, N.S. Svirzhevsky, Y.I. Stozhkov, Variations of the charged particle fluxes in the Earth's troposphere. Bull. Lebedev Phys. Inst. **12**, 13 (2007)
- W.J. Borucki, Z. Levin, R.C. Whitten, R.G. Keesee, L.A. Capone, O.B. Toon, J. Dubach, Icarus **51**, 302 (1982)
- W.J. Borucki, Z. Levin, R.C. Whitten, R.G. Keesee, L.A. Capone, A.L. Summers, O.B. Toon, J. Dubach, Icarus **72**, 604 (1987)
- I.S. Bowen, R. Millikan, H.V. Neher, Phys. Rev. **46**, 641 (1934)
- R. Bütkofer, E.O. Flückiger, L. Desorgher, M.R. Moser, Sci. Total Environ. **391**, 177 (2008)
- L.A. Capone, R.C. Whitten, S.S. Prasad, J. Dubach, Astrophys. J. **215**, 977 (1977)
- L.A. Capone, J. Dubach, R.C. Whitten, S.S. Prasad, Icarus **39**, 433 (1979)
- G.A. Carse, D. MacOwan, Proc. R. Soc. Edinb. **30**, 32, 460 (1910)
- J.A. Chalmers, *Atmospheric Electricity* (Pergamon, Oxford, 1967)
- A.N. Charakhchyan, Sov. Phys. Uspekhi **7**, 358 (1964)
- A.N. Charakhchyan, G.A. Bazilevskaya, Y.I. Stozhkov, T.N. Charakhchyan, Trudy FIAN, Nauka, Moscow **88**, 3 (1976a), (in Russian)
- A.N. Charakhchyan, G.A. Bazilevskaya, A.N. Kvashnin, T.N. Charakhchyan, Trudy FIAN, Nauka, Moscow **88**, 51 (1976b), (in Russian)
- W.E. Cobb, H.J. Wells, J. Atmospheric Sci. **27**, 814 (1970)
- A.H. Compton, E.O. Wollan, R.D. Bennett, Rev. Sci. Instr. **5**, 415 (1934)
- D.J. Cooke, J.E. Humble, M.A. Shea et al., Nuovo Cimento C **14**, 213 (1991)
- L.R. Dartnell, L. Desorgher, J.M. Ward, A.J. Coates, Biogeosciences **4**, 545 (2007)
- L. Desorgher, E.O. Flückiger, M. Gurtner et al., Int. J. Modern Phys. A **20**, 6802 (2005)
- G. Dobson, A comparison of the electrical conditions of the atmosphere at Kew and Eskdalemuir with notes on observations of atmospheric electricity made in other countries. Geophysical Memoirs **7**, 155–169, Meteorological Office, His Majesty's Stationery Office (1914)
- L.I. Dorman, *Cosmic Rays in the Earth's Atmosphere and Underground* (Kluwer, Dordrecht, 2004)
- H. Ebert, Physik Zeitschrift **2**, 662 (1901)
- V.I. Ermakov, G.A. Bazilevskaya, P.E. Pokrevsky, Y.I. Stozhkov, J. Geophys. Res. **102**, 23413 (1997)
- V.I. Ermakov, Y.I. Stozhkov, N.S. Svirzhevsky, in *Proc. 6th Russian Conf. Atm. Electricity*, Nizhni Novgorod (2007), p. 79 (in Russian)
- J. Feynman, A. Ruzmaikin, Geophys. Res. Lett. **26**, 2057 (1999)
- E.L. Fleming, S. Chandra, J.J. Barnett, M. Corney, Adv. Space Res. **10**(12), 11 (1990)
- S.E. Forbush, J. Geophys. Res. **59**, 525 (1954)
- H. Gerdien, Ein neuer Apparat zur Messung der elektrischen Leitfähigkeit der Luft, Nachrichten von der Gesellschaft der Wissenschaften zu Göttingen, 240 (1905)
- A.E. Golenkov, A.K. Svirzhevskaya, N.S. Svirzhevsky, Y.I. Stozhkov, in *Proc. 21st Int. Cosmic Ray Conf.*, Adelaide, vol. 7 (1990), p. 14
- P.K.F. Grieder, *Cosmic Rays at Earth: Researcher's Reference Manual and Data Book* (Elsevier, Amsterdam, 2001)
- M. Gurtner, L. Desorgher, E.O. Flückiger, M.R. Moser, Adv. Space Res. **36**, 2176 (2005)
- M. Gurtner, L. Desorgher, E.O. Flückiger, M.R. Moser, Adv. Space Res. **37**, 1759–1763 (2006)
- R.G. Harrison, Surv. Geophys. **25**, 441 (2004)
- R.G. Harrison, Rev. Sci. Inst. **76**, 126111 (2005)
- R.G. Harrison, Atmos. Res. **84**, 182 (2007)

- R.G. Harrison, A.J. Bennett, *J. Atmos. Sol.-Terr. Phys.* **69**, 515 (2007)
- R.G. Harrison, W.J. Ingram, *Atmos. Res.* **76**, 49 (2004)
- R.G. Harrison, D.B. Stephenson, *Proc. R. Soc. A* **462**, 1221 (2006)
- A. Hensen, J.C.H. van der Hage, *J. Geophys. Res.* **99**, 10693 (1994)
- V.F. Hess, *Phys. Zeitschr.* **13**, 1084 (1912)
- J. Kazil, E.R. Lovejoy, M.C. Barth et al., *Atmos. Chem. Phys.* **6**, 4905 (2006)
- D.R. Kniveton, *J. Atmos. Sol.-Terr. Phys.* **66**, 1135 (2004)
- D.R. Kniveton, M. Todd, *Geophys. Res. Lett.* **28**, 1527 (2001)
- G.A. Kovaltsov, I.G. Usoskin, *Adv. Geosci.* **13**, 31 (2007)
- A.I. Kurguzova, T.N. Charakhchyan, *Geomagn. Aeron.* **23**, 715 (1983)
- L.I. Miroshnichenko, *Solar Cosmic Rays* (Kluwer, Dordrecht, 2004)
- D. Lario, G.M. Simnett, Solar energetic particle variations, in *Solar Variability and Its Effects on Climate*, ed. by J.M. Pap et al., *Geophys. Monograph*, vol. 141 (AGU, Washington, 2004), p. 195
- W.M. Lowder, P.D. Raft, H.L. Beck, in *Proc. National Symp. on Natural and Manmade Radiation in Space*, ed. by E.A. Warman (NASA, 1972), p. 908
- V.S. Makhmutov, G.A. Bazilevskaya, M.B. Krainev, M. Storini, in *Proc. 27th Internat. Cosmic Ray Conf.*, Hamburg (2001), p. 4196
- N. Marsh, H. Svensmark, *Space Sci. Rev.* **94**, 215 (2000)
- K.G. McCracken, J. Beer, *J. Geophys. Res.* **112**, A10101 (2007)
- I.A. Mironova, M.I. Pudovkin, *Geomagn. Aeron.* **45**, 221 (2005)
- A. Mishev, P. Velinov, C.R. Acad. Bulg. Sci. **60**(5), 511 (2007)
- G.J. Molina-Cuberos, J.J. Lopez-Moreno, R. Rodrigo, L.M. Lara, K. O'Brien, *Planet. Space Sci.* **47**, 1347 (1999)
- G.J. Molina-Cuberos, W. Stumptner, H. Lammer, N.I. Kömle, K. O'Brien, *Icarus* **154**, 216 (2001)
- H.V. Neher, W.H. Pickering, *Phys. Rev.* **61**(7), 407 (1942)
- H.V. Neher, *J. Geophys. Res.* **72**, 1527 (1967)
- H.V. Neher, *J. Geophys. Res.* **76**, 1637 (1971)
- N. Nerukar, W.R. Webber, *J. Geophys. Res.* **69**, 815 (1964)
- K. O'Brien, *J. Geophys. Res.* **84**, 423 (1979)
- K. O'Brien, in *Proc. 7th Internat. Symp. on the Natural Radiation Environment*, ed. by J.P. McLaughlin, S.E. Simopoulos, F. Steinhusler (Elsevier, Amsterdam, 2005), p. 29
- V.P. Okhlopkov, Y.I. Stozhkov, *Bull. Russ. Acad. Sci. Phys.* **69**, 998 (2005)
- E. Pallé, C.J. Butler, K. O'Brien, *J. Atmos. Sol.-Terr. Phys.* **66**, 1779 (2004)
- W.D. Pesnell, R.A. Goldberg, C.H. Jackman, D.L. Chenette, E.E. Gaines, *J. Geophys. Res.* **105**(A10), 22943 (2001)
- G. Pfötzer, *Z. Phys.* **102**, 23 (1936)
- C. Plainaki, A. Belov, E. Eroshenko et al., *J. Geophys. Res.* **112**, A04102 (2007)
- M.I. Pudovkin, S.V. Veretenenko, *J. Atmos. Terr. Phys.* **57**, 1349 (1995)
- M.I. Pudovkin, S.V. Veretenenko, *Adv. Space Res.* **17**, 161 (1996)
- E. Regener, *Phys. Zeitschr.* **35**, 784 (1934)
- V.C. Roldugin, B.A. Tinsley, *J. Atmos. Sol.-Terr. Phys.* **66**, 1143 (2004)
- V.K. Roldugin, E.V. Vashenyuk, *Geomagn. Aeron.* **34**, 251 (1994)
- J.M. Rosen, D.J. Hofmann, W. Gringel, *J. Geophys. Res.* **90**, 5876 (1985)
- J.M. Rosen, D.J. Hofmann, *J. Geophys. Res.* **93**, 8415 (1988)
- J. Schröter, B. Heber, F. Steinhilber, M.B. Kallenrode, *Adv. Space Res.* **37**, 1597 (2006)
- J.A. Simpson, *Space Sci. Rev.* **93**, 11 (2000)
- O.I. Shumilov, E.A. Kasatkina, K. Henriksen, E.V. Vashenyuk, *Ann. Geophys.* **14**, 1119 (1996)
- C.M.H. Smith, *A Textbook of Nuclear Physics* (Pergamon, Oxford, 1966)
- P.H. Stoker, *Space Sci. Rev.* **73**, 327 (1994)
- Y.I. Stozhkov, *J. Phys. G* **29**, 913 (2003)
- Y.I. Stozhkov, P.E. Pokrevskii, Z. Zullo et al., *Geomagn. Aeron.* **36**, 211 (1996)
- Y.I. Stozhkov, N.S. Svirzhevsky, G.A. Bazilevskaya et al., *Cosmic ray investigations in the atmosphere of the Arctic and Antarctic*. Arctic and Antarctic collected papers, 3(37), 114, Moscow, Nauka (2004), (in Russian)
- Y.I. Stozhkov, N.S. Svirzhevsky, G.A. Bazilevskaya et al., *Fluxes of cosmic rays in the maximum of absorption curve in the atmosphere and at the atmosphere boundary (1957–2007)*. Lebedev Phys. Inst. Report Series, No. 14 (2007a). Online version: http://sites.lebedev.ru/DNS_FIAN/show.php?page_id=1949
- Y.I. Stozhkov, V.I. Ermakov, N.S. Svirzhevsky, in *Proc. 6th Russian Conf. Atm. Electricity*, Nizhni Novgorod, (2007b), p. 198 (in Russian)
- H. Svensmark, E. Friis-Christensen, *J. Atmos. Sol.-Terr. Phys.* **59**, 1225 (1997)
- H. Svensmark, J.O.P. Pedersen, N.D. Marsh et al., *Proc. Roy. Soc. A* **463**, 385 (2007)

- B.A. Tinsley, G.M. Brown, P.H. Scherrer, *J. Geophys. Res.* **94**, 14783 (1989)
- B.A. Tinsley, G.W. Deen, *J. Geophys. Res.* **96**, 22283 (1991)
- B.A. Tinsley, L. Zhou, *J. Geophys. Res.* **111**, D16205 (2006)
- B.A. Tinsley, G.B. Burns, L. Zhou, *Adv. Space Res.* **40**, 1126 (2007)
- I.G. Usoskin, K. Mursula, S.K. Solanki et al., *J. Geophys. Res.* **107**(A11), 1374 (2002)
- I.G. Usoskin, O.G. Gladysheva, G.A. Kovaltsov, *J. Atmos. Sol.-Terr. Phys.* **66**, 1791 (2004a)
- I.G. Usoskin, N. Marsh, G.A. Kovaltsov et al., *Geophys. Res. Lett.* **31**, L16109 (2004b)
- I.G. Usoskin, K. Alanko-Huotari, G.A. Kovaltsov, K. Mursula, *J. Geophys. Res.* **110**, A12108 (2005)
- I.G. Usoskin, G.A. Kovaltsov, *J. Geophys. Res.* **111**, D21206 (2006)
- I.G. Usoskin, M. Voiculescu, G.A. Kovaltsov, K. Mursula, *J. Atmos. Sol.-Terr. Phys.* **68**, 2164 (2006)
- I.G. Usoskin, S.K. Solanki, G.A. Kovaltsov, *Astron. Astrophys.* **471**, 301 (2007)
- I.G. Usoskin, M. Korte, G.A. Kovaltsov, *Geophys. Res. Lett.* **35**, L05811 (2008a)
- I.G. Usoskin, L. Desorgher, P. Velinov et al., Ionization of the Earth's atmosphere by solar and galactic cosmic rays. *Acta Geophys.* **56** (2008b, in press)
- E.V. Vashenyuk, Y.V. Balabin, B.B. Gvozdevsky, S.N. Karpov, *Geomagn. Aeron.* **46**, 424 (2006)
- P. Velinov, L. Mateev, *Geomagn. Aeron.* **30**, 593 (1990)
- S.V. Veretenenko, M.I. Pudovkin, *J. Atmos. Sol.-Terr. Phys.* **59**, 1739 (1997)
- S. Veretenenko, P. Thejll, *J. Atmos. Sol.-Terr. Phys.* **66**, 393 (2004)
- M. Voiculescu, I.G. Usoskin, K. Mursula, *Geophys. Res. Lett.* **33**, L21802 (2006)
- G.R. Wait, *J. Wash. Acad.* **36**, 321 (1946)
- J.R. Winckler, K.A. Anderson, *Phys. Rev.* **108**, 148 (1957)
- C.T.R. Wilson, *Proc. R. Soc. Lond. A* **80**, 542–537 (1908)
- J.R. Wright, O.F. Smith, *Phys. Rev.* **7**, 49 (1916)

Meteoric Layers in Planetary Atmospheres

J.G. Molina-Cuberos · J.J. López-Moreno · F. Arnold

Originally published in the journal Space Science Reviews, Volume 137, Nos 1–4.
DOI: [10.1007/s11214-008-9340-5](https://doi.org/10.1007/s11214-008-9340-5) © Springer Science+Business Media B.V. 2008

Abstract Metallic ions coming from the ablation of extraterrestrial dust, play a significant role in the distribution of ions in the Earth's ionosphere. Ions of magnesium and iron, and to a lesser extent, sodium, aluminium, calcium and nickel, are a permanent feature of the lower E-region. The presence of interplanetary dust at long distances from the Sun has been confirmed by the measurements obtained by several spacecrafts. As on Earth, the flux of interplanetary meteoroids can affect the ionospheric structure of other planets. The electron density of many planets show multiple narrow layers below the main ionospheric peak which are similar, in magnitude, to the upper ones. These layers could be due to long-lived metallic ions supplied by interplanetary dust and/or their satellites. In the case of Mars, the presence of a non-permanent ionospheric layer at altitudes ranging from 65 to 110 km has been confirmed and the ion $Mg^+\cdot CO_2$ identified. Here we present a review of the present status of observed low ionospheric layers in Venus, Mars, Jupiter, Saturn and Neptune together with meteoroid based models to explain the observations. Meteoroids could also affect the ionospheric structure of Titan, the largest Saturnian moon, and produce an ionospheric layer at around 700 km that could be investigated by Cassini.

Keywords Meteoroids · Ionosphere · Planetary atmosphere

J.G. Molina-Cuberos (✉)

Dept. Física, Universidad de Murcia, Campus Espinardo, 30100, Murcia, Spain

e-mail: gromc@um.es

J.J. López-Moreno

Instituto Astrofísica de Andalucía, CSIC, P.O. Box 3004, 18080, Granada, Spain

e-mail: lopez@iaa.es

F. Arnold

Atmospheric Physics Division, Max-Plank Institut for Nuclear Physics (MPIK), P.O. Box 10399980, 69029, Heidelberg, Germany

e-mail: frank.arnold@mpi-hd.mpg.de

1 Introduction

The ablation of a continuous flux of extraterrestrial dust in the atmosphere gives rise to permanent layers of free neutral and ionized metal atoms in the 80–110 km altitude range. From the initial ground based observations of sodium at the end of the 1930s (Chapman 1938) to the in-situ measurements of metal ions by rocket-borne mass spectrometers (Grebowksy et al. 1998), the density profiles of metallic species as well as their latitude and temporal variability has been established. Magnesium and iron are the most abundant metal species in the atmosphere; others like sodium, aluminium, calcium and nickel are also present in a concentration, at least, one order of magnitude lower. The relative abundance of metal species in the atmosphere is roughly equal to the one exhibited in carbonaceous chondrites (Mason 1971).

In addition to general background of extraterrestrial dust, meteor showers, that are produced when the Earth crosses the dust stream left along a comet orbit, can increase the concentration of metals during short periods of time. The net mass influx to the Earth from each meteor shower is only a small fraction of the total yearly influx from the sporadic background (Hughes 1978). However, an increase by a factor of 2–3 in metallic concentration has been found during such events. The increase can be as much as one order of magnitude during a strong meteor shower (Kopp 1997; Grebowksy et al. 1998), which is often large enough to be manifested as a peak in the total ion and electron density profiles. Figure 1 shows two examples of the distribution of positive ions and electrons in the terrestrial atmosphere, where the increase in the metallic ion concentrations during the Perseid meteor shower is highlighted.

Dust detectors on board several space missions have observed that meteoroids are distributed through the whole interplanetary medium in the Solar System. Meteoroids can thus affect the atmospheric structure of other planets. In this paper we search for evidence of meteoroid layers in the atmospheres of extraterrestrial planets and we review the present knowledge of meteoroid modeling in the Solar System.

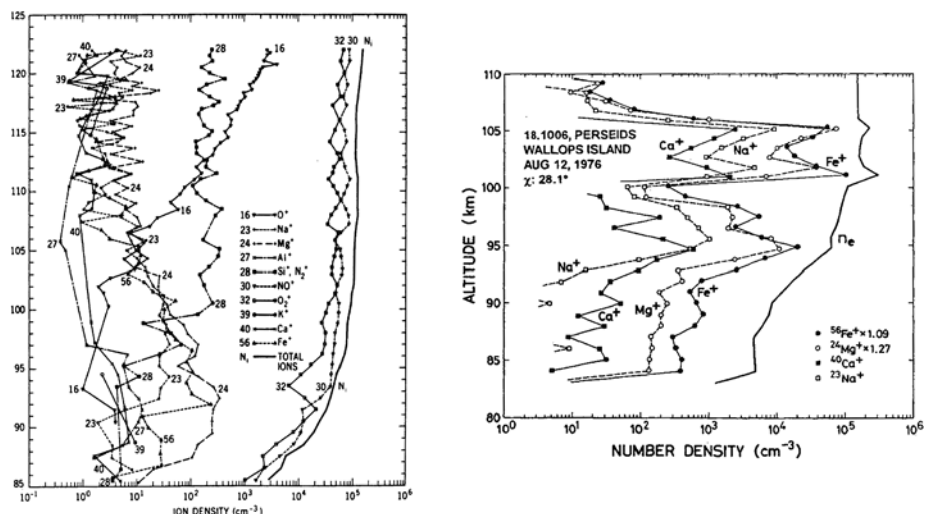


Fig. 1 Observed distribution of positive ion species in the terrestrial ionosphere during the following conditions: (*left*) daytime over Thumba (India) (Aikin and Goldbert 1973); (*right*) Perseid meteor shower on August 12, 1976, above Wallops Islands (Kopp 1997)

2 Evidence of Meteoroid Layers through the Solar System

Planetary ionospheres have been sounded by radio occultation techniques since the beginning of the 1960s; the measurements show a daytime ionosphere with a major peak mainly produced by solar radiation and photoelectrons. Below the main peak, one or more secondary ionospheric layers have been found. Examples of such layers have been found at Venus by Pioneer Venus (Kliore et al. 1979) and Mars by Mariner IV (Fjeldbo et al. 1966), Mars 4 and 5 (Savich et al. 1976) and Mars Express (Pätzold et al. 2005) among others, see Fig. 2. The number of missions to the external planets is not so comprehensive, Galileo (Hinson et al. 1997) and Voyager (Hinson et al. 1998) found evidence of such layers in the Jovian atmosphere, Cassini (Nagy et al. 2006) in the atmosphere of Saturn and Voyager at Uranus (Strobel et al. 1991) and Neptune (Lyons 1995), see Fig. 3.

2.1 Venus

The electron density profile measured by Pioneer Venus in the nightside ionosphere shows low altitude layers below the main ambient ionospheric layer, see Fig. 2. The altitude of the main peak is located at 142.2 ± 4.1 km, very close to the main peak of the dayside terminator ionosphere. The peak density is characterized by a great variability, with a magnitude ranging from 23×10^3 to 40×10^3 cm $^{-3}$ (Kliore et al. 1979). A double-peak structure appears during two closely spaced orbits, 55 and 57, and on orbit 57 the structure appeared in both the entry and exit measurements. It seems that the appearance of such a double-peak structure is a relatively rare temporal phenomenon. The altitude of the layer, ~ 120 km, is in agreement with the maximum for meteoroid ablation. Other ionization sources, such us direct impact ionization by electron precipitation or protons into the nightside, could also explain the nature of the lower ionospheric layer.

2.2 Mars

The atmosphere of Mars has been sounded in more detail than the rest of the extraterrestrial solar system planets, and its ionosphere presents the strongest evidences of metallic layers. The magnesium ion Mg $^{+} \cdot$ CO $_2$ has even been identified as a constituent of the Martian ionosphere (Aikin and Maguire 2005). The daytime ionosphere is well characterized by a main layer produced by solar radiation at an altitude of 140 km with a number density of some teens of thousands electrons per cubic centimeter. Mariner IV found a secondary layer one order of magnitude lower at around 100 km, below the main photoionospheric peak (Fjeldbo et al. 1966). Some years later, the soviet Mars 4 and 5 (Savich et al. 1976) found a layer at around 80 km during nighttime similar, in magnitude, to the daytime one. Mars Express confirmed the existence of a sporadic layer between 65 and 110 km in altitude in 10 of 120 ionospheric electron concentration profiles (Pätzold et al. 2005). Figure 2 shows the measurements developed by Mars 4 and 5 (left) and Mars Express (right). The occurrence of the daytime layer was not limited to specific times of the day or locations, and part of it is hidden in the lower portion of the upper one (Pätzold et al. 2005). Mars Express did not find such layers in the 20 ionospheric observations at night, all of which were at high southern latitudes during winter. The observations are too limited to exclude the occurrence of a layer at night (Pätzold et al. 2005). Theoretical models considering meteoroids ablation indicate that the altitude and magnitude of the observed layers can be explained by long lived metallic ions deposited by meteoroids (Pesnell and Grebowsky 2000; Molina-Cuberos et al. 2003).

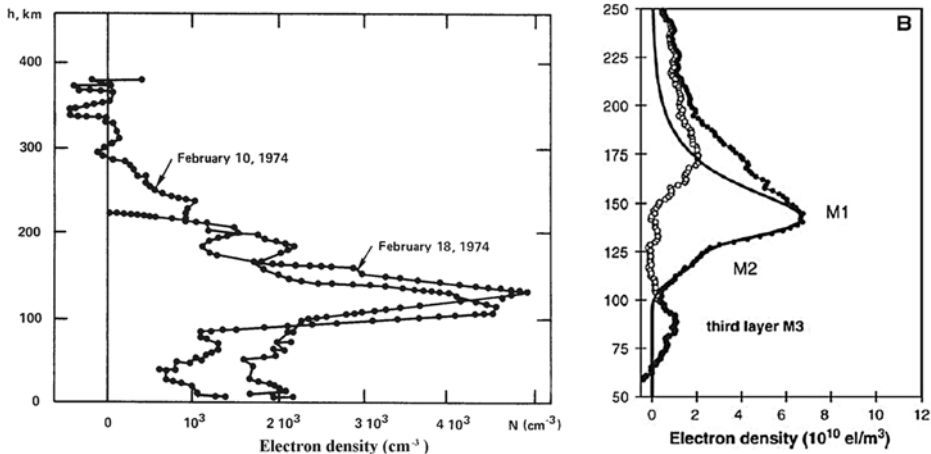
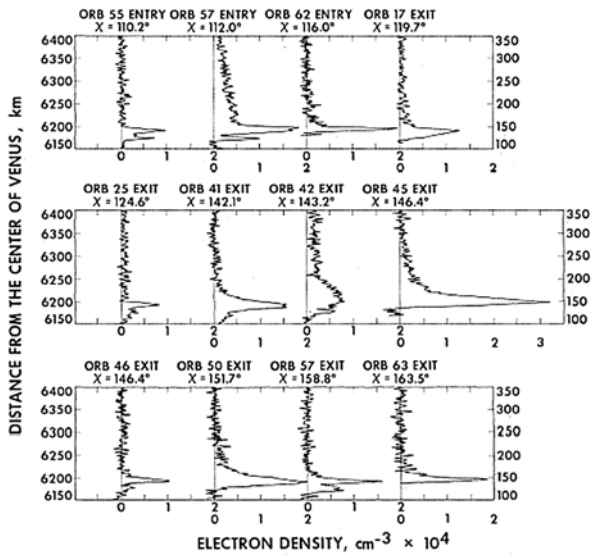


Fig. 2 *Top* electron concentration profiles in the nightside ionosphere of Venus measured by Pioneer Venus. From A.J. Kliore et al., Science 205:99–102 (July 6 1979). Reprinted with permission from AAAS. *Lower-left* distribution of electron concentration in the nighttime ionosphere of Mars measured by Mars 4 and 5 (Savich et al. 1976). *Lower-right* electron concentration in the Martian ionosphere observed by Mars Express (solid circles) and after subtracting a Chapman ionization model (open circles). From M. Pätzold et al., Science 310:837–839 (2005). Reprinted with permission from AAAS

2.3 Jupiter

The Voyager 2 fly-by provided most of the information about the lower ionospheric structure of Jupiter (Hinson et al. 1998). The electron concentration profile obtained during the egress contains two distinct layers: one is centred near 1000 km (relative to the 1 bar altitude) with a peak number density of $46 \times 10^4 \text{ cm}^{-3}$ and the structure of the other is more complex, see Fig. 3. It is formed by a group of fine layers situated between 300 and 500 km

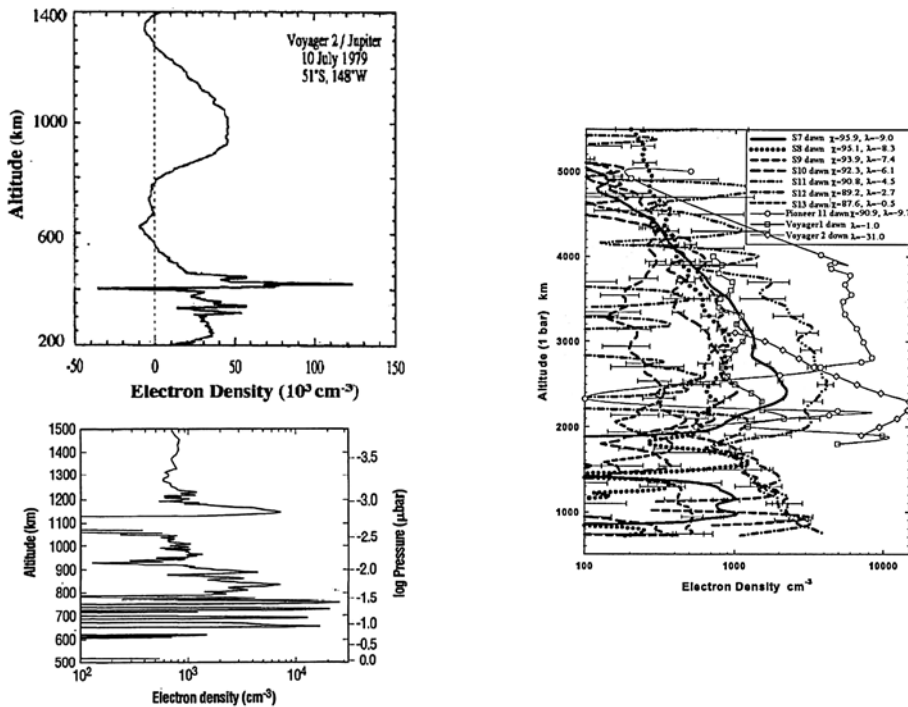


Fig. 3 Electron concentration profile at Jupiter (*top-left*) (Hinson et al. 1998), Neptune (*lower-left*) (From J.R. Lyons, *Science* 268:648 (1995). Reprinted with permission from AAAS) and Saturn (*right*) (Nagy et al. 2006)

with a concentration of $(20\text{--}120) \times 10^3 \text{ cm}^{-3}$ that might be formed in response to vertical shear in the zonal wind or plasma instabilities. Pre-Voyager theoretical models of the lower ionosphere predicted a layer of hydrocarbon ions in the 300–400 km altitude range (Kim and Fox 1994); although the calculated magnitude is around two order of magnitude smaller than the observed one. The difference between theory and observations seems too large to be reconciled by considering atmospheric processes. A plausible explanation is that the lowest layer is composed of long-lived metallic ions supplied by meteoroids or by the Galilean satellites (Hinson et al. 1998).

2.4 Saturn

Saturn presents quite a complex ionosphere where several ionization sources and physical processes take place. In addition to the solar and cosmic radiation, water inflow and particle impact have important influences on the ionospheric structure. The lower part also presents some layered structure, as it has been detected by Cassini (Nagy et al. 2006). Figure 3 shows the electron concentration profile for exit (dawn terminator) measured by Pioneer 11, Voyager 1 and 2, and Cassini. We can observe that only Cassini was able to determine the structure of the lower part of the ionosphere. The peak densities are, in general, larger for the dusk results than for the dawn ones. The profile corresponding to the dawn terminator presents a thick layer in the 900–1500 km range, well below the main peak placed at around 2500 km. For the dusk terminator, the layer is more sharp and could be partially included in

the upper main ionosphere. The magnitude of the lower ionospheric layer is, in both cases, of around 1000 cm^{-3} .

2.5 Neptune

Electron number density profile in Neptune observed during Voyager 2 occultation revealed sharp layers in the lower ionosphere with densities of around 10^4 cm^{-3} (Lyons 1995), see Fig. 3. The magnitude of the layers are even higher than the upper peak. It must be taken into account that the uncertainty in the electron abundance is high in the lower ionosphere, by as much as a factor of two, but the altitude of the layers is well determined from the phase of the received signal. A simple explanation for these layers is that the long-lived metallic ions are compressed by a horizontal wind with a vertical shear acting on the ions in the presence of a magnetic field (Lyons 1995).

3 The Interaction of Meteoroids with a Planetary Atmosphere

In parallel to the experimental observations, many theoretical studies have considered the effect of dust in the atmosphere of Venus (McAuliffe and Christou 2006), Mars (Adolfsson et al. 1996; Pesnell and Grebowsky 2000; Molina-Cuberos et al. 2003), Jupiter (Grebowksy 1981; Hinson et al. 1998; Kim et al. 2001), Saturn (Moses and Bass 2000), Titan (Ip 1990; English et al. 1996; Molina-Cuberos et al. 2001), Neptune (Moses 1992; Lyons 1995) and Triton (Pesnell et al. 2004).

The evaluation of meteoroid effects on planetary atmospheres requires the knowledge of the mass and velocity distributions of the meteoroid flux through the Solar System. Then the dynamical evolution of small particles through the atmosphere has to be calculated in order to determine the deposition profiles of neutrals and ions. The concentration of each metallic compound is calculated by solving the continuity and momentum equations.

3.1 Interplanetary Flux

Collisions between asteroidal parent bodies or grains released by comets are the major source of meteoroids in the Solar System (Liou et al. 1995; Gurnett et al. 1997). Exogenous sources also exist, particles coming from the local interstellar medium cross the Solar System on hyperbolic orbits (Grün et al. 1993). The experimental information of the dust distribution beyond the orbit of the Earth comes from the dust detectors on board of Pioneer 10 and 11, Ulysses, Galileo and Cassini (Humes 1980; Grün et al. 1993; Altobelli et al. 2007):

The measurements by the penetration detector of Pioneer 10 indicate that the spatial density of 10^{-9} g meteoroids is essentially constant between 1 and 18 AU (Humes 1980). The data obtained by the detector on Pioneer 11 show that meteoroids between 4 and 5 AU are not in circular orbits near the ecliptic plane, but they follow randomly inclined orbits of high eccentricity (Humes 1980), which implies a cometary origin. During the Saturn encounters, the on board detectors measured an increase in the flux of about three orders of magnitude, probably as a result of impacts from ring particles (Humes 1980). The data obtained with the penetration detector on board Pioneer 10 and 11 have similar shapes in spite of the differences on the threshold mass, 10^{-9} and 10^{-8} g , respectively, which means that the particle size distribution does not change strongly with the orbital radius (Cuzzi and Estrada 1998).

The high sensitivity Cassini Dust Analyzer (Altobelli et al. 2007) measured the dust particles between Jupiter and Saturn and found two main group. The first group of impacts consists of particles on bound and prograde orbits coming from the dust ram direction, most probably on low eccentric and low inclined orbits, and they show a large spread in mass. The possible sources are short-period Jupiter family comets or circumsolar dust. Impactors of the second group were identified as interstellar dust particles, perhaps including a minority of beta-meteoroids. The upper limit value of the flux and the particles size are in very good agreement with what is expected from the Ulysses data (Grün et al. 1993) and model predictions.

The dust environment in the outer Solar System has been sounded by the Voyagers. The plasma wave instruments were able to detect a small but persistent level of dust impacts (up to 51 AU for Voyager 1 and up to 33 AU for Voyager 2). The average number density obtained is estimated to be around $2 \times 10^{-8} \text{ m}^{-3}$, and the average mass of around 10^{-11} g (Gurnett et al. 1997). The ecliptic latitudes of the paths taken by Voyager 1 and 2 were quite different. After the flyby of Saturn at 9.5 AU, Voyager proceeded northward from the ecliptic plane at an asymptotic ecliptic latitude of about 35° . Voyager 2 remained very close to the ecliptic plane until the flyby of Neptune at 30 AU. Considering the differences in the spacecraft trajectories, the observed variations in number densities were small and (Gurnett et al. 1997) concluded that comets are the most likely source for interplanetary dust particles in the outer Solar System.

3.2 Entry Velocity

For particles on bound orbits, the velocity distribution of dust particles arriving a planet depends on the distance to the Sun and on the planetary gravitational field. The velocity decreases with the distance to the Sun. Cuzzi and Estrada (1998) found the relationship between the orbital velocity of the meteoroids and the distance to the Sun to be:

$$v(R) = \frac{v_1}{\sqrt{R_{AU}}}, \quad (1)$$

where v_1 is the velocity at 1 AU and R_{AU} the distance to the Sun.

Meteoroids penetrate the atmosphere at higher velocities than predicted by (1). The planetary gravitational field accelerates the particle and its orbit becomes parabolic. If v^* is the relative speed of a particle with respect to the planet, then the meteoroid speed $v(r)$ at a distance r from the planetary centre is:

$$v(r) = \sqrt{v_{\text{esc}}^2(r) + v^{*2}}, \quad (2)$$

where $v_{\text{esc}}(r)$ is the planetary escape velocity of an object at a distance r .

The gravitational field also produces an enhancement in the cross section of a planet and, therefore, an increase in the meteoroid flux by a factor (Bauer 1973):

$$G = 1 + \left(\frac{v_{\text{esc}}}{v^*} \right)^2. \quad (3)$$

Table 1 shows the characteristic velocities of meteoroids arriving at Solar System bodies with a noticeable atmosphere. V_{\min} and V_{\max} represent the minimum and maximum velocities reaching the top of the atmosphere, respectively, where meteoroids in heliocentric orbits are assumed. The minimum velocity corresponds to the planetary escape velocity at the top

Table 1 Characteristic velocities (km s⁻¹)

	V_{\min}	V_{\odot}	V_{orb}	V_{\max}
Venus	10	50	35	85
Earth	11	42	30	72
Mars	5	34	24	58
Jupiter	60	19	13	69
Saturn	35.5	13.7	9.7	42.5
Titan ^d	2.6	13.7	5.58	29.1
Uranus	21	9.6	6.8	26.6
Neptune	23.5	7.7	5.5	26.9

^dThe case of Titan includes the gravitational focus of Saturn, V_{orb} is the orbital velocity around Saturn

of the atmosphere. The maximum velocity corresponds to a particle with the solar system escape velocity V_{\odot} orbiting the Sun in a retrograde orbit. V_{orb} is the planetary orbital velocity.

It can be observed that the range of velocities ($V_{\max} - V_{\min}$) is very wide for terrestrial planets due to the combined effect of a low escape velocity and high orbital velocity. For the giant planets this velocity range is much smaller.

3.3 Meteoroid Ablation

The problem of determining the physical evolution of a particle penetrating the atmosphere was first treated in detail by Öpik (1958). Here we briefly describe the processes describing the loss of velocity and mass of a spherical small particle, based in the work of Lebedinets et al. (1973). We do not consider aspects like fragmentation, non spherical shape, mixed compositions or differential ablation which are usually important for the detailed modeling of the Terrestrial atmosphere or for high mass particles.

Meteoroids penetrating the atmosphere are accelerated by the planetary gravitational field and slowed down by collisions with atmospheric constituents. Collisions also remove part of the mass and heat the particle surface producing an additional loss of mass by evaporation. The increase of the particles' temperature by atmospheric collisions is balanced with thermal radiation and loss of heat through ablation.

The dynamical evolution of a small particle penetrating the atmosphere is calculated by solving the motion, ablation and energy equations. The motion equation relates the decrease in relative impact velocity v due to the drag of the atmosphere:

$$\cos \theta \frac{dv}{dz} = \frac{\Gamma A \rho v}{\delta^{2/3} m^{1/3}} \quad (4)$$

where θ is the entry angle, and v , m and δ are the meteoroid velocity, mass and density, respectively. The atmospheric drag depends on the drag coefficient, Γ , the atmospheric mass density, ρ , and on the meteoroid shape, through factor A .

The ablation equation relates the loss of mass m from a meteoroid due to evaporation and sputtering:

$$\cos \theta \frac{dm}{dz} = -\frac{4AK_1m^{2/3}}{\delta^{2/3}vT^{1/2}}e^{-K_2/T} - \frac{\Lambda_S A \rho m^{2/3} v^2}{2Q^{2/3}} \quad (5)$$

where K_1 and K_2 are constants describing the dependence of the evaporation rate on temperature, T . Λ_S is the sputtering coefficient and Q the energy of evaporation of 1 g of the meteoroid.

Finally, the energy equation provides the thermal evolution of the particle as a function of the increase of temperature due to the heating by sputtering, thermal radiation from the body surface and the deposition of energy by evaporation:

$$\cos \theta \frac{dT}{dz} = \frac{4A\rho v^2}{8C\delta^{2/3}m^{1/3}}(\Lambda - \Lambda_S) - \frac{4A\sigma T^4}{C\delta^{2/3}vm^{1/3}} - \frac{4AK_1 Q}{C\delta^{2/3}T^{1/2}m^{1/3}v}e^{-K_2/T} \quad (6)$$

where Λ the heat transfer coefficient, σ the Stefan–Boltzmann constant and C the heat capacity of the meteoroid substance.

The energy, mass and momentum are couple by a system of equations which usually demand a high precision numerical method and a small discretization grid in order to solve it. In principle, the effect of a velocity distribution has to be taken into account in the modeling, mainly if a high precision of the meteoroid mass deposition profile is required, as usually occurs to the Earth case. However, most of the numerical models of the extraterrestrial atmospheres simply consider a monochromatic distribution at the mean velocity, rather than a distribution of velocities, and analyse the effect of different incoming velocities. For low gravity planets a mean angle of 45 degrees for incoming particles can be used. The effect of non-vertical entry is to elevate the altitude at which ablation occurs. For massive planets the gravitational focus shifts the distribution of incident angle towards vertical.

Icy meteoroids coming from comets ablate more easily and at higher altitude than stony meteoroids, which are produced in the asteroid belt. Rocky material introduces a higher amount of metal constituents to the atmosphere than icy meteoroids.

Once the ablation of meteoroids is known, the linear concentration of the individual ion species can be calculated by

$$\alpha_i = -\frac{p_i \beta_i}{m_i v} \frac{dm}{dt} \quad (7)$$

where p_i is the ratio of atom i type to the total, m_i is the atomic mass, and β_i is the ionization probability, which depends on the ion produced and meteoroid velocity. For low velocity $\leq 35 \text{ km s}^{-1}$, for which no secondary ionization or recombination take place, Jones (1997) proposed an empirical expression:

$$\beta_i = k_i(v - v_i)^2 v^{0.8} \quad (8)$$

where k_i is an experimental value, which depends on the element and v_i is a cut off velocity, For high velocity particles, a more general expression can be used (Lebedinets et al. 1973):

$$\beta_i = Cv^{7/2}. \quad (9)$$

The production rate of i type ions (P_i) is calculated as:

$$P_i = \int \alpha_i f(m) dm, \quad (10)$$

where $f(m)$ is the flux per unit of micrometeoroidal mass.

4 Modelling Metallic Layers in Planetary Atmospheres

The meteoroid mass deposition profiles are calculated by adapting the flux of interplanetary dust and solving the dynamical evolution of the particles, as described in the above section.

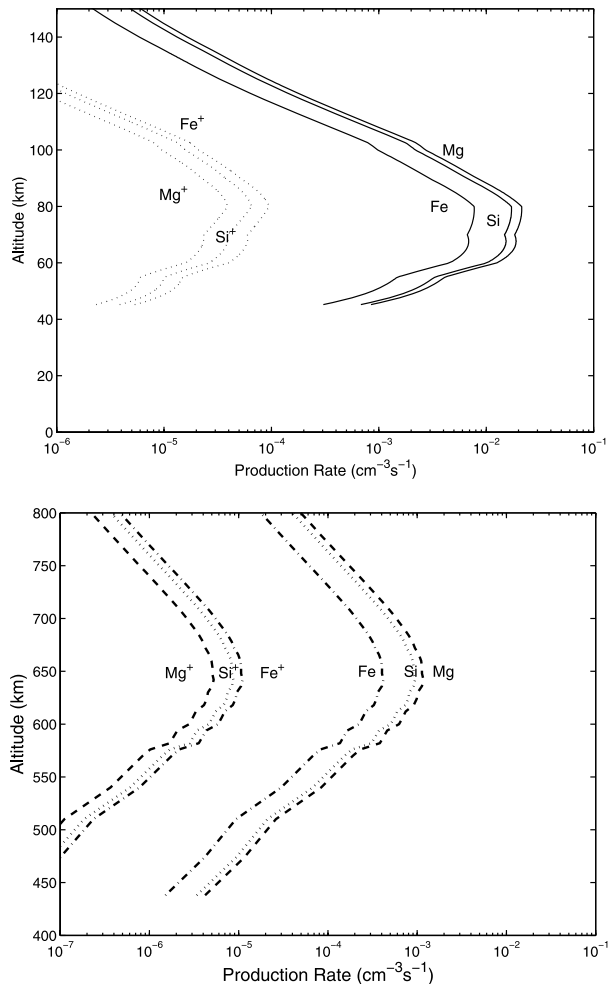


Fig. 4 Neutral and ionic deposition rates of Mg, Fe and Si due to the ablation of meteoroids with entry velocity of 18 km s^{-1} in the atmosphere of Mars (top) (Molina-Cuberos et al. 2003) and Titan (bottom) (adapted from Molina-Cuberos et al. 2001) to consider the same meteoroid composition than on Mars

We have used the model by Grün et al. (1985), which assumes an isotropic flux of meteoroids at Earth's orbit with effective density of 2.5 g cm^{-3} and mean velocity of $v(1 \text{ AU}) = 20 \text{ km s}^{-1}$. The model considers mass ranging from 10^{-18} to 100 g , although the main contribution to the total mass is due to particles ranging from 10^{-7} to 10^{-4} g .

Figure 4 shows the neutral and ion deposition rate of magnesium, iron and silicon in the atmosphere of Mars (top) and Titan (bottom), assuming the interplanetary dust is mainly composed of carbonaceous chondrites, that have a relative concentration of Mg = 6.1%, Si = 5.7% and Fe = 5.1% (Anders and Ebihara 1982).

Table 2 shows the altitude range where the maximum of the meteoroid ablation occurs and the altitude of the ionospheric layers that could consist of metallic ions. Please note that the ionospheric peak is located in all the cases quite close to the ablation altitude.

Table 2 Theoretical predictions of the altitude of the meteoroid deposition peak and altitude of ionospheric layer that could consist on metallic ions. \odot represents ice meteoroids and \bullet silicate ones

Planet	Ablation (km)	Reference	Ionospheric peak (km)
Venus	110–120	<i>This work</i>	120–130 km
Earth	85–95	McNeil et al. 1998	90–100 km
Mars	75–85	Molina-Cuberos et al. 2003	65–100
Jupiter	300–400	Kim et al. 2001	300–550
Saturn	790–1290 \odot	Moses and Bass 2000	900–1200
	610–790 \bullet	Moses and Bass 2000	
Titan	650–700	Molina-Cuberos et al. 2001	No evidences
Neptune	500–800 \bullet	Moses 1992	600–1000 km
	250–500 \odot	Moses 1992	

The altitude of the ablation depends on the physical characteristics of meteoroids (volatility, speed, size and composition). The radio-occultation measurements of ionospheric layers of long-lived metallic ions through the Solar System planets could, therefore, provide information about properties and composition of interplanetary dust. The distribution of metals is, however, affected by transport and layering.

Once the meteoroid deposition in the atmosphere is known, the concentration of each neutral and ion species is calculated from the continuity and momentum equations that, assuming steady state, may be expressed as:

$$P_i - n_i l_i = \frac{\partial}{\partial z} n_i v_i \quad (11)$$

$$\begin{aligned} v_i &= -D_i \left(\frac{1}{n_i} \frac{\partial n_i}{\partial z} + \frac{1}{H_i} + \frac{1}{T} \frac{\partial T}{\partial z} \right) \\ &\quad - K \left(\frac{1}{n_i} \frac{\partial n_i}{\partial z} + \frac{1}{H} + \frac{1}{T} \frac{\partial T}{\partial z} \right) \end{aligned} \quad (12)$$

where i denotes the i th constituent, z the altitude, n_i the concentration, P_i the production, l_i the specific loss, T the temperature. v_i is the mean vertical velocity, D_i and K are molecular and eddy diffusion coefficients, H_i and H are the individual and atmospheric scale heights.

Vertical transport of metallic species is mainly produced by turbulent and molecular diffusion, the former being more effective at lower levels. Diffusion theory provide analytical expressions for the molecular diffusion coefficients D_i (Chapman and Cowling 1970). The turbulent diffusion is the least known factor in the modeling of an atmosphere. It is typically parameterized by means of an eddy diffusion coefficient K .

The production of metallic ions depends on the atmospheric and ionospheric characteristics. Other ionization sources, like solar radiation or electrons, provide atmospheric ions that transfer the charge to metallic atoms by charge exchange reactions, which is a very important source for metallic ions. In addition, the photoionization of metallic neutrals increases the production of metallic ions.

4.1 Earth

Meteoric metals in the terrestrial atmosphere have been modeled in detail. The chemistry and temporal and spatial variations have been extensively treated in the literature (Swider 1969; Aikin and Goldbert 1973; Carter and Forbes 1999; Joiner and Aikin 1996). In particular, special attention has been paid to the most abundant metallic species, magnesium (McNeil et al. 1996; Plane and Helmer 1995), iron (Helmer et al. 1998; Carter and Forbes 1999), silicon (Kopp et al. 1995), potassium (Eska et al. 1999), sodium and calcium (McNeil et al. 1998; Plane et al. 1999) and the chemistry is well known.

Metals constitute a very small fraction of the total atmospheric constituents in the E-region; however the ionized fraction of metallic atoms is very high when compared with other atmospheric compounds. The reason for the relatively high concentration of metallic ions is their low electron recombination rate, several order of magnitude slower than the recombination of the most abundant ambient ions, O_2^+ and NO^+ . The chemical lifetime of metallic ions is very long and their vertical distribution is strongly influenced by transport mechanisms such as eddy diffusion and layering due to wind shears and electric field. Metallic species are removed from the E-layer by downward transport. Three-body association reactions with atmospheric neutrals produce molecules in the gas phase that subsequently condensate and coagulate to aggregates and aerosols (Hungen et al. 1980). Figure 6 shows a schematic diagram of reactions involving magnesium species, as an example of the chemistry of metallic compounds in the terrestrial atmosphere. It was developed from the works by Plane and Helmer (1995), McNeil et al. (1996) and McNeil et al. (1998).

Magnesium ion are mainly produced by charge exchange with atmospheric ambient species (O_2^+ , NO^+ and O^+) (Grebowksy et al. 1998), and also by direct meteoric ionization and photoionization. The recombination of Mg^+ with electrons is not the main loss process of Mg ions. Three body reactions of Mg^+ with O_2 and N_2 produce MgO_2^+ (Plane and Helmer 1995) and MgN_2^+ (McNeil et al. 1996) and two body reaction with ozone leads to the formation of MgO^+ . These ions are recycled to neutral Mg through molecular dissociative recombination. The chemistry of neutral magnesium is determined by two/three body reactions with oxygen species (O , O_2 and O_3), which produce MgO and MgO_2 . The final sink of Mg may be $Mg(OH)_2$ as obtained by Plane and Helmer (1995) or $MgCO_3$ as calculated McNeil et al. (1996).

Grebowksy et al. (1998) compiled all published studies describing rocket flights which measured meteoric ions between 1963 and 1991. They found that the observed Mg^+ concentrations are lower than those yielded by models and they also confirmed that meteor showers do have significant impact on the average ionospheric composition.

4.2 Mars

Terrestrial knowledge is the starting point to model the meteoroid effects on the atmosphere of Mars. The chemistry of metallic ions is quite similar to the terrestrial case, CO_2 playing the role of the third body in three-body reactions in Mars instead of N_2 on Earth.

Magnesium and iron ions are produced by direct meteoric ionization, photoionization and charge exchange with atmospheric ions, mainly O_2^+ . The last one is the main source for production of metallic ions. Magnesium and iron follow quite similar processes. The oxidation by ozone is the most efficient mode of converting atomic metals into neutral oxides. Once MgO and FeO are formed, three body association of CO_2 provides carbonated metallic atoms, which are the more stable neutrals. Metallic ions can undergo electron recombination or be converted to oxygenated ions. At higher pressure, molecular association by three-body

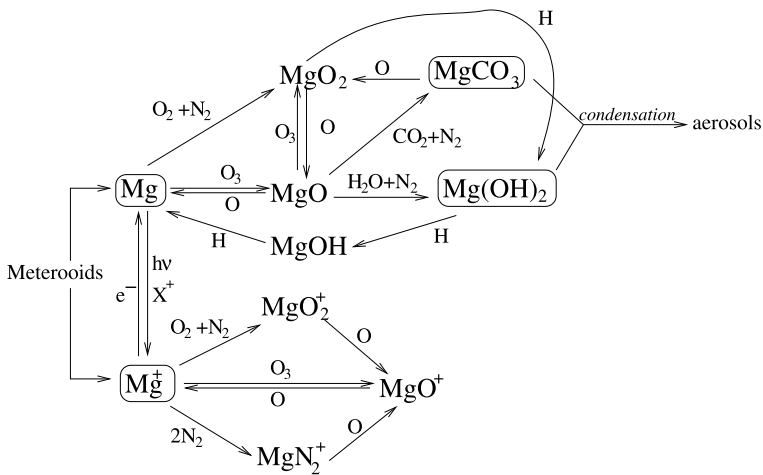
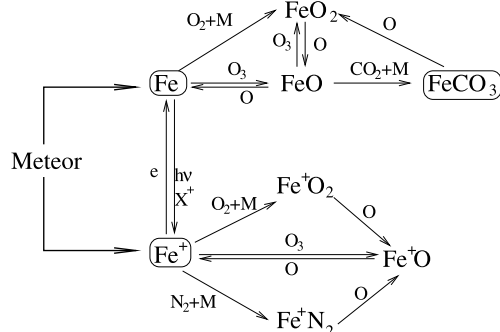


Fig. 5 Schematic diagram of the chemistry of magnesium species in the terrestrial atmosphere, where X^+ represents a non-metallic ion (mainly O^+ and NO^+) and $h\nu$ photoionization. Adapted from Plane and Helmer (1995), McNeil et al. (1996, 1998)

Fig. 6 Schematic diagram of the chemistry of iron species in the martian atmosphere, where X^+ represents a non-metallic ion and $h\nu$ photoionization. Adapted from Molina-Cuberos et al. (2003)



reactions produce molecular ions, which undergo molecular dissociative recombination to form Fe and Mg (Molina-Cuberos et al. 2003). Figure 6 shows a schematic diagram of the chemistry of iron species. For the case of Mg, it follows a general scheme similar to Fe, but with different rates.

Pesnell and Grebowsky (2000) modeled the effect of magnesium in the atmosphere of Mars and predicted a persistent layer of Mg^+ in the order of 10^4 cm^{-3} at around 80 km, which is a factor of around 20 times lower than the main ionospheric peak placed at 130 km. Molina-Cuberos et al. (2003) developed daytime and nighttime models for iron and magnesium produced by meteoric ablation, and the effect of solar activity, and seasonal variations was also explored. They found a meteoric layer formed by Fe^+ and Mg^+ with a magnitude of the order of 10^4 cm^{-3} at noon and decreases by two orders of magnitude during the night. The agreement between the model and the daytime measurements taken by Mars Express (Pätzold et al. 2005) some years later is quite good. Figure 7 shows (solid lines) the electron concentration predicted and a pair of experimental profiles that match better with the theoretical model.

Fig. 7 Theoretical predictions (Molina-Cuberos et al. 2003) (lines) and experimental determination (Pätzold et al. 2005) of meteoroid layers in the Martian ionosphere

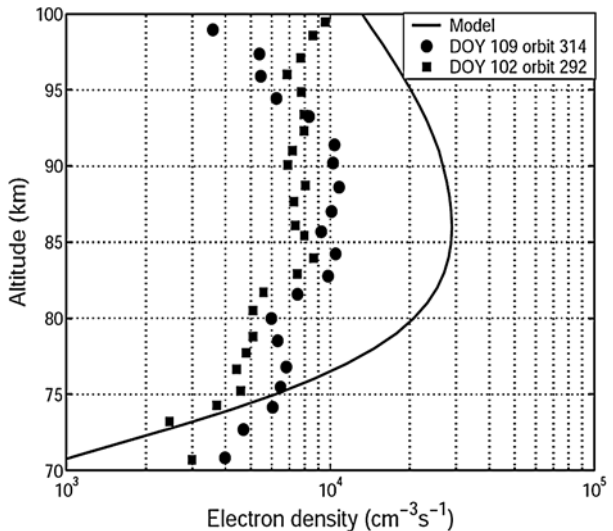
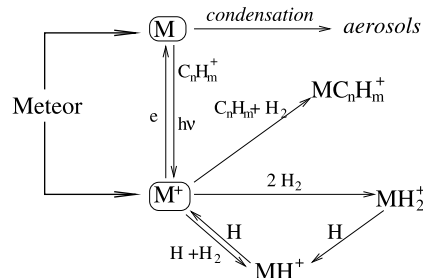


Fig. 8 Schematic diagram of the chemistry of metals in the ionosphere of giant planets, where M represents Mg^+ or Fe^+ . Electron recombination of metals have not been included for higher clarity, adapted from Kim et al. (2001)



4.3 Giant Planets

The hydrogen-hydrocarbons atmosphere of the giant planets is more difficult to model than the Martian one, due to the lack of measurements of reaction rates between hydrocarbons and metallic ions.

The ionospheres of gaseous planets are usually dominated by H^+ in the upper part and H_3^+ prevails below (Kim et al. 2001; Moses and Bass 2000). If metals are not considered in the modeling, then hydrocarbons are the major ionic species in the lower ionosphere (Kim and Fox 1994). However the predicted densities are much lower than the observed ones. The inclusion of meteoric ablation into the atmosphere that produces metal ions that take the place of hydrocarbons as the major ionic species in the lower part of the ionosphere (Kim et al. 2001; Moses and Bass 2000; Lyons 1995). Figure 8 shows a short scheme of the chemistry of metals in the atmosphere of giant planets.

The high gravitational focus of giant planets and the long distance to the Sun results in metallic ions that are mainly produced by charge exchange with atmospheric ions and direct ionization from ablation; the other source, photoionization of metallic neutrals, is much less important. Metallic ions are removed by three-body reactions with hydrocarbons and hydrogen, and the metallic atoms are lost by condensing onto existing aerosols or dust particles. The depletion of atoms is parameterized by assuming a constant lifetime, which depends on the number of dust particles and their size; typical values in the range of (1–6)

$\times 10^5$ s have been used in the modeling of Jupiter (Kim et al. 2001), Saturn (Moses and Bass 2000), and Neptune (Lyons 1995). Three-body reaction between metallic ions (Fe^+ , Mg^+) with the most abundant atmospheric neutral (H_2) has not been confirmed in the laboratory. Even by assuming that the reaction occurs, it results in little net loss of ions, due to the adduct ($\text{Fe}^+\cdot\text{H}_2$ or $\text{Mg}^+\cdot\text{H}_2$) undergoing a sequence of reactions with H atoms which restore metallic ions in the Jovian atmosphere (Kim et al. 2001).

The electron concentration profile of outer planets shows frequent gaps, specially at the dawn terminators, see Fig 3. The layering that is frequently observed in the lower ionospheres of the outer planets could be caused by long-lived atomic ions being moved by horizontal winds that possess vertical shear, such as might occur with atmospheric tides and gravity waves interacting with meteoric ions.

The ablation of meteoroid in the Jovian atmosphere and the chemistry of meteoric ions (O^+ , C^+ , Si^+ , Fe^+ , Mg^+ , Na^+ and S^+) was modeled by Kim et al. (2001). They found a layer of meteoric ions in the altitude region of 350–450 km, above the 1-bar level, with a peak total ion concentration of several times 10^4 cm^{-3} , which are comparable with the observed one. Moses and Bass (2000) studied the effects of external material on the chemistry and structure of Saturn's ionosphere, they found that the ionospheric structure is dominated by two major peak, with H^+ creating the high-altitude peak and Mg^+ , representing the metallic ions, the low-altitude peak with a magnitude in the order of 10^4 cm^{-3} , similar to the upper one. Lyons (1995) also considered metal ions to model the lower ionosphere of Neptune and calculated a concentration of Mg^+ around 1000 cm^{-3} , one order of magnitude lower than the one observed by Voyager 2. The differences are reduced if the magnesium ions are compressed into sharp layers by a sinusoidal vertical wind.

4.4 Titan

The Voyager 1 fly-by of Titan was able to determine an ionospheric peak of $2400 \pm 1100 \text{ cm}^{-3}$ at $1180 \pm 150 \text{ km}$ (Bird et al. 1997), and did not provide any information from below the peak. Therefore, Voyager did not show any evidence for meteoroids effects in its atmosphere. From 2004, Cassini has been orbiting Saturn and several opportunities to sound the ionosphere by radio-occultation and even to determine ionic mass by INMS (Ion and Neutral Mass Spectrometer) will be available in the near future. In spite of the lack of experimental observations of the effects of meteoroids at Titan, some theoretical models have investigated the effects of meteoroids in the composition of neutral (English et al. 1996) and ion (Molina-Cuberos et al. 2001) species. Molina-Cuberos et al. (2001) investigated the ablation of meteoroids and found that long-lived metallic ions considerably change the predictions of the electron number density due to models which only consider solar radiation and electrons trapped in the magnetosphere of Saturn. By using a simple model where metallic ions are lost by termolecular associations with neutral molecules, they concluded that an ionospheric layer could be present at around 700 km, with an electron concentration peak similar in magnitude to the one produced by solar radiation. Petrie (2004) has developed theoretical calculations of Mg^+ reactions with the atmospheric compounds of Titan (N_2 , CH_4 and some nitrogenated hydrocarbons), which allowed the magnesium chemistry to be modelled in more detail and predicted the radical MgNC as the final product.

Acknowledgements This work was supported by contracts ESP2003-00357. The authors thanks Ernesto Martín and Ann and Harry Callaway for their assistance in writing this paper.

References

- L.G. Adolfsson, B.A.S. Gustafson, C.D. Murray, The Martian atmosphere as a meteoroid detector. *Icarus* **119**, 144–152 (1996)
- A.C. Aikin, R.A. Goldbert, Metallic ions in the equatorial ionosphere. *J. Geophys. Res.* **78**, 734–745 (1973)
- A.C. Aikin, W.C. Maguire, Detection in the infrared of $Mg^+ \cdot CO_2$ ion produced via meteoritic material in the Martian atmosphere. *Bull. AAS* **37**, 1567 (2005)
- N. Altobelli, V. Dikarev, S. Kempf et al., Cassini/Cosmic Dust Analyzer in situ dust measurements between Jupiter and Saturn. *J. Geophys. Res.* **112** (2007)
- E. Anders, M. Ebihara, Solar-system abundances of the elements. *Geochemica et Cosmochimica Acta* **46**, 2363–2380 (1982)
- S.J. Bauer, *Physics of Planetary Ionosphere* (Springer, Berlin, 1973)
- M.K. Bird, R. Dutta-Roy, S.W. Asmar, T.A. Rebold, Detection of Titan's ionosphere from Voyager 1 radio occultation observations. *Icarus* **130**, 426–436 (1997)
- L.N. Carter, J.M. Forbes, Global transport and localized layering of metallic ions in the upper atmosphere. *Ann. Geophysicae* **17**, 190–209 (1999)
- S. Chapman, Notes on atmospheric sodium. *Astrophys. J.* **90**, 309–316 (1938)
- S. Chapman, T.G. Cowling, *The Mathematical Theory of Non-Uniform Gases*, 3rd edn. (Cambridge University Press, New York, 1970)
- J.N. Cuzzi, P.R. Estrada, Compositional evolution of Saturn's rings due to meteoroid bombardment. *Icarus* **132**, 1–35 (1998)
- M.A. English, L.M. Lara, R.D. Lorenz, P. Ratcliff, R. Rodrigo, Ablation and chemistry of meteoric materials in the atmosphere of Titan. *Adv. Space Res.* **17**, 157–160 (1996)
- V. Eska, U. von Zahn, J.M.C. Plane, The terrestrial potassium layer (75–110 km) between 71S and 54N: Observations and modeling. *J. Geophys. Res.* **104**(A8), 17173–17186 (1999)
- G. Fjeldbo, W.C. Fjeldbo, V.R. Eshleman, Atmosphere of Mars: Mariner IV models compared. *Science* **153**, 1518–1523 (1966)
- J.M. Grebowsky, Meteoric ion production near Jupiter. *J. Geophys. Res.* **86**, 1537–1543 (1981)
- J.M. Grebowsky, R.A. Goldberg, W.D. Pesnell, Do meteor showers significantly perturb the ionosphere? *J. Atmospheric Sol.-Terr. Phys.* **60**, 607–615 (1998)
- E. Grün, H.A. Zook, M. Baguhl et al., Discovery of Jovian dust streams and interstellar grains by the Ulysses spacecraft. *Nature* **362**, 428–430 (1993)
- E. Grün, H.A. Zook, H. Fechtig, R.H. Giese, Collisional balance of the meteoritic complex. *Icarus* **62**, 244–272 (1985)
- D.A. Gurnett, J.A. Ansher, W.S. Kurth, L.J. Granroth, Micron-sized dust particles detected in the outer solar system by the Voyager 1 and 2 plasma wave instruments. *Geophys. Res. Lett.* **24**, 3125–3128 (1997)
- H. Helmer, J.M.C. Plane, J. Qian, C.S. Gardner, A model of meteoric iron in the upper atmosphere. *J. Geophys. Res.* **103**, 10,913–10,925 (1998)
- D.P. Hinson, F.M. Flasar, A.J. Kliore et al., Jupiter's ionosphere: Results from the first Galileo radio occultation experiment. *Geophys. Res. Lett.* **24**, 2107–2110 (1997)
- D.P. Hinson, J.D. Twicken, E.T. Karayel, Jupiter's ionosphere: New results from Voyager 2 radio occultation measurements. *J. Geophys. Res.* **103**, 9505–9520 (1998)
- D.W. Hughes, Meteors, in *Cosmic Dust*, ed. by J.A.M. McDonnell (Wiley, Chichester, 1978), pp. 123–184
- D.H. Humes, Results of Pioneer 10 and 11 meteoroid experiments: Interplanetary and Near-Saturn. *J. Geophys. Res.* **85**, 5841–5852 (1980)
- D.M. Hunten, R.P. Turco, O.B. Toon, Smoke and dust particles of meteoric origin in the mesosphere and stratosphere. *J. Atmospheric Sci.* **37**, 1342–1357 (1980)
- W.H. Ip, Meteoroid ablation processes in Titan's atmosphere. *Nature* **345**, 511–512 (1990)
- J. Joiner, A.C. Aikin, Temporal and spatial variations in the upper atmospheric Mg^+ . *J. Geophys. Res.* **101**, 5239–5249 (1996)
- W. Jones, Theoretical and observational determinations of the ionization coefficient of meteors. *Mon. Not. R. Astron. Soc.* **288**, 995–1003 (1997)
- Y.H. Kim, J.L. Fox, The chemistry of hydrocarbon ions in the Jovian ionosphere. *Icarus* **112**, 310–325 (1994)
- Y.H. Kim, W.D. Pesnell, J.M. Grebowsky, J.L. Fox, Meteoric ions in the ionosphere of Jupiter. *Icarus* **150**, 261–278 (2001)
- A.J. Kliore, I.R. Patel, A.F. Nagy et al., Initial observations of the nightside ionosphere of Venus from Pioneer Venus orbiter radio occultations. *Science* **205**, 99–102 (1979)
- E. Kopp, On the abundance of metal ions in the lower ionosphere. *J. Geophys. Res.* **102**, 9667–9675 (1997)
- E. Kopp, F. Balsiger, E. Murad, Silicon molecular ions in the D-region. *Geophys. Res. Lett.* **22**, 3473–3476 (1995)

- V.N. Lebedinets, A.V. Manochina, V.B. Shushkova, Interaction of the lower thermosphere with the solid component of the interplanetary medium. *Planet. Space Sci.* **21**, 1317–1332 (1973)
- J.C. Liou, S.F. Dermott, Y.L. Xu, The contribution of cometary dust to the zodiacal cloud. *Planet. Space Sci.* **43**, 717–722 (1995)
- J.R. Lyons, Metal ions in the atmosphere of Neptune. *Science* **267**, 648–651 (1995)
- B. Mason, ed. by B. Mason, Gordon and Breach, *Handbook of Elemental Abundances in Meteorites* (New York, 1971)
- J.P. McAuliffe, A.A. Christou, Modelling meteor ablation in the Venusian atmosphere. *Icarus* **180**, 8–22 (2006)
- W.J. McNeil, S.T. Lai, E. Murad, A model for meteoric magnesium in the ionosphere. *J. Geophys. Res.* **101**, 5251–5229 (1996)
- W.J. McNeil, S.T. Lai, E. Murad, Differential ablation of cosmic dust and implications for the relative abundances of atmospheric metals. *J. Geophys. Res.* **103**, 10,899–10,911 (1998)
- G.J. Molina-Cuberos, H. Lammer, W. Stumpfner et al., Ionospheric layer induced by meteoric ionization in Titan's atmosphere, *Planet. Space Sci.* **49**, 143–153 (2001)
- G.J. Molina-Cuberos, O. Witasse, J.P. Lebreton, R. Rodrigo, J.J. López-Moreno, Meteoric ions in the atmosphere of Mars. *Planet. Space Sci.* **51**, 239–249 (2003)
- J.I. Moses, Meteoroid ablation in Neptune's atmosphere. *Icarus* **99**, 268–383 (1992)
- J.I. Moses, S.F. Bass, The effects of external material on the chemistry and structure of Saturn's ionosphere. *J. Geophys. Res.* **105**, 7013–7052 (2000)
- A.F. Nagy, A.J. Kliore, E. Marouf et al., First results from the ionospheric radio occultations of Saturn by the Cassini spacecraft. *J. Geophys. Res.* **111** (2006)
- E.J. Öpik, *Physics of Meteor Flight in the Atmosphere* (Wiley, New York, 1958)
- M. Pätzold, S. Tellmann, B. Häusle et al., A sporadic third layer in the ionosphere of Mars. *Science* **310**, 837–839 (2005)
- W.D. Pesnell, J. Grebowsky, Meteoric magnesium ions in the Martian atmosphere. *J. Geophys. Res.* **105**, 1695–1707 (2000)
- W.D. Pesnell, J.M. Grebowsky, A.L. and Weisman, Watching meteors on Triton. *Icarus* **169**, 482–491 (2004)
- S. Petrie, Products of meteoric metal ion chemistry within planetary atmospheres I. Mg^+ at Titan. *Icarus* **171**, 199–209 (2004)
- J.M.C. Plane, M. Helmer, Laboratory Study of the Reactions $Mg + O_3$ and $MgO + O_3$. Implications for the chemistry of magnesium in the upper ionosphere. *Faraday Discuss* **100**, 411–430 (1995)
- J.M.C. Plane, R.M. Cox, R.J. Rollason, Metallic layers in the mesopause lower thermosphere region. *Adv. Space Res.* **24**, 1559–1570 (1999)
- N.A. Savich, V.A. Samovol, M.B. Vasilyev et al., The nighttime ionosphere of Mars from Mars-4 and Mars-5 radio occultation dual-frequency measurements, in *Solar-Wind Interaction with the Planets Mercury, Venus, and Mars*, ed. by N.F. Ness. NASA SP-397 (1976), pp. 41–46
- D.F. Strobel, R. Yelle, D.E. Shemansky, S.K. Atreya, *The Upper Atmosphere of Uranus in Uranus* (University of Arizona Press, Tucson, 1991), pp. 65–109
- W.J. Swider, Processes for meteoric elements in the *E* region. *Planet. Space Sci.* **17**, 1233–1246 (1969)

Profiles of Ion and Aerosol Interactions in Planetary Atmospheres

S.N. Tripathi · M. Michael · R.G. Harrison

Originally published in the journal Space Science Reviews, Volume 137, Nos 1–4.
DOI: [10.1007/s11214-008-9367-7](https://doi.org/10.1007/s11214-008-9367-7) © Springer Science+Business Media B.V. 2008

Abstract In planetary atmospheres the nature of the aerosols varies, as does the relative importance of different sources of ion production. The nature of the aerosol and ion production is briefly reviewed here for the atmospheres of Venus, Mars, Jupiter and Titan using the concepts established for the terrestrial atmosphere. Interactions between the ions formed and aerosols present cause (1) charge exchange, which can lead to substantial aerosol charge and (2) ion removal. Consequences of (1) are that (a) charged aerosol are more effectively removed by conducting liquid droplets than uncharged aerosol and (b) particle–particle coagulation rates are modified, influencing particle residence times in the relevant atmosphere. Consequences of (2) are that ions are removed in regions with abundant aerosol, which may preclude charge flow in an atmosphere, such as that associated with an atmospheric electrical circuit. In general, charge should be included in microphysical modeling of the properties of planetary aerosols.

Keywords Ion aerosol attachment · Aerosol charging · Atmospheric conductivity · Planetary dust

1 Introduction

Ion–aerosol interactions are very important in understanding the electrical nature of atmosphere. A direct effect of aerosol charging is the removal of small cluster ions, which reduces the atmosphere’s electrical conductivity (Borucki et al. 1982). Electrical conductivity in an atmosphere is a necessary requirement in permitting an atmospheric electrical global circuit (Aplin 2006a; Aplin et al. 2008).

S.N. Tripathi (✉) · M. Michael

Department of Civil Engineering, Indian Institute of Technology, Kanpur 208016, India
e-mail: snt@iitk.ac.in

R.G. Harrison

Department of Meteorology, University of Reading, PO Box 243, Reading RG6 6BB, UK

Molecular cluster ions, consisting of a few tens of molecules, determine electrical conductivity in the terrestrial lower atmosphere, where weather processes are important. Cluster ions have sufficiently large mobilities to be moved appreciably under the influence of an electric field. The vertical ion concentration profile in the lower atmosphere is determined by various ionizing mechanisms for the production of ions and electrons and the loss processes of these species (Bazilevskaya et al. 2008). Cosmic ray induced ionization, in the lower atmospheres of planets and satellites, lead to the formation of primary negative and positive ions, which readily form ion clusters (Harrison and Tammet 2008). Besides cosmic rays, solar UV photons of very low energies are not absorbed in the ionosphere, and reach the lower atmosphere and surface, causing photoemission of electrons when the energies of the incident photons exceed the threshold energy for photoemission of electrons from particles (Grard 1995; Borucki et al. 2006; Michael et al. 2008).

The cluster ion concentration in a planetary atmosphere is very sensitive to the presence of aerosols, tiny particles suspended in the air originating from various sources. In all atmospheres, aerosols reduce the ion concentrations through the transition of the highly mobile ions into large and massive charged aerosols, by ion–aerosol attachment. As well as ion–aerosol attachment, clusters can be lost by ion–ion or ion–electron recombination. Whereas computation of ion–ion recombination coefficient is relatively straightforward, this is not the case for ion–aerosol attachment coefficient (Hoppel and Frick 1986). Various theories exist for calculating the ion–aerosol attachment coefficient, which depend on the comparative size of the aerosols with the cluster ionic mean free path of the atmosphere. The atmosphere of Venus is very dense and the ionic mean free path is smaller than the aerosol size; this permits ion diffusion to the particle surface. On the other hand, for a tenuous atmosphere like that of Mars, with the ionic mean free path larger than the aerosol size, a kinetic theory approach is required.

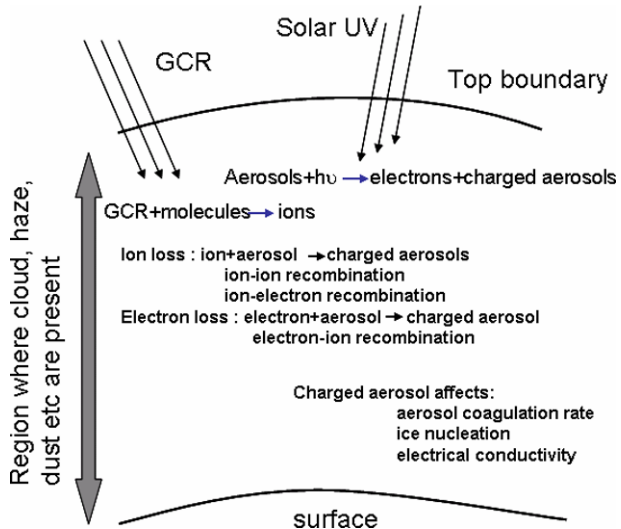
In addition to affecting the conductivity of the atmosphere, aerosol charging reduces aerosol coagulation rate (Harrison and Carslaw 2003), thereby increasing the residence time in the atmospheric column. One consequence is a concentration increase, modifying the optical depth, therefore electrical charging of aerosols is a factor in governing the atmospheric aerosol profiles. Another consequence is an enhancement of aerosol–cloud interactions as the collision efficiency between a particle and a water droplet increases if the particle carries a large charge (Tripathi et al. 2006). In particular, should the drop be supercooled, its freezing probability may be enhanced by the electrically-assisted collection of aerosol facilitating the likelihood of ice nucleation by the contact mode (Tripathi and Harrison 2001, 2002).

In the present review, aerosol charging by ion and electron attachment and the consequences are studied for various atmospheres (see Fig. 1). The review is organized as follows: Ion production in the lower atmospheres of Venus, Mars, Jupiter and Titan is discussed in Sect. 2, Aerosol characteristics (Sect. 3), calculation of ion–aerosol attachment coefficient (Sect. 4), aerosol charging (Sect. 5), and consequences of aerosol charging in atmospheres (Sect. 6). Possible future work is discussed in Sect. 7.

2 Ion Production

Galactic cosmic rays (GCR) have energies spanning a wide range, and contribute to ionization in a planetary atmosphere. GCR have been shown to be the most significant source of ionization (Dubach et al. 1974; Capone et al. 1976, 1977, 1979, 1980), especially in relatively dense regions of a planetary atmosphere with little ionizing solar ultraviolet radiation. GCR originate in interstellar medium, which encounter the solar wind and solar

Fig. 1 Schematic of ion–aerosol processes in a planetary atmosphere. “Top boundary” defines the altitude at which the effect of particles on electrical conductivity ceases; Venus (80 km), Mars (70 km), Jupiter (0.1 mbar), and Titan (400 km)



magnetic field in the heliosphere. In times of higher solar activity the heliosphere deflects GCR from a planet. Therefore, GCR flux is at its minimum during maximum solar activity. The spectrum of the incident cosmic ray flux falls off sufficiently slowly at high energies that a significant portion of the total energy flux is carried by high-energy particles. The largest energy fraction in the cosmic ray flux is typically carried by particles having kinetic energies of at least 1 GeV. Such high energies produce electromagnetic and particle cascades in the atmosphere. A detailed discussion about cosmic rays and their general interaction with planetary atmospheres is presented in Bazilevskaya et al. (2008). Here we consider processes in the planetary atmospheres separately.

2.1 Venus

Cosmic rays incident on the atmosphere interact with the atmospheric gas atoms and molecules. The incident radiation is mainly atomic nuclei, consisting of ~90% protons, ~10% He nuclei, and about 1% heavier nuclei (Upadhyay et al. 1994).

Chen and Nagy (1978) have shown that the ionizing solar ultraviolet radiation does not penetrate much below ~120 km, whereas solar flare X-rays are the most important source of ionization in the 60 to 100 km altitude region. Thus, below ~60 km or during the Venusian night, galactic cosmic rays are the principal ionizing agent for the atmosphere. The shape of the cosmic ray spectrum is such that a significant fraction of the total energy flux is carried by particles with kinetic energies above 1 GeV. In fact, incident cosmic rays with energies as high as 10 TeV contribute to a significant ionization at penetration depths¹ of ~100 g cm⁻². Borucki et al. (1982) used the method developed by O’Brien (1969, 1970, 1971, 1972) to calculate the cosmic ray-induced ionization rates in the Venusian atmosphere. Ionization of the atmosphere by energetic particles produces primary ions CO₂⁺, CO⁺, and O₂⁺ and electrons. Because the collision frequency with neutral species is large, the primary ions and

¹Depth is defined as the integrated mass density of the atmosphere above any given altitude. The total depth of the Venusian atmosphere is approximately 10⁵ g cm⁻².

electrons rapidly form secondary ions and ion clusters. The conductivity of the atmosphere is governed by the mobility of these long-lived secondary ions and ion clusters, rather than by the very mobile, but short-lived, primary ions and electrons. Borucki et al. (1982) estimated that ions such as $\text{H}_3\text{O}^+\cdot\text{SO}_2$ (81 amu), $\text{H}_3\text{O}^+\text{H}_2\text{O}\cdot\text{CO}_2$ (81 amu), $\text{H}_3\text{O}^+\cdot(\text{H}_2\text{O})_3$ (73 amu), and $\text{H}_3\text{O}^+\cdot(\text{H}_2\text{O})_4$ (91 amu) are the most abundant positive ion clusters. In the atmosphere of Venus, sulfur dioxide and oxygen are the major gaseous species to which free electrons may attach. O_2^- readily transfers its charge to sulfur dioxide and the subsequent reactions of SO_2^- are uncertain. The study of Keesee et al. (1980) suggested that $(\text{SO}_2)_2^-$ would prevail above about 25 km.

2.2 Mars

Whitten et al. (1971) carried out a detailed study of the lower ionosphere of Mars. They considered the ionization by GCR and solar radiation in an ion-neutral model, and calculated the concentration of ions and electrons below 80 km. Molina-Cuberos et al. (2001) improved the study of the lower ionosphere of Mars by developing a more detailed ion-neutral model which includes more neutral compounds and improved reaction rates than previous studies. Molina-Cuberos et al. (2001) calculated the cosmic ray ionization rates of CO_2 , N_2 and Ar. The ionization by cosmic rays in the Martian atmosphere is mainly due to the slowing down of protons and Molina-Cuberos et al. (2001) used measurements of the dissociative and non-dissociative ionization of CO_2 and N_2 by proton impact. The maximum ion concentration occurs at the surface. Hydrated hydronium ions $\text{H}_3\text{O}^+(\text{H}_2\text{O})_n$ (n varies from 1 to 4) are the most abundant positive ions for all altitudes below 70 km. CO_2^+CO_2 becomes important at altitudes more than 65 km. The most abundant negative ion is $\text{CO}_3^-(\text{H}_2\text{O})_2$. Recently, Haider et al. (2008) studied in detail the chemistry of the ion production at high latitudes in the atmosphere of Mars.

2.3 Jupiter

In the Jovian atmosphere (from 10 bar to 1 mbar) muon flux component of galactic cosmic rays are the main ionization source (Whitten et al. 2008). They penetrate to the deep atmosphere at levels where the total number density exceeds 10^{25} m^{-3} and ionize the neutral constituents producing the primary ions H_2^+ , He^+ , CH_4^+ , CH_3^+ , CH_2^+ , and electrons. Fast reactions with the neutrals rapidly convert these into secondary ions and ion clusters. The He^+ ions formed initially are converted into CH_5^+ due to the abundance of H_2 and CH_4 and the inverse temperature dependence of three-body association reaction (Hiraoka and Kebarle 1975). CH_5^+ reacts with C_2H_6 and NH_3 to produce C_2H_7^+ and NH_4^+ , respectively (Capone et al. 1979). The formation of the cluster between NH_4^+ and NH_3 controls the loss process of NH_4^+ in the lower deep troposphere of Jupiter. At equilibrium, the cluster ion $\text{NH}_4^+(\text{NH}_3)_n$ is expected to be dominated by ions with ammonia composition $n = 4$ between 10 bar and 1 bar, but by $n = 2$ ions at 100 mbar due to increasing temperature and decreasing ammonia concentration. $\text{CH}_5^+\cdot(\text{CH}_4)_4$ is formed at 0.01 bar, and $\text{CH}_5^+\cdot(\text{CH}_4)_2$ is formed at pressures 0.001 bars (Whitten et al. 2008).

2.4 Titan

Since the intensity of the solar UV radiation decreases with the square of the distance from the Sun, GCR-induced ionization assumes greater relative importance in the atmospheres of the outer planets and satellites. GCR-induced electromagnetic and particle cascade penetrate

Table 1 Ion clusters compositions in planetary atmospheres

	Venus	Mars	Titan	Jupiter
Positive ion cluster	$\text{H}_3\text{O}^+\cdot\text{SO}_2$, $\text{H}_3\text{O}^+\cdot\text{H}_2\text{O}\cdot\text{CO}_2$, $\text{H}_3\text{O}^+\cdot(\text{H}_2\text{O})_3$, $\text{H}_3\text{O}^+\cdot(\text{H}_2\text{O})_4$	$\text{H}_3^+\text{O}(\text{H}_2\text{O})_n$	$(\text{H}_2\text{CN}^+(\text{HCN})_3)$	$\text{NH}_4^+(\text{NH}_3)_n$, $\text{CH}_5^+(\text{CH}_4)_n$
Negative ion cluster	$(\text{SO}_2)_2^-$	$\text{CO}_3^-(\text{H}_2\text{O})_2$	–	–

to relatively great depths (i.e. high pressures) in the extended, massive atmosphere of Titan. Ionization also occurs in the atmosphere of Titan through particles precipitating from the magnetosphere of Saturn.

The ion clusters formed in the lower atmosphere of Titan were studied by Borucki et al. (1987, 2006) and their masses estimated to be 30 to 102 amu. $\text{HCO}^+\cdot\text{H}_2$ and $\text{CH}_5^+\cdot\text{CH}_4$ are the major positive ions at altitudes below 80 km. C_7H_7^+ and $\text{H}_4\text{C}_7\text{N}^+$ are the most abundant positive ion clusters for altitudes 80 to 260 km, and 260 to 400 km, respectively. Studies showed that there is a lack of electrophilic species in the atmosphere of Titan (Borucki et al. 1987, 2006; Lara et al. 1996; Molina-Cuberos et al. 2000), and there is therefore a large abundance of electrons. During the descent of Huygens probe through the atmosphere of Titan on 14th January 2005, electron conductivity and density profiles were derived using the Huygens atmospheric structure instrument (HASI). This carried two different instruments, a relaxation probe and a mutual impedance probe (Hamelin et al. 2007). The observations suggest that the electron concentration is at least a factor of two lower than that predicted by previous studies (Borucki et al. 1987, 2006; Molina-Cuberos et al. 1999). Though it was generally accepted earlier that electrophilic species are absent in Titan's atmosphere, the recent observations by HASI suggest that they could be present with a maximum concentration of a few ppm. The most abundant ion clusters in the atmospheres of Venus, Mars, Jupiter and Titan are presented in Table 1.

3 Aerosol Characteristics

Aerosols are sub-micron to micron sized solid particles or liquid droplets suspended in air. In the terrestrial atmosphere, some aerosols are generated naturally, originating from volcanoes, dust storms, forest and grassland fires, living vegetation, and sea spray. Human activities, such as fossil fuel combustion and the alteration of natural surface cover, also generate aerosols. In planetary atmospheres, the sources of aerosols are also very variable.

3.1 Venus

The clouds of Venus are generally thought of as a photochemical haze observed in the altitude range of 48–70 km. According to Rossow (1977) there are two different mechanisms for the formation of these clouds. Near the cloud top, photochemistry leads to the formation of cloud particles; near the cloud base, condensation of sulfuric acid vapor on hydrated sulfuric acid particles is responsible for the particle formation.

In situ probe measurements detected three cloud layers (upper, middle, and lower) based on distinctive cloud particle size distributions of ~ 0.4 , ~ 2 and $\sim 7 \mu\text{m}$ (Esposito et al. 1983; Crisp et al. 1991; Carlson et al. 1993; Grinspoon et al. 1993). The cloud particles have a number density ranging from 100 to 1000 cm^{-3} and the particle size distribution is bimodal

(Knollenberg and Hunten 1980; Pollack et al. 1993; Grinspoon et al. 1993; Krasnopolksy 1989). The thick opaque cloud region between 48–56 km was clearly observed on Galileo and ground-based near-infra red images of Venus (Crisp et al. 1989; Bell et al. 1991; Carlson et al. 1993; Grinspoon et al. 1993). Microphysical processes in the cloud layer are described in detail in various papers (e.g., Toon et al. 1982; James et al. 1997; Imamura and Hashimoto 1998, 2001). An upper haze layer is observed in the altitude range of 70–90 km, containing particles with an effective radius of 0.2–0.3 μm , composed of $\text{H}_2\text{SO}_4/\text{H}_2\text{O}$ aerosol of 75% sulfuric acid (Kawabata et al. 1980). A transport model between this haze layer and the atmospheric cloud is discussed in Yamamoto and Takahashi (2006).

3.2 Mars

Dust enters the atmosphere of Mars mainly by the thermally driven wind and then by saltation and strong updraft by the dust devils. Dust particle sizes in the Martian atmosphere have been known since the Mariner 9 and Viking missions (Conrath 1975; Pang and Ajello 1977; Toon et al. 1977). Observations of Martian aerosols from Viking orbiter and lander cameras are discussed in Clancy and Lee (1991) and Pollack et al. (1979). Clancy and Lee (1991) suggested that the effective radius of the dust particles, as seen from the Martian surface, is $\sim 2.5 \mu\text{m}$ and the size distribution of dust is constant at sub-solar latitudes. Vertical profiles of the mixing ratio and size of the dust particles in the 15–25 km altitude range were estimated from the solar occultation measurements performed by the Auguste instrument onboard Phobos 2 spacecraft (Korablev et al. 1993; Chassefiere et al. 1992). The effective radius of the particles was found to be $\sim 0.8 \mu\text{m}$ at 25 km and $\sim 1.6 \mu\text{m}$ at 15 km. Their number density is $\sim 0.3 \text{ cm}^{-3}$ in the same altitude range. Chassefiere et al. (1995) extrapolated the solar occultation profiles from the 15–25 km altitude range down to the ground. An effective radius of $\sim 1.25 \mu\text{m}$ was inferred from the analysis of the dust component observed by the ISM infrared spectrometer (Drossart et al. 1991).

Mars aerosol studies with Mars Global Surveyor Thermal Emission Spectrometer during 1999–2001 have been summarized by Clancy et al. (2003). They suggested that the dust particle sizes vary with latitudes. The properties of dust observed by Mars Pathfinder and the Mars Exploration rovers are discussed in Tomasko et al. (1999) and Lemmon et al. (2004). Montmessin et al. (2006) presented the aerosol size distribution from the SPICAM ultraviolet instrument onboard Mars Express. Goetz et al. (2005) studied the dust using Mossbauer spectroscopy and suggest that the dust contains magnetite, olivine and some ferric oxides. The presence of olivine indicates that liquid water did not play a dominant role in the processes that formed the atmospheric dust.

3.3 Jupiter

Haze in the atmosphere of Jupiter extend in altitude as deep as the 10 bar pressure level to as high as the $\sim 0.5 \text{ mbar}$ (Owen 1969; Smith et al. 1977; West 1979, 1988; Hord et al. 1979; Smith 1980; West et al. 1981, 1992; Tomasko et al. 1986; Banfield et al. 1998; Friedson et al. 2002). The haze chemistry is thought to involve coupling among hydrocarbon photochemistry, ion-neutral chemistry, auroral processes, and particle microphysics. Strobel (1985) suggested that ammonia photolysis in the lower stratosphere leads to the production and condensation of hydrazine. The suggestion of Hord et al. (1979) that the auroral breakdown of methane leads to the formation and growth of carbonaceous particles has been supported by other workers (Kim et al. 1985; Pryor and Hord 1991; Vincent et al. 2000;

Wong et al. 2000, 2003). Detailed discussion of Jovian atmospheric aerosol is provided in West et al. (1986) with the particles' physical properties discussed further in Mishchenko (1990), Moreno (1996), and Lebonnois (2005). A detailed discussion on the cloud and haze particles in the Jovian atmosphere using the observations of Galileo instruments, ground based and Hubble Space Telescope is provided in West et al. (2004). The optical and physical properties of the haze particles, like the composition, size and shape and the formation of the particles are also discussed in West et al. (2004). Atreya and Wong (2005) provided a good picture of the structure of Jovian clouds through combining the Galileo data, remote imaging and thermochemical models. The Galileo probe detected tenuous cloud layers at 0.5, 1.3 and 1.6 bar levels (Ragent et al. 1998) which most likely represent the clouds of NH₃-ice, NH₄SH-ice, and H₂O-ice, respectively (Atreya et al. 1999).

3.4 Titan

Spacecraft observations show aerosols are abundant in the Titan atmosphere. Titan's haze particles consist of complex organic molecules, derived from methane and nitrogen photochemistry (Khare and Sagan 1973; McKay et al. 2001; Khare et al. 2002; Atreya 2007). Size information is derived from the Voyager photopolarimeter observations (West et al. 1983), Voyager high-phase-angle images (Rages et al. 1983) and photometry and polarimetry measurements from Pioneer 11 (Tomasko and Smith 1982). Analysis of Voyager 2 images by Rages and Pollack (1983) indicate that between 220 km and 350 km the aerosol particles have radii near 0.3 μm and have number densities that range from about 0.2 particles/cc at 350 km to 2 particles/cc near 220 km. Benzene was detected by the Infrared Space Observatory (Coustonis et al. 2003). Benzene, in a chain of reactions, leads to formation of polyaromatic hydrocarbons (PAH) by continued removal of hydrogen atom and acetylene addition. Cassini instruments detected large positively charged ions (100–350 amu) and negatively charged ions (20–8000 amu) and Waite et al. (2007) confirmed the large negatively charged particles as tholins and predicted the size as ~100–260 nm. Observations of haze particles by Huygens probe Descent Imager / Spectral Radiometer (DISR) were reported by Tomasko et al. (2005). The DISR instrument measured the linear polarization of scattered sunlight and the comparison of polarization with model computations for different sized fractal aggregate particles indicate that the radii of the monomers comprising the aggregate particles is near 0.05 μm, almost independent of the number of monomers in the particle. Contrary to the expectation that the Titan haze clears below an altitude of about 50 km, the DISR downward-looking spectrometer observed significant haze opacity at all altitudes throughout the descent, extending all the way down to the surface (Tomasko et al. 2005).

4 Ion–Aerosol Interactions

The problem of droplet charging by ionic diffusion was originally addressed by Millikan (1911). During the experiment, Millikan (1911) observed that negatively charged droplets were able to catch more negative ions. This was interpreted as evidence that the ions must have sufficient kinetic energy to maintain the surface of the drop against the electrostatic repulsion generated by the charge on the drop. It was concluded that the only way a droplet could lose or gain charge was to capture an ion of appropriate sign. The diffusion of ions to droplets is a real and continuous process. Once captured, ions can never escape because of the work they must do to overcome the local electric image forces. The image force increases faster than the inverse square law and is appreciable for distances considerably less than one mean free path away from the droplet.

Later Arndt and Kallmann (1925) and Frenkel (1946) studied quantitatively the charging of droplets, but the assumptions they adopted were not reasonable. Gunn (1954) estimated the role of ionic diffusion in the electrical charging of drops and noticed that not more than a single ion may be carried by a droplet of radius less than 0.01 μm , unless energetic chemical forces modify. On the other hand, if drops are appreciably larger than the ionic mean free path, relatively many ions may be transferred to the droplet. Gunn (1954) suggested that ions of both signs diffuse into the droplet surface and the ion attachment coefficient can be expressed using the following equations.

$$\beta_+ = \frac{4\pi Q\mu_+}{\exp(Qe/akT) - 1}, \quad (1)$$

$$\beta_- = \frac{4\pi Q\mu_-}{1 - \exp(-Qe/akT)}. \quad (2)$$

Here, β_+ and β_- are the positive and negative ion attachment coefficients, respectively, Q is the free electrical charge resident on the droplet, μ_+ and μ_- are the mobilities of positive and negative ions, respectively, e is the elementary charge, a is the droplet radius, k is the Boltzmann constant and T is the temperature.

The different theories for ion–aerosol attachment are summarized by Fjeld and McFarland (1986). These can be divided into three different types. Diffusion theory applies to particles having radii larger than the ionic mean free path; it assumes ion diffusion to the particles' surface. Here ions are trapped by image force (Keefe et al. 1968; Hoppel 1977). At the other extreme (small particle size) are the free molecular or effusive theories, which use a kinetic approach. Here the attachment occurs via 3-body trapping (similar to the ion–ion recombination). In the intermediate region (size of the particles and the ionic mean free path become comparable), transition regime theory is used. Image capture has a maximal effect for uncharged particles, and its importance relative to the Coulomb force (for charged particles) increases with aerosol particle radius. For aerosols much smaller than the ionic mean free path, attachment is also dominated by image capture, but for discharging events a three-body collision process as in ionic recombination is dominant. In the transition regime, a combination of diffusion and effusion mechanisms is used. The mean free path is smaller than the radius of aerosols in the atmosphere of Venus, whereas the opposite is true in Mars. In Titan's atmosphere the mean free path is smaller for altitudes less than 50 km; above this height the mean free path is larger than the aerosol size.

As discussed in Gunn (1954) the theory of the diffusion of ions to aerosols with radii larger than the ionic mean free path is well established. The study of the attachment of ion to aerosols of radii comparable to or smaller than the ionic mean free path has been more difficult (Hoppel and Frick 1986). The concept of a limiting sphere—concentric with the aerosol but with radius the order of a mean free path larger than the aerosol was defined by Fuchs (1964). The diffusion—mobility treatment holds outside this sphere, with kinetic theory applied for the region inside.

If an aerosol particle carries a single charge then the ion–aerosol recombination coefficient reduces to the ion–ion recombination coefficient and can be explained using 3-body trapping theory, which requires the trapping distance. The ion–aerosol trapping distance is obtained from the ion–ion trapping distance which itself can be calculated from the ion–ion recombination coefficient (Natanson 1960). In addition to the 3-body trapping there can be trapping of the ion by image force. The image force can lead to orbits which spiral into the aerosol, which means any ions which approach the aerosol closer than the image capture distance will spiral into the aerosol under the influence of the image force. The image capture sphere and the resulting attachment coefficient were calculated by Keefe et al. (1968).

Fig. 2 Schematic of image force, and three body trapping distance. Δ is the image capture distance, δ is the three-body trapping distance, a is the radius of the particle and b_Δ is the impact parameter

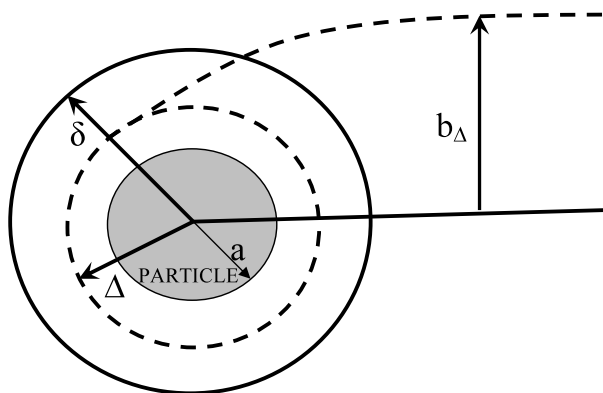
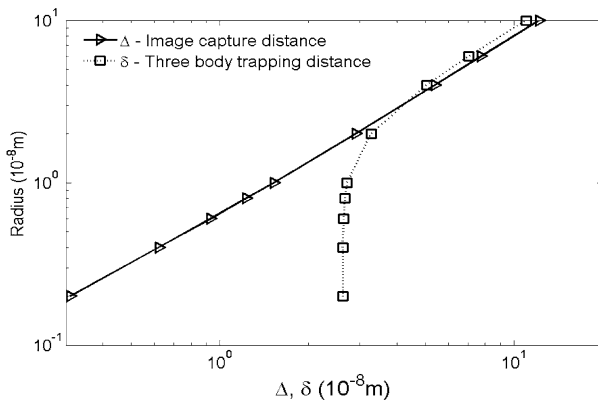


Fig. 3 Importance of image force distance and three body trapping distance with respect to the size of the aerosol. (Data from Hoppel and Frick 1986)



Jensen and Thomas (1991) used the expression developed by Natanson (1960) to calculate the ion capture rates by small ice and meteoric particles in the terrestrial mesosphere.

Hoppel and Frick (1986) estimated the relative importance of image capture and three-body trapping and included both effects in a single theory to calculate the attachment coefficients. Figure 2 demonstrates the two trapping spheres. The image capture sphere extends to the distance (Δ) corresponding to the minimum apsidal distance (i.e. the distance of closest approach where radial velocity vanishes). If the impact parameter is greater than b_Δ , the ion escapes, and if the impact parameter is less than b_Δ , the ion spirals into the aerosol. When an ion collides with an aerosol particle, part of its kinetic energy is lost to the aerosol. If this energy is sufficiently high the ion will be trapped in the coulomb field of the aerosol. The three-body trapping distance δ is defined as the average separation distance where the removed energy is enough to ensure trapping. If the image capture distance Δ is greater than the three-body trapping distance δ , three-body trapping is not important. Δ is always larger than δ for uncharged aerosol, but if the ion and the aerosol have opposite polarity, there is a critical radius of the aerosol below which the three-body trapping becomes important. Hoppel and Frick (1986) calculated Δ and δ as a function of the radius of the aerosol and the same is presented in Fig. 3. The relative importance of Δ and δ at Venus, Mars and Titan are shown in Fig. 4.

Hoppel and Frick (1986) calculated the attachment coefficients for ionic mass 150 amu and found, for radii less than about 2×10^{-8} m, no aerosol is-doubly charged and, for

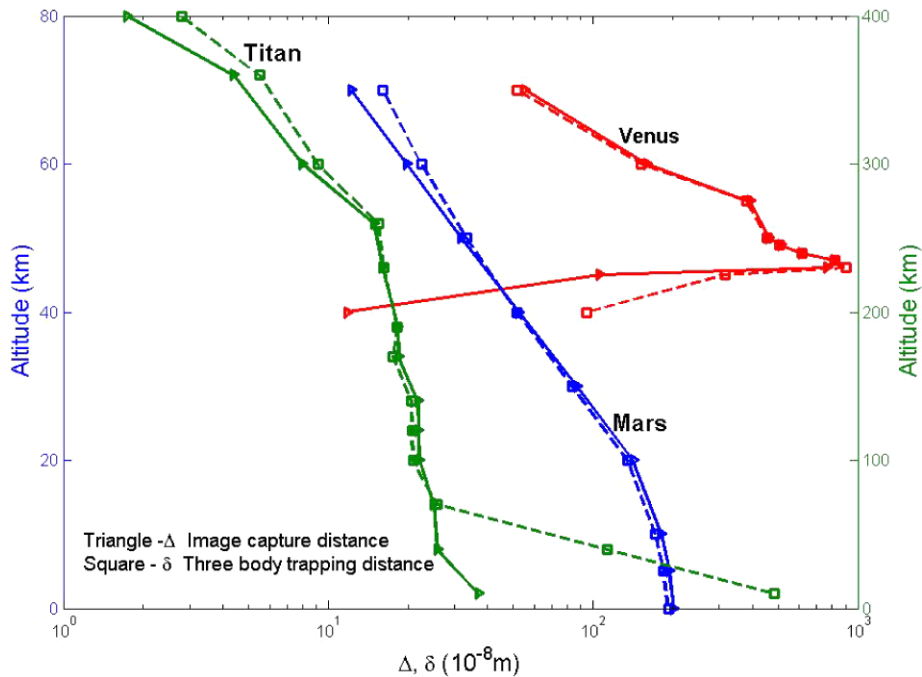
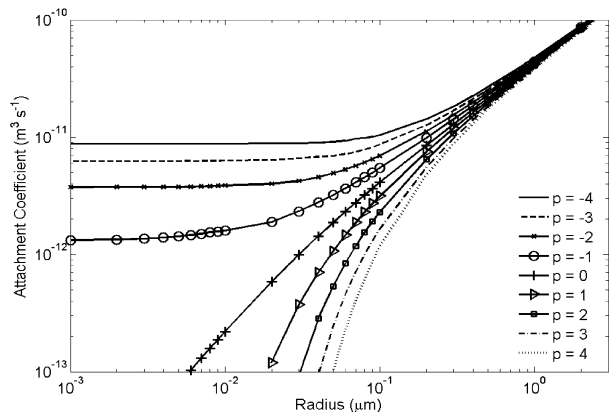


Fig. 4 Relative importance of Δ and δ for various planets. The green lines (Titan) correspond to the right y-axis and the blue (Mars) and red (Venus) lines correspond to the left y-axis

Fig. 5 Ion–aerosol attachment coefficients for ions of 150 amu (Hoppel and Frick 1986)



aerosols less than about 3×10^{-8} m, triply charged aerosols can be neglected. The attachment coefficients as a function of aerosol radius was estimated by Hoppel and Frick (1986), as presented in Fig. 5 and found that the attachment coefficient increases as the radius increases. Tripathi and Michael (2008) describes the calculation of ion–aerosol attachment coefficients using the theory of Hoppel and Frick (1986). Figure 6 presents the attachment coefficients estimated for Venus, Mars and Titan.

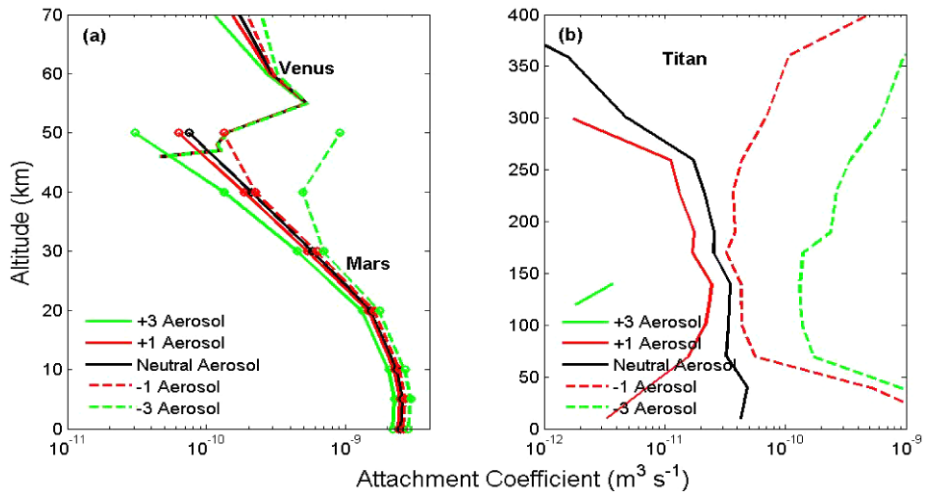


Fig. 6 Attachment coefficients estimated for various planets. (a) Venus and Mars, (b) Titan. Positive aerosols mean they are of opposite polarity (i.e. “+3 aerosol” means the attachment coefficient of a positive ion to a particle of charge −3 or the attachment coefficient of a negative ion to a particle of charge +3). In Venus, the effect of ion–aerosol attachment in the atmospheric conductivity occurs only for altitudes 45–70 km

5 Aerosol Charging

Aerosol charging depends on ion–aerosol attachment coefficients and the ion–ion and ion–electron recombination coefficients. As the attachment coefficients and the recombination coefficients vary with temperature and pressure, and therefore with altitude in atmosphere, the aerosol charging rate also varies with altitude. The concentrations of ions, electrons and aerosols can be found from the three-level probabilistic master equations. These constitute a set of $2s + 4$ simultaneous differential equations, where s is the maximum number of elementary charges allowed on a particle (Yair and Levin 1989). The ion and electron charge balance equations can thus be written as

$$\frac{dn^+}{dt} = q_{\text{ion}} - \alpha n^+ n^- - \alpha_e n^+ n^e - n^+ \sum_i (\beta_1^{(i)} N^i), \quad (3)$$

$$\frac{dn^-}{dt} = q_{\text{ion}} - \alpha n^+ n^- - n^- \sum_i (\beta_2^{(i)} N^i) - F n^-, \quad (4)$$

$$\frac{dn^e}{dt} = q_e - \alpha_e n^+ n^e - n^e \sum_i (\beta_e^{(i)} N^i) + F n^- - n^e \sum_j \beta_j n^j. \quad (5)$$

Here, α is the ion–ion recombination coefficient, α_e is the electron–ion recombination coefficient, q_{ion} is the ion production rate, q_e is the electron production rate, β_j^i is the attachment coefficient for ions of polarity j (1 for positive and 2 for negative) to particles with charge i , β_e^i is the electron attachment coefficient to particles with charge i , β_j is the electron attachment coefficient to species j , and N^i is the density of particles of charge i . F represents the detachment of electrons from negative ions and is evaluated using the equation from

Borucki et al. (1982).

$$F \approx p\pi^{1/2} \frac{L_m}{L_1} \frac{P}{KT} \sigma^2 \left(\frac{8KT}{\pi m} \right)^{1/2} \left(\frac{E_a}{KT} + 1 \right) \exp\left(-\frac{E_a}{KT}\right). \quad (6)$$

Here p is the probability of an energetic collision removing an electron, L_M/L_I is the ratio of the mean free path of neutral molecules to that of ions, P is the pressure, σ is the collision cross section, E_a is the electron affinity of the negative ions, m is the mass of the negative ions, k is the Boltzmann constant, and T is the temperature (Borucki et al. 1982).

Parthasarathy (1976) derived a steady-state recurrence relation to compute the build-up of electric charge on aerosol particles due to collision with positive and negative ions and electrons. Whitten et al. (2007) modified the recurrence expression given by Parthasarathy (1976) to estimate the charge distribution on aerosols and used the method of Jensen and Thomas (1991) to reflect the time dependence of the charge accumulation by aerosols. The time dependent charge balance equations for the aerosols are

$$\frac{dN^i}{dt} = \beta_1^{(i-1)} n^+ N^{(i-1)} + \beta_2^{(i+1)} n^- N^{(i+1)} + \beta_e n^e N^{(i+1)} - \beta_1^{(i)} n^+ N^i - \beta_2^{(i)} n^- N^i - \beta_e n^e N^i \quad (7)$$

where β_e is the electron-aerosol attachment coefficient.

5.1 Venus

Aerosol charging in the Venusian atmosphere is appreciable at altitudes below 80 km. For altitudes above 60 km, additional electrons produced by photodetachment substantially increase the electron concentration. Below this altitude, electrons rapidly attach themselves to neutral molecules, which become more abundant as the atmosphere becomes denser. There is a reduction of 10–20% in the ion and electron densities above 70 km (Borucki et al. 1982).

5.2 Mars

In the Martian atmosphere the charging of aerosols is appreciable below 70 km. Michael et al. (2007) showed that the concentration of charged aerosols decreases as the altitude increases. The aerosols are charged up to 36 elementary charges (i.e. $-36e$ and $+36e$) at 0 km in the atmosphere, but at 70 km the aerosols are charged only up to $\pm 2e$. The concentration of charged aerosols decreases as the charge on the aerosol increases, i.e. the neutral aerosols have a maximum concentration whereas the aerosols with maximum charges have their minimum concentration. It was also noted by Michael et al. (2007) that the steady-state concentration of the aerosols with positive charges is somewhat higher than the corresponding negatively charged aerosols. This is because the positive ions have higher mobility and are attached to the aerosols faster. Michael et al. (2008) studied the day-time charging of aerosols when electrons are also present in the atmosphere along with ions. It was found that more negatively charged aerosols are produced when electrons have a much higher mobility than the ions. More than 80% of the neutral aerosols get charged close to the surface and almost none become charged at the upper boundary (70 km). This is due to the characteristics of the ion–aerosol attachment coefficients and the number density of the aerosols.

5.3 Jupiter

The cloud charging by ion and electron attachment in the atmosphere of Jupiter (for pressures between 5.5 and 0.1 mbar) has been studied by Whitten et al. (2008). For pressures below 4 mbar the electrons are scavenged by cloud particles and thereby increasing the positive ion abundance as the electron–ion recombination decreases. At most atmospheric pressures greater than 2.2 bars, the charge on the low cloud particles is negative and at atmospheric pressures of 2.2 bars and less, the mean charge on the lower cloud particles becomes positive. The charge on the middle and upper cloud particles is negative (Whitten et al. 2008).

5.4 Titan

Aerosol charging during the nocturnal atmosphere for the altitude region 0–400 km is studied by Whitten et al. (2007). During the night, no negative ions are present (Borucki et al. 1987) and for altitudes between 170 and 350 km electrons get attached to the polycyclic aromatic hydrocarbons (PAH, which are similar in mass and mobility with respect to positive ions), and become negatively charged. The densities of positive ions and electrons are similar at altitudes greater than 350 km as the abundance of PAH is very low. At low altitudes the positive ion and electron densities decrease rapidly because of ion–electron recombination. The mean charges attained by the aerosol after the ion-attachment are –6, –6 and –3 at altitudes of 50, 150 and 250 km, respectively (Whitten et al. 2007). The charging of aerosols was modeled by Borucki et al. (2006) for the day-time atmosphere of Titan. During the daytime, solar UV radiation knocks out electrons from aerosols. It was inferred by Borucki et al. (2006) that the charge distribution of aerosols moves to larger positive values as the altitude increases. About 350 positive charges were acquired by aerosols at 350 km altitude. This is a result of the increased solar UV flux at higher altitudes.

6 Atmospheric Consequences of Aerosol Charging

6.1 Electrical Conductivity

The atmospheric conductivity depends on the existence of positive and negative ions, and the resulting conductivity can be found from the number densities and mobilities of the individual charged species. In the lower atmosphere the conductivity is maintained by the small ions. The attachment of ions to aerosols reduces the conductivity as they become almost immobile by attachment to aerosol particles. The conductivity of the atmosphere is calculated as

$$\sigma = e(n_+ K_+ + n_- K_- + n_e K_e) \quad (8)$$

where e is the electronic charge, n and n_e are the number densities of ions and electrons, respectively and K and K_e are the corresponding mobilities. The atmospheric electrification at various bodies in the solar system is reviewed in Aplin (2006a).

Venus: Borucki et al. (1982) modeled the ion–particle interaction and the atmospheric electricity and Aplin (2006b) debated on the existence of the global electric circuit on Venus. With certain assumptions, Borucki et al. (1982) suggested that the effect of particles in the atmosphere for altitudes less than 47 km, on the conductivity is negligible. Between 47 and

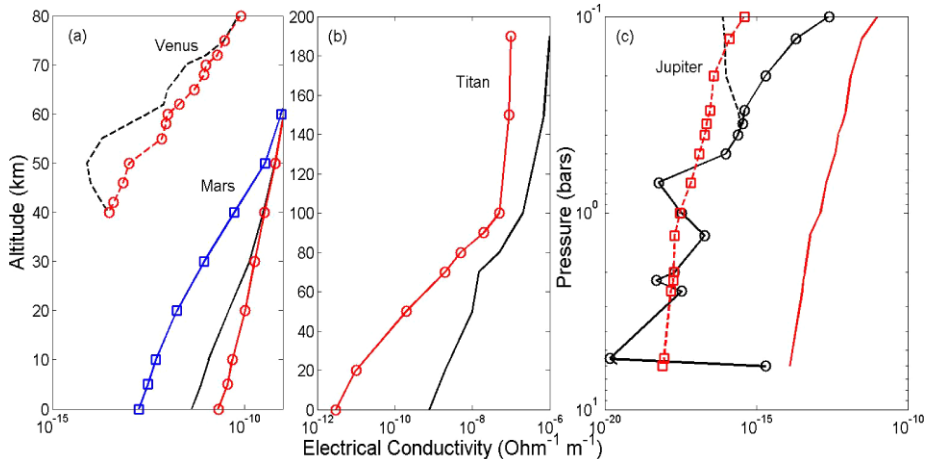


Fig. 7 Effect of aerosols in the atmospheric conductivity in (a) Venus (Borucki et al. 1982), Mars (Michael et al. 2007), (b) Titan (Borucki et al. 2006), and (c) Jupiter (Whitten et al. 2008). Red lines are conductivities of the clear atmospheres and black lines are conductivities in the presence of aerosols. Blue line in (a) shows the effect of dust storm (dust opacity ~ 5) in the atmosphere of Mars (Michael and Tripathi 2008). Solid lines are electron conductivities and dashed lines are ion conductivities in (c)

70 km, the large abundance of particles causes a reduction in conductivity by a factor of about 2–3. The ubiquity of the cloud cover on Venus makes this reduction a global feature. Discovery of frequent lightning discharges (Russell et al. 2007 and references therein) in the atmosphere show the active electrical processes in Venus. The presence of lightning implies that the charge separation mechanisms operate at a rate sufficient to overcome the dissipation of the separated charge by atmospheric conduction. Atmospheric conductivity helps control the local electric field and the current flowing in a global circuit. Figure 7a presents the atmospheric conductivity with and without particles in the atmosphere of Venus.

Mars: Michael et al. (2007) studied the electrical conductivity in the night-time atmosphere of Mars. The maximum variation in conductivity was observed close to the surface (dropped by a factor of five) of the planet and effect of aerosols becomes negligible for altitudes greater than 50 km. The atmospheric conductivity estimated is presented in Fig. 7a. Michael and Tripathi (2008) studied the variation of atmospheric conductivity during the dust storm in 2001. The dust opacity reached a maximum of ~ 5 during the storm, and the conductivity decreased by about 2 orders of magnitude for the maximum dust opacity observed (blue line in Fig. 7a). The atmospheric conductivity during the day-time has been studied by Michael et al. (2008). In addition to ions, electrons are also present in the day-time atmosphere due to the ionization of aerosols by the solar UV radiation. Though the concentration of electrons is about 2 orders of magnitude less than the ions, the high mobility of electrons increases the atmospheric conductivity by a factor of 2.5. But the existing aerosols decrease the conductivity by about a factor of 2 during the day-time.

Jupiter: The consequences for atmospheric conductivity of particle charging by ion and electron attachment in the atmosphere of Jupiter for pressures between 5.5 and 0.1 mbar has been studied by Whitten et al. (2008). Where cloud particles are present, the reduction of the electron conductivity ranges from a factor of 30 at 0.1 bar to 10^4 at 4 bars. At pressures near 1 bar and 4 bars, the positive ion conductivity increases by a factor of 10 over that expected

for the clear atmosphere. Whitten et al. (2008) suggested that negative ions' contributions are likely to be insignificant. The effect of cloud particles in the electron and ion conductivity in the atmosphere of Jupiter from Whitten et al. (2008) is presented in Fig. 7c.

Titan: The atmospheric conductivity of Titan for the night-time was studied by Whitten et al. (2007) and for the day-time was studied by Borucki et al. (2006). For the night-time atmosphere, the conductivity decreases in the diffusion range, where the effective radius of the particles are larger than the ionic mean free path, (below 50 km), while the presence of aerosols does not make a considerable variation in the atmospheric conductivity for altitudes greater than 50 km (effusion range, where the particles are much smaller than the ionic mean free path). During the day-time, a large amount of electrons are produced from aerosols due to the interaction with the solar UV radiation (Borucki et al. 2006) thereby increasing the conductivity by a factor of 2 to more than 2 orders of magnitude. The effect of particles on the electron conductivity during the day-time atmosphere of Titan from Borucki et al. (2006) is presented in Fig. 7b. The direct (HASI) measurements of electrical conductivity in the lower atmosphere of Titan reveal that all models differ from the measurements by a factor about two to three, but the general shapes of modeled and measured profiles are similar (Hamelin et al. 2007). The higher conductivity estimated by Borucki et al. (2006) could be due to the fact that the photoemission threshold used by Borucki et al. (2006) is smaller than the original photoemission cut-off, due to methane absorption.

6.2 Effect of Aerosol Charging on Physical Processes

Scavenging of aerosols by cloud droplets can be enhanced by electrification of the aerosols. Collision efficiency of a particle with a water droplet increases by a factor of 30 for aerosols carrying a large charge (~ 50). For an aerosol population containing a constant fraction of contact nuclei, the droplet's freezing probability can be enhanced by the electrical collection. This is particularly so in the case of small (< 20 microns) super-cooled droplets, or for the few aerosol particles which statistically may transiently carry large charges. A mean charge of $10e$ charges per particle is sufficient to increase the collision efficiency threefold over that for neutral particles (Tripathi et al. 2006). Modest charging of submicron radii aerosols can lead to more collisions with supercooled droplets than neutral aerosol. The change in collision rate occurs from the electrical image force and is, therefore, independent of the charge carried by the water drop (Tripathi and Harrison 2001, 2002). Figure 8 presents the freezing probability with particle charge.

Coagulation of particles in the atmosphere leads to a shift in the aerosol size distribution to larger particles and reduces the build up of extremely high concentrations of ultra-fine aerosols produced by gas-to-particle conversion (Kanawade and Tripathi 2006). The electrical charging of aerosols reduces the aerosol coagulation rate. The lower coagulation rate increases the residence time of the aerosols and thereby increases the aerosol concentration, which affect the optical depth of the atmosphere and hence the atmospheric structure. For ultrafine particles there is a dramatic increase in the coagulation rate if the particles are charged (Harrison and Carslaw 2003). Figure 9 presents the coagulation rate with particle charge. For larger particles the rate of coagulation between particles with like charges is lower than that for neutral particles, while the rate is enhanced for particles with unlike charges (Harrison and Carslaw 2003).

Fig. 8 Freezing probability with particle charge (Tripathi and Harrison 2002)

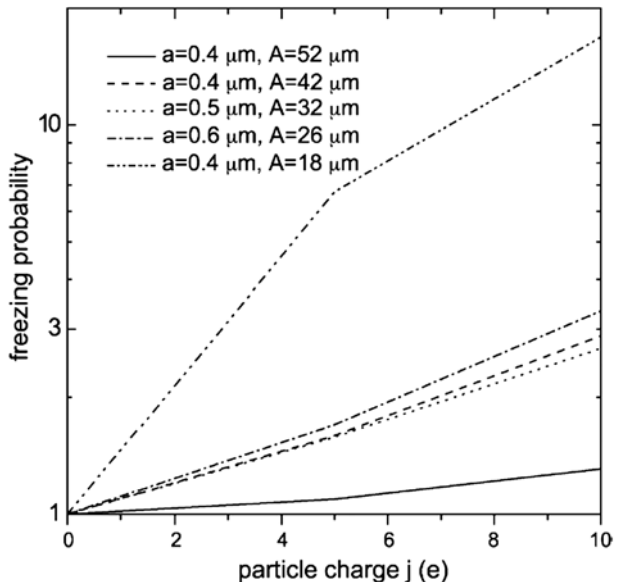
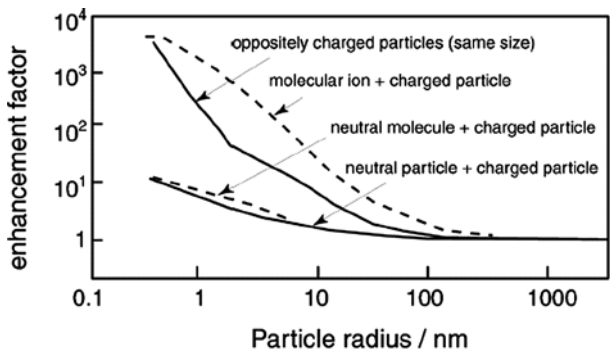


Fig. 9 The enhancement of coagulation rate with particle charge (Harrison and Carslaw 2003)



7 Future Work

Virtually the work on ionic modeling, in regions of interest in the atmosphere of Jupiter from aerosol charging point of view, has not progressed since the seminal work of Capone et al. (1979). Recently the rate constants for ion and ion-neutral reactions occurring in Jupiter's atmosphere have been updated, based on laboratory data. However, these rate constants have not been incorporated into the detailed ion-neutral model of Jupiter's atmosphere. Furthermore, recent detection of electrophilic species leads to the formation negative ion clusters, as shown using simple modeling calculations by Whitten et al. (2008). This needs to be confirmed.

Whereas some experiments have been performed in the laboratory to validate the numerical results pertaining to the aerosol charging in Titan, no such experiments have been performed relevant to Mars. The laboratory simulations for Martian electrification have only been confined to the triboelectric (contact) mechanism (Krauss et al. 2003), however, as shown recently by Michael et al. (2007, 2008) and Michael and Tripathi (2008) that away from the surface dust diffusion charging is the dominant mechanism for calm weather con-

ditions in Mars, which need to be tested, in laboratory on a priority basis. In the terrestrial atmosphere it has been shown that collision rates between electrically charged aerosols and supercooled droplet are greatly enhanced. This should be accounted for while studying cloud formation in the atmosphere of Mars.

Because the smallest particles formed in Titan's ionosphere are electrically charged (Waite et al. 2007), and because aerosol charging can greatly modify the condensation and coagulation processes (Yu and Turco 2001; Toon et al. 1992), it is important to simulate the effect of aerosol charging in an explicit manner in the microphysical models. Planetary aerosol microphysical models currently lack this refinement.

Acknowledgements The authors SNT and MM acknowledge the support of Indian Space Research Organisation PLANEX program.

References

- K.L. Aplin, Surv. Geophys. **27**, 63 (2006a). doi:[10.1007/s10712-005-0642-9](https://doi.org/10.1007/s10712-005-0642-9)
- K.L. Aplin, <http://arxiv.org/abs/physics/0605080> available on 9 May 2006 (2006b)
- K.L. Aplin, G.R. Harrison, M. Rycroft, Space Sci. Rev. (2008, this issue)
- P. Arndt, H. Kallmann, Z. Physik **35**, 421 (1925)
- S.K. Atreya, M.H. Wong, T.C. Owen et al., Planet. Space Sci. **47**, 1243 (1999). doi:[10.1016/S0032-0633\(99\)00047-1](https://doi.org/10.1016/S0032-0633(99)00047-1) Medline
- S.K. Atreya, A.S. Wong, Space Sci. Rev. **116**, 121 (2005). doi:[10.1007/s11214-005-1951-5](https://doi.org/10.1007/s11214-005-1951-5)
- S. Atreya, Science **316**, 843 (2007). doi:[10.1126/science.1141869](https://doi.org/10.1126/science.1141869) Medline
- D. Banfield, B.J. Conrath, P.J. Gierasch, P. Nicholson, Icarus **134**, 11 (1998). doi:[10.1006/icar.1998.5942](https://doi.org/10.1006/icar.1998.5942)
- G. Bazilevskaya, I. Usoskin et al., Space Sci. Rev. (2008, this issue). doi:[10.1007/s11214-008-9339-y](https://doi.org/10.1007/s11214-008-9339-y)
- J.F. Bell, III, D. Crisp, P. Lucey, T. Ozorski, W. Sinton, S. Willis, B. Campbell, Science **252**, 1293 (1991). doi:[10.1126/science.252.5010.1293](https://doi.org/10.1126/science.252.5010.1293) Medline
- W.J. Borucki, Z. Levin, R.C. Whitten, R.G. Keesee, L.A. Capone, O.B. Toon, J. Dubach, Icarus **51**, 302 (1982). doi:[10.1016/0019-1035\(82\)90086-0](https://doi.org/10.1016/0019-1035(82)90086-0)
- W.J. Borucki, Z. Levin, R.C. Whitten, R.G. Keesee, L.A. Capone, A.L. Summers, O.B. Toon, J. Dubach, Icarus **72**, 604 (1987). doi:[10.1016/0019-1035\(87\)90056-X](https://doi.org/10.1016/0019-1035(87)90056-X)
- W.J. Borucki, R.C. Whitten, E.L.O. Bakes, E. Barth, S.N. Tripathi, Icarus **181**, 527 (2006). doi:[10.1016/j.icarus.2005.10.030](https://doi.org/10.1016/j.icarus.2005.10.030)
- L.A. Capone, R.C. Whitten, J. Dubach, S.S. Prasad, W.T. Huntress, Icarus **28**, 367 (1976). doi:[10.1016/0019-1035\(76\)90150-0](https://doi.org/10.1016/0019-1035(76)90150-0)
- L.A. Capone, R.C. Whitten, S.S. Prasad, J. Dubach, Astrophys. J. **215**, 977 (1977). doi:[10.1086/155434](https://doi.org/10.1086/155434)
- L.A. Capone, J. Dubach, R.C. Whitten, S.S. Prasad, Icarus **39**, 433 (1979). doi:[10.1016/0019-1035\(79\)90151-9](https://doi.org/10.1016/0019-1035(79)90151-9)
- L.A. Capone, J. Dubach, R.C. Whitten, S.S. Prasad, Icarus **44**, 72 (1980). doi:[10.1016/0019-1035\(80\)90056-1](https://doi.org/10.1016/0019-1035(80)90056-1)
- R.W. Carlson, L. Kamp, K. Baines, J. Pollack, D. Grinspoon, T. En crenaz, P. Drossart, F. Taylor, Planet. Space Sci. **41**, 477 (1993)
- E. Chassefiere, J.E. Blamont, V.A. Krasopolsky, O.I. Korablev, S.K. Atreya, R.A. West, Icarus **97**, 46 (1992). doi:[10.1016/0019-1035\(92\)90056-D](https://doi.org/10.1016/0019-1035(92)90056-D)
- E. Chassefiere, P. Drossart, O. Korablev, J. Geophys. Res. **100**, 5525 (1995). doi:[10.1029/94JE03363](https://doi.org/10.1029/94JE03363)
- R.H. Chen, A.F. Nagy, J. Geophys. Res. **83**, 1133 (1978). doi:[10.1029/JA083iA03p01133](https://doi.org/10.1029/JA083iA03p01133)
- R.T. Clancy, S.W. Lee, Icarus **93**, 135 (1991). doi:[10.1016/0019-1035\(91\)90169-T](https://doi.org/10.1016/0019-1035(91)90169-T)
- R.T. Clancy, M.J. Wolff, P.R. Christensen, J. Geophys. Res. **108**, 5098 (2003). doi:[10.1029/2003JE002058](https://doi.org/10.1029/2003JE002058)
- B.J. Conrath, Icaurs **24**, 36 (1975). doi:[10.1016/0019-1035\(75\)90156-6](https://doi.org/10.1016/0019-1035(75)90156-6)
- Coustenis et al., Icarus **161**, 383 (2003). doi:[10.1016/S0019-1035\(02\)00028-3](https://doi.org/10.1016/S0019-1035(02)00028-3)
- D. Crisp, W.M. Sinton, K.W. Hodapp et al., Science **246**, 506 (1989). doi:[10.1126/science.246.4929.506](https://doi.org/10.1126/science.246.4929.506) Medline
- D. Crisp, S. McMurdoch, S. Stephens et al., Science **253**, 1538 (1991). doi:[10.1126/science.253.5027.1538](https://doi.org/10.1126/science.253.5027.1538) Medline
- P. Drossart, J. Rosenqvist, S. Erard, Y. Langevin, J.P. Bibring, M. Combes, Ann. Geophys. **9**, 754 (1991)
- J. Dubach, R.C. Whitten, J.S. Sims, Planet. Space Sci. **22**, 525 (1974). doi:[10.1016/0032-0633\(74\)90087-7](https://doi.org/10.1016/0032-0633(74)90087-7)

- L.W. Esposito, R.G. Knollenberg, M.Y. Marov, O.B. Toon, R.P. Turco, in *Venus*, ed. by D.M. Hunte, L. Colin, T.M. Donahue, V.I. Moroz (Univ. Arizona Press, Tucson, 1983), p. 484
- R.A. Fjeld, A.R. McFarland, J. Aerosol Sci. **17**(4), 653 (1986). doi:[10.1016/0021-8502\(86\)90045-5](https://doi.org/10.1016/0021-8502(86)90045-5)
- J. Frenkel, J. Phys., USSR **10**, 151 (1946)
- A.J. Friedman, A.S. Wong, Y.L. Yung, Icarus **158**, 389 (2002). doi:[10.1006/icar.2002.6885](https://doi.org/10.1006/icar.2002.6885)
- N.A. Fuchs, Izv. Geophys. Ser. **4**, 579 (1964)
- W. Goetz, P. Bertelsen, C.S. Binau et al., Nature **436** (2005). doi:[10.1038/nature03807](https://doi.org/10.1038/nature03807) Medline
- R. Grard, Icarus **114**, 130 (1995). doi:[10.1006/icar.1995.1048](https://doi.org/10.1006/icar.1995.1048)
- D. Grinspoon, J.B. Pollack, B. Sitton, R. Carlson, L. Kamp, K. Baines, T. Encrenaz, F. Taylor, Planet. Space Sci. **41**, 515 (1993)
- R. Gunn, J. Meteorol. **11**, 339 (1954)
- S.A. Haider, V. Sheel, V.R. Choksi, V. Singh, W.C. Maguire, G.J. Molina-Cuberos, J. Geophys. Res. (2008, in press)
- M. Hamelin, C. Beghin, R. Grard et al., Planet. Space Sci. **55**, 1964 (2007). doi:[10.1016/j.pss.2007.04.008](https://doi.org/10.1016/j.pss.2007.04.008)
- R.G. Harrison, K.S. Carslaw, Rev. Geophys. **41**(3), 1012 (2003). doi:[10.1029/2002RG000114](https://doi.org/10.1029/2002RG000114)
- R.G. Harrison, H. Tammet, Space Sci. Rev. (2008, this issue). doi:[10.1007/s11214-008-9356-x](https://doi.org/10.1007/s11214-008-9356-x)
- K. Hiraoka, P. Kebarle, J. Chem. Phys. **63**(1), 394 (1975). doi:[10.1063/1.431116](https://doi.org/10.1063/1.431116)
- W.A. Hoppel, G.M. Frick, Aerosol Sci. Tech. **5**, 1 (1986). doi:[10.1080/02786828608959073](https://doi.org/10.1080/02786828608959073)
- W.A. Hoppel, in *Electrical Processes in Atmospheres*, ed. by H. Dolezalek, R. Reiter (Stenopoff Verlag, Darmstadt, 1977), p. 60
- C.W. Hord, R.A. West, K.E. Simmons, D.L. Coffeen, M. Sato, A.L. Lane, J.T. Bergstrahl, Science **206**, 956 (1979)
- T. Imamura, G.L. Hashimoto, J. Geophys. Res. **103**, 31349 (1998). doi:[10.1029/1998JE900010](https://doi.org/10.1029/1998JE900010)
- T. Imamura, G.L. Hashimoto, J. Atmos. Sci. **58**, 3597 (2001). doi:[10.1175/1520-0469\(2001\)058<3597:MOVCI>2.0.CO;2](https://doi.org/10.1175/1520-0469(2001)058<3597:MOVCI>2.0.CO;2)
- E.P. James, O.B. Toon, G. Schubert, Icarus **129**, 147 (1997). doi:[10.1006/icar.1997.5763](https://doi.org/10.1006/icar.1997.5763)
- E.J. Jensen, G.E. Thomas, J. Geophys. Res. **96**, 18603 (1991). doi:[10.1029/91JD01966](https://doi.org/10.1029/91JD01966)
- V. Kanawade, S.N. Tripathi, J. Geophys. Res. **111**, D02209 (2006). doi:[10.1029/2005JD006366](https://doi.org/10.1029/2005JD006366)
- K. Kawabata, D.L. Coffeen, J.E. Hansen, W.A. Lane, M. Sato, L.D. Travis, J. Geophys. Res. **85**, 8129 (1980). doi:[10.1029/JA085iA13p08129](https://doi.org/10.1029/JA085iA13p08129)
- D. Keefe, P.J. Nolan, J.A. Scott, Proc. R. Irish Acad. **66A**, 17 (1968)
- R.G. Keesee, N. Lee, A.W. Castleman Jr., J. Chem. Phys. **73**, 2195 (1980). doi:[10.1063/1.440415](https://doi.org/10.1063/1.440415)
- B.N. Khare, C. Sagan, Icarus **20**, 311 (1973). doi:[10.1016/0019-1035\(73\)90008-0](https://doi.org/10.1016/0019-1035(73)90008-0)
- B. Khare, E.L.O. Bakes, H. Imanaka, C.P. McKay, D.P. Cruikshank, E.T. Arakawa, Icarus **160**, 172 (2002). doi:[10.1006/icar.2002.6899](https://doi.org/10.1006/icar.2002.6899)
- S.J. Kim, J. Caldwell, A.R. Rivolo, R. Wagener, G.S. Orton, Icarus **64**, 233 (1985). doi:[10.1016/0019-1035\(85\)90088-0](https://doi.org/10.1016/0019-1035(85)90088-0)
- R.G. Knollenberg, D.M. Hunten, J. Geophys. Res. **85**, 8039 (1980). doi:[10.1029/JA085iA13p08039](https://doi.org/10.1029/JA085iA13p08039)
- O.I. Korablev, V.A. Krasopolsky, A.V. Rodin, E. Chassefiere, Icarus **102**, 76 (1993). doi:[10.1006/icar.1993.1033](https://doi.org/10.1006/icar.1993.1033)
- V.A. Krasopolsky, Icarus **80**, 202 (1989). doi:[10.1016/0019-1035\(89\)90168-1](https://doi.org/10.1016/0019-1035(89)90168-1)
- C.E. Krauss, M. Horanyi, S. Robertson, New J. Phys. **5**, 70.1 (2003)
- L.M. Lara, E. Lellouch, J.J. Lopez-Moreno, R. Rodrigo, J. Geophys. Res. **101**, 23261 (1996). doi:[10.1029/96JE02036](https://doi.org/10.1029/96JE02036)
- S. Lebonnois, Planet. Space Sci. **53**, 486 (2005). doi:[10.1016/j.pss.2004.11.004](https://doi.org/10.1016/j.pss.2004.11.004)
- M. Lemmon et al., Science **306**, 1753 (2004). doi:[10.1126/science.1104474](https://doi.org/10.1126/science.1104474) Medline
- C.P. McKay, A. Coustenis, R.E. Samuelson, M.T. Lemmon, R.D. Lorenz, M. Cabane, P. Rannou, P. Drossart, Planet. Space Sci. **49**, 79 (2001). doi:[10.1016/S0032-0633\(00\)00051-9](https://doi.org/10.1016/S0032-0633(00)00051-9)
- M. Michael, M. Barani, S.N. Tripathi, Geophys. Res. Lett. **34** (2007). doi:[10.1029/2006GL028434](https://doi.org/10.1029/2006GL028434)
- M. Michael, S.N. Tripathi, Planet. Space Sci. (2008, accepted)
- M. Michael, S.N. Tripathi, S.K. Mishra, J. Geophys. Res. (2008, in press). doi:[10.1029/2007JE003047](https://doi.org/10.1029/2007JE003047)
- R.A. Millikan, Phys. Rev. **32**, 349 (1911)
- M.I. Mishchenko, Icarus **84**, 296 (1990). doi:[10.1016/0019-1035\(90\)90039-C](https://doi.org/10.1016/0019-1035(90)90039-C)
- G.J. Molina-Cuberos, J.J. Lopez-Moreno, R. Rodrigo, L.M. Lara, K. O'Brien, Planet. Space Sci. **47**, 1347 (1999). doi:[10.1016/S0032-0633\(99\)00056-2](https://doi.org/10.1016/S0032-0633(99)00056-2)
- G.J. Molina-Cuberos, J.J. Lopez-Moreno, R. Rodrigo, L.M. Lara, Geophys. Res. Lett. **27**, 1351 (2000). doi:[10.1029/1999GL010771](https://doi.org/10.1029/1999GL010771)
- G.J. Molina-Cuberos, J.J. Lopez-Moreno, R. Rodrigo, H. Lichtenegger, K. Schwingenschuh, Adv. Space Res. **27**, 1801 (2001). doi:[10.1016/S0273-1177\(01\)00342-8](https://doi.org/10.1016/S0273-1177(01)00342-8)
- F. Montmessin, E. Qu'emerais, J.L. Bertaux, O. Korablev, P. Rannou, S. Lebonnois, J. Geophys. Res. **111** (2006). doi:[10.1029/2005JE002662](https://doi.org/10.1029/2005JE002662)

- F. Moreno, Icarus **124**, 632 (1996). doi:[10.1006/icar.1996.0237](https://doi.org/10.1006/icar.1996.0237)
- G.L. Natanson, Zh. Tech. Fiz. **30**, 573 (1960)
- K. O'Brien, Nucl. Instrum. Methods **72**, 93 (1969)
- K. O'Brien, J. Geophys. Res. **75**, 4357 (1970). doi:[10.1029/JA075i022p04357](https://doi.org/10.1029/JA075i022p04357)
- K. O'Brien, Nuovo Cimento A **3**, 521 (1971). doi:[10.1007/BF02823324](https://doi.org/10.1007/BF02823324)
- K. O'Brien, Phys. Rev. D **5**, 597 (1972). doi:[10.1103/PhysRevD.5.597](https://doi.org/10.1103/PhysRevD.5.597)
- T. Owen, Icarus **10**, 355 (1969). doi:[10.1016/0019-1035\(69\)90090-6](https://doi.org/10.1016/0019-1035(69)90090-6)
- K. Pang, J.M. Ajello, Icarus **30**, 63 (1977). doi:[10.1016/0019-1035\(77\)90121-X](https://doi.org/10.1016/0019-1035(77)90121-X)
- R. Parthasarathy, J. Geophys. Res. **81**, 2392 (1976)
- J.B. Pollack, D.S. Colburn, F.M. Flasar, R. Kahn, C.E. Carlson, D.G. Pidek, J. Geophys. Res. **84**, 2929 (1979). doi:[10.1029/JB084iB06p02929](https://doi.org/10.1029/JB084iB06p02929)
- J.B. Pollack, J.B. Dalton, D. Grinspoon, R.B. Wattson, R. Freedman, D. Crisp, D.A. Allen, B. Bezard, C. Bergh, L.P. Giver, Q. Ma, R. Tipping, Icarus **103**, 1 (1993). doi:[10.1006/icar.1993.1055](https://doi.org/10.1006/icar.1993.1055)
- W.R. Pryor, C.W. Hord, Icarus **91**, 161 (1991)
- B. Ragent, K.A. Rages, T.C.D. Knight, P. Arvin, G.S. Orton, J. Geophys. Res. **103**, 22891 (1998). doi:[10.1029/98JE00353](https://doi.org/10.1029/98JE00353)
- K. Rages, J.B. Pollack, Icarus **55**, 50 (1983). doi:[10.1016/0019-1035\(83\)90049-0](https://doi.org/10.1016/0019-1035(83)90049-0)
- K. Rages, J.B. Pollack, P.H. Smith, J. Geophys. Res. **88**, 8721 (1983). doi:[10.1029/JA088iA11p08721](https://doi.org/10.1029/JA088iA11p08721)
- W.B. Rossow, Icarus **36**, 1 (1977). doi:[10.1016/0019-1035\(78\)90072-6](https://doi.org/10.1016/0019-1035(78)90072-6)
- C.T. Russell, T.L. Zhang, M. Delva, W. Magnes, R.J. Strangeway, H.Y. Wei, Nature **450**, 661 (2007). doi:[10.1038/nature05930](https://doi.org/10.1038/nature05930) Medline
- D.W. Smith, T.F. Greene, R.W. Shorthill, Icarus **30**, 697 (1977). doi:[10.1016/0019-1035\(77\)90089-6](https://doi.org/10.1016/0019-1035(77)90089-6)
- D.W. Smith, Icarus **44**, 116 (1980). doi:[10.1016/0019-1035\(80\)90060-3](https://doi.org/10.1016/0019-1035(80)90060-3)
- D.F. Strobel, in *The Photochemistry of Atmospheres*, ed. by J.S. Levine (Academic Press, New York, 1985), p. 393
- M.G. Tomasko, P.H. Smith, Icarus **51**, 65 (1982). doi:[10.1016/0019-1035\(82\)90030-6](https://doi.org/10.1016/0019-1035(82)90030-6)
- M.G. Tomasko, E. Karkoschka, S. Martinek, Icarus **65**, 218 (1986). doi:[10.1016/0019-1035\(86\)90136-3](https://doi.org/10.1016/0019-1035(86)90136-3)
- M.G. Tomasko, L.R. Doose, M. Lemmon, P.H. Smith, E. Wegryn, J. Geophys. Res. **104**, 8987 (1999). doi:[10.1029/1998JE900016](https://doi.org/10.1029/1998JE900016)
- M.G. Tomasko, B. Archinal, T. Becker et al., Nature **438**, 765 (2005). doi:[10.1038/nature04126](https://doi.org/10.1038/nature04126)
- O.B. Toon, J.B. Pollack, C. Sagan, Icarus **30**, 663 (1977). doi:[10.1016/0019-1035\(77\)90088-4](https://doi.org/10.1016/0019-1035(77)90088-4)
- O.B. Toon, R.P. Turco, J.B. Pollack, Icarus **51**, 358 (1982). doi:[10.1016/0019-1035\(82\)90089-6](https://doi.org/10.1016/0019-1035(82)90089-6)
- O.B. Toon, C.P. McKay, C.A. Griffith, R.P. Turco, Icarus **95**, 24 (1992). doi:[10.1016/0019-1035\(92\)90188-D](https://doi.org/10.1016/0019-1035(92)90188-D) Medline
- S.N. Tripathi, R.G. Harrison, Atmospheric Environ. **35**, 5817 (2001). doi:[10.1016/S1352-2310\(01\)00299-0](https://doi.org/10.1016/S1352-2310(01)00299-0)
- S.N. Tripathi, R.G. Harrison, Atmospheric Res. **62**, 57 (2002). doi:[10.1016/S0169-8095\(02\)00020-0](https://doi.org/10.1016/S0169-8095(02)00020-0)
- S.N. Tripathi, S. Vishnoi, S. Kumar, R.G. Harrison, Q.J.R. Meteorol. Soc. **132**, 1717 (2006). doi:[10.1256/qj.05.125](https://doi.org/10.1256/qj.05.125)
- S.N. Tripathi, M. Michael, In *Chemistry and Aerosols in the Atmospheres of Earth and Mars*, ed. by S.A. Haider, V. Sheel, S. Lal (Mcmillan India, 2008, in press)
- H.O. Upadhyay, R.R. Singh, R.N. Singh, Earth, Moon Planets **65**, 89 (1994). doi:[10.1007/BF00572202](https://doi.org/10.1007/BF00572202)
- M.B. Vincent, J.T. Clarke, G.E. Ballester et al., Icarus **143**, 205 (2000). doi:[10.1006/icar.1999.6233](https://doi.org/10.1006/icar.1999.6233)
- H. Waite Jr., D.T. Young, T.E. Cravens, A.J. Coates, F.J. Crary, B. Magee, J. Westlake, Science **316**, 870 (2007). doi:[10.1126/science.1139727](https://doi.org/10.1126/science.1139727) Medline
- R.A. West, Icarus **38**, 12 (1979). doi:[10.1016/0019-1035\(79\)90082-4](https://doi.org/10.1016/0019-1035(79)90082-4)
- R.A. West, C.W. Hord, K.E. Simmons, D.L. Coffeen, M. Sato, A.L. Lane, J. Geophys. Res. **86**, 8783 (1981). doi:[10.1029/JA086iA10p08783](https://doi.org/10.1029/JA086iA10p08783)
- R.A. West, A.L. Lane, H. Hart et al., J. Geophys. Res. **88**, 8699 (1983). doi:[10.1029/JA088iA11p08699](https://doi.org/10.1029/JA088iA11p08699)
- R.A. West, D.F. Strobel, M.G. Tomasko, Icarus **65**, 161 (1986). doi:[10.1016/0019-1035\(86\)90135-1](https://doi.org/10.1016/0019-1035(86)90135-1)
- R.A. West, Icarus **75**, 381 (1988). doi:[10.1016/0019-1035\(88\)90152-2](https://doi.org/10.1016/0019-1035(88)90152-2)
- R.A. West, A.J. Friedson, J.F. Appleby, Icarus **100**, 245 (1992). doi:[10.1016/0019-1035\(92\)90033-4](https://doi.org/10.1016/0019-1035(92)90033-4)
- R.A. West, K.H. Baines, A.J. Friedson, D. Banfield, B. Ragent, F.W. Taylor, in *Jupiter: The Planet, Satellites and Magnetosphere*, vol. 1, ed. by F. Bagenal, T.E. Dowling, W.B. McKinnon (Cambridge University Press, Cambridge, 2004), pp. 79–104
- R.C. Whitten, I.G. Poppoff, J.S. Sims, Planet. Space Sci. **17**, 243 (1971). doi:[10.1016/0032-0633\(71\)90203-0](https://doi.org/10.1016/0032-0633(71)90203-0)
- R.C. Whitten, W.J. Borucki, S.N. Tripathi, J. Geophys. Res. **112** (2007). doi:[10.1029/2006JE002788](https://doi.org/10.1029/2006JE002788)
- R.C. Whitten, W.J. Borucki, K. O'Brien, S.N. Tripathi, J. Geophys. Res. **113**, E04001 (2008). doi:[10.1029/2007JE002975](https://doi.org/10.1029/2007JE002975)
- A.-S. Wong, A. Lee, Y.L. Yung, J.M. Ajello, Astrophys. J. **534**, L215 (2000). doi:[10.1086/312675](https://doi.org/10.1086/312675) Medline
- A.-S. Wong, Y.L. Yung, A.J. Friedson, Geophys. Res. Lett. **30**(8), 1447 (2003). doi:[10.1029/2002GL016661](https://doi.org/10.1029/2002GL016661)
- Y. Yair, Z. Levin, J. Geophys. Res. **94**, 13085 (1989). doi:[10.1029/JD094iD11p13085](https://doi.org/10.1029/JD094iD11p13085)
- M. Yamamoto, M. Takahashi, J. Geophys. Res. **111**, E08002 (2006). doi:[10.1029/2006JE002688](https://doi.org/10.1029/2006JE002688)
- F. Yu, R.P. Turco, J. Geophys. Res. **106**, 4797 (2001). doi:[10.1029/2000JD900539](https://doi.org/10.1029/2000JD900539)

Composition and Measurement of Charged Atmospheric Clusters

K.L. Aplin

Originally published in the journal Space Science Reviews, Volume 137, Nos 1–4.
DOI: [10.1007/s11214-008-9397-1](https://doi.org/10.1007/s11214-008-9397-1) © Springer Science+Business Media B.V. 2008

Abstract Atmospheric charged clusters are formed in a series of rapid chemical reactions after ionisation, leaving a central ion X^+ or X^- clustered with n ligands ($Y)_n$. In solar system tropospheres and stratospheres there are two distinct cluster regimes: the terrestrial planets contain largely hydrated clusters (i.e. $Y = H_2O$), whereas the gas planets and their moons have organic or nitrogenated cluster species. These classifications are largely based on model predictions, since hardly any measurements are available. The few existing composition measurements are reviewed, including the recent detection of massive charged particles in Titan's upper atmosphere. Technologies for both remote sensing and in situ measurements of atmospheric charged clusters are discussed. Preliminary measurements in the terrestrial atmosphere are presented indicating that ambient charged cluster species interact with downwelling infra-red radiation at $9.15\ \mu m$, even in the presence of cloud. This supports the possibility of future infrared detection of charged clusters.

Keywords Atmospheric electricity, lightning · Comparative planetology · Planetary atmospheres · Charged clusters · Ion chemistry and composition; ionisation mechanisms

PACS 92.60.Pw · 96.30.Bc · 96.15.Hy · 36.40.Wa · 94.20.dv

1 Introduction

Ionisation occurs in all planetary atmospheres, principally from cosmic rays (Bazilevskaya et al. 2008). The interaction between an atmospheric molecule and an energetic particle produces an electron and a positive ion. The electron almost immediately attaches to an electronegative molecule (if present) to form a negative ion. After formation of the core ion, there is a rapid (<1 ms) and complex sequence through which it typically reacts with progressively less abundant trace species through ligand exchange until a stable, terminal ion

K.L. Aplin (✉)

Rutherford Appleton Laboratory, Space Science and Technology Department, Chilton, Didcot, Oxon OX11 0QX, UK

e-mail: k.aplin@rl.ac.uk

cluster is produced (Elrod 2003). These “charged clusters”, or “cluster-ions”,¹ comprise the core ion, hydrogen bonded to one or more polar ligands. Charged cluster production occurs in atmospheres dense and/or cold enough for stable clusters to exist (the collision cross-section is proportional to $p/(T^{3/2})$ where p is pressure and T temperature). An additional condition for the existence of charged clusters is that the atmosphere must contain suitable polar ligands: either electrophilic species (to form negative ions which can subsequently cluster) and/or those with a high proton affinity (to form positive clusters).

Charged clusters interact constantly with each other, aerosol particles and the atmosphere. They gain and lose individual molecules, recombine with oppositely charged particles, and attach to larger particles. On the molecular scale, they attach and recombine to form neutral complexes (Klemperer and Vaida 2006). The detailed physics of atmospheric ions and their interaction with aerosol particles is discussed in companion papers by Harrison and Tammet (2008) and Tripathi et al. (2008).

There are several motivations to study charged clusters. The direct condensation of vapour onto ions in highly supersaturated conditions has been known since the early days of the cloud chamber. Though the supersaturations needed for this “Wilson” condensation to occur are impossible in the terrestrial atmosphere, it is expected in some planetary atmospheres, as will be described in Sect. 2. Indirect mechanisms have also been postulated for Earth where charged clusters assist nucleation of larger aerosol particles, on which condensation can occur to form cloud droplets (reviewed in e.g. Harrison and Carslaw (2003) and Kazil et al. (2008)). Charged clusters move in electric fields, which can arise either from a global circuit (Aplin et al. 2008) or local generation of charge (Yair 2008). Therefore, in the presence of electric fields, charged clusters can represent an important mechanism for the transport of trace chemical species. In some planetary environments charged cluster chemistry could also form trace neutral species (Capone et al. 1979). The radiative effects of charged clusters have been detected in laboratory experiments (Carlon and Harden 1980; Aplin and McPheat 2005), and ionic absorption is likely to have some atmospheric relevance, though the sensitivity of the effect to charged cluster concentration and composition is not yet known. As will be discussed in Sect. 3, this technique could be used in the future for remote sensing of charged clusters.

This paper will describe the composition (Sect. 2) and measurement (Sect. 3) of atmospheric charged clusters. The discussion focuses on charged clusters in the troposphere and stratosphere, since these are the regions where processes discussed in the motivation section above take place.

2 Composition of Charged Clusters

2.1 Earth

Typical negative core species in the terrestrial atmosphere are O_2^- , CO_3^- , and NO_3^- , with positive core species H_3O^+ , NO^+ , NO_2^+ and HSO_4^+ , and common ligands H_2O and NH_3 , where $n \sim 2-10$ (Harrison and Carslaw 2003). Near the surface, polar organic species act as ligands producing a wide variety of clusters, depending on trace gas concentrations

¹Chemically homogeneous clusters can also be referred to as a charged oligomer, e.g. the protonated water dimer.

(Elrod 2003; Parts and Luts 2004). Pyridine (an organic heterocyclic molecule with formula C_5H_5N) is a particularly efficient, and therefore common, ligand for positive cluster ions because of its high proton affinity (Elrod 2003), even though it only exists in tiny atmospheric concentrations (Harrison and Tammert 2008). Negative ion species are dominated by relatively simple nitrate and sulphate-based clusters, but some organic core species e.g. $C_3H_3O_4^-$ are also present (Eisele 1989; Eisele et al. 2006). Relatively little is known about ion composition away from the surface, but aircraft mass spectrometer measurements have detected acetone-based cluster ion species e.g. $H^+(CH_3)_2CO(H_2O)_n$ near the tropopause (Möhler et al. 1993). In the upper troposphere there tend to be fewer and less exotic organic charged clusters, and in the lower stratosphere the dominant cluster ions are simpler, such as the protonated hydrate (Smith and Church 1977; Beig and Brasseur 2000). Usually the atomic masses of these ions vary from a few tens to a few hundred atomic mass units (amu), depending on the clustering chemistry which is modulated by e.g. temperature, pressure, and humidity (Harrison and Aplin 2007). Large cluster ions of a few thousand amu have been detected in the upper troposphere using aircraft-borne mass spectrometry (Eichkorn et al. 2002), providing evidence for ion-mediated growth of aerosol particles in cloud-forming regions.

2.2 Venus

Borucki et al. (1982) modelled ion clustering reactions in the dense Venusian atmosphere. The clustering processes included were similar to those on Earth, and the terminal clusters may be similar to those in the terrestrial atmosphere, particularly the protonated hydrate, $H_3O^+(H_2O)_n$ ($n = 3–4$). Other common species are $H_3O^+(SO_2)$ and $H_3O(H_2O^+)(SO_2)$, with average positive ion mass $\sim 80 \pm 40$ amu. Sulphate species appear to dominate negative ion evolution, with mean mass $\sim 150 \pm 75$ amu. Aplin (2006) suggested that, based on data from the Magellan mission, sulphuric acid supersaturations could be sufficient for direct heterogeneous (Wilson) nucleation of sulphuric acid onto ions in the lower cloud-forming regions, for which the cloud production mechanism is not yet understood.

2.3 Mars

Ion formation and evolution in the Martian lower atmosphere was modelled, taking into account measurements of trace gases and water vapour, by Molina-Cuberos et al. (2002). Much of the chemistry is similar to the D region of the terrestrial ionosphere at $\sim 75–95$ km (MacGorman and Rust 1998). The dominant positive species are also similar to those expected on Earth and Venus with the protonated hydrate ($n = 2–4$) most abundant below 70 km. The level of hydration is sensitive to the amount of water vapour present, even though Mars's atmosphere contains an order of magnitude less water vapour than Earth. This is because the proton affinity of water is sufficient for it to attach preferentially to ions, much like pyridine in Earth's atmosphere (Sect. 2.1). Hydrates such as $CO_3^-(H_2O)_n$ are the most common negative ions. Nitric acid can occasionally act as a ligand, since its proton affinity is greater than water, though a more common reaction is one in which it acts as a catalyst to produce more protonated hydrates. Despite this complex chemistry, charged clusters play an insignificant role in the proposed Martian global electric circuit, as the expected existence of free electrons will dominate atmospheric conductivity (Aplin 2006).

2.4 Gas Planets: Jupiter, Saturn, Uranus and Neptune

Ion formation and chemistry at the gas planets was modelled by Capone et al. (1977, 1979) and, recently, as part of a study of Jovian aerosol and cloud droplet charging by Whitten et al. (2008). On Jupiter, ions are formed down to 40 km below the visible clouds, below which the atmosphere has absorbed all the ionising radiation from cosmic rays. Terminal positive ions are expected to be NH_4^+ and the clusters C_2H_7^+ and $\text{NH}_4^+(\text{NH}_3)_n$ (with $2 \geq n \geq 4$), which are stable in the relatively cool, yet dense atmosphere. In cloudy regions, electrons formed by ionisation attach rapidly to cloud particles, so the negative ion concentration is negligible. Above and below the cloud layers, negative cluster ions could be significant charge carriers, depending on electrophile concentrations (Whitten et al. 2008). Ionisation could ultimately enhance synthesis of molecules like C_3H_8 (propane) and CH_3NH_2 (methylamine) in the troposphere. Modelling of ionisation and ion chemistry in the atmospheres of Saturn, Uranus and Neptune predicted that C_2H_9^+ dominated in the lower atmosphere for each planet (Capone et al. 1977, 1979). Negative ions were ignored due to the lack of electrophilic species on Uranus and Neptune, and the rapid reactions expected on Saturn. No further chemical predictions were made, presumably because of the low abundance of reactive trace species known at the time. The models for Saturn, Uranus and Neptune could readily be updated to include more recent measurements of trace species.

2.5 Titan

Titan has an extensive nitrogen atmosphere with a surface pressure of 1.5 bar, but the chemistry is significantly different to the terrestrial planets. The lack of electrophilic species, such as oxygen, to attach to electrons after ionisation has led to uncertainty over the ratio of free electrons to negative ions in the lower atmosphere (e.g. Borucki et al. 1987; Molina-Cuberos et al. 2001). Since electrons are many orders of magnitude more electrically mobile than molecules, negative atmospheric electrical conductivity and aerosol attachment are both poorly constrained. Recent models have assumed that polycyclic aromatic hydrocarbons (PAHs) are the major electrophilic species, present in the upper troposphere/lower stratosphere between 170–350 km, and negative ions are negligible below 100 km (Whitten et al. 2007). PAHs are expected in Titan's atmosphere from laboratory experiments, and benzene, a chemical precursor to PAHs, was also detected remotely by the Cassini Ion Neutral Mass Spectrometer (Waite et al. 2007). The Cassini Plasma Spectrometer (CAPS) has detected large (a few hundred amu) positive organic ions, and massive (a few thousand amu) negatively charged particles in Titan's upper atmosphere (~ 1000 km). The negative particles are thought to play a key role in the formation of the complicated mixture of polymers, called tholins, making up Titan's haze (Coates et al. 2007). This provides further evidence that charge is important for cloud and haze formation in the outer Solar System.

Early results from Huygens have not added much to the earlier modelling work (re-reviewed in Aplin 2006) on the chemical composition of ions in Titan's lower atmosphere. Techniques developed to enable extraction of ion mobility (related to mass: see Sect. 3.1 or Harrison and Tammert (2008)) from the Huygens relaxation probe data (Aplin 2005; Owen et al. 2008) could not be used, due to loss of data from the positive channel (Lebreton et al. 2005). In general, the Huygens atmospheric electricity data has been more complicated than expected to analyse due to calibration problems and inconsistencies between the results from the two conductivity instruments (described in more detail in Hamelin et al. 2007). Only relatively preliminary analysis is available, but it is clear from the negative conductivities of $\sim \text{nS m}^{-1}$ reported in Hamelin et al. (2007) that free electrons are present,

suggesting a lack of electrophilic species. One approach to improve understanding of ion composition would be to combine the ion electrical mobilities predicted in physical models (e.g. Whitten et al. 2007) with up-to-date chemical modelling based on Huygens data e.g. from the Gas Chromatograph Mass Spectrometer, if its detection limit of a mixing ratio of 10^{-8} is sufficient (Niemann et al. 2002). It may also be possible that a trace electrophilic species is required below 50 km to reconcile Huygens measurements and models (Borucki and Whitten 2008), which would presumably lead to negative ion formation.

2.6 Triton

Triton's atmospheric ion processes were only studied after Voyager 2 discovered its tenuous atmosphere and thin cloud layer. The atmosphere consists of molecular nitrogen with methane, carbon monoxide and carbon dioxide as the major trace constituents (Delitsky 2006; Delitsky et al. 1990). The stepwise attachment of nitrogen molecules to CO^+ , NO^+ and C^+ ions produced by cosmic rays or magnetospheric particles is thermodynamically preferred at Triton's low temperatures (37 K at the surface) and forms large nitrogenated clusters e.g. $\text{CO}^+(\text{N}_2)_n$, $\text{NO}^+(\text{N}_2)_n$, or $\text{C}^+(\text{N}_2)_n$ (where $n \leq 50$). Nitrogen can become highly supersaturated near the tropopause at 9 km and is expected to condense directly onto the cluster ions. The “Wilson” mechanism of ion-induced nucleation (Aplin 2006) is the only mechanism explaining cloud formation on this icy moon. Triton is unique in the Solar System for two reasons, firstly charged clusters appear to be the major process controlling cloud formation and, secondly, the existence of charged clusters is only possible because of the low temperatures favouring nitrogen clustering. Otherwise, the atmosphere is so thin that collision probabilities would be low, making clustering unlikely.

3 Measurement of Charged Clusters

This paper will focus on identification of the composition of atmospheric cluster-ions rather than bulk electrical properties, although there is some overlap. In the absence of free electrons, charged clusters control air conductivity through their number concentration and electrical mobility (Harrison and Tammet 2008) and this provides a link to studies of the global electric circuit (Aplin et al. 2008). Measurements of the atmospheric electrical properties of charged clusters have already been reviewed by e.g. Aplin (2000), Harrison and Carslaw (2003) and Aplin (2006).

3.1 In Situ Measurements

The terrestrial atmosphere, where charged clusters have been detected for over a hundred years, is the exemplar for in situ measurements (Aplin et al. 2008). In situ charged cluster identification techniques are based on (1) mass spectrometry and (2) electrical mobility.

3.1.1 Mass Spectrometry

Mass spectrometry of ambient clusters is difficult for several reasons. Firstly the ions can exist in sufficiently small concentrations (mixing ratios of $\sim 10^{-17}$ at the terrestrial surface) that sampling only ambient charged species produces signals that are almost undetectably small. The pressure changes required from ambient pressure down to mass spectrometer

operating levels could further reduce the signal. Secondly, fragmentation of clusters is common within mass spectrometers, requiring separation of ambient species from those produced in the mass spectrometer. However, mass spectrometry of ambient ions both at the surface and in the free troposphere has been achieved using novel techniques, which are briefly outlined in this section. Tandem mass spectrometry involves stripping cluster ions of their ligands in a dissociation chamber, then selecting a core (“parent”) ion using a quadrupole ion trap. This core ion is then fragmented in a buffer gas and the fragments (“daughters”) identified with another quadrupole mass filter. The original charged cluster can be identified by comparing the daughter ion spectrum to reference data from artificially produced ions. This technique was used to identify the ion species described in Sect. 2.1 (Elrod 2003). Similar instruments have been used on planes for measurement of ambient tropospheric ions of up to several thousand amu (Wohlfahrt et al. 2000) and identification of “chemiions”, charged clusters observed in combustion engine exhausts (Möhler et al. 1993; Kiendler and Arnold 2002)).

3.1.2 Electrical Mobility

Electrical mobility is the speed of an ion in a unit electric field and is related to the ion’s mass, charge and the properties of the carrier gas (Harrison and Tammet 2008). Molecular clusters can only carry a single charge, which relates mobility to mass if the carrier gas is known. Ambient ion mobility spectrometers, reviewed by Aplin (2000), separate out ions of different mobilities either by varying the electric field and measuring the change in ion current, or allowing the charged clusters to drift in an electric field and measuring the current as a function of distance. This latter type is known as a drift tube spectrometer, in which ions of different mobility can be identified by their speeds (Nagato and Ogawa 1998). Drift tube spectrometers take a sample of air which is subsequently analysed, but aspiration ion mobility spectrometers continually blow or suck air through a region (often a cylinder) to which an electric field is applied. The current from ions of different mobilities can be determined by either direct measurement (Tammet 1970; Aplin and Harrison 2001; Fews et al. 2005) or inferred from the rate of voltage relaxation (Aplin 2005). Disadvantages of cluster-ion mobility measurements are that the carrier gas must be well-known, and that the conversion of mobility to mass is non-trivial (Harrison and Tammet 2008).

No in situ extra-terrestrial charged cluster composition measurements have yet been carried out, though it may be possible to infer composition from the results of the Pressure Wave Altimetry experiment on the Huygens probe (Fulchignoni et al. 2002). Miniaturisation of an aspiration-type instrument for possible use in space appears relatively straightforward, but drift tube miniaturisation could be more difficult because decreasing sample volume reduces the ambient ion content (terrestrial instruments often employ an ion source to increase the signal). Drift tubes could also lack spatial resolution if samples were taken, for example, during the descent of a probe.

Mass spectrometry has a well-established space heritage, with numerous instruments flown, often to determine precise isotopic ratios for studies of planetary evolution (e.g. Niemann et al. 2002). Ambient ion measurement would require a broader mass range and lower resolution but with much lower signal strength. There seems no objection in principle to modifying a space-qualified quadrupole instrument (e.g. Wright et al. 2007) for in situ detection of atmospheric charged clusters.

3.2 Remote Sensing

Remote sensing refers here to detection of charged clusters at a distance by a spacecraft in orbit, for which there is not yet a standard technique. The measurement of large ions in

Titan's upper atmosphere by the CAPS instrument on Cassini (Sect. 2.5), an electrostatic analyser intended to detect impacts from aligned fast ion fluxes in Saturn's magnetosphere (Young et al. 2004) were effectively in situ rather than remote detection. CAPS was used in a non-standard way during Titan fly-bys to determine the mass-to-charge ratio of clusters and particles directly impacting the detector. As many of the particles appeared to be massive, and would support multiple charges in the plasma environment of the Titan ionosphere, the CAPS technique used is not adequate to determine composition.

3.2.1 Laboratory Tests of Infrared Absorption by Cluster-Ions

It would be possible to detect atmospheric charged clusters remotely through spectroscopy. Just like neutral molecules and clusters, for which spectroscopic remote sensing is well-established, charged molecular clusters have absorption bands from stretch and bend modes between their hydrogen bonds. Absorption regions, possibly associated with the protonated water oligomer, which is common in the terrestrial atmosphere, and probably also on Mars and Venus, have been identified in the mid-infrared in laboratory experiments (Carlon and Harden 1980; Aplin and McPheat 2005) (Fig. 1). In Aplin and McPheat (2005), ambient cluster-ion concentrations were enhanced using a positive corona source. In this experiment, typical charged cluster concentrations were $\sim 8000 \text{ cm}^{-3}$ corresponding to a column concentration in the spectroscopy cell $\sim 10^{13} \text{ m}^{-2}$. As the total column concentration of atmospheric cluster-ions $\sim 10^{14} \text{ m}^{-2}$, the atmospheric absorption signal could be detectable in these bands.

3.2.2 Atmospheric Instrumentation for Measurements of Cluster-Ion Absorption

To investigate the atmospheric application of this finding, a narrowband filter radiometer system has been developed to measure terrestrial downwelling infra-red radiation at a cluster-ion absorption wavelength. The radiometer was deployed at a site where meteorological and electrical measurements are made.

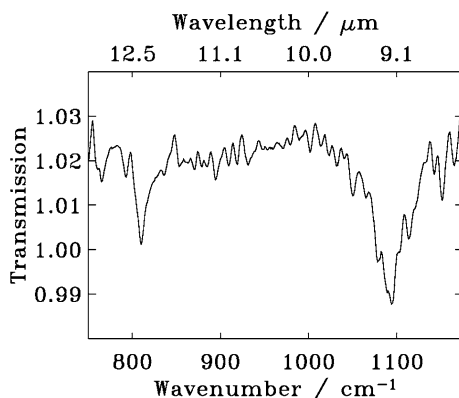


Fig. 1 Transmission spectrum of atmospheric charged clusters measured in artificial terrestrial air ($T \sim 20^\circ\text{C}$, $p \sim 1000 \text{ mbar}$) in a long path cell. The signal shown is the infra-red spectrum at charged cluster column concentrations $\sim 10^{13} \text{ m}^{-2}$, filtered to remove the absorption from neutral water and residual carbon dioxide vapour, and divided by a similarly filtered spectrum obtained at ambient cluster concentrations $\sim 10^{10} \text{ m}^{-2}$. Absorption bands, likely to be from molecular charged clusters can be seen at 12.3 and 9.2 μm (815 and 1090 cm^{-1}). From Aplin and McPheat (2005)

The radiometer was fitted with a narrowband ($9.15 \mu\text{m} \pm 0.75\%$, 5% bandwidth) interference filter, chosen to match the stronger of the two absorption bands in Fig. 1. An auxiliary filter (germanium, outer face coated with diamond-like-carbon, inner face covered with high efficiency anti-reflection coating) was also employed, mounted vertically above the narrowband filter to (1) provide a long-wavelength cutoff and (2) to provide robust environmental protection for the narrowband filter. The space between the two filters was purged with nitrogen to remove any residual water vapour, and sealed. A precision, temperature-stable amplifier ($\times 500$ gain) (Harrison and Knight 2006) was used to raise the voltage output of the radiometer, and a platinum resistance thermometer attached to the radiometer body.

The air conductivity σ is related to the total charged cluster concentration n by

$$\sigma \approx ne\bar{\mu} \quad (1)$$

where $\bar{\mu}$ is the mean ion mobility at that location (Harrison and Aplin 2007). Conductivity can be determined close to the radiometer from local atmospheric electricity measurements of the Potential Gradient (PG) (Aplin et al. 2008) measured with a field mill, and the conduction current J_z

$$\sigma = \frac{J_z}{PG}. \quad (2)$$

The parameters measured during the filter radiometer experiment are summarised in Fig. 2.

3.2.3 Retrieval of Radiometer Response to Cluster-Ion Changes

Preliminary data obtained under clear and foggy conditions are presented here. Nocturnal measurements were chosen to remove solar heating effects. The data are selected for meteorologically quiescent conditions, particularly low wind speed, to minimise effects from lofting of aerosol particles which could modify the local electrical and radiative environment.

As the ion absorption bands shown in Fig. 1 are in the continuum absorption region of the spectrum, the filter radiometer is expected to respond linearly to the column water vapour pressure, represented here by the surface water vapour pressure e . Some of the water vapour continuum absorption is thought to be from neutral water vapour clusters, particularly dimers, with concentration approximately proportional to e^2 (Vaida et al. 2001). The filter radiometer itself will also emit infra-red radiation, proportional to its body temperature T_{fr}^4 . To account for these effects, a multiple linear regression was used to extract the contributions of anomalies in e , e^2 , T_{fr}^4 , T_{fr} , electrical conductivity σ , and the interactions between them, on the fluctuations from the median filter radiometer voltage V_{fr} . The simplest statistically significant model fitting the data was of the form

$$V_{fr} = A + Be + Ce^2 + DT + ET_{fr}e + F\sigma. \quad (3)$$

Between the clear and foggy nights, the electrical conductivity coefficient F did not change, within the errors in the regression. This suggests a consistent electrical response of the filter radiometer in the varying conditions. The response of the filter radiometer to cluster-ion concentration changes, determined using (1) and (2), are shown in Fig. 3.

Figure 3 indicates that, once other linear effects on the filter radiometer have been removed using (3), there is a consistent positive response to changes in ion concentration. This is evidence that the filter radiometer responds to ion changes, and that the signal can

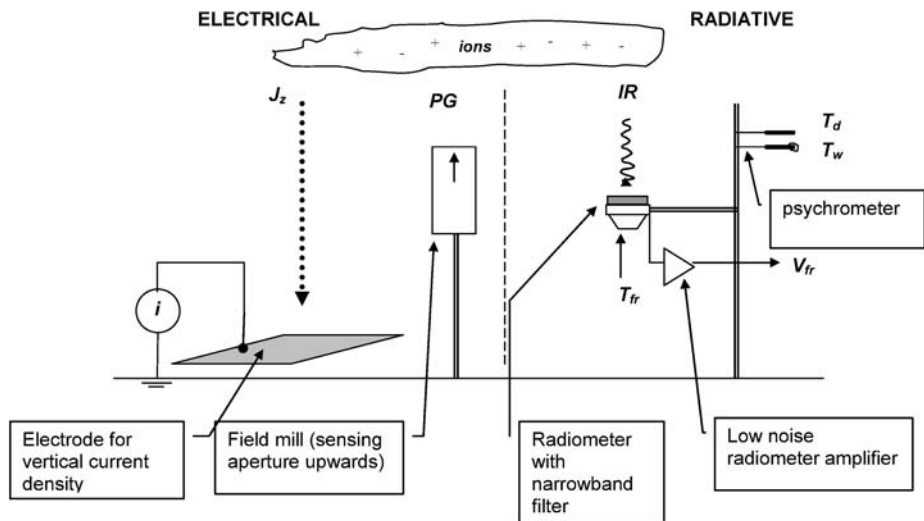


Fig. 2 Schematic diagram of co-located electrical and radiative ion measurements. Potential gradient PG is measured using a JC1131 electrostatic field mill. Conduction current J_z is detected at an insulated metallic electrode (Bennett and Harrison 2008). Dry and wet bulb temperatures T_d and T_w are used to calculate the water vapour pressure e . The filter radiometer body temperature T_{fr} is measured using a platinum resistance thermometer

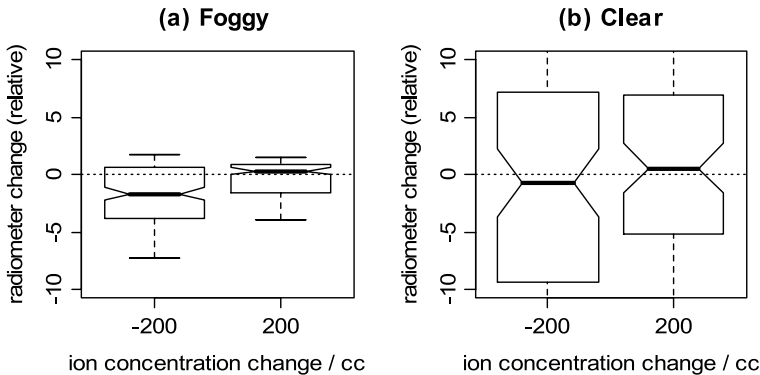


Fig. 3 Relative change in radiometer response, after detrending for vapour pressure, vapour pressure squared and temperature, against the change in ion concentration for (a) foggy (midnight–6am on 5th November 2007, 386 points) and (b) clear conditions (1am–4am on 22nd April 2007, 156 points). 1 minute averages are plotted, from 1 Hz samples, with separated notches indicating 95% significance

be detected in fog, and therefore potentially, through cloud. Further work is required to calculate the expected radiative effect of atmospheric charged water clusters.

Identification of the unique infra-red signals of atmospheric charged clusters even through cloud provides a method for their remote sensing, and therefore also the remote sensing of atmospheric electrical properties (Aplin et al. 2008). The principle could first be demonstrated for the terrestrial atmosphere by comparing satellite observations in the ion absorption bands (appropriate satellite data sets are discussed in e.g. Clerbaux et al. 2003) to in situ ion measurements. For planetary applications, laboratory spectroscopy experiments

would be required to generate charged clusters in simulated planetary atmospheres, identify the species and their characteristic absorption bands. It would then be relatively simple to use infra-red spectrometers e.g. the Cassini Composite Infrared Spectrometer (Flasar et al. 2004) to identify atmospheric charged clusters, much like any other trace species.

4 Discussion

Charged clusters are common in the Solar System, but measurements of their composition are scarce, even in our own atmosphere. Hydrated clusters are the most abundant species at the terrestrial planets where water vapour is present, because of water's large proton affinity. In the dense atmospheres of Earth and Venus there are approximately equal numbers of positive and negative clusters, but at Mars, free electron stability in the lower atmosphere reduces the number of negative cluster species. At the gas planets and their moons, organic and nitrogenated clusters are expected, with negative clusters relatively rare due to the lack of electrophilic species. Very large charged clusters and charged aerosol particles have been detected directly in Titan's upper atmosphere, though their composition could not be explicitly determined (Coates et al. 2007).

In the terrestrial atmosphere, in situ measurements of the composition can be made through mobility spectrometry or tandem mass spectroscopy, described in Sect. 3.1. Mobility spectrometry instrumentation is smaller, cheaper and can be used for continuous data acquisition without the need for reference laboratory measurements. As mobility links the chemical and physical properties of charged clusters, atmospheric ion mobility spectrometers are versatile and can be used to simultaneously infer atmospheric electrical properties such as air conductivity (Aplin 2000). Existing techniques for mass spectrometry of charged clusters are inherently complicated, with scope for future improvement and simplification, but offer better accuracy in identifying composition.

For planetary applications, mass spectrometry may be more promising for studies of cluster composition, at least in the short to medium term, due to its space heritage. If the instrument is well-characterised before launch, then the need to work off-line generating reference data does not compromise the measurements. Atmospheric ion mobility spectrometers could readily be miniaturised for use in space or other applications. Remote sensing of charged clusters from existing satellite spectrometer instruments is potentially a more powerful method with opportunities for wide spatial coverage. Experiments in Earth's atmosphere show that downwelling infra-red radiation in a charged cluster spectral band (Aplin and McPheat 2005) is linked to the cluster-ion concentration, measured independently. This supports the concept of future remote spectroscopic detection of atmospheric charged clusters.

Acknowledgements This research was partially funded by the UK Natural Environment Research Council and the Science and Technology Facilities Council. The filter radiometer housing was designed by B.J. Landowski (RAL), and technical support is also acknowledged from A.G. Lomas (Reading University) and W. Robins (RAL). K.A. Nicoll and R.G. Harrison (Reading University) assisted with the filter radiometer measurements.

References

- K.L. Aplin, Instrumentation for atmospheric ion measurements. PhD Thesis, The University of Reading, UK (2000)
K.L. Aplin, Surv. Geophys. **27**, 63–108 (2006). doi:[10.1007/s10712-005-0642-9](https://doi.org/10.1007/s10712-005-0642-9)

- K.L. Aplin, Rev. Sci. Instrum. **76**, 104501 (2005). doi:[10.1063/1.2069744](https://doi.org/10.1063/1.2069744)
- K.L. Aplin, R.G. Harrison, Rev. Sci. Instrum. **72**(8), 3467–3469 (2001)
- K.L. Aplin, R.G. Harrison, M.J. Rycroft, Space Sci. Rev. (2008, this issue)
- K.L. Aplin, R.A. McPheat, J. Atmos. Sol.-Terr. Phys. **67**(8–9), 775–783 (2005). doi:[10.1016/j.jastp.2005.01.007](https://doi.org/10.1016/j.jastp.2005.01.007)
- G.A. Bazilevskaya, I.G. Usoskin, E. Flückiger et al., Space Sci. Rev. (2008, this issue)
- A.J. Bennett, R.G. Harrison, J. Atmos. Sol.-Terr. Phys. (2008, in press). doi:[10.1016/j.jastp.2008.04.014](https://doi.org/10.1016/j.jastp.2008.04.014)
- G. Beig, G.P. Brasseur, J. Geophys. Res. **105**, 22671–22684 (2000)
- W.J. Borucki, Z. Levin, R.C. Whitten et al., Icarus **51**, 302–321 (1982)
- W.J. Borucki, Z. Levin, R.C. Whitten et al., Icarus **72**, 604–622 (1987)
- W.J. Borucki, R.C. Whitten, Planet. Space Sci. **56**, 19–26 (2008). doi:[10.1016/j.pss.2007.03.013](https://doi.org/10.1016/j.pss.2007.03.013)
- L.A. Capone, J. Dubach, R.C. Whitten et al., Icarus **39**, 433–449 (1979)
- L.A. Capone, R.C. Whitten, S.S. Prasad et al., Astrophys. J. **215**, 977–983 (1977)
- H.R. Carlon, C.S. Harden, Appl. Opt. **19**(11), 1776–1786 (1980)
- C. Clerbaux, J. Hadji-Lazaro, S. Turquety et al., Atmos. Chem. Phys. **3**, 1495–1508 (2003)
- A.J. Coates, F.J. Crary, G.R. Lewis et al., Geophys. Res. Lett. **34**, L22103 (2007). doi:[10.1029/2007GL030978](https://doi.org/10.1029/2007GL030978)
- M.L. Delitsky, R.P. Turco, M.Z. Jacobson, Geophys. Res. Lett. **17**(10), 1725–1728 (1990)
- M.L. Delitsky, Bull. Am. Astron. Soc. **38**, 519 (2006)
- S. Eichkorn, S. Wilhelm, H. Aufmhoff et al., Geophys. Res. Lett. **29**(14), 1698 (2002). doi:[10.1029/2002GL015044](https://doi.org/10.1029/2002GL015044)
- F.L. Eisele, J. Geophys. Res. **94**, 2183–2196 (1989)
- F.L. Eisele, E.R. Lovejoy, E. Kosciuch et al., J. Geophys. Res. **111**, D04305 (2006). doi:[10.1029/2005JD006568](https://doi.org/10.1029/2005JD006568)
- M.J. Elrod, Int. J. Mass Spectr. **228**, 91–105 (2003)
- A.P. Fews, N.K. Holden, P.A. Keitch et al., Atmos. Res. **76**(1–4), 29–48 (2005)
- F.M. Flasar, V.G. Kunde, M.M. Abbas et al., Space Sci. Rev. **115**(1–4), 169–297 (2004)
- M. Fulchignoni, F. Ferri, F. Angrilli et al., Space Sci. Rev. **104**(1–4), 395–431 (2002). doi:[10.1023/A:1023688607077](https://doi.org/10.1023/A:1023688607077)
- M. Hamelin, C. Beghin, R. Grard et al., Planet. Space Sci. **55**, 1964–1977 (2007). doi:[10.1016/j.pss.2007.04.008](https://doi.org/10.1016/j.pss.2007.04.008)
- R.G. Harrison, K.L. Aplin, Atmos. Res. **85**, 199–208 (2007). doi:[10.1016/j.atmosres.2006.12.006](https://doi.org/10.1016/j.atmosres.2006.12.006)
- R.G. Harrison, K.S. Carslaw, Rev. Geophys. **41** (2003). doi:[10.1029/2002RG000114](https://doi.org/10.1029/2002RG000114)
- R.G. Harrison, J.R. Knight, Rev. Sci. Instrum. **77**, 116105 (2006). doi:[10.1063/1.2370752](https://doi.org/10.1063/1.2370752)
- R.G. Harrison, H. Tammet, Space Sci. Rev. (2008, this issue)
- J. Kazil, R.G. Harrison, E. Lovejoy et al., Space Sci. Rev. (2008, this issue)
- A. Kiendler, F. Arnold, Atmos. Environ. **36**, 1757–1761 (2002)
- W. Klemperer, V. Vaida, Proc. Nat. Acad. Sci. **103**(28), 10584–10588 (2006). doi:[10.1073/pnas.0508231103](https://doi.org/10.1073/pnas.0508231103)
- J.P. Lebreton, O. Witassee, C. Sollazzo et al., Nature **438**, 758–764 (2005). doi:[10.1038/nature04347](https://doi.org/10.1038/nature04347)
- O. Möhler, T. Reiner, F. Arnold, Rev. Sci. Instrum. **64**(5), 1199–1207 (1993)
- D.R. MacGorman, W.D. Rust, *The Electrical Nature of Storms* (Oxford University Press, Oxford, 1998), pp. 25–31
- G.J. Molina-Cuberos, J.J. López-Moreno, R. Rodrigo et al., Adv. Space Res. **28**(10), 1511–1516 (2001)
- G.J. Molina-Cuberos, H. Lichtenegger, K. Schwingenschuh et al., J. Geophys. Res. **107**, E5 (2002). doi:[10.1029/2000JE001447](https://doi.org/10.1029/2000JE001447)
- K. Nagato, T. Ogawa, J. Geophys. Res. **103**, 13917–13925 (1998)
- H.B. Niemann, S.K. Atreya, S.J. Bauer et al., Space Sci. Rev. **104**(1–4), 553–591 (2002). doi:[10.1023/A:1023680305259](https://doi.org/10.1023/A:1023680305259)
- N.R. Owen, K.L. Aplin, P.A. Stevens, J. Phys. Conf. Ser. (2008, in press). <http://epubs.cclrc.ac.uk/work-details?w=43535>
- T.E. Parts, A. Luts, Atmos. Env. **38**, 1283–1289 (2004). doi:[10.1016/j.atmosenv.2003.11.030](https://doi.org/10.1016/j.atmosenv.2003.11.030)
- D. Smith, M.J. Church, Planet. Space Sci. **25**(5), 433–439 (1977). doi:[10.1016/0032-633\(77\)90075-7](https://doi.org/10.1016/0032-633(77)90075-7)
- H. Tammet, The aspiration method for the determination of atmospheric ion spectra. Israel program for scientific translations, Jerusalem, 1970
- S.N. Tripathi, M. Michael, R.G. Harrison, Space Sci. Rev. (2008, this issue)
- V. Vaida, J.S. Daniel, H.G. Kjaergaard et al., Q. J. R. Met. Soc. **127**, 1627–1643 (2001)
- J.H. Waite, D.T. Young, T.E. Cravens et al., Science **316**(5826), 870–875 (2007). doi:[10.1126/science.1139727](https://doi.org/10.1126/science.1139727)
- R.C. Whitten, W.J. Borucki, S.N. Tripathi, J. Geophys. Res. **112**, E04001 (2007). doi:[10.1029/2006JE002788](https://doi.org/10.1029/2006JE002788)
- R.C. Whitten, W.J. Borucki, K. O'Brien et al., J. Geophys. Res. **113**, E04001 (2008). doi:[10.1029/2007JE002975](https://doi.org/10.1029/2007JE002975)

-
- K.H. Wohlf from, S. Eichkorn, F. Arnold et al., *Geophys. Res. Lett.* **27**(23), 3853–3860 (2000)
- I.P. Wright, S.J. Barber, G.H. Morgan et al., *Space Sci. Rev.* **128**, 1–4 (2007). doi:[10.1007/s11214-006-9001-5](https://doi.org/10.1007/s11214-006-9001-5)
- Y. Yair, *Space Sci. Rev.* (2008, this issue)
- D.T. Young, J.J. Berthelier, M. Blanc et al., *Space Sci. Rev.* **114**(1–4), 1–112 (2004). doi:[10.1007/s11214-004-1406-4](https://doi.org/10.1007/s11214-004-1406-4)

Atmospheric Ions and Aerosol Formation

Frank Arnold

Originally published in the journal Space Science Reviews, Volume 137, Nos 1–4.
DOI: [10.1007/s11214-008-9390-8](https://doi.org/10.1007/s11214-008-9390-8) © Springer Science+Business Media B.V. 2008

Abstract This paper discusses atmospheric ions and their role in aerosol formation. Emphasis is placed upon the upper troposphere where very low temperatures tend to facilitate new particle formation by nucleation. New measurements addressed include: Laboratory measurements of cluster ions, aircraft measurements of ambient atmospheric ions, atmospheric measurements of the powerful nucleating gas H_2SO_4 and its gaseous precursor SO_2 . The paper also discusses model simulations of aerosol formation and growth. It is concluded that in the upper troposphere new aerosol formation via ions is a frequent process with relatively large rates. However new particle formation by homogeneous nucleation which does not involve ions also seems to be efficient. The bottleneck in the formation of upper troposphere aerosol particles with sizes sufficiently large to be climate relevant is mostly not nucleation but sufficient growth of new and still very small particles. Our recent upper troposphere SO_2 measurements suggest that particle growth by gaseous sulphuric acid condensation can be efficient in certain circumstances. If so, cosmic ray mediated formation of CCN sized particles should at least occasionally be operative in the upper troposphere.

Keywords Atmosphere · Ions · Aerosol

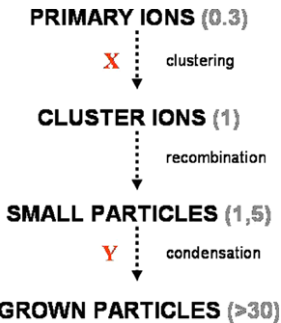
1 Introduction

Atmospheric ions are involved in aerosol formation. Ions may grow sufficiently to become stable aerosol particles. Ion growth requires the presence of atmospheric trace gas molecules which have the ability to attach to ions. The ion growth speed which increases with the concentration of such trace gas molecules must be sufficiently large to allow ion growth within the relatively short ion lifetime. However such conditions are met only in certain atmospheric conditions. Whether ion induced aerosol formation makes a significant contribution to the atmospheric aerosol budget therefore remains an open question.

F. Arnold (✉)

Atmospheric Physics Division, Max Planck Institute for Nuclear Physics (MPIK), P.O. Box 103980,
69029 Heidelberg, Germany
e-mail: frank.arnold@mpi-hd.mpg.de

Fig. 1 Simplified scheme of atmospheric ion-induced formation of aerosol particles followed by particle growth to CCN size. Numbers denote approximate diameters (in nm) of ions and particles. X denotes nucleating gas molecules and Y denotes condensing gas molecules



It has even been speculated that aerosol particles formed via ions may grow to the size of cloud condensation nuclei and thereby may influence clouds and climate (Ney 1959). This ion-climate connection hypothesis has recently attained considerable interest stimulated by several recent reports claiming observational evidence for a cosmic ray climate connection hypothesis (cf. Marsh and Svensmark 2000; Neff et al. 2001; Shaviv 2002; Shaviv and Veizer 2004; Harrison and Stephenson 2006). In particular observations were reported suggesting that low clouds are correlated with cosmic rays (Marsh and Svensmark 2000). However the current discussion of the cosmic ray climate connection hypothesis is highly controversial. A major point of criticism is the apparent lack of an obvious physical mechanism linking climate with cosmic radiation (CR). Several potential mechanisms have been proposed, some of which being only poorly understood. Among the proposed mechanisms, probably the one most often considered (and perhaps least speculative) involves ion induced formation of aerosol particles. Some of these new particles can grow sufficiently to act as cloud condensation nuclei (cf. Arnold 1980a, 1980b, Arnold 1981a, 1981b; Yu and Turco 2001; Eichkorn et al. 2002; Carslaw et al. 2002; Harrison and Carslaw 2003; Lee et al. 2003; Lovejoy et al. 2004; Kazil and Lovejoy 2004; Yu et al. 2002). However, ion induced CCN formation is itself not fully understood and it is uncertain whether it can significantly contribute to the atmospheric CCN population and thereby influence climate.

Aerosols influence climate in numerous direct (WMO 2001) and indirect ways (WMO 2001; Lohmann and Feichter 2005; Chen and Penner 2005). If sufficiently large, they scatter sunlight and eventually act as cloud condensation nuclei (CCN) and cloud ice (freezing) nuclei (IN), if CR mediated aerosol formation was indeed contributing significantly to the atmospheric budget of grown aerosol particles. CR would have a potential to influence climate. CR are modulated by solar activity variations, and so might also be their potential effect on aerosols and CCN. An analysis of Marsh and Svensmark (2000) identified a signature of the 11-years sunspot cycle in low clouds (cloud-coverage).

The present paper is focussed on upper tropospheric processes that lead from CR generated ions to CCN. These processes (Fig. 1) involve clustering of atmospheric trace gas molecules X (particularly H_2SO_4) to ions, mutual recombination (neutralization) of large cluster ions leading to stable but still very small aerosol particles, and growth of fresh aerosol particles preferably by condensation of atmospheric trace gases Y. The first two steps leading from ions to stable aerosol particles are termed ion induced nucleation (hereafter INU). The third step involves trace gases X and in addition also trace gases Y which have a potential to condense on stable aerosol particles and thereby induce particle growth. Several different species Y may be present having different equilibrium saturation pressures and therefore starting at a given temperature to attach to stable particles at different threshold particle sizes. In addition there may be present trace gases which react with particles leading to molecules which remain bound to the particle and therefore contribute to particle growth.

At first glance, ion induced CCN formation seems to be similar to what is taking place in the famous “Wilson cloud chamber” which had an important role in the development of high-energy particle physics. Tracks of ionizing high energy particles traversing the chamber are visualized by converting ions to light scattering water droplets. This is achieved by building up a very high water vapour super-saturation (about 400%) which allows efficient INU and efficient small particle growth. Here $X = Y = \text{H}_2\text{O}$.

In the atmosphere water vapour super-saturation builds up occasionally leading to cloud droplet formation. However, these super-saturations remain very small and only very rarely exceed 1% but almost never reach 2%. In contrast with the situation in a Wilson cloud chamber the minimum water droplet diameter of a stable water droplet in the atmosphere is much larger (300 nm). Hence ions cannot grow sufficiently to become stable water droplets. Ion-induced aerosol particle formation can take place only in the presence of highly supersaturated atmospheric trace gases X . Since such trace gases rapidly (within less than about one hour) condense on pre-existing aerosols, they cannot be efficiently transported in the atmosphere and must therefore be produced locally by photochemical processes.

In this context, sulphuric acid (H_2SO_4) could emerge as one of the most important candidates for X as an nucleating and condensing trace gas. Being very hygroscopic, it tends to co-cluster with water vapour molecules, eventually leading to new stable aerosol particles (bi-molecular nucleation). Due to their strongly hygroscopic nature, sulphuric acid aerosol particles may act as atmospheric CCN already when their diameter exceeds only about 30 nm (at 1% super-saturation; see below).

Low temperatures favour nucleation. Therefore the cold upper troposphere represents a region of primary interest, at the condition that gases of type X are present and that their concentrations are large enough. In fact, so far only a single X -gas has been detected in the upper troposphere, namely, H_2SO_4 (cf. Heitmann and Arnold 1983; Viggiano and Arnold 1995). It is also the only Y -gas known to be present in the upper troposphere. Another feature of the upper troposphere which tends to facilitate new particle formation and growth is the relatively small surface of pre-existing aerosol particles.

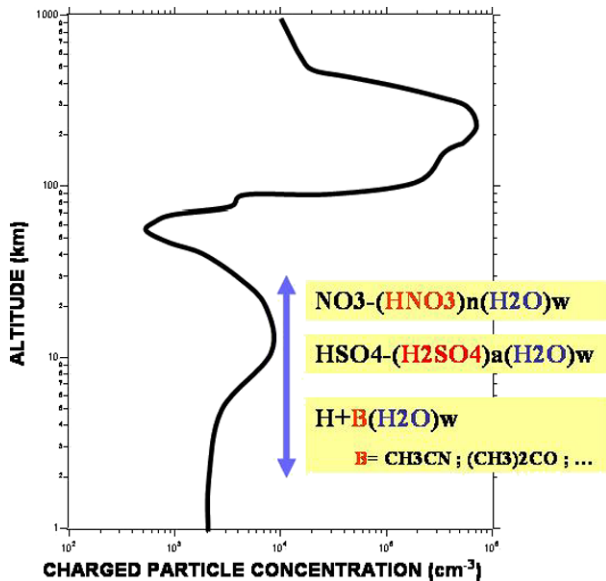
After their formation in the upper troposphere, new particles may undergo downward transport into the middle and lower troposphere where they may act as CCN. Alternatively new particles formed in the upper troposphere may also experience upward transport to the lower stratosphere. If this cross-tropopause transport takes place in the tropics, it is likely that it is followed by further transport from the lower to the middle stratosphere. Hence particles formed in the upper troposphere may also experience transport into the stratosphere and thereby feed the stratospheric aerosol layer.

The present paper critically discusses tropospheric ions and ion induced formation of atmospheric secondary sulphuric acid aerosol particles and CCN in the light of new laboratory experiments and new atmospheric measurements recently made by our MPIK Heidelberg group. Emphasis is placed upon the upper troposphere where low temperatures and low abundances of pre-existing aerosol particles tend to facilitate new particle formation and growth. The present paper also places CR mediated INU into a broader perspective by comparing INU with new particle formation via homogeneous sulphuric acid nucleation (HONU), a mechanism that does not require ions.

2 Atmospheric Ions

Ions are formed in the Earth’s troposphere by numerous processes. The most important ionization sources involving air ionization are galactic cosmic rays, radio activity, and electric discharges particularly including corona and lightning.

Fig. 2 Vertical profile of the total concentration of atmospheric positive ions for daytime conditions. Also indicated are the most abundant positive and negative ion species measured by MPIK Heidelberg



Primary charged species formed by air ionization include free electrons and the simple molecular and atomic ions N_2^+ , O_2^+ , N^+ , and O^+ . Free electrons attach rapidly to O_2 leading to O_2^- . Thereafter primary positive ions and O_2^- undergo ion–molecule-reactions leading to secondary positive and negative ions, mostly complex cluster ions. Ultimately ions are lost by ion-ion recombination, and in aerosol rich air masses, also by attachment to aerosol particles. For upper tropospheric air, in the absence of aerosol particles, a steady state treatment of ion formation and ion loss by ion-ion recombination yields a total ion concentration:

$$n_i = (Q/\alpha)^{1/2} \quad (1)$$

(Q in $\text{cm}^{-3} \text{s}^{-1}$; α in $\text{cm}^3 \text{s}^{-1}$; n_i in cm^{-3}).

In the troposphere below about 12 km the ion-ion recombination coefficient α is about $1.7 \cdot 10^{-6} \text{ cm}^{-3} \text{s}^{-1}$ (Bates 1985), and hence $n_i = 0.0013 Q^{1/2}$.

The rate Q of CR induced ionization is largest at about 14 km altitude. At middle latitudes where the local tropopause is located at about 12 km, the maximum Q is found just above the tropopause in the lowermost stratosphere. Since CR experience partial shielding by the magnetic fields of the Sun and the Earth, Q varies with geomagnetic latitude and solar activity. It is larger at the Earth's poles compared to the equator. However, the variation of Q over a solar sunspot cycle is relatively small. At middle latitudes and around 14 km altitude Q decreases with increasing solar activity (from sunspot minimum to sunspot maximum) only from about 40 to 30 $\text{cm}^{-3} \text{s}^{-1}$. According to expression (1), at middle latitudes the corresponding variation of n_i is only $4200\text{--}4850 \text{ cm}^{-3}$ over a solar cycle.

Therefore, a very sensitive process must be involved if the faint increase in n_i induced by the 11-year solar activity cycle is to lead to a significant increase of CCN formation via INU.

The vertical n_i profile (Fig. 2) has two pronounced maxima, one in the ionosphere (around 100–200 km), and one in the stratosphere (around 10–30 km). The ion lifetime with respect to ion-ion recombination is $t_r = 1/(\alpha \cdot n_i)$. Below 12 km altitude t_r increases

with increasing height from about 120 s (12 km) to 400 s (3 km) (Viggiano and Arnold 1995).

Therefore the time span (t_r) available for the ion chemical evolution is relatively short which implies that atmospheric trace gases involved in the conversion of primary to secondary ions and in the growth of secondary ions must be sufficiently abundant. For example for an altitude of 10 km where $t_r = 200$ s the trace gas concentration must be at least about $3 \cdot 10^6 \text{ cm}^{-3}$ (corresponding to an atmospheric mole fraction of about $3 \cdot 10^{-13}$). Here a typical ion molecule collision rate coefficient of $2 \cdot 10^{-9} \text{ cm}^3 \text{ s}^{-1}$ was considered.

The most abundant ion species observed in the free troposphere and the stratosphere (Fig. 2) have originally been detected by the MPIK Heidelberg group (Heitmann and Arnold 1983; Möhler and Arnold 1992; Viggiano and Arnold 1995) using ion mass spectrometers on flying platforms including aircraft, balloons, and rockets. These observed major ions are complex cluster ions containing H_2SO_4 , H_2O , HNO_3 , $(\text{CH}_3)_2\text{CO}$ and CH_3CN molecules attached to core ions. These cluster ions are formed from precursor ions via ion-molecule-reactions involving the atmospheric trace gases H_2SO_4 , H_2O , HNO_3 , $(\text{CH}_3)_2\text{CO}$, and CH_3CN . Of these gases H_2SO_4 is particularly interesting as it represents a powerful nucleating agent (see above). An interesting question is whether large H_2SO_4 cluster ions involved in INU can in fact build up in the atmosphere. Another interesting question is why the observed major positive ions do not contain H_2SO_4 . Both questions will be answered below.

3 Ion Induced Sulphuric Acid Nucleation

This section of the paper addresses steps 1 and 2 of the scheme shown in Fig. 1 focussing on the case $X = \text{H}_2\text{SO}_4$. Recently, laboratory investigations of H_2SO_4 cluster ions have been made by two laboratories (Aeronomy Laboratory in Boulder, Colorado, and MPIK Heidelberg). The Aeronomy Lab investigations focussed on negative cluster ions containing up to 6 H_2SO_4 molecules and were made at different temperatures (Froyd and Lovejoy 2003; Lovejoy and Curtius 2001; Curtius et al. 2001; Lovejoy et al. 2004). The MPIK investigations were made at only one temperature (295 K), but include also larger negative and positive cluster ions containing up to 24 H_2SO_4 molecules (Wiedner 2000; Eichkorn 2001; Wilhelm et al. 2004; Sorokin et al. 2006). Here some of these MPIK results will be addressed.

Figure 3 shows mass distributions (envelopes) of negative cluster ions obtained in a flow reactor-mass spectrometer experiment of MPIK (Wilhelm et al. 2004; Sorokin et al. 2006). The ion mass spectrometer used was a large ion-mass spectrometer (LIOMAS) with a mass range of up to 10000 amu (atomic mass units). This instrument was developed by MPIK for measurements of atmospheric large cluster ions on aircraft platforms (see below). Synthetic air was passed through the flow reactor and traces of H_2SO_4 vapour and H_2O vapour (relative humidity: 4.1–6.2%) were added. Reagent ions introduced into the flow reactor were of the type $\text{NO}_3^- (\text{HNO}_3)_n (\text{H}_2\text{O})_w$ which are the same ions acting in the atmosphere as precursors of $\text{HSO}_4^- (\text{H}_2\text{SO}_4)_a (\text{H}_2\text{O})_w$ ions (see above). The four mass spectra (Fig. 3) correspond to different gaseous H_2SO_4 concentrations. For the lowest H_2SO_4 concentration the spectrum is narrow, peaking around 200 amu and the major ions are $\text{NO}_3^- (\text{HNO}_3)_n (\text{H}_2\text{O})_w$ reagent ions with $n = 1$ and 2 and mostly $w = 0$. These ions were introduced into the flow reactor and unambiguously identified using a second ion mass spectrometer with higher mass resolution.

As the H_2SO_4 concentration is increased to $[\text{H}_2\text{SO}_4] = 5 \cdot 10^9 \text{ cm}^{-3}$, the spectrum becomes bi-modal and the second mode extends to 2400 amu. Now the major ions are

Wilhelm, Eichkorn, Wiedner, Pirjola, and Arnold (2004)

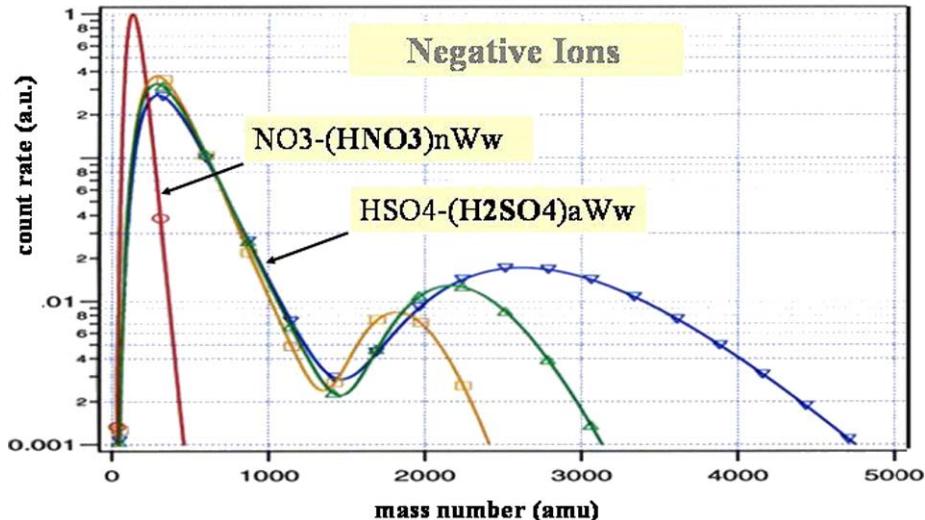
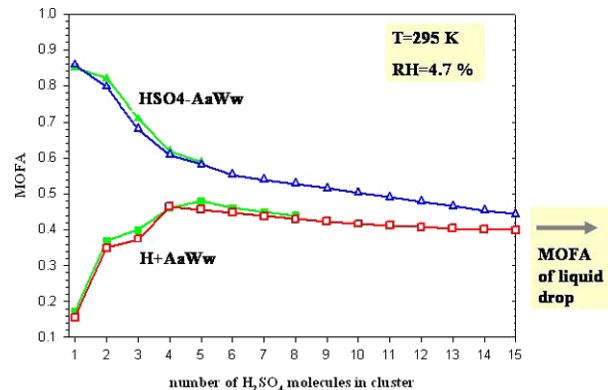


Fig. 3 Mass distributions of negative cluster ions measured in a laboratory flow reactor experiment of MPIK Heidelberg (Wilhelm et al. 2004; Sorokin et al. 2006). Plotted are envelopes of mass peak heights (ion count rates in arbitrary units) versus mass number (in atomic mass units). The four mass distributions correspond to different gaseous H_2SO_4 concentrations. For the lowest $[\text{H}_2\text{SO}_4]$ the ions are $\text{NO}_3^- (\text{HNO}_3)_a(\text{H}_2\text{O})_w$ cluster ions and for the 3 cases with elevated H_2SO_4 the ions are $\text{HSO}_4^- (\text{H}_2\text{SO}_4)_a(\text{H}_2\text{O})_w$ cluster ions. For details see text

Fig. 4 Sulphuric acid mole fraction MOFA of $\text{HSO}_4^- (\text{H}_2\text{SO}_4)_a(\text{H}_2\text{O})_w$ and $\text{H}^+ (\text{H}_2\text{SO}_4)_a(\text{H}_2\text{O})_w$ cluster ions measured in the laboratory flow reactor experiment of MPIK (Sorokin et al. 2006). Also given are model calculations for cluster ions, electrically neutral $\text{H}_2\text{SO}_4/\text{H}_2\text{O}$ droplets, and droplets carrying a single elementary electrical charge. For details see text



$\text{HSO}_4^- (\text{H}_2\text{SO}_4)_a(\text{H}_2\text{O})_w$ cluster ions (hereafter termed $\text{HSO}_4^- \text{A}_a \text{W}_w$) containing numerous H_2O molecules. As $[\text{H}_2\text{SO}_4]$ is further increased the second mode shifts to larger mass numbers extending up to 4700 amu. In an analogous experiment with positive ions, cluster ions of the form $\text{H}^+ \text{A}_a \text{W}_w$ were detected when gaseous H_2SO_4 was present. Again a second mode developed but remained smaller (3000 amu) compared to negative ions.

Figure 4 shows the measured H_2SO_4 mole fraction (MOFA) of $\text{HSO}_4^- \text{A}_a \text{W}_w$ and $\text{H}^+ \text{A}_a \text{W}_w$ cluster ions (a is the number of sulphuric acid molecules and w is the number of water molecules contained in the cluster ion) versus a . Also shown are model simulations for cluster ions. For small a , MOFA is small for positive ions but large for nega-

tive ions. As the parameter a increases, the MOFA of positive and negative ions approach each other. Note that neutral $A_a W_w$ clusters which are also important in theories of homogeneous bi-molecular nucleation have so far not been measured (Laaksonen et al. 1995; Kulmala et al. 2004). Therefore the cluster ion measurements also help to constrain theories on homogeneous nucleation.

The above laboratory investigations of cluster ions confirm the efficiency of co-clustering of gaseous H_2SO_4 and H_2O . This co-clustering relies on strong hydrogen bonds forming between the clustering molecules. The H_2SO_4 molecule has a large gas-phase acidity and therefore tends to form strong hydrogen bonds with H_2O molecules which are not only abundant in the atmosphere but importantly posses an appreciable proton affinity. Small $HSO_4^- A_a W_w$ cluster ions have a large MOFA as the core ion HSO_4^- prefers H_2SO_4 ligands whose gas-phase acidity is much larger than the gas-phase acidity of H_2O ligands. In other words H_2SO_4 ligands bond much more strongly to HSO_4^- . Small $H^+ A_a W_w$ cluster ions have a small MOFA since H_2SO_4 and H_2O have approximately the same proton affinity but in the flow reactor gaseous H_2O was much more abundant than gaseous H_2SO_4 . For larger cluster ions ligand–ligand bonding becomes increasingly important and therefore the MOFA of positive and negative cluster ions approach each other.

The above laboratory experiments also explain why the major positive cluster ions observed in the atmosphere (see Fig. 2) do not contain H_2SO_4 . In the atmosphere, as in the laboratory experiment, gaseous H_2O is far more abundant than gaseous H_2SO_4 . Therefore the most abundant positive cluster ions can not contain H_2SO_4 . Even worse the atmosphere contains trace gas molecules (like $(CH_3)_2CO$ and CH_3CN) which possess substantially larger proton affinities than H_2O and therefore are the preferred inner ligands of small atmospheric positive cluster ions.

The behaviour seen in Fig. 4 indicates that under the conditions of the laboratory experiment A-attachment to $HSO_4^- A_a W_w$ ions becomes faster than thermal A-detachment for mass numbers $> 1300\text{--}1400$ amu corresponding to $a > 6$. It also indicates that for $a > 6$ A-attachment occurs on every collision of a gaseous A-molecule with a cluster ion (Sorokin et al. 2006). The ultimate decrease of the second mode simply reflects a kinetic limitation resulting from the limited time span ($t_{res} = 0.8$ s) an ion resides in the flow reactor. When gaseous H_2SO_4 is added, the ion life time t_c with respect to collision with a gaseous A-molecule ranges between about 0.025 s and about 0.06 s depending on the gaseous A-molecule concentration. Hence the ratio t_{res}/t_c ranges from about 8 to 32. This implies that on average during t_{res} an ion collides with 8–32 gaseous H_2SO_4 molecules depending on the gaseous H_2SO_4 concentration. If each of these collisions would lead to A-attachment the average mass numbers of the ions would be about 1600–6000 amu (including equilibrium H_2O uptake as well). In comparison the second modes of the mass spectra of negative ions extend to largest mass numbers of 2400 to 4700 amu. Our laboratory experiments with $H^+ A_a W_w$ ions also revealed the presence of a second mode. However, compared to the second mode $HSO_4^- A_a W_w$ ions, the second mode $H^+ A_a W_w$ ions are smaller. Probably this reflects more efficient A-detachment from $H^+ A_a W_w$ ions, induced either by thermal collisions or by switching with H_2O molecules.

In the atmosphere at 10 km altitude where temperatures are very low (around 223 K at middle latitudes), thermal A-detachment from ions is expected to be very slow. Hence ion growth is expected to be limited by the number of gaseous H_2SO_4 molecule collisions an ion experiences during its life time $t_r = 200$ s. On average this number is equal to t_r/t_c where $t_c = 1/k[H_2SO_4]$ is the time needed for an ion to collide with a gaseous H_2SO_4 molecule. Here $k = 2 \cdot 10^{-9} \text{ cm}^3 \text{ s}^{-1}$ is the ion–molecule-collision rate coefficient and $[H_2SO_4]$ is the gaseous H_2SO_4 concentration. Hence $t_c = t_r = 200$ s corresponds to

$[H_2SO_4] = 3 \cdot 10^6 \text{ cm}^{-3}$. For efficient formation of $HSO_4^- A_a W_w$ and $H^+ A_a W_w$ cluster ions at 10 km altitude $[H_2SO_4]$ need to be larger than $3 \cdot 10^6 \text{ cm}^{-3}$.

Are H_2SO_4 concentrations sufficiently high in the upper troposphere? This question will be addressed in the following section of the paper.

4 Atmospheric Sulphuric Acid

Gaseous sulphuric acid is present in the upper troposphere. It was originally detected via ambient atmospheric ion measurements by Arnold and Fabian (1980; see also review by Viggiano and Arnold 1995). Moreover, laboratory measurements (Reiner and Arnold 1993, 1994; Kolb et al. 1994; Lovejoy et al. 1996) explored the mechanism by which gaseous sulphuric acid is formed in the atmosphere.

Figure 5 shows a simplified schematic of atmospheric sulphuric acid processes. The sulphur bearing precursor gas from which gaseous H_2SO_4 is formed is SO_2 . Its sources are mostly combustion of sulphur containing fossil fuels, volcanism, and atmospheric photochemical SO_2 formation from oceanic plankton generated $(CH_3)_2S$. Of these sources fossil fuel combustion is clearly dominant. The SO_2 sinks are mostly deposition at the Earth's surface, cloud processes, and the gas-phase reaction with the hydroxyl radical OH . The OH reaction represents also the first and rate limiting step of SO_2 conversion to gaseous H_2SO_4 . Importantly, OH is recycled and therefore acts merely as a catalyst. In the upper troposphere OH is formed via O_3 photolysis and also via the photolysis of acetone $(CH_3)_2CO$ and other organic trace gases. Once formed gaseous H_2SO_4 rapidly condenses on pre-existing aerosol particles PAP (mostly within less than 1000 s). Hence a steady-state treatment yields as a first approximation $k[SO_2][OH] = [H_2SO_4]/t_s$ where $k = 1.5 \cdot 10^{-12} \text{ cm}^3 \text{ s}^{-1}$ is the rate coefficient of the OH -reaction and t_s is the gaseous H_2SO_4 lifetime with respect to condensation. For example, for $t_s = 1000 \text{ s}$ and a typical noon-time $[OH] = 2 \cdot 10^6 \text{ cm}^{-3}$, one obtains $[H_2SO_4] = 0.003[SO_2]$ for cloud-free conditions around noon. Hence for such conditions, gaseous H_2SO_4 is to a large part controlled by SO_2 .

If gaseous H_2SO_4 reaches a sufficiently large super-saturation, nucleation takes place involving INU (ion induced nucleation) and eventually also HONU (homogeneous nucleation) leading to secondary aerosol particles (SAP). These SAP grow by Y-condensation and mutual coagulation. Ultimately SAP may suffer from coagulation scavenging by PAP

Fig. 5 Simplified scheme of atmospheric gaseous H_2SO_4 processes. HONU denotes homogeneous nucleation, PAP denotes pre-existing aerosol particles, and SAP denotes secondary aerosol particles formed by HONU and ion-induced nucleation (arrow labelled IONS)

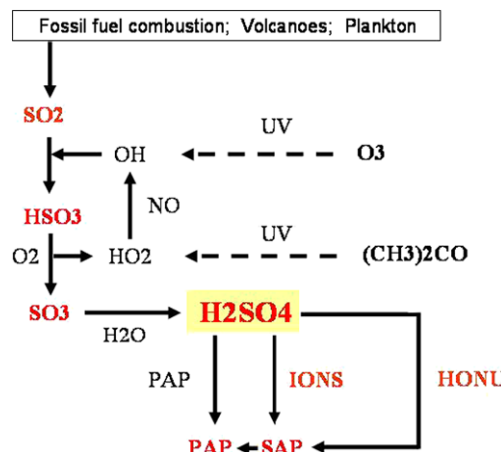
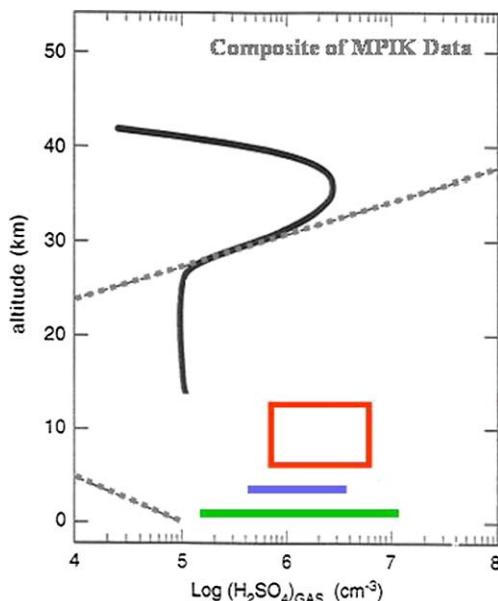


Fig. 6 Compilation of the ranges of daytime atmospheric gaseous sulphuric acid concentrations measured by MPIK Heidelberg using ground-based (green bar), mountain sites (blue bar), aircraft-based (red box), balloon-based (black line), and rocket-based (black line) mass spectrometers. The dotted curve represents an equilibrium saturation curve for gaseous sulphuric acid (see text)



(pre-existing aerosol particles). Importantly, the SAP lifetime increases very markedly with increasing SAP size. Therefore SAP growth has a strong influence on SAP concentrations (see below). Whether INU and HONU become efficient critically depends on the gaseous sulphuric acid concentration [H₂SO₄].

Figure 6 shows in a somewhat schematic form a compilation of the vertical distribution of daytime atmospheric gaseous sulphuric acid number concentration ranges measured by MPIK Heidelberg using mass spectrometers on the ground and on aircraft, balloons, and rockets. At ground-level and for cloud-free daytime conditions the measured [H₂SO₄] range from about $1 \cdot 10^5$ – $1 \cdot 10^7$ cm⁻³. This substantial range of variability reflects to a large part a variability of [SO₂]. Data obtained in the free troposphere on a central European mountain site at 2300 m altitude range from $4 \cdot 10^5$ – $4 \cdot 10^6$ cm⁻³.

Data obtained in the upper troposphere by aircraft-based instruments (box in Fig. 4.2) range from about $6 \cdot 10^5$ – $6 \cdot 10^6$ cm⁻³. Finally data obtained in the stratosphere by balloon-based and rocket-based instruments (only an average daytime profile is shown) are around $1 \cdot 10^5$ – $3 \cdot 10^6$ cm⁻³ and exhibit a pronounced layer with a peak around 35 km.

Also included in Fig. 6 is an equilibrium curve representing the H₂SO₄ saturation concentration of an H₂SO₄–H₂O mixture which is in equilibrium with atmospheric water vapour. Whenever the experimental data fall to the right of the equilibrium curve, gaseous H₂SO₄ is super-saturated. The largest H₂SO₄ super-saturations (saturation ratios >1000) are found in the upper troposphere where temperatures are lowest. These very high super-saturations imply that thermal A-detachment from HSO₄⁻A_aW_w and H⁺A_aW_w cluster ions can be neglected and therefore under these conditions INU should have no thermodynamic limitation.

The upper tropospheric H₂SO₄ concentrations correspond to $t_c = 100$ –1000 s. In comparison, the ion lifetime t_r with respect to ion-ion recombination (around 200 s) falls in between the above t_c . This implies that in many situations a severe kinetic limitation ($t_r > t_c$) exists which prevents INU from becoming efficient. However occasionally t_c becomes smaller than t_r which should allow cluster ions to grow and INU to become efficient.

The major cause of these INU promoting conditions seems to be elevated SO₂. Hence, SO₂ seems to be the major key to upper tropospheric INU and probably also HONU. However, our knowledge of upper tropospheric SO₂ is rather limited since only few data have previously been obtained by advanced instruments. Only very recently a number of advanced SO₂ measurements have been made by our group (Speidel et al. 2006) which revealed that SO₂ concentrations have a high degree of spatial variability. Around 10 km altitude SO₂ mole fractions range mostly from about 30–100 pptv but occasionally have a much larger variability from 10–3000 pptv. This implies highly variable concentrations of gaseous H₂SO₄ which in turn implies highly variable nucleation rates and particle growth rates.

5 Observations of Large Cluster Ions in the Upper Troposphere

Building on the laboratory experiments with H₂SO₄ cluster ions and the atmospheric gaseous H₂SO₄ measurements one expects large HSO₄⁻A_aW_w and H⁺A_aW_w cluster ions to be at least occasionally present in the cold upper troposphere. If so, such ions would induce new aerosol particle formation and therefore would represent fingerprints of INU. Using our aircraft-based large ion-mass spectrometer LIOMAS we have made a search for such large cluster ions in the upper troposphere (Eichkorn et al. 2002; Arnold et al. 2008).

Figure 7 shows as an example time-series of ion composition data obtained by LIOMAS in cloud-free upper troposphere air during one aircraft flight (Arnold et al. 2008). Given are flight altitude and fractional abundances of positive and negative ions with mass numbers larger than 200, 300, and 600 amu. While the aircraft was cruising mostly around 8000 m

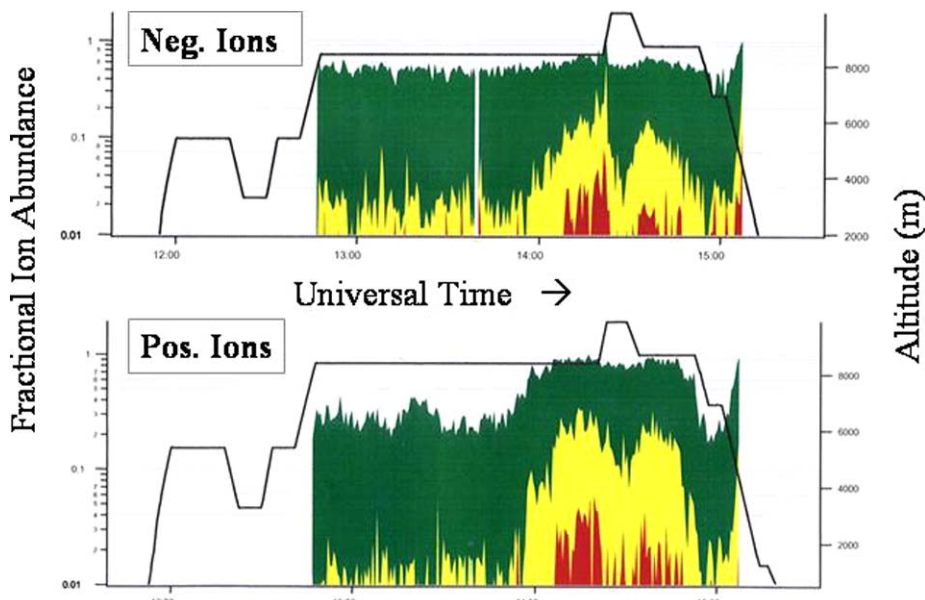


Fig. 7 Fractional abundances of positive and negative ions with mass numbers larger than 200 (green), 400 (yellow), and 600 (red) amu measured by MPIK Heidelberg during an aircraft mission over Central Europe. Also given is the flight altitude profile. (From Arnold et al. 2008)

altitude it occasionally intercepted air masses containing large negative and positive cluster ions with mass numbers larger than 600 amu. Negative and positive ions behave rather similar which suggests that one or several trace gases X are present which cluster to negative and positive ions. From the measured ions the concentrations of X were inferred. These range between $1\text{--}4 \cdot 10^6 \text{ cm}^{-3}$ which is very similar to the gaseous H_2SO_4 concentrations previously measured by our group in the upper troposphere around 8000 m altitude (see Fig. 6). This suggests at least that X is not more abundant than gaseous H_2SO_4 which implies that most likely X can be identified as H_2SO_4 .

Assuming X to be gaseous H_2SO_4 the rate J_i of ion-induced nucleation was calculated (Arnold et al. 2008). Around 8000 m altitude J_i ranges mostly from $3\text{--}25 \text{ cm}^{-3} \text{ s}^{-1}$. The latter value is equal to the maximum possible $J_i = Q$ where Q is the ionization rate. When $J_i = Q$, all ions become stable aerosol particles. Also calculated was the rate J_h of homogeneous bi-molecular nucleation (which does not require ions (Arnold et al. 2008). For the flight sections with low concentration of X , J_i tends to exceed J_h whereas for the section with high X concentrations J_h exceeds J_i . Even the highest J_h of about $100 \text{ cm}^{-3} \text{ s}^{-1}$ are much smaller than the highest possible J_h dictated by the rate at which an H_2SO_4 molecule collides with another H_2SO_4 molecule. Note that a nucleation rate of $3 \text{ cm}^{-3} \text{ s}^{-1}$ is already relatively high allowing the formation of more than 10000 aerosol particles $\text{cm}^{-3} \text{ hr}^{-1}$.

The above example of the atmospheric situation encountered during a single upper troposphere flight demonstrates that in the cold upper troposphere CR mediated INU (ion induced nucleation) can be very efficient. However this example also demonstrates that HONU (homogeneous nucleation) is also efficient and may become even more efficient than INU.

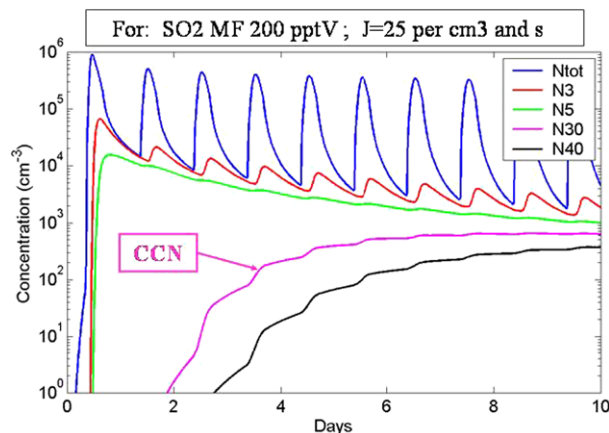
6 Aerosol Growth

Growth of newly formed, still very small aerosol particles is important for at least three reasons. Only sufficiently large particles become long lived, scatter sunlight efficiently, and eventually act as CCN and IN. Particle growth proceeds by Y condensation and coagulation. Growth by Y condensation may involve various types of different trace gases Y_i . Our gaseous H_2SO_4 measurements made in ground level air (Fiedler et al. 2005) indicate that gaseous H_2SO_4 contributes on average only about 5% to the growth of particles with diameters larger than 3 nm. Probably growth is mostly due to so far unidentified condensable organic trace gases. These condensable organics must be formed by chemical reactions involving relatively short lived organic precursor gases.

However in the upper troposphere the situation may be different. Here the short lived organic precursor gases may be less important since they are probably destroyed already during transport from the surface to the upper troposphere. In contrast, SO_2 , the precursor of gaseous H_2SO_4 , lives longer (about 10–20 days; see above) and therefore in the upper troposphere gaseous H_2SO_4 formation can continue for about 10–20 days. Hence new particles generated in the upper troposphere by INU or HONU can grow at least by gaseous H_2SO_4 condensation. Note that gaseous H_2SO_4 condensation does not require particularly low temperatures (see Fig. 6) and therefore can take place also in the middle and lower troposphere. This implies that particles formed in the upper troposphere may still continue to grow by gaseous H_2SO_4 condensation after downward transport and can act as CCN at lower altitudes.

Figure 8 shows as an example a 10 day model simulation (Arnold et al. 2008) considering an air mass which has ascended to 10 km and resided there for 10 days at clear-sky

Fig. 8 Results of a 10 day model simulation, for 10 km altitude, of number concentrations N_d of atmospheric aerosol particles with diameters larger than d nm. The air mass under consideration was assumed to ascend to 10 km altitude and reside there for a period of 10 days in cloud-free conditions. The initial SO_2 mole fraction was assumed to be 200 pptV. For details see text. (From Arnold et al. 2008)



conditions. After arrival at 10 km the initial SO_2 concentration was 200 pptV. The diurnal maximum OH concentration is $1 \cdot 10^6 \text{ cm}^{-3}$ which implies an e-folding lifetime for SO_2 of about 23 days.

On day 1, as the sun is rising, OH increases, leading to H_2SO_4 production. As a consequence H_2SO_4 rises to about $2 \cdot 10^7 \text{ cm}^{-3} \text{ s}^{-1}$ leading to HONO which in turn leads to a rise of the total aerosol particle number concentration N_{tot} to nearly $1 \cdot 10^5 \text{ cm}^{-3}$. Also the number concentrations N_4 and N_6 of particles with diameters larger than 4 and 6 nm rise steeply maximizing on day 1. In the afternoon as the solar elevation decreases OH, H_2SO_4 decrease steeply again. Also N_{tot} and to a lesser extent also N_4 and N_6 decrease due to coagulation. On the following days, the diurnal H_2SO_4 maximum decreases to about $4 \cdot 10^6 \text{ cm}^{-3}$ which is due to the decrease of OH and the increase of the aerosol surface leading to a decrease of the condensational H_2SO_4 lifetime. After day 1 the diurnal N_{tot} maxima nearly vanish, reflecting decreased HONO and increased scavenging of new particles via coagulation. The N_{12} , N_{20} , and N_{30} curves maximize on days 2, 4, and 6.

Note that the model results of particle formation and growth depend very critically on temperature, relative humidity, SO_2 , OH, and the initial aerosol surface. For example, when increasing the initial aerosol abundance, an increasing fraction of the photochemically formed H_2SO_4 will condense on pre-existing particles rather than nucleate.

In the atmosphere water vapour super-saturations are usually less than 1% and almost never exceed 2%. The corresponding minimum diameters of $\text{H}_2\text{SO}_4/\text{H}_2\text{O}$ aerosol particles acting as CCN are about 30 nm and 20 nm respectively.

An inspection of Fig. 8 reveals that within about 6 days the concentration N_{30} of particles with diameters larger than 30 nm (CCN sized particles) increases very substantially from 60 cm^{-3} to nearly 1000 cm^{-3} .

Particle growth is not controlled by temperature but is controlled by the rate of gaseous sulphuric acid formation which in turn is proportional to $[\text{SO}_2] \cdot [\text{OH}]$. The concentration of SO_2 is controlled by emissions of SO_2 and SO_2 -precursors at the Earth's surface, by atmospheric transport of these species, and by SO_2 removal by clouds.

Also, OH concentrations may be higher than considered by the above model case. This is particularly true for summer and for low latitudes. Higher OH will reduce the SO_2 lifetime and increase the rate of gaseous H_2SO_4 formation. In turn this will increase new particle formation and growth.

Variations of the CR ionization rate Q induce a variation of the INU rate J_i . However, the N30 reached after 10 days substantially depends on J_i only if J_i is sufficiently larger than J_h and only if J_i is less than about $1 \text{ cm}^{-3} \text{ s}^{-1}$.

7 Conclusions

The preceding discussion suggests that ion induced nucleation INU is a frequent process in the cold upper troposphere. However, homogeneous nucleation HONU also occurs. According to the model simulations reported by Arnold et al. (2008), upper troposphere INU and HONU rates are relatively high even for typical SO_2 mole fractions. Therefore the bottleneck of upper troposphere CR mediated formation of CCN sized particles seems to be new particle growth and not new particle formation by INU and HONU. In fact, the gaseous $[\text{H}_2\text{SO}_4]$ required to allow new particle growth to become efficient is mostly more than sufficient for INU.

Particle growth by gaseous H_2SO_4 condensation is to a large part controlled by SO_2 . In fact, spatial and temporal variations of upper troposphere SO_2 should have a much stronger effect on N30 (after 6 days) than the small variations of the CR ionization rate. Therefore more information on upper troposphere SO_2 and its spatial and temporal variability is needed. Furthermore efforts should be made to detect additional condensable gases Y which may eventually be present in the upper troposphere.

Acknowledgements The work presented here took place in close collaboration with DLR-IPA and the University of Helsinki. Financial support by the Max Planck Society is appreciated.

References

- F. Arnold, Multi-ion complexes in the stratosphere – Implications for trace gases and aerosol. *Nature* **284**, 610–611 (1980a). doi:[10.1038/284610a0](https://doi.org/10.1038/284610a0)
- F. Arnold, Ion-induced nucleation of atmospheric water vapour at the mesopause. *Planet. Space Sci.* **28**, 1003 (1980b). doi:[10.1016/0032-0633\(80\)90061-6](https://doi.org/10.1016/0032-0633(80)90061-6)
- F. Arnold, Solvated electrons in the upper atmosphere. *Nature* **294**, 732 (1981a). doi:[10.1038/294732a0](https://doi.org/10.1038/294732a0)
- F. Arnold, Ion nucleation – A potential source for stratospheric aerosols. *Nature* **299**, 134 (1981b). doi:[10.1038/299134a0](https://doi.org/10.1038/299134a0)
- F. Arnold, R. Fabian, First measurements of gas phase sulfuric acid in the stratosphere. *Nature* **282**, 55 (1980). doi:[10.1038/283055a0](https://doi.org/10.1038/283055a0)
- F. Arnold, S. Wilhelm, L. Pirjola, Cosmic ray induced formation of aerosol particles and cloud condensation nuclei: First detection of large negative and positive cluster ions in the upper troposphere (2008, in preparation)
- D.R. Bates, Ion–ion recombination in an ambient gas. *Adv. In Atomic and Molecular Physics*, vol. 20 (1985)
- K.S. Carslaw, R.G. Harrison, J. Kirkby, Cosmic rays, clouds and climate. *Science* **298**, 1732–1737 (2002). doi:[10.1126/science.1076964](https://doi.org/10.1126/science.1076964)
- Chen, Penner, Uncertainty analysis of the first indirect aerosol effect. *Atmos. Chem. Phys.* **5**, 2935–2948 (2005)
- J. Curtius, K.D. Froyd, E.R. Lovejoy, Cluster ion thermal decomposition (I): Experimental kinetics study and ab initio calculations for $\text{HSO}_4^- (\text{H}_2\text{SO}_4)_x (\text{HNO}_3)_y$. *J. Phys. Chem. A* **105**, 10867–10873 (2001). doi:[10.1021/jp0124950](https://doi.org/10.1021/jp0124950)
- S. Eichkorn, Development of an aircraft-based ion mass spectrometer with a large mass range: Measurements in the laboratory, aircraft exhaust plumes and the upper troposphere. PhD thesis. University of Heidelberg (2001)
- S. Eichkorn, S. Wilhelm, H. Aufmhoff, K.H. Wohlfahrt, F. Arnold, Cosmic ray-induced aerosol-formation: First observational evidence from aircraft-based ion mass spectrometer measurements in the upper troposphere. *Geophys. Res. Lett.* **29** (2002). doi:[10.1029/2002GL015044](https://doi.org/10.1029/2002GL015044)

- V. Fiedler, M. Dal Maso, M. Boy, H. Aufmhoff, J. Hoffmann, T. Schuck et al., The contribution of sulphuric acid to atmospheric particle formation and growth: a comparison between boundary layers in Northern and Central Europe. *Atmos. Chem. Phys. Discuss.* **5**, 1–33 (2005)
- K.D. Froyd, E.R. Lovejoy, Experimental thermodynamics of cluster ions composed of H_2SO_4 and H_2O . 2. Negative ion measurements and ab initio structures. *J. Phys. Chem. A* **107**, 9812–9824 (2003). doi:[10.1021/jp0278059](https://doi.org/10.1021/jp0278059)
- R.G. Harrison, K.S. Carslaw, Ion-aerosol-cloud processes in the lower atmosphere. *Rev. Geophys.* **41**, 1012 (2003). doi:[10.1029/2002RG000114](https://doi.org/10.1029/2002RG000114)
- R.G. Harrison, D.B. Stephenson, Empirical evidence for a nonlinear effect of cosmic rays on clouds, *Proc. R. Soc. A* (2006)
- H. Heitmann, F. Arnold, Composition measurements of tropospheric ions. *Nature* **306**, 747 (1983). doi:[10.1038/306747a0](https://doi.org/10.1038/306747a0)
- J. Kazil, E.R. Lovejoy, Tropospheric ionization and aerosol production: A model study. *J. Geophys. Res.* **109** (2004). doi:[10.1029/2004JD004852](https://doi.org/10.1029/2004JD004852)
- C.E. Kolb, J.T. Jayne, D.R. Wornshop, M.J. Molina, R.F. Meads, A.A. Viggiano, Gas phase reaction of sulfur trioxide with water vapour. *J. Am. Chem. Soc.* **116**, 10,314–10,315 (1994). doi:[10.1021/ja00101a067](https://doi.org/10.1021/ja00101a067)
- M. Kulmala, H. Vehkamäki, T. Petäjä, M. Dal Maso, A. Lauri, V.-M. Kerminen et al., Formation and growth rates of ultrafine atmospheric particles: a review of observations. *J. Aerosol Sci.* **35**, 143–176 (2004). doi:[10.1016/j.jaerosci.2003.10.003](https://doi.org/10.1016/j.jaerosci.2003.10.003)
- A. Laaksonen, V. Talanquer, D.W. Oxtoby, Nucleation: measurements, theory, and atmospheric applications. *Annu. Rev. Phys. Chem.* **46**, 489–524 (1995). doi:[10.1146/annurev.pc.46.100195.002421](https://doi.org/10.1146/annurev.pc.46.100195.002421)
- Lee et al., Particle formation by ion nucleation in the upper troposphere and lower stratosphere. *Science* **301**, 1886–1889 (2003). doi:[10.1126/science.1087236](https://doi.org/10.1126/science.1087236) Medline
- U. Lohmann, J. Feichter, Global indirect aerosol effects: a review. *Atmos. Chem. Phys. Discuss.* **5**, 715–737 (2005)
- E.R. Lovejoy, J. Curtius, Cluster ion thermal decomposition (II): Master equation modeling in the low pressure limit and fall-off regions. Bond energies for $\text{HSO}_4^-(\text{H}_2\text{SO}_4)_x(\text{HNO}_3)_y$. *J. Phys. Chem. A* **105**, 10,874–10,883 (2001). doi:[10.1021/jp012496s](https://doi.org/10.1021/jp012496s)
- E.R. Lovejoy, D.R. Hanson, G.G. Huey, Kinetics and products of gas-phase reactions of SO₃ with water. *J. Phys. Chem.* **100**, 19,911–19,916 (1996)
- E.R. Lovejoy, J. Curtius, K.D. Froyd, Atmospheric ion-induced nucleation of sulphuric acid and water. *J. Geophys. Res.* **109** (2004). doi:[10.1029/2003JD004460](https://doi.org/10.1029/2003JD004460)
- N.D. Marsh, H. Svensmark, Low cloud properties influenced by cosmic rays. *Phys. Rev. Lett.* **85**, 5004–5007 (2000). doi:[10.1103/PhysRevLett.85.5004](https://doi.org/10.1103/PhysRevLett.85.5004) Medline
- O. Möhler, F. Arnold, Gaseous sulphuric acid and sulfur dioxide measurements in the arctic troposphere and lower stratosphere: Implications for hydroxyl radical abundances. *Geophys. Res. Lett.* **19**, 1763–1766 (1992). doi:[10.1029/92GL01807](https://doi.org/10.1029/92GL01807)
- U. Neff et al., Strong coincidence between solar variability and the monsoon in Oman between 9 and 6 kyr ago. *Nature* **411**, 290–293 (2001). doi:[10.1038/35077048](https://doi.org/10.1038/35077048) Medline
- E.P. Ney, Cosmic radiation and the weather. *Nature* **183**, 451–452 (1959). doi:[10.1038/183451a0](https://doi.org/10.1038/183451a0)
- T. Reiner, F. Arnold, Laboratory flow reactor measurements of the reaction $\text{SO}_2 + \text{H}_2\text{O} + \text{M} \rightarrow \text{H}_2\text{SO}_4 + \text{M}$: Implications for gaseous H_2SO_4 and aerosol formation in the plume of jet aircraft. *Geophys. Res. Lett.* **20**, 2659–2662 (1993). doi:[10.1029/93GL02996](https://doi.org/10.1029/93GL02996)
- T. Reiner, F. Arnold, Laboratory investigations of gaseous sulfuric acid formation via $\text{SO}_2 + \text{H}_2\text{O} + \text{M} \rightarrow \text{H}_2\text{SO}_4 + \text{M}$: Measurements of the rate constant and products identification. *J. Chem. Phys.* **101**, 7399–7407 (1994). doi:[10.1063/1.468298](https://doi.org/10.1063/1.468298)
- N.J. Shaviv, Cosmic ray diffusion from the galactic spiral arms, iron meteorites, and a possible climatic connection. *Phys. Rev. Lett.* **89**, 051102 (2002). doi:[10.1103/PhysRevLett.89.051102](https://doi.org/10.1103/PhysRevLett.89.051102) Medline
- N.R. Shaviv, J. Veizer, Celestial driver of phanerozoic climate? *GSA. Today* **13**(7) (2004)
- A. Sorokin, F. Arnold, D. Wiedner, Flow reactor experiments and model calculations of sulfuric acid-water cluster ion formation and ion-induced nucleation. *Atmos. Environ.* **40**, 2030–2045 (2006).
- Speidel et al., Sulfur dioxide measurements in the lower, middle and upper troposphere: Deployment of a novel aircraft-based chemical ionization mass spectrometer with permanent in-flight calibration. *Atmos. Environ.* (2007)
- A.A. Viggiano, F. Arnold, Ion chemistry and composition of the atmosphere, in *Handbook of Atmospheric Electrodynamics*, vol. 1 (CRC Press, Boca Raton, 1995)
- D. Wiedner, Flow reactor investigations of aerosol particle formation by ion induced nucleation: The $\text{H}_2\text{SO}_4/\text{H}_2\text{O}$ system. Diploma thesis. University of Heidelberg, 2000
- S. Wilhelm, S. Eichkorn, D. Wiedner, L. Pirjola, F. Arnold, Ion-induced aerosol formation: new insights from laboratory measurements of mixed cluster ions $\text{HSO}_4^-(\text{H}_2\text{SO}_4)_a(\text{H}_2\text{O})_w$ and $\text{H}^+(\text{H}_2\text{SO}_4)_a(\text{H}_2\text{O})_w$. *Atmos. Environ.* **38**, 1735–1744 (2004). doi:[10.1016/j.atmosenv.2003.12.025](https://doi.org/10.1016/j.atmosenv.2003.12.025)

- WMO, in *Climate Change 2001: The Scientific Basis*, ed. by J.T. Houghton et al. (Cambridge University Press, Cambridge, 2001)
- F. Yu et al., Altitude variations of cosmic ray induced production of aerosols: Implications for global cloudiness and climate. *J. Geophys. Res.* **107** (2002). doi:[10.1029/2001JA000248](https://doi.org/10.1029/2001JA000248)
- F. Yu, R.P. Turco, From molecular clusters to nanoparticles: Role of ambient ionisation in tropospheric aerosol formation. *J. Geophys. Res.* **106**, 4797–4814 (2001). doi:[10.1029/2000JD900539](https://doi.org/10.1029/2000JD900539)

Tropospheric New Particle Formation and the Role of Ions

Jan Kazil · R. Giles Harrison · Edward R. Lovejoy

Originally published in the journal Space Science Reviews, Volume 137, Nos 1–4.
DOI: [10.1007/s11214-008-9388-2](https://doi.org/10.1007/s11214-008-9388-2) © Springer Science+Business Media B.V. 2008

Abstract Aerosol particles play an important role in the Earth’s troposphere and in the climate system: They scatter and absorb solar radiation, facilitate chemical processes, and serve as condensation nuclei for the formation of clouds. Tropospheric aerosol particles are emitted from surface sources or form *in situ* from the gas phase. Formation from the gas phase requires concentrations of aerosol precursor molecules aggregating to form molecular clusters able to grow faster than they evaporate. This process is called nucleation. Gas phase ions can reduce the concentration of aerosol precursor molecules required for nucleation, as they greatly stabilize molecular clusters with respect to evaporation. Therefore, ions are a potential source of aerosol particles. Since atmospheric ionization carries the signal of the decadal solar cycle due to the modulation of the galactic cosmic ray intensity by solar activity, a possible connection between the solar cycle, galactic cosmic rays, aerosols, and clouds has been a long-standing focus of interest. In this paper, we provide an overview of theoretical, modeling, laboratory, and field work on the role and relevance of ions for the formation of tropospheric aerosol particles, and on subsequent effects on clouds, and discuss briefly related research needs.

Keywords Troposphere · Aerosol nucleation · Ionization · Cosmic rays · Clouds

J. Kazil (✉)

Max Planck Institute for Meteorology, Bundesstr. 53, 20146 Hamburg, Germany

e-mail: jan.kazil@zmaw.de

R.G. Harrison

Department of Meteorology, University of Reading, Earley Gate, PO Box 243, Reading, RG6 6BB, UK
e-mail: r.g.harrison@reading.ac.uk

E.R. Lovejoy

NOAA Earth System Research Laboratory, Chemical Sciences Division, 325 Broadway, R/CSD2,
Boulder, CO 80305-3337, USA
e-mail: edward.r.lovejoy@noaa.gov

1 Introduction

The continuous formation of charged particles in the atmosphere has been recognized since the late nineteenth century. These particles were identified as ions following studies on radioactivity and electrical conduction in gases (see Aplin et al. 2008). In early laboratory experiments, Wilson (1897, 1899) reported ion and particle formation in air and other gases in the presence of ultraviolet radiation and radioactive sources, and was the first to suggest that ions may be involved in atmospheric particle formation, and to realize the importance this could have for clouds (Galison 1997). Particle formation from the gas phase requires the emergence of molecular clusters of a size at which the condensation of further molecules is more likely than their evaporation, a process referred to as nucleation. Molecular clusters forming around ions are more stable compared to their neutral counterparts; ions can therefore trigger nucleation in conditions where neutral molecules would not. In the twentieth century, laboratory studies have confirmed Wilson's initial experiments (e.g. Bricard et al. 1968; Vohra et al. 1969; Raes and Janssens 1985), but research on atmospheric particle formation from ions has intensified only in the dawn of the twenty-first century with the heightened awareness of the relevance of new particle formation from the gas phase, which can significantly increase concentrations of aerosol particles and cloud condensation nuclei in the troposphere (Kulmala et al. 2004a), and thereby establishes a connection between atmospheric chemical composition, aerosols, clouds, and climate. Interest for the topic was also fueled by the possibility that the solar cycle modulation of atmospheric ionization through galactic cosmic rays could give rise to a similar modulation in aerosol and cloud droplet concentrations, and provide a mechanism to explain reported correlations between the decadal solar cycle and tropospheric observables, such as cloud cover (Svensmark and Friis-Christensen 1997; Marsh and Svensmark 2000; Carslaw et al. 2002; Harrison and Carslaw 2003).

2 Tropospheric Aerosol

Tropospheric aerosol particles are either emitted from the surface of the Earth, or form from the gas phase. Transport of aerosol particles from the stratosphere represents only a minor contribution to tropospheric aerosol. Major surface sources of aerosol particles include the oceans, which emit sea-salt particles, arid and semi-arid regions, where wind lifts mineral dust, and volcanoes, which inject particulate sulfate and ash into the atmosphere, while carbonaceous aerosols are produced by wildfires and by the combustion of fossil and biomass fuels. The formation of new aerosol particles from the gas phase requires sufficiently high concentrations of gas phase molecules with low saturation vapor pressure: for example, sulfuric acid which has a very low saturation vapor pressure in atmospheric conditions has been frequently reported as component of freshly formed aerosol, and appears to drive new particle formation in clean areas, such as over oceans (Clarke 1992; Brock et al. 1995). Over continents and, in particular, within the continental boundary layer, recently nucleated aerosol particles may contain, in addition to sulfate, substantial amounts of ammonia (Smith et al. 2005) or organic compounds (Allan et al. 2006; Cavalli et al. 2006), which may be involved in their formation process (Coffman and Hegg 1995; Marti et al. 1997a; Ball et al. 1999; O'Dowd et al. 2002; Kulmala et al. 2004b; Zhang et al. 2004; Burkholder et al. 2007). Freshly nucleated particles measure a few nanometers in diameter, much less than aerosol particles emitted from surface sources. In order to participate in atmospherically relevant processes, nucleated particles need to grow

to sizes of tens of nanometers. Depending on the availability of condensable molecules, this process may proceed on time scales between minutes to days, and result finally in the formation of cloud condensation nuclei, particles which form cloud droplets. Kulmala et al. (2004a) found that nucleation from the gas phase may significantly increase concentrations of tropospheric cloud condensation nuclei. The resulting increase in cloud droplet concentrations may increase cloud albedo via the first (Twomey 1977) and cloud lifetime via the second indirect aerosol effect (Albrecht 1989). Pre-existing aerosol particles however quench the formation of new aerosol from the gas phase as they efficiently remove compounds which may initiate nucleation or contribute to particle growth, as well as the newly forming particles. The role played by gas phase particle formation in tropospheric processes therefore depends not only on the availability and distribution of nucleating and condensing compounds, but also on the presence, growth, transport, and removal of pre-existing particles. Similarly, the importance of charged nucleation in the troposphere depends not only on the availability of ions and molecules condensing on them, but also on the efficiency of competing neutral nucleation pathways.

3 Ionization, Galactic Cosmic Rays, and Clouds

Galactic cosmic rays (GCR) are a major source of ions in the troposphere (Bazilevskaya et al. 2008): upon entering the Earth atmosphere, primary cosmic ray particles, mostly hydrogen and helium nuclei, collide with atmospheric gas molecules and initiate a cascade of nuclear and electromagnetic reactions producing secondary cosmic rays. Due to the shape and orientation of the Earth's magnetic field, the GCR ionization rate increases from the magnetic equator towards the poles; its altitude profile has a peak in the upper troposphere/lower stratosphere. The GCR intensity and ionization rate are anti-correlated with the decadal solar cycle (Forbush 1954; Neher and Forbush 1958). A second important source of ionization in the troposphere is the radioactive decay of radon effusing from rocks and soils (Laakso et al. 2004b, and references therein). This source of ionization is strongest near the surface and in the boundary layer, and is not known to correlate with the solar cycle.

A mechanism linking galactic cosmic rays, aerosols and clouds was initially outlined by Dickinson (1975): sulfate aerosol particles forming from ions produced by GCR might grow to cloud condensation nuclei and eventually become cloud droplets. The variation of GCR ionization over the solar cycle would thus appear in cloud droplet concentrations and hence in cloud albedo via the first (Twomey 1977) and cloud lifetime via the second (Albrecht 1989) indirect aerosol effect. The result would be a solar cycle modulation of radiative forcing of the troposphere. A corresponding correlation was first reported by Svensmark and Friis-Christensen (1997), who found a 3–4% variation of the global cloud cover over a solar cycle based on data of the International Satellite Cloud Climatology Project (ISCCP) (Rossow and Schiffer 1991) for the years 1983–1992. Kristjánsson and Kristiansen (2000) pointed out that the correlation may be purely coincidental, as the ISCCP data showed a divergence of cloud cover and GCR intensity in the years 1991–1994, but concluded that global cloud fraction is higher by 0.0176 and radiative forcing reduced by 0.29 W m^{-2} at solar minimum 1986 compared with solar maximum 1990. Marsh and Svensmark (2000) confined the correlation to low clouds for the period 1983–1994. They estimated that global low cloud fraction is higher at solar minimum by 0.02 and radiative forcing reduced by 1.2 W m^{-2} compared with solar maximum. Kristjánsson et al. (2002, 2004) analyzed the revised ISCCP cloud dataset (Rossow and Schiffer 1999) for the period 1983–2001 and found a weak correlation between low cloud cover and GCR intensity. Harrison and Stephenson

(2006) found a small yet statistically significant effect of cosmic rays on daily regional cloudiness, based on surface radiation measurements. In a recent statistical analysis of the ISCCP data, Sloan and Wolfendale (2008) found only very limited support for a connection between the decadal variation in galactic cosmic ray ionization and low cloud cover.

4 Field Observations of New Particle Formation and Ions

Evidence for the involvement of ions in the nucleation of tropospheric aerosol particles includes observations of bursts of intermediate size ions followed by increases in ultrafine aerosol in the boundary layer (Hörrak et al. 1998), and direct observation of very large cluster ions in the upper troposphere (Eichkorn et al. 2002). Charged nucleation in the upper troposphere is also supported by the observations of Lee et al. (2003), who used results obtained with the laboratory data based model of Lovejoy et al. (2004) to explain the measured high ultrafine aerosol concentrations. Laakso et al. (2004a) and Laakso et al. (2007a) observed nucleation events in the boundary layer over the boreal forest and identified events when charged nucleation was contributing to particle formation by preferential growth of negatively charged clusters. However, during a large fraction of these events, neutral nucleation dominated particle formation, with a marginal contribution from charged nucleation. Similarly, Vana et al. (2006) identified negative molecular clusters as preferred condensation centers in particle formation events observed over the boreal forest. The contribution of charged nucleation appeared highest for comparatively weak particle formation events, while during strong particle formation events, the contribution of charged nucleation was reduced. Eisele et al. (2006) measured size and mobility distributions of charged molecular clusters and aerosol particles at a continental site, and found that while ions contributed to the formation of small charged sulfate clusters, charged nucleation did not play a significant role in aerosol production during these measurements. Laakso et al. (2007b) conducted a study of boundary layer ion and aerosol profiles over the boreal forest with a hot air balloon. These measurements showed a distinct asymmetry between the negative and positive aerosol size distribution, with concentrations of nanometer-sized negative particles exceeding those of corresponding positive particles throughout the mixed layer. This indicates charged nucleation in which negative ions played a significant role; however, neutral nucleation was found to contribute to the observed particle nucleation events as well. Calculations using the method of Kazil and Lovejoy (2007) showed that charged nucleation of sulfuric acid and water was not able to explain the observations alone, indicating a compound other than sulfuric acid stabilizing the negative clusters. Laakso et al. (2007b) proposed that this stabilizing component is an organic molecule.

The contribution of neutral nucleation to the particle formation events reported in the above studies may be driven by organic molecules (O'Dowd et al. 2002) or ammonia (Coffman and Hegg 1995), which are supported as nucleation agents by laboratory studies (Marti et al. 1997a; Ball et al. 1999; Zhang et al. 2004; Kulmala et al. 2006; Burkholder et al. 2007). On the other hand, several field campaigns at forested sites have found no indication for organic molecules participating in boundary layer aerosol nucleation: Marti et al. (1997b) and Sellegli et al. (2005) concluded the organic compounds play a role for condensational growth of aerosol particles, rather than in their nucleation. Similarly, Janson et al. (2001) found that organic molecules were not the nucleating species responsible for nucleation events in the boundary layer, but sulfuric acid and ammonia, while subsequent particle growth ought to have been due to condensation of organic compounds. A role of ammonia in aerosol nucleation is contended as well, as is discussed in the next section.

5 Laboratory Measurements

There has been a significant experimental effort aimed at understanding possible atmospheric nucleation mechanisms (see e.g. reviews by Laaksonen et al. 1995; Curtius 2006; O'Dowd and Wagner 2008). Here we focus our discussion on recent experimental work, and emphasize sulfuric acid-based schemes. Neutral nucleation of sulfuric acid and water has long been regarded as an important source of new particles in the atmosphere, largely due to in situ atmospheric H₂SO₄ production, extremely low H₂SO₄ vapor pressure in the presence of water, and optimistic predictions from classical nucleation theory (discussed in Sect. 6). In a seminal work, Wyslouzil et al. (1991) measured the nucleation rates of H₂SO₄ and H₂O as function of temperature, relative humidity, and H₂SO₄ concentration, and found a strong dependence on these variables. Ball et al. (1999) reported the nucleation rate as a function of the concentration of sulfuric acid for a range of relative humidities. A major achievement of this work was the direct measurement of sulfuric acid concentration within the nucleation reactor. Both experiments yielded nucleation rates that were significantly lower than predictions of classical nucleation theory.

Laboratory studies of atmospheric gas phase H₂SO₄ nucleation have advanced to study the individual elementary clustering reactions in recent years. The goal of these studies is to measure the thermochemical parameters (enthalpy and entropy change) of the step-wise cluster formation reactions, and use these data to develop kinetic models that accurately predict nucleation rates as a function of atmospheric conditions. Such experiments give valuable new insight into the elementary steps involved in particle formation, but are a significant undertaking for even simple binary systems because of the large number of reactions that need to be evaluated to accurately describe the kinetics of the system. However, accurate thermochemical parameters for even the initial few clustering reactions are extremely useful, and can strongly constrain nucleation rates. Clustering of the charged sulfuric acid/water system has received considerable experimental attention, because of the expected atmospheric relevance of sulfuric acid in new particle formation, and because ions are directly observable with mass spectrometry. Eisele and Hanson (2000) were the first to observe and resolve on the molecular scale the nucleation of charged sulfuric acid clusters from precursor ions. Curtius et al. (2001) and Lovejoy and Curtius (2001) measured the thermochemical parameters for sulfuric acid uptake and Froyd and Lovejoy (2003a, 2003b) the thermochemical parameters for water uptake by small neutral and charged sulfuric acid clusters. These experimental data constitute a matrix of thermochemical parameters describing charged nucleation of sulfuric acid and water. Similar experiments were conducted by Wilhelm et al. (2004) and Sorokin et al. (2006). These ion clustering thermochemical studies show that sulfuric acid has a stronger affinity for the hydrated negative ions than the positive ions, and hence the positive ions are less likely to grow in typical tropospheric conditions.

Hanson and Lovejoy (2006) measured the thermochemical parameters for the formation of the neutral hydrated dimer and trimer of sulfuric acid, averaged over the water contents of the particles. These thermochemical data strongly constrain the atmospheric relevance of this process, and show that classical nucleation theory overestimates the stability of the small neutral sulfuric acid/water clusters and the corresponding nucleation rates, consistent with the results of Wyslouzil et al. (1991) and Ball et al. (1999). While these results indicate that the neutral nucleation of H₂SO₄ and H₂O is inefficient in the lower troposphere, Hanson and Lovejoy (2006) show that this mechanism is potentially important in the cold upper troposphere, where it is likely to overwhelm the corresponding charged process.

Berndt et al. (2005) observed new particle formation in the sulfuric acid-water system at H₂SO₄ concentrations exceeding 10¹⁰ cm⁻³, generated by evaporation from a liquid sample,

similar to concentrations reported by Wyslouzil et al. (1991) and Ball et al. (1999). However, when the sulfuric acid was generated in the gas phase photochemically, Berndt et al. (2005) found that much lower H_2SO_4 concentrations, around 10^7 cm^{-3} , such as occurring in the atmosphere, were sufficient to initiate new particle formation. A possible explanation for the low threshold sulfuric acid concentrations and high particle formation rates when using photochemically produced sulfuric acid may be organic molecules used by Berndt et al. (2005) to determine the concentrations of gas phase OH and H_2SO_4 , which may have contributed to the formation of new particles. In a subsequent study, however, Berndt et al. (2006) investigated nucleation of H_2SO_4 and H_2O in the absence of organic compounds, and with H_2SO_4 forming in the gas phase with or without UV photochemistry. In this study, particle formation commenced at sulfuric acid concentrations around 10^7 cm^{-3} , indicating no significant role of the organic compounds used in the Berndt et al. (2005) work. At the same time, no significant differences between the experiments with H_2SO_4 produced in the gas phase with or without UV photochemistry were found, ruling against a possible contribution of charged nucleation due to UV-produced ions in the experiment. Neutral nucleation of sulfuric acid and water proceeding at the low concentrations of gas phase sulfuric acid observed by Berndt et al. (2005) and Berndt et al. (2006) would significantly abate a role of charged nucleation of these compounds in the troposphere.

While the results of Berndt et al. (2006) indicate that the organic compounds used do not promote the formation of $\text{H}_2\text{SO}_4/\text{H}_2\text{O}$ particles from the gas phase, other organic compounds may trigger or support nucleation of sulfate aerosol: Zhang et al. (2004) have observed enhanced formation of neutral sulfuric acid particles from the gas phase in the presence of aromatic organic acids in the laboratory. Based on theoretical work, they postulate that a strong aromatic acid- H_2SO_4 interaction facilitates nucleation.

The role of ammonia for sulfate aerosol formation has not been conclusively established yet: Kim et al. (1998) investigated particle formation from a $\text{NH}_3/\text{SO}_2/\text{H}_2\text{O}/\text{air}$ mixture in the presence of ionizing radiation, and observed enhanced particle concentrations in the presence of NH_3 , although the enhancement depended greatly on the SO_2 , NH_3 and H_2O concentrations. Particle formation was also found to proceed faster in the $\text{NH}_3/\text{SO}_2/\text{H}_2\text{O}/\text{air}$ mixture, with a lower contribution of charged nucleation compared to the $\text{SO}_2/\text{H}_2\text{O}/\text{air}$ mixture. However, charged nucleation was identified as a main mechanism at an early stage of particle generation in both mixtures. Ball et al. (1999) have shown a significant enhancement in the nucleation rate of the neutral $\text{NH}_3/\text{SO}_2/\text{H}_2\text{O}$ system relative to the neutral $\text{H}_2\text{SO}_4/\text{H}_2\text{O}$ system, while Anttila et al. (2005), Yu (2006b), and Kurtén et al. (2007) have found that ammonia may not be an effective nucleation agent. Laboratory measurements of the thermochemical parameters for selected steps of charged $\text{H}_2\text{SO}_4/\text{NH}_3/\text{H}_2\text{O}$ nucleation have been conducted by Froyd (2002).

6 Theory

Classically, the nucleation of neutral particles from the gas phase is described with the Kelvin–Thomson equation (Thomson 1906), which gives the Gibbs free energy ΔG_n released in the uptake of a gas phase molecule by a neutral, spherical liquid droplet:

$$\Delta G_n = -\frac{4}{3}\pi R^3 \frac{kT}{v} \ln S + 4\pi R^2 \sigma, \quad (1)$$

with the droplet radius R , its surface tension σ , and the supersaturation ratio S of the nucleating compound above a flat liquid surface with the composition of the droplet (see e.g.

Curtius 2006 and references therein). T is the temperature of the system, k the Boltzmann constant, and v the volume of the nucleating molecules. Note that adding a molecule is endothermic for radii smaller than a critical radius R^* , and exothermic for larger radii. The critical radius R^* and the Gibbs energy ΔG_n^* required to form a critical droplet can be determined by solving $\frac{\partial \Delta G_n}{\partial R} \doteq 0$. The classical nucleation rate in steady state may then be written (Volmer and Weber 1926) as

$$J = C \exp\left(-\frac{\Delta G_n^*}{kT}\right). \quad (2)$$

The factor C accommodates concentrations of condensable molecules and their reaction coefficients, and has been discussed by Farkas (1927) and Becker and Döring (1935) for a unary and by Reiss (1950) for a binary system. If the droplet is charged, then the uptake of a molecule from the gas phase changes the electric field energy of the charged droplet due to the increase in the volume occupied by a dielectric liquid. Thus for a charge that resides at the center of the droplet, the Gibbs free energy released by the uptake of a molecule is (in SI units)

$$\Delta G_c = \Delta G_n - \frac{q^2}{8\pi} \left(\frac{1}{\epsilon_0} - \frac{1}{\epsilon_1} \right) \left(\frac{1}{R} - \frac{1}{R + \Delta R} \right). \quad (3)$$

ϵ_0 and ϵ_1 are the permittivities of the gas and liquid phase, R and $R + \Delta R$ the radii of the liquid droplet before and after the uptake of the molecule, respectively. Commonly, $\epsilon_1 > \epsilon_0 > 1$ and $R + \Delta R > R > 0$, hence $\Delta G_c < \Delta G_n$, meaning that the charged droplet is more stable than the neutral droplet. Based on this formulation of classical nucleation theory, Yue and Chan (1979) investigated the formation of aerosols through the nucleation of a binary mixture of vapors and in the presence of ion sources, and derived analytical expressions for estimating the composition, radius R^* , and Gibbs energy of formation ΔG_c^* of critical droplets formed through the charged nucleation process.

Yu (2005) extended charged classical nucleation theory by accounting for the interaction between the droplet charge and the dipole moment of the condensing gas phase molecules. The charge–dipole interaction further reduces the Gibbs free energy for the uptake of gas phase molecules molecule and increases the stability of the charged droplet. Accounting for the charge–dipole interaction in the calculation of the entropies and enthalpies for the uptake of molecules by small charged molecular clusters improves the agreement with observations (Yu 2005).

However, the concept of a liquid droplet characterized by a bulk solution and a composition-dependent surface tension breaks down in the context of very small particles (diameters ~ 1 nm and less). Such small particles are better described as molecular clusters: in these, molecules arrange in a different spatial structure compared to molecules in a bulk liquid, resulting in different thermochemical parameters for the uptake and loss of gas phase molecules. As a consequence, classical nucleation theory overestimates the stability of very small particles and nucleation rates; in the case of neutral $\text{H}_2\text{SO}_4/\text{H}_2\text{O}$ clusters, classical steady state nucleation rates are significantly higher than nucleation rates inferred in laboratory measurements (Wyslouzil et al. 1991; Ball et al. 1999; Hanson and Lovejoy 2006). In addition, the structure of the molecular clusters and of the gas phase molecules (Nadykto et al. 2004), as well as the shape of their interaction potential (Langevin 1905; Chesnavich et al. 1980; Nadykto and Yu 2003) affect their collision rate coefficients. Finally, the assumptions of steady state, and of a negligible role of self-coagulation and coagulation with pre-existing aerosol in the formation of supercritical clusters used in classical nucleation theory need not be valid in all conditions. For these reasons, more sophisticated

approaches to aerosol nucleation, which account for the individual cluster–molecule reactions, the structure of the molecules and molecular clusters, and the interaction of subcritical and supercritical particles, have been developed. These approaches are typically not accessible by analytical methods but require numerical modeling, discussed in the next section.

7 Modeling

The most straightforward step beyond classical nucleation theory is the kinetic modeling of particle formation, i.e. as a process of repeated uptake (and loss) of gas phase molecules, with the reaction of two gas phase molecules forming a dimer as the initial step. The thermochemical parameters from the liquid drop model can be used to describe the individual steps, with the same limitations as discussed in the preceding section, except that here steady-state is not assumed, and self-coagulation of the subcritical particles, and their coagulation with pre-existing aerosol are accounted for. At the next level, the structure of the molecular clusters and gas phase molecules involved can be represented implicitly by using thermochemical parameters for the uptake and loss of the molecules from the gas phase by the clusters obtained from extensions of the liquid drop approach, ab initio calculations, or from laboratory measurements. The thermochemical parameters and the corresponding forward and reverse rate coefficients can be calculated based on different assumptions and treatments of the cluster-molecule interaction potential (Langevin 1905; Chesnavich et al. 1980; Su and Chesnavich 1982; Nadykto and Yu 2003; Lovejoy et al. 2004; Yu 2005; Yu 2007). The most widely investigated aerosol nucleation pathway via the clustering of sulfuric acid and water is commonly reduced to a system where only the uptake of sulfuric acid is resolved in individual steps, and uptake and loss of water is described in steady state. This treatment is considered valid in tropospheric conditions, where water vapor concentrations exceed the concentration of sulfuric acid by orders of magnitude, hence allowing sulfuric acid/water clusters to equilibrate with respect to water uptake and loss between individual sulfuric acid uptake/loss events.

In an early combined modeling/experimental study, Raes and Janssens (1985, 1986) investigated neutral and charged nucleation in a mixture of gaseous sulfuric acid and water, using a model of classical neutral and charged nucleation. They observed an increase in particle concentration upon exposure of the mixture to γ radiation, indicating the occurrence of charged nucleation, which could, however, be reproduced only in part in their simulations. Using the same model, Raes et al. (1986) investigated aerosol formation over oceans, and concluded that charged nucleation may be the only source of new aerosol particles forming from the gas phase over the oceans.

Turco et al. (1998) proposed and investigated, using their model of sulfuric acid/water aerosol, the recombination of oppositely charged molecular clusters as the process maintaining tropospheric background aerosol concentrations: this mechanism could produce supercritical aerosol particles in conditions which do not support the formation of such particles by charged (negative or positive) nucleation. Yu and Turco (2000) were able to explain observed ion mobility spectra as well as nucleation events and ultrafine particle concentrations at different sites with charged aerosol nucleation. In a subsequent study, Yu and Turco (2001) found that variations in ionization, e.g. from the modulation of GCR intensity by the solar cycle, are capable of causing a significant variation in aerosol production. Yu (2002) modeled the response of aerosol production to variations in GCR intensity during a solar cycle as a function of altitude. The results show a positive correlation of aerosol production and GCR intensity in the lower troposphere and a negative correlation in the upper

troposphere. In the middle troposphere, the aerosol production was insensitive to changes in the ionization. These findings are consistent with the GCR-cloud correlation of Marsh and Svensmark (2000), apparent for low tropospheric clouds.

Laakso et al. (2002) developed a model of neutral, negative, and positive $\text{H}_2\text{SO}_4/\text{H}_2\text{O}$ aerosol which accounts, above a certain size, for multiply charged particles. One interesting result of this work is that final particle concentrations are very similar independent of whether both negative and positive particles (symmetric case) nucleate and grow, or only negative particles (asymmetric case). In the asymmetric case, however, the size distributions of positive and negative particles differ during nucleation, a fact which may be exploited experimentally to identify the nucleation pathway. Kerminen et al. (2007) investigated this idea in detail and developed an approach for the assessment of the contribution of neutral and charged nucleation to a particle formation event.

The modeling approaches discussed so far employed thermochemical parameters for the formation of neutral and charged molecular clusters that were derived from classical nucleation theory. Lovejoy et al. (2004) developed a detailed aerosol model of neutral and negative $\text{H}_2\text{SO}_4/\text{H}_2\text{O}$ aerosol particles. Small neutral and negative $\text{H}_2\text{SO}_4/\text{H}_2\text{O}$ clusters are resolved individually, and larger particles with geometric bins. Laboratory thermochemical parameters measured by Curtius et al. (2001) and Froyd and Lovejoy (2003b) for the small negative $\text{H}_2\text{SO}_4/\text{H}_2\text{O}$ clusters were used. Thermochemical parameters for small neutral $\text{H}_2\text{SO}_4/\text{H}_2\text{O}$ clusters were obtained from the liquid drop model, adjusted to reproduce the laboratory measurements of Ball et al. (1999). Positive particles were represented summarily by a positive molecular cluster of a given mass. The thermodynamic data for large aerosol particles were derived from H_2SO_4 and H_2O vapor pressures over bulk solutions, and from the liquid drop model. Thermodynamic data for intermediate size particles were obtained by smoothly interpolating the data for the small and large particles. The model predicts that charged nucleation of H_2SO_4 and H_2O proceeds efficiently in the middle and upper troposphere, and explained nucleation events observed in the remote middle troposphere with the charged $\text{H}_2\text{SO}_4/\text{H}_2\text{O}$ mechanism, but not generally nucleation events observed in the boundary layer (Lovejoy et al. 2004). The model also correctly reproduced measurements of subcritical charged $\text{H}_2\text{SO}_4/\text{H}_2\text{O}$ clusters and the simultaneous absence of their growth to larger sizes in the boundary layer at a continental site (Eisele et al. 2006), confirming that charged nucleation of these compounds was not responsible for the observed particle formation events.

Kazil and Lovejoy (2004) applied the Lovejoy et al. (2004) model to the conditions studied by Yu (2002) and investigated the response of aerosol formation to changes in the ionization rate, such as resulting from the modulation of the GCR intensity by the decadal solar cycle. They obtained a positive correlation of aerosol formation and ionization throughout the troposphere in the adopted conditions. Still, depending on conditions, either a negative or a positive correlation of the nucleation and ionization rates was shown to be possible, which was explained as follows: an increase in the ionization rate enhances nucleation when growth of subcritical charged clusters exceeds their loss by recombination, and reduces nucleation in the opposite case.

Yu (2007) developed a detailed model of positive, negative, and neutral $\text{H}_2\text{SO}_4/\text{H}_2\text{O}$ aerosol particles, forming by neutral and charged nucleation of sulfuric acid and water, and growing by uptake of these compounds as well as by condensation of organic molecules. The role of the charge for the composition of small $\text{H}_2\text{SO}_4/\text{H}_2\text{O}$ clusters is accounted for in detail. The model resolves the small $\text{H}_2\text{SO}_4/\text{H}_2\text{O}$ clusters individually, and larger particles with geometric bins. The thermochemical parameters for the uptake/loss of sulfuric acid are implemented via the evaporation rate coefficients: For the neutral $\text{H}_2\text{SO}_4/\text{H}_2\text{O}$ clusters, H_2SO_4 evaporation rate coefficients are calculated after Yu (2006a); for the positive and

negative clusters, the effect of the charge and of the charge-dipole interaction (Yu 2005) on the evaporation rate coefficients are accounted for. The model predicts that charged nucleation can lead to significant new particle formation in the lower atmosphere due to charged nucleation of sulfuric acid and water, supporting a more general role of ions in aerosol nucleation in the boundary layer than indicated by the simulations of Lovejoy et al. (2004). This vigorous particle formation can be possibly traced to the size-resolved treatment of positive clusters in the model, which could extend negative cluster lifetimes, or to the adopted thermochemical parameters.

Kazil et al. (2006) operated the Lovejoy et al. (2004) model on long term average ambient conditions and composition data in the troposphere over the oceans, obtained from reanalysis and chemical transport model runs. These simulations predict negligible charged and neutral nucleation of H_2SO_4 and H_2O in the tropical lower troposphere, even in the absence of pre-existing aerosol. At mid-latitudes, charged nucleation would proceed efficiently, provided that pre-existing aerosol particles are depleted e.g. by precipitation, and exceed neutral nucleation. The simulations also show very efficient charged nucleation in the tropical upper troposphere up to the highest considered model level. At higher altitudes, however, neutral nucleation is likely to dominate (Hanson and Lovejoy 2006). Using correlations between aerosol concentrations and cloud properties derived from satellite observations, Kazil et al. (2006) estimated that the difference in daily mean shortwave radiative forcing between solar maximum and minimum due to the response of cloud cover and albedo to the difference in charged aerosol nucleation in the lower troposphere falls short of the difference of absorbed solar irradiance between solar maximum and minimum of 0.24 W m^{-2} due to the concurrent variation in solar radiative output. This upper limit estimate is much smaller than the difference in radiative forcing of 1.2 W m^{-2} between solar maximum and minimum given by Marsh and Svensmark (2000) due to the variation of low cloud cover based on ISCCP data (Rossow and Schiffer 1999) for the period 1983–1994, but close to the value of Kristjánsson and Kristiansen (2000), who found, based on the same cloud data, that radiative forcing was reduced by 0.29 W m^{-2} at solar minimum 1986 compared with solar maximum 1990.

Most recently, Yu et al. (2008) conducted a global study of charged nucleation of H_2SO_4 and H_2O in a chemical transport model, using nucleation rates calculated with the model of Yu (2007). The resulting nucleation rates compare favorably with a comprehensive dataset of new aerosol formation events, showing agreement in the spatial distribution and strength in aerosol nucleation: At mid-latitudes, in the northern hemisphere, and in particular over continents, lower tropospheric nucleation rates are significantly stronger compared with tropical latitudes, the southern hemisphere, and oceans, respectively. Charged nucleation is also shown to proceed very efficiently in the tropical upper troposphere. A comparison of the simulated nucleation rates with primary particle emissions rates positions charged nucleation as a significant source of aerosol on a global scale, possibly explaining many observed new particle formation events.

8 Summary and Outlook

Groundbreaking studies have cleared some of the fog blurring our understanding of particle formation from the gas phase in the atmosphere and the role of ions therein: Laboratory studies have identified neutral and charged nucleation of sulfuric acid and water as efficient processes for new particle formation from the gas phase in favorable conditions, placed corresponding model simulations on a dependable footing, and helped understanding the relative importance of these processes in the atmosphere. Neutral nucleation of sulfuric acid

and water appears more efficient than charged nucleation of these compounds in the cold upper troposphere, although charged nucleation has been found to proceed in this atmospheric region as well. In the middle and lower troposphere, neutral nucleation of sulfuric acid and water is likely to be negligible. Field observations indicate that while both neutral and charged nucleation proceed in these regions, in the continental boundary layer, where most field studies have been performed, neutral nucleation is more frequent and efficient, and involves chemical compounds beyond sulfuric acid and water. On the other hand, charged nucleation of sulfuric acid and water has been found to explain the observed nucleation events in modeling studies, depending on the implementation of the nucleation process and the thermochemical data used. However, models agree that variations in ionization such as occurring in the course of the decadal solar cycle have a considerable effect on the charged nucleation rate, although no uncontested effect on concentrations of cloud condensation nuclei or on clouds themselves has been found. Possible explanations are that charged nucleation may also arise from ionization due to decay of radon, which does not vary with the solar cycle, and has to compete with neutral nucleation mechanisms and surface aerosol emissions.

In order to quantify the contribution of ions to atmospheric aerosol nucleation and identify the conditions in which charged nucleation matters as well as their spatial distribution, both charged and neutral nucleation processes need to be understood. Conflicting research results complicate the task: The species involved in neutral nucleation in addition to sulfuric acid are thought to be organic molecules and ammonia, but theoretical, field, and laboratory studies have come to contrasting findings on the role of these compounds. An additional complication arises from the possibility that these compounds may be involved in charged nucleation as well. The questions surrounding the relevance of ions for atmospheric nucleation are therefore far from settled, and numerous research challenges await their solution: Methods for the determination of the composition of small clusters observed in the atmosphere need to be improved and corresponding field studies conducted to identify the compounds involved in aerosol nucleation. Laboratory and ab initio studies on the structure and thermochemical parameters for the formation of small neutral and charged molecular clusters, in particular those containing sulfuric acid, ammonia, and water, as well as organic molecules, are needed to understand the relative contributions of neutral and charged nucleation to new particle formation, and to improve the representation of aerosol nucleation in atmospheric models. Such representations will have to be able to simultaneously accommodate different nucleation pathways. They must be computationally efficient on the one hand, but reproduce results obtained with a detailed model with sufficient precision on the other. At the same time, the sensitivity of processes in atmospheric models to aerosol nucleation needs to be investigated: Aerosol nucleation competes against aerosol emissions from the surface, and changes in the nucleation rate need not to translate into similar changes in aerosol and cloud condensation nuclei concentrations, or cloud properties. However, a limited sensitivity of atmospheric models to nucleation rates changes needs not necessarily imply an insensitivity of the actual atmosphere to aerosol nucleation or to changes thereof. These steps will bring us closer to understanding aerosol nucleation in the atmosphere and the contribution of ions, as well as the possible links between solar variability and the troposphere.

Acknowledgements We thank D. O'Donnell (Max Planck Institute for Meteorology) for helpful comments, and two anonymous referees for their thoughtful review of this manuscript.

References

- B.A. Albrecht, Aerosols, cloud microphysics and fractional cloudiness. *Science* **245**, 1227–1230 (1989)
- J.D. Allan, M.R. Alfarra, K.N. Bower, H. Coe, J.T. Jayne, D.R. Worsnop, P.P. Aalto, M. Kulmala, T. Hyötyläinen, F. Cavalli, A. Laaksonen, Size and composition measurements of background aerosol and new particle growth in a Finnish forest during QUEST 2 using an Aerodyne Aerosol Mass Spectrometer. *Atmos. Chem. Phys.* **6**, 315–327 (2006)
- T. Anttila, H. Vehkämäki, I. Napari, M. Kulmala, Effect of ammonium bisulphate formation on atmospheric water-sulphuric acid ammonia nucleation. *Boreal Environ. Res.* **10**, 511–523 (2005)
- K.L. Aplin, R.G. Harrison, M.J. Rycroft, Investigation of Earth's atmospheric electricity: a role model for planetary studies, *Space Sci. Rev.* (2008, this issue)
- S.M. Ball, D.R. Hanson, F.L. Eisele, P.H. McMurry, Laboratory studies of particle nucleation: Initial results for H_2SO_4 , H_2O , and NH_3 vapors. *J. Geophys. Res.* **104**, 23 709–23 718 (1999)
- G.A. Bazilevskaya, I.G. Usoskin, E. Flückiger, R.G. Harrison, L. Desorgher, R. Bütkofer, M.B. Krainev, V.S. Makhmutov, Y.I. Stozhkov, A.K. Svirzhevskaya, N.S. Svirzhevsky, G.A. Kovaltsov, Cosmic ray induced ion production in the atmosphere. *Space Sci. Rev.* (2008, this issue) doi:[10.1007/s11214-008-9339-y](https://doi.org/10.1007/s11214-008-9339-y)
- R. Becker, W. Döring, Kinetische Behandlung der Keimbildung in übersättigten Dämpfen. *Ann. d. Phys.* **416**, 719–752 (1935)
- T. Berndt, O. Böge, F. Stratmann, J. Heintzenberg, M. Kulmala, Rapid formation of sulfuric acid particles at near-atmospheric conditions. *Science* **307**, 698–700 (2005)
- T. Berndt, O. Böge, F. Stratmann, Formation of atmospheric $\text{H}_2\text{SO}_4/\text{H}_2\text{O}$ particles in the absence of organics: A laboratory study. *Geophys. Res. Lett.* **33**, L15817 (2006)
- J. Bricard, F. Billard, G. Madelaine, Formation and evolution of nuclei of condensation that appear in air initially free of aerosols. *J. Geophys. Res.* **73**, 4487–4496 (1968)
- C.A. Brock, P. Hamill, J.C. Wilson, H.H. Jonsson, K.R. Chan, Particle formation in the upper tropical troposphere: a source of nuclei for the stratospheric aerosol. *Science* **270**, 1650–1653 (1995)
- J.B. Burkholder, T. Baynard, A.R. Ravishankara, E.R. Lovejoy, Particle nucleation following the O_3 and OH initiated oxidation of α -pinene and β -pinene between 278 and 320 K. *J. Geophys. Res.* **112**, 10216 (2007)
- K.S. Carslaw, R.G. Harrison, J. Kirkby, Cosmic rays, clouds, and climate. *Science* **298**, 1732–1737 (2002)
- F. Cavalli, M.C. Facchini, S. Decesari, L. Emblico, M. Mircea, N.R. Jensen, S. Fuzzi, Size-segregated aerosol chemical composition at a boreal site in southern Finland, during the QUEST project. *Atmos. Chem. Phys.* **6**, 993–1002 (2006)
- W.J. Chesnavich, T. Su, M.T. Bowers, Collisions in a noncentral field: A variational and trajectory investigation of ion-dipole capture. *J. Chem. Phys.* **72**, 2641–2655 (1980)
- A.D. Clarke, Atmospheric nuclei in the remote free-troposphere. *J. Atmos. Chem.* **14**, 479–488 (1992)
- D.J. Coffman, D.A. Hegg, A preliminary study of the effect of ammonia on particle nucleation in the marine boundary layer. *J. Geophys. Res.* **100**, 7147–7160 (1995)
- J. Curtius, Nucleation of atmospheric aerosol particles. *C.R. Phys.* **7**, 1027–1045 (2006)
- J. Curtius, K.D. Froyd, E.R. Lovejoy, Cluster ion thermal decomposition (I): Experimental kinetics study and ab initio calculations for $\text{HSO}_4^-(\text{H}_2\text{SO}_4)_x(\text{HNO}_3)_y$. *J. Phys. Chem. A* **105**, 10867–10873 (2001)
- R.E. Dickinson, Solar variability and the lower atmosphere. *Bull. Am. Meteorol. Soc.* **56**, 1240–1248 (1975)
- S. Eichhorn, S. Wilhelm, H. Aufmhoff, K.H. Wohlfrom, F. Arnold, Cosmic ray-induced aerosol-formation: First observational evidence from aircraft-based ion mass spectrometer measurements in the upper troposphere. *Geophys. Res. Lett.* **29** (2002)
- F.L. Eisele, D.R. Hanson, First measurement of prenucleation molecular clusters. *J. Phys. Chem. A* **104**, 830–836 (2000)
- F.L. Eisele, E.R. Lovejoy, E. Kosciuch, K.F. Moore, R.L. Mauldin III, J.-N. Smith, P.H. McMurry, K. Iida, Negative atmospheric ions and their potential role in ion-induced nucleation. *J. Geophys. Res.* **111**, D043053 (2006)
- L. Farkas, Keimbildungsgeschwindigkeit in übersättigten Dämpfen. *Z. Phys. Chem.* **125**, 236–242 (1927)
- S.E. Forbush, Worldwide cosmic ray variations, 1937–1952. *J. Geophys. Res.* **59**, 525–542 (1954)
- K.D. Froyd, Ion induced nucleation in the atmosphere: Studies of NH_3 , H_2SO_4 , and H_2O cluster ions. Ph.D. thesis, University of Colorado at Boulder, 2002
- K.D. Froyd, E.R. Lovejoy, Experimental thermodynamics of cluster ions composed of H_2SO_4 and H_2O . 1. Positive Ions. *J. Phys. Chem. A* **107**, 9800–9811 (2003a)
- K.D. Froyd, E.R. Lovejoy, Experimental thermodynamics of cluster ions composed of H_2SO_4 and H_2O . 2. Measurements and ab initio structures of negative ions. *J. Phys. Chem. A* **107**, 9812–9824 (2003b)
- P.L. Galison, *Image and Logic: A Material Culture of Microphysics* (University of Chicago Press, Chicago, 1997)

- D.R. Hanson, E.R. Lovejoy, Measurement of the thermodynamics of the hydrated dimer and trimer of sulfuric acid. *J. Phys. Chem. A* **110**, 9525–9528 (2006)
- R.G. Harrison, K.S. Carslaw, Ion-aerosol-cloud processes in the lower atmosphere. *Rev. Geophys.* **41** (2–1)–(2–26), (2003)
- R.G. Harrison, D.B. Stephenson, Empirical evidence for a nonlinear effect of galactic cosmic rays on clouds. *Proc. R. Soc. A* **462**, 1221–1233 (2006)
- U. Hõrrak, J. Salm, H. Tammet, Bursts of intermediate ions in atmospheric air. *J. Geophys. Res.* **103**, 13909–13916 (1998)
- R. Janson, H.-C. Rosman, K. Karlsson, A. Hansson, Biogenic emissions and gaseous precursors to forest aerosols. *Tellus B* **53**(4), 423–440 (2001)
- J. Kazil, E.R. Lovejoy, Tropospheric ionization and aerosol production: A model study. *J. Geophys. Res.* **109**, D19206 (2004)
- J. Kazil, E.R. Lovejoy, A semi-analytical method for calculating rates of new sulfate aerosol formation from the gas phase. *Atmos. Chem. Phys.* **7**, 3447–3459 (2007)
- J. Kazil, E.R. Lovejoy, M.C. Barth, K. O'Brien, Aerosol nucleation over oceans and the role of galactic cosmic rays. *Atmos. Chem. Phys.* **6**, 4905–4924 (2006)
- V.-M. Kerminen, T. Anttila, T. Petäjä, L. Laakso, S. Gagné, K.E.J. Lehtinen, M. Kulmala, Charging state of the atmospheric nucleation mode: Implications for separating neutral and ion-induced nucleation. *J. Geophys. Res.* **112**, D21205 (2007)
- T.O. Kim, T. Ishida, M. Adachi, K. Okuyama, J.H. Seinfeld, Nanometer-sized particle formation from $\text{NH}_3/\text{SO}_2/\text{H}_2\text{O}/\text{Air}$ mixtures by ionizing irradiation. *Aer. Sci. Tech.* **29**, 111–125 (1998)
- J.E. Kristjánsson, J. Kristiansen, Is there a cosmic ray signal in recent variations in global cloudiness and cloud radiative forcing? *J. Geophys. Res.* **105**, 11851–11864 (2000)
- J.E. Kristjánsson, A. Staple, J. Kristiansen, E. Kaas, A new look at possible connections between solar activity, clouds and climate. *Geophys. Res. Lett.* **29**, 22–1 (2002)
- J.E. Kristjánsson, J. Kristiansen, E. Kaas, Solar activity, cosmic rays, clouds and climate – an update. *Adv. Space Res.* **34**, 407–415 (2004)
- M. Kulmala, H. Vehkämäki, T. Petäjä, M. Dal Maso, A. Lauri, V.-M. Kerminen, W. Birmili, P.H. McMurry, Formation and growth rates of ultrafine atmospheric particles: A review of observations. *J. Aer. Sci.* **35**, 143–176 (2004a)
- M. Kulmala, V.-M. Kerminen, T. Anttila, A. Laaksonen, C.D. O'Dowd, Organic aerosol formation via sulphate cluster activation. *J. Geophys. Res.* **109**, D4205 (2004b)
- M. Kulmala, A. Reissell, M. Sipilä, B. Bonn, T.M. Ruuskanen, K.E.J. Lehtinen, V.-M. Kerminen, J. Ström, Deep convective clouds as aerosol production engines: Role of insoluble organics. *J. Geophys. Res.* **111**, 17202 (2006)
- T. Kurtén, M. Noppel, H. Vehkämäki, M. Salonen, M. Kulmala, Quantum chemical studies of hydrate formation of H_2SO_4 and HSO_4^- . *Boreal Environ. Res.* **12**, 431–453 (2007)
- L. Laakso, J.M. Mäkelä, L. Pirjola, M. Kulmala, Model studies on ion-induced nucleation in the atmosphere. *J. Geophys. Res.* **107**, 4427 (2002)
- L. Laakso, T. Anttila, K.E.J. Lehtinen, P.P. Aalto, M. Kulmala, U. Hõrrak, J. Paatero, M. Hanke, F. Arnold, Kinetic nucleation and ions in boreal forest particle formation events. *Atmos. Chem. Phys.* **4**, 2353–2366 (2004a)
- L. Laakso, T. Petäjä, K.E.J. Lehtinen, M. Kulmala, J. Paatero, U. Hõrrak, H. Tammet, J. Joutsensaari, Ion production rate in a boreal forest based on ion, particle and radiation measurements. *Atmos. Chem. Phys.* **4**, 1933–1943 (2004b)
- L. Laakso, S. Gagné, T. Petäjä, A. Hirsikko, P.P. Aalto, M. Kulmala, V.-M. Kerminen, Detecting charging state of ultra-fine particles: instrumental development and ambient measurements. *Atmos. Chem. Phys.* **7**, 1333–1345 (2007a)
- L. Laakso, T. Grönholm, L. Kulmala, S. Haapanala, A. Hirsikko, E.R. Lovejoy, J. Kazil, T. Kurtén, M. Boy, E.D. Nilsson, A. Sogachev, I. Riipinen, F. Stratmann, M. Kulmala, Hot-air balloon as a platform for boundary layer profile measurements during particle formation. *Boreal Environ. Res.* **12**, 279–294 (2007b)
- A. Laaksonen, V. Talanquer, D.W. Oxtoby, Nucleation: Measurements, theory, and atmospheric applications. *Annu. Rev. Phys. Chem.* **46**, 489–524 (1995)
- P.M. Langevin, Une formule fondamentale de théorie cinétique. *Ann. Chim. Phys.* **8**, 245–288 (1905)
- S.-H. Lee, J.M. Reeves, J.C. Wilson, D.E. Hunton, A.A. Viggiano, T.M. Miller, J.O. Ballenthin, L.R. Lait, Particle formation by ion nucleation in the upper troposphere and lower stratosphere. *Science* **301**, 1886–1889 (2003)
- E. Lovejoy, J. Curtius, Cluster ion thermal decomposition (II): Master equation modeling in the low pressure limit and fall-off regions. Bond energies for $\text{HSO}_4^- (\text{H}_2\text{SO}_4)_x (\text{HNO}_3)_y$. *J. Phys. Chem. A* **105**, 10874–10883 (2001)

- E.R. Lovejoy, J. Curtius, K.D. Froyd, Atmospheric ion-induced nucleation of sulfuric acid and water. *J. Geophys. Res.* **109**, D08204 (2004)
- N. Marsh, H. Svensmark, Cosmic rays, clouds, and climate. *Space Sci. Rev.* **94**, 215–230 (2000)
- J.J. Marti, A. Jefferson, X. Ping Cai, C. Richert, P.H. McMurry, F. Eisele, H_2SO_4 vapor pressure of sulfuric acid and ammonium sulfate solutions. *J. Geophys. Res.* **102**, 3725–3736 (1997a)
- J.J. Marti, R.J. Weber, P.H. McMurry, F. Eisele, D. Tanner, A. Jefferson, New particle formation at a remote continental site: Assessing the contributions of SO_2 and organic precursors. *J. Geophys. Res.* **102**, 6331–6340 (1997b)
- A.B. Nadykto, Yu, Uptake of neutral polar vapor molecules by charged clusters/particles: Enhancement due to dipole-charge interactions. *J. Geophys. Res.* **108**, 4717 (2003)
- A.B. Nadykto, A. Al Natsheh, F. Yu, K.V. Mikkelsen, R. J., Effect of molecular structure and hydration on the uptake of gas-phase sulfuric acid by charged clusters/ultrafine particles. *Aer. Sci. Tech.* **38**, 349–353 (2004)
- H.V. Neher, S.E. Forbush, Correlation of cosmic ray-intensity and solar activity. *Phys. Rev. Lett.* **1**, 173–174 (1958)
- P.A. O'Dowd, K. Hämeri, M. Kulmala, T. Hoffmann, Atmospheric particles from organic vapours. *Nature* **416**, 497–498 (2002)
- C. O'Dowd, P. Wagner, *Nucleation and Atmospheric Aerosols* (Springer, Berlin, 2008)
- F. Raes, A. Janssens, Ion-induced aerosol formation in a $\text{H}_2\text{O}-\text{H}_2\text{SO}_4$ system—I. Extension of the classical theory and search for experimental evidence. *J. Aer. Sci.* **16**, 217–227 (1985)
- F. Raes, A. Janssens, Ion-induced aerosol formation in a $\text{H}_2\text{O}-\text{H}_2\text{SO}_4$ system—II. Numerical-calculations and conclusions. *J. Aer. Sci.* **17**, 715–722 (1986)
- F. Raes, A. Janssens, R. van Dingenen, The role of ion-induced aerosol formation in the lower atmosphere. *J. Aer. Sci.* **17**, 466–470 (1986)
- H. Reiss, The kinetics of phase transitions in binary systems. *J. Chem. Phys.* **18**, 840–848 (1950)
- W.B. Rossow, R.A. Schiffer, ISCCP Cloud data products. *Bull. Am. Meteorol. Soc.* **72**, 2–20 (1991)
- W.B. Rossow, R.A. Schiffer, Advances in understanding clouds from ISCCP. *Bull. Am. Meteorol. Soc.* **80**, 2261–2287 (1999)
- K. Sellegri, M. Hanke, B. Umann, F. Arnold, M. Kulmala, Measurements of organic gases during aerosol formation events in the boreal forest atmosphere during QUEST. *Atmos. Chem. Phys.* **5**, 373–384 (2005)
- T. Sloan, A.W. Wolfendale, Testing the proposed causal link between cosmic rays and cloud cover. *Env. Res. Lett.* **3**, 024001 (2008)
- J.N. Smith, K.F. Moore, F.L. Eisele, D. Voisin, A.K. Ghimire, H. Sakurai, P.H. McMurry, Chemical composition of atmospheric nanoparticles during nucleation events in Atlanta. *J. Geophys. Res.* **110**, D22S03 (2005)
- A. Sorokin, F. Arnold, D. Wiedner, Formation and growth of sulfuric acid-water cluster ions: Experiments, modelling, and implications for ion-induced aerosol formation. *Atmos. Env.* **40**, 2030–2045 (2006)
- T. Su, W.J. Chesnavich, Parametrization of the ion-polar molecule collision rate constant by trajectory calculations. *J. Chem. Phys.* **76**, 5183–5185 (1982)
- H. Svensmark, E. Friis-Christensen, Variation of cosmic ray flux and global cloud coverage—a missing link in solar-climate relationships. *J. Atmos. Terr. Phys.* **59**, 1225–1232 (1997)
- J.J. Thomson, *Conduction of Electricity through Gases* (Cambridge University Press, Cambridge, 1906)
- R.P. Turco, J.-X. Zhao, F. Yu, A new source of tropospheric aerosols: Ion-ion recombination. *Geophys. Res. Lett.* **25**, 635–638 (1998)
- S.A. Twomey, The influence of pollution on the shortwave albedo of clouds. *J. Atmos. Sci.* **34**, 1148–1152 (1977)
- M. Vana, E. Tamm, U. Hörrak, A. Mirme, H. Tammet, L. Laakso, P.P. Aalto, M. Kulmala, Charging state of atmospheric nanoparticles during the nucleation burst events. *Atmos. Res.* **82**, 536–546 (2006)
- K.G. Vohra, M.C. Subba Ramu, K.N. Vasudevan, Behavior of aerosols formed by clustering of molecules around gaseous ions. *Atmos. Env.* **3**, 99–105 (1969)
- M. Volmer, A. Weber, Keimbildung in übersättigten Gebilden. *Z. Phys. Chem.* **119**, 277–301 (1926)
- S. Wilhelm, S. Eichkorn, D. Wiedner, L. Pirjola, F. Arnold, Ion-induced aerosol formation: New insights from laboratory measurements of mixed cluster ions $\text{HSO}_4^- (\text{H}_2\text{SO}_4)_a (\text{H}_2\text{O})_w$ and $\text{H}^+ (\text{H}_2\text{SO}_4)_a (\text{H}_2\text{O})_w$. *Atmos. Env.* **38**, 1735–1744 (2004)
- C.T.R. Wilson, Condensation of water vapour in the presence of dust-free air and other gases. *Phil. Trans. R. Soc. of London A* **189**, 265–307 (1897)
- C.T.R. Wilson, On the condensation nuclei produced in gases by the action of Röntgen rays, uranium rays, ultra-violet light, and other agents. *Phil. Trans. R. Soc. of London A* **192**, 403–453 (1899)
- B.E. Wyslouzil, J.H. Seinfeld, R.C. Flagan, K. Okuyama, Binary nucleation in acid-water systems. II. Sulfuric acid-water and a comparison with methanesulfonic acid-water. *J. Chem. Phys.* **94**, 6842–6850 (1991)

- F. Yu, Altitude variations of cosmic ray induced production of aerosols: Implications for global cloudiness and climate, *J. Geophys. Res.* **107** (2002)
- F. Yu, Modified Kelvin-Thomson equation considering ion-dipole interaction: Comparison with observed ion-clustering enthalpies and entropies, *J. Chem. Phys.* **122**, 084503 (2005)
- F. Yu, Binary H₂SO₄-H₂O homogeneous nucleation based on kinetic quasi-unary nucleation model: Look-up tables, *J. Geophys. Res.* **111**, D04201 (2006a)
- F. Yu, Effect of ammonia on new particle formation: A kinetic H₂SO₄-H₂O-NH₃ nucleation model constrained by laboratory measurements, *J. Geophys. Res.* **111** (2006b)
- F. Yu, From molecular clusters to nanoparticles: second-generation ion-mediated nucleation model, *Atmos. Chem. Phys.* **6**, 5193–5211 (2007)
- F. Yu, R.P. Turco, Ultrafine aerosol formation via ion-mediated nucleation, *Geophys. Res. Lett.* **27**, 883–886 (2000)
- F. Yu, R.P. Turco, From molecular clusters to nanoparticles: Role of ambient ionization in tropospheric aerosol formation, *J. Geophys. Res.* **106**, 4797–4814 (2001)
- F. Yu, Z. Wang, G. Luo, R. Turco, Ion-mediated nucleation as an important global source of tropospheric aerosols, *Atmos. Chem. Phys.* **8**, 2537–2554 (2008)
- G.K. Yue, L.Y. Chan, Theory of the formation of aerosols of volatile binary-solutions through the ion-induced nucleation process, *J. Coll. Int. Sc.* **68**, 501–507 (1979)
- R. Zhang, I. Suh, J. Zhao, D. Zhang, E.C. Fortner, X. Tie, L.T. Molina, M.J. Molina, Atmospheric new particle formation enhanced by organic acids, *Science* **304**, 1487–1490 (2004)

Measurements Effects and Hazards of Thunderstorms and Lightning

Ground-Based and Space-Based Radio Observations of Planetary Lightning

P. Zarka · W. Farrell · G. Fischer · A. Konovalenko

Originally published in the journal *Space Science Reviews*, Volume 137, Nos 1–4.
DOI: [10.1007/s11214-008-9366-8](https://doi.org/10.1007/s11214-008-9366-8) © Springer Science+Business Media B.V. 2008

Abstract We review radio detection of planetary lightning performed by Voyager, Galileo (including in-situ probe measurements), Cassini, and other spacecraft, and compare the information on the underlying physics derived from these observations—especially the discharge duration, at Jupiter and Saturn—with our knowledge of terrestrial lightning. The controversial evidence at Venus is discussed, as well as the prospects for lightning-like discharges in Martian dust-storms (and studies on terrestrial analogues). In addition, lightning sources provide radio beacons that allow us to probe planetary ionospheres. Ground-based observations of Saturn’s lightning have been attempted several times in the past and have been recently successful. They will be the subject of observations by the new generation of giant radio arrays. We review past results and future studies, focussing on the detection challenges and on the interest of ground-based radio monitoring, in conjunction with spacecraft observations or in standalone mode.

Keywords Planetary lightning · Planetary atmospheres · Atmospheric electricity · Planetary ionospheres · Radioastronomy · Radio emission · Radio wave propagation

PACS 92.60.Pw · 52.80.Mg · 94.20.-y · 95.55.Jz

P. Zarka (✉)

Observatoire de Paris, CNRS, UPMC, Université Paris Diderot, 5 Place Jules Janssen, 92190 Meudon, France

e-mail: philippe.zarka@obspm.fr

W. Farrell

Science Exploration Directorate, NASA Goddard Space Flight Center, Greenbelt, MD, USA

G. Fischer

Dept. of Physics and Astronomy, University of Iowa, 203 Van Allen Hall, Iowa City, IA 52242, USA

A. Konovalenko

Institute of Radio Astronomy, National Academy of Sciences of Ukraine, 4 Chervonopraporna Str., Kharkiv 61002 SU, Ukraine

Abbreviations

e.m.	electromagnetic (waves)
f	radio frequency
f_{cutoff}	cutoff frequency
f_{peak}	peak frequency of lightning's radio spectrum
f_{pe}	plasma frequency
HF	high frequency (e.m. waves)
i	stroke current (i_o = current constant; α, β = time constants)
Jy	Jansky
k	wave vector
LT	Local Time
LOFAR	LOw Frequency ARray (in construction)
LWA	Long Wavelength Array (USA)
μ	refractive index
NDA	Nançay decameter array, France
N_e	electron density
$P(f)$	spectral power
RPWS	Radio and Plasma Wave Science instrument on Cassini orbiter
S_{peak}	flux density at f_{peak}
SED	Saturn's electrostatic discharges
S_{min}	noise level/detection threshold
τ	stroke duration
θ	angle of incidence of the radio wave on the ionosphere
UED	Uranus' electrostatic discharges
UTR-2	Ukrainian T-shape Radiotelescope, mark 2 (near Kharkov, Ukraine)
VLF	very low frequency
\oslash	planetary angular diameter

1 Lightning's Radio Signature

1.1 Lightning Basics

Atmospheric lightning is a transient, tortuous high-current electrostatic discharge that occurs when large quantities of electric charge of opposite sign are separated over macroscopic distances (typically a few km). In the chain of atmospheric processes leading to lightning, small-scale particle electrification intervenes first through collisions and charge transfer, followed by large-scale charge separation, resulting for example from the competition of upward convection and gravitation. This results in the build-up of a large-scale electric field. When the amplitude of this electric field becomes larger than a critical value (breakdown field) which depends on the atmospheric pressure and composition, the energy gained by an electron over its mean free path between collisions becomes larger than the energy threshold for ionization of the intervening medium. The medium is thus ionized through a cascade of collisions, and a high intensity current flows to neutralize the electric field. This phenomenon is a lightning stroke, through which the stored electrostatic energy is released. A lightning flash consists of many consecutive strokes. More details on these processes can be found in Yair et al. (2008), and a quantitative discussion in e.g. Gibbard et al. (1997).

1.2 Interest of Planetary Lightning Studies

The interest in studying planetary lightning comes from the fact that (i) lightning plays a role in the atmospheric chemistry, through the production of non-equilibrium trace organic constituents potentially important for biological processes, (ii) lightning is a signature of atmospheric dynamics and cloud structure, that can be correlated with optical and infrared observations, and they provide a comprehensive picture of storm activity, its planetographic and seasonal variations, transient activity ..., (iii) lightning allows comparative studies of electrification processes with the terrestrial case, including the influence of atmospheric composition, and (iv) lightning is a unique tool for probing planetary ionospheres (see Zarka et al. 2004a and references therein).

1.3 Radio (and Other Electromagnetic) Signatures

Lightning discharges produce various electromagnetic waves, among which:

- Optical emission due to intense heating of the lightning channel;
- High-frequency (HF) radio emission (up to a few tens of MHz) originating from the current channel acting as an antenna;
- Very low-frequency (VLF) plasma waves (below a few tens of kHz) in the whistler mode, showing a characteristic time-frequency dispersion (Helliwell 1965).

1.4 Time Profile and Radio Spectrum

The time profile of the stroke current may be described by: $i = i_o (e^{-\alpha t} - e^{-\beta t})$. Typical parameters for a terrestrial discharge are: $i_o \sim 30$ kA, $\alpha \sim 2 \times 10^4$ s $^{-1}$, $\beta \sim 2 \times 10^5$ s $^{-1}$, implying a stroke duration $\tau \approx 100$ μ s. The stroke duration is the fundamental parameter that defines the spectral peak at which radio power is emitted. The corresponding radiated spectrum $P(f)$ decreases as f^{-4} at high frequencies (Farrell et al., 1999a, 2007 and references therein), while at lower frequencies channel tortuosity flattens the spectrum as: $P(f) \propto f^{-1}$ to f^{-2} . Radio emission is thus produced in a broad spectrum peaking (at Earth) about $1/\tau = 10$ kHz. A typical total flash duration at Earth is between a few msec and hundreds of msec.

2 Space-Based Radio Observations of Planetary Lightning

Besides their monitoring by many dedicated ground-based and embarked experiments, terrestrial lightning flashes have been observed in the same conditions as planetary lightning during the Earth fly-bys of Voyager, Galileo, and Cassini spacecraft, with the above characteristics.

2.1 Saturn

The first positive detection of a HF radio emission associated to extraterrestrial lightning occurred at Saturn, where unexpected sporadic spikes of radio emission were discovered by Voyager 1 in 1980 (Warwick et al. 1981). They have been studied with observations from both Voyagers over the Saturn fly-bys of 1980 and 1981, and by Cassini since 2004. Prior to understanding their atmospheric origin (Kaiser et al. 1983), these spikes were named

SED for “Saturn Electrostatic Discharge”. SED characteristics include occurrence within ~ 5 hour “episodes”, a typical duration of 30 to 350 msec per flash (exponential distribution with e-folding time ~ 50 msec), a broadband spectrum nearly flat from $\ll 1$ MHz to 10–20 MHz, then decreasing in f^{-1} to f^{-2} , an instantaneous spectral power ~ 0.1 to 300 W/Hz implying a flux density between 0.4 and 1000 Jy at the distance of Earth ($1 \text{ Jy} = 10^{-26} \text{ W m}^{-2} \text{ Hz}^{-1}$). In 1980, more than 1 event/min. was detected by Voyager 1 with a flux that would translate to ≥ 50 Jy at Earth, and about 10 events/min with a flux ≥ 5 Jy. SED beaming seems to be isotropic. In 1981, Voyager 2 observed SED flux densities and occurrence 2–4 times weaker than for Voyager 1. Cassini measured SED characteristics similar to those from Voyager 1 (peak occurrence rate) and 2 (average rate), with in addition a long-term variable occurrence: lightning emitting storms lasting for days to weeks are separated by weeks/months of inactivity (see Zarka et al. 2006; Fischer et al. 2008 and references therein). Cassini also confirmed directly by radio-goniometry (\mathbf{k} -vector determination) the origin of SED from the planet itself (unpublished measurements), measured accurately an average spectral power of 50–100 W/Hz nearly flat up to 16 MHz (Fischer et al. 2006; Zarka et al. 2006), and observed the correlation of an SED storm in September 2004 with an atmospheric cloud system (“Dragon storm”—Porco et al. 2005), confirmed by a similar correlation for the SED storm of early 2006 (Dyudina et al. 2007). VLF whistlers were reported by Akalin et al. (2006).

2.2 Titan

No lightning from Titan was detected with either Voyager or Cassini flybys of Titan (Desch and Kaiser 1990; Fischer et al. 2007b), implying an upper limit on the flux density at Earth $< 2 \times 10^{-5}$ Jy at 500 kHz. As tentative modelling based on atmospheric composition and dynamics predicted much higher flux densities especially from Titan’s dayside (Lammer et al. 2001; Zarka et al. 2004a), other reasons now invoked for non-detection include a very low flash rate ($< 10^{-2}$ flash/h), or long flash duration ($\gg 0.25$ msec) and thus a VLF spectral peak and an undetectable HF radio component (Sect. 4.3), or very episodic activity.

2.3 Uranus

Broadband radio spikes similar to SED were detected by Voyager 2 during its encounter with Uranus in 1986 (Zarka and Pedersen 1986). These spikes named UED had an occurrence rate much lower than SED (~ 7 events/hour), a comparable duration of 30–250 msec per event, a steeper spectrum, approximately $\sim f^{-2}$ (flatter below 20 MHz, much steeper above 35 MHz), and a weaker spectral power (a few W/Hz) corresponding to a flux density between ~ 0.4 and 40 Jy at the Earth.

2.4 Neptune

At Neptune, only 4 weak events presenting characteristics similar to SED and UED were detected by Voyager 2 during the fly-by (Kaiser et al. 1991), together with a few dispersed VLF whistlers supporting evidence for atmospheric lightning (Gurnett et al. 1990). Measurements of these 4 radio events was consistent with duration of 30–90 msec, a spectrum in f^{-4} , and flux densities of 0.03 to 0.003 Jy at Earth.

2.5 Jupiter

No HF radio emission from lightning was detected at Jupiter by any visiting spacecraft (Voyagers, Galileo, and Cassini), but whistlers and optical flashes were detected (see Desch et al. 2002 and references therein). Two possible explanations for the non-detection of radio waves are discussed in Sects. 3.2 and 4.2. Also, Cassini's sensitive radio observations were dominated by the strong magnetospheric decameter noise environment (Zarka et al. 2004b). The search coil on the Galileo descent probe recorded, up to 90 kHz and below the ionosphere, signals with \sim msec rise time, tentatively attributed to lightning (Lanzerotti et al. 1996).

2.6 Venus

On Venus, the existence of lightning has remained controversial for more than two decades. Russell (1991, 1993) summarized pros (tentative optical or radio detections) and cons (possible spurious origin of these detections) for observational evidence of Venusian lightning, especially from Venera and Pioneer-Venus Orbiter spacecraft. A few isolated spikes were observed by Galileo (Gurnett et al. 1991). During the two close-range fly-bys of Venus by Cassini in 1998 and 1999, Cassini's sensitive radio receiver detected no statistically significant lightning signal, while it recorded hundreds of lightning radio spikes during the Earth fly-by in 1999, up to 40 dB above the detection threshold (Gurnett et al. 2001). It was thus concluded that Venus lightning are either extremely rare ($\ll 1$ flash/hour) or very weak (10^{2-3} times weaker than their terrestrial counterparts). Absence of lightning could be explained by a very low vertical convection inhibited by the strong horizontal atmospheric circulation at this planet. However, whistler-mode waves have been recently detected with the Venus Express Magnetometer, and tentatively associated to the existence of lightning (Russell et al. 2007), keeping the controversy alive. If this detection is confirmed, consistency between Cassini and Venus Express results will imply either the existence of long intervals of atmospheric electrical inactivity at Venus, as for Saturn, or radio emission restricted to low frequencies (e.g. slow strokes with a very steep HF spectrum—see Sect. 4.4) unable to cross Venus' ionosphere. Conversely, the waves detected by Venus Express could be local plasma waves, that are known to occur in a non magnetic ionosphere in interaction with the solar wind (see e.g. Strangeway 2004).

3 Lightning and Ionospheric Probing

3.1 Saturn: LF (Low Frequency) Cutoff, Ionospheric Absorption, and Propagation over the Horizon

Radio emission from lightning is generated within planetary atmospheres. In order to escape the planet and reach distant observers, radio waves must thus propagate through the planet's ionosphere, which is a dispersive and absorbing medium. The most prominent effect comes from the fact that radio waves with frequency f incident on a plasma slab of (peak) plasma frequency f_{pe} (f_{pe} [Hz] $\approx 9 N_e^{1/2}$ with N_e the electron density in [m^{-3}]), with an angle of incidence θ relative to the slab normal, can propagate through the plasma only if $f > f_{pe}/\cos(\theta)$. They are reflected in the opposite case. This causes a LF cutoff of the observed radio emission dependent on the source (storm) position in Local Time (LT). Zarka and Pedersen (1983) and Kaiser et al. (1984) accordingly measured different LF SED cutoffs above Saturn's dayside ($f_{cutoff} \sim 6$ MHz) and nightside ($f_{cutoff} < 1$ MHz). Zarka (1985a)

derived a diurnal profile of the peak electron density in Saturn's ionosphere, between $N_e \sim 3\text{--}6 \times 10^5 \text{ cm}^{-3}$ on the dayside and $N_e \leq 10^3 \text{ cm}^{-3}$ on the nightside.

Another important effect of trans-ionospheric propagation is the attenuation of radio waves with f up to a few times f_{pe} , mainly due to electron-neutral collisions in the lower ionosphere. This chromatic attenuation effect was clearly observed by Voyager (Zarka 1985a) and Cassini (Fischer et al. 2007a), and successfully modelled. The negligible attenuation measured above ~ 20 MHz by Voyager allowed Zarka (1985a, 1985b) to set constraining upper limits on the vertical N_e profile in the dayside and nightside ionosphere.

When comparing SED occurrence during the large storm of September 2004 with simultaneous optical observations of the “Dragon” storm system, a surprising discrepancy of several tens of degrees was found between the average center time of SED episodes and the passage of the Dragon storm at sub-spacecraft meridian (Fig. 1a—see also Fischer et al. (2008) in this issue). SED episodes of occurrence started 0.12 ± 0.02 Saturnian rotation (i.e. $\sim 40^\circ$ to 50°) before the apparition of the Dragon storm at the planet's limb. Both the apparition and disappearance of bursts were frequency-dependent: lower frequencies started earlier than higher ones, and also stopped earlier (Fig. 1b). Cassini was located about 06 h LT in September 2004, so that it observed the storm system emerge from Saturn's nightside and disappear under the dayside ionosphere. At disappearance, the variable LF cutoff at $f_{pe}/\cos(\theta)$ is in good agreement with the observations (Fig. 1b). For the more puzzling chromatic and early apparition of SED, a possible explanation was provided by Zarka et al. (2006) in terms of sub-ionospheric radio propagation: when a wave with frequency above the cutoff enters the ionosphere, it is refracted away from the normal to the plasma layer, and then back towards it when it exits (refractive index for a wave frequency f is: $\mu = (1 - f_{pe}^2/f^2)^{1/2}$). For a plane plasma slab, the net ray deviation is zero, but not for a spherical layer. The effect is dominant for rays entering the ionosphere at large angle from its local normal. 2D ray-tracing of radio waves launched horizontally from the storm source through an ionospheric layer with a Gaussian profile around a peak plasma frequency $f_{pe} \approx 1$ MHz demonstrated that SED could be detected 35° to 70° over the horizon (Fig. 1c,d), consistent with the result of radio/optical comparison. Of special importance is the fact that the ionospheric electron density decreases gradually from dusk to dawn, due to gradual recombination (see e.g. N_e profile in Moore et al. 2004), leading to temporary trapping of the radio waves under the ionosphere before final escape towards the observer. This effect is stronger at lower frequencies (closer to f_{pe}).

Similar ionospheric propagation phenomena were observed for the SED storm of early 2006 (Fischer et al. 2007a), albeit with a lower discrepancy (30° to 40°) between SED occurrence and storm passage at sub-spacecraft meridian. Cassini was located between 03 h and 08 h LT in January/February 2006.

3.2 Jupiter: Low-Altitude Absorption

The first possible explanation for the non-detection of Jovian lightning in the HF radio range was proposed by Zarka (1985b), who demonstrated that the low-altitude Jovian ionospheric layers discovered by Pioneer 10 and 11 would cause very strong absorption (several tens of dB attenuation, again due to electron-neutral collisions) of radio waves generated in the atmosphere. These low-altitude ionospheric layers, with electron concentrations above 10^5 cm^{-3} at an altitude of a few hundred km above the 1 bar level, possibly have a (micro-)meteoritic origin and might thus be non-permanent.

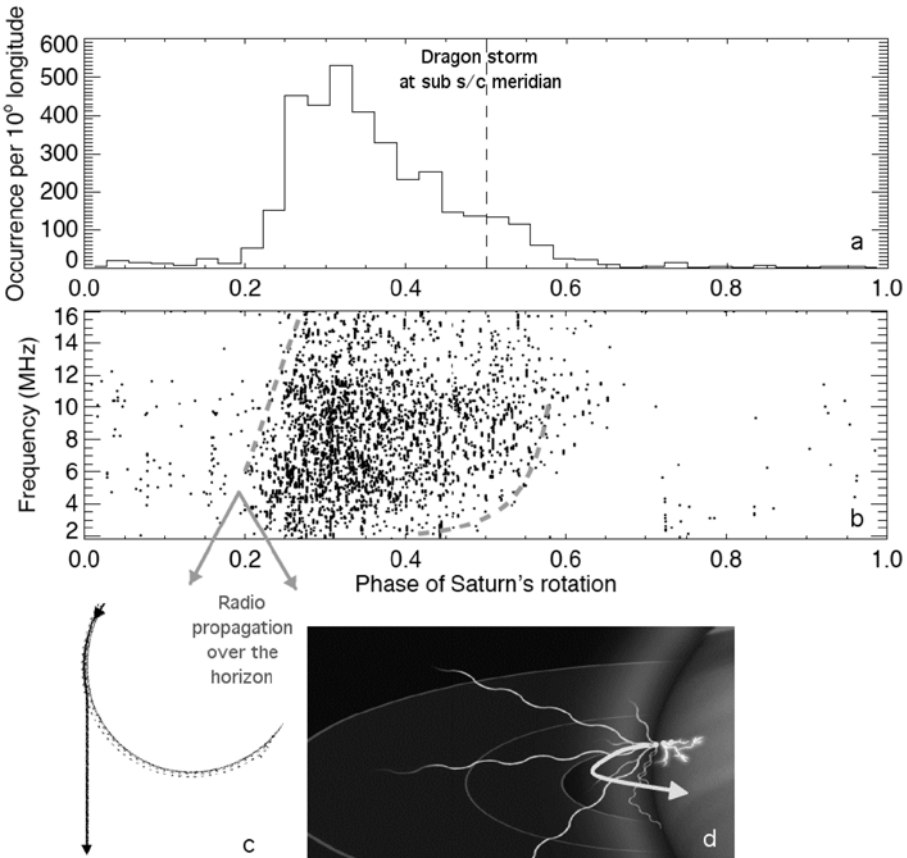


Fig. 1 (a) Stacked SED episodes from 9/2004 compared to position of the “Dragon” storm, showing a discrepancy of $\sim 50^\circ$ to 70° , and implying propagation $\sim 40^\circ$ to 50° over the horizon. (b) SED occurrence versus phase of Saturn’s rotation (with an arbitrary origin) showing frequency-dependent apparition and disappearance of bursts, as outlined by the grey dashed lines. The right one results from computation of the frequency cutoff $f_c = f_{pe} / \cos \theta$ with θ the angle of incidence of radio waves on Saturn’s ionosphere and f_{pe} here taken equal to 2 MHz in Saturn’s morningside ionosphere. (c) Example of deviation of a horizontal ray (top arrow) at 2 MHz refracted through a model ionosphere (dotted lines) with $f_{pe} = 1$ MHz at launch but decreasing versus LT. Overall ray deviation is here $\sim 35^\circ$. (d) Sketch of radio propagation over the horizon, from the lightning source (Dragon storm) to the observer (Cassini). See Fig. 4 of Fischer et al. (2008) in this issue for complementary illustration

4 Compared Temporal and Spectral Characteristics

As explained in Sect. 1.4, lightning’s radio spectrum and peak frequency are directly related to the time profile of the discharge.

4.1 Saturn: Fast Discharges?

With the observed SED spectral power (Sect. 2.1) and a spectrum $\propto f^{-n}$ with $n \sim 1-4$, several authors (Zarka and Pedersen 1983; Williams 1983; Farrell et al. 2007) showed that if the stroke duration is similar to the Earth case (≈ 100 μ s), then SED are very powerful

superbolts with a total energy of $10^{10\text{--}13}$ J. However, Farrell et al. (2007) noted that if the discharge duration is much faster (e.g. $\approx 1\ \mu\text{s}$), then the energy can be much weaker than for terrestrial discharges ($\sim 10^9$ J), down to $10^{3\text{--}6}$ J per flash, since the spectral peaks shifts to higher frequencies. The near-flat SED spectrum favours the latter interpretation. The same question arises for UED.

4.2 Jupiter: Slow Discharges?

Conversely, based on the Galileo probe observation of $\sim\text{msec}$ electrical discharges (Sect. 2.5), Farrell et al. (1999a) and Farrell (2000) proposed an alternative explanation for the non-detection of HF emission from Jovian lightning: Jovian lightning discharges could have much longer time constants than their terrestrial or Saturnian counterparts, up to a few milliseconds. The reason for these possibly “slow” lightning strokes at Jupiter is not known, but they would imply radio emission spectra restricted to very low frequencies, well below Jupiter’s ionospheric cutoff frequency. Similar slow rise times have been observed for cloud-to-ionosphere discharges (sprites) at Earth (Sentman et al. 1995).

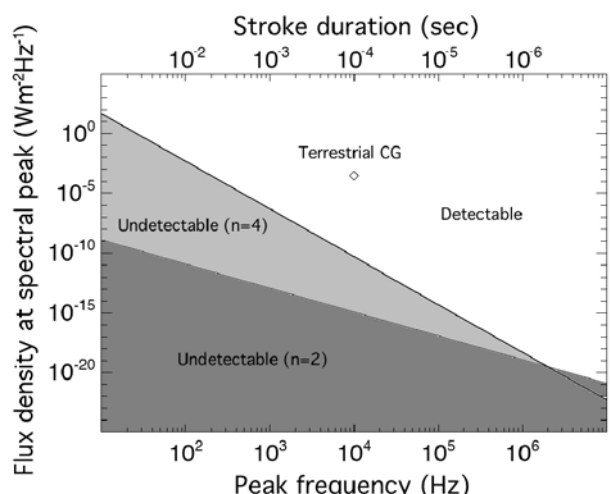
4.3 Titan: Slow Discharges?

Slow discharges on Titan could also prevent detection by Cassini, even from ~ 1000 km range. The noise level and detection threshold of the RPWS experiment onboard Cassini (Radio and Plasma Wave Science—Gurnett et al. 2004) is $S_{\min} \sim 3 \times 10^{-20}\ \text{W m}^{-2}\ \text{Hz}^{-1}$ above $f \sim 2\ \text{MHz}$. Assuming that the radiated spectrum decreases as f^{-n} above a peak frequency f_{peak} , Fig. 2 displays the regions of the plane ($f_{\text{peak}}, S_{\text{peak}} = S_{\min} \times (f/f_{\text{peak}})^n$) where the corresponding HF signals would be undetectable by Cassini. Typical values ($f_{\text{peak}}, S_{\text{peak}}$) = ($10\ \text{kHz}, 3 \times 10^{-4}\ \text{W m}^{-2}\ \text{Hz}^{-1}$) are indicated for terrestrial cloud-to-ground strokes, which would have been easily detected by Cassini/RPWS. Ionospheric attenuation, not taken into account here, would further expand the regions of undetectability.

4.4 Venus: Slow Discharges?

The same explanation as for Jupiter (and perhaps Titan) could solve the Cassini/Venus Express controversy (Sect. 2.6). Russell et al. recently published Venus Express magnetic field

Fig. 2 Ranges of detectability and undetectability of Titan lightning at $f = 2\ \text{MHz}$, as constrained by the absence of detection by Cassini/RPWS (Fischer et al. 2007b), as a function of peak frequency (f_{peak}) and flux density at spectral peak (S_{peak}), for a spectral slope $n = 2$ or $n = 4$. Upper limits on the flux density S at frequency f (at Cassini) can be deduced from this plot according to $S(f) = S_{\text{peak}} \times (f_{\text{peak}}/f)^n$, spectral power as $P(f) = S(f) \times 4\pi r^2$ with $r \sim 1000\ \text{km}$, and flux density at Earth as $S_{\text{Earth}}(f) = S(f) \times (r/R)^2$ with $R \sim 10\ \text{AU}$



measurements of electromagnetic whistler-mode waves claimed to support the detection of lightning. However, as noted by Yair et al. (2008) in this book, lightning whistlers on Earth are typically a factor of 10 shorter. Venus lightning could thus consist of slow discharges, whose origin remains to be explained, with a reduced HF spectrum.

5 The Case of Mars

5.1 Electrostatic Fields in Dust Devils/Storms

Although no lightning has ever been detected on Mars, dust charging and substantial electric field build-up is not excluded (Farrell et al. 1999b; Zarka et al. 2004a, and references therein). Large scale dust storms and “dust devils” (localized dust storms) are thought to be able to generate substantial charge via triboelectric processes (contact electrification). Laboratory experiments indicate that smaller grains tend to become negatively charged and larger grains positively charged (Ette 1971). In convecting dust storms with substantial vertical pressure gradients (vertical winds), the smaller (–) grains tend to be lifted upward relative to the larger (+) grains, generating a large vertical potential difference and a macroscopic electric dipole moment. Particle-in-cell numerical modelling indeed showed that large charge centers and potentials develop in dust devils due to vertical stratification of mass and charge (Melnik and Parrot 1998), and measurements inside dust devils on Earth revealed coherent electric fields exceeding 100 kV/m (Farrell et al. 2004, and references therein).

5.2 Nature of the Martian Discharge?

The exact nature of the discharge (time scale, current flow, spatial size) is unknown. Because of the lower atmospheric pressure on Mars, the atmospheric breakdown voltage is about 1/100 that of Earth’s (or about 20 kV/m). Laboratory experiments involving tribo-electrified dust grains in low pressure Martian-like CO₂ atmosphere were found to generate both coronal glow and filamentary discharges (Eden and Vonnegut 1973; Mills 1977). The former is a slow, sprite-like discharge resulting from electron impact excitation of CO₂ in a collisional plasma, while the latter is a fast discharge ($\tau \approx 5\text{--}50$ nsec) tending to interact more with the walls. By analogy, one might anticipate on Mars grain-grain and/or grain-atmosphere coronal discharges confined to the dust storm, and filamentary discharges to the ground analogous to Earth’s cloud-to-ground lightning (full breakdown requires the presence of secondary electrons, possibly from cosmic ray sources). Farrell et al. (1999b) noted that “leakage” currents associated with glow discharges would dissipate or bleed off charge centers, thereby limiting their maximum voltages. They estimated incoherent HF radiation corresponding to flux densities at Earth of the order of 1 μJy for peak emission frequency $f \sim 20$ MHz ($\tau \approx 50$ nsec) to 1 mJy for $f \sim 200$ MHz ($\tau \approx 5$ nsec). Farrell et al. (2006) noted that discharges in Martian dust storms could have a significant impact on the atmospheric chemistry (such as a methane sink).

6 Prospects for Ground-Based Observations

Zarka et al. (2004a) reviewed the radio detectability of all planetary lightning (Fig. 3), and showed that Saturn’s and Uranus’ lightning (SED and UED) should be detectable above sky background fluctuations with a large ground-based radiotelescope such as

the LOw Frequency ARray (LOFAR—see Van Haarlem et al. 2001 and www.lofar.org) or the UTR-2 array in Kharkov (Braude et al. 1978), or even a more modest instrument such as the Nançay decameter array (NDA—see Boisshot et al. 1980) with use of modern radio frequency interference (RFI) mitigation techniques (Zarka et al. 1997; Zarka 2005, and references therein). Martian discharges may be detectable with large meter-wave instruments such as LOFAR (at its highest frequencies), the GMRT in India or the future Square Kilometer Array (www.skatelescope.org).

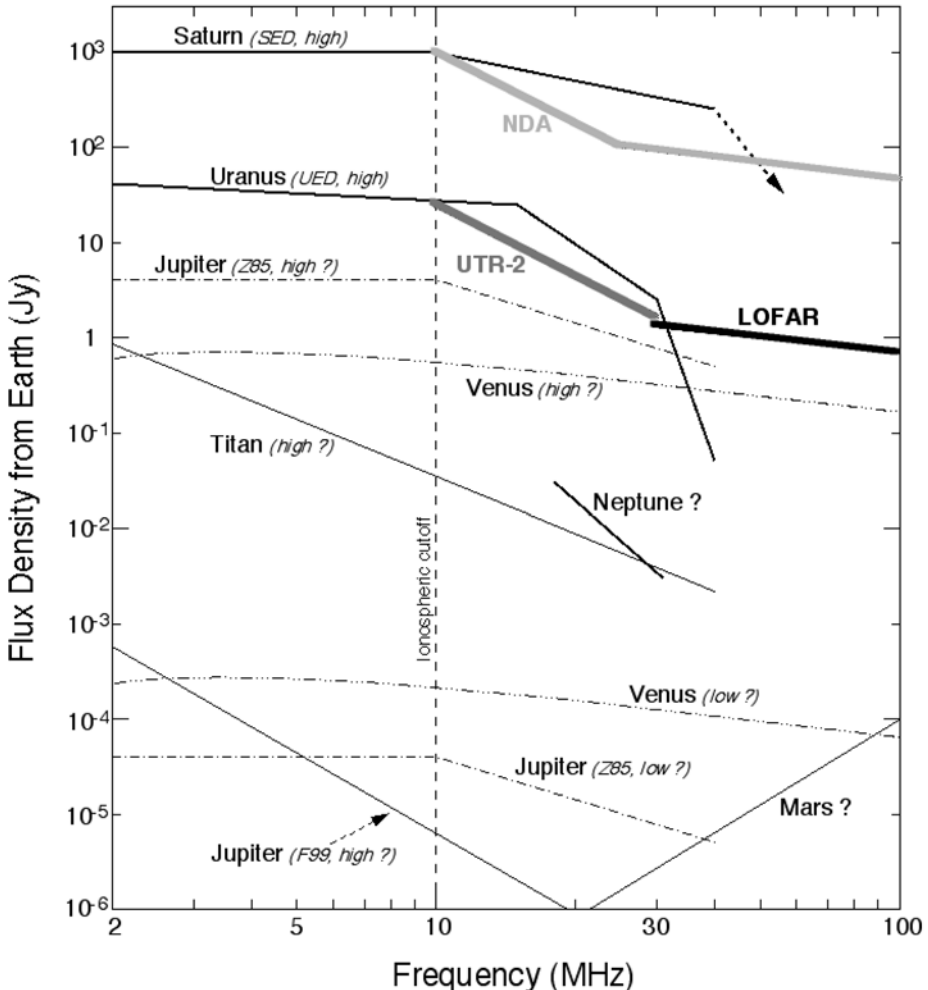


Fig. 3 Summary of planetary lightning radio spectra, adapted from (Zarka et al. 2004a). Spectra for Saturn, Uranus, and Neptune correspond to direct extrapolations of Voyager observations. Light grey lines represent upper limits or models of unobserved planetary lightning radio spectra. Two estimates of the upper limit for Venus lightning are represented. Two models are discussed for Jupiter, each providing a range of predicted spectra (high and low), as well as model estimates for Mars and Titan. Sky background-limited sensitivity of LOFAR, UTR-2 and Nançay Decameter Array (NDA) are displayed over their respective frequency ranges for an integration time of 20 msec and an observation bandwidth of 4 MHz

Previous attempts to detect SED with ground-based radio telescopes were made by Barrow in 1967 with the Arecibo dish, by Carr et al. in 1981 with the Maipu and Florida arrays, by Lecacheux and Biraud (1984) with the Nançay decimeter radiotelescope (see details in Konovalenko et al., to be submitted). Several campaigns were conducted at UTR-2 with various receivers (by Abranin and Bazelyan in 1972, Zarka et al. (1997), and Sidorchuk et al. (2006)). All had negative results, some of them due to insufficient sensitivity, but mostly due to the intrinsic variability of SED occurrence, especially on the long term, making detection unlikely with observations carried at arbitrary times. Using real-time information by Cassini about ongoing lightning activity on Saturn, Zarka et al. (2006) obtained a marginal detection with the Nançay decameter array, and Konovalenko et al. (2006) a more convincing one at UTR-2 in narrow frequency bands. A recent campaign using new digital receivers at UTR-2 during the episode of Saturnian lightning activity of December 2007 resulted in SED detection over the full instrument spectral range 10–30 MHz (Zarka et al., to be submitted). In particular, successful detections resulted from simultaneous observations of “On” and “Off”, allowing SED to be distinguished from interference.

The LOFAR interferometer, presently in construction in the Netherlands, with long baseline extensions in surrounding European countries, will enable arcsecond resolution imaging in the range 30–240 MHz. It will thus be able to resolve lightning sources on the planetary disk of Venus ($\varnothing \sim 60''$), Mars ($\varnothing \sim 18''$), Jupiter ($\varnothing \sim 47''$), Saturn ($\varnothing \sim 19''$), and even Uranus ($\varnothing \sim 4''$), and make possible correlations with optical measurements.

7 Prospects for Space-Based Observations

Future planetary space missions will offer interesting exploratory studies. Prospects for lightning are low for the present or near future missions to Pluto and Mercury, due to the very tenous atmospheres of these planets. In 2015–16, the Juno mission will perform 32 close-by pole-to-pole flybys of Jupiter, allowing it to re-attempt radio detection of lightning activity at Jupiter if discharges are fast and low-altitude high- N_e layers not permanent. Looking forward to \sim 2020, ESA (European Space Agency) missions to Jupiter, Saturn, Titan and/or Enceladus are under study.

8 Conclusions

Monitoring of planetary lightning permits to study electrification processes, breakdown electric field build-up, atmospheric dynamics, composition and cloud structure, geographical and seasonal variations, comparatively to the Earth’s case. Radio observations are a powerful tool for remote sensing of planetary lightning activity, with much higher time resolution than optical observations. When performed from space, they also allow to probe planetary ionospheres above lightning sources. As noted above, future planetary space missions will offer exploratory studies, while ground-based radio observations will complement them by concentrating on the accessible targets Saturn and Uranus (where instantaneous broadband observations should permit high time resolution analysis of SED—and hopefully UED—time profile and radio spectrum). The latter will also help to re-assess/confirm lightning activity at Venus and Titan, existence of Martian discharges, and possible transient activity at Neptune. In the case of successful detection, physical properties of planetary radio discharges can be studied in detail.

Finally, ground-based observations are also of methodological interest for the search for sporadic astrophysical phenomena at radio frequencies: SED detection requires mitigation

of intense man-made RFI and ionospheric effects. This methodology is applicable to studies of other transient sources (active stars, pulsars, radio emission associated with X or γ bursts, search for exoplanets ...). It should be of interest for existing and future (LOFAR, LWA ...) low-frequency instruments.

References

- F. Akalin, D.A. Gurnett, T.F. Averkamp et al., *Geophys. Res. Lett.* **33**, L20107 (2006)
- A. Boischot, C. Rosolen, M.G. Aubier et al., *Icarus* **43**, 399–407 (1980)
- S.Y. Braude, A.V. Megn, B.P. Ryabov et al., *Astrophys. Space Sci.* **54**(1), 3–36 (1978)
- M.D. Desch, M.L. Kaiser, *Nature* **343**, 442–444 (1990)
- S.J. Desch, W.J. Borucki, C.T. Russell, A. Bar-Nun, *Rep. Prog. Phys.* **65**, 955–997 (2002)
- U.A. Dyudina, A.P. Ingersoll, S.P. Ewald et al., *Icarus* **190**, 545–555 (2007)
- H.F. Eden, B. Vonnegut, *Science* **180**, 962–963 (1973)
- A.I.I. Ette, *J. Atmospheric Terr. Phys.* **33**, 295 (1971)
- W.M. Farrell, M.L. Kaiser, M.D. Desch, *Geophys. Res. Lett.* **26**, 2601–2604 (1999a)
- W.M. Farrell, M.L. Kaiser, M.D. Desch et al., *J. Geophys. Res.* **104**, 3795–3801 (1999b)
- W.M. Farrell, in *Radio Astronomy at Long Wavelengths*. Geophysical Monograph, vol. 119 (AGU, 2000), pp. 179–186
- W.M. Farrell, P.H. Smith, G.T. Delory et al., *J. Geophys. Res.* **109** E3, E03004 (2004)
- W.M. Farrell, G.T. Delory, S.K. Atreya, *Geophys. Res. Lett.* **33**, L21203 (2006)
- W.M. Farrell, M.L. Kaiser, G. Fischer et al., *Geophys. Res. Lett.* **34**, L06202 (2007)
- G. Fischer, W. Macher, M.D. Desch et al., in *Planetary Radio Emissions*, vol. VI, ed. by H.O. Rucker, W.S. Kurth, G. Mann (Austrian Academy of Sciences Press, Vienna, 2006), pp. 123–132
- G. Fischer, W.S. Kurth, U.A. Dyudina et al., *Icarus* **190**, 528–544 (2007a)
- G. Fischer, D.A. Gurnett, W.S. Kurth et al., *Geophys. Res. Lett.* **34**, L22104 (2007b)
- G. Fischer, D.A. Gurnett, W.S. Kurth et al., *Space Sci. Rev.* (2008, this issue). doi:[10.1007/s11214-008-9370-z](https://doi.org/10.1007/s11214-008-9370-z)
- S.G. Gibbard, E.H. Levy, G.E. Morfill, *Icarus* **130**, 517–533 (1997)
- D.A. Gurnett, W.S. Kurth, I.H. Cairns, L.J. Granroth, *J. Geophys. Res.* **95**, 20967–20976 (1990)
- D.A. Gurnett, W.S. Kurth, A. Roux et al., *Science* **253**, 1522–1525 (1991)
- D.A. Gurnett, P. Zarka, R. Manning et al., *Nature* **409**, 313–315 (2001)
- D.A. Gurnett, W.S. Kurth, D.L. Kirchner et al., *Space Sci. Rev.* **114**, 395–463 (2004)
- R.A. Helliwell, *Whistlers and Related Ionospheric Phenomena* (Stanford Univ. Press, Stanford, 1965)
- M.L. Kaiser, J.E.P. Connerney, M.D. Desch, *Nature* **303**, 50–53 (1983)
- M.L. Kaiser, M.D. Desch, J.E.P. Connerney, *J. Geophys. Res.* **89**, 2731–2736 (1984)
- M.L. Kaiser, M.D. Desch, W.M. Farrell, P. Zarka, *J. Geophys. Res.* **96**, 19043–19047 (1991)
- A.A. Konovalenko, A. Lecacheux, H.O. Rucker et al., European Planetary Science Congress. Berlin, Germany (2006), p. 229
- H. Lammer, T. Tokano, G. Fischer et al., *Planet. Space Sci.* **49**, 561–574 (2001)
- L.J. Lanzerotti, K. Rinnert, G. Dehmel et al., *Science* **272**, 858–860 (1996)
- A. Lecacheux, F. Biraud, in *Planetary Rings*, ed. by A. Brahic (Cepadues/CNES, 1984), pp. 319–324
- O. Melnik, M. Parrot, *J. Geophys. Res.* **103** A12, 29107–29118 (1998)
- A.A. Mills, *Nature* **268**, 614 (1977)
- L.E. Moore, M. Mendillo, I.C.F. Müller-Wodarg, D.L. Murr, *Icarus* **172**, 503–520 (2004)
- C.C. Porco, E. Baker, J. Barbara et al., *Science* **307**, 1243–1247 (2005)
- C.T. Russell, *Space Sci. Rev.* **55**, 317–356 (1991)
- C.T. Russell, R.N. Clayton, P.R. Buseck et al., *Annu. Rev. Earth Planet. Sci.* **21**, 43–87 (1993)
- C.T. Russell, T.L. Zhang, M. Delva et al., *Nature* **450**, 661–662 (2007)
- D.D. Sentman, E.M. Wescott, D.L. Osborne, D.L. Hampton, M.J. Heavner, *Geophys. Res. Lett.* **22**, 1205–1208 (1995)
- K.M. Sidorchuk, A.A. Konovalenko, V.N. Melnik et al., in *Planetary Radio Emissions*, vol. VI, ed. by H.O. Rucker, W.S. Kurth, G. Mann (Austrian Academy of Sciences Press, Vienna, 2006), pp. 581–588
- R.J. Strangeway, *Adv. Space Res.* **33**(11), 1956–1967 (2004)
- M.P. Van Haarlem et al., LOFAR scientific applications. Report ASTRON-LOFAR-00230, v1.00 (2001). www.lofar.org
- J.W. Warwick, J.B. Pearce, D.R. Evans et al., *Science* **212**, 239–243 (1981)
- M.A. Williams, *Icarus* **56**, 611–612 (1983)

- Y. Yair, G. Fischer, F Simões et al., Space Sci. Rev. (2008, this issue). doi:[10.1007/s11214-008-9349-9](https://doi.org/10.1007/s11214-008-9349-9)
- P. Zarka, B.M. Pedersen, J. Geophys. Res. **88**(A11), 9007–9018 (1983)
- P. Zarka, Icarus **61**, 508–520 (1985a)
- P. Zarka, Astron. Astrophys. **146**, L15–L18 (1985b)
- P. Zarka, B.M. Pedersen, Nature **323**, 605–608 (1986)
- P. Zarka, J. Queinnec, B.P. Ryabov et al., in *Planetary Radio Emissions*, vol. IV, ed. by H.O. Rucker, S.J. Bauer, A. Lecacheux (Austrian Academy of Sciences Press, Vienna, 1997), pp. 101–127
- P. Zarka, W.M. Farrell, M.L. Kaiser et al., Planet. Space Sci. **52**, 1435–1447 (2004a)
- P. Zarka, B. Cecconi, W.S. Kurth, J. Geophys. Res. **109**, A09S15 (2004b)
- P. Zarka, URSI General Assembly, Delhi, India, J05 COM 9 (2005)
- P. Zarka, B. Cecconi, L. Denis et al., in *Planetary Radio Emissions*, vol. VI, ed. by H.O. Rucker, W.S. Kurth, G. Mann (Austrian Academy of Sciences Press, Vienna, 2006), pp. 111–122

Atmospheric Electricity at Saturn

Georg Fischer · Donald A. Gurnett · William S. Kurth ·
Ferzan Akalin · Philippe Zarka · Ulyana A. Dyudina ·
William M. Farrell · Michael L. Kaiser

Originally published in the journal Space Science Reviews, Volume 137, Nos 1–4.
DOI: [10.1007/s11214-008-9370-z](https://doi.org/10.1007/s11214-008-9370-z) © Springer Science+Business Media B.V. 2008

Abstract The Cassini mission provides a great opportunity to enlarge our knowledge of atmospheric electricity at the gas giant Saturn. Following Voyager studies, the RPWS (Radio and Plasma Wave Science) instrument has measured again the so-called SEDs (Saturn Electrostatic Discharges) which are the radio signature of lightning flashes. Observations by Cassini/ISS (Imaging Science Subsystem) have shown cloud features in Saturn's atmosphere whose occurrence, longitudinal drift rate, and brightness were strongly related to the SEDs.

In this paper we will review the main physical parameters of the SEDs. Lightning does not only give us clues about the dynamics of the atmosphere, but also serves as a natural tool to investigate properties of Saturn's ionosphere. We will also discuss other lightning related phenomena and compare Saturn lightning with terrestrial and Jovian lightning.

Keywords Saturn: lightning · Saturn: atmosphere

1 Introduction

In this review paper we will focus on the new Cassini/RPWS observations of lightning on Saturn, which we continue to call Saturn Electrostatic Discharges (SEDs). This term was introduced by Warwick et al. (1981) due to the initially unknown origin of these impulsive radio bursts. When first detected by the Voyagers, an anomalous extension to very low

G. Fischer (✉) · D.A. Gurnett · W.S. Kurth · F. Akalin
Department of Physics and Astronomy, University of Iowa, 203 Van Allen Hall, Iowa City, IA 52242,
USA
e-mail: georg-fischer@uiowa.edu

P. Zarka
Observatoire de Paris, Meudon, France

U.A. Dyudina
150-21 Geological and Planetary Sciences, Caltech, Pasadena, CA 91125, USA

W.M. Farrell · M.L. Kaiser
NASA Goddard Space Flight Center, Greenbelt, MD 20771, USA

frequencies led Warwick et al. (1981, 1982) and Evans et al. (1982) to the conclusion that discharges in Saturn's rings might be responsible for the SEDs. But, using an argument of visibility Kaiser et al. (1983) could show that SEDs should stem from an atmospheric source. As the atmospheric origin is now well established (see Sect. 4) and SEDs are essentially electromagnetic waves the term "SED" could be considered as a kind of misnomer. On the other hand, the total energy of a lightning flash in a thunderstorm stems from the electrostatic energy of oppositely charged clouds. Hence, the usage of "SED" can still be considered appropriate in this sense, and to avoid confusion we refrain from creating a new name.

In Sect. 2 we will briefly describe the instruments which have detected SEDs or related phenomena. In Sect. 3 we will tabulate all SED measurements so far and discuss their occurrence in storms and episodes. Section 4 is devoted to the periodicity of SED episodes providing a first clue about the latitude of the lightning storm in Saturn's atmosphere. In Sect. 5 we will discuss further physical parameters like SED intensity, frequency spectrum, burst duration and rate. SEDs can be used as a natural tool to investigate Saturn's ionosphere, which will be shown in Sect. 6. In Sect. 7 the structure of Saturn's atmosphere and the possible source location of SEDs in the water clouds will be discussed. In Sect. 8 we will mention lightning related phenomena like whistlers and speculate about the possibility of sprites, elves, or gamma ray flashes at Saturn. The final summary of Sect. 9 will be in the form of a table comparing the most important properties of SEDs with terrestrial lightning.

2 Instruments for Lightning Detection at Saturn

2.1 Observations by Spacecraft

SEDS were first detected by the Voyager 1 PRA (Planetary Radio Astronomy) experiment during the Voyager 1 Saturn encounter in November 1980 (Warwick et al. 1981). In August 1981 the identical PRA instrument onboard of Voyager 2 also detected SEDs during Voyager 2's encounter with Saturn (Warwick et al. 1982). The PRA instrument consists of two orthogonal antennas with a length of 10 m, and a frequency sweeping receiver in the frequency range of 1.2 kHz to 40.5 MHz (Warwick et al. 1977). The PRA performs a scan from high to low frequencies within 6 seconds through its whole frequency range, and the receiver dwells at each of its 198 frequency channels for about 30 ms. Most SEDs were detected in the HF part of the PRA (above 1.2 MHz), but on the nightside of Saturn some SEDs were also detected in the LF part below 1326 kHz (Zarka and Pedersen 1983). No SEDs were detected by the PWS (Plasma Wave System) of the Voyagers operating in the frequency range from 10 Hz to 56.2 kHz in 16 logarithmically spaced frequency channels (Kurth et al. 1983).

The Cassini/RPWS instrument can use any of its three electric antennas of 10 m in length (or a combination of them) to detect SEDs in its High Frequency Receiver (HFR) (Gurnett et al. 2004). SEDs were detected only in the HF1 and HF2 band of the HFR, which (like the PRA) acts as frequency sweeping receiver. The time for a scan through these two bands can vary as number of used antennas, start frequency, frequency step size and integration time can be set to different values. The typical mode consists of the following scan lasting for 16 seconds: HF1 sweeps from 325–1800 kHz in 60 frequency steps of 25 kHz with an integration time of 80 ms and using two antennas; followed by a sweep through HF2 from 1825–16025 kHz in 143 frequency steps of 100 kHz with an integration time of 40 ms and using only one antenna. PRA as well as RPWS have a high rate mode to monitor SED

amplitude variations with a time resolution of the order of 0.1–1 ms. RPWS can even use its Wideband Receiver at SED frequencies with a time resolution of a few tens of μ s, and some SEDs were caught recently with this mode. Evans et al. (1983) showed that the SED amplitude envelope exhibits slowly varying fluctuations for several tens of ms as well as more rapid fluctuations lasting less than 1 ms.

Besides producing radio emissions, lightning also produces optical emissions that can be detected by imaging instruments. Unsuccessful attempts were made to image lightning flashes on the nightside of Saturn with the Voyager cameras (Burns et al. 1983), partly due to the sunlight reflected from the rings (ring shine). Similar attempts were made with Cassini/ISS, but no flashes have been seen so far (Dyudina et al. 2007). The Cassini/ISS is also equipped with a narrow-band H α filter (Porco et al. 2004), as this atomic hydrogen line is expected to be prominent for a lightning flash at Saturn (Borucki et al. 1996). Another reason for this non-detection could be that the lightning-producing water clouds at Saturn are at a deeper level compared to Jupiter, which leads to complete absorption of the light from the flashes. This will be further discussed in Sect. 7. Nevertheless, the Cassini/ISS has imaged bright storm cloud eruptions at a latitude of 35° South correlating with the occurrence of SEDs (Porco et al. 2005; Dyudina et al. 2007).

2.2 Earth-based Measurements

The clouds related to the SED storm of early 2006 were, in fact, first observed by amateur astronomers on Earth (Fischer et al. 2007a). The occurrence rate of such remarkable cloud features and lightning storms throughout one Saturnian year (~ 29.5 Earth years) is not known. Hence, such observations could be especially valuable after the end of the Cassini mission, since Konovalenko et al. (2006) have succeeded in detecting SEDs with the world's largest radio telescope UTR-2 in the decametric frequency range in early 2006. As the SEDs are particularly strong radio emissions with a flux of ~ 100 Jansky at Earth their detection from Earth was anticipated (see also Zarka et al. 2008, this issue). Three previous attempts by Lecacheux and Biraud (1984) and Zarka et al. (1997, 2006) had resulted in non-detection for the former and marginal or ambiguous one by the latter.

3 Occurrence Rate of Saturn Electrostatic Discharges

Since both Voyagers detected SEDs during their Saturn encounters it seemed possible that SEDs (like Earth lightning) are a permanently present feature. The Cassini/RPWS measurements displayed in Fig. 1 show that this is clearly not the case. There are long intervals of time with no SED activity. No SEDs were detected from early 2006 until late 2007 for about 21 month. A new SED storm has started on November 27, 2007, and is still ongoing after five months at the time of the correction of this paper (late April 2008). In order to see the various SED storms more clearly we have not displayed this long inactive time interval and the most recent SED storm in Fig. 1. The SED storms after Cassini SOI (Saturn Orbit Insertion, DOY 183, 2004) were labeled A, B, and C by Gurnett et al. (2005). A smaller storm happening before SOI was labeled storm 0 (zero) by Fischer et al. (2006a). Only one storm occurred in 2005 (storm D), and early 2006 RPWS observed the SEDs of the big storm E (Fischer et al. 2007a). The RPWS instrument was capable of SED detection nearly all the time, and sparse data gaps are indicated in Fig. 1 by the light grey background color. There were only two longer time intervals of about 9 days each, when no data were retrieved from RPWS. The first one was right before storm A, and we might have missed some SEDs at

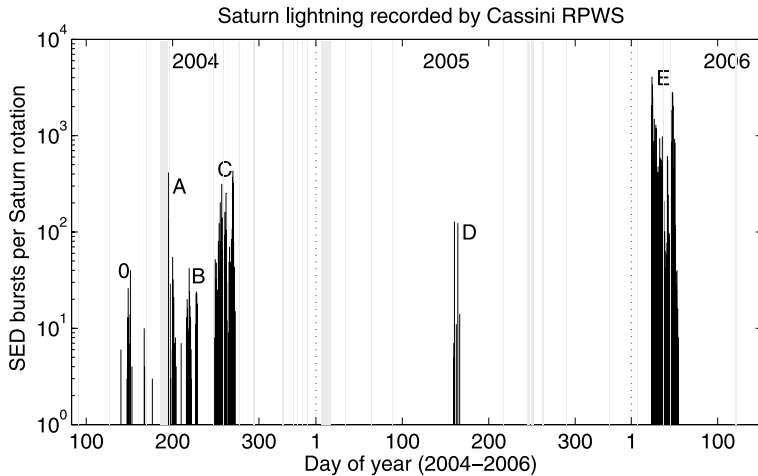


Fig. 1 Number of detected SEDs per Saturn rotation as a function of time. Cassini/RPWS data gaps are indicated by a light gray background color

Table 1 Summary of all SED storms detected by radio instruments on Voyager (V1, V2) and Cassini (0 to F). The table was adapted from Fischer et al. (2007a), and the higher number of V2 episodes here comes from Warwick et al. (1982) instead of Zarka and Pedersen (1983)

Name	Date: month, year	Number of SEDs in number of episodes	Recurrence period of episodes
V1	Nov. 1980	18000 in ~ 16	10 h 09 min (± 6 min)
V2	Aug. 1981	5000 in ~ 14	10 h 00 min (± 7 min)
0	May 2004	100 in 8	10 h 35 min (± 6 min)
A	July 2004	800 in 15	10 h 43 min (± 2 min)
B	Aug. 2004	300 in 16	10 h 40 min (± 2 min)
C	Sept. 2004	4200 in 49	10 h 40 min (± 1 min)
D	June 2005	300 in 6	10 h 10 min (± 10 min)
E	Jan./Feb. 2006	43400 in 71	10 h 39.8 min (± 0.4 min)
F	Nov. 2007 until ?	TBD	Around 10 h 40 min

this instant. The second one was in January 2005 around the landing of the Huygens Probe on Titan, but no SEDs were detected around that time. The Cassini mission gives us the opportunity to follow the full lifetime of a Saturn lightning storm, whereas the Voyagers only captured snapshots due to their single passages.

In Table 1 we have summarized all SED storms observed so far by the Voyagers as well as Cassini. We have listed their identifying name, the month and year when they were recorded, the number of SEDs and episodes, plus the episode's recurrence period. SEDs are organized in episodes simply because the causative lightning storm can be either on the side of Saturn facing the spacecraft or on the opposite site (and below the radio horizon), from where it cannot be detected. In the course of one SED storm the numbers of SEDs per episode (or per Saturn rotation) can exhibit a significant variability. Numbers of SEDs per episode ranged from just a few bursts to several hundreds or even a few thousands in the case of storm E.

Altogether (Voyagers and Cassini) $\sim 72,000$ SEDs (in ~ 195 episodes) have been detected so far, and more than half of them were recorded during the “giant” storm E of early 2006 (Fischer et al. 2007a). Analysis of the SED storm F is not completed yet, and so it is not included in the previous numbers.

4 Periodicity of SED Episodes and Location of Lightning Storms

An inspection of the recurrence periods of episodes of the various storms (last column of Table 1) shows that there are basically only two different classes: Storms 0, A, B, C, and E (and also F) have a period close to 10 h 40 min, whereas storms V1, V2, and D have a period around 10 h 10 min. Storms A, B, and C were associated with a prominent cloud feature at a planetocentric latitude of 35° South, which was nicknamed the “dragon storm”. Its occurrence coincided with the occurrence of SEDs, and from Voyager as well as Cassini wind speed measurements it is known that this latitude is associated with a near-zero wind speed relative to the Voyager radio period, i.e. it has a period close to 10 h 40 min. Furthermore, the brightness of the “dragon storm” clouds correlated well with the number of observed SEDs (Porco et al. 2005; Dyudina et al. 2007). The usage of different filters to image different depth of Saturn’s atmosphere allowed Dyudina et al. (2007) to see dense clouds reaching high altitudes suggesting strong updrafts, which are a well known feature of terrestrial thunderclouds (Rakov and Uman 2003). Similarly, during the “giant” SED storm E there was another prominent cloud feature again at 35° South (the same holds for the recent storm F). This cloud feature can be seen in Fig. 2 on the right side, and the prominent “dragon storm” is on the left. Fainter clouds can be imaged in Saturn’s atmosphere at various latitudes (linked to different wind speeds and periods) practically all the time. But, such prominent clouds like the “dragon storm” were absent on the surface of Saturn during the several-months-long periods when the SEDs were absent.

The parallel occurrence of SEDs from storm E and the cloud feature is illustrated in Fig. 3, where the sub-spacecraft western longitude ranges of Cassini during each SED episode are indicated by nearly vertical lines. The nearly horizontal thick line close to the

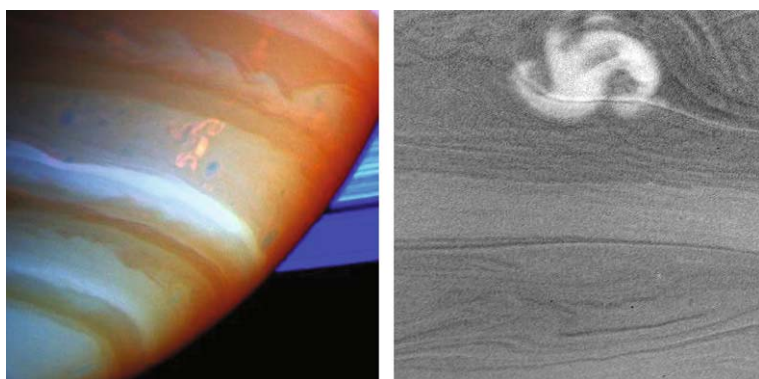


Fig. 2 The “dragon storm” as imaged by Cassini/ISS on September 13, 2004 (left), and the prominent cloud feature during SED storm E imaged on January 27, 2006 (right). The left false—color image was taken on Saturn’s dayside, while the right contrast—enhanced image was taken at the nightside. Both storms were located at a planetocentric latitude around 35° South (from <http://saturn.jpl.nasa.gov/>, © NASA)

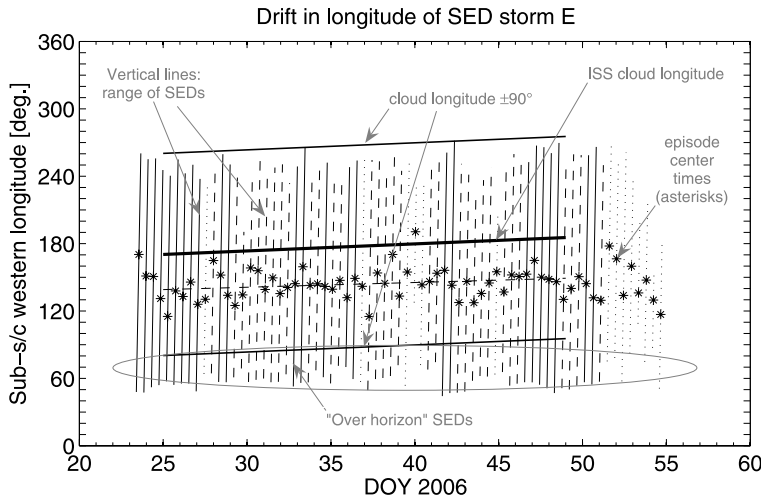


Fig. 3 Sub-spacecraft western longitude ranges (Voyager SLS) for storm E episodes as a function of day of year 2006. Dotted lines denote weak episodes with less than 50 SEDs, dashed lines denote episodes with 50 to 500 SEDs, and solid lines denote strong episodes with more than 500 SEDs. The asterisks mark the western longitudes at the center times of the episodes. The *nearly horizontal lines* and the “over horizon” SEDs are labeled in the figure and are explained in the text (adapted from Fischer et al. 2007a)

middle of the episodes gives the western longitude of the ISS observed cloud system, which was located around 170° on DOY 25 and drifted westward with a rate of 0.6° per day. This line is also shifted by $\pm 90^\circ$ in both directions indicating the appearance and disappearance (at $\sim 90^\circ$ and $\sim 270^\circ$ sub-spacecraft western longitude, respectively) of the visible cloud system at the horizon. Since Cassini was on the morning side of Saturn the cloud system appeared on the nightside, passed the morning terminator, and disappeared on the dayside. The SED episodes end either exactly when the visible cloud disappears at the dayside horizon or slightly before that, which can be attributed to radio wave absorption in Saturn’s ionosphere at grazing incidence angles. But, it is evident from Fig. 3 that the SEDs started before the visible cloud was seen with the Cassini cameras. They are marked by the grey ellipse in Fig. 3 and we call them “over horizon” SEDs, as the radio horizon extends as much as 45° below the visible horizon. Zarka et al. (2006) explains this effect by an electron density decrease with local time at Saturn’s nightside ionosphere which leads to temporary trapping of the SED radio waves. The drift of the ISS imaged cloud system corresponds to a period of (10.665 ± 0.001) h. For the determination of the recurrence period of SED episodes Fischer et al. (2007a) used the so-called center time of an episode, which is the mean time of all SEDs within one episodes. The center times are indicated by the asterisks in Fig. 3, and a straight line fit (from DOY 25 to 48 when the cloud was imaged) is given by the dashed line close to the asterisks. Its slope corresponds to a period of (10.662 ± 0.006) h, which is in good agreement with the period of the imaged cloud.

The period of SED storms V1, V2, and D around 10 h 10 min corresponds to the rotation of Saturn’s equatorial atmosphere. But, no corresponding cloud features by the Voyager cameras have been reported, and also some faint clouds observed at the equator during the small SED storm D do not really match the SED occurrence (Dyudina et al. 2007; Fischer et al. 2007a). Nevertheless, it seems possible that due to strong vertical and latitudinal wind shear in Saturn’s equatorial region, updrafting clouds are diluted and spread over a huge area and therefore cannot be clearly seen. The period and other characteristics (like

episode and flash durations and the low frequency cutoff due to the ionosphere) of these SED storms clearly point to longitudinally extended storms in Saturn's equatorial atmosphere. In summary, up to now only two latitudes at Saturn have been found to produce SED storms, which are the equatorial region and the “storm alley” at 35° South.

5 Some More Physical Parameters of SEDs

5.1 SED Intensity and Frequency Spectrum

The radio emissions of SEDs are much stronger than the radio emissions from terrestrial lightning in the frequency range of a few MHz. Zarka et al. (2006) as well as Fischer et al. (2006b) found spectral radio source powers of the order of 10 to 100 W Hz⁻¹ for SEDs confirming the previous Voyager measurements by Zarka and Pedersen (1983). This is a factor of 10⁴ stronger than terrestrial flashes, which makes SEDs detectable from great distances. With RPWS SEDs were first detected far beyond 300 Saturn radii (Fischer et al. 2006a). This corresponds to a staggering distance of about 3000 Earth radii compared to only 14 Earth radii, within which RPWS detected terrestrial lightning during its Earth flyby (Gurnett et al. 2001). We note that radio emissions detected by RPWS in July 2003 at a distance of more than 1 AU from Saturn, which were initially interpreted as SEDs, turned out to be radio emissions (decametric arcs) from Jupiter (Fischer et al. 2006c). This factor of 10⁴ in radio power, measured in fact only in a relatively small frequency range, has led some authors to conclude that the total energy of SEDs might be 4 orders of magnitude above the typical terrestrial lightning energy of 10⁹ J (“superbolt”). Farrell et al. (2007) have shown that this is not necessarily the case and that this question is actually related to the temporal nature of the discharge itself and the resulting shape of the frequency spectrum. With f denoting the frequency, the spectrum of terrestrial lightning shows a roll-off with f^{-2} or even steeper above 1 MHz. This is distinctly different from what Zarka et al. (2006) and Fischer et al. (2006b) found for the SED spectrum being essentially flat or with a roll-off of only $f^{-0.5}$ from 4–16 MHz. For the Voyager SEDs Zarka and Pedersen (1983) and Zarka et al. (2004) found a relatively flat spectrum up to 20 MHz, and a decrease with f^{-1} to f^{-2} from about 20–40 MHz. This spectral behavior suggests that an SED consists of a series of very short pulses less than 1 μ s (Farrell et al. 1999, 2007).

5.2 SED Burst Duration and Burst Rates

Similar to a terrestrial flash, an SED probably consists of many subpulses, and the total duration of one SED can be as long as a few hundred milliseconds. Most SEDs are somewhat shorter and the SED duration can be well described by a distribution with an exponential decrease in number of SEDs n with increasing burst duration t . In such a distribution described by $n \propto \exp(-t/t_0)$ the storm C SEDs had an e-folding time t_0 of (37 ± 3) ms similar to the 41 ms found for the Voyager 1 SEDs by Zarka and Pedersen (1983). The e-folding times of storms D and E were found to be somewhat longer with (48 ± 12) ms and (49 ± 3) ms, respectively (Fischer et al. 2007a).

SED burst rates (number of recorded SEDs per time interval) depend strongly on the distance of the spacecraft to the thunderstorm in Saturn's atmosphere. The closer the spacecraft is the more low intensity bursts can be observed. The maximum rate found by the Voyagers was 1 SED every 4 seconds, which was measured around closest approach of Voyager 1

when it was just 2 Saturn radii above Saturn's 1-bar level (Zarka and Pedersen 1983). A remarkable burst rate of 1 SED every 2 seconds was measured by RPWS during the second episode of the giant storm E with Cassini at a distance of 45 Saturn radii. If Cassini would have been at a distance of only 2 Saturn radii at that time, the flash rate can be extrapolated to some tens of SEDs per second using the distribution of SED intensities (Fischer et al. 2007a), which is much higher than what was measured by Voyager 1 at this distance. The flash rates also varied significantly in the course of SED storm E, but the high flash rates lasted typically for 3 to 4 Saturn rotations, which is longer than one Earth day. We note that a single thunderstorm on Saturn with a diameter around 2000 to 3000 km (Dyudina et al. 2007) and a depth of the order of 200 km (see Sect. 7) has approximately the same volume as the whole terrestrial troposphere.

6 Saturn Lightning as a Tool to Investigate Saturn's Ionosphere

6.1 Peak Electron Densities Derived from the Low Frequency Cutoff of SED Episodes

The broadband SED radio waves can be measured by RPWS only when their frequency is above the peak plasma frequency of Saturn's ionosphere. Hence, assuming straight line of sight propagation, the peak electron plasma frequency $f_{pe,peak}$ can be easily determined from the low frequency cutoff f_{cutoff} of SED episodes with the equation $f_{pe,peak} = f_{cutoff} \cos(\alpha)$, with α being the angle of incidence. These three quantities change with time in the course of one SED episode, as the storm rotates with Saturn's atmosphere and passes various local times under the ionosphere. The shape of this low frequency cutoff f_{cutoff} is indicated in Fig. 4 for one SED episode. This figure is a so-called dynamic spectrum showing the color-coded intensity of radio emissions as a function of time and frequency. The SEDs are the short vertical bursts, that due to the sweeping nature of the receiver appear as narrow-banded signals, although they are intrinsically broadband. The patchy emission at the bottom is Saturn Kilometric Radiation (SKR). At the abscissa we have indicated the times, when the visible cloud appeared and disappeared at the horizon, and when it was at the central meridian (CM) as seen from Cassini. Hence, all SEDs observed before 22:22 SCET are essentially "over horizon" SEDs, which Zarka et al. (2006, 2008, this issue) attribute to an ionospheric propagation effect. It can also be seen that the SEDs are slightly less intense on the dayside (Cassini is at 6 LT), which is caused by higher electron densities resulting in increased radio wave absorption. In Fig. 4 SEDs disappear about half an hour before the visible cloud disappears at the dayside horizon, which is due to the long ray path through the absorbing ionosphere at angles close to grazing incidence. Using the low frequency cutoff of some SED episodes Fischer et al. (2007a) determined the peak electron density as a function of local time. In the range from midnight to 9 LT the peak electron density increased by more than one order of magnitude from 4×10^3 to $8 \times 10^4 \text{ cm}^{-3}$, consistent with what Kaiser et al. (1984) had found for the Voyager 1 SEDs.

Fischer et al. (2007a) found that the frequency minima of storm E episodes were in the range from 770–2300 kHz where there were enough SEDs to see a clear minimum. In Fig. 4 for example, the frequency minimum is around 1 MHz, in the more noisy HF1 band (below 1.8 MHz) of the HFR. For all observed SEDs in the year 2004 (storms 0, A, B, C) Fischer et al. (2006a) could not identify any SEDs below 1.3 MHz, and the lowest frequency channels where SEDs were observed for storm D and E were close to 1070 kHz and 770 kHz, respectively. Generally, at Saturn the frequency range from 3–1200 kHz is dominated by SKR which has highly variable lower and upper frequency limits. With RPWS

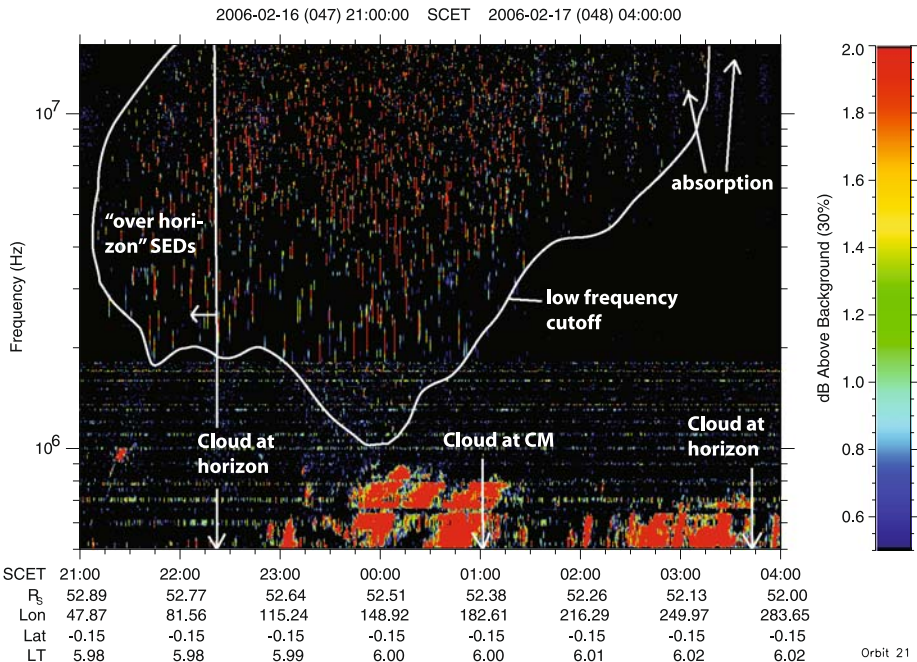


Fig. 4 Dynamic spectrum of SED episode number 56 of storm E. CM stands for central meridian, and it can be seen that the visible cloud is at the CM as seen from Cassini around 01:00 SCET (Spacecraft Event Time). On the abscissa orbital parameters of Cassini are indicated (distance from the center of Saturn in Saturn radii, longitude and latitude, as well as local time). For further explanations see text

clearly no SEDs could be observed below the SKR. An exceptional event had occurred during the SED episode around closest approach of Voyager 1 at Saturn, where SEDs had been observed as low as 20 kHz (Warwick et al. 1981; Zarka and Pedersen 1983). We believe that the anomalous low frequency extension of the Voyager 1 SEDs is either caused by ionospheric holes caused by an influx of water from the rings (Connerney and Waite 1984) or by bursty signals of a different nature that have been misinterpreted as SEDs. Zarka (1985a) and Fischer et al. (2007a) have given convincing arguments showing the consistency of various SED properties with an atmospheric source and the inconsistencies related to a ring source. The combined ISS and RPWS observations (Porco et al. 2005; Dyudina et al. 2007; Fischer et al. 2007a) have finally established a connection between observed cloud features and SEDs. In the next subsection we will discuss that SED radio waves get highly polarized in the magnetoplasma of Saturn's ionosphere, implying that the source of SEDs must be below Saturn's ionosphere.

6.2 Polarization of SEDs

Fischer et al. (2007b) analyzed the polarization measurements of SEDs, which were performed below a frequency of 2 MHz (HF1 band) with RPWS during SED storm E early 2006. They found that SEDs are highly polarized ($\sim 80\%$) with a particularly high degree of circular polarization, and there was exclusively one sense of rotation, which was found to be right-handed with respect to the wave propagation direction. They could explain these measurements in the frame of magneto-ionic theory by calculating Appleton's equation for

typical ionospheric conditions on Saturn's nightside ionosphere. In the magnetoplasma of Saturn's ionosphere the SED radio waves experience two possible modes of propagation, which are generally elliptically polarized with opposite rotation sense. Fischer et al. (2007b) found that different cutoff frequencies of these two modes as well as a differential absorption effect lead to the dominance of the ordinary mode below 2 MHz, and the extraordinary mode is highly attenuated. Since the angle between Saturn's magnetic field at the latitude of the storm at 35° South and the direction of wave propagation is larger than 90°, the ordinary mode should show right-handed polarization (with respect to the direction of wave propagation), which is consistent with the observations. Fischer et al. (2007b) note an interesting analogy between terrestrial TIPPs (Transitionospheric Pulse Pairs) and SEDs, as both are related to intracloud lightning, are strong radiators in the high frequency range and also have a flat spectrum there. Finally, TIPPs (like SEDs) also show a high circular polarization after passage through the ionosphere (Shao and Jacobson 2002).

7 The Structure of Saturn's Atmosphere

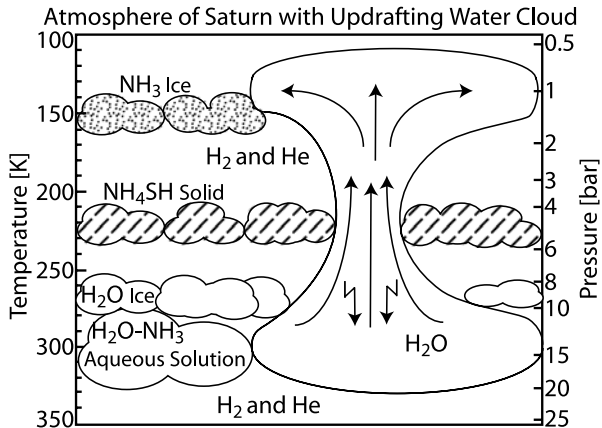
7.1 Lightning on Jupiter as a Comparison

Due to the compositional similarity between Jupiter's and Saturn's atmosphere, we shortly discuss lightning at Jupiter (see comprehensive review by Desch et al. 2002 and new review by Yair et al. 2008, this issue) before proceeding to the structure of Saturn's atmosphere. Lightning at Jupiter was detected optically by the cameras on-board the Voyagers (Cook et al. 1979), Galileo (Little et al. 1999), Cassini (Dyudina et al. 2004), as well as New Horizons (Baines et al. 2007). Radio emissions from Jovian lightning have been detected in the form of whistlers (Gurnett et al. 1979) in Jupiter's magnetosphere as well as sferics with the Galileo Probe inside Jupiter's atmosphere (Rinnert et al. 1998). Interestingly, no high frequency (HF) radio component (similar to SEDs) above the cutoff frequency of Jupiter's ionosphere has been detected, which according to Zarka (1985b) is due to the strong absorption of the radio waves in Jupiter's lower ionospheric layers. Farrell et al. (1999) attributes the non-detection of the HF component to the decrease of spectral power of Jovian spherics with increasing frequency as it was measured by the Galileo Probe. Borucki and Williams (1986) as well as Dyudina et al. (2002) applied a Monte Carlo model to describe the scattering of light from Jovian flashes in Jupiter's atmosphere. In both papers the best agreement between model and observations is obtained when the lightning source is located in a Jovian water cloud at or below a pressure level of 4–5 bars. Gibbard et al. (1995) as well as Yair et al. (1995) have modeled the generation of lightning in Jovian water clouds using a charge separation mechanism similar to that which operates in terrestrial thunderstorms (Rakov and Uman 2003). Both conclude that a Jovian thundercloud is able to build up a strong electric field required for lightning discharges as long as there is sufficient water abundance.

7.2 At What Depth is the SED Source Located?

Figure 5 illustrates the cloud structure in Saturn's hydrogen and helium atmosphere, which shows three distinct cloud layers. The figure was drawn after the equilibrium cloud condensation model of Atreya and Wong (2004), who used elemental abundances of 5 times the solar value. The outermost cloud layer consists of ammonia (NH_3) ice particles and is followed by an intermediate ammonium hydrosulfide (NH_4SH) cloud layer.

Fig. 5 Sketch of the three-layered cloud structure in Saturn's atmosphere with an updrafting water cloud with lightning activity



The deep water cloud (H_2O) has a cloud base around the 20 bar level and might consist of droplets of an aqueous solution of ammonia in water at lower levels and ice particles above. Jupiter's cloud structure is essentially similar, except that the greater gravity of Jupiter leads to a higher temperature lapse rate and clouds condense at lower pressure levels. As observations of Jovian lightning point to the water cloud as source region for lightning, it is straightforward to assume that Saturn lightning also has its origin in the water clouds. Furthermore, the greater depth of water clouds in the model of Saturn's atmosphere allows us to explain why direct flashes of lightning have not been optically detected up to now. Similar to Desch et al. (2006), we presume that SED activity is related to vertical convection driving the water cloud up to the visible atmospheric level, where it has been observed as bright eruptions by Cassini/ISS (Porco et al. 2005; Dyudina et al. 2007) overshooting the uppermost ammonia cloud layer (see also Fig. 2). We have sketched such an updrafting water cloud in Fig. 5, which has been theoretically modeled by Hueso and Sánchez-Lavega (2004). They conclude that water storms on Saturn are more difficult to trigger compared to Jupiter, but they can be very energetic reaching vertical velocities of the order of 150 m s^{-1} . Since external sunlight does not penetrate much further than down to the pressure level around 2 bars, Saturn's weather at deep pressure levels is most likely driven by an internal source of energy, which exhibits thermal gradients initiating the upward convection of the water cloud (Desch et al. 2006).

SEDs might originate from a pressure level around 8 to 10 bars, roughly 200 to 300 km below the 1-bar level. The temperature at those levels is around 255–275 K, which is the same temperature range at which most cloud particles get charged in terrestrial thunderclouds and where the strongest electric fields can be found (Rakov and Uman 2003). At such high pressure levels the breakdown electric field should be higher than in terrestrial thunderclouds. Roussel-Dupré et al. (2008, this issue) found that the hydrogen-helium atmosphere of Saturn decreases the critical electric field necessary for breakdown, in the case of conventional breakdown by a factor of 2, and for runaway breakdown by a factor of 6.3 compared to air at Earth. This has to be linearly related to the gas particle density at standard conditions ($\sim 2.65 \times 10^{25} \text{ m}^{-3}$ at 1 bar and 0°C). At the SED source the particle density should be a factor of ~ 10 higher, leading to a conventional breakdown field of $\sim 1.5 \times 10^7 \text{ V m}^{-1}$ being a factor of ~ 5 above the terrestrial one. Similarly, the threshold field for runaway breakdown at Saturn's 10-bar level would be $\sim 3.4 \times 10^5 \text{ V m}^{-1}$ or a factor of ~ 1.6 above the terrestrial value. These higher breakdown fields would allow more

charges to accumulate before it comes to a breakdown, which supports the idea that Saturn lightning is more powerful than Earth as well as Jupiter lightning.

8 Phenomena Related to Saturn Lightning

8.1 Whistlers at Saturn

The observation of a whistler at Saturn was reported by Akalin et al. (2006). It was detected by the Wideband Receiver of RPWS on October 28, 2004, on a magnetic field line with an L -shell value of $L \approx 6.5$. The whistler signal lasted for about 2 seconds and was recorded in a frequency range of 200–400 Hz, and Akalin et al. (2006) measured a dispersion of $81 \text{ Hz}^{1/2} \text{ s}$. Using a model for the plasma distribution along the magnetic field line they concluded that the whistler originated in the northern hemisphere of Saturn at an invariant latitude of 67° . Another whistler was possibly detected in spring 2007 and is currently under investigation.

The scarcity of whistler observations so far is probably due to the very restrictive conditions for their detection. First, the spacecraft must be relatively close to the planet. Second, the causative lightning must occur very close to the foot of the magnetic field line that passes through Cassini. Third, appropriate wideband observations without interference, such as from Cassini's reaction wheels, must be available. It is easy to explain why Cassini did not detect whistlers during SED activity, as the lightning storms were either located at the equator or at a planetocentric latitude of 35° South, the latter corresponding to $L \approx 1.44$. Only during SOI was Cassini that close to Saturn, but no SEDs were detected at that time, and for most detected SEDs Cassini was even outside of Saturn's magnetosphere. However, there is no good explanation why RPWS did not detect SEDs around the whistler event of October 2004.

8.2 Could There Be a Global Atmospheric Circuit at Saturn?

Aplin (2006) discusses the question of the existence of a global atmospheric circuit at Saturn driven by Saturn lightning. Aplin (2006) argues that some necessary conditions for an electric circuit are not fulfilled at the gas planets like two conductive layers (ionosphere and “surface”) relative to a less conductive atmosphere. Sentman (1990) modeled the conductivity of Jupiter's shallow interior and suggested the existence of a planetary-ionosphere cavity, where Schumann resonances could be excited between the ionosphere and the so-called conduction boundary depending on the wave frequency. A similar model for Saturn is presented in this book, where Simões et al. (2008, this issue) calculated the frequencies of 0.93 Hz, 1.63 Hz, and 2.34 Hz as the three lowest Schumann eigenmodes with a Q-factor around 7.

8.3 Sprites, Elves, and Gamma Ray Flashes at Saturn?

We note that the content of this subsection is rather speculative as neither sprites, nor elves or gamma ray flashes have been detected at Saturn. However, our increasing knowledge about these phenomena at Earth allows us to consider their existence at other planets.

Terrestrial (red) sprites are transient optical emissions above thunderstorms at mesospheric altitudes of 40–90 km. They are believed to be caused by conventional breakdown or runaway electrons due to a strong electrostatic field, which is often produced by a strong

Table 2 A comparison between Saturn and Earth lightning

Saturn lightning	Earth lightning
<ul style="list-style-type: none"> • Sporadic occurrence, but SEDs can go on for several weeks to months with a highly variable flash rate • Flash duration few hundred ms • Spectral radio power ~ 100 W/Hz, but not necessarily “superbolts” • Nearly flat spectrum (up to 20 MHz) • Highly polarized due to propagation in Saturn’s ionosphere • Giant convective storm systems (~ 3000 km in diameter) • Up to now SEDs only observed at equator and 35° South (makes whistler observations difficult) • SED source probably in updrafting water clouds at 8–10 bar • Elves more likely than sprites (modeling needed); gamma ray flashes hardly detectable from space 	<ul style="list-style-type: none"> • Permanent presence of ~ 100 flashes per second, but typically only a few hours at one place • Similar flash duration as SEDs • Power in radio range at a few MHz smaller by factor of $\sim 10^4$ • Spectral fall-off with $1/f^2$ (> 1 MHz) • TIPPs but not return strokes get polarized in Earth’s ionosphere • Individual storms of few tens of km, but grouping possible (“mesoscales”) • Most lightning over land in tropical regions and much less frequent at high latitudes • Charge separation in thunderclouds at a few km altitude around freezing level • Existence of sprites, elves, and gamma ray flashes established in recent years

positive cloud-to-ground stroke (Rakov and Uman 2003). Elves are lightning-induced luminous discs expanding horizontally in a circular form with an observed duration less than 1 ms (Fukunishi et al. 1996). The likely source of elves is the interaction of lightning return-stroke radiation fields with the electrons of the lower ionosphere. The existence of high altitude discharges at Earth was in fact anticipated by Wilson (1956) as the lower gas density at high altitudes combined with thunderstorm electric fields should allow electron acceleration and breakdown.

For the existence of sprites it is necessary that the local thunderstorm electric field exceeds the critical field E_k for conventional breakdown for an interval long enough for the formation of a “streamer”. Roussel-Dupré et al. (2008, this issue) found that the scaled critical electric field E_k/N (divided by the particle density N) for Saturn’s hydrogen atmosphere is about half of that of air or ~ 60 Td (1 Townsend (Td) = 10^{-21} V m 2). We have no knowledge of Saturn’s thunderstorm electric fields, and a macro-physical model would be required for their estimation. We note that an electrostatic dipole field decreases with $1/r^3$ with r as the distance, whereas a lightning radiation field decreases only with $1/r$. Given the extraordinary radio power of SEDs compared to Earth lightning, the existence of elves at Saturn seems more probable than the existence of sprites.

Terrestrial gamma ray flashes (TGFs) were observed by the Burst and Transient Signal Experiment onboard the Compton Gamma Ray Observatory and were related to thunderstorms by Fishman et al. (1994). The source location of TGFs is not yet exactly known; Williams et al. (2006) inferred a source altitude around 15–21 km, i.e. not so far from the thundercloud tops. An important issue for the detection of TGFs is their attenuation in the terrestrial atmosphere. Suszynsky et al. (1996) show an attenuation length of about 100 m for gamma rays with energies in the MeV-range at standard conditions in air, which corre-

sponds to a mass thickness of 11 g cm^{-2} . A mass thickness of the same order of magnitude can be expected in Saturn's atmosphere at the 10-bar level, as the 10 times higher particle density is compensated by a factor of 14 being the ratio between the molecular masses of air and H_2 . Hence, the attenuation length close to the SED source at 10 bar would be $\sim 140 \text{ m}$, which would make their detection with satellites impossible. We estimate that gamma rays caused by bremsstrahlung of runaway electrons at Saturn would be only detectable by satellites in case their source region is above the 100 mbar pressure level, which is 100 km above the 1-bar level.

9 Summary: A Comparison between Saturn and Earth Lightning

Instead of a written summary we present Table 2 comparing the most important properties of Saturn lightning mentioned in this paper with terrestrial lightning (Rakov and Uman 2003).

References

- F. Akalin, D.A. Gurnett, T.F. Averkamp et al., *Geophys. Res. Lett.* **33**, L20107 (2006)
- S.K. Atreya, A.-S. Wong, *Space Sci. Rev.* **114**, 121–136 (2004)
- K.L. Aplin, *Surv. Geophys.* **27**, 63–108 (2006)
- K.H. Baines, A.A. Simon-Miller, G.S. Orton et al., *Science* **318**, 226–229 (2007)
- W.J. Borucki, M.A. Williams, *J. Geophys. Res.* **91**(D9), 9893–9903 (1986)
- W.J. Borucki, C.P. McKay, D. Jebens, H.S. Lakkaraju, C.T. Vanajakshi, *Icarus* **123**, 336–344 (1996)
- J.A. Burns, M.R. Showalter, J.N. Cuzzi, R.H. Durisen, *Icarus* **54**, 280–295 (1983)
- J.E.P. Connerney, J.H. Waite, *Nature* **312**, 136–138 (1984)
- A.F. Cook, T.C. Duxbury, G.E. Hunt, *Nature* **280**, 794–795 (1979)
- M.D. Desch, G. Fischer, M.L. Kaiser et al., in *Planetary Radio Emissions VI*, ed. by H.O. Rucker, W.S. Kurth, G. Mann (Austrian Academy of Sciences Press, Vienna, 2006), pp. 103–110
- S.J. Desch, W.J. Borucki, C.T. Russell, A. Bar-Nun, *Rep. Prog. Phys.* **65**, 955–997 (2002)
- U.A. Dyudina, A.P. Ingersoll, A.R. Vasavada, S.P. Ewald, the Galileo SSI Team, *Icarus* **160**, 336–349 (2002)
- U.A. Dyudina, A.D. Del Genio, A.P. Ingersoll et al., *Icarus* **172**, 24–36 (2004)
- U.A. Dyudina, A.P. Ingersoll, P.E. Shawn et al., *Icarus* **190**, 545–555 (2007)
- D.R. Evans, J.H. Romig, C.W. Hord et al., *Nature* **299**, 236–237 (1982)
- D.R. Evans, J.H. Romig, J.W. Warwick, *Icarus* **54**, 267–279 (1983)
- W.M. Farrell, M.L. Kaiser, M.D. Desch, *Geophys. Res. Lett.* **26**, 2601–2604 (1999)
- W.M. Farrell, M.L. Kaiser, G. Fischer et al., *Geophys. Res. Lett.* **34**, L06202 (2007)
- G. Fischer, M.D. Desch, P. Zarka et al., *Icarus* **183**, 135–152 (2006a)
- G. Fischer, W. Macher, M.D. Desch et al., in *Planetary Radio Emissions VI*, ed. by H.O. Rucker, W.S. Kurth, G. Mann (Austrian Academy of Sciences Press, Vienna, 2006b), pp. 123–132
- G. Fischer, W. Macher, D.A. Gurnett et al., *Geophys. Res. Lett.* **33**, L21201 (2006c)
- G. Fischer, W.S. Kurth, U.A. Dyudina et al., *Icarus* **190**, 528–544 (2007a)
- G. Fischer, D.A. Gurnett, A. Lecacheux, W. Macher, W.S. Kurth, *J. Geophys. Res.* **112**, A12308 (2007b)
- G.J. Fishman, P.N. Bhat, R. Mallozzi et al., *Science* **264**, 1313–1316 (1994)
- H. Fukunishi, Y. Takahashi, M. Kubota et al., *Geophys. Res. Lett.* **23**, 2157–2160 (1996)
- S. Gibbard, E.H. Levy, J.I. Lunine, *Nature* **378**, 592–595 (1995)
- D.A. Gurnett, R.R. Shaw, R.R. Anderson, W.S. Kurth, *Geophys. Res. Lett.* **6**, 511–514 (1979)
- D.A. Gurnett, P. Zarka, R. Manning et al., *Nature* **409**, 313–315 (2001)
- D.A. Gurnett, W.S. Kurth, D.L. Kirchner et al., *Space Sci. Rev.* **114**, 395–463 (2004)
- D.A. Gurnett, W.S. Kurth, G.B. Hospodarsky et al., *Science* **307**, 1255–1259 (2005)
- R. Hueso, A. Sánchez-Lavega, *Icarus* **172**, 255–271 (2004)
- M.L. Kaiser, J.E.P. Connerney, M.D. Desch, *Nature* **303**, 50–53 (1983)
- M.L. Kaiser, M.D. Desch, J.E.P. Connerney, *J. Geophys. Res.* **89**(A4), 2371–2376 (1984)
- A.A. Konovalenko, A. Lecacheux, H.O. Rucker et al., European Planetary Science Congress, Berlin, Germany, 2006, p. 229
- W.S. Kurth, D.A. Gurnett, F.L. Scarf, *Icarus* **53**, 255–261 (1983)
- A. Lecacheux, F. Biraud, in *CNES Planetary Rings*, 1984, pp. 319–324

- B. Little, C.D. Anger, A.P. Ingersoll et al., *Icarus* **142**, 306–323 (1999)
- C.C. Porco, R.A. West, S. Squyres et al., *Space Sci. Rev.* **115**, 363–497 (2004)
- C.C. Porco, E. Baker, J. Barbara et al., *Science* **307**, 1243–1247 (2005)
- V.A. Rakov, M.A. Uman, *Lightning, Physics and Effects* (Cambridge Univ. Press, Cambridge, 2003)
- K. Rinnert, L.J. Lanzerotti, M.A. Uman et al., *J. Geophys. Res.* **103**, 22,979–22,992 (1998)
- R. Roussel-Dupré, J. Colman, E. Symbalisty, D. Sentman, V. Pasko, *Space Sci. Rev.* (2008, this issue)
- D.D. Sentman, *Icarus* **88**, 73–86 (1990)
- X.M. Shao, A.R. Jacobson, *J. Geophys. Res.* **107**(D20), 4430 (2002)
- F. Simões, M. Rycroft, N. Renno et al., *Space Sci. Rev.* (2008, this issue)
- D.M. Suszcynsky, R. Roussel-Dupré, G. Shaw, *J. Geophys. Res.* **101**, 23505–23516 (1996)
- J.W. Warwick, J.B. Pearce, R.G. Peltzer, A.C. Riddle, *Space Sci. Rev.* **21**, 309–327 (1977)
- J.W. Warwick, J.B. Pearce, D.R. Evans et al., *Science* **212**, 239–243 (1981)
- J.W. Warwick, D.R. Evans, J.H. Romig et al., *Science* **215**, 582–587 (1982)
- E. Williams, R. Boldi, J. Bór et al., *J. Geophys. Res.* **111**, D16209 (2006)
- C.T.R. Wilson, *Proc. R. Soc. Lond.* **236**, 297 (1956)
- Y. Yair, Z. Levin, S. Tzivion, *Icarus* **115**, 421–434 (1995)
- Y. Yair, G. Fischer, F. Simões, N. Renno, P. Zarka, *Space Sci. Rev.* (2008, this issue). doi:[10.1007/s11214-008-9349-9](https://doi.org/10.1007/s11214-008-9349-9)
- P. Zarka, in *Planetary Radio Emissions I*, ed. by H.O. Rucker, S.J. Bauer (Austrian Academy of Sciences Press, Vienna, 1985a), pp. 161–182
- P. Zarka, *Astron. Astrophys.* **146**, L15–L18 (1985b)
- P. Zarka, B.M. Pedersen, *J. Geophys. Res.* **88**(A11), 9007–9018 (1983)
- P. Zarka, J. Queinnec, B.P. Ryabov et al., in *Planetary Radio Emissions IV*, ed. by H.O. Rucker, S.J. Bauer, A. Lecacheux (Austrian Academy of Sciences Press, Vienna, 1997), pp. 101–127
- P. Zarka, W.M. Farrell, M.L. Kaiser, E. Blanc, W.S. Kurth, *Planet. Space Sci.* **52**, 1435–1447 (2004)
- P. Zarka, B. Cecconi, L. Denis et al., in *Planetary Radio Emissions VI*, ed. by H.O. Rucker, W.S. Kurth, G. Mann (Austrian Academy of Sciences Press, Vienna, 2006), pp. 111–122
- P. Zarka, W.M. Farrell, G. Fischer, A. Konovalenko, *Space Sci. Rev.* (2008, this issue). doi:[10.1007/s11214-008-9366-8](https://doi.org/10.1007/s11214-008-9366-8)

Atmospheric Electricity Hazards

Ralph D. Lorenz

Originally published in the journal Space Science Reviews, Volume 137, Nos 1–4.
DOI: [10.1007/s11214-008-9364-x](https://doi.org/10.1007/s11214-008-9364-x) © Springer Science+Business Media B.V. 2008

Abstract Atmospheric electricity, and electrostatic discharge in general, can be a significant hazard to aircraft, spacecraft and personnel.

Keywords Lightning injury · Electrocution · Electrostatic discharge · Hazards

1 Introduction

Atmospheric electricity is responsible for a hazard, lightning, that kills perhaps several thousand people worldwide each year: within the USA where statistics are documented quite well by the National Oceanographic and Atmospheric Administration (NOAA), roughly 100 people are killed and 1000 injured annually. The first measures to protect against lightning began in America (albeit not yet the United States—Franklin's advocacy of grounded rods to protect buildings against lightning began in the 1750's, before independence)

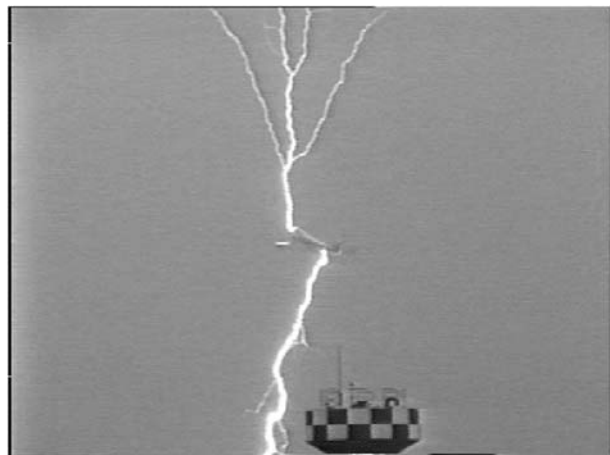
As we discuss later, lightning is responsible for the failure of space launch vehicles, and protective measures are installed on many space probes to other planets, as well as to terrestrial aircraft. More generally, lightning causes economically significant damage—half of wildfires are caused by lightning, requiring an effort of $\sim \$100M/yr$ to fight, some $\sim 5\%$ of all insurance claims are lightning-related, including some $\sim 30,000$ house fires in the 1991–1995 period alone ($\$176M$ damage) and about 30% of power outages are lightning-related.

While lightning is the most obvious atmospheric electricity hazard, there are a number of others, and electrostatic discharge (ESD) and related effects are a known problem in electronic aerospace vehicle design and operation. We briefly review these issues, as well as summarize the various causes and mechanisms of damage and injury. For further reading on lightning effects on aircraft (e.g. Fig. 1), structures and people, there are several excellent

Presented at the International Space Studies Institute Workshop on Atmospheric Electricity, Bern, Switzerland, July 2007.

R.D. Lorenz (✉)
Johns Hopkins University Applied Physics Laboratory, Laurel, MD, USA
e-mail: ralph.lorenz@jhuapl.edu

Fig. 1 Video frame of a lightning strike to a jet aircraft just after takeoff. (Courtesy of Zen Kawasaki and the Self Defense Air Force of Japan)



chapters in the formidable book by Rakov and Uman (2003). For spacecraft hazards specifically, a recent overview is by Harland and Lorenz (2005) and several NASA publications (e.g. Leach and Alexander 1995 and Herr and McCollum 1994) are worthwhile starting points.

Lightning conductors, sometimes referred to as Franklin rods, have prevented untold damages to buildings over the centuries since their application was first advanced. Ironically, many churches suffered lightning damage by failing to install such protection (lightning being considered ‘God’s will’, and thus a worthy church would not require protection).

2 Electrical Effects on Humans

Electrical currents, like our neural signals, cause muscle contractions. When humans are shocked these contractions can lead to injury by causing people to fall, and if the heart muscle is affected, its rhythm may be disrupted causing death. In the early days of the municipal supply of electricity when rival (AC and DC) systems fought to become a standard, the relative safety of the two types was used as an argument to advocate one versus the other. In fact both types are dangerous, but in different ways. AC current is more likely to cause ventricular fibrillation, while DC is more likely to cause burns. Typically, currents may cause muscles to spasm and in the case of DC acquired by manually grasping a conductor, the current forces the hand to clamp onto it, leading to sustained currents and thus burns.

While it is ‘the current that kills’, a certain potential difference is required to cause that current. Skin typically has a resistance (depending on sweatiness and the specific path through or across the body) of 1000 to several thousand ohms. People will begin to feel an electric shock with currents of a few millamps (requiring some tens of volts at least), while 10–20 mA is enough to contract major muscles (the ‘cannot let go’ current). Pain, heart fibrillation and breathing difficulty can be caused by currents above 50 mA and currents above 100 mA can be fatal. Heart defibrillators may typically operate (for short periods) at several amps. Note that from Ohm’s law, a current of one amp will require kilovolt potential, and therefore hundreds of kilowatts: the possibility of acquiring burns in such situations can therefore be understood.

Beyond the use of electrocution to inflict the death penalty, the nonlethal application of electric shocks to cause temporary incapacitation for personal protection and law enforce-

ment has reached some prominence in recent years. Specifically, a device called the Taser (actually a name taken from science fiction—"Thomas A Swift's Electric Rifle") applies a controlled current of 2–4 mA with a potential of 50 kV applied across two adjacent electrodes at the end of a baton or more typically between two needles projected on fine wires a few meters long by springs. The device causes muscle spasm and pain without likely heart fibrillation in healthy adults (although some controversy remains about dangers to individuals with heart problems). The induced spasms cause paralysis while the shock is applied, and lactic acid buildup in the contracted muscles will cause sustained weakness and pain, increasing with the length of applied voltage. These devices have become sufficiently widespread that many also include video cameras to document their application (hopefully for legal purposes). While these devices, like any other weapon, may have controversial applications, they at least provide an option in many settings that is at least less obviously lethal than firearms.

Returning briefly to lightning, about a third of lightning deaths occur among outdoor workers such as farmers, while a similar proportion are associated with outdoor recreation. Very few injuries occur indoors, for obvious reasons: those that do occur are usually the result of contact with conductors such as telephone cabling or plumbing that is struck elsewhere. When death is caused, it is usually by ventricular standstill. Although local burning at the discharge site is common, serious burns are in fact rather rare in lightning injury due to the short application of current. Survivors may have muscle pains and neurological damage (personality change, seizures, deafness—often due to eardrum rupture, confusion or eye damage) which may persist for years after the event.

In addition to direct lightning strikes (to which upright individuals in flat areas are particularly prone) and conducted ESD via telephone wires, people can be injured by induced currents near lightning strikes to the ground—in such settings the horizontal field is the threat and thus individuals sheltering from a storm under a tree would be advised (if they must remain in such a threatening location) to lie circumferentially rather than radially to it. It may be noted that quadruped mammals such as cows are particularly susceptible to currents flowing up forelimbs and down through hindlimbs (or vice versa), the currents passing through their heart. Multiple livestock deaths from a single lightning strike can arise this way.

3 Electrostatic Discharge Effects on Electronics

Electrostatic discharge is estimated to be responsible for perhaps 30% of all electronic failures, although good statistics are hard to acquire. As a general industrial problem, it has been an issue (in powder magazines) since the 1400 s, and specific countermeasures (grounding and flame ionization etc.) have been in operation since 1860. There is even an industrial association (www.esda.org).

Many electronic devices are destroyed by high voltages—in some cases only a few tens of volts, but quite typically a few hundred. Damage thresholds for JFETs can be as low as 150 V, although bipolar transistors are much more robust. Because modern systems are so miniaturized, the charge transfer or ohmic heating needed to destroy a single gate (or diode, resistor, etc.)—and only a single component on a large and expensive chip need be damaged to render the whole part unusable—is very small. The voltage threshold for damage is readily exceeded triboelectrically—walking across a carpet in low-humidity conditions may develop potentials of 35 kV (although perhaps only 2 kV in conditions of 60–90% relative humidity). A part damaged by ESD may show no external signs of damage, and

may even display partial or complete function before failing later. Thus ESD is a major hazard, although precautions such as conductive bags for parts and grounding straps for personnel are effective countermeasures.

Impingement of charged particles onto an antenna can cause substantial voltage noise, and this is the likely principal source of radio noise encountered during dust storms. (The association of radio noise with dust storms was noticed even as early as the first world war.)

While not atmospheric electricity as such, some spacecraft ESD issues merit mention. First, high voltages are required for the operations of some systems such as travelling wave tube amplifiers, mass spectrometers, etc., and may even be encountered on simple antennas. While these voltages may not cause breakdown in vacuum, nor under terrestrial surface (1 bar) conditions, if these systems are powered on when they are exposed to thin atmospheres with low breakdown potential, discharge may occur. This typically happens under a couple of circumstances. One is during launch—as the rocket ascends into thinner air, the pressure in the fairing slowly declines. Similarly transient conditions may occur during ground tests as a chamber is pumped down from 1 bar to vacuum conditions. The other transient thin atmosphere may occur due to outgassing from films of adsorbed moisture or solvents, etc., particularly in plastic materials. If high voltage devices are switched on in these conditions of microbar to tens of millibar pressures, a breakdown discharge may occur.

Note that the declining pressure experienced during launch may be experienced in reverse in vehicles that enter or re-enter planetary atmospheres. The surface conditions at Mars are of particular concern, since the pressure of several millibars is close to the minimum of the Paschen curve, and thus relatively modest potential gradients can cause discharge.

Other discharge can occur in space if surfaces acquire unusually high potentials due to the implantation of charged particles. This so-called deep dielectric discharge occurs during particularly energetic magnetospheric or solar wind conditions on slabs of insulating material. The charged particles have sufficient energy to penetrate the material, where they deposit their charge, but because the material is insulating, this charge can accumulate. When a large enough charge builds up, a breakdown across the surface may occur.

Whatever the cause of the discharge, there can be several deleterious effects (e.g. Leach and Alexander 1995). The discharge may cause conducted or radiated transient signals in nearby circuits—a corrupted telemetry packet is a common result. Similarly, systems performing pulse-counting such as the angular encoders on rotating parts such as antenna despun mechanisms may develop erroneous counts due to spurious pulses. The current associated with a discharge may destroy a conductor by resistive heating causing melting or evaporation. Evaporated materials (whether metals or others) may be redeposited on other surfaces, leading to electrical shorts, optical obscuration, or indirect overheating due to emissivity or absorptivity changes. Examples of such events include the Canadian comsat Anik D2 which suffered a transient glitch due to ESD—although it recovered many components remained at elevated temperatures after the event due to degradation of thermal coatings. The ESA comsat MARECS-A suffered reduced solar array output due to materials deposited on the panels by ESD.

ESD may occur in planetary environments too, where triboelectric effects occur. Blowing dust or sand (Schmidt et al. 1998) is a particular example—blowing sand can accumulate a charge of some 60 mC/kg. It is known that the Russian lander Mars 3 touched down on the Martian surface during a dust storm. Although it is commonly assumed that it toppled over in high winds, a simple inspection of the vehicle configuration shows that this is rather unlikely. Furthermore, the systems operated for 20 seconds after landing before suddenly failing. ESD therefore seems a more plausible scenario.

Charge may be picked up by vehicles ‘flying’ through soils—penetrators. In one experiment (Lorenz and Shandera 2002) a 0.65 kg penetrator shot through dry sand at 40 m/s developed some 3 mA of current for 3 ms, or some 9 uC of charge. Without ballasting capacitors into which to dump such charge, large potentials can be developed, causing ESD damage. Efforts to explore this effect as a possible diagnostic of subsurface composition were unsuccessful, however.

4 Aerospace Vehicle Damage by Lightning and ESD

Lightning strikes to aircraft may occur naturally, with an aircraft merely ‘getting in the way’, although as we discuss later, the presence of the conductive aircraft can trigger lightning discharges where none were previously present. Strikes to commercial airliners occur typically at modest altitudes (up to 6 km, or 20,000 ft—below the typical cruise altitude of jets). On average such aircraft are struck once per 3000 hours. Usually no damage occurs, although a handful of fatal accidents are attributed to lightning strikes (electrical failure causing control difficulties, or in rare cases fuel ignition). A particularly challenging surface to protect is the radome (which is necessarily nonconducting). In cases where there is only minor damage to an aircraft, disrupted radio communications, and magnetic compass offsets are the most typical effect. Lightning and its effects was the subject of study by a dedicated NASA F106B lightning research aircraft (Fig. 2). This aircraft was flown 421 times into clouds seen to have lightning, and was struck 176 times, with 54 near-misses.

Aircraft flying through clouds of charged droplets naturally acquire the charge of those drops that are large enough to impinge upon the vehicle surface. This effect was noted by early aviators who often experienced an electric shock upon alighting from their planes on the ground—this was because the planes had rubber tail wheels, allowing them—and their pilots—to retain their charge after landing. It was soon realized that a conductive skid would allow the aircraft to discharge itself on landing.

One other corrective measure that can be applied is the use of narrow rods to provide locations for point discharge. These discharge wicks are often simply carbon fiber rods, typically mounted on the trailing edge of the wing (Fig. 3): these allow any accumulated charge from cloud droplets to be gradually discharged away, without an impulsive breakdown. As a result of difficulties with the Pioneer Venus probes (which in the end proved to be a materials incompatibility, rather than anything to do with electrostatics) the Galileo probe was equipped with such discharge wicks. The Huygens probe was similarly protected.

Fig. 2 NASA F-104 Lightning research aircraft. The paint has been burned off in hundreds of locations where lightning strikes hit the airframe



Fig. 3 Trailing edge of a commercial airliner—note the narrow discharge wicks to allow accumulated electrical charges to dissipate. (Photo: R Lorenz)

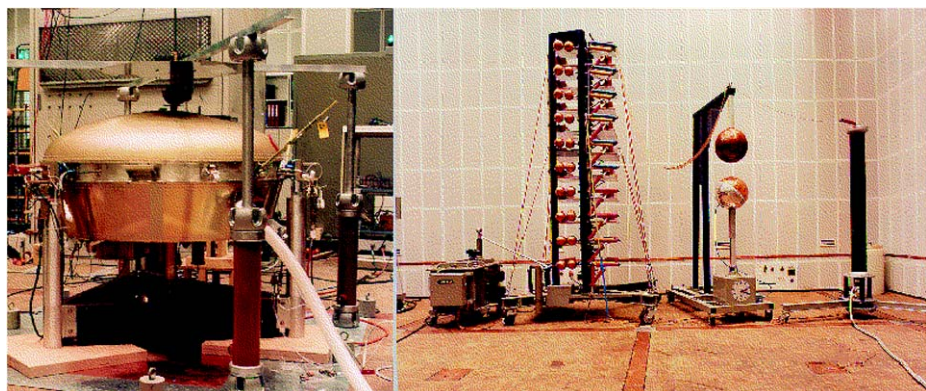


Fig. 4 The ESA Huygens probe (inverted) being set up for electrostatic discharge tests—several kA were applied to the probe's shell, demonstrating that the probe systems continued to function after simulated lightning strike. (Photos: ESA)

External sensors are of course particularly vulnerable. In general space probes are constructed of metals, which are therefore conductive and protect the interior equipment as a Faraday cage. Induced or radiated fields can nonetheless occur. The Huygens probe was tested before launch with 1–5 kA pulses (with 50 kA/ms rise time) applied to its shell from a large Marx generator (Fig. 4). The probe suffered no damage, although telemetry saw occasional corruption ‘hiccups’ (<6 secs). The probe’s robustness was demonstrated by the complete crash of electrical ground support equipment which was some 6 m away and completely isolated from the probe—this equipment had to be reset.

Aircraft, like ships before them, may experience luminous point discharges during electrically active storms—these discharges go by the collective name of ‘St Elmo’s Fire’. Such discharges are usually harmless, although associated radio noise (and sometimes impaired cockpit visibility) are often encountered.

Aircraft can cause lightning to occur where none is observed if they act as a long conductor which intensifies an existing electrical field. Particular examples are launch vehicles (where the hot part of the rocket exhaust, ionized and therefore conductive, serves as an extension of the vehicle itself) or aircraft towing gunnery targets by conductive cables.

The most celebrated launch vehicle lightning strike is Apollo 12 which was struck just over 35 seconds into ascent—the strike caused several circuits and systems to go off-line. A more recent example, which prompted the revision of launch rules to avoid heavy cloud and electric fields—an Atlas-Centaur from Kennedy Space Center (Florida is one of the most



Fig. 5 Atlas-V launch from Kennedy Space Center in Florida. Note the 4 towers to attract lightning away from the launch vehicle itself on the launch pad. Note also the long, luminous (and partly conductive) exhaust which augments any preexisting electric fields. (Photo: NASA)

lightning-active regions of the USA) carrying a communications satellite was struck soon after launch in March 1987, leading to a \$161 Million loss. Because launch vehicles are tall structures that offer a preferred site for cloud-to-ground discharge, lightning protection measures are installed on launch pads (Fig. 5).

Lightning can be a hazard to spacecraft on the ground. For example, lightning triggered premature launch of an Orion sounding rocket (and two smaller calibration rockets) from Wallops Island in June 1987. Although the firing circuits of these rockets were nominally shorted out by safe-arm plugs, the currents induced by the lightning strike were nonetheless high enough to cause ignition. At the time the rocket was mounted in a near-horizontal position and flew several hundred meters before hitting the sea. Ironically the rocket was intended to study lightning effects on the ionosphere. “We were hoping for lightning. We just had it a little closer than we would like,” said Warren Gurkin, Head of NASA Wallops sounding rocket branch.

5 Conclusions

Lightning and electrical discharge is a recognized hazard on Earth for personnel, structures and vehicles. Prudent design of equipment destined for other planets needs to design against not only the terrestrial hazard (to which systems are exposed before they reach their destination), but also the space hazards associated with deep dielectric discharge or outgassing, and the hazards particular to the target body.

On bodies such as Jupiter where the lightning hazard is known to exist, protective measures are similar to those on Earth. Mars is a particularly interesting setting, in that the breakdown field strength in the near-surface atmosphere is low: this may cause electrostatic effects to be common (but perhaps mild in intensity, such that normal engineering design practices against ESD damage are adequate). On Titan and Venus the case for lightning is arguable—the electrically insulating environment of cold Titan may make triboelectric effects significant. On airless bodies, charge separation seems difficult, but electrostatic effects may play a major role in dust adhesion.

Acknowledgements RL acknowledges the support of NASA via the Cassini Project (Huygens SSP Co-Investigator) at JPL.

References

- D.M. Harland, R.D. Lorenz, *Space Systems Failures* (Praxis-Springer, 2005)
- J.L. Herr, M.B. McCollum, Spacecraft environment interactions: Protecting against the effects of spacecraft charging. NASA RP-1354, 1994
- R.D. Leach, M.B. Alexander (eds.), Failures and anomalies attributed to spacecraft charging. NASA RP-1375, 1995
- R.D. Lorenz, S.E. Shandera, Target effects during penetrator emplacement: Crushing, heating and triboelectric charging. *Planet. Space Sci.* **50**, 141–157 (2002)
- V.A. Rakov, M.A. Uman, *Lightning, Physics and Effects* (Cambridge University Press, Cambridge, 2003)
- D.S. Schmidt, R.A. Schmidt, J.D. Dent, Electrostatic force on saltating sand. *J. Geophys. Res.* **103**(D8), 8997–9001 (1998)

Electrical Effects on Atmospheric Chemistry

Ralph D. Lorenz

Originally published in the journal Space Science Reviews, Volume 137, Nos 1–4.
DOI: [10.1007/s11214-008-9360-1](https://doi.org/10.1007/s11214-008-9360-1) © Springer Science+Business Media B.V. 2008

Abstract Electrical discharges in planetary atmospheres, and lightning in particular, can cause otherwise unexpected—but highly important—chemical species to be present. The synthesis of oxidants on Mars, nitrates on Earth and Early Mars, and of organic matter elsewhere can be driven by lightning and related electrical phenomena.

Keywords Lightning · Ozone · Nitrogen fixation · Atmospheric chemistry

1 Introduction

Lightning is an exceptional phenomenon, and its occurrence leads to exceptional chemistry. In this paper we review briefly the role of electrical discharges in creating several important gas species that would otherwise not be present in significant amounts. Lightning-induced chemistry may have been significant in the evolution of the composition of Titan's atmosphere, in the present-day production of oxidants in the Martian near-surface environment, and in the production of nitrate nutrients and prebiotic molecules on the early Earth and Mars.

2 Chemistry in the Lightning Discharge

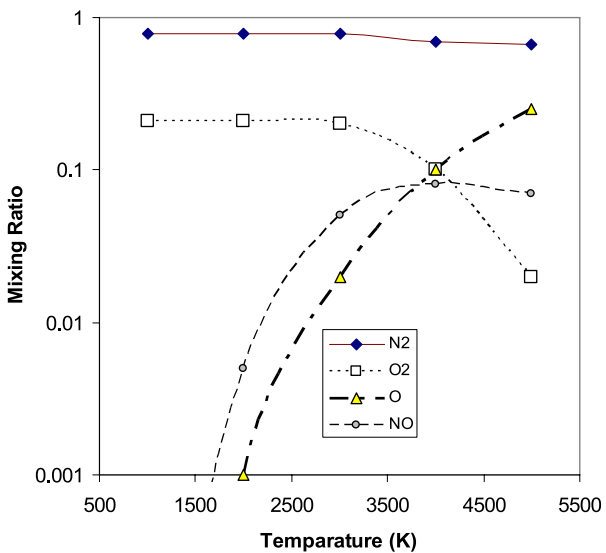
A given collection of atoms such as those in a parcel of air at given pressure and temperature conditions has a preferred molecular arrangement that minimizes free energy (or equivalently, maximizes entropy). This is the so-called equilibrium composition, and will be a function of the pressure and temperature—for example, higher pressure conditions tend, via Le Chatelier's principle, to favor the atoms being arranged to form fewer molecules and thus

Presented at the International Space Studies Institute Workshop on Atmospheric Electricity, Bern, Switzerland, July 2007.

R.D. Lorenz (✉)

Johns Hopkins University Applied Physics Laboratory, Laurel, MD 20723-6099, USA
e-mail: ralph.lorenz@jhuapl.edu

Fig. 1 Schematic of the equilibrium composition of the principal components of air. In a high-temperature discharge O and NO can become much more abundant than at normal conditions, and the rapid expansion of the lightning channel ‘freezes in’ this composition



lower volume. Similarly, the high-temperature conditions in a lightning discharge would favor a different composition from the ambient air. However, there is also a kinetics issue, in that as the lightning channel rapidly expands, some of the high-temperature composition is ‘frozen in’ as the expanded and cooled volume cannot readjust to the cooler equilibrium composition in time (while the equilibration time for typical reactions is microseconds at ~ 4000 K and milliseconds at 2500 K, it is centuries at 1000 K and below—see, e.g., Chameides 1979 or Borucki and Chameides 1984). Thus after a lightning discharge, the gas may contain chemical species that are not found in the equilibrium gas composition at that temperature.

A prime example is ozone (O_3). This molecule is created from molecular oxygen in two ways—by ultraviolet light in the stratosphere, and in the troposphere by lightning discharge. Corona discharge around power lines and in electrical equipment, notably laser printers and photocopiers, similarly can produce it yielding a characteristic ‘electrical’ smell. Humans can detect the smell of ozone at levels not much lower (0.02 ppm) than the recommended exposure limit (0.05 ppm) of this corrosive gas. Ozone, if it doesn’t oxidize some organic matter first, will exothermically convert into oxygen (O_2), and so its presence indicates disequilibrium and thus a nearby and/or recent electrical discharge ozone source.

However, ozone is probably not the most significant chemical species due to lightning in the Earth’s atmosphere. Nitric oxide (NO) is also produced in lightning discharges: in air it rapidly establishes equilibrium with nitrogen dioxide NO_2 , and thus the two together are often referred to as NO_x or sometimes (to contrast it from molecular nitrogen N_2) as ‘odd nitrogen’. NO_2 is rained out of the atmosphere to form nitric acid, and thus represents an important source of nitrogen for living things. In the modern world, the industrial generation of fertilizers by the Haber process is the dominant form of nitrogen fixation, initially producing NH_3 from N_2 in air by heating and pressure, then oxidizing the NH_3 into nitric acid. However, on the early Earth it is likely that lightning was the principal means by which nitrogen was made available for prebiotic and biological chemistry. There are some modern plants such as peas with root nodules containing symbiotic bacteria which can fix nitrogen, but in evolutionary terms these are very recent: nitrogen availability was likely a highly significant bottleneck for the origin and early evolution of life.

On present-day Earth, estimates (see Rakov and Uman 2003) are that lightning produces about 10–20% of the total NO budget, the majority coming from fossil fuel and biomass burning—these representing in a way the accumulation of NO_x in the past. Thus even today, but more so in the past, lightning was an important factor in creating odd nitrogen. One estimate is that the NO production relates to the lightning energy by the factor of 9×10^{16} molecules per Joule (Borucki and Chameides 1984).

Clearly, the ultimate composition will depend on the details of the discharge, but also on the starting composition of the gas mixture. On Titan, where oxygen-bearing species are merely traces in the atmosphere (but not perhaps on the surface—see later) if lightning occurs, then the principal effect is the rearrangement of carbon and nitrogen atoms. On Mars and Venus, CO_2 is the major component, with nitrogen being far less common. On Jupiter it may influence the production of acetylene.

3 Mars and Venus

On Mars, there is only $\sim 1\%$ nitrogen with the bulk of the atmosphere being CO_2 , so NO production might be expected to be less significant than on Earth. An upper limit on nitric oxide abundance has been established spectroscopically (Krasnopolksy 2006).

Lightning on any scale has yet to be observed on Mars, yet it seems likely that some sort of electrical discharge occurs in association with dust devils and dust storms. Such discharges have been identified (Delory et al. 2006) as being a key source of oxidants, in particular hydrogen peroxide H_2O_2 . This compound may be produced by discharge in amounts 200 times higher than those expected from photochemistry alone. In turn this H_2O_2 , or superoxides produced from it, may be responsible for scavenging organic molecules from the regolith (e.g. Atreya et al. 2006), accounting for the nondetection of such molecules by Viking even if some biota were present.

On the other hand, while discharges may be unfavorable towards life at present, the chemistry due to discharges might have been important in providing prebiotic molecules in the possible origin of life on that planet, or in providing nutrients for it. This is because Mars would have faced the same bottleneck of nitrogen fixation as does the Earth—lightning on early Mars, either associated with convective rainfall or more likely with volcanoes, may have produced significant amounts of nitrates and/or hydrogen cyanide (e.g., Segura and Navarro-Gonzalez 2003).

As for Venus, it was recognized quite early on (e.g., Bar-Nun 1980) that lightning could play a major role in the generation of NO. As with Mars, CO_2 is the bulk constituent, but molecular nitrogen makes up about 3.5% of Venus' massive cloud-laden atmosphere. While the existence of lightning on Venus has been long considered controversial since searches with different data types have given positive and negative results (see, e.g., the review by Ksanfomailly et al. 1983 and Krasnopolksy 2006), recent results from Venus Express (Russell et al. 2007) have been given as further support for its presence. Spectroscopic observations (Krasnopolksy 2006) claim to detect an abundance of NO of about 5.5 ppb below 60 km. This abundance is apparently consistent with lightning production. Bar-Nun (1980) notes that while the production by lightning of CO from CO_2 on Venus is overall small compared with the upper atmospheric production by photolysis, the local abundance in the lower atmosphere, far from the photolysis levels, might be enhanced significantly by lightning production.

4 Titan

Borucki et al. (1984) suggested that lightning on Titan could produce HCN and C₂N₂ in amounts that exceed significantly their estimated photochemical production (some other species such as soot and ethylene C₂H₄ would also be produced, but in less important amounts). Another potential, and perhaps more likely, scenario is that in the primordial Titan atmosphere (which may have contained ammonia, methane and some water vapor) lightning discharges may have been important in converting ammonia into molecular nitrogen (McKay et al. 1988). This conversion, which could also occur in impact shocks or perhaps by photolysis, may have been very important in Titan's atmospheric evolution, since molecular nitrogen is too volatile to have been readily incorporated into Titan when it formed in the protoSaturnian nebula—if it had been, then primordial ³⁶Ar should be present in much larger amounts than appears to be the case. Thus the nitrogen atoms were brought to Titan as much less volatile ammonia hydrates, and a mechanism to convert the ammonia into nitrogen is needed.

5 Jovian Planets

Remarkably little work—given the ample evidence for lightning on Jupiter at least—has been done on the chemical impact of lightning on the chemistry of the Jovian planets. As elsewhere, there is a challenge to isolate disequilibrium due to lightning from disequilibrium due to UV photolysis, although one factor is that UV may be absorbed by different species at different altitudes in an atmosphere, thereby preventing the excited radicals and ions from interacting, whereas they will be mixed together in a lightning discharge.

In the Jovian atmosphere, lightning may be a significant source of HCN (Stribling and Miller 1987) and possibly also acetylene (Bar-Nun and Podolak 1985). Indeed, Bar-Nun (1975) used the large abundance of acetylene detected on Jupiter even before the Voyager encounters with that world to argue that substantial lightning might occur there: there was also the suggestion (as yet unresolved) that lightning chemistry might influence the formation of the red and yellow compounds ('chromophores') that give Jupiter its angry appearance. Little work appears to have been done as yet on the chemical effects of lightning in other giant planet atmospheres.

6 Electrostatic Discharge Chemistry beneath the Atmosphere

Disequilibrium chemistry can be driven by lightning in materials other than the atmosphere—a lightning discharge may introduce into the plasma atoms from solid material that is struck. Lightning discharge through the ground can form dendritic, sometimes fused, structures called Fulgerites which crudely resemble tree roots. However, such structures are not merely the partly molten soil—some chemical modification also occurs. As in another disequilibrium environment (the quenching of the vapor cloud in a meteorite impact,) reduced materials may be produced, notably carbon and elemental iron (e.g., Scheffer 2007).

Plankensteiner et al. (2007) have also shown that discharges across the ice–air interface in a simulated Titan environment allow the oxygen in the water ice to participate in the carbon–nitrogen chemistry of the atmosphere to yield prebiotically important species such as nitriles, aldehydes and esters.

7 Conclusions

Electrical discharges may be an important source of disequilibrium chemical species in various planetary atmospheres. In this sense, electrical discharge acts much like ultraviolet light in photochemistry, in that it overcomes kinetic barriers and forms species that otherwise would form only slowly or not at all. Example reactions in particular are the generation of nitrogen species such as NO_x in the atmospheres of the terrestrial planets (notably the Earth). On Mars, discharges in dust devils may be responsible for producing oxidants which in turn may play a role in destroying organic molecules in the regolith. On Titan, lightning may have contributed to the formation of the molecular nitrogen atmosphere, and if lightning occurs at present, to other species. Lightning or other electrical discharges can force chemistry in substrates other than air, forming reduced material such as nanophase iron, or on Titan's surface, prebiotic molecules such as amino acids.

Acknowledgements RL acknowledges the support of NASA via the Cassini Project (Huygens SSP Co-Investigator) at JPL. The reviewers are thanked for useful comments on this chapter.

References

- S.K. Atreya, A.-S. Wong, N.O. Renno, W.M. Farrell, G.T. Delory, D.O. Sentman, S.A. Cummer, J.B. Marshall, S.C.R. Rafkin, D.C. Catling, Oxidant enhancement in Martian dust devils and storms: Implications for life and habitability. *Astrobiology* **9**, 439–450 (2006)
- A. Bar-Nun, Thunderstorms on Jupiter. *Icarus* **24**, 86–94 (1975)
- A. Bar-Nun, Production of carbon and nitrogen species by thunderstorms on Venus. *Icarus* **42**, 338–342 (1980)
- A. Bar-Nun, M. Podolak, The contribution by thunderstorms to the abundances of CO, C_2H_2 and HCN on Jupiter. *Icarus* **68**, 112–124 (1985)
- W.J. Borucki, W.L. Chameides, Lightning: Estimates of the rates of energy dissipation and nitrogen fixation. *Rev. Geophys. Space Phys.* **32**, 363–372 (1984)
- W.J. Borucki, C.P. McKay, R.C. Whitten, Possible production by lightning of aerosols and trace gases in Titan's atmosphere. *Icarus* **60**, 260–273 (1984)
- W.L. Chameides, Effect of variable energy input on nitrogen fixation in instantaneous linear discharges. *Nature* **277**, 123–125 (1979)
- G.T. Delory, W.M. Farrell, S.K. Atreya, N.O. Renno, A.-S. Wong, S.A. Cummer, D.O. Sentman, J.B. Marshall, S.C.R. Rafkin, D.C. Catling, Oxidant enhancement in Martian dust devils and storms: Storm electric fields and electron dissociative attachment. *Astrobiology* **9**, 451–462 (2006)
- V. Krasnopolsky, A sensitive search for nitric oxide in the lower atmosphere of Venus and Mars: Detection on Venus and upper limit for Mars. *Icarus* **192**, 80–91 (2006)
- L.V. Ksanfomailly, F.L. Scarf, W.W.L. Taylor, The electrical activity of the atmosphere of Venus, in *Venus*, ed. by D.M. Hunten et al. (University of Arizona Press, Tucson, 1983), pp. 565–603
- C.P. McKay, T.W. Scattergood, J.B. Pollack, W.J. Borucki, H.T. Van Ghyseghem, High-temperature shock formation of N₂ and organics on primordial Titan. *Nature* **332**, 520–522 (1988)
- K. Plankenstein, H. Reiner, B.M. Rode, T. Mikoviny, A. Wisthaler, A. Hansel, T.D. Mark, G. Fischer, H. Lammer, H.O. Rucker, Discharge experiments simulating chemical evolution on the surface of Titan. *Icarus* **187**, 616–619 (2007)
- V.A. Rakov, M.A. Uman, *Lightning, Physics and Effects* (Cambridge University Press, Cambridge, 2003)
- C.T. Russell, T.L. Zhang, M. Delva, W. Magnes, R.J. Strangeway, H.Y. Wei, Lightning on Venus inferred from whistler-mode waves in the ionosphere. *Nature* **450**, 661–662 (2007)
- A. Scheffer, Chemical reduction of silicates by meteorite impacts and lightning strikes. Ph.D. Thesis, Lunar and Planetary Laboratory, University of Arizona, 2007
- A. Segura, R. Navarro-Gonzalez, Nitrogen fixation on early mars by volcanic lightning and other sources. *Geophys. Res. Lett.* **32**, L05203 (2003). doi:[10.1029/2004GL021910](https://doi.org/10.1029/2004GL021910)
- R. Stribling, S.L. Miller, Electrical discharge synthesis in simulated jovian atmospheres. *Icarus* **72**, 48–52 (1987)

New Missions

TARANIS—A Satellite Project Dedicated to the Physics of TLEs and TGFs

Francois Lefevre · Elisabeth Blanc · Jean-Louis Pinçon · Robert Roussel-Dupré · David Lawrence · Jean-André Sauvaud · Jean-Louis Rauch · Hervé de Feraudy · Dominique Lagoutte

Originally published in the journal Space Science Reviews, Volume 137, Nos 1–4.
DOI: [10.1007/s11214-008-9414-4](https://doi.org/10.1007/s11214-008-9414-4) © Springer Science+Business Media B.V. 2008

Abstract TARANIS “Tool for the Analysis of RAdiations from lightNIngs and Sprites” is a CNES satellite project dedicated to the study of impulsive transfers of energy between the Earth atmosphere and the space environment. Such impulsive transfers of energy, identified by the observation at ground and in space (rocket, balloons, FORMOSAT 2 satellite) of Transient Luminous Events (TLEs) and the detection on satellites (CGRO, RHESSI) of Terrestrial Gamma ray Flashes (TGFs), are likely to occur in other astrophysical environments as well. The TARANIS mission and instrumentation is presented. The way the TARANIS programme (associated ground-based and balloon-based measurements included) may answer questions about the physics of TLEs and TGFs is examined. The questions addressed include: TLEs and TGFs source regions, associated phenomena, transfers of energy between

The TARANIS scientific Team: E. Blanc, J. Blecki, T. Farges, H. de Feraudy, W.C. Feldman, U.S. Inan, F. Lefevre, R.P. Lin, M. Parrot, T. Neubert, R. Pfaff, J.L. Pinçon, Z. Nemecek, J.L. Rauch, R. Roussel-Dupré, O. Santolik, M. Sato, D.M. Smith, M. Suzuki, Y. Takahashi

F. Lefevre (✉) · J.-L. Pinçon · J.-L. Rauch · D. Lagoutte
Laboratoire de Physique et Chimie de l’Environnement—CNRS, Université d’Orléans, 45071 Orléans cedex 2, France
e-mail: lefeuvre@cnrs-orleans.fr

E. Blanc
Commissariat à l’Energie Atomique, DASE/LDG, Bruyères le Châtel, France

R. Roussel-Dupré
Atmospheric and Climate Sciences Group, Los Alamos National Laboratory, Los Alamos, NM, USA

D. Lawrence
Johns Hopkins Applied Physics Laboratory, 11100 Johns Hopkins Road, Laurel, MD 20723, USA

J.-A. Sauvaud
Centre d’Etude Spatiale des Rayonnements, CNRS, Toulouse, France

H. de Feraudy
Centre d’Etudes des environnements Terrestre et Planétaires—CNRS, Université de Versailles et ST Quentin-en-Yvelines, 78140 Vélizy Villacoublay, France

the radiation belts and the atmosphere, TLEs and TGFs generation mechanisms, input parameters to the modelling of the variation of the atmosphere and the electric circuit.

Keywords Earth environment · Lightning · Transient Luminous Events (TLEs) · Terrestrial Gamma ray Flashes (TGFs) · Lightning induced Electron Precipitation (LEPs) · Runaway electron Beams (RBs)

1 Introduction

The discovery in the last decade of both Transient Luminous Events (TLEs) and Terrestrial Gamma-ray Flashes (TGFs) has revolutionized our understanding of the terrestrial environment by pointing out the frequent occurrence of impulsive transfers of energy between the troposphere and the space environment. The implications for our atmosphere are far reaching and range from affecting the chemical balance of ozone and nitric oxides in the upper atmosphere to modifying the global electric circuit and perturbing the population of the radiation belts. Furthermore, the source of these phenomena must by all indications stem from a fundamentally new physical process that could have much broader implications and manifestations throughout the universe. Radio frequency emissions from lightning activity observed in the environment of other planets could be the signature of a physical process (runaway breakdown) proposed by several authors (Roussel-Dupré and Gurevich 1996; Gurevich et al. 2004; Roussel-Dupré et al. 2005) for the Earth environment (Zarka et al. 2004). Such processes could be much more efficient on Jupiter (Dwyer et al. 2006). In the same way, the near linear marking on Saturn's rings called spokes could be caused by lightning induced electron beams striking the rings at locations magnetically connected to thunderstorms (Jones et al. 2006).

The scientific background concerning the physics of TLEs and TGFs is given in Blanc et al. (2007). The aim of the present paper is to present the operational objectives of the CNES TARANIS programme such as they may be defined at the phase B of development. The instruments are listed in Table 1. Tests performed on available ground-based and satellite-based observations are still in progress to fix the physical parameters which will allow to provide the first simultaneous measurements of: (a) TLEs, TGFs and lightning flashes, (b) associated bursts of upward and downward moving energetic electrons, (c) associated electromagnetic wave fields in a very wide frequency band (DC to 30 MHz), and (d) other environmental conditions like large scale fluctuations in the ionosphere/atmosphere coupling.

The science objectives of the TARANIS mission are listed in Table 2 and fall into three broad categories:

- (1) Advance physical understanding of the links between TLEs, TGFs and environmental conditions (lightning activity, geomagnetic activity, atmosphere/ionosphere coupling, occurrence of Extensive Atmospheric Showers, etc.).
- (2) Identify other potential signatures of impulsive transfers of energy (electron beams, associated electromagnetic or/and electrostatic fields) and provide inputs to test generation mechanisms
- (3) Provide inputs for the modelling of the effects of TLEs, TGFs and bursts of precipitated and accelerated electrons (lightning induced electron precipitation, runaway electron beams) on the Earth's atmosphere.

Table 1 List of TARANIS instruments (September 11 2007)

Instrument	Measured parameters	PI, Organizations
MCP	Microcameras and photometers	E. Blanc—CEA/LDG (F) + Univ. Tohoku-Hokkaido, Jaxa (J)
XGRE	X-ray, gamma-ray and relativistic electron experiment	D. Lawrence—JHUAPL (USA) + DNSC (D), UC Berkeley & Santa Cruz, Planetary Science Institute, SciTech Solutions (USA)
IDEE	Energetic electrons (<2 MeV)	J.A. Sauvaud—CESR/CNRS (F) + Univ. Prague (Cz)
IME-BF	Low frequency electric field (<1 MHz) & ion probe	H. de Feraudy—CETP/CNRS (F) + GSFC (USA)
IME-HF	HF/VHF electric field (100 kHz–30 MHz)	J.L. Rauch—LPCE/CNRS (F) + Univ. Prague, IAP (Cz)
IMM	Low frequency magnetic field (<1 Mz) & zero + whistler detector	J.L. Pinçon—LPCE/CNRS (F) + Univ. Stanford (USA)
MEXIC	On-board management	M. Parrot—LPCE/CNRS (F) + CBK (P)

Table 2 Major Science topics and questions addressed by the TARANIS mission

TLEs and TGFs observations	Locate geographical positions and altitudes of TLEs and TGFs source regions Model variations with LT, season, activity indices, etc.
Environmental conditions	Identify parent lightning flashes and associated EM emissions Investigate possible correlations with cosmic rays, micrometeorites, volcanoes, etc.
Transfers of energy between the radiation belts, the ionosphere and the atmosphere	Detect and characterize burst of precipitated electrons (LEPs) and of accelerated electrons (RBs)
TLEs and TGFs generation mechanisms	Provide input data (TLEs and TGFs source regions, association with lightning activities and other environmental parameters like EAS, bursts of precipitated and accelerated electrons) to test generation mechanisms
Contribution to the modelling of the effects on the atmosphere and on the global electric circuit	Provide information on sources of energy (TLEs, TGFs, bursts of precipitated and accelerated electrons) or/and on large scale ionospheric perturbations

This paper first describes the TARANIS mission and instrumentation. It then shows how the TARANIS programme (including associated ground-based and balloon-based measurements) may answer questions about: TLEs and TGFs source regions, associated phenomena, transfers of energy between the radiation belts and the atmosphere, TLEs and TGFs generation mechanisms, input parameters to the modelling of the variation of the atmosphere and of the electric circuit. The final section includes a summary and a conclusion.

2 TARANIS Instrumentation Payload and mission profile

The TARANIS scientific payload is composed of six scientific instruments: MCP (Micro-Cameras and Photometers), XGRE (X-ray, Gamma-ray and Relativistic Electron experiment), IDEE (Instrument Déetecteurs d'Electrons Energétiques), IME-BF (Instrument de Mesure du champ Electrique-Basse Fréquence), IME-HF (Instrument de Mesure du champ Electrique-Haute Fréquence), IMM (Instrument de Mesure du champ Magnétique) and of a Multi Experiment Interface Controller equipment (MEXIC). The TARANIS layout is represented in Fig. 1. The main characteristics of the instruments are given in Table 1.

The scientific payload is operated as a single instrument (Lagoutte and Lefevre 2008). The objective is: first, to make a low time resolution survey of the optical and field/particle events at medium and low latitudes, then, under alert, to record well synchronized high resolution data. Alerts may be triggered by the detection of a priority event (TLEs, TGFs, electron beams, or burst of electromagnetic or electrostatic wave) by one of the instrument. They are controlled by the MEXIC equipments before being transmitted to all the instruments. The recording time intervals depend on the event at the origin of the alert and of the instrument considered. As an example, for a TLE, low frequency electric field measurements must be recorded over time intervals starting a few tens of milliseconds before the alert in order to detect the electromagnetic signature of the parent lightning. This imposes to implement circulating buffers on each instrument.

Two operation modes have been defined: a “Survey mode” and an “Event mode”. Both operate in parallel. The Survey mode is run over each half orbit in the geographical latitude range $[-60^\circ; +60^\circ]$. Except in specific regions where experiments have to be switched off (day time for most optical measurements, South Atlantic Anomaly for gamma ray detectors) low time resolution data are continuously sent by the instruments to the MEXIC equipment which transmits them to the satellite mass memory. The Event mode is triggered on alerts.

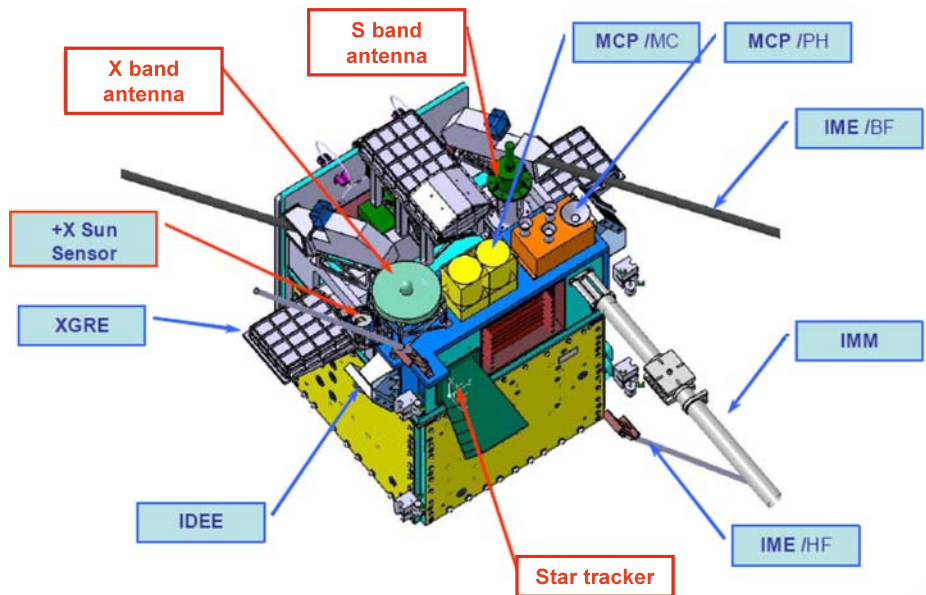


Fig. 1 Lay out of the TARANIS satellite. The instruments are in *blue*. Satellite sub-systems are in *red*

High time resolution data are sent by the instruments to a ring buffer of high storage capacity. Tests performed on available ground-based and satellite-based observations are in progress to precise all needed event parameters. Modifications of these parameters are also possible during the flight.

2.1 The Instruments

2.1.1 *The MicroCamera and Photometer experiment (MCP)*

The objectives of the MCP experiment are: to identify and characterize the TLEs (sprites, halos, elves, etc.), to locate the source regions, and to trigger other TARANIS instruments which may point out associated events. The first specification requires measurements at wavelengths where the different types of TLEs may be discriminated between themselves and from lightning flashes. The second can be fulfilled by observations at the nadir only. The third imposes both observations in the direction where associated events may be detected, i.e. at the nadir (second specification), and a quasi real-time analysis on-board.

The concept of discriminating TLEs from images taken at the nadir has been validated by the LSO (Lightning and Sprite Observations) experiment on-board the International Space Station (Blanc et al. 2004, 2006). It consists in the use of two cameras in parallel. One microcamera (lightning camera) is dedicated to observations in the visible and near-infrared (600–900 nm) the other (TLE camera) to observations in the band 762 ± 5 nm. This band corresponds to the O₂ absorption band of the atmosphere in which lightning are absorbed comparatively to TLEs (Blanc et al. 2006). Thirty images per second, with 512×512 pixels per image, are expected. The zone of observation is of the order of 500 km. The spatial resolution at ground is of the order of 1 km. Knowing that distances between TLEs and parent lightning flashes are found to run from a few km to ~ 50 km (Sao Sabbas et al. 2003), such characteristics will allow to have on the same or on successive images both TLE and parent lightning flash.

The photometers measure the irradiance in four different spectral bands: 762 ± 5 nm, 337 ± 5 nm, 150 to 280 nm, 600 to 900 nm. The three first make observations on a disk of 275 km radius and the fourth, which is dedicated to lightning measurements, on a disk of 700 km. The flux of photons is sampled at 20 kHz. This will allow separating in time lightning flashes from sprites which occur from about 1 ms to hundreds of ms after the parent lightning. The full distinction between lightning and TLEs will be performed by using all photometer responses in the different spectral bandwidths. The TLE response is expected to be important in the UV-FUV (337 nm, 150 to 280 nm) and in the 762 nm O₂ absorption band, whereas the response of lightning will be weak because lightning are absorbed by the atmosphere. ISUAL showed that the lightning response is suppressed in the FUV (Mende et al. 2006). MCP alert signals will be derived from the amplitudes of output signals of 1 to 3 photometers. Thresholds will be modifiable during the flight.

2.1.2 *The X-ray, Gamma-ray and Relativistic electron Experiment (XGRE)*

The purpose of the TARANIS X-ray, Gamma-ray and Relativistic electron Experiment (XGRE) detector is to provide measurements that can determine unambiguously the mechanism(s) that generate TGF events as well as to quantify: (i) the total energy released per event, (ii) the atmospheric altitude at which the burst is initiated, and (iii) the latitude, altitude, and local-time dependent factors that control the evolution of the burst event. The XGRE performance (e.g., detection efficiency and timing parameters) has been designed

based on known TGF fluxes and timing characteristics from previously detected TGFs (Smith et al. 2005; Smith 2007).

The measurement goals require the detection of hard X-ray and gamma-ray transients having photon energies between 20 keV and 10 MeV, rise times as short as 10 s of μ s, and total durations up to several 100 s of milliseconds. The atmospheric altitude of the X-ray/gamma-ray burst (Østgaard et al. 2008) can be derived from both the measured rise time (increased atmospheric scattering will produce a longer rise time, Colman and Roussel-Dupré 2008) and the low-energy portion of the transient energy spectrum (increased atmospheric attenuation will preferentially attenuate lower energy X-rays). Some of the energetic-photon bursts may be accompanied by bursts of relativistic electrons having energies between 1 MeV and 10 MeV.

The XGRE detectors will consist of three rectangular, 10 mm-thick CsI(Na) scintillator sheets, each having 300 cm^2 area. The total area is 900 cm^2 . Each CsI scintillator will be packaged with a 5 mm thick BC400 plastic scintillator in a phoswich arrangement. A phoswich sensor (or phosphor sandwich) consists of two dissimilar scintillators that are optically coupled to a single photomultiplier tube (PMT) where the signals from each scintillator are separately detected by their significantly different rise times. Phoswich techniques are standard for particle detection and are described by Knoll (2000) and references therein. The plastic scintillator acts as a partial anticoincidence shield and a dE/dX identifier of relativistic electrons. This phoswich combination of scintillator elements combined with appropriately-designed front-end electronics, provides the capability of separating the signals of hard X-rays/gamma rays and relativistic electrons, and measuring their separate energy spectra (enabled by the very different fluorescent decay times of plastic and CsI scintillators). The dE/dX element of one of the 300 cm^2 sensors will face downward (for upward-going newly accelerated electrons) and two will face upwards (for downward-going precipitated electrons). The two upward-facing BC400 sensors will be mounted on two of the sides of the spacecraft near the nadir face.

The XGRE detector will record both the dE/dX and total E amplitudes. The information will be stored in a circular buffer. Each time an interaction above threshold is detected an alert signal will be sent to MEXIC.

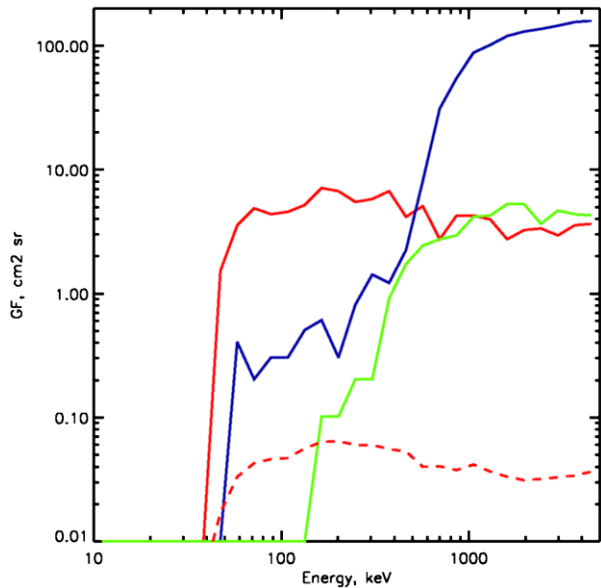
2.1.3 The Energetic Electron Instrument (IDEE)

The objective of the IDEE experiment is: to provide high resolution energetic electron spectra and pitch angle distributions, to separate upgoing accelerated electrons and downgoing precipitated electrons, to detect burst of electrons associated with TGFs, to identify Lightning induced Electron Precipitation (LEP), and to provide alert signals.

The Energetic Electron Instrument (IDEE) is intended to measure energetic electrons in a large dynamic range of fluxes running from $\sim 10^6 \text{ cm}^{-2} \text{ s}^{-1} \text{ keV}^{-1}$ at 60 keV (radiation belts) to $0.2 \text{ cm}^{-2} \text{ s}^{-1} \text{ keV}^{-1}$ at 4 MeV (expected runaway electron beams). Estimations of electron fluxes in the radiation belts are derived from DEMETER data (Sauvaud et al. 2006) and those of runaway electron beams from RHESSI data (Dwyer et al. 2008).

The instrument consists of two spectrometers, each with a maximal field of view of $140^\circ \times 150^\circ$; one with a sight axis making an angle of 60° with the nadir direction, the second making an angle of 30° with the anti-nadir direction. The sensor heads are made of two planes of semi-conductors, the upper plane with silicon and the lower plane with CdZnTe. Each spectrometer measures electron spectra from 70 keV up to 4 MeV. The energy resolution changes with the electron energy: It varies from 10 keV for electrons between 70 and 400 keV up to ~ 100 keV for 4 MeV electrons (see Fig. 2). The angular resolution of each

Fig. 2 Geometrical factors of the different parts of the IDEE spectrometer as a function of the electron energy ($G = S \cdot \Omega \cdot \varepsilon$ where S is the effective detection surface, ε is the detection efficiency, Ω is the solid angle of acceptance). Red: full silicon detection plane. Dashed red: silicon small strip. Blue: full CdZnTe detection plane. Green: geometrical factor of the combined semiconductor detection planes: silicon and CdZnTe



spectrometer is better than 35° . The maximum recordable count rate is 10^7 s $^{-1}$. IDEE will be able to detect very short transient events (<10 ms) with small fluence. Alert signals will be sent by IDEE in the case of electron beams detection.

2.1.4 The Low Frequency Electric Field Instrument (IME-BF) and the Ion Probe

The IME-BF instrument covers the low and medium frequency range (DC—1 MHz). Its main objectives are: the identification of the O $^+$ whistler (name given to a whistler during its first upward propagating path through the ionosphere) of the causative lightning (which completes information provided by the ground-based lightning detection networks, in particular in the case of the Intra Cloud (IC) discharges which are not observed at ground), to monitor the electromagnetic environment, and to provide estimations of the local plasma parameters. Although it is still an open question, measurements of wave-fields in this frequency range are expected to provide electromagnetic and/or electrostatic signatures of electron beams and more specifically of runaway electron beams.

For the sake of convenience (common analyzer) an ion probe has been associated with the IME-BF instrument. Its objective is to detect large scale perturbations of the thermal plasma which could affect the ionosphere/atmosphere coupling in specific geographical regions.

The electric antenna is a heritage of the DEMETER satellite (Berthelier et al. 2006). The electric wave fields are measured by spheres located at the tip of 4 m boom. Accommodation with 6 m at least between the two spheres increases the measurement sensitivity. It is expected to be equal to 126 nV m $^{-1}$ Hz $^{-1/2}$ at 100 Hz and 40 nV m $^{-1}$ Hz $^{-1/2}$ at 10 kHz.

The ion-probe provides a passive measurement of local ion density fluctuations. It is located on a boom (at least 50 cm away from the platform of the satellite) allowing measurements outside the satellite sheath. Ion density fluctuations are expected to identify specific local environmental conditions like plasma depletions (ionospheric “bubbles”).

2.1.5 The High Frequency Electric Field Measurements (IME-HF)

The IME-HF instrument measures electric wave fields in the frequency band: 100 kHz–35 MHz. At the highest frequencies, i.e. at the frequencies where the wave fields are weakly affected by the trans-ionospheric propagation, it has for main objective to point out radio signatures associated with TLEs, TGFs and lightning flashes, and in particular the bi-polar pulses associated with intracloud lightning signals (Jacobson and Light 2003). At the lowest frequencies, i.e. at frequencies overlapping with the IME-BF instrument (<1 MHz), it is expected to contribute to the estimation of polarization characteristics and to the identification of propagation modes (O or X). In the full frequency band, it provides a monitoring of natural emissions (Trans-Ionospheric Pulse Pairs or TIPPs) and man-made emissions (broadcast transmitters). Estimations of cut-off frequencies may be used to derive the values of the local plasma frequency.

The measurements are performed by a dipole antenna composed of 2 monopoles of 1 m length each. The tip to tip distance is 3 m. The sensitivity is equal to $10 \text{ nV m}^{-1} (\text{Hz})^{-1/2}$ at 1 MHz. The electronic works at high impedance to minimize the plasma effect around the plasma characteristic frequencies (f_{ce} , f_{pe}). IME-HF may provide alert signals.

2.1.6 The Magnetic Field Measurement (IMM)

The IMM instrument covers a frequency band running from a few Hz to 1 MHz. Its two main objectives are: first, at VLF frequencies below 20 kHz, to provide accurate estimations of the propagation characteristics of the electromagnetic emissions (sense of polarization, wave normal directions); second, at all frequencies, to complete the IME-BF data i.e. to discriminate electrostatic from electromagnetic wave fields and to provide rough estimates of the propagation characteristics.

The measurements are performed by a triaxial search coil magnetometer. IMM is mounted at the tip of a two meters boom to minimize noise interference from the space-craft. It is composed of three orthogonal magnetic antennas. Two of them are mono-band coils that measure two magnetic field components for frequencies ranging from a few Hz to 20 kHz. The third antenna is a dual-band coil allowing measurements of the remaining magnetic field component for frequency ranging from a few Hz up to 1 MHz. The sensitivity achieved by the IMM instrument is $2 \text{ pT}(\text{Hz})^{-1/2}$ at 10 Hz, $8 \text{ fT}(\text{Hz})^{-1/2}$ at 2 kHz, and $9 \text{ fT}(\text{Hz})^{-1/2}$ at 100 kHz.

The analyzer dedicated to the data processing of IME-BF and IMM data for the MF frequency band [10 kHz–1 MHz] includes a O⁺ whistler detector to perform automatically and continuously the detection and characterization of O⁺ whistlers in order to provide comprehensive statistics of lightning flashes including for Intra Cloud discharges.

2.1.7 MEXIC

The MEXIC equipment powers the scientific instruments and ensures all interfaces between the scientific instruments and the satellite. In this regard, its main functions are: to provide the (basic) secondary voltages, to receive and to decode the scientific payload commands, to manage the instruments (ON/OFF, configuration, modes), to manage the event triggering signals, to time stamp the data packets (absolute date), to manage the data transfer to mass memory, to house the instrument analyzers.

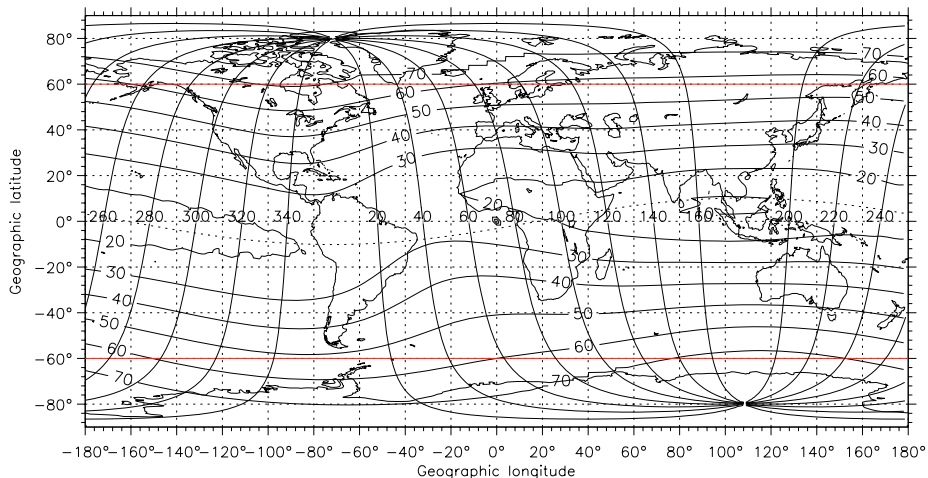


Fig. 3 Geographical domain in which the TARANIS instrument will be switched on (between -60° and $+60^\circ$ geographic latitudes). Invariant latitude and geomagnetic longitude curves respectively point out the L values and conjugate regions which will be covered

2.2 Mission Profile

TARANIS belongs to the CNES Myriade microsatellite family. It is a three axis stabilized satellite. The scientific equipments are mounted on a box $80 \times 60 \times 80$ cm (see Fig. 1). The total weight is around 150 kg, including ~ 30 kg for the scientific payload. The microsatellite subsystems include a mass memory of 16-Gbit capacity, a high rate X band telemetry (16.8 Mbits/s) for the transmission of the scientific data.

The mission profile is very close to the DEMETER profile. TARANIS is forecast to be a two-year mission. It will fly in a 98° polar orbit at altitudes ~ 700 km. It will be sun-synchronous with a drift of 2 hours Local Time per year. In two years, assuming a Local Time ascending node around ~ 22 LT at the launch (which maximises the probability of optical measurements), it will cover 22 to 2 LT during night-time and 10 to 14 LT during day-time. Due to limitations in the power budget, in particular for the night time orbits, the scientific experiments will be switched off at high geographical latitudes (below -60° and above 60°) during the nominal operation modes (see Fig. 3). However, this will allow coverage for most regions where lightning activity is strong and therefore where the probability of observations of TLEs or/and TGFs is high. Data will be transmitted to the ground at least twice per day. As with the DEMETER microsatellite, the TARANIS mission Centre will be developed and operated by the Laboratoire de Physique et Chimie de l'Environnement (Lagoutte et al. 2006).

3 TARANIS Contributions to Major Science Topics

3.1 TLEs and TGFs Source Regions

Numerous ground-based images of TLEs occurring over the tops of thunderstorms have been obtained (Lyons 2006). The most recent observations with high-speed cameras and telescopes have shown a wide variety of optical small scale structures. They have resulted

in the phenomenological identification of a large number of processes named column and carrot sprites, angels, trolls, jets, giant jets, halos, elves, beads, and bars (i.e., Sentman and Wescott 1993; Lyons et al. 2003; Lyons 2006; Cummer et al. 2006a, 2006b). Triangulation techniques have allowed the location of source regions. However, despite well organized campaigns of measurements, to our knowledge, no comparison with TGFs satellite data has been reported so far. Global TLE observations by the ISUAL experiment on-board the FORMOSAT-2 Taiwanese satellite has allowed the mapping of sprites, elves and halos (Mende et al. 2006). The occurrence rate is about 1.7 TLE per operation hour (Chen et al. 2005). However, with the images being taken at the limb, region sources may only be roughly estimated.

By making optical measurements at the nadir, the TARANIS MCP instrument will identify sprites, halos and elves but may have difficulties to well measure with cameras low altitude events such as blue jets. The photometer in the 337 ± 5 nm spectral band is better adapted to such observations. MCP will also provide lightning monitoring. The source regions will be located with a 1 km space resolution and results will be correlated with other satellites, ground-based and balloon-based observations related with thunderstorm activity. This is essential when looking for common physical mechanisms at the origin of the generation of TLEs and TGFs. In particular, this will allow a better description of electrochemical processes associated to breakdown and of associated events like large gravity waves over thunderstorm areas (Sentman et al. 2003) and synchronized ground-based observations of infrasound associated with sprites (Farges et al. 2005).

TGFs, originally discovered above active thunderstorms by the BATSE instrument on board of the CGRO satellite (Compton Gamma-Ray Observatory) (Fishman et al. 1994), are presently being monitored by the RHESSI satellite which to date has observed some 10–20 TGFs per month (Smith et al. 2005). The geographical distribution of TGFs roughly corresponds to the geographical distribution of lightning over continents at low-latitude and also to the distribution of sprites (Christian et al. 2003; Chen et al. 2005). However, TGF emissions are rarely detected over the Southern USA where many sprites are observed at ground level (Smith et al. 2005).

By increasing the sensitivity of the detectors and by providing better estimates of the altitudes of the X and gamma ray source regions, data from the TARANIS XGRE instrument will provide relevant inputs for testing among the TGFs generation models: at low altitudes in the troposphere (Dwyer and Smith 2005; Williams et al. 2006), at high altitude (Moss et al. 2006), or continuously at altitudes between 15 and 60 km (Østgaard et al. 2008).

3.2 Associated Phenomena

TLEs and TGFs are generally associated with lightning activity. This is particularly well demonstrated for TLEs. Sprites and halos occur after an intense positive cloud-to-ground stroke, generally identified using ground-based detection networks, while elves are observed after all lightning flashes that exceed a minimum threshold (Barrington-Leigh and Inan 1999). Delay times are generally below 20 ms but delays up to several hundreds of ms have been reported, in particular for groups of sprites. Remote sensing using broadband ELF sensors at thousands of kilometres from the thunderstorms may be used to estimate charge moment (Cummer and Lyons 2005). Ground-based measurements have shown that ELF slow tail signatures indicating a significant flow of continuing current (Cummer et al. 1998) are associated with 10–20% of sprites (Fullekrug et al. 2001; Cummer et al. 2006b). TGFs have also been associated to lightning activity. Lightning flashes located in a circle of 300 km radius of the subsatellite point were correlated with

RHESSI TGFs (Cummer et al. 2005). BATSE TGFs were related with ELF/VLF signals exhibiting slow tails as signals associated with sprites (Inan et al. 1996a). Other TGFs were observed without associated lightning (Inan et al. 1996a; Cummer et al. 2005). However, Smith (2007) has shown that TGFs observed over nonstormy regions may be interpreted as the result of the propagation of relativistic electrons from a storm at the conjugate point.

By locating source regions of TLEs and/or TGFs at the same time, TARANIS will allow checks of whether the two phenomena are related to the same lightning activity or not. Moreover, on-board wide band wave field measurements will provide the capabilities: (a) to remove ambiguities about missing or/and long delay parent lightning flashes, (b) to identify spherics propagation characteristics, (b) to better track electrostatic or electromagnetic signatures of electron currents, (c) to evaluate the energy transferred by electromagnetic pulses along their propagation across the ionosphere.

In parallel, the IDEE and XGRE high energy electron measurements will provide discrimination between gamma-rays and electron events observed by gamma ray detectors, whereas the ion probe measurements will provide data to test whether the altitude of TLE and TGF sources are affected or not by large scale movements (bubbles) observed just after sunset in the equatorial regions (de La Beaujardière 2004).

In addition, comparisons with ground-based measurements will allow studying seasonal dependence of the association with lightning activity, correlation with: observations of Extensive Atmospheric Showers (EAS), burst of electron precipitations, geomagnetic activity, etc.

3.3 Transfers of Energy Between the Radiation Belts, the Ionosphere and the Atmosphere

Except for a narrow latitude range around the equator, a non-negligible part of the energy of VLF waves emitted at ground (VLF transmitters) or in the atmosphere (electromagnetic waves associated with lightning flashes) may propagate through the ionosphere and interact with radiation belt electrons. Bursts of precipitated electrons associated with subionospheric early VLF perturbations have been observed in one-to-one association with sprites observed at ground (Haldoupis et al. 2004). Electron measurements performed on board the DEMETER spacecraft (Sauvaud et al. 2006) have pointed out short bursts of lightning-induced electron precipitation (LEP) simultaneously with newly-injected upgoing whistlers, and sometimes also with once reflected (from the opposite hemisphere) whistlers. As shown in Inan et al. (2007), for the first time causative lightning discharges have been definitely geo-located for some LEP bursts aboard a satellite. The LEP bursts occur within <1 s of the causative lightning and consist of 100–300 keV electrons.

The direct observation of electron beams accelerated from the atmosphere to the radiation belt is more difficult. In only one instance energetic electrons (~ 1 keV) moving upward were ever measured by a satellite in association with a lightning strike situated in a hurricane (Burke et al. 1992). This lack of success is further exemplified by the data set obtained by the SAMPEX low altitude satellite (Li et al. 2001), which despite continuous monitoring of the radiation belts, shows no evidence for runaway relativistic electron beams in association with lightning. An encouraging case, however, has been identified in RHESSI data. The longer and most intense TGF observed above the SAHARA desert in January 2004, as thunderstorms are frequent at the conjugate point, could be the manifestation of an electron beam hitting the spacecraft (Smith et al. 2005). Other examples have been presented since then (Smith 2007). Indirect observations of electron beams via electromagnetic signatures have also been invoked. Lehtinen et al. (2000) have shown that relativistic runaway electron beams driven by intense lightning generated quasi electrostatic (QE) fields may undergo intense interactions with the background magnetospheric plasma, leading to rapid nonlinear

growth of Langmuir waves. Plasma physics offers other potential interactions and so other potential signatures, like the production of lower hybrid waves (Martin-Solis et al. 2002).

As shown by numerous authors (e.g. Baker et al. 2007; Sauvaud et al. 2008) measurements of energetic electrons on-board low altitude (~ 600 km) satellites like SAMPEX and DEMETER is a good way to monitor variations in the radiation belts. Provided the observations are made in geographical regions where the different sources of energy may be distinguished impulsive events like LEPs may be observed (Inan et al. 2007). By adjusting its sensitivity to the background noise in different geophysical regions, the TARANIS IDEE experiment is tailored to point out impulsive events like bursts of precipitated and accelerated electrons with still higher time and space resolutions. Although it is still a challenge a direct detection of runaway electron beams seems possible. In parallel, indirect detections of electron currents are expected from the wide band wave field measurements.

3.4 TLEs and TGFs Generation Mechanisms

The association of TLEs or/and lightning with TGFs has not been demonstrated so far. TGF spectra measured by RHESSI reveal energies up to 30 MeV (Smith et al. 2005), in agreement with energies predicted by the runaway relativistic electron breakdown mechanism triggered by cosmic rays (Roussel-Dupré and Gurevich 1996; Gurevich et al. 2004; Roussel-Dupré et al. 2005), while most of TLE structures are explained by conventional processes (Pasko 2006). Most recent developments show that for fast (< a few ms), high current (> 100 kA) positive lightning, the high altitude discharge is dominated by a diffusive air glow driven by conventional breakdown and producing TLEs at high altitudes (> 60 –70 km), followed by runaway breakdown, at the origin of TGFs, that initiates at the top of the cloud (~ 15 km) and develop upwards to altitudes exceeding 90 km. For longer duration continuing currents ($>$ a few ms), streamers driven by conventional breakdown develop at high altitudes (~ 75 km) and evolve downward to lower altitudes. The streamers are then followed by runaway discharges that are initiated at the top of the cloud and propagate to high altitudes (Roussel-Dupré et al. 2005; Nelson et al. 2006). However, Gurevich and Zybina (2005) considered that runaway breakdown are produced by EAS and are not associated to TLEs.

By providing: (a) simultaneous and comprehensive measurements of source regions and source altitude for TLEs and TGFs, (b) comprehensive information on the association with lightning activities and on other environmental parameters like the occurrence of Extensive Atmospheric Showers, and (c) characteristic parameters of bursts of precipitated and accelerated electrons, the TARANIS instruments are expected to provide data which will allow to put complementary constraints and to test generation models.

3.5 Contribution to the Modelling of Effects on the Atmosphere and on the Global Electric Circuit

The possible effect on the Earth's atmosphere concerns ionization, chemical changes, and the dynamics of the atmosphere. It has been suggested for numerous years that lightning flashes were a major natural source of NO_x (Stark et al. 1996; Wang et al. 1998). Observations suggest that TLEs may be sources of NO_x and may cause local perturbations (Inan et al. 1996a, 1996b). Significant production of nitric oxide and ozone by single jet was estimated by Mishin (1997) assuming an electron avalanche in the jet wave front. The effects of ionization changes on the Earth-ionosphere wave guide in relation with TLEs and LEP is currently monitored by ground-based VLF measurements (Haldoupis et al. 2004).

Columns of ionization with peak electron densities of $6 \times 10^4\text{--}10^5 \text{ cm}^{-3}$ predicted by the runaway breakdown mechanism were observed by HF radar following intense lightning flashes (Roussel-Dupré and Blanc 1997). The recent observations of details in the streamer structures by high-speed cameras allow a better description of electrochemical processes associated with breakdown (Liu and Pasko 2004; Cummer et al. 2006a, 2006b). Precipitated particles may also produce NO_x, but, except for high latitudes where local mechanisms allow transport to the stratosphere (Callis et al. 2002 and references therein), very energetic particles are required to produce NO_x in the low atmospheric layers. Heating effects have also been pointed out. Ground-based observations of infrasound associated with sprites (Farges et al. 2005) and measurements in the upper atmosphere of large scale gravity waves over thunderstorm area (Sentman et al. 2003) have been reported. A one to one relation between specific infrasound characterized by a chirp signature and sprites indicates the possibility of the heating of ambient atmosphere (Farges et al. 2005).

Although TARANIS cannot by itself measure direct effects on the atmosphere, it may bring an important contribution to modelling activities by providing information on several sources of energy (TLEs, TGFs, bursts of precipitated and accelerated electrons) or/and on large scale ionospheric perturbations. Additional atmospheric data need to be obtained from complementary satellite measurements or/and from ground-based and balloon based experiments. Tests on the effects of TLEs, TGFs, and bursts of precipitated and accelerated electrons on the ionization rate must involve ground based radar measurements.

4 Summary and Conclusions

The TARANIS microsatellite is scheduled to be launched in 2012 into a 98° polar orbit at altitudes $\sim 700 \text{ km}$. The instruments include:

- Microcameras and photometers
- X-ray, gamma-ray and relativistic electron detectors
- Energetic electron detectors
- LF electric fields measurements and ion probe
- HF/VHF electric fields measurements
- LF magnetic field and O⁺ whistler detector
- A controller system including processing of alert signals generated by the instruments

The TARANIS instruments and their main functions have been described. They provide the following capabilities:

- to locate the source regions of TLEs and TGFs and to estimate the altitudes of the TGFs region sources,
- to clarify associations of TLEs and TGFs with lightning activity (delay times with parent lightning flashes, ELF and VLF signatures of associated events, correlation between bipolar pulses and TGFs),
- to detect and characterize potential electromagnetic signatures of physical processes involved
- to investigate the potential effects of large scale movements of the thermal plasma on the source altitudes,
- to check the separation between gamma-rays and electrons,
- to identify and characterize bursts of precipitated and accelerated energetic electrons,
- to test generation mechanisms for TLEs and TGFs,

- to evaluate effects of TLEs, TGFs, RBs and LEPs on the atmosphere and on the radiation belt.

Associated ground-based and balloon-based measurements are necessary both for comparisons between data acquired below the source regions and above and for evaluating effects on the atmosphere. Collaborations are needed with scientific teams involved in other spacecraft programmes in orbit at the same time as TARANIS (in particular, experimenters of the ASIM experiment on-board the International Space Station): (1) to provide data not acquired by TARANIS like atmospheric data, (2) to extend the UT and LT coverage, and (3) to better describe the spatial structures under study.

Acknowledgements TARANIS is a project of the Myriad series of microsatellites developed by CNES. The authors express their thanks to C. Bastien-Thiry (CNES project manager), the CNES Staff, and the scientific and technical TARANIS team members. They also thank the reviewers for very useful comments.

References

- C.P. Barrington-Leigh, U.S. Inan, Geophys. Res. Lett. **26**(6), 683 (1999)
- D.N. Baker, S.G. Kanekal, R.B. Horne et al., Geophys. Res. Lett. **34**, 20 (2007). citeID L20110
- J.J. Berthelier, M. Godefroy, F. Leblanc et al., Planet. Space Sci. **54**, 456 (2006)
- E. Blanc, T. Farges, R. Roche et al., J. Geophys. Res. **109**, A02306 (2004) doi:[10.1029/2003JA009972](https://doi.org/10.1029/2003JA009972)
- E. Blanc, Farges, T. Brebion et al., in *Sprites, Elves and Intense Lightning Discharges*, ed. by M. Fullekrug, V.A. Mareev, M. Rycroft (NATO Science series, Mathematics, Physics and Chemistry, 2006)
- E. Blanc, F. Lefevre, R. Roussel-Dupré, J.A. Sauvaud, Adv. Space Res. **40**, 1268 (2007)
- W.J. Burke, T.L. Aggson, N.C. Maynard et al., Effects of a lightning discharge detected by the DE 2 Satellite over Hurricane Debbie. J. Geophys. Res. **97**(A5), 6359 (1992)
- L.B. Callis, M. Natarajan, J.D. Lambeth, Geophys. Res. Lett. **29**, 2 (2002). doi:[10.1029/2001GL011395](https://doi.org/10.1029/2001GL011395)
- H.J. Christian, R.J. Blakeslee, D.J. Boccippio et al., J. Geophys. Res. **108**(D1), 4005 (2003)
- B. Chen, Y. Lee, R. Hsu et al., AGU Fall meeting, San Francisco, 2005
- J.H. Colman, R.A. Roussel-Dupré, A full kinetic treatment of gamma-ray transport applied to TGF observations from RHESSI. Los Alamos National Laboratory Report (2008, in preparation)
- S.A. Cummer, U.S. Inan, T.F. Bell, C.P. Barrington-Leigh, Geophys. Res. Lett. **25**, 1281 (1998)
- S.A. Cummer, W.A. Lyons, J. Geophys. Res. **110**, A04304 (2005)
- S.A. Cummer, Y. Zhai, D.M. Smith, L.I. Lopez, M.A. Stanley, Geophys. Res. Lett. **32**, L08811 (2005) doi:[10.1029/2005GL022778](https://doi.org/10.1029/2005GL022778)
- S.A. Cummer, N. Jaugey, Li et al., Geophys. Res. Lett. **33**, L04104 (2006a)
- S.A. Cummer, H.U. Frey, S.B. Mende et al., J. Geophys. Res. **111**, A10315 (2006b)
- O. de La Beaujardière, J. Atmos. Sol. Terr. Phys. **66**, 1573 (2004)
- J.R. Dwyer, D.M. Smith, Geophys. Res. Lett. **32**, L22804 (2005)
- J.R. Dwyer, L.M. Coleman, R. Lopez et al., Geophys. Res. Lett. **33**, L22813 (2006). doi:[10.1029/2006GL027633](https://doi.org/10.1029/2006GL027633)
- J.R. Dwyer, B.W. Grefenstette, D.M. Smith, High-energy electron beams launched into space by thunderstorms. Geophys. Res. Lett. **35**, L02815 (2008). doi:[10.1029/2007GL032430](https://doi.org/10.1029/2007GL032430)
- T. Farges, E. Blanc, A. Lepichon, T. Neubert, T.H. Allin, Geophys. Res. Lett. **32**, L01813 (2005). doi:[10.1029/2004GL021212](https://doi.org/10.1029/2004GL021212)
- G.J. Fishman, P.N. Bhat, R. Mallozzi et al., Science **264**, 1313 (1994)
- M. Fullekrug, D.R. Moudry, G. Dawes, D.D. Sentman, J. Geophys. Res. **106**, 20189–20194 (2001)
- A.V. Gurevich, K.P. Zybin, Phys. Today **37** (2005)
- A.V. Gurevich, A.N. Karashtin, A.P. Chubenko et al., Phys. Lett. A **325**, 389 (2004)
- C. Haldoupis, T. Neubert, U.S. Inan et al., J. Geophys. Res. **109**, A10303 (2004). doi:[10.1029/2004JA010651](https://doi.org/10.1029/2004JA010651)
- U.S. Inan, S.C. Reising, G.J. Fishman, J.M. Horack, Geophys. Res. Lett. **23**, 1017 (1996a)
- U.S. Inan, W.A. Sampson, Y.N. Tarantenko, Geophys. Res. Lett. **23**, 1017 (1996b)
- U.S. Inan, D. Piddachiyy, W.B. Peter et al., Geophys. Res. Lett. **34**, 7 (2007). doi:[10.1029/2006GL029238](https://doi.org/10.1029/2006GL029238)
- A.R. Jacobson, T.L. Light, J. Geophys. Res. **108**(D9), 4266 (2003). doi:[10.1029/2002JD002613](https://doi.org/10.1029/2002JD002613)
- G.H. Jones, N. Krupp, H. Kruger et al., Geophys. Res. Lett. **33**, L21202 (2006). doi:[10.1029/2006GL028146](https://doi.org/10.1029/2006GL028146)
- G.F. Knoll, *Radiation Detection and Measurement*, 3rd edn. (Wiley, 2000), p. 344
- D. Lagoutte, J.Y. Brochot, D. de Carvalho et al., Planet. Space Sci. **5**, 428 (2006)

- D. Lagoutte, F. Lefevre, TARANIS Mission Specification, TAR-SP-SY-0-6013-LPCE (2008)
- N.G. Lehtinen, U.S. Inan, T.F. Bell, Geophys. Res. Lett. **27**(8), 1095 (2000)
- X. Li, D.N. Baker, S.G. Kamekal, M. Cooper, M. Temerin, Geophys. Res. Lett. **28**, 3827 (2001)
- N. Liu, V. Pasko, J. Geophys. Res. **109**, A04301 (2004). doi:[10.1029/2003JA010064](https://doi.org/10.1029/2003JA010064)
- W.A. Lyons, in *Sprites, Elves and Intense Lightning Discharges*, ed. by M. Fullekrug, M. Mareev, V.A. Rycroft. NATO Science series, Mathematics, Physics and Chemistry (2006), p. 19
- W.A. Lyons, T.E. Nelson, R.A. Armstrong et al. Bul. Am. Meteo. Soc. **84**(4), 445 (2003)
- J.R. Martin-Solis, R. Sanchez, B. Espósito, Phys. Plasmas **9**(5), 1667 (2002)
- S.B. Mende, Y.S. Chang, A.B. Chen et al., in *Sprites, Elves and Intense Lightning Discharges*, ed. by M. Fullekrug et al. (Springer, Berlin, 2006)
- E. Mishin, Geophys. Res. Lett. **24**(15), 1919 (1997)
- G.D. Moss, V.P. Pasko, N. Liu, G. Veronis, J. Geophys. Res. **111**, A02307 (2006). doi:[10.1029/2005JA011350](https://doi.org/10.1029/2005JA011350)
- M.A. Nelson, L.A. Triplett, J. Colman, R.A. Roussel-Dupré, AGU, Fall meeting (2006)
- N. Østgaard, T. Gjesteland, J. Stadsnes, P.H. Connell, B. Carlson, Production altitude and time delays of the terrestrial gamma flashes: Revisiting the Burst and Transient Source Experiment spectra. J. Geophys. Res. **113**, A02307 (2008). doi:[10.1029/2007JA012618](https://doi.org/10.1029/2007JA012618)
- V.P. Pasko, in *Sprites, Elves and Intense Lightning Discharges*, ed. by M. Fullekrug et al. (Springer, Berlin, 2006)
- R. Roussel-Dupré, E. Blanc, HF echoes from ionization produced by upward propagating discharges. J. Geophys. Res. **102**(A3), 4613–4622 (1997)
- R. Roussel-Dupré, A.V. Gurevich, J. Geophys. Res. **101**, 2297 (1996)
- R.A. Roussel-Dupré, E.M.D. Symbalisty, L. Triplett et al., Cal Meeting, Crete (2005)
- F.T. Sao Sabbas, D.D. Sentman, E.M. Wescott et al., J. Atmos. Sol.-Terr. Phys. **65**, 525 (2003)
- J.A. Sauvaud, T. Moreau, J.-P. Treilhou et al., Planet. Space Sci. **54**(5), 502 (2006)
- J.A. Sauvaud, R. Maggiolo, C. Jacquey et al., Geophys. Res. Lett. (2008, in press)
- D.D. Sentman, E.M. Wescott, Geophys. Res. Lett. **20**, 2857 (1993)
- D.D. Sentman, E.M. Wescott, R.H. Picard et al., J. Atmos. Sol. Terr. Phys. **65**, 537 (2003)
- D.M. Smith, IAGA, JAS006, Perugia (2007)
- D.M. Smith, L.I. Lopez, R.P. Lin, C. Barrington-Leigh, Science **307**, 1085 (2005)
- M.S. Stark, J.T.H. Harrison, C. Anasti, J. Geophys. Res. **101**(D3), 6963 (1996)
- Y. Wang, A.W. De Silva, G.C. Goldenbaum, J. Geophys. Res. **103**, 191149 (1998)
- E. Williams, R. Boldi, J. Bor et al., J. Geophys. Res. **11**, D16209 (2006). doi:[10.1029/2005JD006447](https://doi.org/10.1029/2005JD006447)
- P. Zarka, W.M. Farrell, M.L. Kaiser, E. Blanc, W.S. Kurth, Planet. Space Sci. **52**, 1435 (2004)

Lightning Detection by LAC Onboard the Japanese Venus Climate Orbiter, Planet-C

**Y. Takahashi · J. Yoshida · Y. Yair · T. Imamura ·
M. Nakamura**

Originally published in the journal Space Science Reviews, Volume 137, Nos 1–4.
DOI: [10.1007/s11214-008-9400-x](https://doi.org/10.1007/s11214-008-9400-x) © Springer Science+Business Media B.V. 2008

Abstract Lightning activity in Venus has been a mystery for a long period, although many studies based on observations both by spacecraft and by ground-based telescope have been carried out. This situation may be attributed to the ambiguity of these evidential measurements. In order to conclude this controversial subject, we are developing a new type of lightning detector, LAC (Lightning and Airglow Camera), which will be onboard Planet-C (Venus Climate Orbiter: VCO). Planet-C will be launched in 2010 by JAXA. To distinguish an optical lightning flash from other pulsing noises, high-speed sampling at 50 kHz for each pixel, that enables us to investigate the time variation of each lightning flash phenomenon, is adopted. On the other hand, spatial resolution is not the first priority. For this purpose we developed a new type of APD (avalanche photo diode) array with a format of 8×8 . A narrow band interference filter at wavelength of 777.4 nm (OI), which is the expected lightning color based on laboratory discharge experiment, is chosen for lightning measurement. LAC detects lightning flash with an optical intensity of average of Earth's lightning or less at a distance of 3 R_V. In this paper, firstly we describe the background of the Venus lightning study to locate our spacecraft project, and then introduce the mission details.

Keywords Venus · Lightning · Atmosphere · Electricity · Planet-C · VCO · Orbiter · LAC

1 Background of Venus Lightning Study

It is well known to us that lightning on Earth is usually produced by strong convective clouds. According to recent global surveys from ground and spacecraft, the average

Y. Takahashi (✉) · J. Yoshida

Department of Geophysics, Graduate School of Science, Tohoku University, Sendai, Japan
e-mail: spriteselves@gmail.com

Y. Yair

Department of Life and Natural Sciences, The Open University of Israel, Tel Aviv, Israel

T. Imamura · M. Nakamura

Japan Aerospace Exploration Agency, Tokyo, Japan

global occurrence rate of lightning is \sim 40 to \sim 100 events per second. It is also known that lightning discharges give an impact on the global electric circuit in the atmosphere and the atmospheric chemical processes. Lightning discharges on Earth have several established source mechanisms. Details of the discharge processes can be found in Rakov and Uman (2003). Basically, the discharge requires as its prelude a charging mechanism and a charge separation mechanism to separate opposite polarity charges against their electrical attraction until the developed electric potential difference exceeds the breakdown field of the atmosphere. Terrestrial lightning discharges also occur in volcanic plumes and within dust storms. Recently the cloud to mesosphere/ionosphere discharges such as sprites, elves and blue jets have been discovered successively and these generation mechanisms are investigated with extensive global observations and numerical simulations. Recent planetary exploration missions have revealed that lightning occurs on other planets. On Jupiter, lightning has been detected by optical instruments (Cook et al. 1979; Little et al. 1999; Dyudina et al. 2004) and by the reception of whistlers which appear to be originated from lightning (Gurnett et al. 1979; Lanzerotti et al. 1992). From the results of Galileo and Cassini optical observations, lightning events on Jupiter are found to be associated with storm clouds, and their maximum energy is estimated to be 10^4 times more powerful than that of Earth. The Cassini radio and plasma wave instrument successfully detected many intense impulsive radio signals from Saturn lightning (Gurnett et al. 2005; Fisher et al. 2006).

1.1 Prediction of Venus Lightning

Venus, Earth's sister planet is particularly fascinating, because of its proximity and its permanent obscuring cloud layers. Terrestrial lightning is associated with the generation of electrical charges in convective clouds; hence, there seems a good chance that Venus is also a candidate which has lightning discharge. But the clouds of Venus are mainly composed of sulfuric acid, so it is difficult to induce a charge separation by friction between cryohydrate and hail like Earth. However, depending on the water content of sulfuric acid, there is a possibility that sulfuric acid is in solid state above the middle cloud layer (\sim 51 km). Furthermore, the fact that the clouds are yellow is due to solid sulfur and ferric chloride existing in clouds. Large upward winds detected by Vega balloons *in situ* measurements (Sagdeev et al. 1986) suggest good conditions to generate lightning discharges in the Venus atmosphere. Therefore there is high possibility of the existence of lightning on Venus. If lightning exists on Venus, cloud-to-ground discharges would be very difficult to produce at Venus due to the large breakdown voltage of the dense CO₂ atmosphere and the extreme high altitude of the cloud layers above the surface. Hence, intra-cloud discharges are likely to be the most dominant possibility at Venus. Cloud-to-ionosphere lightning events cannot be ruled out at Venus, particularly because the clouds on Venus are 30 to 40 km nearer to the base of the ionosphere than the case of Earth. If there is volcanic activity on Venus, this can become a source of lightning. Considering that Venus has no intrinsic magnetic field, lightning initiated by cosmic rays may be dominant on Venus. Borucki et al. (1996) made laboratory simulations of lightning in the Venus atmosphere (CO₂: 96%, N₂: 4%) and measured the spectral irradiance in the visible range. From the results obtained by observing laser-induced plasmas, it is clear that the observed spectrum is fairly uniform from 360 nm to 760 nm, but shows a very prominent atomic oxygen feature at 777.4 nm. Ohba et al. (2003, 2004) generated discharges in the CO₂ atmosphere and the strongest emission has also been measured at 777.4 nm, atomic oxygen line. Krasnopolksy (2006) pointed out that lightning is only the known source of NO in the lower atmosphere of Venus, and the detection of NO is a convincing and independent proof of lightning on Venus. He derived 5.5 ± 1.5 ppb

below 60 km as NO mixing ratio by ground-based telescopic observations, hence concluded that the global flash rate is ~ 90 flashes/s and $\sim 6 \text{ km}^2/\text{year}$ if a flash energy on Venus is $\sim 10^9 \text{ J}$.

1.2 Significance of Venus Lightning

Investigation of the Venusian lightning is necessary to progress the following research areas:

Charge separation mechanism: In the generation mechanism of terrestrial lightning, charging and charge separation between cryohydrate and hail are generally considered. However, if Venus lightning is generated in the sulfuric acid clouds, charge separation between droplets is necessary. This will lead to the understanding of sulfuric acid cloud characteristics.

Atmospheric activity: Assuming that Venus lightning is produced by the strong convection like Earth, lightning observation becomes a powerful tool for remote sensing of convective activity in the Venus atmosphere.

Global electric circuit: Earth is considered to be a concentric sphere capacitor surrounded with ground surface and ionosphere, called the global electric circuit. Lightning discharge plays an important role as a generator. From the occurrence rate and the global distribution of Venus lightning, we can estimate the structure of the global electric circuit on Venus.

Chemical effects on atmosphere: Nitric oxides (NOx) production due to lightning discharges is important in the terrestrial troposphere. Particularly, in the equatorial region where lightning discharge occurs most frequently, it is estimated to reach to 40% of the total amount of NOx production. Krasnopol'sky (1983b) reported that Venus lightning produces NO and atomic nitrogen. Levine et al. (1982) suggested that at and below cloud level and in the region where solar ultraviolet radiation cannot penetrate, the dissociation of carbon dioxide by lightning may be a significant source of oxygen atoms. For the estimation of the chemical effect of lightning on the Venus atmosphere, it is necessary to investigate the energy characteristics and occurrence rate of lightning.

Volcanic activity: The Magellan spacecraft reported that there is abundant evidence for volcanoes and lava flows on Venus, but current observations have not yet determined whether the planet is geologically alive or dead today. Na et al. (1994) showed a compilation of sulfur dioxide cloud top measurements in Venus and reported that sulfur dioxide has been advanced for the likely rapid increase and observed slow decline. One of these explanations is the existence of active volcanism (Esposito 1984). If lightning is present in Venus and its occurrence region is consistent with volcanoes, we can indirectly view the volcanic activity in Venus. From the above arguments, it is predicted that lightning activities must have an impact on meteorology, atmospheric electricity, and atmospheric chemistry on Venus.

1.3 Past Observations

Venus lightning activity was investigated by optical measurements and electromagnetic wave observations. These are thoroughly reviewed by Russell (1991), Grebowsky et al. (1997), and Russell et al. (2006a, 2006b). Subsequent sections will describe past observations briefly.

1.3.1 Optical measurements

Major past optical measurements of Venus lightning were made as follows.

Venera 9 and 10: In 1975, the Venera 9 grating spectrometer obtained the first optical evidence for lightning on the nightside of Venus at 19h30m local time and 9°S latitude Krasnopol'sky (1983a, 1983b). That spectrometer scanned the spectral range from 300 nm to 800 nm in 10 s. Similar observations were made on Venera 10, but no nightside signals were detected. Flashes were only seen over a period of 70 s. There were 10 to 20 flashes per 10 s scan with ~ 0.25 s peakwidth—a duration comparable to that of terrestrial flashes. But taking the instrument response time (5 ms) with the sampling time (20 ms) into account, Krasnopol'sky (1983a, 1983b) suggested that the flashes consisted of 10 to 20 short duration strokes which occurred at intervals shorter than 20 to 30 ms. Alternative interpretation is that the flashes have a continuous optical emission. Based on the energy measurement of 3×10^7 J and the assumption of constant energy/wavelength between 400 nm and 1100 nm, the power of 7×10^7 J was estimated for the optical energy emitted per flash assuming long duration 14 flashes without substrokes. On the other hand, Krasnopol'sky (1983a) estimated that if the flash consisted of 10 to 20 short strokes then the visible stroke energy would drop to 2×10^6 J, corresponding to an estimated $\sim 10^{10}$ J for the total energy dissipated in a single flash.

Pioneer Venus Orbiter: Borucki et al. (1981, 1991) devised a creative use of the Pioneer Venus Orbiter (PVO) Star Tracker to search for optical bursts in the nightside ionosphere of Venus. Scanner measurements near periapsis were studied for 53 orbits in 1988 and 55 orbits in 1990. The cloud coverage consisted of patches predominantly from 2230 local time to the dawn terminator but a patch near the dusk terminator was also viewed. But the rate of pulse detection was compared to the false alarm rate (due to high-energy particles) measured outside of eclipse. Estimated upper bounds to the planetary flash rate were 4×10^7 flashes/km²/s for terrestrial-like short-duration (few hundred microsecond) flashes at least 50% as terrestrial flash using the 1988 data and 1×10^{-7} flashes/km²/s for long duration flashes that are at least 1.6% as bright as typical terrestrial flashes using the 1990 data. Despite this study surveying a large area of the nightside of Venus, the total time of search for the two-year 108 orbits study was only 83 s due to very stringent viewing requirements. Nevertheless, this analysis found no evidence of lightning.

Vega 1 and 2 balloons: Vega balloons searched Venus lightning within the cloud layers of Venus in 1985. Sagdeev et al. (1986). Vega 1 and Vega 2 were inserted near midnight local time at 7°N and 7°S latitude, respectively. They floated in the middle cloud layer at altitudes between ~ 50 km and ~ 54 km. Each carried a silicon PIN diode light detector, sensitive from 400 nm to 1100 nm range, which looked downward with a field of view of ± 60 degrees. Both balloons drifted with the wind for 30 hours from midnight through the dawn terminator. No lightning events were detected.

Galileo: In 1990, the Galileo spacecraft flew by Venus on its way to Jupiter. Solid State Imaging (SSI) camera onboard Galileo observed Venus returned 77 useful images from Venus Belton et al. (1991). If Venus lightning flashes have power characteristics and frequency of occurrence similar to those of terrestrial lightning and spectral characteristics similar to those suggested by Borucki et al. (1985), then it is only marginally possible that they could have been detected by the SSI camera. Nevertheless, in view of the considerable interest in Venus lightning, ten frames were devoted to a search. No indications for the presence of lightning flashes were found in these pictures. Roughly estimated upper bound to total optical energy per flash is $\sim 4 \times 10^9$ J.

Ground-based telescope: Hansell et al. (1995) installed the CCD detector at the 153 cm telescope located on Mt. Bigelow, Arizona and searched for light flashes on the nightside of Venus. Their study carefully employed coronagraphic optics, using 2 masks designed in accordance with the specific geometry for each individual night of viewing. An occulting

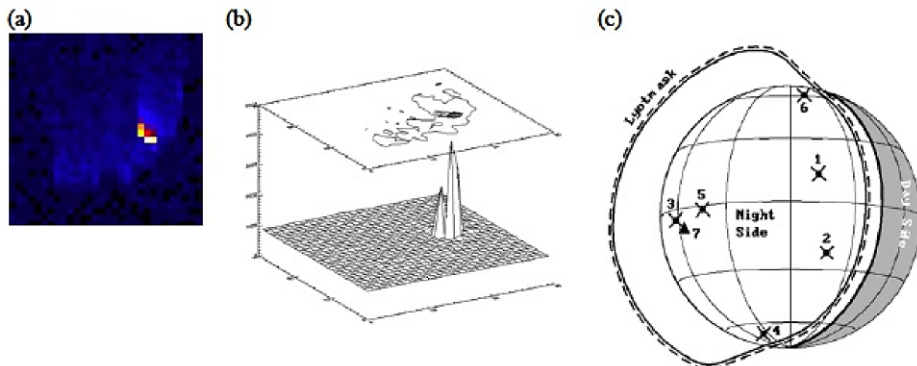


Fig. 1 Example of the CCD image (a) and response (b) for a flash detected at 777.4 nm from Mt. Bigelow, Arizona, (c) Locations of all 7 flash events. Event 7 is the lone burst detected at 658.0 nm and event 1 is the burst depicted in (b) (Hansell et al. 1995)

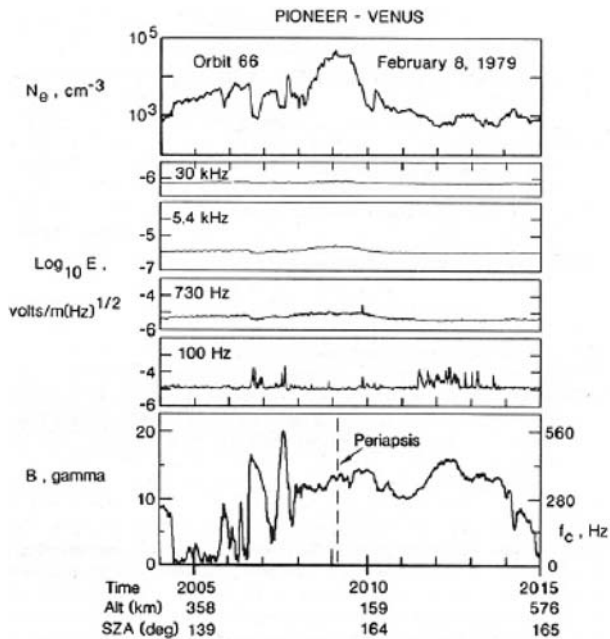
mask was used in the imaging plane and a Lyot mask was used to block diffracted light by the edges and support structure of the secondary mirror. The CCD detector was operated at 18.8 frames/s for 30 pixel Å ~ 30 pixel images of Venus. The observations were made at 777.4 nm (0.7 nm bandwidth) and 656.3 nm (2.0 nm bandwidth). For 8 nights in 1993, the total viewing time was 3 hours at 777.4 nm and 45 minutes at 656.3 nm. The 777.4 nm (atomic oxygen) line is predicted that the strong emission in the Venus lightning spectra by Borucki et al. (1996) and 656.3 nm ($H\alpha$) line was selected as a control measurement, such emissions were not initially expected from lightning discharge on Venus. The dusk side of Venus was facing Earth. Seven events met the stringent criteria (including the requirement that an event must be seen on more than one pixel) that the experimenters used for isolating lightning flashes, as shown in Fig. 1. Six events were detected in the 777.4 nm line. The seventh occurred at 656.3 nm. It was then realized that the spectrum of lightning includes a line at 658.0 nm which is within the rather broad pass band of the filter. The 777.4 nm flashes occur at a rate of 2.7×10^{-12} flashes/km²/s and imply Venus lightning flashes with optical energies from 7×10^7 J to 2×10^9 J.

1.3.2 Electromagnetic Wave Observations

Four electromagnetic wave observations of Venus lightning were made as follows.

Venera 11 and 12 landers: The Venera 11 and 12 probes descended onto Venus in 1978, at similar midday, low latitude locations (Ksanfomality 1980). Each lander carried a high sensitivity loop antenna detector with four narrowband channels centered at 10, 18, 36, and 89 kHz, a wideband signal (8–90 kHz) detector, and an impulse counter. Measurements began at an altitude of ~60 km and continued during the ~1-hour descent and on the surface until contact was lost with the relay spacecraft. Five or six bursts of fine structured wave activity were detected on Venera 11 and two bursts of activity on Venera 12. The duration of the bursts ranged from several to more than 15 minutes. The highest intensities were typically observed in the lowest frequency band centered at 10 kHz. On the surface Venera 12 recorded only one burst of activity 30 minutes after landing, while nothing was recorded from Venera 11. The bursts were composed of pulses occurring at rates ranging from ~10 Hz to ~55 Hz. The pulses seemed to be essentially continuous throughout bursts, with rates that at times exceeded those of radio frequency bursts generated in terrestrial lightning flashes which are typically ≤ 20 Hz.

Fig. 2 Intensity of the whistlers associated with discharges in the atmosphere, recorded by the OEFD instrument on the PVO on 8 February 1979 (Ksanfomality 1980). The vertical scales give the logarithm of the electromagnetic field intensity, the magnetic field intensity (bottom), and the electron density NBeB (top). The whistlers were detected in the 100 Hz channel. At the bottom right is a gyrofrequency scale



Pioneer Venus Orbiter: PVO carried an electric field detector (OEFD) with four (30% bandwidth) frequency bands centered at 100 Hz, 730 Hz, 5.4 kHz, and 30 kHz (Scarf et al. 1980). Figure 2 shows the recorded bursts of 100-Hz activity in the lower ionosphere on the nightside. Because PVO is situated far above the cloud layers; because *in-situ* plasma processes and atmosphere interactions with the spacecraft can generate electric field waves; because propagation paths from the atmosphere into the ionosphere are not well defined; and because there are anomalous OEFD signals, the OEFD measurements in the lower nightside ionosphere have been the subject of much controversy in the (a) (b) (c) literature for more than a decade. This has led to a labyrinth of pro-and-con lightning publications that has made it difficult for those looking from afar to understand issues. Themes of published papers range from the position that all non-spurious OEFD low-altitude signals have a lightning origin (e.g., Russell 1991) to the opposite position of claiming that any inferred association of the OEFD waves with lightning is pure speculation (e.g., Taylor et al. 1995).

Galileo: During the Galileo's Venus flyby, the plasma wave instrument was used to search for Venus lightning signals from 100-kHz to 5.6-MHz range (Gurnett et al. 1991). The data were acquired for 53 minutes in 1990, at distances of 4 to 5 R_V , where R_V is the Venus radius (6052 km), on the dawn flank from the nightside of Venus. All pulses were isolated and nine pulses were identified. However, from anticipated Venus ionosphere conditions under the solar maximum period of the Galileo flyby, lightning generated radio frequency waves can propagate through the ionosphere only if their frequencies exceed the maximum ionospheric electron plasma frequency (~ 1 MHz). So six higher frequency pulses are consistent with a lightning source. A very rough estimate for the flash rate is $\sim 10^{-11}$ flashes/ km^2/s assuming 6 valid flash signatures arising from anywhere on the nightside.

Cassini: The Cassini spacecraft, which was on its way to Saturn, made two gravity-assisted flybys of Venus, the first in 1998, and the second in 1999 (Gurnett et al. 2001). During these fly-bys the Radio and Plasma Wave Science (RPWS) instrument conducted a search for impulsive high-frequency (0.125 to 16 MHz) radio signals from lightning.

Such signals have characteristics of terrestrial lightning, and are commonly heard on AM (amplitude-modulated) radios during thunderstorms. Despite the instrument easily detecting signals from terrestrial lightning during a later flyby of Earth (at a global flash rate estimated to be 70 Hz, which is consistent with the rate expected for terrestrial lightning) and many intense impulsive radio signals were successfully detected from Saturn lightning (Gurnett et al. 2005), no similar signals were detected from Venus. If lightning exists in Venus' atmosphere, the results of these observations indicate that it is either extremely rare, or very different from terrestrial lightning.

1.4 Venus Express and Necessary Observation in the Future Mission

As mentioned above, the existence of Venus lightning has been under investigation and still controversial. Nighttime optical signatures have been detected only on the dusk side of midnight. The observations thus far have been too limited to deduce confidently that this reflects a planetary trend. The PVO OEFD broadband signals, concentrated near 21h00m local time, have been hypothesized to be a consequence of lightning discharges but details of the underlying mechanism or alternate plasma-wave sources have yet to be considered. In 2006, Venus Express which carries a magnetometer (MAG) arrived at Venus, and started to sample magnetic wave at 128 Hz (Russell et al. 2006a, 2006b; Zhang et al. 2006b). From preliminary results (Zhang and Russell 2006a), electromagnetic signals which are likely to originate from Venus lightning have been detected.

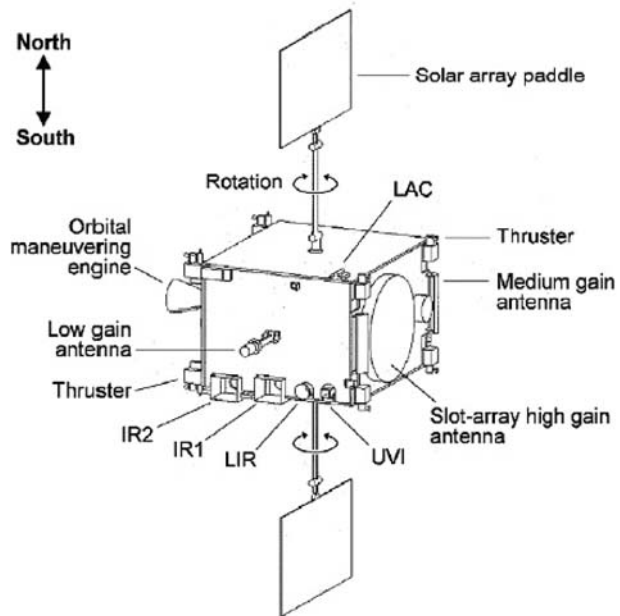
However, it seems that most scientists think the investigations by an optical instrument is essential for the identification of Venus lightning. Venus Monitoring Camera (VMC) and Visible and Infrared Thermal Imaging Spectrometer (VIRTIS) onboard Venus Express has attempted to detect optical lightning flash on the nightside of Venus. Both of the instruments can positively confirm the existence of terrestrial-strength optical lightning flashes if their frequency in the well-scrutinized southern hemisphere is at least one-tenth of one percent of their frequency on Earth (Baines et al. 2006), but no signals have been observed so far (Markiewicz et al. 2006). With respect to the VMC, one reason may be that it does not have the 777.4 nm filter simulated as the strongest line in the Venus lightning spectra by Borucki et al. (1996). In order to conclusively investigate this phenomenon, it is necessary to build an optical instrument which has both high temporal resolution and high sensitivity to detect the temporal variation within one lightning event. If electromagnetic wave observations (~ 100 Hz, $\sim 1\text{--}5$ MHz) can be made simultaneously, it will be possible to confirm whether or not detected signals are originating from lightning.

2 Japanese Venus Climate Orbiter Mission: Planet-C

2.1 Scientific Objectives and Instruments

The Institute of Space and Astronautical Science (ISAS), Japan Aerospace Exploration Agency (JAXA), will launch a Venus Climate Orbiter (VCO) in 2010. This mission, which is called Planet-C, is the third planetary mission in Japan and aims at understanding the meteorology and climate of the Venus atmosphere. This Japanese Venus mission was formally proposed in January 2001 by the Venus exploration working group with members from various universities and institutes. This proposal was approved as one of the M-V satellite projects by the space science committee of ISAS in May 2001, and the mission was named Planet-C. The code name Planet-C means the third Japanese planetary explo-

Fig. 3 Configuration of VCO
(Nakamura et al. 2007)



ration mission; Planet-A mission to Halley's comet and Planet-B mission to Mars which were named *Sakigake* and *Nozomi*, respectively, after their successful launching. In August 2006, the launching vehicle was changed from M-V to H-IIA. The details of this mission are summarized in Japanese Venus Mission Proposal (2001), Ishii et al. (2004), and Nakamura et al. (2007). The VCO is the first meteorological satellite of a Venus orbiter. The science goals are as follows:

- 1) To understand the mechanism of the superrotation of the atmosphere
- 2) To understand the structure of meridional atmospheric circulation
- 3) To survey the global structure of the meso-scale meteorological phenomena
- 4) To understand the mechanism of cloud formation and lightning discharge
- 5) To measure the ground surface radiant emittance and exploration of active volcanoes.

In order to achieve these objectives, five cameras have been developed. These cameras cover the wavelength range of UV (280 and 360 nm), near-IR (1.0, 1.7, 2.0, and 2.3 μm), and long-IR (8–12 μm). The lightning and airglow camera (LAC) measures lightning flashes and airglow emissions on the Venus nightside disk. The Near-IR cameras (IR1 and IR2) measure lower clouds around 50 km altitude and the distribution of carbon monoxide below clouds, while the ultraviolet imager (UVI) and the longwave-IR camera (LIR) measure the cloud top region around 70 km. Multi-wavelength images obtained from concurrent operation of these cameras and the temperature profiles obtained from radio occultation enable us to investigate the three-dimensional structures of atmosphere and their dynamics.

2.2 Spacecraft Design

The specifications of the spacecraft are summarized in Table 1. The VCO will be launched by H-IIA in the early 2010 and arrival at Venus is scheduled for late 2010. The configuration of the spacecraft is illustrated in Fig. 3. The spacecraft has a three-axis stabilized attitude

Table 1 Specifications of the spacecraft

Parameters	Value
Launch	Early 2010
Arrival	Late 2010
Vehicle	H-IIA
Launch site	Tanegashima Space Center (TNSC), Japan
Orbital insertion	Direct insertion (into interplanetary orbit by a rocket)
Orbital period	~180 days (till Venus arrival)
Observation period	More than 2 years (after Venus arrival) Periapsis: ~300 km Quasi-synchronous equatorial orbit
Orbit	Apoapsis: ~78700 km (13 R _V [*]) Period: 30 hours Inclination: ~172° B-Plane angle: ~185°
Shadow duration	Umbra: 90 minutes (including penumbra: 100 minutes)
Size	1450 × 1040 × 1400 mm Wet: 500 kg
Mass	Dry: 313 kg Science payload: 32.50 kg
Attitude control	3-axis stabilized

^{*}R_V: Venus radii (= ~6050 km)

control to give the optimum platform for atmospheric imaging. This orbit allows the angular motion of the spacecraft to be approximately synchronized with the westward mean zonal wind over a span of 24 hours around the apogee region. This geometry enables us to observe temporal evolution of meteorological phenomena. Such 20-hour continuous observations are performed in every orbital revolution over the mission life of more than 2 years. The time scales of atmospheric phenomena recorded in such datasets range from several minutes to several months. The synchronized orbit also allows derivation of the horizontal wind fields from cloud motions with high accuracy. Close-up images of meso-scale features and limb images are obtained near the periapsis. The shadow region along the orbit is utilized for observing lightning flashes and airglow. Radio occultation experiment is performed when the spacecraft is hidden by Venus as viewed from the ground station.

2.3 Lightning and Airglow Camera: LAC

The lightning and airglow camera (LAC), one of the five cameras installed in VCO, has been developed by our team of the Planetary Atmosphere Physics Laboratory, Department of Geophysics, Graduate School of Science, Tohoku University. LAC is a new camera developed for measurements of planetary lightning flashes and global distributions of airglow. The LAC measures Venus lightning flashes and airglows on the nightside disk when the VCO is located within the umbra (shadow region) of Venus. As described in Sect. 1, the existence of Venus lightning is still a controversial issue in spite of optical and electromagnetic wave observations for more than 25 years. We aim to conclude this controversy by LAC observations. The high speed optical detector of the LAC is adopted for optical measurement,

which enables us to distinguish between lightning flashes and electrical noise pulses. The scientific objectives of the LAC are as follows:

- 1) To confirm, for the first time, the existence of Venus lightning
- 2) To obtain information on the durations on flashes, optical flash energies, spatio-temporal distributions, and the global occurrence rates
- 3) To detect volcanic thunderstorms in corporation with near-IR camera 1 (IR1)

Furthermore, using the above observation data, the following subjects are investigated:

- 4) To confirm vertical convection in Venus' atmosphere
- 5) To obtain part of the fundamental information relating to the global electric circuit of the atmosphere
- 6) To evaluate the chemical impact of lightning on the Venus atmosphere
- 7) To explore the relationship between active volcanoes and lightning In addition, the LAC has enough sensitivity to detect airglow emissions in the Venus upper atmosphere. The science goals of LAC airglow observations are listed as follows:
- 8) To investigate the global distributions and the spatio-temporal variations of molecular and atomic oxygen airglows
- 9) To detect the wavelike structures caused by atmospheric gravity waves
- 10) To investigate the vertical profiles of airglow intensities

Furthermore, using the above observation data, the following subjects are investigated:

- 11) To understand the structures and spatio-temporal variations of global circulation in the upper atmosphere
- 12) To investigate the coupling process between the upper atmosphere and the lower atmosphere by evaluating the effect of atmospheric gravity waves
- 13) To understand the atomic oxygen emission mechanism

3 Development of LAC

3.1 Required Performances

We have designed and developed the LAC, carrying out various examinations and experiments since FY 2001. As summarized in Table 2, the LAC has been developed in collaboration with several institutes and corporations.

Table 2

Department	Person or company in charge
Principal investigator	Yukihiro Takahashi (Tohoku University)
Co-investigators	Masaki Tsutsumi (National Institute of Polar Research) Tomoo Ushio (Osaka University)
Electronics and assembly	Meisei Electric Co., Ltd.
Optical system and lenses	Nikon Corporation
Optical sensor	Hamamatsu Photonics K. K.
Filters	Barr Associates, Inc. (Fujitok Corporation)
Satellite system	NEC TOSHIBA Space Systems, Ltd.

In order to achieve scientific objectives as shown in previous section, we set the sensitivity requirement that we can detect the same intensity of typical terrestrial lightning flashes from an altitude of 5 R_V even if they occur under the cloud layer. The optical energies of Venus lightning flashes have been estimated to be $\sim 10^7$ to $\sim 10^9$ J (Krasnopolsky 1983a; Hansell et al. 1995), which are ~ 10 to $\sim 10^3$ times more than those of typical terrestrial lightning flashes ($\sim 10^6$ J). However, weaker flashes may not be detected because of the low sensitivity and low temporal resolution of the instrument. If the above requirement can be satisfied, this instrument allows us to detect 1/1000 intensity of typical terrestrial lightning flash from an altitude of 1000 km. In this study, the required Signal-to-Noise Ratio (SNR) to detect lightning flash is set to be 10.

In order to detect the Venus lightning and airglow with a single camera, the following requirements have to be satisfied.

- 1) To adopt a high-speed and high-sensitivity optical sensor: Although the duration of the Venus lightning flash is unknown, it is expected to be extremely short similar to the case of terrestrial lightning. The intensities of Venus airglow, are expected especially atomic oxygen lines, are expected to be very weak. Therefore, the LAC needs a high-speed and high-sensitivity sensor.
- 2) To detect a lightning flash using pre-trigger sampling: Since the LAC aims to detect temporal evolution in lightning flashes, a high-speed sampling is essential. Since continuous high-speed data sampling is impossible for planetary missions, it is necessary to adopt a pre-trigger sampling method which enables us to save only the pre- and post-trigger data with high sampling rates.

3.2 Design of LAC

We started the design of the LAC in FY2001. The final optical performances of LAC are summarized in Table 3.

3.3 Observing Wavelengths

We selected interference filters for LAC as follows: Lightning observation is made of wavelength at 777.4 nm (atomic oxygen line). The laboratory simulations by Borucki et al. (1996) that this line is the strongest emission in the Venus lightning spectrum. In addition, Hansell et al. (1995) presented evidence on the Venus lightning flashes in the nightside disk at this wavelength. Airglow observation is performed in the wavelength range of 480–605 nm (molecular oxygen Herzberg II band), 557.7 nm (atomic oxygen green line). The Herzberg II band is the strongest emission in the visible wavelength range of Venus airglow (Krasnopolsky 1983a). The atomic oxygen green line emission was discovered by recent ground-based observations (Slanger et al. 2001), while the Venera 9 and 10 orbiters reported the lack of this emission (Krasnopolsky 1983a). In addition, in order to record background, airglow-free images are acquired at 545.0 nm.

3.4 APD Detector

We adopt a multi-anode silicon avalanche photodiode (SiAPD) as a detector. The APD is an opto-semiconductor and high-speed, high-sensitivity photodiode utilizing an internal gain mechanism that functions by applying a reverse voltage. The APD gain (M ; multiplication ratio) depends on the electric field applied across the avalanche layer. Normally, the higher

Table 3 Optical performances of LAC

Parameter	Value
Wavelengths	777.4 nm (lightning) 480–605 nm (O_2 Herzberg II band airglow) 557.7 nm (O_2 line airglow) 545.0 nm (airglow-free background image)
Interference filter	Array bandpass filter
Image sensor	Hamamatsu Si APD (Avalanche photodiode) 4461
Pixel size	2.0 mm × 2.0 mm
Image sensor format	Gap between pixels: 0.20 mm 8 pixels × 8 pixels
Field of view	16.0 degrees × 16 degrees ($2\omega = 23.3$ degrees)
Angular resolution	1.84 degrees/pixel
Spatial resolution	32 km @1,000 km 580 km @3Rv
Optics	Image-side telecentric
Objective lens	Aspheric lens
Entrance pupil (diaphragm)	25.0 mm dia
Focal length (<i>F</i> number)	61.9 mm (<i>F</i> / ~ 2.5)

the reverse voltage (*VR*) becomes, the higher the gain becomes. APDs have excellent vibration and thermal tolerances so that they are suitable for space application. However, the APD gain also has time-dependent characteristics. The gain at a certain reverse voltage becomes small as the temperature rises. Therefore, in order to obtain constant output, it is necessary to adjust the reverse voltage according to the changes in temperature or to keep the APD temperature constant. We developed a new multi anode SiAPD (No. 4461) in collaboration with Hamamatsu Photonics. The design and the view are displayed in Fig. 4. It has 8 by 8 matrix of 2 mm square pixels and the gap between pixels is 0.2 mm. The maximum gain is designed to be 100.

3.5 Array Bandpass Filter

Imaging observations of LAC are made using five filters. A filter wheel system is usually adopted to choose one of filters. However, this system is very heavy (~ 1.5 kg) and there is risk of an electric motor's breaking down. Instead of the filter wheel system, we have developed the rectangular interference filters in corporation with Barr Associates Inc. and Fujitok Corporation. Measurement of lightning flash at 777.4 nm is carried out with 4 × 8 pixels, while measurements of airglow emissions at 551.0–552.5 nm, 557.7 nm, and 630 nm are performed with 1 by 8 pixels, respectively. Airglow-free background images are also acquired at 545.0 nm with 1 × 8 pixels with the same kind of filter. As illustrated in Fig. 5, a complex of these interference filters, which is called as an array bandpass filter (ABPF), is placed on the detector. Each rectangular filter is bonded with black epoxy. Support glass is placed on both side of ABPF to stabilize its structure. In order to improve its vibrational tolerance, it is surrounded with a super invar case made by Nikon Corporation.

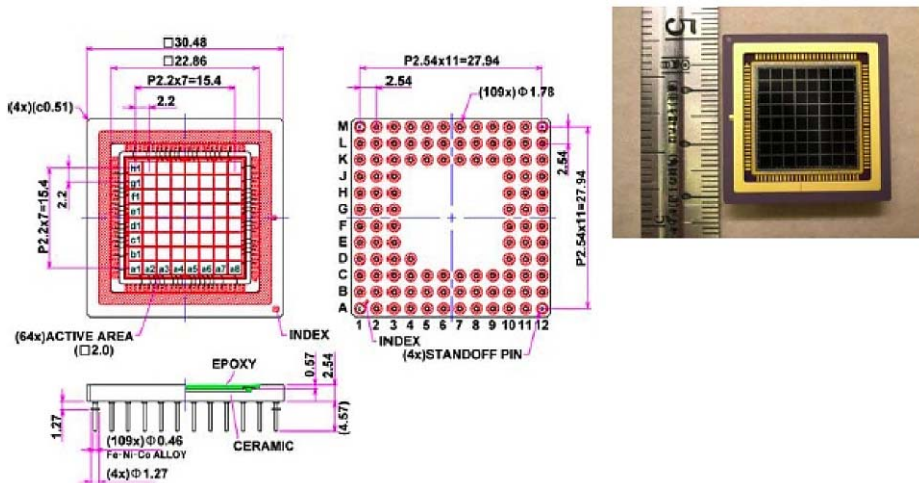


Fig. 4 Design (*left*) and view (*right*) of SiAPD 4461

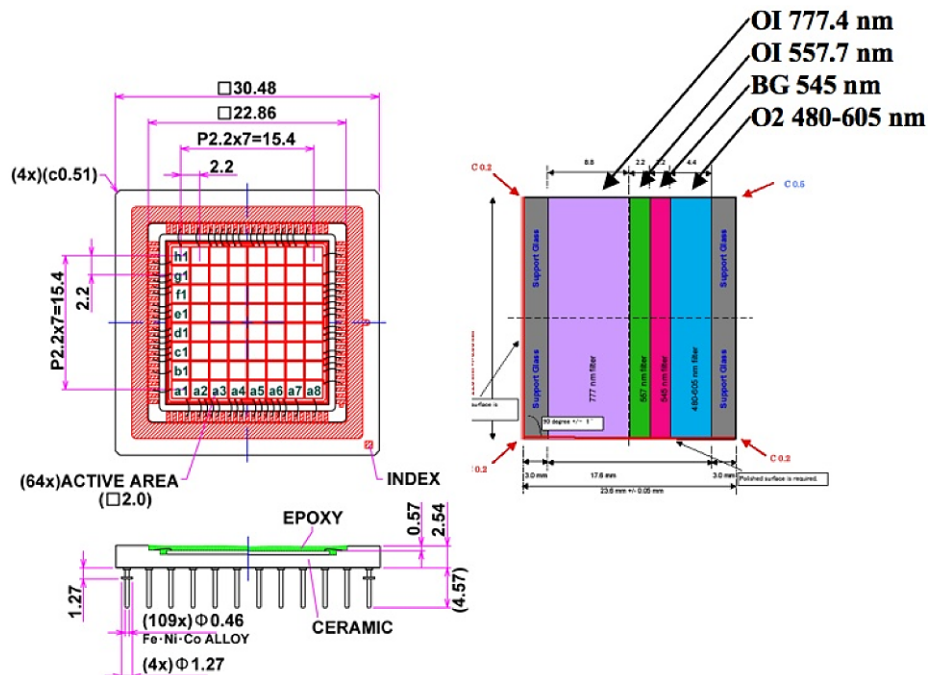


Fig. 5 Schematic view of array bandpass filter

3.6 Optical Design

The LAC is operated when the VCO spacecraft is located within the umbra (shadow region) of Venus. FOV is set to be 16×16 degrees so that it can cover the whole nightside disk using

all of the SiAPD pixels when VCO is located at ~ 5 Rv. Although the half angle corresponding to the image circle (ω) is 11.3 degrees based on paraxial theory, it becomes 11.6 degrees taking the distortion into consideration. Angular resolution per pixel is 1.84 degrees/pixel because of the pixel size and the gap between pixels. Based on the sizes of Si APD and FOV, the focal length of this optics is calculated to be 61.9 mm. The aperture is set as 25.0 mm taking the mass and the size of LAC into consideration. All of the ABPF (interference filters) of the LAC have narrow (or broad) bandwidths (a few nanometers min.); therefore, we have to consider their central wavelength shift as a function of incident angle. We adopted an image-side telecentric system as the optics of LAC. Using this optical design the chief rays become parallel to the optical axis on the image side. This realizes that the maximum incident angle become 11.4 degrees, which is much smaller than that of the non-telecentric system.

The LAC optics is bright (F number is ~ 2.5) by adopting a single aspherical lens to save the mass. The material of the lens is quartz, which has excellent radiation tolerance. The focal length depends on wavelength because chromatic aberration is not considered. According to a spot diagram analyzed by Nikon Corporation, spot size in shorter wavelength range is smaller at object-side defocus position due to axial chromatic aberration. In addition, spot size formed by luminous flux with a large angle of view is smaller at object-side defocus position due to field curvature. We decided an arrangement of ABPF as shown in Fig. 5. In order to stabilize the structure of ABPF, rectangular filters covering 1×8 pixels are placed on the both sides.

The LAC has the structure without filter wheels to satisfy the mass requirement; thus there are no shutters in the LAC optics. According to the orbital analysis by NEC TOSHIBA Space Systems, Ltd., it is reported that direct sunlight illuminates the first component of the optics every orbital revolution, although observations are carried out only when the orbiter is located in the Venus umbra. Normally, power supply is turned off except for observation time; however, extreme amount of light and thermal radiation may cause APD's or ABPF's to break down. In order to reduce light and thermal radiation influx as much as possible, an interference filter which transmits only observing wavelength range is set on the front of LAC optics. Here this filter is called a Solar Blocking Filter (SBF). Reflecting light from the detector and SBF may produce uneligible ghost image. Considering half angle of view with margin, the SBF is inclined 9 degrees relative to principle plane so that ghost image cannot be formed at the receiving side of the detector.

3.7 Observation Plan and SNR Estimation

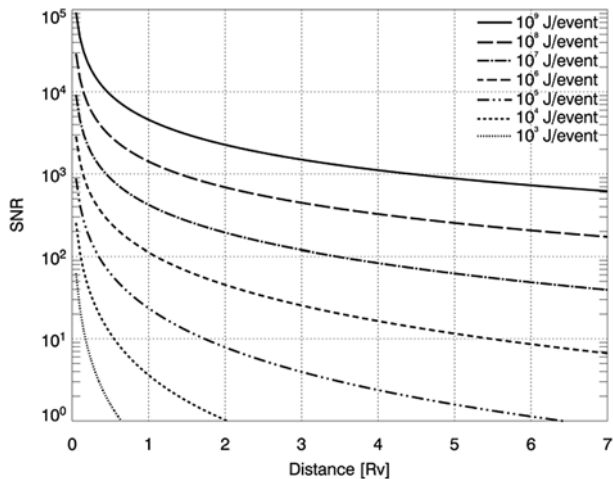
In order to measure the luminous phenomena which show different temporal variations (lightning flashes and airglow emissions), current to voltage conversion amplifiers with high-speed and low-speed time constant are connected to APD's pixels. Note that there are no plans to observe lightning and airglow simultaneously. The planned observation modes are summarized in Table 4 and described here for only lightning observation mode.

Assuming that duration of Venus lightning flashes is the same as that of representative terrestrial ones (~ 20 micro sec), sampling frequency is set to be 50 kHz. This enables us to detect the temporal variations of brightness within one flash so that we can distinguish between lightning flash and electrical noise pulse. However, high temporal sampling produces a large amount of data. We adopt the pre-trigger sampling method, which can acquire 2–2000 ms data from pre- to post-trigger periods depending on the duration of lightning flashes. Estimated SNR of lightning observations as a function of optical energy and distance from light source is shown in Fig. 6. From an altitude of 5 Rv, the LAC enables us to detect the same intensity of typical terrestrial lightning flash (106 J) with SNR of ~ 12 .

Table 4 Observation modes

Parameter	Lightning observation mode	Airglow observation mode
Method	Pre-trigger sampling	Numerical integration
Temporal resolution (Sampling rate)	5×10^4 samples/s/pixel	1 sample/integration time/pixel
Data acquisition time	2, 20, and 200 ms (Sum of pre- and post-trigger time period)	—
Integration time	—	10, 30, and 90 s
Data depth	8 bit/pixel	24 bit/pixel

Fig. 6 Estimated SNR of lightning observations as a function of optical energy and distance from light source. From an altitude of 5 R_V, LAC enables us to detect the same intensity of typical terrestrial lightning flash (106 J) with SNR of ~12



3.8 Proto Model Design

Based on the considerations above a prototype LAC model has been produced. The LAC consists of the sensor (LAC-S) and the electronics (LAC-E). The former includes optics, detector, current-to-voltage conversion amplifiers, Bright Object Sensor (BOS), thermal sensor, high voltage power supply, etc., while the latter includes power supply, followers, Analog-to-Digital Converters (ADCs), multiplexers (MPXs), Field Programmable Gate Array (FPGA), Static Random Access Memories (SRAMs), DC-to-DC converters, etc. 3-dimensional images of LAC-S and LAC-E and the detailed cross section of LAC-S are depicted in Fig. 7. On the assumption that sunlight or reflected sunlight from the Venus dayside disk illuminates the LAC due to some troubles of orbital operation while LAC observes the Venus nightside disk, the bright object sensor (BOS) is placed on the top of LAC-S to protect the APD. The BOS enables us to lower the high voltage and to turn off the power supply before the LAC detects a large amount of light. Configuration of VCO is depicted in Fig. 3. LAC will be set on the +Y panel and view direction look toward -X-axis, which is the same view direction of other cameras.

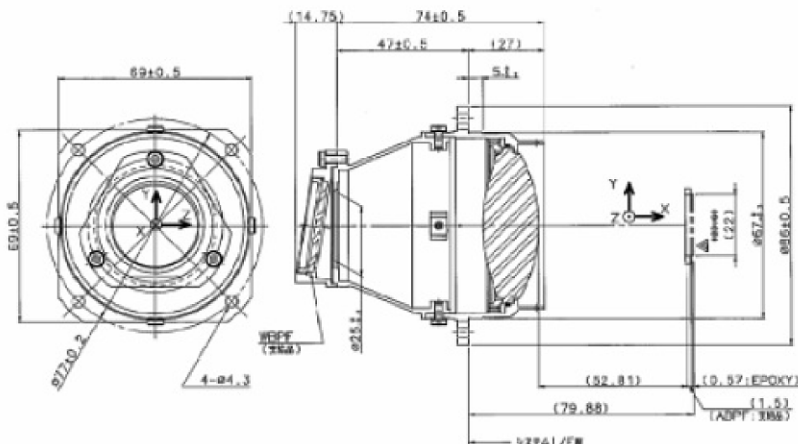
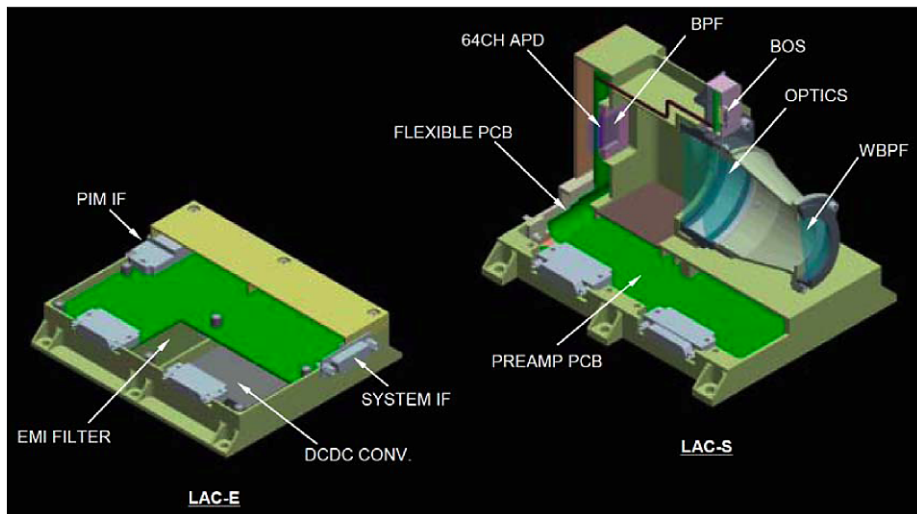


Fig. 7 (Top) 3-dimensional images of LAC-S and LAC-E and (bottom) cross section of LAC-S

4 Summary and Conclusion

LAC is a high-speed imaging sensor which measures lightning flashes and airglow emissions on the nightside disk of Venus from within the umbra (shadow region). One of the major goals of LAC is to settle controversy on the occurrence of lightning in the Venusian atmosphere. Lightning observations will give us information on the charging mechanism, charge separation mechanism, physics of sulfuric acid clouds, mesoscale meteorology and its impacts on atmospheric chemical processes. If lightning discharge occurs in the upwelling cloud regions like as the Earth and Jupiter, we can monitor vertical convections inside the cloud layer via lightning detection. The 777.4 nm [OI] line associated with the excitation of atomic oxygen is expected to be a strong emission from the laboratory discharge experiment in a simulated Venusian atmosphere (Borucki et al. 1996). Possible lightning

flashes were detected on the nightside disk of Venus at this wavelength by a ground-based telescope (Hansell et al. 1995). But, due to the observational difficulties, the existence of lightning in Venus' atmosphere remains controversial.

LAC is designed to detect lightning flashes with an intensity of 1/100 of standard lightning on the Earth when viewed from 1000 km altitude. LAC has a field-of-view of 16 degrees, and the detector uses a multi-anode avalanche photo-diode (APD) that has 8×8 matrix of 2-mm square pixels. We will measure lightning flashes at 777.4 nm [OI] with 4×8 pixel area. A complex of these interference filters is placed on the detector. Individual lightning flash events are sampled at 50-kHz by pre-triggering. The field-of-view of one pixel corresponds to about 35 km on the Venusian surface at 1000 km altitude and 850 km at 3 R_V altitude. LAC onboard VCO will arrive at Venus in 2010 and could conclude controversial situation on lightning activity.

Acknowledgements We would like to acknowledge all members of the VCO project team for developing the mission plan and the spacecraft and instrument designs. The LAC has been developed, collaborating with the Meisei Electric Co., Ltd., Hamamastu, Photonics K. K., Nikon Corp., and Barr Associates, Inc./Fujitoku Corp.

References

- K.H. Baines, S. Atreya, R.W. Carlson, D. Crisp, P. Drossart, V. Formisano et al., To the depths of Venus: Exploring the deep atmosphere and surface of our sister world with Venus Express. *Planet. Space Sci.* **54**, 1263–1278 (2006). doi:[10.1016/j.pss.2006.04.034](https://doi.org/10.1016/j.pss.2006.04.034)
- M.J.S. Belton, P.J. Gierasch, M.D. Smith, P. Helfenstein, P.J. Schinder, J.B. Pollack et al., Images from Galileo of the Venus cloud deck. *Science* **253**, 1531–1536 (1991). doi:[10.1126/science.253.5027.1531](https://doi.org/10.1126/science.253.5027.1531) Medline
- W.J. Borucki, J.W. Dyer, G.Z. Thomas, J.C. Jordan, D.A. Comstock, Optical search for lightning on Venus. *Geophys. Res. Lett.* **8**, 233–236 (1981). doi:[10.1029/GL008i003p00233](https://doi.org/10.1029/GL008i003p00233)
- W.J. Borucki, R.L. Mc Kenze, C.P. McKay, N.D. Duong, D.S. Boac, Spectra of simulated lightning on Venus, Jupiter, and Titan. *Icarus* **64**, 221–232 (1985). doi:[10.1016/0019-1035\(85\)90087-9](https://doi.org/10.1016/0019-1035(85)90087-9) Medline
- W.J. Borucki, J.W. Dyer, J.R. Phillips, P. Phan, Pioneer Venus Orbiter search for Venusian lightning. *J. Geophys. Res.* **96**, 11033–11043 (1991). doi:[10.1029/91JA01097](https://doi.org/10.1029/91JA01097)
- W.J. Borucki, C.P. McKay, D. Jebens, H.S. Lakkaraju, C.T. Vanajakshi, Spectral irradiance measurements of simulated lightning in planetary atmospheres. *Icarus* **123**, 336–344 (1996). doi:[10.1006/icar.1996.0162](https://doi.org/10.1006/icar.1996.0162)
- A.F. Cook, T.C. Duxbury, G.E. Hunt, First results on Jovian lightning. *Nature* **280**, 794 (1979). doi:[10.1038/280794a0](https://doi.org/10.1038/280794a0)
- U.A. Dyudina, A.D. Del Genio, A.P. Ingersoll, C.C. Porco, R.A. West, A.R. Vasavada et al., Lightning on Jupiter observed in the H α line by the Cassini imaging science subsystem. *Icarus* **172**, 24–36 (2004). doi:[10.1016/j.icarus.2004.07.014](https://doi.org/10.1016/j.icarus.2004.07.014)
- L.W. Esposito, Sulfur dioxide—Episodic injection shows evidence for active Venus volcanism. *Science* **223**, 1072–1074 (1984). doi:[10.1126/science.223.4640.1072](https://doi.org/10.1126/science.223.4640.1072) Medline
- G. Fisher, M.D. Desch, P. Zarka, M.L. Kaiser, D.A. Gurnett, W.S. Kurth, W. Macher, H.O. Rucker, A. Lecacheux, W.M. Farrell, B. Cecconi, Saturn lightning recorded by Cassini/RPWS in 2004. *Icarus* **183**, 135–152 (2006). doi:[10.1016/j.icarus.2006.02.010](https://doi.org/10.1016/j.icarus.2006.02.010)
- J.M. Grebowsky, R.J. Strangeway, D.M. Hunten, Evidence for Venus lightning, in *Venus II*, ed. by S.W. Bougher et al. (Univ. of Arizona Press, Tucson, 1997), pp. 125–157
- D.A. Gurnett, R.R. Shaw, R.R. Anderson, W.S. Kurth, F.L. Scarf, Whistlers observed by Voyager 1: Detection of lightning on Jupiter. *Geophys. Res. Lett.* **6**, 511–514 (1979). doi:[10.1029/GL006i006p00511](https://doi.org/10.1029/GL006i006p00511)
- D.A. Gurnett, W.S. Kurth, A. Roux, R. Gendrin, C.F. Kennel, S.J. Bolton, Lightning and plasma wave observations from the Galileo flyby of Venus. *Science* **253**, 1522–1525 (1991). doi:[10.1126/science.253.5027.1522](https://doi.org/10.1126/science.253.5027.1522) Medline
- D.A. Gurnett, P. Zarka, R. Manning, W.S. Kurth, G.B. Hospodarsky, T.F. Averkamp et al., Non-detection at Venus of high-frequency radio signals characteristic of terrestrial lightning. *Nature* **409**, 313–315 (2001). doi:[10.1038/35053009](https://doi.org/10.1038/35053009) Medline
- D.A. Gurnett, W.S. Kurth, G.B. Hospodarsky, A.M. Persoon, T.F. Averkamp, B. Cecconi et al., Radio and plasma wave observations at Saturn from Cassini's approach and first orbit. *Science* **307**, 1255–1259 (2005). doi:[10.1126/science.1105356](https://doi.org/10.1126/science.1105356) Medline

- S.A. Hansell, W.K. Wells, D.M. Hunten, Optical detection of lightning on Venus. *Icarus* **117**, 345–351 (1995). doi:[10.1006/icar.1995.1160](https://doi.org/10.1006/icar.1995.1160)
- N. Ishii, H. Yamanaka, S. Sawai, M. Shida, T. Hashimoto, M. Nakamura et al., Current status of the PLANET-C Venus orbiter design. *Adv. Space Res.* **34**, 1668–1672 (2004). doi:[10.1016/j.asr.2004.07.006](https://doi.org/10.1016/j.asr.2004.07.006)
- V.A. Krasnopolsky, Venus spectroscopy in the 3000–8000 Å region by Veneras 9 and 10, in *Venus*, ed. by D.M. Hunten et al. (Univ. of Arizona Press, Tucson, 1983a), pp. 459–483
- V.A. Krasnopolsky, Lightnings and nitric oxide on Venus. *Planet. Space Sci.* **31**, 1363–1369 (1983b). doi:[10.1016/0032-0633\(83\)90072-7](https://doi.org/10.1016/0032-0633(83)90072-7)
- V.A. Krasnopolsky, A sensitive search for nitric oxide in the lower atmospheres of Venus and Mars: Detection on Venus and upper limit for Mars. *Icarus* **182**, 80–91 (2006). doi:[10.1016/j.icarus.2005.12.003](https://doi.org/10.1016/j.icarus.2005.12.003)
- L.V. Ksanfomality, Discovery of frequent lightning discharges in clouds on Venus. *Science* **284**, 244–246 (1980)
- L.J. Lanzerotti, K. Rinnert, G. Dehmel, F.O. Gliem, E.P. Krider, M.A. Uman et al., The Lightning and Radio Emission Detector (LRD) instrument. *Space Sci. Rev.* **60**, 91–109 (1992). doi:[10.1007/BF00216851](https://doi.org/10.1007/BF00216851)
- J.S. Levine, G.L. Gregory, G.A. Harvey, W.E. Howell, W.J. Borucki, R.E. Orville, Production of nitric oxide by lightning on Venus. *Geophys. Res. Lett.* **9**, 893–896 (1982). doi:[10.1029/GL009i008p00893](https://doi.org/10.1029/GL009i008p00893)
- B. Little, C.D. Anger, A.P. Ingersoll, A.R. Vasavada, D.A. Senske, H.H. Breneman et al., The Galileo SSI Team, Galileo images of lightning on Jupiter. *Icarus* **142**, 306–323 (1999). doi:[10.1006/icar.1999.6195](https://doi.org/10.1006/icar.1999.6195)
- W.J. Markiewicz, D.V. Titov, N. Ignatiev, H.U. Keller, D. Crisp, L. Esposito et al., First results from Venus Monitoring Camera on Venus Express, American Astronomical Society, the 38th DPS meeting, Pasadena, US, 2006
- C.Y. Na, L.W. Esposito, W.E. McClintock, C.A. Barth, Sulfur dioxide in the atmosphere of Venus: II Modeling results. *Icarus* **112**, 389–395 (1994). doi:[10.1006/icar.1994.1193](https://doi.org/10.1006/icar.1994.1193)
- M. Nakamura, T. Imamura, M. Ueno, N. Iwagami, T. Satoh, S. Watanabe, et al., PLANET-C: Venus climate orbiter mission of Japan. *Planet. Space Sci.* **55**, 1831–1842 (2007).
- Y. Ohba, H. Itabashi, Y. Goto, Optical measurements in long gap carbon dioxide discharge, *Proc. Soc. Atmos. Electr. Jpn.* **63** (2003) (in Japanese)
- Y. Ohba, H. Koriyama, Y. Sato, Y. Goto, Spectral measurements of long gap carbon dioxide discharge by 1 MVIG, *Proc. Soc. Atmos. Electr. Jpn.* **64** (2004) (in Japanese)
- V.A. Rakov, M.A. Uman, *Lightning: Physics and Effects* (Cambridge Univ. Press, Cambridge, 2003)
- C.T. Russell, Venus lightning. *Space Sci. Rev.* **55**, 317–356 (1991)
- C.T. Russell, T.L. Zhang, M. Delva, W. Magnes, R.J. Strangeway, H.Y. Wei, Lightning on Venus inferred from whistlemode waves in the ionosphere. *Nature* **450**, (2006a). doi:[10.1038/nature05930](https://doi.org/10.1038/nature05930)
- C.T. Russell, R.J. Strangeway, T.L. Zhang, Lightning detection on the Venus Express mission. *Planet. Space Sci.* **54**, 1344–1351 (2006b). doi:[10.1016/j.pss.2006.04.026](https://doi.org/10.1016/j.pss.2006.04.026)
- R.V. Sagdeev, V.M. Linkin, V.V. Kerzhanovich, A.N. Lipatov, A.A. Shurupov, J.E. Blamont et al., Overview of VEGA balloon in situ meteorological measurements. *Science* **231**, 1411–1414 (1986). doi:[10.1126/science.231.4744.1411](https://doi.org/10.1126/science.231.4744.1411) Medline
- F.L. Scarf, W.W.L. Taylor, C.T. Russell, L.H. Brace, Lightning on Venus: Orbiter detection of whistler signals. *J. Geophys. Res.* **85**, 8158–8166 (1980). doi:[10.1029/JA085iA13p08158](https://doi.org/10.1029/JA085iA13p08158)
- T.G. Slanger, P.C. Cosby, D.L. Huestis, T.A. Bida, Discovery of the atomic oxygen green line in the Venus night airglow. *Science* **291**, 463–465 (2001)
- H.A. Taylor Jr., L. Kramer, P.A. Cloutier, S.S. Walker, Signatures of solar wind interaction with the nightside of Venus. *Earth Moon Planets* **69**, 173–199 (1995). doi:[10.1007/BF00613097](https://doi.org/10.1007/BF00613097)
- Venus exploration working group, Japanese Venus Mission Proposal. The Institute of Space and Astronautical Science, 2001
- T.L. Zhang, C.T. Russell, Magnetometer team, Solar wind interaction with Venus: Venus Express magnetic experiment initial results, American Astronomical Society, the 38th DPS meeting, Pasadena, US, 2006a
- T.L. Zhang, W. Baumjohann, M. Delva, H.-U. Auster, A. Balogh, C.T. Russell et al., Magnetic field investigation of the Venus plasma environment: Expected new results from Venus Express. *Planet. Space Sci.* **54**, 1336–1343 (2006b). doi:[10.1016/j.pss.2006.04.018](https://doi.org/10.1016/j.pss.2006.04.018)

Charge Generation and Separation

Charge Separation Mechanisms in Clouds

Clive Saunders

Originally published in the journal Space Science Reviews, Volume 137, Nos 1–4.
DOI: [10.1007/s11214-008-9345-0](https://doi.org/10.1007/s11214-008-9345-0) © Springer Science+Business Media B.V. 2008

Abstract Mechanisms of thunderstorm electrification are presented and discussed.

Keywords Charge separation mechanisms: drop break-up, ion charging, convective charge transport, inductive processes · Ice particle mechanisms: Workman–Reynolds freezing potentials, contact potentials, dislocation charges, temperature gradients, melting effects, ice splinter charges, fragmentation effects · Ice crystal/graupe1 charging: thunderstorm observations, charging requirements, laboratory studies, ice/ice charging mechanism

1 Introduction

Worldwide thunderstorm activity is responsible for maintaining a weak negative charge on the Earth's surface and a corresponding positive charge in the atmosphere. In general, cloud to ground lightning brings negative charge to ground from a negatively charged region in the cloud that also releases positive ions by point discharge in the strong electric field region below a thunderstorm. The resulting global fair weather electric field is around -120 V m^{-1} at the ground and decreases to zero in the conducting region of the ionosphere. Wilson (1916) assumed a vertical charge dipole within thunderstorms and determined that the charge regions are usually positive above negative: he measured electric field changes at the ground caused by intra-cloud lightning in which the dipole charges neutralised each other. This picture was confirmed with extensive electric field change measurements made by Krehbiel et al. (1979) in New Mexico, in which the locations and values of charges in thunderstorm charge centres were determined. More complicated charge centre distributions have been reported, for example, by Stolzenburg et al. (1998).

The generally accepted concept for the development of the thunderstorm charge dipole is the physical separation of oppositely charged particles within the cloud. Larger cloud particles fall under gravity while smaller particles are transported in the updraught; if these

C. Saunders (✉)

School of Earth, Atmospheric and Environmental Sciences, The University of Manchester, Manchester,
M13 9PL, UK
e-mail: clive.saunders@manchester.ac.uk

particles carry negative and positive charges respectively then the normal charge dipole will result.

2 Charging Mechanisms

2.1 Drop Break-up

Many mechanisms have been proposed to account for the observed charges on cloud particles. Lenard (1892) noted the electrical effects associated with drop break-up near waterfalls. The larger droplets became positively charged while the fragments were negative. This may be explained by the negative electric charge on the surface of water that is carried away on the smaller fragment droplets. Blanchard (1963) observed that bubble bursting over the oceans releases positively charged jet droplets formed from the positive liquid inside the drops; these charged droplets may be carried up into clouds by the local air currents. However, the break-up of individual water droplets in clouds is a rare event, surface tension forces are sufficient to hold all but the largest drops together even in the presence of severe turbulence. Drop break-up may only occur during collisions of two particles, when other, stronger, charging processes may take place leading to an ordered separation of opposite charges in the cloud.

2.2 Ion Charging

Charging processes have been considered involving atmospheric ions produced by cosmic rays and by radioactivity in the ground. The ionisation in a volume of free air over land is around 11 ion pairs per cubic centimetre per second. Thunderstorms themselves produce positive ions in the high field regions below cloud by corona discharge from sharply pointed objects. Lightning bringing negative charge to ground injects large numbers of positive ions into the cloud where the ions may become involved in subsequent cloud particle charging.

Gerdien (1905) used the result that water molecules deposit more readily on negative ions than on positive ions as a process of cloud particle initiation; however, unrealistically high supersaturations of several hundred percent are required to activate droplet growth on ions, as shown by C.T.R. Wilson with his cloud chamber.

Wilson (1929) proposed a mechanism of selective ion capture whereby a cloud particle will be polarised in the pre-existing vertical fair weather electric field and so will carry a positive charge on its lower half and an equal negative charge on its upper half. As it falls, the lower charge attracts negative ions which are captured and lead to the net negative charging of the falling particle. But the process is limited because sufficient build up of negative charge on the particle will lead to the subsequent capture of positive ions. The mechanism may increase the vertical electrical field to about 50 kV m^{-1} before this limiting charge is reached; however, this field strength is inadequate to cause electrical breakdown and is about an order of magnitude lower than the typical maximum field strength measured in thunderstorms. This “influence” mechanism was one of the first to invoke the inductive process of thunderstorm charging, as discussed in Sect. 2.4. Elster and Geitel (1913) used the concept for the charging of polarised drops when smaller droplets rebounded from their underside, thus removing positive charge to be carried up on the smaller droplets while the negative drop fell and strengthened the electric field. However, in stronger fields, coalescence is the likely result of a collision.

2.3 The Convective Mechanism

Wilson proposed a “convective” mechanism involving the movement of charges carried by the natural convection currents in a storm cloud. He suggested that ion capture by cloud particles leads to the initial cloud electrification. This theory was proposed by Grenet (1947) and has been championed by Vonnegut (1953), whose concept is represented in Fig. 1. Positive ions near the ground are attracted to the cloud to be captured by droplets and carried to the cloud top in the updraught. In turn, this positive region attracts negative ions to the cloud that are captured by falling particles whose charge then strengthens the lower negative charge centre. The cycle continues with substantial field intensification.

It is hard to visualise the ordered separation of charge in this process that would lead to an electric field strength capable of initiating lightning. Vonnegut himself made several predictions about the charge distribution in clouds that would be consistent with his theory. He wrote “If this theory is correct, these measurements should disclose large masses of electrically charged air that are some distance from the region of precipitation, a situation that would be unlikely if precipitation were responsible for electrification. Furthermore these measurements should show that in both the positive and negative regions of charge, the greater part of the charge is generally in the form of small charged cloud particles and Aitken nuclei rather than precipitation particles. In some cases one might expect that appreciable electric fields had developed before the precipitation particles had formed.” However, measurements by Reynolds and Brook (1956) showed that rapid electrification of thunderstorms was associated with the development of ice phase precipitation particles. Besides, many measurements of charges on cloud particles in thunderstorms showed them to be significantly charged (e.g., Gaskell and Illingworth 1980).

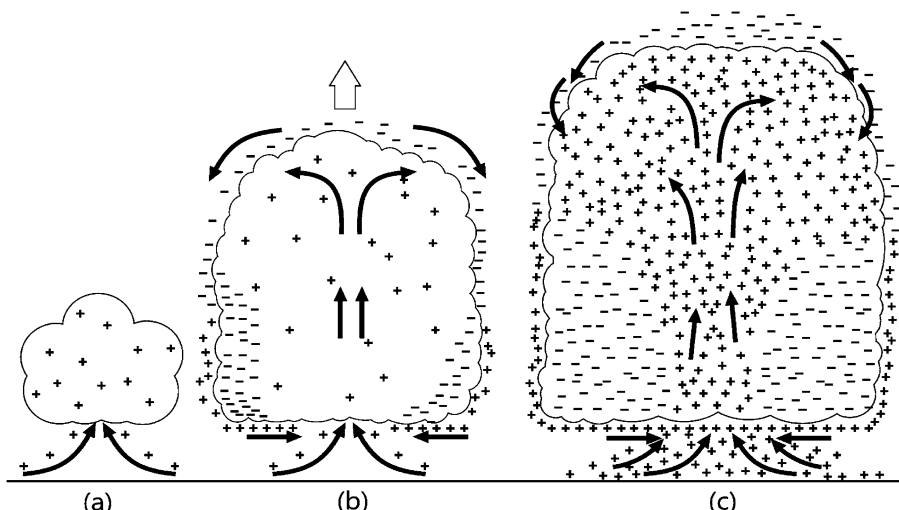


Fig. 1 The convective charging mechanism. (a) Positive space charge ingested into cloud. (b) A negative screening layer forms on the cloud particles on the outside boundary, which moves down the sides toward the cloud base. Additional positive charge is further ingested at the base, and further negative charge flows to the upper cloud boundary to replace the loss of the screening layer that flowed to the cloud base along the sides. (c) The lower accumulation of negative charge increases the electric field strength to a magnitude large enough to generate positive corona from ground objects. The corona becomes an additional source of positive charge that feeds into the cloud. (Emersic 2006)

Masuelli et al. (1997) used a numerical model of the cloud charging involved in the convective process and found an inadequate rate of field development. More recently, Helsdon et al. (2002) examined the convective charging hypothesis using a three-dimensional storm electrification model of a small, weak storm and a larger, severe, storm. With a full treatment of small ions, including attachment to hydrometeors, the inclusion of field-dependent surface point discharge, and the components of the Maxwell current, the results from both storm simulations indicated disorganized, weak electrical structures during the mature and dissipating stages. Furthermore, currents within the storm were dissipative and the cloud acted as a barrier to the external conduction current when convective-only charging was considered. However, since the convective charging hypothesis, by itself, is unable to produce significant charging or strong electric fields in their simulated clouds, they concluded that it is not a viable mechanism for thunderstorm electrification.

2.4 Inductive Charging

The inductive process, shown in Fig. 2, relies on the pre-existing vertical electric field to induce charges so that particle rebounds can separate charge and strengthen the field. Initially, the field may be due to the downward directed fair weather field ($-E$) resulting from positive charges in the atmosphere with a negative ground surface below. The interacting cloud particles have sufficiently high an electrical conductivity that there is time for the induced charges to form in the particles in response to the external electric field. In other planetary atmospheres with materials other than water ice, the particle conductivity and electrical relaxation time needs to be considered both for response to a changing external field and the time required for charge transfer. Collisions of water droplets often leads to coalescence, so the most likely situation in which the inductive process may act in clouds is for rebounding ice/ice or, possibly, ice/water collisions. A smaller cloud particle rebounds from the underside of a larger ice particle in the existing vertical electric field; it removes charge and is carried around the larger particle in the upward moving airstream—gravitational separation then occurs with the larger particle falling while the oppositely charged smaller particle is carried aloft thus strengthening the electric field. But the process does not always work like this; Saunders and Al-Said (1976) showed that when pairs of larger drops collided they partially coalesced, swung around each other and separated induced charge in a way that reduced the ambient field, as shown in Fig. 3.

Experimental studies with ice/ice collisions by Illingworth and Caranti (1985) showed that the charge transfer was limited by the purity of naturally occurring ice. Ice has an

Fig. 2 An uncharged graupel pellet in the environmental vertical electric field. The field induces positive and negative charges as shown. A rebounding cloud particle removes positive charge leaving the graupel negatively charged. The negatively charged graupel falls while the positively charged cloud particle is carried aloft so that the environmental electric field E is strengthened

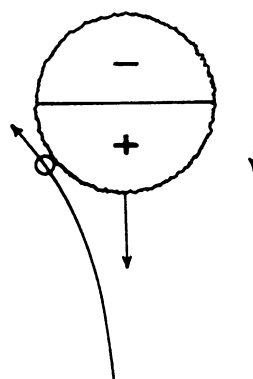
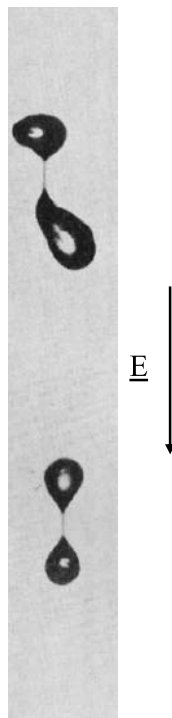


Fig. 3 Collisions between nearly equal sized water drops result in particle separations in the direction of the vertical environmental electric field that are in a direction to dissipate the field. (Al-Said 1977)



electrical conductivity high enough to allow the induced charges to form, but low enough that in the brief collision time, there is insufficient time for a complete transfer of charge. They found that when the ice was doped to increase its electrical conductivity, the theoretical value of induced charge transfer appropriate to two conducting particles was achieved. For this reason the inductive process involving ice/ice collisions has not been considered a viable mechanism for thunderstorm electrification.

Mason (1988) made a convincing case from thunderstorm observations and numerical modelling of the inductive process that it may be a viable mechanism for the case of water droplets rebounding from the underside of ice pellets. Brooks and Saunders (1994) carried out studies of this process in a laboratory cloud chamber in which an ice coated sphere fell through a cloud of supercooled water droplets in a vertical electric field. They showed that measurable and significant charge transfer was achieved when the droplets rebounded off riming graupel pellets, thus reviving the inductive mechanism. This process may help account for observations in thunderstorms of regions of cloud particles that have acquired their charges very rapidly in later stages of storm development when substantial electric fields are already present.

Despite this recent turn around in the fortunes of the inductive process, it does have to overcome a severe problem: observations in the early electrification period of thunderstorms by Christian et al. (1980) showed charges on graupel (small hail pellets) larger than could have been generated in the maximum electric field strength measured in thunderstorms. These results were obtained from an airborne instrument in a New Mexico thunderstorm in which a cloud particle imager and charge induction device gave corresponding values of charge and graupel size for individual precipitation particles. They concluded that cloud particle charges producing the first lightning stroke are unlikely to be due to the inductive

process. Other processes must be responsible for the production of the observed charges in the time available.

3 Particle Charging Involving the Ice Phase

Observations in thunderstorms have shown that strong electrification follows the development of ice particles. Reynolds and Brook (1956) noted a rapid increase in radar reflected intensity from a storm in which the electric field was approaching breakdown leading to lightning. Illingworth and Lees (1992) used radar to observe the position of lightning and precipitation in a UK summer thunderstorm and confirmed that lightning is co-located with the maximum precipitation radar echo; they concluded that the presence of graupel is required for lightning to occur. Most mechanisms considered today involve cloud ice in the charging process.

3.1 Workman–Reynolds Freezing Potentials

When supercooled water droplets are captured by a falling ice pellet, the water freezes. Workman and Reynolds (1950) measured a freezing potential across the ice/water interface during the freezing process. They suggested that this may lead to charge separation by the shedding of charged liquid water due to splashing during the collision process. In a laboratory study in which the freezing potential was measured as a function of time after the water/ice collision, Caranti and Illingworth (1983) found that the potential developed very slowly. In fact it turns out that the full potential develops in bulk ice in a time longer than the freezing time of the captured small supercooled cloud droplets. Thus the process cannot account for significant charge transfer in thunderstorms.

3.2 Contact Potential

Caranti and Illingworth (1980) and Caranti et al. (1985) noted that an ice particle developed a surface contact potential when it accreted supercooled droplets that froze on its surface. The surface charge was negative, and if considered as a “contact potential” (despite the fact that ice is a proton conductor), the negative potential could account for the negative charging of the colliding ice surface having the larger negative contact potential. However, this process could only account for the negative charging of accreting graupel during ice crystal collisions; besides, laboratory studies have shown that the charge sign is controlled by temperature and water accretion rate. Furthermore, it has been observed that ice surfaces growing by vapour diffusion charge positively and sublimating ice surfaces charge negatively during rebounding collisions with smaller ice particles (as discussed below), but when ice surfaces were caused to grow or sublimate by cooling or heating, their contact potential was not affected. So, the contact potential mechanism has been discounted from further consideration in the terrestrial atmosphere.

3.3 Dislocation Mechanism

Keith and Saunders (1990) suggested that charge transfer in ice/ice collisions may be associated with charges on dislocations in the ice lattice. They reported that dislocations carry a positive charge and that during a collision between an ice crystal and a graupel pellet this charged material may be transferred. They calculated that for a typical number

of dislocations per unit area of $5 \times 10^9 \text{ m}^{-2}$, with a charge per unit length of $6 \times 10^{-11} \text{ C m}^{-1}$, (determined by X-ray methods) the charge available on a typical collision area of $55 \times 55 \mu\text{m}^2$ is +50 fC, which is of the observed order of magnitude from laboratory studies of charge transfer. Dislocation concentration depends on the ice growth rate, and as discussed elsewhere, crystals and graupel grow at different rates as a function of cloud conditions so positive or negative charge transfers may occur. However, in ice, there are mobile ions of both signs which are free to move under local electric fields such as would be set up by a charged dislocation. So, any mass transferred during a collision is likely to consist of the dislocation together with surrounding oppositely charged material. However, in other planetary atmospheres where the colliding particles may consist of materials that develop charged dislocations but may not have mobile charges available, this process may be viable.

3.4 Temperature Gradients in Ice

Latham and Mason (1961), working in the laboratory, studied charge transfer during impacts of ice crystals on an ice sphere representing a falling graupel pellet. They noted that a temperature difference between the particles led to charge transfer, such that the warmer ice particle lost positive charge. They required the graupel to be warmed by collection of supercooled droplets in the cloud chamber (riming), however their simulations did not include riming itself—they relied on artificial heating of the ice surface. They attributed this result to the higher mobility of positive ions in ice compared with negative ions: during contact the positive ions are able to move away from the warmer ice surface leaving it negatively charged. They developed a numerical model, however, the actual charges measured in the laboratory were considerably in excess of the theoretical predictions. Later, Marshall et al. (1978), Gaskell and Illingworth (1980) and Jayaratne et al. (1983) showed in laboratory studies that charge transfers could be obtained in the opposite direction to the direction of the temperature gradient between colliding ice particles. Later it was realised that particle growth or sublimation rates control the sign of charge transfer and naturally, these rates are temperature dependent as well as being influenced by the local cloud supersaturation.

3.5 Melting Effects

Despite graupel usually being charged negatively in the lower charge region of thunderstorm dipoles, rainfall measured below cloud is often positively charged. Dinger and Gunn (1946) proposed a charge transfer process associated with melting. Drake (1968) noted that convection in a melting ice sphere produced negatively charged droplets ejected from bursting air bubbles at the surface. The sign of charge and the conditions under which the charges were separated were highly dependent on the impurities in the melting ice. The positive charge on the melted drops may help account for the lower positive charge region in thunderstorms and for the positive charge on precipitation. The capture of positive ions below cloud will also contribute to the drop charge.

3.6 Ice Splinter Charging During Hallett–Mossop Ice Multiplication

Ice splintering has had a long history of possible involvement in charging. Latham and Mason (1961) noted that ice splinters created during the freezing of supercooled droplets (riming) on a larger ice surface were charged. Hallett and Saunders (1979) studied the charges on ice splinters produced during the Hallett and Mossop (1974) ice multiplication process. The Hallett–Mossop mechanism is an important source of ice particles in clouds, particularly in regions where the temperature is between -3°C and -8°C . The process involves

the accretion of supercooled water droplets by falling ice pellets, ice crystals or graupel. The supercooled liquid water immediately freezes and if the conditions are suitable, the freezing droplets form a shell of ice which can shatter under the high stresses involved caused by the effects of expansion upon freezing. The ice surface may break up into fragments, or a spicule of material may be formed through which liquid is ejected that rapidly freezes. The net effect is to produce a large number of small ice particles that grow very rapidly by the diffusion of local water vapour and form ice crystals that can in turn accrete smaller droplets thus continuing the multiplication process.

Hallett and Saunders (1979) investigated this multiplication process with a view to the possibility that the ejected ice fragments were electrically charged and so could contribute to thunderstorm electrification. They found that the growing ice pellet charged positively with a negative charge on an ejected ice fragment of order -10^{-16} C. Interestingly, when the vapour supply used to grow the cloud droplets was turned off, the charge sign reversed; under these conditions the ice pellet would have started to sublimate. The authors concluded that the sign of the charge transfer depends on the physical state of the rime ice surface and its vapour pressure excess or deficit relative to the environment. This turned out to be a far reaching conclusion, as will be seen below, however the magnitude of the charges on the fragments is too small to be able to account for the observed electrification rates in thunderstorms. They did note that in the presence of liquid cloud, the ice crystals grew rapidly and when these larger crystals collided with a riming ice surface, then substantial charges were transferred. This work led to extensive studies of charging during ice crystal collisions with riming graupel, as discussed in Sect. 4 below.

3.7 Fragmentation Effects

The surface of ice is in an environment in clouds in which it grows by vapour diffusion from the environment. It may, therefore, become covered in frost, which can break off, or be knocked off during collisions with other cloud particles. Takahashi (1978) invoked crystal breakup for his observed charging during crystal collisions with riming graupel. In droplet/graupel collisions at speeds between 10 and 30 m s⁻¹, Avila et al. (2003) noted the production of charged fragments. Such speeds are high for terrestrial thunderstorms but may be relevant in other planetary conditions.

Charge transfer associated with surface growth or sublimation has been noted by everyone who has worked in the area of collisional ice charging in clouds. The relative growth rate theory discussed below, has its origins in the often observed result that growing ice surfaces charge positively, while sublimating ice surfaces charge negatively, as noted by Findeisen (1940), Findeisen and Findeisen (1943), Buser and Aufdermaur (1977), Marshall et al. (1978), Gaskell and Illingworth (1980), Jayaratne et al. (1983), Rydock and Williams (1991), Caranti et al. (1991), Dong and Hallett (1992), Saunders et al. (1993), Scavuzzo et al. (1995) and Mason and Dash (2000). Most of these experiments were carried out by artificially cooling or heating an ice surface while its surface was removed by collisions or by fragmentation, thus the laboratory simulations are not representative of the conditions in real clouds. For example, an ice surface grows by diffusion in a real cloud causing the ice surface to be heated by the release of the latent heat of condensation. However, in laboratory simulations, in order to ensure that the ice surface grows, it is artificially cooled. Correspondingly, a sublimating ice surface in clouds loses mass because the surrounding environment is at a lower vapour pressure and it is cooled by the latent heat of sublimation; however, in laboratory simulations the ice would be heated to ensure sublimation. Thus these simulation experiments do not provide realistic cloud or ice surface conditions.

These differences have to be considered when relating the laboratory results to nature—however, the observation that ice surfaces growing by diffusion charge positively and sublimating ice surfaces charge negatively is consistent with observations of the sign of charge on fragments breaking off a growing or sublimating ice surface and provide an important clue to the mechanism of charge transfer when ice crystals rebound from ice particles that are not only growing or sublimating, but are also accreting supercooled water droplets. Various theories have been proposed for these observations, the most recent being a theory relying on the relative diffusional growth rates of two briefly interacting ice particles, as discussed below.

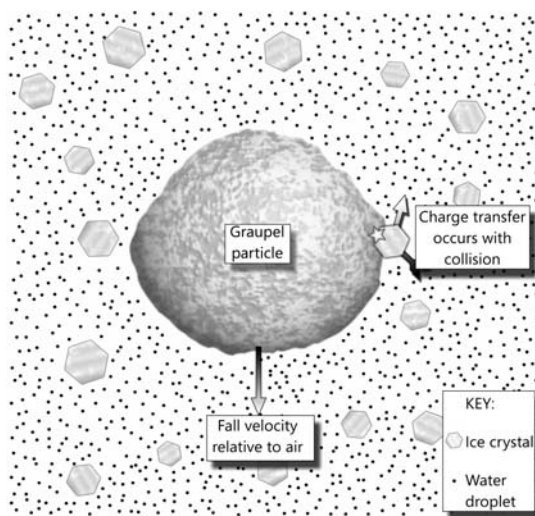
4 Ice Crystal/Graupel Charging

4.1 Background

The beginnings of this non-inductive particle charging mechanism (so-called because the presence of an electric field plays no role in the mechanism) came when Reynolds et al. (1957) measured in the laboratory the charge transferred to riming graupel when ice crystals rebounded and removed the equal and opposite charge. The process is shown in Fig. 4. They reported the negative charging of graupel that could account for the region of negatively charged graupel in thunderstorms. The positively charged ice crystals would be carried aloft to form the upper charge region of the dipole. Takahashi (1978), in similar experiments, showed that the riming graupel charge sign could be negative or positive by crystal rebounds depending on cloud temperature and liquid water content.

Work in this research area started in the Manchester laboratory in 1978 with a search for charged fragments created during the Hallett–Mossop ice multiplication process, as discussed above. It soon became apparent that, although the small ice particles ejected during the process were charged, the charges were too small to be of significance to thunderstorm electrification processes. However, it was noted that after time had been allowed in the cloud chamber for the ice crystals to grow to tens of micrometres in diameter, the charge transfer was considerably increased. It was also noted with interest that under some cloud conditions

Fig. 4 The charging a graupel particle (soft-hail pellet) during droplet accretion (riming) and ice crystal rebounding collisions. (Emersic 2006)



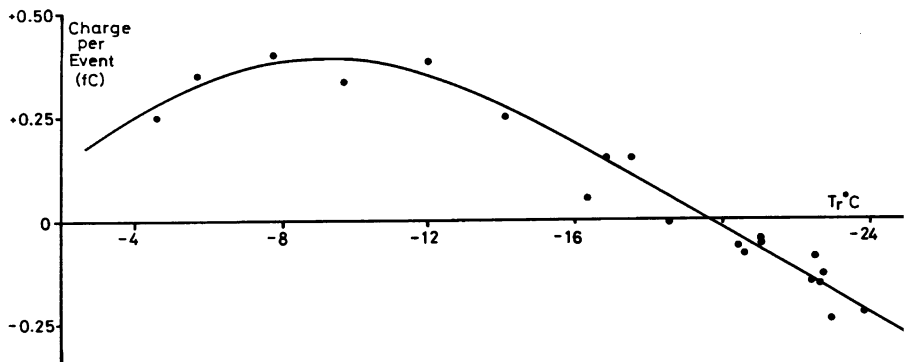
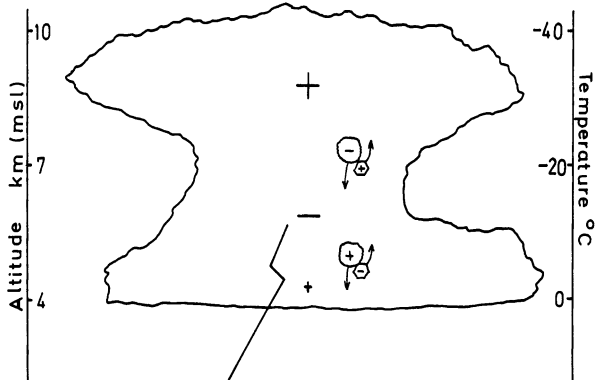


Fig. 5 The charge transferred to a riming graupel pellet by a separating ice crystal following a collision, at constant cloud water content. (Jayaratne 1981)

Fig. 6 The charging of a thunderstorm leading to the tripole charge distribution. Graupel pellets charge negatively at low temperatures and positively at higher temperatures



a riming ice surface could become charged positively, whereas Reynolds et al. (1957) had concentrated on their observation of negative charging of graupel, a result they used to account for the negative charge region in thunderstorms. A more detailed study by Jayaratne et al. (1983) showed that the charge sign could be positive or negative as a function of the cloud temperature and liquid water content; Fig. 5 shows graupel charge sign reversal at -20°C from experiments at a particular water content. Lower water contents moved the reversal point to higher temperatures favouring negative graupel charging in the cloud. The temperature dependence of the charge transfer helps account for the sign of graupel charging required to account for the usual dipole structure of a thunderstorm reported by Wilson (1916, 1929), and the often observed tripole structure noted by Williams (1989). Figure 6 shows a storm with a tripole charge structure: graupel/crystal charge separation events at higher altitudes and lower temperatures lead to negative graupel that falls under gravity while the positive ice crystals are carried aloft; at lower altitudes and higher temperatures, the charge transfer reverses sign leading to the often observed lower positive charge centre, while the negatively charged ice crystals are carried up to reinforce the negative charge centre. The lower positive charge centre has been detected in thunderstorms and is thought to help the initiation of cloud to ground lightning strokes from the lower region of negative charge.

4.2 Thunderstorm Charge Observations

The work on charge transfer mechanisms follows from an understanding of the cloud physical and electrical properties of thunderstorms. There have been many studies of thunderstorm properties, by remote sensing techniques as well as by research flights through storms. Krehbiel (1986) reported on studies in New Mexico in which the location of charge centres was identified by multiple-station analysis of the electric field change associated with intra-cloud lightning. They noted that during the course of a storm, the lower negative charge region maintained a steady altitude around 7 km corresponding to a temperature around -15°C . Meanwhile, the upper positive charge centres were observed to be carried up at 8 m s^{-1} , a rate that corresponded to the updraught speed in the cloud. Krehbiel (1986) also compared data on charge centre location in storms in other locations. Thunderstorms in New Mexico, in Florida, and winter storms over the Sea of Japan all possessed a negatively charged region located around the -15°C level despite the considerable differences in the dynamics and characteristics of these various storms.

In a series of multiple aircraft penetrations through thunderstorms in Montana, Dye et al. (1986) reported on simultaneous measurements of cloud parameters and electrical properties. They noted that increases in electric field strength occurred in regions containing a mix of liquid water and of ice particles. Ice crystals and graupel pellets were identified by airborne laser probes carried on aircraft flying in regions of strong electric field. They also reported that electrification appeared to be occurring at the interface between the updraught and downdraught regions of the clouds.

These observations point strongly to a precipitation based charging process of thunderstorm electrification and they strengthened the growing conviction that ice crystals rebounding from riming graupel in the presence of supercooled liquid water is a requirement of the charge transfer process leading to electric field development and lightning.

4.3 Thunderstorm Charging Requirements

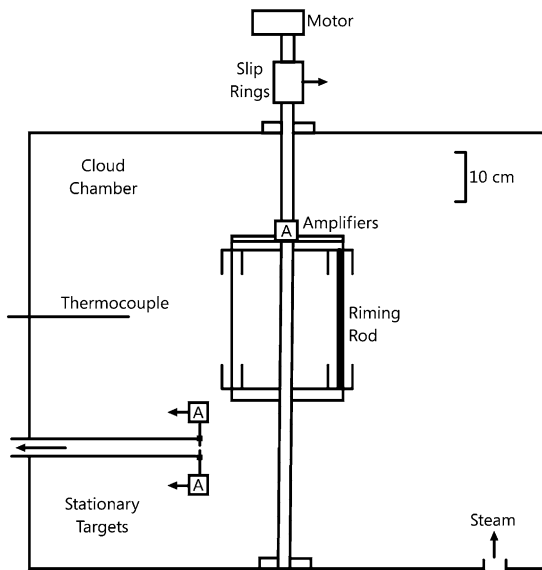
In order to ascertain whether laboratory measured charge transfer values are adequate to account for thunderstorm electrification, Mason (1953) used thunderstorm observations to put forward some basic requirements of a viable theory of charge generation.

- 1) Time available for electric field generation is 30 minutes.
- 2) Charge generation produces 20 to 30 Coulombs per flash.
- 3) Charge separation occurs between the 0°C and -40°C levels in a region of radius 2 km.
- 4) The main negative charge centre is between the -5°C and -25°C levels depending on the cloud physics, the main positive centre is a few kilometres above the negative centre. The lower positive charge is close to the 0°C level.
- 5) Electric field development is associated with the development of precipitation in the form of soft hail (graupel).
- 6) The first lightning occurs within 12 to 20 minutes of the first radar detection of large particles.
- 7) Charge theories/mechanisms must generate 5 to 30 C km^{-3} leading to a charge generation rate of order $1 \text{ C km}^{-3} \text{ min}^{-1}$.

From these basic requirements, Mason determined the magnitude of the charge transfer events needed to account for the observed rates of electrification. Falling graupel pellets, radius R , number density n_h , collide with ice crystals, number density n_i .

The number of collisions/ $\text{m}^3/\text{sec} = \text{d}N/\text{dt} = E\pi R^2 n_h n_i V$ where V is the relative velocity between graupel and crystals and E is the crystal/graupel collision efficiency.

Fig. 7 Cold room cloud chamber and charge transfer apparatus. (Jayaratne 1981)



Graupel precipitation rate, $p = (4/3)\pi R^3 \rho n_h V$ where ρ = the density of a graupel pellet. Each collision produces charge transfer q . To account for observations, the rate of production of charge per unit volume of cloud: $dQ/dt = q(dN/dt) = (3/4)q(En_i p/R\rho) = 1 \text{ C km}^{-3} \text{ min}^{-1}$.

For a typical precipitation rate, $p = 5 \text{ cm hr}^{-1}$. Graupel density = 0.5 g cm^{-3} . $R = 2 \text{ mm}$. $n_i = 0.1 \text{ cc}^{-1}$ for crystals $> 80 \mu\text{m}$.

So, $q = (4/3)(dQ/dt)/(En_i p/R\rho) = 1.6 \times 10^{-14} \text{ C}$ per collision, if $E = 1$ and every ice crystal collision results in a rebound.

4.4 Laboratory Studies of Thunderstorm Charging Processes

There has been a long series of measurements in the Atmospheric Science Laboratory in Manchester where large cold chambers permit the growth of clouds to simulate atmospheric processes. Extensive thunderstorm charge transfer experiments have been performed in which the magnitude and sign of the charge transfer during ice crystal rebounds from riming graupel have been determined as a function of cloud temperature, graupel temperature, cloud water content, cloud droplet size distribution, impurity content of the graupel, ice crystal size, relative velocity between the colliding particles and their collision and separation probabilities. The most recent work points to the importance of ice particle diffusional growth rates controlled by the supersaturation in the cloud.

Figure 7 is a typical laboratory cloud chamber located inside a cold room. A cloud of water droplets condenses from the continuous water vapour input. The droplets supercool to the ambient temperature. Ice crystals are initiated by introducing a fine wire cooled to liquid nitrogen temperature and grow from the available water vapour. Figure 8 shows a three minute sequence of crystal growth from the available water vapour and cloud droplets, whose number and concentration decline and recovery during the run track the variations in cloud supersaturation. Metal rods, typically of 5 mm diameter, are moved through the cloud on a rotating frame; droplets accrete on the rod to form rime ice simulating the growth of a graupel pellet. Ice crystals strike the rod and if they rebound, charge is separated. The

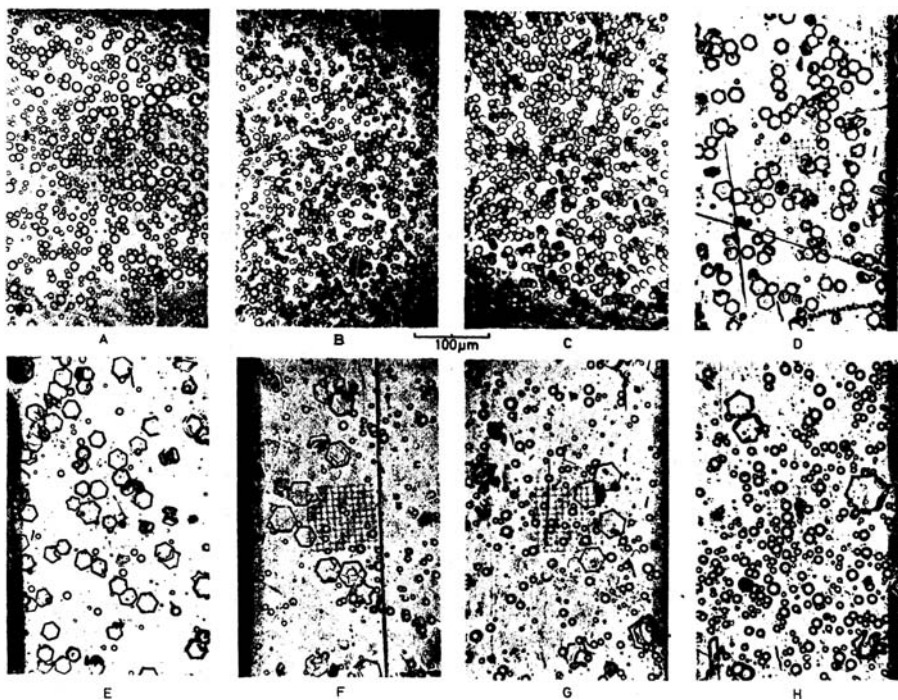


Fig. 8 A time sequence of cloud conditions over a period of three minutes from crystal nucleation. The droplets and cloud vapour provide water vapour for crystal growth. When the crystals have grown, they fall out of the cloud and the continuous vapour supply re-establishes the water droplet cloud. (Jayaratne 1981)

riming target rod is connected via slip rings to an electrometer so that the total charge due to many crystal charge transfer events is measured. Alternatively a stationary target is used while the cloud is drawn past using a suction pump. For the same velocity, between 2 and 9 m s^{-1} , representing the fall speed of a graupel pellet, both stationary and moving targets give similar results.

Figure 9 represents a study of the effect of velocity on charge transfer for positive and negative graupel charging. The dependence of charge transfer on ice crystal size is shown in Fig. 10. These results (Keith and Saunders 1990) confirm that the magnitude of charge transfer determined in these laboratory studies is adequate to account for thunderstorm electrification according to the analysis of Mason (1953). Droplet size also influences the charge transfer as shown by Avila et al. (1999).

4.5 The Thunderstorm Charging Mechanism

A thunderstorm charging mechanism based on vapour deposition rate, first proposed by Baker et al. (1987), has been successful in helping to account for differences between the results from various laboratory studies. The concept follows on from the result described earlier that, during collisions leading to the removal of some surface mass from the larger particle, fast growing ice surfaces charge positively and conversely, sublimating surfaces charge negatively. Baker et al., suggested that an additional variable comes into play when two ice surfaces having different vapour diffusional growth rates come into brief contact, namely the surface state of the smaller particle in the collision process. They suggested that

Fig. 9 Charge transfers when ice crystals rebound from riming graupel, as a function of velocity, for the positive and negative charging regimes. (Keith 1987)

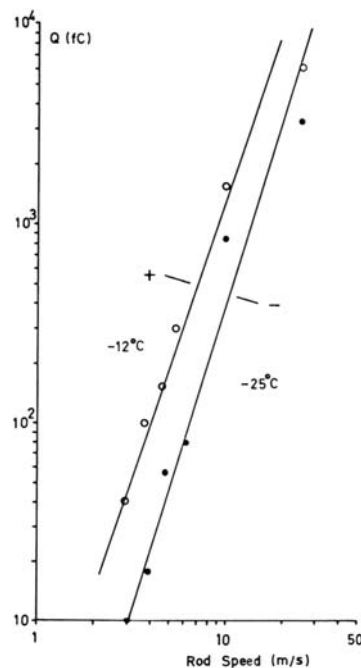
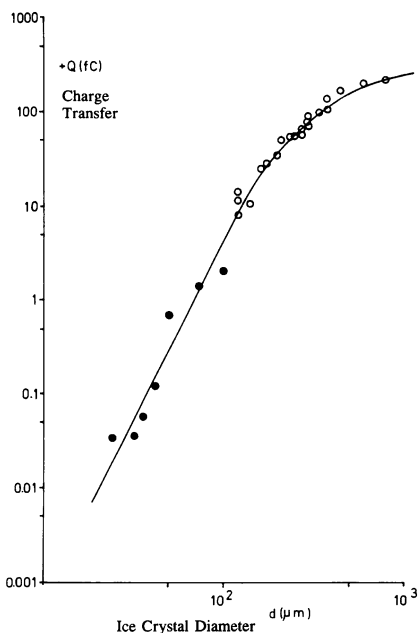


Fig. 10 Charge transfer to a riming target as a function of ice crystal size. (Keith 1987)



the *relative* diffusional growth rates of the interacting ice particle surfaces was the factor that controls the sign of charge transfer. The charge transfer follows the rule that the ice surface that grows faster by vapour diffusion charges positively during ice crystal/graupel

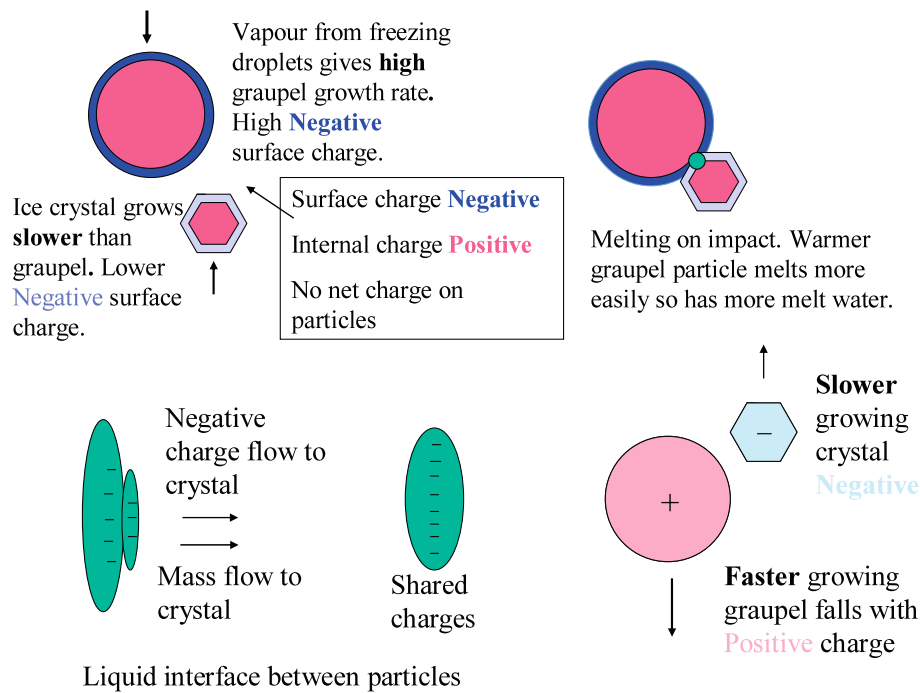


Fig. 11 A graupel pellet, warmed by rime accretion collides with a colder, faster growing, ice crystal. Charges and mass are shared in the melt water. The graupel becomes negatively charged while the crystal carries positive charge

rebounding collisions. This concept has stood the test of time, and has been shown to be consistent with the results obtained in various laboratories.

The theory was developed further by Dash et al. (2001)—the faster growing ice surface has more negative surface charge available for transfer, and hence charges positively. According to Dash et al., rapid vapour deposition to an ice surface produces disordered growth, with ionic defects at vapour and grain boundary interfaces; faster growth leads to higher charge densities. The OH^- ions are held in position by their hydrogen bonds, but positive ions are able to diffuse away from the surface into the bulk ice, leading to a negative surface potential. Two colliding ice surfaces tend to equalise their surface charges so that the faster grown surface loses negative charge. The collisional impact melts a local volume on each surface with the warmer graupel providing more mass than the colder crystal. The charge exchange takes place in the melt water whereby the melted masses and associated charges are shared between the separating ice particles. In this way, the negative charge shared leads to positive charging of the faster growing ice surface. However, the liquid mass transfer is in the opposite direction to the transfer of negative charge, as noted by Mason and Dash (2000). The equalisation of charges occurs on a time scale of microseconds, which is much less than the estimated 0.1 ms contact time. This provides insufficient time for the deeper protons in the ice to react during the available contact time. Figure 11 represents the case of a faster growing ice crystal rebounding from a slower growing graupel pellet, so that the charge and mass exchange during the collision results in the graupel becoming negatively charged.

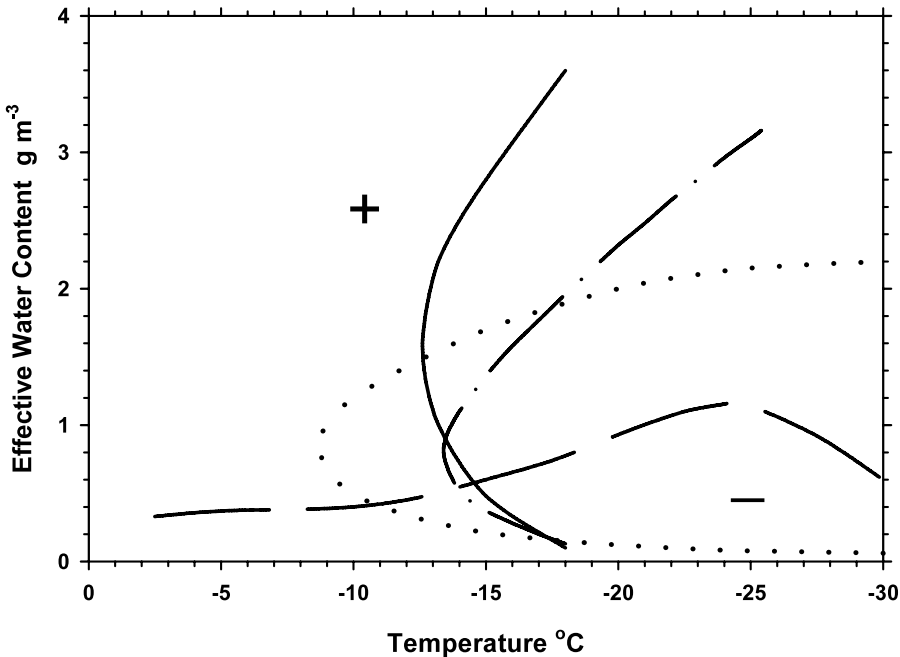
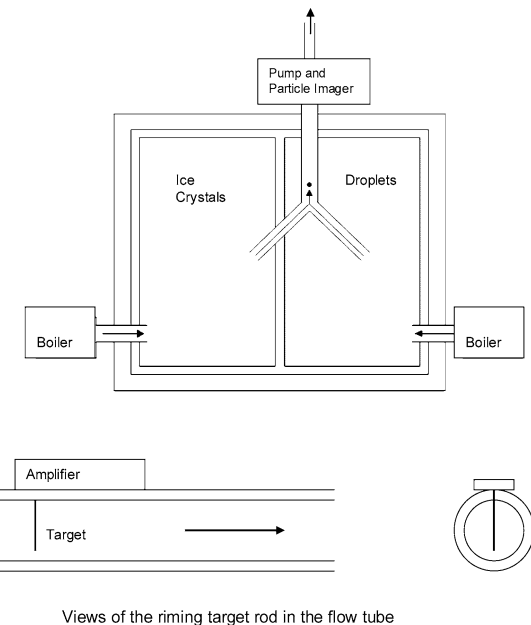


Fig. 12 Rimer charge sign boundaries from various laboratory studies. — Saunders et al. (2006), — · — Pereyra et al. (2000), ····· Takahashi (1978), — — Saunders and Peck (1998)

Figure 12 shows laboratory results from Saunders et al. (2006) together with those from Pereyra et al. (2000), Takahashi (1978) and Saunders and Peck (1998). Plotted on these graphs are the critical values of temperature and cloud effective water content for which the charge transfer during crystal/graupeл collisions is zero. The effective water content, EW, is made up of that portion of the cloud water droplet spectrum that by virtue of the droplet size, graupel velocity and the appropriate collision efficiency, strike the graupel pellet. The lowest of the charge sign reversal lines shown in the figure was obtained in experiments in the Manchester laboratory with cloud chamber apparatus essentially similar to that in Fig. 7 (Saunders and Peck 1998). The differences between this line and the charge sign reversal line obtained by Takahashi (1978) are clear and prompted many laboratory studies aimed at resolving the reasons for the differences. The laboratory studies of Pereyra et al. (2000) provided the breakthrough—they mixed ice crystals into their droplet cloud just before the mixed cloud impacted on the riming target. The studies of Saunders and Peck (1998) however, were performed in a chamber in which the ice crystals grew in the same chamber as the droplets. The importance of the cloud conditions for particle growth was investigated in studies by Saunders et al. (2006) whose data line is shown in Fig. 12. Figure 13 shows their apparatus in which the ice crystals grew in a cloud of supercooled droplets, while the droplets that provided most of the rime ice to the target were grown separately. The two clouds were mixed briefly on their way to the target.

The relative growth rate hypothesis can help to account for the results that led to the range of results in Fig. 12, and in particular is consistent with the apparently conflicting results represented by the highest and lowest of the charge sign reversal lines, both sets being obtained in the same laboratory and cloud chamber in Manchester. According to the hypothesis, in order to strengthen the negative charging of a graupel pellet, the impacting

Fig. 13 The cloud chambers and target in which the ice crystals and supercooled droplets are grown in separate chambers. (Bax-Norman 2004)



Views of the riming target rod in the flow tube

ice crystals need to grow faster than the graupel ice surface. This is achieved in the case where the two clouds are mixed just before impact, because the crystals growing in a droplet cloud reduced the supersaturation in the chamber, while the other chamber containing the supercooled water droplets is at water saturation. On mixing, the ice crystals experience a higher value of supersaturation and so increase their growth rate leading to the high charge sign reversal line. In the case where the crystals grow in the same droplet cloud, their growth rate is appropriate to a mixed cloud and there is no surge of increased supersaturation when they approach the target. This leads to the lowest of the reversal lines shown on Fig. 12.

These results have relevance to thunderstorm conditions where mixing between cloud parcels having different histories will result in faster, or slower, growth of ice crystals. In other cloud situations, there is longer term stability of conditions and the low EW charge sign reversal line will apply.

Given that ice particles grow in supersaturated conditions, such as in cirrus clouds experiencing an updraught, charge transfer will occur during collisions between non-riming ice particles growing at different rates. The relative growth rate hypothesis predicts that the faster growing ice surface will charge positively. Laboratory measurements have confirmed substantial charge transfer in ice/ice collisions in the absence of supercooled droplets. This will be important in other planetary atmospheres where the liquid phase may not be present.

5 Concluding Remarks

The processes of thunderstorm electrification outlined here have all been considered, in their time, as contenders for the dominant mechanism by which terrestrial thunderstorms become sufficiently charged to produce lightning discharges. All the mechanisms result in charges being carried on cloud particles. The two processes generally acknowledged to be the most likely candidates are the process by which ice particles, growing at different diffusional

rates, collide and share charges such that the particle growing fastest charges positively, and the inductive mechanism that relies on the pre-existing electric field to produce induced charges in uncharged particles that may be transferred during collisions.

The reason that these processes are viable is connected with the electrical relaxation time of the earth's atmosphere and the particles' dielectric and physical properties that permit charge transfers in the available contact time and allow the charges to remain on the particles long enough for regions of high electric fields to develop in the cloud volume. In other planetary atmospheres similar considerations must be made in order to identify likely charging processes leading to particle separation under the local gravity. All the processes considered here may well be active in other atmospheres.

References

- S. Al-Said, PhD Thesis. The University of Manchester, 1977
- E.E. Avila, G.M. Caranti, N.E. Castellano, C.P.R. Saunders, Q. J. R. Meteorol. Soc. **125**, 1669–1679 (1999)
- E.E. Avila, G.S. Longo, R.E. Bürgesser, Atmospheric Res. **69**, 99–108 (2003)
- B. Baker, M.B. Baker, E.R. Jayaratne, J. Latham, C.P.R. Saunders, Q. J. R. Meteorol. Soc. **113**, 1193–1215 (1987)
- H. Bax-Norman, PhD Thesis. The University of Manchester, 2004
- D.C. Blanchard, *Progress in Oceanography*, vol. 1 (Pergamon Press, Elmsford, 1963)
- I.M. Brooks, C.P.R. Saunders, J. Geophys. Res. **99**, 10627–10632 (1994)
- O. Buser, A.N. Aufdermaur, in *Electrical Processes in Atmospheres* (Steinkopf, Darmstadt, 1977)
- G.M. Caranti, A.J. Illingworth, Nature **284**, 44–46 (1980)
- J.M. Caranti, A.J. Illingworth, J. Geophys. Res. **88**, 8483–8489 (1983)
- J.M. Caranti, A.J. Illingworth, S.J. Marsh, J. Geophys. Res. **90**, 6041–6046 (1985)
- G.M. Caranti, E.E. Avila, M.A. Ré, J. Geophys. Res. **96**, 15365–15375 (1991)
- H. Christian, C.R. Holmes, J.W. Bullock, W. Gaskell, A.J. Illingworth, J. Latham, Q. J. R. Meteorol. Soc. **106**, 159–174 (1980)
- J.G. Dash, B.L. Mason, J.S. Wetlaufer, J. Geophys. Res. **106**, 20395–20402 (2001)
- J.E. Dinger, R. Gunn, Terr. Magn. Atmos. Electr. **51**, 477 (1946)
- Y. Dong, J. Hallett, J. Geophys. Res. **97**, 20361–20371 (1992)
- J.C. Drake, Q. J. R. Meteorol. Soc. **94**, 176–191 (1968)
- J.E. Dye, J.J. Jones, W.P. Winn, T.A. Cerni, B. Gardiner, D. Lamb, R. Pitter, J. Hallett, C.P.R. Saunders, J. Geophys. Res. **91**, 1231–1247 (1986)
- J. Elster, H. Geitel, Zur Influenztheorie der Niederschlags elektrizität, Phys. Z. 1287–1292 (1913)
- C. Emersic, PhD Thesis. The University of Manchester, UK, 2006
- W. Findeisen, Meteor. Zeit. **57**, 201–215 (1940)
- W. Findeisen, E. Findeisen, Meteor. Z. **60**, 5 (1943)
- W. Gaskell, A.J. Illingworth, Q. J. R. Meteorol. Soc. **106**, 841–854 (1980)
- H. Gerdien, Phys. Z. **6**, 647–666 (1905)
- G. Grenet, Ann. Geophys. **3**, 306–307 (1947)
- J. Hallett, S.C. Mossop, Nature **249**, 26–28 (1974)
- J. Hallett, C.P.R. Saunders, JAS **36**, 2230–2235 (1979)
- J.H. Helston Jr., S. Gattaleeradapan, R.D. Farley, C.C. Waits, J. Geophys. Res. **107**(D22), 4630 (2002). doi:[10.1029/2001JD001495](https://doi.org/10.1029/2001JD001495)
- A.J. Illingworth, J.M. Caranti, J. Geophys. Res. **90**, 6033–6039 (1985)
- A.J. Illingworth, M.I. Lees, Proc. 9th Int. Conf. Atmos. Elec., St. Petersburg, Russia, 1992, p. 9345
- E.R. Jayaratne, Ph.D. Thesis, The University of Manchester, UK, 1981
- E.R. Jayaratne, C.P.R. Saunders, J. Hallett, Quart. J. R. Meteorol. Soc. **109**, 609–630 (1983)
- W.D. Keith, Ph.D. Thesis. The University of Manchester, UK, 1987
- W.D. Keith, C.P.R. Saunders, Atmospheric Res. **25**, 445–464 (1990)
- P.R. Krehbiel, M. Brook, R.A. McCrary, J. Geophys. Res. **84**, 2432–2456 (1979)
- P.R. Krehbiel, Studies in Geophysics, Nat. Ac. Press, 90–113 (1986)
- J. Latham, B.J. Mason, Proc. R. Soc. A **260**, 537–549 (1961)
- P. Lenard, Ann. Phys. Lpz, 46 (1892)
- B.J.P. Marshall, J. Latham, C.P.R. Saunders, Quart. J. R. Meteorol. Soc. **104**, 163–178 (1978)
- B.J. Mason, Quart. J. R. Soc. **79**, 501–509 (1953)

- B.J. Mason, Proc. R. Soc. Lond. **A415**, 303–315 (1988)
- B. Mason, J.G. Dash, J. Geophys. Res. **105**, 10185–10192 (2000)
- S. Masuelli, C.M. Scavuzzo, G.M. Caranti, J. Geophys. Res. **102**, 11049–11059 (1997)
- R.G. Pereyra, E.E. Avila, N.E. Castellano, C.P.R. Saunders, J. Geophys. Res. **105**, 20803–20813 (2000)
- S.E. Reynolds, M. Brook, J. Met. **13**, 376–380 (1956)
- S.E. Reynolds, M. Brook, M.F. Gourley, J. Met. **14**, 426–436 (1957)
- J.P. Rydock, E.R. Williams, Quart. J. R. Met. Soc. **117**, 409–420 (1991)
- C.P.R. Saunders, S. Al-Said, J. Geophys. Res. **81**, 2650–2654 (1976)
- C.P.R. Saunders, M. Hickson, M.D. Malone, J. von Richtofen, Atmospheric Res. **29**, 261–270 (1993)
- C.P.R. Saunders, S.L. Peck, J. Geophys. Res. **103**, 13949–13956 (1998)
- C.P.R. Saunders, H. Bax-Norman, C. Emersic, E.E. Avila, N.E. Castellano, Quart. J. R. Met. Soc. **132**, 2653–2673 (2006)
- C.M. Scavuzzo, E.E. Avila, G.M. Caranti, Atmospheric Res. **37**, 325–342 (1995)
- M. Stolzenburg, W.D. Rust, T.C. Marshall, J. Geophys. Res. 14079–14096 (1998)
- T. Takahashi, J. Atmospheric Sci. **35**, 1536–1548 (1978)
- B. Vonnegut, Bull. Am. Met. Soc. **34**, 378–381 (1953)
- E.R. Williams, J. Geophys. Res. **94**, 13151–13167 (1989)
- C.T.R. Wilson, Proc. R. Soc. A **92**, 555–574 (1916)
- C.T.R. Wilson, J. Franklin Inst. **208**, 1–12 (1929)
- E.J. Workman, S.E. Reynolds, Phys. Rev. **78**, 254–259 (1950)

Charge Structure and Dynamics in Thunderstorms

Maribeth Stolzenburg · Thomas C. Marshall

Originally published in the journal Space Science Reviews, Volume 137, Nos 1–4.
DOI: [10.1007/s11214-008-9338-z](https://doi.org/10.1007/s11214-008-9338-z) © Springer Science+Business Media B.V. 2008

Abstract The electrical structure inside thunderstorm clouds and the changes with time of this structure are fundamental parameters for atmospheric electricity studies on Earth. This paper gives a review of the current state of knowledge about thunderstorm charge structure based primarily on in-cloud vertical profiles through different types of deep convective clouds, cirriform anvil clouds, and stratiform precipitation regions associated with mid-latitude mesoscale convective systems. Results on the dynamical evolution of the vertical charge structure during the early and decay stages from series of balloon soundings through small thunderstorms are described, along with recent findings regarding the importance of the charge structure in determining the current contribution of small and large thunderstorms to the Earth’s global electrical circuit.

Keywords Thunderstorm electricity · Atmospheric electric charge · Thunderstorm electrical evolution · Mesoscale convective system · Global electric circuit

1 Introduction

In many ways, atmospheric electricity as a scientific discipline began with the discovery that thunderstorms are electrical phenomena. Since 1752, when Benjamin Franklin and Jean Francois Dalibard proved this finding, mankind has been attempting to better understand the electrical nature of clouds. The earliest models of thunderstorms were dipolar charge structures proposed by Simpson (1909, 1927) and Wilson (1916, 1920, 1925). Later, to better fit all the available observations, Simpson and colleagues modified the dipole models by proposing a tripolar structure, with a positive charge center near the thundercloud base and negative and positive charge centers successively higher in the cloud (Simpson and Scrase 1937; Simpson and Robinson 1941). This basic tripolar model survived through much of the twentieth century, although there is mounting evidence that it is overly simplified for many situations (e.g., Rust and Marshall 1996). Our current understanding of the electrical

M. Stolzenburg (✉) · T.C. Marshall
Department of Physics & Astronomy, University of Mississippi, University, MS, USA
e-mail: mstolzen@olemiss.edu

structure of thunderstorms, particularly the vertical distribution of charge within different types of storm clouds and the temporal evolution of charge during the life of a storm, is the subject of this review.

Numerous techniques have been developed to study thunderstorm electricity, both remotely and *in situ* (e.g., MacGorman and Rust 1998). Remote measurements, often acquired from ground-based and space-based platforms, are particularly useful for studying large-scale electrical effects of storms. Phenomena such as lightning and mesospheric transient luminous events are also well suited to remote measurement because of their distinct optical and electromagnetic emissions. *In situ* measurements, acquired from the ground beneath a thunderstorm and with airborne instruments that penetrate or fly over clouds, are essential for obtaining detailed information on the location and development of charge inside clouds. Although the deepest knowledge will come from a combination of measurement techniques, this paper highlights results about the fundamental thunderstorm charge structure based primarily on *in situ* electrical measurements.

Airborne studies of thunderstorm electrical parameters have made use of instrumented airplanes, rockets, and balloons (e.g., Weinheimer et al. 1991; Mo et al. 2003; Winn and Moore 1971; Willett et al. 1993; Winn et al. 1978; Chauzy et al. 1985; Byrne et al. 1989). Because balloon-borne electrical measurements are relatively simple and inexpensive to acquire, such observations have become the most prevalent *in situ* data available across different types of thunderstorm clouds. Balloons also have the capability of sampling the entire cloud depth over a reasonably short time, which yields valuable information about the vertical distribution of electrical quantities and their variation with respect to the vertical changes in temperature and microphysical quantities in the storm. For these reasons, this paper focuses primarily on data acquired with balloons. From a vertical profile (sounding) of electric field (E), one can determine the location and density of charge in the storm. Analysis of charge from E soundings is typically done using a one-dimensional approximation to Gauss's Law (e.g., Stolzenburg et al. 1998a), in part because the largest component of E and the largest divergence of E measured in a sounding are usually in the vertical. For charge regions with horizontal extent of at least 5 km, the approximation has been found to fit the sounding observations reasonably well (Stolzenburg et al. 1998b). For the purposes of this review the approximation is used primarily to determine the polarity of the charge regions, with less emphasis on the charge density. Multiple soundings within a single storm, acquired at different locations and times, allow further inferences about the spatial extent and temporal variation of electrical properties. In addition to measuring E , balloons have carried numerous other electrical devices into clouds, including instruments to measure conductivity and the charge on individual hydrometeors (e.g., Rust and Moore 1974; Marshall and Winn 1982; Takahashi and Keenan 2004); results from these various measurements are beyond the space limitations of this review.

2 Charge Distribution in Thunderstorm Convection

Many balloon E soundings through convective regions have been acquired since the early work by Simpson and Scrase (1937) and continuing through recent large field programs in the U.S. Great Plains (e.g., Rust et al. 2005). The three types of convection studied most frequently with balloons include isolated supercells, multicellular squall lines of mesoscale convective systems (MCSs), and small New Mexico mountain storms over Langmuir Laboratory. Because these storms form in very different environments, the thermodynamic forcing, microphysical nature, and kinematic structure of these convective types are quite different (see, e.g., Stolzenburg et al. (1998b) for a brief description, or Houze (1993) for a full

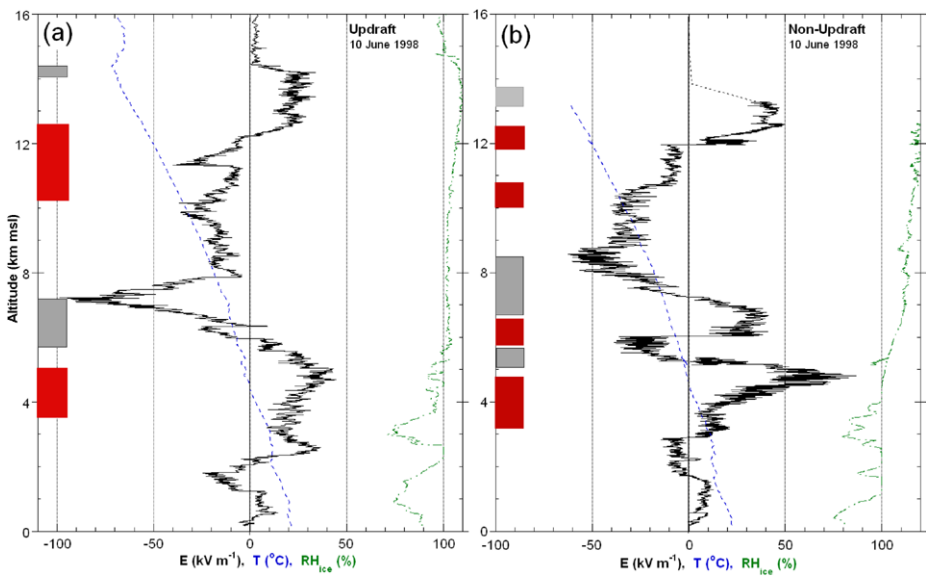


Fig. 1 Representative vertical profiles of electric field (E), temperature (T), relative humidity (RH_{ice}), and inferred charge (red boxes for positive, gray for negative charge regions) through convective clouds. **(a)** Example of a typical convective updraft sounding, showing four charge regions. The main negative charge is at 6–7 km altitude in this case. **(b)** Example of a convective region sounding from a balloon that ascended outside the updraft. The six common charge regions are shown, with the upper positive charge split in two regions between 10 and 12.5 km altitude in this case. (Adapted from Stolzenburg et al. 2002)

discussion). For the purposes of this review it is important to note mainly that the three types have different typical maximum updraft speeds and updraft region sizes, from strong and large (supercells) to moderate (MCSs) to weak and small (New Mexico storms). To describe the vertical electrical structure across convective regions in general, it has proven useful to classify balloon soundings in terms of their location relative to the updraft (Stolzenburg et al. 1998a). Thus, soundings made in convective regions where the vertical air velocity exceeds about 1 m s^{-1} are ‘updraft’ soundings, while those acquired in weaker or downward vertical motion (or in very heavy precipitation) within the convective region are ‘non-updraft’ soundings.

Based upon E soundings through 20 different storms, Stolzenburg et al. (1998c) identified a basic charge structure in convective updrafts comprised of four charge regions. Weak positive charge is lowermost, and above this are the main negative and upper positive charge regions often described as the “main dipole” of the cloud. The fourth and uppermost region has negative charge and is usually shallow. Figure 1a represents a complete balloon E sounding, along with the charge analysis, through the updraft region. (The RH_{ice} profile from the balloon gives humidity relative to liquid water for temperatures warmer than freezing and relative to ice for colder temperatures; RH_{ice} values near or above 100% indicate the balloon is in cloud.) This basic four-charge structure essentially modifies the earlier tripolar charge structure by adding a negative screening charge layer (i.e., a cloud charge region formed primarily by ion attachment (e.g., Vonnegut 1955) near the upper cloud boundary. The effect of the upper negative charge region is to reduce the E magnitude above the cloud to relatively small values of order 1 kV m^{-1} or less, compared to maximum magnitudes of order 100 kV m^{-1} observed within the thundercloud. Outside the updrafts, but still within

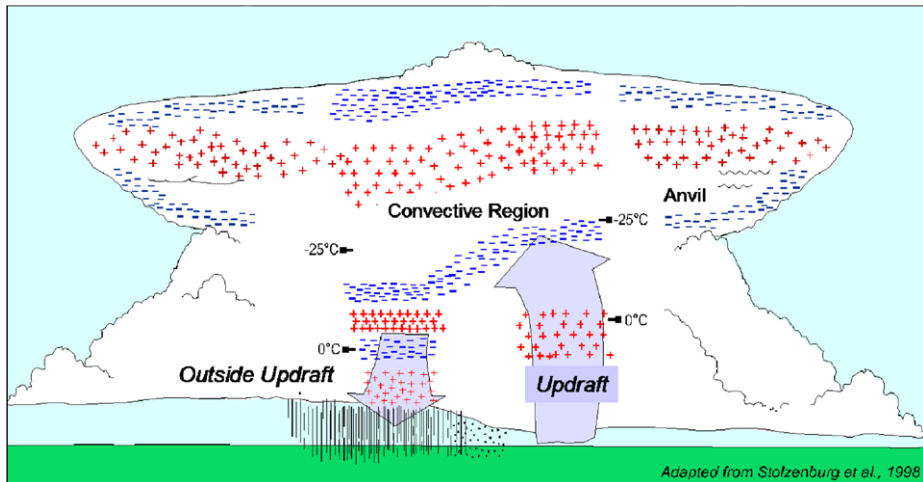


Fig. 2 Conceptual model of the charge structure within an idealized isolated, mature, thunderstorm, based on 49 balloon soundings through different clouds. Four charge regions are commonly found in the convective updraft and at least six charge regions are seen outside the updraft of convection. Forward and rearward anvils typically contain positive charge, and are screened with negatively charged layers. (Adapted from Stolzenburg et al. 1998c)

the storm's convective region, there are typically at least six charge regions, alternating in polarity from lowest to highest, and the uppermost region has negative charge. Figure 1b shows a representative example of a non-updraft E sounding and charge structure. Non-updraft soundings tend to exhibit more variation and complexity from one storm to the next, thus the six-charge structure represents only the most common features.

Stolzenburg et al. (1998c) derived a conceptual model (Fig. 2) to illustrate the basic four- and six-charge structures they identified in typical, mature, midlatitude thunderstorm convective regions. The two parts of this model have been found to occur simultaneously within mature convection (Stolzenburg et al. 2002; MacGorman et al. 2005). It is also likely that the updraft structure, which is similar to that described for thunderclouds in general by Krehbiel (1986), can evolve into the non-updraft structure as a storm develops from the early to mature stage and its updraft weakens. Lightning discharges throughout the cloud can also add complexity to the charge structure as the storm ages. Possible charging mechanisms responsible for the complicated electrical structures in convection are discussed briefly in Stolzenburg et al. (1998c). A more complete review of charging formation in convective clouds is included elsewhere in this issue (Saunders 2008).

Among the three types of convection studied by Stolzenburg et al. (1998c), differences were found in the heights and temperatures at which the basic four charge regions are located. For example, the center height of the main negative charge region averaged 9.1 km (-22°C) in supercell updrafts, 6.9 km (-16°C) in MCS convective region updrafts, and 6.0 km (-7°C) in New Mexico mountain storm updrafts. These differences generally scale with the maximum updraft speeds present in each storm type, although the total storm depth and the surface altitude (in the case of the mountain storms) are also important parameters. Overall, the altitude of the main negative charge region was found to be well correlated with the local updraft speed as estimated from the balloons (Stolzenburg et al. 1998c). Differences in the charge structure with differing updraft speeds in “giant” storms (tornadic supercells) were suggested much earlier by Vonnegut and Moore (1958).

Within a given type of thunderstorm convection, the cloud dynamics or overall convective intensity play an important role in the electrical structure. In comparing typical convective region soundings outside updrafts to those within updrafts, Stolzenburg et al. (1998a, 1998b) found that the maximum E magnitudes of both polarities tend to be smaller and located at higher altitudes (and colder temperatures) within the updrafts. Maximum E magnitudes are typically 80 kV m^{-1} or less in the updraft soundings, while most soundings outside updrafts in convection have maximum E magnitudes of at least 100 kV m^{-1} . (Immediately before nearby lightning, exceptionally large E magnitudes of $150\text{--}200 \text{ kV m}^{-1}$ have been observed with balloons (Marshall et al. 2005; Stolzenburg et al. 2007a).) In addition, most of the inferred charge regions outside updrafts are shallower and have larger charge densities (Stolzenburg et al. 1998c). Outside updrafts the center of the main negative charge region is at lower altitude and warmer temperature (average $5.5 \text{ km}, -6.2^\circ\text{C}$) than within updrafts. Differences in the electrical structure between strong and weak updrafts were also identified by Marshall et al. (1995) in large storms over the U.S. Great Plains.

It is important to note that the conceptual model in Fig. 2 does not represent some supercell storms in which balloon soundings indicate an ‘inverted polarity’ charge structure. Recent work by Rust et al. (2005) describe these atypical storms as having dominant positive charge at mid-levels in place of the typical main negative charge region, and dominant negative charge at upper levels where the upper positive charge region is typically found. Also in contrast to typical thunderstorms in which most cloud-to-ground lightning flashes lower negative charge, these inverted polarity supercell storms produce mainly positive cloud-to-ground lightning. Finally, it should be noted that the conceptual model is based on convective region balloon soundings from storms that occurred in a limited portion of the lower mid-latitudes; the extent to which this model fits storms in other midlatitude regions or those in the tropics and high latitudes (for all of which in situ data are scarce) is not known.

3 Charge Distribution in Layered Clouds Associated with Convection

3.1 Thunderstorm Anvil Clouds

As defined by Houze (1993) and others, anvil clouds are ice particle outflows emanating downshear and upshear from the tops of cumulonimbus clouds. They are high-based, typically cirriform (cirrostratus or cirrus spissatus) clouds, and generally do not produce precipitation at the surface. Non-precipitating anvil clouds associated with isolated and multicellular thunderstorms can last for several hours during and after the parent convection. It is thought that little or no lightning initiates within anvils, although E values of at least 50 kV m^{-1} are common and lightning flashes regularly propagate through the anvil (e.g., Marshall et al. 1989). Since anvil clouds are formed by advection of hydrometeors (ice crystals) from divergence at the tops of convective cells, and since these ice crystals may become charged in the convection and carry their charge with them, it is not surprising that anvils can contain large amounts of charge. The basic charge structure in anvils is simple, with interior positive charge bounded by upper and lower negative screening layers (e.g., Marshall et al. 1989; Byrne et al. 1989), as shown in the conceptual model of Fig. 2. Marshall et al. (1989) estimated 50 C and 7000 C of positive charge in the interior of two anvil clouds associated with a small mountain storm and a large multicellular storm, respectively.

Although the internal dynamics and charging within the anvil have been presumed to be minimal and dissipative, results from a 75-min series of three balloon soundings of E through the anvil of a New Mexico mountain thunderstorm (Stolzenburg et al. 2004) show

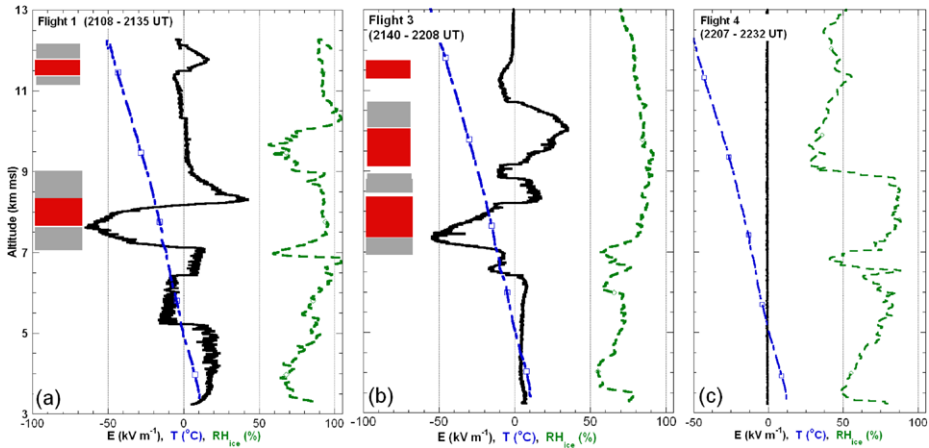


Fig. 3 Series of vertical profiles of electric field (E), temperature (T), relative humidity (RH_{ice}), and inferred charge (red boxes for positive, gray for negative charge regions) through a thunderstorm anvil cloud. (a) Earliest sounding shows three charge regions in the main anvil (7–9 km), plus another three in a higher anvil cloud (above 11 km). (b) About 30 min later, charge in the upper anvil cloud has descended closer to the main anvil (below 9 km). (c) The final sounding in the series had negligible E . (Adapted from Stolzenburg et al. 2004)

interesting features about the evolution and longevity of the charge. The first two soundings of the series (Figs. 3a and 3b) reveal that the main anvil cloud, which was between 7 and 9 km altitude, had the basic structure of positive interior charge and negative screening layers. Large E magnitudes ($>50 \text{ kV m}^{-1}$) and significant charge densities of both polarities were present, although these values were slightly smaller in the second sounding. In comparing to radar data, it was found that even tenuous cloud boundaries had noticeable screening charge layers. These two soundings were made 25–50 min after the last lightning flash had occurred in the parent convection, and the decaying convection was at least 20 km distant. The last sounding in the series (Fig. 3c), made 25 min later through visible but optically less dense anvil cloud, indicated essentially no enhanced E nor any net charge remaining in the anvil.

Unlike previously published data for anvil clouds, the case described by Stolzenburg et al. (2004) shows the effects of a second, older anvil cloud above 10 km in the first sounding and above 9 km in the second sounding. This older anvil also had weak interior positive charge and negative screening layers during the first balloon E sounding. By the time of the second sounding (30 min later), the two anvil clouds were less distinct in altitude, however. The upper negative screening layer of the older anvil had apparently descended into the cloud, and re-screening with positive charge had occurred at the uppermost cloud boundary. Most surprisingly, the E values and amount of charge associated with this older anvil had increased markedly as the two anvils merged: the positive E peak changed from 18 kV m^{-1} (at 11.7 km) to 38 kV m^{-1} (at 10.1 km) in the intervening 30 min. This more complicated charge structure in the later sounding illustrates that internal microphysics of the cloud are important in determining the electrical evolution, even for these relatively quiescent anvil clouds. The results also indicate that ion attachment (or the screening process) should be considered a significant charging mechanism for long-lived layered clouds.

Radar data for this series of anvil soundings have also yielded estimates of the horizontal extent and duration of the charge within the cloud. About 30 min after the last lightning flash, the main interior positive charge region covered approximately 250 km^2 (Fig. 4a) and was

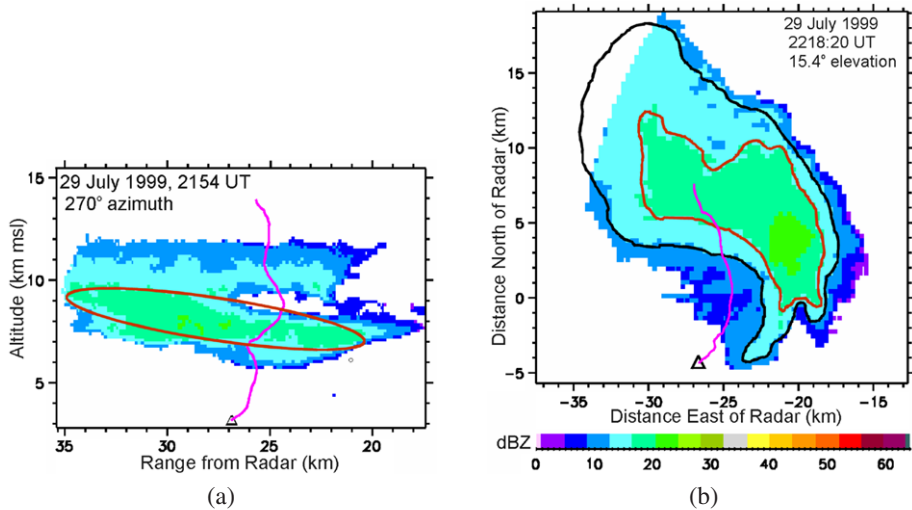


Fig. 4 Radar reflectivity for a thunderstorm anvil cloud. Pink curve is the track of the Flight3 balloon (from Fig. 3b), triangle is launch location. **(a)** Range vs. altitude scan of the cloud about 30 min after the last lightning flash. Red oval indicates the approximate depth of the positive charge in the main anvil. **(b)** Plan view of the anvil cloud about 50 min after the last lightning (scan altitude is near 8.1 km msl at balloon's range from radar). Red curve indicates the estimated area of positive charge; black curve encloses the area of large E values. (Adapted from Stolzenburg et al. 2004)

estimated to have 450 C of charge (Stolzenburg et al. 2004). About 50 min after the last flash, the positive charge region still covered approximately 90 km^2 (Fig. 4b) and was estimated to contain 50 C of charge. The data from this case further provide limited information about the long-term hazards anvils present to aircraft: 32 min after and more than 20 km away from the final lightning flash in the parent storm, E at 10 km altitude (a common jet aircraft cruising altitude) was 35 kV m^{-1} . About 50 min after the last lightning, the spatial extent of potentially hazardous E values of at least 50 kV m^{-1} associated with this anvil was estimated by Stolzenburg et al. (2004) to be 220 km^2 . Thus, the interior positive charge and large E values extended well beyond the lifetime and area of the parent convection.

Recent results by Dye and Willett (2007) based on aircraft measurements in Florida storms also indicate that substantial changes can occur in long-lived anvils. Horizontal aircraft tracks at 9.3 km altitude made 85 min after the last lightning flash in the parent convection showed E of -15 to -40 kV m^{-1} . Although no information was available about the vertical charge structure, the measured negative vertical E was consistent with positive charge above the aircraft in the interior of the anvil and/or negative charge below the aircraft. Another anvil had E of 20 – 35 kV m^{-1} at 9.9 km altitude over a horizontal distance of 70 km. For this case, the measured E suggested interior negative charge in some interior parts of the anvil. Dye and Willett (2007) also describe enhancement in the radar reflectivity and E , indicative of possible weak internal convection and charging in the anvil. It is interesting to note that several anvils studied by Dye and Willett (2007) and by Dye et al. (2007) in Florida had precipitation falling through the melting level (4 km altitude), though not reaching the ground, and the larger E values were often correlated in time with the presence of significant melting of particles lower in the anvils. These features indicate that, in terms of the electrical structure, the distinction between long-lived cirriform “ice particle outflow” anvil clouds and the stratiform precipitation regions that trail MCSs (discussed next) may not be clear in every case.

3.2 MCS Stratiform Precipitation Regions

In the midlatitudes the storms referred to as mesoscale convective systems (MCSs) are characterized by a leading region of deep convective clouds often forming a line or arc, followed by a broad area of deep nimbostratus cloud produced by a combination of advection (of the entire system) and vertical shear (of the horizontal wind within the system). As described by Houze (1993) and others, the typical MCS stratiform cloud has a mesoscale updraft with vertical motion weaker than the fall speed of ice aggregates, has a radar bright band signature associated with melting aggregates, has light to moderate precipitation reaching the ground, and, although generally stratified, often has embedded cellular elements of dying convective cells. An MCS is organized on the mesoscale, both in duration and horizontal scale, thus a typical MCS stratiform cloud lasts for 2–12 hrs and covers 2,000–20,000 km². All these features make the electrical structure of midlatitude MCS stratiform clouds potentially complex. (Balloon measurements in Africa, made by Chauzy et al. (1985), have confirmed this complexity for tropical MCSs, as well.) MCS stratiform region charge structure has been of interest since early studies (e.g., Marshall and Rust 1993) showed that very large amounts of charge reside in these clouds, particularly in a strong charge layer (estimated at 20,000 C) that is often found near the melting level. Additional interest in understanding these clouds comes from observations of sprites and other mesospheric transient luminous events above some MCSs with extensive stratiform clouds, phenomena which are discussed elsewhere in this Volume (Mika 2008).

Marshall and Rust (1993) described two different modes of electrical structure that are typical in MCS stratiform cloud regions. Their ‘Type A’ is more complex in terms of the number of significant charge regions, while ‘Type B’ is relatively simple, with fewer charge regions. Representative examples of these two classic structures are shown in Fig. 5. Note that both these soundings have dense charge regions near 0°C. In analyzing all the available MCS stratiform region soundings, Stolzenburg et al. (2007b) identified a third electrical structure as ‘Anvil Type’ (Fig. 5c). The soundings of this type do not have a strong charge region near 0°C; notably, they also have no cloud at the melting level (i.e., cloud base is higher in altitude), although light precipitation was reaching the ground in three of their four cases. The ‘Anvil Type’ stratiform region charge structure resembles that of anvils (described in the previous Section) in the sense that there is a deep, internal positive charge region and

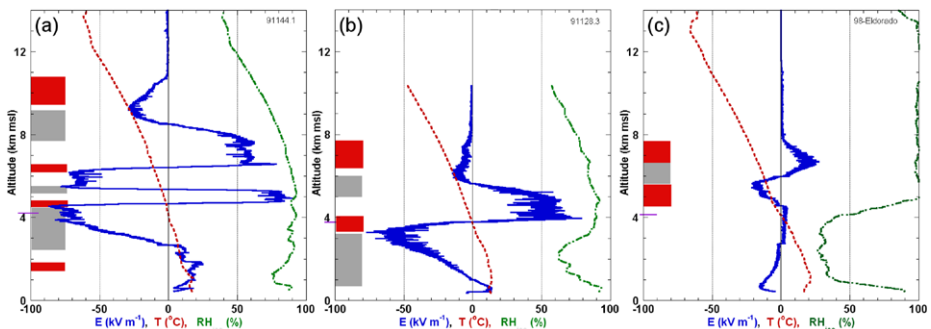


Fig. 5 MCS stratiform region soundings of electric field, temperature, and relative humidity, and inferred charge (red boxes for positive, gray for negative charge regions). (a) Example of the more complicated Type A electrical structure, with negative charge at 0°C in this case. (b) Example of simpler Type B structure, with a positive charge region at 0°C. (c) Sounding with ‘Anvil Type’ structure, where cloud base is above the level of the 0°C isotherm. (Adapted from Stolzenburg et al. 2007b)

a lower negative screening layer. However, the upper negative charge region is found at the upper cloud boundary in only two of the four cases. Stolzenburg et al. (2007b) speculated that this structure is the simplest for MCS stratiform clouds due to the lack of significant numbers of aggregates melting, and possibly becoming charged, near the 0°C isotherm. For the overall charge structure, most of the 28 complete MCS stratiform *E* soundings analyzed by Stolzenburg et al. (2007b) indicate three to six major charge regions inside the cloud. The average center altitude of the uppermost charge region, not including the upper screening layer, was about 8 km (or -20°C). In 17 of the 28 complete soundings, all the net charge regions in the cloud were located below 10 km altitude.

A conceptual model of a midlatitude MCS with Type B stratiform region charge structure was derived by Stolzenburg et al. (1994) from multiple soundings through one MCS. The general similarities among their five soundings through a single MCS stratiform cloud were given as evidence that the basic charge regions are horizontally extensive over at least 100 km and 3 hours. However, aircraft data acquired by Mo et al. (2003) at a constant altitude near the melting level (in the same MCS studied by Stolzenburg et al.) show that smaller scale inhomogeneities in the charge exist in what are probably weak convective elements. Schuur and Rutledge (2000) identified subtle but important differences in the kinematics, thermodynamics, and microphysics between one Type A and one Type B MCS that may explain some of the differences in the two stratiform region charge structures. In particular, the MCS stratiform region with Type A structure had a stronger mesoscale updraft and hence some supercooled cloud water, an ingredient which is needed for non-inductive ice-ice charging (e.g., Saunders 2008).

As noted by Marshall and Rust (1993), Shepherd et al. (1996) and others, MCS stratiform region soundings typically have a dense charge layer near the 0°C isotherm when cloud base is at or below that altitude. From a recent study of all their available balloon *E* soundings through MCS stratiform regions, Stolzenburg et al. (2007b) found strong positive charge at 0°C in 14 cases, and strong negative charge in 16 cases. In another 11 soundings, there was essentially no net charge indicated at 0°C because there was either a relative maximum or minimum in *E* (i.e., a large positive or negative *E* peak) precisely at that altitude. To possibly explain this strong feature in the soundings, Marshall and Rust (1993) pointed to the inductive melting charging mechanism first described by Simpson (1909), which involves the melting of hydrometeors on which charges are induced prior to their breaking apart or shedding. The microphysical state in the melting layer of MCS stratiform clouds, namely large ice aggregates descending (e.g., Willis and Heymsfield 1989), is conducive to the shedding process. Melting charging can occur through a significant depth (100–200 m) because there is often a quasi-isothermal layer near 0°C and because melting of aggregates reaches a maximum at temperatures slightly warmer than 0°C. Since this is an inductive mechanism, melting charging also depends on the polarity and strength of *E* during the melting of the particles.

The basic signatures that fit the inductive melting charging mechanism are described by Stolzenburg et al. (2007b) and shown in Fig. 6: when *E* is *positive* (negative) at 0°C, there would be strong *positive* (*negative*) charge at and just below 0°C and weaker or equivalent *negative* (*positive*) charge further below the 0°C level. However, variations on the basic melting charge signatures are possible in different situations. For example, in cases with a stronger mesoscale updraft extending down to the melting level, the (upper) charge associated with the smaller particles that are shed during melting may extend further upward and be less dense. Also, in cases with heavier precipitation falling through the melting level, the charge region associated with the larger melting particles may be deeper and less dense. In some soundings, the polarity of *E* changes at 0°C or within the melting region; in these,

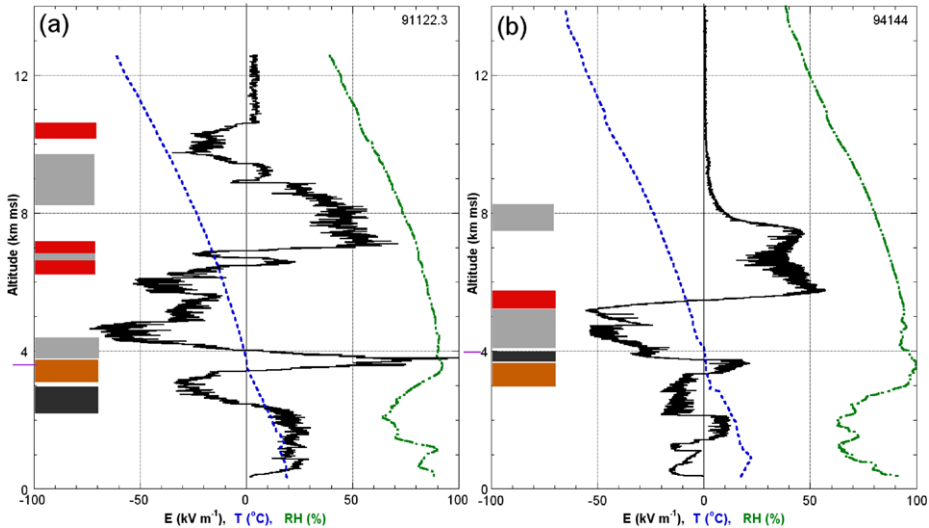


Fig. 6 Two MCS stratiform region soundings of electric field, temperature, relative humidity, and inferred charge (red/orange boxes for positive, gray/black for negative charge regions) which apparently fit the Simpson (1909) melting charging mechanism. (a) Example with positive E at 0°C , positive charge (orange) at and just below 0°C , and negative charge (black) lower in and below the cloud. (b) Example with negative E at 0°C , negative charge (black) at and just below 0°C , and positive charge (orange) lower in and below the cloud. (Adapted from Stolzenburg et al. 2007b)

analyzing the expected effect of an inductive charging mechanism is more complicated, since neither the time history of E in the melting region nor the microphysical detail about the precise level of melting is available. Additionally, the fact that cloud base, with the corresponding screening charge development that occurs there, is sometimes very near the melting level in MCS stratiform clouds further complicates the basic signature that would be present due to the melting charging mechanism alone.

Although Stolzenburg et al. (2007b) concluded that the ‘Type A’ and ‘Type B’ stratiform region charge structures are common, their data show a wide variety about these basic types. Any charging mechanisms at work within the stratiform cloud would thus need to be able to explain this variability, especially at the microphysically and electrically important melting level near 0°C . Most of the data near the 0°C isotherm were interpreted by Stolzenburg et al. to fit with the inductive melting charging mechanism described by Simpson (1909). As they note, this is in part a simple consequence of the fact that many different situations are possible with this mechanism.

4 Charge Dynamics in Thunderstorms

Because the charge structures described above for different cloud types are reasonably reproducible from one storm to another, the reader may have the impression that such ‘basic’ charge structures are static within the appropriate location. In active thunderstorm convection, this impression is perhaps most accurate during the mature stage of the storm (e.g., Fig. 2). However, as a thunderstorm develops or decays, the electrical structure can change rapidly. In this section, the dynamics of the charge structure within small mountain thunderstorms are highlighted to give a sense of the changes that occur.

4.1 Electrical Evolution in the Early Stage

There is relatively little *in situ* information from balloons about E , charge, and first lightning in developing storms. Aircraft measurements (e.g., Dye et al. 1986) of early electrification in Montana hailstorms have shown that E can increase exponentially and the region of maximum electrification is apparently near the updraft/downdraft interface in some developing storms. In addition to the long-standing interest in knowing the charging mechanisms that can explain the character of the electrification, a fundamental question about the early electrical evolution concerns the type of lightning that occurs first in a storm. Although the first lightning flash may be either intracloud (IC) or cloud-to-ground (CG), many storms begin with a series of IC flashes.

Presumably the early evolution of the charge structure inside a cloud is responsible for the type of lightning flash that occurs first. Based on data from a series of balloon soundings made during the early and mature stages of one storm, Stolzenburg et al. (2003) suggested that in storms which initially produce IC flashes only, the early electrification and net charge development occurs at upper altitudes (above 7 km). This early stage of development produces a large negative E at upper levels in the cloud which is necessary to initiate normal IC flashes. However, no large positive E values, needed to initiate normal negative-polarity CG flashes, develop at lower levels. In the storm investigated by Stolzenburg et al. (2003) balloon and lightning data revealed that the initiation of CG flashes was delayed until the development of a lower positive charge region and the growth of a substantial positive E at lower levels. Unlike the basic charge structure found in the mature stage (described above and depicted in Fig. 2), the sounding during the early stage showed only two charge regions: negative charge centered at 7.6 km (-10°C) and positive charge centered at 8.8 km (-20°C). A subsequent sounding acquired about 10 min later had a significant lower positive charge region below 6 km and a positive E maximum at 6 km that was ten times larger than in the early sounding. Thus, the storm evolved from early stage to mature stage within a 10 min period, in which time both a lower positive charge region and substantial positive E had developed, and CG flashes began occurring.

In different geographical conditions, the early development of thunderstorms can be different. For example, Qie et al. (2005) studied thunderstorms that developed at high altitudes (ground level of 4.5 km msl) on the Tibetan Plateau and found that an inverted dipole (positive charge below negative) developed first. Inverted polarity IC flashes and enhanced fair weather polarity E values at the surface were also observed.

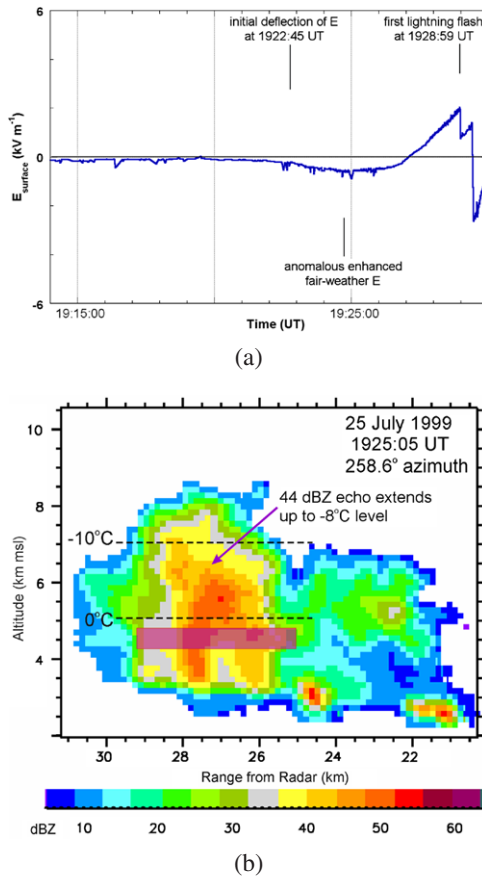
The idea that precipitation particles and electrical charge develop together during the initial electrification of storms has been investigated for many years (e.g., Dye et al. 1986). Several studies have compared growth of the radar reflectivity to growth of the surface E beneath thunderstorms. For example, Reynolds and Brook (1956) found the time between the first indication of electrification at the surface and the first lightning was 10–12 min, and electrification was coincident with substantial vertical echo development. Later, Jameson et al. (1996) found that initial electrification was coincident with the appearance of graupel particles above the -7°C level.

Recent results (Stolzenburg et al. 2007c) from three New Mexico mountain storms with surface E , radar, lightning, and balloon E data shed new light on initial electrification and the correlated development in time and location with precipitation. Analysis of one case showed weak but anomalous (i.e., enhanced fair-weather E) initial electrification at the surface (Fig. 7a) beneath the thunderstorm. The lowest charge region evident in a balloon sounding early in this storm was also anomalous: this region was positively charged, located low in the cloud (near cloud base), and moved downward (as if carried on precipitation) with time (Fig. 7b). Along with the radar echo development, the E data indicate

Fig. 7 (a) Electric field vs. time at the surface beneath a developing thunderstorm.

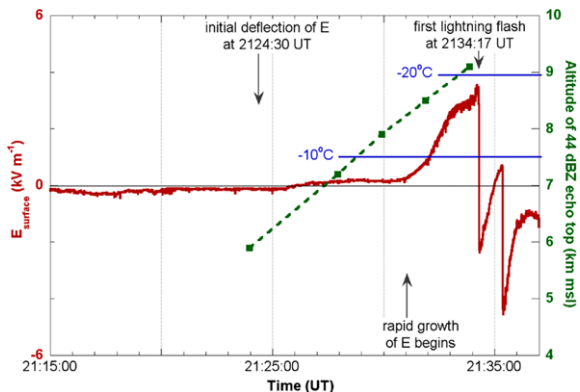
Background, fair weather values are present until about 1922:45 UT, and the first lightning from the storm occurred about 6 min later. Enhanced negative E prior to rapid electrification indicates net positive charge aloft.

(b) Radar reflectivity data for the same storm, acquired at the time of the enhanced fair weather E prior to rapid electrification. Note that all the strong echoes are at low levels in the cloud. Red shaded box shows positive charge inferred from a balloon sounding made 5 min later in the storm. Temperatures shown are also from balloon data. The surface E measurements in (a) were made at 3.2 km altitude and 27 km range. (From Stolzenburg et al. 2007c)



that the anomalous charging occurred at temperatures warmer than -20°C and warmer than the “charge reversal temperature” associated with the non-inductive, ice-ice charging mechanism (e.g., Saunders 2008). As the radar echo subsequently developed into colder parts of the cloud, the surface E reversed to foul weather polarity and rapidly increased. In a second case investigated by Stolzenburg et al. (2007c), electrification began soon after substantial upward growth of the precipitation core began. The temporal evolution of the top of the strong radar echo and the surface E are shown in Fig. 8. The rapid positive E growth at the ground, indicating development of net negative charge aloft, began when the 44 dBZ echo reached 8.3 km (-15°C) in the cloud. A brief plateau in the growth of surface E started at the time the 44 dBZ echo reached -20°C . The first lightning from this cell initiated at -10°C (7.4 km), suggesting that the strongest negative E values in the cloud were near this altitude and between negative and overlying positive charge regions. A corresponding balloon sounding (slightly later and in an adjacent, slightly later cell) indicated negative charge between 7.2 and 8.9 km (-9 to -19°C), with positive charge above and weak positive charge below. In the third case of initial electrification, an early explosive precipitation growth phase was evident in the radar data between 6 and 8 km (-5 to -15°C). A coincident E sounding during that time showed only two net charge regions: positive charge centered at -20°C and negative charge at -10°C near the region of an elongated graupel signature.

Fig. 8 Evolution of electric field at the surface and the maximum altitude of the 44 dBZ radar echo in the cloud through the initial electrification of a storm on 2 August 1999. Echo altitude increases at 6 m s^{-1} , which is also the average updraft speed from a balloon sounding in the storm. Temperatures indicated are from the balloon data. The rapid positive E growth at the surface starts when the 44 dBZ echo reaches 8.3 km (-15°C), and a brief plateau in dE/dt starts when 44 dBZ reaches -20°C . (From Stolzenburg et al. 2007c)



In all three of the storms investigated by Stolzenburg et al. (2007c), the initial electrification began once substantial radar echo developed above the -5°C level, and rapid E growth at the surface began once radar reflectivities indicative of large precipitation particles reached above the level of -15°C . The first lightning flashes occurred within a few minutes of the onset of rapid E growth at the ground and initiated at temperatures between -10 and -21°C . Stolzenburg et al. (2007c) concluded that the initial electrification in each of the storms fit with charging via the non-inductive ice–ice collisional mechanism.

4.2 Electrical Evolution in the Decay Stage

Despite the absence of convective updrafts, the electrical structure during the decay stage of thunderstorms is quite dynamic. Evidence for this evolution is easily found in E measurements at the ground beneath storms, which often exhibit an End Of Storm Oscillation (EOSO). During the EOSO, E makes at least two polarity changes over a period of 30–75 min (Moore and Vonnegut 1977); these are accompanied by substantial changes in the charge structure within the cloud during its decay (Marshall and Lin 1992). A typical EOSO cycle begins during strong positive E at the ground (i.e., dominated by negative charge overhead), then E switches to large negative values, then returns to a slightly weaker positive E , and finally decays to ‘fair weather’ negative E values as the storm completely dies. Figure 9 shows an EOSO observed beneath a New Mexico mountain thunderstorm that occurred above Langmuir Laboratory (Marshall et al. 2007). In addition to the typical features, this EOSO has a final overshoot of negative E that sometimes occurs.

Mechanisms associated with the electrical decay of thunderstorms after their dynamical forcing and associated updrafts die have been the subject of only a few studies. Moore and Vonnegut (1977) suggested that downdrafts in a dying storm allow the upper positive charge to dominate E at the ground, thereby explaining the first oscillation to negative values. Marshall and Lin (1992) used balloon and surface E data along with radar data to show that for two EOSOs, the cloud electrical structure consisted of an internal negative charge with positive screening charge layers at the upper and lower boundaries. (This decay stage charge structure has the opposite polarity of the basic charge structure described above for anvil clouds.) Marshall and Lin also observed negatively charged precipitation descending below cloud base of both decaying storms. For both cases, their data are applicable to the last oscillation of the EOSO. Marshall and Lin (1992) suggested that the final period of large

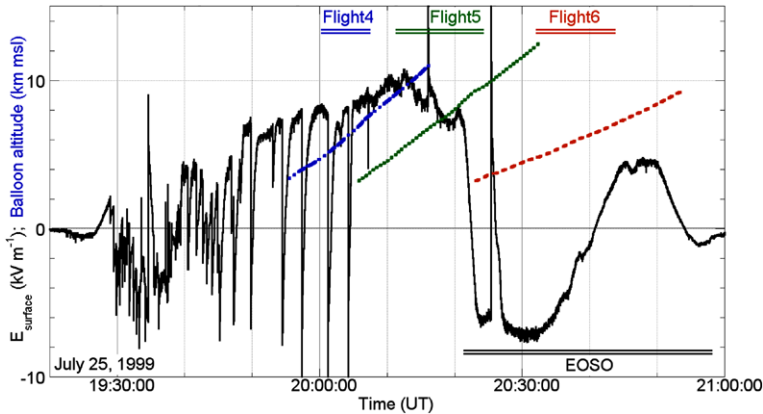


Fig. 9 Time history of surface electric field for a thunderstorm over Langmuir Laboratory, New Mexico. The End Of Storm Oscillation (EOSO) time is indicated. Altitude vs. time of three balloons (Flights 4, 5, and 6) in the storm during the late-mature and decay stage are shown; colored horizontal bars indicate the time each balloon was inside cloud. (From Marshall et al. 2007)

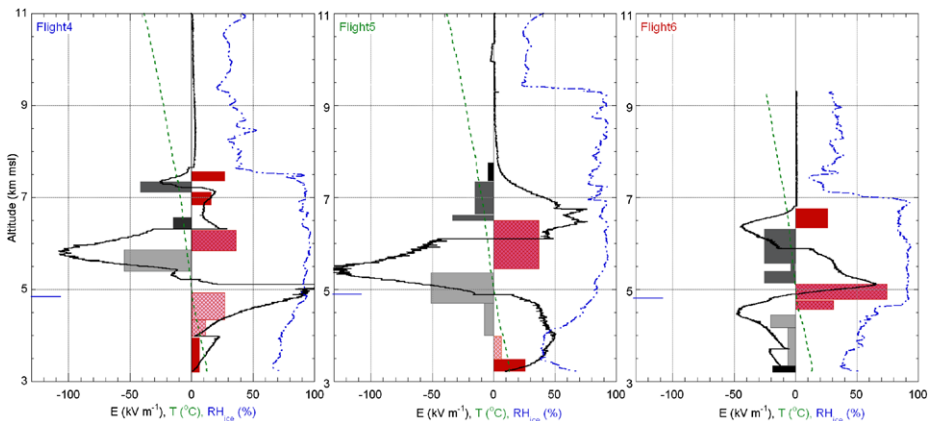


Fig. 10 Balloon electric field, temperature, relative humidity, and charge (shown as *shaded boxes*) for three soundings through a dying storm on July 25, 1999. Times of each flight are shown in Fig. 9. The lower charge regions (especially those indicated by pink, dark blue, and red boxes) descend with time. Loss of the lowest positive charge into the ground and addition of positive charge at the top of Flight 6 lead to the E profile's apparent opposite shape, compared to Flight 5. (Adapted from Marshall et al. 2007)

positive E at the ground is due to a combination of the internal negative cloud charge and the sub-cloud negative charge on precipitation. As the negatively charged precipitation falls to the ground, the screening charge process brings positive charge to the cloud boundaries to maintain a nearly zero E outside the cloud. Thus, when the negatively charged precipitation completely vanishes into the ground, the surface E either returns to fair weather values or becomes slightly negative (the final overshoot) as the screening process continues.

A recent study by Marshall et al. (2007) used E soundings (Fig. 10) and radar data to understand details about the earlier part of one EOSO. Multiple balloon soundings before and during the EOSO that is shown in Fig. 9 indicate substantial changes in the charge

structure over about 50 min through the decaying storm. Note especially in Fig. 10 the change in the E profile from Flight5 (completed just before the EOSO began) to Flight6 (launched 17 min later, just after the EOSO began). Marshall et al. (2007) concluded that the first oscillation of the EOSO to large negative E values is apparently due to the descent of negatively charged precipitation, which dominates the surface E as it approaches the ground. Then, after the period of strong negative E at the ground, E returns to positive values due to the subsequent descent of positively charged precipitation and to an increase in negative charge and a decrease in positive charge within the cloud. These changes lead to the addition of an uppermost positive screening charge (as indicated at the top of the Flight6 sounding). Interestingly, these changes also lead to the Flight6 sounding appearing as nearly a mirror image (in E polarity) of the earlier Flight5 profile. Finally, the part of the EOSO described by the Marshall and Lin (1992) study occurs: the screening process coupled with the descent of negatively charged precipitation causes the final oscillation of the EOSO.

5 Thunderstorm Charge Structures in the Earth's Electric Circuit

As reviewed elsewhere in this issue (Aplin et al. 2008), the Earth's global electric circuit can be considered a paradigm for planetary electricity. Wilson (1920) hypothesized that thunderstorms are the main generators in the global electric circuit, effectively driving negative charge from the ionosphere to the Earth in what is now called the Wilson current. In this section, studies indicating that the internal thunderstorm charge structure can effect the contribution that storms have to the Earth's global electric circuit are reviewed.

Some of the earliest attempts to measure the Wilson current above thunderstorms (Gish and Wait 1950; Stergis et al. 1957) indicated an upward current flow, in support of Wilson's hypothesis. More recent airplane measurements by Blakeslee et al. (1989) of E and conductivity above 15 thunderstorms of various sizes showed E values of 0.4 to 6 kV m⁻¹. From their data and the approximate storm sizes, Blakeslee et al. estimated Wilson currents in the range from 0.09 to 3.7 A, with an average of 1.7 A. This average current, combined with simple estimates (\sim 1000) of the number of worldwide simultaneous thunderstorms, added further support to Wilson's hypothesis that thunderstorms are the main generator in the global circuit.

Recent above-cloud balloon E measurements (Stolzenburg et al. 2006) for one small thunderstorm are shown in Fig. 11. Using the same technique and empirical conductivities as Blakeslee et al. (1989), Stolzenburg et al. estimated that the Wilson current ranged from 0.1 to 0.3 A during part of this storm's lifetime. An important criterion in determining the strength of the Wilson current in this case is whether or not the convective updraft has a screening charge layer above it. As noted in early work by Vonnegut et al. (1966), the convective updraft and internal cloud charge may not be fully screened at the top if divergent outflow carries away the particles (to which attracted ions have attached) too quickly. In this scenario, E above the cloud is of order 1–10 kV m⁻¹ (as shown in Fig. 11, particularly in Fig. 11a) rather than near-zero; such a relatively large E can drive a relatively large above-cloud current. In addition, since small storms like those studied by Stolzenburg et al. (2006) may make up a large portion of the global storm population, the average Wilson current used by Blakeslee et al. (1989) in their test of the Wilson (1920) hypothesis may be an overestimate.

Modeling of thunderstorms as generators in the global circuit began with Holzer and Saxon (1952), who represented the storm as positive and negative current sources of equal strength embedded in an atmosphere with an exponential conductivity profile between two

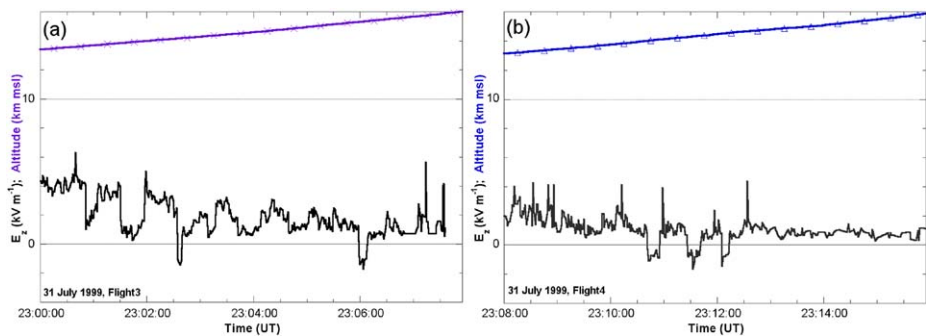


Fig. 11 Above-cloud vertical component of E (E_z) and altitude from two balloons over a New Mexico storm. (a) Earlier balloon at increasing altitude (13 to 16 km) and increasing distance from storm's updraft (2 to 6 km away). E_z is positive most of the time, except after some lightning flashes. Average current density estimated is 3.7 nA m^{-2} ; estimated Wilson current is 0.3 A. (b) Data from a later balloon at increasing altitude and increasing distance from storm core (4 to 8 km away). E_z is smaller and positive most of the time, except after some lightning flashes. Average current density estimated is 2.0 nA m^{-2} ; estimated Wilson current is 0.2 A. (Adapted from Stolzenburg et al. 2006)

perfectly conducting planes. The positive current source was located near the top of the cloud, and the negative source was a few kilometers lower. Holzer and Saxon showed that such a dipolar structure of current sources does act as a generator in the global circuit and transfers negative charge to the Earth. They also showed that the Wilson current output from a storm depended on the charge separation distance within the storm. During the next 30 years, many improvements were made in models of thunderstorms as generators in the global circuit (see Roble and Tzur 1986, for a review). However, in these improved models, there was still little detail included about the charge structure inside the storms or about the overall range of horizontal scales of thunderstorms. Intuitively, it can be expected that if the charge separation distance is important in the current output, then the internal vertical charge structure, including its complexity beyond a positive dipole, is also important in estimating the Wilson current due to a storm. Furthermore, since a typical MCS has lateral extent which is an order of magnitude greater than that of an ordinary thunderstorm (and at least twice the distance between the Earth's surface and the ionosphere), one might expect a more effective coupling to the ionosphere over a substantially longer period for MCSs than for an isolated thunderstorm.

Recently, Davydenko et al. (2004, 2005) investigated the contribution of individual MCSs to the global electric circuit. These authors found that one MCS stratiform region with Type A structure had a Wilson current of 32 A, while a Type B MCS stratiform region had a Wilson current of -25 A. In both these MCSs, the convective region had an estimated Wilson current of less than 0.5 A, similar to that of an ordinary thunderstorm. Based on their examination of 32 balloon soundings through MCS stratiform regions, Stolzenburg et al. (2007b) inferred that the above-cloud E for 15 cases indicated the stratiform cloud was charging the global circuit, while the other 17 indicated the cloud was discharging the global circuit. Thus, the overall effect of MCSs on the global circuit could be very large or very small, but it remains essentially unknown.

Wilson's 1920 hypothesis that thunderstorms are the main generators in the Earth's global electric circuit seems likely to be proven correct, based on the data collected and the models constructed to date. However, a comprehensive test of the hypothesis awaits comprehensive data on the Wilson current provided by storms of different sizes and flash rates, with different

dynamics, and at different times in their evolution. A comprehensive test will also require a comprehensive knowledge of the number and percentage of different types of thunderstorms, including deep convection in the tropics, that occur simultaneously around the globe and the variations in those numbers and percentages as the Earth rotates. Finally, as pointed out by Williams (2007) and others, improved estimates about other possible current sources in the circuit (such as non-thunderstorm shower clouds mentioned by Wilson (1920)) are needed to determine whether thunderstorms are indeed the main generators in the global circuit.

6 Concluding Remarks

As is evident from this review, the electrical nature of thunderstorms on Earth is neither simple nor fully known. Some important basic charge structures have been identified in common types of layered and convective clouds and within certain periods of the convective activity. In most cases, however, it is clearly not enough to know only that a cloud is making lightning to know its charge structure; one needs additional information regarding the storm type, cloud type, location, and life stage, to make informed guesses about the internal charge structure. Furthermore, little electrical data currently exist for some storm types in important regions of the Earth (e.g., the tropics); knowledge of these storms is needed to understand their effects on the global circuit and other phenomena important to the planet's electricity. The interactions within a cloud between water in its various phases (i.e., hydrometeor microphysics and latent heat release) and air motions, driven by the broad range of atmospheric forces, are fundamental to terrestrial storm electricity. Whether or to what extent these interactions and forces are relevant or have counterparts in other planetary electrical systems remains an open question for future investigations.

Acknowledgements Much of the research reviewed herein has been supported by the National Science Foundation (recent grant nos. ATM-0220842 and ATM-0605026). The lead author's involvement in the Planetary Electricity workshop was made possible by the University of Mississippi Office of Research and Sponsored Programs.

References

- K. Aplin, G. Harrison, M. Rycroft, *Space Sci. Rev.* (2008, this issue)
R.J. Blakeslee, H.J. Christian, B. Vonnegut, *J. Geophys. Res.* **94**, 13135 (1989)
G.J. Byrne, A.A. Few, M.F. Stewart, *J. Geophys. Res.* **94**, 6297 (1989)
S. Chauzy, M. Chong, A. Dellanoy, S. Despiau, *J. Geophys. Res.* **90**, 6091 (1985)
S.S. Davydenko, E.A. Mareev, T.C. Marshall, M. Stolzenburg, *J. Geophys. Res.* **109** (2004). doi:[10.1029/2003JD003832](https://doi.org/10.1029/2003JD003832)
S.S. Davydenko, M. Stolzenburg, E.A. Mareev, T.C. Marshall, *EOS Trans. AGU* **86**(52), Fall Meet. Suppl., AE23A-1003 (2005)
J.E. Dye, J.C. Willett, *Mon. Weather Rev.* **135**, 3362 (2007). doi:[10.1175/MWR3484.1](https://doi.org/10.1175/MWR3484.1)
J.E. Dye, J.J. Jones, W.P. Winn et al., *J. Geophys. Res.* **91**, 1231 (1986)
J.E. Dye, M.G. Bateman, H.J. Christian et al., *J. Geophys. Res.* **112** (2007). doi:[10.1029/2006JD007550](https://doi.org/10.1029/2006JD007550)
O.H. Gish, G.R. Wait, *J. Geophys. Res.* **55**, 473 (1950)
R.E. Holzer, D.S. Saxon, *J. Geophys. Res.* **57**, 207 (1952)
R.A. Houze Jr., *Cloud Dynamics* (Academic, San Diego, 1993), p. 573
A.R. Jameson, M.J. Murphy, E.P. Krider, *J. Appl. Meteorol.* **35**, 343 (1996)
P.R. Krehbiel, in *The Earth's Electrical Environment*, ed. by E.P. Krider, R.G. Roble (Natl. Acad. Press, Washington, 1986), pp. 90–113
D.R. MacGorman, W.D. Rust, *The Electrical Nature of Storms* (Oxford Univ. Press, New York, 1998), p. 422
D.R. MacGorman, W.D. Rust, P.R. Krehbiel et al., *Mon. Weather Rev.* **133**, 2583 (2005)
T.C. Marshall, B. Lin, *J. Geophys. Res.* **97**, 9913 (1992)

- T.C. Marshall, W.D. Rust, Bull. Am. Meteorol. Soc. **74**, 2159 (1993)
- T.C. Marshall, W.P. Winn, J. Geophys. Res. **97**, 7141 (1982)
- T.C. Marshall, W.D. Rust, W.P. Winn, K.E. Gilbert, J. Geophys. Res. **94**, 2171 (1989)
- T.C. Marshall, W.D. Rust, M. Stolzenburg, J. Geophys. Res. **100**, 1001 (1995)
- T.C. Marshall, M. Stolzenburg, C.R. Maggio et al., Geophys. Res. Lett. **32** (2005). doi:[10.1029/2004GL021802](https://doi.org/10.1029/2004GL021802)
- T.C. Marshall, M. Stolzenburg, P.R. Krehbiel et al., Proc. 13th Intl. Conf. on Atmos. Elec., Beijing, China, 2007
- A. Mika, Space Sci. Rev. (2008, this issue)
- Q. Mo, A.G. Detwiler, J. Hallett, R. Black, J. Geophys. Res. **108**, 4225 (2003)
- C.B. Moore, B. Vonnegut, in *Lightning (1)*, ed. by R.H. Golde (Academic, San Diego, 1977), pp. 51–98
- X. Qie, T. Zhang, C. Chen et al., Geophys. Res. Lett. **32**, L05814 (2005). doi:[10.1029/2004GL022162](https://doi.org/10.1029/2004GL022162)
- S.E. Reynolds, M. Brook, J. Meteorol. **13**, 376 (1956)
- R.G. Roble, I. Tzur, in *The Earth's Electrical Environment*, ed. by E.P. Krider, R.G. Roble (Natl. Acad. Press, Washington, 1986), pp. 206–231
- W.D. Rust, T.C. Marshall, J. Geophys. Res. **101**, 23499 (1996)
- W.D. Rust, C.B. Moore, Q. J. R. Meteorol. Soc. **100**, 450 (1974)
- W.D. Rust, D.R. MacGorman, E.C. Bruning et al., Atmos. Res. **76**, 247 (2005). doi:[10.1016/j.atmosres.2004.11.029](https://doi.org/10.1016/j.atmosres.2004.11.029)
- C.P.R. Saunders, Space Sci. Rev. (2008, this issue)
- T.J. Schuur, S.A. Rutledge, J. Atmos. Sci. **57**, 1961 (2000)
- T.R. Shepherd, W.D. Rust, T.C. Marshall, Mon. Weather Rev. **124**, 919 (1996)
- G.C. Simpson, Philos. Trans. R. Soc., Lond. **A209**, 379 (1909)
- G.C. Simpson, Proc. R. Soc. Lond. **A114**, 376 (1927)
- G. Simpson, G.D. Robinson, Proc. R. Soc. Lond. **A177**, 281 (1941)
- G. Simpson, F.J. Scrase, Proc. R. Soc. Lond. **A161**, 309 (1937)
- C.G. Stergis, G.C. Rein, T. Kangas, J. Atmos. Terr. Phys. **11**, 83 (1957)
- M. Stolzenburg, T.C. Marshall, W.D. Rust, B.F. Smull, Mon. Weather Rev. **122**, 1777 (1994)
- M. Stolzenburg, W.D. Rust, B.F. Smull, T.C. Marshall, J. Geophys. Res. **103**, 14059 (1998a)
- M. Stolzenburg, W.D. Rust, T.C. Marshall, J. Geophys. Res. **103**, 14079 (1998b)
- M. Stolzenburg, W.D. Rust, T.C. Marshall, J. Geophys. Res. **103**, 14097 (1998c)
- M. Stolzenburg, T.C. Marshall, W.D. Rust, D.L. Bartels, J. Geophys. Res. **107**, 4352 (2002)
- M. Stolzenburg, T.C. Marshall, L.M. Coleman et al., Proc. 12th Intl. Conf. on Atmos. Elec., Versailles, France, 2003
- M. Stolzenburg, T.C. Marshall, P.R. Krehbiel, EOS Trans. AGU **85**(47), Fall Meet. Suppl., AE33A-0191, 2004
- M. Stolzenburg, T.C. Marshall, C.R. Maggio et al., EOS Trans. AGU **87**(52), Fall Meet. Suppl., AE42A-07, 2006
- M. Stolzenburg, T.C. Marshall, W.D. Rust et al., Geophys. Res. Lett. **34**, L04804 (2007a). doi:[10.1029/2006GL028777](https://doi.org/10.1029/2006GL028777)
- M. Stolzenburg, T.C. Marshall, W.D. Rust et al., Proc. 13th Intl. Conf. on Atmos. Elec., Beijing, China, 2007b
- M. Stolzenburg, T.C. Marshall, P.R. Krehbiel et al., Proc. 13th Intl. Conf. on Atmos. Elec., Beijing, China, 2007c
- T. Takahashi, T.D. Keenan, J. Geophys. Res. **109**, D16208 (2004). doi:[10.1029/2004JD004667](https://doi.org/10.1029/2004JD004667)
- B. Vonnegut, Geophys. Res. Pap. 42, AFRC-TR-55-222. Air Force Cambridge Res. Ctr., Bedford, MA, 1955, pp. 169–181
- B. Vonnegut, C.B. Moore, in *Recent Advances in Atmospheric Electricity*, ed. by L.G. Smith (Pergamon, Elmsford, 1958), pp. 399–410
- B. Vonnegut, C.B. Moore, R.P. Espinola, H.H. Blau Jr., J. Atmos. Sci. **23**, 764 (1966)
- A.J. Weinheimer, J.E. Dye, D.W. Breed et al., J. Geophys. Res. **96**, 20809 (1991)
- J.C. Willett, D.C. Curtis, G.Y. Jumper, W.F. Thorn, Rep. PL-TR-93-2182. Phillips Lab, Hanscom AFB, Mass., 1993
- E.R. Williams, Proc. 13th Intl. Conf. on Atmos. Elec., Beijing, China, 2007, pp. 1–4
- P.T. Willis, A.J. Heymsfield, J. Atmos. Sci. **46**, 2008 (1989)
- C.T.R. Wilson, Proc. R. Soc. Lond. **A92**, 555 (1916)
- C.T.R. Wilson, Phil. Trans. R. Soc. Lond. **A221**, 73 (1920)
- C.T.R. Wilson, Proc. R. Soc. Lond. **A37**, 32D (1925)
- W.P. Winn, C.B. Moore, J. Geophys. Res. **76**, 5003 (1971)
- W.P. Winn, C.B. Moore, C.R. Holmes, L.G. Byerley III, J. Geophys. Res. **83**, 3079 (1978)

Formation of Charge Layers in the Planetary Atmospheres

Evgeny A. Mareev

Originally published in the journal Space Science Reviews, Volume 137, Nos 1–4.
DOI: [10.1007/s11214-008-9396-2](https://doi.org/10.1007/s11214-008-9396-2) © Springer Science+Business Media B.V. 2008

Abstract This section focuses on the physical phenomena, leading to large-scale space-charge and electric field generation (electric dynamo) in the planetary atmospheres, and ways of their theoretical description. The main attention is paid to charge-layer formation in atmospheres. Under terrestrial conditions, a problem of charge-layer formation in the atmosphere is important from the viewpoint of both thunderstorm and fair weather electricity. It is important also for the problems of intense layer generation under perturbed ionization conditions, charge layer formation over deserts, high field generation in the mesosphere etc. On the other hand, charge-layer treatment allows verifying electrification theories being applied to more or less simple 1D conditions such as the electrode effect, cloud screening layers, long-term charge layers in mesoscale convective systems. The paper reviews the results of recent research in this field. General conditions of the electro-hydro-dynamic description and their applications to the planetary atmospheres are discussed in terms of the Debye length, mean free path length of charged particles, Langmuir frequency and electrical conductivity. In terms of electrostatic interaction energy, it is found that three phases for charge carriers co-exist in strongly electrified clouds in the Earth's atmosphere. Crucial role of turbulent motion of conducting media for electric dynamo realization is revealed. The results of recent research in the modeling of the electrode effect, fog electrodynamics, screening layers in clouds and aerosol/dust structures, long-term charge layers in mesoscale convective systems are presented. Nonlinear solutions, demonstrating the formation of charge layers in planetary atmospheres, are examined.

Keywords Electric field generation · Charge layer · Atmospheric electric circuit · Conductivity · Thunderstorm electrification · Fair weather · Modeling · Electric dynamo

1 Introduction

Planetary atmospheric electricity is an interdisciplinary research area, but the problem of basic importance for that area is the problem of generating a large-scale electric field in a

E.A. Mareev (✉)

Institute of Applied Physics, Russian Academy of Sciences, 603950 Nizhny Novgorod, Russia
e-mail: mareev@appl.sci-nnov.ru

weakly conducting medium. We will refer to it below as the *electric dynamo* (ED) problem. A partial case of ED is the generation of electric current by means of a conductor moving through a magnetic field. In this more narrow sense the term electric dynamo (or simply *dynamo*) is often used when dealing with magneto-hydro-dynamic (MHD) problems, first of all for ionospheric applications (e.g., Whitten and Poppoff 1971). In atmospheric electrodynamics, the generation of a large-scale electric field is caused usually with the microphysical separation of electric charges (e.g., on cloud and precipitation particles) and their subsequent transfer by a weakly conducting medium, which is not affected substantially by the magnetic field. The motion of the medium, however, plays a principal role leading to the transformation of a micro-scale electric field to the macro-scale field and providing the electric energy growth in a system. Therefore, this term is adequate for electric field generation in weakly conducting atmospheres with a large enough time of space charge relaxation.

This approach is convenient also due to the possibility of direct comparison with magnetic-field generation processes widely investigated in space physics. Indeed, as compared to the problem of generating a large-scale magnetic field in a highly conducting medium, referred usually as magnetic dynamo, ED problem has been generally less developed so far, probably due to the fact that weakly conducting media are less abundant in the universe, and visible manifestations of ED (first of all, electrostatic discharges) require more special observation facilities. However, recent progress in experimental technique calls forth the growing interest to atmospheric electricity both under terrestrial and space conditions. It allows us to hope for more rapid elaboration of ED problems in the nearest future.

In the present part the principles of electro-hydro-dynamic (EHD) description and their applications as applied to *charge-layer formation* in atmospheres are briefly reviewed. Under terrestrial conditions, a problem of charge-layer formation in the atmosphere is important from the viewpoint of both thunderstorm and fair weather electricity. It is important also for the problems of intense layer generation under perturbed ionization conditions, charge layer formation over deserts, high field generation in the mesosphere etc. A special interest to charge layers is caused by the search for possible mechanisms of solar activity action on weather and climate (e.g., Tinsley and Zhou 2006).

On the other hand, charge-layer treatment allows verifying electrification theories being applied to more or less simple 1D conditions (such as the noted-above electrode effect, cloud screening layers, long-term charge layers in mesoscale convective systems). This paper reviews the results of recent research in this field and especially in the modeling of the electrode effect (under fair weather and fog conditions), screening layers in clouds and aerosol/dust structures, long-term charge layers in mesoscale convective systems. A special attention is paid to the role of turbulence and finding for dynamical analytical solutions. Due to their clear physical sense, such solutions, after verification under terrestrial conditions, can be used for analysis of extraterrestrial electrical phenomena. It is the more so important that according to recent studies the existence of charged layers caused by the conductivity perturbations can be considered as a global feature of different extra-terrestrial atmospheres, at least for Venus, Jupiter and Titan (e.g. Yair et al. 1995; Aplin 2006).

2 Electric Field Generation: General Conditions

2.1 Parameterization of Planetary Atmospheres

Planetary atmospheres can be considered in general as weakly conducting media (plasmas) where moderate ionization level is supported by different ionization sources: galactic cosmic rays, UV solar radiation, energetic particles from planetary magnetospheres and solar wind,

radionuclide emanations. Fundamental plasma characteristics are the Langmuir frequency $\omega_L = (\sum N_i q_i^2 / \epsilon_0 M_i)^{1/2}$ and the Debye length $\lambda_D = (\sum N_i q_i^2 / k T_i \epsilon_0)^{-1/2}$, and summation is performed over the charged species (electrons and ions, in the lower atmosphere—light and heavy ions), k is the Boltzmann's constant, ϵ_0 is the permittivity of free space (the dielectric constant); N_i and q_i are the number density and mean charge of carriers respectively, M_i and T_i are their masses and temperatures. The Debye length is simply expressed through the thermal velocities of the charged components: $\lambda_D = (\sum \omega_{Li}^2 / v_{Ti}^2)^{-1/2}$.

Common definition of plasma as a quasi-neutral medium requires that characteristic spatial scale of the medium is large as compared to Debye length because the latter is considered as the measure for a spatial scale of space-charge density perturbations. A characteristic feature of a weakly conducting medium, however, is a large value of an effective collision frequency of charged particles with the neutral gas particles, so that the medium conductivity becomes small. Indeed, the medium conductivity is defined as $\sigma = \sum \sigma_i = \sum (N_i q_i^2 / M_i v_i)$, where v_i is the effective collision frequency of the i -th charged component, so that $\sigma = \sum \epsilon_0 (\omega_{Li}^2 / v_i)$.

In most space and laboratory plasmas $\omega_{Li} \geq v_i$, while for lower atmospheric layers an opposite condition $\omega_{Li} \ll v_i$ holds. It means that the Debye length $\lambda_{Di} = v_{Ti} / \omega_{Li}$ turns out to be large as compared to the mean free path of the charges $l_i = v_{Ti} / v_i$ and does not serve already as the measure of quasi-neutrality. As a result, charged components are trapped by the motion of the neutral medium and become the subject of large-scale charge separation occasionally in a case of respective mechanisms (charge separation due to particle collisions, ion capture, thermodynamic phase bifurcations etc.) at work. It is obvious from the above formulas that the inequality $\lambda_{Di} \gg l_i$ is equivalent to the condition that the inverse relaxation time determined by conductivity $\tau_r^{-1} = \sigma / \epsilon_0$ is much less than the Langmuir frequency. On the other hand, the relaxation time itself should be big enough to ensure the effective work of separation mechanisms. It implies that the relaxation time should exceed the characteristic temporal scales of respective aero-dynamical and thermo-dynamical processes determining the large-scale electric-field evolution in the atmosphere.

Therefore, the study of electric field generation in planetary atmospheres should start from the analysis of their general plasma parameters: whenever inequality $\sigma / \epsilon_0 < \omega_L$ holds, large-scale space-charge separation can take place if respective aero-dynamical and thermo-dynamical conditions (e.g., intensive convection) are present.

In the Earth's lower atmosphere electric conductivity, Langmuir frequency and Debye length are dominated by light ions until the altitudes 40–50 km, where free electrons give some contribution due to their small mass and high mobility. It is easily to find that near the ground surface the Debye length is about 4 cm, while the Langmuir frequency $\omega_L \approx 5.5 \times 10^3 \text{ s}^{-1}$ (for $N_{i+} = N_{i-} = 500 \text{ cm}^{-3}$, $T_i = 300 \text{ K}$, and $M_i = 60 \text{ a.m.u.}$). These parameters do not change substantially with altitude in the lower several tens km: ω_L increases about 3 times up to 12–15 km, where the ionization rate maximizes (Gringel et al. 1986), and then slowly decreases until about 40–50 km. Even small addition of free electrons 10 cm^{-3} at the height 50 km makes electron contribution to the plasma frequency dominating: $\omega_{Li} \approx 1.7 \times 10^4 \text{ s}^{-1}$, $\omega_{Le} \approx 1.7 \times 10^5 \text{ s}^{-1}$. In the ionosphere the Langmuir frequency is defined by the electron profile and reaches its maximum of $\omega_{Le} \approx 8 \times 10^7 \text{ s}^{-1}$ at the altitudes 250–300 km (e.g., Kelley 1989). In contrary, the conductivity changes many orders of magnitude in the atmosphere, increasing from about $3 \times 10^{-14} \text{ S/m}$ near the ground (so that $\sigma / \epsilon_0 \omega_L \approx 10^{-6}$) up to 10^{-5} – 10^{-3} S/m in the D region. It should be noted that above 70–75 km the conductivity becomes anisotropic due to the geomagnetic field. One can see that normalized conductivity σ / ϵ_0 reaches the Langmuir frequency level at the height of about 90–100 km. Therefore, the whole region between the ground surface and about

100 km should be considered as a weakly conducting medium where electric dynamo can be realized, and it does (as we know due to recent TLE studies and rocket-borne measurements of electric field perturbations) not only in the troposphere but in the middle atmosphere as well.

For comparison, in the Venusian atmosphere the conductivity is estimated to vary from about 2×10^{-16} S/m above the surface up to 10^{-10} S/m at 80 km altitude (Borucki et al. 1982). The Langmuir frequency varies from $\omega_L = \omega_{Li} \approx 1.7 \times 10^3$ s⁻¹ near the surface to $\omega_L = \omega_{Le} \approx 1.7 \times 10^5$ s⁻¹ at 80 km. Respective range of $\sigma/\epsilon_0\omega_L$ relation is from 10^{-8} to 10^{-4} .

In the Martian rarefied atmosphere the conductivity estimated as 10^{-12} – 10^{-11} Sm/m, is caused primarily by photoelectrons (Grard 1995; Berthelier et al. 2000) with the density 1 – 10^2 cm⁻³ near the surface. It means that the relation $\sigma/\epsilon_0\omega_L$ is about 10^{-6} .

Due to the Cassini/Huygens mission, Titan's atmosphere has attracted much attention recently. Cosmic ray radiation is the main mechanism for ionizing the lower atmosphere of Titan. Their higher penetration power, in comparison with solar photons, allows cosmic rays to penetrate deep into the atmosphere of Titan, ionizing the neutral molecules and generating an ionosphere (Molina-Cuberos et al. 1999). In contrast to the atmospheres of Venus and Earth, no species were found in the Titan's atmosphere that lead to the formation of appreciable concentrations of negative ions. As a result, the predicted conductivity is quite different in that a substantial concentration of electrons exists all the way to the surface of Titan (Borucki et al. 1987). However, in light of the PWA-MIP experiment results derived from the Cassini/Huygens entry probe to Titan's atmosphere in January 2005, there is presently no consensus between the models of conductivity and electron density profiles for Titan's atmosphere. Around the altitude 63 km, all models differ from measurements by a factor ~ 2 – 3 , while the general shapes of conductivity and electron density profiles are similar (Hamelin et al. 2007). Larger differences develop at altitudes from 80 to 100 km, and even 140 km where the measured conductivity falls down to less than 0.3 nS/m. This emphasizes in particular the major role of aerosols (Borucki et al. 2006).

The main contribution of the PWA-MIP experiment is the discovery of an ionospheric layer between ~ 50 and 80 km, characterized by a maximum conductivity of 3 nS/m and a peak electron density of ~ 650 cm⁻³ at an altitude of about 63 km, and by small conductivity and electron density from 80 up to at least 140 km. The ionized layer shows relatively steep boundaries ~ 400 and 800 m scale heights for the upper and lower boundaries, respectively (Hamelin et al. 2007). Therefore, in the maximum of ionospheric layer the relation $\sigma/\epsilon_0\omega_L$ is about 10^{-6} .

In conclusion, all the above examples demonstrate that in the wide enough region of planetary atmospheres ED dynamo conditions are satisfied so that large-scale space-charge separation can take place there. Respective equations should describe not only the influence of medium motion (wind, convection etc.) on the charge transfer, but also a possible action of electrostatic force on the medium flow. It makes sense to present these equations for a simple case of one-component medium to illustrate a possible role of additional physical factors, e.g. turbulence, magnetic field, and to analyze the main differences from the magnetic dynamo problem (see below Sects. 2.2 and 2.3).

Before going to these equations, note that along with the $\sigma/\epsilon_0\omega_L$ relation (equivalent to λ_D/l relation), there is another aspect of weakly conducting plasma very important for its behavior. Commonly used gas (or weak-interaction) approximation implies that the mean potential energy of electrostatic interaction between the charged particles in the medium is small compared with the mean kinetic energy of their thermal motion. As a rule, it is equivalent to the assertion that the Debye length sphere contains large number of charged

particles. This approximation holds for light ions in the air, but it is drastically violated for highly charged particles in the active ED systems like thunderstorm clouds. For example, under the Earth's cloudy atmosphere, for highly-charged precipitation particles the mean potential energy of electrostatic interaction can be estimated as $(4\pi\epsilon_0)^{-1} Q_p^2 N_p^{1/3} \approx 10^{-11}$ J (if the particle charge $Q_p \approx 20$ pC and particle density $N_p \approx 125$ m⁻³) (e.g., Bateman et al. 1995), while the mean kinetic energy of thermal motion $kT \approx 4 \times 10^{-21}$ J is many orders of magnitude smaller. It means that highly charged storm regions contain strongly coupled plasma. This situation is analogous to strongly coupled dusty plasmas attracted much attention recently (see the paper by Goertz 1989) reviewing dusty plasmas in the Solar systems, and many other recent publications (e.g., Bhatuthram et al. 2002), but it is more complicated due to the higher values of non-ideality parameter compared to usual dusty plasmas (almost 10^{10} in the above presented example) and complicated phase composition of the cloudy medium. Indeed, for small cloud particles which are abundant in the highly charged storm regions and carry significant total charge, the mean potential energy of electrostatic interaction can be estimated as 4×10^{-21} J (if $Q_c \approx 20$ e and $N_q \approx 10^8$ m⁻³), i.e. of the same order magnitude as the mean kinetic energy of their thermal motion. It means that this fraction (ice particles in the higher part of the cloud, or droplet particles in the lower part) is under quasi-liquid state from the viewpoint of statistical thermodynamics, therefore all the three phases for charge carriers co-exist in strongly electrified clouds in the Earth's atmosphere. The possibility of a similar situation occurring in other planetary atmospheres requires a special analysis.

2.2 Electric Dynamo Problem Formulation

Theoretical studies of most atmospheric electricity problems (fair weather, cloud electrification, global electric circuit operation etc.) imply the presence of at least two different characteristic scales—microphysical one, determined by charge separation processes, and large scale, i.e. the size of generated electric field (EF), determined by the external scales of the system (e.g., the scales of temperature and conductivity profiles, the cloud height), and connect them analyzing Maxwell equations together with quasi-hydrodynamical equations for several charge-carrier components upon certain parameterizations for microphysical processes. The noted above approach is identified adequately by the term *electric dynamo*, which by definition is the generation of large-scale quasi-stationary electric field and space charge due to the motion (laminar or turbulent) of a weakly ionized medium (Mareev and Trakhtengerts 1996; Mareev 1999).

A weakly ionized medium is typically considered as a multi-component system, providing both separation (charging) and dissipation (discharging) currents. In a rigorous formulation, the description of the conducting fluid implies solution of kinetic equations for the distribution functions of all species (neutral, positive and negative) over velocities (e.g., Holzworth 1995). As applied to cloud electrification, the distribution over the electric charges in precipitation and cloud particles should be taken into account as well. Due to extremely wide variety of spatial and temporal scales of processes involved (from microphysical to global-scale ones) and many other complications (inhomogeneous conductivity, non-stationary character of processes, nonlinear dynamics of systems, such as the lightning channel, thunderstorm cloud, global electric circuit etc.) different simplifying approaches are used instead of the full and rigorous analysis. The modern models of thunderstorm electrification usually include conservation equations for mixing ratios of water vapor and hydrometeors, and charge densities and ion concentrations (e.g., Schuur and Rutledge 2000; Mansell et al. 2005). For example, the microphysics package of the Straka Atmospheric

Model (Mansell et al. 2005) has two liquid hydrometeor categories (cloud droplets and rain) and ten ice categories characterized by habit and size: two ice crystal habits (column and plate), rimed cloud ice, snow (ice crystal aggregates), three graupel densities, frozen drops, small hail, and large hail.

In a very simplified approach just illustrating general operation principles, electric dynamo may be considered even for a one-component medium. In this case the set of equations includes the equation for space charge density ρ , and hydrodynamic (aerodynamic) equations of a conducting medium:

$$\frac{\partial \rho}{\partial t} + \frac{\sigma}{\varepsilon_0} \rho = -\operatorname{div} \rho \mathbf{v} + D \Delta \rho - \sigma \mathbf{B} \operatorname{rot} \mathbf{v}, \quad (1)$$

$$\frac{\partial \rho_a}{\partial t} + \operatorname{div} \rho_a \mathbf{v} = 0, \quad (2)$$

$$\rho_a \frac{\partial \mathbf{v}}{\partial t} + \rho_a (\mathbf{v} \nabla) \mathbf{v} = -\nabla P + \rho E - \frac{1}{2} \nabla E^2 + \varepsilon (\mathbf{E} \nabla) \mathbf{E}. \quad (3)$$

The medium is characterized by the density ρ_a , the velocity \mathbf{v} , the pressure P , the conductivity σ , the temperature T , the charge diffusion coefficient D and permittivity ε , which is unity in many atmospheric applications. Thermodynamic quantities are connected by the state equation: $P = P(\rho_a, T)$. Space charge density and electric field are coupled through the Poisson equation: $\varepsilon_0 \operatorname{div} \mathbf{E} = \rho$. In (1) the last term is caused by the account of the correction $[\mathbf{v} \mathbf{B}]$ in Ohm's law expression for the conductivity current in the moving medium: $\mathbf{j} = \sigma (\mathbf{E} + [\mathbf{v} \mathbf{B}])$. This term leads to the space charge density growth for the vortex motion of a weakly conducting medium in magnetic field (e.g., for the shift flow or the convective cell, rotating in a magnetic field).

If electric currents are not too big, the magnetic field induction \mathbf{B} in the lower atmosphere may be considered as a given function of time and coordinates. Otherwise it is found from the equation:

$$\frac{\partial \mathbf{B}}{\partial t} + \frac{\varepsilon_0}{\sigma} \frac{\partial^2 \mathbf{B}}{\partial t^2} = \frac{1}{\mu_0 \sigma} \Delta \mathbf{B} + \operatorname{rot} [\mathbf{v} \mathbf{B}] + \frac{1}{\sigma} \operatorname{rot} \rho \mathbf{v}. \quad (4)$$

Here μ_0 is the magnetic permeability of vacuum. Equations (1)–(4) together with the Poisson equation and thermodynamic state equation form a full set of electro-magnetohydrodynamic equations of a conducting medium. The examples of their analysis, laminar electric dynamo solutions and general criteria for large-scale electric field generation in a continuous conducting medium are presented by Mareev and Trakhtengerts (1996). It was shown in particular that the sound wave reveals dispersion at large scales when propagating in the highly charged medium (for example, the charge layer in a thunderstorm cloud) with space charge density ρ_0 distributed: $\omega^2 = \omega_e^2 + k u_0^2$, where k is the wave number, u_0 is the sound wave velocity in a neutral medium, $\omega_e = (\rho_0^2 / \varepsilon_0 \rho_a)^{1/2}$ is the characteristic frequency.

It should be noted that in most practical ED applications (4) is not required, so that the ED problem in its general formulation can seem less complicated as compared to MD problem because of potential character of the electric field determined by the scalar electric potential. But many complications in atmospheric electrodynamics are concerned to the inhomogeneity, turbulent motion and multi-component composition of the medium.

2.3 Turbulence

Experiments show that turbulence plays a very important role in atmospheric electricity both under storm and fair-weather conditions. However the study of the dynamo in a turbulent

weakly conducting medium in the general case is not much developed. The main question is whether turbulence can operate occasionally as a factor supporting large-scale electric field generation. It turns out that it can at least for a case of intensive electrification with the participation of induction mechanisms (Mareev 1999). Note for comparison that in the MD problem the main achievements of recent decades were associated just with the studies of magnetic fields generated in a turbulent medium, in particular with the discovery of so-called α -effect in turbulence with certain helicity (Krause and Radler 1980; Beck et al. 1996; Wilkin et al. 2007).

The turbulent electric dynamo investigation implies an analysis of averaged (over the characteristic turbulent scales) equations for the mean electric field or the mean space charge density. For their derivation (in what follows the magnetic field is not accounted for) the functions $\rho(\mathbf{r}, t)$, $\mathbf{E}(\mathbf{r}, t)$ and $\mathbf{v}(\mathbf{r}, t)$ are represented as the sums of mean and random terms:

$$\begin{aligned}\rho(\mathbf{r}, t) &= \rho_0 + \rho', \quad \langle \rho' \rangle = 0; & \mathbf{v}(\mathbf{r}, t) &= \mathbf{v}_0 + \mathbf{v}', \quad \langle \mathbf{v}' \rangle = 0; \\ \mathbf{E}(\mathbf{r}, t) &= \mathbf{E}_0 + \mathbf{E}', \quad \langle \mathbf{E}' \rangle = 0,\end{aligned}\tag{5}$$

where brackets mean the average over the realizations ensemble. The average procedure implies the existence of two characteristic scales in the problem: $L \gg l$, where L is the external scale of (global) mean fields change, while l is a characteristic scale of turbulence. Under one-component approach, inserting the expressions (5) into (1), one can get:

$$\frac{\partial \rho_0}{\partial t} + \frac{\sigma_0}{\varepsilon_0} \rho_0 = -\operatorname{div} \rho_0 \mathbf{v}_0 - \operatorname{div} \langle \rho' \mathbf{v}' \rangle - \frac{\langle \sigma' \rho' \rangle}{\varepsilon_0} + D_T \Delta \rho_0.\tag{6}$$

A similar procedure is known in statistical hydromechanics to lead to the Reynolds tensor $\langle v'_i v'_j \rangle$ for the mean field motion equation. There is no any simple method to express this tensor via mean flow velocity due to the necessity to solve nonlinear equations. In the electric (magnetic) dynamo theory a similar tensor is expressed analytically because the space charge (magnetic field) equation is linear (e.g., Moffatt 1978).

In the framework of (6) the presence of random fluctuations of the space charge and medium velocity provides an additional term $\langle \sigma' \rho' \rangle / \varepsilon_0$ on the right hand side of the averaged space-charge continuity equation. The expression $\mathbf{J} = \langle \rho' \mathbf{v}' \rangle$ represents the turbulent flux of the space charge, or the turbulent electromotive force. The divergence of this function defines the distribution of space charge sources in the medium. Usually the turbulent flux of the space charge is taken in the form: $\mathbf{J} = -D_T \nabla \rho_0$, where D_T is the coefficient of the space charge turbulent diffusion, which is written by analogy with the molecular diffusion coefficient. However this approach suggests *a priori* a search of stationary solutions in the equilibrium medium. A problem of the turbulent electric dynamo requires more general consideration with account for the charging current arising due to microphysical charge-separation processes. To study the mean field formation in a weakly ionized atmospheric medium, taking into account charging of hydrometeors/aerosols due to their collisions in the turbulent flow, it is more practical to use an averaging procedure as applied to the equation for electric field (Mareev 1999; see also Sect. 3.6 below). It can be illustrated with a simplest example of a distributed “plane capacitor” model based on the solution of a non-linear diffusion equation for electric field evolution in a cloud:

$$\frac{\partial E_0}{\partial t} = \varepsilon_0^{-1} (j_{sep} - j_{dis}) + D_c \frac{\partial^2 E_0}{\partial z^2}.\tag{7}$$

In this equation, the charging current j_{sep} describes the field growth due to charge separation by cloud and precipitation particles, the dissipation current j_{dis} is caused mainly by the

conductivity, the charge-diffusion coefficient $D_c \simeq V_c L_c$ is determined by the characteristic velocity V_c and scale L_c of turbulent eddies.

Our theory is based on the calculation of turbulent convective current (assuming small-scale random fluctuations) and its further account in the large-scale evolution equations. The key problem is calculation of turbulent current in two-flow system with charge transfer via particle collisions. Particles accumulate charge still charging current is greater than leakage one. The velocity difference arises due to air velocity fluctuations. Inductive and non-inductive charging mechanisms are taken into account, but it is turned out that just for inductive mechanism quasi-stationary aerodynamic turbulence might support the large-scale charge separation. Therefore, the effect of mean field growth has been found, caused by induction charging of colliding particles. This phenomenon takes place for the turbulence intensive enough when the air conductivity is sufficiently small. The estimations have been performed for thunderstorm cloud conditions when the Kolmogorov spectrum for wind turbulent perturbations is valid. They showed that the relation of parameters ν_1 , ν_2 and $k_0 \sigma_v$ is important, where ν_1 and ν_2 are the drag coefficients in the motion equations for heavy and light colliding particles respectively, $k_0 = 2\pi/L_0$, L_0 is the outer scale of Kolmogorov turbulence, σ_v is the dispersion of the distribution function for the neutral gas velocity ($\sigma_v \approx 0.1$ m/s). For a typical case $\nu_1 \gg k_0 \sigma_v \gg \nu_2$ in the first order on $\nu_2/k_0 \sigma_v$, the integration over the wave numbers and frequencies of the turbulent eddies mixing cloud particles gives the following relation:

$$j_{sep} = \alpha_s E_0 = a E_0 \xi \varepsilon_t^{2/3} r^2 R^2 n N \nu_i^{-1} k_0^{-2/3}, \quad (8)$$

where ξ is the parameter determined by the contact time of colliding particles and their conductivities and varies in a wide enough range 10^{-3} – 1 (MacGorman and Rust 1998); $a \approx 0.5$ is a non-dimensional factor, R and r are the radii of heavy and light particles, N and n are their densities, ε_t is the energy flow in the inertial interval for the Kolmogorov turbulence, ν_i^{-1} is the inverse time of charge relaxation of a cloud particle due to attachment of ions, so that ν_i is determined by the ion attachment coefficient multiplied by the mean ion concentration. It is necessary for the mean electric field growth: $\alpha_s > \sigma/\varepsilon_0$. To estimate α_s , one can take parameters typical for intensive thunderstorm clouds: $\xi = 10^{-1}$, $\nu_i = 10^{-1}$ s $^{-1}$, $r = 10^{-4}$ m, $R = 10^{-3}$ m, $n = 10^8$ m $^{-3}$, $N = 5 \times 10^3$ m $^{-3}$, $L_0 = 10^2$ m, $\varepsilon_t = 10^{-2}$ m 2 s $^{-3}$. We find $\alpha_s \approx 2 \times 10^2$ s $^{-1}$, i.e. turbulence can operate occasionally as a factor supporting large-scale electric field generation. It is seen from the presented expressions that the increase of particle sizes and concentrations along with increase of the external scale of turbulence and decrease of the conductivity help to the electric field growth.

The results of the above consideration could be used for the explanation of high electric fields (including horizontal field) in thunderstorm cells with the high level of turbulence. They can be applied also to other planetary atmospheres, particularly to Martian atmosphere, characterized by strong turbulence during dusty storms.

3 Charged Layers in the Atmosphere and Their Theoretical Description

Planetary environments represent the consequence of spherical envelopes. In a case of the Earth they are called sometimes geospheres. Their important property is that spatial scales of their inhomogeneity in the vertical (radial) and horizontal (zonal and meridian) directions are substantially different, and they can be often considered as the layers, which greatly simplifies theoretical treatment, allowing 1D analysis.

Electromagnetic phenomena are observed in all the Earth's envelopes including the Earth's interior—the core, the mantle and the crust, and external envelopes—atmosphere, ionosphere and magnetosphere. But only the narrow layer of the lower atmosphere of about 100 km height is a place where the macroscopic charge formation is possible due to the very low conductivity of this layer in accordance with the above noted general properties of ED in the Earth's atmosphere. In the following chapters we will consider several examples of charge-layer formation in the atmosphere.

3.1 Large-Scale EF Profiles in the Global Circuit

If the conductivity of the atmosphere were uniform, it would be a passive dissipating medium with no charge accumulation in response to external electromotive force applied. Atmospheric conductivity, however, increases with the height very quickly—for many applications it can be approximated by the exponential function (see Rycroft et al. 2008 for more details). Space charge is generated: (1) due to the gradient of conductivity, and (2) due to the presence of a boundary—ground surface.

Large-scale gradient of conductivity leads to space charge generation in accordance with the equation:

$$\rho = \varepsilon_0 \nabla \cdot \mathbf{E} = \frac{\varepsilon_0}{\sigma} (\nabla \cdot \mathbf{J} - \mathbf{E} \cdot \nabla \sigma). \quad (9)$$

Under stationary conditions the first term on the right-hand side vanishes. Therefore, usually all the fair-weather part of the atmosphere represents the layer of positive charge, because the electric field in the fair-weather atmosphere is directed downwards usually.

Large-scale fair-weather field profile which at the same time illustrates both noted mechanisms of space charge generation is presented in Fig. 1. It is an example of balloon EF soundings performed under fair weather conditions (Markson 2007). An electric field maximum caused by a thin aerosol layer at 3 km is revealed. Another feature of this profile is

Fig. 1 Balloon electric field sounding in clean air at Hilo, Hawaii (from Markson 2007)

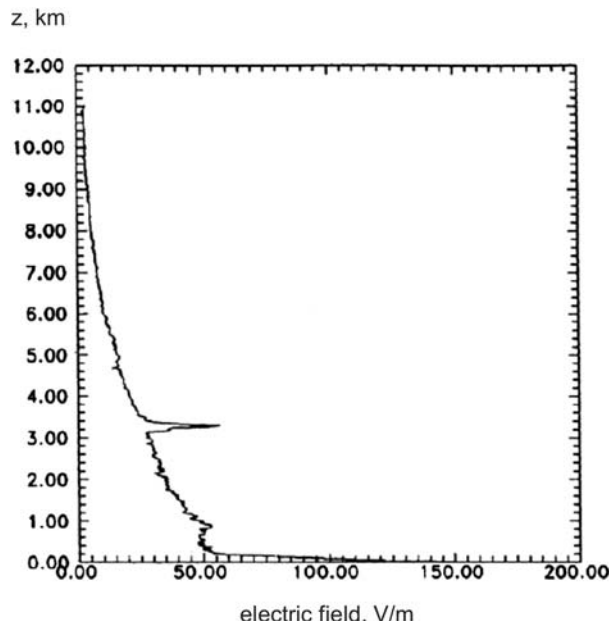
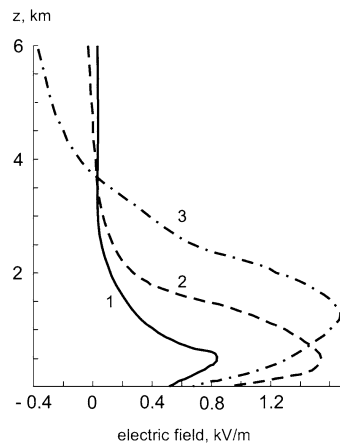


Fig. 2 Electric field profiles of so called third group (with increasing electric field strength in the boundary layer) after several hundreds of air flights:
 1—Leningrad, 2—Kiev,
 3—Tashkent (from Imyanitov and Chubarina 1967)



the large increase in electric field close to the ground due to a layer of positive space charge in the lowest 200 m. According to Markson (2007), this is caused by the accumulation of positive ions drifting downward which is not counterbalanced by negative ions drifting upward (so called electrode effect). This effect is often observed over the ocean. Over land surfaces it does not typically observed but in this case it exists because there is no radiation or radioactive gases in the volcanic soil of Hawaii where the sounding was carried out.

The most comprehensive airplane measurements of electric field profiles under fair-weather and cloudy atmosphere have been performed in 1958–1959 (Imyanitov and Chubarina 1967). Their results demonstrate variability of the profiles even for clear sky. Very often charge layers were observed, which is revealed in the changes of the sign for electric field and its derivative on certain altitudes. In particular, about 40% of all the profiles (about 2000 profiles in total) revealed the electric field decrease in the lowermost part of the troposphere (one example from this group of profiles is presented on Fig. 2). The observed layers can be caused in particular by the charge transfer processes (inhomogeneous convection or advection) (Anisimov and Dmitriev 1999) or by the ionization rate gradient above the ground. Attachment to aerosol particles can play a substantial role in these processes as well (see below Sects. 3.3 and 3.4).

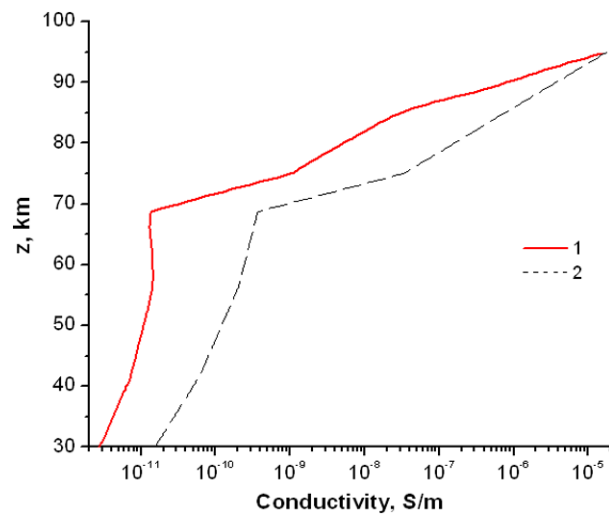
3.2 Large-Scale EF Dynamical Perturbations

Recently a great attention has been attracted to EF transient processes due to their ability to excite optical emissions and stimulate quick ionization in the middle atmosphere. In fact, the main features of the electric field changes after the lightning flash can be understood on the basis of 1D approximation, analyzing thereby dynamics of alternating EF layers. In particular, the following equation (Mareev et al. 2006) can be used for calculation of the vertical component of electric field in the conducting atmosphere:

$$\frac{\partial E}{\partial t} + \frac{\sigma(E, z)}{\varepsilon_0} E = \frac{\partial E_{ex}}{\partial t}, \quad (10)$$

where $E_{ex} = 2P/4\pi\varepsilon_0 z^3$ is the external dipole field, $P = 2hIt + d_{eff}$ is the full dipole moment, h is the mean height of the region, where the electric charge, transferred by the lightning current, is distributed. In the expression for P , the first term describes the growth of

Fig. 3 Variation of conductivity as a function of height (for 8 ms) due to electron heating in the electric field, generated due to the flash with continuing current magnitude 10 kA; maximum of M-component current 23 kA. 1—conductivity profile perturbed by electric field; 2—conductivity profile in the absence of electric field (from Yashunin et al. 2007)



the dipole moment at the stage of the continuing current, while the second term is the contribution of the perturbation caused by lightning-channel dynamics, in particular by the M-component of the flash. Note that lightning M-components are transient perturbations in the relatively steady continuing current that follows the return-stroke pulse and in the associated channel luminosity (Rakov and Uman 2003).

At times that are sufficiently small (10) gives the dipole field in the vicinity of the source, while it is an approximate equation, ignoring the horizontal components of electric field. It is seen from (10) that the conducting medium causes the field relaxation with the characteristic time $\varepsilon_0/\sigma(E, z)$, depending on the electric field magnitude. Such a nonlinear effect caused by the collision frequency change due to heating of electrons is pronounced at heights of the lower ionosphere for lightning currents of the order of 1 kA. Focusing on the search for breakdown conditions, we were disregard the change in conductivity due to electron density perturbation, which is a slower process compared to the electron heating in the field. We used in field calculations a conductivity profile experimentally obtained during night conditions (Holzworth et al. 1985). The M-component velocity was assumed to be equal $0.1c$ (c is the speed of the light in vacuum). The charge source height h was taken to be 5 km. We assume that the lightning discharge (return stroke followed by continuing current) lasts for 10 ms, after the field relaxation takes place. M-component starts 7 ms after the beginning of the continuing current stage.

To illustrate the transient charge layer formation, we present here the Fig. 3, showing the importance of the effect of conductivity perturbation by the field of M-component (Yashunin et al. 2007). It is seen that the conductivity decreases in the electric field, and this effect becomes more substantial with increasing the altitude (up to 75–80 km) due to the fact that the electric field decreases according to the power law, while the plasma field decreases exponentially. At higher altitudes, this effect diminishes because of the influence of conductivity on the electric field, which due to fast relaxation does not penetrate into the plasma. In particular, this effect leads to more effective field penetration to greater altitudes and increases the potential of M-components to initiate transient luminous events in the middle atmosphere during the continuing current stage of the lightning flash (Yashunin et al. 2007).

3.3 Electrode Effect

Across any horizontal area in the atmosphere stressed by a vertical electric field, positive and negative ions flow in opposite directions. However at a boundary ions of one sign can flow to that boundary, but there is no compensating flow of opposite sign away from it. This imbalance called the electrode effect gives rise to a space charge layer in the vicinity of the boundary (Hoppel et al. 1986). The importance of this phenomenon is in its ability to separate rather big amounts of charge near the Earth's surface, because due to the turbulence this charge is distributed over much thicker layers.

The theory of the electrode effect has been extensively developed with account for aerosols, turbulence and non-uniform volume ionization (Willett 1979, 1983; Tuomi 1982; Hoppel et al. 1986). For the case of uniform volume ionization without aerosol the electrode effect is described by the balance equations for positive and negative ions (their densities will be denoted below as n_1 and n_2 respectively in accordance with common notations in this theory) together with Poisson's equation:

$$\frac{\partial n_1}{\partial t} + \operatorname{div} n_1 \mathbf{v}_1 = q - \alpha n_1 n_2, \quad \frac{\partial n_2}{\partial t} + \operatorname{div} n_2 \mathbf{v}_2 = q - \alpha n_1 n_2, \quad (11)$$

$$\varepsilon_0 \operatorname{div} \mathbf{E} = e(n_1 - n_2), \quad (12)$$

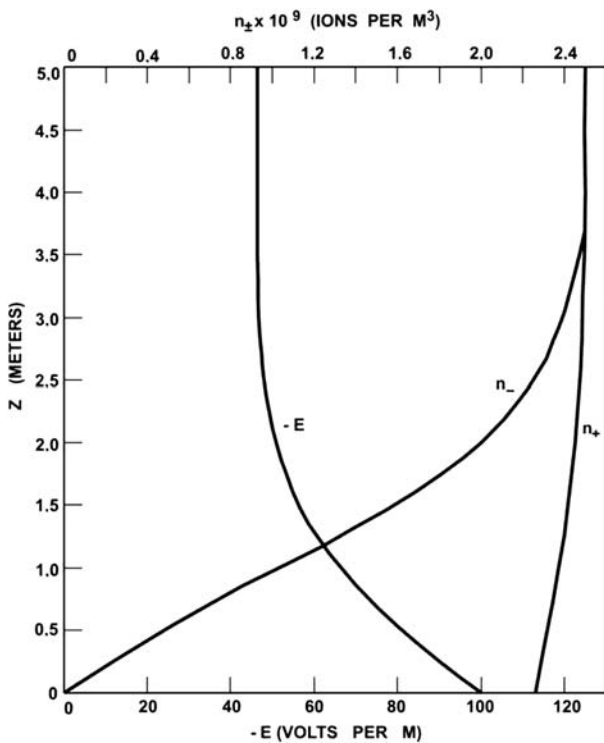
where $\mathbf{v}_{1,2} = \pm \mu_{1,2} \mathbf{E} + \mathbf{v}_0 - D_{T1,2} \nabla n_{1,2} / n_{1,2}$ are the velocities of ions determined by their drift in electric field \mathbf{E} , transport in the neutral gas flow and diffusion, so that the diffusion coefficients $D_{T1,2}$ are determined by turbulent transfer of ions; $\mu_{1,2}$ are the mobilities of positive and negative ions; q is the intensity of the external ionization source; α is the ion recombination rate. For the diffusion coefficients the following expressions are used: $D_{T1,2} = D_T = D_0 + Kz$, where $D_0 \approx 5 \times 10^{-6} \text{ m}^2/\text{s}$ is the molecular diffusion coefficient of small ions, K is a constant, characterizing the linear increase of the turbulent eddy scales with height. The boundary conditions on these equations are $n_1(z \rightarrow \infty) = n_2(z \rightarrow \infty) = (q/\alpha)^{1/2}$, $n_2(0) = 0$. The electric field is given at the lower boundary $E(z = 0) = E_0$ or at the infinity $E(z \rightarrow \infty) = E_\infty$. For the non-turbulent atmosphere the positive ion density on the lower boundary must be determined as a result of the solution. In a case of strong turbulence the condition $n_1(0) = n_2(0) = 0$ is often assumed, while for real land surfaces more general boundary conditions relating the densities and their derivatives on the surface are proper (Willett 1983; Mareev et al. 1996).

For the non-turbulent atmosphere the thickness of the charge layer is determined by the lifetime of small ions $\tau_i = (\alpha n_i)^{-1}$ and their drift velocity $v_{d1,2} = \mu_{1,2} E_0$ in the ambient electric field $E_0 : L_{cl} = j_0 / 2eq$, where j_0 is the electric current density which can be assumed constant under stationary conditions. Estimations show that L_{cl} does not exceed several meters. The solution of (11)–(12) for so-called classical (non-turbulent) case is presented in Fig. 4 (Hoppel 1967), where $L_{cl} \approx 2 \text{ m}$. The height of the electrode effect in the turbulent atmosphere is determined by the following expression (Willett 1978):

$$L_{ct} = (\varepsilon_0 K / \mu e) \sqrt{\alpha/q}. \quad (13)$$

The following values of the parameters can be taken for estimations: $K \approx 0.2 \text{ cm/s}$, $\alpha = 1.6 \times 10^{-12} \text{ m}^3/\text{s}$, $\mu = 1.5 \times 10^{-4} \text{ m}^2 \text{ V}^{-1} \text{ s}^{-1}$, $q = 10^7 \text{ m}^{-3} \text{ s}^{-1}$ which gives much bigger values for the electrode-layer thickness compared to the classical case: $L_{ct} \approx 30 \text{ m}$. It is interesting that the aerosol particles increase further the thickness of the turbulent charge layer (by increasing the electrical relaxation time) while reduce the thickness of the non-turbulent charge layer (due to ion attachment resulting in their lifetime decrease).

Fig. 4 Simple electrode effect in nonturbulent air with constant volume ionization rate of 10^7 ion pairs per m^3 per second over a plain surface (from Hoppel 1967)



In general, the models of the electrode effect developed up to the moment give the quasi-stationary profiles being often in a good agreement with measurements (e.g., Hoppel et al. 1986; Qui et al. 1994). Note, however, that there are still open questions in the theory of the electrode effect, concerning its temporal dynamics, the choice of adequate boundary conditions for different meteorology, and the account for particular “ion-aerosol climate” of a considered site. It can be illustrated by the results of some balloon-borne soundings.

We have presented already in Sect. 3.1 the electric field profile (Fig. 1) demonstrated the enhancement of the electric field near the ground surface for fair-weather conditions in Hawaii, which can be attributed to the electrode effect (Markson 2007). The observed charge-layer thickness was about 200 m, which can not be explained by the classical electrode effect and was caused probably by the vertical turbulent transfer of charged particles. In this sounding, however, may be revealed an additional effect of positive space charge from sea spray blown by trade winds over the island, or some reduction in the conductivity due to marine aerosols. All these factors should be taken into account when analyzing the particular height profiles (not numerous so far, unfortunately) of the electric field in the boundary layer.

Several series of electric field soundings with tethered balloons made in the lowest few hundred meters above the ground at Florida were presented by Marshall et al. (1999). On most of the days considered there was an anomalous enhancement in the ground-level electric field often referred as sunrise effect. Marshall et al. (1999) found that electrode-layer charge density began increasing at about the same time as the local enhancement in the electric field magnitude at the ground level. They suggested that enhanced positive electrode layers accumulated before sunrise very close to the surface because there is relatively little radioactivity in the soil or air. The typical decrease in charge density was from 0.2

to 0.05 nC m^{-3} while the charge layer thickness increased from less than 20 m to almost 200 m.

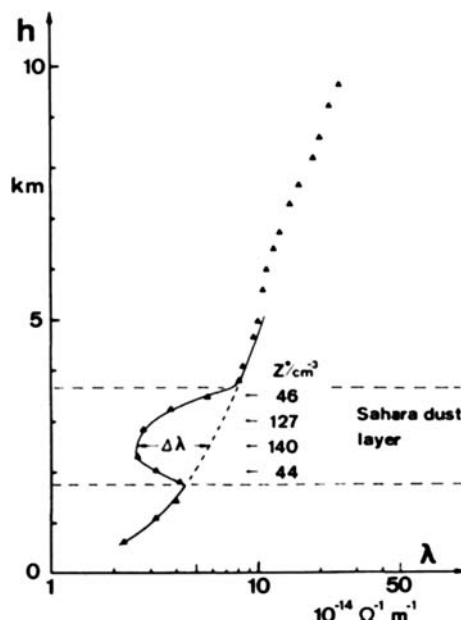
3.4 Fog, Clouds and Aerosol Layers

The conductivity in the atmosphere is reduced in the areas where ions attach to aerosol or cloud particles, therefore charged layers are often generated near the upper and lower surfaces of cloud or aerosol layers. One example of a double space-charge layer (with the positive charge below and negative charge above) caused by a thin aerosol layer is seen on Fig. 1. As another extreme, Fig. 5 shows a conductivity profile through a Sahara dust layer between 1.7 and 3.7 km height and 2200 km west of the West African coast (Gringel and Muhleisen 1978). The dust concentration responsible for the conductivity decrease is also shown. The authors report a mean mass concentration of 1200 g^{-3} throughout the layer. Owing to the low altitude of the layer the total columnar resistance increased up to 50% over large-scale North-Atlantic areas. In terms of space charge density the effect can be similar in a case of stratus clouds (Gringel et al. 1986). Regions of negative and positive space charge as large as 50 e/cm^3 have been observed in non-thunderstorm shower clouds (Imyanitov and Chubarina 1967).

In a theory of similar (screening) layers the balance equations for light ions (11) should be supplemented by the terms describing the linear sinks of ions due to their attachment; at the same time the balance equations for heavier charged components appear, and their contribution comes to the Poisson's equation (12). In general heavier components (cluster ions, aerosol or cloud particles) are dispersed over the size and mass which leads to the charge dispersion as well. A common simplification consists in the separation of several fractions with certain size and phase state (water droplets, ice particles, graupel etc.) to represent a complicated real charging process.

This procedure can be considered as applied to fog modeling—a case, allowing for direct experimental verification. Fog is an important object of long-term rather controversial

Fig. 5 Polar conductivity as a function of altitude and the concentration of mineral dust particles Z^* derived from the conductivity decrease (from Gringel and Muhleisen 1978)



investigations dictated by a number of practical problems such as possible means for the fog forecast and control (Hoppel et al. 1986; Israelsson 1999). On the other hand, fog is a wonderful natural laboratory for the study of charging of water droplets (or ice crystals) coupled to the aero-electric state of the boundary layer and cloud development.

Charging of water drops in a fog is a key point for analysis of quasi-stationary distribution of the field and its fluctuations. If the diffusion regime of charging is realized (Fuchs 1947), for the stationary state we easily find the mean stationary charge acquired by a fog particle of radius R : $Q_0 = Q_T \ln(\mu_1 n_1 / \mu_2 n_2)$, where $Q_T = kT_i R/e$ is the characteristic diffusion charge, caused by the thermal motion. For typical fog conditions with $R = 5 \mu\text{m}$ and temperature 300 K we have $Q \cong 180e$, where e is the electron charge value. As we noted, usually $n_1 > n_2$ in the surface layer due to the increase of the air conductivity with height, and even the case $n_1 \gg n_2$ can be realized near the Earth's surface due to the electrode effect, so that at heights where $\mu_1 n_1 > \mu_2 n_2$, fog particles acquire a positive charge on average. But if the ion densities are not too different, the drop charge appears negative due to the higher mobility of negative ions. For instance, taking $n_1 = n_2$ and $\mu_1 = 1.2 \times 10^{-4} \text{ m}^2 \text{ V}^{-1} \text{ s}^{-1}$, we have $Q_0 = -72e$ for $\mu_2 = 1.8 \times 10^{-4} \text{ m}^2 \text{ V}^{-1} \text{ s}^{-1}$, and $Q_0 = -27e$ for $\mu_2 = 1.4 \times 10^{-4} \text{ m}^2 \text{ V}^{-1} \text{ s}^{-1}$. This mechanism of fog particle charging is known as the diffusion charging (Pruppacher and Klett 1978).

In a case of identical particle ensemble, particle charging will produce, in the stationary case, some distribution of particles over charges (Fuchs 1963):

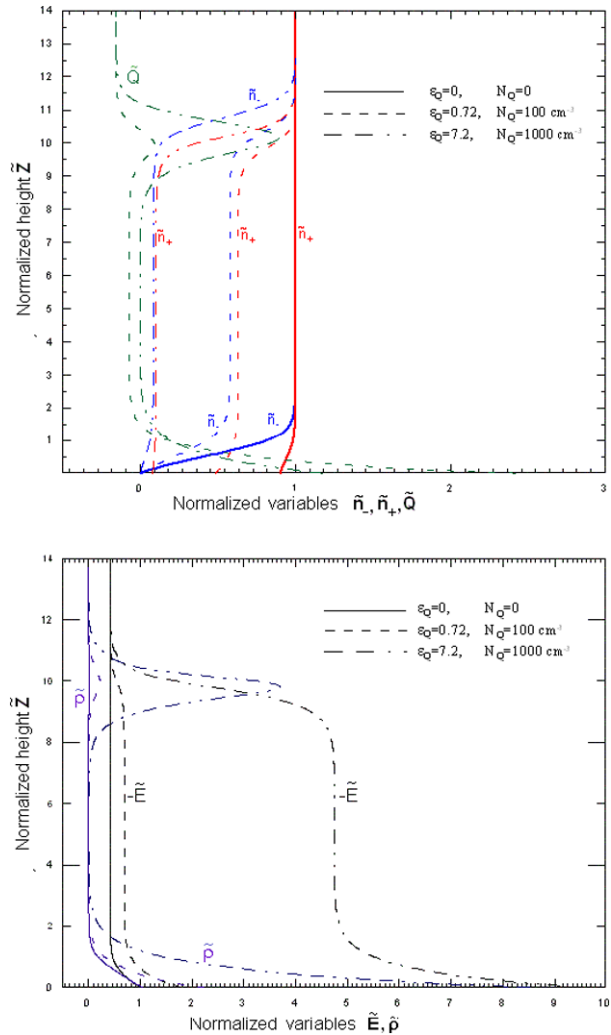
$$f_Q(Q, Q_T, \dots) = C_n \frac{Q_T}{Q} \operatorname{sh}\left(\frac{Q}{2Q_T}\right) \exp\left[-\frac{(Q - Q_0)^2}{2Q_T e}\right], \quad (14)$$

where C_n is the normalization constant, the effect of the external field is not considered, and charging is assumed to be due to diffusion only. Equation (14) shows in particular that the diffusion mechanism ensures not only a fairly high average charge, but also a broad charge distribution of drops. The width of the charge distribution is governed by the parameter $(Q_T e)^{1/2}$. Thus, under typical conditions, fog particles have a sufficiently broad charge-distribution function with an average charge Q_0 , whose sign depends on the ratio $\mu_1 n_1 / \mu_2 n_2$. This conclusion is important from the viewpoint of electric field generation, because the turbulent mixing of particles with $|Q| \gg e$ and sufficiently broad distribution should cause significant increase of the amplitude of small-scale fluctuations. The dependence of charge Q_0 on the height is an additional factor contributing to the field fluctuations because of fluctuations of the vertical velocity of gas.

Using the system of equations describing fog electrodynamics (Anisimov et al. 2005), the influence of fog-particle parameters and the characteristics of air ionization on diffusion-charging of particles has been investigated numerically. Stationary vertical profiles of the fog-particle charge, electric field, charge density, and light-ion concentration have been found (see Fig. 6 where the vertical coordinate is normalized by $z_0 = \varepsilon_0 E_0 / en_0$; E_0 and n_0 are the unperturbed electric field and ion density respectively). It is important to note that these profiles are controlled mainly by the single parameter $\varepsilon_Q = Q_T N_Q / en_0$, where N_Q is the equilibrium density of fog particles.

A most simple and well-known consequence of fog presence is the electrical conductivity decreasing and electric field growth. This effect is revealed usually in ground-based measurements under fog conditions, while it is accompanied by very pronounced electric-field fluctuations (Anisimov et al. 2005). Another feature seen on the profiles is the charge-density layer in the vicinity of the upper boundary of the fog. A layer forming near the ground is the electrode effect modified by the fog influence.

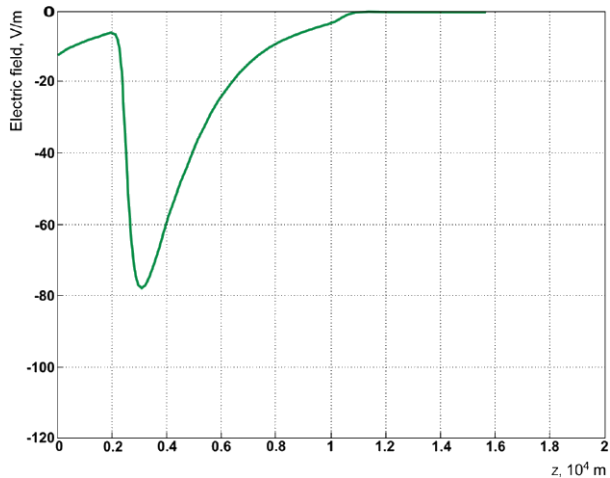
Fig. 6 Height profiles of electric field, droplet charge, net volume charge density and ion concentration for three control parameter values (from Anisimov et al. 2005)



In a similar way, the difference in clear air and cloud conductivities causes a layer of space charge to form at cloud boundaries region. For a component of the electric field normal to the boundary under stationary conditions we have $\sigma E_c = \sigma_{ex} E_{ex}$, where subscripts c and ex relate to the cloud and external values of conductivities and electric field strength, respectively. Then from the Poisson equation we get for the boundary charge density $\rho_s \approx \epsilon_0 E_c (1 - \sigma_c / \sigma_{ex}) / \Delta z_s$, where Δz_s is the thickness of the layer. A crude estimate for Δz_s shows that it is determined by mean free path of ions l_i , typically about 50 m, and so $\rho_s \approx \epsilon_0 E_c / l_i$ for $\sigma_c \ll \sigma_{ex}$ (Pruppacher and Klett 1978). More detailed studies on the formation and structures of charge screening layer can be found in Phillips (1967); Brown et al. (1971); Klett (1972).

Interestingly, we have not found in the literature any convenient numerical models allowing for the detail study of the intensity and thickness of charge layers near the cloud boundaries as dependent on the cloud parameters and external factors in a global atmospheric circuit. As an example of such layer formation the results of numerical calculations in the

Fig. 7 Electric field profile for the horizontally extended cloud (from Mareev and Mezentzev 2008)



framework of a simple 1D model (Mareev and Mezentzev 2008) are presented in Figs. 7–9. In spite of usual approach using the given conductivity, the microscopic description was used where the conductivity profile develop due to the permanent operation of the ionization source increasing with height: $q(z) = q_0 \exp(2z/H)$, where $q_0 = 10^7 \text{ cm}^{-3} \text{ s}^{-1}$, $H = 6 \times 10^3 \text{ m}$. Light-ion mobility profile (the same for positive and negative ions) was taken as $\mu(z) = \mu_0 \exp(2z/H_b)$, where $H_b = 7 \times 10^3 \text{ m}$, $\mu_0 = 1.5 \times 10^{-4} \text{ m}^2 \text{ V}^{-1} \text{ s}^{-1}$. The voltage between the ground and ionosphere was supported to be 250 kV. The lower and upper boundaries of the cloud at the heights 2.5 km and 10.5 km were determined by the following cloud-particle density distribution: $M(z) = M_0 \exp(-(z - z_m)^{16}/(\Delta/2)^{16})$, where $M_0 = 10^8 \text{ m}^{-3}$, $z_m = 6.5 \text{ km}$, $\Delta = 8 \text{ km}$. A large value of the power under the exponent function ensures the pronounced boundaries of the cloud. It is obvious from Fig. 7 that the intensity of the layer near the lower boundary is bigger compared to the upper boundary where the ion mobility is much lower. Analogous calculations for more thin aerosol or cloud layers give similar pictures of electric field distributions. They are presented in Fig. 8 along with space-charge density profiles. Two layers centered on different altitudes (3 km and 5.5 km) are shown for direct comparison. Note that charge-density perturbations are concentrated on cloud (aerosol) particles in much more narrow layers. The charge-density magnitude decreases with the altitude due to light-ion mobility increase.

A similar approach can be used for the estimation of charge layer parameters for extra-terrestrial conditions.

3.5 Small-Scale EF Dynamics in the Lower Atmosphere

Electric field and charge dynamics in the Earth's boundary laye (e.g. Israel 1973) has been the subject of intensive studies in recent several decades. In particular, 10^{-3} –1 Hz electric field pulsations were measured during 1999–2001 under the fair-weather and fog conditions (Anisimov et al. 2002). At the frequencies of 10^{-2} – 10^{-1} Hz these pulsations have a power-law spectrum with the spectral index varying from -1.23 to -3.36 . The most probable values of the index fall into the range from -2.25 to -3.0 , unlike the temperature fluctuation spectra which obey the Kolmogorov power law with the spectral index close to $-5/3$ in the inertial subrange. Under the fog conditions the intensity of electric-field pulsations increases by about an order of magnitude compared to the fair-weather conditions.

Fig. 8a Electric field profiles for two horizontally extended layers 2 km thickness at different altitudes (from Mareev and Mezentzev 2008)

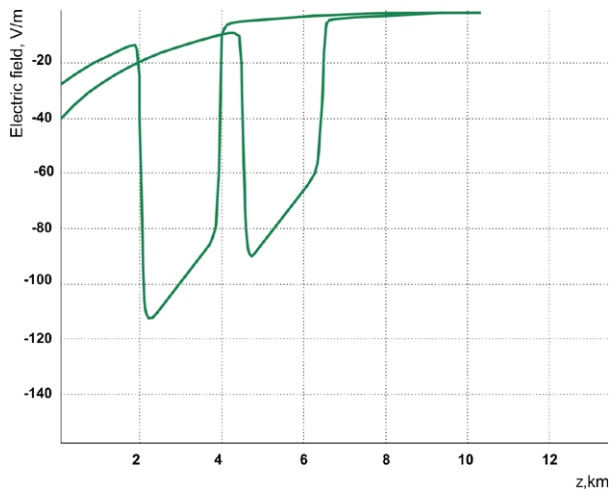
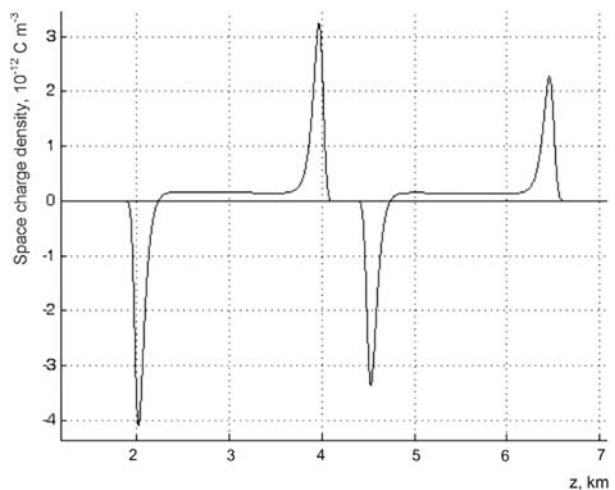


Fig. 8b Space-charge density on cloud particles for two horizontally extended layers of 2 km thickness at different altitudes (from Mareev and Mezentzev 2008)



The relation of spectral characteristics to the formation of aero-electric structures (AESs) was found. Figure 8 (from Anisimov et al. 2002) illustrates how the fluctuations of space charge developing in the atmosphere, are reflected in the remote sensing of the electric field pulsations. Analysis of the mechanisms explains the relationship between electric-field spectra and the neutral-gas turbulence and AES formation and allows one to recover the parameters of the neutral gas motion (Shatalina et al. 2005). We have suggested in particular that measuring the short-period (10^{-3} –1 Hz) pulsations of the electric field is a convenient instrument for the fog prognosis and fog studies (Anisimov et al. 2005). We can conclude that EF pulsation analysis serves as a powerful mean for electrodynamics/turbulence monitoring under different conditions, being of special interest for extra-terrestrial in-situ atmospheric measurements.

Analysis of spectra and structure function of EF pulsations (Anisimov et al. 1999, 2003) shows nontrivial properties of space-charge structures including effective increase of charge relaxation time and existence of long-term horizontally extended (up to several km) charge

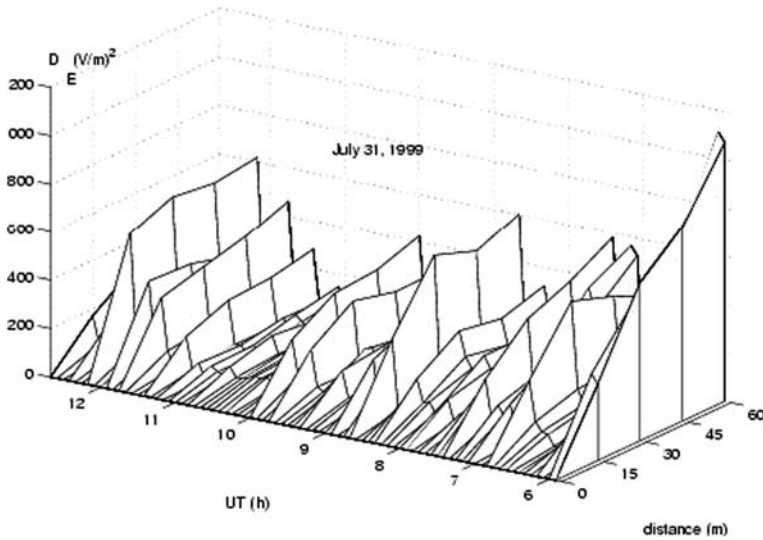


Fig. 9 Aero-electric structures in the atmosphere detected at the Borok Geophysical Observatory on July 31, 1999. The distance between the sensors in the line is 15 m (from Anisimov et al. 2002)

layers. The modeling of such layers requires the use of modern methods of nonlinear dynamics. As an example, the analytical solutions of (11)–(12) can be found, corresponding to self-consistent charge layers forming in the light-ion environment (Mareeva et al. 1999). It is interesting that in this case the dynamical stationary state and wave velocity depend on the difference of mobilities of positive and negative ions, leading to different ion-drift velocities V_{1d} and V_{2d} . The running step of space-charge density $\rho = \rho_0[1 + \exp(-\rho_0 \zeta C)]^{-1}$ appears, where $\zeta = z - Vt$, $\rho_0 = -\sigma_0 E_0 (V + \Delta V_d) / V_{1d} V_{2d}$; $C = A \varepsilon_0 E_0 / (1 - a)$, $a = \alpha / 4\pi e(\mu_1 + \mu_2)$, $\Delta V_d = V_{2d} - V_{1d}$, $A = 1 - V(V + \Delta V_d) / V_{1d} V_{2d}$. The nonlinear nature of this solution is obvious. The positive value of the step velocity corresponds to the motion along the external electric field. The value of quasi-stationary space-charge density ρ_0 is not so big if condition $V \cong -a \Delta V_d$ for the step velocity is satisfied. In the most interesting case $A \rightarrow 0$ the narrow step of the space charge density of the width C/ρ_0 forms.

For relatively small perturbations of space-charge density and equal values of positive and negative ion mobilities the set of equations (11)–(12) reduces to one nonlinear equation for the variable $I = n_1 - n_2$:

$$\frac{\partial^2 I}{\partial t^2} + (\alpha + \gamma)N \frac{\partial I}{\partial t} - V_d^2 \frac{\partial^2 I}{\partial z^2} - V_d(4\gamma - \alpha)I \frac{\partial I}{\partial z} = -q\gamma\alpha N^2 I - 2V_d \frac{\partial q}{\partial z}, \quad (15)$$

where $\gamma = 4\pi e\mu$, $N = n_1 + n_2 \approx N_0 = (4q/\alpha)^{1/2}$. Significance of nonlinear effects is defined by the parameter $R_e = I_0(4\gamma - \alpha)z_0/V_d$, where z_0 is the characteristic scale of the charge density change, I_0 is its magnitude. It is analogous to the Reynolds number in common hydrodynamics and can be called the effective “electro-kinetic” Reynolds number. Under certain conditions (15) reduces to the modified Burgers equation, which has universal analytical solutions.

Estimations show that found non-stationary self-consistent solutions can be realized both in fair weather and beneath electrified clouds. Their parameters are defined by micrometeorological conditions and give the signature of nonlinear processes of electric interaction in the atmosphere (Mareeva et al. 1999).

3.6 Thunderstorm Clouds and MCSs

The charge-layer formation is a classical problem of thunderstorm electrification. It has been discussed recently in particular due to the fact that the stratiform region of a typical mesoscale convective system (MCS) was found to have a number of horizontally extensive charge layers that exist for 6–12 hours. This problem is extensively investigated nowadays (e.g., Stolzenburg et al. 2008).

In general there are two approaches useful for the analysis of thunderstorm charge layers. The first one (which is described in more detail in the present chapter) is based on the description of external currents supporting the experimentally observed layers independently of the microphysical processes leading to these currents. This approach directly connected to the experimental data is especially useful for the analysis of thunderstorm energetics and their role in the global electric circuit. Another approach implies the construction of detail microphysical models for the charge layer generation, including 3D numerical models of storm electrification (e.g., Mansell et al. 2005).

Our description uses the external currents as the most convenient parameter forming the electrical structure of thunderstorms and at the same time playing the basic role in the global atmospheric electric circuit. For the external current we use the following expression:

$$\mathbf{j}_{ex}(\mathbf{r}, z) = \begin{cases} 0, & z < z_-, z > z_+, \\ j_{ex}(\mathbf{r})\mathbf{z}_0, & z_- < z < z_+, \end{cases} \quad (16)$$

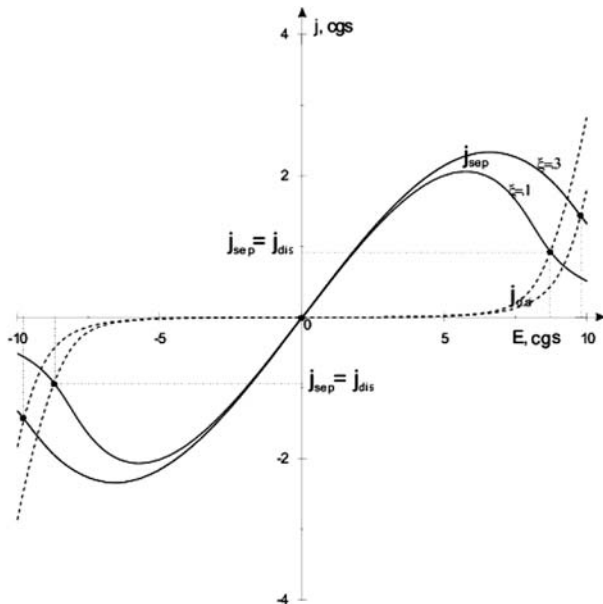
where z_- and z_+ are the lower and upper boundaries of the current layer, i.e. the heights of the main negative and positive charges in the cloud, $j_{ex}(\mathbf{r})$ is the distribution of the external current in the horizontal plane, \mathbf{z}_0 is the single vector directed upward. As was demonstrated by Davydenko et al. (2004), this representation is useful for linear analysis of rather complicated thunderstorms like MCSs. In the latter case one can model a thunderstorm as a set of currents in the form (16) chosen in accordance with experimental data.

To model a typical thunderstorm in the global circuit, one can represent it by one current layer (16) flowing between the lower and upper levels z_- and z_+ respectively and forming corresponding charge layers at these levels. It allows finding the dependence of energetic characteristics of a thunderstorm cloud upon the geometrical factors and conductivity distribution. Usually the conductivity profile is assumed to be exponential: $\sigma(z) = \sigma_0 \exp(z/H)$, $z > 0$. The Earth's surface is considered to be ideal. If the electric field is quasi-stationary $\mathbf{E} = -\nabla\varphi$, the conductivity current density takes the form $\mathbf{j} = -\sigma \nabla\varphi$. The equation for the electric potential is as follows: $\text{div}[-\sigma \nabla\varphi + \mathbf{j}_{ex}(\mathbf{r}, z)] = 0$. Boundary conditions are: $\varphi(r \rightarrow \infty, z) = 0$, $\varphi(r, z \rightarrow \infty) = 0$. Assuming that the current distribution is axially symmetrical, we can use the Fourier transform on the transverse coordinates. Writing the current in the form $j_{ex}(r) = j_0 \exp(-r^2/a^2)$, we easily find the energetic characteristics, including the energy accumulated in the vertical electric field and in the horizontal electric field (Mareev and Anisimov 2007).

Sufficiently simple expressions for the energy and their dissipation rate can be derived only for a small enough compared to H and for a big enough compared to H . Omitting the details, we will present the final formulas for these limiting cases only for the total energy W_Σ and total ohmic dissipation rate P . For $a < H$ we have: $W_\Sigma = 4W_0[\exp(-2z_-/H) + \exp(-2z_+/H)]$, $P = P_0[\exp(-z_-/H) + \exp(-z_+/H)]$, where

$$W_0 = \sqrt{\frac{\pi}{2}} \cdot \frac{\pi \varepsilon_0 j_0^2 \cdot a^3}{32\sigma_0^2}, \quad P_0 = \sqrt{\frac{\pi}{2}} \cdot \frac{\pi j_0^2 \cdot a^3}{4\sigma_0}. \quad (17)$$

Fig. 10 Dependences of the separation and dissipation currents on the electric-field intensity in a thundercloud



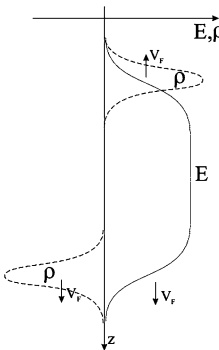
In an opposite case $a > H$ we have: $W_\Sigma = W_1[2 \exp(-2z_-/H) + \exp(-2z_+/H) + \exp(-2(z_+ + z_-)/H)]$, $P = P_1[\exp(-z_-/H) + \exp(-z_+/H)]$, where

$$W_1 = \frac{\pi \varepsilon_0 j_0^2 \cdot a^2 H}{8\sigma_0^2}, \quad P_1 = \frac{\pi j_0^2 \cdot a^2 H}{2\sigma_0}. \quad (18)$$

These expressions show the dependence of the electric energy and ohmic dissipation on the parameters a , H , σ_0 , z_- , z_+ . They lead to reasonable energy estimations for the current densities of order of 1–10 nA/m² for typical thunderstorms and MCSs, and can be used for energy estimations under extraterrestrial conditions.

In terms of thunderstorm charge layer analysis the model nonlinear equations like (7) are useful. In our analysis of this equation (Mareev and Sorokin 2001) we have taken into account different parameterizations of inductive and non-inductive mechanisms, leading to different expressions for the charge separation current, as well as corona discharge dissipation current. At the stage of intense electrification, the charging current is dominant. However, a sharp increase in conductivity occurs in a sufficiently strong field due to the corona effect around the strongly charged particles. To allow for this effect, one can use the corresponding empirical dependence $j_{dis} = \sigma_c E_c [\exp(E/E_c) - 1]$, where σ_c is the unperturbed conductivity of the cloud medium and E_c is the critical electric field leading to the sharp growth of the corona current (Beesley et al. 1977). We show in Fig. 10 the dependences of the separation and dissipation currents on the electric-field intensity in the cloud for typical cloud particle parameters: $r = 10^{-4}$ m, $R = 10^{-3}$ m, $n = 4 \times 10^6$ m⁻³, $N = 5 \times 10^4$ m⁻³, $E_c = 60$ kV m⁻¹ and two values of the parameter ξ . Several equilibrium states of the cloud electrification determined by the equality of separation and dissipation currents are shown. Of particular interest is the solution in the form of a traveling front of electric field and space charge perturbation, separating the stable and unstable equilibrium states $j_{sep} = j_{dis}$. This solution shown schematically in Fig. 11, describes the growth of the thunderstorm cell at the stage of its intense electrification due to the slow oppositely-directed motion of charge layers

Fig. 11 Solution in the form of a pair of traveling fronts



on its boundaries. Detail discussion of different mechanisms of charge transfer in thunderstorm clouds forming the charge separation current is presented in the other chapter of this issue (Saunders 2008).

3.7 Charge Layers Near the 0°C Isotherm

Rather complicated multi-layer charge structures are frequently observed in stratiform precipitation regions of MCSs (Stolzenburg et al. 2008). But the narrow layer of positive electric charge near the 0°C isotherm serving as “reservoir” for the positive ground flashes appears to be a very characteristic feature (Stolzenburg et al. 1994, 2008; Shepherd et al. 1996). We suggest a quantitative model treating the formation of the positive charge layer near the 0°C isotherm as a result of the melting charging process (Evtushenko et al. 2007). It is one of mechanisms, which have been discussing for rather long time, especially as applied to MCS stratiform regions (e.g., Stolzenburg et al. 1994). There is experimental evidence for its significance, while the detail microphysics of charge separation during melting is not completely understood up to now.

We assume that previously uncharged precipitation particles (large aggregates of vapor-grown crystals or smaller precipitation particles) acquire negative charge as they melt by shedding smaller, cloud-size particles (either liquid or solid). One of the main goals of this study was the investigation of inductive mechanism effectiveness during the charge separation near the 0°C isotherm. In a positive electric field, positive charge is induced on the upper part of the melting aggregate while an equal negative charge is induced on the lower part. Charge is separated when the particle melts. An actual typical profile of the vertical velocity profile in a stratiform region is taken into account. The upper charge layer in the stratiform region is assumed to form due to advection. Typical examples of electric field profile and field dynamics are presented in Fig. 12a, b. In Fig. 12 the formation and rather quick stabilization of charge layers can be seen. We can conclude that after melting charging mechanism start the field magnitude grows reaching 30–120 kV/m in 300–2000 s (depending on the parameters of charge transfer). It should be noted however that the role of light ions has not been completely studied so far, while it appeared to be important for narrow charge layer formation. Balloon measurements in MCS stratiform regions seem to be in accordance with the presented modelling results but suggest further development of charge-layer formation theory to make more reliable conclusions on their nature and stability mechanisms (Stolzenburg et al. 2008).

Fig. 12a Electric field dynamics in the stratiform region of a mesoscale convective system in a case of inductive charging near the 0° isotherm

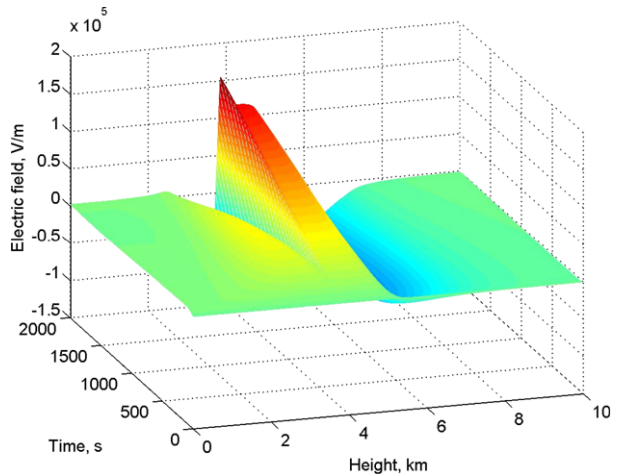
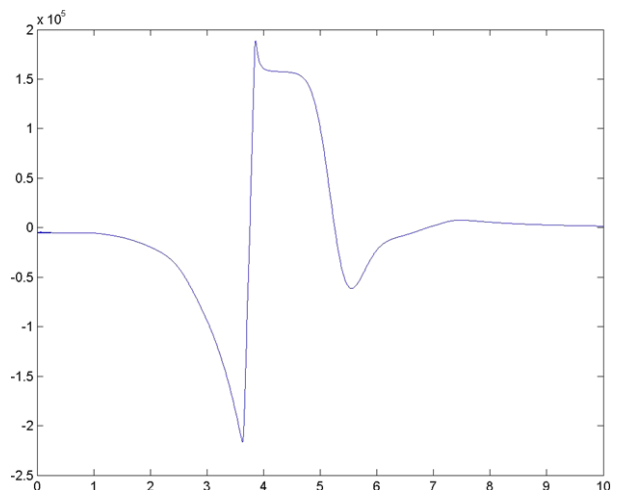


Fig. 12b The calculated electric field profile in the stratiform region at the moment $t = 2000$ s



4 Summary

The motion of weakly ionized disperse-phase medium leads to the electric charge separation and generation of large-scale quasi-stationary electric field (electric dynamo) as well as to short-period pulsations of electric field, current and space charge density. Their study is of fundamental importance to investigate intra-cloud, cloud-to-ground and high-altitude discharge inception, to understand the nature of volcano lightning, dust and sand storms, to recognize global and local components of planetary electricity.

General conditions of the electro-hydro-dynamic description and their applications to the planetary atmospheres are available in terms of the Debye length, mean free path length of charged particles, Langmuir frequency and electrical conductivity; the relation of latter two parameters is important for the charge layer forming. In terms of electrostatic interaction energy, it is found that three phases for charge carriers co-exist in strongly electrified clouds in the Earth's atmosphere.

Laboratory modeling and analysis of field experimental data demonstrate clearly the effects of electro-hydro-dynamical turbulence. They can be used for planetary electricity research.

The problem of charge-layer formation in atmospheres is important from the viewpoint of both thunderstorm and fair weather/disturbed fair weather electricity, and allows verifying electrification theories being applied to more or less simple 1D conditions such as the electrode effect, cloud screening layers, long-term charge layers in mesoscale convective systems.

Acknowledgements The author wishes to thank Drs. S. Anisimov and A. Mezentzev for valuable discussions. This work was partially supported by the Russian Foundation for Basic Research (grant #07-02-01342) and Russian Academy of Science Program “Physics of the atmosphere: electric processes, radio-physical methods”.

References

- S.V. Anisimov, E.A. Mareev, N.M. Shikhova, E.M. Dmitriev Geophys. Res. Lett. **29**, 2217 (2002). doi:[10.1029/2002GL015765](https://doi.org/10.1029/2002GL015765)
- S.V. Anisimov, E.A. Mareev, S.S. Bakastov, J. Geophys. Res. **104**, 14359 (1999). doi:[10.1029/1999JD900117](https://doi.org/10.1029/1999JD900117)
- S.V. Anisimov, N.M. Shikhova, E.A. Mareev, M.V. Shatalina, Izv. Atmos. Ocean. Phys. **39**, 766 (2003)
- S.V. Anisimov, E.M. Dmitriev, J. Atmos. Electr. **19**, 25 (1999)
- S.V. Anisimov, E.A. Mareev, N.M. Shikhova, A.E. Sorokin, E.M. Dmitriev, Atmos. Res. **76**, 16 (2005)
- K.L. Aplin, Surv. Geophys. **27**, 63 (2006). doi:[10.1007/s10712-005-0642-9](https://doi.org/10.1007/s10712-005-0642-9)
- M.G. Bateman, W.D. Rust, B.F. Smull, T.C. Marshall, J. Geophys. Res. **100**, 16341 (1995) doi:[10.1029/95JD01280](https://doi.org/10.1029/95JD01280)
- R. Beck, A. Brandenburg, D. Moss, A. Shukurov, D. Sokoloff, Annu. Rev. Astron. Astrophys. **34**, 155 (1996) doi:[10.1146/annurev.astro.34.1.155](https://doi.org/10.1146/annurev.astro.34.1.155)
- G. Beesley, A.J. Illingworth, J. Latham, in *Electrical Processes in Atmospheres*, ed. by H. Dolezalek (Steinkopf, Darmstadt, 1977), p. 279
- J.-J. Berthelier, R. Grard, H. Laakso, M. Parrot, Planet. Space Sci. **48**, 1193 (2000)
- R. Bhatnagar, M.A. Hellberg, P.K. Shukla, F. Verheest (eds.), *Dusty Plasma in the New Millennium* (Springer, New York, 2002), p. 516
- W.J. Borucki, Z. Levin, R.C. Whitten et al., Icarus **51**, 302 (1982)
- W.J. Borucki, Z. Levin, R.C. Whitten et al., Icarus **72**, 604 (1987)
- W.J. Borucki, R.C. Whitten, E.L.O. Bakes, E. Barth, S. Tripathi, Icarus **181**, 527 (2006)
- K.A. Brown, P.R. Krehbiel, C.B. Moore, G.N. Sargent, J. Geophys. Res. **76**, 2825 (1971)
- S.S. Davydenko, E.A. Mareev, T.C. Marshall, M. Stolzenburg, J. Geophys. Res. **109**, D11103 (2004). doi:[10.1029/2003JD003832](https://doi.org/10.1029/2003JD003832)
- A.A. Evtushenko, E.A. Mareev, T.C. Marshall, M. Stolzenburg, in *Proc. 13th Int. Conf. on Atmospheric Electricity*, Beijing, China, 2007, pp. 286–289
- N.A. Fuchs, Geofis. Pura Appl. **56**, 185 (1963)
- N.A. Fuchs, Izv. Acad. Sci. USSR Geogr. Geophys. Ser. **11**, 341 (1947)
- C.K. Goertz, Dusty plasmas in the solar system. Rev. Geophys. **27**, 271 (1989)
- R. Grard, Icarus **114**, 130 (1995)
- W. Gringel, J.M. Rosen, D.J. Hofmann, in *The Earth's Electrical Environment*, ed. by E.P. Krider, R.G. Roble (Natl. Acad. Press, Washington, 1986), pp. 166–182
- W. Gringel, R. Muhleisen, Beitr. Phys. Atmos. **51**, 121 (1978)
- M. Hamelin, C. Beghin, R. Grard et al., Planet. Space Sci. **55**, 1964 (2007)
- R.H. Holzworth, M.C. Kelley, L.C. Siefring, L.C. Hale, J.D. Mitchell, J. Geophys. Res. **90**, 9824 (1985)
- R.H. Holzworth, in *Handbook on Atmospheric Electrodynamics*, vol. 1, ed. by H. Volland (CRC Press, Boca Raton, 1995), pp. 65–109
- W.A. Hoppel, J. Atmos. Terr. Phys. **29**, 709 (1967)
- W.A. Hoppel, R.V. Anderson, J.C. Willett, in *The Earth's Electrical Environment*, ed. by E.P. Krider, R.G. Roble (Natl. Acad. Press, Washington, 1986), pp. 149–165
- I.M. Imyanitov, E.V. Chubarina, *Electricity of the Free Atmosphere* (Isr. Program for Sci. Transl., Jerusalem, 1967)
- H. Israel, *Atmospheric Electricity*, vol. 2 (Isr. Program for Sci. Transl., Jerusalem, 1973), pp. 408–416

- S. Israelsson, in *Proc. 11-th Int. Conf. on Atmospheric Electricity*, Guntersville, USA, 1999, pp. 587–590
- M.C. Kelley, *The Earth's Ionosphere: Plasma Physics and Electrodynamics*. Int. Geophys. Ser., vol. 43 (Academic, San Diego, 1989)
- J.D. Klett, *J. Geophys. Res.* **77**, 3187 (1972)
- F. Krause, K.-H. Radler, *Mean-Field Electrodynamics and Dynamo Theory* (Pergamon, Elmsford, 1980)
- D.R. MacGorman, W.D. Rust, *The Electrical Nature of Storms* (Oxford University Press, London, 1998)
- E.R. Mansell, D.R. MacGorman, C.L. Ziegler, J.M. Straka, *J. Geophys. Res.* **110**, D12101 (2005). doi:[10.1029/2004JD005287](https://doi.org/10.1029/2004JD005287)
- E.A. Mareev, S.V. Anisimov, in *Proc. 13th Int. Conf. on Atmospheric Electricity*, Beijing, China, 2007, pp. 21–24
- E.A. Mareev, S. Israelsson, E. Knudsen, A.V. Kalinin, M.M. Novozhenov, *Ann. Geophys.* **14**, 1095 (1996)
- E.A. Mareev, V.Yu. Trakhtengerts, *Radiophys. Quantum Electron.* **39**, 797 (1996)
- E.A. Mareev, A.E. Sorokin, *Radiophys. Quantum Electron.* **44**, 148 (2001)
- E.A. Mareev, in *Proc. 11th Int. Conf. on Atmospheric Electricity*, Guntersville, USA, 1999, pp. 272–275
- E.A. Mareev, A.A. Evtushenko, S.A. Yashunin, in *Sprites, Elves and Intense Lightning Discharges*, ed. by M. Fullerkrug, E. Mareev, M. Rycroft. NATO Science Series, vol. 225 (Springer, Berlin, 2006), pp. 313–340
- E.A. Mareev, A.Yu. Mezentzev, *Izv. Atmos. Ocean. Phys.* (2008, submitted)
- O.V. Mareeva, E.A. Mareev, S. Israelsson, S.V. Anisimov, in *Proc. 11th Int. Conf. on Atmospheric Electricity*, Guntersville, USA, 1999, pp. 614–617
- R. Markson, *Bull. Am. Math. Soc.* **88**, 223–241 (2007). doi:[10.1175/BAMS-88-2-223](https://doi.org/10.1175/BAMS-88-2-223)
- T.C. Marshall, W.D. Rust, M. Stolzenburg et al., *J. Geophys. Res.* **104**, 24455 (1999)
- H.K. Moffatt, *Magnetic Field Generation in Electrically Conducting Fluids* (Cambridge Univ. Press, Cambridge, 1978)
- G.J. Molina-Cuberos, J.J. López-Moreno, R. Rodrigo, L.M. Lara, K. O'Brien, *Planet. Space Sci.* **47**, 1347 (1999)
- B.B. Phillips, *Mon. Weather Rev.* **95**, 854 (1967)
- H.R. Pruppacher, J.D. Klett, *Microphysics of Clouds and Precipitation* (Reidel, Dordrecht, 1978)
- X. Qui, S. Soula, S. Chauzy, *Ann. Geophys.* **12**, 1218 (1994)
- V.A. Rakov, M.A. Uman, *Lightning, Physics and Effects* (Cambridge Univ. Press, Cambridge, 2003)
- M.J. Rycroft, R.G. Harrison, K.A. Nicoll, E.A. Mareev, *Space Sci. Rev.* (2008, this issue)
- C. Saunders, *Space Sci. Rev.* (2008, this issue)
- M.V. Shatalina, E.A. Mareev, S.V. Anisimov, N.M. Shikhova, *Radiophys. Quantum Electron.* **48**, 648 (2005)
- R.T. Shepherd, W.D. Rust, T.C. Marshall, *Mon. Weather Rev.* **124**, 919 (1996)
- T.J. Schuur, S.A. Rutledge, *J. Atmos. Sci.* **57**, 1983 (2000)
- M. Stolzenburg, T.C. Marshall, W.D. Rust, B. Smull, *Mon. Weather Rev.* **122**, 1777 (1994)
- M. Stolzenburg, T.C. Marshall, W.D. Rust, *Space Sci. Rev.* (2008, this issue)
- B.A. Tinsley, L. Zhou, *J. Geophys. Res.* **111**, D16205 (2006). doi:[10.1029/2005JD006988](https://doi.org/10.1029/2005JD006988)
- T.J. Tuomi, *J. Atmos. Terr. Phys.* **44**, 737 (1982)
- R.C. Whitten, I.G. Poppoff, *Fundamentals of Aeronomy* (Wiley, New York, 1971)
- J.C. Willett, *J. Geophys. Res.* **83**, 402 (1978)
- J.C. Willett, *J. Geophys. Res.* **84**, 703 (1979)
- J.C. Willett, *J. Geophys. Res.* **88**, 8453 (1983)
- S.L. Wilkin, C.F. Barenghi, A. Shukurov, *Phys. Rev. Lett.* **99**(13), 134501 (2007)
- Y. Yair, Z. Levin, S. Tzivion, *Icarus* **115**, 421 (1995)
- S.A. Yashunin, E.A. Mareev, V.A. Rakov, *J. Geophys. Res.* **112**, D10109 (2007). doi:[10.1029/2006JD007631](https://doi.org/10.1029/2006JD007631)

Electrical Charging of Volcanic Plumes

M.R. James · L. Wilson · S.J. Lane · J.S. Gilbert ·
T.A. Mather · R.G. Harrison · R.S. Martin

Originally published in the journal Space Science Reviews, Volume 137, Nos 1–4.
DOI: [10.1007/s11214-008-9362-z](https://doi.org/10.1007/s11214-008-9362-z) © Springer Science+Business Media B.V. 2008

Abstract Many explosive terrestrial volcanic eruptions are accompanied by lightning and other atmospheric electrical phenomena. The plumes produced generate large perturbations in the surface atmospheric electric potential gradient and high charge densities have been measured on falling volcanic ash particles. The complex nature of volcanic plumes (which contain gases, solid particles, and liquid drops) provides several possible charging mechanisms. For plumes rich in solid silicate particles, fractoemission (the ejection of ions and atomic particles during fracture events) is probably the dominant source of charge generation. In other plumes, such as those created when lava enters the sea, different mechanisms, such as boiling, may be important. Further charging mechanisms may also subsequently operate, downwind of the vent. Other solar system bodies also show evidence for volcanism, with activity ongoing on Io. Consequently, volcanic electrification under different planetary scenarios (on Venus, Mars, Io, Moon, Enceladus, Tethys, Dione and Triton) is also discussed.

Keywords Volcanic eruptions · Lightning · Fractoemission · Tribocharging · Particle aggregation

PACS 91.40.Dr · 91.40.Ft · 96.12.XY

M.R. James (✉) · L. Wilson · S.J. Lane · J.S. Gilbert
Lancaster Environment Centre, Lancaster University, Lancaster LA1 4YQ, UK
e-mail: m.james@lancaster.ac.uk

T.A. Mather
Department of Earth Sciences, University of Oxford, Parks Road, Oxford OX1 3PR, UK

R.G. Harrison
Department of Meteorology, University of Reading, Earley Gate, Reading RG6 6BB, UK

R.S. Martin
Department of Earth Sciences, University of Cambridge, Downing Street, Cambridge CB2 3EQ, UK

Fig. 1 Volcanic lightning photographed during the 1982 eruption of Galunggung volcano, Indonesia. The photograph was taken by R. Hadian and is reproduced courtesy of the US Geological Survey



1 Introduction

The dark, silicate-particle laden plumes produced by explosive volcanic eruptions on Earth are frequently associated with observable electrical phenomena (such as vivid lightning displays, Fig. 1). Compilations of historical descriptions of such effects, that illustrate the large magnitude of electrical charging involved, can be found in Pounder (1978, 1980b) and Mather and Harrison (2006). However, such plumes can be considered to represent one end of the spectrum of plume silicate-contents. At the other end, white plumes, dominated by condensing gases and droplets and with only a small silicate particle component, can be produced by gentle degassing activity. For a comprehensive review of different terrestrial plume types and the styles of volcanism involved, the reader is referred to Sparks et al. (1997). In this paper, the electrification of plumes and the subsequent effects are discussed, for both terrestrial and extraterrestrial volcanism.

2 Electric Charge in Terrestrial Volcanic Plumes

On Earth, volcanic plumes are three-phase mixtures composed of variable proportions of solid particles (dominantly fractured fragments of silicate rock, in various forms including crystals, glassy shards and vesicular particles, in a wide range of sizes), volcanic gases (mainly H_2O , but also CO_2 , SO_2 , N_2 , H_2S , H_2 , CO and others), and aerosols and droplets of condensed volcanic gases and atmospheric water vapour (Sparks et al. 1997). Additional solid particles can be present in the form of salts, if the activity involved significant boiling of seawater, or in the form of ice, in the case of high altitude plumes (Rose et al. 1995).

2.1 Silicate-Rich Plumes

The bulk of research on volcanic charging has been carried out on silicate-rich plumes produced by explosive eruptions. Such plumes are characteristically produced by subduction-related volcanoes erupting viscous magmas and can vary in height from a few kilometres (e.g. those from small Vulcanian eruptions, Wilson and Self 1980) to more than 30 km for major Plinian eruptions (e.g. the 1991 eruption of Mt. Pinatubo in the Philippines; Lynch and Stephens 1996). As the magma under the volcano ascends, its high viscosity prevents exolving volatiles from expanding or escaping. The resulting internal pressure eventually leads to brittle failure and explosive fragmentation of the magma. Although blocks up to

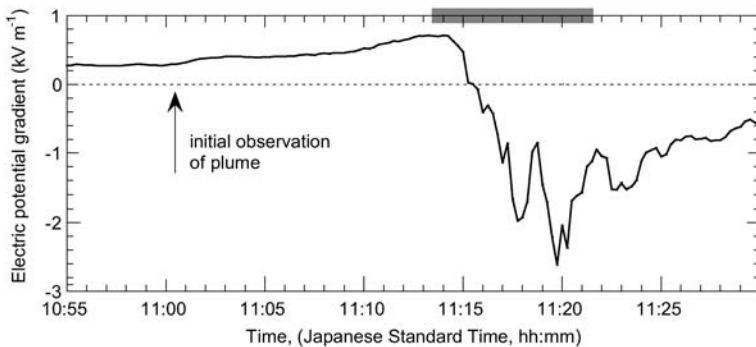


Fig. 2 Atmospheric electric potential gradient data recorded at Sakurajima volcano, Japan, approximately 2.7 km from the vent, during a small explosive eruption (James et al. 1998; James 1999). After the initial observation of the plume ascending above the crater, the plume was blown towards the instrument site, producing positive perturbations. The shaded bar on the upper axis denotes the duration of light ash fall at the instrument site, during which strong negative perturbations were recorded

metres in size can be erupted, small particles, generally in the range of micrometres to millimetres in diameter (with particles smaller than 2 mm classified as ‘ash’) can be transported horizontally by winds in the atmosphere for thousands of kilometres.

Interest in the electrification of plumes as a fundamental natural process has led to measurements using three techniques: (1) detecting perturbations of the atmospheric electric potential gradient at the surface (which is directly related to the vertical electric field), (2) measuring the charge on particles falling from a plume, and (3) remote (radio-frequency) lightning detection. Most measurements have been aimed at ascertaining plume electrical structure by recording atmospheric electric potential gradient (PG) perturbations as plumes pass near, or over, surface measurement sites (e.g. Hatakeyama 1943; Nagata et al. 1946; Hatakeyama 1949). Many of the results are dominated by strong negative perturbations, indicating the proximity of net negative charge in the plumes to the measurement site; however, others are dominantly positive (e.g. Hatakeyama and Uchikawa 1952) and most have perturbations of both polarities (Lane and Gilbert 1992; Lane et al. 1995; James et al. 1998; Miura et al. 2002; Fig. 2). Compilations and summaries of such measurements are given in James (1999), Miura et al. (2002) and Mather and Harrison (2006).

The dominantly bipolar nature of the perturbations is interpreted as indicating a dipole charge structure with (in most cases) a net positive charge in the higher portions of the plume and a net negative charge in the lower regions. In plumes being dispersed by atmospheric winds, the higher regions of the plumes will usually be advected faster than the lower regions, producing ground-level potential gradients that initially show positive perturbations as a plume approaches (Fig. 2). When the lower regions of the plume approach (possibly also involving ashfall), then the increasing proximity of the negative charge begins to dominate and the surface potential gradient reverses polarity. This dipole model has been used to explain data collected at Sakurajima volcano in Japan (Lane and Gilbert 1992; Lane et al. 1995; James et al. 1998) and from plumes rising above pyroclastic flows at Unzen, also in Japan (Miura et al. 1996). However, for other data collected at Sakurajima, a tripole model with an additional lower positive charge has also been suggested (Miura et al. 2002).

Thus, most plumes are thought to contain at least two vertically separated regions of opposite charges, with potential gradient data suggesting space charge densities, ρ , of order 10^{-10} to 10^{-9} C m^{-3} and charge magnitudes up to 10 C during the eruptions measured (Lane

et al. 1995). This macro-scale charge distribution results from the gravitational separation of plume components; lower regions will have larger particles than the upper regions and the upper regions will be more aerosol- and gas-rich than lower, more particle-rich regions. Thus, the charge distribution could indicate polarity differences between the net charges held on either particles of different sizes or, alternatively, on different phases (i.e. a net negative charge on the solid silicate particles and a net positive charge on the volcanic gases and aerosols, Lane and Gilbert 1992). This latter hypothesis is the favoured one and is in line with a fractoemission charging mechanism (see Sect. 3.1) and with measurements of positive potential gradient perturbations during periods of acid droplet fall, produced by condensation of volcanic gases (Lane and Gilbert 1992). However, whatever the initial charge distribution, subsequent scavenging processes will inevitably modify the charge distribution and are very likely to produce polarity differences as a function of particle size. The impact of ion and aerosol scavenging (Harrison and Tammet 2008) on electric charge distribution in volcanic plumes has not yet been systematically explored, but a basic thermodynamic approach has been illustrated by Mather and Harrison (2006).

Some atmospheric potential gradient (PG) data recorded during eruptions have shown rapid step-like changes that have been attributed to lightning discharges. Many such changes were recorded during the eruption of Mount St. Helens, USA, in 1980 (Hobbs, P.V. and Lyons, J.H., 1983, Electrical activity associated with the May 18, 1980 volcanic eruption of Mount St. Helens, *unpublished internal report for the IRT Corporation*). Within 60 km of the mountain, the PG was generally negative (with a maximum magnitude of 3.5 kV m^{-1}) and changes were predominantly positive (from 5 to 6 kV m^{-1} , equivalent to lowering negative charge to the ground, at up to 12 per minute), with both observations indicating the proximity of negative charge to the ground. Further from the mountain, the PG was generally positive (up to about 10 kV m^{-1}) with less frequent, smaller amplitude and predominantly negative (equivalent to lowering positive charge to the ground) changes, indicative of positive charge close to the ground. The authors explained the PG polarities in terms of the fallout of net negatively charged “heavy ash particles” close to the volcano and net positively charged “lighter ash particles” at greater distances, an interpretation in line with a positive-above-negative charge distribution model for the plume, with the lower regions initially dominated by the charge on larger particles, and the upper regions by charge on smaller particles (or aerosol).

Lightning-induced step-like changes in PG are distinct from other continuous and rapid changes in potential gradient polarity that have also been recorded. Changes in the potential gradient polarity during ashfall from an eruption of Mt. Usu, Japan (Kikuchi and Endoh 1982) were accompanied by simultaneous changes in the polarity of the electrical current resulting from the falling ash (which represented current densities, J , of magnitude $\sim 10^{-9} \text{ A m}^{-2}$). Such rapid changes in the net polarity of ashfall indicate a complex heterogeneous charge distribution in silicate-rich plumes, with the presence of relatively small, closely located regions of differing polarity. Note that $J = \rho v$, where v is the average velocity and, for the values cited above, is inferred to be $\sim 1\text{--}10 \text{ m s}^{-1}$, somewhat faster than the typical fall velocities of ash particles.

The net charge on falling ash particles has been measured directly by collecting ashfall in Faraday cup sensors. At distances less than 10 km from the vent, ash with a net charge of order $10^{-5} \text{ C kg}^{-1}$ (and of both positive and negative polarity during different eruptions) has been collected at Sakurajima (Gilbert et al. 1991; Miura et al. 2002). By exposing falling ash to horizontal electric fields, particles can also be separated by their charge and such experiments have indicated the simultaneous presence of both positively and negatively charged particles in ashfall, with specific charge densities of up to order $10^{-4} \text{ C kg}^{-1}$

(Gilbert et al. 1991; Miura et al. 2002). Modelling particles as spheres, this represents an approximate surface charge density, σ , of $\sim 10^{-5}$ C m $^{-2}$, close to the theoretical maximum of $\sim 2.6 \times 10^{-5}$ C m $^{-2}$, as estimated (for large particles) by equating the surface field strength, $E = \sigma/\epsilon_0$, to the breakdown strength of air (3×10^6 V m $^{-1}$), where ϵ_0 is the permittivity of free space. Gilbert et al. (1991) thus suggested that the particles were close to their charge limit, so that they were nearly ‘saturated’ with charge under atmospheric conditions.

As well as visual observations and the effect of discharges on PG data, lightning has also been detected by standard detection systems, demonstrating that at least some volcanic lightning has a similar radio signature to that of meteorological lightning (Hoblitt 1994). After eruptions at Redoubt, USA, in 1990, lightning polarity usually started as ‘negative’ (lowering negative charge to ground), but often then turned ‘positive’, with the first detected strikes lagging behind the onset of eruption seismicity by 5 to 15 minutes and located away from the volcano’s summit (often in an area of rugged highlands 15 km to the northeast of the summit). During the eruptions of Mount Spurr, USA, in 1992, lightning strength was found to correlate with seismic and geochemical (magmatic gas content) indicators of eruption intensity (McNutt and Davis 2000). However, the number of lightning events was thought to be additionally influenced by different wind, temperature and relative humidity conditions. More recently, a portable system was employed during the 2006 eruption of Mt Augustine, USA (Thomas et al. 2007) and identified both short discharges at or near the vent region, and long-duration flashes with branches over ten kilometres in length.

Basaltic volcanoes do not generally produce large silicate-rich plumes because their lower-viscosity magmas allow exolving gases to escape much more freely and less explosively. Consequently, basalt fragmentation can often be considered to be similar to a ductile liquid spray process (rather than one of brittle failure) producing mostly relatively large liquid clots, as opposed to ash. However, violently explosive basaltic eruptions can occur, particularly when ascending magma encounters significant volumes of water, for example the sea, a groundwater aquifer, or meltwater produced during eruptions through icesheets. Such phreato-magmatic eruptions generate significant electrification, not only by increasing the amount of brittle failure (due to steam expansion increasing strain rates and water cooling the magma surfaces (Büttner and Zimanowski 1998)), but also by involving additional water-boiling mechanisms (see Sect. 3.2). On Iceland during the 1998 subglacial eruption of Grímsvötn, the lightning produced was detected by a local lightning location system and the Arrival Time Difference (“ATD”) sferics measurement system of the UK Met Office (Arason 2005).

2.2 Silicate-Poor Plumes

Much less is known about the electrification of silicate poor-plumes, with only those produced by lava flows entering the sea having been studied in detail. These plumes are dominated by condensing steam (from boiled seawater) and entrained atmospheric air, but also contain salt particles produced during the boiling process, and generally small amounts of silicate material spalled from rapidly quenched lava. Such plumes appear to hold a net positive charge and, during the eruption of Surtsey, Iceland, in 1963, PG data suggested charge densities of up to 10 $^{-7}$ C m $^{-3}$ (Anderson et al. 1965). Similar data were collected during the 1973 eruption of the Icelandic volcano Heimaey, with perturbations of the surface PG in excess of +7 kV m $^{-1}$, including rapid changes correlated with lightning events (Brook et al. 1974). These transients suggested that the discharges were single, rapid, upward movements of negative charge from the plume base that neutralized slowly ascending positive charge in the lowest 100 m of the plume; none could be interpreted as the multiple strokes that typify thunderstorm lightning strikes.

There has been only one report of measurements made at Strombolian-type eruptions, during which small, initially negative, then positive perturbations were recorded at Stromboli (Büttner et al. 2000). No measurements of the electrification of plumes from fire-fountaining, persistent basaltic systems or lava flows have been reported. Typically, where plumes are dominated by condensing volcanic gases (mainly H₂O) and entrained air they are not associated with observable electrical effects, although some degree of electrification cannot be discounted. At Sakurajima, in contrast to large PG perturbations (up to 3 kV m⁻¹) from dark silicate-rich plumes, perturbations have not been detected from similarly-produced white plumes of condensing gases (Lane and Gilbert 1992). However, light-brown or light-grey plumes suggesting a dilute silicate content have produced measurable PG perturbations, with the inferred charging mechanism being brittle magma fragmentation (James et al. 1998). It is likely that other dilute plumes (e.g. those produced by rockfall from active domes) would be similarly charged.

3 Charging Mechanisms

Both qualitative observations and quantitative measurements have indicated that, for volcanic plumes on Earth, high degrees of electrification are strongly correlated with either vigorous water boiling, extensive magma fragmentation, or both. Generic particle or droplet plumes can become electrified either: (1) initially, as a result of their formation process, or (2) subsequently, by the self-generation of charge by radioactive decay, by particle interactions with existing space charge or external radiation, or by particle–particle interactions within the plume. The chemically complex and multiphase nature of volcanic plumes suggests that several charging processes could operate and the dominant process may well change with a plume's age and distance from the volcano.

If a charging process produces detectable macro-scale electrification, it can be described in terms of an initial charge generation, representing the atomic- or micro-scale separation of charge, and the subsequent charge separation, covering the ensuing macro-scale separation process to produce detectable electric fields. In common with thunderclouds, the gravitational separation of particles (or droplets) with different fall velocities is assumed to dominate the charge separation process. However, charge generation is much less well understood, with the most likely processes described below.

3.1 Solid-Based Charging

Solid particles can become electrically charged by a wide range of processes, most of which have been suggested for volcanic charging at some stage. In line with the earliest awareness of the generation of electricity, frictional charging (tribocharging) is often suggested to cause volcanic plume charging in early literature (e.g. Perret 1924). Tribocharging involves charge transfer when materials are rubbed together, and experimentally it is extremely difficult to isolate from contact charging (charge transfer by contact alone between materials with different work functions). Indeed, in many cases the terms are used interchangeably and work function differences are used to explain tribo-effects (e.g. Farrell et al. 2006; Desch and Cuzzi 2000). These processes are still not fully understood and, where theories exist, they are generally applicable only to clean material surfaces in a vacuum.

Triboelectric effects have been shown to charge a wide range of industrial powders (e.g. during pneumatic transport) to between 10⁻⁷ and 10⁻³ C kg⁻¹ (Boschung and Glor 1980), with some of the differences in both charge magnitude and polarity attributable to specific

area and particle size, with the higher charge densities on powders of higher surface area (about $500 \text{ m}^2 \text{ kg}^{-1}$, Cross and Farrer 1982). Early electrification experiments on volcanic ash, which involved pouring ash particles down inclined planes (e.g. Kikuchi and Endoh 1982; Hatakeyama and Uchikawa 1952), have probably been dominated by ‘frictional’ effects. For these experiments, charge densities varied from 10^{-9} to $10^{-5} \text{ C kg}^{-1}$, with the polarity changing between different particle size fractions and between samples from different volcanoes.

Consequently, tribo-charged particles have demonstrated many of the charge characteristics of ashfall measured in the field but there are uncertainties as to how applicable a frictional mechanism is in volcanic plumes, what the relevant fundamental physics actually is, and whether the high charge densities can be reliably reproduced. An alternative mechanism, which relies on bulk material properties rather than surface properties and can be explained in terms of atomic physics, is fractoemission. This is a process by which electrons, positive ions, neutral atoms and various frequencies of electromagnetic radiation, from radio waves to light, are released from a material due to fracture. Typically, emission starts at the time of onset of crack generation, but can continue from the fresh surfaces for up to several seconds after the break (Dickinson et al. 1984). It may be possible to consider triboelectric effects as resulting from fractoemission on a small scale (Molina et al. 2001), due to friction-producing asperities between sliding surfaces becoming damaged or broken. In line with this, research into material wear processes has identified particle emission during the abrasion of solids and termed this ‘triboemission’ (Mazilu and Ritter 2005; Nakayama 2004; Nakayama and Hashimoto 1992). Thus, ‘emission’ may be the key underlying physical process, regardless of whether it is excited by fracture or friction at the sample scale. This implies that, for understanding macro-scale charge distributions in plumes, charge held in the gas and liquid phases is probably just as important as that on the solid silicate phase.

Fractoemission research has been dominated by the physics and materials science communities, mainly on oxide coatings of metals (Dickinson et al. 1981b), crystals (Dickinson et al. 1981a) and adhesives (Dickinson et al. 1982) under high vacuum. However, minerals such as mica and quartz have also been investigated with electron emission (of up to 7000 electrons per second decaying rapidly over 3 seconds) and charged macroscopic fracture debris (around $10^{-14} \text{ C per particle}$) being detected (Dickinson et al. 1981b, 1984; Donaldson et al. 1988). Macro-scale experiments have also been carried out on rock samples with optical emission observed during the compressional fracture of granite (Brady and Rowell 1986) and positive and negative charge release being detected from indented andesite, dolerite and basalt (Enomoto and Hashimoto 1990). In many cases the light emission results from the atmospheric response to emitted electrons (e.g. Brady and Rowell 1986). In similar experiments, charge movement has also been attributed to the motion of mobile hole charge carriers (defect electrons on the O^{2-} sublattice). Experiments have provided evidence for this by detecting mobile charge carriers in olivine (Freund et al. 1988), fused silica (Freund 1985) and a variety of igneous rocks (Freund 2000). Much of this work has been aimed at explaining the occurrence of earthquake lights, transient atmospheric luminous phenomena associated with earthquakes, and other seismo-electromagnetic phenomena (Takeuchi et al. 2006; St-Laurent et al. 2006; Takeuchi and Nagahama 2002; Freund 2000).

Fractoemission has been investigated as a charging mechanism for volcanic plumes in laboratory experiments in which ash particles were produced by fragmenting pumice (cold magmatic foam) by repeated pumice-pumice collisions (James 1999; James et al. 2000). The particles produced were highly charged and experiments carried out under a range of pressure and relative humidity conditions indicated that net charges of up to $\sim 10^{-5} \text{ C kg}^{-1}$ can

be produced under atmospheric pressure and closer to 10^{-4} C kg $^{-1}$ in low pressure environments. Furthermore, these net charges were demonstrated to result from small imbalances in particle charges of both polarities that were at least one order of magnitude greater (10^{-4} to 10^{-3} C kg $^{-1}$). The general trend was for particles to be net negatively charged but some samples suggested that geochemistry and atmospheric pressure could exert some influence over charge polarity. The fact that atmospheric pressure can be a factor strongly suggests that ion scavenging may play an important role, with ions being retained in the vicinity of particles for longer (and hence with increased chance of scavenging) in denser atmospheres. During the experiments, a net opposite polarity charge was detected above the samples and was attributed to the collection of ions (or to very small numbers of highly charged particles for which electrostatic forces had outweighed gravitational forces). These experiments thus demonstrated that fractoemission occurring during the production of ash particles by pumice fragmentation was capable of generating the charge magnitudes and distributions measured during ashfall.

3.2 Liquid-Based Charging

Terrestrial volcanic events can be associated with both the boiling and freezing of water; on other planetary bodies, other liquids are also involved (e.g. SO₂ on Io). In the context of volcanic charging on Earth, processes involving ice are generally only applicable to high altitude plumes, and consequently we leave their electrical effects to be encompassed within thundercloud-type mechanisms (see Sect. 3.3). Water boiling also produces charging and the exact mechanisms responsible can be explained in terms of shearing double electric layers at the water interface and, in the case of boiling saline solutions, also solid-solid charging of the salt crystals produced (Pounder 1980a).

At water interfaces, the polar nature of water molecules leads to the formation of double electric layers with negative charge aligned outward at the liquid surface. Consequently, rapid mechanical disruption of water (e.g. spraying, bubble bursting or vigorous boiling) can produce charge separation if the electric layers are sheared more quickly than they can rearrange to maintain charge balance. This process ('waterfall' or 'Lenard' charging) results in small, negatively charged droplets and a few larger, positively charged droplets and is responsible for negative space charge around waterfalls. However, the process is sensitive to the water chemistry, and bursting bubbles in seawater produce droplets and salt particles (with diameters ≥ 3 µm) that are positively charged (Blanchard 1955, 1958). In more saline waters from the Mediterranean Sea, a net negative space charge, resulting from charge on particles smaller than 3 µm, is produced by the same process (Reiter 1994).

Boiling saline solutions have been shown to produce charge separation (Blanchard 1964; Björnsson et al. 1967; Pounder 1978; Sheldon 1974) with the process explained in terms of both liquid disruption and solid-solid charging of salt crystals produced (Pounder 1980a). Seawater droplets falling on lava samples sufficiently hot to have a molten surface layer, produce positive charges of order 10^{-5} C kg $^{-1}$ (Björnsson et al. 1967). Charge separation varies with droplet size and solution concentration (Pounder 1972), and increases by about an order of magnitude if rough lava, with only some melted protuberances, is used (producing condensing steam plumes with space charge densities of 10^{-6} C m $^{-3}$). The importance of solid-solid charging mechanisms within this boiling process is illustrated by the fact that the results change significantly when experiments are repeated with rock surfaces contaminated by organic materials which are possibly only monolayers thick (Blanchard 1964; Björnsson et al. 1967).

A particularly efficient variant of this process is Leidenfrost boiling, where a boiling liquid droplet is supported above a hot surface by a vapour layer (Pounder 1978, 1980a).

If the liquid contains dissolved salts, the vapour layer periodically collapses due to crystallisation at the base of the droplet, the surfaces contact, and charged particles are emitted during fragmentation of the crystal layer. Rapid liquid vaporisation quickly forms another insulating vapour layer, and the process starts again. This Leidenfrost process is capable of producing particles with specific charges of up to 10^{-3} C kg $^{-1}$, with the charge generation resulting from solid-solid charging (by contact, frictional or fracture effects) and shear of the double layer in the liquid (Pounder 1980a).

To investigate charge generation during explosive phreato-magmatic eruptions, Büttner et al. (1997, 2000) carried out molten fuel-coolant interaction (MFCI) experiments using hot silicate melts injected with water. As the water in contact with the melt vaporises and expands, disruption of the melt provides more hot surface area to vaporise more water in a runaway event. These experiments generated significant charge and voltages measured on a sensing mesh were interpreted as being induced by negatively charged silicate particles driven by a positively charged steam cloud. The charge generation was attributed to water disruption as well as to the brittle fragmentation of the material. The charge magnitudes detected increased with the energy of the explosion and, consequently, with the surface area of the products. In similar experiments carried out to compare MFCI explosions produced by pure water and NaCl solution, lower explosion intensities were observed with the solution (Grunewald et al. 2007). This was interpreted as indicating that chemical reactions with the saline water were reducing the energy available for the explosion and, although charge was not measured, this is likely to have an effect on charging too.

3.3 Thundercloud-Type Charging

Thundercloud electrification may involve a range of microphysical charging mechanisms and similarities in size and electrical activity with volcanic plumes have led to ‘thundercloud charging’ being suggested for volcanic plumes (Williams and McNutt 2005). The physics of thundercloud charging has been the subject of many detailed investigations over a long period, and many diverse theories for the origin of the thunderstorm electrification have been proposed (Saunders 2008; Chapter 3, this issue). Current understanding is built around the charge distribution on (and in) ice surfaces growing by diffusion from vapour-phase water, and rebounding collisions between small growing hailstones and ice particles (Dash et al. 2001; Saunders 2008). Faster growing ice surfaces are more negatively charged than slower growing ones so, during brief ice particle collisions, charge transfer (facilitated by localized melting) allows faster growing ice surfaces to lose negative charge and hence to become positively charged. Fall velocity differences then produce the macro-scale charge separation responsible for lightning.

Large volcanic plumes contain significant volumes of water, not only from the magmatic volatiles which drive the eruption (usually several percent by weight of the magma) but also from entrained, moist tropospheric air, and substantial ice formation can occur. However, because the thunderstorm charge generation mechanism relies on delicate molecular-level balances, there could be significant differences in how it may operate under the conditions inside volcanic plumes. No attempt has yet been made to experimentally reproduce hailstone and ice charging in a physico-chemical environment appropriate to a volcanic plume, or to provide quantitative theoretical simulations of the charging environment. Nevertheless, even if this precise thundercloud charging mechanism is not appropriate, particle–particle interactions will continue to occur even at significant distances from the vent and some degree of down-plume charging is inevitable. Unfortunately, field measurements are currently insufficient to distinguish between the continued down-plume separation of charge initially

generated by fragmentation within or near the vent, and any *in situ* generation of ‘new’ charge by distal mechanisms in ageing sections of a plume.

3.4 External Charging Mechanisms

With Earth relatively well protected from the solar wind and space-borne radiation by its magnetosphere and atmosphere, the charging of volcanic particles by external radiation is not, in relative terms, an important process at low altitudes, although photoelectric charging is much increased at high altitude and some cosmic ray ionisation occurs at surface levels (Bazilevskaya et al. 2008). However, on planetary bodies with little or no atmosphere, for example, the Moon, Mercury and Io, significant charging could result from the absorption of externally generated atomic particles or photons.

In ‘bombardment’ charging, a receptor surface absorbs an incident ion or electron and hence, also, its charge. If the incident particle has sufficient energy it may also cause secondary emission from the target. This can result in further charge adjustment, and the process will vary with the existing sign and magnitude of the charge held on the target. In contrast, photoelectric charging is caused by the ejection of electrons from the target due to the absorption of energy from an uncharged incident particle (photon). However, this will only occur if each photon is sufficiently energetic to allow an electron to escape from its potential well and this is not generally the case for photons of visible light.

On the Moon, photoelectric charging and bombardment charging by the solar wind is significant and is inferred to be responsible for the electrostatic levitation of dust particles from the surface (Abbas et al. 2007, and references therein). Similarly for dusts in space, consideration of these processes is an integral part in understanding the relevant dynamics (Graps and Jones 2008; Horányi 1996).

4 Charging in Extraterrestrial Volcanism

The observations of ongoing volcanic activity on Io (Fig. 3) illustrate that electrification from volcanism may not be solely a terrestrial phenomenon. Consequently, the ranges of pressure, temperature and chemical conditions that need to be considered for potential charging mechanisms have had to be considerably expanded.

4.1 Silicate Volcanism

Some of the most familiar planetary volcanic scenarios will be those in which, as on Earth, the ‘magma’ is a molten silicate rock. Venus, Mars, the Moon and probably Mercury have had such silicate volcanism, but with considerable differences due to, amongst other factors, the different surface atmospheric pressures on these bodies. Where there is insufficient atmosphere to develop a buoyant dispersing plume, or eruption conditions prevent it, a fountain is produced in which particles follow ballistic or near-ballistic trajectories. Both Earth and Mars have, or have had, the necessary conditions for both plumes and fountains, but on bodies with no substantial atmosphere, such as the Moon and Io, only fountains can be produced. However, note that in the case of Io this distinction is not often made, and Io’s fountains are misleadingly referred to as ‘plumes’.

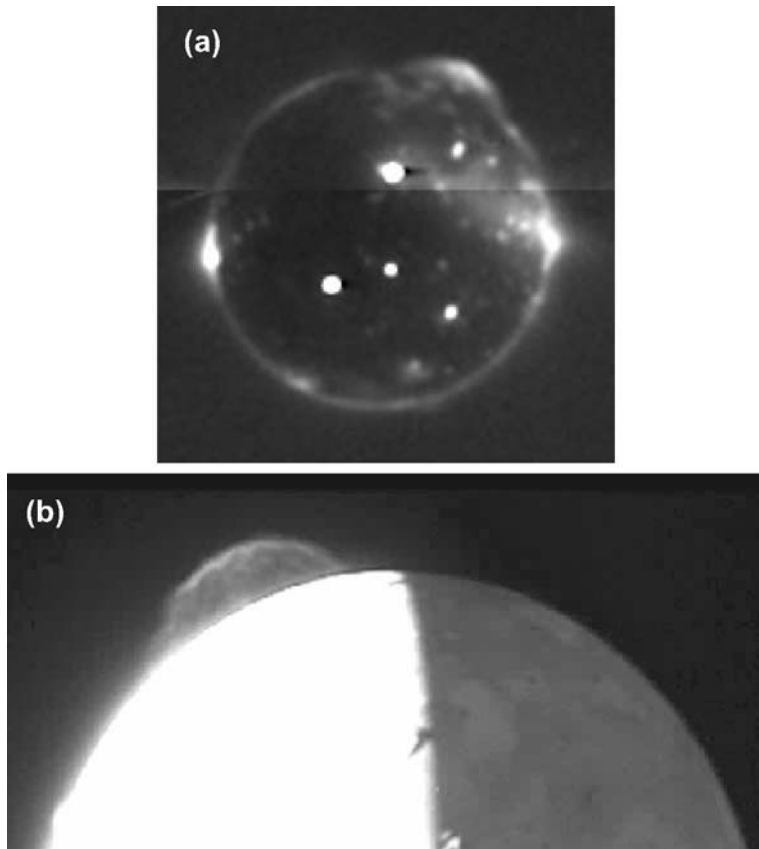


Fig. 3 Volcanic activity on Io as observed by the New Horizons spacecraft, which passed the Jupiter system in February 2007 en route to Pluto. (a) In eclipse from Jupiter, the extent of Io's volcanic activity is apparent, with hot lava (the *brightest spots*), volcanic plumes and auroral displays in the tenuous atmosphere outlining the disk being detectable. The largest plume (the diffuse glow at ~ 1 o'clock) is ~ 330 km high and from the Tvashtar volcano. This image is a heavily processed mosaic and the horizontal line is a processing artefact. (b) A closer view of the Tvashtar plume caught on the limb of the sunlit side illustrates its umbrella shape and shows minor internal inhomogeneities. Image credit: PIA09354 & PIA09357—NASA/Johns Hopkins University, Applied Physics Laboratory/Southwest Research Institute

4.1.1 Plumes on Venus and Mars

Although the size and composition of Venus suggest that it should be in a similar thermal and chemical state to the Earth (Nikolaeva and Ariskin 1999), no unambiguous detection of active volcanic eruptions has yet been made from Earth or from spacecraft missions. However, morphologically very fresh lava flows, detected by radar imaging through the opaque atmosphere (Carter et al. 2006), are abundant on the surface of Venus and it is very likely that volcanic activity on some scale is still taking place. Relatively steady, long-lived explosive volcanic eruptions should be less common than on Earth due to the very high pressure (ranging from 4×10^6 to 9×10^6 Pa) of the hot (average surface temperature ~ 750 K), dry (negligible water content below ~ 50 km), CO₂-dominated atmosphere (Bézard and de Bergh 2007). However, localized build-up of volatiles in shallow magma reservoirs or intrusions can lead to energetic transient explosions (Fagents and Wilson 1995). Assuming

H_2O and CO_2 are the most common volatiles in these magmas (as on Earth), prolonged explosive activity can only take place if volatile contents are relatively high compared with terrestrial values (Head and Wilson 1986). Even when explosive activity does occur, for a given mass eruption rate, plumes will rise to less than half the height that would be reached in the Earth's atmosphere (Robinson et al. 1995). Thus, the hot, dry and high pressure atmospheric conditions on Venus suggest that the only significant mechanisms which could cause volcanic charging are likely to be triboelectric effects and fractoemission.

Mars has a bulk chemistry similar to that of the Earth (Foley et al. 2005), and erupted magmas appear to be dominantly basalts to basaltic andesites (McSween et al. 2001). Impact crater counts on martian volcanoes suggest that numerous summit eruptions took place ~ 100 – 200 Ma ago (Neukum et al. 2004), with a few eruptions being less than 10 Ma old. This is consistent with theoretical predictions (Wilson et al. 2001) that much martian volcanic activity should be episodic with major intervals of ~ 100 Ma between cycles of activity. The most common volatiles in these magmas are likely to be H_2O and CO_2 and, with the low atmospheric pressure on Mars (a mean pressure of ~ 600 Pa at the surface) encouraging volatile exsolution and expansion, it is likely that a greater proportion of volcanic eruptions will be explosive on Mars than on Earth (Wilson and Head 1994).

Recent studies (Wilson and Head 2007) have shown that there may be two possible classes of martian eruption plume. At low mass eruption rates, plumes rising to heights less than ~ 20 km entrain the surrounding atmosphere in the same way as plumes on Earth. The martian atmosphere is very dry and its temperature is less than the freezing point of water everywhere, so magmatic water vapour is rapidly converted to ice, and formation of ice-bound particle aggregates is likely in low-mass-flux eruption plumes. At higher mass eruption rates, the jet of magmatic gases and entrained pyroclasts emerging from the vent would normally be expected simply to entrain more atmospheric material and convect to greater heights. However, at heights above ~ 20 km, the martian atmospheric density is so low that the mean free path of molecules is much greater than the sizes of typical volcanic particles (Glaze and Baloga 2002) and the gas laws no longer apply: volcanic particles and gases (both magmatic and atmospheric) interact in the Knudsen regime and essentially no atmospheric entrainment occurs. As a result, there are many combinations of high mass eruption rate, enhanced by high magma volatile content, for which the erupting jet has so much inertia that it effectively punches a hole through the lower atmosphere and forms an umbrella-shaped plume, or fountain, like those seen in current eruptions on Io.

Finally, conditions on Mars in its early history (higher atmospheric pressure and, hence, temperature) may have been such as to allow liquid water to reside on its surface. However, for most of its history the surface has been very cold, and liquid water has been confined to depths between ~ 3 and ~ 10 km where the combination of the geotherm and the available pore space allows its presence. There is abundant evidence that in many places volcanic activity has fractured the frozen outer few kilometres and allowed water to escape. In some of these places violent mixing interactions between magma and water have occurred producing phreato-magmatic eruptions. Thus, as a result, essentially all charging mechanisms that operate in volcanic eruptions on Earth are likely to have operated at some time and place on Mars, although any thundercloud-type charging mechanism which relies on latent heat release to drive updrafts may only be relevant in the early wetter martian environment. Additionally, the current low atmospheric density means that ultra-violet levels at the surface of Mars are orders of magnitude greater than at Earth's surface and, for long lived plumes that survive for several days (Wilson and Head 2007), photoelectric charging could be significant.

4.1.2 Fountains on Io and Moon

Jupiter's satellite Io and Earth's Moon are similar in size (with radii of 1821 and 1738 km respectively), gravity (1.8 and 1.6 m s⁻² respectively), and lack of atmosphere. The Moon was volcanically active mainly between 4 and 3 Ga B.P., with activity being driven by radiogenic heat sources, whereas Io is active now (Fig. 3) as a result of dramatic tidal heating by Jupiter due to Io's orbital resonance with Europa and Ganymede (Peale et al. 1979). The absence of a dense atmosphere means that on both bodies the expansion of gases released during explosive eruptions must be dramatic (Kieffer 1984). Solid or liquid particles (both silicates and any condensates from the volatiles) decouple from the expansion of the residual gas a very small distance above the vent as the Knudsen regime is reached (Wilson and Keil 1997) and continue along ballistic trajectories, the envelope of which defines the classic umbrella-shaped structure (Fig. 3b) first recognized on Io (Strom and Schneider 1982).

The Moon has always been essentially devoid of volatiles but many ascending magmas produced small amounts of a CO volatile phase as a result of a chemical smelting reaction between carbon (graphite) grains and oxides such as FeO (Sato 1979; Fogel and Rutherford 1995). As a result, explosive as well as purely effusive eruptions took place when the Moon was volcanically active in its early history (Wilson and Head 1981). The products of these eruptions are sub-mm sized, glass-dominated, spherical to ellipsoidal clasts and it can be assumed that charging will have taken place by triboelectric and fractoemission mechanisms as the clasts were ejected, and photoelectric and bombardment charging subsequently.

There is every reason to think that Io was formed from a mixture of materials rich in volatiles, like the other three main satellites of Jupiter. However, the enormous heat source provided by the Jupiter body-tide in Io causes planetary-scale resurfacing at a rate of at least a few mm per year (Johnson et al. 1979), i.e. two orders of magnitude faster than on Earth. Over more than 4 Ga this amounts to a ten-fold overturn of the entire interior of the body and has led to almost complete outgassing so that only the highest molecular weight species remain. As a result, sulphur allotropes and sulphur compounds, especially SO₂, abound on and just beneath the surface and are recycled into rising silicate magmas to provide the driving force for the many violently explosive eruptions seen at any one time (Smith et al. 1979). Thus, explosive activity on Io has many similarities to lava–water interactions on Earth and similar processes are likely to operate (Kokelaar and Busby 1992). The lack of any substantial atmosphere means that bombardment and photoelectric charging are also potentially important, and in tall plumes that penetrate the ionosphere, electron capture has been shown to be a highly efficient charging mechanism (Flandes 2004).

4.2 Non-silicate Volcanism (Enceladus, Tethys, Dione and Triton)

The presence of large proportions of water ice in the surface materials of many of the satellites of the gas-giant planets suggested the possibility that they are the sites of cryo-volcanism, a form of volcanism in which liquid water replaces liquid rock as the ‘magma’ and compounds such as ammonia and methane replace H₂O and CO₂ as the driving volatiles (Kargel 1992). Although a variety of landforms suggestive of cryo-volcanism have been identified on bodies such as the Jupiter satellites Europa and Ganymede and Saturn’s large satellite Titan, it was initially only Neptune’s large satellite Triton that displayed overt evidence of activity (Fig. 4), with gaseous nitrogen being identified issuing from subsurface liquid nitrogen reservoirs to form plumes in the extremely low density nitrogen atmosphere (Duxbury and Brown 1997). Although it is unlikely that this liquid nitrogen boiling process

Fig. 4 The south polar terrain of Triton, imaged by the Voyager spacecraft in 1989, shows about 50 dark streaks emanating from what appear to be vents on the icy surface. The vent regions are generally several kilometres in diameter and the dark streaks, thought to be deposits from wind-blown plumes, can be more than 150 km long. Image credit: PIA00059—courtesy of NASA/JPL-Caltech

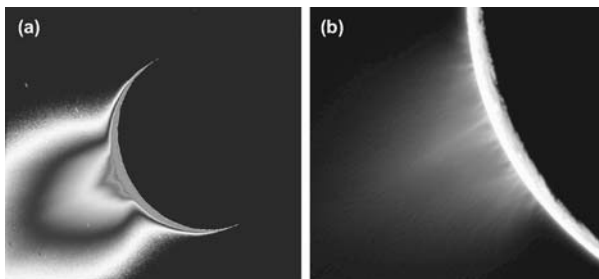


Fig. 5 The fountains of Enceladus, a moon of Saturn, as discovered by the Cassini spacecraft. (a) A heavily processed image shows the extent of the material emanating from the Tiger Stripes area (south polar region) as it is backlit by the Sun. For scale, Enceladus has a diameter of 500 km. In (b) a less-enhanced close-up of the source region shows the fine scale detail revealing the multitude of individual fountains responsible. Image credit: PIA07759 & PIA08386—NASA/JPL/Space Science Institute

will produce charge itself (unlike water, as a diatomic molecule, N_2 is not polar), as an insulator, N_2 would maintain the charge on any solids entrained within it.

Subsequently, detailed evidence has been gathered by the Cassini spacecraft in orbit around Saturn for a gaseous water plume being erupted from the small satellite Enceladus (Hansen et al. 2006; Fig. 5). The size, composition and temperature of the plume, and the temperature of its source area near the south pole, have all been measured a number of times. Significant amounts of volatiles other than H_2O are present, and it is very likely that decomposition of clathrates (Kieffer et al. 2007) is the main potential source of particles and vapour in the Enceladus plume, the presence of which is indicated by plume interaction with Saturn's planetary magnetic field (Burger et al. 2007). Charging of the plume will occur due to fractoemission processes where clathrates decompose violently (Kieffer et al. 2007) and particles will also become charged as they travel to the surface. If any liquid water

is involved, then boiling charging will occur when the water is exposed to the near-vacuum surface conditions. Once above the surface, material forming the plume will be subject to the usual photoelectric and bombardment charging effects. Very recently, evidence has emerged that a similar form of water release may be taking place on two other small satellites of Saturn, Tethys and Dione (Burch et al. 2007).

5 Charge-Driven Processes

5.1 Physical Effects

The most obvious effects of terrestrial plume charging are atmospheric discharge phenomena, particularly lightning, but with others such as St. Elmo's fire—a local plasma discharge—also having been observed. As a volcanic hazard, lightning strikes are not very important in relative terms, although a few people have been killed (Blong 1984), and monitoring equipment can be vulnerable. Similarly, in planetary exploration, volcanically induced discharges would have to be considered a minor hazard when compared with the primary volcanic event itself (Mather and Harrison 2006).

A less observable, but more pervasive effect of particle charge is the driving of electrostatic particle aggregation, which can be very efficient due to the high charge densities on particles and the opposing polarities. During the Mount St. Helens 1980 eruption, dry aggregates (generally <1 cm) were collected on the ground and, during a flight into the plume, fist-sized dry aggregates were observed (Sorem 1982). The aggregation process changes the effective particle size distribution (producing relatively large, low density 'aggregate' particles), which then alters the rate of sedimentation from a dispersing plume. Consequently, predicted deposit thicknesses are inaccurate unless aggregation processes are incorporated into sedimentation models. Common indicators of the importance of aggregation are bimodal particle size distributions in fall deposits (reflecting a fall velocity equivalence of some silicate particles with larger, but less dense clusters of smaller particles) and regions in which deposit thickness temporarily increases with distance from the vent, reflecting optimum aggregate sedimentation at a certain distance from the volcano (Carey and Sigurdsson 1982). Although other aggregation processes (involving water) are also known to operate, the dry electrostatic aggregation of particles has been shown to produce low-density ($100\text{--}200 \text{ kg m}^{-3}$) clusters of the sizes and morphologies observed in the field (James et al. 2002, 2003). Furthermore, these characteristics also fit those required by tephra sedimentation models in order to best-fit field data (Carey and Sigurdsson 1982; Cornell et al. 1983; Scollo et al. 2007), indicating the importance of electrostatic aggregation in plume dynamics.

Aggregation is generally most effective with the smallest particles, which have the highest specific charge densities and consequently are subject to the largest ratio of electrostatic to gravitational forces. These small particles (e.g. PM₄, particulate matter with an aerodynamic diameter $<4 \mu\text{m}$) are also known to have the most significant health effects (Horwell and Baxter 2006), so concentration of PM₄ material through aggregate deposition can be linked to potential health issues.

In planetary environments, aggregation of charged silicate volcanic ejecta is also likely where there is sufficient atmosphere to provide non-ballistic trajectories. Due to falloff with the square of the distance, electrostatic forces are poor at attracting particles together, but good at binding particles which do collide or approach very closely. Consequently, electrostatic aggregation would be anticipated to be significantly reduced in more 'ballistic' particle

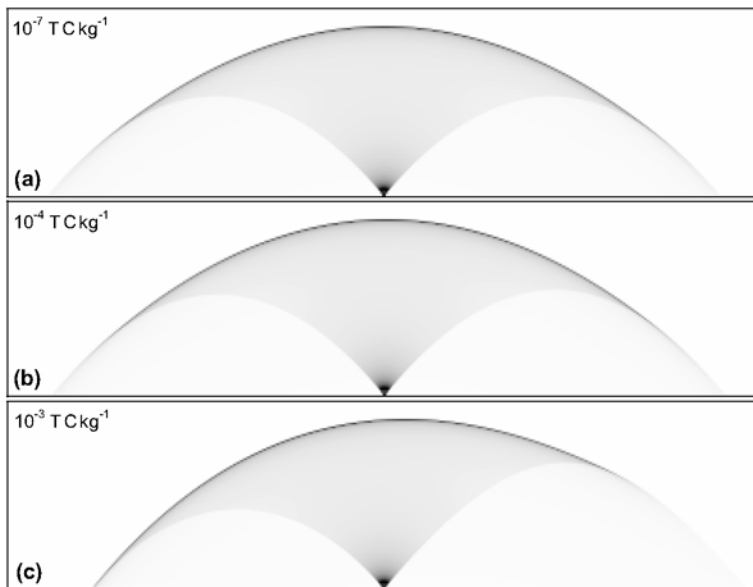


Fig. 6 Distortion of a volcanic fountain (such as Io's 'plumes') by interaction of electrically charged particles with a magnetic field (James 1999). The shading represents the particle number density in a cross section through a simulated fissure eruption (each panel is 110×440 km). Particles were erupted at 600 m s^{-1} , at angles of up to 40° from the vertical and the magnetic field is horizontal and perpendicular to the page. The degree of distortion is determined by the product of the magnetic flux density, B , and the specific particle charge, $q \text{ m}^{-1}$. In order to achieve noticeable distortion from the electromagnetic interactions, $Bq \text{ m}^{-1}$ needs to be around $10^{-3} \text{ T C kg}^{-1}$, roughly three orders of magnitude larger than thought applicable for Io. Note this is a first-order model that considers particle trajectories individually; no bulk electrostatic forces are included

regimes, such as the plumes on Io. However, this leaves the possibility of large numbers of highly charged particles existing individually within plumes on near-ballistic trajectories.

Any moving charge will experience a force if subject to a magnetic field, so such charged particles could potentially distort otherwise symmetric plumes in the presence of a planet's magnetic field. On Io, if it is assumed that particles are charged to $10^{-3} \text{ C kg}^{-1}$, this is estimated to be three orders of magnitude less than required to produce observable plume asymmetry (Fig. 6). However, satellite-detected dust streams from the Jovian system (Grün et al. 1993; Krüger et al. 2006; Postberg et al. 2006) have been traced back to Io as their source (Graps et al. 2000), with particles thought to escape Io's gravity due to electromagnetic accelerations (Flandes 2004). For the levels of charge required, only electron capture in the upper regions of the highest plumes (which are exposed to the ionospheric plasma of Io) can be responsible (Flandes 2004).

5.2 Chemical Effects

On Earth, it has been proposed that lightning produced by volcanic plumes could have had an important effect on the evolution of life by affecting the chemical evolution of the atmosphere. During a discharge, highly energetic (and conductive) plasma channels at temperatures $>10,000 \text{ K}$ are briefly produced, then rapidly cooled. The thermodynamic equilibration of gases at these temperatures, followed by rapid cooling, leads to the formation and

retention of reaction products that would not otherwise be present in the atmosphere. Furthermore, within volcanic plumes, lightning may have access to significantly elevated concentrations of reduced gases such as CH₄ and NH₃ compared with the normal atmosphere, and reducing conditions are required in order to synthesise key compounds such as HCN and HCHO, fundamental to the generation of life (Navarro-González et al. 1996). Consequently, volcanic lightning could have been of significantly more evolutionary importance than ‘standard’ thunderstorm lightning in an early atmosphere.

For the terrestrial atmosphere, experiments generating discharges in gases of known composition have shown that volcanic lightning can fix nitrogen into the more reactive forms required for involvement with biological or early-life reactions (Navarro-González et al. 1998). For the atmosphere of Venus (96.5% CO₂, 3.5% N₂), thermodynamic modelling using the methodology of Martin et al. (2007) and temperatures characteristic of lightning discharges, suggests that a large (~0.1%) NO/N₂ ratio is produced. Thus, if volcanic lightning does indeed occur on Venus, discharges could convert a significant proportion of atmospheric equilibrated N₂ to NO.

Similar models for the martian atmosphere (95.3% CO₂, 2.7% N₂, 1.6% Ar, 0.13% O₂, 0.08% CO) yield NO/N₂ ratios that are close to those for Venus, even though the atmospheric pressures and oxygen contents are very different. Early martian volcanic gases are thought to have been more reduced than those of Earth (due to the presence of metallic Fe in Mars’ upper mantle), and to have contained more CH₄ and H₂ (Kuramoto 1997). Consequently, volcanic lightning could have been a significant source of fixed nitrogen and key molecules (e.g., HCN, a precursor for amino acids) relevant for the origins of life on early Mars (Navarro-González and Basiuk 1998; Segura and Navarro-González 2001, 2005). However, note that HCN and NO generation in discharges cannot be contemporaneous because different chemical conditions are required (reducing, for HCN and oxidising for NO). Phosphorous, another essential component of life, can also be reduced from non-reactive minerals such as fluorapatite into reactive phosphites by lightning (Glindemann et al. 1999; De Graaf and Schwartz 2000).

6 Future Measurements

Future research into the electrification of terrestrial volcanic plumes is likely to be driven by a requirement to further elucidate intra-plume processes (e.g. particle sedimentation or turbulence conditions), to further investigate the origins of life or to develop a possible remote sensing tool. All of these directions require the nature of macro-scale charge distribution to be understood better, for which many more eruptions need to be densely instrumented, with a variety of instrument types. For example, arrays of ground-based field meters should be augmented with simultaneous lightning detection and ash current measurements. Balloon- and rocket-based instruments (or possibly even instruments on model aircraft (Taddeucci et al. 2007)) should sample ash and aerosols through the plumes, including collecting data on their charges and measurements of the electric field. A sustained campaign of such deployments, integrated with detailed meteorological and volcanological observations, would undoubtedly extend understanding considerably, possibly allowing the relative importance of any distal-plume charging (i.e. thundercloud type) with respect to near-vent mechanisms to be demonstrated.

Once plumes have dispersed from the vent region and the larger particles have fallen out, the resulting dilute plumes of fine-grained particles can be difficult to detect. In particular, although these plumes remain a hazard to aircraft, pilots rely only on information sent

to them (often originating from satellite data) and their own observations to avoid plume encounters. It may be possible that electric potential gradients could be used as a remote sensing tool to augment existing satellite data in tracking dilute plumes. However, more needs to be understood about the lifetime of charges in plumes as well as their long-term distribution.

As exploration of the solar system continues, further opportunities exist to detect electrical effects of volcanism on other planets. As on Earth, discharges from eruptions are likely to pose a negligible hazard to craft (e.g. landers on Venus), particularly when compared with the causative eruptions. Remotely detecting volcanic activity through discharges alone is also likely to be extremely difficult because, in the absence of discharge location information, it would be hard to discount other non-volcanic sources of electrification; equally, however, remote electrostatic discharges on planets should not be assumed solely to arise from meteorological processes. Possibly the best opportunities to observe discharge phenomena exist on Io, where the characteristics and locations of the plumes are now relatively well known and visible or radio-frequency anomalies could be searched for. However, due to the near-zero pressure, it is likely that discharge phenomena would be very much more diffuse than on Earth, which while generating interesting or even characteristic signatures, would make them more difficult to detect.

7 Summary

Terrestrial volcanism produces electrically charged plumes in a variety of scenarios, with the charging linked to rapid water boiling and disruption (e.g. where lava enters the sea), the production of fine-grained particles during explosive fragmentation of magma, or both mechanisms during phreato-magmatic activity. Silicate particles produced in this manner are thought to be charged to their atmospheric limit and ash generally holds a net negative charge resulting from a small imbalance in particle charges of both polarities. The dominant charging mechanism is thought to be fractoemission, which also imparts a net opposite charge to the volcanic gas and aerosol. This charging is envisaged to occur dominantly in and near to the vent, but subsequent charge scavenging processes may significantly change initial charge distributions. Furthermore, subsequent charging processes may also operate, similar to those in thunderclouds and occurring as plumes age and disperse from the volcano, although their contribution has yet to be quantified.

Volcanic-related charging is likely to have occurred on other planets and is probably happening now on moons such as Io and Enceladus. However, Earth, with sufficient volatile content to drive explosive eruptions, water stable in all three states on the surface and in the atmosphere, and an atmospheric pressure insufficient to prevent explosive volcanism, yet sufficient to maintain large convective plumes, possesses all the qualities to maximise this process.

Acknowledgements We thank two anonymous reviewers whose constructive comments have helped to clarify the text.

References

- M.M. Abbas, D. Tankovic, P.D. Craven et al., *Planet. Space Sci.* **55**, 953 (2007)
- R. Anderson, S. Björnsson, D.C. Blanchard et al., *Science* **148**, 1179 (1965)
- P. Arason, *Geophys. Res. Abstr.* **7**, 05369 (2005).

- G.A. Bazilevskaya, I.G. Usoskin, E.O. Flückiger et al., *Space Sci. Rev.* (2008, this issue). doi:[10.1007/s11214-008-9339-y](https://doi.org/10.1007/s11214-008-9339-y)
- B. Bézard, C. de Bergh, *J. Geophys. Res.* **112**, E04 (2007) S07
- D.C. Blanchard, *Nature* **175**, 334 (1955)
- D.C. Blanchard, *J. Meteorol.* **383**, 15 (1958)
- D.C. Blanchard, *Nature* **201**, 1164 (1964)
- S. Björnsson, D.C. Blanchard, A.T. Spencer, *J. Geophys. Res.* **72**, 1311 (1967)
- P. Boschung, M. Glor, *J. Electrostat.* **8**, 205 (1980)
- B.T. Brady, G.A. Rowell, *Nature* **321**, 488 (1986)
- M. Brook, C.B. Moore, T. Sigurðsson, *J. Geophys. Res.* **79**, 472 (1974)
- J.L. Burch, J. Goldstein, W.S. Lewis et al., *Nature* **447**, 833 (2007)
- M.H. Burger, E.C. Sittler, R.E. Johnson, *J. Geophys. Res.* A06219 (2007)
- R. Büttner, B. Zimanowski, *Phys. Rev. E* **57**, 5726 (1998)
- R. Büttner, H. Röder, B. Zimanowski, *Appl. Phys. Lett.* **70**, 1903 (1997)
- R. Büttner, B. Zimanowski, H. Röder, *J. Geophys. Res.* **105**, 2819 (2000)
- R.J. Blong, *Volcanic Hazards: A Sourcebook on the Effects of Eruptions* (Academic Press, Sydney, 1984)
- S.N. Carey, H. Sigurdsson, *J. Volcanol. Geotherm. Res.* **7**, 7061 (1982)
- L.M. Carter, D.B. Campbell, B.A. Campbell, *J. Geophys. Res.* **111**, E06005 (2006)
- J.A. Cross, D. Farrer, *Dust Explosions* (Plenum, New York, 1982)
- W. Cornell, S. Carey, H. Sigurdsson, *J. Volcanol. Geotherm. Res.* **17**, 89 (1983)
- J.G. Dash, B.L. Mason, J.S. Wetzlaufer, *J. Geophys. Res.* **106**, 20395 (2001)
- R.M. De Graaf, A.W. Schwartz, *Orig. Life Evol. B* **30**, 405 (2000)
- S.J. Desch, J.N. Cuzzi, *Icarus* **143**, 87 (2000)
- J.T. Dickinson, E.E. Donaldson, M.K. Park, *J. Mater. Sci.* **16**, 2897 (1981a)
- J.T. Dickinson, E.E. Donaldson, D.B. Snyder, *J. Vac. Sci. Technol.* **18**, 238 (1981b)
- J.T. Dickinson, M.K. Park, E.E. Donaldson et al., *J. Vac. Sci. Technol.* **22**, 436 (1982)
- J.T. Dickinson, L.C. Jenson, A. Jahan-Latibari, *J. Vac. Sci. Technol. A* **2**, 1112 (1984)
- E.E. Donaldson, J.T. Dickinson, S.K. Bhattacharya, *J. Adhesion* **25**, 281 (1988)
- N.S. Duxbury, R.H. Brown, *Icarus* **125**, 83 (1997)
- Y. Enomoto, H. Hashimoto, *Nature* **346**, 641 (1990)
- S.A. Fagents, L. Wilson, *J. Geophys. Res.* **100**, 26327 (1995)
- W.M. Farrell, J.R. Marshall, S.A. Cummer et al., *J. Geophys. Res.* **111**, E11004 (2006)
- A. Flandes, *Geophys. Res. Lett.* **31**, L16802 (2004)
- R.A. Fogel, M.J. Rutherford, *Geochim. Cosmochim. Acta* **59**, 201 (1995)
- F. Freund, J. Non-Cryst. Solids **71**, 195 (1985)
- F. Freund, *J. Geophys. Res.* **105**, 11001 (2000)
- F. Freund, F. Battlo, R.C. LeRoy, *Eos. Trans. Am. Geophys. Union* **69**, 1300 (1988)
- C.N. Foley, M. Wadhwa, L.E. Borg et al., *Geochim. Cosmochim. Acta* **69**, 4557 (2005)
- J.S. Gilbert, S.J. Lane, R.S.J. Sparks et al., *Nature* **349**, 598 (1991)
- L.S. Glaze, S.M. Baloga, *J. Geophys. Res.* **107**, 5086 (2002)
- D. Glindemann, R.M. De Graaf, A.W. Schwartz, *Orig. Life Evol. B* **29**, 555 (1999)
- A. Graps, G. Jones, *Space Sci. Rev.* (2008, this issue)
- A.L. Graps, E. Grün, H. Svedhem et al., *Nature* **405**, 48 (2000)
- E. Grün, H.A. Zook, M. Baguhl et al., *Nature* **362**, 428 (1993)
- U. Grunewald, B. Zimanowski, R. Büttner et al., *J. Volcanol. Geotherm. Res.* **159**, 126 (2007)
- C.J. Hansen, L. Esposito, A.I.F. Stewart et al., *Science* **311**, 5766 (2006)
- R.G. Harrison, H. Tammet, *Space Sci. Rev.* (2008, this issue). doi:[10.1007/s11214-008-9356-x](https://doi.org/10.1007/s11214-008-9356-x)
- H. Hatakeyama, *J. Met. Soc. Jpn. II* **21**, 420 (1943). 2nd Report
- H. Hatakeyama, *J. Geomag. Geoelectr.* **1**, 48 (1949)
- H. Hatakeyama, K. Uchikawa, *Pap. Meteor. Geophys.* **2**, 85 (1952)
- J. Head, L. Wilson, *J. Geophys. Res.* **91**, 9407 (1986)
- R.P. Hoblitt, *J. Volcanol. Geotherm. Res.* **62**, 499 (1994)
- M. Horányi, *Annu. Rev. Astron. Astrophys.* **34**, 383 (1996)
- C.J. Horwell, P.J. Baxter, *Bull. Volcanol.* **69**, 1 (2006)
- M.R. James, Electric charge within volcanic plumes on Earth and Io. PhD thesis, Lancaster University, 1999
- M.R. James, S.J. Lane, J.S. Gilbert, *J. Geol. Soc. Lond.* **155**, 587 (1998)
- M.R. James, S.J. Lane, J.S. Gilbert, *J. Geophys. Res.* **105**, 16641 (2000)
- M.R. James, S.J. Lane, J.S. Gilbert, *J. Geophys. Res.* **107**, 2191 (2002)
- M.R. James, S.J. Lane, J.S. Gilbert, *J. Geophys. Res.* **108**, 2435 (2003)
- T.V. Johnson, A.F. Cook II, C. Sagan et al., *Nature* **280**, 246 (1979)
- S.J. Kargel, *Icarus* **100**, 556 (1992)

- S.W. Kieffer, in *Explosive Volcanism; Inception, Evolution, and Hazards*, ed. by F.M. Boyd (Nat. Acad. Sci., Washington, 1984)
- S.W. Kieffer, X. Lu, C.M. Bethke et al., *Science* **314**, 1764 (2007)
- K. Kikuchi, T. Endoh, *J. Meteor. Soc. Jpn.* **60**, 548 (1982)
- P. Kokelaar, C. Busby, *Science* **257**, 196 (1992)
- H. Krüger, D. Bindshadler, S.F. Dermott et al., *Planet. Space Sci.* **54**, 879 (2006)
- K. Kuramoto, *Phys. Earth Planet. Inter.* **100**, 3 (1997)
- S.J. Lane, J.S. Gilbert, *Bull. Volcanol.* **54**, 590 (1992)
- S.J. Lane, J.S. Gilbert, A.J. Kemp, Bull. in 8th Report of Geophysical and Geochemical Observations at Sakurajima Volcano (1995), p. 105
- J.S. Lynch, G. Stephens, in *Fire and Mud: Eruptions and Lahars on Mount Pinatubo, Philippines*, ed. by C.G. Newhall, S. Punongbayan (University of Washington Press, Seattle, 1996)
- R.S. Martin, T.A. Mather, D.M. Pyle, *Geochim. Cosmochim. Acta* **71**, 3673 (2007)
- T.A. Mather, R.G. Harrison, *Surv. Geophys.* **27**, 387 (2006)
- D.A. Mazilu, A.L. Ritter, *Wear* **258**, 1384 (2005)
- S.R. McNutt, C.M. Davis, *J. Volcanol. Geotherm. Res.* **102**, 45 (2000)
- H.Y. McSweeney, T.L. Grove, R.C.F. Lentz et al., *Nature* **409**, 487 (2001)
- T. Miura, T. Koyaguchi, Y. Tanaka, *Geophys. Res. Lett.* **23**, 1789 (1996)
- T. Miura, T. Koyaguchi, Y. Tanaka, *Bull. Volcanol.* **64**, 75 (2002)
- G.J. Molina, M.J. Furey, A.L. Ritter et al., *Wear* **249**, 214 (2001)
- T. Nagata, K. Hirao, M. Fukushima et al., *Bull. Earthq. Res. Inst.* **24**, 221 (1946)
- K. Nakayama, *Surf. Coat. Technol.* **188**, 599 (2004)
- K. Nakayama, H. Hashimoto, *Tribol. Trans.* **35**, 643 (1992)
- R. Navarro-González, V.A. Basiuk, in *Exobiology: Matter Energy and Information in the Origin and Evolution of Life in the Universe*, ed. by J. Chela-Flores, F. Raulin (Springer, New York, 1998)
- R. Navarro-González, V.A. Basiuk, M. Rosenbaum, in *Chemical Evolution: Physics of the Origin and Evolution of Life*, ed. by J. Chela-Flores, F. Raulin (Kluwer, Netherlands, 1996)
- R. Navarro-González, M.J. Molina, L.T. Molina, *Geophys. Res. Lett.* **25**, 3123 (1998)
- G. Neukum, R. Jaumann, H. Hoffmann et al., *Nature* **432**, 971 (2004)
- O.V. Nikolaeva, A.A. Ariskin, *J. Geophys. Res.* **104**, 18889 (1999)
- S.J. Peale, P. Cassen, R.T. Reynolds, *Science* **203**, 892 (1979)
- F.A. Perret, *The Vesuvius Eruption of 1906* (Carnegie Institute of Washington, Washington, 1924)
- F. Postberg, S. Kempf, R. Srama et al., *Icarus* **183**, 122 (2006)
- C. Pounder, *J. Phys. D* **5**, 753 (1972)
- C. Pounder, Investigation of a reproducible boiling phenomenon with relevance to volcanic lightning. Ph.D. Thesis, Open University, 1978
- C. Pounder, *J. Electrostat.* **9**, 177 (1980a)
- C. Pounder, *Weather* **35**, 357 (1980b)
- R. Reiter, *J. Geophys. Res.* **99**, 10807 (1994)
- C.A. Robinson, G.D. Thornhill, E.A. Parfitt, *J. Geophys. Res.* **100**, 11755 (1995)
- W.I. Rose, D.J. Delene, D.J. Schnelder et al., *Nature* **375**, 477 (1995)
- C.P.R. Saunders, *Space Sci. Rev.* (2008, this issue). doi:[10.1007/s11214-008-9345-0](https://doi.org/10.1007/s11214-008-9345-0)
- M. Sato, *Proc. Lunar Planet. Sci. Conf.* **10**, 311 (1979)
- S. Scollo, P. del Carlo, M. Coltelli, *J. Volcanol. Geotherm. Res.* **160**, 147 (2007)
- A. Segura, R. Navarro-González, *Adv. Space Res.* **27**, 201 (2001)
- A. Segura, R. Navarro-González, *Geophys. Res. Lett.* **32**, L05203 (2005)
- J.W. Sheldon, *J. Phys. D* **7**, 91 (1974)
- B.A. Smith, E.M. Shoemaker, S.W. Kieffer et al., *Nature* **280**, 738 (1979)
- R.K. Sorem, *J. Volcanol. Geotherm. Res.* **13**, 63 (1982)
- R.S.J. Sparks, M.I. Bursic, S.N. Carey et al., *Volcanic Plumes* (Wiley, Chichester, 1997)
- F. St-Laurent, J.S. Derr, F.T. Freund, *Phys. Chem. Earth* **31**, 305 (2006)
- R.G. Strom, N.M. Schneider, in *Satellites of Jupiter*, ed. by D. Morrison (Univ. Arizona Press, Tucson, 1982)
- J. Taddeucci, P. Scarlato, D. Andronico et al., *Eos, Trans. Amer. Geophys. Union* **88**, 253 (2007)
- A. Takeuchi, H. Nagahama, *Phys. Earth Planet. Inter.* **130**, 285 (2002)
- A. Takeuchi, B.W.S. Lau, F.T. Freund, *Phys. Chem. Earth* **31**, 240 (2006)
- R.J. Thomas, P.R. Krehbiel, W. Rison et al., *Science* **315**, 1097 (2007)
- E.R. Williams, S.R. McNutt, in *Recent Progress in Lightning Physics*, ed. by C. Pontikis (Research Signpost, Kerala, 2005)
- L. Wilson, J.W. Head, *J. Geophys. Res.* **86**, 2971 (1981)
- L. Wilson, J.W. Head, *Rev. Geophys.* **32**, 221 (1994)
- L. Wilson, J.W. Head, *J. Volcanol. Geotherm. Res.* **163**, 83 (2007)
- L. Wilson, K. Keil, *Meteorit. Planet. Sci.* **32**, 813 (1997)
- L. Wilson, S. Self, *J. Geophys. Res.* **85**, 2567 (1980)
- L. Wilson, E.D. Scott, J.W. Head, *J. Geophys. Res.* **106**, 1423 (2001)

Electrical Activity and Dust Lifting on Earth, Mars, and Beyond

Nilton O. Renno · Jasper F. Kok

Originally published in the journal Space Science Reviews, Volume 137, Nos 1–4.
DOI: [10.1007/s11214-008-9377-5](https://doi.org/10.1007/s11214-008-9377-5) © Springer Science+Business Media B.V. 2008

Abstract We review electrical activity in blowing sand and dusty phenomena on Earth, Mars, the Moon, and asteroids. On Earth and Mars, blowing sand and dusty phenomena such as dust devils and dust storms are important geological processes and the primary sources of atmospheric dust. Large electric fields have been measured in terrestrial dusty phenomena and are predicted to occur on Mars. We review the charging mechanisms that produce these electric fields and discuss the implications of electrical activity to dust lifting and atmospheric chemistry. In addition, we review theoretical ideas about electric discharges on Mars. Finally, we discuss the evidence that electrostatics is responsible for dust transport on the Moon and asteroids.

Keywords Saltation · Dust lifting · Dust electrification · Electrostatics · Electric discharges

1 Introduction

Mineral dust aerosols affect climate by absorbing and scattering radiation (Myhre and Stordal 2001; Fenton et al. 2007). On Earth, dust aerosols also play an important role in cloud formation by serving as cloud condensation and ice nuclei (DeMott et al. 2003). Indeed, the ‘climate forcing’ produced by the interactions of radiation with dust and clouds are among the most uncertain processes in climate change predictions (IPCC 2007). Part of this uncertainty arises from the limited ability of current models to accurately simulate the quantity and size distribution of dust lifted from the surface (Cakmur et al. 2006).

Atmospheric dust aerosols generally have diameters smaller than a few microns (DeMott et al. 2003) and therefore are subject to large interparticle forces that prevent them from being directly lifted by wind (Greeley and Iversen 1985; Shao and Lu 2000; Merrison et al.

N.O. Renno (✉) · J.F. Kok
Atmospheric, Oceanic, and Space Sciences, University of Michigan, Ann Arbor, MI, USA
e-mail: renno@umich.edu

N.O. Renno · J.F. Kok
Applied Physics Program, University of Michigan, Ann Arbor, MI 48109, USA

2007). On Earth, dust aerosols are predominantly lifted into the air by saltation, a process by which larger sand particles are moved by wind and bounce on the surface, ejecting the smaller, harder to lift, dust particles (aerosols) into the air (Bagnold 1941). Saltation lifts dust in blowing sand, dusty plumes, dust devils, and dust storms. Moreover, both on Earth and Mars saltation is an important geological process that leads to the formation of sand dunes and the erosion of geological features.

The lifting of dust aerosols on Mars is still poorly understood, but as on Earth it is possibly caused mainly by saltation (Greeley et al. 2002). Other dust lifting mechanisms include the breakup of low-density aggregates of dust particles (Merrison et al. 2007), and lifting aided by moving low-pressure centers of dust devils (Greeley et al. 2003).

The understanding of saltation and dusty phenomena is thus important to a wide range of atmospheric and geological processes on Earth, Mars and beyond. Recent studies have shown that on Earth, saltation and dusty phenomena can be highly electrified, with electric fields (E -fields) exceeding 100 kV/m (Stow 1969; Schmidt et al. 1998; Renno et al. 2004; Jackson and Farrell 2006; Kok and Renno, 2006, 2008). Theory and laboratory experiments suggest that these E -fields reduce the wind stress necessary to initiate saltation, thereby increasing the concentration of saltating particles at a given wind speed (Kok and Renno, 2006, 2008). Moreover, electric forces arising from sand electrification can be strong enough to significantly affect the motion of saltating particles (Schmidt et al. 1998; Zheng et al. 2003). Indeed, their inclusion in numerical models of saltation can resolve observed discrepancies between measurements and theory (Kok and Renno 2008; Zheng et al. 2006).

On Mars, electric forces might also play a role in dust lifting by reducing the threshold wind stress necessary to initiate saltation (Kok and Renno 2006). Moreover, several studies suggest that E -fields generated in Martian dust storms can cause electric discharges (Eden and Vonnegut 1973; Melnik and Parrot 1998; Krauss et al. 2006; Farrell et al., 2003, 2006a; Zhai et al. 2006; Kok and Renno 2008). The possible occurrence of large E -fields and the associated electric discharges has potentially important implications for Martian atmospheric chemistry, human exploration, habitability (Atreya et al. 2006; Delory et al. 2006), and even the possible development of life (Miller 1953). In particular, E -fields exceeding \sim 10 kV/m might produce large quantities of hydrogen peroxide, a strong oxidant that could make the martian surface inhospitable to life as we know it (Atreya et al. 2006).

This article reviews electrical activity in dusty phenomena on Earth, Mars, the Moon, and asteroids. In the next section, we review measurements of electrification in saltation and dusty phenomena, discuss the charge transfer between colliding sand/dust particles, and describe the effects of the resulting E -fields on dust lifting, possible electric discharges, and atmospheric chemistry on both Earth and Mars. Finally, in Sect. 3, we discuss possible electrostatic dust lifting on celestial bodies without atmospheres, such as the Moon and asteroids.

2 Dust/Sand Electrification and Its Effects on Dust Lifting and Atmospheric Chemistry

The electrification of blowing sand and dusty phenomena is caused by charge transfer during collisions among saltating sand particles, between saltating sand particles and the ground, and between sand particles and dust particles (Harper 1967; Renno et al. 2004; Kok and Renno 2008). The physical mechanism that governs this charge transfer is not

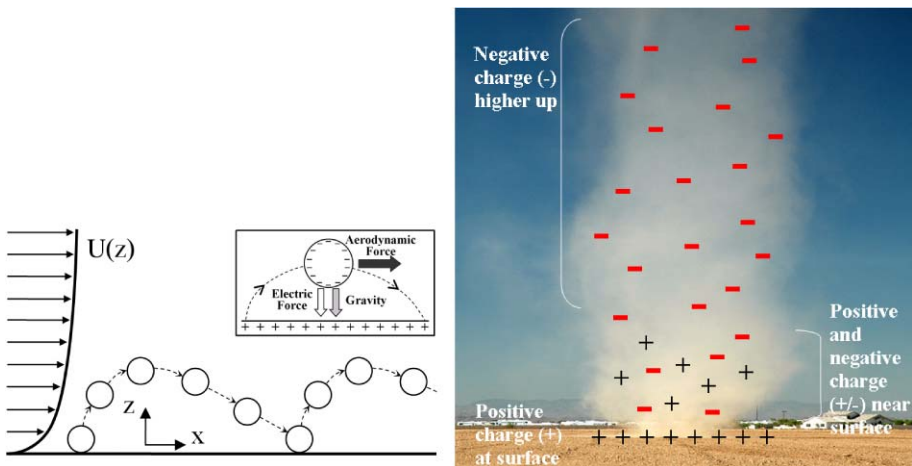


Fig. 1 (a) Schematic of saltation, showing the logarithmic wind profile $U(z)$ to the left of a sand particle propelled by the wind and bouncing along the surface. Saltating particles absorb horizontal momentum from the wind, which is partially converted into vertical momentum upon collision with the soil bed. The inset illustrates the charge distribution in saltation in the absence of suspended dust, and shows the force diagram of a negatively charged sand grain saltating over the positively charged soil surface. After Kok and Renno (2008). (b) Hypothesized charge distribution in dusty phenomena (i.e., a dust storm or dust devil). Collisions with saltating particles are expected to charge the soil surface positively, and dust particles negatively (see main text). The net charge held by saltating particles thus depends on the relative frequency of collisions with the surface and suspended dust, and can probably be both negative and positive. The small dust particles are transported upwards through convection or turbulent diffusion, while the larger and heavier saltating particles stay closer to the surface. This charge separation can produce large electric fields

clear (see Sect. 2.2), but measurements indicate that, on average, the larger particle becomes positively charged with respect to the smaller particle (Freier 1960; Schmidt et al. 1998; Inculet et al. 2006; Duff and Lacks 2008). Since the ground can be interpreted as the surface of an infinitely large particle, it is expected to charge positively with respect to saltating particles (Kok and Renno 2008). This is consistent with measurements of upward-pointing near-surface E -fields in saltation (Schmidt et al. 1998; Zheng et al. 2003; Qu et al. 2004), dust devils (Freier 1960; Renno et al. 2004), dust storms (Stow 1969), and saltating snow (Schmidt et al. 1999). While the ground is thus expected to charge positively in dusty phenomena, the net charge of saltating particles depends on the relative frequencies of collisions with the surface (which charges them negatively) and suspended dust particles (which charges them positively). In the absence of suspended dust particles, saltating particles are therefore expected to charge negatively (Zheng et al. 2003; Kok and Renno 2008).

After undergoing collisions, the smaller (negatively charged) dust particles can be lifted by turbulent eddies and updrafts, while the larger particles (whose charge can be either positive or negative) stay close to the positively charged surface. Figure 1 shows the hypothesized charge distribution in saltation and dusty phenomena and is based on the measurements reviewed in the next section.

2.1 Measurements of Electrification in Saltation and Dusty Phenomena

Electrification in blowing sand (saltation), dust devils, and dust storms has been studied in laboratory and field experiments. These studies have been performed under Earth ambient

conditions, but they also serve as analog studies of the electrification of saltation and dusty phenomena on other planetary bodies, especially Mars (Farrell et al. 2004; Jackson and Farrell 2006).

Field measurements by Schmidt et al. (1998) found E -fields of up to 160 kV/m in saltation. These E -fields were found to be upward-pointing, indicating negatively charged saltating particles over a positively charged surface (Fig. 1a). Surprisingly, Schmidt et al.'s simultaneous measurement of particle charge found saltating particles at 5 cm above the surface to be positively charged, in disagreement with their finding of upward-pointing E -fields uniformly increasing towards the surface. However, wind-tunnel studies by other investigators found negatively charged saltating particles, and upward-pointing E -fields in saltation (Zheng et al. 2003; Qu et al. 2004).

A significant number of measurements of E -fields have also been made in dust devils. Freier (1960) made the first reliable measurement of the E -fields in dust devils. He used a grounded electric field mill to measure the E -field produced by a dust devil tens of meters away and found a significant deviation from the fair-weather value. This result is consistent with the idea that dust devils have a negative dipole moment (i.e., negative over positive charges). Freier's measurements were confirmed by Crozier (1964, 1970). Field measurements by Farrell et al. (2004) and Renno et al. (2004) also found negative charges aloft, with measured E -fields exceeding the instrument range of 4 and 20 kV/m respectively, well before the dust devil passed over their sensors. More recently, Jackson and Farrell (2006) measured the horizontal E -field in dust devils and found values of up to 120 kV/m.

Though detailed measurements of E -fields in dust devils are numerous, fewer measurements have been made in dust storms. There is anecdotal evidence of significant electrification of dust storms observed during the 'dust bowl' on the American Great Plains in the 1930s (Keith 1944). Later measurements in the Sahara found both downward (Demon et al. 1953) and upward-pointing (Stow 1969) E -fields, with values of 1–15 kV/m at about 1 m above the ground, increasing to 50–200 kV/m at the ground (Stow 1969). Kamra (1972) made a series of measurements in dust storms in the southwestern deserts of the United States and found both upward and downward-pointing E -fields with magnitudes similar to those measured by Demon et al. (1953) and Stow (1969). He also reported measurements of both positive and negative space charges at a height of 1.25 m. More recently, Williams et al. (2008) reported measurements during dust storms ('haboobs') in the Sahel and also found E -fields pointing both up and downwards, although most measurements indicated upward-pointing fields.

In summary, most measurements in saltation, dust devils and dust storms show upward pointing E -fields. These measurements support the hypothesis that saltating particles charge negatively upon collision with the ground, and that dust particles become negatively charged after collisions with larger saltating particles (Fig. 1). However, the situation appears to be more complex in dust storms, with E -fields pointing both up and downwards (Kamra 1972; Williams et al. 2008). This apparent discrepancy between measurements in saltation and dust devils on the one hand, and measurements in dust storms on the other, stresses the need for a better understanding of the charging processes involved in dust/sand electrification. The current state of knowledge of this charging process is reviewed in the next section.

2.2 Charge Transfer in Colliding Dust/Sand Particles

While the electrification of blowing sand and dusty phenomena is well documented (see Sect. 2.1), the physical process responsible for it is still a puzzle. It is well established that two objects get charged when rubbed against each other, and that the charge transfer depends on the difference in contact potential between their materials (Harper 1967;

Desch and Cuzzi (2000). Thus, little or no charge transfer is expected when particles of identical material such as sand and/or dust collide with each other. Since measurements show that significant charging does occur, a mechanism different than the ‘traditional’ contact electrification (Harper 1967) must play an important role in dust/sand electrification.

Lowell and Truscott (1986) proposed a heuristic model for charge transfer during collisions of particles of similar dielectric materials. According to their model, electrons confined in the high-energy states of one particle tunnel to more abundant empty low-energy levels on the other particle when they rub against each other. Thus, the particle that rubs a larger surface area with the other loses more electrons and therefore charges positively. Thus, ‘asymmetric rubbing’ during collisions of smaller with larger particles leads to a net transfer of electrons from the larger to the smaller particles (Kok and Renno 2008). This prediction is consistent with measurements in blowing sand and dusty phenomena.

An alternative, but related model was proposed by Duff and Lacks (2008). They used particle dynamics simulations to show that the mere presence of confined high-energy states in insulators can lead to the transfer of electrons from larger to smaller particles, even without explicit ‘asymmetric rubbing.’ The physical reason for the charge transfer is that, after multiple collisions in which high-energy electrons from one particle are transferred to empty, low-energy, states on the other particle, the smaller particles lose a larger fraction of its electrons than the larger. The ability of smaller particles to give up electrons is therefore reduced, such that the smaller particles become negatively charged after multiple collisions.

Though the hypotheses put forth by both Lowell and Truscott (1986) and Duff and Lacks (2008) are promising, they have not been rigorously tested yet. In the absence of a clear physical understanding of the mechanism driving ‘collisional charge transfer’ between particles, various simple parameterizations have been proposed to describe the charging of colliding sand and/or dust particles. Melnik and Parrot (1998) proposed that when sand/dust particles collide with each other, the amount of negative charge that the smaller particle acquires depends on its radius, while the larger particle acquired an equal and opposite amount of positive charge. Though appealing in its simplicity, this idea is problematic because it does not take into account pre-existing charges on the colliding particles and therefore poses no limit to the amount of charge transferred after many collisions. Moreover, the amount of charge transferred per collision is likely too large to be realistic (Zhai et al. 2006). Desch and Cuzzi (2000) developed a more sophisticated parameterization in which the charge transferred during each collision depends on the pre-existing charge, the particle radii, and the difference in contact potential between them. Based on previous research summarized by Harper (1967), they proposed that

$$q_S = C_1(q_S + q_L) - C_2 \Delta \Phi; \quad (1a)$$

$$q_L = (1 - C_1)(q_S + q_L) + C_2 \Delta \Phi, \quad (1b)$$

where q_S and q_L are the charges of the smaller and larger particles before a collision, q'_S and q'_L are the charges after a collision, $\Delta \Phi$ is the difference in particle contact potential, and C_1 and C_2 are functions of the mutual capacitances of the two particles, as defined by (5)–(10) of Desch and Cuzzi (2000). As noted above, the second term in (1a) and (1b) is zero for particles of similar composition such as typical sand/dust particles because $\Delta \Phi = 0$. Therefore, this model is not technically applicable to sand/dust electrification, as it predicts that no charge is transferred during collisions of uncharged particles of identical material. This led Farrell et al. (2003) to postulate a contact potential difference between sand and dust. Kok and Renno (2008) expanded upon this idea and proposed an *effective* potential

difference $\Delta\Phi_{\text{eff}}$ between particle pairs of similar composition but different sizes,

$$\Delta\Phi_{\text{eff}} = S(r_L - r_S)/(r_L + r_S), \quad (2)$$

where S (in volts) is a physical parameter that scales the collisional charge transfer, and r_S and r_L are the radii of the smaller and larger particles. Using a detailed numerical model of saltation, Kok and Renno (2008) calibrated the parameter S with E -field measurements in saltation, finding $S = 6 \pm 4$ volts. Since typical dust/sand particles are of identical material, this *effective* potential difference is thus likely not due to an actual difference between the contact potentials of the colliding particles. Rather, the physical mechanism that drives the transfer of charge (such as the ‘asymmetric rubbing’ described above) can be expressed as an *effective* potential difference, and therefore the Desch and Cuzzi model can be used to describe the charge transfer.

The simple model described by (1) and (2) has a functional form consistent with observations—smaller particles acquire net negative charge during collisions with larger particles, and the charge transfer increases with the relative difference in particle size. However, this model does not account explicitly for other variables that likely affect the charge transfer such as temperature, humidity (Guardiola et al. 1996) and particle speed (Poppe and Schrapler 2005). Moreover, it assumes that particles get fully charged after a single collision. That is, multiple collisions between two particles yield the same final charges as only one collision, which is probably not realistic (Kwetkus et al. 1992). Detailed measurements of the collisional charging of similar materials are thus required to facilitate the formulation of realistic charging parameterizations.

2.3 The Effects of Electric Forces on Saltation and Dust Lifting

The electrification of blowing sand and dusty phenomena affects saltation and dust lifting. First, electric forces affect the trajectories of saltating particles, as first suggested by Schmidt et al. (1998) and Zheng et al. (2003). Indeed, the presence of electric forces might explain the puzzling discovery that the height to which saltating particles bounce does not increase with wind speed (Greeley et al. 1996; Namikas 2003). This is in direct contradiction with saltation theory (Bagnold 1941; Owen 1964), which predicts that the height of the saltation layer increases markedly with wind speed. A possible explanation for this discrepancy between theory and measurements is the presence of downward-pointing electric forces on the saltating particles as illustrated in Fig. 1a (Kok and Renno 2008). As the wind speed increases, so does the concentration of saltating particles and therefore the E -field. Thus, the downward-pointing electric forces increase with wind speed and counteract the increased momentum that saltating particles obtain from the wind. Kok and Renno (2008) show that the inclusion of electric forces in saltation models can resolve the discrepancy between theory and measurements (Fig. 2). Detailed numerical simulations of saltation by Zheng et al. (2006) also showed better agreement with wind-tunnel measurements by Shao and Raupach (1992) and Rasmussen and Mikkelsen (1998), when electrostatic forces were included in the model.

A second effect of electrification on saltation and dust lifting is that electric forces facilitate the lifting of particles from the surface by wind, leading to an increase in the concentration of saltating particles. This occurs because the negatively charged cloud of saltating particles attracts the positively charged particles on the surface, facilitating their lifting by wind and ejection into the air by saltating particles. Kok and Renno (2006) derived an expression

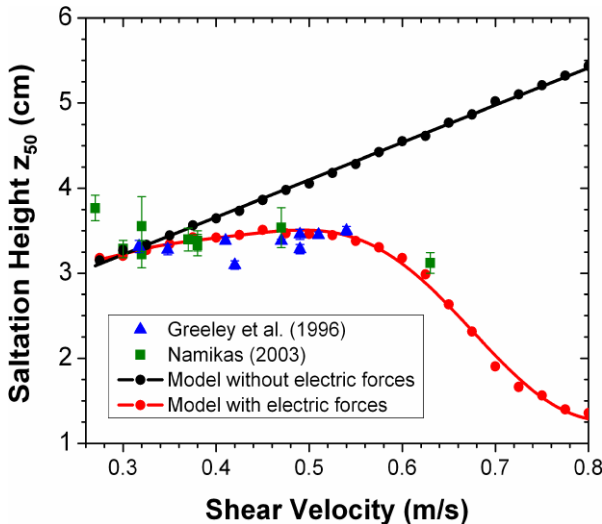


Fig. 2 Numerical study by Kok and Renno (2008) of the dependence of the saltation height z_{50} on the wind shear velocity. z_{50} is defined as the height below which 50% of the mass transport in saltation occurs, and the wind shear velocity is the square root of the wind shear stress divided by the air density. Classical saltation theory predicts that z_{50} increases strongly with shear velocity (Bagnold 1941; Owen 1964), which the numerical model also predicts when electric forces are not included (black circles). However, field measurements [squares Namikas (2003) and triangles Greeley et al. (1996)] show that z_{50} remains approximately constant with shear velocity. The inclusion of sand electrification in the numerical model (red circles) apparently resolves the discrepancy between theory and measurements

for the threshold shear velocity required to lift particles from the surface that includes the effect of electric forces,

$$u_{\text{thr}}^* = \sqrt{\frac{A_n}{\rho_{\text{air}}} \left(\rho_{\text{part}} g d + \frac{6\beta G}{\pi d} - \frac{8.22 \varepsilon_0 E_{\text{surf}}}{c_s} \right)}, \quad (3)$$

where $A_n \approx 0.0123$ is a dimensionless parameter that scales the aerodynamic forces (Shao and Lu 2000), ρ_{air} and ρ_{part} are the densities of air and of soil particles, g denotes the gravitational acceleration, d is the average size of the surface grains, c_s is a dimensionless correction factor for the non-sphericity of soil particles, β scales the soil cohesive forces and lies in the range of 10^{-5} to 10^{-3} kg/s², G is a geometric parameter that depends on the bed stacking and is of order 1 (Shao and Lu 2000), ε_0 is the electric permittivity, E_{surf} is the surface E -field, and the shear velocity $u^* = \sqrt{\tau/\rho_{\text{air}}}$ is a measure of the wind shear stress τ . Kok and Renno (2008) use (3) to parameterize the effect of electric forces on particle lifting in their model of saltation and find that electric forces can substantially increase the concentration of saltating particles (see their Fig. 4). They also find that the lower near-surface wind speed (due to the reduction of the surface shear stress through (3)) leads to a decrease in the velocity of the saltating particles. Thus the simulations of Kok and Renno predict that electrification leads to an increase in saltating particles impacting the soil, but that the saltating particles have smaller speeds than in the absence of electric forces. The effect of the combination of these two processes on the ejection of dust aerosols is unclear and needs to be investigated further.

In addition to aiding aerodynamic lifting, electric forces can also directly lift particles from the surface. Kok and Renno (2006) derived an expression for the threshold E -field

necessary to lift sand particles by the action of electric forces alone,

$$E_{\text{thr}}(d) = \sqrt{c_s \left(\frac{\beta}{1.37\pi\varepsilon_0 d} + \frac{\rho_{\text{part}} dg}{8.22\varepsilon_0} \right)}. \quad (4)$$

Kok and Renno (2006) found the E_{thr} for sand particles to be around 175–250 kV/m, which is at the upper range of the ground-level E -fields measured in saltation and dusty phenomena (see Sect. 2.1).

As summarized above, significant progress has been made in assessing and quantifying the effects of electrification on saltation and dust lifting on Earth. However, the importance of electric forces to saltation and dust lifting on Mars remains unclear, especially because E -fields on Mars are probably limited by the relatively low breakdown E -field of ~ 25 kV/m (Melnik and Parrot 1998). Thus, electrification is probably not as important to Martian saltation as it is for terrestrial analogs, but the possible occurrence of electric discharges in Martian dusty phenomena could be highly significant. The unique thermodynamic conditions created by electric discharges could have significant effects on atmospheric chemistry (Miller 1953; Schumann and Huntrieser 2007). Experiments (Eden and Vonnegut 1973; Krauss et al. 2006) have clearly demonstrated the potential of electrified dust and sand to produce discharges in the thin Martian atmosphere. Simple numerical studies generally confirm these experimental results. Melnik and Parrot (1998) were the first to numerically investigate the generation of E -fields in Martian dust storms and predicted that electric discharges are readily produced, although their charge transfer model was probably not realistic (see above). More recently, Renno et al. (2004), Farrell et al. (2003, 2006a), and Zhai et al. (2006) developed simple models of the E -fields in terrestrial and Martian dust devils. These models also suggest the occurrence of electric discharges in Martian dusty phenomena.

In addition to electric discharges, increases in the atmospheric conductivity can also limit the bulk E -fields on Mars. A recent study by Delory et al. (2006) found that E -fields exceeding 5 kV/m accelerate free electrons to energies sufficiently large to ionize CO₂ and H₂O molecules. These additional ions lead to large increases in the air conductivity that can reduce the charge in sand and dust particles, thus also limiting the E -fields in Martian dusty phenomena. Moreover, the production of energetic electrons by E -fields (Delory et al. 2006) has potentially important effects on Martian atmospheric chemistry, as these energetic electrons can catalyze chemical reactions that would not otherwise occur.

2.4 An Example of the Effects of Electric Fields on Atmospheric Chemistry

The planetary science community was surprised that no trace of organics was found at the surface of Mars by the Viking Gas Chromatograph Mass Spectrometer (GCMS) experiments. This was a surprise because meteorites and space dust bring complex organics to the surface of Mars. Indeed, meteorites alone deliver approximately 300 g s⁻¹ of micrometeoritic dust to Mars (Flynn 1996), of which about 3% is organic material. More recently, the Mars Express Planetary Fourier Spectrometer (Formisano et al. 2004), and ground-based measurements (Krasnopolsky et al. 2004; Mumma et al. 2004) found trace amounts of methane in the martian atmosphere. These recent findings suggest the possibility of extant or extinct life on Mars. However, chemolithotrophic microbial colonies are only one of several possible sources of methane or more complex organic molecules (Atreya et al. 2007). Indeed, serpentinization at low temperatures and involving the hydration of ultramafic silicates could be just as effective in producing methane (Atreya et al. 2007).

An understanding of potential sinks of methane and other organics on Mars is important for constraining their sources. Oxidizers such as hydrogen peroxide can destroy organics at the surface (Oyama et al. 1977). Hydrogen peroxide (H_2O_2) is produced by photochemical processes (Atreya and Gu 1994; Nair et al. 1994), and it was recently detected on Mars (Encrenaz et al. 2003, 2004; Clancy et al. 2004). The abundance of H_2O_2 was observed to vary between 20 ppbv and 40 ppbv around the planet (Encrenaz et al. 2004), in agreement with predictions of photochemical models at the season of the observations. At the surface, the concentration of hydrogen peroxide is estimated to vary between 1 ppm (Zent and McKay 1994) and 250 ppm (Mancinelli 1989), on the basis of the reactivity of the surface measured by the Viking Gas Exchange experiment. A problem with these estimates is that this H_2O_2 abundance is too small to efficiently remove organics from the martian surface. Interestingly, laboratory studies also show that, even with 100–1000 times larger concentrations of H_2O_2 the surface would not be sterilizing (Mancinelli 1989). Therefore, a substantially larger concentration of hydrogen peroxide or others oxidants are necessary to explain the lack of detection of organics in the martian soil. Atreya et al. (2006) showed that electric fields in excess of 20 kV/m in dust storms can produce more than 100 times the amount of hydrogen peroxide produced by photochemical processes. Farrell et al. (2006b) show that the electric fields predicted in Martian dust storms can directly dissociate methane.

3 Other Dust Electrification Processes and Their Effect on Dust Lifting

3.1 Dust Lifting on the Moon

The Surveyor-6 and 7 Landers photographed bright glows along the western lunar horizon after sunset (Rennilson 1968; Criswell 1973). This horizon glow (HG) follows the contour of surface features such as rocks (Fig. 3). The HG usually persists for ~90 min after sunset (Gault et al. 1968a, 1968b). It is not polarized (Shoemaker et al. 1968) and extends vertically 3 to 30 cm above the surface, ruling out the idea that it is caused by secondary ejecta from the impact of micrometeorites (Criswell 1973). Moreover, the HG is not due to solar corona because it is much brighter and is parallel to the horizon, not elliptical like the corona. Since the Surveyor cameras are sensitive to light at wavelengths between 0.4 and 0.6 μm , scattering at these wavelengths must cause the HG.

The Lunar Ejecta And Meteorite (LEAM) Experiment was designed to measure the impact of micrometeorites and their hypervelocity ejecta (Berg et al. 1976). However, most

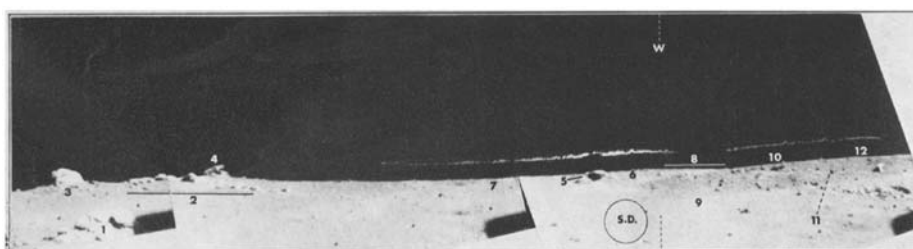


Fig. 3 Composite of morning and evening (about 1 hour after sunset) images of the western lunar horizon taken by the Surveyor-7 Lander. The horizon glow (HG) is probably the result of forward scattering by soil regolith particles of ~10 μm at concentrations of ~50 particles/ cm^3 levitating between ~3 and 30 cm above the surface (Criswell 1973). After Rennilson and Criswell (1974)

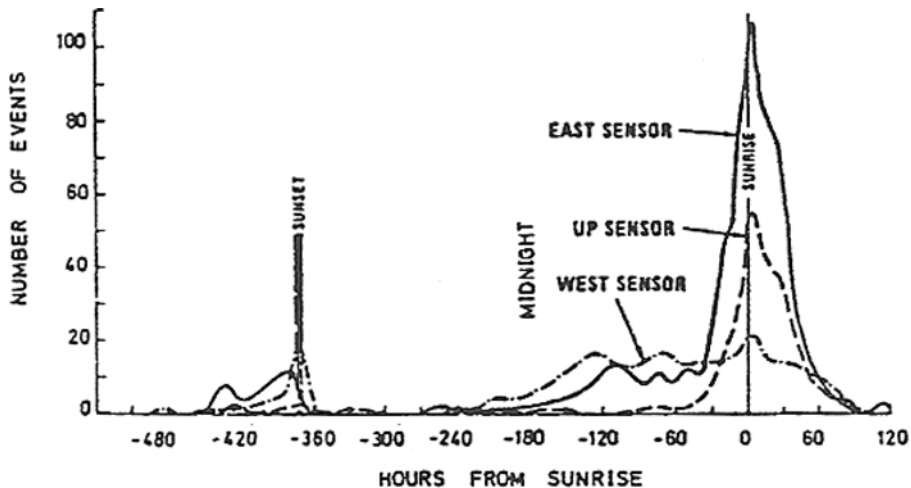


Fig. 4 Number of particle impacts (events) on the LEAM instrument sensors. Hypervelocity impacts from micrometeorites were rare, but impacts of particles with velocities of up to 1 km/s were detected. After Berg et al. (1976)

impacts detected were not from hypervelocity particles, and they occurred at the terminator as illustrated in Fig. 4. Stubbs et al. (2006) suggests that most of the impacts detected by the LEAM sensors were from particles lifted from the surface of the Moon by electrostatic forces. They hypothesized that electric fields eject highly charged particles from the surface. Then, the particles follow ballistic trajectories and return to the surface (Vondrak et al. 2005; Stubbs et al. 2006). The Lunohod-2 astro-photometer showed that the “twilight” lunar sky is 20 times brighter at visible wavelengths than expected from starlight alone (Severny et al. 1975). This suggests that dust particles levitating above the Moon’s surface scatter solar light and make the sky brighter. The observation of crepuscular rays at the terminator by Apollo astronauts provides further evidence of dust lifting on the Moon (McCoy 1976). These lunar crepuscular rays are probably caused by the scattering of sunlight by small dust particles with diameters of $\sim 0.2 \mu\text{m}$ at altitudes ranging from 1 to 100 km (Berg et al. 1976).

Rennilson and Criswell (1974) estimates that the HG can be explained by forward scattering from particles with diameters of $\sim 10 \mu\text{m}$ levitating a few cm above the surface. Moreover, they estimate that the concentration of levitating particles necessary to explain the HG is 7 orders of magnitude larger than what is ejected by the impact of micrometeorites. Indeed, they suggest that electrostatic forces eject these particles from the surface and keep them levitating a few cm above the surface.

Both intense solar radiation and the solar wind turn the lunar surface into a complex plasma environment (Manka 1973; Stubbs et al. 2006; Farrell et al. 2007). Surface particles are charged by photoelectric emission, impingement of electrons and ions, and secondary ejection of electrons from the lunar regolith by the impact of energetic particles. Photoemission dominates the current budget on the dayside and charges the surface positively, leading to positive surface potentials of a few volts (Manka 1973; Freeman and Ibrahim 1975; Stubbs et al. 2006; Farrell et al. 2007). On the nightside, electron currents from the wake of the solar wind are much larger than ion currents and the surface charges negatively. Moreover, the plasma Debye length, a characteristic length-scale of the E -field, is much larger on the night side because of the increased electron temperature (Halekas et al. 2005;

Farrell et al. 2007). The resulting E -fields on the night side are of the order of a few V/m, similar to what is expected on the day side (Farrell et al. 2007).

At the terminator, where most lunar dust is lifted, the processes producing E -fields are more complex. Manka (1973) and Farrell et al. (2007) use a plasma model to study the surface potential at this region. They find that the lunar surface potential at the terminator is enhanced relative to the dayside, and is on the order of -50 volts. Measurements of the suprathermal ion detector experiment (SIDE) on the Apollo landers (Freeman and Ibrahim 1975) are consistent with these predictions. The plasma Debye length at the lunar terminator is also enhanced to ~ 10 m (Manka 1973; Freeman and Ibrahim 1975; Stubbs et al. 2006; Farrell et al. 2007), such that the large-scale E -field at the terminator does not exceed about 10 V/m. It is unclear whether such small E -fields could actually lift dust particles from the surface. Sickafoose et al. (2002) and Farrell et al. (2007) show that the force on a spherical surface particle in a plasma environment is

$$F_E = \frac{2\pi\epsilon_0 d\phi^2}{\lambda}, \quad (5)$$

where ϕ is the surface potential, and λ is the Debye length. A simple balance of the electric force with the vertical gravitational, $F_g = (\pi/6)\rho_{\text{part}}g_m d^3$, and cohesive force, $F_c = \beta d$ (see Shao and Lu 2000) suggests that the electric potential necessary to lift dust particles from the lunar surface is

$$\phi_{\text{lift}} = \sqrt{\lambda \left(\frac{\rho_{\text{part}}d^2 g_m}{12\epsilon_0} + \frac{\beta}{2\pi\epsilon_0} \right)}, \quad (6)$$

where g_m is the lunar gravitational acceleration. For terrestrial soil particles, $\beta \sim 10^{-4}$ – 10^{-3} kg/s² (Shao and Lu 2000; Kok and Renno 2006), while on the Moon β is probably much smaller because of the absence of moisture and therefore capillary forces (Merrison et al. 2007). Indeed, on the Moon β is expected to be smaller than on Mars, where it is in the range 10^{-5} – 10^{-4} kg/s² (Merrison et al. 2007). If we conservatively assume that $\beta > 10^{-7}$ kg/s² on the lunar regolith, the second term in the square root of (6) dominates the balance of forces for the particles of diameter < 10 μm that are observed to levitate above the surface (Rennilson and Criswell 1974). Therefore,

$$\phi_{\text{lift}} \approx \sqrt{\frac{\lambda\beta}{2\pi\epsilon_0}}. \quad (7)$$

Thus, the threshold electric potential necessary to lift particles < 10 μm from the surface depends primarily on the cohesion of the lunar regolith and the Debye length-scale of the lunar plasma. Notably, ϕ_{lift} for small particles does not depend on the gravitational acceleration, and therefore this approximation is general for celestial bodies surrounded by plasmas.

Although Stubbs et al. (2006) suggest that dust can be lifted by E -fields due to the large-scale lunar surface potential predicted by theoretical models (Manka 1973; Stubbs et al. 2006; Farrell et al. 2007) and the Apollo SIDE measurements (Freeman and Ibrahim 1975), they neglected the cohesive force, which is probably the dominant force on particles < 10 μm . Figure 5 shows the threshold electric potential necessary to lift particles from the surface of the Moon as a function of the parameter β that scales the cohesive forces. This threshold electric potential is significantly larger than the large-scale potential at the lunar terminator, even for very small values of β .

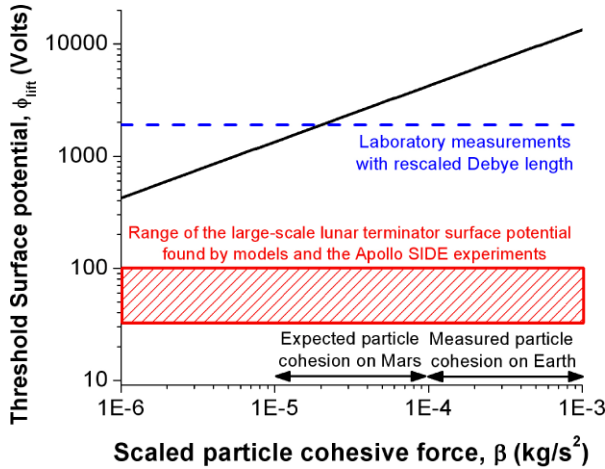


Fig. 5 Threshold electric surface potential required to lift micron and submicron dust from the lunar surface (*solid black line*) as a function of particle cohesive forces, using (7) with $\lambda = 10$ m (Manka 1973; Stubbs et al. 2006; Farrell et al. 2007). Included for comparison is the large-scale surface potential at the lunar terminator (*red rectangle*) found by models (Manka 1973; Stubbs et al. 2006; Farrell et al. 2007) and the Apollo SIDE experiment (Freeman and Ibrahim 1975). Laboratory experiments by Sickafoose et al. (2002) found that particles can be electrically lifted at negative potentials in excess of 30 volts, with a Debye length of ~ 0.25 cm. The *blue dashed line* represents their measured value, rescaled for $\lambda = 10$ m using (7). Measured values of β for soils on Earth are in the range of 10^{-4} – 10^{-3} kg/s 2 (Shao and Lu 2000; Kok and Renno 2006), while β is expected to lie in the range of 10^{-5} – 10^{-4} kg/s 2 on Mars (Merrison et al. 2007)

An explanation for the observation of lunar dust lifting, despite both measurements and theory showing that the large-scale surface E -field is not strong enough to lift dust particles, is that surface heterogeneities on much smaller scales could enhance the local E -field to above the threshold required for dust lifting (Criswell 1973; Borisov and Mall 2006). A simple upper limit on the local enhancement of the lunar surface E -field was proposed by Criswell (1973). He assumed that the photoelectric effect removes electrons and increases the potential of the illuminated surface until the stopping voltage V_{stop} with respect to nearby surfaces is reached and the photoelectric current (I_p) vanishes. The stopping voltage is

$$V_{stop} = \frac{U_e}{e}, \quad (8)$$

where U_e is the kinetic energy and e the charge of the electron. When the energy of incoming light is large enough (UV or more energetic light such as soft X-rays) a few eV is spent to overcome the material work function and remove electrons from its surface. The remaining photon energy is used to increase the electrons' kinetic energy E_e . This kinetic energy, in turn, forces the free electrons to move against local potentials until the stopping potential value is reached. Since the work function (<10 eV) of materials is small compared to the energy of X-ray photons, we have that

$$V_{stop} \approx \frac{(500 - 1500) \text{ eV}}{e} = (500 - 1500) \text{ V}. \quad (9)$$

Therefore, neglecting leaking currents due to surrounding conducting plasmas, soft X-rays could generate small-scale potentials of up to 50–150 kV/m between shadows and illumi-

nated areas of cm-scale surface protuberances. This is an upper bound to the E -fields that would occur in the absence of the conducting plasma generally found at the lunar surface.

More recently, Borisov and Mall (2006) showed that small-scale protuberances such as small craters can enhance the local potential at the lunar terminator. The slope associated with such craters makes it easier for solar wind electrons to penetrate the crater's wake than for solar wind protons, leading to a substantial increase in the negative surface potential.

The hypotheses of locally enhanced E -fields to explain the mystery of lunar dust levitation can be tested with measurements of E -fields near the surface of the Moon with a sensor that is both small enough to probe the small scale E -fields, and can distinguish the effects of charged particles impacting on it from that of the local space field (Renno et al. 2008).

3.2 Dust Lifting on Asteroids and Comets

The formation of regolith on asteroids is different from that on the Moon because of the large difference in gravity accelerations (Chapman et al. 2002). On asteroids, impact ejecta are usually spread uniformly over the entire surface, while on the Moon they are sorted by sizes and larger ejecta get confined to the areas around impact craters. In addition, asteroid regoliths appear to be deficient in dust and agglutinates when compared to the lunar regolith. Lee (1996) suggests that this happens because the smallest particles are preferentially lost when surface particles are levitated electrostatically. Moreover, Lee argues that levitated fine dust with diameters ranging from 0.01 to 1 μm may escape from asteroids, while larger particles with diameters of up to 100 μm migrate and get trapped in shadowed areas on craters and grooves.

Low altitude images (up to 1 m per pixel) of asteroid Eros by the NEAR-Shoemaker spacecraft show that craters and grooves are filled with fines (Veverka et al. 2001). High-resolution images (up to 6 mm per pixel) of the surface of asteroid Itokawa by the Hayabusa spacecraft show that it is covered with mm-size and larger particles (Fig. 6). Moreover, it shows that none of the smallest particles stay on top of boulders without being supported by other particles (Miyamoto et al. 2007). The high-resolution images also show craters with flat floors filled with fines. These findings suggest that the smallest particles migrate

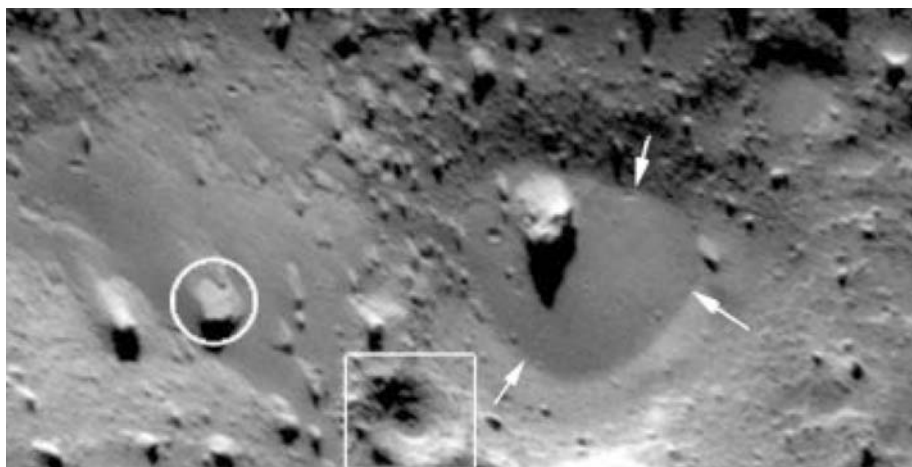


Fig. 6 Image of the surface of asteroid Eros showing evidence of dust particles moving downhill, filling craters and accumulating upslope of rocks

to gravitationally stable areas. Miyamoto et al. (2007) suggests that vibrations forced by impacts, tides and thermal fluctuations are responsible for these global migrations. However, electrostatic lifting of surface particles, similar to what is observed on the moon, could also explain the migration of dust to low terrains (Fig. 6).

4 Summary and Conclusions

We review theoretical and observational studies of electric fields in dusty phenomena, and their role in saltation and dust lifting on Earth, Mars, the Moon, and asteroids. Near-surface electric fields larger than 100 kV/m can occur in terrestrial dusty phenomena, and might play an important role in saltation and dust lifting. Electric forces reduce the threshold wind speed required to lift surface particles (Kok and Renno 2006), significantly affect saltation trajectories (Schmidt et al. 1998; Zheng et al. 2003) and their inclusion in numerical models improves agreement with measurements (Zheng et al. 2006; Kok and Renno 2008). On Mars, there is evidence that electric fields in dusty phenomena dissociate water vapor, catalyze the production of hydrogen peroxide, and dissociate methane (Delory et al. 2006; Atreya et al. 2006; Farrell et al. 2007). Moreover, electric fields in saltation and dusty phenomena on Mars might produce electric discharges (Melnik and Parrot 1998).

Finally, there is evidence dust particles of diameters $< 10 \mu\text{m}$ are lifted from the surface of the Moon by electrostatic forces, and perhaps also from the surface of asteroids. However, large-scale surface potentials predicted by plasma models (Manka 1973; Farrell et al. 2007) and confirmed by measurements (Freeman and Ibrahim 1975) are not large enough to lift dust particles from the lunar surface, but locally enhanced surface potentials might become large enough to lift dust particles (Criswell 1973; Borisov and Mall 2006). This hypothesis can be tested with measurements of small-scale electric fields at the lunar surface or from low orbit with “picosatellite sensors.”

Acknowledgements We thank the National Aeronautics and Space Administration (NASA) and the National Science Foundation (NSF) for partially funding this research under award numbers NASA/06-PIDDP06-0111 and NSF/ATM 0622539. In addition we thank the organizers of the workshop on “Planetary Atmospheric Electricity” and our hosts at the International Space Science Institute in Bern Switzerland for the wonderful experience. Finally, we thank Earle Williams and two anonymous reviewers for helpful comments that improved the original manuscript.

References

- S.K. Atreya, Z. Gu, *J. Geophys. Res.* **99**, 13133–13145 (1994). doi:[10.1029/94JE01085](https://doi.org/10.1029/94JE01085)
- S.K. Atreya, P.R. Mahaffy, A.S. Wong, *Planet. Space Sci.* (2007). doi:[10.1016/j.pss.2006.02.005](https://doi.org/10.1016/j.pss.2006.02.005)
- S.K. Atreya, A.S. Wong, N.O. Renno et al., *Astrobiology* **6**(3), 439–450 (2006). doi:[10.1089/ast.2006.6.439](https://doi.org/10.1089/ast.2006.6.439)
Medline
- R.A. Bagnold, *The Physics of Blown Sand and Desert Dunes* (Methuen, London, 1941)
- O.E. Berg, H. Wolf, J.W. Rhee, in *Interplanetary Dust and Zodiacal Light*, ed. by H. Elsasser, H. Fechtig. Lecture Notes Phys., vol. 48 (Springer, New York, 1976), pp. 233–237
- N. Borisov, U. Mall, *Planet. Space Sci.* **54**, 572 (2006). doi:[10.1016/j.pss.2006.01.005](https://doi.org/10.1016/j.pss.2006.01.005)
- R.V. Cakmur et al., *J. Geophys. Res.* **111**, D06207 (2006). doi:[10.1029/2005JD005791](https://doi.org/10.1029/2005JD005791)
- C.R. Chapman, W.J. Merline, P.C. Thomas et al., *Icarus* **155**, 104–118 (2002). doi:[10.1006/icar.2001.6744](https://doi.org/10.1006/icar.2001.6744)
- R.T. Clancy, B.J. Sandor, G.H. Moriarty-Schieven, *Icarus* **168**, 116–121 (2004). doi:[10.1016/j.icarus.2003.12.003](https://doi.org/10.1016/j.icarus.2003.12.003)
- D.R. Criswell, Photon and Particle Interactions with Surfaces in Space, 545–556 (1973)
- W.D. Crozier, *J. Geophys. Res.* **69**, 5427 (1964). doi:[10.1029/JZ069i024p05427](https://doi.org/10.1029/JZ069i024p05427)
- W.D. Crozier, *J. Geophys. Res.* **75**, 4583 (1970). doi:[10.1029/JC075i024p04583](https://doi.org/10.1029/JC075i024p04583)

- G.T. Delory, W.M. Farrell, S.K. Atreya, N.O. Renno et al., *Astrobiology* **6**, 451–462 (2006). doi:[10.1089/ast.2006.6.451](https://doi.org/10.1089/ast.2006.6.451) Medline
- L. Demon, P. Defelice, H. Gondet, Y. Kast, L. Pontier, *Journal des Recherches du C.N.R.S.* **24**, 126 (1953)
- P.J. DeMott, K. Sassen, M.R. Poellot et al., *Geophys. Res. Lett.* **30**(14), 1732 (2003). doi:[10.1029/2003GL017410](https://doi.org/10.1029/2003GL017410)
- S.J. Desch, J.N. Cuzzi, *Icarus* **143**, 87–105 (2000). doi:[10.1006/icar.1999.6245](https://doi.org/10.1006/icar.1999.6245)
- N. Duff, D.J. Lacks, *J. Electrost.* **66**, 51 (2008). doi:[10.1016/j.elstat.2007.08.005](https://doi.org/10.1016/j.elstat.2007.08.005)
- H.F. Eden, B. Vonnegut, *Science* **180**(4089), 962–963 (1973). doi:[10.1126/science.180.4089.962](https://doi.org/10.1126/science.180.4089.962) Medline
- T. Encrenaz, B. Bézard, Greathouse et al., in *IAU Circular 8254: Hydrogen Peroxide Detection on Mars* (Central Bureau for Astronomical Telegrams, Cambridge, 2003)
- T. Encrenaz, B. Bézard, T. Greathouse et al., *Icarus* **170**, 424–429 (2004). doi:[10.1016/j.icarus.2004.05.008](https://doi.org/10.1016/j.icarus.2004.05.008)
- W.M. Farrell, G.T. Delory, S.A. Cummer et al., *Geophys. Res. Lett.* **30** (2003)
- W.M. Farrell, P.H. Smith, G.T. Delory et al., *J. Geophys. Res. Planets* (2004). doi:[10.1029/2003JA010130](https://doi.org/10.1029/2003JA010130)
- W.M. Farrell, N. Renno, G.T. Delory et al., *J. Geophys. Res. Planets* **111**(E1) (2006a)
- W.M. Farrell, G.T. Delory, S.K. Atreya, *Geophys. Res. Lett.* (2006b). doi:[10.1029/2006GL027210](https://doi.org/10.1029/2006GL027210)
- W.M. Farrell, T.J. Stubbs, R.R. Vondrak, G.T. Delory, J.S. Halekas, *Geophys. Res. Lett.* **34**, L14201 (2007). doi:[10.1029/2007GL029312](https://doi.org/10.1029/2007GL029312)
- G.D. Freier, *J. Geophys. Res.* **65**, 3504 (1960). doi:[10.1029/JZ065i010p03504](https://doi.org/10.1029/JZ065i010p03504)
- L.K. Fenton, P.E. Geissler, R.M. Haberle, *Nature* **446**(7138), 934 (2007). doi:[10.1038/nature05790](https://doi.org/10.1038/nature05790)
- G. Flynn, *Earth Moon Planets* **72**, 469–474 (1996). doi:[10.1007/BF00117551](https://doi.org/10.1007/BF00117551) Medline
- V. Formisano, S.K. Atreya, T. Encrenaz et al., *Science* **306**, 1758–1761 (2004). doi:[10.1126/science.1101732](https://doi.org/10.1126/science.1101732) Medline
- J.W. Freeman, M. Ibrahim, *Moon* **14**, 103 (1975). doi:[10.1007/BF00562976](https://doi.org/10.1007/BF00562976)
- D.E. Gault, J.B. Adams, R.J. Collins et al., Surveyor project final report. Part 2: Science results. *JPL Tech. Rep.* 32-1265 (1968a), p. 401
- D.E. Gault, J.B. Adams, R.J. Collins et al., Surveyor project final report. Part 2: Science results. *JPL Tech. Rep.* 32-1265 (1968b), p. 308
- J. Guardiola, V. Rojo, G. Ramos, *J. Electrost.* (1996). doi:[10.1016/0304-3886\(96\)00002-2](https://doi.org/10.1016/0304-3886(96)00002-2)
- R. Greeley, J.D. Iversen, *Wind as a Geological Process on Earth, Mars, Venus, and Titan* (Cambridge University Press, New York, 1985)
- R. Greeley, D.G. Blumberg, S.H. Williams, *Sedimentology* **43**, 225 (1996). doi:[10.1111/j.1365-3091.1996.tb01458.x](https://doi.org/10.1111/j.1365-3091.1996.tb01458.x)
- R. Greeley, *Planet. Space Sci.* **2**, 151 (2002). doi:[10.1016/S0032-0633\(01\)00127-1](https://doi.org/10.1016/S0032-0633(01)00127-1)
- R. Greeley et al., *J. Geophys. Res.* **108**, 5041 (2003). doi:[10.1029/2002JE001987](https://doi.org/10.1029/2002JE001987)
- J.S. Halekas, S.D. Bale, D.L. Mitchell, R.P. Lin, *J. Geophys. Res.* **110**, A07222 (2005). doi:[10.1029/2004JA010991](https://doi.org/10.1029/2004JA010991)
- W.R. Harper, *Contact and Frictional Dissipation* (Clarendon Press, Oxford, 1967)
- I.I. Inculet, G.S. Peter Castle, G. Aartsen, *Chem. Eng. Sci.* **61**, 2249–2253 (2006). doi:[10.1016/j.ces.2005.05.005](https://doi.org/10.1016/j.ces.2005.05.005)
- IPCC, *Climate Change 2007: The Physical Science Basis. Contribution of Working Group I to the Fourth Assessment Report of the Intergovernmental Panel on Climate Change* [S. Solomon, D. Qin, M. Manning, Z. Chen, M. Marquis, K.B. Averyt, M. Tignor, H.L. Miller (eds.)]. Cambridge University Press, Cambridge, United Kingdom and New York, NY, USA (2007)
- T.L. Jackson, W.M. Farrell, *IEEE T. Geosci. Remote* **44**, 2942 (2006). doi:[10.1109/TGRS.2006.875785](https://doi.org/10.1109/TGRS.2006.875785)
- A.K. Kamra, *J. Geophys. Res.* **30**, 5856 (1972). doi:[10.1029/JC077i030p05856](https://doi.org/10.1029/JC077i030p05856)
- B.A. Keith, *Trans. Kans. Acad. Sci.* **47**, 95 (1944). doi:[10.2307/3625473](https://doi.org/10.2307/3625473)
- J.F. Kok, N.O. Renno, *Geophys. Res. Lett.* **33**, L19S10 (2006). doi:[10.1029/2006GL026284](https://doi.org/10.1029/2006GL026284)
- J.F. Kok, N.O. Renno, *Phys. Rev. Lett.* (2008). doi:[10.1103/PhysRevLett.100.014501](https://doi.org/10.1103/PhysRevLett.100.014501) Medline
- V.A. Krasnopolsky, J.P. Maillard, T.C. Owen, *Icarus* **172**, 537–547 (2004). doi:[10.1016/j.icarus.2004.07.004](https://doi.org/10.1016/j.icarus.2004.07.004)
- V.A. Krasnopolsky et al. (1993)
- C.E. Krauss, M. Horanyi, S. Robertson, *J. Geophys. Res. Planets* (2006). doi:[10.1029/2004JE002313](https://doi.org/10.1029/2004JE002313)
- B.A. Kwetkus, K. Sattler, H.C. Siegmann, *J. Phys. D Appl. Phys.* **25**, 139 (1992). doi:[10.1088/0022-3727/25/2/002](https://doi.org/10.1088/0022-3727/25/2/002)
- P. Lee, *Icarus* **124**, 181–194 (1996). doi:[10.1006/icar.1996.0179](https://doi.org/10.1006/icar.1996.0179)
- J. Lowell, W.S. Truscott, *J. Phys. D Appl. Phys.* **19**, 1281–1298 (1986). doi:[10.1088/0022-3727/19/7/018](https://doi.org/10.1088/0022-3727/19/7/018)
- R.L. Mancinelli, *Adv. Space Res.* **9**, 191–195 (1989). doi:[10.1016/0273-1177\(89\)90229-9](https://doi.org/10.1016/0273-1177(89)90229-9) Medline
- R.H. Manka, *Photon and Particle Interactions with Surfaces in Space* (1973), pp. 347–361
- J.E. McCoy, *Proc. Lunar Sci. Conf.* 7th (1976), pp. 1087–1112
- O. Melnik, M. Parrot, *J. Geophys. Res. Space Phys.* **103**(A12), 29107–29117 (1998). doi:[10.1029/98JA01954](https://doi.org/10.1029/98JA01954)
- J.P. Merrison, H.P. Gunnlaugsson, P. Nornberg, A.E. Jensen, K.R. Rasmussen, *Icarus* **191**, 568 (2007)
- S.L. Miller, *Science* **117**(3046), 528–529 (1953). doi:[10.1126/science.117.3046.528](https://doi.org/10.1126/science.117.3046.528) Medline

- H. Miyamoto, H. Yano, D.J. Scheeres et al., *Science* **316**, 1011–1014 (2007). doi:[10.1126/science.1134390](https://doi.org/10.1126/science.1134390)
Medline
- M.J. Mumma, R.E. Novak, M.A. diSanti et al., in *DPS Meeting 36* (American Astronomical Society, Washington, 2004) [abstract 26.02]
- G. Myhre, F. Stordal, *J. Geophys. Res.* **106**, 18,193–18,204 (2001). doi:[10.1029/2000JD900536](https://doi.org/10.1029/2000JD900536)
- H. Nair, M. Allen, A.D. Anbar et al., *Icarus* **111**, 124–150 (1994). doi:[10.1006/icar.1994.1137](https://doi.org/10.1006/icar.1994.1137) Medline
- S.L. Namikas, *Sedimentology* **50**, 303 (2003). doi:[10.1046/j.1365-3091.2003.00556.x](https://doi.org/10.1046/j.1365-3091.2003.00556.x)
- V.I. Oyama, B.J. Berdahl, G.C. Carle, *Nature* **265**, 110–114 (1977). doi:[10.1038/265110a0](https://doi.org/10.1038/265110a0)
- P.R. Owen, Saltation of uniform grains in air. *J. Fluid Mech.* **20**, 225–242 (1964). doi:[10.1017/S0022112064001173](https://doi.org/10.1017/S0022112064001173)
- T. Poppe, R. Schrapler, *Astron. Astrophys.* (2005). doi:[10.1051/0004-6361:20042327](https://doi.org/10.1051/0004-6361:20042327)
- J.J. Qu et al., *Sci. China Ser. D* **47**, 529–539 (2004). doi:[10.1360/01yd0478](https://doi.org/10.1360/01yd0478)
- K.R. Rasmussen, H.E. Mikkelsen, *Sedimentology* **45**, 789 (1998). doi:[10.1046/j.1365-3091.1998.00179.x](https://doi.org/10.1046/j.1365-3091.1998.00179.x)
- J.J. Rennilson, Surveyor project final report, Part 2: Science results. *JPL Tech. Rep.* 32-1265 (1968), p. 119
- J.J. Rennilson, D.R. Criswell, *Earth Moon Planets* **10**, 121–142 (1974)
- N.O. Renno et al., *J. Geophys. Res.* **109**(E7), E07001 (2004). doi:[10.1029/2003JE002219](https://doi.org/10.1029/2003JE002219)
- N.O. Renno, J.F. Kok, H. Kirkham et al., *J. Phys.* (2008)
- D.S. Schmidt, R.A. Schmidt, J.D. Dent, *J. Geophys. Res.* **103**(D8), 8997–9001 (1998). doi:[10.1029/98JD00278](https://doi.org/10.1029/98JD00278)
- D.S. Schmidt, R.A. Schmidt, J.D. Dent, *Boundary-Layer Meteorol.* **93**(1), 29–45 (1999). doi:[10.1023/A:1002045818907](https://doi.org/10.1023/A:1002045818907)
- U. Schumann, H. Huntrieser, *Atmos. Chem. Phys.* **7**, 3823 (2007)
- A.B. Severny, E.I. Terez, A.M. Zvereva, *Earth Moon Planets* **14**, 123 (1975)
- Y. Shao, M.R. Raupach, *J. Geophys. Res.* **97**, 20559 (1992)
- Y. Shao, H. Lu, *J. Geophys. Res.* **105**, 22437–22443 (2000). doi:[10.1029/2000JD900304](https://doi.org/10.1029/2000JD900304)
- E.M. Shoemaker, R.M. Batson, H.E. Holt, E.C. Morris, J.J. Rennilson, E.A. Whitaker, Surveyor 7 mission report: Science results. *JPL Tech. Rep.*, 32-1264 (1968), p. 66
- A.A. Sickafuse, J.E. Colwell, M. Horanyi, S. Robertson, *J. Geophys. Res.* **107**, 1408 (2002). doi:[10.1029/2002JA009347](https://doi.org/10.1029/2002JA009347)
- C.D. Stow, *Weather*, 24,134–24,137 (1969)
- T.J. Stubbs, R.R. Vondrak, W.M. Farrell, *Adv. Space Res.* **37**, 59 (2006). doi:[10.1016/j.asr.2005.04.048](https://doi.org/10.1016/j.asr.2005.04.048)
- J. Veverka, P.C. Thomas, M. Robinson et al., *Science* **292**, 484–488 (2001). doi:[10.1126/science.1058651](https://doi.org/10.1126/science.1058651)
Medline
- R.R. Vondrak, T.J. Stubbs, W.M. Ferrell, A dynamic fountain model for dust in the lunar exosphere. *Workshop on Dust in Planetary Systems 2005* (2005), p. 4071
- E. Williams et al., (2008, revised)
- A.P. Zent, C.P. McKay, *Icarus* **108**, 146 (1994). doi:[10.1006/icar.1994.1047](https://doi.org/10.1006/icar.1994.1047)
- Y. Zhai, S.A. Cummer, W.M. Farrell, *J. Geophys. Res. Planets* **111**(E6), (2006)
- X.J. Zheng, N. Huang, Y.-H. Zhou, *J. Geophys. Res.* **108**(10), 4322 (2003). doi:[10.1029/2002JD002572](https://doi.org/10.1029/2002JD002572)
- X.J. Zheng, N. Huang, Y. Zhou, *Eur. Phys. J. E* **19**(2), 129–138 (2006). doi:[10.1140/epje/e2006-00020-9](https://doi.org/10.1140/epje/e2006-00020-9)
Medline

The Charging of Planetary Rings

A.L. Graps · G.H. Jones · A. Juhász · M. Horányi ·
O. Havnes

Originally published in the journal Space Science Reviews, Volume 137, Nos 1–4.
DOI: [10.1007/s11214-008-9406-4](https://doi.org/10.1007/s11214-008-9406-4) © Springer Science+Business Media B.V. 2008

Abstract This chapter will review what is known about the charging of planetary rings, in particular the sum of the individual currents from the time-varying charge dQ/dt , of the planetary ring particle. For the smallest ring particles, in addition to checking the plasma conditions for the charging currents, one must consider if collective effects in the ring environment are relevant. Two planetary ring environments that have held a strong interest for ring scientists in the last two decades are Saturn's spokes in the B Ring and the environment of Saturn's E ring. Two sections of this chapter will describe these planetary ring charging environments in detail. Finally, we describe two charging effects that demonstrate areas of future studies while providing fresh examples of the intriguing effects from planetary ring charging processes.

Keywords Charged dust · Plasma · Photoelectron emission · Secondary electron emission · Saturn's rings · Jupiter's rings · Saturn's E ring · Saturn's spokes · Dusty plasma · Dust-in-plasma · Mach cones · Electrostatic braking

A.L. Graps (✉)
Southwest Research Institute, Boulder, CO, USA
e-mail: amara@boulder.swri.edu

A.L. Graps
Planetary Science Institute, Tucson, AZ, USA

G.H. Jones
Mullard Space Science Laboratory, Centre for Planetary Sciences, University of College London,
London, UK

A. Juhász
KFKI Research Institute for Particle and Nuclear Physics, Budapest, Hungary

M. Horányi
Laboratory for Atmospheric and Space Physics, Boulder, CO, USA

O. Havnes
Dept. of Physics, University of Tromsø, Tromsø, Norway

1 Introduction

Planetary rings have an undeniable aesthetic appeal, resulting in media icons of ringed planets as descriptive of the planetary sciences field as a whole. Such far-reaching symbolism might not be misplaced, however, because planetary rings represent a fundamental class of planetary structure (Greenberg and Brahic 1984), that invites interdisciplinary investigations from specialists in dust, gravitational, plasma, collisional, and radiative transfer physics, due to: its sub-micron to meters-sized particles, its emersion in the planet's magnetic field, its embedded moonlets and its close proximity to the ringed planet's ionosphere and innermost moons. As such, planetary rings are a metaphoric bridge through a wide range of planetary physical processes. Therefore, it is fitting that the topic of the charging of planetary rings, which, at first, appears to be narrowly-defined, is similarly interdisciplinary for the same reasons as given above. Processes that charge ring particles have different relative dynamical effects, dependent upon the rings' particle sizes, and the ring's plasma, magnetic and gravitational environments. Therefore, the focus for this chapter will be on the ring charging processes, dotted with highlights of several of the diverse dynamical ring charging effects.

The charging of planetary rings is the sum of the individual currents from the time-varying charge dQ/dt , of the planetary ring particle. The individual currents could be any of the following, depending on the environmental plasma conditions: number density, flow speed, temperature, mass: electron and ion capture from the plasma, ion currents to a moving grain, photoelectron emission, secondary electron emission, thermionic effects, with stochastic charging influences all of the above. Since rings are an ensemble of particles, (“cloud” \approx Ring), we will define an ensemble, and consider the above currents, including those for the smallest ring particles, the dust particles, to arrive at a table giving charge potential and other relevant parameters.

For the smallest ring particles, in addition to checking the plasma conditions for the charging currents, one must consider if collective effects in the ring environment are relevant. The Debye screening length provides our first indication of whether collective processes might be important, giving clues to whether we have a “dust-in-plasma” (isolated particle) or a “dusty plasma” (nonisolated particle). For a dusty plasma, however, the Debye screening length is a minimum condition, and a more sensitive check on the dust plasma conditions measures the ratio for the charges on the dust particle compared to the electrons in the plasma.

Two planetary ring environments that have held a strong interest for ring scientists in the last two decades are Saturn's spokes in the B ring and the environment of Saturn's E ring. Two sections of this chapter will describe these planetary ring charging environments in detail. The Spokes section will present the spoke characteristics, previously-proposed formation processes, recent Cassini observations and one possible spoke formation process with tests that one can apply to determine their origin. The section on Saturn's E ring will present another class of details. Because it is the largest ring in the solar system and its particles can be studied as isolated particles, Saturn's E ring is probably the most studied ring. This section will describe the results of the ring's charging and dynamics which demonstrate that the ring's primary origins can be traced to the Saturn's moon: Enceladus. The ring's most relevant forces should include plasma drag, it has a noticeable seasonal variation and the secondary electron emission current is known best for this ring due to direct charge measurements by Cassini's CDA instrument.

Finally, we close this chapter with several special charging effects: Electrostatic braking and Mach cones.

2 Charging Equation

The charge of a ring particle is the sum of the individual currents from the time-varying charge dQ/dt , which varies with time according to (Horányi 1996),

$$\frac{dQ}{dt} = \sum_k I_k = I_{e,i,\text{moving}} + I_{\text{sec}} + I_v$$

where k ranges over the different charging processes, and the current of the k th charging process is denoted as I_k . The other variables on the right side: $I_{e,i,\text{moving}}$ = electron and ion currents to a moving or stationary grain, I_{sec} = secondary electron currents, and I_v = photoelectron currents. The individual currents depend on the environmental plasma conditions' number density, flow speed, temperature, and mass, with stochastic charging influencing all of the above.

2.1 Electron and Ion Capture

Given an isotropic, thermal (Maxwellian) plasma, the electron and ion capture currents are (Goertz 1989):

$$I_{e,i} = q_{e,i} 4\pi r_g^2 n_{e,i} \sqrt{\left(\frac{kT_{e,i}}{2\pi m_{e,i}}\right)} \begin{cases} \exp(-\psi_{i,e}) & \psi_{i,e} > 0 \\ 1 - \psi_{i,e} & \psi_{i,e} < 0 \end{cases}$$

where,

$$\psi_{i,e} = \mp \frac{q_{i,e} \varphi_{i,e}}{kT_{e,i}},$$

$q_{i,e}$ is the charge of the plasma species, $n_{e,i}$ is the plasma number density, k is the Boltzmann constant, $m_{e,i}$ is the plasma particle mass, $T_{e,i}$ is the plasma temperature, $\varphi_{i,e}$ is the charge potential, the \mp the signs correspond to electrons and ions, and the e, i indices indicate electrons and ions, respectively.

If the plasma particle velocity distribution possesses a non-Maxwellian high-energy tail, then a generalized Lorentzian (kappa) distribution is more appropriate. The generalized Lorentzian distribution is characterized by a spectral index κ which varies as the energy goes to $(\kappa + 1)$ at high velocities, and approaches a Maxwellian distribution as κ goes to infinity. The ion and electron capture currents will change accordingly; see equations 21ab and 22ab in (Chow et al. 1993).

Ion currents generated due to a moving particle of grain size is a more general scenario for the ion capture, which reduces to the above expression under special circumstances. More generally, if the dusty ring particles are not at rest in the plasma, and the dust-to-plasma relative velocities are comparable to, or exceed, the ion thermal velocities (a situation which often arises when the particle resides in the solar wind), then the ion currents to the moving particle ("modified proton currents") must be added to the other currents. The I_{moving} current has two different expressions, each depending whether the grain potential is positive or negative.

For a negative grain potential, the modified proton current is:

$$I_{\text{moving}} = \frac{4\pi r_g^2 q_i n_i \sqrt{\left(\frac{kT_i}{2\pi m_i}\right)}}{2} \left[\left(M^2 + \frac{1}{2} - \psi_i \right) \sqrt{\frac{\pi}{M}} \operatorname{erf}(M) + \exp(-M^2) \right]$$

where M = the ratio of the dust-to-plasma relative velocity w over the ion thermal speed (M = “Mach” number (Horányi et al. 1988), and $\operatorname{erf}(x)$ is the *error function*):

$$M = \frac{w}{\sqrt{\frac{2kT_i}{m_i}}} \quad \operatorname{erf}(x) = \frac{2}{\pi} \int_0^x \exp(-y^2) dy.$$

For a positive grain potential, the modified proton current is:

$$I_{\text{moving}} = \frac{4\pi r_g^2 q_i n_i \sqrt{\left(\frac{kT_i}{2\pi m_i}\right)}}{4} \left\{ \begin{array}{l} \left(M^2 + \frac{1}{2} - \psi_i \right) \sqrt{\frac{\pi}{M}} [\operatorname{erf}(M + \sqrt{\psi_i}) + \operatorname{erf}(M - \sqrt{\psi_i})] \\ + \left(\sqrt{\frac{\psi_i}{M}} + 1 \right) \exp[-(M - \sqrt{\psi_i})^2] \\ - \left(\sqrt{\frac{\psi_i}{M}} - 1 \right) \exp[-(M + \sqrt{\psi_i})^2] \end{array} \right\}.$$

In the limit of $M \rightarrow 0$, the above expressions are identical to the ion capture expression.

2.2 Photoelectron emission

The absorption of solar UV radiation releases photoelectrons, and hence, constitutes a positive charging current (Horányi et al. 1988). Its magnitude depends on the material properties of the grain, i.e., its photoemission efficiency, and on the grain’s surface potential, which may, if positive, recapture a fraction of the photoelectrons. The spectrum of the photoelectrons released is often assumed to be of Maxwellian distribution with a temperature T_{photo} , which corresponds to an energy $kT \sim 2$ eV. The photoelectric current is (Eqn. 10, Horányi et al. 1988):

$$I_v = \begin{cases} \pi r_g^2 q_e f_1 & \varphi < 0 \\ \pi r_g^2 q_e f_1 \exp\left(-\frac{q_e \varphi}{kT}\right) & \varphi > 0 \end{cases}.$$

Here, r_g is the particle radius, q_e is the charge on the electron, kT is the average energy of the photoelectrons and, $f_1 \approx 2.5 \times 10^{10} \chi \text{ s}^{-1}$, is the flux of photoelectron emission at 1 AU with the “photoelectron efficiency factor” χ spanning the range: $\chi \approx 1.0$ for conducting magnetite (metals) grains, and $\chi \approx 0.1$ for dielectric olivine particles.

The photoelectric current described here follows from Horányi et al. (1988)’s work, which, in turn, refers to Feuerbacher et al. (1973). They carried out calculations for grains of high (material: Al_2O_3) and low (material: C) photoelectric yields, taking into account the material’s full frequency dependence and the energy distribution of the emitted photoelectrons. The photoelectric threshold theoretically and observationally increases with decreasing particle radii (Kimura and Mann 1998). The smallest dust grains can be characterized by the physical properties of *solid spherical* particles, which is a typical particle geometry used for modeling work, as a first approximation.

2.3 Secondary Electron Emission

The effect of electrons or ions with high energies bombarding the dust grain can lead to an ionization of the grain material and ejection of electrons from the grain. This process is called *secondary electron emission*. This current has the largest effect on the charging of the dust particles, and is, in turn, highly sensitive to the dust particle's material properties. The three processes that can occur during secondary electron emission: 1) reflection, 2) backscattering and 3) true secondary emission, are usually treated as distinct secondary electron yield processes by both *electron* impacts from solid particles as well as by *ion* impacts (Whipple 1981).

The flux of secondary electrons depends on the energy of the plasma electrons/ions E and on the grain's surface potential. The number of secondary electrons—the *yield*—also depends on the material properties of the charged grains, which is characterized by the secondary electron emission yield parameter δ . If the secondary electron yield is greater than 1, then positive dust charging occurs. For some materials, the yield is greater than 1 for $kT_e = 50$ eV, and for other materials, the yield is greater than 1 at $kT_e = 1000$ eV and higher. The yield also increases with decreasing grain size. For example, the maximum secondary electron emission yield from ions/electrons impacting onto 0.01 μm -sized particles, for both conductors and insulators, is about 3.5 times higher than onto 1 μm -sized particles (Chow et al. 1993).

2.3.1 Secondary Electron Emission—Electron impact

Sternglass published an expression for the secondary current by electron impact using the yield function (Sternglass 1954):

$$\delta(E) = 7.4\delta_m \left(\frac{E}{E_m} \right) \exp \left[-2\sqrt{\left(\frac{E}{E_m} \right)} \right]$$

where E_m is a characteristic energy, at which the release of a secondary electron reaches a maximum (Goertz 1989), which corresponds to a maximum δ_m .

This extensively-used formula for the secondary emission yield, which uses semi-infinite slabs of material, approximates the theoretical derivations of Bruining and Jonker from the 1950s ("Jonker yield", Bruining 1954 and Jonker 1952), however experimental data might be better fit using expressions in (Kimura and Mann 1999). For small spherical grains (not a planar slab), secondary electrons are not limited to the point of incidence of the primary electron. Instead, it is possible for secondary electrons to exit from all points of the dust grain surface, thus increasing the yield over that determined by the Sternglass formula (Chow et al. 1993). Sometimes this effect is referred to as the *small-particle approximation*. For this reason, we double the secondary electron emission yield when the dust particle is $\leq 0.1 \mu\text{m}$. At low primary energies, the smaller grains have higher yields for both insulators and conductors because, within these smaller grains, excited secondary electrons have shorter distances to travel to reach the surface. However, as the primary energy increases, the yield curves for different size grains may cross and larger grains may have higher yields than the smaller grains.

Meyer-Vernet (1982) demonstrated that the charge on a grain is not always unique: the equilibrium potential may have multiple roots, which is important to note, especially for a plasma environment with high plasma temperatures or densities. Secondary-electron yield of electron impact onto other grain materials, such as onto ice grains, can influence that

type of grain's charging, also. Useful secondary electron emission values can be found in Table 5 (Draine and Salpeter 1979) for graphite, SiO_x , Mica, Fe, Al, MgO, lunar dust), Table 1 (Suszczynsky et al. 1993) for H_2O , CO_2 , NH_3 , CH_3OH , Table 2 (Whipple 1981) for Al_2O_3 , SiO_2 , Teflon, Kapton, Mg, and from M. Horányi and A. Heck's work (Horányi et al. 1997, 1988; Heck 1999) for SO_x and Apollo 17 lunar dust. The latter data is particularly valuable for being among the few data available of secondary electron emission of low-energy electron impacts.

2.3.2 Secondary Electron Emission—Ion impact

Following from Sternglass, Horányi et al. (1988) gave expressions for the secondary current by ion impact, using the yield function:

$$\delta(E) = 2\delta_m \left(\frac{E}{E_m} \right) \frac{\sqrt{\left(\frac{E}{E_m} \right)}}{\left(\frac{1+E}{E_m} \right)}.$$

In addition to the charging processes in this section, there exists stochastic influences on the charging processes, as well as: gradients in the plasma parameters, velocity modulation of the ion current, and/or modulation of the photoelectron current by the planet's shadow.

3 Equilibrium Potential

Ring particle equilibrium potential is reached when the sum of all of the charging currents is zero. The dominant electron capture from the plasma leads to negative charges, and the other charging processes: ion capture, secondary electron emission and photoelectron emission, facilitate positive currents. Secondary electron and photoelectron emission charging processes are highly material dependent. If the charged dust particle is located in a high-energy or high density region of a planetary magnetosphere, then dust particles may be charged positively or negatively (Graps and Grün 2000; Graps et al. 2007). The time to acquire the equilibrium charge may be longer than the flight trajectory time of the particle.

4 Dust-in-Plasma versus Dusty Plasma

For the smallest ring particles, in addition to checking the plasma conditions for the charging currents, one must consider if collective effects in the ring environment are relevant. The Debye screening length λ_D , the distance over which the Coulomb field of an arbitrary charge in the plasma is shielded, provides our first indication of whether collective processes might be important, giving clues to whether we have a “dust-in-plasma” (isolated particle) or a “dusty plasma” (nonisolated particle). These two regimes are defined depending on the concentration of the dust grains (Verheest 2000):

- ‘Dust-in-Plasma’: If $r_g \ll \lambda_D < d$, then, we have a plasma containing isolated screened dust grains and can treat the dust from a particle dynamics point of view.
- ‘Dusty Plasma’: If $r_g \ll d < \lambda_D$, then collective effects of the charged dust can be relevant.

where d is the average intergrain distance, r_g is the dust grain size, and λ_D is the plasma Debye length (here for electrons): $\lambda_D = \sqrt{\frac{\epsilon_0 k T_e}{q_e^2 n_e}}$ where ϵ_0 = the permittivity of free space ($8.854 \times 10^{-12} \text{ C}^2 \text{ N}^{-1} \text{ m}^{-2}$), k = the Boltzmann constant ($1.381 \times 10^{-23} \text{ J K}^{-1}$), T_e is the electron plasma temperature (K), q_e is the charge on the electron ($1.602 \times 10^{-19} \text{ C}$), and n_e is the electron plasma density (m^{-3}).

For a dusty plasma, the Debye screening length, however, is a minimum condition, and a more sensitive check on the dust plasma conditions measures the ratio for the charges on the dust particle compared to the electrons in the plasma. This sensitive check, the Havnes parameter “ P ” is defined as:

$$P \equiv \frac{4\pi\epsilon_0 r_g}{q_e^2 n_e} n_d k T$$

where r_g = the dust grain radius (m) and n_d = dust number density (m^{-3}). The potential solutions as a function of P (Figure 1, Havnes et al. 1990) illustrate that collective effects of the dust ensemble occur when the parameter $P \sim 1$, which is when the derivative with respect to P for the relative plasma potential caused by the dust, is at a maximum. When the parameter P is very small, then the grain potential φ approaches the negative equilibrium potential of a stationary grain in a plasma with the only currents to the grain being ion and electron collection currents. This so-called Spitzer single-grain value of $-2.51kT_e/q_e$ can be understood by noting that the electrons are 43 times more mobile than the protons when the surface potential of the grain is initially 0, therefore, the electron current exceeds the ion current. As the surface potential becomes negative, electrons are repelled, the electron current is reduced the ion current is increased. The process proceeds until the grain acquires the Spitzer value that makes these two currents equal in magnitude (Goertz 1989). Then the grain can be treated as a test particle and the grain’s charge has a negligible effect on the plasma environment, and on the electric and magnetic fields (Horányi et al. 2004).

Since rings are an ensemble of particles, (“cloud” \approx Ring), we can compare the charge potential for a singly-charged grain to that of an ensemble or cloud of grains, each carrying a charge Q_i . In the first instance, that is, for each particle carrying charge Q , the surface electric field is (Goertz et al. 1988):

$$E_s = \frac{Q}{4\pi\epsilon_0 r_g^2}.$$

For $r_g/\lambda_D \ll 1$, the charge potential decreases as (Goertz 1989; Whipple et al. 1985):

$$\varphi(r) = \varphi_s \left(\frac{r_g}{r} \right) e^{-(r-r_g)/\lambda_D},$$

where the exponential factor represents the Debye screening by the plasma.

In the second instance, the solution must be solved numerically, but one can see the range of solutions for equally-spaced infinite sheets in (Figure 4, Goertz 1989), that illustrates the effects of placing grains close to each other. If the interparticle distance between the ring particles is *larger* than the Debye length, the maximum potential between the grains is almost zero, and the surface charge density of the planetary ring is:

$$\sigma = \frac{E_s}{\epsilon_0} \approx \frac{\varphi_s}{\lambda_D \epsilon_0}.$$

Table 1 Nominal values for various planetary ring environments

Rings	n_e (m $^{-3}$)	kT/e (eV)	τ	H (m)	r_g (m)	P
A B	10^5	2	2	10^2	5	2×10^1
					1	1×10^2
F	10^7	10^2	0.1	10^3	10^{-2}	2×10^1
					10^{-6}	2×10^5
Spokes	10^5	2	0.1	3×10^4	10^{-6}	1×10^4
	10^8					1×10^1
Uranus α	5×10^7	30	0.35	10^2	5×10^{-2}	10^1
	2×10^8					10^0
Uranus ϵ	5×10^7	30	1.8	10^2	0.2	1×10^1
	2×10^8					3×10^0
Jupiter	10^8	10^2	10^{-5}	3×10^4	2×10^{-6}	2×10^{-1}
G	10^7	10^2	3×10^{-4}	3×10^5	3×10^{-4}	10^{-2}
		10^{-6}	10^6	10^{-6}		2×10^{-3}
E	10^7	10^2	10^{-6}	10^6	10^{-6}	2×10^{-3}
			10^{-7}	3×10^7		10^{-5}

When the distance between the ring particles is *smaller*, then the potential between the grains is smaller, and the average charge density on each sheet is reduced. The same effect occurs in the three-dimensional case. That is, when the intergrain distance d is smaller than the Debye length, then the average charge density on the ring as a whole is reduced (charge is spread over the ring). The charge on each ring particle is therefore, for $r_g \ll \lambda_D$:

$$Q = (\varphi_s - V_p)4\pi\epsilon_0 r_g$$

where V_p is the maximum plasma potential between the ring particles. The average charge on the grains is thus smaller than that of an isolated grain at the same surface potential.

Considering these charging processes, Goertz et al. (1988) derived the values in Table 1, which gives plasma density n_e , optical depth τ , ring thickness H , ring particle size r_g , Havnes parameter P and charge potential φ . The P value in the last column has been scaled by $4\pi\epsilon_0/q_e$ to correspond with the current definition of P given in this text. The numbers in Goertz et al.'s table need updating, but such is beyond the scope of this review chapter.

5 Saturn's Ring Spokes

5.1 Overview

On approach to Saturn in 1980, Voyager 1 returned the first clear images of dark spokes in Saturn's rings: a phenomenon whose existence had been only hinted at in previous ground-based observations.

Detailed descriptions of the spokes' phenomenology and other characteristics were provided by Doyle and Grün (1990), Eplee and Smith (1984), Grün et al. (1983), and Grün et al. (1992). These studies' main results can be summarized as follows: Spokes are usually near-linear markings that almost exclusively occur in the outer region of Saturn's B-ring, typically, but not exclusively, between 1.5 and 1.9 Saturn radii from the planet's centre, near

to or spanning the corotation distance where ring particles' circular orbital periods match the rotation period of Saturn itself. Keplerian velocity shear acts on the spokes following formation: due to the increased orbital velocity of the inner spoke sections compared to those further from Saturn, the spokes are elongated and are oriented at an ever-increasing angle with respect to the local anti-Saturnward vector. Spokes' reflectance properties and phase angle dependence—dark in backscattered light but bright at high phase angles—indicate that their constituent particles have a fairly narrow size distribution, with mean effective radii of around 0.6 microns.

The initial appearance of spokes must occur in a matter of minutes or less, as some appeared between the acquisition of Voyager images taken only 5 minutes apart. No radial spreading of the spokes was observed to take place: spokes initially appeared covering their entire radial range. The times at which the features initially appeared were calculated in these studies under the assumption that spokes were all formed when radially-aligned, an assumption that is not universally-accepted. Under this assumption, however, the Voyager 1 and 2 images reveal that most formation occurs in the midnight-dawn local time sector. Spoke complexes typically build up over a period of 1–2 hours, and once formation ceases, they gradually fade, but can sometimes persist over a full Saturn rotation.

It was found that some spokes reformed when their ring location returned to the vicinity of the local time in which they originated, which suggested a link with Saturn itself, and that Saturn's magnetic field plays a significant role in their formation. This periodicity in the formation of spokes (Porco and Danielson 1982), was later found to encompass two discrete periods around 641 and 611 minutes (Porco 1988), in agreement, respectively, with the then-current Saturn Kilometric Radiation (SKR) and Saturn Electrostatic Discharge (SED) periods observed at radio wavelengths. For the 5-day period of Voyager 2 observations from which this result was derived, it was noted that the sector of the planet facing local dawn at the inferred time of spoke formation was at local noon at the time of maximum emission of SKR.

5.2 Spoke formation Theories

In the period immediately following the Voyager flybys, several spoke formation theories were proposed, including the alignment of charged grains by electric fields (Bastin 1981; Carberry et al. 1982). Assuming that the grains are predominantly composed of water ice, Weinheimer and Few (1982) suggested that such alignments could not be caused by the effects of electric fields.

Hill and Mendis (1981) postulated electrostatic effects to explain the spokes' occurrence, and suggested that beams of electrons strike the rings to cause localised enhancements in ring particle charging. The source of these electron beams was suggested to be magnetic field-aligned drops in potential caused by an interaction between the solar wind's convective electric field and Saturn's magnetospheric plasma. However, as the spoke formation region is magnetically-connected to lower latitude regions than those connected to the magnetotail, the viability of this process is questioned. We note that Connerney (1986) also addressed the matter of the magnetic connection of Saturn's atmosphere and the rings, albeit in a different context.

The formation theory that was by far the most widely-accepted for many years involved the effects on localized sections of the rings by meteoroid impacts (Goertz and Morfill 1983). It was postulated that the plasma cloud resulting from an impact would spread radially, due to an azimuthal polarization electric field caused by the relative motion of the orbiting, negatively charged dust grains and the corotating magnetospheric plasma. In this environment,

the local electric fields would be strong enough to overcome the gravitational force on small dust particles, and that these smallest particles would thus form spokes elevated above the ring plane. The case for the Goertz and Morfill model was strengthened by the study of Cuzzi and Durisen (1990): they investigated the velocities of interplanetary particles at the Saturnian system, and concluded that the most energetic impacts with the rings would coincide with the ring sector where spoke formation appeared to be most prevalent.

The meteoroid-impact model was questioned by Farmer and Goldreich (2005), who stated that the radial spreading of spokes, as postulated by Goertz and Morfill, could not occur quickly enough to appear as instantaneous in a 5-minute cadence image sequence. However, Morfill and Thomas (2005) expressed their continued belief in the validity of the Goertz and Morfill model.

Alternative formation theories include that of Tagger et al. (1991), who postulated that spokes are a manifestation of magnetosonic waves generating radial structures in the vicinity of corotation in a thin Keplerian ionized disk. They suggested that meteor strikes or electron beams could be the drivers of such waves. More recently, Hamilton (2006) proposed an alternative meteor impact-induced formation process: he suggested that such impacts release clouds of ejecta, not all of whose constituents are large enough to be visible. The smallest grains are accelerated out of the ring plane by electromagnetic forces, and then return to the plane at slightly different locations, and at high speeds, producing more ejecta. This collisional cascade continues over several cycles, and particles released by these impacts are observed as spokes when of large enough size.

Although spokes were observed several times in the 1990s by the Hubble Space Telescope, they were not observed after 1998 (McGhee et al. 2005). McGhee and colleagues suggested that this was due to viewing angle with respect to the ring plane, and that observers needing to be located close to the plane for successful detection. Contrary to predictions, despite being afforded an apparently favourable viewing geometry, instruments aboard Cassini failed to observe spokes between the spacecraft's arrival at Saturn in July 2004 and September 2005 (Mitchell et al. 2006a). At the time of this writing, several more spoke observations have been reported by the Cassini ISS imaging team (e.g. Mitchell and Porco 2006b). Although fewer in number than the Voyager events, they appear to share many characteristics. A slight deviation from Keplerian motion was reported, suggesting the influence of electromagnetic effects.

Other factors were also suggested to affect the observability of spokes: Farrell et al. (2006), partially citing Cassini RPWS observations of electron density above Saturn's main rings, proposed that the ring surface potential changes with Saturnian season. They suggested that during the Voyager epoch, the rings were uniformly negatively charged, whereas in the first years following Cassini's arrival at Saturn, due to increased photoemission on the sunward-facing ring surface, the ring polarity was bipolar. They also suggested that spokes only form on negatively-charged ring surfaces, so Cassini's first few years at Saturn coincided with a time when spokes were concentrated on the unlit ring face. Suggestions were made that spokes could return in abundance on the sunlit rings in 2008, but that solar activity may prove to have a significant effect on spokes' formation, due to increased flare activity. Mitchell et al. (2006a) also suggested a dependence on background plasma environment, expanding on an earlier work by Nitter and Havnes (1992).

Recently, an alternative formation process has been proposed which suggests that, although the electrostatic charging mechanism is responsible for spoke formation as first postulated by Hill and Mendis (1981), the exact cause of the charging is linked to electrical storms in the atmosphere of Saturn itself (Jones et al. 2006). As presented by Fischer et al. (2008) in this issue, following a lightning discharge, it is believed that a strong electric

field exists above terrestrial thunderstorms. The ionization of atmospheric particles by an incoming cosmic ray during the existence of this electric field can lead to the formation of an electron avalanche, as has been suggested to cause gamma ray emission from above thunderstorms. When the atmospheric density is low enough, such electron avalanches can escape into the magnetosphere (e.g. Lehtinen et al. 2000). The escaping electrons are guided by the planetary magnetic field to the thunderstorm's magnetic conjugate point in the opposite hemisphere. At Saturn, if this occurs within a certain range of latitudes, the escaping electrons will strike the rings. Jones et al. suggest that this process is the cause of electrostatic charging in the rings, and that thus, ultimately, thunderstorms cause spokes. The ionospheric density varies with local time, and reaches a minimum near local dawn (Moore et al. 2004), where spoke formation is most relevant.

The curious, changing morphology of spokes as observed by the two Voyagers appears to agree with this suggested process. Seasonality in the spokes' appearance could be tied to the occurrence latitudes of thunderstorms on Saturn, and the changing ionospheric conditions at the planet (e.g. Moore et al. 2004), which can affect the likelihood of electron avalanches escaping the atmosphere. The confirmation of this process's operation ideally requires the positive identification of a thunderstorm on Saturn together with spokes at the location on Saturn's rings to which the thunderstorm is magnetically mapped. This is, however, challenging: storms cannot easily be identified by imaging on Saturn: the planet's nightside is largely illuminated by light scattered by the ring system, precluding the acquisition of long-exposure images. Although radio emissions termed Saturn Electrostatic Discharges, SEDs, are known to be linked to Saturnian thunderstorms (Fischer et al. 2006), the detection of whistler in the absence of an SED (Akalin et al. 2006) suggests that SEDs may not be as reliable thunderstorm markers as at first thought. Jones and colleagues also reported that Cassini's MIMI instrument has detected a pair of magnetic field-aligned electron beams which in many respects are similar to those expected from thunderstorms (Lehtinen et al. 2000).

There was no SED emission or whistler events during this time, so a link with thunderstorms is unproven. A curious phenomenon, possibly related to spokes, is the observed emission at X-ray wavelengths from the rings, and the enhancement of that emission in the dawn local time sector (Ness et al. 2004). The emission is dominated by photons in the energy range centered on atomic oxygen K-alpha fluorescence (Bhardwaj et al. 2005).

Due to the difficulty in recognizing the locations of thunderstorms, a final answer regarding the origin of spokes may not be forthcoming for some time. Even if any of the above spoke initiation processes involving the charging of the rings is proven to be correct, the details of the charging process still need to be resolved. Do electron beams charge the ring particles directly, leading to dust levitation purely through mutual repulsion of like-charged grains, or is it an enhancement in the electron number density of the ring plasma sheath that initiates the levitation of submicron particles?

If, as anticipated, spoke activity becomes vigorous around Saturnian equinox in 2009, data from the Cassini orbiter will allow us to at least narrow down the range of possible spoke formation processes in the near future.

6 E Ring

6.1 Introduction

Saturn's E ring is the largest planetary ring in the solar system. This faint ring spans a radial distance of 3–8 Saturnian radii ($1 R_S = 60330$ km) including the orbit of five major satellites,

Mimas ($R_M = 3.08 R_S$), Enceladus ($R_E = 3.95 R_S$), Tethys ($R_T = 4.89 R_S$), Dione ($R_D = 6.26 R_S$) and Rhea ($R_R = 8.75 R_S$). Due to its low optical depth $\tau \simeq 1.5 \times 10^{-5}$ (Showalter et al. 1991) the E ring provides an excellent opportunity to study single particle dynamics in a planetary ring as collisions or collective effects are negligible in this region.

Several observations, including ground-based detections during the Earth's ring plane crossings, Hubble Space Telescope (HST), and Voyager imaging show that the brightness of the E ring peaks sharply close to the orbit of Enceladus and that it is composed mainly of small, $0.3 < r_g < 3$ micron radius dust particles (Nicholson et al. 1996, 2004). The peak of the optical depth distribution, in fact, lies outside the orbit of Enceladus, with a displacement of approximately 10^4 km (de Pater et al. 2004). The ring's thickness increases with increasing distance to Saturn from 4000 km (at $r = 3 R_S$) to 15000 km (at about $r = 8 R_S$). Recent in situ observations by Cassini Cosmic Dust Analyzer (CDA) show that the E ring material continuously extends much further from Saturn, engulfing even the orbit of Titan ($R_{Ti} = 20.3 R_S$) (Srama et al. 2006; Kempf et al. 2006, 2008).

As the ring's optical depth distribution sharply peaks close to Enceladus' orbit, this satellite has been long suspected to be the main source of dust particles comprising the E ring. A dense cloud of icy dust grains was observed by the high-rate detector (HRD) subsystem of CDA that appeared asymmetric relative to the closest approach position, indicating a locally enhanced dust production in the south polar region of Enceladus. A comprehensive study of the CDA data suggested that at least 85% of the grains (above the HRD detection threshold) are generated near Enceladus' south pole (Spahn et al. 2006a, 2006b). These grains are either entrained in the outflow of the plumes, or grow in situ in the expanding and cooling gas. They can attain velocities larger than the escape velocity from the surface of Enceladus ($v_{esc} = 210$ m/s), or gain energy from the gas flow, so that they have a nonzero residual velocity on the order of $v_z = 50\text{--}100$ m/s after leaving the gravity field of the satellite (Porco et al. 2006a, 2006b). Interestingly, most of the ejecta particles generated via bombardment by interplanetary micrometeoroids are also expected to have a characteristic residual velocity of about 110 m/s (Krivov 1994).

6.2 Dust Dynamics and Charging

Here we briefly describe an E ring model developed by Juhász and Horányi (2002, 2004), Juhász et al. (2007) and Horányi et al. (2008) that can reproduce many of the observed features of the E ring.

The considered forces in the equation of motion of a dust grain are: the gravitational force due to Saturn (including its oblateness, $J_2 = 1.667 \times 10^{-2}$), the solar radiation pressure force, the Lorentz force and the drag forces due to direct collisions of a dust grain with plasma and neutral particles. It can be shown that the drag force acting on a dust particle is dominated by direct collisions as opposed to distant Coulomb interactions. These forces depend on the particle size, charge, and velocity, and the ambient plasma parameters. The expressions for the first three forces are readily available (Horányi et al. 1992). Expressions for plasma and neutral drags due to direct collisions were taken from Morfill et al. (1980). The magnetic field is calculated using the Z3 model (Connerney 1993). For the calculation of the electric field, fractional corotation was assumed (Richardson 1995). Calculation of dust charge and drag forces requires the knowledge of plasma parameters in the magnetosphere. Juhász and Horányi (2002) used the two-dimensional (2-D) model of Richardson et al. (1998) and Richardson (1995) that gives the density and temperature of cold (ce) and hot (he) electrons and ions (O^+ , H^+ , and OH^+) and the density of neutrals (mainly OH). In the E ring region ($|3 R_S < r < 8 R_S|$), typical plasma density values are

$5 < n < 110 \text{ cm}^{-3}$, decreasing with increasing radial distance from Saturn, and the temperatures are: $1 < T_{ce} < 11 \text{ eV}$, $80 < T_{he} < 200 \text{ eV}$, $13 < T_{O^+} < 180 \text{ eV}$, and $8 < T_{H^+} < 20 \text{ eV}$, increasing with r . Sittler et al. (2006) presented an estimates of the ion fluid parameters from the CAPS instrument on Cassini for the Saturn's inner plasmasphere. Their results have shown that they are qualitatively consistent to those estimated from Voyager plasma measurements, however the temperatures of electrons and protons are somewhat lower than what Voyager determined.

The charge on a dust particle is calculated by solving the current balance equation. As was described in the earlier section, the charging currents are functions of the ambient plasma parameters (density, temperature, and composition), the grain potential, the relative velocity between the grain and plasma, and the material properties of the dust particle (photoelectron and secondary electron yields and size) (Horányi 1996). In calculating the charge the thermal fluxes of hot and cold electrons and ions, the photoelectron emission, and the secondary electron emission currents were considered and dielectric dust grains with a secondary electron yield of $\delta_M = 1.5$ with an optimum impact energy of $E_M = 400 \text{ eV}$, a characteristic secondary electron energy of $kT_s = 2.5 \text{ eV}$, and a photoelectric yield of $\kappa = 0.1$ (Whipple 1981) were assumed.

Figure 1 shows the equilibrium dust potential in the (r, z) plane. In the E ring region, the equilibrium dust potential is $-7 < \Phi_V < +5$. The negative potentials are expected in the cold, dense plasma regions. Above and below the ring plane, the plasma density rapidly drops with distance, and the photoelectron production turns the charge of the dust particles positive. We note that for larger values of secondary yield parameter δ_M , the resulting dust potential is larger. Electrostatic dust charge measurements by the CDA indicated somewhat different dust potential; about -2 V inside Rhea's orbit and $+3 \text{ V}$ outside of it (Kempf et al. 2006). The authors state that these potential values cannot be matched by any model calculations based on the Richardson's plasma model. However, an updated comprehensive model

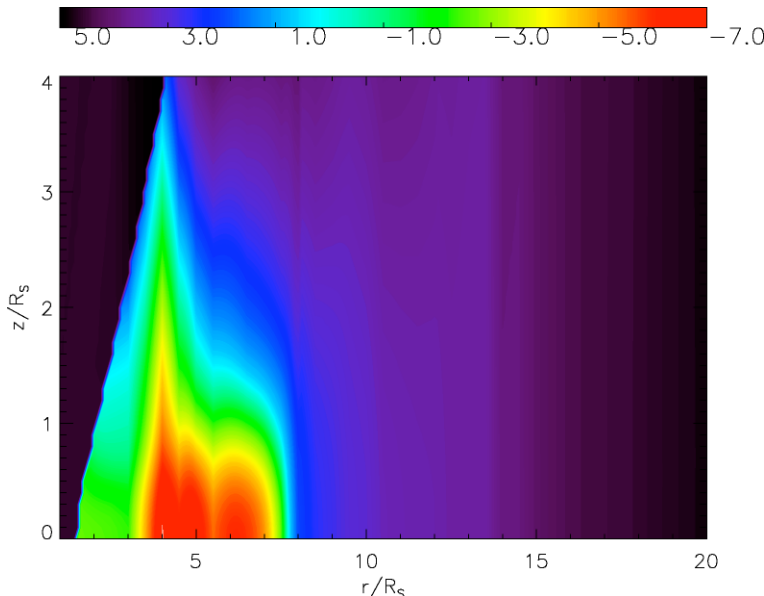


Fig. 1 Equilibrium dust potential distribution in the E ring ($\delta_M = 1.5$, $E_M = 400 \text{ eV}$)

for the inner plasma environment of Saturn that is based on Cassini's plasma measurements is still not available.

Due to sputtering, the radius of a dust particle decreases in time at a rate that is a function of the energy distribution of the bombarding ions, but roughly independent of the particle size, so that a grain with initial size of 1 μm would disappear in about 50 years (Jurac et al. 2001). The instantaneous size of a dust grain due to sputtering was integrated simultaneously with the equation of motion and the current balance equation.

6.3 Effects of Different Perturbing Forces

Here we briefly summarize the dynamical characteristics of the motion. The grain's eccentricity variation exhibits a periodicity driven by the radiation pressure and orbital precession. The planetary oblateness is responsible for the precession, while the Lorentz force causes the orbit of a negatively charged particle to regress with a rate depending on the particle charge and location (Horányi et al. 1992). The near cancellation of these for $r_g^* \simeq 1.2 \mu\text{m}$ radius dust grain allows solar radiation pressure to induce large eccentricities. As a consequence, these particles will be dispersed swiftly owing to their eccentric orbit. This cancellation occurs only for negatively charged dust grains and the corresponding grain radius can be approximated as $r_g^* \simeq \sqrt{0.1 * \Phi_V a_S^{0.5}}$ where a_S is the semimajor axes of the particle's orbit (in R_S). The parameter $r_g^* \simeq 1.2$ micron for $\Phi = -7$ V [Richardson's plasma model] and $r_g^* \simeq 0.6$ micron for $\Phi = -2$ V [corresponding to the CDA measurements, Kempf et al. (2006)]. These charged grains will quickly (in a few years) collide with the A ring of Saturn due to their large eccentricities.

The out-of-plane component of radiation pressure will also force particles on inclined orbits (which determines the thickness of the ring). While this effect is modest for negatively charged grains, it can have a large effect for positively charged grains, that are unstable against vertical oscillations (Howard et al. 1999). In Saturn's magnetosphere dust particles around $a_S \simeq 7$ will turn positively charged. This is because of the combined effects of the enhanced secondary electron production due to increasing electron temperature, and the relative increase of UV induced photoelectron production as the plasma density is decreasing with distance. In situ charge measurements by the Cassini CDA instrument also observed the switch of the sign of the dust potential at this distance (Kempf et al. 2006).

Plasma drag leads to a secular growth of the semimajor axis of the dust particle orbit. The growth rate of the semimajor axis is inversely proportional to the size of the dust grain, the outward transport of smaller grains due to plasma drag is faster than for larger grains.

For very small grains ($<0.1 \mu\text{m}$), the Lorentz force is large and eventually the negatively charged dust particles will be picked up by the corotating magnetic field of Saturn. Particles that have positive charge will be ejected from the magnetosphere due to the corotational electric field, forming the high speed stream of grains leaving the planet (Kempf et al. 2005).

Figure 2 shows the dust density distributions in the E ring for various particle size ranges. The entire region between the outskirts of the A ring and Titan is populated by particles with $r_\mu < 0.5$, with a quite large vertical extent of about $0.5 R_S$ at Enceladus, reaching over $2.5 R_S$ outside the orbit of Rhea (top panel). Due to the transition from negative to positive charges the spatial distribution of particles with radii $r_\mu < 1$ exhibit a structural change at $\simeq 7 R_S$. Particles with $r_\mu > 1$ remain confined to the 'classical' E ring region (bottom panel), that do not reach beyond $\sim 9 R_S$. The competition between the outward dust transport due to plasma drag and mass loss due to sputtering sets the spatial range that particles with a given initial size can reach (Horányi et al. 2008).

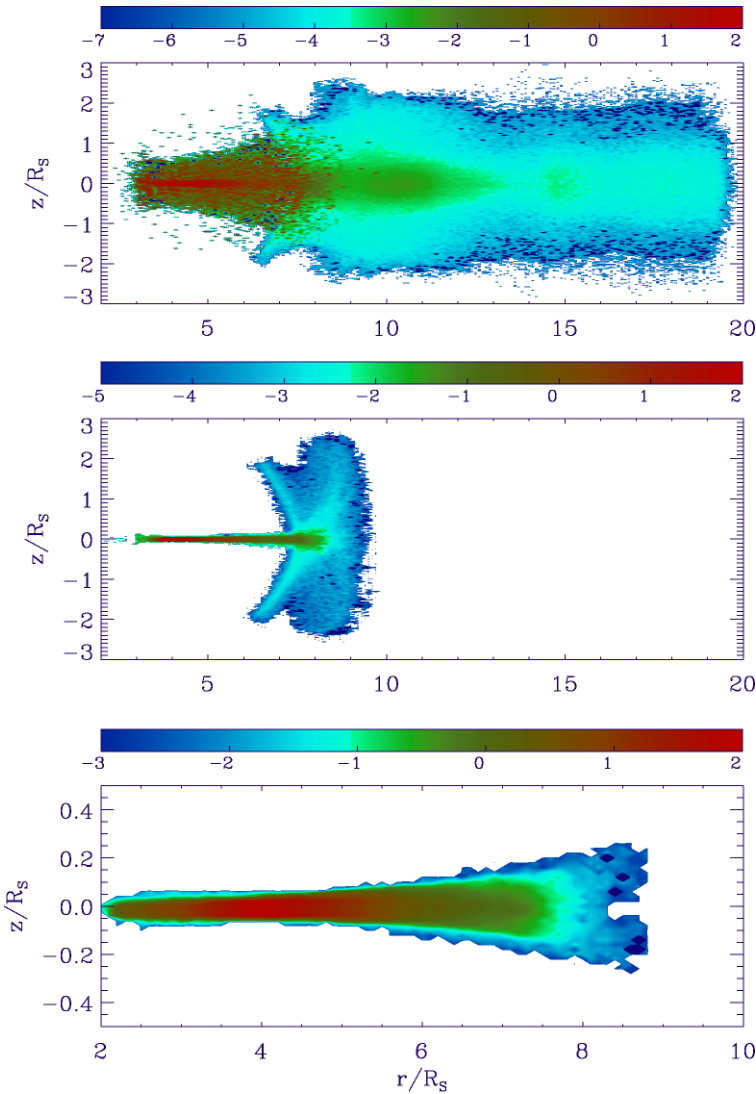


Fig. 2 The azimuthally averaged dust density distribution with radii: $0.1 < r_\mu < 0.5$ (*top*); $0.5 < r_\mu < 1$ (*middle*); and $1 < r_\mu < 3$ (*bottom*). The largest grains remain confined to the classical E ring, while the smallest particles can reach the orbit of Titan. All particles were released from Enceladus with an initial southward velocity of $v_z = 100$ m/s. The color scale is logarithmic, and normalized to 100 (percentage). The corresponding maximum number densities are: 7, 1.2, and 0.3 m^{-3}

The double-banded structure of the these grains at $z \simeq \pm 1000$ km near Enceladus (Fig. 2, bottom panel) is caused by their initial southward velocity of about 100 m/s with respect to their source, was also observed by Cassini (Porco et al. 2006a; Juhász et al. 2007). Outside $\simeq 9 R_S$ only particles with $r_\mu < 0.5$ can be found, consistent with the in situ observation (Srama et al. 2006).

The initial decoupling velocity of the dust grains from Enceladus (nonzero v_z) is ultimately responsible for the formation of the outward shift of the peak optical depth in the

E ring. This is due to the greatly prolonged lifetimes of grains with radii $r_g > 0.5 \mu\text{m}$ against re-collision with Enceladus, combined with their outward transport due to plasma drag. Finally, we note that the combined effects of all the forces (gravity, plasma drag, solar radiation pressure and Lorentz force) is responsible for shaping the E ring. Also, it is interesting to mention that, due to their longer lifetimes, grains from Enceladus alone could be responsible for the entire E ring.

7 Special Charging Effects

Finally, we describe two charging effects that demonstrate areas of future studies at the same time of providing fresh examples of the intriguing effects from planetary ring charging processes.

7.1 Electrostatic Braking

One charging effect on a dusty planetary ring, called electrostatic braking (Havnes et al. 1992), is a mechanism where dust particles arriving from outside of the ring and impacting it, will have a maximum electric charge and its speed dramatically reduced by the electrostatic field of the ring. This effect causes particles to be preferentially absorbed at the ring edges to contribute to the characteristic “M” shape frequently seen in the radial density structure of rings.

The mechanism begins with the ring’s screening electrostatic field, with the greatest field at the ring edge. Any (charged) small particle travelling from the outside of the ring and upon approach to the ring, will be nearly stopped by the ring’s electrostatic field. If the particle can penetrate the ring, then it will be discharged inside and given less acceleration by the ring electrostatic field upon leaving. If the particle oscillates through the ring, then it will gradually become absorbed by it. Particles are preferentially absorbed at the ring edges.

The conditions for electrostatic braking are that the maximum potential difference from the outside to the inside of a ring structure should be comparable to the energy in the charging plasma (one might regard the dusty ring as a very large dust particle which also is charged up), in order for the speed of a particle to be dramatically reduced. For example, in a 10 eV hot plasma (and disregarding secondary electron production), the maximum potential difference V from the outside to the inside will be of the order of about twice $*V$, $V = -10$ volt (20 volt). In addition, the conditions require a dense ring, a dusty plasma, i.e., the P -parameter value is close to 1 or more. In tenuous rings, the potential difference will be much lower, and the overall ring potential is much reduced compared to the maximum attainable value.

The electrostatic braking effect, while on the particle’s inbound trajectory, leads to an energy loss of $Z(\text{dust}) * V$ (eV). The dust charge number can be fairly high, which will increase the energy loss. One should also consider that if it passes through the ring structure, it will be accelerated as it travels out again, but there will be a net energy loss because the charge of the impacting dust particle is reduced inside of the cloud. For this reason, the energy gain (at a reduced charge compared to the charge as it encounters the ring structure) as the particle travels out will be lower than the energy loss while traveling in. Note that in a tenuous ring, the reduction in (negative) dust charge as the particle traverses the ring structure, will also be much smaller than in a dense ring. The braking effect therefore falls off roughly proportional to the square of the P -value of the ring structure.

7.2 Mach Cones

Mach cones are the V-shaped cone patterns visible in the laboratory around a charged body moving through, or close to, a layer of dusty plasma (Havnes et al. 2001). They are the result of an application of low-frequency, long-wavelength electrostatic waves; dust acoustic waves in an unmagnetized dusty plasma. This phenomena can yield information about the conditions in the dusty plasma, such as the velocity of the dust acoustic waves, the damping length, and the dust charge frequencies. Predicted to be seen also in planetary rings, this ~ 100 m-sized phenomena has so far has not been detected due to Cassini's lower ~ 1 km resolution.

Acknowledgements The authors thank Eberhard Grün for valuable discussions, ALG thanks the INAF Istituto di Fisica dello Spazio Interplanetario for its financial support January 2003 to October 2007, AJ acknowledges the support of the Hungarian OTKA grant K62617.

References

- F. Akalin et al., Geophys. Res. Lett. **33**, L20107 (2006)
- J.A. Bastin, Moon Planets **24**, 467 (1981)
- A. Bhardwaj, R.F. Elsner, J.H. Waite et al., Astrophys. J. **627**, L73 (2005)
- H. Bruining, *Physics and Applications of Secondary Electron Emissionx* (Pergamon, New York, 1954)
- J.F. Carbary, P.F. Bythrow, D.G. Mitchell, Geophys. Res. Lett. **9**, 420 (1982)
- V.W. Chow, D.A. Mendis, M. Rosenberg, Role of grain size and particle velocity distribution in secondary electron emission in space plasmas. J. Geophys. Res. **98**, 19065–19076 (1993)
- J.E.P. Connerney, Geophys. Res. Lett. **13**(8), 773 (1986)
- J.E.P. Connerney, Magnetic fields of the outer planets. J. Geophys. Res. **98**, 18659 (1993)
- J.N. Cuzzi, R.H. Durisen, Icarus **84**, 467 (1990)
- I. de Pater, S.C. Martin, M.R. Showalter, Keck near-infrared observations of Saturn's E and G rings during Earth's ring plane crossing in August 1995. Icarus **172**, 446 (2004)
- L.R. Doyle, E. Grün, Radiative transfer modeling constraints on the size of the spoke particles in Saturn's rings. Icarus **85**, 168–190 (1990)
- B.T. Draine, E.E. Salpeter, On the physics of dust grains in hot gas. Astrophys. J. **231**, 77–94 (1979)
- R.E. Eplee, B.A. Smith, Icarus **59**, 188 (1984)
- A.J. Farmer, P. Goldreich, Icarus **179**, 535 (2005)
- W.M. Farrell, M.D. Desch, M.L. Kaiser, W.S. Kurth, D.A. Gurnett, Geophys. Res. Lett. **33**, L07203 (2006)
- B. Feuerbacher, R.F. Willis, B. Fitton, Electrostatic potential of interstellar grains. Astrophys. J. **181**, 101–114 (1973)
- Fischer, Space Sci. Rev. (2008, this issue)
- G. Fischer et al., Icarus **183**, 135 (2006)
- C.K. Goertz, G. Morfill, Icarus **53**, 219 (1983)
- C.K. Goertz, Linhua-Shan, O. Havnes, Electrostatic forces in planetary rings. Geophys. Res. Lett. **15**, 84–87 (1988)
- C.K. Goertz, Dusty plasmas in the solar system. Rev. Geophys. **27**, 271–292 (1989)
- A.L. Graps, E. Grün, Properties, charging, and dynamics of interplanetary dust particles in Earth's magnetosphere, Final Report of ESA contract 13145/98/NL/WK, European Space Agency, July 2000, pp. 1–73
- A.L. Graps, S.F. Green, N.M. McBride, J.A.M. McDonnell, K. Bunte, H. Svedhem, G. Drolshagen, GEO debris and interplanetary dust: Fluxes and charging behavior, in *Dust in Planetary Systems*, ed. by H. Krüger, A. Graps. ESA SP-643, (ESA, Noordwijk, 2007)
- R. Greenberg, A. Brahic, eds., *Planetary Rings* (1984)
- E. Grün, G.E. Morfill, R.J. Terrile, T.V. Johnson, G. Schwehm, Icarus **54**, 227 (1983)
- E. Grün, C.K. Goertz, G.E. Morfill, O. Havnes, Icarus **99**, 191 (1992)
- D.P. Hamilton, Bull. Am. Astron. Soc. **38**, 578 (2006)
- O. Havnes, T.K. Aanesen, F. Melandsø, On dust charges and plasma potentials in a dusty plasma with dust size distribution. J. Geophys. Res. **95**(A5), 6581–8585 (1990)
- O. Havnes, T. Aslaksen, F. Melandsø, T. Nitter, Collisionless Braking of dust particles in the electrostatic field of planetary dust rings. Physica Scripta **45**, 491–496 (1992)

- O. Havnes, F. Li, T.W. Hartquist, T. Aslaksen, A. Brattli, Mach cones in dusty plasmas in planetary rings and in laboratory experiments. *Planet. Space Sci.* **49**, 223–220 (2001)
- A. Heck, Modellierung und Analyse der von der Raumsonde Galileo im Jupitersystem vorgefundenen Mikrometeoroiden-Populationen. PhD thesis, Ruprecht-Karls-Universität Heidelberg, February 1999
- J.R. Hill, D.A. Mendis, *Moon Planets* **24**, 431 (1981)
- M. Horányi, H.L.F. Houpt, D.A. Mendis, Charged dust in the Earth's magnetosphere. *Astrophys. Space Sci.* **144**, 215–229 (1988)
- M. Horányi, J.A. Burns, D.P. Hamilton, The dynamics of Saturn's E ring particles. *Icarus* **97**, 248 (1992)
- M. Horányi, Charged dust dynamics in the Solar System. *Ann. Rev. Astr. Astrophys.* **34**, 383 (1996)
- M. Horányi, E. Grün, A. Heck, Modeling the Galileo dust measurements at Jupiter. *Geophys. Res. Lett.* **24**, 2175–2178 (1997)
- M. Horányi, T.W. Hartquist, O. Havnes, D.A. Mendis, G.E. Morfill, Dusty plasma effects in Saturn's magnetosphere. *Rev. Geophys.* **42**, 4002 (2004)
- M. Horányi, A. Juhász, G.E. Morfill, The large-scale structure of Saturn's E-ring. *Geophys. Res. Lett.* **35**, L04203 (2008). doi:[10.1029/2007GL032726](https://doi.org/10.1029/2007GL032726)
- J.E. Howard, M. Horányi, G.R. Stewart, Global dynamics of charged dust particles in planetary magnetospheres. *Phys. Rev. Lett.* **83**, 3993 (1999)
- G.H. Jones et al., *Geophys. Res. Lett.* **33**, L21202 (2006)
- J.H. Jonker, On the theory of secondary electron emission. *Phillips Res. Rep.* **7**, 1 (1952)
- A. Juhász, M. Horányi, Saturn's E ring: a dynamical approach. *J. Geophys. Res.* **107**, A6 (2002). doi:[10.1029/2001JA000182](https://doi.org/10.1029/2001JA000182)
- A. Juhász, M. Horányi, Seasonal variations in Saturn's E-ring. *Geophys. Res. Lett.* **31**, L19703 (2004)
- A. Juhász, M. Horányi, G.E. Morfill, Signatures of Enceladus in Saturn's E-ring. *Geophys. Res. Lett.* **34**, L09104 (2007). doi:[10.1029/2006GL029120](https://doi.org/10.1029/2006GL029120)
- S. Jurac, R.E. Johnson, C. Richardson, Satellite sputtering in Saturn's magnetosphere. *Planet. Space Sci.* **49**, 319 (2001)
- S. Kempf, R. Srama, M. Horányi, M. Burton, S. Helfert, G. Moragas-Klostermeyer, M. Roy, E. Grün, High-velocity streams of dust originating from Saturn. *Nature* **433**, 289 (2005)
- S. Kempf, U. Beckmann, R. Srama, M. Horányi, S. Auer, E. Grün, The electrostatic potential of E ring particles. *Planet. Space Sci.* **54**, 999 (2006)
- S. Kempf, U. Beckmann, G. Moragas-Klostermeyer, F. Postberg, R. Srama, T. Economou, J. Schmidt, F. Spahn, E. Grün, The E ring in the vicinity of Enceladus: Spatial distribution and properties of the ring particles. *Icarus* **193**, 420–437 (2008)
- H. Kimura, I. Mann, The electric charging of interstellar dust in the solar system and consequences for its dynamics. *Astrophys. J.* **499**, 454–462 (1998)
- H. Kimura, I. Mann, Filtering of the interstellar dust flow near the heliopause: the importance of secondary electron emission for the grain charging. *Earth, Planets Space* **51**, 1223–1232 (1999)
- A.V. Krivov, On the dust belt of Mars. *Astron. Astrophys.* **291**, 657 (1994)
- N.G. Lehtinen, U.S. Inan, T.F. Bell, Trapped energetic electron curtains produced by thunderstorm driven relativistic runaway electrons. *Geophys. Res. Lett.* **27**, 1095 (2000)
- C.A. McGhee, R.G. French, L. Dones et al., HST observations of spokes in Saturn's B ring. *Icarus* **173**, 508–521 (2005)
- M. Meyer-Vernet, 'Flip-flop' of electric potential of dust grains in space. *Astr. Astrophys.* **105**, 98–106 (1982)
- C.J. Mitchell, M. Horanyi, O. Havnes, C.C. Porco, *Science* **311**, 1587 (2006a)
- C.J. Mitchell, C.C. Porco, Abstract P23E-0107. *Fall Meeting 2006*, American Geophysical Union (2006b)
- G. Morfill, E. Grün, T.V. Johnson, Dust in Jupiter's magnetosphere: Physical processes. *Planet. Space Sci.* **28**, 1087 (1980)
- G.E. Morfill, H.M. Thomas, *Icarus* **179**, 539 (2005)
- L.E. Moore, M. Mendillo, I.C.F. Mueller-Wodarg, D.L. Murr, *Icarus* **172**, 503 (2004)
- J.-U. Ness, J.H.M.M. Schmitt, S.J. Wolk, K. Dennerl, V. Burwitz, *Astron. Astrophys.* **418**, 337 (2004)
- P.D. Nicholson, M.R. Showalter, L. Dones, R.G. French, S.M. Larson, J.J. Lissauer, C.A. McGhee, B. Sicardy, P. Seitzer, G.E. Danielson, Observations of Saturn's ring-plane crossing in August and November. *Science* **272**, 509–516 (1996)
- P.D. Nicholson, M.R. Showalter, L. Dones, R.G. French, S.M. Larson, J.J. Lissauer, C.A. McGhee, B. Sicardy, P. Seitzer, G.E. Danielson, *Astron. Astrophys.* **418**, 337 (2004)
- T. Nitter, O. Havnes, *Earth, Moon, Planets* **56**, 7 (1992)
- C.C. Porco, *Bull. Am. Astron. Soc.* **20**, 852 (1988)
- C.C. Porco, Cassini Imaging Central Laboratory for Operations/SSI News Release July 5 (2006b)
- C.C. Porco, G.E. Danielson, *Astron. J.* **87**(5), 826 (1982)
- C.C. Porco et al., Cassini observes the active south pole of Enceladus. *Science* **311**, 139 (2006a)
- J.D. Richardson, An extended plasma model for Saturn. *Geophys. Res. Lett.* **22**, 1177 (1995)

- J.D. Richardson, A. Eviatar, M.A. McGrath, V.M. Vasyliunas, OH in Saturn's magnetosphere: Observations and implications. *J. Geophys. Res.* **103**, 20245 (1998)
- M.R. Showalter, J.N. Cuzzi, S.M. Larson, Structure and particle properties of Saturn's E ring. *Icarus* **94**, 451 (1991)
- E.C. Sittler et al., Cassini observations of Saturn's inner plasmasphere: Saturn orbit insertion results. *Planet. Space Sci.* **54**, 1197 (2006)
- F. Spahn et al., Cassini dust measurements at Enceladus and implications for the origin of the E ring. *Science* **311**, 1416 (2006a)
- F. Spahn et al., E ring dust sources: Implications from Cassini's dust measurements. *Planet. Space Sci.* **54**, 1024 (2006b)
- R. Srama et al., In situ dust measurements in the inner Saturnian system. *Planet. Space Sci.* **54**, 967 (2006)
- M. Tagger, R.N. Hendersen, R. Pellat, *Icarus* **91**, 297 (1991)
- E.J. Sternglass, *Sci. pap.*, 1772, Westinghouse Res. Lab., 1954
- D.M. Suszcynsky, J. Borovsky, C.K. Goertz, Secondary-electron yields of solar system ices. *Astrophys. Space Sci.* **13**(10), 187 (1993)
- F. Verheest, *Waves in Dusty Space Plasmas* (Kluwer, 2000)
- A.J. Weinheimer, A.A. Few, *Geophys. Res. Lett.* **9**, 1139 (1982)
- E.C. Whipple, Potentials of surfaces in space. *Rep. Prog. Phys.* **44**, 1197–1250 (1981)
- E.C. Whipple, T.G. Northrop, D.A. Mendis, The electrostatics of a dusty plasma. *J. Geophys. Res.* **90**, 7405 (1985)

Electromagnetic Signatures of Discharges in the Atmosphere

Schumann Resonances as a Means of Investigating the Electromagnetic Environment in the Solar System

**F. Simões · M. Rycroft · N. Renno · Y. Yair · K.L. Aplin ·
Y. Takahashi**

Originally published in the journal Space Science Reviews, Volume 137, Nos 1–4.
DOI: [10.1007/s11214-008-9398-0](https://doi.org/10.1007/s11214-008-9398-0) © Springer Science+Business Media B.V. 2008

Abstract The propagation of extremely low frequency (ELF, 3 Hz to 3 kHz) radio waves and resonant phenomena in the spherical Earth-ionosphere cavity has been studied for almost fifty years. When such a cavity is excited by naturally occurring broadband electromagnetic radiation, resonances can develop if the equatorial circumference is approximately equal to an integral number of wavelengths of the propagating electromagnetic waves; these are termed Schumann resonances. They provide information not only about thunderstorm and lightning activity on the Earth, and their relation to climate, but also on the properties of the low ionosphere. Similar investigations can be performed for any other planet or satellite, provided that it has an ionosphere.

F. Simões (✉)

Centre d'Etude des Environnements Terrestre et Planétaires, 4 Avenue de Neptune, 94107 Saint Maur,
France

e-mail: fernando.simoes@cetp.ipsl.fr

M. Rycroft

CAESAR Consultancy, 35 Millington Road, Cambridge CB3 9HW, UK

M. Rycroft

International Space University, 1 rue J-D Cassini, 67400 Illkirch-Graffenstaden, France

N. Renno

Department of Atmospheric, Oceanic and Space Sciences, University of Michigan, Ann Arbor,
MI 48109, USA

Y. Yair

Department of Life and Natural Sciences, Open University of Israel, Ra'anana 43107, Israel

K.L. Aplin

Space Science and Technology Department, Rutherford Appleton Laboratory, Chilton, Didcot, Oxon,
OX11 0QX, UK

Y. Takahashi

Department of Geophysics, Tohoku University, Aramaki-aoba, Sendai 980-8578, Japan

There are important differences between the Earth and other celestial bodies regarding, for example, the surface conductivity, the atmospheric conductivity profile, the geometry of the ionospheric cavity, and the sources of excitation. To a first approximation, the size of the cavity defines the fundamental resonant frequency, the atmospheric electron density profile controls the wave attenuation, the nature of the sources influences the electromagnetic field distribution in the cavity, and the body surface conductivity indicates to what extent the subsurface can be explored. The frequencies and attenuation rates of the principal eigenmodes depend upon the electrical properties of the cavity. Instruments that monitor the electromagnetic environment in the ELF range on the surface, on balloons, or on descent probes provide unique information on the cavity.

In this paper, we present Schumann resonance models for selected inner planets, some gaseous giant planets and a few of their satellites. We review the crucial parameters of ELF electromagnetic waves in their atmospheric cavities, namely the electric and magnetic field spectra, their eigenfrequencies, and the associated Q -factors (damping factors). Then we present important information on theoretical developments, on a general model that uses the finite element method and on the parameterization of the cavity. Next we show the distinctiveness of each planetary environment, and discuss how ELF radio wave propagation can contribute to an assessment of the major characteristics of those planetary environments.

Keywords Atmospheric electricity · Planets · Moons · Atmosphere · Ionosphere · Wave propagation · Schumann resonance · Lightning

1 Introduction

The Earth can be regarded as a nearly conducting sphere, wrapped in a thin dielectric atmosphere that extends up to the ionosphere, for which the conductivity is also substantial. The surface and ionosphere of the Earth form a cavity that, when excited with a broadband electromagnetic spectrum, can develop resonant states for which the average equatorial circumference is approximately equal to an integral number of wavelengths of the electromagnetic waves trapped in the resonator. This phenomenon was studied first theoretically by Schumann (1952, for an historical perspective, see Besser 2007) and later observed by Balser and Wagner (1960). For Schumann resonances to exist a broad initial electromagnetic source spectrum is required. This can be provided by lightning activity and, together with other lower frequency phenomena (Bösinger and Shalimov 2008), is a property of the AC global electric circuit (Aplin et al. 2008).

The DC global electric circuit is characterized by a quasistatic vertical “fair weather” electric field that decreases with altitude; close to the surface it has a value $\sim 120 \text{ V m}^{-1}$. The potential difference between the surface and the ionosphere amounts to $\sim 250 \text{ kV}$, which is sustained by a dynamic equilibrium between thunderstorm generators and losses in the fair weather atmosphere (Rycroft et al. 2000). The amplitude of the Schumann resonance electric field is a fraction of mV/m in a 1 Hz bandwidth. Schumann resonances exhibit amplitude and frequency variability related to the location of the lightning (e.g., Nickolaenko and Hayakawa 2002) and sprites (Boccippio et al. 1995).

Schumann resonances may also occur on other planets or moons, namely the rocky planets, icy moons, and gaseous giants of the solar system. The significance of atmospheric electricity for our understanding of celestial bodies was reviewed by Aplin (2006), with lightning playing a major role even though its existence in several planetary environments remains controversial (Yair et al. 2008). However, the standard cloud-to-ground and cloud-to-cloud discharges that act as radiating dipoles are not the only possible way of exciting

the cavity. Discharging phenomena due to triboelectric dust (e.g., Farrell and Desch 2001) might play a primordial role in atmospheric electrification of the Martian environment.

With the possible exception of phenomena recorded by the Huygens Probe in Titan's atmosphere (Simões et al. 2007; Béghin et al. 2007), Schumann resonances have never been identified on any celestial body other than the Earth. Modelling of Schumann resonances in planetary cavities contributes nevertheless to assessing wave propagation conditions and to defining instrument requirements aiming at planetary atmospheric electricity *in situ* measurements. The work of Nickolaenko and Hayakawa (2002, and references therein) testifies to the importance of Schumann resonance studies on Earth (for additional reviews, see Galejs 1972; Bliokh et al. 1980, and Sentman 1995) providing a reference for comparison with investigations in other planetary environments. Although cavity boundary conditions play a role on the assessment of wave propagation and Schumann resonances, the study of specific phenomena that take place on the surface and in the ionosphere of planetary environments is not the main objective of this work. The following reviews provide detailed descriptions of surface and ionospheric phenomena related to atmospheric electricity and wave propagation: Earth (Hargreaves 1979, 1992; Allen 1997); Venus (Brace and Kliore 1991; Donahue and Russell 1998; Pettengill et al. 1998); Mars (Christensen and Moore 1993; Nagy et al. 2004); outer planets (Atreya 1986; Majeed et al. 2004).

Here we revisit work related to Schumann resonances in planetary environments. We start by summarizing those observations and models of Schumann resonances at the Earth that contribute to establishing similarities and differences with other planets. Subsequently, we present the general theory about Schumann resonances and numerical models of them, followed by a review of theoretical work for Venus, Mars, Jupiter, Io, Europa, Saturn, Titan, Uranus, and Neptune. Finally, we briefly highlight several recommendations concerning Schumann resonance future modelling and measurement strategies.

2 Schumann Resonances on Earth

Schumann resonance spectrum fluctuations reflect the dynamic state of the surface-ionosphere cavity. Unlike the cavity inner boundary that is sharp, stable, approximately uniform, and can be considered to be a Perfect Electric Conductor (PEC), the outer boundary is neither sharp nor constant. Several processes contribute to such a complication, namely the day-night ionospheric asymmetry and polar heterogeneity, combined with the eccentric geomagnetic field (e.g., Nickolaenko and Hayakawa 2002). Ionospheric asymmetry and the inhomogeneous distribution of lightning increase cavity intricacies; consequently, both data interpretation and cavity characterization are rather difficult, but they provide additional information about atmospheric electricity.

The outer boundary variability has significant implications on Schumann resonance spectra. For example, the eigenfrequencies of the cavity were found to be shifted downwards by about 0.5 Hz due to high altitude nuclear explosions (Madden and Thompson 1965). The interaction between the solar wind and the ionosphere distorts and modulates (by the solar cycle) the upper boundary and influences cavity eigenfrequencies, which also respond to solar flares (Reid 1986).

Observations have shown that the signal amplitude, frequency, and cavity *Q*-factor (damping factors) all increase during solar proton events (Schlegel and Füllekrug 1999). Under normal conditions, the five lowest Schumann eigenfrequency peaks are close to 8, 14, 20, 26, and 32 Hz, and the respective *Q*-factors are about 5 (e.g., Nickolaenko and Hayakawa 2002). The maximum number of peaks of 13 detected so far was obtained for controlled experimental conditions during strong lightning activity (Füllekrug 2005).

One major interest of Schumann resonance studies on Earth is concerned with the processes linking lightning and thunderstorm activity to the global electric circuit and to climate change. This began when Williams (1992) established the connection between worldwide thunderstorm activity and climate variability.

The amplitude, frequency, and Q -factors of the resonance peaks show daily variations that are related to the development of thunderstorms around the globe, whose maximum activity is reached in the late afternoon Local Time (near the dusk terminator). This produces an amplitude variation by a factor of 2 or 3 and a few percent deviation on frequency. These observations provide evidence that lightning is the major natural electromagnetic source of energy for the Earth-ionosphere cavity.

Perturbations in the ionospheric boundary produce frequency splitting. According to numerical calculations made by Galejs (1972), frequency splitting due to day–night asymmetry is small because the altitude of the lower boundary of the ionosphere varies from approximately 60 km at the subsolar point to 90 km in the night side. The polar non-uniformity is largest at high latitudes and is related, for example, to transient polar cap absorption events initiated by coronal mass ejections, arriving in the Earth's vicinity. The penetration of solar wind particles deep in the magnetosphere changes the ionization rate and, consequently, the conductivity profile. The geomagnetic field distorts the upper boundary further, and this may be the dominant effect. Using ELF transient data, Sentman (1989) measured the transverse and parallel components of the horizontal magnetic field and observed that the peak frequency difference of the spectral components is in the order of 1 Hz; this difference was attributed to line splitting. Recent observations have shown additional evidence for line splitting and amplitude variations due to cavity heterogeneity, namely the day-night asymmetry (Sátori et al. 2007; Nickolaenko and Sentman 2007).

Currently, Schumann resonance studies of the Earth-ionosphere cavity are driven by three major research fields, specifically climate change, the global electric circuit and transient luminous events such as sprites, and space weather. The connection between Schumann resonances, lightning, and thunderstorm activity at the global scale presents a reliable method of monitoring climate variability and its response to space weather events (Williams 1992; Williams and Sátori 2007). Schumann resonance measurements also contribute to sprite investigations (Williams et al. 2007).

3 Wave Propagation and Resonances in Planet-Ionosphere Cavities

3.1 Analytical Approximation

The simplest approximation that can be made to estimate the Schumann resonance frequencies is to consider a thin cavity formed by two highly conductive, concentric, spherical shells. Schumann (1952), considering a lossless thin cavity, estimated the Earth-ionosphere cavity eigenfrequencies (angular frequencies), which are given by

$$\omega_n = \sqrt{n(n+1)} \frac{c}{R}, \quad (1)$$

where c is the velocity of light in the medium, R the cavity radius, and n an integer. These frequencies correspond to the resonant modes of the cavity, which are known as Schumann resonances, and fall within the ELF range for most celestial objects, particularly the Earth.

The characterization of electromagnetic wave propagation in the cavity, specifically to study the resonant states, requires Maxwell's equations to be solved. The analytical method developed by Greifinger and Greifinger (1978) for the Earth-ionosphere cavity has also been applied to other planets (e.g., Pechony and Price 2004). The Greifingers' model, later generalized by Sentman (1990a), considers the decoupling between transverse electric and magnetic modes that is acceptable when the cavity thickness, h , is much smaller than the radius ($h \ll R$). In general, the conductivity profile is described by an exponential law within the cavity with two scale heights ("knee model"), known often as the height of cut-off of the electric field and the height of diffusion of the magnetic field. The analytical models valid for the Earth's cavity have some limitations that weaken their applicability to other planets; in fact, subsurface losses, medium permittivity, and intricate atmospheric conductivity profiles neglected for Earth models must be taken into account when studying more complex planetary cavities (Simões et al. 2008a).

The Earth's surface is a good electrical conductor (e.g., Lide et al. 2006; Rycroft et al. 2008) and the PEC condition is applicable in the ELF range. The skin depth, δ_d , of the Earth's surface at ELF is ~ 1 km, two orders of magnitude lower than cavity thickness. Consequently, models put the cavity's inner boundary at the Earth's surface. For the lower ionosphere the skin depth is similar at about 80 or 90 km altitude, which therefore defines the upper boundary. Similar considerations can be employed to define the boundary conditions of planetary cavities. For example, Titan's surface is a poor reflector because its conductivity is very low ($\sim 10^{-9}$ S m $^{-1}$, Grard et al. 2006); this corresponds to $\delta_d > 10^3$ km, and ELF waves can propagate in the subsurface (Simões et al. 2007). The lower bound of the ionosphere represents the outer boundary of a cavity.

3.2 Numerical Modelling

Although some analytical approximations are accurate enough for the Earth-ionosphere cavity, they are not applicable to other planetary environments. Several simplifications are, nevertheless, useful because they can provide an overview of the physical parameters that control ELF radio wave propagation. Numerical modelling gives higher accuracy and is applicable to more complex cavities.

Numerical tools have been developed for applications with elaborate conductivity profiles, subsurface losses, or arbitrary distributions of electromagnetic sources within the cavity. Three types of numerical methods have been used to model planetary cavities: (i) Transmission Line Modelling (TLM), (ii) Finite Difference Time Domain (FDTD), and (iii) Finite Element Method (FEM). The TLM method described by Morente et al. (2003) employs a circuit-like approach with resistor and capacitor networks for modelling the evolving electromagnetic field. The FDTD technique is extremely popular for the computational modelling of various electrodynamics situations, and utilizes the finite difference approach (Yang et al. 2006; Navarro et al. 2007; Soriano et al. 2007). The FEM technique is often used for solving partial differential equations for complex domains by employing unstructured meshes (Simões et al. 2008a). The FDTD and FEM algorithms are suitable for solving eigenfrequency, time harmonic, and transient problems, by employing 2D axisymmetric or 3D descriptions.

3.3 Cavity Parameterization

Solar system planetary environments can be grouped into one of two major classes—those with (i) partly rocky/icy surface conditions, or (ii) entirely gaseous cavities. General cavity

parameterizations are described in the remainder of the paper, and applied to Venus, Mars, Jupiter, Io, Europa, Saturn, Titan, Uranus, and Neptune.

The Earth-ionosphere cavity is relatively simple compared with those of other planetary environments. Several simplifications can be made, namely:

- (i) the surface can be considered to be a PEC because the skin depth of ELF waves is lower than ~ 1 km and therefore represents the inner boundary;
- (ii) the atmospheric relative permittivity does not deviate much from vacuum conditions and only the conductivity profile must be taken into account;
- (iii) the altitude of the upper boundary is small compared to the cavity radius ($h/R \sim 0.01$), which allows several simplifications to be made in analytical approaches—for example, the electric field horizontal component is only a few percent of the vertical one and can be neglected to a first approximation.

At least one of these simplifications cannot be made for each of the other planets or moons of the solar system.

The electron conductivity profile is derived from electron density and thermodynamic parameters such as temperature and pressure; the permittivity profile is derived from the gas density and refractivity equations. Although the conductivity profile is the dominant determinant of the cavity parameters (see Rycroft et al. 2008), permittivity corrections should also be considered when the gas density is significant, namely for the atmosphere of Venus and for the interior of giant planets. The refractivity of a neutral gas is a linear function of density at low pressure and negligible for most atmospheres. However, on the giant planets, following gas density increasing with depth, a permittivity profile is required. Medium conductivity usually includes heterogeneities though any sort of anisotropy is neglected; for example, corrections due to static magnetic fields are not taken into account though they may be significant for studying some environments.

After discussing the relevant phenomena that play a role in determining the properties of the cavity, we briefly address cavity parameterization following the general approach presented by Simões et al. (2008a) and visualized in Fig. 1:

- (a) *Surface radius (R_P)*. Most planetary or moon radii are estimated assuming spherical shapes. By definition, the surface of the gaseous giants corresponds to the 1-bar reference level.

Fig. 1 Sketch of the model used for calculating the properties of Schumann resonances.

R_P : planet radius;

R_{int} : lower boundary radius;

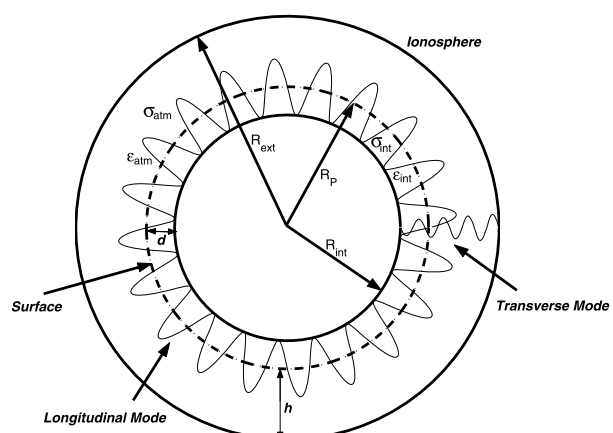
R_{ext} : ionosphere radius;

h : altitude of the ionosphere;

d : depth of the lower boundary;

ε_{int} , ε_{atm} , σ_{int} , σ_{atm} :

permittivities and conductivities of the interior and atmosphere, respectively



- (b) *Height of the ionosphere (h) and cavity upper boundary (R_{ext})*. The upper boundary of the cavity is located where the skin depth of propagating ELF waves is much smaller than the ionospheric height. Cavities are spherically symmetric unless specified otherwise.
- (c) *Depth of the subsurface interface (d) and cavity lower boundary (R_{int})*. The surface and inner boundary do not, in general, coincide; the giant planets represent a fair example of such a scenario; the Earth is an exception because of high surface conductivity.
- (d) *Conductivity profile of the atmosphere and lower ionosphere (σ_{atm})*. The ionospheric conductivity profile of most planets has only been measured down to the electron density peak of what is generally known as the Chapman layer (Chapman 1931); the outer boundary of the cavity always lies beneath that. The atmospheric conductivity profile is known with good accuracy only for the Earth; other conductivity profiles for solar system bodies rely, at least partially, on modelling.
- (e) *Permittivity profile of the atmosphere (ϵ_{atm})*. The relative permittivity of a vacuum, $\epsilon = 1$, is generally assumed for the atmosphere of most planets, but this is a crude approximation for Venus because the atmospheric pressure is so high.
- (f) *Conductivity profile of the interior (σ_{int})*. In general, the surface of rocky/icy celestial bodies is not a perfect conductor and, consequently, cannot be considered to be the inner boundary. To a first approximation, the conductivity does not vary with depth unless better estimates are available. This assumption is not applicable to the giant planets because the density increases with depth and the model must include a conductivity profile.
- (g) *Permittivity profile of the interior (ϵ_{int})*. The approach that is applied to the subsurface conductivity profile is also valid for the permittivity. For Mars and Titan, the permittivity is usually considered to be independent of frequency, temperature, and depth; the dielectric properties of typical materials, namely silicates and ices, have to be considered. The subsurface permittivity profile of the gaseous giant planets follows similar assumptions used for the atmosphere of Venus, and information about the composition and density is required.

Detailed descriptions of the cavity parameters can be found in Sentman (1990b) for the cavity of Jupiter. Simões et al. (2007, 2008b) generalize that study to other planetary bodies.

4 Planetary Cavities

Whereas lightning is the major electromagnetic source on Earth, some other phenomena contribute to pump the cavity, including triboelectric phenomena, corona effect, and magnetospheric broadband radio noise (e.g. Rakov and Uman 2003). Schumann resonances are most likely present on the Jovian planets, where lightning detection is confirmed by whistlers and other radio frequency signals and also optical measurements (Gurnett et al. 1979; Kurth et al. 1985; Fischer et al. 2006). The phenomenon is less certain to occur on the Uranian planets and Venus because radio signals have not been widely confirmed by optical instruments (Zarka and Pedersen 1986; Gurnett et al. 1990, Farrell 1996; Rakov and Uman 2003). Mars and several moons require alternative sources of energy. If Schumann resonances are excited on Mars and Titan, the most probable electromagnetic sources are dust storms and magnetospheric plasma of Saturn, respectively (Farrell and Desch 2001; Bégin et al. 2007). In the flowing we review Schumann resonance modelling of each planetary cavity.

4.1 Venus

Knowledge about the environment of Venus has been gathered from ground-based observations, and orbiters, flybys, balloons, and landers space missions. In particular, the Venera 11 and 12 probes collected electric field data at very low frequencies (10–80 kHz) during their descent through the atmosphere.

The first estimates of Schumann resonances for the Venus cavity were made by Nickolaenko and Rabinovich (1982). The major contribution of this work was to show that Schumann resonances are suitable for studying planetary electricity and can be used to infer lightning activity. The existence of lightning on Venus was a controversial issue for a long time (e.g., Strangeway 2004; Yair et al. 2008). Recent whistler-mode waves collected on-board Venus Express have been attributed to lightning signatures and apparently solved the dispute (Russell et al. 2007). There, Schumann resonance measurements would provide an alternative approach to inferring lightning activity.

Pechony and Price (2004) utilized a variation of the knee model and the theoretical conductivity profile developed by Borucki et al. (1982) to compute the eigenmodes of the Venusian cavity. Whereas the eigenfrequencies are only slightly larger than on Earth, the Q -factors are larger, ~ 10 , suggesting that wave attenuation is lower on Venus than on Earth. Yang et al. (2006) employing the FDTD method have obtained similar results. Interestingly, all approaches predict similar eigenfrequencies, though the Nickolaenko and Rabinovich (1982) model halves the Q -factor. Simões et al. (2008a), using a FEM algorithm and similar conductivity profiles, assessed the contribution of subsurface losses to the Q -factor; they found similar eigenfrequencies and Q -factors to those reported by Yang et al. (2006) unless the surface conductivity is lower than 10^{-5} – 10^{-4} S m $^{-1}$.

The Venusian atmosphere is very dense with a surface pressure of ~ 90 bar and, consequently, atmospheric refractivity phenomena play a role in radio wave propagation. Using a numerical approach, and also analytical approximations employing a variant of Sentman (1990b) model, Simões et al. (2008b) assessed the contribution due to corrections of atmospheric permittivity and found a peak on the electric field profile at ~ 32 km, which is close to the altitude of critical refraction. Although ELF measurements are not available and interpretation is difficult due to gaps in the electric field profiles, modelling and Venera 11 and 12 very low frequency data show some similarities.

The slow spin of Venus, the absence of a significant magnetic dipole, and specific atmospheric chemistry and plasma dynamics produce an asymmetric cavity (e.g., Strangeway 2004). Simões et al. (2008b) predict that this cavity asymmetry produces a line splitting larger than 1 Hz for the lowest frequency. Eigenmode degeneracy is partially removed; this effect should be easier to observe on Venus than on Earth because the cavity asymmetry produces considerable line splitting and also sharper peaks.

Table 1 shows a synopsis of Schumann eigenfrequencies, including those for the Venus cavity. Improved studies require information on the conductivity profile and surface properties. Venus Express and future space missions can contribute to an assessment of some of these hypotheses, mainly on the upper boundary, though *in situ* measurements are required to confirm some of the previous results. Improved models should take into account ionospheric anisotropy due to a static magnetic field, mainly on the night-side.

4.2 Mars

The Martian environment has been explored using Earth-based, remote sensing, and *in situ* observations, but the electrical properties of the lower atmosphere and of the surface are

Table 1 Schumann resonance frequencies (f) and damping factors (Ω) of planetary cavities considering several parameters. Model: A—analytical; N—numerical, including the type of algorithm. Spacecraft measurements and typical models used to derive the conductivity profile are included

Body	1 st mode			2 nd mode			3 rd mode			Cavity parameterization	Electromagnetic Sources	Conductivity profile	Model	Reference
	f [Hz]	Ω	f [Hz]	Ω	f [Hz]	Ω	f [Hz]	Ω	f [Hz]					
Venus	9	5.1	15.8	5.1	22.7	5.2						Pioneer Venus, Magellan data	A	Nickolaenko and Rabinovich (1982)
	9.3	10.5	16.3	11.3	23.3	11.7								Pechony and Price (2004)
	9.05	10.1	15.9	10.2	22.64	10.3								Yang et al. (2006)
	9.01	8.0	15.81	8.1	22.74	8.0								N-FDTD
	8.80	4.8	15.77	5.7	22.67	6.4								Russell et al. (2007)
Mars	7.95	5.4	14.17	5.9	20.37	6.4								Sukhorukov (1991)
	13–14	3.3–3.7	25–26	3.5–3.8	37–38	3.7–40								A/N-FEM
	8.6	2.3	16.3	2.4	24.4	2.4								Pechony and Price (2004)
	8.8	2.27	16.1	2.35	23.6	2.45								Yang et al. (2006)
	7.3	2.5	13.1	2.5	19.2	2.8								N-FDTD
Jupiter	11–12	-	21.7–24.9	-	21.7–24.9	-								N-TLM
	8.31	1.9	15.64	1.8	23.51	1.8								Molina-Cuberos et al. (2006)
	7.93	1.9	14.93	1.9	22.41	1.9								N-FEM
	8.55	2.1	15.93	2.2	23.13	2.1								Simões et al. (2008a)
	10.97	2.4	20.34	2.4	30.19	2.3								Cummer and Farrell (1999)
Saturn	11.19	2.6	20.66	2.5	30.59	2.4								Soriano et al. (2007)
	9.67	2.5	17.88	2.4	26.46	2.3								N-FDTD
	0.76	7.2	1.35	7.2	1.93	7.3								Sentman (1990b)
	0.68	8.5	1.21	8.6	1.74	8.7								N-FEM
	0.93	7.8	1.63	6.8	2.34	6.5								Simões et al. (2008a)
Uranus	11–15	-	21.2–27.3	-	35.6–41.6	-								N-TLM
	19.9	2.6	35.8	2.7	51.8	2.8								Moretto et al. (2003)
	17.6	1.98	32.4	2.02	47.4	2.04								Nickolaenko et al. (2003)
	11.8	1.8	22.5	1.9	34.1	2.0								A
	10.6	1.40	20.5	1.49	30.8	1.54								Pechony and Price (2004)
Neptune	8.2	0.92	17.4	0.99	27.3	1.06								Yang et al. (2006)
	9.4	1.04	14.3	0.82	31.4	1.23								N-FDTD
	8.8	-	17.4	-	26.7	-								Béghin et al. (2007)
	10.9	-	20.4	-	30.1	-								Navarro et al. (2007)
	13.43	1.1	28.13	1.3	43.93	1.6								
Uranus	2.44	20.3	4.24	19.3	6.00	20.0								Voyager data
	1.02	2.0	1.99	2.0	3.03	2.3								Low water content – Voyager data 1
	2.47	20.6	4.27	19.4	6.04	18.9								Zarka and Pedersen (1986)
	1.12	1.7	2.17	1.9	3.26	2.0								Gurnett et al. (1990)
	2.33	9.7	4.12	9.4	5.90	9.5								Farrell (1996)
Neptune	1.10	1.0	2.03	1.1	2.96	0.9								Low water content
														High water content

still poorly known. Using propagation techniques, radio science instruments measured the electron density down to ~ 70 km, where a sporadic layer is observed (e.g., Pätzold et al. 2005, and references therein), but the conductivity profile is unknown at lower altitudes. Several profiles are found in the literature and, in some instances, ELF wave propagation is questionable due to significant losses in the cavity (e.g., Soriano et al. 2007). The atmosphere consisting mostly of CO₂ has a density which is about 60–70 times lower than on Earth, and surface conductivity estimates in the literature vary between 10⁻¹² and 10⁻⁷ S m⁻¹ (Aplin 2006). The dielectric properties of the regolith should vary with latitude, depth, and composition, especially if water/ice/brines are embedded in the medium.

There is no evidence of lightning activity on Mars but it is generally accepted that, due to triboelectricity effects, massive dust storms might produce large electric fields like on Earth (Farrell and Desch 2001; Kok and Renno 2008). Potential gradients up to 5 kV m⁻¹ have been measured during dust devils on Earth and, in some cases, discharging was observed (Crozier 1964; Rakov and Uman 2003). Spectral features of these emissions should, however, considerably differ from those observed on the Earth; whereas atmospheric low density favours discharges on Mars, development of large potential gradients is more difficult due to dust electrification mechanisms efficiency (Buhler et al. 2003). Classification of atmospheric breakdown conditions deserves further investigations, namely measurements of Paschen curves, because atmospheric electricity is also relevant concerning risk assessment of robotic and human missions.

Sukhorukov (1991) computed the Schumann resonances of the Martian cavity and found the lowest mode peaking at 13–14 Hz, with a *Q*-factor of the order of 3.5. Pechony and Price (2004) found significantly lower values, of the order of 8.6 Hz and *Q* \sim 2.3 using a different conductivity profile (Cummer and Farrell 1999). Yang et al. (2006) used the FDTD method employing a few conductivity profiles with different surface conductivities and obtained 7–14 Hz for the lowest eigenmode and *Q* \sim 2–4. Molina-Cuberos et al. (2006) considered an alternative conductivity profile; they obtained 11 Hz for the first Schumann resonance frequency. Soriano et al. (2007) employed several conductivity profiles including Viking and Mariner data and specific contributions due to meteoroids; they found *Q*-factors of the order of 2.5 and 11 Hz for the lowest eigenfrequency. Table 1 presents typical values of the predicted Schumann resonances on Mars. It shows that the eigenfrequencies are extremely sensitive to the selected conductivity profile. The significance of subsurface losses is related to the inner boundary and to what depth the PEC condition is valid.

Ongoing and future missions that are able to investigate the subsurface, namely the radars onboard Mars Express and Mars Reconnaissance Orbiter, might provide information to constrain surface losses. Considering the conductivity profile of Cummer and Farrell (1999), all models predict considerable attenuation. In fact, higher conductivity values impair propagation leading to evanescent modes.

4.3 Jupiter

Lightning has been identified on Jupiter by several spacecraft (see review by Yair et al. 2008) and the Schumann resonance frequencies were first estimated by Sentman (1990b). The atmospheric density increases significantly with depth and the vacuum approximation is no longer valid for the permittivity. Deep in the molecular hydrogen envelope, theoretical models predict a phase transition from gas to liquid hydrogen. The permittivity, which is related to the gas density, increases with depth until reaching ~ 1.25 when hydrogen condenses. The normalized radius of the liquid interface is ~ 0.76 .

Sentman (1990b) calculated the Schumann resonance parameters for Jupiter taking into account the conductivity profile not only of the ionosphere and atmosphere but also deeper in

the gaseous envelope. Simões et al. (2008a) used an updated conductivity profile (Liu 2006) and also considered the contribution due to gas permittivity. Table 1 shows the estimated Schumann frequencies that are significantly smaller than on Earth because the cavity is much larger.

4.4 Io and Europa

This work reviews not only planetary cavities but also the electric environments of a few moons. The environments of Titan, Europa, and Io are different and unique. Schumann resonance characteristics on Io have been estimated by Nickolaenko and Rabinovich (1982), though it is unlikely that they occur because the conductivity close to the surface is high leading to evanescent modes (Simões et al. 2008a). Volcanoes might be an ELF source of electromagnetic energy on Io but wave attenuation prevents the development of resonant states. Although Europa possesses an ionosphere (Kliore et al. 1974, 1997), the conductivity seems to be too high down to the surface and, consequently, no resonant state is reached. Unlike Titan, it does not seem conceivable that Schumann resonances can be used to study the ionosphere or the interior of the Galilean moons.

4.5 Saturn

The approach used to study the Jupiter cavity is also valid for Saturn, where the liquid interface is expected at a normalized radius of ~ 0.48 . Lightning has been detected with the multiple instruments onboard Cassini, confirming previous observations (Fischer et al. 2006; Yair et al. 2008). Simões et al. (2008a) derived the conductivity profile of the ionosphere taking into account information from the electron density, pressure, temperature, and composition data collected by the Voyager and Cassini spacecraft. The conductivity of the atmosphere is interpolated between values for the lower ionosphere and for the upper interior (Liu 2006). The expected eigenfrequencies (Table 1) are slightly higher than for Jupiter and the corresponding Q -factors are about 7.

4.6 Titan

Titan, the largest satellite of Saturn, is a remarkable celestial body; it is the only moon in the solar system with a thick atmosphere, which might resemble that of the primordial Earth, several billion years ago. Voyager flybys, in the early 1980s, revealed an atmosphere composed of nitrogen with a small amount of methane, and permeated with a haze that impaired surface observations. The observation of possible prebiotic conditions on Titan was one of the major objectives of Cassini-Huygens, a mission dedicated to the Kronian system—Saturn, its rings and its moons (Matson et al. 2002; Lebreton and Matson 2002). The spacecraft included an entry probe, Huygens, designed to perform *in situ* experiments of the composition and electrification of Titan's atmosphere, namely measurement of ELF electric fields. The Permittivity, Waves, and Altimetry (PWA) analyzer, a sub-unit of the Huygens Atmospheric Structure Instrument, recorded an electric field with frequency of 36 Hz with average amplitude of $\sim 2 \text{ mV m}^{-1}$ (Simões et al. 2007). However, the true nature of this signal is not yet fully understood; possible signals induced by vibrations of the antenna are not completely ruled out. Béghin et al. (2007) considered several hypotheses that could provide an interpretation of the origin of such an intriguing signal; they proposed a model involving the production of ELF ion-acoustic turbulence in the ionospheric regions that load the wake currents, which are driven by the interaction of

the co-rotating Saturn's magnetosphere with Titan ionosphere, and a subsequent coupling mechanism between the electrostatic turbulence and whistler-mode wavelets able to emerge downwards in the atmospheric cavity. The signal resembles that of a Schumann resonance, but further investigations are necessary to identify the energy source more rigorously.

Most Schumann resonance models of Titan's cavity consider the conductivity profiles of Borucki et al. (1987) and Molina-Cuberos et al. (2004) developed before the Cassini-Huygens measurements. Although PWA data were only recorded below 140 km altitude, it is clear that the theoretical conductivity profile was overestimated by almost two orders of magnitude at 100 km. The identification of a local conductivity peak at about 60–70 km makes the conductivity profile more complex than previously expected (Hamelin et al. 2007). Additionally, the effect of aerosols on the conductivity profile is not fully understood (Borucki et al. 2006; Borucki and Whitten 2008).

The Cassini-Huygens data are expanding our knowledge of Titan's atmospheric environment. The most relevant results to Schumann resonance studies include:

- (i) the detection of clouds, mainly in the polar regions (Griffith et al. 2006),
- (ii) the lack of lightning detection after several Cassini flybys (Fischer et al. 2007),
- (iii) the Huygens data that might contain lightning signatures are still under investigation but, if present at all, lightning was not as ubiquitous as on Earth during the probe descent (Simões 2007),
- (iv) high aerosol concentrations in the atmosphere (Tomasko et al. 2005), and
- (v) a very low surface conductivity at the Huygens landing site (Grard et al. 2006).

Several models of Titan's Schumann resonances have been published. The first models were developed by Morente et al. (2003) and Nickolaenko et al. (2003). They estimated the lowest eigenfrequency to be in the range 11–20 Hz. Pechony and Price (2004) and Yang et al. (2006) calculated improved values using analytical and numerical models (Table 1). The discrepancies with the earlier models are related not only to the conductivity profile but also to the location of the upper boundary. Navarro et al. (2007) used a FDTD model and the conductivity profile of Molina-Cuberos et al. (2004) to estimate the Schumann frequencies; they obtained 9 Hz and 11 Hz for a perfect reflector on the surface and at a depth of 250 km, respectively (Table 1). Simões et al. (2007) included Huygens data to correct the conductivity profile at low altitude and to calculate the cavity eigenfrequencies as a function of several parameters, namely soil permittivity and conductivity, and depth of the inner boundary; they concluded that Titan interior can be investigated because the surface is a weak reflector of ELF waves, which can propagate in the subsurface. Therefore, Schumann resonances are a useful tool to assess the subsurface ocean predicted by theoretical models (e.g., Lunine and Stevenson 1987). Interpretation of recent Cassini radar data suggests that such a buried ocean may exist (Lorenz et al. 2008).

The electric environment of Titan is different from that found on Earth and from what was expected before the Cassini-Huygens mission. Lightning, if it exists, does not seem to be very frequent and so our understanding of the chemical processes acting in the atmosphere must be revised. The nature of the 36 Hz signal detected by the Huygens probe has yet to be resolved though it seems unrelated to lightning activity; a substitute electromagnetic source of energy is therefore required. The Schumann resonance can be used to estimate the buried ocean depth but the nature of the 36 Hz signal must be clarified. The intricate conductivity profile is certainly driven by electron attachment on aerosols and, consequently, the atmospheric chemistry models require further developments, particularly above 100 km. The hypothetical global electric circuit on Titan requires further investigations but is certainly different from that of Earth.

4.7 Uranus

The cavity of Uranus is quite different from those of Jupiter and Saturn. Voyager 2 measured the electron density (Lindal et al. 1987) with some discrepancy between ingoing and outgoing passes. Lightning is probably the major source of electromagnetic energy in the ELF range (Zarka and Pedersen 1986; Yair et al. 2008). The interior of Uranus is significantly different from that of the Jovian planets. A solid mantle of ices is substituted for the liquid hydrogen metallic mantle of Jupiter and Saturn. The water content of the Uranus environment is unknown and a concentration of only a few percent could increase the conductivity by several orders of magnitude.

Simões et al. (2008a) presented estimates of the Uranian Schumann resonances considering different ionospheric conductivity profiles. Table 1 shows the frequencies calculated with a few ionospheric conductivity profiles and varying water content. It is clear that Schumann resonances are sensitive to the water content in the gaseous envelope. The Schumann resonance frequencies of a water-rich envelope might be halved compared with those for a water-depleted scenario; the Q -factors would decrease by as much as a factor of ten.

4.8 Neptune

Like the other gaseous giants, Neptune is wrapped in an envelope composed of hydrogen and helium. A single ionospheric conductivity profile is available (Capone et al. 1977; Chandler and Waite 1986) and the evidence for lightning on Neptune is less convincing than for the other outer planets (Gurnett et al. 1990; Yair et al. 2008). The structure of the interior of Neptune is similar to that of Uranus, where an icy solid mantle is expected (e.g., Lewis 1995). The water content in the gaseous envelope is uncertain, but should induce significant variability of the conductivity profile, as in the case of Uranus (Liu 2006). High and low interior conductivity profiles produce significant changes in the cavity (Table 1).

5 Comparative Planetology Results

Modelling ELF electromagnetic wave propagation in various planetary cavities of the solar system provides a suitable method for studying the AC global electric circuits and atmospheric phenomena in different environments. Although cavity parameterization is, to date, somewhat limited, the study of Schumann resonances in different planetary cavities becomes a useful tool for assessing the properties of both the atmosphere and subsurface conditions.

Three major characteristics distinguish the cavity of Venus from that of the Earth: the surface is not a perfect reflector, the cavity is significantly asymmetric, and the atmospheric density is much greater. According to modelling, surface losses might change the Schumann resonant frequency estimates by as much as ~ 1 Hz with respect to those of a PEC surface; cavity asymmetry partially removes eigenmode degeneracy and produces significant line splitting (~ 1 Hz). Given the observed atmospheric permittivity, it is predicted that the Schumann resonance electric field profile should show a maximum at ~ 32 km altitude induced by refraction phenomena. The expected high Q -factor of the cavity ($Q \sim 10$) testifies that attenuation is lower than on Earth and, consequently, ELF wave propagation conditions should be better.

Although the Martian cavity radius suggests higher eigenfrequencies than on Earth, the significant atmospheric conductivity decreases the Schumann resonance frequencies and

implies low Q -factors as well. The subsurface contribution to the Q -factor is not significant, unless dry conditions extend deep into the crust, because the planetary surface and the inner boundary of the cavity are expected to nearly coincide. The lowest eigenfrequency falls in the range 8–13 Hz, though the most significant result expected is the low Q -factor (~ 2 or below), which implies significant wave attenuation. Thus, strong electromagnetic sources are required; it is not clear whether triboelectric phenomena, even in massive dust storms, are able to sustain ELF resonances of the cavity.

The eigenfrequencies of the Jupiter cavity are one order of magnitude lower than on Earth, and this is strictly related to the cavity radius; the Q -factor is higher than that of the Earth's cavity and has similar values for the first three eigenmodes; similar considerations are valid for the cavity of Saturn. The large variability of the estimated conductivity profile for Uranus and Neptune shows that Schumann resonances can be used to determine the most suitable profile and, indirectly, to assess the water content in the gaseous envelope. On Uranus, high and low interior conductivity profiles produce significant changes in the cavity; the Q -factor is in the order of 20 and 2, for low and high conductivity profiles, respectively. The Q -factors of Neptune cavity are smaller than for Uranus and propagation conditions are less favourable when the water content is high. Since high and low electron conductivity profiles are related to water content in the gaseous envelope, it is possible, in principle, to estimate the water content in the cavity from Schumann resonance measurements.

Possible Schumann resonances in the surface-ionosphere cavities of a few moons have also been investigated. The cavities of Io and Europa do not seem to be able to sustain standing waves because the expected conductivity is high and resonance states are not reached.

Although it is not obvious that a global circuit exists, ELF wave propagation in Titan's cavity is possible. However, this cavity is quite different from that of the Earth because a low altitude conductive layer related to cosmic rays was identified there and the surface is a weak reflector of ELF waves. Therefore, calculation of the cavity eigenfrequencies must include a subsurface contribution and the cosmic ray layer should have significant implications for a possible global circuit. Additionally, the ELF signal detected by Huygens, if real, should provide useful information regarding cavity characterization.

6 Summary

This paper reviews the major advances made concerning Schumann resonances on Earth that can be used in comparative planetary sciences, including the assessment of model predictions published for Venus, Mars, Jupiter, Saturn, Uranus, and Neptune, and the moons Io, Europa, and Titan. To date, Schumann resonances have been identified only on Earth. Titan *in situ* measurements performed by the Huygens Probe are still under investigation and should confirm whether ELF surface-ionosphere resonances have been observed or not. Schumann resonance measurements are useful to characterize the environment of the lower ionosphere and atmosphere, and possibly to investigate the subsurface of planets. Schumann resonances are likely, at least, on the Jovian planets, where unquestionable electromagnetic sources have been identified.

Schumann resonance measurements would contribute to studies of the following characteristics of planetary cavities:

- Venus—lightning detection, identification of the electric field maximum expected at an altitude of about 32 km, assessment of frequency line splitting, and global electric circuit;
- Mars—triboelectricity phenomena induced by dust, climate variability, global electric circuit, and monitoring of the sporadic low ionospheric layer;

- Jupiter, Saturn, Uranus, and Neptune—monitoring of lightning activity and quantification of global water content of the gaseous envelopes;
- Titan—validation of the Huygens Probe measurements, monitoring of the global electric environment, studies of the interaction with the magnetosphere of Saturn, and investigations of substrate dielectric properties and of the buried ocean.

Future models of planetary cavities must include better estimates of the conductivity profiles. Observations of the night-side of the ionospheres of Venus and Mars revealed intricate heterogeneous ionospheres; for example, the influence of multiple magnetic “cusp” that connect the crustal magnetic sources to the Martian tail and shocked solar wind plasma is not taken into account in electron density profiles. The contribution of static magnetic fields has been neglected in the models; the conductivity profiles have included scalar components only though anisotropic corrections may be significant in some planetary environments.

Balloons or airships that include electric and magnetic sensors are especially suitable platforms on which to perform measurements in the atmospheres of Venus, Titan, and the giant planets. Surface static modules are suitable for studying ELF wave phenomena on the surface of Mars and Titan.

The study of extraterrestrial Schumann resonances is an efficient way to investigate the electrical properties of surface-ionosphere cavities elsewhere in the solar system. ELF radio wave propagation models can contribute to improvements of our knowledge of planetary atmospheric electricity wherever, and whenever, they can be validated against *in situ* measurements.

References

- P.A. Allen, *Earth Surface Processes* (Blackwell, Oxford, 1997)
- K.L. Aplin, Surv. Geophys. **27**, 63–108 (2006). doi:[10.1007/s10712-005-0642-9](https://doi.org/10.1007/s10712-005-0642-9)
- K.L. Aplin et al., Space Sci. Rev. (2008, this issue)
- S.K. Atreya, *Atmosphere and Ionospheres of the Outer Planets and Their Satellites* (Springer, Heidelberg, 1986)
- M. Balser, C.A. Wagner, Nature **188**, 638–641 (1960). doi:[10.1038/188638a0](https://doi.org/10.1038/188638a0)
- C. Béghin, F. Simões, K. Karsnoselskikh et al., Icarus **191**, 251–266 (2007). doi:[10.1016/j.icarus.2007.04.005](https://doi.org/10.1016/j.icarus.2007.04.005)
- B.P. Besser, Radio Sci. **42**, RS2S02 (2007). doi:[10.1029/2006RS003495](https://doi.org/10.1029/2006RS003495)
- P.V. Bliokh, A.P. Nickolaenko, Yu.F. Filippov, in *Schumann Resonances in the Earth-Ionosphere Cavity*, ed. by D.L. Jones (Peter Peregrinus, Oxford, 1980)
- D.J. Boccippio, E.R. Williams, W.A. Lyons, I. Baker, R. Boldi, Science **269**, 1088–1091 (1995)
- W.J. Borucki, R.C. Whitten, Planet. Space Sci. **56**, 19–26 (2008)
- W.J. Borucki, Z. Levin, R.C. Whitten et al., Icarus **51**, 302–321 (1982)
- W.J. Borucki, Z. Levin, R.C. Whitten et al., Icarus **72**, 604–622 (1987)
- W.J. Borucki, R.C. Whitten, E.L.O. Bakes, E. Barth, S. Tripathi, Icarus **181**, 527–544 (2006)
- T. Bösinger, S. Shalimov, Space Sci. Rev. (2008, this issue)
- L.H. Brace, A.J. Kliore, Space Sci. Rev. **55**, 81–163 (1991)
- C.R. Buhler, C.I. Calle, E. Nelson, LPSC **34**, 17–21 (2003)
- L.A. Capone, R.C. Whitten, S.S. Prasad, J. Dubach, Astrophys. J. **215**, 977–983 (1977)
- M.O. Chandler, J.H. Waite, Geophys. Res. Lett. **13**, 6–9 (1986)
- S. Chapman, Proc. Phys. Soc. **43**(1), 26–45 (1931)
- P.R. Christensen, H.J. Moore, The Martian surface layer, in *Mars*, ed. by H.H. Kieffer, B.M. Jakosky, C. Snyder, M.S. Matthews (University of Arizona Press, Tucson, 1993)
- W.D. Crozier, J. Geophys. Res. **69**, 5427–5429 (1964)
- S.A. Cummer, W.M. Farrell, J. Geophys. Res. **104**(6), 14149–14158 (1999)
- T.M. Donahue, C.T. Russell, The venus atmosphere and ionosphere and their interaction with the solar wind: An overview, in *Venus*, ed. by S.W. Bougher, D.M. Hunten, R.J. Phillips (University of Arizona Press, Tucson, 1998)

- W.M. Farrell, Geophys. Res. Lett. **23**, 587–590 (1996)
- W.M. Farrell, M.D. Desch, J. Geophys. Res. **106**, 7591–7595 (2001)
- G. Fischer, M.D. Desch, P. Zarka et al., Icarus **183**, 135–152 (2006)
- G. Fischer, W.S. Kurth, U.A. Dyudina et al., Icarus **190**, 528–544 (2007)
- M. Füllekrug, Geophys. Res. Lett. **32**, L13809 (2005)
- J. Galejs, *Terrestrial Propagation of Long Electromagnetic Waves* (Pergamon, New York, 1972)
- R. Grard, M. Hamelin, J.J. López-Moreno et al., Planet. Space Sci. **54**, 1124–1136 (2006)
- C. Greifinger, P. Greifinger, Radio Sci. **13**, 831–837 (1978)
- C.A. Griffith et al., Science **313**, 1620–1622 (2006)
- D.A. Gurnett, R.R. Shaw, R.R. Anderson, W.S. Kurth, Geophys. Res. Lett. **6**, 511–514 (1979)
- D.A. Gurnett, W.S. Kurth, I.H. Cairns, L.J. Granroth, J. Geophys. Res. **95**, 20967–20976 (1990)
- M. Hamelin, C. Béghin, C.R. Grard et al., Planet. Space Sci. **55**, 1964–1977 (2007)
- J.K. Hargreaves, *The Upper Atmosphere and Solar-Terrestrial Relations* (Van Nostrand Rheinhold, UK, 1979)
- J.K. Hargreaves, *The Solar-Terrestrial Environment* (Cambridge University Press, UK, 1992)
- A. Kliore, D.L. Cain, G. Fjeldbo, B.L. Seidel, S.I. Rasool, Science **183**, 323–324 (1974)
- A.J. Kliore, D.P. Hinson, F.M. Flasar, A.F. Nagy, T.E. Cravens, Science **277**, 355–358 (1997)
- J.F. Kok, N.O. Renno, Phys. Rev. Lett. **100**, 014501 (2008)
- W.S. Kurth, B.D. Strayer, D.A. Gurnett, F.L. Scarf, Icarus **61**, 497–507 (1985)
- J.-P. Lebreton, D.L. Matson, Space Sci. Rev. **104**, 59–100 (2002)
- H. Lammer et al., Planet. Space Sci. **49**, 561–574 (2001)
- J.S. Lewis, *Physics and Chemistry of the Solar System* (Academic Press, San Diego, 1995)
- D.R. Lide et al., *CRC Handbook of Chemistry and Physics*, 86th edn. (Taylor and Francis, Boca Raton, 2006)
- G.F. Lindal, J.R. Lyons, D.N. Sweetnam, V.R. Eshleman, D.P. Hinson, J. Geophys. Res. **92**, 14987–15001 (1987)
- J. Liu, Interaction of magnetic field and flow in the outer shells of giant planets. PhD Thesis, Caltech, California (2006)
- R.D. Lorenz et al., Science **319**, 1649–1651 (2008)
- J.I. Lunine, D.J. Stevenson, Icarus **70**, 61–77 (1987)
- T. Madden, W. Thompson, Rev. Geophys. **3**, 211–254 (1965)
- T. Majeed, J.H. Waite, S.W. Bouger, R.V. Yelle, G.R. Gladstone, J.C. McConnell, A. Bhardwaj, Adv. Space Res. **33**, 197–211 (2004)
- D.L. Matson, L.J. Spilker, J.-P. Lebreton, Space Sci. Rev. **104**, 1–58 (2002)
- G.J. Molina-Cuberos, J. Portí, B.P. Besser et al., Adv. Space Res. **33**, 2309–2313 (2004)
- G.J. Molina-Cuberos, J.A. Morente, B.P. Besser et al., Radio Sci. **41**, RS1003 (2006)
- J.A. Morente, G.J. Molina-Cuberos, J.A. Portí, K. Schwingenschuh, B.P. Besser, Icarus **162**, 374–384 (2003)
- A.F. Nagy, D. Winterhalter, K. Sauer et al., Space Sci. Rev. **111**, 33–114 (2004)
- E.A. Navarro, A. Soriano, J.A. Morente, J.A. Portí, Radio Sci. **42**, RS2S04 (2007). doi:[10.1029/2006RS003490](https://doi.org/10.1029/2006RS003490)
- A.P. Nickolaenko, M. Hayakawa, *Resonances in the Earth-Ionosphere Cavity* (Kluwer, Academic Publishers, Dordrecht, 2002)
- A.P. Nickolaenko, L.M. Rabinovich, Kosmicheskie Issledovaniya **20**, 82–87 (1982) (in Russian)
- A.P. Nickolaenko, D.D. Sentman, Radio Sci. **42**, RS2S13 (2007). doi:[10.1029/2006RS003473](https://doi.org/10.1029/2006RS003473)
- A.P. Nickolaenko, B.P. Besser, K. Schwingenschuh, Planet. Space Sci. **51**(13), 853–862 (2003)
- M. Pätzold, S. Tellmann, B. Häusler et al., Science **310**, 837–839 (2005)
- O. Pechony, C. Price, Radio Sci. **39**, RS5007 (2004)
- G.H. Pettengill, B.A. Campbell, D.B. Campbell, R.A. Simpson, Surface scattering and dielectrical properties, in *Venus*, ed. by S.W. Bouger, D.M. Hunten, R.J. Phillips (University of Arizona Press, Tucson, 1998)
- V. Rakov, M. Uman, *Lightning* (Cambridge Univ. Press, Cambridge, UK, 2003)
- G.C. Reid, in *Study in Geophysics: The Earth's Electrical Environment*, ed. by E.P. Krider, R.G. Roble (National Academy Press, Washington, 1986), pp. 183–194
- C.T. Russell, T.L. Zhang, M. Delva et al., Nature **450**, 661–662 (2007)
- M.J. Rycroft, S. Israelsson, C. Price, J. Atmos. Sol.-Terr. Phys. **62**, 1563–1576 (2000)
- M.J. Rycroft et al., Space Sci. Rev. (2008, this issue)
- G. Sátori, M. Neska, E. Williams, J. Szendrői, Radio Sci. **42**, RS2S10 (2007). doi:[10.1029/2006RS003483](https://doi.org/10.1029/2006RS003483)
- K. Schlegel, M. Füllekrug, J. Geophys. Res. **104**, 10111–10118 (1999)
- W.O. Schumann, Z. Naturforschung A **7**, 149–154 (1952) (in German)
- D.D. Sentman, J. Atmos. Terr. Phys. **51**, 507–519 (1989)
- D.D. Sentman, J. Atmos. Terr. Phys. **52**, 35 (1990a)
- D.D. Sentman, Icarus **88**, 73–86 (1990b)

- D.D. Sentman, in *Handbook of Atmospheric Electrodynamics*, 1st edn., ed. by H. Volland (CRC Press, Boca Raton, 1995), pp. 267–298
- F. Simões, PhD thesis. Université Pierre et Marie Curie, Paris 6, France (2007)
- F. Simões, R. Grard, M. Hamelin et al., *Planet. Space Sci.* **55**, 1978–1989 (2007)
- F. Simões, R. Grard, M. Hamelin et al., *Icarus* **194**, 30–41 (2008a)
- F. Simões, M. Hamelin, R. Grard et al., *J. Geophys. Res.* (2008b). doi:[10.1029/2007JE003045](https://doi.org/10.1029/2007JE003045)
- A. Soriano, E.A. Navarro, J.A. Morente, J.A. Portí, *J. Geophys. Res.* **112**, 06311 (2007). doi:[10.1029/2007JA012281](https://doi.org/10.1029/2007JA012281)
- R.J. Strangeway, *Adv. Space Res.* **33**, 1956–1967 (2004)
- A.I. Sukhorukov, *Planet. Space Sci.* **39**, 1673–1676 (1991)
- M.G. Tomasko et al., *Nature* **438**, 765–778 (2005)
- E.R. Williams, *Science* **256**, 1184–1187 (1992)
- E.R. Williams, G. Sátori, *Radio Sci.* **42**, RS2S11 (2007). doi:[10.1029/2006rs003494](https://doi.org/10.1029/2006rs003494)
- E.R. Williams, V.C. Mushtak, R. Boldi, R.L. Dowden, Z.-I. Kawasaki, *Radio Sci.* **42**, RS2S20 (2007). doi:[10.1029/2006RS003498](https://doi.org/10.1029/2006RS003498)
- Y. Yair et al., *Space Sci. Rev.* (2008, this issue)
- H. Yang, V.P. Pasko, Y. Yair, *Radio Sci.* **41**, RS2S03 (2006). doi:[10.1029/2005RS003431](https://doi.org/10.1029/2005RS003431)
- P. Zarka, B.M. Pedersen, *Nature* **323**, 605–608 (1986)

Blue Jets: Upward Lightning

Evgeny V. Mishin · Gennady M. Milikh

Originally published in the journal Space Science Reviews, Volume 137, Nos 1–4.
DOI: [10.1007/s11214-008-9346-z](https://doi.org/10.1007/s11214-008-9346-z) © Springer Science+Business Media B.V. 2008

Abstract Blue jets are beams of blue light propagating from the tops of active thunderclouds up to altitudes of \sim 50 km. They resemble tall trees with quasi-vertical trunk and filamentary branches. Their apparent speeds are in the range of 10 s to 100 s km/s. Other events, having essentially lower terminal altitudes (<26 km), are named blue starters. These phenomena represent the first documented class of upward electrical discharges in the stratosphere. Some of upward discharges, termed gigantic jets, propagate into the lower ionosphere at much higher speeds in the final phase. We describe salient features of the upward discharges in the atmosphere, give an assessment of the theories of their development, and discuss the consequences for the electrodynamics and chemistry of the stratosphere. We argue that this upward lightning phenomenon can be understood in terms of the bi-directional leader, emerging from the anvil.

Keywords Blue jets · Upward lightning · Transient discharges · Bi-leader

1 Introduction

Luminous flashes above thunderstorms have been reported by eyewitnesses for over a century (e.g., see review Vaughan and Vonnegut 1989) and eventually documented from low-light optical observations on the ground (Franz et al. 1990; Lyons 1994), airborne platforms (Sentman and Wescott 1993), and the space shuttle (Vaughan et al. 1992). However, only during the Sprites94 aircraft campaign Wescott et al. (1995) identified the class of upward-propagating stratospheric flashes, named blue jets (BJ) due to primarily blue color, as opposed to the red-color sprites at mesospheric altitudes (Sentman et al. 1995). Brief upward

E.V. Mishin (✉)
Boston College, Chestnut Hill, MA, USA
e-mail: evgenii.mishin@hanscom.af.mil

G.M. Milikh
University of Maryland, College Park, MD, USA
e-mail: milikh@umd.edu

jets, which propagate only a few km and terminate below 26 km, were dubbed blue starters (BS) (Wescott et al. 1996). A number of BJ/BS and similar events were captured during the ground and aircraft observations (Wescott et al. 1998, 2001); Lyons et al. 2000, 2003) and apparently from the space shuttle (Boeck et al. 1995, 1998). Pasko et al. (2002) and Su et al. (2003) discovered the so-called gigantic jets (GJ), propagating into the mesosphere/lower ionosphere (6 events). Recently, eight GJ events have been identified from the imager ISUAL onboard Formosat-2 (Kuo et al., *Workshop on streamers, sprites, leaders, lightning: From micro- to macro-scales*, Leiden, 2007).

The BJ/BS phenomena were quickly recognized as manifesting upward transient discharges in the stratosphere. Earlier BJ theories included the runaway breakdown (Roussel-Dupré and Gurevich 1996) and streamers of the positive (Pasko et al. 1996) and negative (Sukhorukov et al. 1996) polarity as the underlying physical mechanisms (see reviews Sukhorukov and Stubbe 1998; Rowland 1998). As the streamer models require seemingly extreme conditions, Sukhorukov and Stubbe (1998) and Petrov and Petrova (1999) suggested that BJ is rather formed by the streamer corona of a leader. This idea was further explored by Pasko and George (2002), who numerically simulated the streamer corona of a positive leader as a stochastic (fractal) process. However, likewise customary cloud to ground (CG) lightning, single-headed leaders require unrealistic rates of the thundercloud charge transport. To clear this hurdle, Raizer et al. (2006, 2007) suggested that the bi-directional uncharged leader (Kasemir 1960) forms in the anvil. As the leader channel transfers the thundercloud potential upward, the overall growth can be maintained by fairly moderate cloud charges and currents.

We next present the salient features of BJ/GJ (or Jets) and related upward discharges, then discuss theory of their evolution and consequences for the electrodynamics and chemistry of the upper atmosphere. We do not dwell on theoretical details, describing the underlying physical processes and basic limitations on a semi-qualitative level, just sufficient for comparison with the observations.

2 Observations of Upward Discharges in the Atmosphere

2.1 Blue Jets and Blue Starters

Four consecutive video frames, 67 ms apart, in Fig. 1 adapted from Wescott et al. (1996) (hereafter referred to as W96) shows the typical BJ development over continental thunderstorms. Note that hereafter the images (most in false color) are adjusted to show the faint

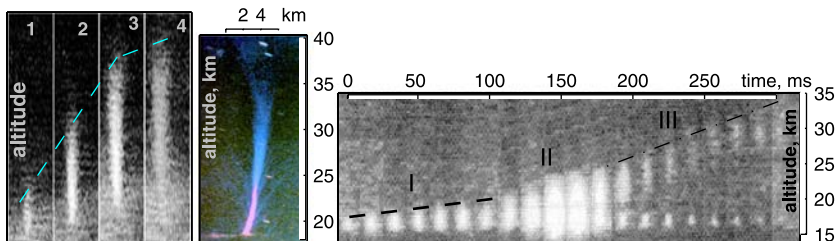


Fig. 1 (Left) Four video frames, 67 ms apart, during the 4 July 1994 BJ event from the Westwind 2 aircraft. (Middle) A 2-min exposure color photograph (in false color) of a blue jet north of Réunion Island and (right) a 350-ms sequence of narrow field TV images (16.67 ms apart) of the 22 July 1998 BJ event captured during the EXL98 aircraft campaign (adapted from W01). Dashed lines mark the BJ tip. Reprinted by permission from the American Geophysical Union

features and then annotated. One can see a slightly-conical ($\sim 10^\circ$ angle) jet propagating upward out of the top of the anvil at a $\simeq 100$ -km/s speed to a terminal altitude of ~ 40 km. Hereafter, ‘speeds’ designate ‘apparent vertical speeds’. Note that the jet in frame 1 nearly resembles a dim starter (cf. Fig. 1 W96 and Fig. 5 Lyons et al. 2003 (L03)). Near the terminus, the jet decelerated and its brightness seems to decay along the column simultaneously.

The next two frames show BJ over the Indian Ocean and over Iowa, respectively (Wescott et al. 2001 (W01)). The ‘oceanic’ BJ resembles a tree with filamentary branches (streamers) in the lower part and a forked tip crowned with two faint prongs (evident in Fig. 1 W01). An apparent diameter at the base is ~ 400 m and broadens to ~ 2 km at an altitude $h \simeq 30$ km, whereas the lower branches are ~ 50 – 100 m wide (W01). The brightest, pencil-like lower part appears white due to saturation of the film, whilst the upper conical part is blue (cf. Fig. 3–4 L03). W01 found that the brightness of a saturated pixel exceeds 6.7 MR and that they account for $\simeq 25\%$ of the total (blue) optical energy of ≥ 0.5 MJ. Assuming the jet duration 0.25 s yields the total optical power ≥ 2 MW.

The jet development can change abruptly. Indeed, the stage I in the right frame of Fig. 1 resembles a ‘persistent’ starter propagating upward at $\simeq 23$ km/s. Then it suddenly brightened (II) and finally separated into two parts (III). The lower part shrinks to the origination point, while the upper streak continues upward at ~ 90 km/s, disappearing from sight at $h \sim 35$ km. Note that a number of starters were also detected during the EXL98 campaign (W01). Multispectral video observations revealed that the second positive band 2PN2 contributed $\sim 90\%$ to a ~ 1 -MR starter, whilst the flux of 427.8-nm photons amounted to ~ 10 kR. This indicates the huge ionization rate.

Finally, L03 reported on observations by the ultrablue LLTV system of 83 very small (~ 100 -m in size), < 16 -ms duration, bright ‘pixies’ and of 17 compact (< 1 -km) bright starters (‘gnomes’) during a 20-min period of rapid vertical development of a convective dome near Yucca Ridge, Kansas. The overall observations show that (1_b) BJ/BS and gnomes/pixies are not coincident with CG flashes of either polarity, (2_b) the BJ/BS speeds are in the range of ~ 25 – 220 km/s, (3_b) the typical jet duration is ~ 0.2 – 0.3 s at the base. Wescott et al. (1998) stressed an association of BS with very large hail; however, it does not seem to be a persistent feature, and (4_b) some jets seem to originate from the same location as preceding BS/BJ tens of ms apart.

2.2 Gigantic Jets

The bottom panel in Fig. 2 shows a ~ 215 -ms sequence of video fields at the beginning of the GJ event captured from the ground by Pasko et al. (2002 (P02)) on 15 September 2001 over the Atlantic Ocean. Evidently, the jet structure and apparent speed vary significantly from field to field. Initially (until field #11), the jet resembles two trunks (with faint branches) growing in step with the average speed ~ 60 km/s. Further, the left trunk brightened and sped up to ~ 200 km/s (#11–12), then decelerated (#12–13) and again brightened and accelerated to ~ 500 km/s (#13–14). We designate this period of a ‘smooth’ average growth as stage A (cf. Fig. 1). At the beginning of stage B (#15), the upper part of the left trunk (beyond ~ 30 km) strongly brightened. Its forked tip seems to have propagated to ~ 48 km at ~ 500 km/s and ‘ejected’ two prongs, which move at ~ 1200 km/s and connect with bright diffuse spots at $h \sim 70$ km (cf. the GJ₄ #2→#3 transition in the top panel). Except for the uppermost part, the structure resembles a tall version of the ‘oceanic’ BJ in Fig. 1 (cf. Fig. 10 Pasko and George 2002).

Meanwhile, the right trunk’s tip (marked by dots), growing barely between #11–15, then ‘exploded’ in #16. Its wide and bright tip near 50 km is crowned with several prongs that

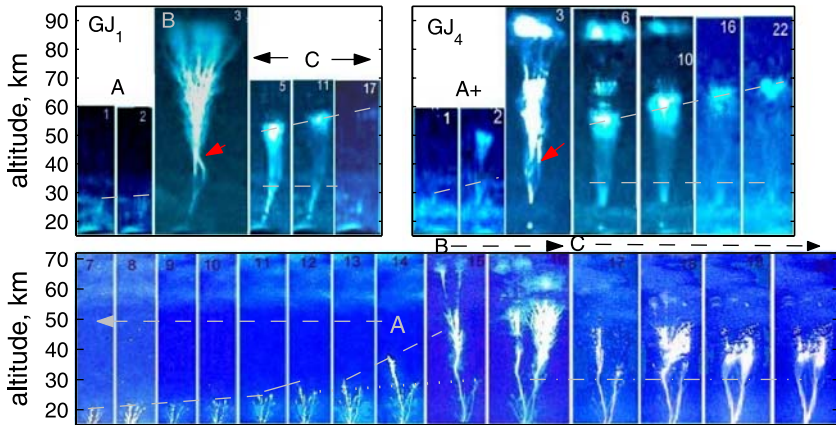


Fig. 2 (Bottom) Video fields 7–20 (~ 17 ms each) during the 15 Sep 2001 GJ event ~ 200 km northwest of Arecibo Observatory, Puerto Rico (adapted from P02 Suppl. Info.). (Top) Two sequences of video images (~ 17 ms each) of the GJ events 1 (left) and 4 (right) on 22 July 2002 over the South China Sea (adapted from Su03). The red arrows mark apparent merging of two branches. Reprinted by permission from *Nature*

extend farther, mapping into a bright diffuse spot a few km above. Next (stage *C*), the uppermost spots faded away, whilst the forked structure at $h \leq 32$ km persisted for the rest of the event. The thick prongs appear Y-like (due to overlapping at the base) and connected via conical ‘flare’ with brighter diffuse tops between ~ 35 and < 50 km that occasionally brighten and expand. After #22 (see P02), the faint prongs and their brighter tops seem to decay in step. At low resolution, the overall decaying structure would appear consisting of a pencil-like trunk (emanating faint flare) and a diffuse top well apart (cf. stage III in Fig. 1). Rebrightening at seemingly the same location (cf. 4_b) occurs at #36 and forms a luminous structure alike stage *C* with the top at ~ 50 km.

The top panel in Fig. 2 shows two GJ (Su et al. 2003 (Su03)) apparently emerging from the convective core. Su03 distinguished three stages of the GJ evolution: ⁽¹⁾leading jet (#1–2), ⁽²⁾fully developed jet, and ⁽³⁾trailing jet. We estimate the speed of the tip (marked by the dashed line) in GJ₁⁽¹⁾/GJ₄⁽¹⁾ roughly to be $\geq 120/230$ km/s. GJ₄⁽¹⁾ in #2 appears to comprise of a trunk below ~ 32 km, and a structured upper part, propagating at ~ 1000 km/s to ~ 50 km (cf. the left jet below 50 km in the bottom #15–16). It seems to be the initial step in the GJ₄⁽¹⁾ \rightarrow GJ₄⁽²⁾ transition (cf. #15 in the bottom panel). GJ₁⁽²⁾ in #3 and GJ₄⁽²⁾ in #3–4 resemble a tall version of the right and left jet in #16 (bottom), respectively.

Notwithstanding their durations, the overall features of GJ⁽¹⁾ and GJ⁽²⁾ are similar to stages *A* and *B* in the bottom panel, respectively. When stage *B* ends, there grows the trailing jet (cf. 4_b). Its structure, i.e. a trunk at the base connected via conical faint flare with diffuse top near 50–60 km (cf. rebrightening above), is alike the decaying GJ₄⁽²⁾, except for a chute-shape region between 70 and 90 km. Note again that at low resolution GJ⁽³⁾ would be reminiscent of stage III above. Overall, the leading and trailing jets seem nearly resembling the (enlarged) BJ. On the other hand, GJ⁽²⁾ (stage *B*) seems to be distinguished by the upper luminous structures beyond the standard BJ terminus and their vivid dynamics. P02 stressed that these structures do not match the established sprite features.

In Fig. 2 red arrows mark the merging of two branches in GJ_{1,4}⁽²⁾, which resembles those observed in laboratory streamers (Fig. 5b). Briels et al. (2006) explained the (electrostatic) attraction of two *non-conductive* streamers as consequent to a ‘return stroke’ piercing the early streamer. Cummer et al. (2006) suggested that a similar merging in sprites is due to

'mirror' charges induced in the *conductive* channel of the earlier streamer by the charged tip of the later streamer. We argue that the charge distribution in the long streamer (Fig. 7d) provides a natural explanation for the observed merging.

Finally, P02 reported on observations of VLF spherics of the positive polarity, coincident with the rebrightening event (trailing jet), and suggested negative cloud-to-ionosphere ($-CI$) breakdown to be their cause. Su03 detected ELF transients of the positive polarity during the GJ events and also interpreted as $-CI$ discharges with the charge moment change 1–2 kC·km. However, there may be a slight chance that these transients were associated with $+CG$ lightning in the nearby thunderstorm. If GJ were $-CI$ discharges, each would remove about 30 C from the thundercloud and ionosphere, thereby decreasing the potential difference in the whole gap (Su03).

2.3 Jets and Lightning Activity

Likewise the BJ/BS family, the GJ events were not observed to be associated with preceding CG flashes of either polarity. Furthermore, they were detected mainly over oceans and shores where the rate of lightning flashes is low. This is evident in Fig. 3, where the locations of all known GJ events (red stars) are superimposed with the lightning distribution over the globe. Besides, black squares indicate some of eighty intense UV (300–400 nm) flashes, detected at ~ 950 km onboard the student microsatellite 'Tatiana' (Garipov et al. 2005). They were almost equally distributed between two groups with durations 1–4 ms and 10–64 ms, corresponding to the lifetimes of individual streamers and of leaders, respectively (see below). Their radiated energy (~ 0.1 MJ) is close to that from GJ (Su03). Thus, we suggest that these flashes are indicative of GJ. As it follows from Fig. 3, alike GJ, the UV flashes are detected mainly over regions with low CG/IC lightning activity.

The generation of locally-enhanced charges initiating Jets has not yet been understood. The charge distribution in the thundercloud depends on various processes, including CG and IC activity (e.g., Stoltzenburg and Marshal 2008). Sukhorukov et al. (1996) noted that Jets should be linked to exceptional thunderstorm conditions and suggested that long IC 'spiders', which are usually missed by the NLDN, can collect enough (negative) charge in the anvil. However, as Fig. 3 shows, this is unlikely during the GJ and UV events. Nor does there appear to be any clear relationship of IC lightning to brief discharges arising out of the anvil mostly during quiet intervals (W96; L03).

W96 have found that following a starter the average rate of nearby $-CG$ flashes drops shortly by a factor of 5 and resumes in ≈ 3 s (a 2-s gap is found for BJ). In our opinion, this in-

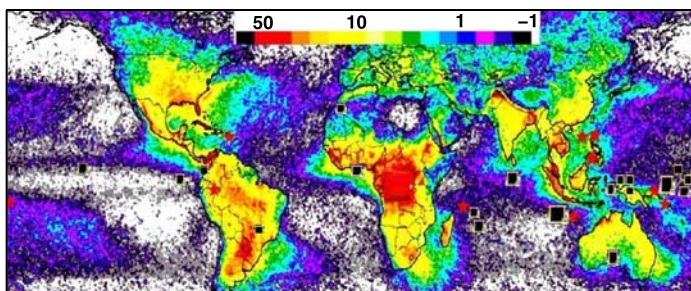


Fig. 3 Global lightning map (<http://thunder.nsstc.nasa.gov/data/query/2004>) with superimposed locations of the GJ events (stars) and ≤ 64 -ms, ≤ 0.1 -MJ, 300–400-nm UV flashes (squares) from the student microsatellite 'Tatiana' (Garipov et al. 2005)

dicates that –CG flashes and BJ/BS ‘compete’ for the same source (cf. Pasko et al.’s (1996) pre-discharge concept). By the same token, we suggest that GJ ‘prefer’ oceanic storms as highly-conductive sea water cannot maintain pointed ‘towers’, which initiate CG lightning in continental storms. Note that initiation of the conventional breakdown inside a cloud poses a serious problem as the observations (e.g., Bazelyan and Raizer 2000 (BR00); Stoltzenburg and Marshal 2008) show that electric fields very seldom exceed a few kV/cm. It is well below the threshold value $E_{th} = \eta \cdot E_{th0}$, where $E_{th0} \approx 32$ kV/cm and $\eta(h) = N(h)/N_0$ is the scaling factor (N_0 is the air density at sea level). However, the runaway breakdown can develop at $E \geq E_{rb} \simeq 0.1 E_{th}$, provided that ‘seed’ MeV-electrons are supplied by cosmic rays and the size of the region exceeds $l_{rb} \simeq 50/\eta$ m (Gurevich and Zybin 2001).

Abrupt (within 17 ms) changes in the Jets’ dynamics indicate rapid variations in the source (charge) that apparently are unrelated to CG flashes. L03 questioned whether the pixies might be related to compact ($l \leq 1$ km in size) IC discharges, accompanied by broadband radio emissions of a few ms duration, or to $\ll 1$ -ms radio bursts observed in upper portions of a cupercell (e.g., Rakov and Uman 2003). Trakhtengerts and Iudin (2005) show that strong convection flows in the developed dome can become unstable, creating ‘microscale’ ($l_{ms} \sim 1$ to 10s m) charged convection cells within a few minutes. The microscale electric field can reach the breakdown value E_{th} (note that $l_{ms} < l_{rb}$) and initiate a microdischarge, manifested by a $\ll 1$ -ms radio burst. The discharge from one micro cell triggers neighboring cells. Ultimately, a cluster of micro cells with the near-breakdown electric field can be formed, while the average field in the cloud remains well below E_{th} . The formation of such cluster near the top might initiate an upward discharge. Given all necessary conditions, the latter should occur rather rarely.

3 Modeling Jets

3.1 Basics of Transient Discharges

We outline some basic features of the streamer/leader discharges in air, relevant to our topic (e.g., Raizer 1991 (R91); Bazelyan and Raizer 1998 (BR98), 2000 (BR00)). Positive *or* negative (single-headed) streamers/leaders are initiated near an anode or cathode, transporting ‘+’ or ‘–’ charge toward the opposite electrode. In negative streamers, electrons drift upstream, so seed electrons are not needed. In positive streamers, electrons drift downstream and seed electrons are mainly due to photoionization by UV radiation from the front. Between electrodes, double-headed (positive *and* negative) or bi-leaders can be formed. Each head of the bi-leader develops as in the corresponding single-headed leader, while zero net charge is transported.

Developed streamers represent low-conductive cold plasma filaments growing in the applied electric field E_a , which exceeds the critical value $E_s^{(-)} \simeq 3E_s^{(+)} \simeq 0.45E_{th}$. If E_a decreases with distance, streamers can cross the gap of length d under applied voltage U_a only if the mean field $\langle E_a \rangle = U_a/d \geq E_s$. The space charge in front of the streamer tip amplifies E_a . As a result, the total field E exceeds E_{th} and drives electron avalanche. The drift (current) of newly-born electrons makes the ‘old’ tip the leading segment of the plasma channel, while the avalanche region becomes the ‘new’ charged tip. This process has the nature of a self-sustained ionization wave moving along the axis $\mathbf{z} \parallel \mathbf{E}_a$ at a speed $u_s = dl_s/dt$, where l_s is the streamer length. Usually, the wavefront frame of reference $\xi = z - \int_0^t u_s dt'$ is used.

Figure 4 shows a schematic of the positive streamer tip of radius r_s and spatial distributions of E , the electron density n_e , and the space charge $\rho = e(n_i - n_e)$, where e/n_i is the

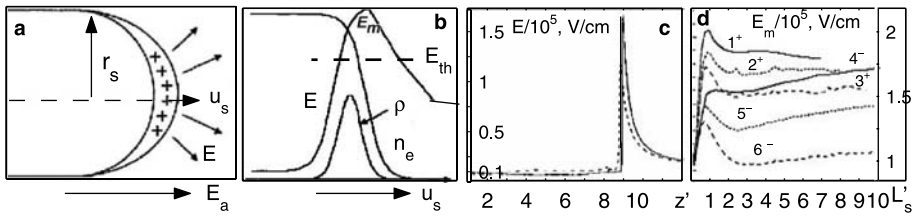


Fig. 4 Schematic of (a) the *spherical* tip of a positive streamer with the *cylindrical* channel of the radius r_s and (b) the spatial distribution of E , space charge ρ , and the electron density n_e . The dashed line indicates the breakdown threshold E_{th} . (c) The magnitude of the electric field in the positive/negative (solid/dotted line) streamers vs. $z' = z/r_0$ at $l_s \simeq 9r_0$. (d) The peak value E_m of the electric field in the positive ($1^+, 3^+$) and negative ($4^-, 6^-$) streamers vs. $L'_s = l_s/r_0$ (see text). The plots are adapted from Raizer et al. (1998) (a, b) and BN97 (c, d). Printed by permission from IOP Publishing Ltd. and IEEE

ion charge/density. Also shown are the results of 2D numerical simulations of *cylindrical* streamers growing along the applied field $\mathbf{E}_a \parallel \mathbf{z}$ from a charged sphere of radius $r_0 = 1$ mm and potential U_0 at $p = p_0$ (Babaeva and Naidis 1997 (BN97)). The total field comprises of two parts $\mathbf{E}(\mathbf{r}) = -\nabla(U_\rho + U_L)$. Here U_ρ is defined by ρ via Poisson's equation and U_L is the Laplacian potential of the charged sphere, yielding $E_{L0} = U_0/r_0 + 3E_a$ at the sphere surface and $E_L \rightarrow E_a$ at $z > 3r_0$. In the BN97 simulations $E_{L0} = 115$ kV/cm and $E_a = 15$ (frames c and d ($3^+, 6^-$)), 25 ($2^+, 5^-$), and 35 ($1^+, 4^-$) kV/cm. Note that $E_a = 15$ kV/cm barely exceeds $E_s^{(-)}$ and equals $\simeq 3E_s^{(+)}$.

The distribution of ρ is defined by the continuity equation $\partial\rho/\partial t + \nabla\mathbf{j}_s = 0$. Here $\mathbf{j}_s \simeq -en_e\mathbf{u}_e \simeq \sigma_e\mathbf{E}$ is the electric current density, $\mathbf{u}_e \simeq -(ev_{en}^{-1}/m)\mathbf{E}$, v_{en} , and $\sigma_e = (e^2/m)n_e/v_{en}$ are the electron drift speed, collision frequency, and conductivity, respectively. Note that the ion motion is neglected. The narrow front width $\delta\xi_f \ll r_s$ (see Figs. 4a and 4c) makes possible simple 1D estimates of the streamer parameters (e.g., BN97; BR98). As the field is enhanced at $\xi \sim r_s$, from the electron continuity equation in the front frame it follows (e.g., BN97)

$$u_s \pm u_{em} \simeq v_{im} \cdot r_s / \ln(n_m/n_a). \quad (1)$$

Here the $+/-$ sign corresponds to positive/negative streamers, n_a is the electron density upstream, $E_m, n_m, v_{im} = v_i(E_m) \simeq 2.9 \cdot 10^{11} \eta \exp(-\frac{10E_{th}}{E_m})$ s $^{-1}$, and $u_{em} = u_e(E_m)$ are the peak values of the electric field, electron density, ionization frequency, and electron drift speed, respectively. Note that v_i and the dielectric relaxation time $\tau_\sigma = \epsilon_0/\sigma_e$ (ϵ_0 is the permittivity of vacuum) are very sensitive to the value of E . This is a key factor in the formation of the narrow front.

For given u_s and r_s , positive streamers have greater values of E_m than negative streamers (cf. Figs. 4c, 4d). From the charge continuity equation it follows that $\rho \simeq en_eu_e/u_s \simeq \sigma_e E/u_s \ll en_e$ at $u_s \gg u_{em}$ and that the space charge lifetime is close to the relaxation time τ_{σ_m} downstream. This implies (Raizer et al. 1998 (R98)) that at least the last electron generation in the avalanche is born during this time, i.e. $v_{im}\tau_{\sigma_m} \gtrsim 1$ or

$$n_m \gtrsim (\epsilon_0/e) \alpha_m \cdot E_m \quad (2)$$

where $\alpha_m = \alpha(E_m)$ and $\alpha = v_i/u_e$ is the Townsend ionization coefficient.

The values of r_s and E_m are related via the potential at the charged streamer tip $\Delta U_t = U_t(l_s) - U_a(l_s) \simeq 2r_s \cdot E_m$, where the account for the conductive segment of the channel is taken (R98; BR98). Figure 4d shows that far from the launching electrode, $E_m = c_m(E_a) \cdot$

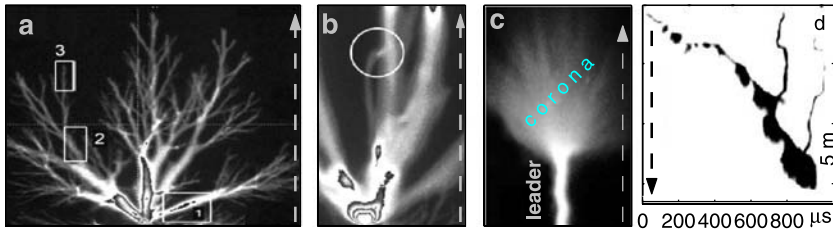


Fig. 5 (a, b) Positive streamer patterns growing from an anode in 8/4-cm gaps at atmospheric pressure and applied voltages $U_a = 60/54\text{-kV}$ (adapted from Briels et al. 2006). (c, d) Examples of positive leaders (adapted from R07// Domens et al. 1991). Reprinted by permission from the IOP Publishing Ltd. and American Geophysical Union

$E_{th} \simeq \text{const}$. R98 argued that for the strong streamers ('ss'), i.e. $u_s \gg u_{em}$ or $E_a \gg E_s$, the coefficient $c_m = c_{ss} \approx 5$. For the weak streamers ('ws'), i.e. $u_s \gtrsim u_{em}$, we take $c_m = c_{ws} \approx 3.2$ (cf. Fig. 4d). It is worth to note that the streamer speed $u_s \propto r_s \propto \Delta U_t$ at $E_a > E_s$.

Let us pool the streamer tip parameters ($n_m/r_s/U_t/u_s$ in $\text{cm}^{-3}/\text{cm/kV/m}\cdot\text{s}^{-1}$) at $E_a > E_s$ (cf. R98)

$$E_m = c_m E_{th} \cdot \eta; \quad n_m \simeq 10^{14} \cdot \eta^2; \quad r_s \simeq 0.015 c_m^{-1} \cdot \Delta U_t / \eta; \quad u_s \simeq 5 \cdot 10^4 \cdot \Delta U_t. \quad (3)$$

We next discuss some relevant results of laboratory experiments. Figure 5(a–b) shows snapshots of positive streamers growing in a $\sim 15\text{-}\mu\text{m}$ -point anode-plane cathode configuration in air at normal pressure (Briels et al. 2006). Applied voltages provided $\langle E_a \rangle > E_s$, thereby streamers could cross the gap. This has not yet happened in frame a, where boxes labelled 1, 2, and 3 indicate streamers with radii $r_{1/2/3} \simeq 2.5/0.5/0.1$ mm. Type 1/2/3 streamers carry currents $J_{1/2/3} \simeq 20/1/0.01$ A with the current densities $j_{1/2/3} \simeq 1/3/0.5$ MA/m 2 . The total current in the gap remains virtually constant, indicating that the total charge is conserved, being redistributed over the ensemble of streamers.

The observations show that the streamer radius remains virtually constant until branching, which has not yet been fully understood (e.g., Niemeyer et al. 1984; Arrayás et al. 2002). Anyway, subsequent (thinner) streamers travel shorter distances at smaller speeds. The overall range of speeds is $u_{1/2/3} \simeq 10/5/1 \cdot 10^5$ m/s. Note that $u_2/u_3 \simeq r_2/r_3$, i.e. $u_s \propto r_s$. It is likely that a $\simeq 0.1$ -mm radius of type 3 streamers is close to the lower limit at normal pressure, i.e. the *minimal* radius r_{\min} , at which the front width $\delta\xi_f \rightarrow r_{\min}$. From (3) at $c_m = c_{ws}$ we obtain $\Delta U_{\min} \simeq 2.2$ kV and $u_{\min} \approx 10^5$ m/s, in excellent agreement with u_3 . Taking $r_s = r_3$ in (2) gives $u_s^{(+)} \simeq u_{\min}$ at $c_m \simeq 1.8$, corresponding to $n_{\min} \simeq 8 \cdot 10^{11}$ cm $^{-3}$ (the 'minimal' streamer).

In frame b, thick streamers have crossed the gap. After that, type 3 streamers start near the anode. Some of these late streamers merge with existing thick streamers, as shown in the circle. This (electrostatic) attraction is consequent to a 'return stroke', piercing the thick streamer and changing its polarity (Briels et al. 2006).

Developed leaders (like in Fig. 5c) represent highly conductive plasma channels, continuously emitting a fan of streamers of the same polarity, termed the streamer zone or corona. The tip moves at a speed much slower than that of individual streamers. Gas in the leader channel is heated by the current to $T \geq 1000$ K. A huge number of short-lived streamers in the corona generate the space-charge field $\langle E_c \rangle \simeq E_s$ (BR00). As streamers move along some distance until termination, their charge covers the leader channel and prevents its expansion and cooling. The overall process has not yet been fully understood, and no rigorous solution is found. Note that the average number of the coronal streamers is roughly

$d_l^2/\langle 4r_s^2 \rangle \sim 10^6\text{--}10^9$, where d_l is the leader diameter and $\sqrt{\langle r_s^2 \rangle}$ is the average streamer radius.

For positive leaders in a $\sim 17\text{-m}$ gap under voltages 2.3–2.4 MV, three types of propagation were documented: continuous (c), oscillatory (o), and restrike (r) (Domens et al. 1991). That the average field in the gap $\langle E_a \rangle \approx 1.4 \text{ kV/cm}$ is well below $E_s^{(+)}$ indicates that the high potential is transferred along the gap by the conductive leader. The length and diameter of the c -type leader increase smoothly with time, whereas the corona fluctuates. The speed of the leader tip is related to the discharge current J_l as $V_l = 9.5 + 10 \cdot J_l \text{ km/s}$. Type o is manifested by strong sub-millisecond oscillations in the current and in the brightness of the corona and channel. However, the current never vanishes, and its mean value is close to $J_l \sim 1 \text{ A}$.

Intermittent r -type discharges (like in Fig. 5d) develop a large bright corona. It generates the space-charge field so large that it chokes the discharge, and the current briefly vanishes. The controlling factor is the charge per unit of the leader length q_l . If q_l is too large or too small, the propagation stops due to an excess of ions (choking effect) or a lack of electrons. Ultimately, the charge per unit length of propagating leaders is nearly the same $\sim 50 \mu\text{C/m}$. The discharge resumes (restrike) following the field recovery near the anode. Each restrike uses the imprint of the old leader, giving a luminous transient and a new corona (cf. rebrightenings/trailing jets in Sect. 2).

Finally, leaders of the negative polarity develop stepwise (step leader) with the time between steps $\sim 30\text{--}100 \mu\text{s}$ and the step length in the range of 5–200 m. There are slow α -leaders, traveling at an average speed $(1\text{--}8) \cdot 10^5 \text{ m/s}$, and β -leaders that are faster and have more branches and longer steps. The electric fields required for propagation of the positive and negative leaders are nearly identical (R91).

3.2 Earlier Streamer Models of Jets

Sukhorukov et al. (1996 (S96)) and Pasko et al. (1996 (P96)) considered BJ/BS as upward streamers launched from thunderstorm tops at $\sim 18\text{--}20 \text{ km}$. Figure 6 shows a schematic of the distributions of charges and electric fields suggested for (a) negative (S96) and (b) positive (P96) *conical* streamers. This is a clear illustration of the alternatives, whatever the charge source (see Sect. 2.3). Shown next is the magnitude of the vertical electric field $E_a(h)$ from a Gaussian-shape of radius $r_0 = 3 \text{ km}$ thundercloud charge $Q_c = 120 \text{ C}$ placed at altitude $h_c = 15 \text{ km}$ (Pasko and George 2002 (PG02)). These conditions correspond to the cloud potential $U_c \sim Q_c/(4\pi\epsilon_0 r_0) \sim 300 \text{ MV}$. Dashed lines indicate the critical field values, scaled according to $E_{th}(h) = \eta \cdot E_{th0}$ and $E_s(h) = \eta \cdot E_{s0}$ with $\eta = N/N_0 = \exp(-h/H)$ and $H \approx 7.2 \text{ km}$.

Near the source $E_a > E_s^{(+)}$, thereby the positive streamer could be initiated. If the (negative) charge were located at $h_c \geq 18 \text{ km}$, the negative streamer would be possible. In addition, Fig. 6d shows the nighttime atmospheric conductivity $\sigma_0(h)$ at low latitudes with values of $\tau_{\sigma_0}(h) = \epsilon_0/\sigma_0(h)$ superimposed (PG02). Clearly, if the applied field fell below E_s before the streamer arrival, it would stop shortly.

S96 suggested that the maximum field at the front (E_m) barely exceeds E_{th} , thereby the negative streamer propagates at the constant speed $u_{\min} \simeq 10^5 \text{ m/s}$. As the relaxation time τ_{σ_0} at $h \simeq 40 \text{ km}$ is close to the streamer propagation time ($\sim 0.2 \text{ s}$), it ultimately terminates near this altitude (cf. Fig. 1). S96 also noticed that $E_a(h)/\eta(h)$ has a minimum between 20 and 30 km (see Fig. 6c). Thus, streamers of either polarity, initiated by the ‘marginal’ cloud charge, cannot pass through this region, thereby becoming starters (cf. Fig. 4(a,b) PG02). However, notwithstanding u_{\min} is the lower limit for the streamer speed, the value

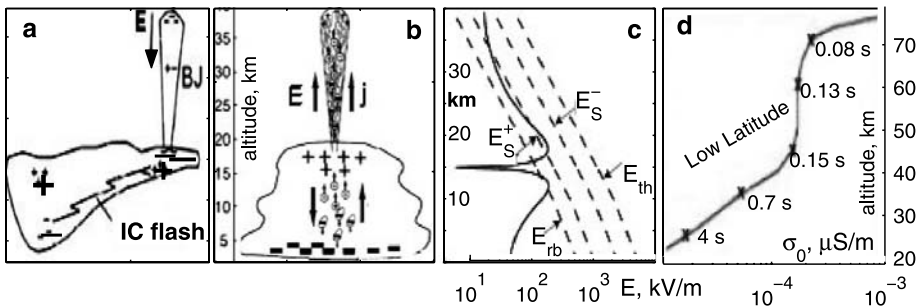


Fig. 6 Schematic of charges and electric fields for (a) negative and (b) positive streamers, respectively. (c) The vertical electric field (solid line) produced by a 120 C thundercloud charge located at $h_c = 15$ km. Dashed lines show E_{rb} , E_{th} , and $E_s^{(\pm)}$. (d) Profiles of the nighttime low-latitude atmospheric conductivity, with τ_σ superimposed. The plots are adapted from S96 (a), P96 (b), and PG02 (c, d). Printed by permission of the American Geophysical Union

$E_m \simeq E_{th}$ is too low (see Sect. 3.1). In turn, the P96 positive streamer model does not account for electron attachment and arbitrarily bounds n_m , which is hardly applicable in the stratosphere (Sukhorukov and Stubbe 1998).

The apparent shortcoming of the streamer models is that they require the large thundercloud charge (potential) to sustain the streamer propagation. Therefore, Sukhorukov and Stubbe (1998), Petrov and Petrova (1999), and PG02 suggested that BJ is rather formed by the streamer corona of an upward-growing positive leader. The leader transfers the cloud potential from its origination point $U_c(h_0) = U_c$ upward. As a result, at any altitude h_l the leader tip potential $U_l = U(h_l)$ is close to U_c and can provide the necessary voltage to support long streamers.

However, unrealistic charge transport (electric current) in the thundercloud is required to sustain a single-headed leader. Indeed, currents ≥ 1 A maintain a single steady-growing streamer. Given ~ 1 nC/m³ density of the (attached to hydrometeorites) charge in a thundercloud (e.g., Saunders 2008), microparticles must be collected from the volume ≥ 1 km³ and transferred into a narrow leader channel within 0.1–0.2 s. The conventional lightning theory circumvents this obstacle by applying the uncharged bi-directional leader (Kasemir 1960; Mazur and Ruhnke 1998). As the opposite-polarity leaders, propagating in opposite directions, are connected via the highly-conductive channel, their charges compensate each other. Thus, virtually no charge is taken from the cloud.

Next, we discuss the Raizer et al. (2006 (R06), 2007(R07)) model of the bi-directional leader, which describes the formation of long coronal streamers escaping into the ionosphere, alike GJ⁽²⁾ (stage B) in Fig. 2.

3.3 Bi-leader Model of Jets

Apparently, if the bi-leader is initiated in the anvil, one of them can extend beyond the cloud top, as depicted in Fig. 7a. The bi-leader is likely triggered near the bending point B , where the vertical electric field $E_a = -dU_c/dh$ is maximum. R06 and R07 presumed an upward-propagating positive leader. However, the negative net charge in the anvil (cf. Fig. 6a) might result in the bi-leader with the negative leader upward.

Coronal streamers develop upward in the space-charge field of the corona (E_c). Its generation mechanism has not yet been quantitatively described. However, numerous experiments

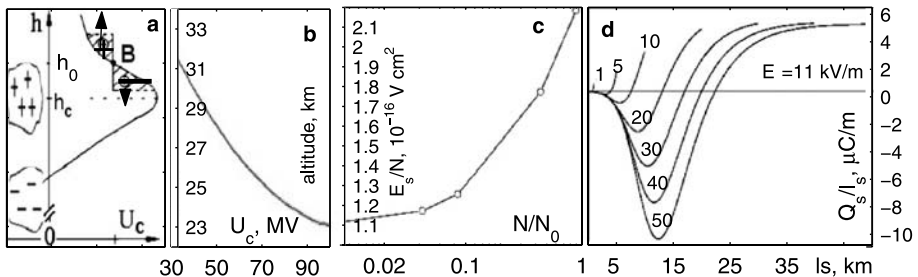


Fig. 7 (a) A schematic of the bi-leader initiation. (b) The escape altitude of a streamer from the leader tip into ionosphere vs. the cloud potential. (c) The critical value of $\bar{E}_s^{(+)}/N$ vs. $\eta = N/N_0$ in the exponential atmosphere. (d) The charge per unit length vs. the length of the positive streamer in the exponential atmosphere. Numbers 1, 5, etc. indicate the streamer length in km. The plots are adapted from R06 (a) and R07 (b-d). Printed by permission of the Elsevier Ltd and American Geophysical Union

established that the mean coronal field under normal conditions is close to E_{s0} (RB00). Likewise the principle of least action, in the exponential atmosphere $\langle E_c(h) \rangle$ is suggested to be close to $E_s(h) \propto \eta(h)$, i.e. just enough to maintain the streamer propagation. As a result, streamers would grow preferentially upward at small angles with the trunk, thereby forming a narrow cone (cf. Figs. 1 and 2).

R07 describe the evolution of long *conical* ($dr_s/dz \ll 1$) streamers growing from the tip of the positive upward leader by a system of equations of a long distributed line (e.g., BR00)

$$\frac{\partial q}{\partial t} = -\frac{\partial J}{\partial z}; \quad \frac{\partial U}{\partial z} = -J \cdot R \quad (4)$$

and (3). Here $z = h - h_l$, J is the current in the channel, R , $q = C \cdot (U - U_a)$, and $C \approx 2\pi\epsilon_0/\ln(l_s/r_s) \simeq 8-10 \text{ pF/m}$ are the resistance, charge, and capacity per unit length of the streamer channel, respectively. The boundary condition at the base, $z = 0$, is $U(0) \simeq U_c$, whereas that at the front, $z = l_s$, relates the current and charge of the newly formed tip

$$J(l_s) = q(l_s) \cdot u_s = C \cdot (U_t - U_a) \cdot u_s. \quad (5)$$

The resistance $R(z) = (\pi r_s^2 \sigma_e)^{-1}$ is defined by the local conductivity $\sigma_e(z) \propto n_e(z)/v_{en}(z)$, which depends mainly on the electron attachment rate $v_a \simeq 1.3 \cdot 10^7 \eta^2 \text{ s}^{-1}$ downstream (BR98). Basically, the streamer channel is a poor conductor, except for its leading section $l_s - u_s/v_a < z_{sc} \leq l_s$, where $n_e \simeq n_m$ (3). The R07 simulations performed in the uniform atmosphere at various densities N and applied fields E_a show that long streamers grow continuously if E_a exceeds the critical value $\bar{E}_s^{(+)}$. Figure 7c shows that at $\eta < 0.1$ or above $\simeq 17 \text{ km}$ the ratio $\bar{E}_s^{(+)}/N$ approximately follows a scaling law $\bar{E}_s^{(+)}/N \simeq 1.3 \cdot 10^{-16} \text{ V cm}^2$, which yields $\bar{E}_{s0}^{(+)} \approx 0.65 \cdot E_{s0}^{(+)}$ (R07). At lower altitudes, electron attachment rapidly reduces the channel conductivity, thereby the similarity law is violated.

Following R06 and R07, we estimate the conditions for a streamer from the leader corona to reach the ionosphere. Let us recall that at $N = \text{const}$ and decreasing E_a , the ultimate length l_∞ of a streamer is defined by the condition $l_\infty \cdot E_s = - \int_0^{l_\infty} E_a dz = U_a$ (the applied voltage). For the leader-streamer corona system, U_a is replaced by the potential drop between the leader tip and the edge of the corona at $h_\infty = h_l + l_\infty$, i.e. $\Delta U_{ls}(h_\infty) \simeq U_c - U(h_\infty)$. As streamers stop at $\Delta U_t < \Delta U_{\min} \ll U_c$ (see Sect. 3.1), we get $\Delta U_{ls}(h_\infty) \simeq U_c - U_a(h_\infty)$, where $U_a(h_\infty)$ is the potential drop between h_∞ and the ionosphere's lower edge.

In the exponential atmosphere, integrating $E_s(h)$ over the streamer zone yields explicitly (R06)

$$\langle E_s \rangle \cdot H = U_c - U_a; \quad \langle E_s \rangle = E_s(h_l) [1 - \exp(-l_\infty/H)]. \quad (6)$$

Let us assume that the front of the streamer zone is located at such distances from the ionosphere that $U_a(h_\infty) \ll U_c$. Neglecting U_a in (6) defines the altitude extent of the corona (R06)

$$l_\infty = -H \cdot \ln(1 - (\langle E_s \rangle H / U_c)^{-1}). \quad (7)$$

Apparently, the streamer zone extends indefinitely ($l_\infty \rightarrow \infty$), i.e. the streamers escape into the ionosphere, at $\langle E_s \rangle h_{l\infty} = U_c / H$. This condition determines the escape altitude $h_{l\infty} = H \cdot \ln(H \bar{E}_{s0} / U_c)$. Figure 7b shows $h_{l\infty}^{(+)}$ as a function of U_c (R07). One can see that the positive leader tip at $h > 26$ km emits streamers that reach the ionosphere at rather moderate values of the cloud potential $U_c < 60$ MV. For comparison, the potential at the surface of a charged sphere of radius r_0 [km] and charge Q_c [C] is $U_c \simeq 10 Q_c / r_0$ MV. Assuming the same scaling law for the negative upward leader yields the escape altitudes $h_{l\infty}^{(-)} = h_{l\infty}^{(+)} + H \cdot \ln(\bar{E}_{s0}^{(-)} / \bar{E}_{s0}^{(+)}) \approx h_{l\infty}^{(+)} + 8$ km.

We suggest that the escape altitude is also the terminal altitude of the leader, since the escaping streamer would likely cause the return stroke from the ionosphere and temporarily discharge the gap, likewise CG flashes. This conjecture is in good agreement with Fig. 2 (stage B), where the trunk top is near 30–35 km.

Figure 7d shows the charge distribution per unit channel of the positive streamer growing in the exponential atmosphere under the applied electric field $E_a(h) \propto \bar{E}_s^{(+)}(h)$ (R07). The streamer starts from the leader tip at $h_l = 25.2$ km, where the applied field $E_a(h_l) = 11.0$ kV/m is slightly above $\bar{E}_s^{(+)}(h_l) = 10.6$ kV/m. Apparently, substantial negative charges are generated in the trailing part of the channel, though the net charge is positive. This is the consequence of the long streamer length (BR98). Indeed, as the applied field moves electrons further downstream, the positive charge is accumulated in the streamer tip. As long as the streamer channel is short and the electron attachment is negligible, the current flows through the whole channel ‘freely’. As soon as the conductivity reduces near the base ($v_a \propto N^2$), the channel plasma polarizes in order to maintain the current.

Note that this type of the charge distribution can cause the electrostatic attraction of the tip of the later streamer to the trailing part of the earlier streamer, irrespective of the streamer (net) polarity (cf. Fig. 2).

4 Jets Observables

4.1 Optical Emissions

The upward-growing leader channel represents the bright white trunk of Jets, whereas the coronal streamers form branches and a faint ‘flame’ near the terminus. First, let us estimate the radiation of the trunk. The energy flux from unit volume of heated air of the temperature T [K] is given by $\Phi_e = \kappa \sigma_T T^4$, where σ_T is the Stefan constant and $\kappa = 2 \cdot 10^{-13} T^3 \cdot \eta^{3/2} \text{ m}^{-1}$ is the inverse characteristic length (Gurevich et al. 1997). Then, the column emission rate, the surface brightness in Rayleighs (megaphoton · cm⁻² s⁻¹), is found by integrating Φ_e along the line of sight

$$I_l \simeq (4\pi \varepsilon_\lambda 10^6)^{-1} \kappa \sigma_T T^4 d_l \quad [\text{R}] \quad (8)$$

(ε_λ is the mean energy of the radiated photons of the wavelength λ). At $T = 1000$ K, $\varepsilon_\lambda \sim 10$ eV, and the leader diameter $d_l \sim 100$ m, Eq. (8) yields $I_l \sim 15$ MR at altitudes ~ 30 km (cf. W01).

Let us estimate the intensity of optical emissions from the coronal streamers. The main contributors to the red- and blue-line emissions are known to be the first (1PN2) and second (2PN2) positive bands of molecular nitrogen, respectively. Besides, $\simeq 2.3\%$ of the N_2 ionization radiates in the band 1NN2+ at $\lambda = 427.8$ nm (Vallance-Jones 1974). Likewise ionization, the excitation rates, v_λ , are very sensitive to the value of E/N (R91), thereby the front region with $E \rightarrow E_m = c_m E_{th}$ is most luminous. As $E_m/N = \text{const}(h)$, the value of v_λ varies as $\propto N$, until the streamer slows down and E_m falls. To estimate the brightness of the fast-moving tip of a streamer, the limited excitation time must be accounted for

$$I_\lambda \simeq (4\pi 10^6)^{-1} \Delta r_{\parallel} n_{em} v_\lambda [1 - \exp(-\tau_f/\tau_\lambda)] / (1 + A_\lambda^{-1} k_\lambda N) \quad [\text{R}]. \quad (9)$$

Here $\Delta r_{\parallel} \sim r_s$ is the glow dimension along the line of sight, $\tau_\lambda = (A_\lambda + k_\lambda N)^{-1}$ is the lifetime of excited quanta, $A_2 \approx 120 A_1 \approx 1.4 A_+ \approx 2 \cdot 10^7 \text{ s}^{-1}$ and $k_1 \approx 1.4 k_2 \approx 0.25 k_+ \approx 10^{-10} \text{ cm}^3 \text{ s}^{-1}$ are the radiation probabilities and quenching rates, respectively (Vallance-Jones 1974), and $\tau_f \sim \alpha_m^{-1}/u_s$ is the front transit time. Hereafter, subscripts ‘+’, ‘1’, and ‘2’ indicate 1NN2+, 1PN2, and 2PN2, respectively.

As $v_1 \sim v_2$ at $E > E_{th}$ and $A_1 \ll A_2$, the blue-line emissions dominate, thereby setting the blue color of Jets. Evidently, the luminosity range is set up by the parameters for the strong and minimal streamers with the excitation rates $v_2^{(ss)} \approx 5 \cdot v_+^{(ss)} \approx 5 \cdot 10^{10} \eta \text{ s}^{-1}$ and $v_2^{(\min)} \approx 100 \cdot v_+^{(\min)}$, respectively (Fig. 3a PG02). An ideal event to compare with is the EXL98 starter, where the reported intensity I_+ and the ratio I_+/I_2 in the brightest part are about 10 kR and 0.01, respectively (W01). Let us presume that the starter terminated at $20 \leq h_t \leq 25$ km, where $0.05 \leq \eta_t \leq 0.03$ and $\tau_f^{(\min)} \gg \tau_\lambda \gg \tau_f^{(ss)}$. For the strong streamers (9) reduces to $I_\lambda^{(ss)} \simeq 10^{-7} n_{em} r_s \tau_f \cdot A_\lambda v_\lambda^{(ss)}$, giving the ratio $I_+^{(ss)}/I_2^{(ss)} \simeq 1/7$, which greatly exceeds the observed ratio. The opposite is true for the minimal streamer, as $\tau_+(h_t) \ll \tau_2(h_t)$.

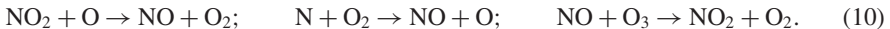
Therefore, as anticipated, the weak streamers are characteristic of the starter corona. The sought-for ratio matches the observed value at $c_m^* \approx 2.45$, when $\tau_2^{(*)} \gg \tau_f^{(*)} > \tau_+^{(*)}$. At $v_+^* \approx 10^9 \eta \text{ s}^{-1}$ (Fig. 3a PG02), $r_s^* \sim 5 \cdot 10^{-2}/\eta \text{ cm}$, and $n_{em}^* \approx 10^{12} \eta^2 \text{ cm}^{-3}$, from (9) we get the ‘instant’ brightness of the streamer tip $I_+(h_t) \simeq 120 \text{ MR}$ (cf. Stenbaek-Nielsen et al. 2007). The coronal glow dimension in the exponential atmosphere is of the order of d_l (implying the cone angle $\leq 15^\circ$). The ‘instant’ radiating layer, i.e. the path $\xi_\lambda = u_s/A_\lambda \sim 1 \text{ cm}$, covered by the front within the radiation time, is much smaller than the size of one pixel, say, $l_0 \sim 10^2 \text{ m}$. Reducing the radiated flux $I_+(h_t)$ by a factor $\xi_+ d_l / l_0^2 \sim 10^{-4}$ yields 12 kR, in fair agreement with the observed value. Note that the total blue-line radiation power from a single streamer amounts to $\sim 0.1 \text{ MW/m}^3$, whereas that from the whole corona $\sim 3 \text{ TW/m}^3$.

4.2 Long-Lived Effects of Jets in the Stratosphere

4.2.1 Ozone Layer Perturbations

Sentman and Wescott (1996) suggested that upward discharges might create long-lived by-products and thus have long term consequences in the atmosphere. In particular, Jets crossing the ozone layer can affect its chemical composition. In the stratosphere, nitric oxide

(NO) and dioxide (NO_2) molecules are known to limit the content of ozone due to the reactions (Crutzen 1970)



As the rate coefficients of the last two reactions sharply increase with T , the NO production and O_3 destruction by an ordinary lightning is based on the heating of gas up to $T \geq 1000$ K (Lawrens et al. 1995). This scheme is hardly applicable for streamers, as the gas temperature in the front is virtually unchanged (Mishin 1997). However, ionization and dissociation by energetic electrons in discharges trigger the chain of chemical reactions resulting in NO and O_3 perturbations (e.g., Kossyi et al. 1992).

Mishin (1997) and Smirnova et al. (2003) explored a plasmochemical model to study NO and O_3 perturbations in the front (tip) of a negative streamer. Besides the basic reactions (10), the model includes electron impact ionization, excitation, and dissociation processes, along with dissociative recombination and charge exchange (Kossyi et al. 1992). Using the (underestimated) streamer parameters from the S96 model, they found that local perturbations of NO (O_3) by a single Jet amount to tens (tenths) per cent and last for a few minutes.

A fairly accurate estimate of the NO perturbation can be derived from the power dissipated in the front, $W_f \sim \sigma_e E_m^2$. As the energy needed to create one NO molecule is $\Delta\epsilon \sim 50$ eV (Kochetov et al. 1986), one gets $[\text{NO}]_{\text{max}} \sim W_f / \Delta\epsilon \cdot r_s / u_s$ (Mishin 1997). Using the streamer tip parameters from (3) yields $W_f \sim 10 \cdot \eta^3 \text{ MW/cm}^3$ and $[\text{NO}]_{\text{max}} \sim 10^{14} \eta^2 \sim 10^{11} \text{ cm}^{-3}$ at 25 km, which well exceeds the background NO content. In the leader-corona system, the composition of the heated gas in the leader channel is affected due to the basic reactions (10). Additionally, NO, NO_2 , and O components can be produced by the streamer coronal. At $T \sim 1000$ K, Eq. (10) predicts that the O_3 content inside the leader at 20–30 km depletes by an order of magnitude within ~ 20 –50 ms. However, only numerical modeling can account for every possible reaction to give accurate predictions. Finally, vibrationally-excited NO molecules radiate in the infrared band at 5.3 μm (the time const ≈ 12 s). Simple estimates show that the emitting layer of 10 km and $[\text{NO}] \sim 10^{11} \text{ cm}^{-3}$ yields the energy flux $\sim 10 \text{ W/m}^2$, well above the strongest infrared fluxes from the auroral zone.

4.2.2 Conductivity Perturbations and Effects

Holtzworth and Hu (1995) suggested that Jet-associated conductivity perturbations might be significant for the global electric circuit. Indeed, Sukhorukov and Stubbe (1998) estimated that during the final phase Jets represent conducting channels, short-circuiting the gap between the thundercloud top and ionosphere. They stressed that the plasma in the channel decays slowly, supporting the conductivity perturbation for much longer time after the optical emission ceases. This conjecture agrees well with the Lehtinen and Inan (2007) modeling, showing that gigantic jets leave the ionization trail above 50–60 km, which lasts for a few minutes.

The persistence of highly-conductive ‘wires’ will discharge (charge) the ionosphere in the case of upward transfer of the negative (positive) charge. Anyway, the thundercloud charge will be reduced. For example, ~ 300 -A currents remove ~ 30 C within ~ 0.1 s. This effect might be responsible for the reported temporary decrease of the local lightning activity after occurrence of a blue jet/starter (Sect. 2.3). Furthermore, as the electron density decays much faster at lower altitudes (Sect. 3.3 and Fig. 2 (Lehtinen and Inan 2007)), the conductivity below ~ 50 km virtually recovers, whilst that at higher altitudes remains greater

than the background. This implies that the effective ‘ionospheric’ boundary is moved down to 50–60 km, thereby explaining the altitude extent of the trailing jets and their bright tops (Fig. 2).

5 Conclusion

We describe the salient features of upward discharges (Jets) in the atmosphere. The state-of-the-art in theoretical and laboratory modeling of transient discharges in air pertinent the physics of Jets is outlined. An assessment of the models of the blue jet development is given. The bi-directional leader concept seems to explain the basic features of Jets. The possible role of Jets in the electrodynamics and chemistry of the middle atmosphere is discussed.

Acknowledgements EVM thanks the International Space Science Institute for its hospitality during this Workshop as also the authors of the contributions contained in the chapter on electric discharges. Work by EVM is partly supported by AFRL contract FA8718-04-C-0055 with Boston College. Dr. Hsiu is acknowledged for sending the original movie of one of the gigantic jets.

References

- M. Arrayás, U. Ebert, W. Hundsdorfer, Phys. Rev. Lett. **88**, 174502-1–174502-4 (2002)
- N. Babaeva, G. Naidis, IEEE Trans. Plasma Sci. **25**, 375 (1997)
- E. Bazelyan, Y. Raizer, *Spark Discharge* (CRC Press, Boca Raton, 1998)
- E. Bazelyan, Y. Raizer, *Lightning Physics and Lightning Protection* (IOP Publishing, Bristol, 2000)
- T. Briels, J. Kos, E. van Veldhuizen et al., Appl. Phys. D **39**, 5201 (2006)
- W. Boeck, O. Vaughan, R. Blakeslee et al., J. Geophys. Res. **100**, 1465 (1995)
- W. Boeck, O. Vaughan, R. Blakeslee et al., J. Atm. Sol. Terr. Phys. **60**, 669 (1998)
- P. Crutzen, Quart. J.R. Met. Soc. **96**, 320 (1970)
- S. Cummer, N. Jaugey, J. Li, W. Lyons et al., Geophys. Res. Lett. **33**, L04104 (2006). doi:[10.1029/2005GL024969](https://doi.org/10.1029/2005GL024969)
- P. Domens, A. Gibert, J. Dupuy et al., Appl. Phys. D **24**, 1748 (1991)
- R. Franz, R. Nemzek, J. Winckler, Science **249**(4964), 48051 (1990)
- G. Garipov, M. Panasyuk, V. Tulupov et al., JETP Lett. **82**, 185 (2005)
- A. Gurevich, N. Borisov, G. Milikh, *Physics of Microwave Discharge. Artificially Ionized Regions in the Atmosphere* (Gordon and Breach, Reading, 1997)
- A. Gurevich, K. Zybin, Physics-Uspekhi **44**, 1119 (2001)
- R. Holtzworth, H. Hu, Adv. Space Res. **16**(5), 131 (1995)
- H. Kasemir, J. Geophys. Res. **65**, 1873 (1960)
- I. Kochetov, E. Mishin, V. Telegin, Sov. Phys. Doklady **31**, 990 (1986)
- I. Kossyi, A. Kostinsky, A. Matveyev et al., Plasma Sources Sci. Technol. **1**, 207 (1992)
- M. Lawrens, W. Chameides, P. Kasibhatla et al., in *Handbook of Atmospheric Electrodynamics*, vol. 1, ed. by H. Volland (CRC Press, Boca Raton, 1995), p. 189
- N. Lehtinen, U. Inan, Geophys. Res. Lett. **35**, L08804 (2007). doi:[10.1029/2006GL029051](https://doi.org/10.1029/2006GL029051)
- W. Lyons, Geophys. Res. Lett. **21**, 875 (1994)
- W. Lyons, M. Stanley, T. Nelson et al., EOS **81**, F131 (2000)
- W. Lyons, T. Nelson, R. Armstrong et al., Bull. Am. Meteorol. Soc. **84**, 445 (2003)
- V. Mazur, L. Ruhnke, J. Geophys. Res. **103**, 23299 (1998)
- E. Mishin, Geophys. Res. Lett. **24**, 1919 (1997)
- L. Niemeyer, L. Pietronero, H. Wiesmann, Phys. Rev. Lett. **52**, 1033 (1984)
- V. Pasko, M. Stanley, J. Mathews et al., Nature **416**, 152 (2002)
- V. Pasko, J. George, J. Geophys. Res. **107**(23299), 1458 (2002). doi:[10.1029/2002JA009473](https://doi.org/10.1029/2002JA009473)
- V. Pasko, U. Inan, T. Bell, Geophys. Res. Lett. **23**, 301 (1996)
- N. Petrov, G. Petrova, Tech. Phys. **44**, 472 (1999)
- Y. Raizer, *Gas Discharge Physics* (Springer, Berlin, 1991)
- Y. Raizer, G. Milikh, M. Shneider et al., Appl. Phys. D **31**, 3255 (1998)
- Y. Raizer, G. Milikh, M. Shneider, Geophys. Res. Lett. **33**, L23801 (2006). doi:[10.1029/2006GL027697](https://doi.org/10.1029/2006GL027697)

- Y. Raizer, G. Milikh, M. Shneider, *J. Atm. Sol. Terr. Phys.* **69**, 925 (2007)
- V. Rakov, M. Uman, *Lightning: Physics and Effects* (Cambridge, Cambridge, 2003)
- R. Roussel-Dupré, A. Gurevich, *J. Geophys. Res.* **101**, 2297 (1996)
- H. Rowland, *J. Atmos. Sol. Terr. Phys.* **60**, 831 (1998)
- C. Saunders, *Space Sci. Rev.* (2008, this issue)
- D. Sentman, E. Wescott, *Geophys. Res. Lett.* **20**, 2857 (1993)
- D. Sentman, E. Wescott, *EOS Trans., AGU* **77**, 1 (1996)
- D. Sentman, E. Wescott, D. Osborne et al., *Geophys. Res. Lett.* **22**, 1205 (1995)
- N. Smirnova, A. Lyakhov, S. Kozlov, *Int. J. Geom. Aeron.* **3**, 281 (2003)
- H. Stenbaek-Nielsen, M. McHarg, T. Kanmae et al., *Geophys. Res. Lett.* **34**, L11105 (2007). doi:[10.1029/2007GL029881](https://doi.org/10.1029/2007GL029881)
- M. Stoltzenburg, T. Marshal, *Space Sci. Rev.* (2008, this issue). doi:[10.1007/s11214-008-9338-z](https://doi.org/10.1007/s11214-008-9338-z)
- H. Su, R. Hsu, A. Chen, Y. Wang et al., *Nature* **423**, 974 (2003)
- A. Sukhorukov, E. Mishin, P. Stubbe et al., *Geophys. Res. Lett.* **23**, 1625 (1996)
- A. Sukhorukov, P. Stubbe, *J. Atmos. Sol. Terr. Phys.* **60**, 725 (1998)
- V. Trakhtengerts, D. Iudin, *Radiophys. Quant. Electron.* **48**, 720 (2005)
- A. Vallance-Jones, *Aurora* (Reidel, Dordrecht, 1974)
- O. Vaughan Jr., B. Vonnegut, *J. Geophys. Res.* **94**, 13179 (1989)
- O. Vaughan Jr., R. Blakeslee, W. Boeck et al., *Mon. Weather Rev.* **120**(7), 1459 (1992)
- E. Wescott, D. Sentman, D. Osborne et al., *Geophys. Res. Lett.* **22**, 1209 (1995)
- E. Wescott, D. Sentman, M. Heavner et al., *Geophys. Res. Lett.* **23**, 2153 (1996)
- E. Wescott, D. Sentman, M. Heaver et al., *J. Atm. Sol. Terr. Phys.* **60**, 713 (1998)
- E. Wescott, D. Sentman, H. Stenbaek-Nielsen et al., *J. Geophys. Res.* **106**, 21549 (2001)

VLF Studies During TLE Occurrences in Europe: A Summary of New Findings

Á. Mika · C. Haldoupis

Originally published in the journal Space Science Reviews, Volume 137, Nos 1–4.
DOI: [10.1007/s11214-008-9382-8](https://doi.org/10.1007/s11214-008-9382-8) © Springer Science+Business Media B.V. 2008

Abstract The paper reviews the past few years' European efforts for characterising the effects of TLEs, in particular sprites and elves, on the lower ionosphere. A mostly experimental approach was applied for the analysis of data collected during the EuroSprite campaigns by optical cameras, very low frequency (VLF, 3–30 kHz) receivers and lightning detection systems. The new findings of these multi-instrumental studies can be summarised as follows: 1) A close relationship between sprites and early VLF perturbations was established which constitutes evidence of upper D-region electron density changes in association with sprites. 2) VLF backscatter from the sprite-affected regions exists but it occurs rarely. 3) Long-delayed sprites were present in a large percentage, contrary to previous reports; they occurred in relation to long-lasting continuing currents that contribute to the build-up of sprite-causative quasi-electrostatic fields. 4) Intracloud lightning was found to be the key-factor which determines the sprite morphological features. 5) A new subcategory of VLF events was discovered, termed *early/slow*, characterised by long onset durations from 100 ms up to \sim 2 s. The slow onsets, which were attributed to a gradual ionisation build-up, are driven by a dense sequence of intracloud electromagnetic pulses that accompany the sprite-causative discharge. 6) A D-region chemical model was applied to simulate the measured recovery phases of the early VLF perturbations. This led to estimates about the mean altitude and electron density enhancements of the sprite-related ionospheric perturbations. 7) Early VLF events were identified for the first time to occur in association with elves, providing evidence that corroborates theoretical predictions on lower-ionospheric ionisation production by lightning-emitted electromagnetic pulses.

Keywords D region · TLE · Early VLF perturbation

Á. Mika (✉)
ARGOSS B.V., Marknesse, The Netherlands
e-mail: mika@argoss.nl

C. Haldoupis
Department of Physics, University of Crete, Heraklion, Greece
e-mail: chald@physics.uoc.gr

1 Introduction

Lightning discharges radiate electromagnetic energy in a wide spectral range with the bulk of their power released in the very low frequency (VLF, 3–30 kHz) band. At these frequencies, electromagnetic waves can propagate large distances (many Mm-s) via reflections from the conducting Earth surface and the lower ionosphere at about 85 km altitude. These waves cause the electrons of the lower-ionospheric plasma to accelerate and thus can lead to heating, the optical emissions called ‘elves’ and the production of extra ionisation near the VLF reflection height. Elves belong to the family of the so-called transient luminous events (TLEs). They consist of a rapidly expanding ring of luminosity and can be observed for less than about 1 ms. In addition, the sudden charge rearrangement in the thundercloud which follows a cloud-to-ground (CG) discharge can set up strong quasi-electrostatic (QE) fields above the cloud tops. These can cause breakdown around 70 km altitude and lead to the spectacular optical emissions called sprites which last for about 10 to 100 ms.

The changes in ionospheric conductivity associated with the lightning-induced electric fields can affect the propagation of the powerful VLF transmissions of navigation beacons situated all around the globe causing perturbations in their amplitude and/or phase. These perturbations appear in the form of early/fast events which are sudden jumps in the recorded VLF time series (Johnson et al. 1999). They occur within 20 ms of a causative CG lighting discharge (‘early’) and have rapid onsets (<20 ms, ‘fast’, i.e. within one sampling interval of the receiver) followed by relatively long signal recoveries (10 to more than 100 s). Although the early VLF perturbations have been studied extensively over the last 15 years, mostly by the VLF group at Stanford University (e.g., see Inan et al. 1993; Johnson and Inan 2000; Moore et al. 2003), and also by University of Otago researchers (e.g., Dowden et al. 1996b; Dowden et al. 1996a), their complex properties are still not well understood. Early VLF events were reported to occur in association with both negative and positive CG discharges and were observed to accompany a subset of sprites (Inan et al. 1995). Using data from an array of closely-spaced receivers, the ionospheric disturbances were seen to cause forward scattering of the incident VLF waves and were estimated to be diffuse regions having typical transverse extents of ~100–150 km (Johnson et al. 1999). On the other hand, researchers from the University of Otago reported that sprites within about 500 km of the receivers were always accompanied by VLF perturbations, irrespective of their distance from the transmitter-receiver (TX-RX) great circle path (GCP). These events showed evidence of wide-angle scattering, often even backscatter towards the VLF transmitter (Dowden et al. 1996a). This requires structured ionised regions with scales smaller than the VLF wavelength, which were hypothesised to coincide with the ionised sprite columns (Hardman et al. 1998; Rodger et al. 1998b; Rodger et al. 1999). Recent Stanford analyses (Marshall et al. 2006) found only rare examples of backscatter, always in relation to the most spatially extended, usually multiple, sprites, thus apparently contradicting the findings of the Otago group. These controversial results strongly suggest that the relation between TLEs and VLF perturbations is highly complex. Therefore further experimental studies are needed to understand better the link between the TLE and VLF phenomena, that is, to learn more about the effects of lightning discharges on the overlying lower ionospheric plasma.

The present paper aims at summarising the European contributions to this intriguing field of research. VLF studies are presented which tackle a number of open questions. These include the effects of lightning-induced TLE-producing electric fields on the lower ionosphere and in turn on VLF wave propagation, the structure of the TLE-related ionisation changes (i.e. forward vs. backscatter), the role of intracloud discharges in the sprite

generation process, and the magnitude of excess ionisation produced during sprite occurrences.

2 Instrumentation

In a response to the need for more experimental TLE studies, the Danish National Space Center has been organising the so-called EuroSprite campaigns each summer since 2000. The aim of these campaigns is to stimulate collaboration between a number of institutes and to deploy a variety of instruments to study the different aspects of the TLE phenomena (Neubert et al. 2005). The data used in the studies summarised in this review were collected during the EuroSprite2003 and EuroSprite2005 campaigns. The essential components of the observing system were two remote-controlled, low-light optical cameras, mounted on mountain tops, in the Observatoire du Pic du Midi in the French Pyrénées and on Puy de Dôme in the Central Massif in France. These provided the information on TLE occurrences. Data on the cloud-to-ground and intracloud (IC) lightning activity was provided by the French Météorage and SAFIR lightning detection systems. The core data used for the analyses presented herein were provided by VLF receivers. VLF observations were conducted at two sites, on the island of Crete in Greece (35.31°N , 25.08°E) and at Nançay, France (47.38°N , 2.19°E). The Crete receiver was recording the amplitude and phase time series of VLF navigation beacons operating at well-defined frequencies with a sampling frequency of 50 Hz. The Nançay receiver was recording the VLF background noise in the 350 Hz–50 kHz range with 100 kHz sampling frequency. It was possible to post-process this broadband signal and extract from it narrowband VLF transmitter signal time series (Bainbridge and Inan 2003).

3 Summary of New Results

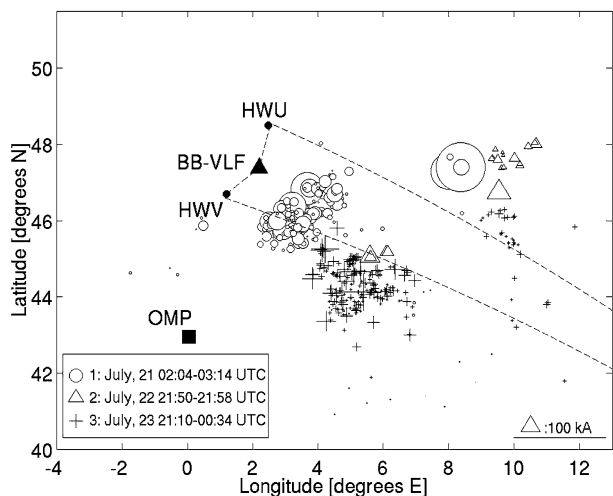
3.1 Sprites and Early VLF Perturbations

As emphasised in Sect. 1, the relationship between sprites and VLF perturbations still constitutes an area of debate and ongoing research. The unique dataset of optical sprite observations, lightning detection data and simultaneous VLF recordings collected during the EuroSprite2003 campaign was exploited in an attempt to find out more about the nature of the association between these two phenomena (Haldoupis et al. 2004; Mika et al. 2005).

Figure 1 shows the locations of the +CG discharges produced by three thunderstorms occurring over central France on 21 (circles), 22 (triangles), and 23–24 July 2003 (crosses). The Pic du Midi cameras captured 27 sprites during a 70-minute period of the first storm when the Météorage system reported a total of 1273 –CG and 207 +CG discharges. There were only 2 sprites recorded during a short storm period on 22 July during which there were 108 –CG and 18 +CG discharges observed by the lightning detection system. During the last storm, the cameras observed 13 sprites during a period when 5148 –CG and 247 +CG discharges were detected. All the storms were situated at distances between ~ 100 and 600 km to the southeast of the two French transmitters (HWV—18.3 kHz and HWU—20.9 kHz), more or less along their GCPs to Crete. Due to the proximity of the storms to the GCPs, these transmitter signals were likely to be perturbed by lightning-induced conductivity changes in the lower ionosphere above the storms.

Inspection of the sprite occurrence sequence and the VLF amplitude time series revealed a striking coincidence between the detected sprites and the onsets of abrupt amplitude

Fig. 1 Locations of the +CG discharges occurring during the 21–24 July 2003 sprite observation periods. The marker sizes are linearly scaled to the peak current intensities. The GCPs from the HWU and HWV transmitters to the Crete and Nançay (BB-VLF) receivers are shown by dashed lines. OMP marks the location of the optical cameras in the Observatoire du Pic du Midi in the French Pyrenees. From Mika et al. (2005)



Sprites / VLF sprites 2003, July 21, 0230-0252 UT

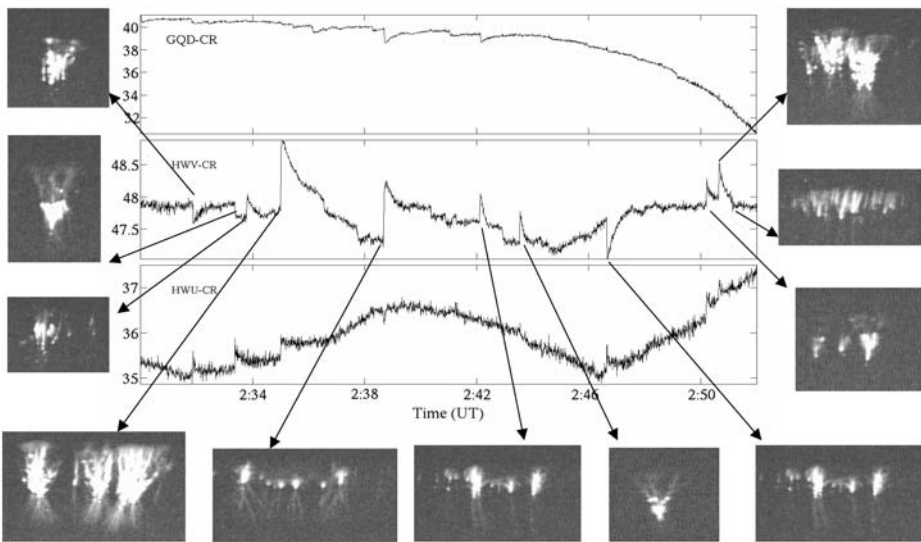


Fig. 2 VLF amplitude time series recorded on Crete and the optical images of 11 sprites captured from OMP during a 22-minute storm interval. All the sprites were accompanied by VLF perturbations. From Haldoupis et al. (2004). Copyright 2004 American Geophysical Union. Reproduced by permission of the American Geophysical Union

perturbations which were identified as early VLF events. This association is illustrated in Fig. 2, which corresponds to a storm interval on 21 July when 11 out of the 27 sprites were observed. The VLF time series display the signal amplitude in dB for the HWU–CR (HWU–Crete) and HWV–CR links traversing the storm region, and the 22.1 kHz GQD (Anthorn, Great Britain)–CR link north of the storm.

In total, 24 out of the 27 sprites observed during the 21 July 2003 storm coincided with an abrupt jump in VLF amplitude. High time-resolution plots showed that the perturbation onsets occurred within about 20 ms (time resolution of the data) relative to the sprite times. This signifies a sudden change in ionospheric conductivity produced directly by a process relating to the sprite-causative +CG discharge perturbations. There were no VLF events observed in relation to the numerous lightning discharges that did not produce sprites, which included 180 +CG and 1273 –CG flashes.

Inspection of the entire dataset for the two storms during 22–24 July 2003 revealed early VLF perturbations on the HWV signal amplitude in association with 12 out of the 15 observed sprites. On the other hand, there were also 10 cases of early-like VLF perturbations which were not accompanied by sprites. A re-examination of the optical images, which was unfortunately possible only for three out of these ten events, led to the discovery of one more sprite which, obviously, was missed originally, whereas for the other two cases the discharges were too low on the horizon for the cameras to capture a possible sprite.

Taking into account the entire dataset considered here, 37 out of the 43 sprites observed during 21–24 July 2003 were accompanied by VLF perturbations, that is, about 85%. On the other hand, there were 9 VLF events which did not relate to observed sprites. These results imply a close relationship between sprites and early VLF perturbations. The electron density changes occurring during sprite events located close to the TX–RX GCP seem to perturb VLF propagation in most cases, though they might not be the sole reason behind early VLF events.

The statistical properties of the sprite-related VLF signatures were also assessed using a sample of 26 selected events which had amplitudes higher than about 0.2 dB (since this is the minimum perturbation that is clearly discernible without significant data processing) and relatively low-level sferic contamination. Most of the perturbation magnitudes were between 0.2 and 1.0 dB in line with existing statistics for early/fast events (Johnson et al. 1999); there were also two events with magnitudes reaching values near 3.0 dB, departing considerably from the rest. The recovery times were mostly between 20 and 150 s, which compare well with those of early/fast events reported elsewhere (Strangeways 1996; Rodger 1999). An interesting new observational fact is that in 12 cases the perturbation onset durations (the time between the abrupt onset and the time of the maximum mean level of the amplitude perturbation) were larger than 100 ms and out of this subset 6 VLF events had onset durations greater than 500 ms reaching values up to about 2 s. These perturbations, termed ‘early/slow’, constituted a new category which had never been dealt with before. Results from studies examining their properties in more detail (Haldoupis et al. 2006) are presented in Sect. 3.5.

3.2 VLF Backscatter in Association with Sprites

The proximity of the 21–24 July sprite-producing storms at distances less than 500 km to the southeast of the broadband VLF receiver (e.g., see Fig. 1) and the controversy in the published observational results mentioned in Sect. 1 motivated a search for VLF backscatter perturbations in association with the observed sprites. In order to identify VLF backscatter signatures in the Nançay recordings, the HWV signal was extracted from the broadband time series by applying the same narrowband digital filter which is employed in real time at the Crete receiver and searched for sprite-related early VLF perturbations.

Inspection of the HWV–Nançay narrowband time series revealed only five cases out of the 38 sprites for which broadband data were available to be accompanied by weak early-like VLF perturbations having onsets coincident with the sprites. All five events occurred

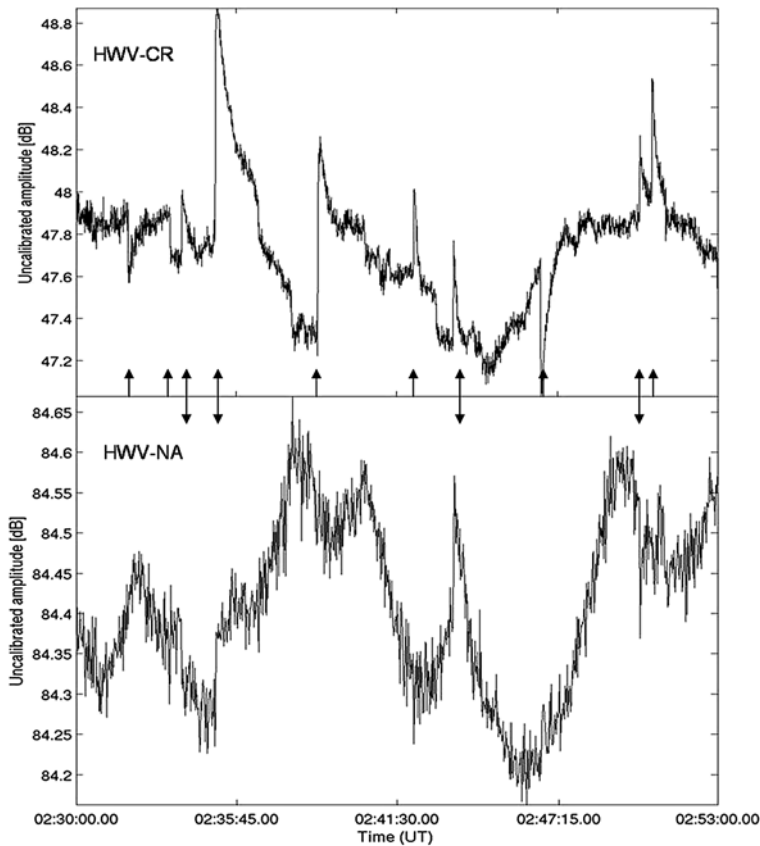


Fig. 3 Concurrent intervals of HWV signal amplitude time series showing sprite-related VLF perturbations (marked by arrows) received on Crete through forward scattering (top) and at Nançay possibly through backscatter (bottom) from conductivity changes in the lower ionosphere during sprite occurrences. From Mika et al. (2005)

during the storm of 21 July which was the nearest one to Nançay, at about 100 to 200 km to the southeast. No similar perturbations were identified to accompany the sprites captured during the 22–24 July storms, possibly because these were located further away from the receiver, at distances between about 230 and 500 km.

Figure 3 shows 23 minutes of recordings when 4 out of the 5 early VLF events were seen in the HWV–Nançay signal (bottom panel). Also shown for comparison in the top panel are simultaneous records from the HWV–Crete link. The sprite-related early VLF events are marked by arrows. As seen, there were 10 early VLF perturbations in the HWV–Crete time series, all in relation to sprites, but only four of these had counterparts in the HWV–Nançay signal. As evidenced by Fig. 3, the Nançay perturbations were considerably weaker than those observed at Crete, having magnitudes less than 0.2 dB. In addition, these few backscatter events did not appear to have any preference to either the early/fast or early/slow VLF perturbations. The HWV recordings were investigated for backscatter-like signatures also for the storms of 27 July, 22, 24, 25, and 28–29 August 2003, when broadband data was available for a total number of 47 sprites. During these storms, the +CG discharges detected by Météorage were located at distances larger than about 300 km from the HWV–

Nançay GCP. The results of the search were negative, there were no early VLF perturbations identified during the entire duration of the storms, probably due to their larger distances from the GCP.

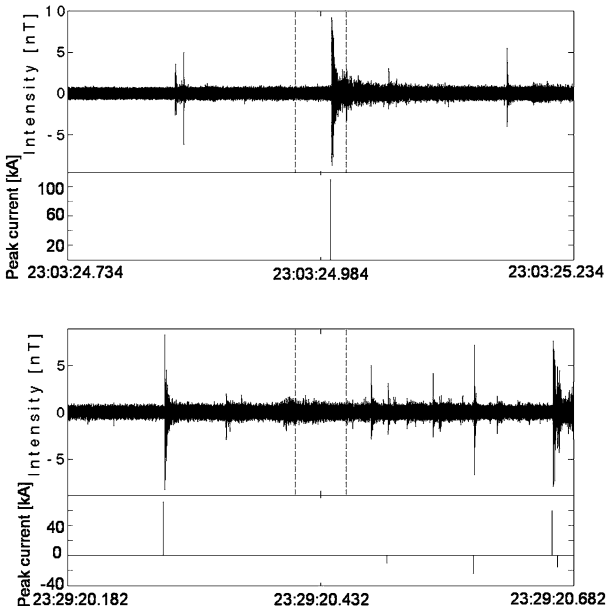
In summary, considering the entire number of sprites recorded, only about 5% associated with identifiable backscatter-like VLF perturbations. Taking into account only those events which were located at distances less than about 500 km from the Nançay receiver this ratio becomes 7%, a figure which departs considerably from the one-to-one relationship reported by Dowden et al. (1996b). Note that the weak backscatter-like perturbations were observed during a single storm situated closer than 200 km to the Nançay receiver. In contrary to the findings of Marshall et al. (2006) there was no relationship between the sprite morphology (meaning here single sprites vs. large clusters) and the existence of backscatter. Alternatively, there might be another explanation for the presumed backscatter perturbations (substantiated by the findings of Mika et al. 2006 and also mentioned in Marshall et al. 2006). The distances of 100–200 km from the +CG location to the Nançay receiver can place these events in a disturbed ionospheric region associated with undetected sprite halos or elves (the possibility for the latter is examined in Sect. 3.7) that may overlap the receiver. Then, in this case, the early VLF signatures observed at Nançay may be the result of a direct change in the local propagation conditions (e.g. change in the reflection height) and thus not associate necessarily with VLF backscatter.

3.3 Long-Delayed Sprites

It is widely accepted that sprites initiate a few milliseconds after a +CG discharge accompanied by charge moment changes sufficiently large to set up a strong enough QE field in the upper atmosphere that is capable of causing locally an electrical breakdown. Despite this conviction, however, the nature of the relation between sprites and their causative +CG discharges is not yet clear and well understood. This is particularly true for the so-called long-delayed sprites, believed to represent a small percentage in which the sprite onsets are delayed relative to the +CG discharge by more than 30 ms (e.g., see Bell et al. 1998; Cummer and Füllekrug 2001). In the following, results from studies investigating the delays between sprites observed during the EuroSprite2003 campaign and the +CG discharges preceding their occurrence using lightning and VLF observations are presented (Mika et al. 2005).

First, the distribution of the time difference between the sprite occurrence and the time of the nearest +CG discharge preceding it up to \sim 300 ms was investigated. A total of 103 sprites were used, observed during the storms of 21–27 July (44 sprites) and of late August 2003 (59 sprites). Since the sprite images were taken over 20 ms and their times were correct to within \pm 12 ms, +CG discharges preceding or following the sprite time by about 30 ms were taken to be nearly coincident, and considered as causative to the sprites. 64 out of the 103 sprites observed, that is \sim 62%, were accompanied by +CG discharges occurring near their onset time. These were termed ‘short-delayed’ sprites. From the rest, 30 sprites (\sim 29%) were lagging the +CG discharge by times ranging from about 30 to 220 ms (termed herein ‘long-delayed’), whereas 9 sprites (\sim 9%) were not preceded by any +CG discharges up to at least 2.5 s prior to their occurrence. This means that nearly 40% of the observed sprites were either long-delayed or had no relation to a causative +CG discharge. Given that Météorage is a state-of-the-art lightning detection system having adequate coverage and a high detection efficiency of more than 90%, it is unlikely that it had missed such a high number of causative discharges. On the other hand, the software algorithms of systems such as Météorage are known to occasionally reject large lightning discharges with complex waveforms (typically +CGs), meaning that Météorage is more likely to miss sprite-associated CGs.

Fig. 4 Typical examples of broadband VLF data recorded at Nançay (*top*) 250 ms before and after a short-delayed (*left*) and a long-delayed (*right*) sprite. The sprite observation time is marked by two vertical dashed lines accounting for both the image exposure time of 20 ms and the time uncertainty of 12 ms. CG discharges recorded by Météorage are shown in the bottom panels. From Mika et al. (2005)



To further investigate the relation between sprites and preceding +CG flashes, the Nançay broadband VLF time series were inspected in order to assess the radio-sferic activity accompanying these events. VLF observations can more accurately link lightning activity to sprite occurrence, since all lightning discharges produce sferics and the receiver sferic-detection efficiency for CG discharges is precisely 1 at such short distances to the thunderstorm (from about 100 to 1000 km). Therefore, sferic detection could also identify the ~9% of CG discharges which were apparently missed by the lightning detection network. Since broadband measurements were carried out from 21:00 to 03:00 UTC only, VLF recordings were available only for 51 short-delayed, 28 long-delayed, and 6 no +CG-related sprites. Close inspection of the Nançay VLF time series revealed the presence of a burst of sferic activity coincident with the +CG discharge always in relation to the short-delayed sprites. On the other hand, there was no significant level of sferic activity present in the broadband VLF signal during the observation times of the long-delayed sprites. Also, there were no additional sferics corresponding to potential causative CG discharges missed by Météorage which endorses that these events were indeed long-delayed sprites. As for the 6 sprites which, according to Météorage, were not preceded by a +CG discharge up to at least 2.5 s prior to their occurrence, the broadband VLF records revealed sferic clusters occurring simultaneously with all of them. This suggests that Météorage had indeed missed the causative discharges of these sprites. These data showed, for the first time, that the short- and long-delayed sprites occur with a ratio of about 2:1, which is much smaller than thought previously.

The radio-sferic and CG lightning activity for the short-delayed (left) and long-delayed (right) sprites is shown in Fig. 4. The left panel of Fig. 4 shows a strong burst of sferics in connection with the short-delayed sprite and its causative +CG discharge. The example in the right panel is representative of the long-delayed sprites showing only weak sferic activity during the sprite observation time.

An explanation put forward for the long-delayed sprites assumes the presence of long-lasting cloud-to-ground continuing currents flowing after the return stroke of the +CG dis-

charge (Bell et al. 1998; Reising et al. 1999; Cummer and Füllekrug 2001) which neutralise charge on a relatively long timescale. This leads to a gradual build-up of the QE fields in the upper atmosphere which, when the field strength exceeds the air breakdown threshold, generate sprites. The VLF data used here cannot provide direct evidence either for or against this mechanism. On the other hand, in order to achieve such long-lasting continuing currents, a significant in-cloud component is required to feed the +CG discharge. In the next section, results from studies on the role of IC discharges in the sprite generation process are presented (van der Velde et al. 2006).

3.4 Intracloud Lightning Activity and Sprite Morphology

There exist a number of modelling studies (e.g., Valdivia et al. 1997; Rycroft and Cho 1998) and observations of spider lightning (Stanley 2000) accompanying sprites which suggest that IC discharges might play an important role in the sprite generating process. The existence of long-delayed sprites also substantiates this idea since it suggests a gradual build-up of the mesospheric electric fields due to long-lasting charge neutralisation by the continuing current and probably IC currents feeding it (Uman 2001, p. 171). Further observational evidence was provided by broadband VLF and ELF observations which revealed IC sferic clusters accompanying sprites (Ohkubo et al. 2005). It must be noted, that in the following, the term intracloud lightning is meant to describe all phases of lightning in the cloud or air involved in one flash event including leader activity accompanying a CG flash.

Sprite-producing thunderstorms traversed the area covered by the SAFIR lightning detection system, capable of detecting IC discharges (for a description of the shortcomings of interferometric systems see e.g., Mazur et al. 1998), on three nights during the EuroSprite2003 campaign. The best quality data were obtained during the night of 23–24 July 2003, when 15 sprites were observed from Pic du Midi. Broadband VLF observations were made by the Nançay receiver which was expected to detect sferics related to IC discharges occurring in the nearby (<500 km) thunderstorm. The sprite events were classified according to their morphology into two groups, column (narrow, straight, short, mostly uniform elements) and carrot (taller, irregular shapes, usually with well-visible streamers extending upwards and downwards from a bright body) sprites and their characteristics compared. Apart from their distinct shapes, these two groups seem to also be related to somewhat different physical processes. E.g., McHarg et al. (2007) observed that column sprites are initiated by downwards propagating (negative) streamers while in the case of carrot sprites upward moving (positive) streamer heads are also present.

Column sprites were found to associate with relatively few (3 to 8) very high frequency (VHF, 30–300 MHz) IC sources in a ±250 ms time interval (relative to the start of the video frame), as detected by the SAFIR system. They followed the +CG closely, with delays up to 40 ms, having an average value of 12 ms relative to the start of the video frame integration time of 20 ms. Thus these events classified as short-delayed sprites, in accord with the analysis presented in Sect. 3.3.

The average duration of VLF sferic clusters was about 25–30 ms for column sprites. Figure 5 shows the VLF and lightning data for a typical column sprite event. Both the broadband VLF time series (top) and the corresponding spectrogram (middle) show a short burst of VLF sferic energy (lasting for about 30 ms) in the time frame when the sprite occurred (marked by the two vertical dashed lines) corresponding to a +CG discharge detected by Météorage (bottom).

All carrot sprites associated with a relatively large number (between 17 and 88) of VHF IC sources. The delay between the +CG discharges and the sprites ranged from 18 to

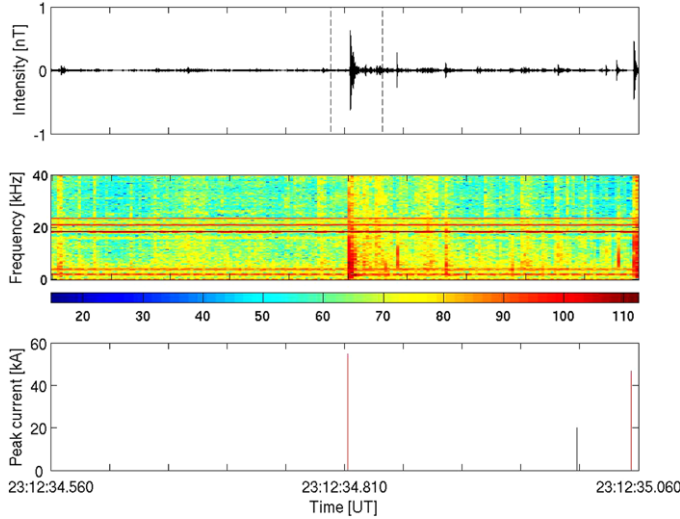


Fig. 5 East-west component of the broadband VLF signal intensity (*top*, in arbitrary units) and the corresponding VLF spectrum (*middle*, dB) 250 ms before and after a column sprite event. The two vertical dashed lines indicate the sprite observation time, accounting for the video frame integration time of 20 ms plus the timing uncertainty of 12 ms. The *bottom panel* shows the peak currents of CG discharges recorded by Météorage (red) and the VHF sources detected by SAFIR (black), the latter scaled arbitrarily. From van der Velde et al. (2006). Copyright 2006 American Geophysical Union. Reproduced by permission of the American Geophysical Union

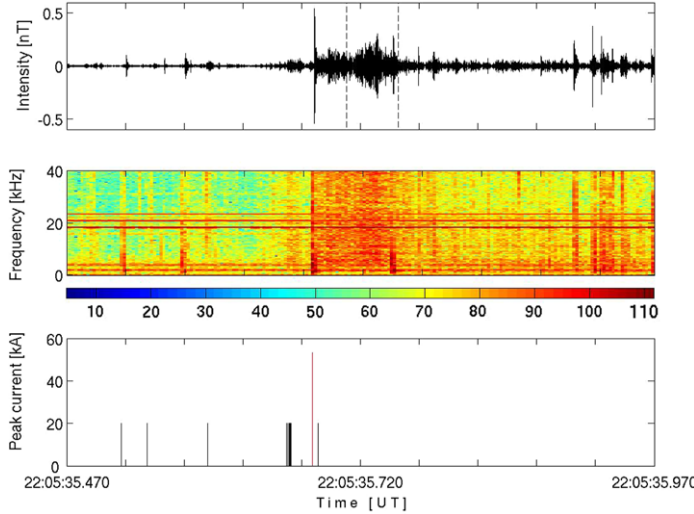


Fig. 6 Same as in Fig. 5 but for a carrot sprite event. From van der Velde et al. (2006). Copyright 2006 American Geophysical Union. Reproduced by permission of the American Geophysical Union

205 ms, with an average value of 63 ms thus carrot sprites classified, on average, as long-delayed sprites. This suggests that continuing currents are likely playing a role in the generation of carrot sprites. The duration of the VLF clusters was also longer, with averages of 100–110 ms. Figure 6 shows the VLF time series (*top*), the corresponding spectrogram (*mid-*

dle), the Météorage cloud-to-ground strokes, and the VHF sources detected by the SAFIR system (bottom) for a typical carrot sprite event.

The results presented in this section show that the IC phase of a lightning discharge plays an important role in the generation of carrot sprites but appears relatively unimportant for column sprites. The physics behind this role is far from being clear and needs to be further studied. These results seem to indicate that carrot sprites associate with longer-lasting continuing currents which help to build-up and sustain strong electric fields in the upper atmosphere for a longer time than in the case of column sprites.

3.5 An Explanation for Early/Slow VLF Perturbations

As described in Sect. 1, early/fast events are abrupt perturbations in the amplitude and/or phase of subionospheric VLF transmissions occurring within 20 ms of a causative CG lightning discharge (i.e., early) having rapid onsets (<20 ms, i.e., fast) followed by relatively long signal recoveries ranging from about 10 to more than 100 seconds. In this section, recent studies are summarised which provide evidence showing that a sizable group of sprite-related early VLF perturbations do not display a ‘fast’ onset, instead they have long onset durations of 100 ms to 2 seconds and thus were labelled ‘early/slow’ events (Haldoupis et al. 2006). The existence of slow onsets implies an underlying mechanism which causes a gradual build-up of ionisation following a causative CG discharge. Next, the observed characteristics of early/slow events are presented and the physical mechanism proposed in (Haldoupis et al. 2006) is described.

The analyses presented herein were based on data collected during the EuroSprite2003 and 2005 campaigns (see Sect. 2). VLF data of the 18.3 kHz transmitter, collected on Crete during 85 sprite events, 75 from four different storms on the nights of 21–24 July and 28–29 August 2003, and 10 from 29 July 2005 were analysed and lead to the identification of 73 early VLF events. From this dataset, only the VLF perturbations with clearly discernible onsets were kept for further inspection which reduced the number of usable events to 27. Out of these 27 VLF events, at least 15, that is, about 55% of the cases, classified clearly as early/slow, 8 events were early/fast, whereas the rest exhibited rather complicated onsets (a few associated with closely spaced sequential sprites), which made their categorisation ambiguous. Figure 7 displays typical examples of early/slow and early/fast perturbations along with the images of the sprites associated with them. The sprite onset is marked by the dashed line. The early/fast event (bottom panel) has an instant (fast) onset followed by the usual signal recovery of several tens of seconds. On the other hand, the early/slow signature, shown in the top panel, has a slow onset, characterised by a gradual growth which lasts for \sim 1.0 to 1.5 s. The recovery back to pre-onset signal levels is similar in duration to that of the early/fast events.

The early/slow events were analysed in conjunction with high-resolution broadband VLF recordings made at Nançay and Météorage lightning data. The storms under consideration were located in central France at distances ranging between 100 and 400 km from the Nançay receiver which made the detection of sferics radiated by IC discharges possible. The analysis revealed a recurring lightning pattern for early/slow events which displayed the following characteristics: 1) Météorage recordings showed a post-onset sequence of a few individual CG discharges originating from the same area. 2) The Nançay VLF time series showed a large number of relatively weak and densely-clustered sferics which were not seen by Météorage and thus probably originated from IC discharges. 3) The sferic clusters sometimes initiated before the sprite but mostly occurred after it and coincided with the VLF perturbation onset growth. 4) The IC sferic clusters originated from about the same storm area.

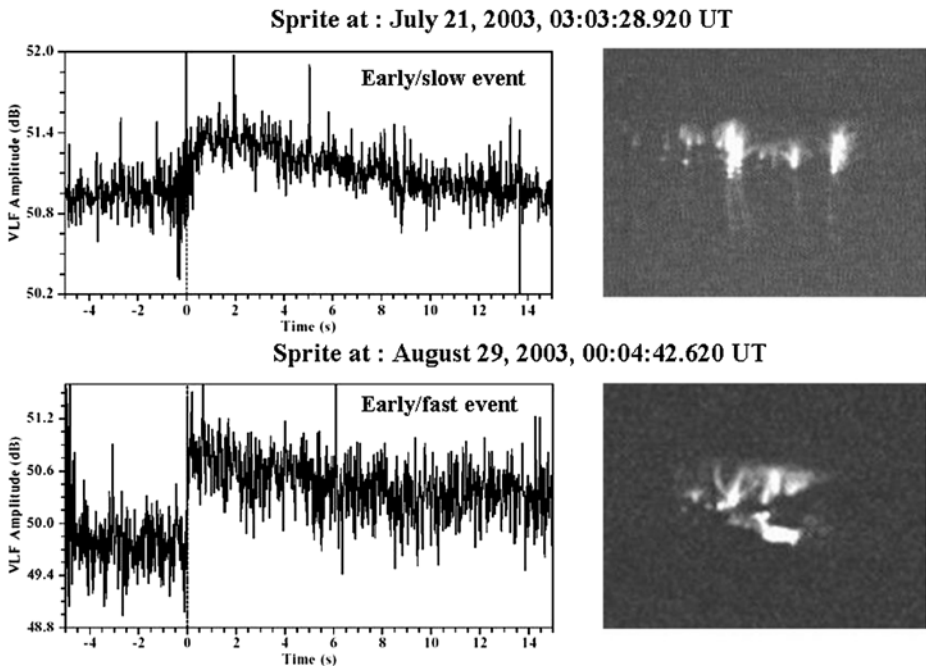
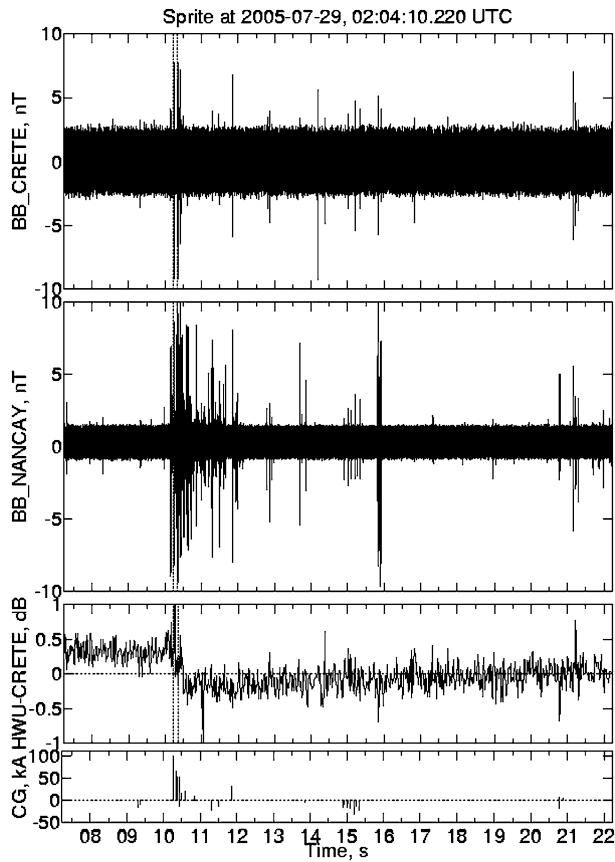


Fig. 7 Typical sprite-related early/slow (top) and early/fast (bottom) VLF perturbations. The optical images of the corresponding sprites are shown on the right. From Haldoupis et al. (2006). Copyright 2006 American Geophysical Union. Reproduced by permission of the American Geophysical Union

During EuroSprite2005 the Crete VLF station operated also as a single-channel broadband receiver. This provided the possibility of testing if the cluster of sferics, observed at Nançay simultaneously with the growth phase of early/slow events, was indeed caused by IC discharges. This relies on the fact that IC lightning sferics are not expected to propagate at large distances (e.g., see Johnson and Inan 2000), thus they should not be observable on Crete, more than 2000 km away from the storms in France. This was confirmed by analysing two early/slow events observed in relation to sprites during a brief storm on 29 July 2005. The findings are summarised in Fig. 8. As seen in the bottom panel, Météorage detected at least 6 +CG flashes following the sprite-causative +CG discharge, all originating from the same region. The related early/slow event shown in the third panel, started with the sprite and had a growth phase of about 2 s, accompanied by a strong burst of numerous sferics seen by the Nançay broadband VLF receiver (second panel). The angles of arrival of these sferics (not shown here) all pointed towards the storm region under consideration. The Crete receiver detected only a small number of discrete sferics all in relation to the CG discharges seen by Météorage. It did not detect the sferic clusters seen at Nançay, probably because these were due to IC lightning and thus could not propagate at distances larger than some 500 to 800 km (e.g., see Johnson and Inan 2000). In contrary, the onsets of the early/fast events were not accompanied by enhanced clusters of sferics.

A mechanism behind the early/slow events needs to explain why soon after a sprite, the VLF perturbation undergoes, for about 1 to 2 s, a gradual growth to a maximum amplitude instead of an abrupt jump as in the case of the early/fast events. This suggests a process of gradual ionisation build-up initiated by the sprite breakdown which seems to be compatible with the presented observations showing the onsets of early/slow events to be accompanied

Fig. 8 An early/slow event seen on Crete (third panel) compared to CG lightning strokes (bottom panel) and broadband VLF data recorded near the storm at Nançay (second panel) and about 2200 km away from the storm on Crete (top panel). The two vertical dashed lines mark the occurrence of the sprite which was seen in two successive video frames. From Haldoupis et al. (2006). Copyright 2006 American Geophysical Union. Reproduced by permission of the American Geophysical Union



by a burst of lightning activity, comprised of a few discrete CG strokes and clusters of IC discharges. The following scenario was proposed for early/slow events: The sprite-causative +CG discharge and the associated charge moment change set up a QE field above the thunderstorm that causes electric breakdown, triggers the sprite and creates some extra ionisation in the upper D region. However, this ionisation production is not strong enough to raise the lower-ionospheric conductivity so much that it would prevent the electric fields related to further discharges from penetrating to higher altitudes. Next, the enhanced CG and IC lightning activity that follows the sprite onset generates QE and EMP (electromagnetic pulse) fields which penetrate in the upper D region and energise the electrons further, which leads to additional (secondary) ionisation. Since the times of interest (0.5 to about 2 s) are much shorter than the electron lifetimes at these altitudes, this process can lead to electron density accumulation which can account for the growth phase, or the long onset duration, of the early/slow events. In this scheme, IC discharges may play the key role as suggested by the VLF and lightning observations. The radiation pattern of horizontal IC discharge channels has a maximum of the emitted energy directly above the discharge and thus they are optimal sources of vertical EMP heating of the upper D region. Also, EMP fields can penetrate more easily to higher altitudes compared to QE fields because of their much shorter time scales due to which ambient conductivity shielding is much less severe. Furthermore, the absence of additional sprite displays in relation to the observed post-onset +CG discharges argues against important CG lightning-induced breakdown effects in the overlying ionosphere. All

this suggests that the EMP role in secondary ionisation production is possibly much more decisive than that of QE fields.

The proposed mechanism is consistent with the observation of enhanced clusters of IC discharges accompanying the growth phases of early/slow perturbations. A key element is that the sprite breakdown is needed for producing seed electrons in the upper D region, which then can be energised to produce additional (secondary) ionisation under the action of subsequent EMPS. A key implication of this interpretation is the production of diffuse regions of elve-like or halo-like optical emissions above the storm during the growth phase of early/slow events since the energy thresholds for excitation are smaller than those required for ionisation. However, these would probably be weak and short-lasting (<1 ms), as in the case of elves. The existence of these weak emissions and thus the validity of the proposed interpretation remains to be proved or disproved by carefully designed experiments using high-speed optical imagers and photometers.

3.6 Estimating D-Region Electron Density Changes Related to Sprites

There are no conclusive measurements of sprite-related ionisation available to date, therefore any bit of independent information constitutes a valuable input for sprite-generation models and theoretical interpretations. Previous studies of modelling VLF scattering off the sprite plasma and comparing the results to VLF observations by Rodger et al. (1998a) estimated an increase in the D-region electron density of more than a factor of 10^4 at 75 km. Roussel-Dupré and Blanc (1997) observed HF (high frequency, 3–30 MHz) radar echoes attributed to reflection off the sprite plasma, requiring minimum electron densities of 6×10^4 – 10^5 cm $^{-3}$ at 55–65 km altitudes, corresponding to relative electron density enhancements of about 7 to 8 orders of magnitude.

In the study presented in this chapter, a D-region chemistry model, originally developed for modelling the recovery times of lightning-associated VLF LEP (Lightning-induced Electron Precipitation) perturbations (Glukhov et al. 1992; Pasko and Inan 1994), was applied to estimate the electron densities involved in sprite events. The model accounts for four constituents: electrons (N_e), single positive ions (N^+), single negative ions (N^-), and positive cluster ions (N_x^+); and six different charge exchange processes: attachment, detachment, dissociative recombination, recombination of positive cluster ions, ion–ion recombination (mutual neutralisation), and conversion of positive ions into positive cluster ions, characterised by their rate coefficients: β , γ , α_d , α_d^c , α_i , and B , respectively. The values of these coefficients can be found in Glukhov et al. (1992) and Pasko and Inan (1994). The time evolution of each of the four constituents obeys its own continuity equation, which together form the following system of ordinary differential equations (Glukhov et al. 1992):

$$\frac{dN_e}{dt} = I + \gamma N^- - \beta N_e - \alpha_d N_e N^+ - \alpha_d^c N_e N_x^+ \quad (1a)$$

$$\frac{dN^-}{dt} = \beta N_e - \gamma N^- - \alpha_i N^- (N^+ + N_x^+) \quad (1b)$$

$$\frac{dN^+}{dt} = I - BN^+ - \alpha_d N_e N^+ - \alpha_i N^- N^+ \quad (1c)$$

$$\frac{dN_x^+}{dt} = -\alpha_d^c N_e N_x^+ + BN^+ - \alpha_i N^- N_x^+. \quad (1d)$$

Here I is the electron (and consequently positive ion) production term which can be expressed as $I = v_i N_e$, where v_i is the ionisation rate which is a function of the electric field

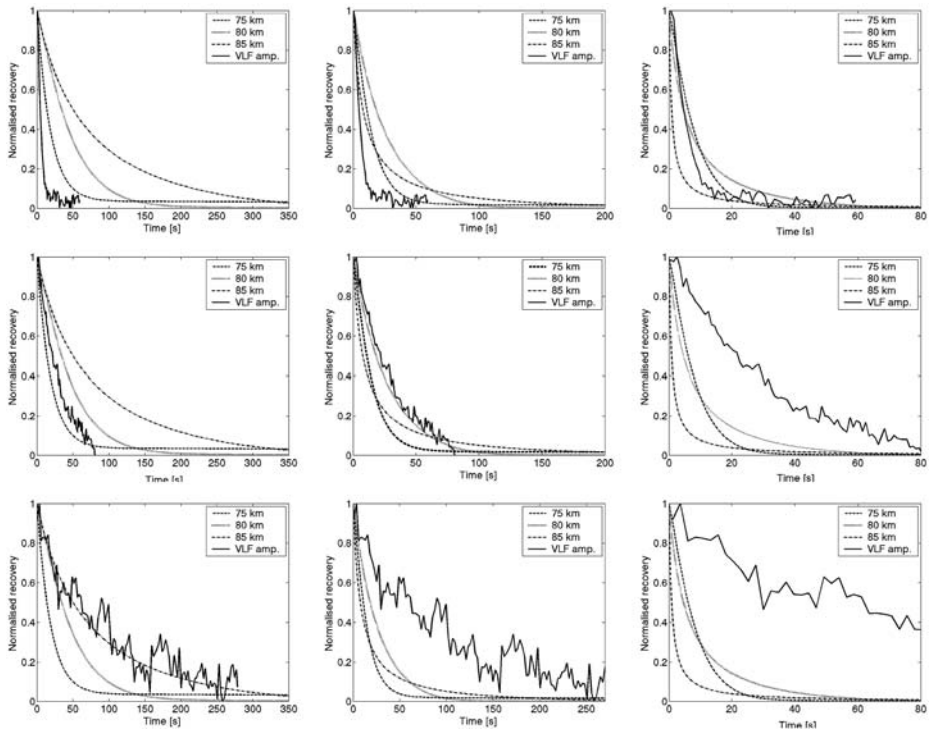


Fig. 9 Model fits of observed VLF perturbation recoveries. The left panels show recoveries from an initial electron density of $100 \times N_{e0}$, the middle ones from $1000 \times N_{e0}$, and the right panels from $10000 \times N_{e0}$. Each row corresponds to a different VLF event (solid line), representing short (top), medium (middle), and long (bottom) recovery durations for altitudes of 75 (dashed), 80 (dotted), and 85 km (dash-dotted)

(Papadopoulos et al. 1993). In order to model the relaxation of excess ionisation, the ordinary differential equation system (1) was solved numerically to produce the excess ionisation followed by the electron density relaxation. The ambient number densities of the four species, constituting the initial conditions for solving the equations, were extracted from their altitude profiles given in Glukhov et al. (1992). The model was set to produce different electron density enhancement levels N_e by manipulating the electric field properties (duration, peak amplitude) entering the electron and ion production term I . Then, by selecting values for the reaction rates corresponding to specific altitudes, it was possible to model the electron density relaxation at a given altitude.

Modelled electron density relaxation times were computed for altitudes of 75, 80, 85 km and initial electron densities of 100, 1000, and 10000 times the ambient values. The model results were then compared to observed VLF perturbation recoveries to provide some estimates on the electron density enhancements occurring during sprite events in the lower D region. Figure 9 shows three examples of early VLF events, representing short (~ 30 s), average (~ 100 s), and long (~ 250 s) recovery times. The modelled curves were superimposed on the measured early VLF amplitude recoveries, and normalised to their maximum values.

Early VLF events with short recoveries (< 50 s) could be modelled assuming regions of large electron density enhancements of up to about 10^4 times the ambient values confined at lower altitudes around 75 km. VLF perturbations with recovery times around 100 s could be reproduced by the model by considering electron density elevations around 80 km, hav-

ing an initial value about 10^3 times the undisturbed electron density levels. Finally, long recovery early VLF events (>200 s) could be accounted for by taking relatively low electron density enhancements ($\sim 10^2$ times the ambient values) to be located at upper D-region altitudes, at ~ 85 km. In the 75–85 km altitude range the key electron loss process governing the recoveries of the early VLF events is electron–ion recombination. Taking into account this and considering the dynamics of the sprite-producing QE fields a simple explanation can be put forward as follows. Strong and long-lasting QE fields are expected to exceed the breakdown threshold and produce large excess ionisation levels at upper D-region heights (say at ~ 75 km) without significantly affecting higher altitudes because of drastic conductivity shielding effects. In this case, an early VLF event will have a short recovery phase not only because electron attachment is still effective at lower heights but also, and possibly mainly, because the electron–ion recombination losses will be higher there since the produced electron densities are high. On the other hand, a weaker QE field can penetrate to higher altitudes near the VLF reflection height before exceeding the breakdown threshold and produce some, relatively weak, ionisation. This may also result in an early VLF perturbation which now, however, will last longer (recover slowly) because electron attachment in this region is small to negligible, and the main electron loss process, that is, electron–ion recombination, will be slow since it depends strongly on electron density ($\sim N_e^2$), which is now lower at these heights.

The results described herein indicate that electron density enhancements related to sprites can vary over two orders of magnitude and can be concentrated at a range of altitudes from about 75 to 85 km. This, in addition to the observed strong forward scattering, suggests that the early VLF perturbations observed on Crete in association with sprites relate to electron density enhancements corresponding to the upper diffuse sprite regions and/or associated halos in line with the findings of Barrington-Leigh et al. (2001) and Moore et al. (2003).

3.7 Elves and Early VLF Perturbations

Electromagnetic pulses released by lightning discharges into the lower ionosphere can lead to momentary optical emissions called elves (e.g., see reviews by Rowland 1998 and Rodger 1999). These phenomena appear at altitudes between 75 and 105 km as a rapidly expanding ring of luminosity reaching lateral extents of about 500 km. Elves are visible for less than 1 ms, which makes their detection from the ground rather difficult. They can be captured from space more easily due to the much lower atmospheric attenuation rates and unobstructed viewing conditions (Chern et al. 2003). Theoretical models predict that in addition to optical emissions, impact ionisation of N_2 can also be caused by an EMP at 80–95 km altitudes, leading to electron density enhancements from a few to a few tens of per cent (Taranenko 1993). Successive EMPs can cause a density increase of many hundreds of per cent of the ambient values (Taranenko et al. 1993; Rodger et al. 2001), affecting a large area of $\sim 3 \times 10^5 \text{ km}^2$ (Barrington-Leigh and Inan 1999). At lower altitudes, where electrons are only mildly heated, dissociative attachment to molecular oxygen dominates, leading to decreases in the electron density of several per cent (Inan et al. 1996; Sukhorukov et al. 1996). The anticipated electron density enhancements due to ionisation and the depletions caused by dissociative attachment lead to a sharpening of the electron density profile in the upper D region. At elve-altitudes this ionisation is expected to be lasting for a few to many minutes (e.g., Rodger et al. 2001; Rodger and McCormick 2004) and may affect VLF radio wave propagation inside the Earth-ionosphere waveguide (Taranenko 1993). For instance, the name ‘elves’ was orig-

inally introduced by Fukunishi et al. (1996) as an acronym for ‘Emissions of Light and VLF perturbations due to EMP Sources’, although there were no reports of accompanying VLF perturbations. In his review, Rodger (2003) pointed out that, despite the efforts, experimental evidence in favour of elve-related ionisation was still lacking. Recently, Mende et al. (2005) presented indirect evidence of electron density enhancements in relation to an elve event observed by the ISUAL (Imager of Sprites and Upper-Atmospheric Lightning) instrument onboard the Taiwanese FORMOSAT-2 satellite. They combined multi-wavelength photometric observations and theoretical model results and estimated the average electron density to be ~ 210 electrons cm^{-3} over a circular region with a diameter of ~ 165 km at ~ 90 km altitude having an assumed vertical extent of 10 km. A direct evidence of elve-related ionisation changes would be the detection of VLF perturbations occurring in association with elves. However, this topic has received little attention so far and the few published studies referring to the topic (Hobara et al. 2001; Hobara et al. 2003; Dowden et al. 1996c) did not provide proof of ionisation production in relation to elves.

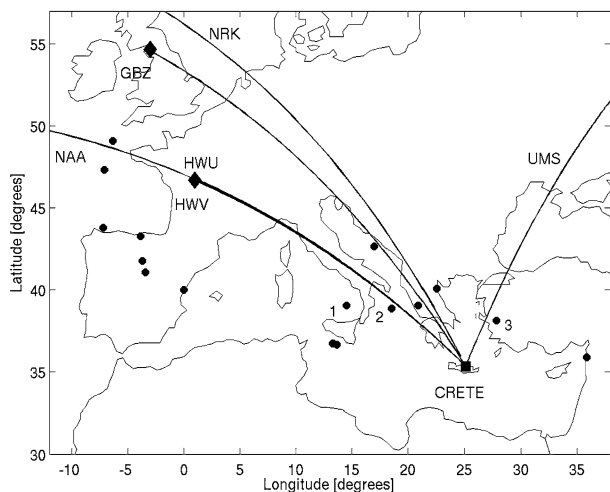
The study summarised herein and published in Mika et al. (2006) aimed at investigating the existence of elve-related VLF perturbations which would constitute direct evidence of electron density changes caused by the elve-generating lightning EMP. For this purpose, a large dataset comprising both ground- and space-based optical observations was used. Five elve events captured during the EuroSprite2003 campaign were analysed along with the largest dataset of elves used for VLF studies so far, collected by the ISUAL instrument of the FORMOSAT-2 satellite (Chern et al. 2003). VLF data for the elves observed over Europe were supplied by the Crete and Nançay receivers, while for those observed over North America data were obtained from various Stanford University VLF receivers located in the United States and Antarctica.

During the two month duration of the EuroSprite2003 campaign, six elves were captured by the optical cameras on Pic du Midi on the nights of 22–24 July 2003. The locations of the storms are shown in Fig. 1. VLF data were available for five events, from the Crete and Nançay receivers. The perturbation magnitudes varied from 0.15 to 0.4 dB and the onset durations were in the range of 20 ms–2 s, including both early/fast and early/slow type events, while the relaxation times were ~ 2 –3 min. The elve-producing discharges were all located at ~ 1950 km from the Crete receiver, at distances < 650 km from the TX–RX GCPs.

In order to get more insight into the nature of the relationship between elves and VLF perturbations, a large dataset of satellite-based elve observations was analysed in conjunction with VLF recordings. The dataset consisted of 18 elves observed over Europe between October 2004 and March 2005 and 282 captured over North America between July 2004 and July 2005 by the ISUAL payload of the Taiwanese FORMOSAT-2 satellite. Out of the 18 elves observed by ISUAL over Europe VLF data was available for 17 events from the Crete receiver. The GCPs of the transmitters monitored during this period to the Crete receiver are shown in Fig. 10 along with the locations of the elve-producing lighting discharges (marked by circles). Eight elves were situated at lateral distances less than ~ 300 km to the closest GCP, while the rest were located between ~ 550 and 1150 km. Six VLF perturbations were observed on multiple links in association with three elves (marked by numbered circles on Fig. 10) which were all located close (at < 500 km) to the GCPs. The distances to the Crete receiver were ~ 400 –950 km. All perturbations were of the early/fast type having onset durations of < 50 ms and magnitudes in the range of 0.2–0.7 dB.

All three early VLF perturbations seen in the HWV transmitter (18.3 kHz) signal had relaxation times of ~ 2 min. The VLF events identified in the higher frequency NAA (24.0 kHz) and NRK (37.5 kHz) signals had a slower relaxation which was eventually masked by other variations in the signal level. This suggests that the higher frequency waves,

Fig. 10 Locations of the elves observed by the ISUAL payload over Europe (*circles*) during the October 2004–March 2005 period, along with the GCPs from the VLF transmitters to the Crete receiver. The elves accompanied by VLF perturbations are marked by numbers. From Mika et al. (2006)



which reflect from higher electron densities and therefore can penetrate to higher altitudes, detected the upper, and thus longer-lived, regions of the EMP-induced ionisation perturbations.

As for the 282 elves observed by the ISUAL over North America, VLF data was supplied by eight receivers, four of them being part of the Stanford HAIL (Holographic Array for Ionospheric and Lightning research) network (Johnson et al. 1999): Cheyenne, Boulder, Parker, and Las Vegas, while the other four being the Taylor, Boston, Arecibo receiver sites and Palmer station in Antarctica. The VLF receiver specifications were identical to those of the Crete station (see Sect. 2). Amplitude and phase time series from the NPM (21.4 kHz, Lualualei, Hawaii), NAA (24.0 kHz, Cutler, Maine), NLK (24.8 kHz, Arlington, Washington), and NAU (40.75 kHz, Aguada, Puerto Rico) VLF transmitters were recorded daily from 01:00 to 13:00 UTC, except for Palmer station which was operating synoptically (recording for only 10 minutes out of every hour). VLF data was only available for 51 elves out of the 282, in most cases for multiple TX–RX combinations. 42 out of the 51 elves were situated at lateral distances less than 500 km from the nearest GCP, whereas the distances of the elves from the receivers were >2000 km, that is, much larger than those found previously for the European sector (<1200 km). The amplitude and phase time series were thoroughly analysed for each receiver–transmitter combination, but no perturbations were found to accompany the elves.

In summary, all five elves captured during EuroSprite2003 were accompanied by VLF perturbations seen in the HWV and GQD signals. Out of the 17 elves observed by ISUAL over Europe three were accompanied by early/fast VLF perturbations seen on multiple transmitter–receiver GCPs. In contrary, there were no VLF perturbations accompanying any of the 51 elves observed by ISUAL over North America, which, however, occurred at rather large distances from the receivers. The occasional existence of early VLF perturbations accompanying elves constitutes a clear proof of electron density changes caused by the elve-generating lightning EMP.

The observations summarised here showed for the first time that the ionisation changes caused by the lightning EMP can occasionally be detected via VLF remote sensing. However, the possibility of detection seems to be highly dependent on the observing geometry. It is interesting that no VLF perturbations were observed in relation to the numerous elves captured over North America. One possible reason can be that these events were located

at distances >2000 km from the receivers, while those observed over Europe were much closer. Theory and numerical calculations predict strong inter-modal scattering upon incidence on lower-ionospheric ionisation enhancements (e.g., see Nunn 1997). These modes can be attenuated over the long propagation distances to the receiver and thus the VLF perturbations can be masked by noise. Another reason can be the absence of ionisation during elves in cases when the EMP intensity is enough to excite optical emissions (the electron energy threshold is ~ 7.5 eV for the first positive band of N_2), but it is insufficient to produce ionisation due to the higher energies (15.6 eV for N_2) required for this process. This can be either due to the low intensity of the EMP or to high ambient electron densities. In the latter case, the electron mean free path is so short that the electric energy goes into excitation during the frequent collisions rather than ionisation which would require that the electrons attain higher energies by being accelerated by the electric field over larger distances.

4 Summary

The new contributions from the European VLF studies of TLE-related phenomena can be summarised as follows: 1) Sprites occurring close to a TX–RX GCP and also to the VLF transmitter are found to be nearly always accompanied by early VLF perturbations. This and more evidence from the observed recovery times of the perturbations are indicative of strong forward VLF scattering from a region of diffuse ionisation enhancement that develops during a sprite, generated by QE fields impacting on the upper D region above about 75 km. 2) Early VLF perturbations due to wide-angle VLF scattering (also backscatter) from conductive filamentary structures associated with the sprite discharges might also occur but are weak and infrequent relative to the strong forward scatter events. The VLF perturbations possibly due to backscatter were observed to accompany only about 5% of the sprites, a much smaller number than it is predicted by scattering theories. 3) Long-delayed sprites were observed to occur much more frequently than thought before, since about 30% of the sprites were delayed with respect to their causative +CG discharges by more than 30 ms up to 220 ms. Apparently, these sprites are caused by QE fields which build up slowly during long continuing currents and thus reach the levels needed for excitation and air-breakdown later compared to short-delayed sprites. 4) Sprite morphology appears to be affected by intracloud lightning. As evidenced by broadband VLF recordings and lightning detection measurements, carrot sprites are concurrent with bursts of sferics of intracloud origin, while such action is absent in column sprites. Moreover, carrot sprites seem to fall in the category of long-delayed sprites, while column sprites are on average short-delayed. This suggests that carrot sprites associate with IC discharge processes and long-lasting continuing currents, leading to electric fields which exceed the air breakdown thresholds for longer times. 5) A new category of early VLF perturbations in relation to sprites was discovered. These are characterised by a slow onset duration or growth. Their onset is nearly coincident with the sprite (early) but is followed by a slow growth lasting up to ~ 2.5 s. These events were named ‘early/slow’ in contrast to the well known ‘early/fast’ perturbations having short onset durations of about 50 ms or less. There is evidence suggesting that early/slow events are due to secondary ionisation build-up in the D region caused by subsequent intracloud discharges. 6) Lightning-induced electron density relaxation times were computed using a D-region model which accounts for charge exchanges between four types of charged particles and various electron loss mechanisms. Model results were fitted to early VLF event recoveries to infer estimates of electron density enhancements and their altitudes of occurrence. Early VLF perturbation recovery times from about 20 to more than 250 s could be

explained by assuming electron density increases of $\sim 10^2$ to 10^4 times the ambient values at altitudes between ~ 75 and 85 km. 7) Elves, which are theoretically understood in terms of molecular excitation produced by strong EMPs impacting on the upper D region—lower E region of the ionosphere, are sometimes accompanied by early VLF perturbations similar to those seen with sprites. This implies the presence of ionisation production during elves providing experimental proof corroborating EMP theories.

Acknowledgement Ágnes Mika would like to acknowledge the support provided by ISSI and EuroPlanet for her participation at the Planetary Atmospheric Electricity workshop held in Bern in July 2007 and also the European Union RTN fellowship programme (contract nr. HPRN-CT-2002-00216) which made the studies presented in the paper possible. The authors express their gratitude to their collaborators: Umran S. Inan, Torsten Neubert, Robert A. Marshall, Oscar A. van der Velde, René J. Steiner, and all the RTN-CAL project young scientists who donated a lot of their time to operating the instruments during the EuroSprite campaigns. In particular we wish to thank Umran S. Inan for providing the Crete VLF receiver and for his continuous encouragement, guidance and support during the entire period of these studies.

References

- G. Bainbridge, U.S. Inan, Ionospheric d region electron density profiles derived from the measured interference pattern of VLF waveguide modes. *Radio Sci.* **38**(4), 1077 (2003)
- C.P. Barrington-Leigh, U.S. Inan, Elves triggered by positive and negative lightning discharges. *Geophys. Res. Lett.* **26**, 683–686 (1999)
- C.P. Barrington-Leigh, U.S. Inan, M. Stanley, Identification of sprites and elves with intensified video and broadband array photometry. *J. Geophys. Res.* **106**(A2), 1741–1750 (2001)
- T.F. Bell, S.C. Reising, U.S. Inan, Intense continuing currents following positive cloud-to-ground lightning associated with red sprites. *Geophys. Res. Lett.* **25**(8), 1285–1288 (1998)
- J.L. Chern, R.R. Hsu, H.T. Su, S.B. Mende, H. Fukunishi, Y. Takahashi, L.C. Lee, Global survey of upper atmospheric transient luminous events on the ROCSAT-2 satellite. *J. Atmos. Sol.-Terr. Phys.* **65**, 647–659 (2003)
- S.A. Cummer, M. Füllekrug, Unusually intense continuing current in lightning produces delayed mesospheric breakdown. *Geophys. Res. Lett.* **28**(3), 495–498 (2001)
- R.L. Dowden, J.B. Brundell, W.A. Lyons, Are VLF rapid onset, rapid decay perturbations produced by scattering off sprite plasma? *J. Geophys. Res.* **101**(D14), 19175–19183 (1996a)
- R.L. Dowden, J.B. Brundell, W.A. Lyons, T. Nelson, Detection and location of red sprites by VLF scattering of subionospheric transmissions. *Geophys. Res. Lett.* **23**(14), 1737–1740 (1996b)
- R.L. Dowden, J. Brundell, C. Rodger, O. Mochanov, W. Lyons, T. Nelson, The Structure of Red Sprites Determined by VLF Scattering. *IEEE Antennas Propag. Mag.* **38**(3), 7–15 (1996c)
- H. Fukunishi, Y. Takahashi, M. Kubota, K. Sakanoi, U.S. Inan, W.A. Lyons, Elves: Lightning-induced transient luminous events in the lower ionosphere. *Geophys. Res. Lett.* **23**, 2157–2160 (1996)
- V.S. Glukhov, V.P. Pasko, U.S. Inan, Relaxation of transient lower ionospheric disturbances caused by lightning-whistler-induced electron precipitation bursts. *J. Geophys. Res.* **97**(A11), 16971–16979 (1992)
- C. Haldoupis, T. Neubert, U.S. Inan, A. Mika, T.H. Allin, R.A. Marshall, Subionospheric early VLF signal perturbations observed in one-to-one association with sprites. *J. Geophys. Res.* **109**, A10303 (2004)
- C. Haldoupis, R.J. Steiner, Á. Mika, S. Shalimov, R.A. Marshall, U.S. Inan, T. Bösinger, T. Neubert, “early/slow” events: A new category of VLF perturbations observed in association with sprites. *J. Geophys. Res.* **111**, A11321 (2006)
- S.F. Hardman, C.J. Rodger, R.L. Dowden, J.B. Brundell, Measurements of the VLF scattering pattern of the structured plasma of red sprites. *IEEE Antennas Propag. Mag.* **40**(2), 29–35 (1998)
- Y. Hobara, N. Iwasaki, T. Hayashida, M. Hayakawa, K. Ohta, H. Fukunishi, Interrelation between ELF transients and ionospheric disturbances in association with sprites and elves. *Geophys. Res. Lett.* **28**, 935–938 (2001)
- Y. Hobara, M. Hayakawa, K. Ohta, H. Fukunishi, Lightning discharges in association with mesospheric optical phenomena in Japan and their effect on the lower ionosphere. *Adv. Polar Upper Atmos. Res.* **17**, 30–47 (2003)
- U.S. Inan, J.V. Rodriguez, V.P. Idone, VLF signatures of lightning-induced heating and ionization of the nighttime D region. *Geophys. Res. Lett.* **20**, 2355–2358 (1993)

- U.S. Inan, T.F. Bell, V.P. Pasko, D.D. Sentman, E.M. Wescott, W.A. Lyons, VLF signatures of ionospheric disturbances associated with sprites. *Geophys. Res. Lett.* **22**(24), 3461–3464 (1995)
- U.S. Inan, W.A. Sampson, Y.N. Taranenko, Space-time structure of optical flashes and ionization changes produced by lightning-EMP. *Geophys. Res. Lett.* **23**, 133–136 (1996)
- M.P. Johnson, U.S. Inan, Sferic clusters associated with Early/Fast VLF Events. *Geophys. Res. Lett.* **27**, 1391 (2000)
- M.P. Johnson, U.S. Inan, S.J. Lev-Tov, T.F. Bell, Scattering pattern of lightning-induced ionospheric disturbances associated with early/fast VLF events. *Geophys. Res. Lett.* **26**(15), 2363–2366 (1999)
- R.A. Marshall, U.S. Inan, W.A. Lyons, On the association of early/fast very low frequency perturbations with sprites and rare examples of vlf backscatter. *J. Geophys. Res.* **111**, D19108 (2006)
- V. Mazur, X.-M. Shao, P.R. Krehbiel, “Spider” lightning in intracloud and positive cloud-to-ground flashes. *J. Geophys. Res.* **103**(D16), 19811–19822 (1998)
- M.G. McHarg, H.C. Stenbaek-Nielsen, T. Kammae, Observations of streamer formation in sprites. *Geophys. Res. Lett.* **34**, L06804 (2007)
- S.B. Mende, H.U. Frey, R.R. Hsu, H.T. Su, A.B. Chen, L.C. Lee, D.D. Sentman, Y. Takahashi, H. Fukunishi, D region ionization by lightning-induced electromagnetic pulses. *J. Geophys. Res.* **110**, A11312 (2005)
- Á. Mika, C. Haldoupis, R.A. Marshall, T. Neubert, U.S. Inan, Subionospheric VLF signatures and their association with sprites observed during EuroSprite-2003. *J. Atmos. Sol.-Terr. Phys.* **67**, 1580–1597 (2005)
- Á. Mika, C. Haldoupis, T. Neubert, H.T. Su, R.R. Hsu, R.J. Steiner, R.A. Marshall, Early VLF perturbations observed in association with elves. *Ann. Geophys.* **24**, 2179–2189 (2006)
- R.C. Moore, C.P. Barrington-Leigh, U.S. Inan, T.F. Bell, Early/fast VLF events produced by electron density changes associated with sprite halos. *J. Geophys. Res.* **108**(A10), 1363 (2003)
- T. Neubert, T.H. Allin, E. Blanc, T. Farges, C. Haldoupis, Á. Mika, S. Soula, L. Knutsson, O. van der Velde, R.A. Marshall, U. Inan, G. Sátori, J. Bór, A. Hughes, A. Collier, S. Laursen, I.L. Rasmussen, Coordinated observations of transient luminous events during the EuroSprite2003 campaign. *J. Atmos. Sol.-Terr. Phys.* **67**(3), 807–820 (2005)
- D. Nunn, On the numerical modelling of the vlf trimp effect. *J. Atmos. Sol.-Terr. Phys.* **59**(5), 537–560 (1997)
- A. Ohkubo, H. Fukunishi, Y. Takahashi, T. Adachi, VLF/ELF sferic evidence for in-cloud discharge activity producing sprites. *Geophys. Res. Lett.* **32**, L04812 (2005)
- K. Papadopoulos, G. Milikh, A. Gurevich, A. Drobot, R. Shanny, Ionization rates for atmospheric and ionospheric breakdown. *J. Geophys. Res.* **98**(A10), 17591–17596 (1993)
- V.P. Pasko, U.S. Inan, Recovery signatures of lightning-associated VLF perturbations as a measure of the lower ionosphere. *J. Geophys. Res.* **99**(A9), 17523–17537 (1994)
- S.C. Reising, U.S. Inan, T.F. Bell, ELF sferic energy as a proxy indicator for sprite occurrence. *Geophys. Res. Lett.* **26**(7), 987–990 (1999)
- C.J. Rodger, Red sprites, upward lightning, and VLF perturbations. *Rev. Geophys.* **37**, 317–336 (1999)
- C.J. Rodger, Subionospheric VLF perturbations associated with lightning discharges. *J. Atmos. Sol.-Terr. Phys.* **65**, 591–606 (2003)
- C.J. Rodger, R.J. McCormick, Remote sensing of the upper atmosphere by VLF. NATO Advanced Study Institute on ‘Sprites, Elves and Intense Lightning Discharges’ in Corte, Corsica, July 24–31, 2004
- C.J. Rodger, J.R. Wait, R.L. Dowden, N.R. Thomson, Radiating conducting columns inside the Earth-ionosphere waveguide: Application to red sprites. *J. Atmos. Sol.-Terr. Phys.* **60**, 1193–1204 (1998a)
- C.J. Rodger, J.R. Wait, R.L. Dowden, VLF scattering from red sprites – theory. *J. Atmos. Sol.-Terr. Phys.* **60**, 755–763 (1998b)
- C.J. Rodger, N.R. Thomson, J.R. Wait, VLF scattering from red sprites: vertical columns of ionisation in the Earth-ionosphere waveguide. *Radio Sci.* **34**(4), 913–921 (1999)
- C.J. Rodger, M. Cho, M.A. Clilverd, M.J. Rycroft, Lower ionospheric modification by lightning-EMP: Simulation of the night ionosphere over the United States. *Geophys. Res. Lett.* **28**, 199–202 (2001)
- R.A. Roussel-Dupré, E. Blanc, HF echoes from ionization potentially produced by hight-altitude discharges. *J. Geophys. Res.* **102**(A3), 4613–4622 (1997)
- H.L. Rowland, Theories and simulations of elves, sprites and blue jets. *J. Atmos. Sol.-Terr. Phys.* **60**, 831–844 (1998)
- M.J. Rycroft, M. Cho, Modelling electric and magnetic fields due to thunderclouds and lightning from cloud-tops to the ionosphere. *J. Atmos. Sol.-Terr. Phys.* **60**, 889–893 (1998)
- M.A. Stanley, Sprites and their parent discharges. Ph.D. thesis, New Mexico Institute of Mining and Technology, 2000
- H.J. Strangeways, Lightning, trimpis, and sprites. *Review of Radio Science 1993–1996*, 1996, pp. 741–780
- A.I. Sukhorukov, E.A. Rudenchik, P. Stubbe, Simulation of the strong lightning pulse penetration into the lower ionosphere. *Geophys. Res. Lett.* **23**, 2911–2914 (1996)

- Y.N. Tarantenko, Interaction with the lower ionosphere of electromagnetic pulses from lightning: heating, attachment, ionization, and optical emissions. Ph.D. thesis, Stanford University, 1993
- Y.N. Tarantenko, U.S. Inan, T.F. Bell, Interaction with the lower ionosphere of electromagnetic pulses from lightning: heating, attachment, and ionization. *Geophys. Res. Lett.* **20**, 1539–1542 (1993)
- M.A. Uman, *The Lightning Discharge* (Dover, New York, 2001)
- J.A. Valdivia, G. Milikh, K. Papadopoulos, Red sprites: Lightning as a fractal antenna. *Geophys. Res. Lett.* **24**(24), 3169–3172 (1997)
- O.A. van der Velde, Á. Mika, S. Soula, C. Haldoupis, T. Neubert, U.S. Inan, Observations of the relationship between sprite morphology and in-cloud lightning processes. *J. Geophys. Res.* **111**, D15203 (2006)

DEMETER Observations of EM Emissions Related to Thunderstorms

M. Parrot · J.J. Berthelier · J.P. Lebreton ·
R. Treumann · J.L. Rauch

Originally published in the journal Space Science Reviews, Volume 137, Nos 1–4.
DOI: [10.1007/s11214-008-9347-y](https://doi.org/10.1007/s11214-008-9347-y) © Springer Science+Business Media B.V. 2008

Abstract The paper is related to specific emissions at frequency <3 MHz observed by the low altitude satellite DEMETER in relation with the thunderstorm activity. At its altitude (~ 700 km), the phenomena observed on the E-field and B-field spectrograms recorded by the satellite are mainly dominated by whistlers. Particular observations performed by DEMETER are reported. It concerns multiple hop whistlers and interaction between whistlers and lower hybrid noise. Two new phenomena discovered by the satellite are discussed. First, V-shaped emissions up to 20 kHz are observed at mid-latitude during night time. They are centered at the locations of intense thunderstorm activity. By comparison with VLF saucers previously observed by other satellites in the auroral zones it is hypothesized that the source region is located below the satellite and that the triggering mechanism is due to energetic electrons accelerated during sprite events. Second, emissions at frequency

M. Parrot (✉) · J.L. Rauch
LPCE/CNRS, 3A Avenue de la Recherche, 45071 Orléans cedex 2, France
e-mail: mparrot@cnrs-orleans.fr

J.J. Berthelier
CETP, Observatoire de Saint Maur, 4 Avenue de Neptune, 94107 Saint Maur des Fossés cedex, France
e-mail: jean-jacques.berthelier@cftp.ipsl.fr

J.P. Lebreton
Research and Scientific Support Department, ESA/ESTEC, Noordwijk, The Netherlands
e-mail: Jean-Pierre.Lebreton@esa.int

R. Treumann
Geophysics Section, Department of Geophysics and Environmental Sciences, Munich University,
Theresienstr. 41, 80333 Munich, Germany
e-mail: rudolf.treumann@geophysik.uni-muenchen.de

R. Treumann
International Space Science Institute, Hallerstr. 6, 3012 Bern, Switzerland
e-mail: treumann@issibern.ch

R. Treumann
e-mail: treumannr@gmail.com

~2 MHz are observed at the time of intense whistlers. These emissions are produced in the lower ionosphere in probable relation with Transient Luminous Events (TLEs).

Keywords Lightning · Ionosphere · VLF and HF emissions: whistlers

1 Introduction

DEMETER is a satellite devoted to the study of ionospheric perturbations in relation with the seismic and anthropogenic activities. Its payload consists of wave and particle analysers. Concerning the wave experiment the main phenomena observed by DEMETER are whistlers. They are observed mainly during night time at low and mid latitudes. Since the pioneering work of Storey (1953) a multitude of papers have been published dealing with the generation, propagation, and the effect of such ionospheric and magnetospheric waves. To only quote DEMETER results:

- Inan et al. (2007) have reported short bursts of lightning induced electron precipitation (LEP) simultaneously with upgoing whistlers. The LEP bursts are seen within <1 s of the causative lightning and consist of 100–300 keV electrons.
- Ferencz et al. (2007) observed whistlers with a specific signal structure of numerous fractional-hop whistlers, which they called “Spiky Whistler” (SpW). These signals appear to be composed of a conventional whistler combined by the compound mode-patterns of guided wave propagation, suggesting a whistler has been excited by a lightning “tweek” spheric.
- Chum et al. (2006) studied the penetration of lightning induced whistler waves through the ionosphere by computing all the possible differences between the times when the whistlers were observed on the satellite and times when the lightning discharges were detected by an European network. They demonstrated that the width of the area in the ionosphere through which the ElectroMagnetic (EM) energy induced by a lightning discharge enters into the magnetosphere as whistler mode waves amounts up to several thousands kilometres.

In the past years, the interest in thunderstorm activity has been boosted by the discovery of Transient Luminous Events (TLEs) occurring between the top of the thunderstorm clouds and the lower ionosphere (see for example Fulkekrug et al. 2006 and references therein). DEMETER does not carry any optical experiments but some electromagnetic waves that have been recorded onboard the spacecraft could be related to EM signatures of TLEs.

Section 2 briefly describes the wave experiment which is a part of the DEMETER’s scientific payload. Specific phenomena observed by DEMETER will be presented and discussed in Sect. 3. Some conclusions will be given in Sect. 4.

2 The DEMETER Project

DEMETER is a low-altitude (700 km) satellite with a polar and circular orbit. It measures EM waves over the Earth with the exception of the auroral zones (Cussac et al. 2006). The frequency range for the electric field is from DC up to 3.5 MHz, and for the magnetic field from a few Hz up to 20 kHz. The instruments are operated in two scientific modes: a survey mode where spectra of one electric and one magnetic component are computed onboard up to 20 kHz and a burst mode where waveforms of one electric field component and one

magnetic field component are recorded up to 20 kHz. The burst mode allows performing a spectral analysis with higher time and frequency resolution. In the frequency range up to 3.5 MHz, the same electric component is used as in the Very Low Frequency (VLF) range. The signals are sampled at 6.66 MHz and digitized with 8 bits. The LF data acquisition is performed on 40 data snapshots each 0.6144 ms long and evenly spaced in the 2.048 s elementary interval of the VLF channel acquisition. Individual power spectra are calculated for each snapshot with a frequency resolution of 3.25 kHz and averaged to provide a power spectrum every 2.048 s. In burst modes, the averaged power spectrum and waveform data for a single 0.6144 ms interval are available. Through a telecommand order, the selected waveform interval can be either the first of the 40 intervals or the one with the maximum total power over the entire bandwidth. In survey modes, the power spectra are the only information available. Details of the wave experiment can be found in Parrot et al. (2006) and Berthelier et al. (2006a, 2006b).

3 Phenomena Recorded by DEMETER

Two common events which had already been observed on previous satellites as multiple hop whistlers or interaction with lower hybrid noise will be described here. These classical examples have been chosen because their characteristics are particularly pronounced.

3.1 Multiple Hop Whistlers

Figure 1 shows a spectrogram of VLF electric field data recorded by DEMETER on November 27, 2004 between 10:58:32 and 11:00:30 UT. The frequency range is from 0 up to 20 kHz, and the power spectral density is color-coded according to the scale on the right. The parameters below the spectrogram indicate Universal Time (UT), Local Time (LT), geographic latitude and longitude, and the McIlwain parameter L . The continuous and dashed horizontal lines in Fig. 1 are due to traces from VLF ground-based transmitters whereas the vertical lines are due to the lightning activity. At the time of a lightning in the atmosphere a pulse named sferic is emitted in a wide frequency band. This pulse can be observed directly by the satellite. It propagates into the magnetosphere following a magnetic field line, can be reflected in the opposite hemisphere, and may return (Storey 1953). During the propagation, a frequency dispersion is observed and the wave is called whistler. The sferic can also propagate in the Earth-ionospheric wave guide and a part can leak out of the ionosphere and become observable by a satellite. This is the reason why so many vertical lines are observed on the Fig. 1. At 10:58:37 UT a sferic was generated that produces multiple hop whistlers. Up to 17 whistlers can be identified with at each time a change in their frequency dispersion. Their frequency band lies between 1 and 5 kHz in the beginning and decreases regularly with the time. The elements are separated by ~ 3 s which is the typical time for a wave to bounce back and forth in the magnetosphere. These ducted whistlers are observed during ~ 75 seconds which means that the dimension of the duct is of the order of 520 km. Such duct thickness has been already observed in the past (Strangeways 1999). Another particularity of this event is that, at least initially, the whistlers are twofold, meaning that the sferic took two different paths to leave the ionosphere. When it returns to the original hemisphere two whistlers are detected by the satellite (see Fig. 1 of Smith and Carpenter 1982). Another possibility is that there might have been two distinct lightning discharges producing the two-fold structure but only one relatively strong fraction hop whistler is observed immediately before the whistler train.

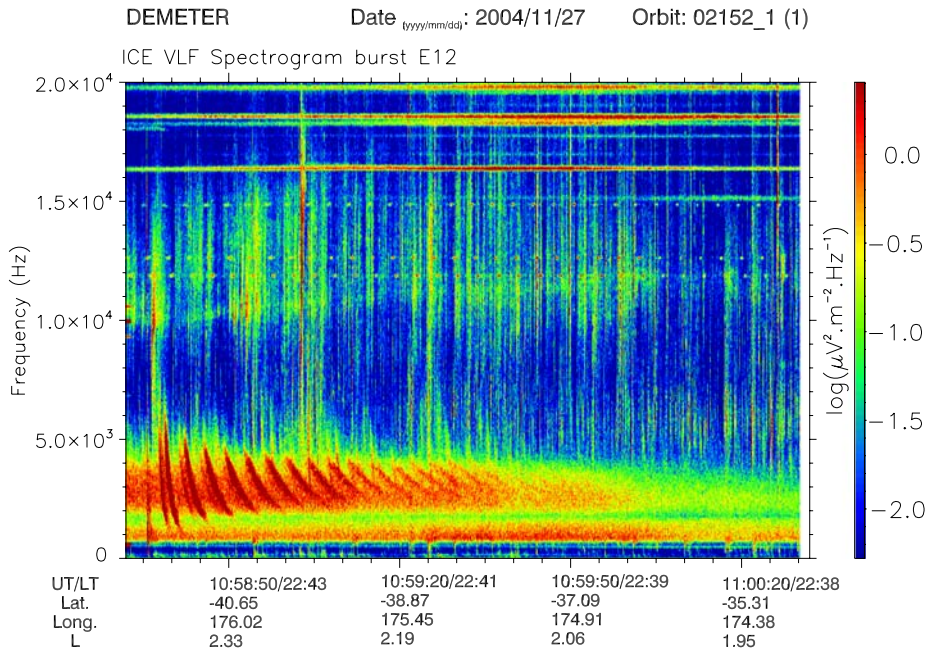


Fig. 1 A multiple hop whistler observed by DEMETER on a VLF night time spectrogram of an electric component recorded on November 27, 2004 between 10:58:32 and 11:00:30 UT during a burst mode. The frequency range is between 0 and 20 kHz

3.2 Strong Interaction with LH Noise

Figure 2 displays a VLF E-field spectrogram that is similar to Fig. 1 recorded on February 17, 2006 between 10:35:32 and 10:37:30 UT. In the lower part of the figure one distinguishes whistlers. The dispersions of the whistlers are almost identical corresponding to 0⁺ whistlers just leaving the ionosphere. Following the classification given by Smith and Angerami (1968), 0⁺ whistler is a whistler that propagates to the satellites without crossing the magnetic equator. But the most important part of the figure is related to the Lower Hybrid (LH) noise. This noise was first observed in the sixties by the Canadian satellite Alouette 1 (Brice and Smith 1964, 1965). Its updated characteristics can be found in Shklyar and Washimi (1994) and Morioka et al. (2005) and references therein. The LH frequency is clearly seen on the figure: at 10:35:32 UT this frequency is roughly equal to 14 kHz and decreases slowly with time (12 kHz at 10:37:30 UT). The noise above the LH frequency is enhanced when it interacts with spherics and whistlers (Brice and Smith 1964, 1965). It is the source of particularly intense emissions lasting several seconds after each whistlers. The generation mechanism of these emissions has been discussed by Lee and Kuo (1984). They showed that intense whistlers are able to excite LH waves and field-aligned density striations in the ionosphere within a few seconds. LH noise observed during rocket experiment was also discussed by Baker et al. (2000). During a magnetic storm, Berthelier et al. (2008) reported another LH event when DEMETER was crossing a plasma bubble. They have shown strong LH turbulence triggered by EM whistlers originating from thunderstorm lightnings in the atmosphere beneath the satellite in association with small-scale plasma density irregularities.

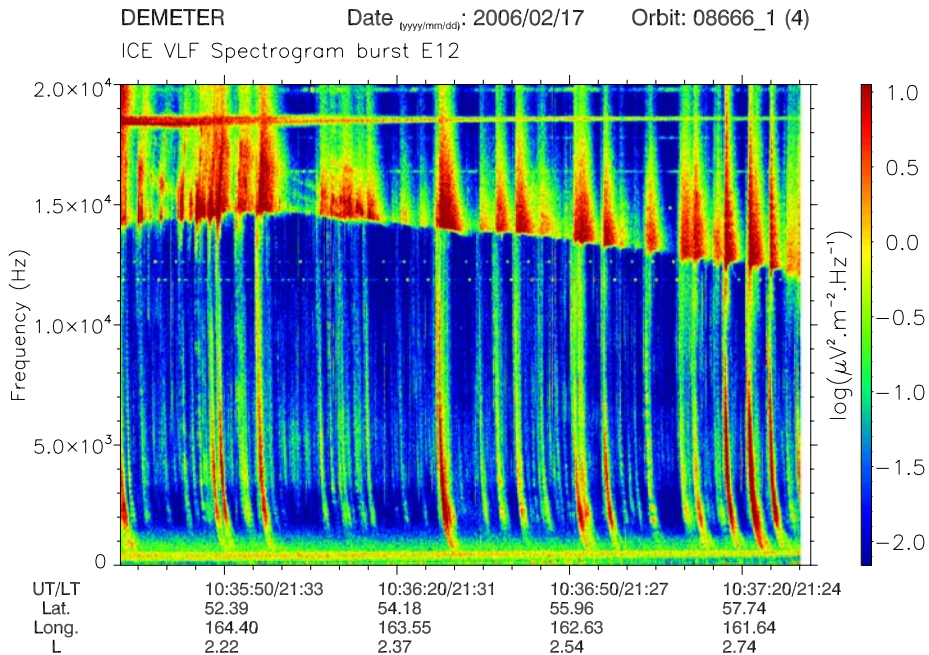


Fig. 2 A two-minute spectrogram similar to Fig. 1 recorded on February 17, 2006. It shows a strong interaction between whistlers, and the related LH noise

Although other past satellites have covered the same near Earth environment, new events associated with thunderstorm activity have been found by DEMETER in the frequency range up to 3 MHz.

3.3 Burst of Lightning Associated with V-shaped Emissions

Figure 3 shows a VLF spectrogram of the electric field recorded on September 13, 2005 between 17:25:00 and 17:33:00 UT. Many whistlers occur during these 8 minutes. Around 17:28:30 UT their number and their intensity reach a maximum, which probably indicates that the satellite is just above the thunderstorm region. In addition to the whistlers many V-shaped emissions centred on this location can be observed. On each side of this region many arms with different slopes are seen. This is not a single event and many examples of such emissions were registered by DEMETER during night time. During three years, 87 events with V-shaped emissions associated with intense and numerous whistlers in VLF range have been observed. In the past these hyperbolic shapes in the frequency-time spectrogram had been observed solely in the auroral zones by Smith (1969), Mosier and Gurnett (1969), and James (1976). It is the first time here that they are reported in association with thunderstorm activity at mid-latitudes. Such V-shaped emissions can be perhaps explained by analogy with the emissions observed solely in the auroral zones. Studies of Poynting flux indicate that the auroral emissions (also called VLF saucers) are due to whistler mode waves originating below the satellite (Mosier 1971). More recently, similar events were observed by VIKING (Lonnqvist et al. 1993) and FAST (Ergun et al. 2001, 2003). FAST observations have shown that electrons (>10 eV) provide the energy source of such VLF saucers. The electron beams are accelerated by a magnetic field-aligned electric field. On DEMETER the particle experiment cannot detect these electrons for two reasons: the lower band

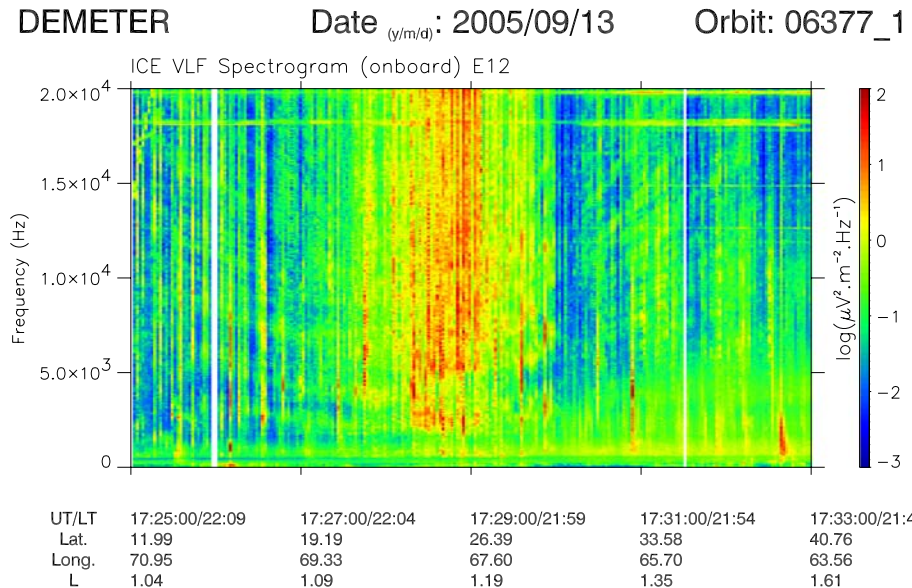


Fig. 3 Onboard computed spectrogram of an electric component recorded on September 13, 2005 between 17:25:00 UT and 17:33:00 UT showing an intense thunderstorm activity. The power spectral density is color-coded according to the scale on the right. The parameters below the spectrogram indicate Universal Time (UT), Local Time (LT), geographic latitude and longitude, and the McIlwain parameter L. Between the two white vertical lines the data is recorded in the burst mode

of the energy (70 keV) is too high and the pitch angle of detected particles is close to 90° (Sauvaud et al. 2006). Furthermore DEMETER does not detect variations of the DC electric field at the altitude of the observations. But it is hypothesized that such electrons can be the source of the emissions also in case of the thunderstorm activity because they have been observed. Energetic electrons (~ 1 keV) moving upward were measured by the DE 2 satellite in association with a lightning strike situated in a hurricane (Burke et al. 1992). Their analysis suggests that these electrons were accelerated by a parallel electric field of ~ 1 mV/m. During occurrences of sprites, Kuo et al. (2005) have found electrons with energies in the range of 4.5–9.2 eV and electric fields of strength between 2.1 and 3.7 times the breakdown E-field at these altitudes. The presence of sprites during the event shown in Fig. 3 cannot be ruled out because the thunderstorm activity was particularly intense. During one of such large thunderstorms occurring above South Poland on July 20, 2007 around 20.10 UT, a sprite has been observed from the ground (J. Blecki, personal communication, 2008). In this case, a mechanism similar to the one in the auroral zone could well be a viable mechanism producing these V-shaped emissions at mid-latitudes as well. The different slopes of the branches of the emissions can be explained by sources located at different altitudes below the satellite. However it must be noticed that the time scale of the V-shaped emissions related to thunderstorm activity is much more important than for the VLF saucers observed in the auroral zones. The thunderstorm and then the source region of these V-shaped emissions has a dimension which is no more than a few tens kilometres. This could be assimilated to a single point and the wave emission could be then similar to the emission of a ground-based VLF transmitter in the Earth-ionosphere guide but at several frequencies. A map of the wave intensity measured by a satellite above a VLF transmitter shows concentric circles with alternately enhanced and decreased intensities (Molchanov et al. 2006;

Clilverd et al. 2008). This could also explain our observations. Other discussion about the generation mechanism can be found in Treumann et al. (2008).

3.4 Emissions in the Frequency Range up to 3 MHz Related to Some Powerful Lightning

Figure 4 is related to an event recorded on August 14, 2005 during one minute when the acquisition system was in burst mode. The top panel shows the onboard computed spectrogram of an electric component between 0 and 3 MHz. The middle panel represents the VLF spectrogram of the same component between 0 and 20 kHz, and the bottom panel displays the VLF spectrogram of a magnetic component between 0 and 2 kHz. These two last spectrograms have been computed from the full resolution data of the experiment. At \sim 04:00:30 UT one observes an increase in the top spectrogram around 2 MHz. This corresponds to the time of an intense whistler in the middle and bottom panels (note that the apparent time broadening of the emission is due to the low resolution time of the spectrogram in this frequency range). During two years, DEMETER has found 130 similar events at night time. They always correspond to intense whistlers, but few of the intense whistlers

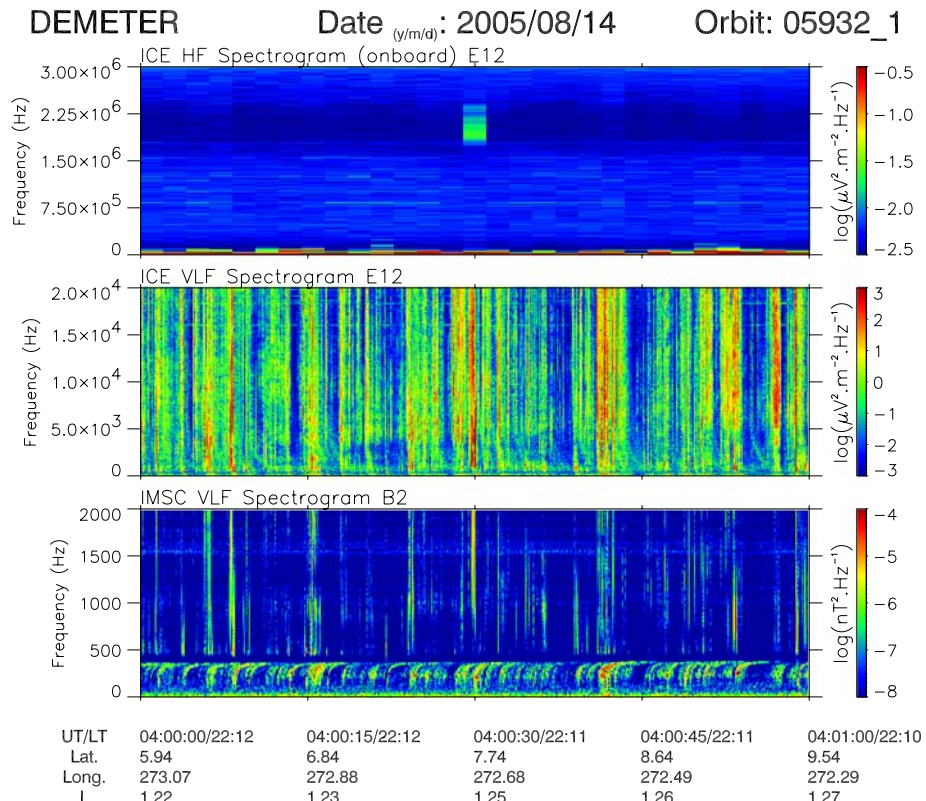
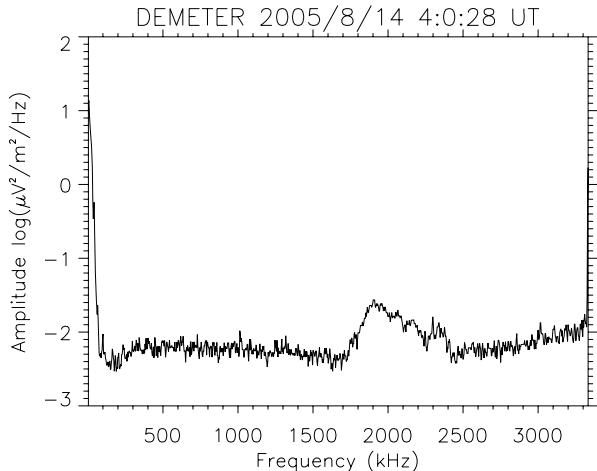


Fig. 4 Spectrograms recorded by DEMETER on August 14, 2005 during one minute. It concerns: *Top*: electric component in the HF range up to 3 MHz. *Middle*: the same component in the VLF range up to 20 kHz. *Bottom*: a magnetic component up to 2 kHz. In this last spectrogram some interference lines alter the data above 1 kHz. The parameters below the spectrograms indicate Universal Time (UT), Local Time (LT), geographic latitude and longitude, and the McIlwain parameter L . The VLF spectrograms are dominated by whistlers. Proton whistlers can be also seen in the bottom panel below \sim 400 Hz

Fig. 5 Single HF spectrum at the time of the increase in the top panel of Fig. 4



produce such emissions. In the past similar emissions had already been observed but at much higher frequencies (several tens of MHz) by the satellite FORTE (Holden et al. 1995; Jacobson et al. 1999). Their generation mechanism must be different from the emissions observed by DEMETER. At ionospheric altitudes, Kelley et al. (1997) reported another observation of an EM pulse in connection with a lightning. This occurs at a frequency below than 2 MHz. A single spectrum at the time of the increase in Fig. 4 is shown in Fig. 5. It can be seen that this emission is between 1.7 and 2.4 MHz. The local electron gyrofrequency was 0.7 MHz, the local plasma frequency determined by the Langmuir probe (Lebreton et al. 2006) was 0.98 MHz, yielding a local upper hybrid frequency of 1.21 MHz. Clearly these local frequencies do not correspond to the frequency band of the increase seen in Fig. 5. The source of this emission must therefore lie below the satellite and could correspond to a TLE. Possible generation mechanisms are discussed by Treumann et al. (2008). Simulations have shown that runaway electrons can initiate high-altitude discharges and then afterwards can produce emissions at high frequencies (Roussel-Dupré et al. 1998). Normally if an emission at ~ 2 MHz occurs at the altitude of a TLE (40–80 km) it will be reflected at the level of the F-layer where the plasma frequency is much higher. In this particular case, the emission will only cross the ionosphere if plasma density irregularities are induced by intense lightning or by the TLE. Radars have already observed field-aligned plasma density striations, also called explosive spread F, resulting from lightning-induced EM effects (Liao et al. 1989; Lonnqvist et al. 1993). Therefore it can be considered that an emission at high frequencies produced in the lower ionosphere could be observed at the DEMETER altitudes during thunderstorm activity.

4 Conclusion

The ionospheric satellite DEMETER has recorded a number of emissions in relation with the thunderstorm activity. Noteworthy events have been presented in this paper. They underline the importance of the LH noise and they provide evidence of strong coupling between the thunderstorm activity and the ionosphere. Further work will be necessary to fully understand the new phenomena discovered by DEMETER and their possible relation with TLE. For example all events at high frequencies recorded by DEMETER will be globally studied and it will be the subject of a future paper.

Acknowledgement The authors thank CNES people involved in the mission development of the DEMETER satellite and those currently in charge of the operations in Toulouse.

References

- S.D. Baker, M.C. Kelley, C.M. Swenson, J. Bonnell, D.V. Hahn, J. Atmos. Sol. Terr. Phys. **62**, 1393 (2000). doi:[10.1016/S1364-6826\(00\)00127-9](https://doi.org/10.1016/S1364-6826(00)00127-9)
- J.J. Berthelier et al., Planet. Space Sci. **54**, 456 (2006a). doi:[10.1016/j.pss.2005.10.016](https://doi.org/10.1016/j.pss.2005.10.016)
- J.J. Berthelier et al., Planet. Space Sci. **54**, 487 (2006b). doi:[10.1016/j.pss.2005.10.018](https://doi.org/10.1016/j.pss.2005.10.018)
- J.J. Berthelier, M. Malingre, R. Pfaff et al., Nature Geosci. **1**, 101 (2008). doi:[10.1038/ngeo109](https://doi.org/10.1038/ngeo109)
- N.M. Brice, R.L. Smith, Nature **203**, 926 (1964)
- N.M. Brice, R.L. Smith, J. Geophys. Res. **70**, 71 (1965). doi:[10.1029/JZ070i001p00071](https://doi.org/10.1029/JZ070i001p00071)
- W.J. Burke, T.L. Aggson, N.C. Maynard et al., J. Geophys. Res. **97**(A5), 6359 (1992). doi:[10.1029/92JA00305](https://doi.org/10.1029/92JA00305)
- J. Chum, F. Jiricek, O. Santolik et al., Ann. Geophys. **24**, 2921 (2006)
- M.A. Clilverd, C.J. Rodger, R.J. Gamble et al., J. Geophys. Res. **113**, A04211 (2008). doi:[10.1029/2007JA012602](https://doi.org/10.1029/2007JA012602)
- T. Cussac et al., Planet. Space Sci. **54**, 413 (2006). doi:[10.1016/j.pss.2005.10.013](https://doi.org/10.1016/j.pss.2005.10.013)
- R.E. Ergun, C.W. Carlson, J.P. McFadden et al., Geophys. Res. Lett. **28**(19), 3805 (2001). doi:[10.1029/2001GL013024](https://doi.org/10.1029/2001GL013024)
- R.E. Ergun, C.W. Carlson, J.P. McFadden et al., Phys. Plasmas **10**(2), 454 (2003). doi:[10.1063/1.1530160](https://doi.org/10.1063/1.1530160)
- O.E. Ferencz, Cs. Ferencz, P. Steinbach et al., Ann. Geophys. **25**, 1103 (2007)
- M. Fullekrug et al. (eds.), *Sprites, Elves and Intense Lightning Discharges*. NATO Science Series, Mathematics, Physics and Chemistry (Springer, Berlin, 2006)
- D.N. Holden, C.P. Munson, J.C. Devenport, Geophys. Res. Lett. **22**, 889 (1995). doi:[10.1029/95GL00432](https://doi.org/10.1029/95GL00432)
- U.S. Inan, D. Piddyachiy, W.B. Peter et al., Geophys. Res. Lett. **34**, L07103 (2007). doi:[10.1029/2006GL029238](https://doi.org/10.1029/2006GL029238)
- A.R. Jacobson, S.O. Knox, R. Franz et al., Radio Sci. **34**, 337 (1999). doi:[10.1029/1998RS900043](https://doi.org/10.1029/1998RS900043)
- H.G. James, J. Geophys. Res. **81**(4), 501 (1976)
- M.C. Kelley, S.D. Baker, R.H. Holzworth et al., Geophys. Res. Lett. **24**(9), 1111 (1997). doi:[10.1029/97GL00991](https://doi.org/10.1029/97GL00991)
- C.-L. Kuo et al., Geophys. Res. Lett. **32**, L19103 (2005). doi:[10.1029/2005GL023389](https://doi.org/10.1029/2005GL023389)
- J.P. Lebreton et al., Planet. Space Sci. **54**, 472 (2006). doi:[10.1016/j.pss.2005.10.017](https://doi.org/10.1016/j.pss.2005.10.017)
- M.C. Lee, S.P. Kuo, J. Geophys. Res. **89**, 10,873 (1984). doi:[10.1029/JA089iA12p10873](https://doi.org/10.1029/JA089iA12p10873)
- C.P. Liao, J.P. Freidberg, M.C. Lee, J. Atmos. Terr. Phys. **51**(9/10), 751 (1989)
- H. Lonnqvist, M. Andre, L. Matson et al., J. Geophys. Res. **98**, 13565 (1993)
- O. Molchanov, A. Rozhnoi, M. Solovieva et al., Nat. Hazards Earth Syst. Sci. **6**, 745 (2006)
- A. Morioka et al., Ann. Geophys. **23**, 723 (2005)
- S.R. Mosier, D.A. Gurnett, J. Geophys. Res. **74**(24), 5675 (1969). doi:[10.1029/JA074i024p05675](https://doi.org/10.1029/JA074i024p05675)
- S.R. Mosier, J. Geophys. Res. **76**(7), 1713 (1971). doi:[10.1029/JA076i007p01713](https://doi.org/10.1029/JA076i007p01713)
- M. Parrot et al., Planet. Space Sci. **54**, 441 (2006). doi:[10.1016/j.pss.2005.10.015](https://doi.org/10.1016/j.pss.2005.10.015)
- R. Roussel-Dupré, E. Symbalisty, Y. Taranenko et al., J. Atmos. Sol. Terr. Phys. **60**(7/9), 917 (1998). doi:[10.1016/S1364-6826\(98\)00028-5](https://doi.org/10.1016/S1364-6826(98)00028-5)
- J.-A. Sauvaud et al., Planet. Space Sci. **54**(5), 502 (2006). doi:[10.1016/j.pss.2005.10.019](https://doi.org/10.1016/j.pss.2005.10.019)
- D.R. Shklyar, H. Washimi, J. Geophys. Res. **99**(A12), 23, 695 (1994)
- R.L. Smith, Nature **224**(5217), 351 (1969). doi:[10.1038/224351a0](https://doi.org/10.1038/224351a0)
- R.L. Smith, J.J. Angerami, J. Geophys. Res. **73**(1), 1 (1968). doi:[10.1029/JA073i001p00001](https://doi.org/10.1029/JA073i001p00001)
- A.J. Smith, D.L. Carpenter, J. Atmos. Terr. Phys. **44**(11), 973 (1982). doi:[10.1016/0021-9169\(82\)90062-9](https://doi.org/10.1016/0021-9169(82)90062-9)
- L.R.O. Storey, Philos. Trans. R. Soc. **246**, 113 (1953). doi:[10.1098/rsta.1953.0011](https://doi.org/10.1098/rsta.1953.0011)
- H.J. Strangeways, J. Atmos. Sol. Terr. Phys. **61**, 1067 (1999). doi:[10.1016/S1364-6826\(99\)00074-7](https://doi.org/10.1016/S1364-6826(99)00074-7)
- R.A. Treumann, Z. Klos, M. Parrot (2008, this issue)

On ULF Signatures of Lightning Discharges

T. Bösinger · S.L. Shalimov

Originally published in the journal Space Science Reviews, Volume 137, Nos 1–4.
DOI: [10.1007/s11214-008-9333-4](https://doi.org/10.1007/s11214-008-9333-4) © Springer Science+Business Media B.V. 2008

Abstract Recent works on magnetic signatures due to distant lightning discharges are reviewed. Emphasis is laid on magnetic signatures in the ULF range (in the old definition from less than 1 mHz up to 1 Hz), that is in the frequency range below the Schumann resonance. These signatures are known to be of importance for the excitation of the ionospheric Alfvén resonator (IAR) which works only at night time conditions. This emphasizes the difference between night and day time ULF signatures of lightning. The IAR forms a link between the atmosphere and magnetosphere. Similarities and differences of this link in the VLF (Trimp effect) and ULF range are worked out. A search for a unique signature of sprite-associated positive cloud-to-ground (${}^+\text{CG}$) lightning discharges ended with a negative result. In this context, however, a new model of lightning-associated induced mesospheric currents was built. Depending on mesospheric condition it can produce magnetic signatures in the entire frequency range from VLF, ELF to ULF. In the latter case it can explain signatures known as the Ultra Slow Tail of ${}^+\text{CG}$ lightning discharges. A current problem on the magnetic background noise intensity has been solved by taking more seriously the contribution of ${}^+\text{CG}$ lightning discharges to the overall background noise. Their low occurrence rate is more than compensated by their large and long lasting continuing currents. By superposed epoch analysis it could be shown that the ULF response to ${}^-\text{CG}$ is one to two orders smaller than in case of ${}^+\text{CG}$ with similar peak current values of the return stroke.

Keywords Lightning · Plasma · ULF magnetic fields · MHD · Cavity resonances · Atmospheric-magnetospheric coupling

T. Bösinger (✉)
Department of Physical Sciences, University of Oulu, Oulu, Finland
e-mail: tilmann.bosinger@oulu.fi

S.L. Shalimov
Institute of Physics of the Earth, Russian Academy of Sciences, Moscow, Russia
e-mail: pmsk5@mail.ru

S.L. Shalimov
e-mail: shalimov@ifz.ru

1 Introduction

This paper is not a strict review aiming at an overview on recent development in the given field. For this end more than some 15 pages of text were needed. Here we draw attention to some recent development in an—as we believe—apparently neglected area. It concerns observations in a frequency range above the geomagnetic pulsations regime but still below the Schumann resonance. Throughout this paper it is nevertheless tried to preserve the review character by adding a recent and extended list of references to all covered topics.

1.1 Main Stream

The Schumann resonance (SR) is undoubtedly an impressive phenomenon that has attracted theoreticians and experimentalists for more than half a century (for a recent review see Nickolaenko and Hayakawa 2002). The phenomenon is still the subject of ongoing research due to its high diagnostic potential in connection with space weather and space climate (Williams 2004; and references therein). This is demonstrated also in the present issue of Space Sci. Rev. (Simoes et al. 2008).

It is well known that electromagnetic emission from world-wide thunderstorm activity is responsible for the excitation of the Earth-Ionosphere Cavity (EIC) giving rise to the Schumann resonance with a fundamental frequency at 7.8 Hz. It can be observed in the electric as well magnetic field components on the ground, in the atmosphere and should be detectable even in the Earth's ionosphere due to wave energy leakage from the atmosphere to the ionosphere (Grimalsky et al. 2005). The global presence of the Schumann resonance is also reflected by the fact that it can be used in physics education, for instance, by building simple devices to measure the Schumann resonance either by magnetic or electric field sensors (e.g. <http://wavelab.homestead.com/Schumanns.html>). Since the fundamental frequency is rather low, around 8 Hz, that is not far from zero (!), one may wonder why it is interesting to look at magnetic signatures of lightning discharges still below this frequency. We would be dealing with the utmost low frequency end in the spectrum of electromagnetic emission from lightning discharges in spite of their power peak being located well in the VLF range (several kHz to tens of kHz).

1.2 Neglected Frequency Band

When dealing with geomagnetic pulsations one prefers to deal with periods instead of frequencies. The classic period range runs from 1 s up to 600 s (Jacobs et al. 1964). Flux gate pulsation magnetometers on the ground as well as on space probes usually sample with 1 or 2 Hz. Measurements in the ELF and VLF range are nowadays carried out with often fantastically high sampling rates, but the spectral analysis usually starts at 4 Hz and higher up (e.g. Füllekrug and Reising 1998). There is in fact a narrow frequency band between the upper end of geomagnetic pulsations and the lower end of ELF/VLF research that is regarded as being of little interest and for which few instrumental equipment and spectral analysis tools exist to function best in a frequency range between, say 1 and 8 Hz. The Finnish chain of pulsation magnetometers is the only extended network in Europe optimized just for measurements in this frequency range (<http://spaceweb.oulu.fi/projects/pulsations/>). It has been operating on a continuous basis since the early seventies of the last century. Most of the experimental work referred to below was carried out with data of this meridional chain of pulsation magnetometers.

1.3 Another Cavity Resonance

Ironically enough, just below the fundamental frequency of the SR another resonance frequency exist. As in the case of SR also this resonance is primarily excited by world-wide lightning activity. Only some 100 km above the EIC in the Earth's ionosphere there another cavity is formed. This cavity is bounded by a steep gradient of the Alfvén wave refractive index at the bottom (E-region) and top sides (upper F-region) of the ionosphere. If ionospheric conditions allow, the gradient at the top side may be so steep that the condition for the validity of geometric optics breaks down. In this case the top side ionosphere acts as a “reflecting” sphere for shear Alfvén waves (SAW) just as the bottom side does. A cavity is formed between the bottom and top sides of the ionosphere where SAW can get trapped. Standing waves may form and a resonance is set up. This cavity is referred to as the ionospheric Alfvén resonator (IAR). Depending on ionospheric conditions its fundamental frequency is varying between 0.1 and 2 Hz. Frequently many harmonics are simultaneously observed forming, the so-called spectral resonance structure (SRS, Belyaev et al. 1990). It can be observed in the electric and magnetic field components on the ground (e.g. Belyaev et al. 1990; Bösinger et al. 2002; Yahnić et al. 2003) and in the ionosphere (Grzesiak 2000; Hirano et al. 2005). The coupling between the Earth's atmosphere and ionosphere is due to mode conversion in the current-layer of the E-region: upwards from the EIC the electromagnetic TM wave mode to SAW mode in the ionosphere, and from the IAR downwards the SAW mode to TE wave mode in the EIC atmosphere (Belyaev et al. 1989, 1990).

The IAR represents a cavity resonance not only for large (perpendicular) scale SAW but also for short (perpendicular) scale kinetic Alfvén waves (KAW). These waves are excited by strong ionospheric convection E-fields and may lead to MHD turbulence such that the whole IAR forms a turbulence layer across the auroral region where the convection is strongest. Here we do not deal with this aspect of the IAR since KAW are not linked to atmospheric electricity and they cannot be observed on the ground due to their small perpendicular scale length (ionospheric screening). They play, however, an important role in substorm dynamics and in auroral acceleration processes. In Rother et al. (2007) references can be found to as well classic works as to information on most recent studies.

1.4 New Interest by the Discovery of Sprites

Besides the IAR, another phenomenon has recently increased the interest in the “neglected” frequency band. It is related to sprites and similar transient luminous events (TLE, see Mika and Haldoupis 2008). Since ground-based observations of sprites always require a clear sky and considerable instrumental investments, one was looking for related measurements, which could serve as a proxy for the appearance of sprites (e.g. Fukunishi et al. 1997). It seemed plausible that the magnetic signatures of positive cloud-to-ground (+CG) lightning discharges carry a unique signature related to sprites. Note that +CG are a necessary condition for the generation of sprites but only some 10% of +CG produce sprites (Sentman et al. 1995; Lyons 1996). The sprite itself is known to emit electromagnetic emission in the lower VLF range (Rodger 1999) and currents have been measured in the sprite columns as well (Cummer 2003).

1.5 Large ULF Magnetic Fields nearby Thunderstorm Centers

Transient ULF electric and magnetic fields following a lightning discharge were first addressed by Greifinger and Greifinger (1976). Since then much work has been done (e.g.

Cummer 2003; and references therein) on this phenomenon. Fraser-Smith (1993) could show that in the vicinity of thunderstorm centers (within a distance of up to 500 km) the background magnetic noise level in the ULF range increased by up to 50 times above the normal level (in the absence of magnetic activity). The near-by magnetic and electric fields in association with lightning can be really large and may form a hazard for sensitive instruments. In this paper we will not deal with observations in the vicinity of thunderstorm centers. The observational results reported here were all obtained in the far-field of lightning discharges (at distances of at least 2000 km). However, Fraser-Smith's question about the significance of ULF magnetic fields generated by electrical storms in view of geomagnetic pulsation generation still awaits a satisfying answer. We will briefly come back to this question at the end of this paper.

2 Observations

The Finnish chain of pulsation magnetometers has traditionally been used in geomagnetic pulsation and substorm studies. Its chain spanning nowadays from the magnetic equator to the polar cap has proved to be a unique tool also in thunderstorm related studies.

2.1 Day-Night Difference

Figure 1 shows a dynamic spectrum of one week of data obtained at the Island of Crete (Bösinger et al. 2002). The Crete station belongs to the Finnish chain. The abscissa of the

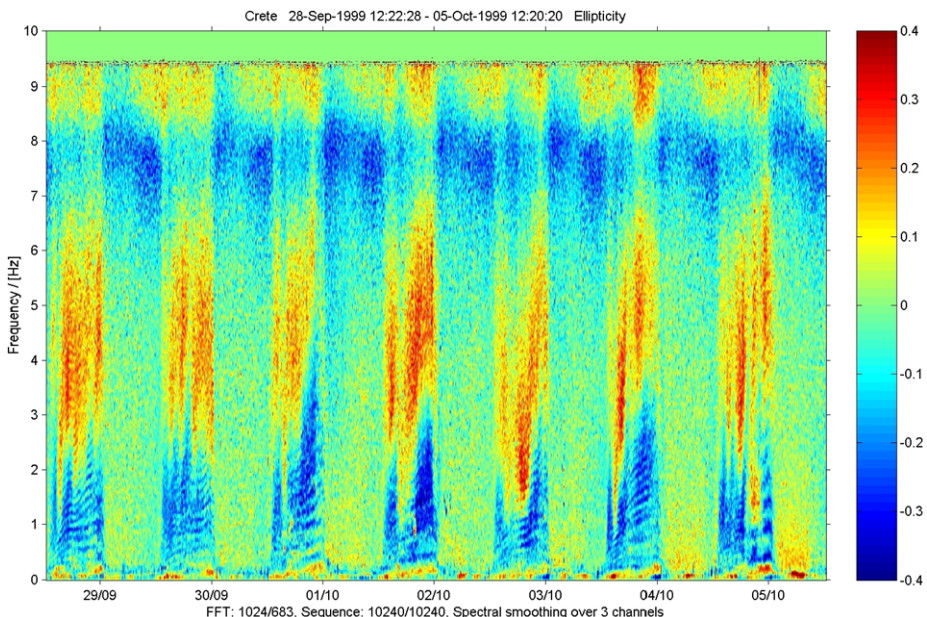


Fig. 1 A dynamic spectrum of magnetic background noise observed on the island of Crete from September 28th to October 5th, 1999. The quantity displayed as a function of frequency and time is the ellipticity ε of the magnetic background noise. This noise is primarily caused by world-wide lightning activity. Deep red of the color code corresponds to $\varepsilon = +0.4$ and deep blue to $\varepsilon = -0.4$. A linearly polarized wave is characterized by $\varepsilon = 0$ (green). The time tick marks indicate 04 LT (early morning) of the ongoing day. For a detailed discussion see the text

spectrum's coordinates displays time, the ordinate frequency. Note the SR as a continuous band around 8 Hz. The time tick marks are given at 04 LT of each day, indicating early morning. The quantity displayed in a color code is the ellipticity. It covers the range between +1 and -1. The value +1 stands for left-handed circularly polarized waves, the value -1 for right-handed circularly polarized waves. The zero-value indicates a linearly polarized wave. Uniformly yellow-greenish colored portions over frequency are observations covering day time. They start with early morning (tick marks) and finish at early evening. In the display the night time portions of the spectrum are highly structured over frequency. Between zero and about 2.5 Hz the background color is bluish. On top of it are equally distant, slightly ascending lines of light blue color. These are the set of multiple harmonics representing the spectral resonance structure (SRS) of the IAR. They are visible at any night, but the distances between adjacent lines are often different from one night to the other. The night time portions of the spectrum between about 2.5 Hz and 6 Hz exhibit strong red-brown quasi oscillatory bands with periods of several hours. These long period oscillations are most likely caused by the apparent propagation of thunderstorm centers around the globe. The spectrogram displays the polarization properties of the magnetic background noise. In this frequency range it is primarily caused by the global lightning activity. This figure demonstrates that the ULF response to distant lightning is totally different between day and night time (cf. Bösinger and Shalimov 2004). During day time the high solar ionization of the upper D- and lower E-region acts as a high conducting "metallic" upper boundary of the EIC. The atmosphere is totally screened from what is going on in the ionosphere. During night time, however, this screening sphere disappears and the atmosphere is open to the iono- and magnetosphere. During night time any ULF signal received on the Earth surface contains information not only from the primary source and the atmosphere (propagation effects; e.g. SR) but also from propagation and resonance effects (IAR) in the iono- and magnetosphere (Bösinger et al. 2004).

2.2 Coupling between Atmosphere, Ionosphere and Magnetosphere

The well known Trimp effect (Helliwell et al. 1973) is a manifestation of the coupling between the atmosphere, ionosphere, and magnetosphere operating in the VLF range: The lightning induced electromagnetic wave can propagate in the Earth's ionosphere and magnetosphere along magnetic field lines as a whistler wave mode. In the equatorial region of the magnetosphere the whistler wave may interact with energetic electrons of the radiation belt in an electron cyclotron wave particle interaction type of process. As a result the wave is amplified and energetic electrons (50 to 500 keV) are precipitated. This lightning induced electron precipitation or LEP starts with ~ 0.6 s delay with respect to the parent lightning flash due to the propagation time of the whistler wave from the ionosphere to the equatorial region and the time needed by the pitch-angle scattered particles to precipitate from the equatorial region to the ionosphere. The onset of the Trimp effect lasts typically 1 to 2 s and the recovery may last up to 100 s. The Trimp effect associated electron precipitation region (LEP) is widespread $\sim (1000 \times 500$ km) and at the northern hemisphere located some 100 to 300 km north of the location of the parent lightning flash due to magnetic field line guiding. The energetic electrons of LEP cause ionization in the upper D-region. It can be probed by scattering and damping effects of VLF radio waves crossing the precipitation region (Mika and Haldoupis 2008). Whistler wave observations in space by the Demeter satellite can be found in Parrot et al. (2008).

There exist far reaching analogues between electron-cyclotron and ion-cyclotron wave particle interactions in the Earth's magnetosphere but there are also distinct differences in the

corresponding scenarios. As in the case of the lightning induced whistler waves propagating along magnetic field lines, there exist also lightning induced SAW which propagate along magnetic field lines (i.e. IAR). Contrary to the case of lightning induced SAW, the whistler waves do not meet a resonator in the ionosphere and can freely continue their propagation from the ionosphere to the equatorial region in the magnetosphere where electron-cyclotron wave interactions may occur. The lightning induced SAW may in turn get trapped already in the ionosphere since the top side ionosphere functions as a sort of reflecting boundary (IAR). This boundary, depending on ionospheric conditions, is, however, not rigid and some leakage towards the magnetosphere occurs in any case. It is one item among others which determines the Q-factor of IAR. More important to note is that the IAR and the equatorial ion-cyclotron wave-particle interactions form a compound system of two coupled resonators as is witnessed in the so called Alfvén sweep maser (ASM), a basic concept of geomagnetic pulsation generation of the Pc 1 pearl type pulsations (Trakhtengerts et al. 2000). These pulsations play an important role in the ion budget of the ring current (Kozyra et al. 1997) and magnetospheric energy deposition as a whole. An evaluation of the importance of SAW energy concentration in the IAR is still missing having in mind that this energy originates in lightning activity of some 2000 thunderstorms all over the globe, at any time.

2.3 Types of Distant ULF-Response to Lightning Discharge

A survey on the ULF response at the Finnish chain at night time to well documented ${}^+CG$ lightning discharges (result of the *EuroSprite2003* campaign; Neubert et al. 2005; Bösinger et al. 2006) revealed two basic types of magnetic signatures: type I is a single, unipolar deflection from background level, a simple peak, so to speak, and type II is again a simple peak, however, with a subsequent asymptotic decay (often referred to as the “tail”) from the peak level to the zero line over time scales of several peak widths. As a frequent variation of these basic types the unipolar peaks are followed by some oscillations. A straightforward explanation for type I and II would be that there are ${}^+CG$ discharges with and without a continuing current. If this is true it has quite an impact on cloud electricity scenarios. If the ${}^+CG$ are necessarily associated with a continuing current then the absence of a tail might be a destructive interference effect of the electromagnetic wave in the EIC. In any case it seems that the observation of two types is a challenge for the interpreter.

An example of type 2 is shown in Fig. 2. It displays two orthogonal magnetic field components around the time of a ${}^+CG$ lightning discharge. The data has been corrected for the frequency and phase response of the instruments, and the coordinate system was rotated such that the response maximizes (in absolute terms) in one component (H-component). This was achieved by rotating the horizontal H-D plane of the Cartesian coordinate system (H, D, Z) around its vertical Z-axis by a suitable amount. In doing so the anticlockwise rotated, negative abscissa of the coordinate system (D-component) points into the direction of the source (${}^+CG$), as should be the case for a TM-mode. The oscillations are primarily Schumann resonances with some contributions possibly from IAR overhead the station. The peak width of 100 to 200 ms is of the order of the impulse response length of the magnetometer.

Note that there are world-wide on average about 60 lightning flashes per second. Only if the lightning flash is sufficiently big or if it occurs sufficiently close to the observation point individual signals are discernible from the background. The term Q-burst was created as a label for large Schumann resonance bursts (transients) which exceed the usual magnetic background noise to such an extent that they can be treated as single, individual events (e.g. Füllekrug and Fraser-Smith 1996; Füllekrug and Reising 1998). Figure 2 shows a typical Q-burst.

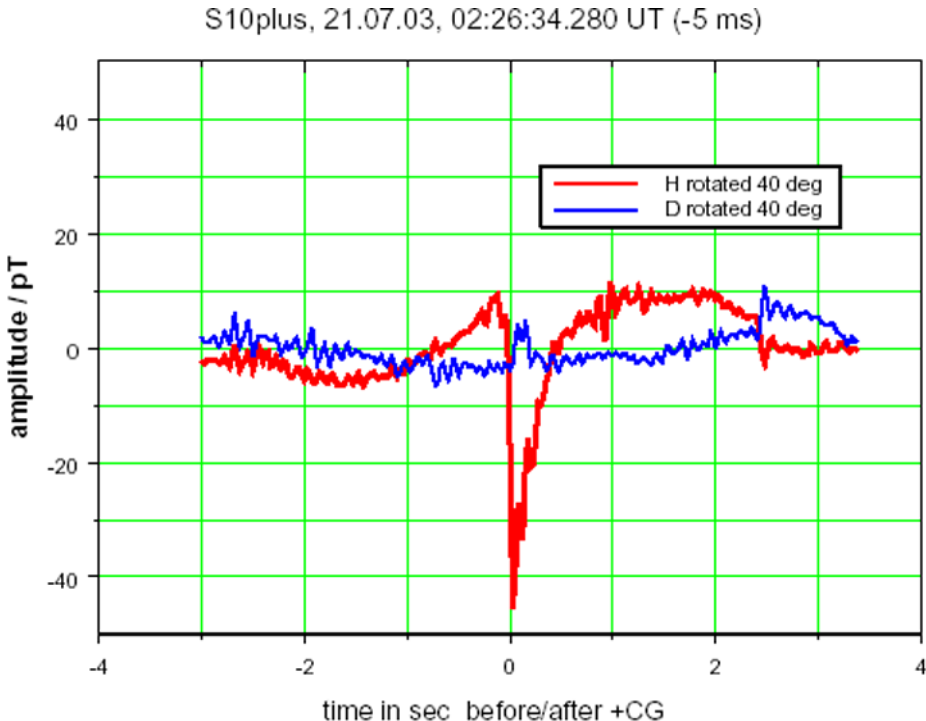


Fig. 2 The ULF response to a sprite-associated ${}^+\text{CG}$ lightning discharge observed in southern Finland at a distance of ~ 2000 km from the parent thunderstorm. The orthogonal coordinates of the horizontal disturbance vector were rotated such that the disturbance maximizes in one and minimizes in the other component for a direction finding triangulation process. S10plus stands for a running code in a lightning detection network list (Météorage). The time lag of -5 ms leads to the sprite observation

Little is known so far about the ULF response to intra-cloud (IC) flashes of lightning in spite of the fact that these flashes are much more frequent than cloud-to-ground lightning discharges. For an analysis one would need the exact coordinates, times, peak current values and flow direction, as well orientation of the discharge channel within the cloud. This kind of information is expected to be obtainable by the Japanese radio interferometer system under construction (Kawasaki 2008). Recently attention has been paid to intra-cloud lightning activity as a possible constituent for sprite generation (Ohkubo et al. 2005). Intra-cloud lightning activity is also witnessed by a new category of VLF perturbations observed in relation with sprites (Haldoupis et al. 2006).

2.4 The Weak ULF Response to ${}^-\text{CG}$ Discharges

Having studied the ULF response to hundreds of sprite and non-sprite associated ${}^+\text{CG}$ we were curious to check on the ULF response to ${}^-\text{CG}$. Since they are more frequent than ${}^+\text{CG}$ we had even a larger collection of well documented ${}^-\text{CG}$ from the EuroSprite2003 campaign at our disposal (courtesy of Météorage). It is known that ${}^-\text{CG}$ are characterized by smaller and shorter continuing currents (Jones 1970; Uman and Krider 1982; Uman 2001). So the ULF response is expected to be smaller than in case of ${}^+\text{CG}$ (Shalimov and Bösinger 2008). A quick survey from one event to another confirmed this expectation. We could verify that

the ULF response to ${}^-\text{CG}$ is one to two orders smaller than in case of ${}^+\text{CG}$ with similar peak current values of the return stroke (Shalimov and Bösinger 2008; their Fig. 3).

2.5 The Negative Answer

Everyone doing measurements in relation to sprites would have been more than happy to find a unique signature of sprite occurrence. Also we started our investigation on the ULF response to lightning discharges hoping for a revealing uniqueness in sprite-associated ${}^+\text{CG}$. Unfortunately we could not find it. The comparison did not reveal any unique and identifiable ULF signatures relating to sprites (Bösinger et al. 2006). The analysis resulted, however, in categorizing a collection of ULF responses to ${}^+\text{CG}$ (and actually also to ${}^-\text{CG}$), which has—to our knowledge—in a similarly systematic fashion not been compiled so far. Some of the items reported here are the outcome of this collection and subsequent investigations.

For our search of a unique signature of sprite-associated ${}^+\text{CG}$ it was essential to have enough certainty on the selection of non-sprite-associated ${}^+\text{CG}$ forming the control group. The interested reader is kindly referred to our original paper (Bösinger et al. 2006) where he or she can find a thorough discussion on this issue.

3 Theoretical Estimates and Models

3.1 The Ultra-Slow-Tail

The subsequent oscillation following the decay from the unipolar pulse in the ULF response to distant ${}^+\text{CG}$ (cf. Fig. 2) sometimes exhibits quasi periodic oscillations around one Hz lasting up to 6 s. They have been first reported by Fukunishi et al. (1997) and Füllekrug et al. (1998). In analogue to the slow-tail in VLF observations (e.g. Rodger 1999) Füllekrug et al. (1998) suggested the name “Ultra-Slow-Tail” (UST) to label it as an ULF phenomenon. Stimulated by the theoretical work of Sukhorukov et al. (1996) and Sukhorukov and Stubbe (1997), Füllekrug et al. (1998) attributed the oscillations to the overhead excitation of IAR by a sprite-associated ${}^+\text{CG}$ lightning discharge. No explanation was given how the information from the IAR overhead the lightning flash could be transferred to the distant point of UST observation. On one side propagation in the ionospheric wave guide (IWG) would imply time delays of several seconds (propagation speed of the fast magnetosonic wave typically around 500 km/s) and also considerable damping due to isotropic propagation from the source region. On the other side propagation in the EIC is not far reaching since the TE wave mode is evanescent in this frequency range. It is known that the SRS is portraying conditions of the local ionosphere overhead the observation point. This is because of SAW conversion takes place preferentially to TE-wave modes (see above).

Shalimov and Bösinger (2006) made a new approach to the UST problem by developing an entirely new model of induced currents in the upper mesosphere in connection with sprite-associated ${}^+\text{CG}$ lightning discharges. Its basic principles are sketched in Fig. 3. As a consequence of electrical breakdown in the mesosphere above the intense IC or CG discharges and/or their clusters a plasma column of enhanced ionization is formed (cf. Fig. 3). Subsequently, electromagnetic wave energy from ongoing thunderstorm activity (either by a strong quasi-electrostatic field or an intense electromagnetic pulse) penetrates (depending on ionization level) into this plasma column where it drives currents. The magnetic signatures of these induced currents can be observed over large distances. Characteristic for this scenario is that the induced currents penetrate into the plasma column in a diffusive

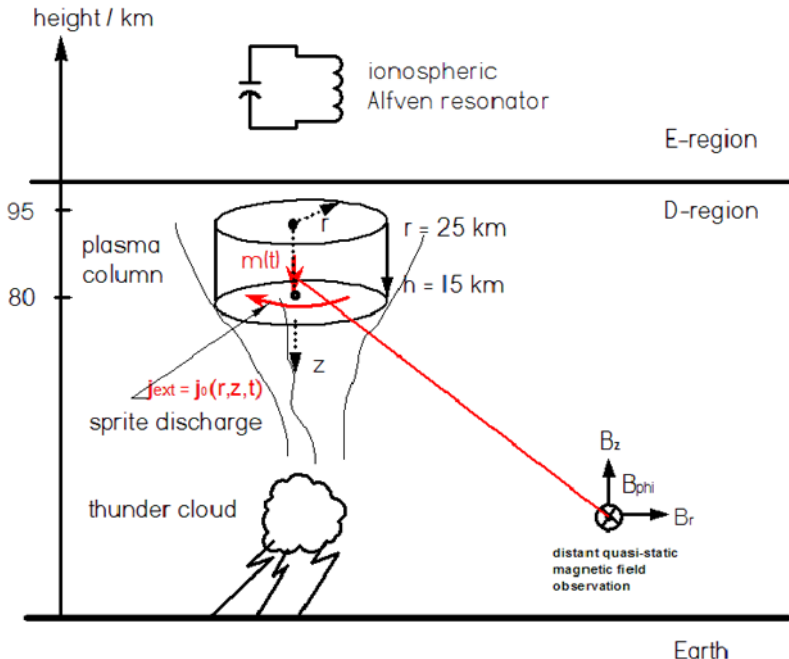


Fig. 3 The model: a plasma column in the mesosphere permeated by a driving (external) current induces secondary (oscillating) currents which are associated with a magnetic moment $m(t)$ which is observed remotely as a secondary magnetic field perturbation. The dimensions and given parameters represent typical values and may be subject to considerable variations. The ionospheric Alfvén resonator is symbolized by a R-C circuit. For details see text

type of wave, which is subject to eigen-oscillations. The observed quasi-periodic oscillations in the UST are witnessing these eigen-oscillations of the induced currents. The mathematical approach is classic, starting from Maxwell's equation, generalized Ohm's law and the gyrotrropic properties (Hall-current) of the magnetized plasma in the plasma column of finite width and height (cf. Fig. 3). The solutions are strongly governed by the high degree of symmetry and characterized by a diffusion time, eigen-frequencies, damping rate, and the magnetic field $B_r(r)$ at a distance r from the plasma column (for details see the original paper). Using typical mesospheric and plasma column parameters reported in the literature it was shown that in spite of the strong decay of magnetic field strength $B_r(r)$ with distance r , the magnetic signatures of the induced currents are observable with standard pulsation magnetometer over distances of up to 10,000 km. The best merit of this model is, however, to be seen that it works as well in the VLF as in the ULF range. Thus this model provides also an explanation to the slow tail in VLF observations (e.g. Rodger 1999, and references therein). It can also explain why the slow-tail in VLF observations is more frequently observed than the UST: Only in extreme cases of high ionization (in the plasma column) the quasi-periodic eigen-oscillations fall into the period range of some seconds that is the ULF range. Moreover, the model works also in the vicinity of the lightning discharge and is therefore in tune with the observations of large magnetic field signatures close to thunderstorm centers (e.g. Fraser-Smith 1993). A weakness of the model is that sometimes sprites themselves carry currents (Cummer 2003) which are not taken into account in our model. The best witness of currents in the sprite itself is ELF radiation. It is characterized by an upper limit of spectral power around 1 kHz (e.g. Cummer et al. 1998;

Cummer 2003, and references therein) thus the current rise and decay times are slow in comparison with those of the parent lightning return stroke, however, ULF radiation must come from transient currents with time constants still large compared to those of currents carried by sprites.

3.2 An Answer to a Current Problem on IAR Excitation

A problem discussed in the literature over the last \sim 5 years can be stated as follows: In the frequency range below SR ground observations exhibit more power in the magnetic background noise than is explained by world-wide lightning activity according to standard lightning discharge models (e.g. Fedorov et al. 2006; their Fig. 4). This finding is especially important in view of the excitation mechanism of IAR, and provoked researchers to look for alternative mechanisms of IAR excitation (Surkov et al. 2004, and references therein). In a recent work the authors “revisited” the classic model of IAR excitation by world-wide lightning activity taking into account the contribution by ${}^+CG$. In earlier works these have been regarded as negligible due to their low occurrence rate in comparison with negative cloud-to-ground (${}^-CG$) lightning discharges (for the pioneering work see Belyaev et al. 1989; specifically in this context see Surkov et al. 2004, 2005, 2006).

The sprite issue has recently increased enormously the interest in ${}^+CG$ and with the aid of new statistics on their occurrence rate and their continuing current properties (e.g. Lyons et al. 2003) the authors could show that the gap in the magnetic background noise intensity below SR can be filled by simply adding even distant ${}^+CG$ contributions to the overall noise intensity (Shalimov and Bösinger 2008). Thus there is not an absolute necessity to look for alternative excitation mechanisms of IAR. It does not mean that there may not operate other mechanisms such as already suggested and/or still to be found, especially in regions far from thunderstorm centers like in the polar cap. Also here IAR observations have been reported (Semenova et al. 2005, 2008).

3.3 Outlook

The near-field of ULF electromagnetic emissions from lightning discharges was only briefly mentioned here. It should, however, be stressed that the local resonances in the mesosphere and ionosphere above lightning discharges may have far reaching consequences in the entire complex of atmosphere-ionosphere-magnetosphere coupling especially in view of thousands of thunderstorms world-wide at any time. It would be nowadays possible to check on lightning induced energetic proton precipitation in analogy to LEP by means of the Far UltraViolet imager onboard the IMAGE spacecraft which provides a global display of proton precipitation regions detached form the main auroral oval (Mende et al. 2000). This method has been successfully applied to the detection of energetic proton precipitation in association with ion-cyclotron waves (Yahnin and Yahnina 2007; Yahnin et al. 2007).

The authors are not aware of any work related to the magnetic signatures of Trimpf effects but the large magnetic signatures, especially in the lowest ULF range, at distances within 500 km from the thunderstorm centers reported by Fraser-Smith (1993) may contain LEP induced magnetic variations. We pointed to the long period oscillations (periods of hours) in the night time ellipticity of magnetic background noise shown in Fig. 1. All this can tell is that a final evaluation of the significance of ULF magnetic fields generated by electrical storms still awaits realization. This is especially true for frequencies below the Schumann resonance.

Acknowledgements The authors thank ISSI for the invitation to the Workshop on “Planetary Atmospheric Electricity” in July 2007, and EuroPlanet for support. Our thanks go also to Torsten Neubert from the Danish National Space centre, leader of the European Union project, Coupling of Atmospheric Layer, for providing an integrated list of sprite and non-sprite associated $^+$ CG and $-$ CG events observed over Southern France during the EuroSprite2003 campaign. The Météorage data was made available by Stéphane Pédeboy of the Météorage Company. Data from the Finnish chain of pulsation magnetometers were kindly provided by the Sodankylä Geophysical Observatory. S.S. appreciated two exchange visits to the University of Oulu in autumn 2006 and summer 2007, financed by the Academy of Finland, which herewith is deeply acknowledged.

References

- P.P. Belyaev, S.V. Polyakov, V.O. Rapoport, V.Y. Trakhtengerts, *Radiofizika* **32**, 802–810 (1989)
- P.P. Belyaev, S.V. Polyakov, V.O. Rapoport, V.Y. Trakhtengerts, *J. Atm. Terr. Phys.* **52**, 781–789 (1990)
- T. Bösinger, S.L. Shalimov, *Ann. Geophys.* **22**, 1–12 (2004)
- T. Bösinger, C. Haldoupis, P.P. Belyaev et al., *J. Geophys. Res.* **107**(A10), 1281 (2002). doi:[10.1029/2001JA005076](https://doi.org/10.1029/2001JA005076)
- T. Bösinger, A.G. Demekhov, V.Y. Trakhtengerts, Ch. Haldoupis, A.A. Ostapenko, *Geophys. Res. Lett.* **31**, L18802 (2004). doi:[10.1029/2004GL020777](https://doi.org/10.1029/2004GL020777)
- T. Bösinger, A. Mika, S.L. Shalimov, C. Haldoupis, T. Neubert, *J. Geophys. Res.* **111**, A10310 (2006). doi:[10.1029/2006JA011887](https://doi.org/10.1029/2006JA011887)
- S.A. Cummer, *J. Atm. Sol.-Terr. Phys.* **65**, 499–508 (2003). doi:[10.1016/1364-6826\(02\)00318-8](https://doi.org/10.1016/1364-6826(02)00318-8)
- S.A. Cummer, U.S. Inan, T.F. Bell, C.P. Barrington-Leigh, *Geophys. Res. Lett.* **25**(8), 1281–1284 (1998). doi: [10.1029/98GL50937](https://doi.org/10.1029/98GL50937)
- E. Fedorov, A.J. Schekotov, O.A. Molchanov, M. Hayakawa, V.V. Surkov, V.A. Gladishev, *Phys. Chem. Earth* **31**, 462–468 (2006)
- A.C. Fraser-Smith, *Geophys. Res. Lett.* **20**, 467–470 (1993)
- M. Füllekrug, A.C. Fraser-Smith, *Geophys. Res. Lett.* **23**(20), 2773–2776 (1996). doi:[10.1029/96GL02612](https://doi.org/10.1029/96GL02612)
- M. Füllekrug, S.C. Reising, *Geophys. Res. Lett.* **25**(22), 4145–4148 (1998). doi:[10.1029/1998GL900133](https://doi.org/10.1029/1998GL900133)
- M. Füllekrug, A.C. Fraser-Smith, S.S. Reising, *Geophys. Res. Lett.* **25**, 3497–3500 (1998)
- Y. Fukunishi, Y. Takahashi, M. Sato et al., *Geophys. Res. Lett.* **24**, 2973–2976 (1997)
- C. Greifinger, P. Greifinger, *J. Geophys. Res.* **81**, 2237–2247 (1976)
- V. Grimalsky, S. Koshevaya, A. Kotsarenko, R. Perez Enriquez, *Ann. Geophys.* **23**, 2559–2564 (2005). SRef-ID: 1432-0576/ag/2005-23-2559
- M. Grzesiak, *Geophys. Res. Lett.* **27**(7), 923–926 (2000)
- C. Haldoupis, R.J. Steiner, A. Mika et al., *J. Geophys. Res.* **111**, A11321 (2006). doi:[10.1029/2006JA011960](https://doi.org/10.1029/2006JA011960)
- R.A. Helliwell, J.P. Katsufakis, M.L. Trimpi, *J. Geophys. Res.* **78**, 4679–4688 (1973)
- Y. Hirano, H. Fukunishi, R. Kataoka et al., *J. Geophys. Res.* **110**, A0728 (2005). doi:[10.1029/2003JA010329](https://doi.org/10.1029/2003JA010329)
- J.A. Jacobs, Y. Kato, S. Matsushita, V.A. Troitskaya, *J. Geophys. Res.* **69**, 180–184 (1964)
- D.L. Jones, *J. Atm. Terr.-Phys.* **32**, 1077–1093 (1970)
- Z.I. Kawasaki, *Space Sci. Rev.* (2008 this issue)
- J.U. Kozyra, V.K. Jordanova, R.B. Horne, R.M. Thorne, AGU monograph on magnetic storms, in *Geophysical Monograph 98* (AGU, Washington, 1997), pp. 187–202
- W.A. Lyons, *J. Geophys. Res.* **101**, 29641–29652 (1996). doi:[10.1029/96JD01866](https://doi.org/10.1029/96JD01866)
- W.A. Lyons, T. Nelson, E.R. Williams, S.A. Cummer, M.A. Stanley, *Mon. Weather Rev.* **131**, 2417–2427 (2003)
- S.B. Mende, H. Heetderks, H.U. Frey et al., *Space Sci. Rev.* **91**, 243–270 (2000)
- A. Mika, C. Haldoupis, *Space Sci. Rev.* (2008 this issue)
- T. Neubert, T.H. Allin, E. Blanc et al., *J. Atm. Sol.-Terr. Phys.* **67**, 807–820 (2005)
- A.P. Nickolaenko, M. Hayakawa (Kluwer Academic, Dordrecht, 2002)
- A. Ohkubo, H. Fukunishi, Y. Takahashi, T. Adachi, *Geophys. Res. Lett.* **32**, L04812 (2005). doi:[10.1029/2004GL021943](https://doi.org/10.1029/2004GL021943)
- M. Parrot, J.J. Berthelier, J.P. Lebreton, J.L. Rauch, R.A. Treumann, *Space Sci. Rev.* (2008 this issue)
- C.J. Rodger, *Rev. Geophys.* **37**, 317–336 (1999)
- M. Rother, K. Schlegel, H. Luehr, *Ann. Geophys.* **25**, 1603–1615 (2007). www.ann-geophys.net/25/1603/2007
- N.V. Semenova, A.G. Yahnnin, A.N. Vasiliev, S.P. Noskov, A.I. Voronin, in *Kola Sci. Cent.*, vol. 5 (Russ. Acad. of Sci., Apatity, 2005), pp. 120–131
- N.V. Semenova, A.G. Yahnnin, A.N. Vasiliev, O. Amm, *Geomagn. Aeron.*, N. 1 (2008 in press)

- D.D. Sentman, E.M. Wescott, D.L. Osborn, D.L. Hampton, M.J. Heavner, Geophys. Res. Lett. **22**(10), 1205–1208 (1995). doi:[10.1029/95GL00583](https://doi.org/10.1029/95GL00583)
- S.L. Shalimov, T. Bösinger, J. Atm. Sol.-Terr. Phys. **68**(7), 814–820 (2006). doi:[10.1016/j.jastp.2005.12.001](https://doi.org/10.1016/j.jastp.2005.12.001)
- S.L. Shalimov, T. Bösinger, J. Geophys. Res. **113**, A02303 (2008). doi:[10.1029/2007JA012614](https://doi.org/10.1029/2007JA012614)
- F. Simoes, N. Renno, I. Ueshima, M. Rycroft, Space Sci. Rev. (2008 this issue)
- A.I. Sukhorukov, E.A. Rudenchik, P. Stubbe, Geophys. Res. Lett. **23**, 2911–2919 (1996)
- A.I. Sukhorukov, P. Stubbe, Geophys. Res. Lett. **24**, 829–832 (1997)
- V.V. Surkov, O.A. Pokhotelov, M. Parrot, E.N. Fedorov, M. Hayakawa, Ann. Geophys. **22**, 2877–2889 (2004)
- V.V. Surkov, O.A. Molchanov, M. Hayakawa, E.N. Fedorov, J. Geophys. Res. **110**, A04308 (2005). doi:[10.1029/2004JA010850](https://doi.org/10.1029/2004JA010850)
- V.V. Surkov, M. Hayakawa, A.J. Schekotov, E.N. Fedorov, O.A. Molchanov, J. Geophys. Res. **111**, A01303 (2006). doi:[10.1029/2005JA011320](https://doi.org/10.1029/2005JA011320)
- V.Y. Trakhengerts, A.G. Demekhov, S.V. Polyakov, P.P. Belyaev, V.O. Rapoport, J. Atm. Sol.-Terr. Phys. **62**, 231–238 (2000)
- M.A. Uman, *The Lightning Discharge* (Dover, New York, 2001)
- M.A. Uman, E.P. Krider, IEEE Trans. EMC-24 **2**, 79–112 (1982). doi: [10.1109/TEMC.1982.304006](https://doi.org/10.1109/TEMC.1982.304006)
- A.G. Yahnnin, T.A. Yahnina, J. Atm. Sol.-Terr. Phys. **69**, 1690–1706 (2007). doi:[10.1016/j.jastp.2007.02.010](https://doi.org/10.1016/j.jastp.2007.02.010)
- A.G. Yahnnin, N.V. Semenova, A.A. Ostapenko et al., Ann. Geophys. **21**, 779–786 (2003)
- A.G. Yahnnin, T.A. Yahnina, H.U. Frey, J. Geophys. Res. **112**, A10223 (2007). doi:[10.1029/2007JA012501](https://doi.org/10.1029/2007JA012501)
- E.R. Williams, Lightning and climate: a review. J. Atm. Res. **76**(1–4), 272–287 (2004). doi:[10.1016/j.atmosres.2004.11.014](https://doi.org/10.1016/j.atmosres.2004.11.014)

Space Science Series of ISSI

1. R. von Steiger, R. Lallement and M.A. Lee (eds.): *The Heliosphere in the Local Interstellar Medium*. 1996 ISBN 0-7923-4320-4
2. B. Hultqvist and M. Øieroset (eds.): *Transport Across the Boundaries of the Magnetosphere*. 1997 ISBN 0-7923-4788-9
3. L.A. Fisk, J.R. Jokipii, G.M. Simnett, R. von Steiger and K.-P. Wenzel (eds.): *Cosmic Rays in the Heliosphere*. 1998 ISBN 0-7923-5069-3
4. N. Prantzos, M. Tosi and R. von Steiger (eds.): *Primordial Nuclei and Their Galactic Evolution*. 1998 ISBN 0-7923-5114-2
5. C. Fröhlich, M.C.E. Huber, S.K. Solanki and R. von Steiger (eds.): *Solar Composition and its Evolution – From Core to Corona*. 1998 ISBN 0-7923-5496-6
6. B. Hultqvist, M. Øieroset, Goetz Paschmann and R. Treumann (eds.): *Magnetospheric Plasma Sources and Losses*. 1999 ISBN 0-7923-5846-5
7. A. Balogh, J.T. Gosling, J.R. Jokipii, R. Kallenbach and H. Kunow (eds.): *Co-rotating Interaction Regions*. 1999 ISBN 0-7923-6080-X
8. K. Altwegg, P. Ehrenfreund, J. Geiss and W. Huebner (eds.): *Composition and Origin of Cometary Materials*. 1999 ISBN 0-7923-6154-7
9. W. Benz, R. Kallenbach and G.W. Lugmair (eds.): *From Dust to Terrestrial Planets*. 2000 ISBN 0-7923-6467-8
10. J.W. Bieber, E. Eroshenko, P. Evenson, E.O. Flückiger and R. Kallenbach (eds.): *Cosmic Rays and Earth*. 2000 ISBN 0-7923-6712-X
11. E. Friis-Christensen, C. Fröhlich, J.D. Haigh, M. Schüssler and R. von Steiger (eds.): *Solar Variability and Climate*. 2000 ISBN 0-7923-6741-3
12. R. Kallenbach, J. Geiss and W.K. Hartmann (eds.): *Chronology and Evolution of Mars*. 2001 ISBN 0-7923-7051-1
13. R. Diehl, E. Parizot, R. Kallenbach and R. von Steiger (eds.): *The Astrophysics of Galactic Cosmic Rays*. 2001 ISBN 0-7923-7051-1
14. Ph. Jetzer, K. Pretzl and R. von Steiger (eds.): *Matter in the Universe*. 2001 ISBN 1-4020-0666-7
15. G. Paschmann, S. Haaland and R. Treumann (eds.): *Auroral Plasma Physics*. 2002 ISBN 1-4020-0963-1
16. R. Kallenbach, T. Encrenaz, J. Geiss, K. Mauersberger, T.C. Owen and F. Robert (eds.): *Solar System History from Isotopic Signatures of Volatile Elements*. 2003 ISBN 1-4020-1177-6
17. G. Beutler, M.R. Drinkwater, R. Rummel and R. von Steiger (eds.): *Earth Gravity Field from Space – from Sensors to Earth Sciences*. 2003 ISBN 1-4020-1408-2
18. D. Winterhalter, M. Acuña and A. Zakharov (eds.): *"Mars" Magnetism and its Interaction with the Solar Wind*. 2004 ISBN 1-4020-2048-1
19. T. Encrenaz, R. Kallenbach, T.C. Owen and C. Sotin: *The Outer Planets and their Moons* ISBN 1-4020-3362-1
20. G. Paschmann, S.J. Schwartz, C.P. Escoubet and S. Haaland (eds.): *Outer Magnetospheric Boundaries: Cluster Results* ISBN 1-4020-3488-1
21. H. Kunow, N.U. Crooker, J.A. Linker, R. Schwenn and R. von Steiger (eds.): *Coronal Mass Ejections* ISBN 978-0-387-45086-5

22. D.N. Baker, B. Klecker, S.J. Schwartz, R. Schwenn and R. von Steiger (eds.): *Solar Dynamics and its Effects on the Heliosphere and Earth* ISBN 978-0-387-69531-0
23. Y. Calisesi, R.-M. Bonnet, L. Gray, J. Langen and M. Lockwood (eds.): *Solar Variability and Planetary Climates* ISBN 978-0-387-48339-9
24. K.E. Fishbaugh, P. Lognonné, F. Raulin, D.J. Des Marais, O. Koralev (eds.): *Geology and Habitability of Terrestrial Planets* ISBN 978-0-387-74287-8
25. O. Botta, J.L. Bada, J. Gomez-Elvira, E. Javaux, F. Selsis, R. Summons (eds.): *Strategies of Life Detection* ISBN 978-0-387-77515-9
26. A. Balogh, L. Ksanfomality, R. von Steiger (eds.): *Mercury* ISBN 978-0-387-77538-8
27. R. von Steiger, G. Gloeckler, G.M. Mason (eds.): *The Composition of Matter* ISBN 978-0-387-74183-3
30. F. Leblanc, K.L. Aplin, Y. Yair, R.G. Harrison, J.P. Lebreton and M. Blanc (eds.): *Planetary Atmospheric Electricity* ISBN 987-0-387-87663-4

Springer – Dordrecht / Boston / London